CHEMICAL RESEARCH, DEVELOPMENT & ENGINEERING CENTER

CRDEC-SP-024

PROCEEDINGS OF THE 1989 U.S. ARMY CHEMICAL RESEARCH, DEVELOPMENT AND ENGINEERING CENTER SCIENTIFIC CONFERENCE ON CHEMICAL DEFENSE RESEARCH 14-17 NOVEMBER 1989

Joseph D. Williams, Jr.

RESEARCH DIRECTORATE

August 1990

U.S. ARMY ARMAMENT MUNITIONS CHEMICAL COMMAND

Aberdeen Proving Ground, Maryland 21010-5423

DISCLAIMER

The findings in this report are not to be construed as an official Department of the Army position unless so designated by other authorizing documents.

DISTRIBUTION STATEMENT

Approved for public release; distribution is unlimited.

REPORT DOCUMENTATION PAGE

Form Approved
OMB No. 0704-0188

1. AGENCY USE ONLY (Leave blank)	2. REPORT DATE	3. REPORT TYPE AND DATES COVERED
	1990 August	Final, 89 Nov - 89 Nov

4. TITLE AND SUBTITLE
Proceedings of the 1989 U.S. Army Chemical Research, Development and Engineering Center Scientific Conference on Chemical Defense Research, 14-17 November 1989

5. FUNDING NUMBERS
PR-1L161102A71A

6. AUTHOR(S)
Prepared by Joseph D. Williams, Jr.

7. PERFORMING ORGANIZATION NAME(S) AND ADDRESS(ES)
CDR, CRDEC, ATTN: SMCCR-RS, APG, MD 21010-5423

8. PERFORMING ORGANIZATION REPORT NUMBER
CRDEC-SP-024

9. SPONSORING/MONITORING AGENCY NAME(S) AND ADDRESS(ES)

10. SPONSORING/MONITORING AGENCY REPORT NUMBER

11. SUPPLEMENTARY NOTES

12a. DISTRIBUTION/AVAILABILITY STATEMENT
Approved for public release; distribution is unlimited.

12b. DISTRIBUTION CODE

13. ABSTRACT (Maximum 200 words)

In this report, 113 papers presented at the 1989 Scientific Conference on chemical Defense Research are included under the heading of Decontamination, Detection, Protection, Computational Chemistry, Fluid Dynamics, Toxicology, Materials, Biotechnology, and Synthesis and Properties. In addition, papers are included for posters of each subject.

14. SUBJECT TERMS				15. NUMBER OF PAGES
Decontamination	Computational Fluid dynamics	Properties	Conference	1040
Biotechnology	Protection	Materials	Chemistry	16. PRICE CODE
Detection	Synthesis	Toxicology	Posters	

17. SECURITY CLASSIFICATION OF REPORT	18. SECURITY CLASSIFICATION OF THIS PAGE	19. SECURITY CLASSIFICATION OF ABSTRACT	20. LIMITATION OF ABSTRACT
UNCLASSIFIED	UNCLASSIFIED	UNCLASSIFIED	UL

BLANK

PREFACE

The 1989 U.S. Army Chemical Research, Development and Engineering Center Scientific Conference on Chemical Defense was held 14-17 November 1989 at the Edgewood Area of Aberdeen Proving Ground, Maryland. The Conference is held annually under the auspices of the Director of Research.

The Conference is an informal forum for scientific exchange and stimulation among investigators in the wide disciplines related to chemical defense research.

The participants develop some familiarity with U.S. Army basic research in chemical defense and also become personally acquainted with the other investigators and their research interests and capabilities. Each attendee is invited to talk on any aspect of a topic of interest and may make last-minute changes or alterations in his talk as the flow of ideas in the Conference develops.

The papers in these proceedings tend to correspond closely to what was presented at the Conference; however, there is not an exact correspondence.* The reader will find the items related to the Conference itself (the list of attendees, the agenda, and the contents of the Conferences' sessions) in the appendixes following the papers collected for these proceedings and the indexes pertaining to them.

Distribution of this document is limited to Conference attendees to reduce the risk of its unauthorized disclosure while providing a valuable exchange of unclassified information. The proceedings are not to be used as reference material for other persons or organizations. It is incumbent on the recipient to safeguard the contents, control the dissemination, and destroy properly in accordance with DoD 5200.22-M, Industrial Security Manual, Section II-19, or DoD 5200.1-R, Information Security Program Regulation, Chapter IX.

ACKNOWLEDGMENTS

The compiler of the proceedings acknowledges Patricia J. Reeves for her critical review of the compilation.

---

*In some instances, papers from the Conference are not included. The titles of the missing papers are listed on the first page of the applicable section.

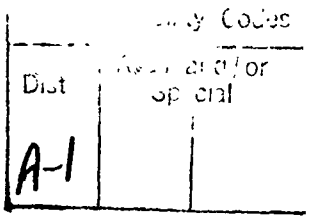

BLANK

CONTENTS

I. DECONTAMINATION

NOTE: Papers with the following titles were presented at the Conference but are not included in this document:

Biological Degradation of a Simulable Chemical Warfare Agent

Reaction of 2-Chloroethyl Methyl Sulfide with Phenolates and Thiophenolates, Mechanistic Dependence on Solvent and Nucleophile

The following paper presented at the Conference was received too late to be included in this section; it is contained in Appendix C.

Soman Detoxifying Enzyme from Escherichia Coli

BLANK

IMPROVEMENT OF THE "GERMAN EMULSION"

Stefan H. Hüttenhain*, Wolfgang Balzer, Ralf Feldmann
Fraunhofer-Institut für Umweltchemie und Ökotoxikologie
D-5948 Schmallenberg

Abstract. Our experience on the mechanism of the detoxification reaction in the "German Emulsion" allowed us to signifikantly decrease its active chlorine concentration. This was the essential prerequisite for using organic solvents other than chlorinated ones. Studies of the extraction potency of several common organic solvents revealed that they were not worse or even better as compared to perchloroethylene. Experiments on their stability against aqueous hypochlorite solution revealed most of them to be sufficiently stable.

Introduction. From the ecological point of view it is critical to expose large quantities of chlorinated hydrocarbon to nature - as will happen when using the original "German Emulsion". For that reason the replacement of perchloroethylene as organic phase of the detoxification emulsion was one of the major targets of the improvement. This research had presupposed the investigation of the structure of the emulsion (1, 2) and the reaction mechanism of the detoxification (3) which had been successfully completed.

Improvements from the ecological point of view should not, however, deteriorate the efficiency of the emulsion as a whole; the extraction potency of the future organic phase against S-Mustard - or a corresponding sulfide - from painted plates must be similar to that shown by perchloroethylene.

Material and methods; Material. The paint was obtained from the German Army Research Institut at Munster, and it was used to paint iron plates of 2 cm^2 size each (1,0 * 2,0). 2-chloroethylmethylsulfide was employed as S-Mustard simulator. The other chemicals used were obtained in analytical grade from Aldrich GmbH. The gaschromatographical analyses was performed with a Sigma 3B gas chromatograph (Bodenseewerk Perkin Elmer).

Defined contamination of painted plates. The painted plates were contaminated in accordance with the method described by Schoene et al (4) :

FIGURE 1

Apparatus for defined gasphase contamination of painted plates

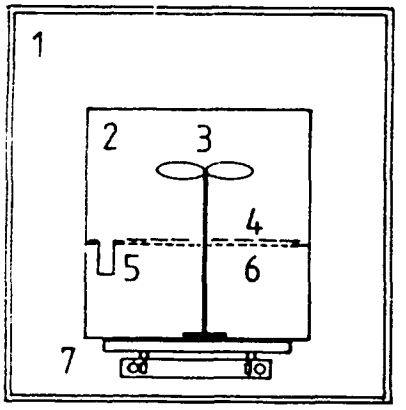

1. climated chamber
2. vapor container
3. ventilator
4. painted plates
5. reservoir
6. net
7. stirrer

In an exsiccator the plates were exposed to a saturated sulfide atmosphere for several hours. A small open flask was used as reservoir. A ventilator, driven externally by a magnetic stirrer, was used to ensure the homogenization of the gas phase, and thus a constant contamination was obtained. The complete apparatus was kept at a temperature of 30 °C in a climated chamber.

Extraction. In a sealed 10 ml test tube painted plates of 2 cm^2 size each were exposed to 3 ml of the solvent to be tested. The extraction was performed on a shaker over a certain period of time Δt (between 0 and 2 min) at room temperature. The remaining content of sulfide was extracted by exhaustive extraction with perchloroethylene; for this purpose the plates were left in 5 ml of this solvent for at least 2 hours.

The sulfide content of both phases was determined gaschromatographically; column: SE 54 Megabor capillary; carrier gas: helium, 20 ml/min; injector temperature: 180 °C; detector temperature: 250 °C; oven temperature: T_1 80 °C (0.5 min) ===> T_2 130 °C (0.8 min), ramp rate 30.0 °C/min; detector: FPD.

For each value 6 plates were extracted. By plotting %-residue in the plates versus Δ t the extraction kinetics were determined.

Stability against hypochlorite. The selected organic solvents were exposed to calciumhypochlorite solution (1 % w/w; about 60 % active chlorine)) to the degree that complied with the formulation of the emulsion.

This mixture was thoroughly stirred without emulsifier so that a pseudo-emulsion was obtained. The active chlorine content of the aqueous solution had been determined by means of jodometric titration at the beginning of the experiments. Now samples of the reaction mixture were taken at regular intervals, over a period of 5 hours or longer, and the active chlorine content was determined after phase separation. The decrease of the oxidizing agent is a measure for the reactivity of the solvent against hypochlorite.

Results and discussion; Stability of the painting. First of all preliminary experiments were carried out in order to investigate how long the painted plates resist to the used solvents without causing considerable damage.

TABLE 1

Stability of painting against selected solvents

Solvent	Stability of the painting	
Hexane Perchloro- ethylene Nitromethane	stable for several hours	
Toluene	paint	30 min
AcOEt	peeling	20 min
AcOMe	off	20 min
Dioxane	after	10 min
Tetrachloro-	approx.	10 min
methane		10 min
Acetone		10 min
DMF		< 10 min

As can be seen from the table, almost all common extraction agents cause damage to the paint, in the long run. But this aspect can be neglected because the extraction takes place much quicker in each case.

Extraction kinetics. The rest contamination of sulfide in the plate was plotted versus time of extraction. As expected, the logarithmic plot showed a linear curve. Apart from the rest contamination at a particular time, the extraction potency of the different solvents is clearly characterized in the ascent of this kinetic curve. It is evident that the extraction potency of all the tested solvents is not worse, or even better as compared to perchloroethylene.

FIGURE 2

Extraction kinetics: plots of the rest contamination versus time for several solvents

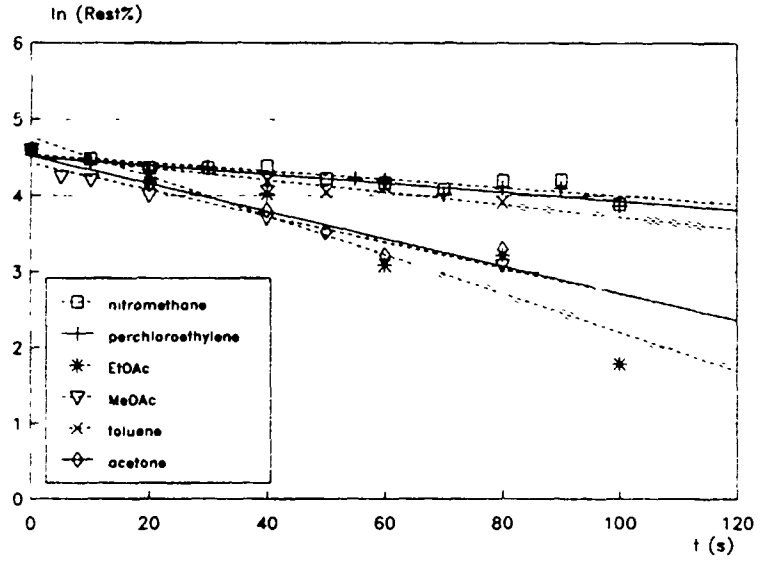

Contamination density and extraction. In view of the varying sorption of sulfide in the paint, the solvents were not tested at plates with identical degree of contamination. The question was whether the extraction is also a function of the total contamination density - i.e. whether the extraction from more contaminated plates is higher. In accordance with the procedure described above we carried out extractions with perchloroethylene as solvent, for 60 s, at plates that were contaminated to different degrees. The extracted amount showed a correlation to the total quantity of sulfide that was absorbed in the paint (Figure 3). The lower the contamination, the higher the extraction. However, a distinct effect was only

found up to approx. 750 µg/plate; as in our experiments the contamination exceeded 1000 µg/plate in all cases it could be neglected.

FIGURE 3

Plot of the extracted amount (%) of sulfide versus the total contamination

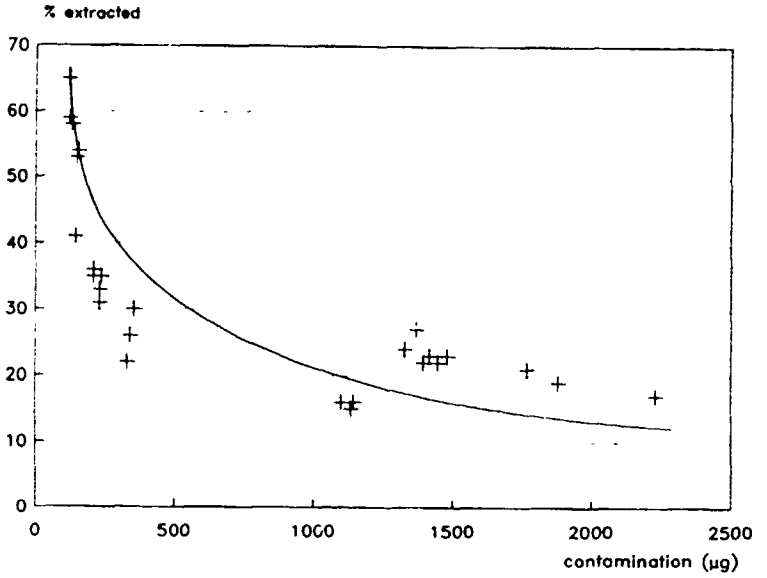

Stability against hypochlorite. Some selected common solvents including diesel as a mixture of aliphates and aromates, were tested for their stability against aqueous hypochlorite solution.

As expected the results showed that the more activated compounds were much stronger attacked. However, hydrocarbons can be used without problems, and there are no objections to the use of diesel or ethylacetate when used within their given limits of consumption.

FIGURE 4

Kinetics of the oxidation of several solvents with aqueous hypochlorite solution

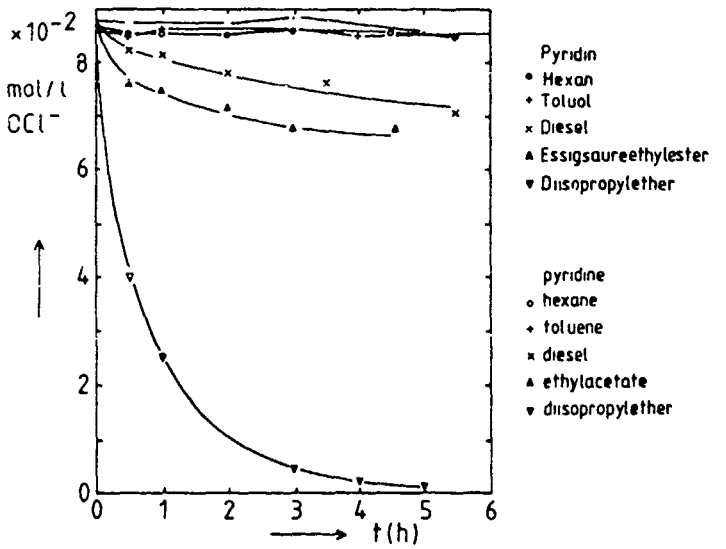

Conclusion. The experiments revealed that the tested solvents from different classes of chemicals are at least just as efficient as perchloroethylene in their extraction potency of sulfide from paint. It is essential for their application in the detoxification emulsion that they do not react at all - or only very little - with the hypochlorite solution.

REFERENCES

(1) K. Görgens; Die Entgiftungsemulsion; WWD Bericht Nr.93; 1986

(2) K. Görgens; Das Lösungsverhalten von Calciumhypochlorit in Entgiftungsemulsionen; WWD Bericht Nr.113; 1989

(3) S. H. Hütt nhain, W. Balzer; Zur Reaktionsweise der Entgiftungsemulsion; IUCT Forschungsbericht; 1988

(4) K. Schoene, H.-J. Bruckert, G. Schreiber, G. Wodtke; An experimental approach for assessing the risk of skin contact to materials containing S-mustard; FOA report C 40266-4.6,4.7 (supplement); 1989

Author of correspondence: *Dr. S.H. Hüttenhain;
Fraunhofer-Institut für Umweltchemie und Ökotoxikologie;
5948 Schmallenberg, West Germany

EFFECT OF REACTIVE INGREDIENTS IN DECONTAMINATION BY THE M280 KIT

J. Richard Ward

Linda L. Szafraniec

William T. Beaudry

Sheldon E. Day

Gintaras A. Dragunas

U.S. Army Chemical Research, Development and Engineering Center

Aberdeen Proving Ground, MD 21010-5423

ABSTRACT

The M280 kit for decontaminating individual equipment contains two packets which are used to wipe agent from contaminated gloves, boots, mask hood, and rifle. An earlier study showed the ingredients in packet I rapidly reacted with G agents while packet II rapidly detoxified HD; VX reacted slowly with the ingredients in either packet. The Army is interested in replacing packet I, so an extensive test program was performed at Dugway Proving Ground to compare the decon efficacy of two packet II vs standard decon procedure of packet I followed by a packet II.

An unintentional sidelight of this test is the opportunity to see what affect, if any, is afforded by placing reactive ingredients in materials for hasty decon. The test data confirmed that agent in all cases was removed (>98%) regardless of the order of packets. For G agents and for HD, there was a small but statistically significant difference when the packet with the reactive ingredient was first.

I. INTRODUCTION

The M280 Decontamination Kit, Individual Equipment (DKIE), was developed to provide the field soldier a capability for decontaminating his individual protective equipment and weapon. It is to be used for basic soldier skill decontamination to remove gross liquid contamination, reduce contact hazard, and help extend the wear life of individual protective items. The DKIE is not intended for complete decontamination. The M280 DKIE consists of twenty individual hard packages in a squad container. Each individual hard package contains two foil packets (I and II). Packet I contains a towelette prewetted with a liquid containing ethanol, water, phenol, and ammonia. Packet II contains a towelette impregnated with 1.36 grams (g) of chloramine-B and glass ampoules containing a solution of ethanol, water, and zinc chloride. The composition of each of these solutions is shown in Table 1.

Previous development and operational tests demonstrated that the kit effectively decontaminates surfaces contaminated with the standard agents G, V and H.[1] In these tests, the surfaces were monitored after decontamination with the kit to see if any residual agent remained. No attempt was made to determine if actual chemical reaction between the agents and the components of the DKIE were occurring or whether chemical reactivity influenced the degree of decontamination. In an earlier report, we established relative reaction rates of the agents with the solutions in packets I and II.[2] These results showed that packet I reacts rapidly with G agents, while packet II

reacts rapidly with HD. In this report we review results when decontamination tests are repeated with two packet II kits as well as packets I and II.[3] Such test data will enable us to see if changing ingredients in the M280 kit to increase chemical reactivity toward agents will enhance decontamination.

II. REACTIVITY OF AGENTS WITH PACKETS I AND II

The M280 Decontamination Kits, Individual Equipment (Contract DAAK11-84-C-0073, MFD 5-85, Lot No. MSA-1-2) were obtained from the Physical Protection Directorate. The solution from packet I was extracted from the prewetted towelette by squeezing it until ca.35 mls were obtained. This solution was used as is. A synthetic solution of packet II was prepared by adding 0.34 g of authentic chloramine-B to one of the four ampoules contained in packet II. This concentration was chosen based on the fact that each impregnated towelette packet II was known to contain a minimum of 1.36 g of chloramine-B.[2]

Because aging of the solution might decrease its effectiveness, fresh solutions were made immediately before preparation of all samples.

The ^{13}C and ^{31}P NMR spectra were recorded using a Varian XL-200 Super-conducting FTNMR System operating at 50 MHz for ^{13}C and 81 MHz for ^{31}P. In all cases, spectra were obtained unlocked at probe temperature, (ca 21^{o}C). External 85% phosphoric acid was used as the reference for the ^{31}P spectra and tetramethylsilane (TMS) in chloroform was used as the external reference for the ^{13}C spectra.

For each sample analyzed, data were accumulated for 4 minutes to 18 hours depending on the signal-to-noise level required or desired. All spectra were obtained using a pulse width of 3.5 usec (33°), an acquisition time of 1.6 sec and a pulse delay of 2.5 - 3.0 sec. A sweep width of 12 KHz was used for the ^{13}C spectra along with full proton (WALTZ) decoupling. For the ^{31}P spectra, a sweep width of 20 KHz and gated decoupling were used. All quantitative data were obtained by digital integration of the peak areas of interest.

A weighed amount of CASARM agent (GA, GB, HD or VX) was placed into a 5 mm O.D. Pyrex NMR tube and 1.0 ml of the decontaminating solution was added. The tube was capped, wrapped with Parafilm and shaken to ensure complete dissolution of the agent. Spectra were taken periodically to monitor the decomposition process and to identify the products. Samples were stored at room temperature (20°C $\pm$ 2°). The initial concentration of the agent was 0.01M for the nerve agents and 0.1M for HD.

Table 3 summarizes the results for the agent reactions with the ingredients in each of the two packets. G agents react rapidly in the solution from packet I while HD is deconned by the ingredients from packet II. Hence, if chemical reactivity contributes to decontamination, two packet II should augment HD decontamination and degrade GB decontamination when compared to the standard decon procedure.

Table 4 summarizes the data from the reaction between GB and packet I solution. As the data shows, GB is rapidly neutralized by simultaneous nucleophilic attac' ' phenoxide, ethoxide, and hydroxide to form the three products indicated. We presume that the reactions occur in parallel, since the three products are relatively stable, and all are observed in the first spectrum.

In packet II the mustard reacts with chloramine-B to form the sulfoxide and the sulfimide: [4]

$$R^1R^2S + ArSO_2NCl^-Na^+ \xrightarrow{H_2O} \begin{matrix} R^1R^2SNSO_2Ar + Na^+Cl^- \\ R^1R^2SO + ArSO_2NH_2 + Na^+Cl^- \end{matrix} \quad (1)$$

The ratio of the sulfoxide to sulfimide depends on the relative amount of water to ethanol and the nature of the R-group.[5]

III. FULL SCALE TESTING WITH PACKET I AND II VS TWO PACKET II

Testing was performed at DPG on the items that the DKIE would be required to decontaminate in the field. These items were:

a) The chemical protective gloves.

b) The chemical protective overboots.

c) The hood for the protective mask and areas of the mask not covered by the hood, and

d) A rifle

Contamination and decontamination of the test items were performed in the same manner as was done during IPT.[1] Sequence of decontamination was gloves, boots, gloves, mask/hood, gloves, rifle, and gloves. This process was followed to minimize the transfer of agent from one item to the next. Testing was performed with thickened GD (TGD), HD, and VX. Contamination density was 2.5 g/m^2 for all trials. Eight replicates were run for packet I-packet II and for two packet II. For GB and HD, residual agent after decontamination was estimated by bubbling the items for twelve hours. Less volatile VX was estimated by measuring the amount of agent transferred by surface contact onto silicone rubber.[1,3]

Tables 4 and 5 collect pertinent data for thickened GD (TGD) decontamination and for HD decontamination. The results for the boot covers, hood, and protective gloves were collected together as elastomeric materials.

Table 6 converts results in Tables 4 and 5 into percent aget deconned. A two way analysis of variance was performed as well[3] to see if there were a statistically significant difference between packet I and II vs two packet II decon.

For elastomeric materials either decon procedure removed over 99% agent. For both HD and TGD there was a small, but statistically significant, improvement when the packet with reactive ingredients was used first. For the rifle, results were different in that there was no statistically significant difference between packets, although over 99% of the agent was removed regardless of the order of the packets.

It would appear, then, for hasty decon using the M280 DKIE, that decon is accomplished almost exclusively by physical removal. Addition of ingredients which are known to react rapidly with the agent enhances decontamination of elastomers. However, the augmented decontamination constitutes only one percent of the total agent originally present.

VX has such a low vapor pressure that decontamination was measured by means of surface contact. Since VX reacts slowly if at all, with either packet, we would expect that decontamination would be equally good regardless of order. The results confirm that there was no statistically significant difference with either elastomers or the rifle.[3]

These results confirming that the M280 DKIE primarily decons by physical removal are consistent with a recent similar study by McMahon and Wilkinson[6] from Calspan who evaluated the effectiveness of the M280 kit to decon the same military equipment. These authors found that over 99% of TGD or HD was removed using packet I followed by packet II.

It also appears that hasty decon by itself will not reduce the contamination level in this test below where one would unmask[7]. Hence, any increase in decon effectiveness will contribute to lowering the hazard from agent contamination, thus reactive ingredients should be incorporated into decontaminants for individual equipment.

ACKNOWLEDGEMENT

The authors wish to thank L. Sturdivan and R. Crosier of CRDEC for results of the analysis of variance.

CONCLUSION

Hasty decontamination of individual equipment with the M280 DKIE removes over 98% of agent regardless of the order of using the packets. When the packet containing ingredients which react rapidly with the agent is used first, there is a slight but statistically significant increase in the amount of agent removed.

REFERENCES

1. J.A. Hazelka, "Initial Production Test, M280 DKIE," Dugway Proving Ground Technical Report, DPG-FR-88-303, June 1989.

2. L.L. Szafraniec, W.T. Beaudry, D.K. Rohrbaugh, and J.R. Ward, "Stoichiometry of Reaction of GA, GB, VX, and HD in Mixed Aqueous Solution," Proceedings of the 1988 Chemical Defense Research Conference, CRDEC-SP-013, August 1989.

3. Sheldon E. Day, et. al. "Report of the Activities of the CAM/M280 Task Force," CRDEC-TN-007, May 1989.

4. F. Ruff and A. Kucsman, "Mechanism of the Reaction of Sulfinides with N-Chloroarenesulfonamides," J. Chem. Soc. Perkin II, 1975, 509.

5. M.M. Campbell and G. Johnson, "Chloramine T and Related N-Halogeno-N-metallo Reagents," Chem Rev., 78, 65 (1978).

6. T.M. McMahon and E.P. Wilkinson, "Study of the Decontamination Kit, Individual Equipment: M280," CRDEC-CR-88081, July 1988.

7. H.R. Carlon, "Compendium of Hazard Definition Data for Chemical Agents GA, GB, GD, GF, HD, HT, and VX, Including Selected Bibliography," CRDEC-SP-88023, August 1988.

Table 1

Composition of the Solutions in the M280 Packets

Component	Weight %
Packet I	
Ethanol	72 ± 2
Phenol	10.0 ± 0.5
Sodium hydroxide	5.0 ± 0.5
Ammonia	0.2 ± 0.05
Water	12.8
Packet II	
Ethanol	45 ± 2
Zinc chloride	5 ± 0.5
Water	50

Table 2

First - Order Rate Coefficients
for Solvolysis of Agents in M280 Chemicals[a]

	PACKET I		PACKET II[b]	
AGENT	k, hr^{-1}	$t_{1/2}$, hr	k, hr^{-1}	$t_{1/2}$, hr
GA	FAST	--	0.3 ± 0.02	2.3
GB	FAST	--	0.4 ± 0.1	1.8
HD	0.06 ± 0.003	12	FAST	--
VX	0.083 ± 0.003	9	0.01 ± 0.003	70.0

[a] Concentration of agent ~0.02M

[b] Apparent first order rate coefficients to illustrate relative reactivity

Table 3

Decontamination of GB[a] in Packet I Solution, Mole Percent

Chemical Shift (ppm)[b]

TIME	δ 28.7	δ 31.8	δ 24.6
2-4 min[c]	76.1	12.6	11.3
15 min	74.2	13.1	12.7
24 hours	48.1	23.2	28.7

[a] 7.0 mg GB in 1 ml of solution (0.05M)

[b] Tentative Assignments:

δ 24.6 Isopropyl Methylphosphonic Acid
δ 28.7 Isopropyl Phenyl Methylphosphonate
δ 31.8 Ethyl Isopropyl Methylphosphonate

[c] No GB was observed in first spectrum

Table 4

Summary of Data Obtained on HD Using Packet I Wipe Followed by Packet II Wipe and Two Packet II Wipes

Trial	Packets	Amount of Agent Recovered, mg	
		Elastomers[a]	Rifle[b]
1	I & II	20.10	16.16
2	I & II	11.47	16.67
3	2 IIs	1.78	13.46
4	I & II	15.76	5.31
5	2 IIs	0.73	5.64
6	I & II	20.15	13.89
7	2 IIs	2.05	5.64
8	2 IIs	1.48	8.69
9	2 IIs	1.99	10.79
10	I & II	27.42	3.21
11	2 IIs	0.57	2.24
12	2 IIs	3.32	2.74
13	I & II	11.97	5.91
14	2 IIs	1.99	2.33
15	I & II	8.28	7.20
16	I & II	13.55	8.23

a 2,215 mg HD initially applied to elastomeric materials

b 370 mg HD initially applied to rifle

Table 5

Summary of Data Obtained on TGD Using Packet I Wipe Followed by Packet II Wipe and Two Packet II Wipes

Trial	Packets	Amount of Agent Recovered, mg	
		Elastomers[a]	Rifle[b]
1	I & II	3.64	0.20
2	2 IIs	17.14	2.67
3	2 IIs	1.43	0.31
4	I & II	1.28	0.95
5	2 IIs	6.47	3.01
6	2 IIs	4.47	8.05
7	I & II	3.14	1.77
8	2 IIs	3.74	4.69
9	2 IIs	3.30	3.38
10	2 IIs	5.94	1.46
11	I & II	2.37	0.76
12	I & II	3.31	0.77
13	I & II	0.67	3.39
14	I & II	0.60	3.63
15	2 IIs	4.81	0.96
16	I & II	0.95	9.59

a 2,125 mg of TGD initially applied

b 370 mg of TGD initially applied

Table 6

Percent Agent Removed by Two Different

Combinations of the M280 Kit

Packet	Mean Agent Recovered, mg		Percent Deconned	
		ELASTOMERS[a]		
	TGD	HD	TGD	HD
I & II	2.0 ± 1.2	16.2 ± 6.2	99.9	99.2
II & II	4.3 ± 1.7	1.7 ± 0.9	99.8	99.9
		RIFLE[b]		
I & II	1.6 ± 1.4	9.6 ± 5.2	99.6	97.4
II & II	3.1 ± 2.5	6.4 ± 4.2	99.2	98.3

[a] 2,125 mg agent initially applied; error is sample standard deviation.

[b] 370 mg agent initially applied; error is sample standard deviation.

DECONTAMINATION OF SOMAN IN FREON MIXTURES

William C. Johnson
Kenneth R. Collins
J. Richard Ward
James A. Richmond

U.S. Army Chemical Research, Development and Engineering Center
Aberdeen Proving Ground, MD 21010-5423

ABSTRACT

Freon solubilizes hydrophobic chemical warfare agents, such as soman, without damaging sensitive electronic equipment, such as night-vision goggles or communication equipment. Freon is used in this manner in the Non-Aqueous Equipment Decontaminating System (NAEDS) under development at CRDEC. The contaminated freon is returned to a still after which it is distilled through an aqueous layer containing bleach to decontaminate the residual agent.

This article describes results of experiments to measure how effectively agent is destroyed in the NAEDS. It is shown that residual agent is still left in the redistilled freon, and there is little difference whether the active decontaminant is removed from the aqueous layer. A mixture was prepared consisting of a 1:1:1 mixture of ethanol, 8 m sodium hydroxide, and freon. It was demonstrated that the use of this mixture in the NAEDS would destroy all agent and that the redistilled freon was free of soman.

I. INTRODUCTION

The U.S. Army has recognized a need for an effective method of decontaminating avionics and other electronics without degradation to such equipment. The fact that trichlorotrifluoroethane (FC-113) is electrically nonconductive, compatible with electronic components, and is used as a cleaning solvent suggests the use of it for the removal of chemical contaminants from military equipment. Several types of commercially available recycling systems which use fluorocarbon solvents are manufactured for the removal of nuclear contaminants from a wide range of equipment.

The nuclear industry uses closed-loop recycling systems with flourocarbon solvents for the removal of contaminants from equipment. These systems use filtration for the removal of the particulate contaminants from the solvent and distillation for the removal of fluxes, oils, and greases. The systems offer rapid one-cycle decontamination requiring only electrical support. The hardware comes in a variety of configurations to accommodate the different types of equipment requiring nuclear decontamination. One such type system

is a tool and parts cleaner, which is constructed in a glovebox configuration. This device makes use of pressurized fluorocarbon applied by a hand held spray gun for removal of the contaminants. A modification to this system for the removal of chemical contaminants was fabricated for evaluation as a non-aqueous equipment decontamination system (NAEDS). This prototype chemical decontamination system collects the contaminated solvent in a still tank. The still tank contains an aqueous solution (10% NaOH, 1% HTH) through which the contaminated solvent is distilled.

An evaluation was undertaken to demonstrate the feasibility of a fluorocarbon wash decontamination concept. To accomplish this, the evaluation was subdivided into three objectives. The first objective was to prove that the solvent, FC-113, was capable of solubilizing the chemical agents and removing them from various substrates. The second objective was to prove that through distillation and filtration, contaminants can be removed from the solvent. The third goal was to demonstrate a prototype system which could be used to decontaminate a variety of equipment with minimal effort.

This article will focus on the results of the laboratory distillation experiments and a brief feasibility study to improve the decontamination of soman in the freon.

2. DISTILLATION OF FREON FROM AGENTS

The distillation studies were conducted with chemical agents HD, GB, and VX. All of the experiments were simple distillations from which three fractions of distillate were collected from each test. Each fraction was analyzed by gas chromatography for the presence of the solute. The first group of distillations was performed with 50 ml of FC-113 and three different concentrations of GB or VX. The second group of distillations was performed with 250 ml of FC-113 and three different concentrations of HD. The concentration of the remaining solvent/solute in the distillation flask was analyzed by gas chromatography after the distillation fractions were collected. The third group of distillations were performed with 200 ml of FC-113, 200 ml of NaOH/bleach, and three different concentrations of HD. Table 1 lists pertinent physical properties of freon-113 and the agents with data from references 1 and 2.

The results of the simple distillation experiments (Tables 2-5) indicated that simple distillation would significantly reduce the concentration of the chemical agents in FC-113, but as expected, would not totally remove these contaminants from the solvent. The addition of aqueous neutralizer into the distillation flask containing HD and FC-113 did little to further reduce the concentrations of HD found in the distillate. Based on these results, it was concluded that a recycling system based on distillation of the solvent was feasible, but an additional means of treating the solvent would be required to totally remove chemical contaminants from FC-113.

Table 1

Pertinent Physical Properties for Freon-113

and Chemical Agents

	MW, g/mole	b.p., °C	P, g/ml	P, torr, 25°C
freon-113[a]	187.5	48	1.57	334
sarin[b]	140.1	158	1.09	2.9
mustard[b]	159.1	217	1.27	0.11
soman[b]	182.2	198	1.022	0.40
VX[b]	267.4	298	1.008	0.0007

[a] Ref 1

[b] Ref 2

Table 2

Removal of GB from Freon 113

SAMPLE	Vol, ml	[GB], ug/ml
FLASK (INITIAL)	50.0	108.0
FRACTION 1	8.7	41.6
FRACTION 2	8.2	44.8
FRACTION 3	3.5	153.1
FLASK (INITIAL)	50.0	54.0
FRACTION 1	4.8	12.9
FRACTION 2	12.2	16.8
FRACTION 3	7.4	28.5
FLASK (INITIAL)	50.0	10.8
FRACTION 1	9.2	0.4
FRACTION 2	6.6	1.3
FRACTION 3	3.8	3.6

Table 3

Removal of VX from Freon 113

SAMPLE	Vol, ml	[VX], ug/ml
FLASK (INITIAL)	50.0	1,169
FRACTION 1	10.4	6.2
FRACTION 2	8.2	18.5
FRACTION 3	9.4	33.0
FLASK (INITIAL)	50.0	584
FRACTION 1	9.4	5.6
FRACTION 2	7.6	10.4
FRACTION 3	7.9	43.6

Table 4

Removal of HD from Freon 113

SAMPLE	Vol, ml	[HD], ug/ml
FLASK (INITIAL)	250	1,004
FRACTION 1	64	12.1
FRACTION 2	74	43.5
FRACTION 3	63	205.9
FLASK (INITIAL)	250	500
FRACTION 1	60	1.4
FRACTION 2	80	4.5
FRACTION 3	58	37.0
FLASK (INITIAL)	250	100
FRACTION 1	76	2.6
FRACTION 2	42	3.0
FRACTION 3	45	5.1

Table 5

Removal of HD from Freon 113 and Aqueous Caustic-Bleach Mixture

SAMPLE	VOL, ml	[HD], ug/ml
FLASK (INITIAL)	200	990
FRACTION 1	46	8.0
FRACTION 2	48	8.1
FRACTION 3	50	15.0
FLASK (FINAL)		7,174
FLASK (INITIAL)	200	495
FRACTION 1	46	4.2
FRACTION 2	56	4.9
FRACTION 3	40	11.5
FLASK (FINAL)		2,915

Table 6

Removal of Soman from Freon 113 and Water Mixture[a]

	Vol, ml	GD, mg[b]	Vol, ml	GD mg[c]
FRACTION 1	49	0.11	40	0.22
FRACTION 2	58	.11	38	.12
FRACTION 3	56	.07	48	.26

[a] Initial GD concentration is 200 mg in 200 ml of freon mixed with 200 ml water

[b] 10% sodium hydroxide and 1% HTH solution

[c] water only

More recently we redid the distillation experiment with soman in the presence of the aqueous layer.[3] In one run, the sodium hydroxide-bleach solution was replaced with water. These results are summarized in Table 6 in which it shows that the majority of soman is decontaminated by the sodium hydroxide-bleach in contrast with mustard. Nonetheless, measureable quantities of soman still are present in the initial fractions of distilled freon.

Recently we were asked by the Physical Protection Directorate to relook at the freon decontamination system since development tests found that bleach was corroding metal parts in the NAEDS. We also used this opportunity to test ways to completely detoxify the agent in the current system design. One approach is to use alcohol as an extender to increase the concentration of caustic in the freon. In the current Army decontaminating solution, DS-2, the methylcellosolve acts as the extender to dissolve sodium hydroxide, which is virtually insoluble in diethylenetriamine (DETA).[4]

In order to screen some freon-alcohol-caustic mixtures, we estimated the amount of caustic in the freon by titration with hydrochloric acid. Such a procedure is similar to ASTM Test Method D-974, used to estimate acidity of oil samples, such as vacuum pump oils.[5]

Screening tests were performed with 3 ml each of freon, 8 m sodium hydroxide, and alcohol. It was found that ethanol transferred the greatest amount of sodium hydroxide to the freon. Further, by adjusting the relative amounts of freon/alcohol/base, either a multi-phase system or a solution could be concocted. Since one presumably wants freon to dissolve the agent on the contaminated electronic equipment, the multi-phase, freon-alcohol-caustic mixture was tested.

One hundred thirty-five ml of solution containing one mg of GD per ml of freon were added to 270 ml of a 1:1 mixture of ethanol and an 8 molal solution of sodium hydroxide contained in a 500 ml distillation flask and heated for sample collection.

Samples were collected at the time period and temperatures as indicated in the table below:

Fraction Number	Temperature (°C)	Time (Min)	Volume (ml)
1	42	3	36
2	42	4	40
3	43-44	4	31
4	44-47	4.5	26

Chromatographic analysis using a Flame Photometric Detector and capillary columns showed that trace amounts of GD (concentrations less than 0.3 ug/ml) were not detected in these samples. The first fraction showed a small peak having a high retention time and temperature that would be indicative of a phosphate heavier than GD. The second and third fractions showed several phosphate decomposition products but none at the retention time expected for GD. Although this system is far from optimized, this is the first time that an agent was deconned in the NAEDS system.

Any future work in the NAEDS system will be predicated on finding an alternative for the FC-113. When the replacement is identified and testing starts, it is recommended that efforts to improve deconability be addressed from the beginning. It is our view that the bleach can be removed from the solution since it seems ineffective toward mustard anyway. Any decon taking place in the present system is likely due to the caustic.

REFERENCES

1. Material Safety Data Sheet, E.I du Pont de Nemours & Co., Inc., Wilmington, DE, 1988.

2. "Military Chemistry and Chemical Compounds," Army Field Manual FM3-9, October 1975.

3. "Decontamination of Organosphosphorus Esters by Hydrolysis Catalyzed by Transition-Metal Ions," J.M. Albizo, J.W. Hovanec, and J.R. Ward, U.S. Army Chemical Research, Development and Engineering Center Technical Report, CRDEC-TR-88061, March 1988.

4. "Development of Decontaminating Solution DS2," J.B. Jackson, CWLR 2368, April 1960.

5. "Measurement of the Acidity of Vacuum Pumps Oils," Technical Brief No. 1, IVAX Industries, Inc., Churchville, NY.

EPR STUDIES OF MICELLES AS COMPARTMENTS

Barney L. Bales[1] and Jack Deaton

A new method to study number distributions of additive molecules associated with micelles is introduced which exploits the fact that magnetic interactions between paramagnetic particles can yield EPR spectra that depend uniquely on the number of interacting particles. To illustrate the method, the stable free radical 5-doxyldecane has been used as an additive in micellar solutions of hexadecyltrimethylammonium bromide and studied by EPR in order to test the assumption that uncharged molecules distribute among micelles randomly, i.e. according to the Poisson distribution. Linewidth and line shape changes of the EPR spectrum as a function of the average number of additives per micelle are inconsistent with a random distribution. This suggests that particle-particle interactions, which result in a reduction of the dispersion of the number distribution, need to be taken into account. A modified Lennard-Jones potential showing effective attraction between additives at low concentrations and repulsion at higher concentrations improves significantly the agreement between theory and experiment.

INTRODUCTION

One of the outstanding properties of micelles is their ability to solubilize water-insoluble molecules[2]. For any physical process that occurs faster than the time required for these additives to migrated from one micelle to another, the number of additive molecules associated with a particular micelle is well defined leading to the idea of the additives residing in *compartments*.[3] This, in turn, leads to the interesting and important concept of the *number distribution* [4] of the particles associated with the micelles.

To bring the problem into focus, we show schematically in Fig. 1 a small system of micelles (compartments), shown as large spheres, and some additive particles, shown as black dots. Ignore, for the moment, the arrows. There are 34 compartments and 102 particles so the average number of particles per compartment, $\langle N \rangle = 3.0$. There are some compartments that have no particles associated with them and some with as many as seven. Fig. 1 is not easy to draw without paying attention because, try as one may, the tendency is to draw more compartments with three particles and diminish the number removed from three. However, Fig. 1 is very nearly what a computer would draw, on average, if it were asked to distribute the particles randomly, i.e. according to the Poisson distribution. Fig. 2(a) shows the distribution expected according to the Poisson distribution and the actual distribution of Fig. 1. The Poisson distribution is given by

$$P_{N<N>} = \frac{<N>^N \exp(-<N>)}{N!}, \qquad (1)$$

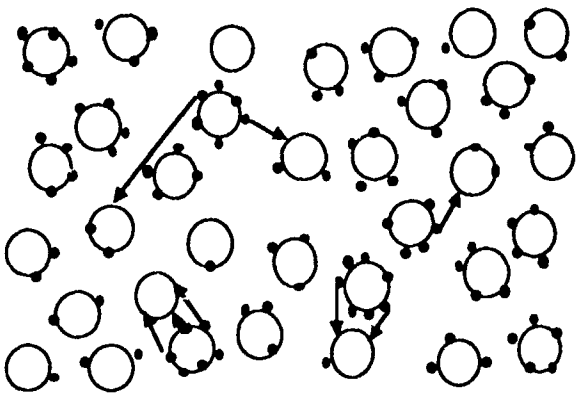

Fig. 1. Schematic system of micelles, large circles, with additive molecules, black dots. There are 34 micelles and 102 additive molecules, yielding an average number of additives per micelle <N> = 3.0. The distribution of additives over the micelles is nearly that predicted by the Poisson distribution, so some micelles have no additives while others have as many as seven. The arrows suggest a reorganization of the additives if particle–particle repulsion is envisioned at high numbers of particles on a given micelle

where $P_{N<N>}$ is the probability of a micelle with N additive particles occurring in a system with an average number of <N> particles per micelle.The Poisson distribution is derived by assuming that there are no interactions between the additive particles, so in building up a system such as Fig. 1, one places another particle on a micelle irrespective of the number already on it , in principle, continuing all the way up to an infinite number. Of course, in a real system, this is not a reasonable assumption because, at the very least sooner or later there will be no further "room" on a given micelle. Thus one does not expect the Poisson distribution to hold to high values of <N>, but even at values as small as <N>=3, one can imagine that interactions could disturb the random distribution. As a concrete example, if we imagine that repulsive interactions were sufficient to cause eight of the 102 particles to migrate from compartments containing larger numbers to those containing smaller numbers of particles, then the number distribution shown in Fig. 2(b) would result. The outstanding feature of the Poisson distribution is its very large dispersion, i. e. the breadth of the plot in Fig. 2(a) is large. One can show[5] from Eq. (1) that the dispersion is equal to <N>. The imagined repulsion between particles that led to Fig. 2(b) results in a smaller number dispersion.

The purpose of this paper is to introduce a new method to study number distributions in micellar solutions and to give preliminary results that show significant departures from Eq. (1) even for uncharged, relatively small additive molecules at small values of <N>. We show that a very simple modified Lennard-Jones interaction between the particles gives a satisfactory account of the experimental facts.

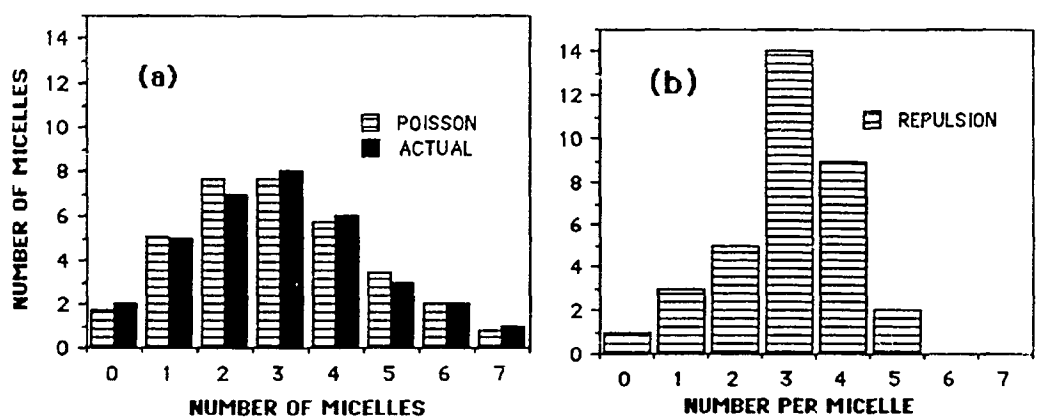

Fig. 2(a). The actual number distribution of additives in the schematic system of Fig. 1 together with the prediction of the Poisson distribution, Eq. (1). (b). The number distribution in the system of Fig. 1 after the redistribution of particles suggested by the arrows. The breadth of the distribution is sharply reduced relative to the Poisson distribution.

EXPERIMENTAL STRATEGY TO STUDY NUMBER DISTRIBUTIONS

We employ paramagnetic molecules as the additive particles and exploit three facts in order to use EPR measurements to study number distributions in micellar solutions. First, owing to magnetic interactions between paramagnetic molecules, the signal due to a micelle containing a given number of paramagnetic molecules is different than that due to micelle containing a different number. Second, since spin exchange between paramagnetic molecules on different micelles is negligible, a fact that we demonstrate below, the observed signal is a superposition of signals due to singly, double, triply, etc. occupied micelles rather that a single number-averaged result that tends to hide the details of the number distribution. Third, since EPR is a sensitive technique, one can study number distributions at very small values of <N>.

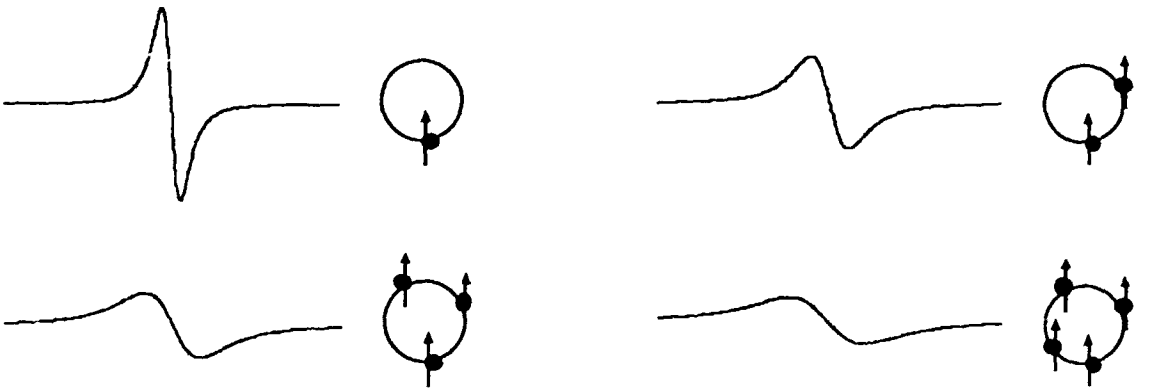

Fig. 3. Schematic description of the composition of the EPR spectrum. The spectrum due to the ensemble of micelles containing a single additive free radical, shown to the left of the icon for a singly-occupied micelle, is different from the spectrum due to the doubly occupied micelle and so on. The doubly-integrated spectrum in each case is proportional to the number of free radicals contributing to the signal. Since the height of first-derivative EPR spectra are inversely proportional to the square of the linewidth for equivalent line shapes, the heights of the spectra *decrease* with N even though the doubly-integrated intensity increases. The composite EPR spectrum is comprised of a sum of spectra such as the above, each of which is multiplied by the probability that a micelle has the corresponding number of additive particles.

The method is presented schematically in Fig. 3 where one line of the three-line free radical EPR spectrum is shown for various occupation numbers of additives illustrated by the accompanying icons. An observed EPR spectrum would be the superposition of spectra like those in Fig. 3, each one being multiplied by the probability of the occurrence of the corresponding occupation number. For the distribution in Fig. 1 , for example, the spectra in Fig. 3 would be multiplied by similar probabilities, resulting in a domination of the linewidth by the singly-occupied signal. Increasing the broadening due to magnetic interactions does not change this reality because the height of the spectra in Fig. 3 are inversely proportional to the square of the linewidth[6] which preserves the dominance by the singly-occupied micelle no matter what the broadening might be. By contrast, the distribution of Fig. 2(a) would emphasize the importance of the broader triply-occupied micelle at the expense of the singly-occupied, resulting in a broader spectrum. We shall see below that experimental linewidths are broader than can be explained by the Poisson distribution.

EXPERIMENTAL

FPR spectra were obtained with a Bruker 200 X-band spectrometer interfaced with an IBM 9000 computer. Precautions were taken to assure faithful reproduction of the spectra as before[7]. Hexadecyltrimethylammonium bromide (CTAB), used as obtained from Sigma, was stirred in triply-distilled water at 30 °C to produce 0.1 M solutions which were "aged" for four hours before being added to a vial containing a film of 5N10 which had been deposited in a known amount from a chloroform solution. Stirring for 30 min produced a clear solution that remained clear at 25 °C at which temperature the measurements were taken. Nondegassed samples were sealed into 50 ml disposable pipets and placed into a quartz dewar in the microwave cavity for the measurements. The temperature was controlled to ± 0.1 C by passing thermostated kerosene (Neslabs RTE-5DD) through the dewar and was measured with a thermocouple The linewidths and a line shape parameter[7], ψ, which is a measure of the height of the wings of the spectrum, were measured using software developed by Chris Stenland described previously[8]. The concentration of micelles was computed from the surfactant concentration by [micelles] = (0.1 M - CMC)/N_A where the CMC was taken to be 0.92 mM and the aggregation number $N_A = 60$[1], and <N>=[5N10]/[micelles].

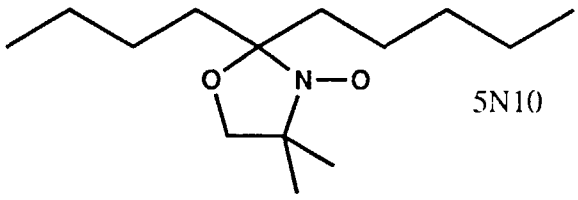

5N10

RESULTS

EPR spectra of 5N10 in CTAB micelles are shown in Fig. 4. The top trace resulted from a low concentration sample and is due mostly to singly-occupied micelles. The second trace corresponds to <N> = 3.0 and shows the expected line broadening while the third trace is due a sample prepared from the <N> = 3.0 sample after a 1:1 dilution with water. In this latter sample, there are approximately one-half as many micelles and one-half as many additives so <N> is also nearly 3.0, so after multiplication by two, the second and third traces ought to be identical if there is no intermicelle interactions affecting the EPR. The final trace, which is two times the third trace subtracted from the second trace and shown at a receiver gain twice as large, shows that this is so to a high degree of accuracy. This also shows that the mechanisms that determine the number distribution function operate at the individual micelle level rather than involving micelle-micelle interactions. The residual signal in the last trace is mostly due to a small partitioning of the free radical into the water, as shown by a comparison of its nitrogen hyperfine coupling constant with that of 5N10 dissolved in water and amounts to < 0.3 % of the micelle-bound signal. A small admixture (< 0.2 %) of signal due to singly-occupied micelles also contributes to the residual.We may thus proceed with the assumption that the observed spectra are superpositions of spectra due to single compartments with no intercompartmental interactions. The experimental linewidth and line shape variations with <N> are given in Fig. 5 together with the predictions of the Poisson distribution. The only parameter involved in the calculations is the amount of broadening induced by bimolecular encounters δ_A, employing the plausible assumption that the number of bimolecular encounters increases as (N-1) so the average induced broadening in a micelle housing N additives is $(N-1)\cdot\delta_A$. Using the Poisson distribution, increasing the value of δ_A can not account for the discrepancy between theory and experiment, as discussed below Fig. 3 and verified in Fig. 5. The largest linewidth occurs at $\delta_A = 0.8$ G (solid line) and is less for both 0.4 G (triangles) and 1.2 G (solid squares).

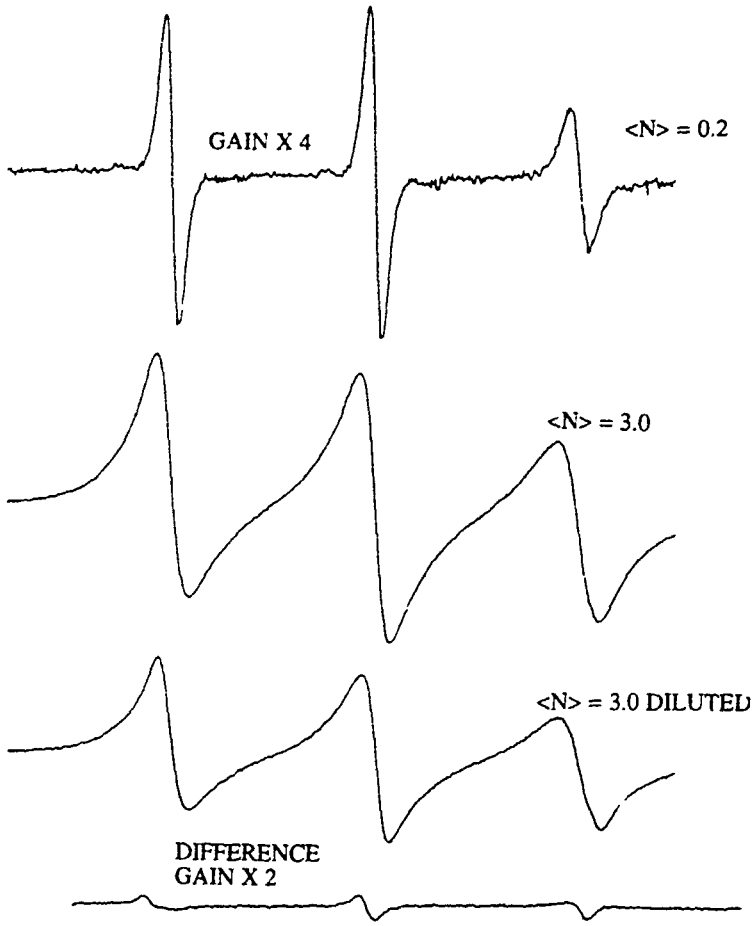

Fig.4. EPR spectra of 5N10 in CTAB micelles at 25 °C at a low (top trace) and at high concentrations. The third trace is measured from a sample that is a 1:1 dilution with water of the sample yielding the second trace. The final trace is two times the difference between the the second and twice the third traces and is mostly due to a small amount of 5N10 partitioned into the water phase. The similarities of the linewidths and line shapes of theEPR due to the <N> = 3 sample and the diluted sample show that intermicelle interactions are unimportant.

DISCUSSION

The discrepancy between experiment and theory can be reduced by taking into account additive-additive interactions. That this is so may be inferred without doing any calculations from the qualitative arguments that produced the distribution in Fig. 2(a). Interactions can decrease the number of singly-occupied micelle and reduce their dominance on the linewidth. In order to proceed quantitatively, one needs a theoretical framework in which to proceed. We have produced such a framework[9] using classical statistical mechanics in the grand canonical ensemble[5] neglecting interactions between particles on different micelles and taking into account the fact that if particles interact on the same micelle,they must be indistinguishable. The probability is

$$P_{N<N>} = \frac{1}{z} \cdot \frac{1}{N!} \cdot \exp\{[\mu N - \varepsilon(N)]/kT\} \qquad (2)$$

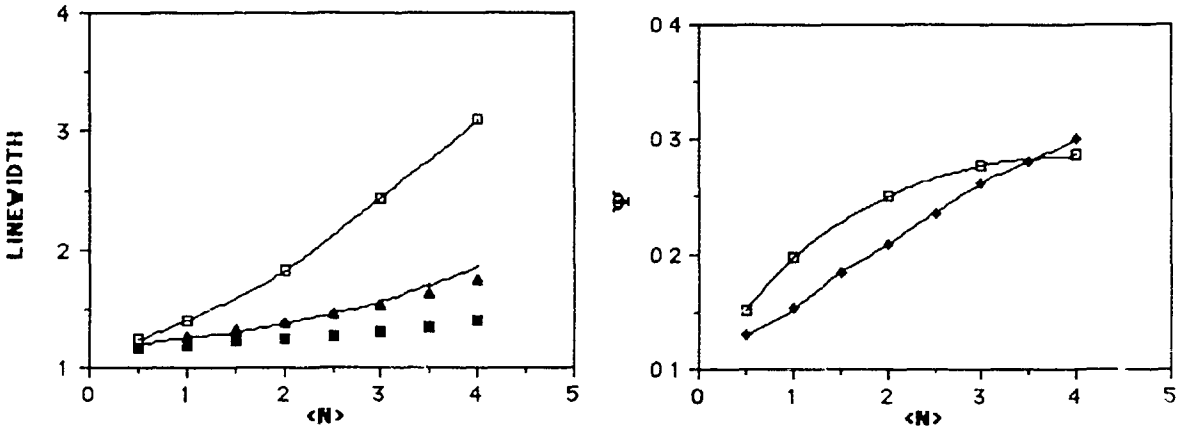

Fig. 5. Experimental EPR linewidth and line shape data for 5N10 in CTAB micelles vs <N> (open squares) and theoretical attempts using the Poisson distribution with δ_A=0.8 G (solid lines), 0.4 G (triangles) and 1.2 G (solid squares).

where the single-micelle grand partition function is given by

$$z = \sum_{N=0}^{\infty} \frac{1}{N!} \cdot \exp\{[\mu N - \varepsilon(N)]/kT\} \quad , \qquad (3)$$

and the chemical potential per additive particle μ is adjusted to give the proper <N>. The interaction model is embodied in the interaction $\varepsilon(N)$. For $\varepsilon(N)$=0.Eq (2) = Eq. (1).

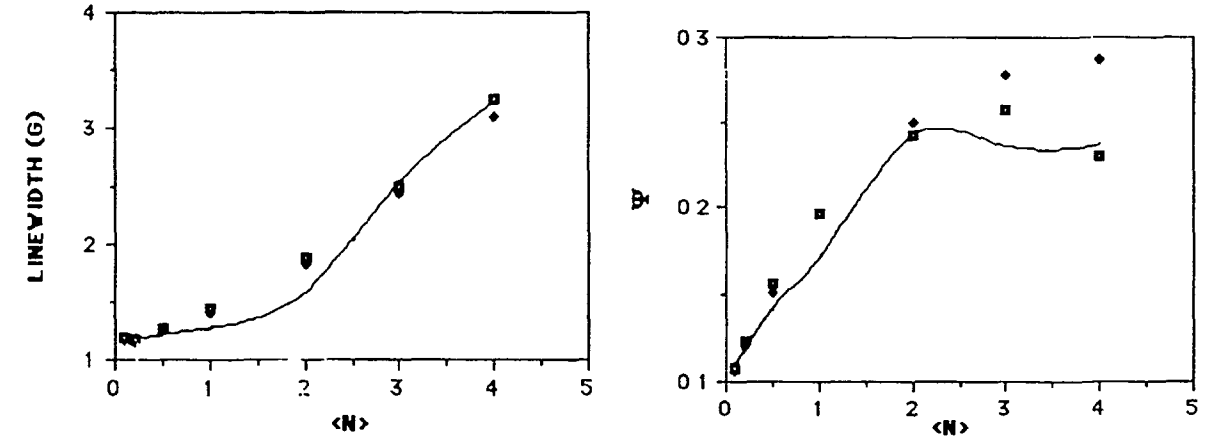

Fig. 6. Experimental EPR linewidth and line shape data for 5N10 in CTAB micelles vs <N> (open squares) and a theoretical fit with δ_A=1.2 G (solid lines) using a modified Lennard-Jones (pair-attraction) model Eq. (4) with ε_A/kT = 1.5 and ε_R/kT = 0.3 Two sets of experimental points come from the low-field and center-field lines and their scatter is of the order of the experimental error.

As a physically plausible model to try to begin to rationalize these results, we propose a modified Lennard-Jones potential that is attractive at large separations (small N) and is repulsive at the other extreme. We present the simplest possible interaction potential that embodies attraction at low values of N and repulsion at higher values as follows:

$$\varepsilon(N) = -\varepsilon_A \delta_{N,2} + \varepsilon_R N(N-1) \quad , \tag{4}$$

i. e. there is attraction between the additives for pairs (N=2) and a repulsive tail that grows as the square of N. The results for $\varepsilon_A/kT = 1.5$ and $\varepsilon_R/kT = 0.3$ are shown together with the experimental results in Fig.6. There is a remarkable improvement in the agreement between experiment and theory for such a simple model.

CONCLUSIONS

EPR is an effective method to study number distributions of additive molecules in micelles. For the uncharged additive molecule 5N10, at concentrations as low as one molecule per micelle, the results are inconsistent with the Poisson distribution. A simple model of additive-additive interactions involving attraction at low concentrations and repulsion at higher concentrations improves the agreement between experiment and theory considerably.

ACKNOWLEDGMENT

This work was supported by the Army Research Office, contract DAALO 3-88-K-0006.

REFERENCES

1. Department of Physics and Astronomy, California State University at Northridge, Northridge, California 91330.

2. J. H. Fendler and E. J. Fendler, *Catalysis in Micellar and Macromolecular Systems*, Academic Press, Inc. New York (1975).

3. J. H. Fendler, *J Phys. Chem.* ***89***, 2730 (1985).

4. P. P. Infelta and M. Gratzel, *J. Chem Phys.* ***70***, 179 (1974); R. C. Dorrance and T. F. Hunter, *J. Chem Soc. Faraday Trans.* 1, ***70***, 1572 (1974); R. C. Dorrance and T. F. Hunter, *J. Chem Soc Faraday Trans.* 1, ***73***, 1891 (1977); D. J. Miller, *J. Chem Ed.* ***55***, 776 (1978)

5. R. Kubo, *Statistical Mechanics*, North-Holland, New York (1965)

6. D. B. Chesnut, *J. Magn Reson* ***25***, 373 (1977).

7. B. L. Bales, *J. Magn. Reson* ***48***, 418 (1982).

8. B. L. Bales, *Biological Magnetic Resonance* ***8***, 77 (1989).

9. B. L. Bales, to be submitted to the *J. Chem. Phys.*

BLANK

SYNTHESIS OF ORGANO-RUTHENIUM COMPLEXES FOR LUMINESCENCE PROBES IN MICROEMULSION DROPLET SIZE DETERMINATION

H. Dupont Durst[1], Frederick R. Longo[2],
Stephanie M. Garlick[3], Keith G. Haddaway[3]

ABSTRACT

Systems of the type RuL_3^x were synthesized where the overall charge (x) on the complex was varied from +2 to -4. These complexes were subsequently used to determine droplet size in microemulsion media. The ligands (L) were derived from the 1,10-phenanthroline or 2,2'-bipyridine nucleus. Syntheses involved the preparation of ligands and/or complexes. The preparation of additional ligands was attempted through a variety of routes in order to further vary the charge of the complex.

Systems of the general structure RuL_3^x where x is some overall charge and L is a ligand having either the 1,10-phenanthroline (**1**) or 2,2'-dipyridyl (**2**) nucleus have previously been used as luminescent probes in micellar and microemulsion systems.[4] In the presence of an electron acceptor, the luminescence of these

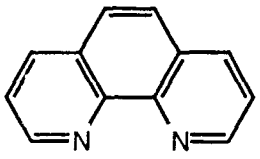

1

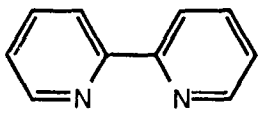

2

compounds is efficiently quenched. Static and dynamic quenching can be used to determine aggregation numbers in micellar systems. Our goal was to examine how the charge of the complex affected the results in these studies.

The premise of these types of studies is that the donors are associated with the aggregate in the interfacial region. The acceptor, on the other hand, is soluble only in the hydophobic core of the micelle or microemulsion. The charge on the donor

should effect the the location of the donor relative to the interface. We set out to synthesize a variety of donor molecules with varying charge in order to investigate these effects. This effort required the synthesis of ligands and the subsequent complexation of these ligands to a Ruthenium (II) species.

Some of the previously synthesized ligands **3-5**[5a] are listed below. The charge on these ligands is 0. When ligated to Ru^{II} the resulting complexes would have a net charge of +2. The microemulsion systems which we intended to study

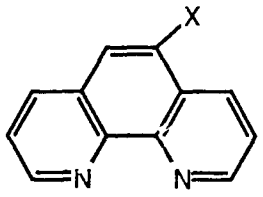

3a X=Cl
3b X=Br
3c X=CH_3
3d X= Ph
3e X=NO_2

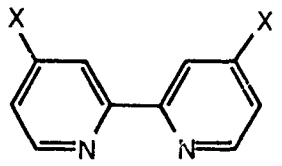

5a X=H
5b X=CH_3
5c X=Ph

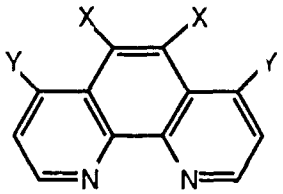

4a X=Y=CH_3
4b X=H; Y=CH_3
4c X=CH_3; Y=H
4d X=H; Y=Ph

contain cationic tetraalkylammonium surfactants. We were concerned that the overall positive charge on the donors would lead to a significant electrostatic repulsion beween the donor and the the positively charged ammonium head groups. It was therefore necessary to synthesize negatively charged complexes. One such compound in the literature uses 4,7-di(phenylsulfonato)-1,10-phenanthroline (bathophenanthroline disulfonic acid, **6**) as the ligand.[6] Although several researchers have utilized this compound, synthetic details were sketchy.

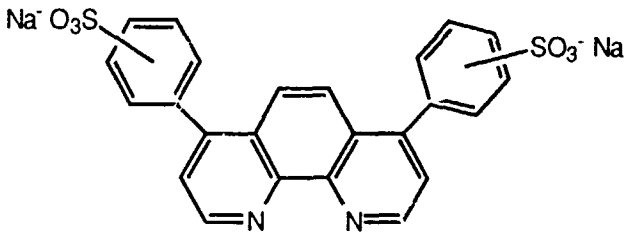

6

Synthesis and characterization of Ru(II) complexes of 6

This complex has been extensively utilized by Demas[6]. A review of these references failed to uncover a specific synthesis. Since the ligand **6** is commercially available, a general approach to the synthesis, applicable to other bidentate, ligands

was pursued (Scheme I).[5a] The nature of the reagent used in the final

Scheme 1

$$K_2RuCl_5 \cdot H_2O + L \xrightarrow[2)\ Na_2HPO_2]{1)\ \Delta} \xrightarrow[\text{Reagent}]{\text{Precipitating}}$$

step of this sequence is dependant upon the ligand. For neutral ligands (yielding cationic complexes), HCl is used to precipitate the complex as the chloride salt. Several reagents were tried when **6** was used as the ligand. Initially, the use of $CsClO_4$ was tried in order to precipitate the cesium salt[5b]. Several drawbacks were encountered in these efforts. First, the relatively low solubility of $CsClO_4$ in water required excess solvent be removed. Secondly, $CsClO_4$ tended to precipitate with the complex. Several recrystallizations of this material failed to give satisfactory elemental analysis. Next, NaCl was used, Again, however, recraystallization failed to give material with satisfactory elemental analysis.

Concurrent with these synthetic efforts, luminescence studies were being conducted using the crude materials previously prepared[7]. These studies were repeated with micelles[4a]. These physical studies seemed to indicate that the crude complexes gave results consistent with those already published. However, we were unable to confirm the structure by elemental analysis. Our attention was also drawn to a paper where anionic bipyridine complexes were purified by chromatography on Sephadex LH-20[8]. In order to prepare a more crystallizable complex, precipitation was accomplished with tetraethylammonium chloride. After crystallization, this complex was chromatographed on Sephadex LH-20 with water as eluent followed by rechromatographing and elution with 15% acetone in water. Again, luminescent studies were consistent with previously reported results.

Elemental Analysis and NMR Results

Elemental analysis of $(NEt_4)_4Ru^{II}L_3 \cdot xH_2O$ where L=**6** seemed to be consistent with a structure containing only four sulfonate groups rather than the six which would be expected (actual analysis reads that the complex is ca. 60% pure). Further, the counterion was found to be sodium. Subsequent preparations used NaCl as the precitant. These discrepancies led to a more in depth analysis of the commercial compound **6**. In house NMR analysis[9] showed the this commercial material was less than 100% pure, assuming that the SO_3 groups are both in the para position. The company providing the compound was also contacted. Their elemental analysis and TLC data were consistent with the structure **6**.[10] There are a few explanations of this data. First of all, it is possible that the material as supplied is a mixture of ortho-para (**6a**) and para-para isomers. This is consistent with the NMR results, but contradicts those of the elemental analysis. A second possibility is that the commercial compound contains a large amount of monosulfonated material. While this explains the elemental and the NMR results, it is inconsistent with data provided by the manufacturer. Lastly, problems may exist with the synthesis, causing desulfonation. This too seems unlikely.

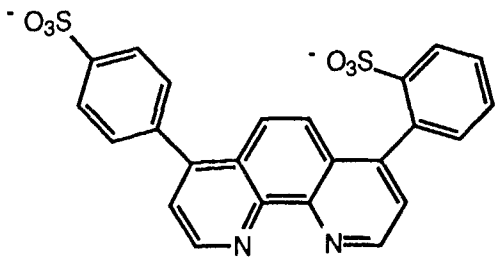

6a

A satisfactory explanation does not exist at this time to justify all of the available data. Importantly, the results of the luminescence experiments for which these compounds were synthesized do not appear to be effected by any impurities which might be present. (It is significant to note that the experiments are not dependant upon knowing the exact concentration of the donor complex if $< 7.2 \times 10^{-5}$.) Apparently, the structural differences do not effect results.

Other Complexes and Luminescence Results

Using the method outlined in Scheme I, complexes of the general formula $Ru^{II}L_3Cl_2$ where L= 1,10-phenahthroline (**1**) or 4,7-diphenyl-1,10-phenanthroline (**4d**) were also synthesized. All of these complexes were subjected to the luminescence experiments. When all of these results are taken together, both of the complexes containing phenyl groups give satisfactory (and self-consistent) results in determination of aggregation numbers for microemulsions. There is some evidence that the results of aggregation number determination is dependant on the size:charge ratio of the ruthenium(II) complex. These results are discussed more fully elsewhere.[7]

The conclusion to be drawn from these results is that when the ligand is sufficiently bulky, the positive charge of the ruthenium is unimportant. Only when the ligands are relatively small does this charge become important. This observation is most likely related to the surface area to charge ratio for the complex.

Attempted Synthesis of Other Ligands

In order to determine the extent to which charge and size were interrelated, we sought to synthesize a small ligand having a negative one charge. It was felt that carboxylation of **1** or **2**, would accomplish this goal. While these attempts were not successful, the attempts are outlined here.

Carboxy-1,10-Phenanthroline- Oxidation of 5-methyl-1,10-phenanthroline was attempted by using $KMnO_4$ and Selenium Dioxide. These gave only starting material.

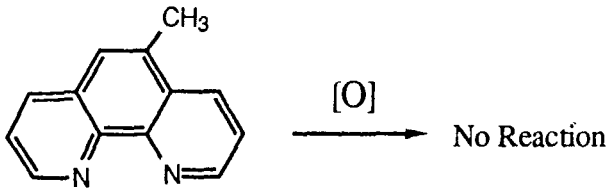

Additionally, attempts were made at replacing the chloride of 5-chloro-1,10-phenanthroline with either a nitrile (for hydrolysis to the acid) or with SO_3^-. These attempts also resulted only in recovery of starting material.

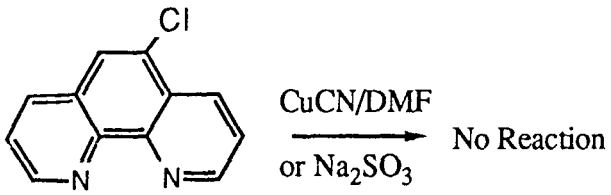

Carboxy-2,2'-dipyridyl- Alkylation of 2,2'-dipyridyl was accomplished by reaction with n-butyllithium (Scheme 2). This gave predominantly 5-carboxy-2,2'-dipyridyl. A side product, separable by TLC is tentatively identified as **7**. Permanganate and chromic acid oxidation of this material gave only decomposition products.

Scheme 2

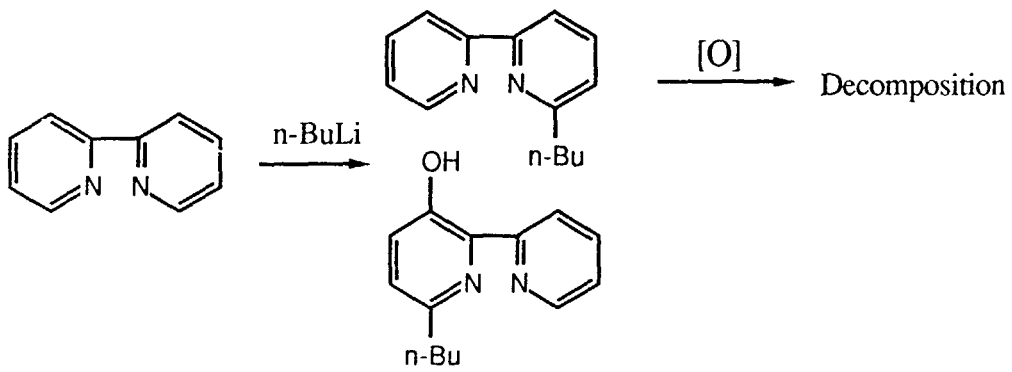

7

Conclusions

A variety of tris-phenanthroline complexes have been prepared using general procedures. High purity of these complexes is somewhat difficult to obtain. Fortunately, for use in luminescence studies related to aggregation numbers for microemulsions, the impurities present do not affect the method.

Acknowledgement

The authors are especially grateful to Linda Szafraniec for conducting ^{13}C NMR analysis of the complexes and ligands and the expert analysis provided. Ray Herd of CRDEC is thanked for performing AA and ICP analyses.

Experimental

General Bathophenanthrolinedisulfonic acid (**6**), 1,10-phenanthroline, 5-methyl-1,10-phenanthroline and n-butyllithium were obtained from Aldrich and used as received. Bathophenanthrolinedisulfonic acid was supplied as the hydrate of the disodium salt. Conversations with technical representatives at Aldrich further revealed that their supplier for this material was Sigma Chemical Co. Potassium aquopentachlororuthenate (III) ($K_2Cl_5 \cdot H_2O$) and 2,2'-Dipyridyl were obtained from Alfa Products. After opening, these materials were stored under a dry nitrogen atmosphere. Sephadex LH-20 was obtained from Sigma Chemicals and prepared for use with standard procedures[11]. Elemental analyses were performed by Schwarzkopf Laboratories (Westbury, NY). NMR analysis was conducted at CRDEC on a Varian 400 MHz FT-NMR.

Synthesis of Ru(II) Complexes Synthises were conducted by the method of Sutin[6a]. Precipitation was carried out by adding a 6-fold excess of the precipitating reagent. The solids obtained were recrystallized twice from hot water. The sodium and tatraethlylammonium salts of the bathophenanthroline disulfonis acid complex were further purified by passage through a Sephadex LH-20 column (2cm) and eluting with water, followed by a second chromatography on a different column of the same material and eluting with 15% acetone in water. Only the central portion of the intense red band was collected.

Oxidations of 5-Methyl-1,10-phenanthroline

$KMnO_4$ 5-Methyl-1,10-phenanthroline (321.3 mg, 1.65 mmol) was dissolved in water (7 mL) and the solution heated to 50°C. a solution of potassium permanganate (533 3 mg, 3.375 mmol) in 10 mL water was added in two portions about 30 min apart. This solution was then stirred for 40 min at 50°, at which time the permanganate color had dissipated. The solution was then poured into water and the flask rinsed with 2N NaOH. The solution was filtered and acidified with conc. HCl. The water was removed under reduced pressure leaving a brown solid, insoluble in both CH_2Cl_2 and $CHCl_3$. The solids were dissolved in 2N NaOH and extracted with CH_2Cl_2 The organic portion was dried over Na_2SO_4 and concentrated in vacuo. The residue gave no clear NMR.

Selenium Dioxide[12] A slurry of selenium dioxide (230.2 mg, 2.07 mmol) in 3mL p-dioxane containing 0.2 mL water was warmed until the selenium dioxide dissolved. 5-Methyl-1,10-phenanthroline (291.0 mg, 1.498 mmol) in 15 mL dioxane was added dropwise over 15 min. A black precipitate formed during this time. The liquid was

decanted, $CHCl_3$ added, and the mixture rinsed with water. The organic layer was dried and concentrated in vacuo. No evidence of CHO was evidenced in the NMR. chromatographed using prep TLC (Silica Gel GF, 5% MeOH in $CHCl_3$). The main fraction was identified as 5-Methyl-1,10-phenanthroline by IR and NMR.

Substitution Reactions of 5-Chloro-1,10-phenanthroline

CuCN A mixture of copper (I) Cyanide (89.6 mg, 1.192 mmol) and 5-chloro-1,10-phenanthroline (214.7 mg, 0.8525 mmol) was refluxed in 15 mL DMF. The solution was poured into ice water, extracted with CHCl3 , dries and concentrated in vacuo. TLC (MeOH) showed only starting material.

Na_2SO_3 A mixture of sodium suifite (350.0 mg, 2.78 mmol) and 5-chloro-1,10-phenanthroline (406.0 mg, 1.89 mmol) was refluxed in 15 mL water for 7 days. TLC (acetone) showed only starting material.

Alkylation and Attempted Oxidation of 2,2'-Bipyridine

A solution of n-BuLi (2.5M, 4.0 mL, 10 mmol) was added dropwise to a solution of bipyridine (1.56 mg, 10.0 mmol) in 50 mL ether. After addition, the solution was poured into water, extracted with ether, dried over sodium sulfate and concentrated in vacuo. The crude mixture was chromatographed on Silica Gel (3:2 hexane:ether). (A good deal of starting material was isolated and yields were not calculated in these preliminary experiments.) The major product was 6-butyl-2,2'-bipyridine and a minor product identified as 6-butyl-3-hydroxy-2,2'-bipyridine (**7**).

For 6-butyl-2,2'-bipyridine- ^1H NMR 0.95 (t, 3H, $-CH_3$, J=7 Hz), 1.4-1.8 (m, 4H, $-CH_2CH_2-$), 2.85 (t, 2H, Ar-CH_2-, J= 7.7 Hz), 7.1-8.6 (m, 7H, Ar-H) ^{13}C NMR 13.8, 22.3, 31.7, 37.9 (Aliphatic C's), 118.0 (C-3), 121.0 (C-3'), 122.5 (C-5), 123.2 (C-5'), 136.5 (C-4'), 136.8 (C-4), 148.9 (C-6'), 155.3 (C-2), 156.5 (C-2'), 161.7 (C-6)

For **7** ^1H NMR 0.96 (t, 3H, $-CH_3$, J=7.1 Hz), 1.4-1.75 (m, 4H, $-CH_2CH_2-$), 2.77 (t, 2H, Ar-CH_2-, J= 7.4 Hz), 7.0-8.65 (m, 6H, Ar-H), 13.96 (br, 1H, OH) ^{13}C NMR 14.0, 22.4, 32.0, 37.2 (Aliphatic C's), 120.8 (C-3'), 122.6 (C-5'), 125.0 (C-4),125.9 (C-5), 135.4 (C-2), 137.7 (C-4'), 145.3 (C-6'), 152.2 (C-3), 154.4 (C-6), 158.6 (C-2')

Oxidation of 6-butyl-2,2'-bipyridine-$KMnO_4$ 6-Butyl-2,2'-bipyridine (294.0 mg, 1.38 mmol) was in 7 mL water was heated to 80°C. A solution of potassium permanganate (598 mg, 3.78 mmol) in 10 mL water was added in 5 portions over 6 h. After aqueous work-up and extraction with chloroform, only starting material was isolated.

Chromic Acid- Sodium Dichromate dihydrate (2.416 g, 10.2 mmol) and 6-butyl-2,2'-bipyridine (321.4 mg, 1.52 mmol) were combined in 7 ml water and 3.3 mL conc. H_2SO_4 was added dropwise. After addition, the mixture was poured into ice water and filtered. The filtrate was adjusted to pH 7-8 with 2N NaOH giving a black precipitate which could not be purified.

Addendum Near the completionn of this work, our attention was been drawn to several other reports which give alternative methods for the synthesis of ruthenium(II)

complexes[8,13] and some monofuctionalized ligands[8]. Thes methods were not used in this study.

FOOTNOTES AND REFERENCES

[1] U.S. Army Chemical Research, Development and Engineering Center, Aberdeen Proving Ground, MD 21010-5423

[2] Drexel University, Philadelphia, PA

[3] GEOCENTERS, Inc., Fort Washington, MD 20744

[4] (a) Turro, N.J.; Yekta, A. JACS 1978, 100, 5951-52; (b) Turro, N.J.; Geiger, M.W.; Hautala, R.R.; Schore, N.E. *Surfactants in Solution, Vol 1*; Mittal, K.L. and Lindman, B. Ed., Plenum Press: New York, 1984, pp 75-6.; (c) Loforth, J-E.; Almgren, M. *Surfactants in Solution, Vol 1*; Mittal, K.L. and Lindman, B. Ed., Plenum Press: New York, 1984, pp 627-43.

[5] (a) Lin, C-T.; Böttcher, W.; Chou, M.; Creutz, C.; Sutin, N. *J. Amer. Chem. Soc.* **1976**, *98*, 6536-6544. (b) Personal communication with C. Creutz, Brookhaven National Laboratories, Long Island, New York, 11973.

[6] (a) Demas, J.N.; Harris, E.W.; McBride, R.P. *J. Amer. Chem. Soc.* **1977**,*99*, 3547-51. (b) Mandal, K.; Hauenstein, B.L.; Demad, J.N.; DeGraff, B.A. *J. Phys. Chem.* . **1983**, *87*, 328-31. (c) Hauenstein, B.L.; Dressick, W.J.; Buell, S.L.; Demas, J.N.;DeGraff, B.A. *J. Amer. Chem. Soc.* **1983**, *105*, 4251-55. (d) Snyder, S.W.; Buell, S.L.; Demas, J.N.;DeGraff, B.A. *J. Phys. Chem.* . **1989**, *93*, 5265-71.

[7] Garlick, S.M.; Mackay, R.A.; Durst, H.D.; Haddaway, K.G.; Christesen, S.D.; Longo, F.R. "Chemiscal and Physical Studies in Microemulsions Containing 1-Alkyl-2-pyrrolidinones as Cosurfactants" The 1989 CRDEC Conference on Chemical Defense Research, November 1989, Abstract #6.

[8] Anderson, S.;Constable, E. C.; Seddon, K. R.; Turp, J. E.; Baggott, J.E.; Pilling, M. J. *J. Chem. Soc., Dalton Trans.* **1985**, 2247-2261.

[9] Conducted by L. Szafraniec, CRDEC

[10] Personal Communicaion with Sigma Chemical Co., St. Louis, MO, 63178.

[11] *Sephadex LH-20, Chromatography in Organic Solvents*, Pharmacia Fine Chemicals: Uppsala, Sweden, 1978; pp 1-17.

[12] Ghosh, P.K.; Spiro, T.G. *J. Electrochem Soc. (Electrochem. Sci. and Tech.)*, **1981**, *128*, 1281.

[13] (a) Rose, D.; Wilkinson, G. *J. Chem. Soc. A*, **1970**, 1791-5. (b) Oishi, S.; Tajime, K. Sjiojima, I. *J. Mol. Cat.* **1982**, *14*, 383-6.

CHEMICAL AND PHYSICAL STUDIES IN MICROEMULSIONS CONTAINING 1-ALKYL-2-PYRROLIDINONES AS COSURFACTANTS

Stephanie M. Garlick,[1,3] Steven D. Christesen,[2] Keith G. Haddaway,[1] Raymond A. Mackay,[2] H. Dupont Durst,[2] Frederick R. Longo[2,3]

[1] Geo-Centers, Inc.
Fort Washington, MD 20744

[2] U. S. Army Chemical Research, Development, and Engineering Center.
Aberdeen Proving Ground, MD 21010-5423

[3] Drexel University
Philadelphia, PA 19104

Abstract

Microemulsions are effective chemical reactors, primarily because they bring together materials of widely different polarities. We have examined the *o* -iodosobenzoate (IBA) catalyzed hydroiysis of *p* -nitrophenyldiphenyl phosphate (PNDP) in microemulsions containing the 1-alkyl-2-pyrrolidinones as cosurfactants. We present pseudo-ternary phase maps for systems containing the surfactant, cetyltrimethylammonium bromide (CTAB), the cosurfactants 1-methyl-2-pyrrolidinone (MP) or 1-cyclohexyl-2-pyrrolidinone (CHP), the oils toluene (TOL) or 4-tert-butyl toluene (t-BuTOL), and 0.03 M borate buffer as the aqueous phase (AQ). In addition, we have calculated the aggregation number of several microemulsions from the results of time-resolved luminescence quenching experiments.

Introduction

We have reported the second order rate constants for the hydrolysis of PNDP in several IBA catalyzed and uncatalyzed CTAC and CTAB microemulsions.[1-4] In recent studies, we varied the choice of cosurfactant not only to increase the solubility and the rate of hydrolysis of the phosphate esters in microemulsions,[5,6] but also to increase the penetration of the microemulsion into polymeric materials.

In this study we prepared pseudo ternary phase maps for (and measured the

second order rate constants for the hydrolysis of PNDP in) microemulsions containing CTAB as surfactant, 1-alkyl-2-pyrrolidinones as cosurfactants, TOL and t-BuTOL as oils, 0.03 M borate buffer as AQ, and IBA as catalyst. The 1-alkyl-2-pyrrolidinones are widely employed as chemical reaction media,[7] possess superior solubilizing potential,[7-9]are biodegradable,[8,10] and are non-corrosive, and chemically inert. The vapor pressure of the pyrrolidinones (neat) is < 1 mm at 20 °C, and they are stable at environmental extremes.[11] The *N* -alkyl-2-pyrrolidinones are aprotic, dipolar liquids whose high polarity can be attributed to their resonance stabilization.[7,12] The *N* -alkyl-2-pyrrolidinones are probably zwitterionic at pH 9.2.

Materials

CTAB was purchased from Aldrich (95 %) and used as received. The cosurfactants 1-methyl-2-pyrrolidinone (MP), 1-ethyl-2-pyrrolidinone (EP), 1-isopropyl-2-pyrrolidinone (iso-PP), 1-allyl-2-pyrrolidinone (AP), and 1-cyclohexyl-2-pyrrolidinone (CHP) were supplied as gifts from Virginia Chemicals, BASF Corp. and GAF Corp. The 2-pyrrolidinone (2-P; 98 %), 1-vinyl-2-pyrrolidinone (VP; 98 %), toluene (TOL; 98 %) and 4-*tert* - butyltoluene (t-BuTOL; 95 %) were purchased from Aldrich. Buffer solutions, 0.03 M in sodium tetraborate decahydrate (AQ; Fischer; 99 %), pH 9.2 - 9.4, were prepared using glass distilled, deionized water. The catalyst, *o* - iodoso benzoic acid (IBA), was obtained from Sigma, converted to the sodium salt, and dissolved in borate buffer prior to use. The substrate, PNDP, was prepared as a custom synthesis by Biomol Research Laboratories, Inc.

Experimental Procedure

The discussion of general experimental methods, the acquisition and analysis of rate data and the determination of k_{IBA} and k_{OH} have previously been described in great detail.[1-5] The computer programs used to collect the rate data and to calculate the rate constants were developed by Dr. Barry L. Knier.[13] Luminescence spectra were acquired on a LeCroy 3500 with Model TR8828C transient recorder. Excitation provided by a doubled Quanta-Ray Nd:YAG laser was detected by a RCA 31034 photomultiplier coupled to a Spex 1403 double monochromator. The donor, tris [[(1,10- phenanthroline-4,7-diyl) bis [benzenesulfonato]] (4/3 -)-*N,N* ']-disodium ruthenate (2 -) decahydrate was synthesized by the method of Sutin.[14] The quencher was 9-methylanthracene.

Results of Phase Map Studies

Pseudo-ternary, four component phase maps were constructed for the CTAB/MP/TOL/AQ, and CTAB/CHP/t-BuTOL/AQ systems. Their compositions are defined in terms of %-emulsifier(E), %-oil (TOL, or t-BuTOL) and %-buffer (AQ). Each phase map is determined at a fixed surfactant to cosurfactant (emulsifier, E) ratio. Mixtures of E and oil or E and buffer were titrated along lines of constant E to oil or E to AQ ratios with buffer or oil , respectively. The results obtained for the four component systems do not depend on the order of mixing.

The phase maps for the CTAB/MP/TOL/AQ microemulsion system at E ratios of 0.5, 0.76, 1.0, and 1.5 are depicted in Figure 1. The clear regions increase in size as the E

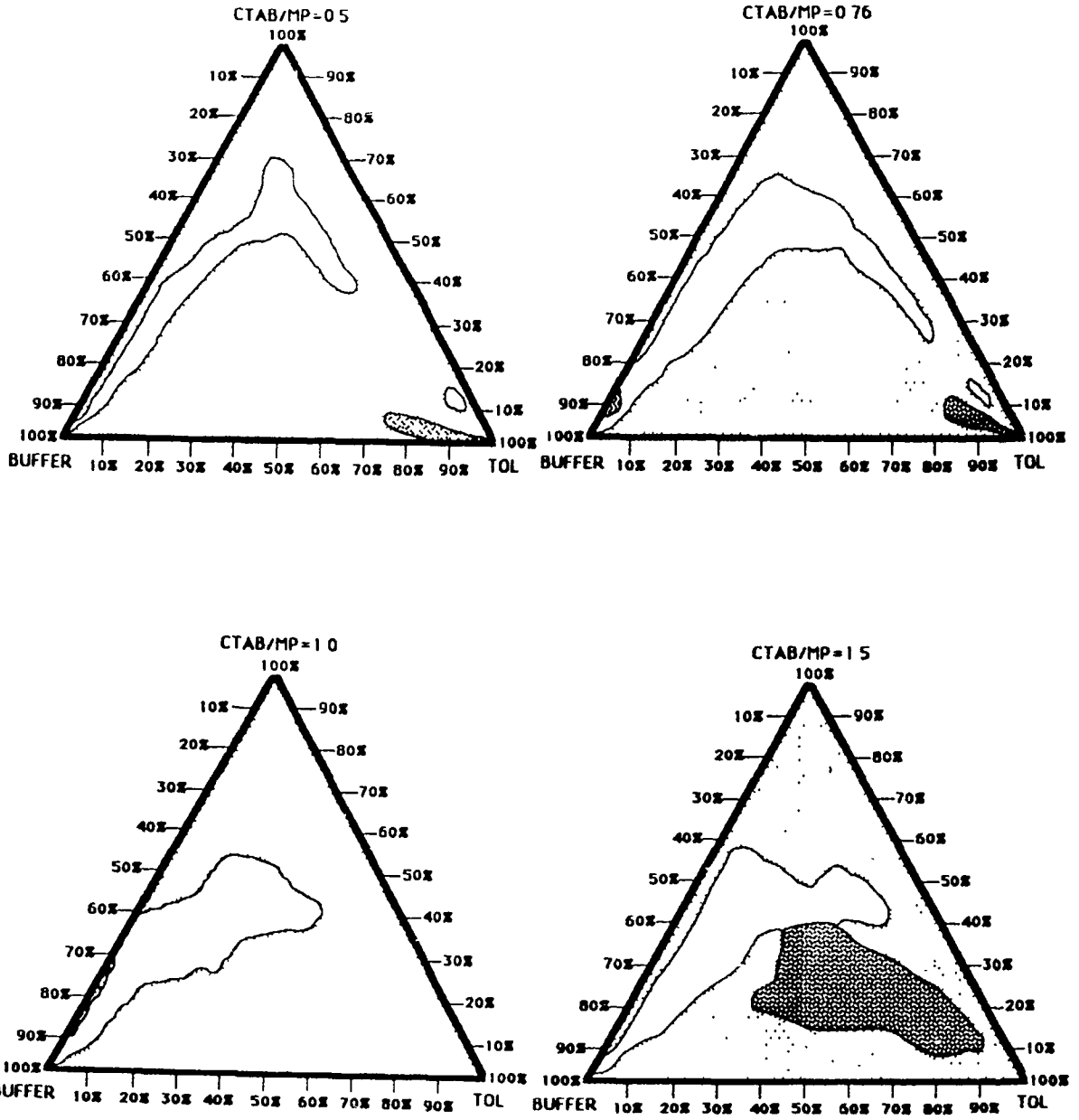

Figure 1. Pseudo-ternary phase maps for CTAB / MP / TOL / AQ systems. Regions are clear ◯, gel ⊛, turbid liquid crystalline ⊘, clear liquid crystalline ≋, and turbid ◯.

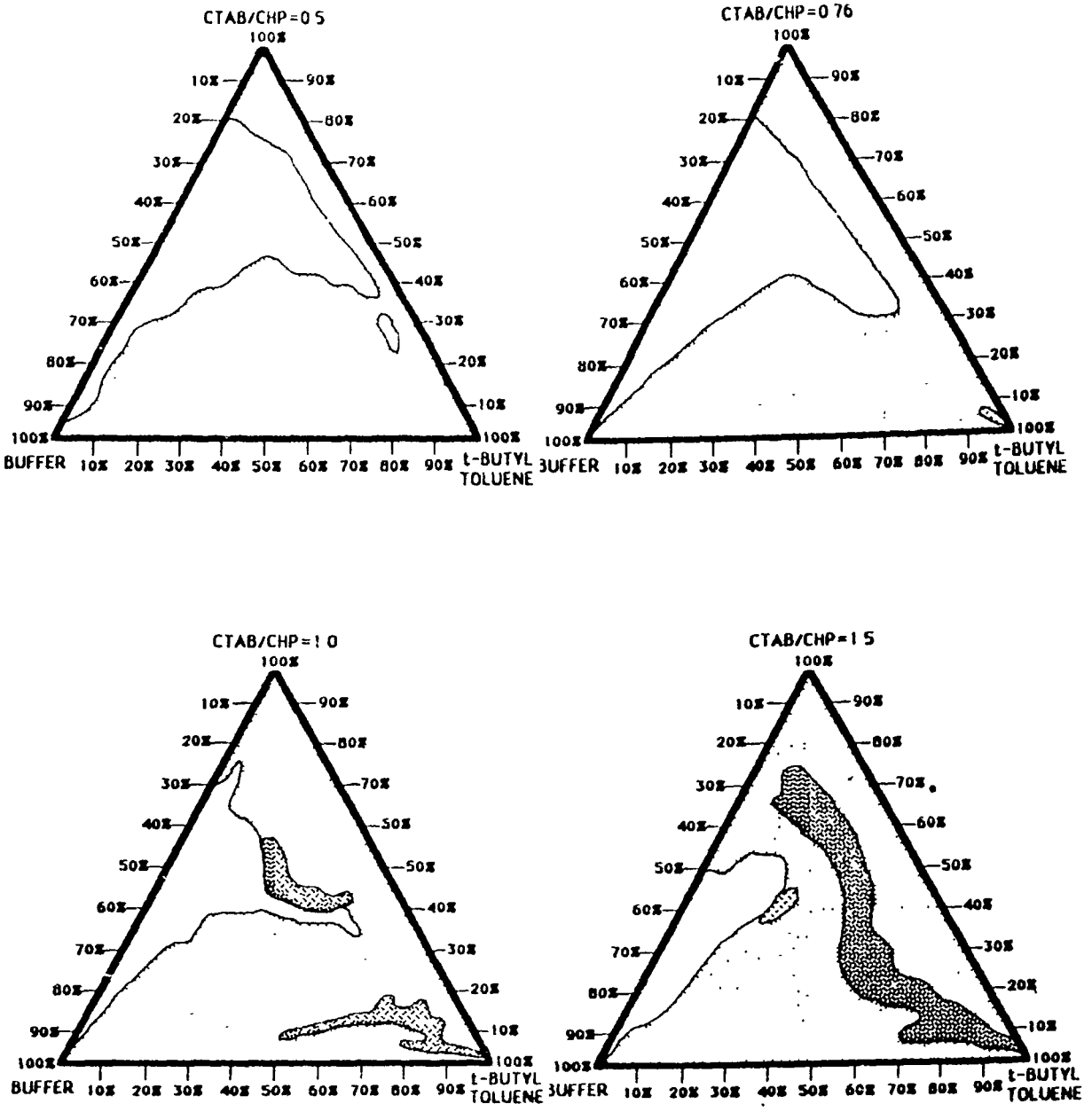

Figure 2. Pseudo-ternary phase maps for CTAB / CHP / t-BuTOL / AQ systems. See Figure 1 for legend.

ratio increases. At an E ratio of 0.76, a small, clear, liquid crystalline region exists at ~ 90 % AQ; at high % TOL a small microemulsion island, probably water in oil (W/O), and a larger gel region are observed. At an E ratio of 1.0 a narrow, turbid, liquid crystalline region is observed between ~70 and 90 %AQ. A large gel region occurs when the E ratio is equal to 1.5.

The phase maps for the CTAB/CHP/t-BuTOL/AQ system at E ratios of 0.5, 0.76, 1.0, and 1.5 are presented in Figure 2. In this system, the clear microemulsion regions decrease in size as the E ratio increases from 0.76 to 1.5. When the E ratio is equal to 0.76, a small, turbid, liquid crystalline area occurs at high % oil. Considerable gel regions exist at the higher E ratios.

Results of Kinetic Studies

The rate constants obtained for the IBA catalyzed hydrolysis of PNDP were previously[15] compared in CTAB/1-alkyl-2-pyrroldinone/TOL/AQ systems. The order of hydrolytic effectiveness of the microemulsions is: MP > 2-P > EP > iso-PP > AP > VP > CHP. The rate constants decrease as the bulk of the alkyl group increases.

Because the cosurfactants CHP and MP provided the extremes in preliminary

TABLE 1

K_{IBA} VALUES FOR PNDP HYDROLYSIS IN CTAB /MP/TOL/AQ MICROEMULSIONS

%S	%CoS	E Ratio	%AQ	%Oil	pH	$k_{IBA}(s^{-1}M^{-1})$
In Order of Increasing E Ratio						
15.0	30.0	0.50	50.0	5.0	9.3	4.71 ± 0.03
19.4	25.6	0.76	50.0	5.0	9.3	4.50 ± 0.17
22.5	22.5	1.00	50.0	5.0	9.2	4.46 ± 0.07
27.0	18.0	1.50	50.0	5.0	9.3	4.95 ± 0.16
28.6	16.4	1.75	50.0	5.0	9.1	5.10 ± 0.08
In Order of Increasing % AQ						
24.4	24.4	1.00	35.0	16.2	10.8	4.01 ± 0.13
20.6	20.6	1.00	45.0	13.8	10.4	5.11 ± 0.15
22.5	22.5	1.00	50.0	5.0	9.2	4.46 ± 0.07
16.9	16.9	1.00	55 0	11.2	10.1	6.08 ± 0.11
18.0	18.0	1.00	60.0	4.0	9.3	6.34 ± 0.18
13.1	13.1	1.00	65.0	8.8	9.9	7.31 ± 0.13
13.5	13.5	1.00	70.0	3.0	9.3	8.62 ± 0.12
9.4	9.4	1.00	75.0	6.2	9.7	11.6 ± 0.28
9.0	9.0	1.00	80.0	2.0	9.3	12.4 ± 0.55
5.6	5.6	1.00	85.0	3.8	9.6	17.3 ± 0.19
4.5	4.5	1.00	90.0	1.0	9.4	25.1 ± 0.26
In Order of Increasing % Oil						
21.0	21.0	1.00	47.0	11.0	9.3	3.66 ± 0.09
17.0	17.0	1.00	54.0	12.0	9.3	3.08 ± 0.15
26.0	26.0	1.00	31.0	17.0	9.3	2.67 ± 0.05
21.5	21 5	1.00	34.0	23.0	9.3	2.00 ± 0.02

kinetics studies, we investigated PNDP hydrolysis in CTAB microemulsions containing MP and CHP over wide ranges of compositions. These systems are also interesting because our observations indicate that CTAB microemulsions containing MP or EP as cosurfactants effectively penetrate polymers.[6]

In CTAB/MP/TOL/AQ systems, as the emulsifier ratio varies from 0.50 to 1.75 (section 1, Table 1) at constant % of oil and AQ, the second order rate constants, k_{IBA}, do not significantly change. At an emulsifier ratio of 1.0 (section 2, Table 1), the k_{IBA} values measured at an emulsifier to oil mass ratio of either 3 or 9, range from 4.0 to 6.3 $s^{-1}M^{-1}$ as % AQ increases from 35 % to 60 %. When % AQ is increased from 65 % to 85 %, k_{IBA} values increase dramatically from 7.31 to 17.3 $s^{-1}M^{-1}$ at an E equal to 1.0. In similar systems,[4,5,15,16] the rate constants generally increase as % AQ increases. A k_{IBA} value of 25.1 $s^{-1}M^{-1}$ was measured in the medium containing 90 % AQ and 1 % oil, suggesting that the system probably contains micellar aggregates. In the last section of Table 1, the rate constants decrease at increasing % TOL and decreasing % AQ.

The second order rate constants change only slightly when t-BuTOL is substituted for TOL in CTAB/MP/TOL/AQ systems, or when TOL is substituted for t-BuTOL in CTAB/CHP/t-BuTOL/AQ systems. Therefore, TOL was replaced by the less volatile t-BuTOL in systems containing CHP.

TABLE 2

K_{IBA} VALUES FOR PNDP HYDROLYSIS IN CTAB/CHP/t-BuTOL/AQ MICROEMULSIONS

%S	%CoS	E Ratio	%AQ	%Oil	pH	$k_{IBA}(s^{-1}M^{-1})$
In Order of Increasing E Ratio						
15.0	30.0	0.50	50.0	5.0	9.5	2.33 ± 0.01
19.4	25.6	0.76	50.0	5.0	9.4	2.86 ± 0.01
22.5	22.5	1.00	50.0	5.0	9.4	3.05 ± 0.02
27.0	18.0	1.50	50.0	5.0	9.3	4.32 ± 0.07
28.0	17.0	1.65	50.0	5.0	9.3	3.34 ± 0.13
28.6	16.4	1.75	50.0	5.0	9.1	3.37 ± 0.20
In Order of Increasing % AQ						
36.0	36.0	1.00	20.0	8.0	9.6	3.43 ± 0.06
31.5	31.5	1.00	30.0	7.0	9.6	3.01 ± 0.03
27.0	27.0	1.00	40.0	6.0	9.5	2.98 ± 0.06
22.5	22.5	1.00	50.0	5.0	9.4	3.05 ± 0.02
18.0	18.0	1.00	60.0	4.0	9.4	3.94 ± 0.08
13.5	13.5	1.00	70.0	3.0	9.3	4.39 ± 0.15
9.0	9.0	1.00	80.0	2.0	9.2	6.66 ± 0.03
4.5	4.5	1.00	90.0	1.0	9.4	12.6 ± 1.0
In Order of Increasing % Oil						
21.0	21.0	1.00	47.0	11.0	9.4	2.78 ± 0.04
17.0	17.0	1.00	54.0	12.0	9.4	3.55 ± 0.26
26.0	26.0	1.00	31.0	17.0	9.4	2.45 ± 0.03
21.5	21.5	1.00	34.0	23.0	9.4	2.94 ± 0.01

Lower rate constants are obtained when CHP is substituted for MP in microemulsions containing TOL or t-BuTOL as the oil. In CTAB/CHP/t-BuTOL/ AQ systems, the k_{IBA} values (section 1, Table 2) increase only slightly as the emulsifier ratio increases from 0.50 to 1.75. Maintaining a constant emulsifier ratio of 1.0, and increasing % AQ at an emulsifier to oil ratio of 9, results in approximately constant k_{IBA} values ranging from 3.43 $s^{-1}M^{-1}$ at 20 % AQ to 3.94 $s^{-1}M^{-1}$ at 60 % AQ. The k_{IBA} values increase to 12.6 $s^{-1}M^{-1}$ when % AQ is increased to 90 %. As % t-BuTOL is varied from 11 % to 23 %, only slight variations in the k_{IBA} values are noted. A plot of k_{IBA} versus % AQ from 20 % to 90 % AQ for these two systems, is analogous to plots that have been obtained in similar systems.[3-5]

The structure of the 1-alkyl-2-pyrrolidinones and the hydrolytic effectiveness of microemulsions containing these cosurfactants suggested that these materials may be functioning as nucleophiles in the hydrolysis of PNDP. However, experiments in our laboratory indicate that MP and iso-PP are not directly involved in the hydrolysis of PNDP in pH 9.2 borate buffer.

An empirical scale of solvent polarity for the 1-alkyl-2-pyrrolidinones tested as cosurfactants was established by dissolving Reichardt's dye (2,6-diphenyl-4-(2,4,6-triphenyl-N-pyridinio) phenolate) in equal volumes of the 1-alkyl-2-pyrrolidinones and borate buffer at pH 11.9. The shift in maximum absorbance of this dye is used to establish a scale indicating relative solvent polarity.[17,18] With the exception of VP, the pyrrolidinone polarity and the second order rate constants are similarly ordered.

Results of Luminescence Quenching Studies

The time-resolved luminescence technique developed by Infelta[19] was used to determine the average aggregation number (number of surfactant monomers/ aggregate; N) in microemulsions containing CTAB or CTAC /OIL/AQ and different cosurfactants (Table 3).

TABLE 3

AVERAGE AGGREGATION NUMBERS FOR 4.5%S/ 4.5%COS/ 1%OIL/ 90%AQ MICROEMULSIONS

	S	CoS	Oil	N
1.	CTAB	1-Butanol	$C_{16}H_{34}$	154 ± 19
2.	CTAB	MP	TOL	174 ± 30
3.	CTAB	CHP	t-BuTOL	269 ± 134
4.	CTAB	*N,N* -dimethylformamide	TOL	247 ± 12
5.	CTAB	*N,N* -diethylformamide	TOL	124 ± 17
6.	CTAB	*N,N* -diisopropylformamide	TOL	274 ± 137
7.	CTAC	Adogen 464	$C_{16}H_{34}$	740 ± 32

CONCLUSIONS

The N-alkyl-2-pyrrolidinones, as a class, are capable of clarifying CTAB microemulsions, and, therefore, they behave like alcoholic cosurfactants. Since the rates of phosphate ester hydrolysis are dependent on the specific nature of the N-alkyl group, and the pyrrolidinones do not function as nucleophiles in the hydrolysis of PNDP, we can infer that the pyrrolidinones are present at the reaction site, but are not directly involved in the hydrolysis. The function of the pyrrolidinone in the microemulsion may involve factors which only indirectly influence PNDP hydrolysis; the size and shape of the microdroplet and/or the nature of the aggregate interface.

Microemulsions containing 1-alkyl-2-pyrrolidinones as cosurfactants provide media in which the hydrolysis of phosphate esters is rapid. In our studies, larger k_{IBA} values are only observed when Adogen 464 is used as a cosurfactant. However, the oil dissolving power of microemulsions is greatly enhanced when 1-alkyl-2-pyrrolidinones are employed as cosurfactants; such systems are, therefore, very attractive as microreactors, in synthesis, and as decontamination media.

Our studies in CTAC and in CTAB microemulsions indicate that the time-resolved luminescence quenching technique is valid for most of the cases studied. The failure of the technique provides some evidence of a broad size distribution and/or very large aggregates.

ACKNOWLEDGMENT

Financial assistance for this project was provided by Geocenters Inc., and the U. S. Army Chemical Research, Development, and Engineering Center.

REFERENCES

1. Mackay, R. A.; Longo, F. R.; Knier, B. L.; Durst, H. D.*J. Phys. Chem.* **1987**, *91,* 861.

2. Knier, B. L.; Durst, H. D.; Burnside, B. A.; Mackay, R A.; Longo, F. R. *J. Soln. Chem.* **1988**, *17,* 77.

3. Burnside, B. A.; Szafraniec, L. L.; Knier, B. L.; Durst, H. D.; Mackay, R. A.; Longo, F. R. *J. Org. Chem.* **1988**, *53,* 2009.

4. Burnside, B. A.; Knier, B. L.; Mackay, R. A.; Durst, H. D.; Longo, F. R. *J. Phys. Chem.* **1988**, *92,* 4505.

5. Mackay, R. A.; Burnside, B. A.; Garlick, S. M.; Knier, B. L.; Durst, H. D.; Nolan, P. M.; Longo, F. R. *J. Disp. Sci. and Tech.* **1989**, *9,* 493-510.

6. Garlick, S. M.; Burnside, B. A.: Mackay, R. A.; Knier, B. L.; Durst, H. D.; Nolan, P. M.; Haddaway, K. G.; Longo, F. R. *Proc.U. S. Army CRDEC Chem. Def. Res.* **1988,** 3.

7. *M-Pyrol ® Handbook;* GAF Corp.; New York, **1985**, pp vii - 31.

8. *M-Pyrol ®* Pamphlets; GAF Corp.; Wayne, New Jersey **1986**.

9. *N-Methylpyrrolidone (NMP);* BASF Corp.; West Germany, **1985**.

10. Kirk, J. S., U. S. Patent # 2,872,277 February 3, 1959.

11. Data from MSDS supplied by BASF Corp., GAF Corp., and Virginia Chemicals, Inc.

12. Zaugg, H. E.; Horrom, B. W.; Borgwardt, S. *J. Am. Chem. Soc.* **1960,***82,* 2895.

13. EAI Corporation, P.O. Box 764, Toele, UT. 84074

14. Lin, C-T.; Böttcher, W.; Chou, M.; Creutz, C.; Sutin, N. *J. Am. Chem. Soc.* **1976,** *98,* 6536-6544.

15. Garlick, S. M.; Mackay, R. A ; Durst, H. D.; Longo, F. R. *J. Coll. Int. Sci.* **1989**, *132.*

16. R.A.Mackay and C.Hermansky, *J. Phys. Chem.* **1981,** *85,* 739.

17. Dimroth, K.; Reichardt, C.; Siepmann, T.; Bohlmann, F. *Ann.* **1963**, *661,* 1.

18. Zachariasse, K. A., Van Phuc, N. Kozankiewicz, B *J. Phys.Chem.* **1981**,*85,* 2676.

19. Infelta, P. P.; Gratzel, M., Thomas, J. K. *J. Phys. Chem.* **1974,** *78,* 190.

BLANK

Electrochemical Impedance Spectroscopic Study of the Penetration of CARC by DS-2 and by Microemulsions

P. L. Cannon Jr.[a], F. R. Longo[a,b] and S. M. Garlick[b,c]

a. U. S. Army CRDEC APG MD 21010-5423
b. Drexel Unversity Philadelphia PA 19104
c. GeoCenters Inc, Fort Washington MD 20744

Abstract

Employing a combination of alternating current (AC) circuit theory and electrochemical techniques we have studied the penetration rates of DS-2 and six microemulsions through sand colored, aliphatic polyurethane chemical agent resistant coating (CARC). The microemulsions were prepared with 1-cyclohexyl-2-pyrrolidinone (CHP) as cosurfactant. The rate at which these formulations penetrate the CARC is dependent upon the emulsifier ratio, E (the mass ratio of surfactant to cosurfactant). In addition, the E-value controlled the rate of degradation of the intact coating as indicated by the change in pore resistance, the number of time constants and the absence or presence of Warburg impedance.

1.0 Introduction to Electrochemical Impedance Spectroscopy

Electrochemical impedance spectroscopy (EIS) permits the electrochemist to follow the penetration of an aggressive reagent through a protective coating in "real time". In addition, the time of coating failure and the initiation of corrosion can also be determined by this technique. EIS provides information even in media of low conductivity where classical direct current (DC) methods cannot be applied.[1,2]

The flow of AC current is more complex process than flow of DC current. The AC current is governed by resistors, capacitors and inductors all of which affect the AC

current flow. Also, the impedance is also frequency dependent . The total resistive effect of all of the elements in a circuit is the ciruit impedance measured in ohms. These elements can cause the applied sinusoidal potential to be out of phase with the measured AC current waveform; however, the applied potential and the current waveforms will remain in phase when a circuit consists of purely resistive elements.

In the systems in which we have studied the total impedance, |Z|, is dependent upon the capacitive and resistive elements in the circuit. Often, the total impedance is represented as a vector with real, Z', and imaginary, Z", components:

$$|Z| = [(Z')^2 + (Z'')^2]^{1/2}$$

The shift in the phase between the responding current and applied potential is equal to -Z"/Z'.

We have examined CARC protected, cold rolled steel specimens using EIS. For purposes of explanation we shall compare uncoated and coated specimens.
An electric double layer exists between an electrolyte and a clean metal surface. For an anode (positively charged electrode) the double layer consists of an electron deficiency at the metal surface and a layer of anions which are held rigidly. See Figure 1. This double layer of charge is referred to as the Helmholtz double layer and is analogous to a parallel plate capacitor. A coated metal specimen represents an additional capacitance and that capacitance, and that capacitance will increase as an aggressive reagent penetrates. At the same time, the pore resistance decreases. The determination of the magnitudes of the various elements in the experimental cell are diagnostic of the state of the protective coating and the metal specimen.

Equivalent Circuit

The analysis of EIS data requires the design of an electric circuit model which corresponds to the electrochemical system of interest. Uncoated and coated metal specimens, when subjected to an AC potential source, can be modelled by the electric circuits depicted in Figures 2 and 3. The applied sinusoidal perturbation, which overlays the open circuit potential, is influenced by the the resistive and capacitive properties of the cell. The resultant current waveform is characterized and determined by the amplitude, the phase shift, and the frequency. (See Equation 1 and Figure 4)

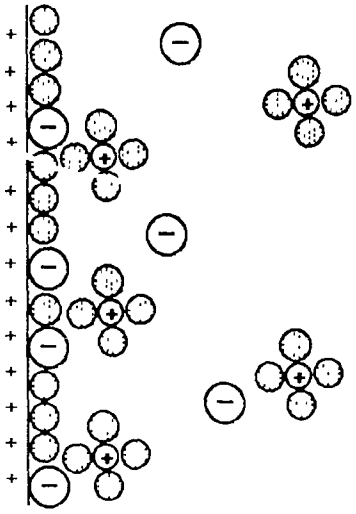

Figure 1 The electrode solution double layer

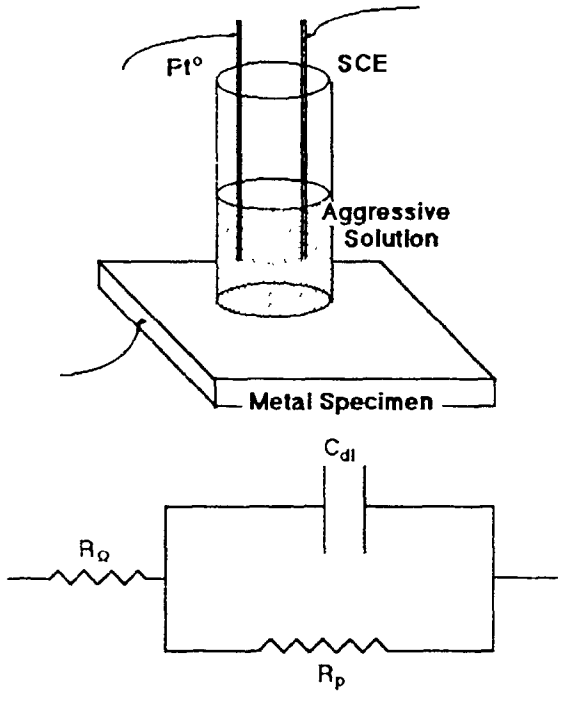

Figure 2 The cell and the equivalent circuit for the electrochemical impedance studies of an uncoated metal specimen

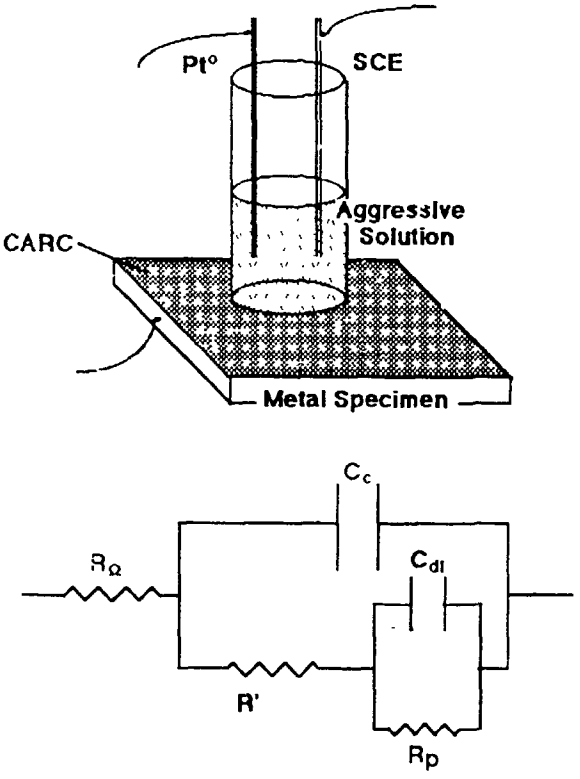

Figure 3. The cell and the equivalent circuit for the electrochemical impedance studies of a coated metal specimen

$$I = A \sin(\omega t + \Theta) \qquad \text{Eq 1}$$

where I = instantaneous current; A = maximum amplitude; ω = frequency (radians per second); t = time; and Θ= phase shift (radians).
In DC applications Ohm's Law, E = IR, applies; however, when AC signal is applied,R, the resistance , is replaced by Z, the impedance; the magnitude of I varies with shifts in the phase angle.

Various analyses of the data allow the determination of the real and imaginary components of the impedance, Z', Z" and the current phase shift. Values of the capacitances and resistances calculated from the data permit the determination of the extent of penetration of the coating and the charge transfer resistance of the under lying metal. By monitoring the capacitance it is also possible to determine the extent of solvent absorbtion by the coating.

DS-2 and Microemulsions

The official decontamination solution of the U. S. Army is DS-2, which is prepared from 70% diethylenetriamine, 28% methyl cellosolve and 2% sodium hydroxide. Our group (Applied Chemistry Branch, Chemical Division, Research Directorate, CRDEC APG MD) has investigated various microemulsions as possible replacements for DS-2.[4-7] Microemulsions are systems in which microdroplets of oil are stabilized by surfactants. In addition, medium length alcohols, N,N-dialkylformamides or N-alkylpyrrolidinones may be used as clarifying agents or "cosurfactants". Microemulsions can physically catalyze or inhibit chemical reactions by compartmentalization or concentration of reactants and products. Appreciable quantities of both polar and non-polar substances dissolve in these systems. Hence, microemulsions serve as reactors for chemical species which ordinarily could not be present in the same phase and this is the property which makes microemulsions strong candidates for decontamination systems: many chemical warfare agents are non-polar while the degradation reagents are generally polar; in microemulsions polar and non-polar reagents are brought into intimate contact and chemical reaction rates are enhanced.

The components of DS-2 and various microemulsions may penetrate, dissolve and/or degrade the protective coatings (CARC) which are normally applied to vehicles and

other equipment. Therefore,we have designed a program for the electrochemical examination of the effect of DS-2 and microemulsion contact with CARC-protected steel.

Materials and Procedures

The DS-2 was received as a gift from Dr. Frank Block. Cetyltrimethylammonium chloride (CTAC) was purchased from Eastman Kodak as a dry chemical powder and as a 29% aqueous solution (Arquad 16-29) from Akzo Chemie America Sodium tetraborate decahydrate was purchased from Fischer. (aqueous 0.03 M borate buffer solutions designated as AQ were prepared from deionized, glass distilled water. The 1-cyclohexyl-2-pyrrolidinone (CHP) containing less than 1 % H_2O was received as a gift from the Virginia Chemicals Inc and from the GAF Corporation. A sample of 99+ % n-hexadecane was obtained from the Sigma Chemical Company. The six μE's which were employed were composed of varying amounts of CTAC, CHP, HEX and AQ. See Table 2.

The coated metal used in this investigation was a cold rolled-steel that had been pretreated with zinc phosphate before the application of the epoxy primer and the polyurethane topcoat. The dry film thickness of the primer was 0.001 inch (Military Specification MIL-P-52192). The topcoat was a 0.002 inch film sand colored CARC in conformance with MIL-C-46168.

The body of the corrosion cell consisted of a size 9 glass O-ring joint clamped to the coated side of the experimental sample. A platinum wire counter electrode and an EG&G PARC G0115 saturated calomel reference electrode inserted in a G0114 reference electrode bridge tube were positioned close to the sample surface through the open end of the O-ring joint. An EG&G PARC G0100 vycor tip, held in place with heat shrunken Teflon™, completed the reference electrode bridge tube assembly. The reference electrode bridge tube was then filled wit a saturated KCl solution. At this point either DS-2 or a microemulsion was introduced, half-filling the cell body. The open circuit potential was then established on an area of 1.54 cm^2.

The experimental system hardware consisted of an EG&G PARC M 173D/276 potentiostat/interface-current response module and an M 5206 phase sensitive lock-in amplifier connected through an IEEE-488 interface bus to an Apple //e Microcomputer.

An Apple Duodisk™ drive was used to manipulate the EG&G PARC M368-1 Impedance Software and data storage disk.

The perturbation signal amplitude was 5mV or 10mV rms. The integration time was set at five cycles for each frequency. The frequency range studied was 1 mHz to 100 kHz by a combination of three measurement methods. Below 1Hz the FFT technique was employed for the measurements. Above 10Hz phase-sensitive lock-in amplification was employed. Between 1 and 10Hz a combination of the FFT and lock-in methods was used.

Results and Discussion

A graphical presentation of EIS data as log|Z| versus log frequency results in a Bode plot in which the value of |Z| extrapolated to the lowest frequencies is a measure of the condition of the coating. When the value of |Z| = or > 10^7 ohm the coating is considered to be intact and protective; when |Z| is below 106 ohm the coating is considered to be in failure. Figure 4 depicts the changes which occur when a CARC protected sample of steel is expcsed to a microemulsion for a period of 63 days. See Entry 7, Table 1. On the 1st and 14th days the CARC is still intact as the values of |Z| exceed 10^7; after 23 days the CARC is in failure as |Z| at low frequencies is less than 10^7. The decrease in impedance is due to the drop in the pore resistance as the microemulsion penetrates the CARC.

Figure 5 is another Bode plot. In this case the penetrant microemulsion (See Entry 6, Table 1) contains a higher fraction of CHP. It is very clear that the coated steel specimen is in failure at 63 days as the low frequency value of |Z| is ~ 10^6.

A plot of the phase angle Θ versus log frequency is called a Bode phase plot. When a coating is intact the applied potential and the current should be out of phase by 90°. When the coating is completely compromised it should behave as a pure resistance with the potential and the current in phase; Θ = 0. The Bode phase plot of Figure 6 demonstrates that a CARC coated steel specimen is severely impaired after only 8 days of exposure to a microemulsion as Θ has decreased from ~80° to ~15°. At 63 days the coating is in complete failure as Θ ≈ 0°. See Entry 4, Table 1 and Table 2 for microemulsion composition.

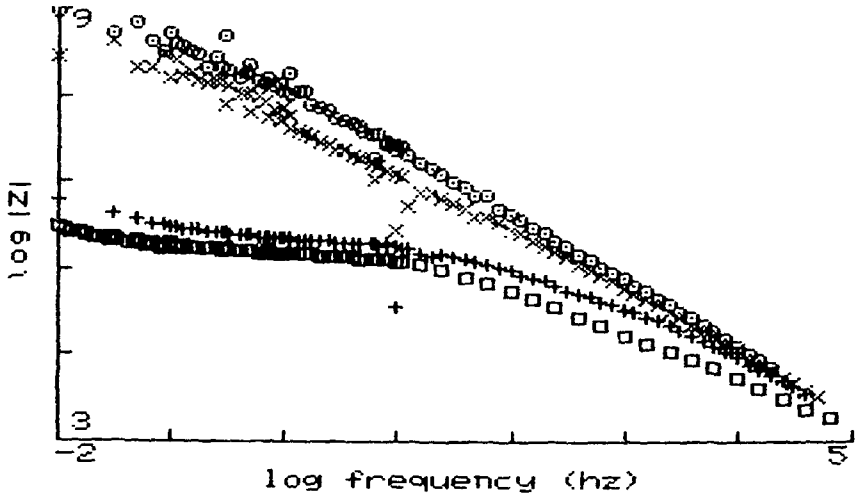

Figure 4. Bode plots of data taken after 1, 14, 23 and 63 days exposure (to μE d, Table 2) show a continual decease in the low frequency impedance.

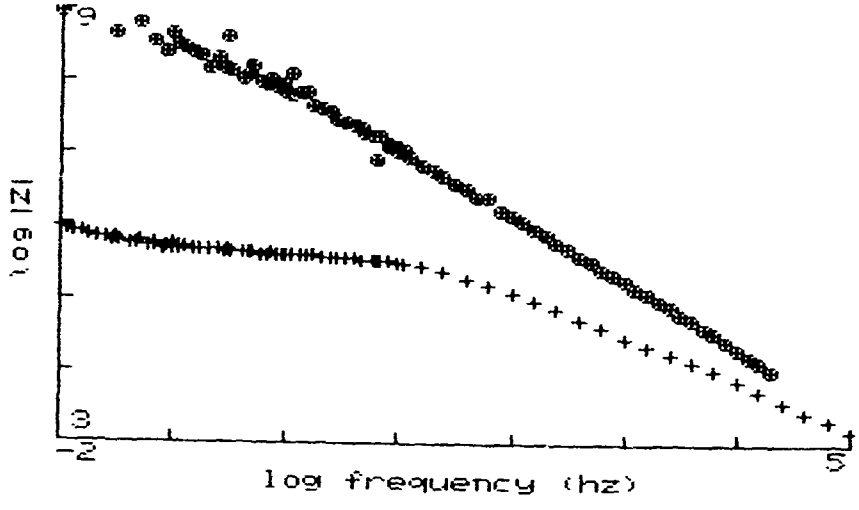

Figure 5. Bode plots after 1 and 63 days indicate that the μE penetrates and degrades the polyurethane topcoat.

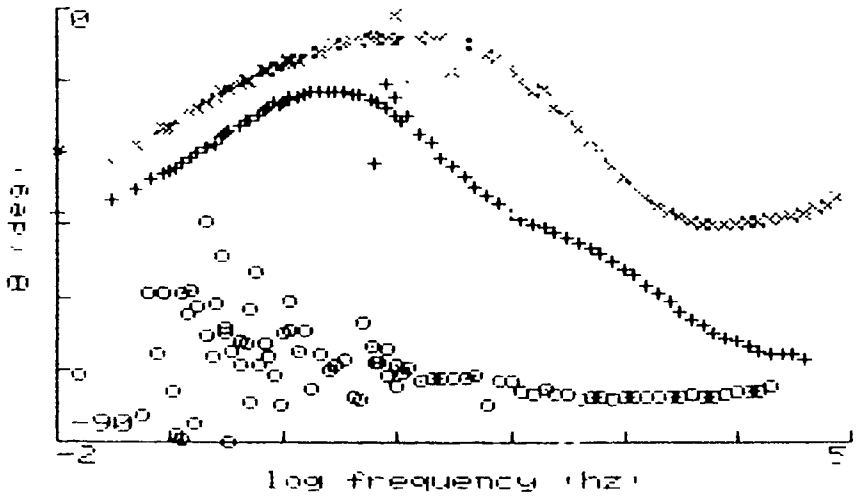

Figure 6. Bode phase plots prepared from data taken after 0, 8 and 63 days illustrate the capacitive behavior of the CARC before 1 day has elapsed and the eventual compromise of the CARC caused by the μE. See μE a, Table 2.

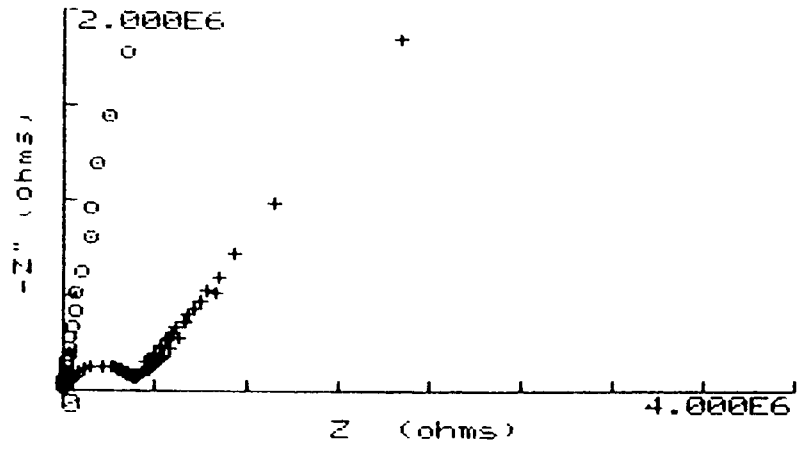

Figure 7. Complex plane plots indicate Warburg diffusion after 63 days exposure to a μE . See μE d, Table 2.

Table 1. EIS CARC Penetration Studies

Medium	Ω, 0 da	Ω n da	Warburg Impedance	%CHP
1. DS-2	10^8	10^7; 3	yes	---- ----
2. Dist H2O	10^9	10^8; 3	no	---------
3. Sea Water	10^8	10^8; 5	no	---------
4. µE 10/90[a]	10^9	10^7; 7	yes	51.6
5. µE 20/80[b]	10^9	10^7; 9	yes	45.6
6. µE 30/70[c]	10^8	10^7; 14	yes	40.4
7. µE 40/60[d]	10^9	10^6; 23	no	34.8
8. µE 60/40[e]	10^8	10^8; 29	no	17.0
9. µE 60/40[f]	10^{10}	10^8; 28	no	18.5

Table 2. Compositions of CTAC / CHP / HEX / AQ microemulsions tested in the penetration studies. The pH range of the borate buffer is 9.2 - 9.4.

	% S	% CoS	E ratio	% TOL	% AQ
a.	5.7	51.6	0.11	6.4	36.3
b.	11.4	45.6	0.25	6.3	36.7
c.	17.3	40.4	0.43	6.4	35.9
d.	23.2	34.9	0.66	6.4	35.5
e.	25.6	17.0	1.50	2.2	55.2
f.	27.7	18.5	1.50	5.1	48.7

The Nyquist or Cole-Cole presentation of the data involves a plot of the imaginary component of the impedance, Z", versus the real component, Z. For an uncompromised coating the plot should result in a semicircle with its diameter collinear with the abscissa. (The semicircle abscissa intersections correspond to ohmic resistance and to the sum of the ohmic and polarization resistances. When the coating is compromised the semicircle does not form completely. Instead, a spike is produced at 45o. This is indicative of CARC failure accompanied by corrosion of the underlying metal (Warburg impedance. Figure 7 demonstrates a Nyquist plot with Warburg impedance obvious after 63 days exposure to a mE. (See Entry 7, Table 1 and Table 2 for mE composition.)

We have performed penetration studies on many CARC treated steel specimens. The results of our studies are summarized in Table 1 where the CARC failure times are given; the compositions of the mE's are included in Table 2. It is obvious that failure times decrease as the percentage of CHP increases. We plan to continue our penetration studies in order to define and discover the parameters and empirical rules related to CARC failure.

References

1. EG&G PARC Application Note AC-1, Basics of AC Impedance Measurements, Applied Instruments Group, Princeton NJ 08540, **1983**

2. EG&G PARC Application Note Corr 1, Basics of Corrosion Measurements, Applied Instruments Group, Princeton NJ 08540, **1983**

3. Equivalent Circuit Analysis of the Impedance Response of Semi-conductor/Electrolyte/Counter Electrode Cells, J. F. McCann and S. P. S. Badwal, J Electrochem Soc **1982***129* 551

4. Iodosobenzoate Catalyzed Hydrolysis of 4-Nitrophenyl diphenyl phaosphate in a CTAB Microemulsion R. A. Mackay; F. R. Longo; B. L. Knier, H. D. Durst. *J. Phys Chem.*, **1987** *91* 861.

5. Catalytic Hydrolysis of Phosphate Esters in Microemulsions. B. L. Knier, H. D. Durst, B. A. Burnside, and F. R. Longo. J. Solution Chem. **1988** *17* 77

6. Catalytic Hydrolysis of Phosphate Esters in Microemulsions III. Analysis of the Hydrolysis Products of p-Nitrophenyl diphenyl phosphate via ^{31}P NMR. B. A. Burnside, L. L. Szafraniec, B. L. Knier, H. D. Durst, R. A Mackay, and F. R. Longo. J. Org. Chem., **1988** *53* 2009

7. Inherent Bias in Nonlinear Least Squares Analysis of tFirst Order Kinetic Data. B. L. Knier and F. R. Longo U S Army CRDEC Aberdeen Proving Ground, CRDEC-TR-88157, June **1989**.

8. Catalytic Hydrolysis of Phosphate Esters in Microemulsions. V. The Effect of Cosurfactants, Mackay, R.A., B.A. Burnside, S.M. Garlick, B.L. Knier, H.D. Durst, P.M. Nolan, K.G. Haddaway, and F.R. Longo. J. Disp. Sci. & Tech **1988** *9* 493.

BLANK

STUDIES IN MICROEMULSIONS SIMILAR TO THE MULTIPURPOSE CHEMICAL/BIOLOGICAL DECONTAMINANT

Stephanie M. Garlick,[1,3] H. Dupont Durst,[2] Keith G. Haddaway,[1]
Raymond A. Mackay,[2] Frederick R. Longo[2,3]

[1] Geo-Centers, Inc.
Fort Washington, MD 20744

[2] U. S. Army Chemical Research, Development, and Engineering Center.
Aberdeen Proving Ground, MD 21010-5423

[3] Drexel University
Philadelphia, PA 19104

Abstract

We have measured the second order rate constants for the *o* - iodosobenzoate catalyzed hydrolysis of *p* - nitrophenyldiphenyl phosphate (PNDP) in microemulsions containing cetyltrimethylammonium chloride as surfactant, tetraalkylammonium chlorides and bromides as cosurfactants, tetrachloroethylene as the oil, and 0.03 M borate buffer as the aqueous component. Pseudo-ternary phase maps have been prepared for systems containing tetrabutylammonium chloride and Adogen®464, mass ratio of 8.2. We have also measured the first order rate constants for the catalyzed hydrolysis of PNDP in borate buffer as a function of % TBACl.

Introduction

The MCBD (Multipurpose Chemical/Biological Decontaminant) microemulsion[1] has been investigated as a potential decontamination medium. This microemulsion contains 16.5 %CTAC, 11.6 %TBAOH, 1.4 %Adogen® 464, 53.0 %H_2O, and 7.5 % PERC. Since the pH of this system is >13.5, it is necessary to add ~0.25 M H_3BO_3 to adjust the pH to 11.2. However, if the pH falls below ~ 11 cetyltrimethylammonium borate salts precipitate. Fichlor (sodium salt of dichloroisocyanuric acid) is added to oxidize H, HD, and VX and IBA is added to hydrolyze the G agents.[2]

Tetraalkylammonium (C_4-C_{10}) hydroxides and halides (TAAX) function as phase-

transfer catalysts in organic synthesis,[3] and have been employed as hydrotropes[4] to increase the aqueous solubility of organic compounds.[5] It has previously been demonstrated that, while TAAX function as cosurfactants in CTAC/Ad/ HEX/AQ [6] systems, tetraalkylammonium (C_4-C_{10}) ions do not aggregate to form micelles.[7-9] Instead, TAAX may increase the hydrolysis rate of phosphate esters by: providing an hydrophobic environment for substrate and nucleophile to form a tight ion-pair;[7] forming nonmicellar aggregates that could be catalytically active;[8] simple salt effects;[10] actuating solvent effects.[4,11]

Since the MCBD formulation is complex and unstable[12] (salts precipitate on standing), we attempted to simplify the microemulsion methodology. Simplification techniques included: substituting other tetraalkylammonium halides for TBAOH and Ad; determining the minimum concentration of TBAX necessary for microemulsion formation and for good hydrolysis rates ($\geq 10\ s^{-1}M^{-1}$) of PNDP; determining the dependency of the microemulsion formulation on emulsifier (E) ratio and % AQ; acsertaining the importance of Ad. Tetraalkylammonium ions (C_1-C_8) containing four identical alkyl groups were employed in this study.

Materials

Cetyltrimethylammonium chloride (CTAC) was purchased from Eastman Kodak Co. as a dry chemical and was obtained as a 29 % aqueous solution (Arquad 16-29) from Akzo Chemie America. Borate buffer (0.03 M) was added to the aqueous CTAC solution before use. The cosurfactants, tetramethylammonium chloride (TMACl), tetraethylammonium chloride (TEACl), tetra-*n*-propylammonium chloride (TPrACl), tetra-*n*-butylammonium chloride (TBACl) and bromide (TBABr), tetra-*n*-pentyl ammonium bromide (TPABr), tetra-*n*-hexylammonium chloride (THACl) and bromide (THABr), tetra-*n*-octylammonium bromide (TOABr) and Adogen® 464 (Ad) were purchased from Eastman Kodak and Aldrich Chemical companies. Tetra-*n*-butyl ammonium hydroxide (TBAOH; 40 % in H_2O), boric acid (H_3BO_3), and tetrachloroethylene (PERC), were purchased from Aldrich.

Buffer solutions (AQ), 0.03 M in sodium tetraborate decahydrate, pH 9.2, were prepared using glass distilled water. The catalyst, *o*-iodosobenzoic acid (IBA), was obtained from Sigma, converted to the sodium salt, and dissolved in borate buffer prior to use. The substrate, PNDP, was prepared as a custom synthesis by Biomol Research Laboratories, Inc.

Experimental Procedure

The discussion of general experimental methods, the acquisition and analysis of rate data and the determination of k_{IBA} and k_{OH} have previously been discussed in great detail.[6,13-14] The computer programs used to collect and analyze the rate data were developed by Dr. B. L. Knier (EAI Corporation, P.O. Box 764, Tooele, UT. 84074).

Results of Phase Map Studies

Because TBAOH was received as a 40 % aqueous solution, it was necessary to determine pseudo-ternary phase maps for CTAC/ (TBACl,Ad) /PERC/AQ systems. A

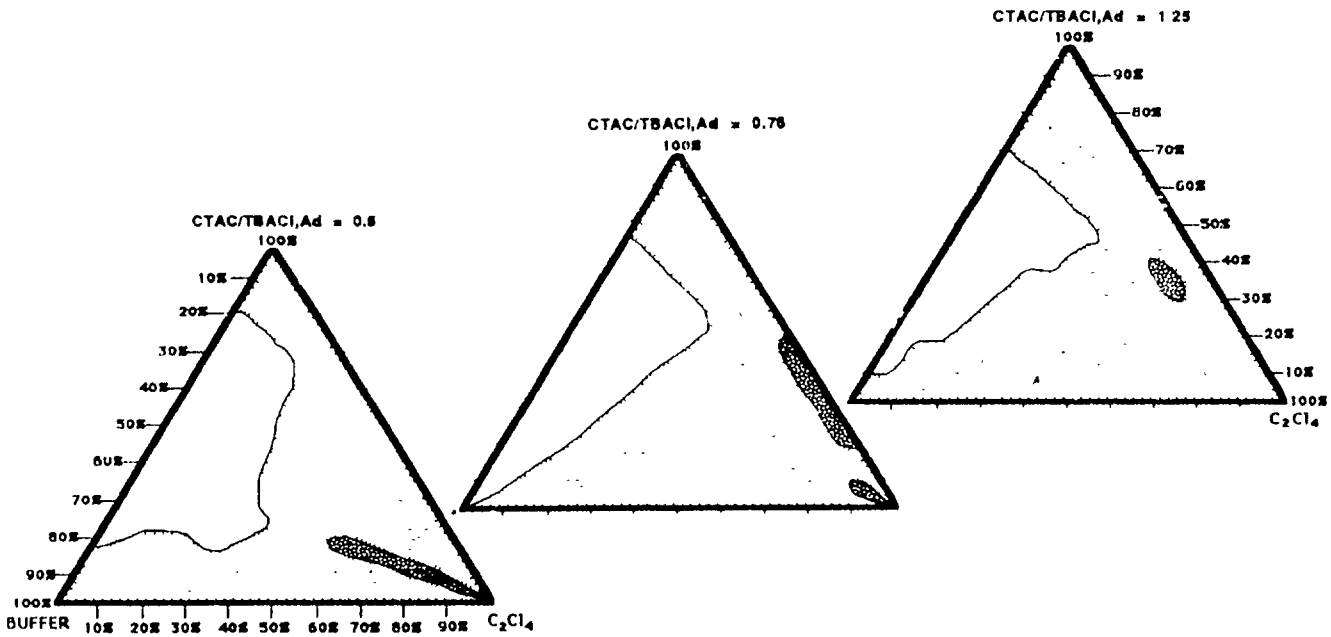

Figure 1. Pseudo-ternary phase maps for CTAC / TBACl, Ad / PERC / AQ systems. Regions are clear ○, gel ◎, and turbid ○.

mixture of two hydrotropes, TBACl and Adogen® 464, at a mass ratio of 8.2, TBACl/Ad, was employed as a cosurfactant. The E ratio in the MCBD microemulsion is 1.26. Pseudo-ternary phase maps were constructed in CTAC/ (TBACl,Ad) /PERC/AQ systems at E ratios of 0.5, 0.76, and 1.25 (Figure 1). Clear regions, whose areas seem to be independent of E ratio, extend from 20 % to 80 % S and from low to moderate (50 %) oil. Gel regions occur in the low % AQ, high % oil portions of the maps. The remaining portions of the maps are turbid.

Results of Kinetic Studies

We have measured the second order rate constants, k_{IBA}, for the IBA catalyzed hydrolysis of PNDP in CTAC/ (TBACl,Ad) /PERC/AQ microemulsions. Values of k_{IBA} measured at an E to oil ratio of ~ 4, (first section;Table 1) increase from 4.99 $s^{-1}M^{-1}$ to 6.37 $s^{-1}M^{-1}$ at 50 % AQ and 10 % oil, and from 5.90 $s^{-1}M^{-1}$ to 8.05 $s^{-1}M^{-1}$ at 60 % AQ and 8 % oil as the E ratio increases from 0.50 to 1.25. As % AQ increases from 20.0 % to 79.7 % at an E ratio of 0.76 (second section;Table 1), k_{IBA} values increase from 4.53 $s^{-1}M^{-1}$ to 12.5 $s^{-1}M^{-1}$.

TABLE 1

K_{IBA} VALUES FOR PNDP HYDROLYSIS IN CTAC/ (TBACL,Ad) /PERC/AQ SYSTEMS

%S	%CoS	E Ratio	%AQ	%Oil	k_{IBA}($s^{-1}M^{-1}$)
In Order of Increasing E Ratio					
13.3	26.7	0.50	50.0	10.0	4.99 ± 0.18
17.3	22.8	0.76	49.9	10.0	6.24 ± 0.21
22.1	18.2	1.25	49.7	10.0	6.37 ± 0.05
10.7	21.3	0.50	60.0	8.0	5.90 ± 0.12
13.8	18.4	0.76	59.8	8.0	7.05 ± 0.23
17.7	14.7	1.25	59.6	8.0	8.05 ± 0.13
In Order of Increasing % AQ					
28.0	36.0	0.76	20.0	16.0	4.53 ± 0.09
18.4	29.6	0.76	40.0	12.0	4.43 ± 0.12
17.3	22.8	0.76	49.9	10.0	6.24 ± 0.21
13.8	18.4	0.76	59.8	8.0	7.05 ± 0.23
6.9	9.4	0.76	79.7	4.0	12.5 ± 0.83

Since previous kinetics studies in the MCBD microemulsion were completed at pH 11.2 with different substrates,[1] it was necessary to measure k_{IBA} for the hydrolysis of PNDP in the MCBD microemulsion at pH ≈11 for comparison. A value for k_{IBA} of 17.6 $s^{-1}M^{-1}$ was obtained. Rate constants measured in several additional systems are included in Table 2.

First order rate constants, k_{obsd}, for the catalyzed ($1x10^{-3}$ [IBA], pH 9.2) hydrolysis of PNDP in 0.03 M borate buffer containing TBACl, increase from 4.63×10^{-4} s^{-1} at 0 mass % TBACl to a constant value of ~ 12×10^{-4} s^{-1} at a mass % TBACl > 4 or 5 % (Table 3). Values of k_{obsd} versus % TBACl are plotted in Figure 2.

Approximately 50 mg PNDP was added to 5 mL of 0.03 M borate buffer at pH 9.4 and 11.2 with and without 13 % TBACl. These solutions were incubated at room

TABLE 2

A COMPARISON OF K_{IBA} VALUES OBTAINED IN SEVERAL MICROEMULSIONS

% CTAC	% CoS	% Oil	% AQ	pH	k_{IBA} ($s^{-1}M^{-1}$)
16.5	11.6 TBAOH 1.4 Ad	7.5 PERC	63.0	11.3	17.6
16.5	11.6 TBACl 1.4 Ad	7.5 PERC	63.0	9.4	10.1
21.2	1.8 Ad	9.6 PERC	67.4	9.4	< 7
15.9	4.8 TBACl	8.5 PERC	70.8	9.4	13.3
---	13.0 TBACl	----	87.0	9.4	1.7
8.0 CTAB	11.6 TBAOH 8.0 MP	4.0 TOL	68.4	11.2	10.3

TABLE 3

VALUES OF k_{obsd} FOR THE HYDROLYSIS OF PNDP IN 0.03 M BORATE BUFFER

% TBACl	[TBACl]	k_{obsd} x 10^{+4} (s^{-1})
0	0	4.63
0.5	0.017	4.52
1.0	0.035	6.08
2.0	0.069	7.03
4.0	0.138	12.4
5.0	0.173	12.7
7.0	0.242	11.2
9.0	0.311	11.8
11.0	0.380	11.1
13.0	0.449	11.5
15.0	0.518	12.0

temperature, and aliquots (1mL) of supernatant were removed at 10, 60, and 180 minutes, diluted with 1 mL of water, and centrifuged. Absorbances were recorded at 402 nm. Results indicate that the uncatalyzed rate of hydrolysis of PNDP is similar at pH 9.4 and at pH 11.2 in the absence of TBACl. However, when 13 % TBACl is added to borate buffer at pH 9.2, the hydrolysis rate of PNDP increases. At pH 11.2, the rate increase is even more dramatic. The reaction between PNDP and OH^- seems to be accelerated by TBACl. Similar results have been reported for other TAAX.[7-9]

Solutions of 0.03 M borate buffer containing ≤ 4 to 5 mass % of either THABr or TBABr and 3 x 10^{-5} M PNDP were turbid.[12] However, results in Table 3 and Figure 2

FIGURE 2

PSEUDO FIRST ORDER RATE CONSTANTS (TABLE 3) VERSUS % TBACl

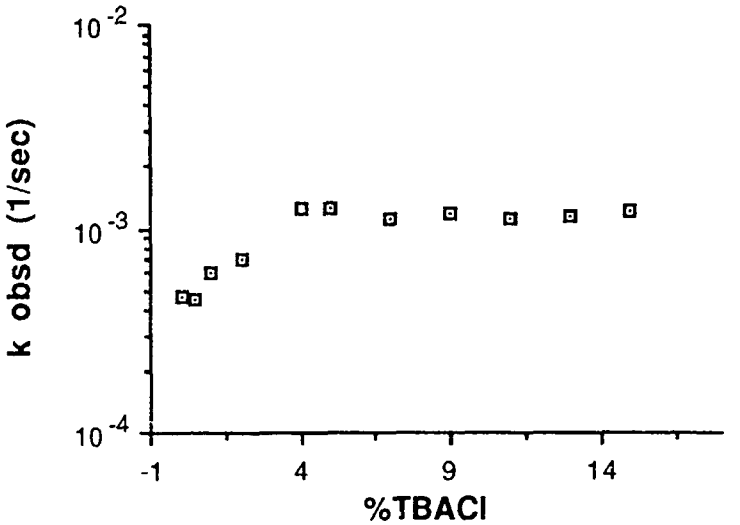

indicate that second order rate constants could be measured in systems containing 15.9 % CTAC/4.8 % TAAX/8.5 % PERC/70.8 % AQ (Table 4). The k_{IBA} values are

~ constant and vary from 13.3 $s^{-1}M^{-1}$ to 9.4 $s^{-1}M^{-1}$ for the cosurfactants, TEACl (C_2) to THABr (C_6) in the absence of Ad. Due to the low solubility of TOABr in water, only microemulsions containing ≤ 2.5 % TOABr could be prepared. In fact, gels form at higher % TOABr. Clear media could not be prepared with TMACl.

TABLE 4

SECOND ORDER RATE CONSTANTS IN CTAC/TAAX/PERC/AQ SYSTEMS; pH 9.2

% S	CoS	% CoS	% AQ	% Oil	k_{IBA} ($s^{-1}M^{-1}$)
15.9	TMACl	4.8	70.8	8.5	----
15.9	TEACl	4.8	70.8	8.5	11.8 ± 1.8
15.9	TPrACl	4.8	70.8	8.5	13.0 ± 0.15
15.9	TBACl	4.8	70.8	8.5	13.3 ± 0.10
15.9	TBACl, Ad	4.8	70.8	8.5	13.8 ± 0.22
16.5	TBACl, Ad	13.0	63.0	7.5	10.1 ± 0.06
17.6	TBABr	3.1	70.8	8.5	12.0 ± 0.26
15.9	TBABr	4.8	70.8	8.5	12.7 ± 0.14
15.9	TPABr	4.8	70.8	8.5	10.2 ± 0.17
15.9	THACl	4.8	70.8	8.5	10.9 ± 0.33
15.8	THABr	1.1	75.2	7.9	10.7 ± 0.22
15.9	THABr	4.8	70.8	8.5	9.4 ± 0.19
15.9	TOABr	0.6	75.5	8.0	10.2 ± 0.05
15.8	TOABr	1.4	74.9	7.9	10.4 ± 0.35
16.4	TOABr	2.5	72.6	8.5	10.8 ± 0.22

CONCLUSIONS

Results of phase map studies indicate that the MCBD microemulsion is suitable for kinetics studies when the E ratio equals 0.50, 0.76, or 1.26. Formulations tested have been reasonably fluid, and can be prepared even when Ad is not included.

Second order rate constants for the catalyzed hydrolysis of PNDP (Table 1) increase as E ratio increases at constant % AQ and % oil. Also, increasing % AQ at constant E ratio increases k_{IBA} values. In similar systems,[14,15] the rate constants generally increase as % AQ increases.

Since TAAX (C_2-C_8) are only slightly soluble in water,[12] and clarify S/Oil/Aq systems, they are probably functioning as cosurfactants in CTAC/TAAX/PERC/AQ systems. It has previously been reported that tri-*n* -octylethyl ammonium bromide (TEABr), chloride (TEACl), and tri-*n* -octylethylammonium mesylate (TEAMs) comicellize with CTAX.[11]

Second order rate constants for the catalyzed hydrolysis of PNDP in 15.9 % CTAC/ 4.8 % TAAX/8.5 % PERC/70.8 % AQ (Table 4) do not depend on the N-alkyl substituents or the TAAX cosurfactants. Slightly larger rate constants, however, are obtained when the counterion is chloride as opposed to bromide ion.

In Table 4, as % TBACl,Ad increases from 4.8 % to 13.0 % at decreasing % AQ, the k_{IBA} value decreases from 13.8 $s^{-1}M^{-1}$ to 10.1 $s^{-1}M^{-1}$. Similarly, k_{IBA} decreases slightly as % THABr increases from 1.1 % to 4.8 %, Also, as % TOABr increases from 0.6 to 2.5 % at approximately constant % S, % AQ, and % oil, k_{IBA} values do not change. The complete function of the tetraalkylammonium ions therefore, cannot be clearly established in microemulsion media.

First order rate constants, k_{obsd}, for the catalyzed hydrolysis of PNDP at pH 9.2 in 0 03 M borate buffer are independent of % TBACl above ~ 4 to 5 % (Table 3). Since 3 x 10^{-5} M PNDP aqueous solutions appear turbid when TBACl < 4 % , and since conductivity and kinetics studies indicate that tetraalkylammonium (C_2-C_8) ions do not aggregate to form micelles,[7-9] it can be concluded that, in non-micellar solutions, tetraalkylammonium ions may function as hydrotropes for PNDP.

We may, therefore, infer that, since rates of phosphate ester hydrolysis in aqueous solutions of hydrophobic ammonium ions surpass rates obtained in micellar CTAB,[7,8,16] and since tetraalkylammonium ions (C_2-C_8) do not form micellar aggregates,[7-9] they may instead form sub-micellar aggregates that provide an environment suitable for uncharged substrate (PNDP) and anionic catalyst (IBA) to interact at close proximity.

In conclusion, studies in CTAC/TAAX/PERC/AQ systems have provided us with the following information: tetraalkylammonium halides (C_2-C_8) may be substituted for TBACl as cosurfactants; the concentration of TBAX necessary for microemulsion formation and for reasonable hydrolysis rates of PNDP seems to be independent of the nature of the N-alkyl groups in tetraalkylammonium ions (C_2-C_8), however gels form at % TOABr > 2.5 %. Therefore, a maximum % TAAX (C_2-C_7) equal to 4.8 % is satisfactory. At an E ratio of 0.76, reasonable rate constants are obtained for the hydrolysis of PNDP in fluid, non-viscous, microemulsion media. Also, if sufficient mixing time is alloted for microemulsion formation, it is probably not necessary to include Adogen®464 as an additional cosurfactant. Since other work (this conference) indicates that isopropanol decreases the rate constant for PNDP hydrolysis, and is included in the industrial formulation of Ad, it is undesirable to include Ad.

ACKNOWLEDGMENT

Financial assistance for this project was provided by Geocenters, Inc., and the U. S. Army Chemical Research, Development, and Engineering Center.

REFERENCES

1. Developed by J. R. Hovanic, U. S. Army CRDEC, APG., MD 21010-5423.

2. "Chemical Agent Data Sheets" Volume 1, Edgewood Arsenal Special Report, U. S. Army Report # EO-SR-74001, December 1974, pp 29-48, pp 167 179.

3. Herriott, A. W.; Picker, D. *J. Am. Chem. Soc.* **1975,** *96,* 2345.

4. Neuberg, C. *Biochem. Z.* **1916,** *76,* 107.

5. Pearson, J. T. *J. Coll. Int. Sci.* **1971,** *37,* 509.

6. Mackay, R. A.; Burnside, B. A.; Garlick, S. M.; Knier, B. L.; Durst, H. D.; Nolan, P. M.; Longo, F. R. *J. Disp. Sci. and Tech.* **1983,** *9,* 493.

7. Okahata, Y.; Ando, R.; Kunitake, T. *J. Am. Chem. Soc.* **1977,** *99,* 3067.

8. Bunton, C. A ; Hong, Y. S.; Romsted, R. S.; Quan, C. *J. Am. Chem. Soc.* **1981,** *103,* 5788.

9. Bunton, C A.; Quan, C. *J. Org. Chem.* **1985,** *50,* 3230.

10. Long, F. A.; McDevit, W F. *Chem. Rev.* **1952,** *51,* 119.

11. *Proc.4th Int. Con. Surf. Active Subs Vol 2;* J Th. G. Overbeek, Ed.; Gordon and Breach: NY,1967; a) Lawrence, A. S. C.; Pearson, J. T., 709.
b) Lawrence, A. S C.; Boffey, B.; Bingham, A.;Talbot, K., 673.

12. Experimentally determined value; personal observation.

13. Mackay, R. A.; Longo, F. R.; Knier, B. L.; Durst, H. D. *J. Phys. Chem.* **1987,** *91,* 861.

14. Burnside, B. A.; Knier, B. L.; Mackay, R. A ; Durst, H D.; Longo, F. R. *J. Phys Chem.* **1988,** *92,* 4505

15. Garlick, S. M.; Mackay, R. A.; Durst, H. D.; Haddaway, K. G.; Longo, F. R. *J. Coll. Int. Sci.* **1989,** *132.*

16. Bunton, C. A.; Hong, Y. S.; Romsted, L. S.; Quan, C. *J. Am. Chem. Soc.* **1981,** *103,* 5784.

CATALYTIC DECOMPOSITION OF CW-AGENTS BY TERNARY CHELATES OF COPPER (II)

K. S. Rajan and S. Mainer, IIT Research Institute, Chicago, Illinois,
and J. E. Walker, D. Remy, and J. Halliday, U. S. Army Natick,
RD & E Center Natick, Maryland

ABSTRACT

The formation and structure of Cu(II)-glucosamine (GA) 1:1 and 1:2 chelates involving coordination with aminonitrogen and C-1 hydroxyl groups with stability constants, i.e , Log β_1 = 9.88 ± 0.02 and Log β_2 = 17.96 ± 0.02 respectively were determined. The hydrolysis and disproportionation of the 1:1 chelate are eliminated through its additional coordination with an equimolar amount of each of the bidentate amines, viz , dipyridyl (DP), ethylenediamine (EN), 1,3-diaminopropane (DAP), N,N'-diethylethylenediamine (DEEN), N,N,N',N'-tetraethylethylenediamine (TEEN), N,N,N',N'-tetra-methylethylenediamine (TMEN) with overall stabilities (Log β_{LA}) respectively, 15.94 ± 0.09, 19.37 ± 0.02, 18.57 ± 0.02, 17.80 ± 0.01, 10.24 ± 0.03, and 16.34 ± 0.02. Similar studies carried out with 1-methoxyglucosamine (MGA) indicated the coordination of Cu(II) with aminonitrogen and the C-3-hydroxyl group with stability constants, i.e., Log β_1 = 9.61 ± 0.03 and Log β_2 = 17.53 ± 0.03. The rates of decomposition of SARIN and SOMAN in aqueous 0.02M PIPES buffer (pH 7.2) by the binary and ternary chelates decreased in the order: Cu-TMEN (1:1) > Cu-TMEN-GA (1:1:1) > Cu-DEEN (1:1) > Cu-DP (1:1) > Cu-GA (1:1) > Cu-GA (1:2) > Cu-DP-GA (1:1:1) > Cu-DAP (1:1). Data on the catalytic activity of the chelates are examined in the light of their stabilities, structures and percent distribution with a view to delineate a possible mechanism.

INTRODUCTION

Studies on the metal chelate catalyzed hydrolysis of SARIN and DFP reported in the literature[1-4] have been confined to binary chelates. However, their corresponding ternary chelates should provide an interesting class of catalysts from the point of view of mechanistic insight. Further, through the coordinate attachment of a second ligand, the destabilizing tendencies of the binary chelates, viz., hydrolysis and disproportionation are largely obviated. It is therefore of interest to investigate a number of ternary chelates.

The specific objective of this research is to investigate the interactions of copper (II) with glucosamine in the presence of equimolar amounts of each of a number of bidentate nitrogen donor ligands. They consisted of: (i) dipyridyl (DP); (ii) ethylenediamine (EN); (iii) 1,3-diaminopropane (DAP); (iv) 1,6-diaminohexane (DAH); (v) N,N'-diethylethylenediamine (DEEN); (vi) N,N,N',N'-tetraethylethylenediamine (TEEN); and (vii) N,N,N',N'-tetramethylethylenediamine (TMEN). The influence of the secondary ligands on the hydrolytic stability of the mixed ligand chelates (thus formed) is examined. Similar studies have been extended to 1-methoxyglucosamine. Finally, the overall objective of this research is to investigate the homogenous catalytic activities of the binary and ternary chelates for the decomposition of SARIN (GB) and SOMAN (GD) and critically examine them against their thermodynamic stabilities and their percent distribution.

EXPERIMENTAL PROCEDURE

Procedure:

Aqueous stock solutions (0.02M) of D-glucosamine, 1-methoxyglucosamine, and the bidentate nitrogen donor amines were prepared by dissolving appropriate quantities of the respective (reagent grade) amine hydrochlorides in CO_2-free distilled water, standardized by potentiometric titration and stored in the refrigerator. Aqueous stock solution (0.02M) of copper (II) was prepared by using reagent grade copper nitrate and standardized by complexometric titrations against EDTA.

The potentiometric equilibrium pH method was used in this investigation. The method consists in determining the proton association equilibria of the different amines (hydrochlorides) in the presence and in the absence of Cu(II) ion in equimolar or higher molar ratios by means of a glass-calomel electrode system in a thermostatted electrometric cell. All the titrations were carried out at 25.0 ± 0.1°C and an ionic strength of 1.0 (1.0M KNO_3). Using the potentiometric equilibrium data, titration curves for the different metal-ligand systems were traced. In Figure 1 are shown the titration curves for Cu(II) interactions with glucosamine (GA) and tetramethylethylenediamine (TMEN). Possible metal-binding reactions occurring in solutions were then postulated on the basis of an analysis of these titration curves. The reactions thus assumed constituted the basis for appropriate mathematical treatments and the determination of the metal chelate formation constants. Details of the potentiometric equilibrium pH method were reported in a number of earlier publications.[1-10] The calculations of the metal chelate stability constants and the distribution of the different chelate species over the pH range 2-12 were carried out with a computer program (BEST) provided by Dr. R. J. Motekitis and Dr. A.E. Martell, Texas A & M University, College Station Texas.

The rates of hydrolysis of DFP, **SOMAN** and **SARIN** brought about by the Cu(II) chelates were determined by using a fluoride ion electrode to measure the amount of F^- produced by the hydrolysis of the substrate. The reactions were conducted at 25°C in $2x10^{-2}$M pH 7.2 PIPES (piperazin-N,N'-bis[2-ethanesulfonic acid]) with 0.4M KCl. The fluoride ion electrode was calibrated with $2x10^{-3}$ and $2x10^{-5}$M NaF standards in the PIPES buffer, and the electrode efficiency was better than ~97% throughout the test period. Both the neat Soman and DFP were less than 1% hydrolyzed but the neat Sarin was about 10-12% hydrolyzed.

The agent-hydrolysis experiment was begun by adding 22 or 23 ml of the PIPES buffer to the temperature-controlled (jacketed) cell and placing the F^- electrode in the buffer. Next 0.1 millimole of the neat agent was added to the buffer and the rate of hydrolysis without catalyst was measured for 10 minutes. Then 0.1 millimole of the Cu(II) chelate was added and the final solution volume was made up to 25 ml. The concentration of the chelate and

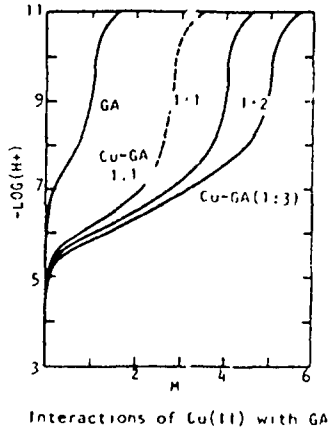

Interactions of Cu(II) with GA

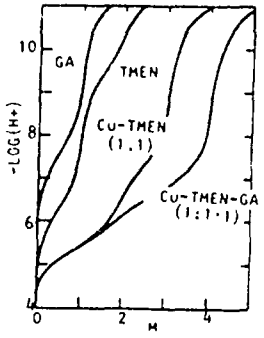

Interactions of TMEN with Cu(II) and Cu(II)-GA

FIGURE 1. INTERACTIONS OF CU(II) WITH GLUCOSAMINE AND TETRAMETHYLETHYLENE DIAMINE.

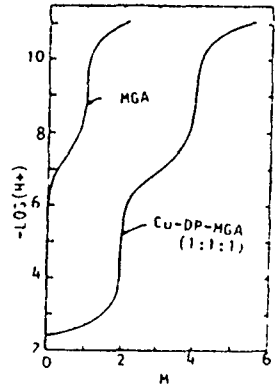

Interactions of MGA with Cu(II)-DP

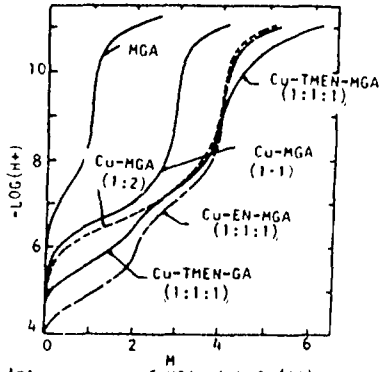

Interactions of MGA with Cu(II), Cu(II)-EN and Cu(II)-TMEN

FIGURE 2. INTERACTIONS OF CU(II) WITH 1-METHOXYGLUCOSAMINE, DIPYRIDYL, ETHYLENEDIAMINE, AND TETRAMETHYLETHYLENE DIAMINE.

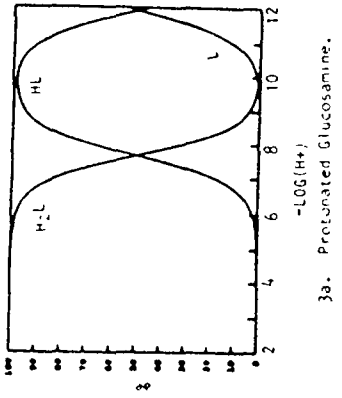

3a. Protonated Glucosamine.

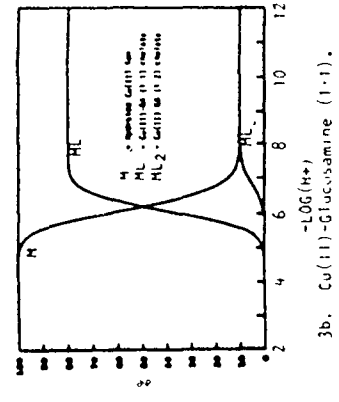

3b. Cu(II)-Glucosamine (1:1).

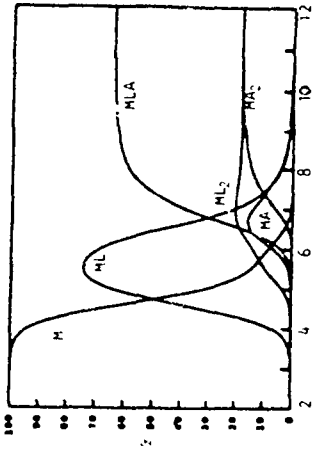

3d. Cu(II)-Ethylenediamine Glucosamine (1:1:1).

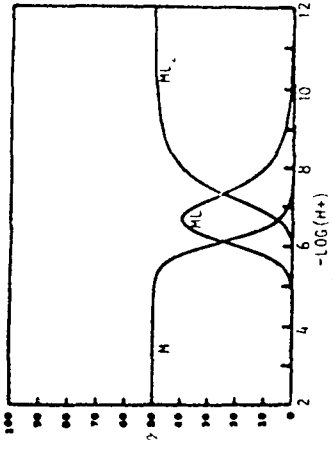

3c. Cu(II)-Glucosamine (1:2).

Figure 3. Species distribution in (a) glucosamine, (b) Cu(II)-glucosamine (1 1), (c) Cu(II)-glucosamine (1 2), and (d) Cu(II)-ethylenediamine glucosamine systems.

the initial concentration of the agent was each $4x10^{-3}M$ in all of the tests. The hydrolysis of the agent in the presence of the Cu(II) chelate was then recorded for ten to twenty minutes. In tests with a slow (less than four micromoles/min) hydrolysis rate, the rate was constant throughout the test period and the constant value was recorded. The tests with high rates of hydrolysis showed a substantial decrease in the hydrolysis rate as the agent concentration decreased during the test period. Thus, when the hydrolysis rate was greater than 4_{μ} moles/min, the largest change in $[F^-]$ per minute was recorded.

RESULTS AND DISCUSSION

Titration curve for the free ligand, glucosamine (GA) and those for the Cu(II)-GA (1:1), (1:2) and (1:3) systems are shown in Figure 1 in which the number of moles of base added per mole of total ligand or total metal (i.e., m) are plotted against the correspondingly measured values of -Log $[H^+]$. The Cu(II)-GA (1:1) curve shows an inflection at m=2.5 to 3.0 with precipitation occurring at m≈ 2.5. This could be taken to indicate the interaction of Cu(II) with GA involving the $-NH_2$ and the -(OH) groups of the glucosamine molecule. The curve further indicates that the partially coordinated Cu(II)-GA chelate undergoes hydrolysis followed by disproportionation, resulting in the separation of solid phase (precipitate). It is noted that the destabilization associated with Cu(II)-glucosamine (1:1) chelate has been obviated through its interaction with a second mole either of glucosamine or the other bidentate amines.

Among the secondary ligands examined, TMEN, DEEN, TEEN, EN, and DP exhibit additional coordination with Cu-GA resulting in the formation of a ternary chelate each. N,N,N',N'-tetramethyethylenediamine (TMEN) interacts with Cu(II) forming a 1:1 chelate in the buffer region m = 0 to m = 2 (Figure 1) followed by hydrolysis and formation of a stable Cu(II)-TMEN-monohydroxo chelate in the second buffer region, i.e., m = 2 to m = 3. The formation of a Cu(II)-TMEN-GA (1:1:1) ternary chelate is indicated by a single strong inflection at m = 4 proceeded by a buffer region between m = 0 and m = 4. The equilibrium interactions occurring in the different systems investigated during this reporting period along with the corresponding stability constants determined are summarized in Table 1.

The stabilities of the 1:1 chelates of Cu(II) with the different amines decrease in the order: **Cu(II)-EN > Cu(II)-GA ≈ Cu(II)-DAP > Cu(II) DEEN > Cu(II)-TMEN > Cu(II)-DP.** With respect to the 1:2 chelates, the order is: **Cu(II)-EN > Cu(II)-GA > Cu(II)-DAP > Cu(II)-DEEN > Cu(II)-DP > Cu(II)-TMEN.** In regard to the formation of a ternary chelate of Cu(II)-GA with each of the amines, the decreasing order is: **Cu(II)-GA-EN > Cu(II)-GA-DAP > Cu(II)-GA-DEEN > Cu(II)-GA-TMEN > > Cu(II)-GA-DP.**

If the molecular structure and nature of the donor groups (along with their pk's) of the glucosamine molecule as well the established coordination geometry of the aquo Cu(II) ion are considered along with the magnitude of the chelate stability constant determined in this research, it is possible to visualize the involvement of the amine nitrogen and one of the hydroxyl groups

TABLE 1. EQUILIBRIUM INTERACTIONS AND THE CORRESPONDING STABILITY CONSTANTS

M	Reaction	Log K	Sigma
	Glucosamine HCl (H_2A^+)		
0-1	$HA + H^+ \rightleftharpoons H_2A^+$	7.67	0.01
0-2	$A^- + H^+ \rightleftharpoons HA$	11.92	0.02
	Cu-Glucosamine.HCl (1:2)		
0-4	$Cu^{2+} + A^- \rightleftharpoons CuA^+$	9.88	0.02
	$CuA^+ + A^- \rightleftharpoons CuA_2$	8.08	0.02
	Ethylenediamine 2HCl (H_2L^{2+})		
0-1	$HL^+ + H^+ \rightleftharpoons H_2L^{2+}$	7.41	0.01
1-2	$L + H^+ \rightleftharpoons HL^+$	10.04	0.01
	Cu-Ethylenediamine.2 HCl (1:1)		
0-2	$Cu^{2+} + L \rightleftharpoons CuL^{2+}$	10.60	0.005
	$CuL^{2+} + L \rightleftharpoons CuL_2^{2+}$	9.26	0.005
	Cu-Ethylenediamine.2HCl-Glucosamine.HCl (1:1:1)		
0-2	$Cu^{2+} + L \rightleftharpoons CuL^{2+}$	10.68	0.04
2-4	$CuL^{2+} + A^- \rightleftharpoons CuLA^+$	8.85	0.06
	$Cu^{2+} + L + A^- \rightleftharpoons CuLA^+$	19.37	0.02
	1,3-Propanediamine.2 HCl (H_2L^{2+})		
0-2	$HL^+ + H^+ \rightleftharpoons H_2L^{2+}$	9.05	0.01
	$L + H^+ \rightleftharpoons HL^+$	10.67	0.01
	Cu-Glucosamine.HCl-1,3-propanediamine.2 HCl (1:1:1)		
0-4	$Cu^{2+} + A^- + L \rightleftharpoons CuAL^+$	18.57	0.02
	1,6 - hexanediamine 2HCl (H_2L^{2+})		
0-2	$HL^+ + H^+ \rightleftharpoons H_2L^{2+}$	10.32	0.01
	$L + H^+ \rightleftharpoons HL^+$	11.02	0.01
	Cu(II)-1,6-hexanediamine.2HCl (1:1)	No chelation formation	
	N,N,N',N' tetramethylethylenediamine.2 HCL (H_2L^{2+})		
0-1	$HL^+ + H^+ \rightleftharpoons H_2L^{2+}$	6.31	0.01
1-2	$L + H^+ \rightleftharpoons HL^+$	9.42	0.01
	Cu-tetramethylethylenediamine 2 HCl (1:1)		
0-2	$Cu^{2+} + L \rightleftharpoons CuL^{2+}$	7.57	0.02
2-4	$CuL^{2+} + L \rightleftharpoons CuL_2^{2+}$	4.70	0.02
	Cu-Glucosamine HCl-tetramethylethylenediamine. 2HCl (1:1:1)		
0-4	$Cu^{2+} + A^- + L \rightleftharpoons CuAL^+$	16.34	0.02
	N,N,N',N'-tetraethylethylenediamine 2 HCl (H_2L^{2+})		
0-1	$HL^+ + H^+ \rightleftharpoons H_2L^{2+}$	6.81	0.01
1-2	$L + H^+ \rightleftharpoons HL^+$	9.99	0.01

TABLE 1. EQUILIBRIUM INTERACTIONS AND THE CORRESPONDING STABILITY CONSTANTS (Cont.)

M	Reaction	Log K	Sigma
	Cu(II)-tetraethylethylenediamine.2HCL	No chelation formation	
	Cu-Glucosamine HCl-tetraethylethylenediamine 2 HCl (1:1:1)		
0-4	$Cu^{2+} + A^- + L^+ \rightleftharpoons CuAL^+$	10.24	0.03
	N,N'-diethylethylenediamine.2 HCl (H_2L^{2+})		
0-1	$HL^+ + H^+ \rightleftharpoons H_2L^{2+}$	7.63	0.02
1-2	$L + H^+ \rightleftharpoons HL^+$	10.35	0.01
	Cu-diethylethylenediamine.2 HCl (1:1)		
0-2	$Cu^{2+} + L \rightleftharpoons CuL^{2+}$	9.05	0.01
	$CuL^{2+} + L \rightleftharpoons CuL_2^{2+}$	6.09	0.01
	Cu-Glucosamine HCl-diethylethylenediamine.2HCl (1:1:1)		
0-4	$Cu^{2+} + A^- + L \rightleftharpoons CuAL^+$	17.80	0.01
	2,2' dipyrdyl.2HCl (H_2L^{2+})		
0-1	$HL^+ + H^+ \rightleftharpoons H_2L^{2+}$	2.40	0.01
1-2	$L + H^+ \rightleftharpoons HL^+$	4.91	0.04
	Cu-dipyridyl.2 HCl (1:2)		
0-2	$Cu^{2+} + L \rightleftharpoons CuL^{2+}$	7.11	0.01
	$CuL^{2+} + L \rightleftharpoons CuL_2^{2+}$	6.88	0.01
	Cu-dipyridyl.2 HCl-glucosamine HCl (1:1:1)		
0-2	$Cu^{2+} + L \rightleftharpoons CuL^{2+}$	4.75	0.08
2-4	$CuL^{2+} + A^- \rightleftharpoons CuLA^+$	8.97	0.01
	$Cu^{2+} + L + A^- \rightleftharpoons CuLA^+$	15.94	0.09
	Bistrispropane.2HCl (H_2L^{2+})		
0-1	$HL^+ + H^+ \rightleftharpoons H_2L^{2+}$	7.11	0.03
1-2	$H^+ + L \rightleftharpoons HL^+$	9.19	0.02
	Cu(II)-Bistrispropane.2HCl (1:1)		
0-2	$Cu^{2+} + L \rightleftharpoons CuL^{2+}$	11.01	0.02
	$CuL + H_2O \rightleftharpoons CuL(OH)^+ + H^+$	5.89	0.07
	$CuL(OH) \rightleftharpoons CuL(OH)_2 + H^+$	8.57	0.04
	Cu(II)-Bistrispropane.2HCl (1:2)		
0-2	$Cu^{2+} + L \rightleftharpoons CuL^{2+}$	10.80	0.10
2-4	$CuL^{2+} + L \rightleftharpoons CuL_2^{2+}$	5.90	0.10
	Cu(II)-Bistrispropane.2HCl.Glucosamine.HCl (1:1:1)		
0-4	$Cu^{2+} + L + A^- \rightleftharpoons CuLA^+$	20.07	0.20

(of the ligand molecule) in the coordination of the metal ion leading to the formation of a (1:1) chelate as illustrated in structure 1. The ligand hydroxyl could be either from the C-1 or the C-3 position of the glucosamine molecule. This observation is consistent with literature reports.[11-13] In order to gain further insight into this, C-1-methoxy derivative was prepared and included in this research and its mode of chelation with Cu(II) was investigated. Structure II indicates the hydrolysis of the 1:1 chelate. The formation of a ternary chelate of Cu(II)-GA with a secondary ligand is illustrated in Structure III.

INTERACTIONS OF Cu(II) WITH 1-METHOXYGLUCOSAMINE

The titration curves for 1-methyoxyglucosamine (MGA), Cu(II)-MGA (1:1) and (1:2), Cu-EN-MGA, Cu-DP-MGA, and Cu-TMEN-MGA (1:1:1) are shown in Figure 2. The inflection at m=3 in the Cu(II)-MGA 1:1 curve can be taken to indicate the formation of a hydrolyzed Cu(II)-MGA chelate involving the coordination of the NH_2 group of methoxyglucosamine and the C-3 hydroxyl group followed by the dissociation of a proton from a Cu(II) coordinated water molecule. The Cu(II)-MGA (1:2) system exhibits an inflection point at M=4 (Figure 2) indicating the displacement of the protons from both the protonated amine group and the C-3 hydroxyl group on each of the MGA molecule to form a 1:2 chelate. All three of the (1:1:1) ternary systems, viz., Cu(II)-TMEN-MGA, Cu(II)-EN-MGA, and Cu(II)-DP-MGA - show inflection points at m=2 and m=4 indicating the formation of the 1:1 chelate of Cu(II) with each of the diamines followed by their interaction with a mole of MGA resulting in the formation of the 1:1:1 ternary chelate at a slightly high pH (i.e., 6-8.5). The equilibrium constants for the postulated reactions are given in Table 2 along with the values for the corresponding reactions with glucosamine. A possible mode of binding of 1-methoxy glucosamine with Cu(II) and the attachment of a secondary ligand (i.e., ethylenediamine) are shown in structure IV.

DISTRIBUTION OF CU(II)-CHELATES

On the basis of the stability constants of the different chelates, their equilibrium concentrations over the pH range 2-12 were computed and the corresponding distribution profiles were plotted, a few of which are shown in Figure 3. Data on the nature and extent of distribution of the Cu(II) chelate species were generated in order to develop a proper mechanistic insight into the catalytic activity of the Cu(II) chelates for a decomposition of toxic phosphonofluoridates. In Tables 3 and 4 are summarized the percent distribution of the aquo Cu(II) ion and the different Cu(II)-chelates at pH 7.2 in the different chelate systems being examined in this research for their agent-decomposing activity.

The data obtained for the hydrolysis of Sarin (GB), Soman (GD) and diisopropylfluorophosphate (DFP) by a number of Cu(II)-chelates are reported in Table 5. The equilibrium constants for the formation of the corresponding Cu(II) chelates are also included. For GB and GD the order of the hydrolysis caused by the Cu(II) chelates is: **Cu-TMEN>Cu-TMEN-GA> Cu-DEEN>Cu-GA ≈ Cu-DP> Cu-GA(1:2)> Cu-DP-GA> Cu-DAP> Cu-BTP.** With DFP, the Cu-DP chelate is relatively more effective so the order becomes: **Cu-TMEN> Cu-TMEN-GA ≈ Cu-DEEN≈Cu-DP>Cu-GA> Cu-DP-GA> Cu-GA(1:2) >Cu-DAP>Cu-BTP≈0.** The hydrolysis rates for GB are slightly faster than the rates for GD hydrolysis. But the hydrolysis rates for either GB or GD are better (i.e., 4 and 16 times faster) than those for DFP.

Structure I. Cu(II)-Glucosamine (1 1) Chelate.

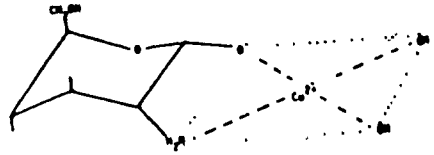

Structure II Hydrolysis of Cu(II)-Glucosamine Chelate.

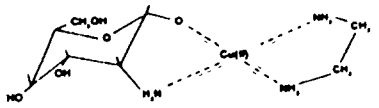

Structure III. Cu(II)-Glucosamine-Ethylenediamine (1 1 1) Chelate (C_1-OH bound to Cu(II)).

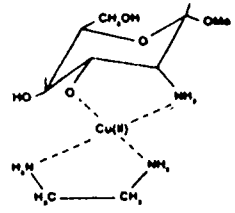

Structure IV. Cu(II)-Methoxy Glucosamine-Ethylenediamine (1,1 1) Chelate (C_3-OH bound to Cu(II)).

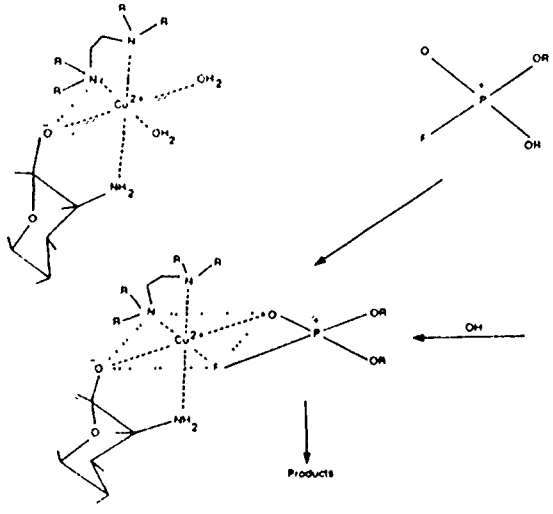

Mechanism 1 For Catalysis by Ternary Cu (II) Chelate

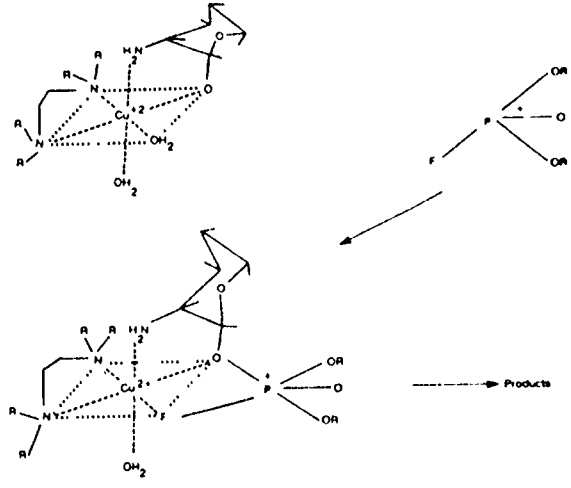

Mechanism 2 For Catalysis by Ternary Cu (II) Chelate

TABLE 2. REACTIONS OF 1-METHOXYGLUCOSAMINE (MGA) WITH Cu(II) AND Cu(II) AMINE CHELATES

m	Reaction	Log K	Sigma	β Values With Glucosamine
	1-methoxyglucosamine-HCl (H_2A^+)			
0-1	$HA + H^+ \rightleftharpoons H_2A^+$	7.39	0.01	7.67
1-2	$A^- + H^+ \rightleftharpoons HA$	12.30	0.01	11.92
	$(A^- + 2H^+ \rightleftharpoons H_2A^+)$	19.69		19.59
	Cu-MGA HCl (1:2)			
0-4	$Cu^{2+} + A^- \rightleftharpoons CuA^+$	9.61	0.03	9.88
	$CuA^+ + A^- \rightleftharpoons CuA_2$	7.92	0.03	8.08
	$(Cu^{2+} + 2A \rightleftharpoons CuA_2$	17.53	0.03	17.96
	Cu-Dipyridyl HCl-MGA-HCl			
0-4	$Cu^{2+} + A^- + L \rightleftharpoons CuAL^+$	15.85	0.03	15.94
	Cu^{2+} - EN.2HCl - MGA - HCl			
0-4	$Cu^{2+} + A^- + L \rightleftharpoons CuAL^+$	18.77	0.03	19.37
	Cu-TMEN.2HCl-MGA-HCl			
0-4	$Cu^{2+} + A^- + L \rightleftharpoons CuAL^+$	15.39	0.08	16.34
	Cu-MGA.HCl (1:1)			
0-3	$Cu^{2+} + A^- \rightleftharpoons CuA^+$	9.46	0.01	9.88
	$CuA^+ + OH^- \rightleftharpoons CuA(OH)$	2.29	0.01	

TABLE 3. CU(II) CHELATE SPECIES DISTRIBUTION AT PH 7.2

System	Chelate Stability β_2	Stoichiometry	% of Total Cu(II) in the Respective Chelate Forms
Cu-TMEN (1:1)		1:0	4.8
	7.57	1:1	92.8
		1:2	2.4
Cu-TMEN-GA (1:1:1)		1:0:0	0.3
		1:1:0	23.3
		1:2:0	2.7
		1:0:1	8.8.
		1:0:2	4.4
	16.34	1:1:1	60.5
Cu-DEEN (1:1)		1:0	4.5
	9.05	1:1	93.4
		1:2	2.1
Cu-GA (1:1)		1:0	12.4
	9.88	1:1	79.4
		1:2	8.1
Cu-DP (1:1)		1:0	30.3
	7.11	1:1	39.4
		1:2	30.3
Cu-GA (1:2)		1:0	0.6
		1:1	46.9
	17.96	1:2	52.5
Cu-DP-GA (1:1:1)		1:0:0	0.5
		1:1:0	5.7
		1:2:0	36.6
		1:0:1	21.7
		1:0:2	14.3
	15.94	1:1:1	21.2
Cu-DAP (1:1)		1:0	9.3
	9.90	1:1	87.8
		1:2	2.9
Cu-BTP		1:0	0.3
	10.86	1:1	99.4
		1:2	0.3

The rates obtained from the experiments on GB hydrolysis by the Cu(II)-MGA chelates are shown in Table 6 along with the rates previously obtained for the corresponding Cu(II)-glucosamine chelates. Table 4 shows the percent of total copper existing as the designated species at pH 7.2 for each of the MGA chelate systems. The rates of hydrolysis of GB by the different Cu(II)-MGA-chelates follow the order: **Cu-TMEN-MGA > Cu-TMEN-GA > Cu-GA (1:1) > Cu-MGA (1:1) > Cu-GA (1:2) ≈ Cu-MGA (1:2).**

The catalytic hydrolysis of GB and GD by the Cu(II)-GA chelates follows the order: **Cu-TMEN > Cu-TMEN-GA > Cu-DEEN > Cu-GA (1:1) Cu-DP > Cu-GA (1:2) > Cu-DP-GA > Cu-DAP.**

It should be noted that from a consideration of the overall thermodynamic stabilities of the chelates and their agent-hydrolyzing activities, a simple correlation between the two is not possible. In order to determine the nature of the catalyst chelate species that might be predominantly involved in the hydrolysis of the agents, it is of interest to consider and compare the rank order of the above-hydrolysis activity with those of the percent distribution of the different species, i.e., aquo-Cu(II) ion, Cu(II)-ligand (1:1 and 1:2) chelates and the ternary chelates of Cu(II)-glucosamine secondary big and (1:1:1) at pH 7.2 at which the agent-hydrolysis reactions were carried out (see Tables 3 through 6).

For the aquo Cu(II)-ion the rank order of its distribution in the different systems is: **Cu-DP > Cu-GA > Cu-DAP > Cu-TMEN > Cu-DEEN > Cu-GA > Cu-DP-GA > Cu-TMEN-GA.**

For Cu(II)-Ligand 1:1 Chelates: **Cu-DEEN ≈ Cu-TMEN > Cu-DAP > Cu-GA > Cu-GA (1:2) > Cu-DP > Cu-TMEN-GA > Cu-DP-GA.**

For Cu(II)-Ligand 1:2 Chelates: **Cu-GA (1:2) > Cu-DP-GA (Cu-DP) > Cu-DP > Cu-DP-GA (Cu-GA) > Cu-GA (1:1) > Cu-TMEN-GA (Cu-GA) >Cu-DAP > Cu-TMEN-GA (Cu-TMEN) > Cu-TMEN > Cu-DEEN.**

For the ternary chelates: **Cu-TMEN-GA > Cu-DP-GA.**

A critical examination of the above would indicate that neither the aquo-Cu(II) ion nor the different Cu(II)-chelates (i.e., 1:1, 1:2, or the 1:1:1) could be considered to be the predominant moiety solely responsible for the catalytic activity. Alternately, on the basis of a critical examination of the structure and steric factors associated with the different chelate systems, it seems reasonable to state that bidentate chelation of Cu(II) with alkyl substitution on the amine nitrogens favors catalytic activity. While ternary chelation helps overcome the destabilizing tendency of a number of the partially coordinated Cu(II)-chelates (i.e., having 1:1 stoichiometry), it does not constitute a sufficient or necessary criterion for conferring maximal catalytic activity on the Cu(II)-chelate moiety. It seems important to have as one of the Cu(II)-coordinating ligands, di- or tetra-N,N,N',N'-substituted diamines (bidentates) in order to confer maximal agent-hydrolysis activity. This, as Martell et al.[1] have pointed out helps stabilize the catalyst chelates (1:1) against their disproportionation tendency.

TABLE 4. SPECIES DISTRIBUTION OF Cu(II)-MGA CHELATES AT pH 7.2

	Log β	Stoichiometry			% of Total Cu(II) In The Respective Chelate Forms
Cu-MGA			Cu	MGA	
(1:1)	-		1	0	18.0
	9.61		1	1	82.0
			Cu	MGA	
Cu-MGA	-		1	0	3.6
(1:2)	9.61		1	1	69.1
	17.53		1	2	27.3
		TMEN	Cu	MGA	
Cu-TMEN-MGA	-	0	1	0	1.0
(1:1:1)	7.57	1	1	0	59.6
	12.27	2	1	0	5.0
	9.61	0	1	1	14.9
	17.53	0	1	2	4.7
	15.39	1	1	1	14.9
Cu-EN-MGA		EN	Cu	MGA	
(1:1:1)	-	0	1	0	1.5
	10.60	1	1	0	30.1
	19.86	2	1	0	27.5
	9.61	0	1	1	20.4
	17.53	0	1	2	5.7
	18.77	1	1	1	14.8
Cu-DP-MGA		DP	Cu	MGA	
(1:1:1)	-	0	1	0	2.4
	7.11	1	1	0	12.0
	13.99	2	1	0	35.1
	9.61	0	1	1	26.7
	17.53	0	1	2	6.0
	15.85	1	1	1	17.9

TABLE 5. HYDROLYSIS OF GB, GD AND DFP BY CU(II) CHELATES

Chelate System	Log K ML or Log K MAL	Hydrolysis (μmoles/min) GB	GD	DFP
Cu-TMEN (1:1)	7.57	28.9	27.9	2.53
Cu-TMEN-GA (1:1:1)	16.34	26.8	16.3	1.67
Cu-DEEN (1:1)	9.05	18.6	11.9	1.57
Cu-GA (1:1)	9.88	11.3	5.31	1.04
Cu-DP (1:1)	7.11	10.3	6.39	1.64
Cu-GA (1:2)	17.96	7.99	3.26	0.44
Cu-DP-GA (1:1:1)	15.94	5.78	2.82	0.73
Cu-DAP (1:1)	9.90	1.98	0.99	0.04
Cu-BTP (1:1)	10.86	0.74	0.36	0

Initial concentration of agent and Cu(II) chelate is 4×10^{-3}M
Buffer: 0.02M pH 7.2 pipes with 0.4M KCl
Temperature 25°C

TABLE 6. COMPARISON OF HYDROLYSIS RATES OF GB BY Cu(II) CHELATES OF GLUCOSAMINE AND THOSE OF 1-METHOXYGLUCOSAMINE

Chelate System	Log β	Maximum Hydrolysis Rate (μ moles/min)
Cu-GA (1:1)	9.88	11.3
Cu-MGA (1:1)	9.61	8.8
Cu-GA (1:2)	17.96	8.0
Cu-MGA (1:2)	17.53	8.1
Cu-TMEN-GA (1:1:1)	16.34	26.8
Cu-TMEN-MGA (1:1:1)	15.39	36.6

4×10^{-3}M chelate and initially 4×10^{-3}M GB
2×10^{-2}M pH 7.2 PIPES buffer with 0.4M KCl
30°C for MGA systems, 25°C for GA systems

Thus, in order to overcome such a destabilizing tendency on the part of the Cu(II)-glucosamine (1:1) system and to confer maximal catalytic activity, the attachment of a secondary ligand such as TMEN is found to help. It is possible to consider two alternate mechanisms for the catalytic action of such a ternary chelate moiety along the lines proposed by Martell et al., viz.[1], (i) combination of the metal chelate with the agent being hydrolyzed followed by attack of this complex with hydroxide ion, and (ii) an analogous push-pull mechanism of Swain's. In order to consider both mechanisms, we have to invoke distorted hexa-coordination geometry of Cu(II) in the ternary chelate catalysts as illustrated in mechanisms I and II.

ACKNOWLEDGMENT

This work was supported by the U.S. Army Natick Research Development and Engineering Center, Natick, MA.

REFERENCES

1. R. C. Courtney, R. L. Gustafson, S. J. Westerback, H. Hyytiainen, S. C. Chaberek, Jr., and A. E. Martell, J. Amer. Chem Soc., 79 3030-3036 (1957).

2. T. Wagner-Jaueregg et al., J. Amer. Chem. Soc., 77, 922 (1955).

3. J. Epstein and D. Rosenblatt, J. Amer. Chem. Soc., 80, 3596 (1958).

4. R. L. Gustafson, S. Chaberek, and A. E. Martell, J. Amer. Chem. Soc., **1963**, 85, 598-601.

5. G. Schwarzenbach and H. Flaschka, "Complexometric Titrations", Methuen & Co., Ltd., (London) 1969.

6. K.S. Rajan, R.W. Colburn and J.M. Davis., J. Neurochem., 18, 345 (1971).

7. K.S. Rajan, J.M. Davis, R.W. Colburn and F.H. Jarke, J. Neurochem., 19, 1099 (1972).

8. K.S. Rajan, J.M. Davis and R.W. Colburn, J. Neurochem., 21, 137 (1974).

9. K.S. Rajan and A.E. Martell, J. Inorg. Nucl. Chem., 26, 1927 (1964).

10. K.S. Rajan and A.E. Martell, Inorg. Chem., 4, 462 (1965).

11. G. Micera, S. Deiana, P. Decock, B. DuBois, and H. Kozlowski, Inorg. Chim. Acta, **1985**, 107, 45.

12. J. Lerivry, B. DuBois, P. Decock, kG. Micera, J. Urbanski, and H. Kozlowski, Inorg. Chim. Acta, **1985**, 125, 189-190.

13. A. Pusino, D. Drama, P. Decock, and H. Kozlowski, Inorg. Chemica Acta., 1987, 138, 5-8.

BLANK

MICELLAR EFFECTS UPON THE REACTION OF HYDROXIDE ION WITH THIOPHENYL PHOSPHINATES

Andrei Blasko and Clifford A. Bunton

Department of Chemistry
University of California
Santa Barbara, CA 93106

ABSTRACT

Cationic micelles of cetyltrimethylammonium bromide and mesylate (CTABr and CTAOMs) assist reaction of OH^- with $Ph_2PO{\cdot}SEt$ (1), $Ph_2PO{\cdot}SPh$ (2) $(EtO)_2PO{\cdot}SPh$ (3) and $(EtO)_2PS{\cdot}OC_6H_4NO_2$-p (4). First order rate constants, k, go through maxima with increasing [surfactant], although there are unexpected double rate maxima for reactions of 1-4, but not for reactions of OH^- with aryl phosphates and phosphinates. A quantitative distribution model fits these rate-surfactant profiles, except at the double maxima. Second-order rate constants are lower at the micellar surface than in water, by factors of 5-20, as for reactions of aryl phosphinates and phosphates. Thiophenyl are only slightly more reactive than phenoxy derivatives and alkoxy substituents inhibit reaction.

Attack of nucleophiles, e.g., OH^-, upon thioesters of phosphorus (V) has been examined in aqueous-organic solvents[1] and we have now examined these reactions in water and in aqueous micelles of cetyltrimethylammonium bromide and mesylate ($C_{16}H_{33}NMe_3X$, CTAX, X^-=Br^-, $MeSO_3^-$). We used the following substrates:

$Ph_2PO{\cdot}SEt$	$Ph_2PO{\cdot}SPh$	$(EtO)_2PO{\cdot}SPh$	$(EtO)_2PS{\cdot}OC_6H_4NO_2$-p
1	2	3	4

The thioalkyl and thioaryl derivatives were chosen as models for toxic thiophosphinates and their reactions were compared with those of aryl phosphinates and phosphates.

Cationic micelles typically speed reactions of anionic reagents with neutral substrates[2] and reactions of anionic nucleophiles with nonionic nitrophenyl phosphates and phosphinates have been examined in a variety of micelles and microemulsions derived from cationic surfactants.[3,4]

For a given concentration of nucleophile observed first order rate constants, k, go through maxima with increasing concentration of surfactant.[2-6] These results are explained by a pseudophase model that treats

water and micelles as distinct reaction media. The overall rate constant depends upon the distribution of both reactants between water and micelles and the second order rate constants in each pseudophase. Initially k increases as reactants are brought together at the micellar surface, but with increasing [surfactant] reactants are "diluted" at the micellar surface and values of k go through maxima. The calculated second order rate constants at the micellar surface are generally similar to, or smaller than, those in water and rate enhancements are due to high concentrations of reactants at micellar surfaces.[2] Rate enhancements in microemulsions or in alcohol-modified micelles fit similar kinetic models.

Results and Discussion

The low solubility of the substrates forced us to follow nonmicellar reactions with OH^- in aqueous MeCN, and second order rate constants k_W in water were calculated by a short extrapolation. A decrease in the water content of the solvent slowed all the reactions because initial state stabilization of hydrophobic substrates by organic solvents more than compensates for the increased nucleophilicity of OH^-.

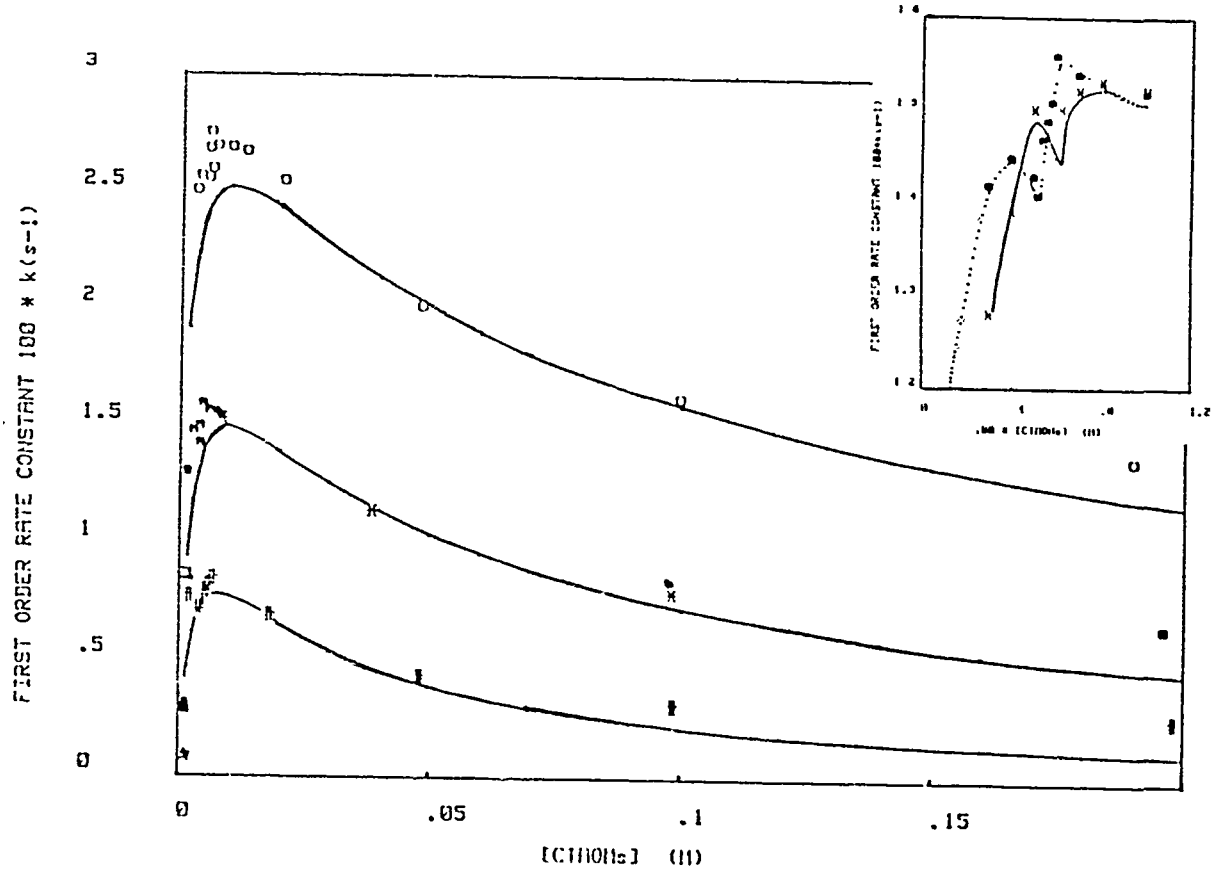

Figure 1. Reaction of $(EtO)_2PO.SPh$ with OH^- in CTAOMs. #; ■, *; □; 0.03; 0.1 and 0.3M OH^- respectively: ■, *; 10^{-5} and $7.5x10^{-5}$ M substrate respectively.

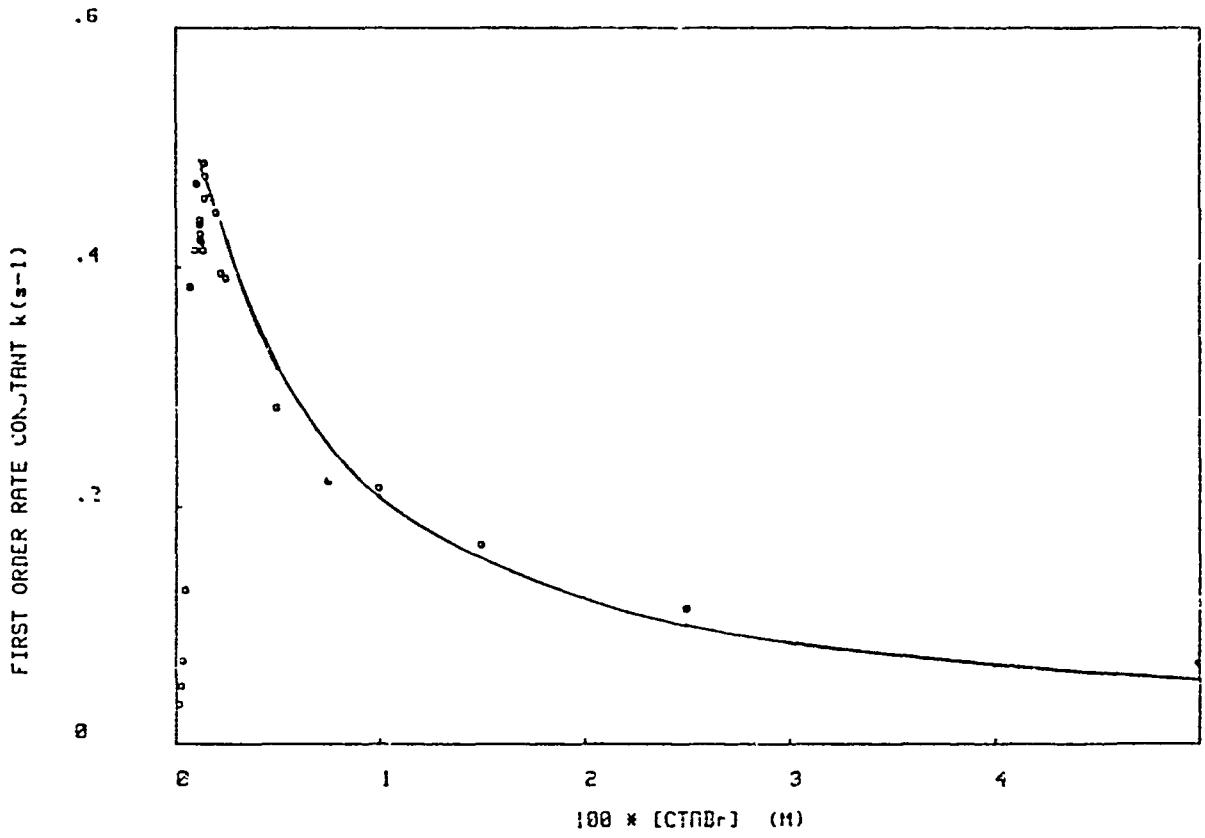

Figure 2. Reaction of 10^{-5}M $Ph_2PO.SPh$ with 0.01M OH^- in CTABr.

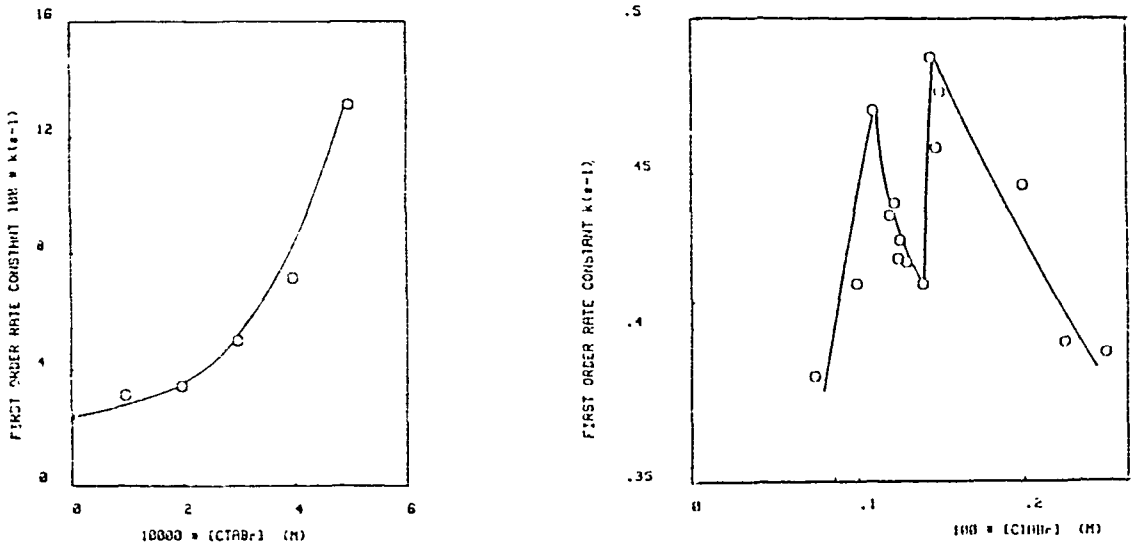

Figure 3. Expanded plots of Figure 2. Left, in dilute CTABr; right, the double rate maxima.

Variations of k with [surfactant] at various [OH^-] are shown in Figures 1-3. The general form of these rate-surfactant profiles is very similar to those found for many micellar-assisted bimolecular reactions, except that with several substrates we saw double rate maxima. The expanded scale insert in Figure 1 shows the double rate maxima for reaction of $(EtO)_2PO{\cdot}SPh$ with 0.1 M OH^- in CTAOMs. The positions of the maxima depend on [substrate], but this dependence disappears at higher [CTAOMs]. Figure 2 shows the rate constant-surfactant profile for reaction of 10^{-5} M $Ph_2PO{\cdot}SPh$ with 0.01 M OH^- in CTABr and Figure 3 shows expanded plots for this reaction at [CTABr] < cmc, and at the double rate maxima.

Most quantitative models of micellar rate effects involve the assumption that the solution contains only monomeric surfactant, whose concentration is the critical micelle concentration, and fully-formed micelles.[2] Only micelles are assumed to bind reactants, but these assumptions are probably oversimplifications. A hydrophobic solute, such as a thiophosphinate, may bind to monomeric surfactant or form small clusters with it, and, if these short-lived complexes react with OH^-, there may be rate enhancements in very dilute surfactant, as shown in Figure 3 (left hand). However, this plot shows that there is little rate increase with [CTABr] < $2x10^{-4}$ M, so submicellar clusters, rather than monomeric surfactant, are apparently speeding reaction. The surfactant concentration is well below the cmc of CTABr, which is $6x10^{-4}$ M in 0.01 M NaOH.[7]

These interactions with submicellar surfactant cannot be treated in terms of any existing model, but rate-surfactant profiles at higher surfactant concentration can be fitted by models that predict the concentration of OH^- at the micellar surface.[2,4-6] We assume that OH^- is attracted coulombically by the cationic micelle. This attraction depends upon the micellar surface potential, which cannot be measured directly, but can be estimated by solving the Poisson-Boltzmann equation (PBE) in spherical symmetry.[4,6] The surface potential depends upon the charge density at the micellar surface, i.e., upon the aggregation number and micellar radius, with allowance for inert counterions, Br^- or $MeSO_3^-$ (OMs^-) that are bound specifically at the micellar surface. This calculation has been described and we use parameters from the literature.[4a,b] Reaction can occur in water or at the micellar surface and the observed first order rate constant is given by:

$$k = \frac{k_W[OH_W^-] + k_2^m K_S([CTAX]\text{-cmc})[OH^-]_{2.4\text{Å}}}{1 + K_S([CTAX]\text{-cmc})} \qquad (1)$$

where k_W is the second order rate constant in water, k_2^m that in a shell of 2.4 Å thickness at the micellar surface and K_S is the substrate binding constant.[4a,b] The concentration of OH^- in the shell, $[OH^-]_{2.4\text{Å}}$ is calculated from the PBE. The value of the cmc is that for CTAX under the reaction conditions. Except in very dilute surfactant, where there are double rate maxima, the model fits the data reasonably well over a range of concentrations of surfactant and OH^-, as shown by the plots in Figures 1 and 2 predicted by equation 1, with the parameters given in Table 1.

TABLE 1

Reactions in Water and Cationic Micelles[a]

Substrate	k_W $M^{-1}s^{-1}$	k_2^m $M^{-1}s^{-1}$	k_2^m/k_W
1, $Ph_2PO{\cdot}SEt$	0.27	0.034	0.13
2, $Ph_2PO{\cdot}SPh$	2.5	0.33[b]	0.13
3, $(EtO)_2PO{\cdot}SPh$	0.037	0.005[b]	0.14
4, $(EtO)_2PS{\cdot}OC_6H_4NO_2$-p	1.0×10^{-3}	1.3×10^{-4} [b]	0.08
5, $Ph_2PO{\cdot}OPh$	1.2	0.05	0.04[c]
6, $Ph_2PO{\cdot}OC_6H_4NO_2$-p	18.0	3.4	0.19[c]
7, $(PhO)_2PO{\cdot}OC_6H_4NO_2$-p	0.48	0.06	0.12[c,d]

[a] Reaction with OH^- at 25.0°C in CTABr; [b] data in CTAOMs also fitted these values; [c] ref. 4d; [d] ref. 4a, b.

In nonmicellar systems reactions are first order in substrate and in OH^-, but the micellar reactions have an order lower than one in OH^- (Figure 1). This situation is general and is readily understandable in terms of pseudophase models that describe competition between reactive and inert ions and surfaces of micelles or other colloidal assemblies,[2,4-6] and reactions in the micellar pseudophase are first order in OH^-, even though the overall reactions are not. Comparisons of values of overall first or second order rate constants for reactions of different nucleophiles, for example, can be grossly misleading unless distribution of reagents between aqueous and micellar pseudophases is taken into account.

The second order rate constants in water and at the micellar surface, k_W and k_2^m, respectively, are given in Table 1 together with data for phenyl and p-nitrophenyl diphenyl phosphinate (5) and (6) and p-nitrophenyl diphenyl phosphate (7).[4]

$Ph_2PO{\cdot}OPh$ (5) $\quad$ $Ph_2PO{\cdot}OC_6H_4NO_2$-p (6) $\quad$ $(PhO)_2PO{\cdot}OC_6H_4NO_2$-p (7)

For all the substrates $k_W > k_2^m$, i.e., observed rate enhancements are due to an increased concentration of reactants at the micellar surface rather than to an increased rate constant at that surface. This behavior is typical of anion-molecule reactions at surfaces of CTA^+ micelles.[2,4-6]

The similarity of the values of k_2^m/k_W for reactions of the various substrates (Table 1) shows that structural effects upon reactivities are similar in water and at the micellar surface. Reactivity is affected by the leaving group and by substituents at phosphorus (V). Comparison of reactivities of phosphate and phosphinate esters 7 and 6 shows that replacement of both phenoxy groups in 7 by phenyl groups speeds reaction with OH^- by factors of ca. 38 in water and ca. 64 in cationic micelles[4d] with a p-nitrophenoxy leaving group (Table 1). Interaction of the p-orbitals of oxygen with the d-orbitals of phosphorous should reduce substrate electrophilicity.

p-Nitrophenyl diphenyl phosphinate (6) is more reactive than analog (5) by factors of 15 in water and 57 in cationic micelles, even though a

p-nitro group increases the acidity of phenol by a factor of ca. 500. This comparison suggests that P-O bond breaking is not extensive in the transition state, c.f. ref. 1. Consistently thiophenyldiphenyl phosphinate, (2), is more reactive than the thioethyl analog (1) by a factor of less than 10 (Table 1), showing that P-S bond-breaking is not extensive in the transition state. Another structural comparison involves phenoxy and thiophenoxy leaving groups. Thiophenyl diphenyl phosphinate (2) is more reactive than phenyl diphenyl phosphinate (5) by factors of ca. 2 is water and ca. 6 in micelles (Table 1), even though thiophenol is more acidic than phenol by a factor of more than 10^2.

Although both phenyl and ethoxy are inductively electron-withdrawing groups replacement of the phenyl gr ups at phosphorus in 2 by ethoxy groups in 3 inhibits reactions by a factor of ca. 65 in both water and micelles (Table 1). This rate reduction is due to p-d conjugation which reduces electrophilicity at phosphorus (V), cf., the relative reactivities of 6 and 7. Parathion (4) is relatively unreactive towards OH^-, even though it has a p-nitrophenyoxy leaving group (Table 1). These low reactivities are typical of P=S as compared with P=O compounds.[1] A strong overlap of the d orbitals on phosphorus and sulfur should stabilize the initial, relative to the transition, state and hydration in the anionic transition state should be relatively weak at sulfur as compared with oxygen.

These structural effects on reaction rate are similar to those observed by Cook et al for alkaline reactions in aqueous organic solvents.[1] For dialkyl phosphinates the thioalkyl esters are more reactive than the corresponding alkoxy esters, but differences are generally small, corresponding to transition states with little bond-breaking.[1] These rate comparisons suggest that attempts to decontaminate VX by nucleophilic attack will be unsuccessful because of competing loss of the ethoxy and thioalkyl residues even though relative rates of P-O and P-S bond-breaking will depend to some extent upon the reaction medium. In 90% H_2O-10% iPrOH reaction of VX with OH^- initially gives 78% P-S and 22% P-O bond fission and complete loss of the thioalkyl group is very slow.[8]

Double Rate Maxima. Double rate maxima in micellar-mediated bimolecular reactions had been observed only in aromatic nucleophilic substitutions and not in reactions of carboxylic or phosphorus(V)esters.[9] We believe that these double rate maxima are due to complexation of hydrophobic substrates with monomeric surfactant or small clusters of it. These complexes are probably too small to bind counterion but they will encounter OH^- and the positive charge of the surfactant should increase the reactivity of complexed substrate in a bimolecular reaction with OH^-. Hydrophobic quaternary ammonium ions, or small clusters of them, are very effective in speeding spontaneous and bimolecular anionic reactions, even though they do not micellize.[10,11]

Formation of these complexes depends upon substrate concentration, and it affects the shape of the double rate maxima (Figure 1) whereas when micelles are fully formed first order rate constants are unaffected by the concentration of (dilute) substrate. With increasing [surfactant] micelles form and, in effect, "dissolve" these complexes. Therefore double maxima become less evident when a counterion, such as Br^-, stabilizes the micelles and promotes micellization.

The various pseudophase models that fit rate-data at [surfactant] above the rate maxima (Figures 1 and 2) do not explain the double rate maxima, because the models consider only monomeric and micellized surfactant.[2,4-6]

Experimental

Materials. The preparation and purification of the surfactants has been described.[4] Substrates were prepared from the acid chloride and thiolate or were commercial samples. Reactions were followed at 25.0°C in CO_2-free N_2 saturated water.

Kinetics. Reactions were generally followed spectrophotometrically by using an HP diode array 8541 spectrometer at the following wavelengths: 1, 245-250 nm; 2, 3, 270-280 nm; 4, 405 nm. The second order rate constant, k_W, in water was obtained by extrapolation of rate constants in H_2O-MeCN. In H_2O-MeCN first order rate constants varied linearly with [KOH].

Data Simulation. The fits of rate constants to [surfactant] were obtained by using a program for solving the PBE in spherical symmetry.[4a,b] Values of the micellar radius and aggregation number were consistent with literature values. The specific binding parameters for Br^- and OMs^- were those used in other simulations. The values of K_S are 3000, 5000, 500 and $5x10^4$ M^{-1} for 1, 2, 3 and 4 respectively, but the fitting is not very sensitive to these values.

CONCLUSIONS

1. Micellar rate enhancements of reactions of OH^- with a variety of thiophosphinates are due to concentration of both reactants at micellar surfaces where second order rate constants are slightly lower than in water.
2. In dilute surfactant submicellar aggregates assist reaction.
3. In water and micelles reaction rates are lower for $(EtO)_2P$ as compared with Ph_2P esters and for P=S as compared with P=O esters. Leaving group efficiencies, relative to PhS are: PhO, 0.5; EtS, 0.1. It will be difficult to remove RS groups selectively by nucleophilic attack if RO groups are present, unless coordination of a metal ion to sulfur is used to assist P-S bond-breaking

ACKNOWLEDGEMENT

Support of this work by the U.S. Army Research Office is gratefully acknowledged.

SULFUR-ASSISTED OXIDATION OF 2-CHLOROETHYL SULFIDES TO SULFOXIDES BY DIMETHYL SULFOXIDE

Yu-Chu Yang, Linda L. Szafraniec, William T. Beaudry and Fu-Lian Hsu
Research and Physical Protection Directorates
U.S. Army Chemical Research, Development and Engineering Center,
Aberdeen Proving Ground, MD 21010-5423

ABSTRACT

While regular dialkyl sulfides and alkyl 2-hydroxyethyl sulfides were not oxidized by dimethyl sulfoxide, the alkyl 2-chloroethyl sulfides and mustard slowly reacted with dimethyl sulfoxide to produce the corresponding sulfoxides at 25-70 °C. The mechanism of the oxidation is proposed to involve the neighboring sulfur-participation of a transient sulfonium ion with a four-membered structure. The sulfonium ion intermediate rapidly reacts with the chloride ion to produce 2-chloroethyl sulfoxides. 2-Hydroxyethyl sulfoxides were also produced probably due to the presence of trace amount of water in the dimethyl sulfoxide. This reaction demonstrates, for the first time, the unique reactivity of alkyl 2-chloroethyl sulfides in dimethyl sulfoxide.

INTRODUCTION

The versatile chemical nature of DMSO is well appreciated and documented in organic chemistry.[1,2] Besides being one of the most prominent members of the family of polar, aprotic solvents, DMSO also functions as a nucleophilic reagent at both the oxygen and sulfur terminals, and thus behaves as either a "hard" or a "soft" base. Because of this characteristic, DMSO has often been used as a mild oxidizing agent in organic synthesis. More importantly, Epstein and Sweat[3] showed that the oxidizing capacity of DMSO was somewhat dependent on its ability to act as a nucleophile. There was also a strong indication that most of the DMSO oxidations involved the same dimethylalkoxysulfonium salt intermediate, **1**. This intermediate can be formed via the activating process illustrated in *eq. 1*. For example, the

oxidation of a primary alcohol to an aldehyde usually follows this mechanism. On the other hand, the oxidation of a primary alkyl halide or tosylate to its corresponding aldehyde, known as the Kornblum reaction, usually follows the mechanism described by *eq. 2*. However, in either case, a base is required in order to achieve the formation of the aldehyde or ketone.

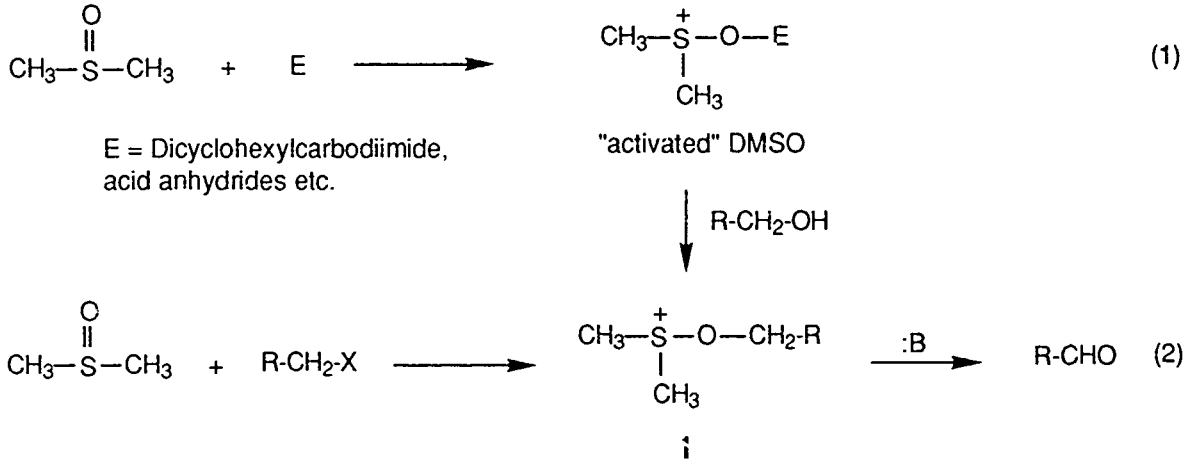

Bis(2-Chloroethyl) sulfide (Mustard, **2a**), is a toxic chemical agent due to its high reactivity toward proteins and DNAs to induce systematic biochemical and morphological changes in mamalian tissue.[4] Its tendency to form a reactive, three-membered ring sulfonium ion in polar media also accounts for its susceptibility to a variety of nucleophiles including water.[5] Interestingly, its sulfoxide and especially its hydrolysis product, thiodiglycol, are relatively harmless[4], and these compounds are often goals in the chemical detoxication of mustard. It is the purpose of this study to examine the possible oxidation of mustard and other 2-chloroethyl sulfides by the nucleophilic oxidizing agent, dimethyl sulfoxide (DMSO) in the absence of any other reagents such as base.

Results and Discussion

Identification of Products. In order to use ^{13}C NMR to follow the compositions of the reaction mixtures, the ^{13}C NMR chemical shifts of many sulfides and their sulfoxides were measured and compared. The results are summarized in Table 1. When a sulfide is oxidized to its sulfoxide, the chemical shifts of the carbon atoms adjacent to sulfur shift downfield 15-23 ppm. This characteristic was utilized to analyze the products in this study.

A 1.0 M solution of 2-chloroethyl methyl sulfide (CEMS, **2b**) in DMSO was converted to 28% 2-chloroethyl methyl sulfoxide (CEMSO), 6% 2-hydroxyethyl methyl sulfoxide (HEMSO), and dimethyl sulfide (DMS) in the absence of base after 30 days at room temperature. The formation of CEMSO and HEMSO was greatly enhanced at 70 ^{o}C. Interestingly, the amount of the hydrolysis product, HEMSO, increases with decreasing concentration of CEMS as shown in Table 2. Similar

TABLE 1

^{13}C NMR Chemical Shifts (δ) of Sulfides and Sulfoxides in DMSO

Compound	CH_3S	CH_3CH_2S	CH_3CH_2S	SCH_2CH_2X	SCH_2CH_2X
$(CH_3)_2S$ (DMS)	16 5	-	-	-	-
$(C_2H_5)_2S$ (DES)	-	13 6	23 5	-	-
$CH_3SCH_2CH_2Cl$ (CEMS)	13 8	-	-	34 4	42 4
$CH_3SOCH_2CH_2Cl$ (CEMSO)	37 1	-	-	54 7	37 2
$CH_3CH_2SCH_2CH_2Cl$ (CEES)	-	13 9	24 4	37 2	42 8
$CH_3CH_2SOCH_2CH_2Cl$ (CEESO)	-	5 6	43 8	52 1	37 2
$CH_3SCH_2CH_2OH$ (HEMS)	14 1	-	-	35 0	59 4
$CH_3SOCH_2CH_2OH$ (HEMSO)	37 6	-	-	53 2	55 9
$CH_3CH_2SCH_2CH_2OH$ (HEES)	-	17 6	28 6	36 3	63 9
$CH_3CH_2SOCH_2CH_2OH$ (HEESO)	-	5 6	43 8	53 2	53 0
C6H5SCH2CH2Cl (CEPS)	-	-	-	33 9	41 9
$C_6H_5SOCH_2CH_2Cl$ (CEPSO)	-	-	-	57 0	36 7
$ClCH_2CH_2SCH_2CH_2Cl$ (HD)	-	-	-	32 5	42 9
$ClCH_2CH_2SOCH_2CH_2Cl$ (HDO)	-	-	-	52 5	37 2
$ClCH_2CH_2SCH_2CH_2OH$[a] (CH)	-	-	-	37 7 38 1	47 0 (X = Cl) 65 3 X = OH)
$ClCH_2CH_2SOCH_2CH_2OH$ (CHO)	-	-	-	52 9 53 0	37 3 (X = Cl) 53 6 (X = OH)
$HOCH_2CH_2SCH_2CH_2OH$[b] (TG)	-	-	-	36 2	63 2
$HOCH_2CH_2SOCH_2CH_2OH$ (TGO)	-	-	-	53 2	54 1

[a]Solvent acetone
[b]Sovent water

behavior was obser[illegible]r solutions of 2-chloroethyl ethyl sulfide (CEES, **2c**) and mustard (HD) in DMSO (cf. Table 2). In all cases, the oxidation was highly selective and no sulfone was detected. The products were identified by ^{13}C NMR and subsequently confirmed by GC/MS.

TABLE 2
The reaction of 2-chloroethyl sulfides with DMSO

	Initial Conc (M)	Rx Cond. Temp (°C)	Time	Composition (%)[a]				
				CEMS	CEMSO	HEMSO		
	1.0	25	30 days	66	28	6		
CEMS	0 5	70	14 h	14	42	44		
	0.2	70	14 h	9	53	38		
				CEES	CEESO	HEESO		
	1.7	25	30 days	46	48	6		
CEES	0.9	70	14 h	62	29	9		
	0.4	70	14 h	11	23	66		
				HD	HDO	CHO	TGO	CH
HD	1 0	25	30 days	17	9	33	38	4

[a]The percentages (±5%) were determined from the ^{13}C NMR integration of specific peaks in the compounds (cf. Table 1)

Reaction Mechanism. Based on the ^{13}C NMR spectra of sulfides and their sulfoxides (see Table 1), it was concluded that oxidation of the 2-chloroethyl sulfides was occurring since the chemical shifts of the methyl groups in CEMS and CEES shifted from δ 13.8 to 37.1 and from δ 13.9 to 5.6, respectively. In addition, the $ClCH_2\underline{C}H_2S$ moiety in CEMS shifted from δ 34.3 to 54.7, while the $CH_3\underline{C}H_2S$ moiety in CEES shifted from δ 24.4 to 43.8 and the $ClCH_2\underline{C}H_2S$ group shifted from δ 37.2 to 52.1. For HD, the chemical shift of the SCH_2 moieties also moved downfield by ca. 15-20 ppm indicating again the oxidation of the sulfur in HD. Furthermore, DMS, δ 16.5, was observed in all three solutions, presumably from the reduction of the DMSO.

The mechanism of the DMSO oxidation proposes that these reactions involve the formation of a three-membered ring sulfonium ion intermediate **3** shown in Scheme 1 in the first step followed by the nucleophilic addition of DMSO to form **4**. Alternately, it is also possible that **4** forms directly from an SN2 nucleophilic substitution of chloride by DMSO without the formation of **3**. Particularly, Harris *et al.*[6] reported that the displacement of a series of 2-chloroethyl sulfides by a number of strong nucleophiles in DMSO proceeds *via* an SN2 mechanism. Subsequently, the neighboring sulfur-assisted displacement of DMS occurs in **4** to form a sulfonium ion, **5** as the rate-determing step for oxidation. Due to ring strain, this four-membered cyclic sulfonium ion rapidly reacts with any nucleophiles present in the DMSO, such as chloride ion or water, to yield 2-chloroethyl and 2-hydroxyethyl sulfoxide, **6** and **7**, respectively.

Scheme 1

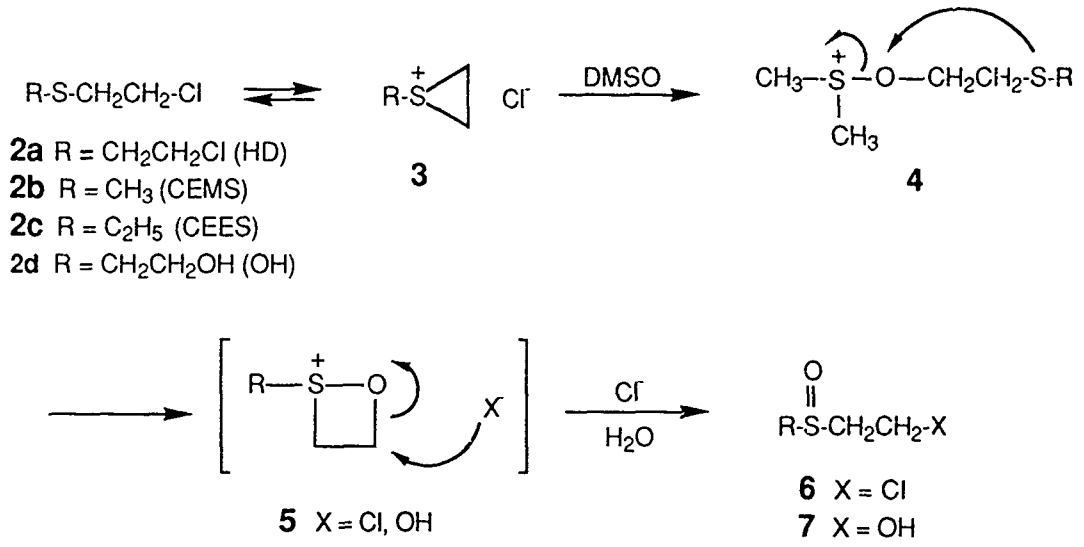

The presence of the intermediate **4** was detected in the ^{13}C NMR spectra of both CEMS and CEES in DMSO. A methyl resonance at 25.3 ppm consistent for a CH_3S^+ moiety was observed in each solution before oxidation was complete. However, no resonances consistent with the intermediate **5** were detected.

To ascertain the participation of the neighboring sulfur atom in **2** and **4** in the reaction mechanism, a solution of 0.1 M 2-chloroethyl phenyl sulfide (CEPS) in DMSO was examined, since the nucleophilicity of the sulfur in CEPS is poor relative to that in CEMS and CEES.[7] Indeed, no sulfoxide was observed when the solution was kept either at room temperature for 60 days or heated at 70 ^oC for 40 hours. This indicates that oxidation is dependent on the nucleophilicity of the sulfur in the substrates. Furthermore, under identical conditions, diethyl sulfide was found inert to DMSO oxidation. This is not surprising, since both diethyl sulfide and DMSO behave as nucleophiles. Nevertheless, it was reported that diakyl sulfides, such as n-propyl, n-butyl, and tetramethylene sulfide, could be oxidized to the corresponding sulfoxides at 160-175 ^oC in DMSO.[8]

Although the mechanism in Scheme 1 has never been proposed, it has been reported that chloromethyl methyl sulfide was oxidized by DMSO to produce formaldehyde, dimethyl sulfide and other products generated from methanesulfenyl chloride similar to *eq. 2*.[9] In contrast, 2-chloroethyl sulfides react with DMSO to form sulfoxides.

Hydrolysis Products. Because of a small amount of water present in DMSO, the formation of the 2-hydroxyethyl sulfoxides, **7,** from DMSO oxidation might be derived *via* three possible routes: (1) The direct oxidation of the 2-hydroxyethyl sulfides, a possible hydrolysis product from the 2-chloroethyl sulfides; (2) The hydrolysis of the 2-chloroethyl sulfoxide **6**; and (3) The nucleophilic addition of water to the sulfonium

ion **5** (cf. Scheme 1). To examine these possible pathways, the oxidation 2-hydroxyethyl methyl sulfide (HEMS) by DMSO was investigated. No oxidation product was detected either at room temperature for 16 days or at 70 °C for 40 hours. This result was not unexpected since HEMS does not have a leaving group for nucleophilic substitution either by DMSO or by a neighboring sulfur-assisted SN1 mechanism. As described before, alcohols are inerts in DMSO and require an "activated" DMSO as shown in *eq. 1.* Furthermore, the hydrolysis of 2-chloroethyl sulfide to 2-hydroxyethyl sulflides in highly unlikely as the dimmeric products predominate.[10]

It has been reported that there is no hydrolysis of 2-chloroethyl sulfoxides, such as CEMSO and CEESO in aqueous DMSO or water.[11] This observation rules out the possible formation of 2-hydroxyethyl sulfoxide 7 from 2-chloroethyl sulfoxide **6**. Thus, the formation of the 2-hydroxyethyl sulfoxide **7** from the oxidation of CEMS, CEES, and HD in the DMSO solution most likely results from the attack of water on the intermediate **5**. This is supported by the observed increase in the amount of the hydrolysis products with decreasing concentration of substrate (cf. Table 2)

EXPERIMENTAL

The samples were placed into 5-mm o.d. pyrex NMR tubes, and the ^{13}C NMR spectra were recorded using a Varian XL-200 FTNMR system operating at 50 MHz. Spectra were recorded at probe temperature (ca. 20 °C) in double precision using a pulse width of 3.1-5.1 μsec (36-60°); an acquisition time of 1.6 sec; a pulse delay of 1-2.5 sec and full proton WALTZ decoupling. Accumulation times varied depending on the signal-to-noise ratio required or desired. Spectra were internally referenced to the DMSO resonance at δ 39.5 ppm, and quantitative information was obtained from the digital integration of peak areas from similar type resonances (i.e., SCH_2 *vs* SCH_2 or CH_3 *vs* CH_3).

CONCLUSIONS

The 2-chloroethyl sulfides are known to be less reactive than alkyl or aryl sulfides towards a neutral, non-nucleophilic oxidant[7], since the presence of the electron-withdrawing chlorine reduces the nucleophilicity of the sulfur making its less reactive. On the other hand, because of the nucleophilic character of DMSO and the electrophilic property of 2-chloroethyl sulfoxides, 2-chloroethyl sulfides become more reactive than diakyl and alkyl aryl sulfides in DMSO oxidation. Thus, the selection of mustard simulants for any oxidation study should be carefully evaluated.

The oxidation of 2-chloroethyl sulfides to sulfoxides by DMSO is very selective under relatively mild condition and the reaction is near completion after 14 hours at 70 °C. Further oxidation of sulfoxide product to sulfone by DMSO is not possible, since the sulfonyl sulfur atom is no longer to act as a nucleophile to displace the chloride in the first step. In addition, the neighboring sulfur-participation of the intermediate **4** is also highly unlikely. Therefore, to the best of out knowledge, this represents the first example that demonstrates the unique oxidative reactivity of 2-

chloroethyl sulfides in DMSO and the active participation of the intramolecular sulfur in the Kornblum reaction.

ACKNOWLEDGEMENT

The authors thank Dennis K. Rohrbaugh, Chemical Research, Development, and Engineering Center, for providing the GC/MS spectra.

REFERENCES

1. Szmant, H. H. In Dimethyl Sulfoxide, Jacob, S. W.; Rosenbaum, E. E.; Wood, D. W., Eds.; Marcell Dekker: New York, **1971**; pp 1-97.

2. Martin, D.; Weise, A.; Niclas, H.-J. *Angew. Chem. internat. Edit.* **1967**, *6*, 318.

3. Epstein, W. W.; Sweat, F. W. *Chem. Rev.* **1967**, *67*, 247.

4. Anslow, W. P.; Carnofsky, D. A.; Val Jager, B.; Smith, H. W. *J. Pharmacol. Exp. Ther.* **1948**, *48*, 129.

5. Barlett, P. D.; Swain, C. G. *J. Am. Chem. Soc.* **1949**, *71*, 1406.

6. Sdeaght-Herati, M. R.; McManus, S. P.; Harris, J. M. *J. Org. Chem.* **1988**, *53*, 2539.

7. Yang, Y.-C.; Szafraniec, L. L.; Beaudry, W. T.; Davis, F. A. Proceeding of the 1988 U.S. Army CDREDC Scientific Conference on Chemical Defense Research 15-18 November, 1988, p. 97.

8. Searles, Jr. S.; Hays, H. R. *J. Org. Chem.* **1958**, *23*, 2028.

9. Ratz, R.; Sweeting, O. J. *Tetrahedron Lett.* **1963**, 529; *J. Org. Chem.* **1963**, *28*, 1612.

10. Yang, Y.-C.; Szafraniec, L. L.; Beaudry, W. T.; Ward, J. R. *J. Org,. Chem.* **1988**, *53*, 3293.

11. Reid, E. E. in "Chemistry of Bivalent Sulfur", Chemical Publishing Company, New York, N.Y. 1960

BLANK

CATALYTIC AGENT DEGRADATION ON OXIDE FILMS AND IN MICROHETEROGENEOUS SOLUTION SYSTEMS

C.K. Grätzel, M. Grätzel, and M. Jirousek
Swiss Federal Institute of Technology

ABSTRACT

TiO_2 in the form of colloidal dispersions (anatase) and as fractal film coated electrodes was used in the photodecomposition of CW simulants. Adjunction of powerful oxidants and catalysts enhances this degradation, not only in photochemically induced but also in thermally initiated reactions. Thermal mineralizations of these organophosphorous compounds in presence of these same oxidant/catalytic agent combinations (without TiO_2) are likewise very efficient.

Electrochemical and photoelectrochemical studies on the TiO_2 fractal film coated electrodes leads to a better understanding of the mechanistic details of this surface mediated decomposition.

INTRODUCTION

Both thermal and photolytic degradations of aqueous solutions (with and without colloidal TiO_2) of the model compound 4-NPDEP in presence of various oxidants and catalytic agents were undertaken with success. These experiments were extended to the study of the photodegradation of agents deposited on metal electrodes coated with TiO_2 fractal films. All decompositions were performed in a solar simulator.

A mechanism of photodecomposition of active phosphates on the semiconductor surface in aqueous TiO_2 colloidal suspensions is proposed, electrochemical and photoelectrochemical investigations being used in order to scrutinize this proposed pathway.

EXPERIMENTAL

Paraoxon (4-NPDEP) was supplied by Dr S. u. I. Ehrenstorfer. $K_2S_2O_8$ (puriss. p.a., Fluka) H_2O_2, (puriss. p.a., Fluka), $CuSO_4$ (purum, Fluka) and $Fe_2(SO_4)_3$ (purum, Fluka) were all used as supplied without further purification.

All aqueous dispersions were prepared by the following technique. The appropriate quantity of 10^{-1}M simulant compound (THF solvent) was injected onto the reaction vessels' walls and the solvent evaporated by heating until no traces of solvent were left. Doubly distilled water and TiO_2 and/or the appropriate oxidizing species are then added. The concentration of TiO_2 (P-25, Degussa; 80% anatase, 20% rutile) was kept at 10 gm/liter throughout all the experiments. TiO_2 fractal film coated metal electrodes with a surface area of 16 cm^2 were used in the dry decomposition experiments. Twenty monolayers of simulant corresponding to a concentration of ~6.10^{-5} mole/cm^2 were injected onto the electrode and the solvent left to evaporate. This number of monolayers was found to be the optimum for efficient photodegradation.

The TiO_2 fractal film coated electrodes were prepared by thermal decomposition of titanium ethoxide ($Ti(OC_2H_5)_4$) solutions on the surface of Ti sheets (Siber Hegner Rohstoff AG, Zurich, Switzerland, ASTM grade 2, size 2 x 2 cm, thickness 0.05 cm). The titanium surface on which the oxide layer was deposited was subjected to a pretreatment consisting of boiling for 0.5 h in 18% HCl. The titanium ethoxide solution was prepared by dissolving 21 mmol of

freshly distilled $TiCl_4$ in 10 ml of absolute ethanol (Fluka puriss.). The solution was then diluted with absolute methanol (Fluka puriss.) to give a titanium concentration of either 25 or 50 mg/ml. The deposition of the oxide layer was carried out in a similar way as described by Stalder and Augustynski.[1] A droplet of the alkoxide solution was spread over the surface to produce a thin coating. Subsequently, the titanium alkoxide layer was hydrolyzed at room temperature for 30 min. in a special chamber where the humidity was kept at 48 ±1% of the equilibrium saturation pressure of water. The precise control of the humidity during the hydrolysis step tunnel out to be of crucial importance to obtain electrodes with high sensitization yields. The electrode was subsequently heated in air in a tubular oven kept at 450°C. Preheating it in the entrance of the oven for 5 min. was followed by 15 min. of heating in the interior. Three more layers were produced in the same way. Subsequently, 10 thicker layers were deposited each by using the titanium ethoxide solution containing the higher Ti concentration, i.e., 50 mg/ml. The same procedure as for the first layers was applied except that the heating of the last layer lasted for 30 min. The total thickness of the oxide film was about 20μ.

The doping of the TiO_2 film was carried out by heating it in highly purified Ar (Air Liquide, Belgium, 99.997%). A horizontal tubular oven composed of quartz tubes with suitable joints was employed. After insertion of the electrodes, the tube was twice evacuated and purged with Ar. The electrode was then heated under Ar flux (2.5 L/h) at a rate of 500°C/h up to 550°C which was maintained for 35 min. The electrodes were removed after cooling.

The simulant/TiO_2 samples (either dry electrodes or aqueous dispersions) were then placed in a Hanau (AMI) solar simulator and irradiated the desired amount of time. The temperature for the thermally initiated reactions was controlled by carefully heating the reaction recipients in a thermostated water-bath to 70°C. For CO_2 detection all of the reaction vessels are sealed and 500μl aliquots of the gas volume are checked by gas chromatography (Gow Mac TCD detector at 70°C, He carrier gas, poropak Q column) at the appropriate time intervals.

Electrochemical and photoelectrochemical experiments were performed using a standard potentiometric set-up and monochromatized light. Essential components of the potentiostat were a Keithley 169 multimeter and a Pine Instrument's RDE3 power generator. The lamp and monochromator were supplied by PTI (Photon Technology International).

4-NPDEP Mineralization

The effect of added oxidants such as $K_2S_2O_8$, H_2O_2, $KBrO_3$ and $NaIO_4$ on the photocatalytic decomposition of 4-NPDEP in aqueous dispersions of TiO_2 has previously been demonstrated in our laboratory.[2]

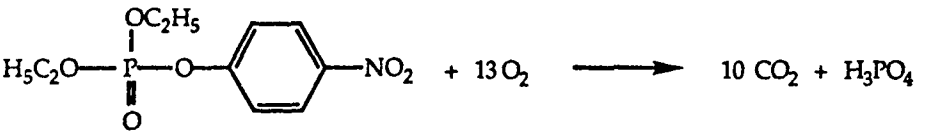

$$+ \ HNO_3 + 5 \ H_2O \qquad (1)$$

$AgNO_3$ was likewise shown to drastically enhance these reaction rates even in the thermal reactions (and notably at room temperature) in absence of TiO_2. Due to these encouraging results, decomposition of 4-NPDEP was tested using the oxidants $K_2S_2O_8$ and H_2O_2 in presence of other less expensive and more readily available catalytic agents such as $CuSO_4$ and $Fe_2(SO_4)_3$. In irradiated TiO_2 dispersions containing 0.1 M $K_2S_2O_8$ and either 10^{-3}M $CuSO_4$ or $Fe_2(SO_4)_3$ the reaction rate is seen to augment relative to solutions in presence of persulfate uniquely (see Table I).

Table I

[4-NPDEP]=5 10^{-4}M	irradiated TiO_2 (10g/l)	thermal TiO_2 (10g/l)	thermal no TiO_2
0.1M $K_2S_2O_8$ 10^{-3}M $CuSO_4$	7 min	12.5 min	7 min
0.1M $K_2S_2O_8$ 10^{-3} M $Fe_2(SO_4)_3$	25 min	12.5 min	12 min
* 0.1 M H_2O_2 10^{-3}M $CuSO_4$	50 min	19 min	22 min
* 0.1 M H_2O_2 10^{-3} M $Fe_2(SO_4)_3$	38 min	18 min	10 min
0.1M $K_2S_2O_8$	60 min	-	60 min

Reaction half-times, $\tau_{1/2}$, for CO_2 evolution (4-NPDEP loss) under various conditions. λ irradiation > 350 nm; thermal reactions at 70°C. *Incomplete decomposition of simulant.

Under these conditions $CuSO_4$ is seen to be more effective as a catalyst than $Fe_2(SO_4)_3$. This situation is reversed when H_2O_2 is used as oxidant. The concentration of H_2O_2 apparently must be optimized to obtain total decomposition of 4-NPDEP. Although the evolution of CO_2 reaches a certain limiting concentration, the initial concentration of 4-NPDEP (corresponding to complete mineralization) is not attained. Under these conditions $Fe_2(SO_4)_3$ is seen to be more effective in augmenting the initial reaction rate than $CuSO_4$ (see Fig. I).

Fig. I

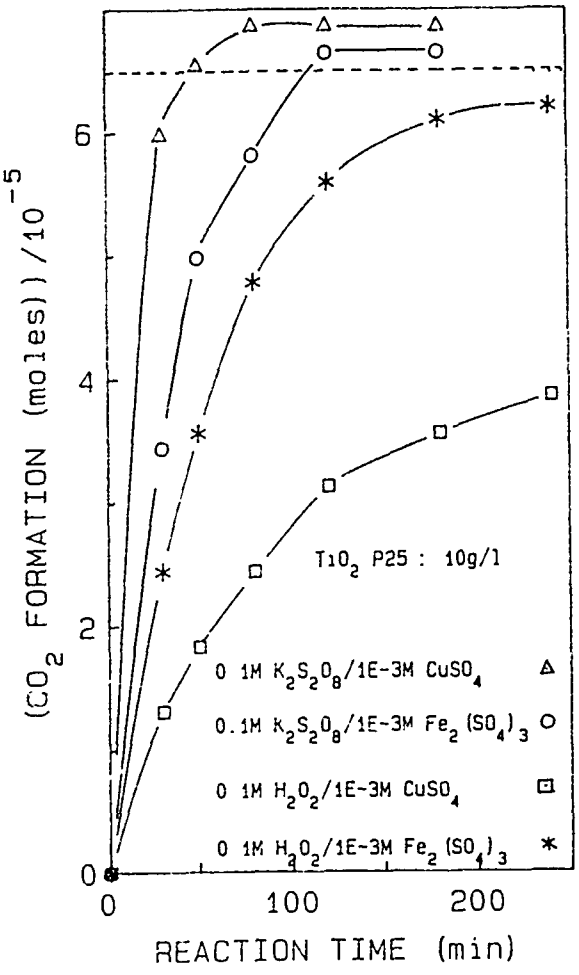

4-NPDEP Decay in Irradiated TiO_2 Dispersions with Added Oxidants and Catalysts

Thermal decomposition of agents in TiO_2 dispersions in presence of these same oxidants and catalytic agents were equally if not more efficient in augmenting the mineralization reaction rate relative to irradiated solutions (see Table I and Fig. II).

Fig. II

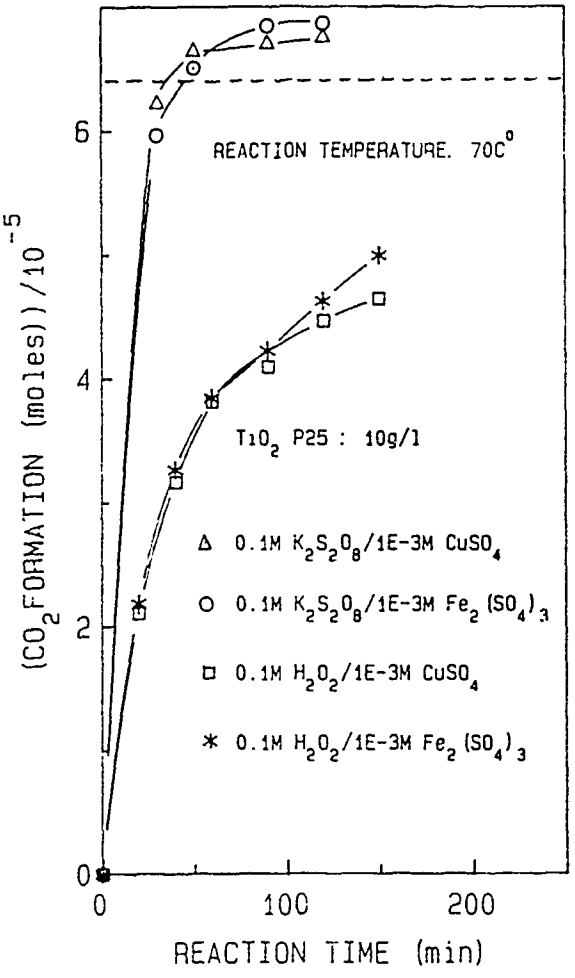

4-NPDEP Thermal Decomposition in TiO_2 Dispersions with Added Oxidants and Catalysts

In the thermal degradations employing aqueous solutions containing strong oxidants, combinations of oxidants and catalytic agents [i.e. $K_2S_2O_8$ and H_2O_2 with $CuSO_4$ and $Fe_2(SO_4)_3$] other than those used in previous studies were examined. Extremely efficient reaction rates were observed (see Table I). The thermal decomposition of 4-NPDEP (which normally does not take place in presence of H_2O_2 alone was rapid in presence of these catalysts, although still less efficient than the degradation using $K_2S_2O_8$ as oxidant (see Fig. III).

Fig. III

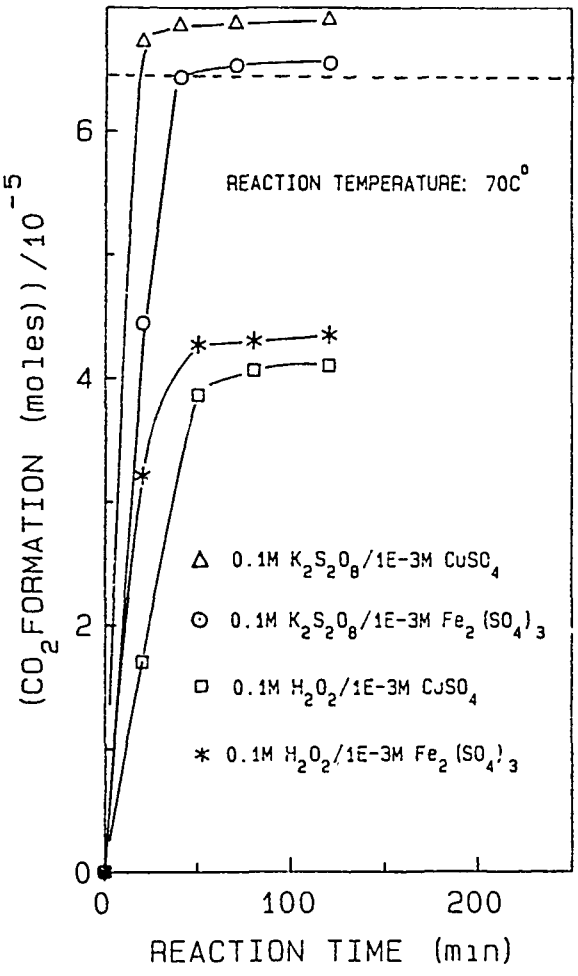

4-NPDEP Thermal Decomposition with Added Oxidants and Catalysts

Fractal TiO_2 film coated metal electrodes (16 cm^2) were prepared for the study of the photodecomposition of CW simulants in the dry state. Twenty monolayers of 4-NPDEP (corresponding to a concentration of ~6.10^{-5} mole/cm^2) were deposited onto these electrodes, and the solvent allowed to evaporate. A substantial photodegradation (in solar simulator) had taken place after ~$7\frac{1}{2}$ hours of irradiation. Total mineralization was observed within ~20 hours of photolysis (see Fig. IV).

Figure IV

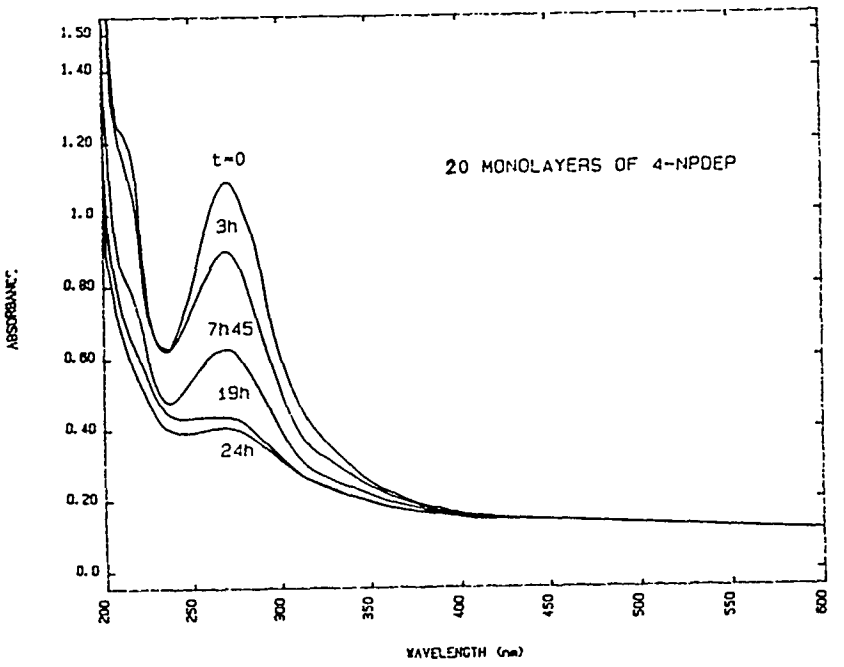

Photodecomposition of 4-NPDEP on TiO_2 Fractal Films Deposited on Metal Electrodes (16 cm^2); Irradiation Solar Simulator ($\lambda > 350$ nm).

This decomposition reaction rate was slightly enhanced (especially initially) by the adjunction of ten monolayers of H_2O_2. A coverage of ten monolayers was seen to be optimum for successful results (see Fig. V).

Figure V

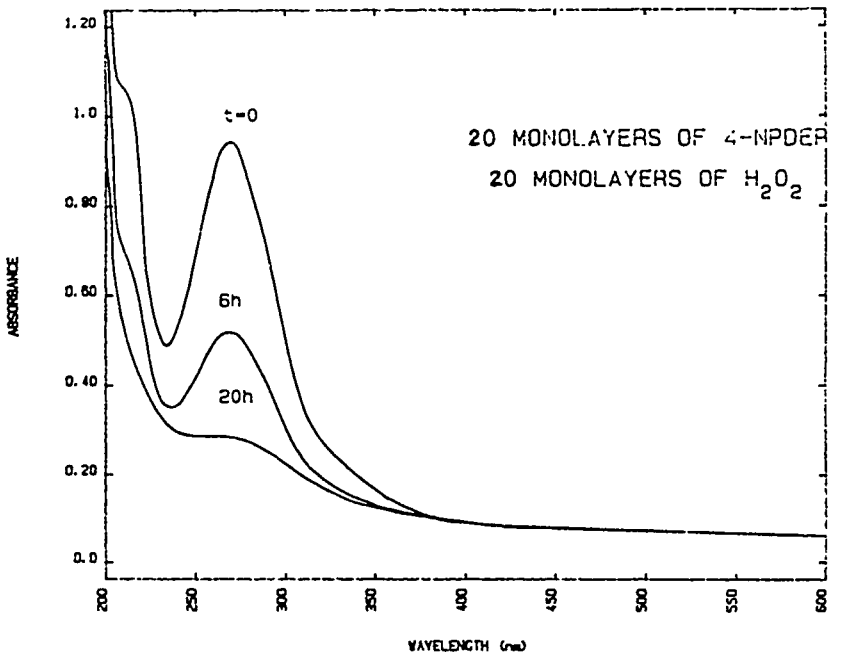

Photodecomposition of 4-NPDEP on TiO_2 Fractal Films Deposited on Metal Electrodes (16 cm^2); Irradiation Solar Simulator ($\lambda > 350$ nm); 20 Monolayers H_2O_2.

Photodegradative Mechanism of Organophosphates on TiO_2 Surface

A summary of the oxidative photodegradation mechanism of simulants on the TiO_2 surface using 4-NPDEP as the model compound is outlined below.[3] In aqueous solution at ambient temperature the surface of TiO_2 should be essentially totally hydroxylated. One could imagine the organophosphorous compound to be attached either to a surface hydroxide group via hydrogen bonding as depicted in structure 1 or via a phosphoryl oxygen-titanium bond as shown in structure 2. The isoelectric point for anatase TiO_2 occurs at pH = 6.5. Thus, under our normal working conditions (i.e. pH between 5 and 6) the surface is well represented by a network containing occasional protonated surface O atoms with a net positive charge.

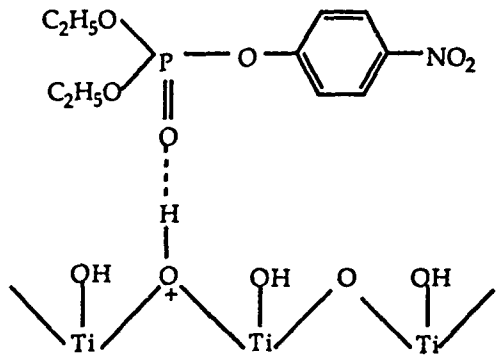

1

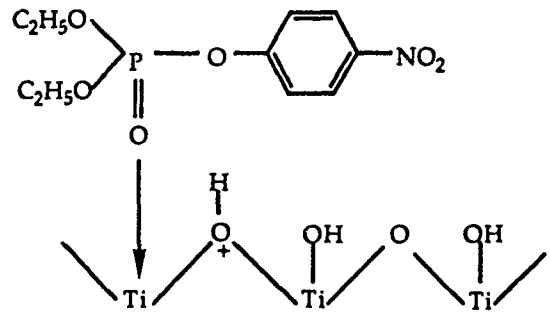

2

Structure 1 will be employed as an illustrative example in all of the reaction schemes for the degradation of 4-NPDEP on the TiO_2 surface.

Prior to irradiation, initial nucleophilic attack by a basic surface hydroxide on the phosphorous atom displacing the nitrophenolate group is postulated. Immediate protonation of this leaving group leads to the formation of nitrophenol. Intervention of the species formed by band-gap irradiation of the aerated or oxygen purged aqueous colloidal TiO_2 suspensions then occurs. Surface hydroxyl radicals generated by water oxidation are instrumental in the photodestruction of the aromatic ring. Surface peroxides can be formed either by hydroxyl radical pairing (hole pairing) or by sequential capture of two holes by the same hydroxide. In presence of air, O_2 can likewise be reduced by conduction band electrons to form superoxide radicals. These superoxide radicals, which are known to absorb strongly to TiO_2's surface, dismutate in neutral (or acidic) solution into O_2 and peroxide. Alternatively, O_2^- is further reduced by e^-_{cb} to yield (O_2^{2-}) surface.

Before the nitrophenol is allowed to escape from the surface into the solution the aromatic ring is cleaved by reaction with these peroxo groups on the TiO_2 particle. We thus speculate epoxidation, by an oxygen atom liberated

from the surface peroxo species, of one of the double bonds of the aromatic compound to form (1) [Eq. 2(a)][4,5]. Hydrolytic rearrangement concomitant with ring opening forms the bifunctional species, (2), [Eq. 2(b)], which after undergoing further oxidation by the surface peroxides [Eq. 2(c)] leads to the α-hydroxymuconic acid derivative (3).

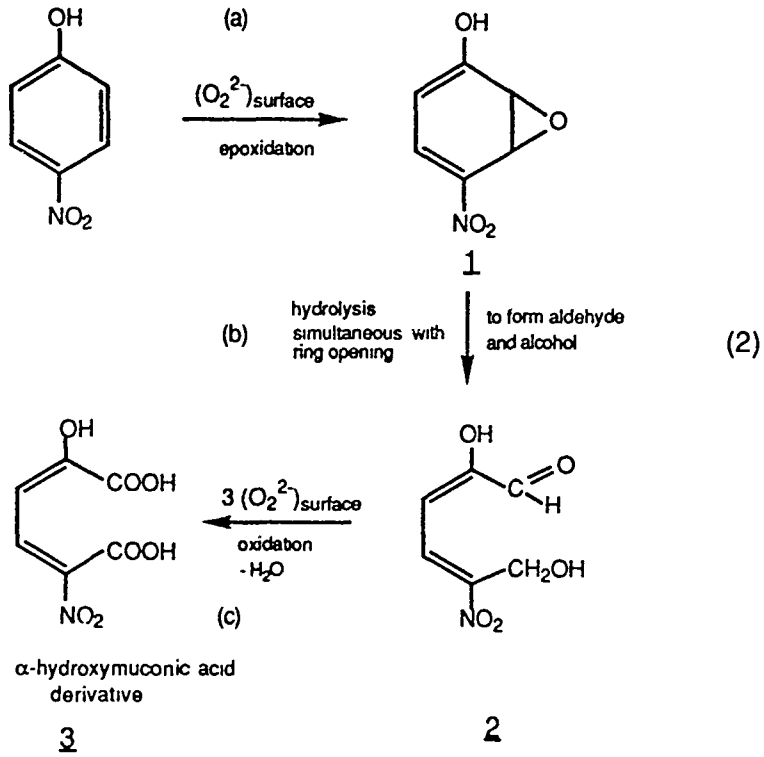

Oxidation of the resulting dicarboxylic acid (3) with the valence band holes results in a photo-Kolbe type decarboxylation [Eq. 3(a-c)] as documented by Bard[6] and Sakata[7], amongst others. Consecutive epoxidation reactions by surface peroxos coupled with direct oxidation of the resultant carboxylic acid by the valence band holes and reduction of appropriate radical species by conduction band electrons

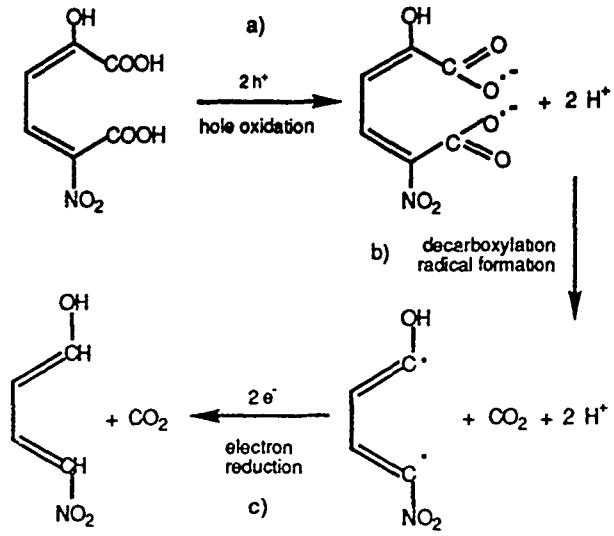

(3)

result in complete decomposition of the aromatic compound with formation of the corresponding inorganic acids and CO_2.

Hydrolytic cleavage of the ester linkage of this organophosphorous compound is initiated through aliphatic α-hydrogen abstraction by a surface hydroxyl radical (formed by hole oxidation of the surface hydroxide) leading to the formation of (in the case of our prototype molecule, 4-NPDEP) an ethyl alcohol radical and the corresponding monoethylphosphate as shown in Eq. 4(b).

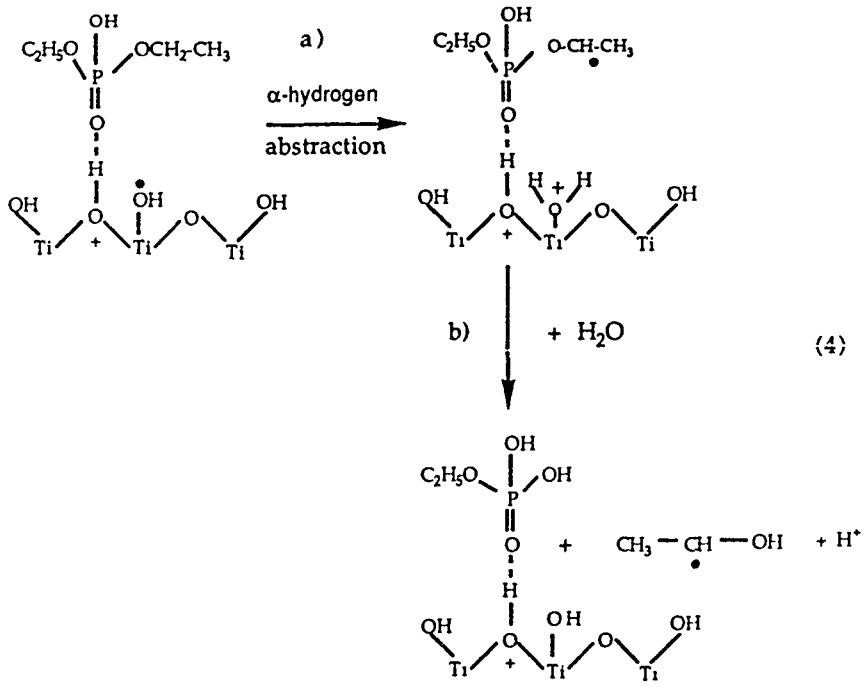

The α-alcohol radical can decompose through several pathways. Electron injection into the semiconductor's conduction band resulting in current doubling and the formation of acetaldehyde is a well documented reaction pathway. A competing reaction is the radical disproportionation to form acetaldehyde and ethanol. In addition ambient O_2 reaction with this α-radical forms a short-lived dimer precursor, which after O_2 liberation, cleaves heterolytically to form acetaldehyde and acetic acid. These products then decarboxylate in successive steps by hole oxidation to form CO_2 as explained previously.

Electrochemical and Photoelectrochemical Investigations of Agent Decomposition on TiO_2 Films:

These films were formed by a sol-gel type procedure yielding layers with a specific surface texture and a high porosity, the roughness factor being 100 to 200. Hydrolysis and oxidative decontamination were tested with agents deposited on the surface which, due to the fractal-type pore geometry, shows a very high capacity for uptake of adsorbent. The decomposition of adsorbed agent was examined both with the film in the dry state and in contact with electrolyte.

Electrochemical and photoelectrochemical techniques were applied in order to analyze the accelerated decomposition of agents on the surface of TiO_2 films. The films were deposited on a conducting substrate and used as a working electrode in a conventional electrochemical cell. The destruction of the

agent by valence band holes manifests itself by an enhancement of the anodic photocurrent. This is shown in Figure VI. Here the photocurrent observed under illumination with 380 nm light is plotted as a function of applied potential. It is evident that in the region where the TiO_2 potential is close to flat band conditions, the anodic photocurrent is markedly enhanced when the film is coated with active phosphate ester.

This shows that the valence band holes produced by light in the TiO_2 films can directly attack the adsorbed phosphate ester. Presumably, in the case of 4-NPDEP the hole reaction leads to abstraction of a hydrogen atom from the α-CH_2 group, i.e.

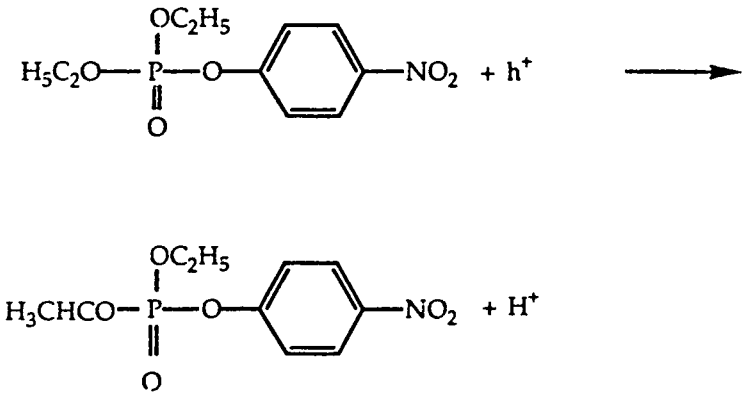

(5)

The hydrogen abstraction destabilizes the ester bond which is readily cleaved by water yielding phosphate and the HO-CH-CH_3 radical. In the presence of O_2 the latter is oxidized to acetaldehyde and, ultimately, carbon dioxide. Further kinetic analysis of this interesting heterogeneous charge transfer process is presently being carried out.

Figure VI

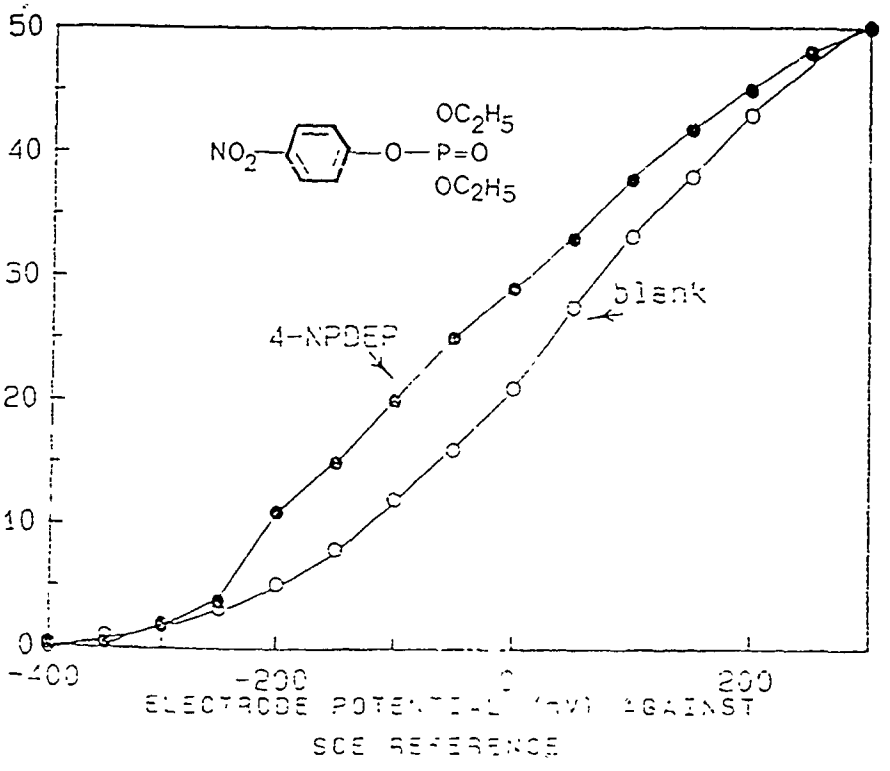

Photoelectrochemical investigations of TiO_2 Films Loaded with Simulant. The Anodic Photocurrent Resulting from the Reaction of the Simulant with Valence Band Holes is Plotted as a Function of Applied Potential.

The photoformation of peroxogroups on TiO_2 fractal films by monochromatic irradiation (λ = 360 nm) is demonstrated in Fig. VII as a function of exposure time. As stated in the section concerning the photodegradative mechanism of organophosphorous compounds these peroxos are believed to intervene as epoxidizing agents in the destruction of the organic moieties.

Figure VII

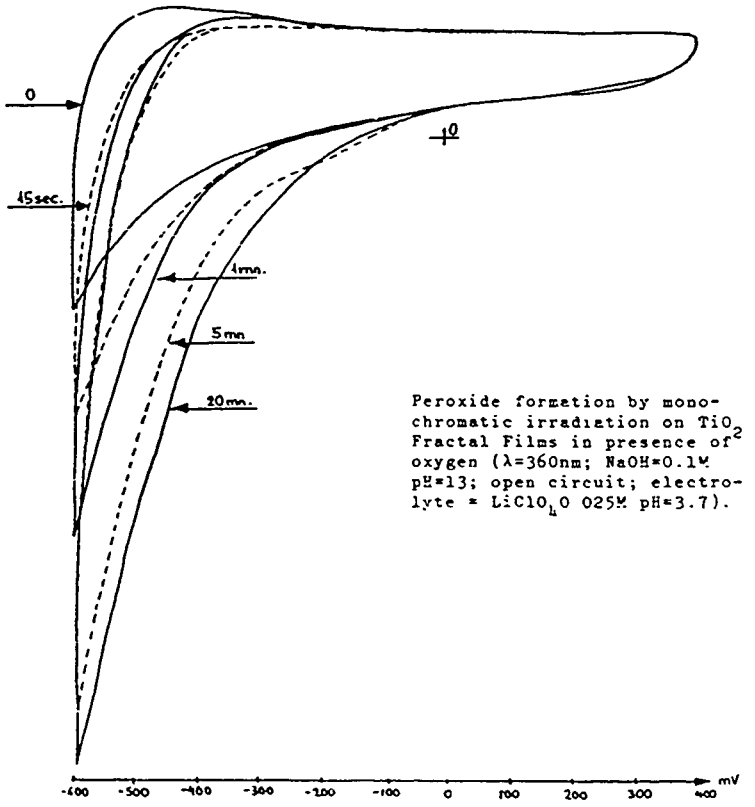

Peroxide formation by monochromatic irradiation on TiO_2 Fractal Films in presence of oxygen (λ=360nm; NaOH=0.1M pH=13; open circuit; electrolyte = $LiClO_4$ 0 025M pH=3.7).

We have previously observed that oxygen plays a key role in the photocatalyzed decomposition of threat agents on TiO_2 surfaces. The role of O_2 is to scavenge conduction band electrons formed concomitantly with the valence band holes by light excitation of TiO_2. In colloidal or powder suspension the valence and conduction band processes always occur simultaneously and therefore cannot be separately investigated. In contrast, the TiO_2 films allow separation of electron and hole transfer processes. The electron reaction was studied in the dark by measuring cathodic currents from the reduction of O_2 using TiO_2 films deposited on a rotating disc electrode. Results are shown in Fig. VIII. The cathodic current is plotted as a function of regular frequency for two potentials, i.e. -0.375 and -0.45 V (SCE). The data are plotted according to the Levich equation. From the slope of the straight lines one obtains the number of electrons (n), transferred to O_2 at the electrode surface. Interestingly, n increases from 1 to 4 as the potential decreases from -0.375 to -0.45 V indicating that the reaction mechanism changes from a one-electron reduction:

$$e^-_{cb}(TiO_2) + O_2 \longrightarrow O^-_2 \qquad (2)$$

to a four electron process:

$$4e^-_{cb} + O_2 + 4H+ \longrightarrow 2H_2O \qquad (3)$$

over a relatively narrow potential range. These results are very valuable in view of the important role of O^-_2 and peroxides in the nucleophilic and oxidative degradation of threat agents at the TiO_2 surfaces.

Fig. VIII

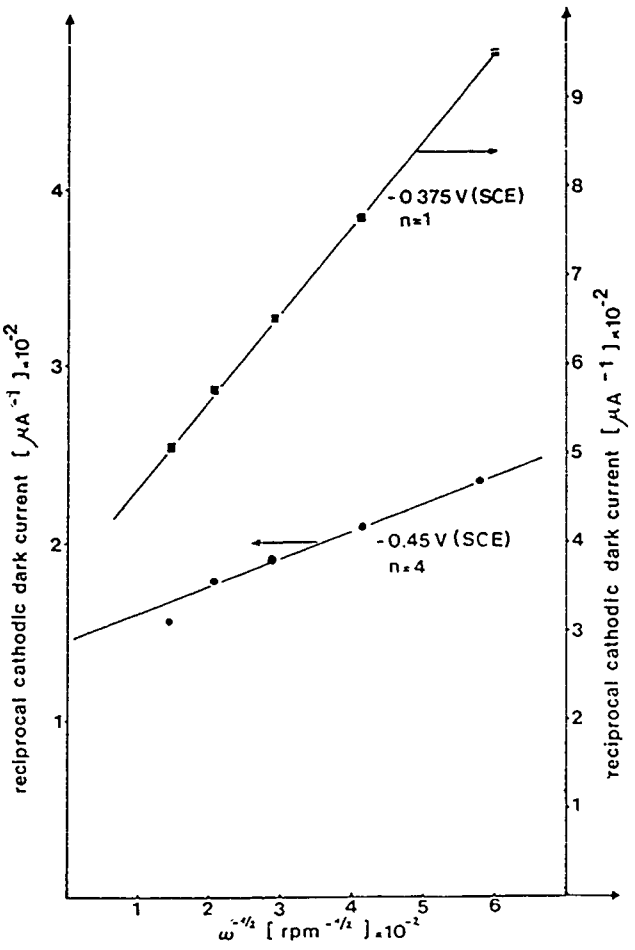

Rotating Disc Experiments Depicting Cathodic Currents Generated by O_2 Reduction at the Surface of TiO_2 Films.

REFERENCES

1. Stalder, C., Augustynski, J. Electrochem. Soc., 1979, 126, 2007.

2. C.K. Grätzel, M. Jirousek and M. Grätzel, Proc. 1988 CRDC, Conference on Chemical Defense.

3. C.K. Grätzel, M. Jirousek and M. Grätzel, accepted for publication (Oct. 1989) in the J.Mol.Cat.

4. H. Hidaka, H. Kubota, M. Grätzel, N. Serpone, Nouv. J. de Chimie, 9 (2), p.67 (1985).

5. A.J. Pandell, J. Org. Chem., 41, (25), p.3992 (1976).

6. (a) B. Krauetler and A.J. Bard, JACS, 100 (7), p. 2239 (1978).
   (b) B. Krauetler and A.J. Bard, JACS, 100 (19), p.5985 (1978).

7. (a) T. Sakata, J. of Photochemistry, 29, p.205 (1985).
   (b) K. Hashimoto, T. Kawai, T. Sakata, J. Phys. Chem., 88, p.4083-8 (1984); idem. p. 2344.
   (c) H. Harada, T. Sakata, T. Ueda, JACS, 107, p. 1773 (1985).
   (d) H. Harada, T. Ueda, T. Sakata, J. Phys. Chem., 93, p. 1542 (1989).

BLANK

THE METAL CATALYZED OXIDATION OF MUSTARD SIMULANTS WITH PEROXIDES

Russell S. Drago,[1] Thomas R. Cundari, Alan S. Goldstein,
Douglas E. Patton, John P. Hage and Yu-Chu Yang[2]

ABSTRACT

The oxidation of organic sulfides can proceed via two distinct paths: (a) oxygen atom transfer (b) one-electron oxidation involving sulfur radicals. A variety of transition metal catalysts have been studied to ascertain the effectiveness of the two paths and the factors influencing reactivity. The problems encountered in extending these reactions to aqueous systems are discussed.

INTRODUCTION

In view of the hydrolytic stability of mustard[3] there is increased interest in oxidative decontaminants. Mechanisms by which sulfide substrates can be oxidized[4] fall into two principal categories: (1) Radical, one electron oxidations, (2) Non-radical, oxygen atom transfer.

The radical path involves the following steps:

$$M^{n+} + OX \longrightarrow M^{n+1} + OX^- \quad (1)$$

$$M^{n+1} + R_2S \longrightarrow R_2S\cdot^+ + M^{n+} \quad (2)$$

$$R_2S\cdot^+ + O_2 \longrightarrow R_2SO_2\cdot^+ \quad (3)$$

$$R_2SO_2\cdot^+ + R_2S \longrightarrow R_2S\cdot^+ + R_2SO_2 \quad (4)$$

$$R_2SO_2 + R_2S \longrightarrow 2\ R_2SO \quad (5)$$

In these equations, OX is an external oxidant such as Ce(IV) or even O_2 in the high temperature and pressure aerobic oxidation of organic sulfides.[4b]

The oxygen atom transfer route occurs by the same mechanism as hydrocarbon epoxidations.[5] As with the oxidation of olefins by similar complexes, conflicting pathways[6] are proposed. They involve: pre-coordination of the sulfide to the metal[6] with a peroxo-metallocycle intermediate and nucleophilic attack of the substrate on a metal-oxo or peroxo oxygen.[6b] Sulfur behaves as a nucleophile toward either a high valent metal-oxo species or a coordinated alkyl hydroperoxide.[5] The metal oxo path involves the following steps:[4c]

$$M^{n+} = O + R_2S \longrightarrow M^{n+}\text{-}O\text{-}SR_2 \longrightarrow \quad (6)$$

$$M^{n-2}\text{-}O = SR_2 \longrightarrow M^{n-2} + R_2SO \quad (7)$$

A molecular orbital investigation of sulfide[7a] and olefin[7b] oxidations by a six-coordinate Ru(IV)-oxo complex indicates that both substrates are oxidized by the concerted transfer of an oxygen atom with a concomitant two oxidation state reduction of the metal. Catalytic oxygen atom transfer via metal peroxo species proceeds via the following path

$$(RO)M = O + ROOH \longrightarrow \quad (8)$$

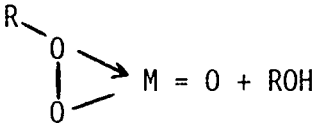

$$M = O + ROH$$

$$R_2S + RO_2M = O \longrightarrow \quad (9)$$

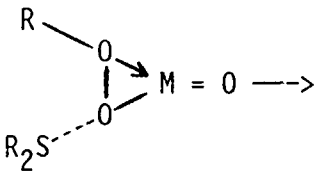

$$M = O \longrightarrow$$

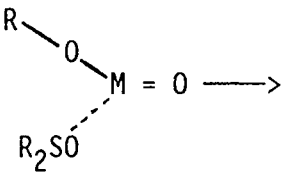

$$R_2SO + ROMO$$

Other proposed mechanisms can be found[8,9] but the results suggest that they could fall into one of the above schemes.

RESULTS AND DISCUSSION

Oxidations of the simulant, n-butyl sulfide, were carried out in acetonitrile using catalysts, expected on the basis of hydrocarbon oxidations,[10,11] to function by one of the above mechanisms. As can be seen in Table 1, some of the most effective catalyst systems arise from activation of the t-butyl hydroperoxide by coordination to d^0 metals. A 0.16 M solution of n-butyl sulfide is completely oxidized with molybdenyl and vanadyl catalysts in two minutes. The oxidant is efficiently used for sulfide oxidation. Stoichiometric amounts of oxidant and substrate yield complete conversion with excess oxidant leading to formation of sulfone.

Catalysts expected to function by radical paths are also efficient catalysts. More research is required to establish that this is the mechanism of sulfide oxidation. The oxygen atom transfer catalysts selected for this study catalyze the oxidation but are much less effective.

Catalyst, oxidant and substrate concentration, constitute variables that are shown to effect the catalysis but which have not been optimized in this study.

Upon addition of water to the reaction mixture all of the catalysts proposed to function by oxygen atom transfer from a coordinated alkyl hydroperoxide, MOOR, became inactive. The large excess of water prevents formation of MOOR from MOR, and rapidly hydrolyzes any that may form as indicated in the following equations:

$$MOR + H_2O \longrightarrow MOH + ROH \quad (10)$$

$$MOOR + H_2O \longrightarrow MOH + ROOH \quad (11)$$

Coordination of the alkyl hydroperoxide is essential for activation, Equation (9).

Activity in CH_3CN/H_2O was observed for radical and metal-oxo catalysts as shown in Table 2. One problem in these experiments involves solubility. Consequently, study of CH_3CN/H_2O is not expected to lead to a practical system but to provide information of the effect of H_2O on the catalysis. To use this type catalyst, systems will have to be designed that permit the catalyst and oxidant to function in non-aqueous media.

The simple transition metal salt $CuCl_2$ is very active in CH_3CN/H_2O. One disadvantage of this system is the lack of stability of t-BuOOH in the presence of low metal concentration. When the oxidant is stirred with the metal prior to substrate addition, (for $\approx$ 10 minutes) the extent of oxidation drops from 70 to 30%. This will probably be typical of most radical catalysts for the Haber-Weiss[12] alkyl hydroperoxide decomposition will be competitive with the catalysis of substrate oxidation. Accordingly, procedures would have to be developed to circumvent this problem by adding the catalyst upon application of the decon solution.

CONCLUSIONS

These studies have shown that there are a large number of transition metal complexes that can activate peroxidic oxidants. Several of these systems are inhibited by water. Oxygen atom transfer from metal-oxo complexes probably have the best potential for catalyzing the oxidation in systems where the complex and peroxide must coexist prior to use.

ACKNOWLEDGEMENT

The authors acknowledge the support of this research by the U.S. Army Research Office under a STAS contract.

Table 1 - $(CH_3)_3COOH/CH_3CN$

Catalyst	Moles	Moles of Substrate	Moles of $(CH_3)_3COOH$	Conversions[c]	Reaction Time-Min.	Comments
Radical Paths						
$CuCl_2$	1.0×10^{-5}	1.6×10^{-3}	4.9×10^{-3}	> 98%	2	Mostly sulfoxide.
$MnCl_2$	1.0×10^{-5}	1.6×10^{-3}	4.9×10^{-3}	80%	3	Catalyst not soluble in MeCN. Added small amount of H_2O. Mostly sulfone.
$Fe_3O(acetate)_6$ •3 acetone	1.0×10^{-4}	2.0×10^{-3}	2.0×10^{-3}	50%	3	
$Ru_3O(pfb)_6^+$	1.0×10^{-5}	1.6×10^{-3}	4.9×10^{-3}	80%	5	Mostly sulfone.
O-Atom Transfer from MOOR						
$MoO_2(acac)_2$	1.0×10^{-3}	1.6×10^{-3}	4.9×10^{-3}	100%	2	Green soln. Turned yellow w/t-BuOOH addition (instantaneous) addition. GC showed no sulfide peak and no sulfoxide peak.
$MoO_2(acac)_2$	1.0×10^{-4}	1.6×10^{-3}	1.6×10^{-3}	100%	2	GC showed no sulfide peak.
MoO_2Cl_2	1.0×10^{-3}	1.6×10^{-3}	4.9×10^{-3}	100%	2	Sulfide added last. Yellow soln., GC no sulfide peak and no product.
$VO(acac)_2$	2.5×10^{-3}	1.6×10^{-3}	1.6×10^{-3}	90%	2	Mostly sulfoxide.
O-Atom Transfer from Metal-Oxo						
$[Ru(DMP)_2(CH_3CN)_2]^{2+}[PF_6^-]_2$	1.0×10^{-4}	1.6×10^{-3}	4.9×10^{-3}	3% 75% 80% 90%	10 60 240 540	Mostly sulfoxide. Monitored via NMR & GC.
Mn(TPP)Cl	1.0×10^{-4}	3.0×10^{-3}	1.0×10^{-2}	50%	15	Mostly sulfone.
$[Mn(TPP)]^+[PF_6^-]$	1.0×10^{-4}	1.6×10^{-3}	4.9×10^{-2}	55%	15	Mostly sulfone.

Table 2 - $(CH_3)_3COOH/H_2O/CH_3CN$

(n-Bu_2S substrate. All 1:1 CH_3CN/H_2O unless indicated)

Catalyst	Moles	Moles of Substrate	Moles of Oxidant	Conversions	Reaction Time(Min.)	Comments
$CuCl_2$	1.0×10^{-5}	1.6×10^{-3}	1.0×10^{-3}	65%	5	A
$CuCl_2$	1.0×10^{-5}	1.6×10^{-3}	1.0×10^{-3}	30%	5	B, Mostly R_2SO
$Ru_3O(pfb)_6^+$	1.0×10^{-5}	1.6×10^{-3}	1.0×10^{-3}	60%	5	A
$Ru_3O(pfb)_6^+$	1.0×10^{-5}	1.6×10^{-3}	1.0×10^{-3}	22%	5	B, Mostly R_2SO
$Ru(DMP)_2^{2+}$	1.0×10^{-5}	1.6×10^{-3}	1.0×10^{-3}	8%	10	Mostly sulfoxide.
$MnCl_2$	1.0×10^{-4}	1.6×10^{-3}	1.6×10^{-3}	N.R.	2	
$CoCl_2 \cdot 6H_2O$	1.0×10^{-4}	1.6×10^{-3}	1.7×10^{-3}	N.R.	2	

a) A - In this experiment the catalyst and substrate were stirred and the oxidant added.
B - In this experiment the catalyst and TBHP are stirred and the substrate added after ten minutes.

REFERENCES

1. Department of Chemistry, University of Florida, Gainesville, Florida 32611-2046.

2. U.S. Army Chemical Research, Development, and Engineering Center, ATTN: SMCCR-PPD, Aberdeen Proving Ground, Maryland 21010-5423.

3. (a) Edgewood Arsenal Special Report EO-SR-74001 Volume 1, 1974, p.47. (b) Yang, Y. C.; Szafraniec, L. L.; Beaudry, W. T.; Ward, J. R. J. Org. Chem. **1988**, Vol. 53, No. 14, 3293.

4. (a) Riley, D. P.; Correa, P. E. JCS, Chem. Comm. **1986**, 1097. (b) Riley, D. P.; Smith, M. R.; Correa, P. E. J. Am. Chem. Soc. **1988**, 110, 177. (c) Roecker, L.; Dobson, J. C.; Vining, W. J.; Meyer, T. J. Inorg. Chem. **1987**, 26, 779.

5. DiFuria, F.; Modena, G. in "Fundamental Research in Homogeneous Catalysis," Tsutsui, M., Ed. Plenum: New York, 1979, 433.

6. (a) Mimoun, H.; Seree de Roch, I.; Sajus, L. Tetrahedron **1970**, 26, 37. (b) Sharpless, K. B.; Townsend, J. M.; Williams, D. R. J. Am. Chem. Soc. **1972**, 94, 295.

7. (a) Cundari, T. R.; Drago, R. S. - unpublished results. (b) Cundari, T. R.; Drago, R. S. Inorg. Chem. - in press. (c) Cundari, T. R.; Drago, R. S. Int. Journal of Quantum Chemistry - in press.

8. Riley, D. P. Inorg. Chem. **1983**, 22, 1965.

9. Root, M. J.; Deutsch, E. Inorg. Chem. **1985**, 24, 1464.

10. Bailey, C. L.; Drago, R. S. Coord. Chem. Rev. **1987**, 79, 321.

11. Davis, S.; Drago, R. S. Inorg. Chem. **1988**, 27, 4759.

12. Schrauzer, D. N. "Transition Metals in Homogeneous Catalysis," Dekker: New York, 1971, p. 131.

BLANK

SELECTIVE, CATALYTIC CONVERSION OF THIOETHER HD ANALOGUES TO THE CORRESPONDING SULFOXIDES. THE R_2S/TBHP/$H_5PV_2Mo_{10}O_{40}$ SYSTEM.

Craig L. Hill * and Mahmoud Faraj
Department of Chemistry, Emory University, Atlanta, GA 30322

ABSTRACT

The system *t*-butylhydroperoxide (TBHP) / $H_5PV_2Mo_{10}O_{40}$ oxidizes thioethers to the corresponding sulfoxides catalytically and selectively by a complex mechanism. With an equivalent amount or less of TBHP present, no sulfone is produced. Rate studies with authentic thioethers, sulfoxides, and sulfones, and the isolation and characterization of a completely stable protonated sulfoxide salt of the catalyst establish the true stability of the sulfoxide under the reaction conditions. The substrate oxidation/polyoxometalate reduction process is the first and rate determining step in the overall mechanism. The oxidations are first order in thioether, second order in polyoxometalate, and variable order in H^+.

INTRODUCTION

The impetus for this work derives from the fact that the sulfoxide obtained from mustard (HD) is substantially less toxic than the corresponding sulfone. At the outset of this project, we searched the literature on thioether oxidation systems exhaustively with respect to their selectivity for production of sulfoxide versus sulfone or other products. Examination of all these thioether oxidation systems, stoichiometric and catalytic alike, indicated that several systems have values for k_1/k_2 (eq 1 and 2) of 5 to 100 but k_2 appears to be finite in all cases, thus some sulfone could be produced.[1] If k_2 is finite then decon of

$$R_2S + OX \xrightarrow{k_1} R_2SO + RED \qquad (1)$$

$$R_2SO + OX \xrightarrow{k_2} R_2SO_2 + RED \qquad (2)$$

HD by such systems would gradually produce more sulfone, thus becoming more toxic with time.

With the goal in mind of finding an effective nontoxic and transportable system for thioether oxidation system for which $k_2 = 0$, we reported preliminary data a year ago on a thioether oxidation system comprised of the the inexpensive, accessible and transportable oxidant *t*-butylhydroperoxide (TBHP) and the vanadium-substituted heteropoly acid, $H_5PV^V_2Mo^{VI}_{10}O_{40}$ that appeared to effect the quantitative oxidation of several thioethers only to the corresponding sulfoxides.[2] An exemplary reaction is eq 3.

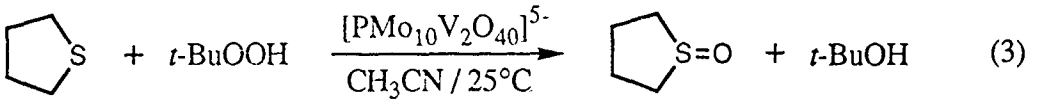

(3)

The conversions not only with tetrahydrothiophene (THT), eq 3, but also for a number of other thioethers including half mustard are virtually quantitative.

Inasmuch as the system in eq 3 appeared to have considerable promise, we undertook over the last year to examine this chemistry in detail. We report here the results of this work.

EXPERIMENTAL

Materials and Methods. Benzene solutions (~3.6M) of TBHP were prepared and titrated as described previously.[2] The thioethers and their oxidation products, sulfoxides and sulfones, were purchased from Aldrich or Fluka. Purities (>98% in all cases) were checked by chromatography. The *N*-acetyliminotetramethylenesulfonium bromide was prepared and purified by literature procedures,[3] mp: 66°C (lit. mp = 66-68°C). The infrared and ^{1}H NMR spectra were also consistent with the product. The $H_5PV_2Mo_{10}O_{40}{\cdot}x(H_2O)$ was prepared and purified by literature methods.[4] The purity of the polyoxometalate catalyst was checked spectroscopically (ir, ^{31}P NMR, UV-visible).[4] Gas chromatographic analyses were performed using an H/P 5890 gc equipped with FID detectors and a 5% phenyl methyl silicone capillary column. The ir spectra were made using a PE spectrometer operating between 4000-250 cm^{-1} and electronic absorption spectra were recorded on a Hewlett/Packard 8451A multidiode array instrument. ^{1}H and ^{13}C NMR measurements were made using a 300-MHz General Electric Model QE-300 spectrometer. The ^{31}P NMR spectra were made using a IBM WP200SY spectrometer.

Preparation of tetrakis(hydroxytetrahydrothiophenesulfonium) salt of the catalyst: $(THTOH^+)_4(H^+)(PV^V_2Mo^{VI}_{10}O_{40}{}^{5-})$. To 1 mmol of $PV^V_2Mo^{VI}_{10}O_{40}$ in 50 ml of acetonitrile at 25°C, was added slowly dropwise, 5.5 mmol of tetrahydrothiophene oxide (THTO). A yellow precipitate was formed quickly. The mixture was stirred for 15 min then the complex was separated from the mixture by filtration (medium fritted glass funnel). The product was then washed with several 2-mL portions of acetonitrile then ether. The complex was dried in vacuo to give 75% of the title complex. $\{^1H\}^{13}C$ NMR: (dilute D_2O solution [~ 10^{-5} M]; δ in ppm): 24.51 (s, β-C, 2H); 52.78 (s, α-C, 2H). (The $\{^1H\}^{13}C$ NMR literature values for free THTO; δ in ppm: 25.4 (s, β-C, 2H); 54.3 (s, α-C, 2H)).[5] ^{1}H NMR: (~ 10^{-5} M in D_2O); δ in ppm: 1.95 (m, CH_2 anti to SO group, 2H); 2.14 (m, CH_2 syn to SO group, 2H): 2.83 (m, 4H, CH_2 α to SO group). Infrared (cm^{-1}): 1080 (m), 950 (s), 860 (m, broad), 700-830 (broad). Elemental analysis was satisfactory for C, H, and S.

Conditions for Reactions and Kinetics Measurements. In a typical reaction, 56.8 mmol of thioether substrate, 56.8 mmol of TBHP and 1 mmol of catalyst, $PV^V_2Mo^{VI}_{10}O_{40}{}^{5-}$ in 5 mL of CH_3CN in a Schlenk flask under Ar were allowed to react until all the oxidant had been consumed (usually just a few min). Reactions were followed by reduction of the catalyst (UV-visible of reduced complex: λ_{max} = 780 nm with ε = 1,430 M^{-1} cm^{-1}) and/or by generation of organic oxidation products (gc or gc/ms) using a Schlenk cuvette as the reaction vessel. First-order plots of the reactions to several half-lives indicated significant curvature only in the latter stages of reaction. The organic products were quantified using internal standard techniques.

RESULTS AND DISCUSSION

The oxidations of several aliphatic and mixed aromatic/aliphatic thioethers by TBHP catalyzed by $H_5PV_2Mo_{10}O_{40}$ were examined, eq 4. Unlike several other polyoxometalates

$$R_2S + t\text{-BuOOH} \xrightarrow[\text{under Ar or } N_2]{H_5PV_2Mo_{10}O_{40}} R_2SO + t\text{-BuOH} \qquad (4)$$

Where R_2S = THT, half mustard, dibutyl sulfide, diphenyl sulfide, other thioethers.

the latter complex leads to the production of sulfoxide only. To determine if in fact k_2 (eq 2) was effectively zero in this case, we sought evidence for sulfoxide oxidation products under the reaction conditions (eq 4). Repeated efforts turned up no such evidence.

In addition we sought to isolate a sulfoxide complex of the oxidized form of the catalyst. A complex of formula $(THTOH^+)_4(H^+)(PV^V_2Mo^{VI}_{10}O_{40}{}^{5-})$ based on elemental analysis was isolated from the the reaction when TBHP was absent and made independently from THTO and $H_5PV_2Mo_{10}O_{40}$. Based on elemental analyses and spectroscopic properties the complexes from the two different sources were identical. It was established that this complex was thermally stable -- the sulfoxide-based cations were not oxidized by the polyoxometalate anion.

One general feature of these thioether oxidations (eq 4) is that there are two fundamental and experimentally separable steps in the reaction: direct oxidation of the thioether substrate by the polyoxometalate producing sulfoxide and reduced polyoxometalate, eq 5, and reoxidation of the reduced polyoxometalate by TBHP, eq 6. TBHP is known to oxidize sulfoxides to sulfones albeit very slowly. In the presence of the catalyst, however, the rates of eq 5 and 6 are orders of magnitude faster than the rate of direct TBHP oxidation of thioether and for this reason as long as there is not a molar excess of TBHP present, no sulfone is generated whatsoever.

$$R_2S + 2\,(H^+)_5(PV^V_2Mo^{VI}_{10}O_{40}{}^{5-}) + H_2O \text{ ------>}$$
$$(R_2SOH^+)(H^+)_4(PV^{IV}V^VMo^{VI}_{10}O_{40}{}^{6-}) + (H^+)_6(PV^{IV}V^VMo^{VI}_{10}O_{40}{}^{6-}) \qquad (5)$$

$$2\,(H^+)_6(PV^{VI}V^VMo^{VI}_{10}O_{40}{}^{6-}) + t\text{-BuOOH} \text{ ------> } 2\,(H^+)_5(PV^V_2Mo^{VI}_{10}O_{40}{}^{5-})$$
$$+ t\text{-BuOH} + H_2O \qquad (6)$$

Reaction 5 is first order in R_2S, second order in polyoxometalate, variable order in H^+ and minimally sensitive to water. Analyses indicate that the catalyst itself contains several water molecules of crystallization. The substrate activation step most likely involves electron transfer from the thioether sulfur to one of two molecules of the catalyst in the rate determining transition state. Reoxidation of the reduced complex, $PV^{IV}V^VMo^{VI}_{10}O_{40}{}^{6-}$, by TBHP is considerably less complex and appears to first order in TBHP.

The most likely initial intermediate derived from oxidation of substrate given the kinetics data and the literature on thioether oxidations is the thioether cation radical, $R_2S^{+\bullet}$. It has been documented that thioether cation radicals react readily with water, O_2 and acetonitrile.[3,6] Water is present in small quantities in our reactions and is the most likely trapping agent for these intermediates in our reactions. O_2 could be generated in these reactions from radical chain ("Haber-Weiss") decomposition of TBHP. Thioether radical cations and O_2 are known to produce thioether hydroperoxy radicals, $R_2S^+OO^\bullet$, which can function as chain carriers in radical chain autoxidation of thioethers.[6b] We do not feel that this type of process is important in the thioether reactions reported here as the catalyst, $H_5PV_2Mo_{10}O_{40}$, does not appear to have appreciable activity for inducing the homolytic

breakdown of TBHP under the reaction conditions. We cannot rule out some component of this chemistry, however. Furthermore, there is remote chance that O_2 could be generated from TBHP under the reaction conditions via heterolytic mechanisms.

The final fate of the thioether cation radicals we addressed was the possible reaction with the acetonitrile solvent to generate the *N*-acetyliminosulfonium cations, **1**, eq 7. One exemplary such cation, that derived from attack on THT radical cation, (i.e. R_1R_2

$$R_1R_2\dot{S}^{+} + CH_3CN \rightleftharpoons R_1R_2\dot{S}\text{-}N{=}\overset{+}{C}\text{-}CH_3 \xrightarrow[\text{Oxidation and Hydrolysis}]{} \underset{\mathbf{1}}{R_1R_2\overset{+}{S}\text{-}NH\text{-}CO\text{-}CH_3} + H^{+} \qquad (7)$$

in eq 7 = $-CH_2CH_2CH_2CH_2-$) was prepared from an independent method,[3] purified, and shown to be completely stable under the reaction conditions. As a consequence, the importance of eq 7 in this chemistry appears to be marginal at best.

CONCLUSIONS

The complex $H_5PV_2Mo_{10}O_{40}$ catalyzes the oxidation of thioethers including half mustard and other HD analogues by *t*-butylhydroperoxide (TBHP) selectively to the sulfoxide. The overall process is comprised of two parts, the oxidation of the substrate by the polyoxometalate catalyst and reoxidation of the reduced catalyst by TBHP. Not only does this system fail to produce any sulfone from sulfoxide under the reaction conditions, but protonated sulfoxide complexes of the oxidized form of the catalyst have been isolated from the reactive system and prepared independently. The latter are completely stable to further thermal reaction establishing that we have a thioether oxidation system that is not only catalytic but one that generates no sulfone. The mechanistic information obtained on this system permits a rational and simple method, manipulation of polyoxometalate composition and protonation state, to control the selectivity-determining ratio of rates in the thioether oxidations, $k_{thioether}$[thioether][oxidant]/$k_{sulfoxide}$[sulfoxide][oxidant] and other features of the reaction.

ACKNOWLEDGEMENTS

We thank the U.S. Army Research Office for support.

REFERENCES

1. A tabular review of stoichiometric and catalytic thioether oxidation systems is available (Chambers, R. C.; Hill, C. L.) on request.
2. Hill, C. L.; Faraj, M.; Chambers, R. C. *Proceedings of the 1988 CRDEC Conference on Chemical Defense Research.*
3. Kise, H.; Whitfield, G. F.; Swern, D. *J. Org. Chem.* **1972**, *37*, 1121.
4. (a) Domaille, P. J.; Watunya, G. *Inorg. Chem.* **1986**, *25*, 1239; see also Domaille P. J., *J. Amer. Chem. Soc.*, **1984**, 106, 7677-87; (b) Tsigdinos G. A.; Hallada C. J. *Inorg. Chem.* **1968**, *7*, 437.
5. Kalinowski, H. O.; Berger, S.; Braun, S. *^{13}C NMR Spectroscopy* John Wiley: New York, 1988; p 359.
6. (a) Block, E. In *Chemistry of ethers, crown ethers, hydroxyl groups and their sulphur analogues* Part 1; Patai, S, Ed.; John Wiley: New York, 1980; Chapter 13; (b) Riley, D. P.; Smith, M. R.; Correa, P. E. *J. Am. Chem. Soc.* **1988**, *110*, 177; (c) Shine, H. J. In *The Chemistry of the Sulphonium Group* part 2, Patai S., Ed.; John Wiley & Sons: New York, 1981; Chapter 14.

PHOTOCATALYTIC C-H AND C-S BOND CLEAVAGE IN MUSTARD ANALOGUES

Craig L. Hill and R. Carlisle Chambers
Department of Chemistry, Emory University, Atlanta, GA 30322

ABSTRACT

Polyoxotungstate complexes catalyze the photochemical oxidative degradation of half mustard and other thioether analogues of mustard under both aerobic and anaerobic conditions. Under anaerobic conditions two unusual modes of thioether degradation are noted, C-S bond cleavage and C-H bond cleavage. The catalytic anaerobic photochemical degradation of the exemplary thioether tetrahydrothiophene (THT) by decatungstate, $W_{10}O_{32}^{4-}$, although first order in complex and light intensity is variable order in THT and fairly complex. The addition of O_2 to these reactions increases the rates and conversions for thioether degradation. The aerobic reactions are exceedingly complex mechanistically but lead to complete and rapid degradation of the thioethers.

INTRODUCTION

One year ago we reported preliminary results indicating that some readily accessible, inexpensive, and environmentally acceptable polyoxometalates could degrade thioether analogues of mustard catalytically and under mild conditions in the presence of O_2 and light (e.g. eq 1).[1] These results and the fact that polyoxometalates can be formulated to function

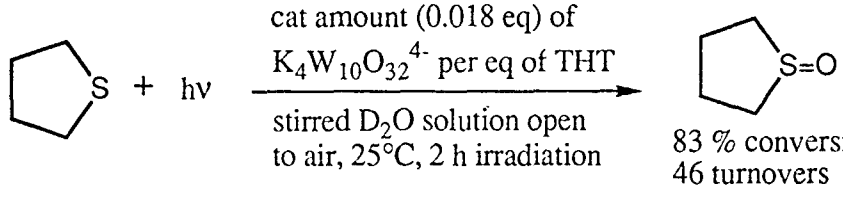

(1)

in aqueous, anhydrous, microemulsion or other media, indicated significant potential for these materials in decontamination. As a result, we have examined these photochemical oxidative thioether degradations and related processes in detail. We report here the products and the principal energetic and mechanistic features of these reactions.

EXPERIMENTAL

The polyoxometalate photoinitiators/photocatalysts $H_3PW_{12}O_{40}$, $[(C_4H_9)_4N]_3PW_{12}O_{40}$, $[(C_4H_9)_4N]_4W_{10}O_{32}$, and $Na_4W_{10}O_{32}$, were prepared using literature procedures.[2] The thioethers and all products derived therefrom were commercial samples. The purity of all materials was assessed by one or more of the following methods: UV-visible, gas chromatography (gc), ^1H NMR.

In a typical aerobic or anaerobic reaction, 5 mL of acetonitrile solvent 10 mM in thioether substrate, 0.2 mM in polyoxometalate, and 9 mM in internal standard were degassed in a 30-mL pyrex Schlenk flask fitted with a Teflon stopper. For aerobic reactions, 25cc of O_2 (1 atm) were added; anaerobic reactions were maintained under ~1 atmosphere of Ar. The reactions were then irradiated using a 550-W Hg vapor lamp or a

1000-W ozone-free Xe arc lamp at a constant temperature of 20°C. Product analyses were performed immediately after reaction by GC or NMR. GC/MS was used to identify some products. The kinetics measurements were made using cylindrical Schlenk quartz cuvettes (2.0mm-pathlength). Other experimental procedures have been reported.[1-3]

RESULTS AND DISCUSSION

Several polyoxometalates catalyze the photochemical oxidative degradation of a range of thioethers including the mustard analogue, 2-chloroethyl ethyl sulfide (half mustard) not only under aerobic conditions but also under anaerobic conditions. The aerobic reactions lead to greater levels and more rapid conversion of the substrates. Exemplary aerobic reactions are given in Table I. Under these conditions thioether produces principally sulfone. Any sulfoxide produced is oxidized further to the sulfone. The product balances for the reactions in Table I are poor. That is, much of the thioether reactant is not accounted for by the quantities of sulfoxide and sulfone present. The nature of the

Table I. Polyoxometalate Initiated Aerobic Oxidation Of Thioethers[a]

Thioether(mM)	Initiator(mM)	time (h)	% loss of R_2S
1. THT (10)	$Na_4W_{10}O_{32}$(0.2)	14	100
2. THT(25)	$Na_4W_{10}O_{32}$ (0.4)	16	100
3. THT (10)	$Na_4W_{10}O_{32}$ (0.4)	1	>95
4. THT (10)	$Na_4W_{10}O_{32}$ (0.4)	0.5	54
5. THT(25)	$Q_4W_{10}O_{32}$ (0.4)	16	~50
6. THT (25)	$H_3PW_{12}O_{40}$(0.4)	16	55
7. PhSPh (10)	$Na_4W_{10}O_{32}$ (0.4)	14	62
8. $EtS(CH_2)_2Cl$ (10)	$Na_4W_{10}O_{32}$ (0.4)	14	100
9. $PhSCH_3$ (10)	$Na_4W_{10}O_{32}$ (0.4)	14	100
10. BuSBu (10)	$Na_4W_{10}O_{32}$ (0.4)	14	100

[a] Reaction conditions given in EXPERMIENTAL. Reactions 3,4 irradiated with 1000-W Xe lamp.

oxidative degradations not involving the conventional and facile oxidations at the sulfur atom are clarified in the anaerobic studies discussed below. Attempts to determine rate constants of exemplary aerobic reactions met with difficulty. Kinetics measurements even at early reaction times and under pseudo-first-order conditions were not satisfactorily reproducible to be of value. Doubtless the presence of several simultaneous and competing thioether substrate oxidation processes renders a close examination of these systems impractical if not misleading. The radicals generated by the photoinduced oxidation of substrate (at sulfur, and as we shall see below, at the C-H bonds and elsewhere) initiate free radical chain autoxidation of the substrate. The latter process itself is quite complex.

Partly in light of the intractability of the catalytic aerobic reactions and partly because the presence of O_2 and radical chain oxidation processes would obscure unusual or potentially significant reactivities, we turned to the examination of the photochemical anaerobic oxidation of thioethers catalyzed by polyoxometalates, and in particular by the highly reactive complex, decatungstate. These reactions were sufficiently simple that they could be studied with some rigor. First, product distribution studies with half mustard and diphenyl sulfide as substrates gave direct evidence for C-H bond cleavage and C-S bond cleavage respectively -- the products in eqs 2 and 3 have been identified. Neither of these reactions although highly novel are surprising given the documented reactions of polyoxometalate excited states with alkanes and other organic compounds.[3] The kinetics followed principally by production of the reduced form of the catalyst, proved to be first order in complex and light intensity and variable order in THT. Clearly even the anaerobic

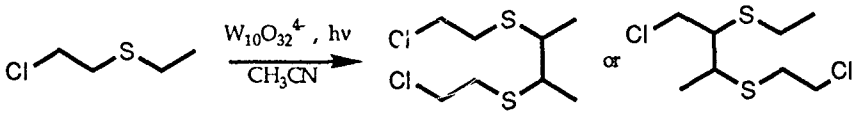

(2)

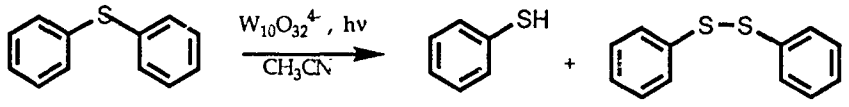

(3)

reactions are fairly complex. The data are in accord with a mechanism involving rate determining oxidation of the thioether substrate by the charge transfer excited state of decatungstate (accessible by absorption of one photon of light). The mechanisms of these unusual and potential useful reactions are under continuing investigation.

CONCLUSIONS

Some polyoxometalates, and in particular, decatungstate ($W_{10}O_{32}^{4-}$) catalyze the rapid and high conversion oxidative degradation of thioether mustard analogues in the presence of air not only by oxidation at sulfur but also by cleavage of C-H and C-S bonds. The latter reactions can be effected under anaerobic conditions. Although the aerobic reactions involve many simultaneous oxidation processes including those associated with radical chain autoxidation, the anaerobic reactions are simpler. The rate law (first order in decatungstate, and light intensity and variable order in thioether substrate) is compatible with a rate determining oxidation of the substrate by the excited state of the decatungstate. Multiple mechanisms of substrate attack appear to be operable even in the anaerobic reactions. The rates, products, and tractability of these decatungstate-catalyzed photochemical degradations indicate their potential value in decontamination of HD and HD by-products.

ACKNOWLEDGEMENTS

We thank the U.S. Army Research Office for support.

REFERENCES

1. Hill, C. L.; Faraj, M.; Chambers, R. C. *Proceedings of the 1988 CRDEC Conference on Chemical Defense Research.*
2. Wu, H., *J. Biol. Chem.* 1920, *43*, 189; (b) Chemseddine, A., Sanchez, C., Livage, J., Launay, J. P., Fournier, M., *Inorg Chem.* 1984, *23*, 189; (c) Renneke, R. Ph.D. thesis, Emory University, 1989.
3. (a) Hill, C. L.; Bouchard, D. A. *J. Am. Chem. Soc.* **1985**, *107*, 5148;
(b) Renneke, R. F.; Hill, C. L. *ibid.* **1988**, *110*, 5461;
(d) Hill, C. L.; Bouchard, D. A.; Kadkhodayan, M.; Williamson, M. M.; Schmidt, J. A.; Hilinski, E. F. *ibid.* **1988**, *110*, 5471, and references cited therein.

BLANK

MECHANISMS OF VX OXIDATION I. OXIDATION BY PEROXIDES AND OXONE

Yu-Chu Yang*, Linda L. Szafraniec, William T. Beaudry
and Dennis K. Rohrbaugh

Physical Protection* and Research Directorates, U.S. Army Chemical Research,
Development and Engineering Center,
Aberdeen Proving Ground, MD 21010-5423

abstract

The nerve agent VX is an unusally selective oxidation substrate. In addition to sulfur, the nitrogen present as a tertiary amino group was a more reactive site for oxidation. The oxidation mechanisms of VX and its derivatives by a broad range of peroxygen compounds were examined in organic, polar organic, and aqueous solvents. VX was found to be either inactive or reactive by two separate mechanisms: 1. In organic and neutral solvents, the nitrogen was oxidized first to an N-oxide, which was stable in polar solvents but decomposed by a Cope reaction in organic solvents. 2. After the nitrogen had been oxidized or protonated in an acidic aqueous solvent, the sulfur was further oxidized followed by nucleophilic substitution at the P-S bond. Detoxification can be accomplished by the second mechanism.

INTRODUCTION

The hydrolysis of VX(**1a**, S-(diisopropylamino)ethyl O-ethyl methylphosphonothiolate) was slow even at very high and low pH values.[1] The observed rate of the spontaneous hydrolysis of VX in pure water in the absence of any pH control was estimated to have a half-life of 80 hours.[2] Furthermore, multiple hydrolysis paths have been reported: As shown in Equations (1) through (3), VX hydrolyzed via simultaneous cleavage of the P-S, S-C and P-O bonds.[1,2] Although both the ethyl methylphosphonic acid(**1b**) and the O-ethyl methylphosphonothioic acid(**1c**) products are relatively non-toxic, the displacement of the better-leaving O-ethyl group produces the S-(diisopropylamino)ethyl methylphosphonothioic acid(**1d**), which is almost as toxic as VX.[3] This almost precludes hydrolysis as an effective reaction to detoxify VX.

The rate and mechanism of the oxidation of VX are investigated in order to identify the controlling factors for the detoxification of VX by oxidation. Stable

commercial peroxygen compounds such as m-chloroperoxybenzoic acid, t-butyl hydroperoxide, and OXONE (active component HSO_5^-)[4,5] were used in solvents ranging from pure t-butanol, t-butanol-water mixtures, to pure water. In all cases, the VX oxidation was compared with that of a simple phosphonothiolate derivative, O-ethyl S-ethyl methylphosphonothiolate(**1e**, see Equation (7)), to determine the effect of the diisopropylamino group in VX on the mechanism of oxidation.

VX, 1a **1b** **2a**

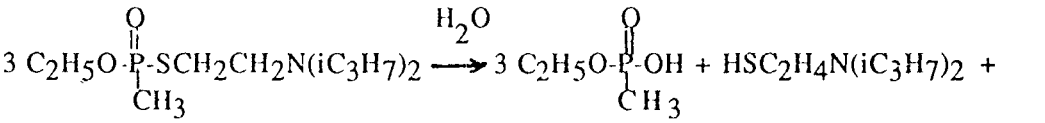

$$3\ C_2H_5O\text{-}P(=O)(CH_3)\text{-}SCH_2CH_2N(iC_3H_7)_2 \xrightarrow{H_2O} 3\ C_2H_5O\text{-}P(=O)(CH_3)\text{-}OH + HSC_2H_4N(iC_3H_7)_2 +$$

$$(iC_3H_7)_2NC_2H_4S\text{-}SC_2H_4N(iC_3H_7)_2 \qquad (1)$$

2b

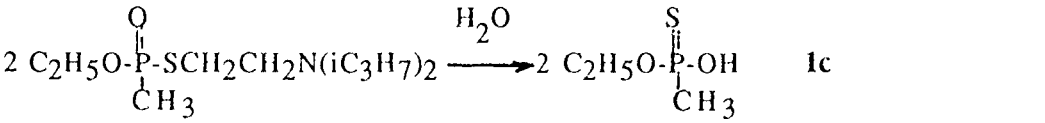

$$2\ C_2H_5O\text{-}P(=O)(CH_3)\text{-}SCH_2CH_2N(iC_3H_7)_2 \xrightarrow{H_2O} 2\ C_2H_5O\text{-}P(=S)(CH_3)\text{-}OH \quad \textbf{1c}$$

$$+\ (iC_3H_7)_2{}^+N\langle\bigcirc\rangle N^+(iC_3H_7)_2 \qquad (2)$$

3a

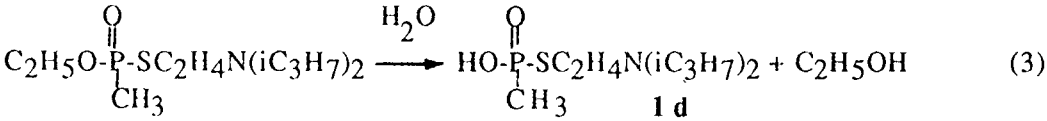

$$C_2H_5O\text{-}P(=O)(CH_3)\text{-}SC_2H_4N(iC_3H_7)_2 \xrightarrow{H_2O} HO\text{-}P(=O)(CH_3)\text{-}SC_2H_4N(iC_3H_7)_2 + C_2H_5OH \qquad (3)$$

1d

Detailed experimental procedures are described in a future publication.[6] All of the oxidation studies were monitored at 19-21°C by ^{31}P NMR. Observed first-order rate constants were determined in the presence of 10 to 30 moles excess oxidant per mole substrate, which was typically 0.01-0.04 M. For fast oxidations, first-order rate coefficients were obtained in dilute D_2O solutions of 0.0005 M substrates by ^1H NMR. The products from each reaction were further identified by ^{13}C NMR and GC/MS and by comparison with the NMR and GC/MS spectra of model compounds. For GC/MS analyses of aqueous samples, the organic components were extracted in CH_2Cl_2, while the ionic products were identified by Direct Exposure Probe (DEP) Mass Spectrometry. The active oxygen content was quantitatively determined for each oxidant with a standard thiosulfate solution in an iodometric titration.

RESULTS AND DISCUSSION

1. Oxidations by m-Chloroperoxybenzoic acid (m-Cl-$C_6H_4C(O)OOH$) in t-Butanol and t-Butanol-Water Mixtures

In pure t-butanol and a 50 vol% t-butanol solution, an equal molar mixture of VX (0.03 M) and m-chloroperoxybenzoic acid reacted instantaneously to form an N-oxide (**1g** in Equation (4)). One equivalent of active oxygen([O]) was consumed per mole of VX reacted. In pure t-butanol, **1g** subsequently decomposed to **1f** (O-ethyl S-vinyl methylphosphonothiolate, see Equation (5)), apparently by a Cope reaction[7] with a

half-life of approximately 2 hours at 20 °C. On the other hand, the N-oxide was quite stable in the 50 vol% t-butanol-water solution. Only 10% of **1g** was decomposed to **1f** in 27 hours. Both **1g** and **1f** are believed to be toxic.[3] Therefore, the oxidation at the nitrogen can not completely detoxify VX.

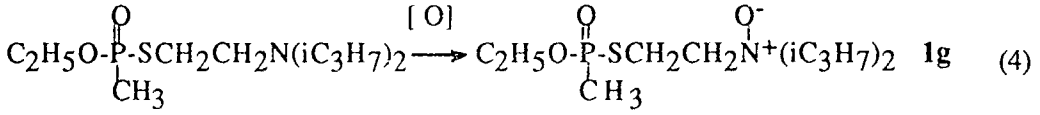

(4)

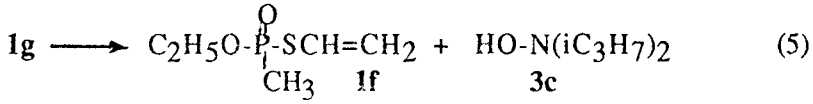

(5)

In the presence of excess peroxybenzoic acid in 50 vol% t-butanol, the sulfur in **1g** was subsequently oxidized followed by hydrolysis at the phosphorus. The reaction is represented by Equation (6), in which the sulfonic acid product(**2c**) was believed to be the initial oxidation product from VX. As the final solution was further analyzed by ^{13}C NMR and by GC/MS after 24 hours, it was decomposed and presumably as a result of further oxidations at the nitrogen.

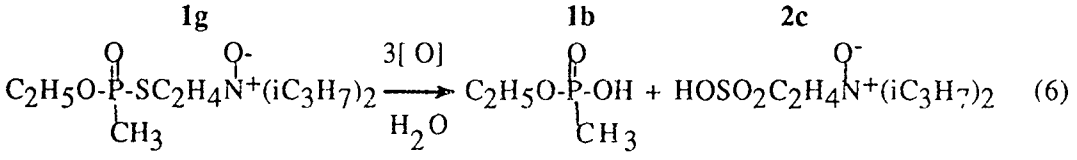

(6)

FIGURE 1

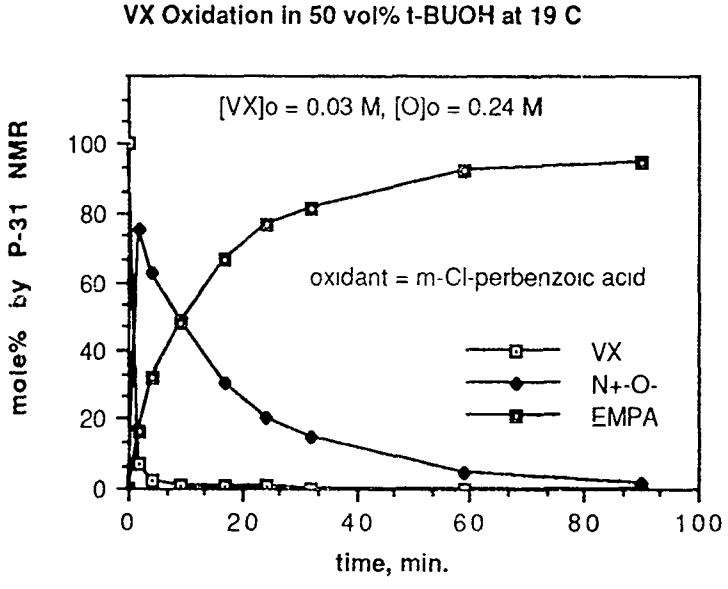

The reaction profile shown in Figure 1 was obtained using ^{31}P NMR. It clearly demonstrates that the sulfur atom can not be oxidized unless all of the VX has been converted to the N-oxide, **1g**. Since the hydrolysis of **1g** is expected to be slow in 50% t-butanol, it is believed that the sulfur in **1g** is oxidized first, followed by hydrolysis at the P-S bond. If this is true, the first-order rate constant at 19°C for sulfur

oxidation at 0.25 M peroxybezoic acid (20 moles of active oxygen per mole VX) has a half-life of 11 min in 50% t-butanol.

The oxidation of the sulfur and the displacement reaction at the phosphorus were further examined using **1e** (Equation (7)). It was observed that while a significant amount of **1e** could be dissolved in pure water, it remained unchanged during the entire monitoring duration of 7 months. No hysrolysis was detected at neutral pH, indicating the S-ethyl was a poor leaving group and that **1e** was hydrolytically less reactive than VX.

In pure t-butanol, the oxidation of **1e** produced a stable intermediate **1j** ((Equation (7)), which subsequently decomposed by reacting with itself, t-butanol, and trace amount of water to produce three products **1k, 1l** and **1m** shown in Equations (8) to (10). The reaction profile is illustrated in Figure 2.

FIGURE 2

Oxidation of 1e by Excess m-Cl Peroxybezoic acid in t-Butanol

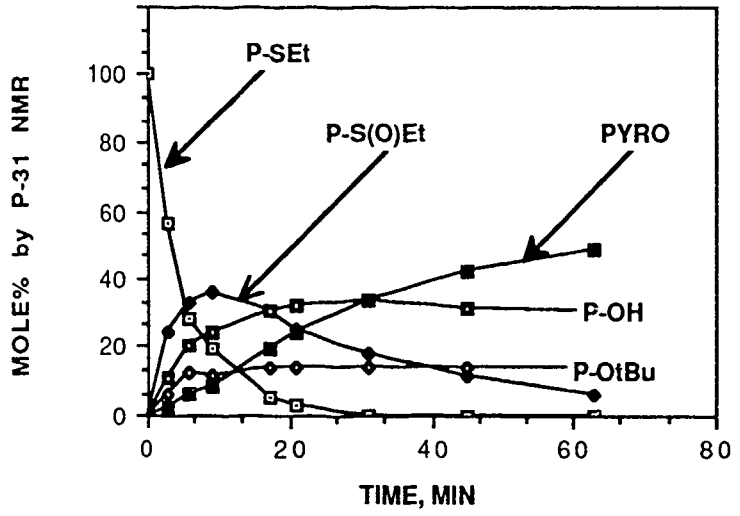

1e **1j**

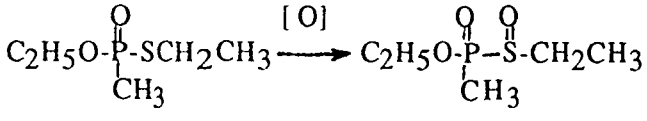

(7)

1j **1k** **2d**

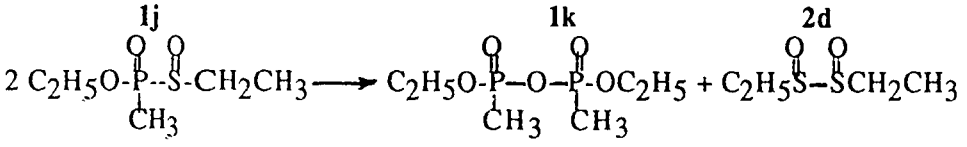

(8)

1j **1l** **2e (?)**

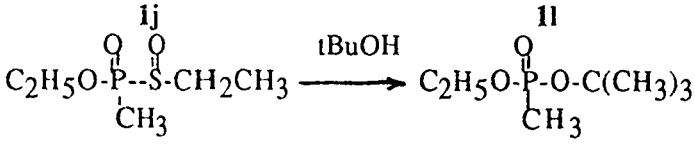

(9)

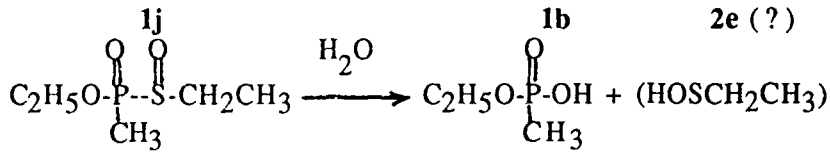

(10)

While compounds **1j**, **1l**, **1b** and **2d** were identified by ^{13}C and/or ^{31}P NMR and by GC/MS, the ethylsulfenic acid **2e** was not detected. Presumably **2e** once formed was immediately oxidized to **2f** (Equation (11)), which was positively identified in the final reaction mixture. In fact, competition of **2e** with the substrate **1e** for the oxidant at low oxidant concentrations was observed. A minimum of 3 moles of active oxygen was required to react with one mole of **1e**, indicating that the oxidation of **2e** in Equation (11) was much faster than that of **1e** in Equation (7).

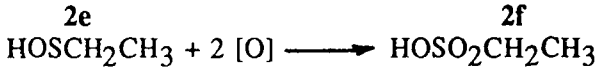

(11)

The formation of the pyrophosphate **1k** in Equation (8) was very interesting since **1k** has been frequently detected as a degradation product of neat VX and **1e** under storage at both room and elevated temperatures.[8] The reaction was presumably initiated by trace amount of moisture. As shown in Figure 2, the formation of **1k** was slower in the beginning but became faster than that of **1l** and **1b** because the formation of **1k** required the accumulation of a significant amount of **1j**. However, the toxicity of **1k** is significant, and for the purpose of detoxification a large amount of a good nucleophile such as water is still required even if after the sulfur is oxidized. This nucleophilic substitution must be fast to compete effectively with Equation(8) so that **1k** is eliminated completely.

In a 50% t-butanol-water mixture, **1e** was quickly converted to **1b** and ethylsulfonic acid(**2f**) according to Equation (12). **1j** could not be detected as a stable reaction intermediate in the presence of water. Since water is a better nucleophile than t-butanol, the displacement reaction must have occurred immediately after the sulfur is oxidized.

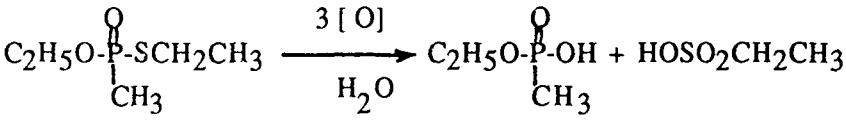

(12)

The absence of hydrolytic reactivity of **1e**, the identification of **1j** as an oxidation intermediate, and the fast oxidation of both VX and **1e** make it possible to conclude that in aqueous solutions, hydrolysis of both VX and **1e** occur only after the sulfur has been oxidized and become a good leaving group; and that the alternate mechanism, which assumes that oxidation of the sulfur is preceeded by hydrolysis at the P-S bond, is very unlikely.

2. Oxidation by OXONE ($2KHSO_5 \cdot K_2SO_4 \cdot KHSO_4$) in Water and in t-Butanol-Water Mixtures

As shown in Equation (13), VX reacted with OXONE to form the corresponding phosphonic acid(**1b**) and sulfonic acid(**2c**) via P-S bond cleavage in pure water. Two moles of OXONE (containing 3 equivalents of active oxygen) are required to oxidize one mole of VX. No reaction intermediate could be detected. In the presence of 15

moles excess OXONE, ^{13}C NMR showed that the nitrogen in VX was not attacked even after 24 hours.

$$C_2H_5O\text{-}\underset{\underset{CH_3}{|}}{\overset{\overset{O}{\|}}{P}}\text{-}SC_2H_4N(iC_3H_7)_2 \xrightarrow[H_2O]{3[O]} C_2H_5O\text{-}\underset{\underset{CH_3}{|}}{\overset{\overset{O}{\|}}{P}}\text{-}OH + HOSO_2C_2H_4N(iC_3H_7)_2 \quad (13)$$

2c

The observed first-order rate constant for the oxidation of 0.0005 M VX by 0.01 M excess OXONE(active oxygen=0.017 M) was determined by ^1H NMR in D_2O. This rate, with a half-life of 19 min at 0.01 M OXONE, is sufficiently large for fast detoxification of VX at practical concentrations. The single oxidation step followed by P-S bond cleavage is perhaps due to the fact tnat the nitrogen in VX is completely protonated. The oxidation of VX was slower in 50% t-butanol than in pure water. In addition to **1b** and **2c**, a small amount of **1g** was produced. The protonation of the nitrogen was apparently not as effective in 50% t-butanol as in pure water.

To verify the hypothesis that the nitrogen once protonated would not be oxidized, the oxidation of 0.01 M VX by 0.04 M peroxybenzoic acid (0.032 equivalents of active oxygen) in the presence of 0.05 M HCl was examined in 50% t-butanol. Almost all of the VX was converted to **1b** and **2c**. Only a trace amount of **1g** was produced initially for a short time, and was subsequently oxidized to the observed products. No **1f** was ever produced.

The reaction of **1e** with OXONE in pure water was instantaneous, and the same products shown in Equation (12) above were formed. The observed first-order rate constant at 0.010 M OXONE (a mixture of 0.017 M [O] and 0.0005 M **1e**) in D_2O was equivalent to a half-life of 4.8 min, about five times that of VX. VX reacted slower perhaps partly as a result of the bulky amino group. The faster oxidation and slower hydrolysis of **1e** relative to VX indicate once again that the oxidation of **1e** is independent of any prior hydrolysis. The simple and fast oxidation of the phosphonothiolates makes the peroxypersulfate an attractive oxidant to detoxify VX. In particular, VX has a large solubility via the protonation of the nitrogen in the acidic solution of OXONE (pH=2.3 at 20°C). The oxidation rate of **1e** by OXONE was also reduced in a 50 vol% t-butanol solution. However, in the presence of a stoichiometric amount of the oxidant, the oxidation of the sulfur atom by OXONE was faster than by the peroxybenzoic acid discussed in 1. above.

3. t-Butyl Hydroperoxide(t-BuOOH) in Water, t-Butanol, and t-Butanol-Water

The oxidation of both VX and **1e** by t-BuOOH was monitored by ^{31}P NMR in three solvent systems, t-butanol, water, and the 50 vol% t-butanol solution for a period of 24 hours. Neither VX nor **1e** reacted with t-BuOOH in any of the three solvent systems. During this period, the only reaction detected was that for VX in water: VX hydrolyzed via the same parallel reaction paths (Equations (1) to (3)) to produce the three phosphorus-containing products as in pure water. The hydrolysis rate was a little faster, perhaps as a result of the subsequent oxidations of the sulfide products from hydrolysis. However, no hydrolysis could be detected for **1e**.

4. Proposed Oxidation Mechanism for VX

Based on the above observations, the mechanism of VX oxidation is proposed in Scheme 1. In the presence of a reactive oxidant in a neutral organic or neutral

aqueous solution, VX is oxidized at the nitrogen to form an N-oxide. The N-oxide is stable in aqueous solutions but decomposes slowly in both polar and apolar organic solvents by a Cope reaction. In polar solvents, the sulfur of the N-oxide can be further oxidized by excess oxidant followed by nucleophilic substitution or hydrolysis at the P-S bond. The rate of oxidation at the sulfur (k_{NOS}) is smaller than k_N. In acidic solutions, VX is converted to an ammonium salt (VXH^+), and can only be oxidized at the sulfur. The rate of the sulfur oxidation, k_{VHS}, is significantly faster than k_{NOS} perhaps as a result of acid-catalyzed hydrolysis at the phosphorus.[1] In a less-polar acidic solution, a significant amount of unprotonated VX can still exist; the nitrogen, then, will be oxidized first.

Scheme 1

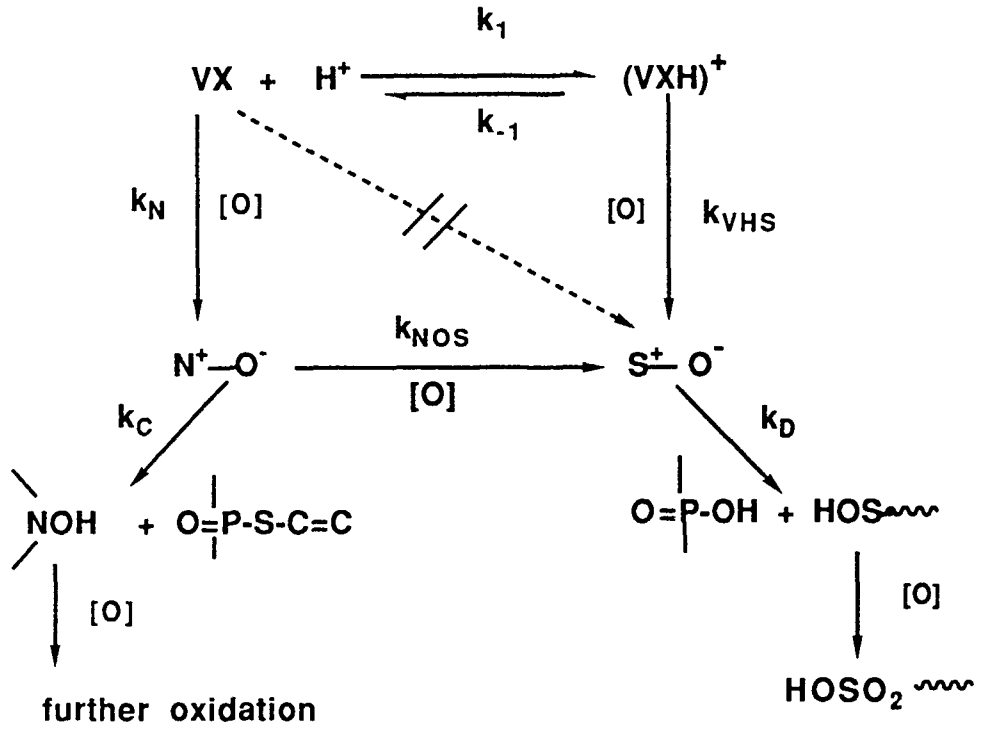

Therefore, in addition to pH, the polarity of the solvent as well as the relative magnitudes of both k_N and k_{VHS} affect the equilibrium between VX and VXH^+(k_1 and k_{-1}), and consequently affect the mechanism and products of oxidation. No direct oxidation of the sulfur in VX was ever observed, therefore, k_S as represented by the dotted arrow in Scheme 1 does not exist. In the two extreme cases, organic solvents promote the reactions in the directions of k_{-1}, k_N and k_C (k_C for the Cope reaction, which is negligible in polar solvents); whereas aqueous acidic solutions promote the reactions in the directions of k_1, k_{VHS} , and k_D (k_D for the displacement or hydrolysis at the P-S bond after the sulur is oxidized). In both cases the secondary oxidation of the sulfide and amine products is faster than the oxidation of VX. The observed first-order rate constants for the oxidation of both VX and **1e** by excess oxidant at 19-20 ^{o}C are expressed in half-lives and summarized in Table 1.

TABLE 1
Oxidation Half-Lives with Excess Oxidant at 19-20°C

SUBSTRATE	SOLVENT	OXIDANT	[O], M	HALF-LIFE, min	
VX	$CDCl_3$	N-sulfonyloxaziridine[a]	0.10	4.1	(k_N)
	t-BuOH-H_2O	peroxybenzoic acid	0.20	< 1	(k_N)
	D_2O	OXONE	0.017	19	(k_{VHS})
	t-BuOH-H_2O	peroxybenzoic acid	0.20	11	(k_{NOS})
1e	D_2O	OXONE	0.017	4.8	(k_S)

a. The rate of oxidation was reported in Reference 9.

REFERENCES

1. Epstein, J.. Callahan, J. J., Bauer, V. E., Phosphorus, (1974) 4, 157-163

2. Szafraniec, L. J., Szafraniec, L. L., Beaudry, W. T., and Ward J. R., On the Stoichiometry of Phosphonothiolate Ester Hydrolysis, in Preceedings of the CRDEC Scientific Conference on Chemical Defense, Aberdeen Proving Ground, MD, November. 1988

3 Private communications with Dr. Herbert Aaron and Mr. William Ashman of the Research Directorate, CRDEC, APG, MD.

4. Trost, B. M.; Curran, D. P.; Tet. Lett., (1981) 22, 1287-1290

5. Kennedy, R. J.; Stock, A. M.; J. Org. Chem., (1960) 25, 1901-1907

6. Yang, Y.-C.; Szafraniec, L. L.; Beaudry, W. T.; Rohrbaugh, D. K.; The Oxidation Mechanism of Phosphonothiolate, in preparation

7. Cope, A. C.; LeBel, N. A.; Lee, H. H., Moor, W. R.; J. Am. Chem. Soc., (1957) 79, 4720

8. D'Agostino, P. A.; Provost, L. R.; Visentini, J., J. Chromatgr. (1987) 402, 221-232

9. Yang, Y.-C.; Szafraniec, L. L.; Beaudry, W. T.; and Davis, F. A.; On Simulating the Oxidation Reactivities of Mustard and VX; in Proceedings of the CRDEC Scientific Conference on Chemical Defense, Aberdeen Proving Ground, MD, November, 1988.

EQUILIBRIA AND REACTIVITY OF PEROXO COMPLEXES OF Mo(VI) and W(VI) IN BASIC SOLUTION

Richard C. Thompson

Department of Chemistry, University of Missouri-Columbia, Columbia, MO 65211

ABSTRACT

We have shown that the reactivity of hydrogen peroxide in acidic and neutral solutions is markedly and catalytically enhanced by Mo(VI) and W(VI), due to the rapid formation of oxodiperoxo complexes. A recent report by Aubry and Cazin shows that hydrogen peroxide is catalytically decomposed to water and singlet oxygen by Mo(VI) in basic solution. A scheme was proposed that implicated MoO_6^{2-} as the reactive species. We have tested the proposed scheme by means of spectrophotometrically monitored stopped-flow and equilibrium experiments. It is concluded that the known reactivity of oxodiperoxo complexes of Mo(VI) and W(VI) coupled with the formation of singlet oxygen in basic solution may allow mixtures of excess hydrogen peroxide and Mo(VI) and/or W(VI) in mildly basic solution to be effective in certain decontamination processes

INTRODUCTION

We have shown previously that Mo(VI) and W(VI) are effective catalysts for oxidations by hydrogen peroxide in aqueous solution.[1-4] Substrates examined include oxygen atom acceptors (sulfides, sulfoxides, coordinated thiolates and sulfenates, and halide ions) and one-equivalent reductants (iron(II), europium(II), methyl viologen radical cation, and dithionite). The active catalysts are the oxodiperoxo complexes $MO(O_2)_2(H_2O)_2$ and their hydrolyzed forms {pK_a = 1.9 for Mo(VI) and 0.1 for W(VI)}, $MO(OH)(O_2)_2(H_2O)^-$. Equilibrium and kinetic parameters were determined for the formation and dissociation of these complexes over the pH range 0 to 8. We were able to demonstrate that direct attack by the substrate at the η^2 bound peroxo ligand is the predominant mechanistic pathway in the catalytic reactions.

It has long been known that molybdate and tungstate ions catalyze the decomposition of hydrogen peroxide in basic solution.[5] A recent report demonstrates that the oxygen formed under these conditions with MoO_4^{2-} is quantitatively $^1\Delta_g$.[6] This is a remarkable observation, particularly since the overall reaction $2\ H_2O_2 \rightarrow {}^1O_2 + 2\ H_2O$ neither consumes nor produces acid or base. The catalyzed reaction is promising as a chemical

means of producing singlet oxygen due to its apparent simplicity and the feature that the only "feed" chemical required is hydrogen peroxide.

A mechanism was proposed based on kinetic effects of $[H_2O_2]$, $[MoO_4^{2-}]$, and pH on the decomposition rate of hydrogen peroxide, and is summarized in eqns 1 - 4

$$MoO_4^{2-} + 2\,H_2O_2 \Leftrightarrow MoO_6^{2-} + 2\,H_2O \qquad K_1 \quad (1)$$

$$MoO_6^{2-} \rightarrow MoO_4^{2-} + {}^1O_2 \qquad k_d \quad (2)$$

$$HMoO_6^{-} \Leftrightarrow MoO_6^{2-} + H^+ \qquad k_{a2} \quad (3)$$

$$H_2O_2 \Leftrightarrow HO_2^{-} + H^+ \qquad K_a \quad (4)$$

Values of log K_1, k_d, and pK_{a2} at 25 °C derived from this study were 3.4, 4.6×10^{-3} s^{-1}, and 9.1 respectively, using the literature value of $pK_a = 11.6$. The decomposition rate has a maximum value at pH 10.5, and is limited at lower pH by protonation of MoO_6^{2-} and at higher pH by deprotonation of H_2O_2.

The formula suggested for the inactive form of the catalyst, $HMoO_6^-$, is identical except for aquo ligands to the hydrolyzed oxodiperoxo complex we had studied at lower pH. The active catalyst, MoO_6^{2-}, is a doubly hydrolyzed form with the structural formula $MoO_2(O_2)_2(H_2O)^{2-}$ if it is pentagonal bipyramidal or $MoO_2(O_2)_2^{2-}$ if it has a distorted tetrahedral geometry.

We are studying the equilibrium and kinetic parameters associated with reactions 1 and 3 by more direct methods for both Mo(VI) and W(VI). In addition, equilibria between the diperoxo complexes considered above and the known tetraperoxo complexes are being examined. Protonated tetraperoxochromium(V) is known to decomposed to singlet oxygen,[7,8] and it is possible that the analogous Mo(VI) and W(VI) species plays an important role in the the present systems.

RESULTS

Spectral Studies. The formation constants for $MO(OH)(O_2)_2^-$ are very large at pH 4, and solutions containing >99% of the Mo(VI) or W(VI) as the oxodiperoxo complex require little excess hydrogen peroxide. These solutions were mixed with appropriate buffer solutions (the biological buffers MES, MOPS, CHES, or CAPS) on the stopped-flow instrument and monitored spectrophotometrically in the UV region. The idea behind these experiments is that immediately after mixing (1-3 msec) protonation equilibria of the oxodiperoxo complex is complete, but dissociation is considerably slower and the low levels of hydrogen peroxide present should prevent higher peroxocomplexes from forming. We hoped to detect spectral differences (i.e., differing ε_{obs} values at various pH's) at appropriate wavelengths for the singly hydrolyzed $MO(OH)(O_2)_2^-$ and doubly hydrolyzed $MO_2(O_2)_2^{2-}$ forms (with water ligands omitted in the formulations). This method worked

very well for the Mo(VI) system - we were able to determine the UV spectra for the two forms of the oxodiperoxo complex, and more importantly to correlate the variation of ε_{obs} with pH to determine the second hydrolysis constant. The resulting value of pK_{a2} was 9.8.

The method did not work for W(VI) - no spectral changes were observed. We believe, and will justify later, that the reason is simply that the spectral differences between the two forms is too small to be detected by this technique.

We also monitored the subsequent decay of the oxodiperoxo complexes. This decay was considerably more rapid that the redox reaction shown in eq 2, and is due to the loss of the peroxo ligands at the low $[H_2O_2]$ employed. The kinetic parameters associated with the formation and decay of the oxodiperoxo complexes from pH 7 to 12 have been examined in detail during the course of this work; the detailed results will not be presented in this report, although the qualitative features will be given (*vide infra*).

Equilibrium Studies. Experiments similar to those described above were performed except with varying amounts of hydrogen peroxide present in the buffer solution, such that between 10 and 90% of the Mo(VI) or W(VI) was complexed at equilibrium. In addition, 5 μM Dequest 2060 was present in the buffer solution to effectively eliminate the usual trace metal catalyzed decomposition of hydrogen peroxide during workup prior to initiating the experiment. The equilibrium data at each pH examined were consistent with the formation of a diperoxo complex. The possible effect of different buffers was shown to be minimal at pH 11 since the results obtained in 0.05 M CAPS buffer were quite close to those obtained in H_2O_2, HO_2^- buffer. Values of the conditional formation constant (25 °C) in terms of eq 5 were: {for Mo(VI)} $(3.75\pm0.26)\times10^4$, $(1.75\pm0.15)\times10^4$, $(8.72\pm0.25)\times10^3$, and $(4.88\pm0.15)\times10^3$ at pH 9.0, 9.4, 10.0, and 11.0, respectively, and {for W(VI)} $(2.73\pm0.28)\times10^4$, $(1.25\pm0.07)\times10^4$, $(4.92\pm0.33)\times10^3$, and $(2.35\pm0.09)\times10^3$, respectively at the same indicated pH's. The $[H_2O_2]$ in these calculations refers simply to the hydrogen peroxide that was not complexed.

$$MO_4^{2-} + 2\,H_2O_2 \Leftrightarrow \text{diperoxo complex} \qquad (5)$$

We discovered from experiments performed with excess NaOH relative to H_2O_2 that HO_2^- is not effective in complexing the metal centers.

The pH dependence of these formation constants are consistent with eqns 1, 3, and 4. The derived values of log K_f and pK_{a2} are {for Mo(VI)} 3.81 and 9.68, and {for W(VI)} 3.49 and 9.89, respectively. The value of pK_{a2} for Mo(VI) is in satisfactory agreement with that determined in the spectral studies. and the value determined for W(VI) fortifies the suggestion that the acid-base chemistry of the two systems are similar, but that the spectral differences between HWO_6^- and WO_6^{2-} happen to be small in the UV region.

Equilibrium Studies of the Conversion of Diperoxo Mo(VI) to Tetraperoxo Mo(VI). These experiments have not been completed, but the preliminary results obtained at pH 11 for the Mo(VI) system are revealing. The experiments were monitored at 330 nm to allow

higher concentrations of hydrogen peroxide to be employed without undue spectral interference. The [diperoxo complex]$_0$ was 5.0×10^{-4} M, and the $[H_2O_2]_{total}$ varied from 0.0090 to 0.40 M. With relatively low $[H_2O_2]$ we again observed a decrease in absorbance with time as the diperoxo complex dissociated to its equilibrium value. However, at the higher concentrations a very rapid *increase* in absorbance was observed. This suggests the formation of a new, more highly absorbing peroxo complex. The data were consistent with the scheme summarized in eqns 6 - 8.

$$MoO_4^{2-} + 2\,H_2O_2 \Leftrightarrow MoO_2(O_2)_2^{2-} + 2\,H_2O \quad (6)$$

$$MoO_2(O_2)_2^{2-} + 2\,H_2O_2 \Leftrightarrow Mo(O_2)_4^{2-} \ \{or\ HMo(O_2)_4^-\} + 2\,H_2O \quad (7)$$

$$H_2O_2 \Leftrightarrow HO_2^- + H^+ \quad (8)$$

It can be shown that, according to this scheme, a plot of $\varepsilon_{obs} / \{[H_2O_2]_{eq}^2 \times (\varepsilon_{2,1} - \varepsilon_{obs})\}$ vs $\{[H_2O_2]_{eq}^2 \times (\varepsilon_{4:1} - \varepsilon_{obs})\} / (\varepsilon_{2,1} - \varepsilon_{obs})$ should be linear with a slope of K_6K_7 and an intercept of K_6. in this equation ε_{obs} is $A_{\infty,corr} / [Mo(VI)]_{total}$, $\varepsilon_{2,1}$ is the extinction coefficient of MoO_6^{2-} and is available from our spectral studies, and $\varepsilon_{4,1}$ is the extinction coefficient of the tetraperoxo complex and was determined independently. Such a plot was in fact reasonably linear, with values of log $K_6 = 4.0$ and log $K_7 = 3.2_0$. The former value is in reasonable agreement with the value of log $K_1 = 3.81$ as determined in the equilibrium studies. The value of K_7 indicates that under conditions where most of the Mo(VI) is complexed at pH 11, both di- and tetraperoxocomplexes will be present except at very large $[H_2O_2]$. Minor corrections for the tetraperoxo complex probably present in our equilibrium studies may need to be applied when this portion of the project is completed.

X-ray Crystallographic Studies. We have found no evidence for detectable triperoxo complexes in our studies to date. However, triperoxo complexes in the related vanadium(V) systems have been reported. Since no definitive structural data were available, we have performed low temperature crystal structures of compounds reported to be $Na[V(O_2)_3]$[9] and $Na_2[V(O_2)_3F]$[10]. We find that in both cases the anion is actually $[V(O_2)_4]^{3-}$.

DISCUSSION

We summarize in the following Table our results that relate to the work of Aubry and Cazin. An earlier value of 9.1 for pK_{a2} was reported by Csanyi[11] based on potentiometric titrations. However, our equilibrium data demonstrate that this value is too low due to incomplete complexation of the Mo(VI) as the diperoxo complex under his experimental conditions. Our rate studies indicate that the kinetic parameters for the formation and dissociation of the diperoxo complexes are rapid relative the the redox decay under most conditions.

While there are differences in the details, the agreement between the two quite different

types of studies is striking. However, in our opinion it is still premature to conclude that the scheme outlined in eqns 1 - 4 is correct. One concern is why the doubly deprotonated

SUMMARY TABLE

	log K_f		pK_{a2}		k_d, s^{-1}
System	ref. 5	this work	ref. 5	this work	ref. 5
Mo(VI)	3.4	3.81	9.1	9.8, 9.68	4.6×10^{-3}
W(VI)	----	3.49	----	9.89	----------

diperoxo complex MoO_6^{2-} is active as a mode of singlet oxygen formation, whereas the protonated form is quite unreactive. A possible explanation might be that the coordination number of Mo(VI) and presumably W(VI) changes (i.e., the geometry becomes pseudo tetrahedral) as a consequence of the second deprotonation. Values of ΔH^o and ΔS^o should answer this question, and we plan to determine them through a temperature dependence study of K_{a2}. We are also measuring k_d as a function of pH for the W(VI) system, both to test whether the scheme analogous to that for Mo(VI) is applicable and consistent with our data, and also in the hopes that the production of singlet oxygen may be more rapid.

We are also entertaining the notion that the protonated tetraperoxomolybdenum(VI) complex may be the reactive form. Both the MoO_4^{2-}, diperoxo Mo(VI) and the diperoxo Mo(VI), tetraperoxo Mo(VI) pairs are related by the square of the hydrogen peroxide concentration. Our preliminary results indicate that both pairs are simultaneously present under a fairly wide range of conditions, at least at pH 11. It is definitely possible that the *protonation* constant for $Mo(O_2)_4^{2-}$ is similar to the *deprotonation* constant of $HMoO_6^-$. If so, then it appears that despite the appeal of the simple scheme proposed by Aubry and Cazin the true situation may be more subtle. Considerable additional data will be required to settle this fundamental point.

A final point concerns why triperoxo complexes seem to be unimportant. We were dubious about the formulation of the compound $Na[V(O_2)_3]$ from the outset. The geometry of the stable oxodiperoxo complex is pentagonal bipyramidal, with the η^2 peroxo ligands in the equatorial plane, while the tetraperoxo complex may be viewed as a severely distorted tetrahedron. It is difficult, and it turns out to be unnecessary, to construct a reasonable structure for a $V(O_2)_3^-$ anion. The formulation $V(O_2)_3F^{2-}$ is more plausible, but it requires one peroxo ligand to be formally half-bonded in the preferred equatorial plane and half-bonded in a strained apical position if the anticipated pentagonal bipyramidal geometry holds. This is not the case, and it may explain why we observe a facile transition from the diperoxo Mo(VI) complex directly to the tetraperoxo form.

CONCLUSIONS

In the near future we should have defined the speciation, equilibria, and kinetic parameters for the peroxo complexes of Mo(VI) and W(VI) in basic aqueous solution. While we have not yet tested the inherent reactivity of these complexes towards suitable substrates in this medium, it is very likely that considerably enhanced reactivity above and beyond that already demonstrated in lower pH regimes will be found. The reason for this optimism is that, in addition to the already active oxodiperoxo complexes, tetraperoxo complexes will be formed in addition to singlet oxygen. It is unclear at this stage what practical applications may be viable in this fairly caustic regime, but the feature of requiring only hydrogen peroxide as an input stoichiometric reagent coupled with the strictly catalytic behavior of Mo(VI) and W(VI) offers promise in certain decontamination processes

ACKNOWLEDGMENT

This research was supported by the U.S. Army Research Office.

REFERENCES

1. Lydon, J.D.; Schwane, L.M.; Thompson, R.C. *Inorg. Chem.* **1987**, *26*, 2606.
2. Ghiron, A.F.; Thompson, R.C. *Inorg. Chem* **1988**, *27*, 4766.
3. Ghiron, A.F.; Thompson, R.C. *Inorg. Chem.* **1989**, *28*, 3647.
4. Schwane, L.M.; Thompson, R.C. *Inorg. Chem.* **1989**, *28*, 3938.
5. Baxendale, J.H. *Adv. Catal.* **1952**, *4*, 31.
6. Aubry, J.M.; Cazin, B. *Inorg. Chem.* **1988**, *27*, 2013.
7. Quane, D.; Earley, J.E. *J. Am Chem. Soc* **1965**, *87*, 3823.
8. Peters, J.W.; Bekowies, P.J.; Winer, A.M.; Pitts J.N. *J Am Chem. Soc.* **1975**, *97*, 3299.
9. Chaudhuri, M.K.; Ghosh, S.K.; Islam, N.S. *Inorg. Chem.* **1985**, *24*, 2706.
10. Chaudhuri, M.K.; Ghosh, S.K. *Inorg. Chem.* **1982**, *21*, 4020
11. Csanyi, L.J. *Acta Chim Acad. Sci. Hung.* **1958**, *14*, 79.

STARBURST® DENDRIMERS: MOLECULAR LEVEL CONTROL OF SIZE, SHAPE, SURFACE CHEMISTRY, TOPOLOGY AND FLEXIBILITY FROM ATOMS TO MICROSCOPIC MATTER

Donald A. Tomalia
Michigan Molecular Institute, 1910 West St. Andrews Road
Midland, Michigan 48640

ABSTRACT

Atomic level architecture has been successfully mimicked at the molecular level by the construction of Starburst® dendrimers. Precise organizations of repeat units (electron analogs) into concentric generation shells around a nucleus (initiator core) with covalent connectivity provides the molecular level motif for mimicry. These generation shells possess quantitized occupation levels that expand according to core (N_c) and branch juncture (N_b) multiplicities. This represents a molecular level *Aufbau* situation which allows complete control of the above five critical molecular design parameters. Practically speaking Starburst® dendrimers are approximately the size of micelles (i.e. ≅10-500A°) with closed surface topologies that mimic liposomes at higher generations (i.e. G = 8-10). These dendrimers are fundamental molecular level building blocks that allow systematic *mesoscopic* constructions as well as *ordered, infinite, network* syntheses.

INTRODUCTION

It is well known that atomic level space is organized and controlled in the elements by the arrangement of electron shells around various attractors (nuclei). This occupation of electron shells around atomic nuclei according to the *Aufbau principle* is the atomic level architectural motif of the elements and constitutes the very essence of contemporary chemistry. These organizations are so precise and dependable that they are accepted as the fundamental building blocks of the universe.

One must ask the question -- "Can this architectural theme be extended to higher dimensional molecular level entities?" If they are not found to be in nature, can such prototypes be designed and synthesized?

Chemistry and molecular structures demonstrating this concept were first reported in 1984. [1-8] Mimicry of atomic architecture at the molecular level involved the assembly of elemental building blocks (C,H,N,O) into *repeat units* (β-alanines) which were organized in a radial fashion around an initiator core to produce concentric

shells [9] ensembles of *branch cells* as shown in Figure 1. Synthetic branching rules were introduced to organize these branch cells into symmetrical cascading ensembles with covalent connectivity to the initiator core. These are referred to as *dendrons*. Multiples of dendrons assembled around an initiator core are referred to as possessing Starburst® topology and these molecular level entities have been coined Starburst® dendrimers. Two dimensional projections of such a dendrimer series are illustrated in Figure 1. It becomes apparent that this controlled organization of branch cells, possessing specific excluded volumes, into defined molecular level shells (generations) around a reference point provides a molecular level *Aufbau* strategy. As such, these fundamental dendrimer building blocks may be viewed as *molecular level analogs to atoms* and become members of molecular level periodic tables within a particular series.

FIGURE 1

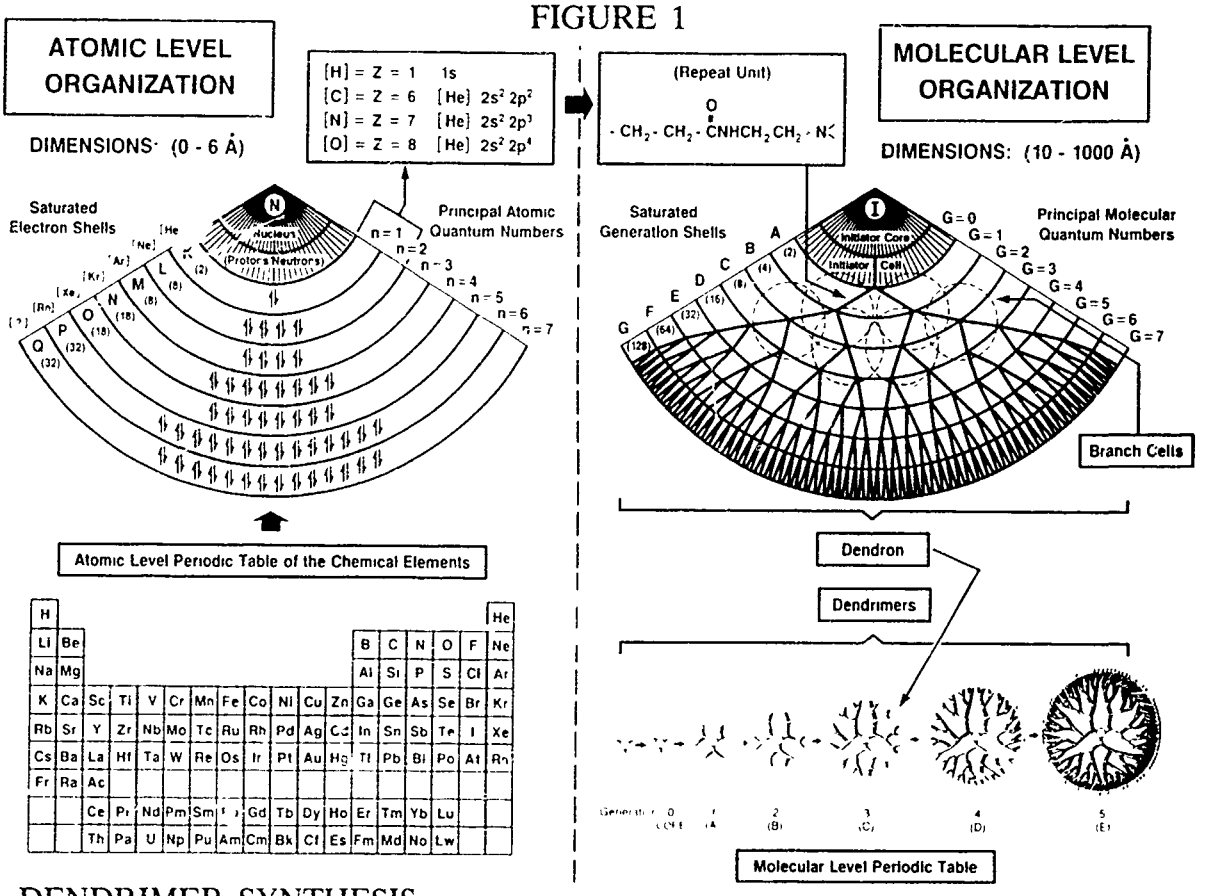

DENDRIMER SYNTHESIS

Presently, dendrimer synthesis involves either of two strategies; (a) *in-situ* construction of branch cells, or (b) coupling of pre-formed branch cell reagents. This allows one to use different chemistries as well as various branch juncture multiplicities for the interior design of the dendrimers. It also follows that a variety of surface groups will result during the course of these constructions, thus allowing modifications or control of these surface moieties throughout the dendrimer synthesis. The *in-situ* branch cell construction is illustrated by the synthesis of STARBURST poly(amidoamines); PAMAM's. Alternatively, coupling of a pre-formed, functional branch cell was used to prepare a STARBURST polyether series, but will not be described here. [6]

STARBURST POLY(AMIDOAMINE) DENDRIMERS

A variety of initiator cores Ⓘ have been used in this series, wherein ammonia with a multiplicity of three (N_c=3) was preferred [1-8]. The branch cell (branch juncture) construction is performed *in-situ*. It involved first, Step A: exhaustive Michael addition of methyl acrylate to an amine, followed by Step B: amidation of the terminal ester groups to produce concentric generations as shown in Figure 2.

Reaction steps A and B are essentially quantitative under optimized conditions. Nearly ideally branched structures are obtained through generation=10 by using optimized reaction conditions and ultra-filtration work-up methods [10]. Under non-ideal reaction conditions, one can observe *intra*molecular cyclization of branches, branch defects, and *inter*molecular dendrimer bridging. These aspects, as well as analytical methods for structure verification, have been described elsewhere [11].

FIGURE 2

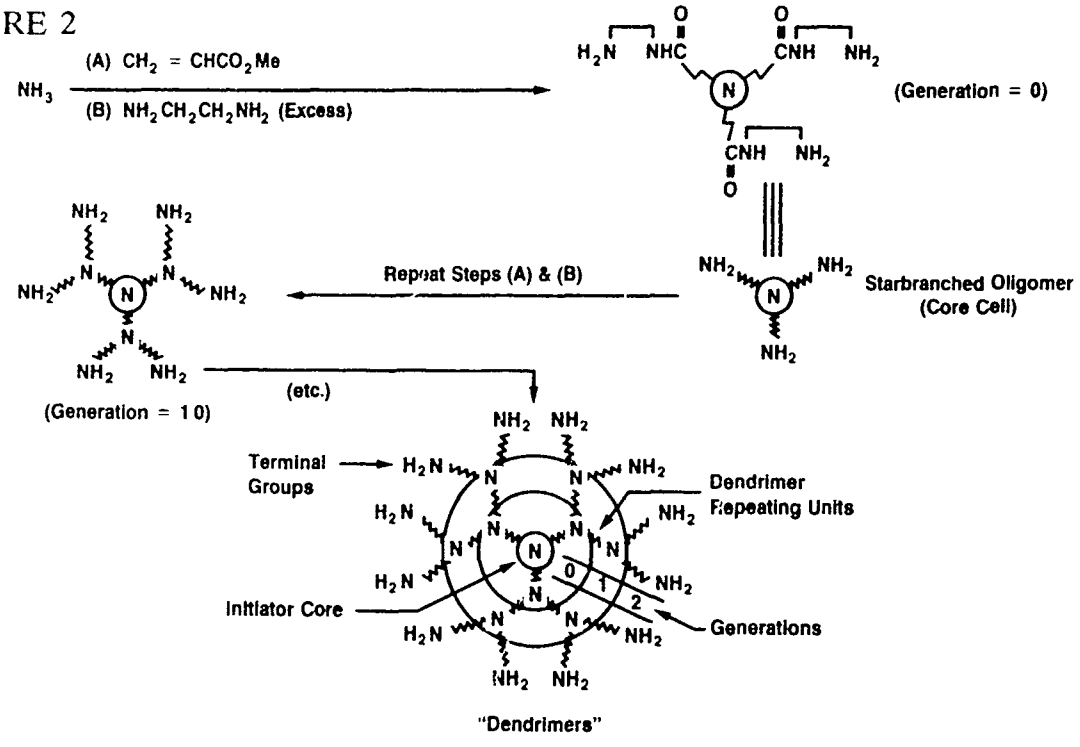

Computer assisted molecular simulation of STARBURST PAMAM dendrimers shows the systematic development of size, shape, and surface congestion as a function of generation [12], where N_c=3 and N_b=2 (Figure 3). It should be noted that there is an approximate doubling in molecular weight as one advances generation to generation, whereas the number of terminal surface groups (Z) accumulate exponentially. Stoichiometric surfaces are formed at each generation wherein the number of moieties follows a geometric progression. The number of terminal groups can be proliferated according to the following expression where G equals the number of generations.

$$\text{Number of terminal groups (Z)} = \left[\text{Initiator Core Multiplicity } (N_c)\right] \left[\text{Branch Juncture Multiplicity } (N_b)\right]^{G}$$

FIGURE 3

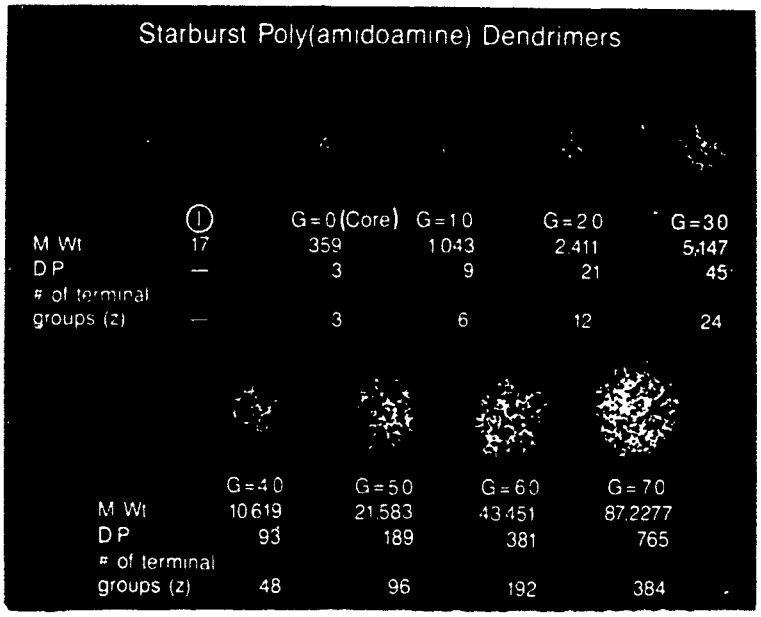

Examination of CPK models in this series showed that these dendrimers would be expected to grow ≅10A°/generation, with the possibility of unimolecularly encapsulating substantial amounts of solvent filled void space at higher generations. This was experimentally observed at generation=9, by scanning transmission electron microscopy (STEM) [13]. Since the diameters of these dendrimers are growing in an approximately linear fashion, whereas the surface groups are accumulating exponentially, one would expect to reach a sterically crowded generation wherein the surface would not accommodate the anticipated number of surface groups. This was described by deGenne and Hervet [14] as the *"STARBURST limited"* generation. It was predicted to occur near the tenth generation. Experimental evidence supports this prediction in that the alkylation rate of the Michael addition reaction (Gen:9 → = Gen:10) is decreased over 10 fold compared to Gen:1 → Gen:2 and is accompanied by substantial amounts of branch defects.

CONTROL OF SIZE

Molecular dimensions of STARBURST dendrimers are determined by the size of the initiator core plus a summation of the branch cell diameters projected radially from the core (see Figures 1 and 2). The flexibility, lengths, and chemical nature of the repeat units in the branch cell determine the compressibility and potential for the dendrimer to possess solvent-filled interior void spaces. Examination of Corey-Pauling-Koltun (CPK) models allows one to predict upper (three-dimensional extended) limits and lower (three-dimensional compressed) limits for the various dendrimer families as a function of generation. Experimental determination of hydrodynamic diameter (H_2O or MeOH) by use of size-exclusion chromatography (comparison to known polymer standards) and intrinsic viscosity measurements [calculated by treatment as Einstein spheroid and use of the Hester-Mitchell relationship [15]] were found to be in excellent agreement. These values were also in close agreement with predicted upper and lower limits that were predicted from CPK models as shown in Figure 4.

FIGURE 4

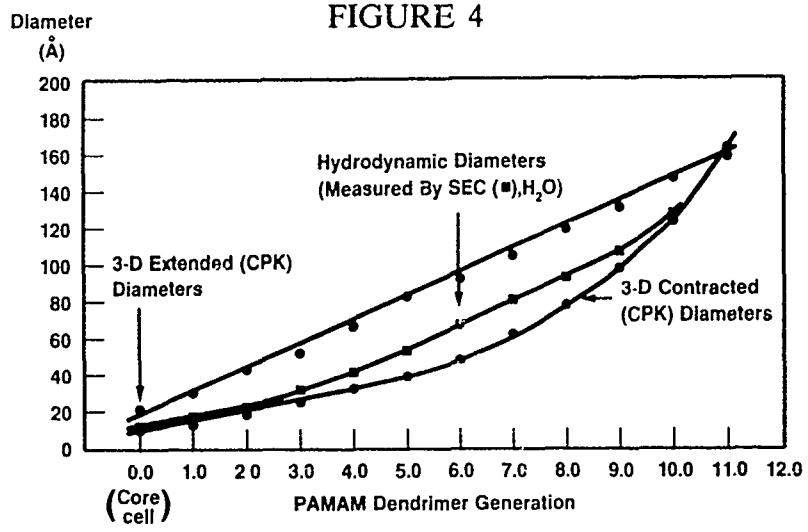

CONTROL OF SURFACE

The surface functionality of the dendrimer determines its physical properties and solubilities. Surface stoichiometry is predictable at each generation stage (see Figure 3); therefore, chemical reactions to produce either hydrophilic or hydrophobic surfaces are straightforward. In view of the size (20-124A°) and shape (spheroidal) of these microdomains, these products have been noted to be reminiscent of covalently fixed regular and inverse micelles, respectively, as illustrated in Figure 5 [15]. Calculation of surface areas from the hydrodynamic diameters determined for STARBURST PAMAM's (where: terminal group (Z) = $-NH_2$ and comparing these areas to the theoretical number of surface groups expected at that generation allows us to determine the surface area/head group (Z). For the first five generations, the surface areas/Z group range from ≅105-130A^{o2}/Z. Beyond this generation, there is a steady decrease to a minimum of 32A^{o2}/Z group (see Figure 6). These more open, large values are reminiscent of surface areas/head group observed for spherical micelles [16] wherein the more compressed values (i.e., 30-50A^{o2}/Z group observed for the higher generations (i.e., Gen=8-9) are usually associated with bilayer formation such as on the surface of liposomes. These data suggest that at lower generations, surface congestion produces unimolecular species which have sizes and shapes reminiscent of micelles, whereas at higher generations, the surface congestion begins to imitate that of a liposome.

CONTROL OF SHAPE AND TOPOLOGY

Computer assisted molecular simulations [12] of the STARBURST PAMAM series has shown that dramatic morphological changes occur as one advances from lower to higher generations. These changes are very consistent with the above surface congestion observations. Using energy minimized procedures, it has been found that Generations=1-3 are open, disk-like entitities; Generations=4-5 are asymmetric, oblate spheroids, whereas Generations=6-8 are nearly symmetrical spheroids. These predictions also parallel spin-lattice relaxation data which have been obtained for guest molecules such as aspirin. Carbon-13, spin lattice relaxation times for aspirin (micelle-guest procedure according to Menger, et.al.) [17] decrease to a minimum at Generations=3-4. This suggests that dendrimer development to provide a hollow

interior occurs essentially at the same stage that predicted morphological change and surface congestion is found to occur (see Figure 7). Therefore, it is apparent that the "tethering effect" resulting from the connectivity of the surface groups to the initiator core, in concert with exponential accumulation of surface groups according to STARBURST branching criteria, provides a new and unique strategy for controlling the shape and topology of these macromolecules.

FIGURES 5 and 6

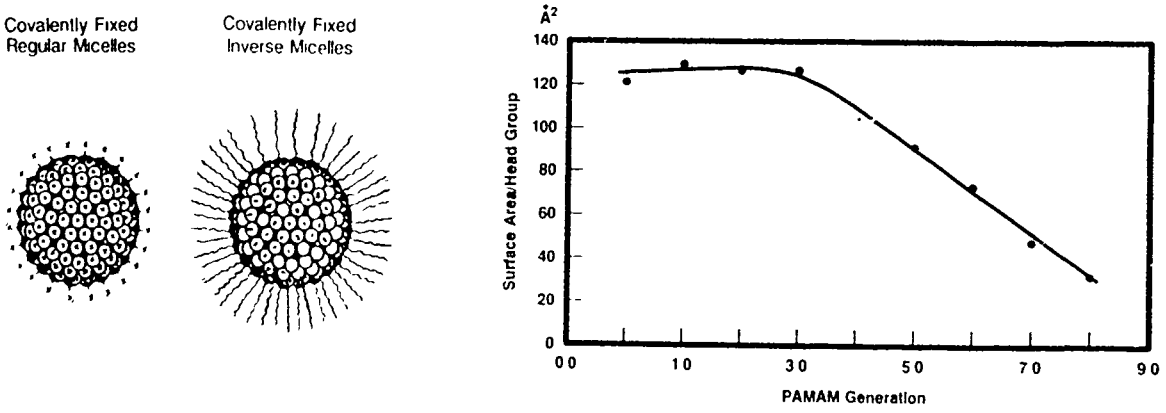

FIGURE 7

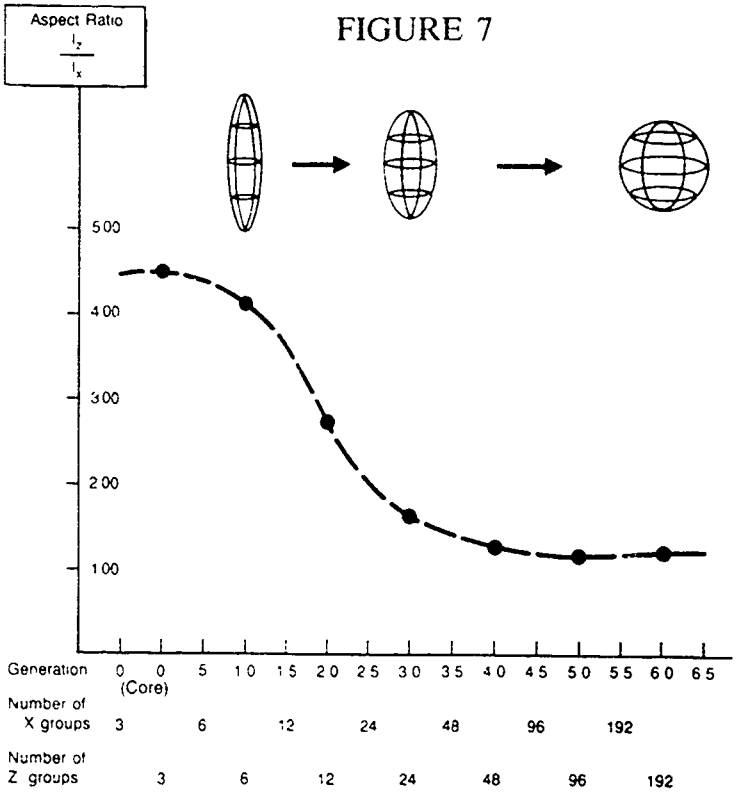

CONCLUSIONS

Starburst dendrimers are mesoscopic building blocks that allow development of ordered complexity and covalent control from atoms to macroscopic matter. The variety and complexity of advanced materials possible from these constructions are only limited by one's imagination. These possibilities are examined in a forthcoming review [18] and may be put into perspective by comparing to previous developments in classical polymer science as shown in Figure 8.

FIGURE 8

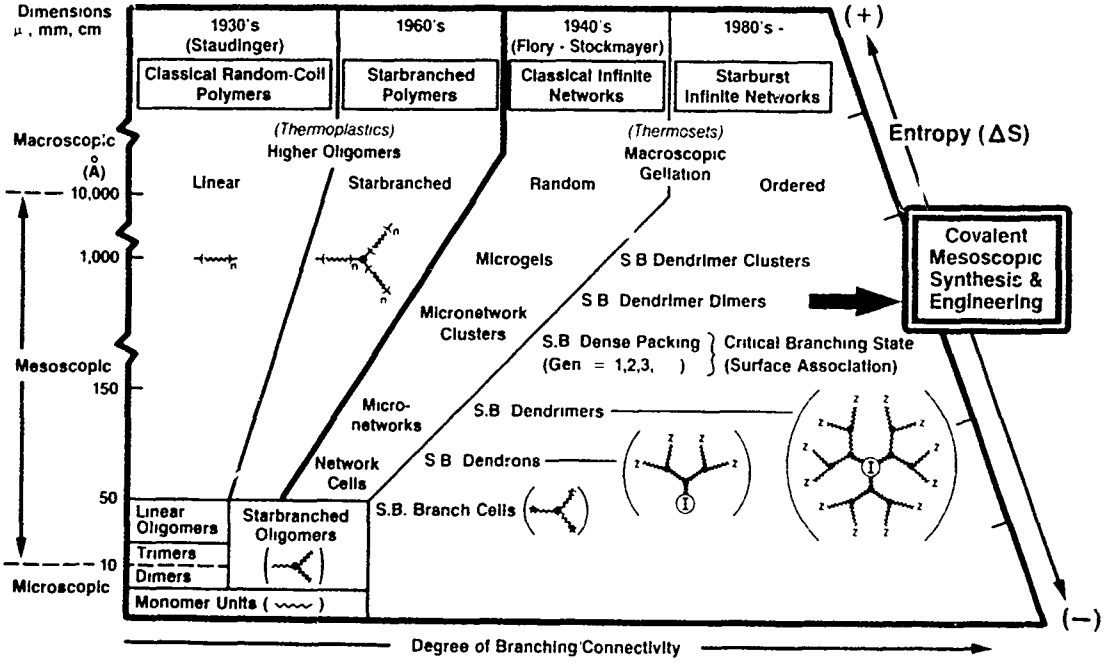

ACKNOWLEDGEMENTS

The author is very grateful to Drs. Hedstrand, Meier, Hoffman and Hotchkiss for valuable discussions.

REFERENCES

1. D.A. Tomalia, Presented at the First Society Polymer Science, Japan International Conference, Kyoto, Japan, August (1984).

2. D.A. Tomalia, H. Baker, J. Dewald, M. Hall, G. Kallos, S. Martin, J. Roeck, J. Ryder, and P. Smith, Polym. J. (Tokyo), 17, 117-132 (1985).

3. *Ibid*, Macromolecules, 19, 2466 (1986).

4. D.A. Tomalia and J.R. Dewald, U.S. Patent #4,507,466, (1985); U.S. Patent #4,558,120, (1985); U.S. Patent #4,568,737, (1986); U.S. Patent #4,587,329, (1986); and U.S. Patent #4,631,337, (1986); U.S. Patent 4,694,064, (1987); U.S. Patent 4,713,975, (1987); U.S. Patent 4,737,550, (1988).

5. D.A. Tomalia, V. Berry, M. Hall, and D.M. Hedstrand, Macromolecules, 20, 1164 (1987).

6. H. Hall, A. Padias, R. McConnell, and D.A. Tomalia, J. Org. Chem., 52, 5305 (1987).

7. D.A. Tomalia, M. Hall, and D.M. Hedstrand, J. Am. Chem. Soc., 109, 1601 (1987).

8. D.A. Tomalia, D.M. Hedstrand, L.R. Wilson, and D.M. Downing, "Frontiers of Macromolecular Science", edited by T. Saegusa, T. Higashimura, and A. Abe, IUPAC (1983), Blackwell Scientific.

9. The dendrimer generation numbering system used in earlier work (see references 1-8) designated the first starbranched species derived from the initiator core as generation = 1.0. The present system is preferred wherein that starbranched intermediate is designated, generation = 0, thus making it consistent with geometric progression, $Z = N_c N_b^G$, for the number of terminal groups.

10. L. Wilson and D.A. Tomalia, Polym. Preprints, 30, 115 (1989)

11. P.B. Smith, S.J. Martin, M.J. Hall, and D.A. Tomalia, Applied Polymer Analysis and Characterization, Edited by J. Mitchell Jr., Hanser Publishers, New York (1986), 375-385.

12. A. Naylor, W.A. Goddard III, G.B. Keifer, and D.A. Tomalia, J. Am. Chem. Soc., 111, 2339 (1989).

13. D.A. Tomalia and H. Baker (unpublished results).

14. P.G. deGenne and H.J. Hervet, Phys. Lett. (Paris), 44, 351 (1983).

15. R.D. Hester and P.H. Mitchell, J. Polym. Sci. Chem. Ed., 18, 1729 (1980).

16. C. Tanford, The Hydrophobic Effect, 2nd Edition, Wiley, New York (1980).

17. F.M. Menger and J.M. Jerkunica, J. Am. Chem. Soc., 100, 688 (1978).

18. D.A. Tomalia, A. Naylor, and W. Goddard, Angew. Chem. Int. Ed. Engl. (to be published) (1990).

II. COMPUTATIONAL CHEMISTRY

NOTE: Papers with the following titles were presented at the Conference but are not included in this document:

Comparison of the Electronic Structure of the P-O and P-S Bonds

Theoretical Studies of Reaction Rates: Application to H_2+CN

Applications of "MNDO"-Type Semi-Empirical Methods

Quantum Chemical Calculations Using a Grid of Evenly Spaced S-Functions

BLANK

MOLECULAR SURFACE PROPERTIES AS GUIDES TO CHEMICAL REACTIVITY

Peter Politzer, Per Sjoberg, Jane S. Murray and Tore Brinck
University of New Orleans
Department of Chemistry
New Orleans, LA 70148

ABSTRACT

We show that molecular reactive behavior can be effectively studied and predicted by examining the magnitudes of certain key properties on a three-dimensional surface encompassing the molecule. Among these properties are the electrostatic potential and the average local ionization energy. The surface is defined in terms of the charge distribution of the molecule; it corresponds to the 0.002 electrons/bohr^3 contour of the molecular electronic density. This general approach has been successful in interpreting reactivity toward both electrophiles and nucleophiles, as well as in treating biological recognition interactions. It offers certain advantages over calculating the same properties in planes through the molecule.

INTRODUCTION

The interpretation and prediction of molecular reactive behavior is a continuing focus of our computational studies[1-5]. In this work, we demonstrate that computing molecular properties, such as the electrostatic potential and the average local ionization energy, on a three-dimensional surface designed to encompass nearly all the electronic charge of the molecule is a useful and promosing new tool for the study of molecular reactivity.

METHODOLOGY

1. Properties on Molecular Surfaces.

We have used an ab initio self-consistent-field (SCF) molecular orbital approach [GAUSSIAN 82[6] and GAUSSIAN 86[7]] to compute wave functions for the molecules of interest. These have been used to compute key molecular properties on three-dimensional surfaces corresponding to the contour of constant electronic density equal to 0.002 electrons/bohr^3. It has been shown, for a group of diatomic molecules and for methane, that this contour gives physically reasonable molecular dimensions, encompassing at least 95% of the electronic charge[8-10]. This surface is defined in terms of a molecular property, the electronic density function $\rho(\mathbf{r})$, and therefore reflects features such as bond formation, lone pairs, etc. that are unique to a molecule. This means of designating a molecular surface is in contrast to earlier methods in which it has been defined as the outer surface of a set of intersecting spheres centered on the nuclei of the molecule[10-21]; such surfaces cannot take into account the very properties that are characteristic of a molecule.

2. The Electrostatic Potential.

The electrostatic potential $V(\mathbf{r})$ that the electrons and nuclei of a molecule create in the surrounding space is given rigorously by eq. (1).

$$V(\mathbf{r}) = \sum_A \frac{Z_A}{|\mathbf{R}_A - \mathbf{r}|} - \int \frac{\rho(\mathbf{r}')\, d\mathbf{r}'}{|\mathbf{r}' - \mathbf{r}|} \qquad (1)$$

Z_A is charge on nucleus A, located at $\mathbf{R}_A$. $\rho(\mathbf{r})$ is the electronic density function of the molecule. $V(\mathbf{r})$ is a real physical property, which can be determined either computationally, or experimentally, by diffraction methods.

The electrostatic potential is well-established as an effective tool for interpreting and predicting molecular reactive behavior toward electrophiles[1,22,23] and for the study of biological recognition interactions[3,5]. An approaching electrophile will go to those regions in which $V(\mathbf{r})$ attains its most negative values (the local minima) since this is where the effects of the molecules' electrons are most dominant [eq. (1)].

The use of the electrostatic potential to analyze reactivity toward nucleophiles is not as straightforward as that toward electrophiles. This can be understood by first recognizing that $V(\mathbf{r})$ for any free neutral atom is positive everywhere, increasing to a maximum at the nucleus[24-26]. This simply reflects the highly concentrated nature of the nuclear charge as contrasted to the dispersed electronic distribution. When atoms interact to form a molecule, the accompanying rearrangement of electrons normally produces one or more regions of negative electrostatic potential. Each region has at least one minimum to which an approaching electrophile may be attracted. The positive regions, on the other hand, generally do not have maxima other than at the positions of the nuclei; these are so large in magnitude that they would mask any weaker local maxima that might indicate sites for nucleophilic attack. This problem can be avoided by computing $V(\mathbf{r})$ on the molecular surface[27], as shall be discussed later in this paper.

3. Average Local Ionization Energies.

The average local ionization energy, $\bar{I}(\mathbf{r})$, is rigorously defined within the framework of self-consistent-field molecular orbital (SCF-MO) theory, as given by equation (2):

$$\bar{I}(\mathbf{r}) = \sum_i \frac{\rho_i(\mathbf{r})\, \varepsilon_i}{\rho(\mathbf{r})} \qquad (2)$$

$\rho_i(\mathbf{r})$ is the electronic density of the i^{th} molecular orbital at the point $\mathbf{r}$, ε_i is the orbital energy, and $\rho(\mathbf{r})$ is the total electronic density; these quantities are obtained using an ab initio SCF-MO approach. Since Koopmans' theorem justifies regarding the orbital energies as good approximations to the ionization potentials of the respective electrons[28], $\bar{I}(\mathbf{r})$ can be interpreted as the average energy needed to ionize an electron at any particular point in the space of the molecule. Thus, the positions where $\bar{I}(\mathbf{r})$ has its lowest values are the points at which are found, on the average, the highest energy electrons. The applicability of $\bar{I}(\mathbf{r})$ for predicting sites and relative reactivities for electrophilic attack in aromatic systems has recently been demonstrated.[29]

THE ELECTROSTATIC POTENTIAL AT THE MOLECULAR SURFACE IN RECOGNITION INTERACTIONS

The interaction of a molecule with a receptor is an example of a "recognition" process, in which the receptor recognizes that the molecule has certain key features that will promote their

interaction. This precedes the formation of any covalent bonds. In the past, such key features have been successfully identified through the analysis of the electrostatic potential that the molecule's nuclei and electrons create in the surrounding space.[3,5,30] It is through this potential that the molecule initially interacts with any other system in its vicinity.

In earlier studies we have presented the electrostatic potentials of dibenzo-p-dioxins, including the highly toxic 2,3,7,8-tetrachlorodibenzo-p-dioxin (TCDD, II), and several structural analogues of TCDD (such as III and IV). We have identified patterns in these potentials that are

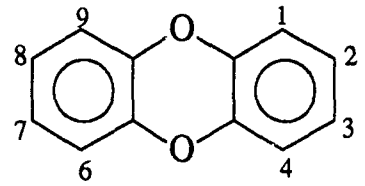

I

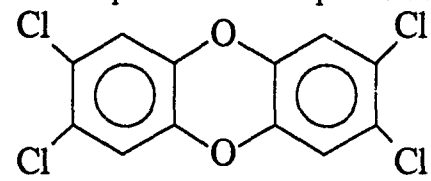

II

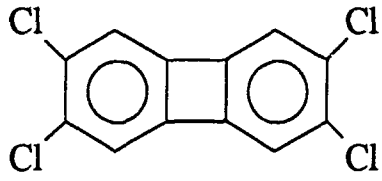

III

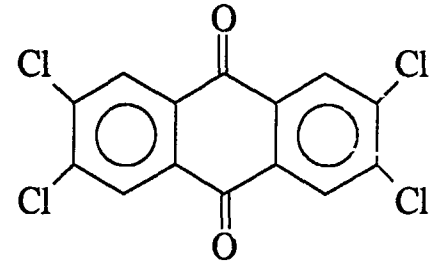

IV

associated with high degrees of biological activity,[31-34] including toxicity, aromatic hydrocarbon hydroxylase (AHH) induction and receptor binding.

In light of the evidence that the toxic effects produced by the dibenzo-p-dioxins and related systems are receptor-mediated,[35,36] our earlier work focused on the initial recognition process involved in this receptor interaction. We computed V(**r**) at a distance of 1.75 Å above the molecular plane, which corresponds to the approximate van der Waals radius of the largest atom in this group of molecules (chlorine).[37] This is the potential that a receptor would encounter during a recognition process.

Recently we have demonstrated that the electrostatic potential plotted on the molecular surface is well suited for the study and analysis of recognition interactions,[38] such as are involved in the biological activities of the dibenzo-p-dioxins and other aromatic systems, e.g. the benzoflavones. We present now highlights of this study. Figures 1-4 show the surface electrostatic potentials of I - IV. These were computed at the STO-5G level using crystallographic geometries or modifications thereof, and will be discussed in light of the molecules' respective biological activities. (All of the electrostatic potential plots presented in this paper are black and white reproductions of computer-generated color figures.)

The calculated electrostatic potentials on the molecular surfaces of the parent inactive dibenzo-p-dioxin, I, and the highly toxic TCDD, II, are shown in Figures 1 and 2. In Figure 1, negative potentials extend over the outer two rings, becoming stronger near the central oxygens. The lateral regions (near positions 2,3, and 7,8) are positive, as is the surface above the central dioxin ring. The negative potentials above the outer rings can be interpreted as being due to the aromatic π electrons.

The surface V(**r**) of TCDD (Figure 2) is in extreme contrast to that of I. Negative lateral regions associated with the chlorines are separated by a large positive V(**r**) region. The negative potentials above the outer rings of I are completely eliminated, as was seen also in our earlier two-dimensional V(**r**) plots.[31] In addition, the oxygen negative potentials in II are greatly diminished

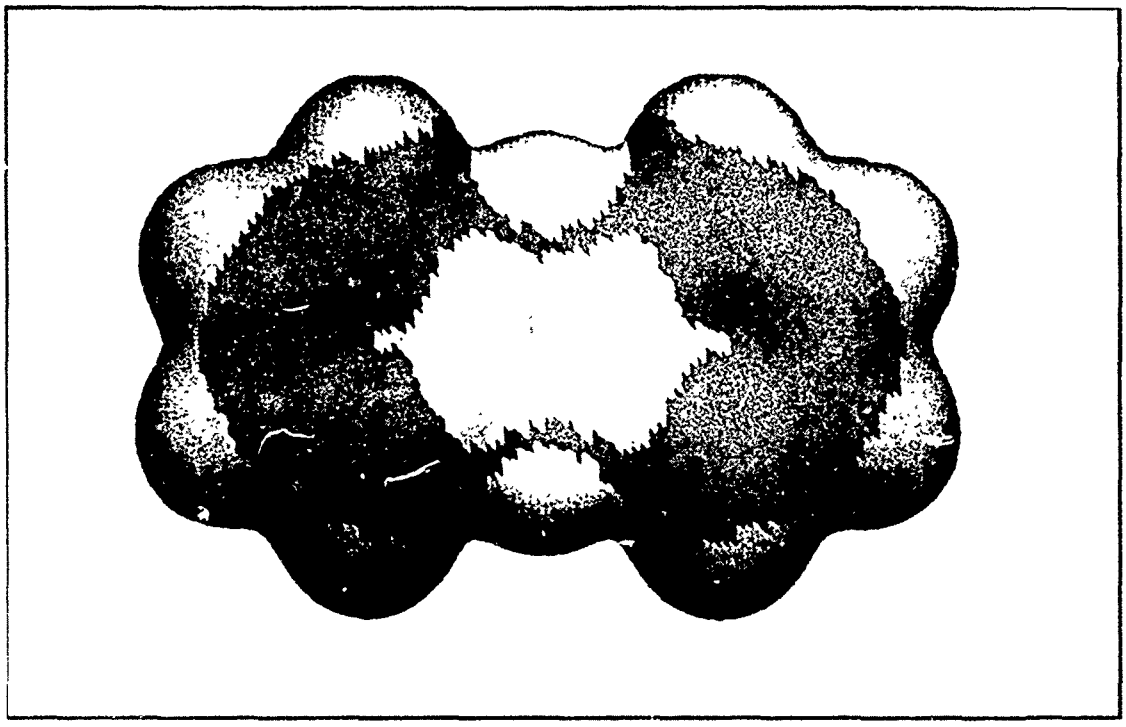

Figure 1. Calculated electrostatic potential on the molecular surface of dibenzo-p-dioxin (I). Gray is for $V(\mathbf{r}) > 0$ kcal/mole, black for $-10 < V(\mathbf{r}) < 0$ kcal/mole, and white for $V(\mathbf{r}) < -10$ kcal/mole.

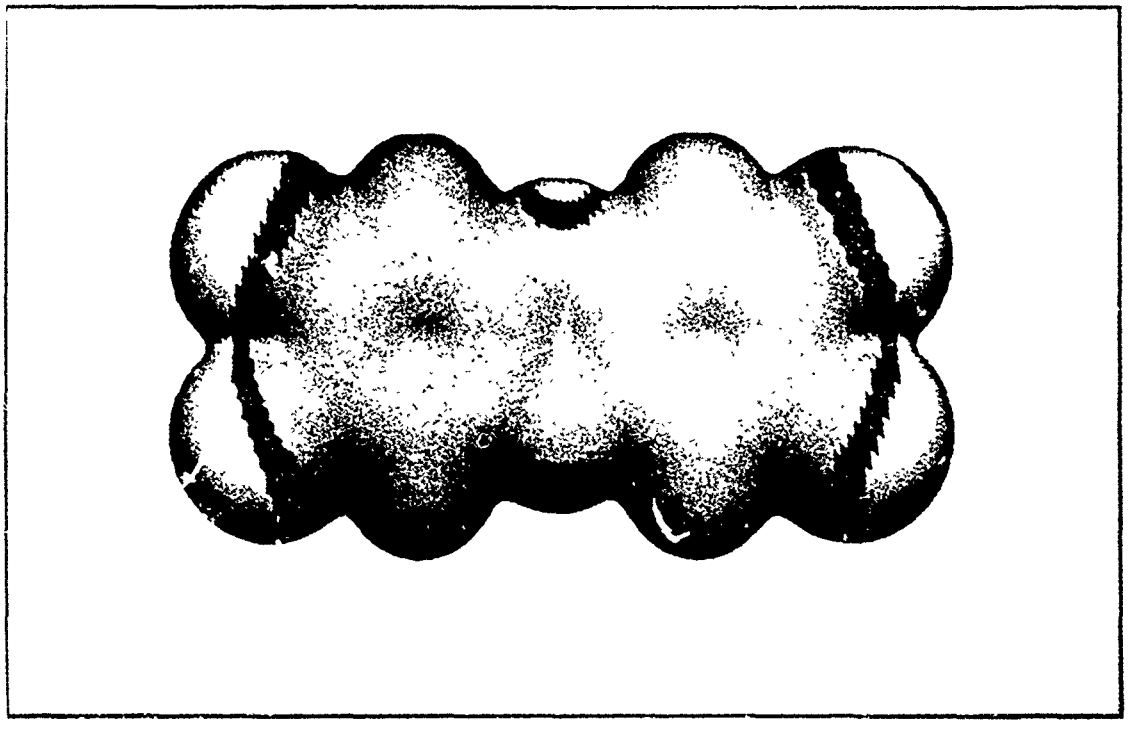

Figure 2. Calculated electrostatic potential on the molecular surface of 2,3,7,8-tetrachloro-dibenzo-p-dioxin (II). Gray is for $V(\mathbf{r}) > 0$ kcal/mole, black for $-10 < V(\mathbf{r}) < 0$ kcal/mole, and white for $V(\mathbf{r}) < -10$ kcal/mole.

relative to I, and appear on the sides of the surface, largely masked from view. These various features reflect the strong electron-attracting inductive power of the chlorine substitutents.

2,3,6,7-tetrachlorobiphenylene (III) is a non-oxygen-containing analogue of TCDD, very similar to II in toxicity, AHH induction and receptor binding. Its surface electrostatic potential, presented in Figure 3, is also strikingly similar to that of TCDD (Figure 2); negative lateral regions are separated by an extensive area of positive potential. This points out, as we have suggested earlier,[34] that oxygens in the central portion of the molecule are not required for high activity.

It is seen in Figure 4 that the surface V(**r**) of the relatively inactive 2,3,6,7-tetrachloro-anthraquinone (IV) has a pattern similar to those of II and III (Figures 2 and 3). However, the negative potentials associated with the central oxygens in IV are farther apart from each other and more accessible than those of TCDD (Figure 2). This difference between the potentials of II and IV, which is steric in nature, is clearly brought out by Figures 2 and 4. These results are consistent with our earlier speculation that the biological inactivity of IV may be due in part to the carbonyl oxygen negative regions being in a position to inhibit an attractive interaction between IV and some portions of the receptor binding site, whatever that may be.[34]

Our present results for I - IV support our earlier observations regarding factors that are linked to high biological activities in the dibenzo-p-dioxins and similar systems.[31,34] Negative regions above all or most of the lateral positions of the molecule, separated by an area of positive potential, appear to be necessary for high activity; oxygens in the central portion of the molecule are not. Our results for the highly toxic II and the relatively inactive IV suggest that in cases with central oxygens, a high level of biological activity requires their characteristic negative potentials to be small, relatively weak and close to the center of the molecule. These features are graphically depicted by the electrostatic potentials on the molecular surfaces of the highly active II and III (Figures 2 and 3). In the case of IV, the steric factor that may be responsible for its low activity (more widely separated and accessible negative oxygen potentials) is also clearly shown by its surface potential (Figure 4).

AVERAGE LOCAL IONIZATION ENERGIES ON MOLECULAR SURFACES OF AROMATIC SYSTEMS

We have recently demonstrated that the average local ionization energy, $\bar{I}(\mathbf{r})$, computed on the molecular surfaces of a series of aromatic systems, V, where X is a hydrogen or a substituent group, provides site specific predictions for preferred positions of electrophilic aromatic substitution.[29]

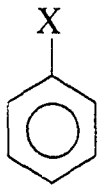

V

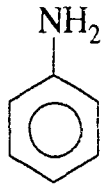

VI

The magnitudes of the smallest $\bar{I}(\mathbf{r})$ values ($\bar{I}_{min}$) for these systems decrease as relative reactivity toward electrophiles increases.

Figure 5 shows the average local ionization energy $\bar{I}(\mathbf{r})$ plotted on the molecular surface of aniline, VI. $\bar{I}(\mathbf{r})$ was computed at the 6-31G* level using an STO-3G optimized structure. The lowest average local ionization energies are found above the ortho and para positions; slightly higher ones are associated with the amine lone pair. The magnitudes of the $\bar{I}_{min}$ values of VI are less than those of benzene. These data are consistent with the experimentally observed ortho and para directing and overall activating tendencies of the $-NH_2$ group.[39,40]

We have found an excellent correlation between the Hammett constants σ_p and σ_m and the corresponding $\bar{I}_{min}$, indicating that our calculated surface $\bar{I}_{min}$ values are good indices of the relative electron-withdrawing and -donating effects of substituents on benzene rings. This relationship, which

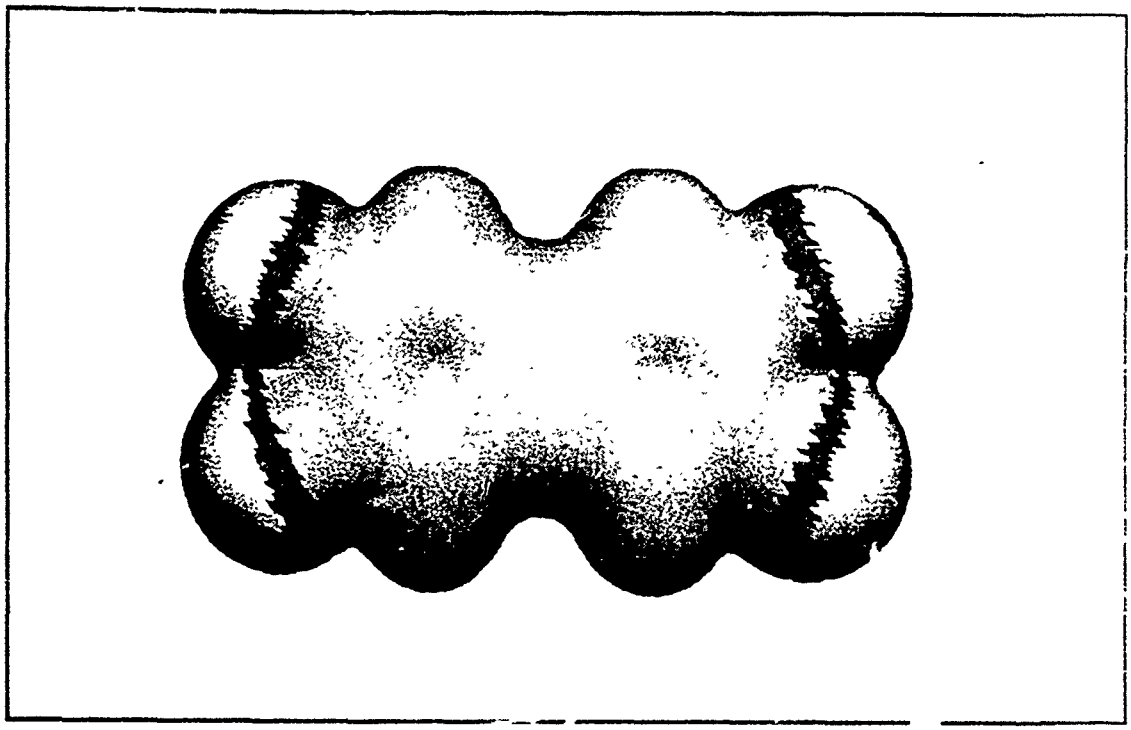

Figure 3. Calculated electrostatic potential on the molecular surface of 2,3,6,7-tetrachlorobiphenylene (III). Gray is for $V(\mathbf{r}) > 0$ kcal/mole, black for $-10 < V(\mathbf{r}) < 0$ kcal/mole, and white for $V(\mathbf{r}) < -10$ kcal/mole.

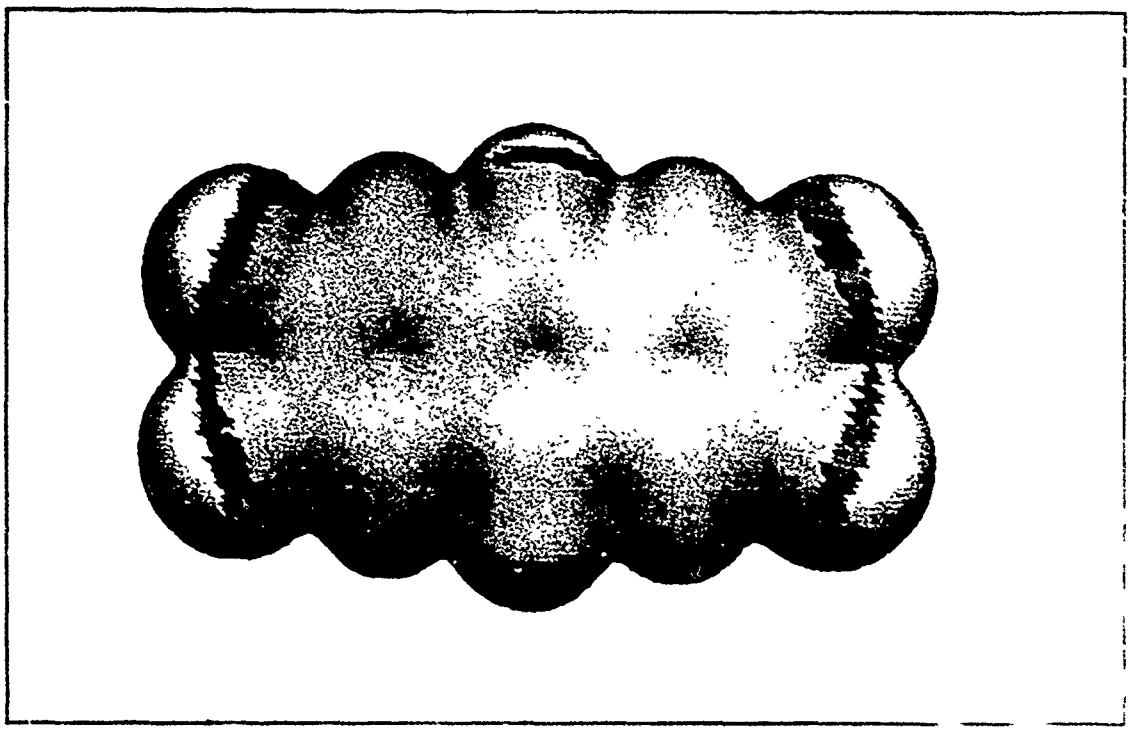

Figure 4. Calculated electrostatic potential on the molecular surface of 2,3,6,7-tetrachloroanthraquinone (IV). Gray is for $V(\mathbf{r}) > 0$ kcal/mole, black for $-10 < V(\mathbf{r}) < 0$ kcal/mole, and white for $V(\mathbf{r}) < -10$ kcal/mole.

has a linear correlation coefficient of 0.99[29], allows us to predict Hammett constants for substituents which have not yet been studied.

ELECTROSTATIC POTENTIALS ON MOLECULAR SURFACES AS GUIDES TO NUCLEOPHILIC PROCESSES

We have recently shown, for a series of cases including acrolein, VII, that the electrostatic potential plotted on the molecular surface can be used effectively for interpreting and predicting nucleophilic processes.[27] Acrolein is an example of an α,β-unsaturated carbonyl compound, VIII.

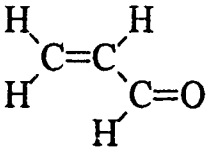

VII

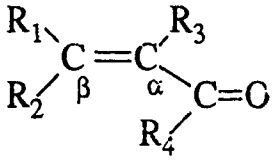

VIII

These are known to undergo nucleophilic attack at the carbonyl and the β carbons;[39] in the particular case of acrolein, this occurs primarily at the carbonyl carbon.

We showed earlier that electrostatic potential plots in planes through the ground-state acrolein molecule reveal no features that indicate the carbonyl carbon to be the favored site for nucleophilic attack.[41] This preference, however, is brought out quite clearly when the potential is plotted on the molecular surface (Figure 6). The surface V(**r**) of VII was computed at the 3-21G level using an optimized STO-3G geometry.

CONCLUSIONS

The computation and presentation of key molecular properties on a three-dimensional surface defined by the contour of constant electronic density equal to 0.002 electrons/bohr^3 is demonstrated to be an effective analytical tool for the study, interpretation and prediction of molecular reactive behavior. This surface encompasses nearly 95% of the total electronic charge of a molecule, and thus effectively reflects molecular dimensions and shape.

The electrostatic potential V(**r**) plotted on the molecular surface is well suited for the study of biological recognition interactions. Surface potential patterns associated with high activity have been identified for the halogenated dibenzo-p-dioxins and related systems. The use of surface potentials eliminates all uncertainty related to choosing the most appropriate plane in which to compute the potential; all molecules are treated in a consistent manner. The surface V(**r**) clearly reveal steric features that may affect the recognition process being investigated. The electrostatic potential plotted on the molecular surface is also effective for the study of nucleophilic processes. These have previously been less straightforward to interpret using the potential than reactivity toward electrophiles, since positive maxima are generally found only at the positions of the nuclei.

The average local ionization energy $\bar{I}(\mathbf{r})$ computed on the molecular surface of aromatic systems provides site specific predictions for preferred positions of electrophilic aromatic substitution. The smallest surface $\bar{I}(\mathbf{r})$ values ($\bar{I}_{min}$) for these systems decrease as relative reactivity toward electrophiles increases. An excellent relationship, with a correlation coefficient of 0.99, has been found between the Hammett constants and $\bar{I}_{min}$, suggesting that the latter are good indices of the total electron-withdrawing and -donating tendencies of the corresponding substitutents.

ACKNOWLEDGEMENT

We greatly appreciate the support of this work by the Environmental Protection Agency, CR-813013-01-0, and the Office of Naval Research, #N00014-85-K-0217.

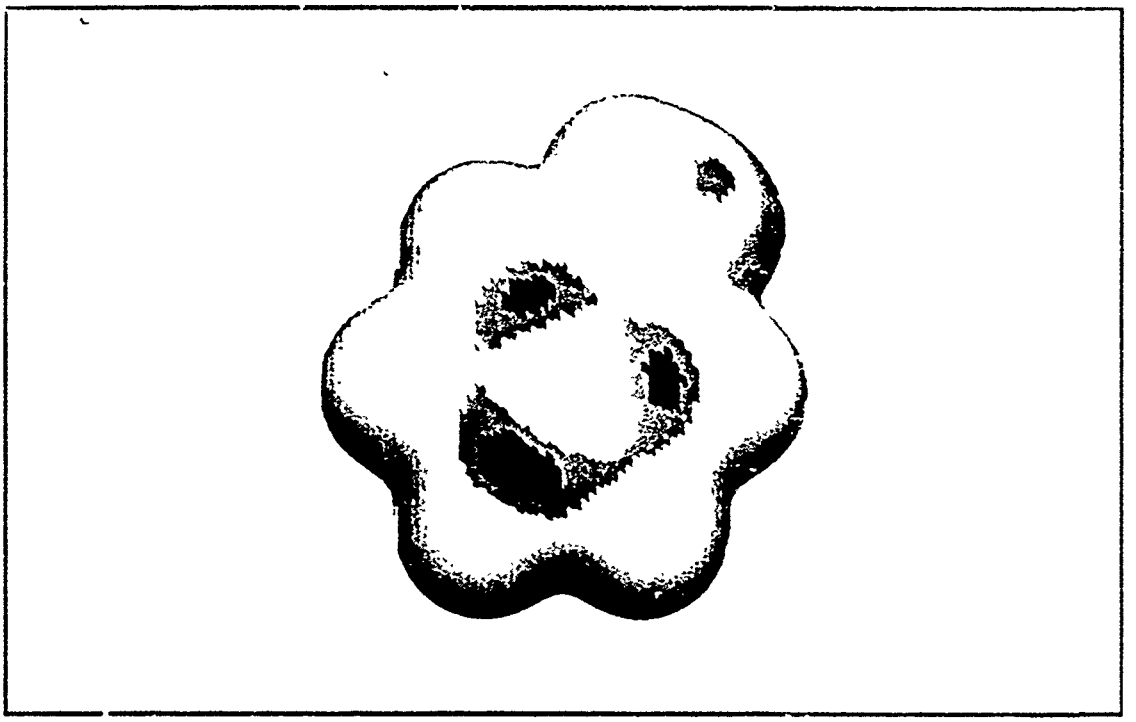

Figure 5. Calculated $\bar{I}(\mathbf{r})$ on the molecular surface of aniline (VI). Black is for $\bar{I}(\mathbf{r}) < 11.84$ eV; gray is for 11.84 eV < $\bar{I}(\mathbf{r})$ < 12.11 eV.

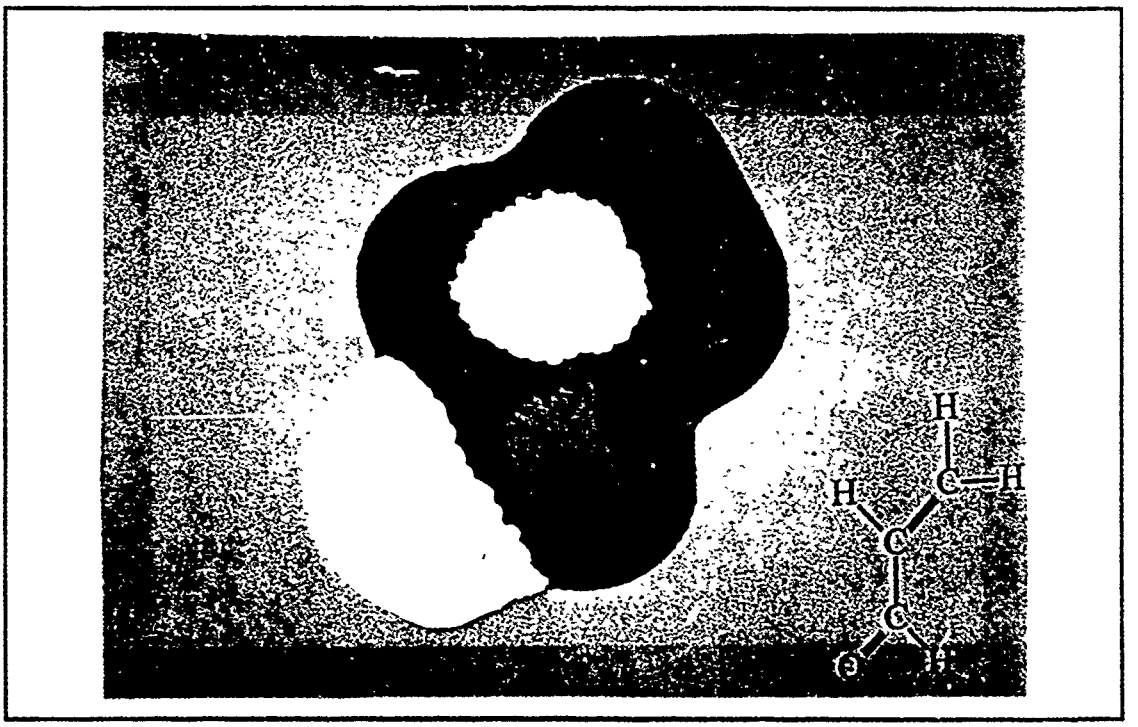

Figure 6. Calculated electrostatic potential on the molecular surface of acrolein (VII). Gray is for $V(\mathbf{r}) > 10$ kcal/mole, black for $10 > V(\mathbf{r}) > 0$ kcal/mole, and white for $V(\mathbf{r}) < 0$ kcal/mole.

REFERENCES

1. P. Politzer and K. C. Daiker, In The Force Concept in Chemistry, B. M. Deb, ed., Van Nostrand Reinhold, New York, 1981, p. 294.

2. P. Politzer and D. G. Truhlar, Eds., In Chemical Applications of Atomic and Molecular Electrostatic Potentials, Plenum Press, New York, 1981.

3. P. Politzer, P. R. Laurence and K. Jayasuriya, Environ. Health Perspect., 61, 191 (1985) (Special Issue on Structure-Activity Correlation in Mechanism Studies and Procedure Toxicology).

4. P. Politzer and J. S. Murray, In Structure and Reactivity (Molecular Structure and Energetics); J. F. Liebman and A. Greenberg, eds., VCH Publishers, New York 1988, Ch. 1.

5. P. Politzer and J. S. Murray, In Theoretical Biochemistry and Molecular Biophysics: A Comprehensive Survey, D. L. Beveridge and R. Lavery, eds., Adenine Press, in press (1989).

6. GAUSSIAN 82: J. S. Binkley, M. J. Frisch, D. J. DeFrees, R. Krishnan, R. A. Whiteside, H. B.Schlegel, E. M. Fluder, and J. A. Pople GAUSSIAN 82, Carnegie-Mellon Quantum Chemistry Publishing Unit, Pittsburgh, PA, 15213.

7. GAUSSIAN 86: M. J. Frisch, J. S. Binkley, H. B. Schlegel, K. Raghavachari, C. F. Melius, R. L.Martin, J. J. P. Stewart, F. W. Bobrowicz, C. M. Rohlfing, L. R. Kahn, D. J.DeFrees, R. Seeger, R. A. Whiteside, D. J. Fox, E. M. Fleuder, and J. A. Pople, Carnegie-Mellon Quantum Chemistry Publishing Unit, Pittsburgh, PA, 1984.

8. R. F. W. Bader, W. H. Henneker and P. E. Cade, J. Chem. Phys. 46, 3341 (1967).

9. R. F. W. Bader and H. J. T. Preston, Theor. Chim. Acta 17, 384 (1970).

10. S. D. Kahn, C. F. Parr and W. J. Hehre, Int. J. Quantum Chem., Quantum Chem. Symp. 22, 575 (1988).

11. B. Pullman, D. Perahia and D. Cauchy, Nucl. Acids Res. 6, 3821 (1979).

12. P. K. Weiner, Langridge, J. M. Blaney, R. Schaefer and P. A. Kollman, Proc. Nat. Acad. Sci. (U.S.) 79, 709 (1982).

13. M. L. Connolly, Science 221, 709 (1983).

14. P. A. Bash, N. Pattabiraman, C. Huang, T. E. Ferrin and R. Langridge, Science 222, 1325 (1983).

15. M. M. Francl, R. F. Hout, Jr., and W. J. Hehre, J. Am. Chem. Soc. 106, 563 (1984).

16. P. Quarendon, C. B. Naylor and W. G. J. Richards, J. Mol. Graph. 2, 4 (1984).

17. M. L. Connolly, J. Am. Chem. Soc. 107, 1118 (1985).

18. J. P. Ritchie, J. Am. Chem. Soc. 107, 1829 (1985).

19. J. M. Burridge, P. Quarendon, C. A. Reynolds and P. J. Goodford, J. Mol. Graph. 5, 165 (1987).

20. R. F. W. Bader, M. T. Carroll, J. R. Cheeseman and C. J. Chang, J. Am. Chem. Soc. 109, 7968 (1987).

21. G. A. Arteca, V. B. Jammal, P. G. Mezey, J. S. Yadav, M. A. Hermsmeier and T. M. Gund, J. Mol. Graph. 6, 45 (1988).

22. E. Scrocco and J. Tomasi, Adv. Quantum Chem., 11, 115 (1978).

23. P. Politzer and D. G. Truhlar, Eds., Chemical Applications of Atomic and Molecular Electrostatic Potentials, Plenum Press, New York, 1981.

24. P. Politzer and R. G. Parr, J. Chem. Phys. 61, 4268 (1974).

25. H. Weinstein, P. Politzer and S. Srebrenik, Theoret. Chim. Acta (Berl.) 38, 159 (1975).

26. P. Politzer, in Homoatomic Rings, Chains and Macromolecules of Main-Group Elements, A. L. Rheingold, Ed., Elsevier, New York, 1977, Chap. 4.

27. P. Sjoberg and P. Politzer, J. Phys. Chem., submitted.

28. T. A. Koopmans, Physica 1, 104 (1933).

29. P. Sjoberg, J. S. Murray, T. Brinck and P. Politzer, Canadian J. Chem., submitted.

30. H. Weinstein, R. Osman, J. P. Green and S. Topiol, in Chemical Applications of Atomic and Molecular Electrostatic Potentials, P. Politzer and D. Truhlar, Eds., Plenum, New York, 1981, p. 309.

31. J. S. Murray, B. A. Zilles, K. Jayasuriya and P. Politzer, J. Amer. Chem. Soc., 108, 915 (1986).

32. J. S. Murray and P. Politzer, Theoret. Chim. Acta 72, 507 (1987).

33. P. Politzer, Toxicol. Lett. 43, 257 (1988).

34. J. S. Murray, P. Evans and P. Politzer, Int. J. Quantum Chem., in press.

35. A. Poland, W. F. Greenlee and A. S. Kende, Ann. N. Y. Acad. Sci. 330, 214 (1979).

36. A. Poland and J. C. Knutson, Ann. Rev. Pharmacol. Toxicol., 22, 517 (1982).

37. A. Bondi, J. Phys. Chem. 68, 441 (1964).

38. P. Sjoberg, J. S. Murray, T. Brinck and P. Politzer, J. Mol. Graphics, submitted.

39. R. T. Morrison and R. N. Boyd, In Organic Chemistry, 3rd ed., Allyn & Bacon: Boston, 1973, Chap. 11.

40. Francis A. Carey and Richard J. Sundberg, In Advanced Organic Chemistry, Part A: Structure and Mechanisms, Plenum Press, New York, 1977, Chap. 9.

41. P. Politzer, S. J. Landry and T. Warnheim, J. Phys. Chem. 86, 4767 (1982).

COMPUTATIONS OF VIBRATIONAL INFRARED FREQUENCIES OF SOME AMINES

Hendrik F. Hameka[1], George R. Famini[2], James O. Jensen[2], and E. Irene Newhouse[3]

ABSTRACT

We have computed the infrared vibrational modes and frequencies of a group of four primary amines, four secondary amines and three tertiary amines. The computations make use of the Gaussian 86 Program Package with the 3-21G basis set and the Hartree-Fock option. The agreement between the computed values and the available experimental data seems reasonable.

1. Introduction

The work described in the present report constitutes a continuation of our computation of vibrational infrared frequencies of organic molecules. In a previous technical report[4] we presented computations on alcohols, mercaptans and sulfides. In the present report we describe computations on a group of amines: (1) two primary amines: methyl amine and ethyl amine and the corresponding chloro-substituted molecules, (2) two secondary amines, dimethyl amine and diethyl amine and the corresponding chloro-substituted molecules dichloromethyl amine and methyl, chloromethyl amine and (3) three tertiary amines, trimethyl amine, triethyl amine and methyl, diethyl amine.

The theoretical prediction of vibrational infrared spectra is of practical importance for the identification of known and unknown compounds. Of course, if a compound has been synthesized and if its infrared or Raman spectrum have been measured then the compound is readily identified by comparing its spectrum with the available experimental spectrum. However, in many instances we wish to identify an unknown compound by measuring its vibrational infrared or Raman spectrum or we wish to identify a molecule of known composition which has not yet been synthesized. In the latter case it would be helpful if the vibrational frequencies and intensities could be predicted theoretically since they cannot be determined experimentally. It should be noted also that the computation of a vibrational infrared spectrum of an organic molecule is considerably cheaper than the synthesis of the molecule and the experimental determination of its spectrum.

We will show that vibrational frequencies may be computed by means of ab-initio quantumchemical methods with possible errors that vary between 1 and 12%, depending on the type of vibrational mode. However, it is well known that in organic molecules many of the vibrational modes are localized and that many functional groups have characteristic frequencies that do not

vary much between different molecules. We feel therefore that the accuracy of computed frequencies may be improved by considering groups of similar molecules and by introducing correction factors that bring the computed frequencies in line with the available experimental data. We have found that it is not advisable to use a uniform correction factor for all vibrational modes. It is preferable instead to introduce different correction factors for different types of vibrational modes, for instance we should differentiate between C-H, C-C and C-Cl stretch frequencies, H-C-H bend frequencies, etc. In this way the unknown vibrational frequencies are predicted by computations and by interpolation or extrapolation of the available experimental data.

2. Computational Methods

Our computations are based on the Gaussian 86 Program Package[5]. The computation of vibrational frequencies by means of this method is extensively discussed in the book by Hehre, Radom, Von Schleyer and Pople[6]. The accuracy of the results depends on the type of basis set that is used and on the type of computation, Hartree-Fock, Hartree-Fock with configuration interaction, etc. We performed some preliminary computations and we concluded that the use of the straightforward Hartree-Fock procedure (no CI) with the 3-21G basis set constitutes a satisfactory compromise of sufficient accuracy and reasonable computational effort. Our preliminary work indicated also that the results obtained from the STO-3G basis set are not of sufficient accuracy to be of practical use. The use of more elaborate basis sets than 3-21G and the addition of configuration interaction does not improve the accuracy of the frequency calculations significantly but it requires considerably more computational efforts. All our observations are consistent with the analysis and discussion presented by Hehre el al[6]. It should also be noted that we are interested in large organic molecules and that in many of our computations the use of basis sets larger than 3-21G is not feasible. Since we wish all our theoretical results to be consistent we feel that the use of the HF/3-21G option constitutes a suitable compromise of sufficient accuracy and manageable computational effort.

We have considered a total of eleven amines and corresponding chloro-substituted amines and we discuss the primary, secondary and tertiary amines separately in the follow three sections.

3. Primary amines

We have computed the 3-21G optimized geometries and the corresponding vibrational frequencies of four primary amines: methyl amine, chloromethyl amine, ethyl amine and 2-chloromethyl amine.

The primary amines have an NH_2 group and this functional group has five characteristic frequencies: two N-H stretch frequencies around 3700 cm^{-1}, two H-N-H bend modes around 1250 cm^{-1} and 1700 cm^{-1} and a NH_2 wagging motion around 750 cm^{-1}. In addition there is an N-C stretch mode with a frequency which varies between 1100 and 1250 cm^{-1}. This group of six frequencies is characteristic of all primary amines.

The presence of the chlorine atom may be detected by observing the C-Cl stretch frequency, which is at 505 cm^{-1} for the methyl compound and at 626 cm^{-1} for the ethyl compound. There is no experimental information available for the chloro-substituted molecules and we cannot offer any explanation for

the difference in C-Cl stretch frequency between the two molecules.

All molecules exhibit a number of C-H stretch modes, the number is of course equal to the number of C-H bonds in the molecule. In ethyl amine we identify two stretch modes that we denote by C_m-H modes and which are localized in the middle CH_2 group. The others which we denote by C_e-H modes are localized in the CH_3 or CH_2Cl end groups. All C-H stretch frequencies are grouped together in a narrow range between 3130 and 3440 cm^{-1}. The ethyl amines also exhibit a C-C stretch mode around 950 cm^{-1}.

It is not easy to identify and characterize the various H-C-H bending modes because most of them are delocalized and we often have difficulty even assigning them to a specific CH_2 or CH_3 group. An exception is the CH_2 or CH_3 wagging mode, which occurs at 900 or at 1100 cm^{-1}, we have listed those separately. All other H-C-H bending modes are listed as a group.

We were unable to find experimental information for the two chloro-substituted compounds but there is an abundance of experimental information available for methyl amine and there is a report of the Raman spectrum of ethyl amine. We present a comparison of our computed frequencies and the experimental data in Table 1.

TABLE 1

methyl amine			ethyl amine		
comp	IR[7]	Ram[8]	Ram[9]	comp	Ram[8]
753	780	-	781	435	414
1096	-	1039	1044	933	889
1256	-	-	-	1079	1046
1456	-	-	-	1152	1082
1614	1385	-	-	1242	1122
1680	1470	1466	1460	1386	1223
1702	-	-	-	1457	1293
1851	1625	-	-	1547	1376
3135	2820	2808	2820	1664	1450
3230	2930	2879	2883	3131	2834
3264	2964	2945	2960	3196	2867
3678	3360	3312	3360	3231	2904
3775	3410	3372	3470	3254	2926
-	-	-	-	3282	2960
-	-	-	-	3664	3305
-	-	-	-	3762	3367

Comparison of computed and experimental frequencies of methyl amine and ethyl amine.

In the case of methyl amine we compare our computed values with the infrared frequencies reported by Owen and Barker[7] and with the Raman frequencies reported by Kohlrausch[8] and by Kirby-Smith and Bonner[9]. We found an additional four or five reports on the IR and Raman spectra of methyl amine, the experimental results seem to be quite consistent and we did not see any point in listing them all. Kohlrausch[8] also reported the Raman spectrum of ethyl amine, we were not able to find any other experimental information for that molecule.

It may be seen in Table 1 that there is a systematic difference between the computed and the experimental C-H and N-H stretch frequencies, the ratio between the experimental and the computed values is 0.9 with a possible deviation of 0.015. In the group of H-C-H bend frequencies the corresponding ratio is slightly smaller, it is 0.875 with a possible deviation of 0.01. In the case of the other frequencies, the N-C and C-C stretch, the H-N-H bend and the CH_2 and NH_2 wag the computed and the experimental frequencies are fairly close together and it is not practical to introduce any correction factor other than unity.

4. Secondary amines

We have computed the 3-21G optimized geometries and the corresponding vibrational modes and frequencies of four secondary amines: dimethyl amine, diethyl amine, dichloromethyl amine and methyl, chloromethyl amine.

The secondary amines have a NH group and this functional group has three characteristic vibrational modes, a N-H stretch mode with a frequency between 3700 and 3800 cm^{-1} and two N-H bend modes, the first has a frequency around 700 cm^{-1} and the second has a frequency around 1650 cm^{-1}. The secondary amines are also characterized by a C-N-C scissor mode with a frequency between 400 and 500 cm^{-1} and two C-N stretch modes with frequencies between 1000 and 1300 cm^{-1}. These six characteristic frequencies are typical of the secondary amines. It should be noted that the C-N stretch frequencies of dimethyl and diethyl amine are practically identical, they are at 1194 and at 1242 cm^{-1}. The lower frequency is shifted downwards by as much as 200 cm^{-1} by chlorine substitution and the higher frequency is shifted upwards by about 50 cm^{-1}.

TABLE 2

dimethyl amine		diethyl amine	
comp	Ram[8]	comp	IR[10]
400	390	-	-
717	826	689	724
970	931	1071	1045
1195	1078	1192	1099
1375	1236	1241	1134
1634	1438	1276	1186
1701	1472	1436	1264
-	-	1454	1282
-	-	1526	1325
-	-	1568	1370
-	-	1639	1449
3116	2776	3155	2800
3122	2816	3202	2880
3220	2890	3272	2956
3713	3343	3700	3268

Comparison of computed and experimental frequencies of dimethyl amine and diethyl amine.

All four molecules have one N-H stretch mode and as many C-H stretch modes as there are C-H bonds. The C-H stretch frequencies are grouped in a fairly narrow range between 3100 and 3450 cm^{-1}. The chloro-substituted molecules have one or two C-Cl stretch modes with frequencies between 500 and 600 cm^{-1}. Diethyl amine exhibits two C-C stretch modes around 1000 cm^{-1} and two N-C-C bend modes around 1200 cm^{-1}. In addition we have identified two CH_2X wag modes in the dimethyl compounds and an additional CH_2 wag in the diethyl compound.

We had difficulty identifying the many H-C-H bending modes since they correspond to delocalized vibrational modes involving the whole molecule.

The Raman spectrum of dimethyl amine was reported by Kohlrausch[8] and the IR spectrum of diethyl amine is listed in the Aldrich Library of Infrared Spectra[10]. We were not able to find experimental information on the chloro-substituted amines.

We have listed the experimental and our computed frequencies of dimethyl and dimethyl amine in Table 2. The ratio between the experimental and the computed C-H and N-H stretch frequencies is the same as for the primary amines, the same is true for the H-C-H bend frequencies. The assignment of the other frequencies (1045, 1099 and 1134 cm^{-1}) of diethyl amine is less straightforward. We have assigned 1045 to the computed 1071 wag frequency, 1099 to the 1192 C-N stretch frequency and 1134 to the 1241 C-N stretch frequency, but these assignments are subject to some uncertainties since our computations do not predict intensities.

5. Tertiary amines

We have computed the 3-21G optimized geometries and the corresponding vibrational modes and frequencies of three tertiary amines: trimethyl amine, triethyl amine and methyl, diethyl amine. The first molecule was computed on a Microvax and the latter two molecules were computed at the Cray computer at the Alabama Supercomputer Network.

The tertiary amines are characterized by three C-N stretch mode frequencies and by three C-N-C bend mode frequencies. In the case of c_{3v} symmetry two of the stretch modes and two of the bend modes are doubly degenerate, in other words, two of the stretch frequencies are equal and two of the bend frequencies are equal. We found that dimethyl amine and diethyl amine are extremely close to c_{3v} symmetry, the nitrogen and carbon skeletons have c_{3v} symmetry but the rotation of the C-H bonds cause a very slight distortion of the symmetry. In both molecules two of the C-N stretch frequencies and also two of the C-N-C bend frequencies are very close together, this is consistent with a very slightly distorted c_{3v} structure. In methyl, diethyl amine there is no c_{3v} symmetry and the C-N frequencies are all different.

In addition to the C-N modes each molecule has a number of C-H stretch modes equal to the number of C-H bonds in the molecule and a number of C-C stretch modes equal to the number of C-C bonds. All these stretch and the six C-N modes are clearly identified. There are also three CH_3 wag modes in each molecule and as many CH_2 wag modes as there are CH_2 groups.

The Raman spectrum of trimethyl amine has been reported by Kohlrausch[8] and the IR spectrum of triethyl amine has been reported in the Aldrich Library[10]. We present a comparison of the computed and the experimental frequencies in Table 3. Since there are no N-H bonds we do not observe any

N-H stretch or bend frequencies. Some of the C-H stretch frequencies are very close together and we suspect that many of the experimental IR lines represent two or more of the computed frequencies. The ratio between the experimental and the computed C-H stretch frequencies is again 0.90 with a possible deviation of 0.01. We have also identified two C-N stretch frequencies and two C-N-C bend ferquencies, in each case one mode is doubly degenerate. The ratio between the experimental and the computed values is 0.95 for the C-N stretch frequencies and 0.89 for the C-N-C bend frequencies. In the triethyl molecule we have also identified the CH_2 and the CH_3 wag modes and a C-C stretch mode. The other frequencies correspond to H-C-H bend modes. here the ratio is again equal to 0.875.

TABLE 3

trimethyl am.		triethyl am.	
comp	Ram[8]	comp	IR[10]
841	827	770	734
-	-	881	800
-	-	983	917
1124	1036	1150	1064
-	-	1198	1076
-	-	1211	1094
1330	1177	1280	1136
1413	1278	1355	1209
1668	1442	1676	1449
1690	1463	1690	1466
3144	2765	3176	2800
3196	2815	3214	2865
3250	2945	3264	2958
3254	2970	3274	2976

Comparison of computed and experimental vibrational frequencies of trimethyl amine and triethyl amine.

CONCLUSIONS

We feel that our computations of the vibrational modes and frequencies of the eleven amines constitute a useful basis for the theoretical prediction of the vibrational frequencies of amines. We mentioned already that triethyl amine and methyl, diethyl amine were computed on a Cray Supercomputer, we should add that all the other molecules were computed on a Microvax. We believe that computations on larger tertiary amines or on chloro-substituted tertairy amines may be successfully completed on a Cray Supercomputer, but we do not believe that molecules of such size can be handled by a Microvax.

It may be seen in Tables 1, 2 and 3 that the differences between computed and experimental frequencies are at most 12%. After introducing correction factors the errors may be reduced to 1 or 2%. Here it is important to note that different correction factors should be used for different types of vibrations. It is not advisable to use the same correction factor for all

types of vibrational modes since this leads to significantly larger errors in the theoretical predictions.

It should also be noted that certain types of vibrational modes are much more readily identified than others. For instance, the C-N stretch modes and the C-N-C bend modes are clearly recognized in all amines. On the other hand, many of the H-C-H bend modes are delocalized throughout the whole molecule and we find it difficult to label these modes or to differentiate between them. Fortunately, the H-C-H bend frequencies are not all that relevant for identification purposes, since they suggest only the presence of C-H bonds and usually we know that already. The more relevant characteristic frequencies such as the C-N stretch and bend modes, the N-H bend and stretch modes, and C-Cl stretch mode, etc., are clearly identified and assigned.

In summary, we believe that the computations of the vibrational frequencies of a group of similar amines may lead to accurate frequency predictions if the computations are combined with an analysis of the available experimental information.

FOOTNOTES

1. Hendrik F. Hameka, Dept. of Chem., University of Pennsylvania, Philadelphia, PA 19104.

2. George R. Famini and James O. Jensen, Chemical Research, Development and Engineering Center, Aberdeen Proving Ground, MD 21010-5423.

3. E. Irene Newhouse, Dept. of Chem., Auburn University, Auburn, AL 36849.

4. H. F. Hameka, S. L. Emery, G. R. Famini, J. O. Jensen, J. M. Leonard and D. J. Reutter, Computation of Vibrational Frequencies in Mercaptans, Alcohols and Sulfides, CRDEC-TR-069, U. S. Army Chemical Research, Development and Engineering Center, Aberdeen Proving Ground, MD, May 1989, Unclassified report.

5. J. S. Binkley, M. J. Frisch, D. J. DeFrees, K. Raghavachair, R. A. Whiteside, H. B. Schlegel, E. M. Fluder and J. A. Pople, Gaussian 86, Carnegie-Melon University, Pittsburgh, PA (1982).

6. W. J. Hehre, L. Radom, P. von R. Schleyer and J. A. Pople, Ab Initio Molecular Orbital Theory, Wiley-Interscience, New York, NY (1985).

7. R. G. Owens and E. F. Barker, The Infra-Red Absorption Spectrum of Methyl Amine, J. Chem. Phys. 8, 229 (1940).

8. K. W. R. Kohlrausch, Studien zum Ramaneffek· ./.II. Das Raman-Spektrum Organischer Substanzen, Monatshefte f. Chemie 68, 349 (1936).

9. J. S. Kirby-Smith and L. G. Bonner, The Raman Spectra of Gaseous Substances. 1. Apparatus and the Spectrum of Methylamine, J. Chem. Phys. 8, 880 (1939).

10. C. J. Pouchert, The Aldrich Library of Infrared Spectra, Aldrich Chemical Company, Milwaukee, WI (1975).

BLANK

THEORETICAL PREDICTION OF VIBRATIONAL CIRCULAR DICHROISM SPECTRA

Daniel Zeroka [1a], George R. Famini [1b], James O. Jensen [1b], Arthur H. Carrieri [1b], and Cary F. Chabalowski [1c]

ABSTRACT

A molecular species that is chiral possesses a Vibrational Circular Dichroism (VCD) spectrum. This study is the first step toward the development of a library of theoretically predicted VCD spectra. At this time we report the results of theoretical studies on several molecules, the dominant species being sugars with 3 to 6 carbon atoms. The procedures used involves stepwise optimizations using MMADS, MOPAC and Gaussian type calculations. Optimizations at the 3-21G Gaussian level are completed using the Gaussian 82 or CADPAC version 4.0 programs. Frequencies and rotational strengths are determined based on the method of P. J. Stephens which is incorporated in the CADPAC version 4.0 program. Calculated optimized structures, frequencies and rotational strengths will be presented. Where available comparison will be made to experimental results and other calculations; also, a comparison of results using nonscaled versus scaled force fields will be presented. For a more detailed description of the work described in this report the reader is referred to reference 2 (2).

1. INTRODUCTION

A requirement for this study was the interest of the Detection Group at CRDEC in being able to detect biological materials in the field. A reasonable means to this objective is through the recognition that sugars are distinguishing features of biological materials. Sugars are optically active and can be studied through a variety of techniques. The technique of interest here is vibrational circular dichroism (VCD). The predicted VCD spectra can also be related to the (1,4) matrix element of the Mueller matrix, to be discussed below. A procedure to obtain all of 16 elements of the (4x4) Mueller matrix simultaneously by a two laser spectroscopic measurement is presently being implemented by one of the authors (AHC). The calculated spectra of sugars, at a minimum, should assist laboratory measurements on sugars. The practical questions as to whether real biological materials can be detected and the limits of detectability await future experimental studies. Because the techniques of computational chemistry are now cheaper and faster than extensive experimental techniques, quantum chemistry is employed to identify spectral regions

of interest and what compounds can be detected by VCD. Furthermore, a library can be constructed that will permit matching of experimental results to unambiguously identify unknown compounds. This report will focus on the application of current computational techniques to the study of sugars, sugar-like molecules and other molecules of interest. This study can be viewed as the beginning phase of the generation of a library of theoretically predicted VCD spectra. For a more detailed report of the work described in this report the reader is referred to reference 2 (2).

2. BACKGROUND

2.1 Vibrational Circular Dichroism

Molecules that interact differently with left circularly polarized (LCP) and right circularly polarized (RCP) radiation are optically active. Two phenomena linked to optical activity are:

(1) optical rotation
(2) circular dichroism

Optical rotation involves the rotation of a plane of linearly polarized radiation as it is passed through a sample. Circular dichroism is the difference in the absorption of LCP and RCP radiation by a sample. In the absence of applied fields, optical activity arises from chirality, which exists when a molecule is not superimposable on its mirror image - i.e. a molecule must not possess any elements of symmetry to be optically active.

In the early 1970's instrumentation was devised to measure the VCD spectrum of a chiral molecule. Here, the difference in absorptivity of a sample between LCP and RCP radiation is plotted as a function of wavenumber. A typical VCD spectrum is shown in Figure 1. Figure 1 includes both the VCD spectrum of methyl thiirane over the wavenumber range of 1500-800 cm^{-1} and the IR spectrum for the purpose of comparison. As can be noted the rotational strengths, i.e. the difference in absorptivity of a sample between LCP and RCP radiation, can be positive or negative and the intensities are not related to the infrared and Raman intensities. The essential points to be studied in this investigation are frequencies, magnitudes of intensities and signs of intensities. All notations used in the following sections are consistent with those of Stephens (3,4).

2.2 Stephens' Formulation of the Rotational Strength

P. J. Stephens (3,4) has developed a theory for the determination of the rotational strength of a vibrational transition g→ e, R(g→ e), for a chiral molecule;

$$R(g \rightarrow e) = \sum_{\beta} \mathrm{Im}[\langle g | (\mu_{el})_{\beta} | e \rangle \langle e | (\mu_{mag})_{\beta} | g \rangle] \qquad [\beta = x, y, z] \tag{1}$$

where g and e are ground and excited states and μ_{el} and μ_{mag} are electric and magnetic dipole moment operators. For a given fundamental vibrational mode of frequency ω_i, the electric and magnetic dipole transition moments for the 0→ 1 vibrational transition is given by;

$$<o|(\mu_{el})_\beta|1>_i=(\hbar/2\omega_i)^{.5}\sum_{\lambda\alpha} P^{\lambda}_{\alpha\beta}\ S_{\lambda\alpha,i} \tag{2}$$

$$<o|(\mu_{mag})_\beta|1>_i=-(2\hbar^3\omega_i)^{.5}\sum_{\lambda\alpha} M^{\lambda}_{\alpha\beta}\ S_{\lambda\alpha,i}. \tag{3}$$

$P^{\lambda}_{\alpha\beta}$ and $M^{\lambda}_{\alpha\beta}$ are atomic polar and atomic axial tensors defined by

$$P^{\lambda}_{\alpha\beta}=E^{\lambda}_{\alpha\beta}+N^{\lambda}_{\alpha\beta} \tag{4}$$

$$M^{\lambda}_{\alpha\beta}=I^{\lambda}_{\alpha\beta}+J^{\lambda}_{\alpha\beta} \tag{5}$$

$$E^{\lambda}_{\alpha\beta}=[(\partial/\partial X_{\lambda\alpha})<\psi_G(\vec{R})|(\mu^e_{el})_\beta|\psi_G(\vec{R})>]_{\vec{R}_o} \tag{6}$$

$$N^{\lambda}_{\alpha\beta}=Z_\lambda e\,\delta_{\alpha\beta} \tag{7}$$

$$I^{\lambda}_{\alpha\beta}=<(\partial\psi_G(\vec{R})/\partial X_{\lambda\alpha})_{\vec{R}_o}|(\partial\psi_G(\vec{R}_o,H_\beta)/\partial H_\beta)_{H_\beta=0}> \tag{8}$$

$$J^{\lambda}_{\alpha\beta}=(i/4\hbar c)\sum_{\gamma}\epsilon_{\alpha\beta\gamma}(Z_\lambda e)R^{o}_{\lambda\gamma} \tag{9}$$

where

$\vec{R}$	=	the nuclear geometry
$\vec{R}_o$	=	the equilibrium nuclear geometry
$X_{\lambda\alpha}$	=	cartesian displacement coordinates(α =x,y,z) from equilibrium of nucleus λ
$Z_\lambda e$	=	charge on nucleus λ
$\vec{R}^{o}_{\lambda}$	=	equilibrium position of nucleus λ
G	=	electronic ground state
μ^e_{el}	=	electronic contribution to μ_{el}
$\psi_G(\vec{R}_o,H_\beta)$	=	electronic wavefunction of G at $\vec{R}_o$ in the presence of the perturbation $H=-(\mu^e_{mag})_\beta H_\beta$
$\epsilon_{\alpha\beta\gamma}$	=	antisymmetric unit third rank tensor

Note that;

$$X_{\lambda\alpha}=\sum_i S_{\lambda\alpha,i}\,Q_i$$

i.e. $S_{\lambda\alpha,i}$ is a matrix element in the transformation between the cartesian coordinates and the normal coordinates.

2.3 Mueller Matrix

Let us now turn to a very brief discussion of the definition and use of a a Mueller matrix. The interaction of polarized radiation with a scatterer can be described by specifying the polarization state of incident and scattered radiation. One convenient description of the radiation involves use of Stokes vectors and the use of a transformation between the scattered radiation, σ_s and the incident radiation σ_i which is termed the Mueller matrix (5), S

$$\sigma_s = S\sigma_i \tag{10}$$

where

σ_s = Stokes vector for scattered light
σ_i = Stokes vector for incident light

All of the information concerning the transmission of radiation by an optical element is contained in the 16 elements of the transformation Mueller matrix. The Stokes parameters, components of a Stokes vector are defined by

$$I = \langle E_{\parallel} E_{\parallel}^{*} + E_{\perp} E_{\perp}^{*} \rangle \tag{11}$$

$$Q = \langle E_{\parallel} E_{\parallel}^{*} - E_{\perp} E_{\perp}^{*} \rangle \tag{12}$$

$$U = \langle E_{\parallel} E_{\perp}^{*} + E_{\perp} E_{\parallel}^{*} \rangle \tag{13}$$

$$V = i\langle E_{\parallel} E_{\perp}^{*} - E_{\perp} E_{\parallel}^{*} \rangle \tag{14}$$

where the angular brackets indicates a time average over an interval long compared with the period of a quasi-monochromatic beam described by an electric field $\vec{E}$ with orthogonal axes perpendicular to the direction of propagation. If the incident light is right-circularly polarized, then the irradiance I_R of the the scattered light is related to $S_{11} + S_{14}$. Also, the irradiance I_L of the scattered light is related to $S_{11} - S_{14}$. The Mueller scattering matrix element S_{14} can be expressed as

$$S_{14} = (I_R - I_L)/2I_i \tag{15}$$

where I_i is the intensity of the incident light. The matrix element S_{14} is readily interpretable in terms of the difference of the irradiances of scattered light for incident right-circularly and left-circularly polarized light. In this case the VCD intensity is directly proportional to the S_{14} matrix element. As a result a VCD theoretical spectrum can be used to predict the magnitude of the Mueller matrix element S_{14}.

3. RESULTS

The Chemometric and Biometric Modeling Branch (CBM) of CRDEC has undertaken the task of generating a library of theoretically determined VCD spectra for sugars, sugar-like molecules and other molecules of interest. The calculations have proceeded in the following stepwise manner:

1. the software package MMADS (6) was run using the option MODEL in order to obtain a crude geometry
2. the structure obtained in step (1) was then optimized using MOPAC version 3.0 (7)
3. optimized structures using the Gaussian programs Gaussian 82 (8-11) or CADPAC version 4.0 (12) were obtained. (Both packages yield identical results both in terms of total energy and optimized structure.)
4. frequencies and rotational strengths were obtained by running CADPAC version 4.0 (12) on a CRAY-XMP computer.

The calculations at this point have been largely carried out at the 3-21G level. This level was selected because past experience indicates very reasonable optimized structures are found as compared to experimental structures. As is well known with ab initio determination of vibrational motion, the vibrational frequencies are typically too high - e.g. the C-H stretch predicted for 3-21 G level calculations multiplied by a scaling factor of 0.89, found empirically, is in very good agreement with experimental data (13).

Attention has been focussed on the following areas:

1. determination of the VCD spectrum for molecules for which literature results are available - the molecules selected here are ethylene oxide (14), the isotopically substituted ammonia molecule (NHDT) (15,16), and methyl thiirane (17-19).
2. prediction of VCD spectral parameters for molecules that have functionalities similar to sugars (hydroxyacetaldehyde, hydroxymethyl ether, ethylene glycol and dimethyl ether) and sugars with 3 carbon atoms (D-glyceraldehyde) and 4 carbon atoms (D-erythrose, and D-threose).

Our objectives are the following:

1. develop the VCD parameters (frequency and rotational strengths) in the range range 800-1200 cm^{-1} that indicate transitions of high rotational strength and predict the correct sign.
2. develop the VCD parameters as accurately as possible, within a procedure that is computationally reasonable, for sugars in order that the results can be dovetailed into the experimental program on Mueller Matrix Spectroscopy directed by one of the authors (AHC).

3.1 Ethylene Oxide, Isotopomer of Ammonia (NHDT) and Methyl Thiirane

In order to assess the feasibility of theoretically predicting VCD spectra, as a reasonable first step it seemed appropriate to carry out calculations on molecules for which experimental and theoretical results already existed in the literature. First, ethylene oxide has been previously investigated by Amos et. al. (14) The geometry used by these investigators (14) was used here also and in one study 4-31G level calculations were performed using the CADPAC package. The atomic polar tensor and the atomic axial tensor, given by equations (4) and (5), agree with Table 3 of reference (14).

Next, the isotopomer of ammonia (NHDT) was studied with the following geometric parameters: nitrogen - hydrogen distance (r_{NH}) = 1.011609 A and hydrogen - nitrogen - hydrogen bond angle (θ_{HNH}) = 106.697815 a.u. Calculations were carried out at both the 3-21G and 4-31 G levels. The energies and dipole moments agree with quantities reported in reference (15). An important point to note here is that, for the most part, signs of transitions with high rotational strengths remain unchanged with basis set and even though the magnitude of the rotational strength changes for transitions of high magnitude, the magnitude remains high as the basis set is changed. For transitions of low magnitude the sign of the rotational strength can change as the basis set is changed. The frequencies calculated here have not been scaled or adjusted in any way at this time.

Then, attention was turned to methyl thiirane. Experimental and theoretical work was carried out by Polavarapu et. al. (17) and calculations were carried out by Dothe, Lowe and Alper (18,19). A comparison of results are given in Table 1. Calculated frequencies are qualitatively similar to the 6-31G level calculation. A comparison of the rotational strengths with the rotational strengths determined by a scaled quantum mechanical(SQM) force field determined from a 6-31G * level calculation shows the agreement is reasonable as to the relative magnitude and the sign. For the most part a transition corresponding to a high rotational strength at the 3-21G level of calculation agrees in sign with the more extensive scaled 6-31G * level of calculation.

3.2 Sugar-like Molecules and Sugars

Next, attention was focussed on molecules that are sugar-like in terms of functional groups and sugars with three to six carbon atoms (19). The sugar-like molecules studied were isotopomers of hydroxyacetaldehyde, hydroxymethyl ether, ethylene glycol and dimethyl ether. Calculated frequencies, rotational strengths and optimized geometries were determined and are reported in reference 2 (2). In addition optimized structures for the three carbon atom sugar D-glyceraldehyde and the four carbon atom sugar D-erythrose have been obtained.

3.3 Discussion

Through examination of given spectral ranges, it is possible to scan each table of frequencies and rotational strengths to predict at which frequency a maximum rotational strength should be observed. The quality of the results can be seen by focusing on the VCD results found for methyl thiirane which are summarized in Table 1. The key points to note are the following:

1. The calculation is sensitive, because of the nature of the quantum mechanical operators involved - namely the angular momentum, to the choice of origin of the coordinate system. Comparisons in the literature at present find better agreement with the choice of origin as the center of mass of the molecule. Very key to the calculation is the level of the calculation. As mentioned our calculations are carried out at the 3-21G level, the origin chosen was the center of mass.
2. The inaccuracies that result will be manifest in
   - force field generated
   - atomic polar tensor
   - atomic axial tensor

   Our calculation of rotational strengths, compared to 6-31G level calculations, for the majority of fundamental frequencies predict transitions of high rotational strengths and the correct sign. Transitions with low strengths can have their magnitude and sign changed as one uses another basis set.

The calculations on ammonia agree with results reported in the literature as to the values of the atomic polar and atomic axial tensors and the rotational strengths. The frequencies determined in the references (15,16) have been arrived at by an empirical force field (Duncan-Mills). As has been mentioned the ab initio unscaled frequencies will be somewhat high compared to experimental frequencies.

4. SUMMARY

We have undertaken the generation of a library of theoretically predicted VCD spectra. The approach involves the use of Stephens' theoretical formulation of the rotational strength and the use of Gaussian calculations at the 3-21G level. The results on molecules studied up to this point indicate that for transitions corresponding to high rotational strengths the signs remain insensitive to the basis set level used; in addition the magnitude of the rotational strength of a transition is sensitive to the basis set level that is used but a transition of high rotational strength at one level of calculation will tend also to be high at another level of calculation. It should be emphasized that the key assumptions being used are:

1. use of Stephens' theoretical formulation
2. use of Gaussian 3-21G level of calculation

The level of calculation affects the frequencies, atomic polar tensor, atomic axial tensor, and thereby the rotational strength.

REFERENCES

1. (a) Department of Chemistry 6, Lehigh University, Bethlehem, PA 18015.
(b) U. S. Army Chemical Research, Development and Engineering Center, Aberdeen Proving Ground, MD 21010.
(c) U. S. Army Ballistic Research Laboratory, Aberdeen Proving Ground, MD 21005.
2. D. Zeroka, G. R. Famini, J. O. Jensen, A. H. Carrieri, and C. F. Chabalowski, "Theoretical Prediction of Vibrational Circular Dichroism Spectra", CRDEC-CR-in publication (1990).
3. P. J. Stephens and M. A. Lowe, Ann. Rev. Phys. Chem. **36**, 213-41 (1985).
4. P. J. Stephens, J. Phys. Chem. **89**, 748-52 (1985).
5. (a) H. Mueller, J. Opt. Soc. Am. **38**, 661 (1948).
(b) C. F. Bohren and D. F. Huffman, "Absorption and Scattering of Light by Small Particles", Wiley-Interscience, New York (1983), Chapters 2 and 3.
6. J. M. Leonard and G. R. Famini, "A User's Guide to the Molecular Modelling, Analysis, Display System (MMADS)", 2nd ed., CRDEC-TR-030 Report (1989).
7. M. J. S. Dewar, QCPE 455.
8. J. S. Binkley, M. J. Frisch, D. J. DeFrees, K. Raghavachari, R. A. Whitesde, H. B. Schlegel, E. M. Fluder and J. A. Pople, "Gaussian 82", Department of Chemistry, Carnegie-Mellon University, Pittsburgh, PA.
9. M. J. Frisch, "Gaussian 82 User's Manual", Department of Chemistry, Carnegie-Mellon University, Pittsburgh, PA (1984).
10. W. J. Hehre, L. Radom, P. von R. Schleyer and J. A. Pople, "Ab Initio Molecular Orbital Theory", John-Wiley, New York (1986).
11. T. Clark, "A Handbook of Computational Chemistry", Wiley-Interscience, New York (1985).
12. R. D. Amos, "The Cambridge Analytical Derivative Package Publication", CCP 1/84/4 SERC, Daresbury Laboratory, Daresbury, Warrington WA4 4AD (1984).
13. H. F. Hameka, S. L. Emery, G. R. Famini, J. O. Jensen, J. M. Leonard and D. L. Reutter, "Computation of Vibrational Frequencies in Mercaptans, Alcohols, and Sulfides",CRDEC-TR-069 Report (1989).
14. R. D. Amos, N. C. Handy, K. J. Jalkanen and P. J. Stephens, Chem. Phys. Letters, **133**, 21-26 (1987).
15. K. J. Jalkanen, P. J. Stephens, R. D. Amos and N. C. Handy, Chem. Phys. Letters, **142**, 153-58 (1987).
16. K. J. Jalkanen, P. J. Stephens, P. Lazzerti and R. Zanasi, J. Chem. Phys. **90**, 3204-13 (1989).

17. P. L. Polavarapu, B. A. Hess, Jr., L. J. Schaad, D. O. Henderson, L. P. Fontana, H. E. Smith, L. A. Nafie, T. B. Freedman and W. M. Zuk, J. Chem. Phys. **86**, 1140-46 (1987).

18. H. Dothe, M. A. Lowe and J. S. Alper, J. Phys. Chem. **92**, 6246-49 (1988).

19. J. S. Alper and M. A. Lowe, J. Chem. Phys. **121**, 189-97 (1988).

20. A. L. Lehninger, "Biochemistry",Worth Publishers, New York (1970).

Table 1. A Comparison of Wavenumbers ν and Rotational Strengths R for Methyl Thiirane

$\tilde{\nu}$ (cm^{-1})			R (x 10^{-44} esu^2cm^2)	
Ref. a	Ref. b	This work	Ref. a	This work
220	-	238.23	7.9	2.196
301	305	312.65	-0.82	-8.078
377	391	427.46	-1.7	3.568
585	592	538.24	-14.4	-9.637
628	644	602.72	22.1	11.396
861	885	925.39	-36.8	-14.875
896	957	943.69	54.2	21.076
908	1011	1043.99	-21.6	-19.318
992	1098	1108.86	73.2	21.285
1043	1151	1172.80	40.9	52.519
1078	1197	1207.44	-173.7	-98.711
1151	1224	1248.83	5.2	-1.470
1169	1268	1324.05	35.9	-11.557
1341	1446	1506.98	15.0	46.377
1387	1543	1586.01	0.85	-2.889
1434	1578	1624.52	17.7	4.697
1446	1605	1655.00	-5.4	8.194
1452	1614	1664.66	-3.5	-14.743
2861	3089	3205.64	0.59	-1.512
2919	3146	3264.62	-2.0	7.475
2943	3168	3272.64	9.4	-6.989
3018	3235	3344.02	3.6	-0.427
3040	3276	3378.51	-10.5	6.182
3098	3317	3444.78	3.2	0.016

Ref. a = H. Dothe, M.A.Lowe and J.S.Alper, J. Phys. Chem. **92**, 6246-49 (1988). These authors have used the scaled quantum mechanical (SQM) force field to obtain vibrational frequencies and the transformation matrix from cartesian coordinates to normal coordinates that is needed in the VCD calculation of rotational strengths. Original calculations were carried out at the 6-31 G^* level.

Ref. b = P. L. Polavarapu et. al., J. Chem. Phys. **86**, 1140-46 (1987). These authors carry out ab initio calculations at the 6-31 G level.

This work = Calculations carried out at the 3-21 G level.

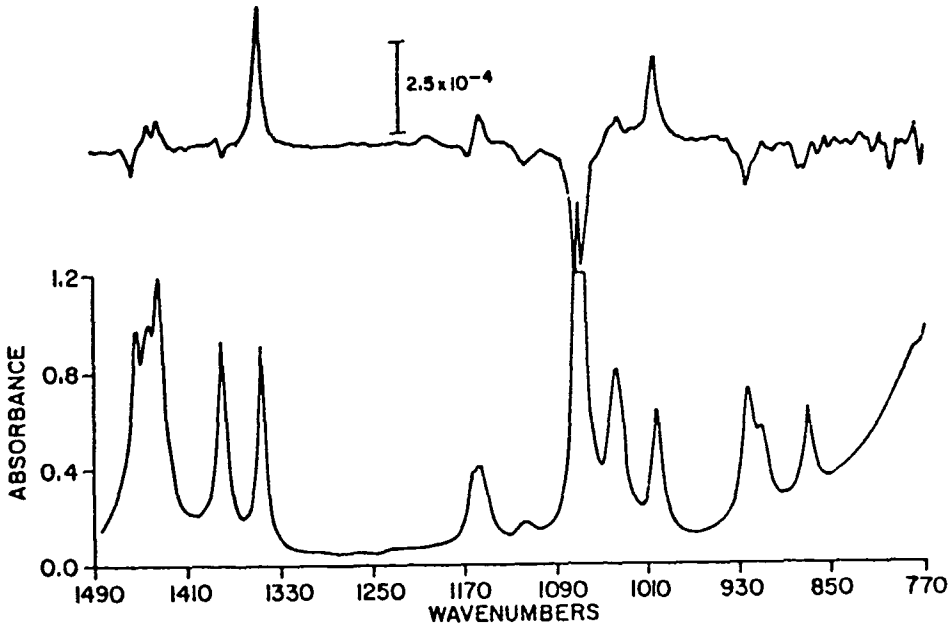

Figure 1. Infrared absorption (bottom) and circular dichroism(top) of (R)-methylthiirane in the 1500-800 cm^{-1} region. The measurements were made with neat liquid in a variable path length cell using minimum path lengths 15 μ). This figure is taken from the reference P. L. Polavarapu et. al., J. Chem. Phys. **86**, 1140-46 (1987).

BLANK

THE CALCULATION OF HYDROGEN-BONDING PROPERTIES

James P. Ritchie, Edward M. Kober[1] and Ian C. Faloona

ABSTRACT

Hydrogen-bonding characteristics of molecules are extremely important in determining their boiling points, densities and water-solubilities, and these properties are important in understanding the adsorption of gases on charcoal. We show that empirical scales that measure hydrogen-bonding interactions can be correlated with the electrostatic properties of the molecules which agrees with previous worker's assessment that the hydrogen-bonding interaction is electrostatic in nature. Correlations both with single molecule properties as well as with the interaction energy between two molecules are found. This establishes a method for calculating these important properties which were previously available only through experiment or empirical scales.

INTRODUCTION

The adsorption of gases on charcoal is a complex problem which depends upon the properties of the charcoal and the adsorbate molecule, and on the ambient conditions (temperature and humidity, in particular). Our long-term goal is to develop a model that explains this behavior and which then can be used to predict sorption properties.[2] Three macroscopic molecular properties that have proven to be useful in correlating with various sorption properties are boiling points, fluid densities and water solubilities. All three of these properties have been demonstrated to be strong functions of hydrogen-bonding interactions, which promopts our interest in understanding this phenomena.

Several empirical solvent scales have been developed to measure hydrogen-bonding properties.[3] Two of the most popular and successful sets in various correlations are the Gutmann Donor Number (DN) and Acceptor Number (AN) scales[4,5] and the Taft-Kamlet solvent scales with α, β and π^* parameters.[6] These scales rely upon physical measurements where we are interested in predicting the properties of novel compounds as well as relating particular physical measurement to molecular properties. It has been demonstrated that strong hydrogen-bonding interactions with molecules such as alcohols, carboxylic acids and amides can be well-described simply in terms of their electrostatic interactions.[7] Here, we examine whether the weaker hydrogen-bonding interactions "measured" by the empirical scales above can also be described by electrostatic interactions.

RESULTS AND DISCUSSION

Empirical Scales. First, a brief description and critique of the Gutmann and Taft scales is given so as to provide an understanding of the types of interactions that are involved in determining these properties. Values of these parameters for selected molecules are given in Table 1, where "bulk" values have been found to be preferable over "single molecule" values. (For modeling purposes,

TABLE 1

Gutmann, Taft and Electrostatic Parameters For Selected Molecules.

Compound	AN	DN	α	β	π*	EP(max)	EP(min)
hexane	0.0	0.0	0.00	0.00	-0.08	+28.8	-15.0
perfluorohexane	–	–	0.00	0.00	-0.40	+81.6	-11.9
diethylether	3.9	19.2	0.00	0.47	0.27	+27.9	-80.5
tetrahydrofuran	8.0	20.0	0.00	0.55	0.58	+38.5	-87.0
benzene	8.2	0.1	0.00	0.10	0.59	+39.4	-40.1
carbontetrachloride	8.6	0.0	0.00	0.00	0.28	+50.2	-9.0
dioxane	10.8	14.8	0.00	0.37	0.55	+41.3	-80.2
acetone	12.5	17.0	0.08	0.48	0.71	+43.0	-75.7
pyridine	14.2	33.1	0.00	0.64	0.87	+52.0	-95.5
nitrobenzene	14.8	4.4	0.00	0.39	1.01	+61.9	-65.4
dimethylformamide	16.0	26.6	0.00	0.69	0.88	+50.7	-85.6
acetonitrile	18.9	14.1	0.19	0.31	0.75	+56.7	-76.8
dimethylsulfoxide	19.3	29.8	0.00	0.76	1.00	+59.2	-99.3
methylenechloride	20.4	0.0	0.30	0.00	0.82	+76.9	-32.5
nitromethane	20.5	2.7	0.22	0.22	0.85	+71.8	-63.4
chloroform	23.1	4.0	0.44	0.00	0.58	+83.3	-14.6
ethanol	37.0	29.0	0.83	0.77	0.54	+82.1	-85.6
methanol	41.3	32.0	0.93	0.63	0.60	+83.1	-86.8
water	54.8	40.0	1.17	0.47	1.09	+80.0	-92.1

ethane and perfluoroethane were used in place of the analogous hexane compounds.) The numerous correlations that have been established with these parameters, as well as particular viewpoints favoring one scale over another, have been summarized in review articles.[3-6]

The Gutmann DN scale was designed to measure the ability of a molecule to act as an electron pair donor (i.e., Lewis base), which is also an effective definition of a hydrogen-bond donor. It was originally experimentally defined as the heat of formation (in kcal/mol) of the adduct with the Lewis acid $SbCl_5$ in 1,2-$C_2H_4Cl_2$.[4,5] The Taft β scale was designed to directly measure the ability of a solvent to act as a hydrogen-bond donor by comparing shifts of the absorption bands of several pairs of related dye molecules which have alkyl groups in place of amino- or alcoholic-hydrogens.[6] Because it is directly based on measurements of several systems with moderate to strong hydrogen bonds, the β scale appears to be reasonably well-designed. In contrast, the DN scale can be criticized for relying on a single measurement which might include additional specific interactions with $SbCl_5$, and especially for over-emphasizing covalent interactions, i.e., the heats of $SbCl_5$ adduct formation range upwards to 60 kcal/mol whereas a typical strong hydrogen bond is only ≈6 kcal/mol. Despite this, there is a reasonably good correlation between the two scales as shown in equation 1. Two of the furthest

(1) $DN = 39.185\,\beta - 0.389$; $n = 76$, $r^2 = 0.920$, $sd = 3.07$

outlying points in this correlation are nitromethane and nitrobenzene which are characterized as weak donors by the Gutmann scale (DN ≈ 3), but are ranked as moderate donors by the Taft scale (β ≈ 0.3). A possible explanation for this discrepancy is that $SbCl_5$ will bind to only a single donor site (i.e., one of the nitro oxygens) whereas the amino-dyes of the β scale are much less sterically demanding. Suggested revisions of the DN scale often increase the values for nitro compounds to DN ≈ 10 which would considerably reduce this discrepancy.[5]

The Gutmann AN scale was designed to measure the ability of a molecule to act as an electron pair acceptor (i.e., Lewis acid), which is an effective definition of a hydrogen-bond acceptor.[4] It is experimentally defined by the ^{31}P NMR shift upon adduct formation of $Et_3P{=}O$ (which is a Lewis base through the O atom) in 1,2-$C_2H_4Cl_2$. The direct analog to this is the Taft α scale which is based on a

combination of NMR and absorption band shifts of a variety of molecules that contain donor sites such as ketones, sulfoxides or nitro groups.[6] What is important is that it is the absolute shifts which are not accounted for by the Taft π^* scale that are used to define the α scale. The π^* scale, which was defined to measure a solvent's polarity/polarizability, is based upon the absolute absorption band shifts of a variety of dye molecules which also contain either nitro or ketone groups, so it inherently contains hydrogen-bonding interactions. A direct comparison of the AN and α scales reveals a fair linear correlation shown in equation 2. The main outlying points are weak acceptors where molecules with

(2) $AN = 32.064\ \alpha + 11.481$; $n = 37$, $r^2 = 0.896$, $sd = 4.75$

AN < 20 tend to have the uniform assignment of $\alpha = 0.0$. Because of this, our studies reveal much better correlations with the AN scale rather than the α scale alone. The correlation between AN and α is dramatically improved upon inclusion of the π^* parameter as shown in equation 3 which supports the

(3) $AN = 31.667\ \alpha + 15.404\ \pi^* + 1.1899$; $n=36$, $r = 0.969$, $sd = 2.49$

contention that the π^* scale includes hydrogen-bonding effects. Other workers have similarly noted a high level of cross-correlation between the α and π^* scales.[8]

Electrostatic Potentials Previous work on strong hydrogen-bonding interactions, which involve a protic hydrogen, has shown that these interactions can be characterized as being predominantly electrostatic in nature[7] and that reasonable correlations can be found between the electrostatic potentials of the molecules and the strength of these interactions.[9] We examine here whether this is also true for the weaker interactions since a distinction is sometimes made between strong "hydrogen-bonds" (which involve a protic hydrogen) and weaker "electrostatic" interactions.

The method by which the electrostatic potentials are calculated is described in detail elsewhere.[10] The basic method is to perform an *ab initio* molecular orbital calculation (typically a Gaussian 82 run with 3-21G basis set) to obtain the electron density distribution around the molecule, assign the electron density to atomic centers using the Hirschfeld procedure, and then analyze the atomic electron density distributions in terms of the multipole moments to obtain the Atom Centered Multipole Expansions (ACME's). With these expansions are carried out at least to the octupole level, this method provides an accurate and rapid way to evaluate the electrostatic potentials and fields around a molecule.

The electrostatic potentials of the19 organic molecules listed in Table I were calculated by this means. Plots of the potentials around ethane, perfluoroethane, nitromethane, benzene, pyridine and methanol are shown in Figure 1. Atoms and bonds that lie in the viewing plane are shown by the larger size letters and heavy solid lines, respectively. Atoms and bonds that are out of the viewing plane are show by the smaller letters and dashed lines. The blanked out regions show the areas within the "van der Waals" radii of the atoms[11] within which the multipole expansion series does not converge. The dashed contours show regions of negative potential where a positive charge would be attracted, and the solid contours show regions of positive potential where a positive charge would be repelled. The increment between contours is 5 kcal/e

The potentials demonstrate mostly the expected behavior around the molecule, and clearly show the moieties that would be involved in hydrogen-bonding or electrostatic interactions. Hydrocarbons exhibit weak electrostatic fields with regions of slight positive potential around the hydrogen atoms consistent with the standard assignment of slight positive charges to them by Mulliken population analysis and other similar schemes. The fields around aromatic hydrocarbons are more intense than those around paraffins demonstrating that aromatic molecules are more "polar" in this sense than normal paraffins, and the π-electron clouds tend to show as regions of moderate negative potential. The locations of nucleophilic lone pairs of electrons, such as on pyridine and methanol, are clearly delineated by regions of large negative potential. The introduction of electron withdrawing moieties such as nitro groups enhances the positive potentials of neighboring hydrogen atoms appreciably, and these then become moderate electrophilic sites. Hydroxylic hydrogens show regions of strong positive potentials consistent with the large positive charges assigned to them by various population schemes and with their strong electrophilic nature

Figure 1

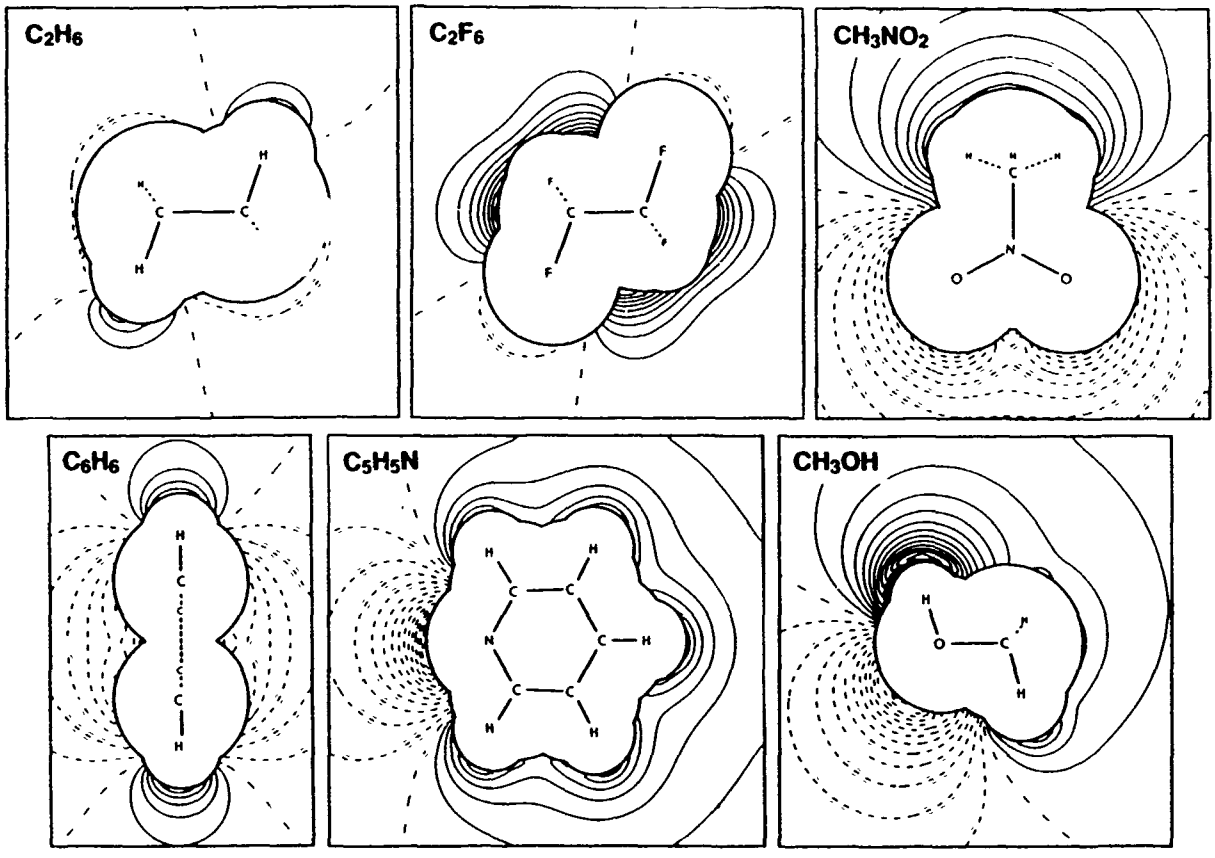

The method chosen to provide a quantitative measure of these characteristics is to evaluate the maximum, EP(max), and minimum, EP(min), values of the electrostatic potential on the van der Waals surface[11] of the molecule. These values in units of kcal/e are given in Table I. This method has its limitations in that there are ambiguities in defining such a surface and not all points on this surface are accessible to other molecules for interaction or are equally accessible to molecules with different steric constraints. However, a previous similar scheme has been used successfully in a correlation with molecules involved in strong hydrogen-bonds.[9]

Since large negative potentials are commonly associated with nucleophilic lone pairs of electrons, a reasonable correlation might be expected between the minimum value of the electrostatic potential on the molecular surface, EP(min), and the electron pair donating ability of a molecule as measured by either DN or β. The correlation between β and EP(min) is the better of the two and this is shown in Figure 2A. The major difference between the β and DN correlations is that the nitro compounds (with EP(min) ≈ -60 kcal/e) are more in line with the β scale assessment of their being weak-moderate donors as opposed to the DN scale assessment of them as very weak donors. The electrostatic potential maps (Figure 1) show large negative potentials in the region between the two oxygen atoms, with less negative potentials on the surfaces of the oxygen atoms on the sides of the nitro group. Since $SbCl_5$ probably only coordinates to one oxygen atom, it probably can not sample the region between the oxygen atoms but only the side of one oxygen atom. Thus, the experimental measure for the DN scale likely de-emphasizes the donating ability of a nitro group on steric grounds.

The maximum value of the electrostatic potential on the molecular surface, EP(max), would then be expected to parallel the electrophilic nature of the molecule as measured by AN or α (and π^*). As mentioned above, the better correlation (shown in Figure 2B) is with AN because half of the α values are zero. Obviously, a two parameter fit with α and π^* would also yield a good correlation (in line with eq 3), but there is not enough data at present to justify such an attempt. The major deviation from the AN-EP(max) correlation is with the alcohols, which have larger values of AN than would be expected from their EP(max) values. (Note that a steeper and improved correlation would result if the points for

Figure 2A

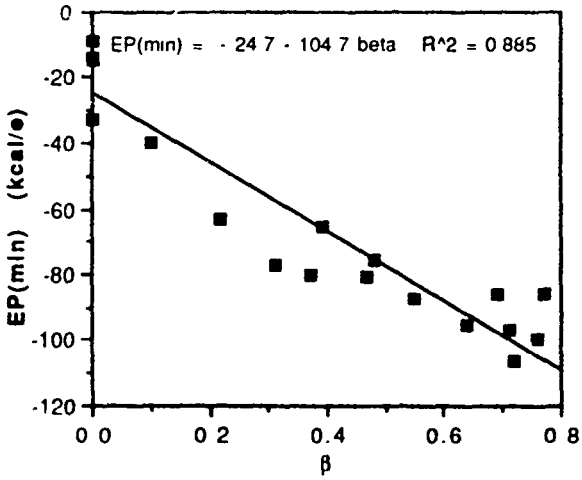

Figure 2B

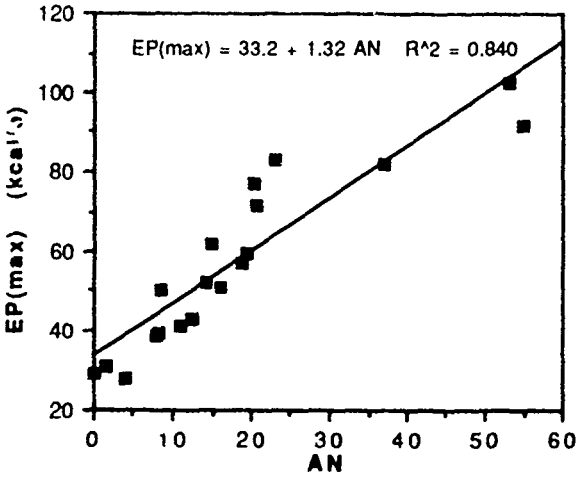

water, methanol and ethanol were eliminated.) The origin for this probably lies in the problem of defining the van der Waals surface of the molecule. The potentials around the protic hydrogens were evaluated with a radius of 1.0 Å rather than with the suggested van der Waals radius for protic hydrogens of 0.8 Å. (The radius of a non-protic hydrocarbon hydrogen is typically 1.2 Å.) The reason for this is that the multipole expansion does not converge for distances <1.0 Å, so the longer radius with the resultant less positive potential had to be used. An alternative scheme would be to reevaluate *all* of the electrostatic potentials at the van der Waals radii plus some set amount (such as 1 Å). Such calculations have not been completed yet, but show promise of providing a more consistent correlation.

Since fluorocarbons are of particular interest, it is worthwhile to analyze their results in more detail. Their hydrogen-bonding properties have not been studied extensively, but tentative values of $\alpha = 0.0$, $\beta = 0.0$ and $\pi^* = -0.4$ have been assigned to perfluorocarbons.[5] Using the relationships shown in eqs 1 and 3, values of DN = 0 and AN = -6 are suggested. Comparison of the electrostatic potentials shown in Figure 1 for C_2H_6 and C_2F_6 reveals some interesting contrasts. First is the expected change in polarity in that the hydrogens tend to be surrounded by regions of positive potential while the fluorines tend to be surrounded by regions of negative potential. What is surprising is the magnitudes of these potentials: the potential around the fluorines has a minimum value of -8 kcal/e while the potential around the hydrogens has a maximum value of +14. Typically, the magnitude of the charge assigned to hydrocarbon hydrogens (by Mulliken population analysis) is quite small (≈ +0.05) while that assigned to fluorines is appreciably larger (≈ -0.15-0.3). From that limited analysis, much larger negative potentials around the fluorines would be expected. What needs to be considered in more detail though is the non-spherical arrangement of electrons in the p orbitals of the fluorine, a complication that does not arise for the hydrogen atoms. The simple charge analysis does reflect the behavior of potentials around the carbon atoms however. In hydrocarbons, the carbon is typically assigned a small negative charge (≈ -0.1) consistent with the small EP(min) value of -6 kcal/e. In contrast, the carbons of fluorocarbons are assigned larger positive charges (≈ +0.6) consistent with the larger EP(max) value of +80 kcal/e. Comparing these values to the correlations suggested in Figure 2, the assignments of DN = β = 0 and AN = 0 for hydrocarbons is supported as is the assignment of DN = β = 0 for fluorocarbons. However, a value of AN ≈ 20-40 for fluorocarbons is implied by this analysis compared to the value of AN = -6 suggested above.

Molecular Interactions. The proper inclusion of steric effects necessitates the modeling of the interactions between two (or more) molecules. This is particularly important in understanding the vagaries of using one parameter to describe a complex interaction particularly where specific couplings between certain pairs of molecules are not feasible for others. Steric constraints are most simply modeled by using atomic hard spheres with the appropriate "van der Waals" radii.[11] The discontinuity in the potentials using this model retard the optimization process, however, so a "firm" sphere model with steeply rising exponential repulsive potential is used as shown in eq 4. Here, r_i and r_j are the van der Waals radii of atoms i and j, which belong to molecules M and N, respectively, and R_{ij} is the distance

$$(4)\quad E_{tot} = E_{es} + \sum_{i \in M} \sum_{j \in N} A \exp\left(-B \left[r_i + r_j - R_{ij} \right] \right)$$

between those two atomic centers. Despite the similarity in form to the standard exchange-repulsion potential, it is emphasized that the values selected for A and B are somewhat arbitrarily chosen (A = 0.0003 hartree, B = 20/bohr) so that the distances of closest approach would be equal to the sum of the van der Waals radii ±0.02 Å. More realistic models of the repulsion potential are not warranted at this time since polarization and dispersion forces have not been included.

The total electrostatic energy of interaction, E_{es}, can be simply expressed by the multipole-multipole interactions of the ACME's described above as shown in eq 5. Here, the multipole

$$(5)\quad E_{es} = \sum_{i \in M} \sum_{j \in N} \left[\frac{q_i q_j}{R_{ij}} + \frac{q_j(\mu_i \cdot \mathbf{R}_{ij})}{R_{ij}^3} + \frac{q_i(\mu_j \cdot \mathbf{R}_{ij})}{R_{ij}^3} + \frac{(\mu_i \cdot \mu_j) R_{ij}^2 - 3(\mu_i \cdot \mathbf{R}_{ij})(\mu_j \cdot \mathbf{R}_{ij})}{R_{ij}^5} + \ldots \right]$$

moments (charge, dipole, etc.) of atom i are q_i, μ_i, etc., and $\mathbf{R}_{ij}$ is the distance vector between atoms i and j. The calculations here included up to octupole-octupole interactions. In the test cases studied, inclusion of up to hexadecapole-hexadecapole interactions resulted in very slight changes in the optimized geometry and energy at the cost of significant additional computing time. Truncating the expansion at quadrupole-quadrupole interactions decreased the computing time somewhat, but noticeable differences in geometrical results were found compared to the octupole-octupole results. This approach is very similar to that used by the Stone and Buckingham groups.[12]

Geometrical optimization to find a local energy minimum from some initial position (with and without constraints) was accomplished by standard techniques. Because of the irregularity of the potential functions, there is no simple method for proving that the absolute minima has been located. However, chemical intuition can readily identify all likely candidates, except possibly in the case of very weak interactions. The general procedure adopted here was to select either a strong donor (such as pyridine) or a strong acceptor (such as methanol) and examine the interactions of that molecule with all of the other molecules acting as the complementary acceptor/donor. Usually, some sort of mixed interaction would result where, for example, the designated acceptor would also act as a weak donor back to the designated donor molecule. Such interactions were found to be quite common simply because the spatial locations of donor and acceptor sides within a molecule are typically in close proximity to one another. To discern the importance of these, constraints were used during the optimizations to ensure that only a single donor-acceptor interaction occurred. That geometry could then be relaxed to allow the secondary interactions to occur, and the two energies compared. These comparisons showed that the secondary interactions are generally about 20% of the primary when either a strong donor or acceptor is involved, but become more important when either weaker interactions are involved or when a molecule is both a good donor and acceptor.

The interactions between the donor pyridine and a variety of acceptors were examined in this manner. The calculated energies of interaction for both constrained (filled squares) and unconstrained (open squares) optimizations are shown in Figure 3A plotted vs. the AN of the acceptor. A very good correlation is found to result with an intercept near zero for AN = 0. The difference in energy between the constrained and unconstrained points is small and comparable to the scatter from the linear correlation. The largest discrepancies are for the three points with the largest AN values: ethanol (37), methanol (41) and water (55). The interaction energies for these three are all very similar despite the spread in AN. A possible explanation for this is that, since only pairwise interactions are considered, the capability of water utilizing both of its acceptor sites is not considered nor are the steric differences between methanol and ethanol of importance here. The calculated interactions energies of pyridine with CF_4 and C_2F_6 are in the range of -1.5-2.5 kcal/mol which would be consistent with a value of AN ≈15 for the fluorocarbons. This result can be contrasted with the assignments of AN = -6-0 from the Taft anaysis and AN = 20-40 from the single molecule electrostatic potentials assessment. This

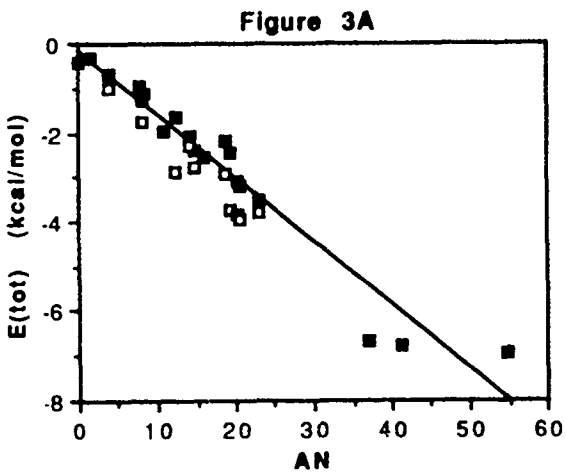

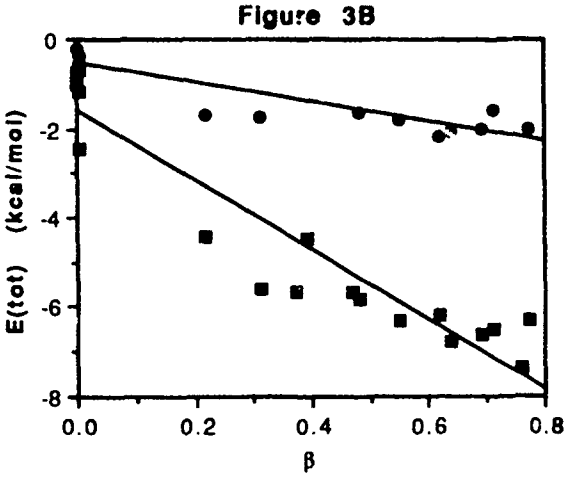

illustrates the pitfalls of attempting a simple analysis, though the electrostatic work clearly suggests that fluorocarbons should function as weak to moderate acceptors.

The interactions between a variety of donors and the strong acceptor methanol (AN = 41) and moderate acceptor pyridine (AN = 14) were also examined. The calculated energies are shown plotted in Figure 3B vs. β of the donor (squares = methanol, circles = pyridine). Reasonable correlations are seen to result although the scatter of the plots is larger than before. It is noteworthy that the slope for the methanol correlation is three times as large as for pyridine data in concert with the factor of three difference in AN. Correlations using DN in place of β were found to be of slightly lower quality which can be directly attributed the results for the nitromethane and nitrobenzene being further out of line when DN is used. The optimized geometries for these two species were found to have donor interactions from both oxygen atoms of the nitro group. If the geometry was constrained so that only a single oxygen could donate, the energy of interaction decreased by roughly a factor of two, and this result would be more in line with the DN scale as was suggested above.

CONCLUSIONS

The net correlations found here between the electrostatic properties of molecules (and their electrostatic interactions with one another) and the empirically defined hydrogen-bond (or electron pair) donor-acceptor scales is reasonably good. It is clearly suggested that this donor-acceptor interaction, if not being predominantly electrostatic in nature, at least parallels the electrostatic contribution. This now provides a method by which these properties can be calculated directly which can then be employed in the estimation of properties such as boiling points, densities and water solubilities.

REFERENCES

(1) T-14, MS B214, Los Alamos National Laboratory, Los Alamos, NM 87545.

(2) (a) Stampfer, J. F.; Wood, G. O.; Ritchie, J. P. "Predicting Air Cleaning Efficiencies of Activated Carbons" **LA-UR**-88-379, 1988 (b) Ritchie, J. P.; Kober, E. M. *Proc. 1988 US Army CRDEC Sci. Conf. Chem. Def. Res.*, 1988, p. 421.

(3) Reichardt, C. "Solvents and Solvent Effects in Organic Chemistry," VCH, New York, 1988.

(4) Gutmann, V.; Resch, G.; Linert, W. *Coord. Chem. Rev.* **1982**, *43*, 133.

(5) Marcus, Y. *J. Soln. Chem.* **1984**, *13*, 599.

(6) Kamlet, M. J.; Abboud, J.-L. M.; Abraham, M. H.; Taft, R. W. *J. Org. Chem.* **1983**, *48*, 2877.

(7) Umeyama, H.; Morokuma, K. *J. Am. Chem. Soc.* **1977**, *99*, 1316.

(8) Swain, C. G.; Swain, M. S.; Powell, A. L.; Alunni, S. *J. Am. Chem. Soc.* **1983**, *105*. 502.

(9) Kollman, P.; McKelvey, J.; Johansson, A.; Rothenberg, S. *J. Am. Chem. Soc.* **1975**, *97*, 955.

(10) Ritchie, J. P. *J. Am. Chem. Soc.* **1985**, *107*, 1829.

(11) Bondi, A. "Physical Properties of Molecular Crystals, Liquids and Gases," 1968.

(12) (a) Buckingham, A. D.; Fowler, P. W. *Can. J. Chem.* **1985**, *63*, 2018. (b) Price, S. L.; Stone, A. J. *J. Chem. Phys.* **1987**, *86*, 2859.

BLANK

MOLECULAR ORBITAL CALCULATIONS OF CU(II)-TETRAMETHYLETHYLENEDIAMINE TYPE COMPLEXES

Landa Hoke
U.S. Army Natick Research, Development and Engineering Center
Natick, Massachusetts 01760-5020

ABSTRACT

Molecular orbital calculations using the intermediate neglect of differential overlap technique are performed on Cu(II)-diamine complexes and results are obtained for geometry optimizations and electronic properties. Comparisons are made with Cu(II)-glucosamine which is a similar but larger structure. Calculated electronic absorption spectra for square planar Cu(II) complexes are considered.

INTRODUCTION

Certain metal chelates can catalyze the detoxification of phosphorous containing chemical agents. Various transition metal ions have been shown to be effective and Cu(II) displays one of the highest activities. The chelate can consist of smaller molecules such as diamines or a biopolymer such as chitosan. A great deal of experimental work has been done to characterize the nature of the catalytic reaction and also the nature of the metal chelate bonding. One of the most effective ligands is tetramethylethylenediamine (TMEN). The approach of this current work is to use computational chemistry to examine the molecular basis for the differences in reactivity of several diamine complexes including Cu(II)-TMEN. An initial characterization of a reactive biopolymer subunit Cu(II)-glucosamine (GA) is included here.

METHODS

Spectroscopic intermediate neglect of differential overlap (INDO/S) was used. This is a self consistent field (SCF) zero differential overlap (ZDO)

technique which retains one center exchange integrals. This method is appropriate to spectral calculations of transition metals since the retention of these exchange terms are important in order to identify states of different multiplicities which have the same electronic configuration. For geometry optimizations, an unrestricted Hartree-Fock (UHF) wavefunction and theoretical gammas were used for these open shell doublet calculations. In order to predict ground state electronic properties, Mataga-Nishimoto type gammas were used. Parameters for resonance integrals which affect sigma and pi MO ordering and which were suggested by Del Bene and Jaffe (1) and also by Ridley and Zerner (2) were used. In order to examine the low energy transitions of tetra coordinated Cu(II) in a square planar environment, absorption spectra were calculated for the tetraaquo Cu(II) complex. Since metal ligand overlap can be relatively small, these transitions can be expected to have a d-d character. Therefore MOs which have a large metal contribution from the eg and t2g manifold would be important to include in spectral calculations. A singles only CI was performed using a restricted open shell wavefunction (ROHF). The nine highest occupied orbitals and the six lowest virtual orbitals of this model complex were included in the CI. Inclusion of additional orbitals did not significantly affect the predicted lowest energy absorptions.

Structures of Cu(II) complexes are shown in Figure 1.

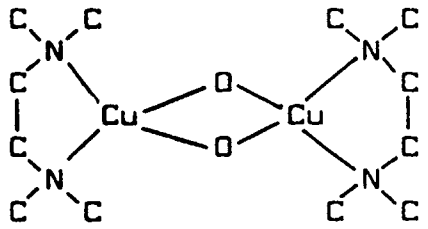

1a. $[Cu(TMEN)OH]^{+2}_2$

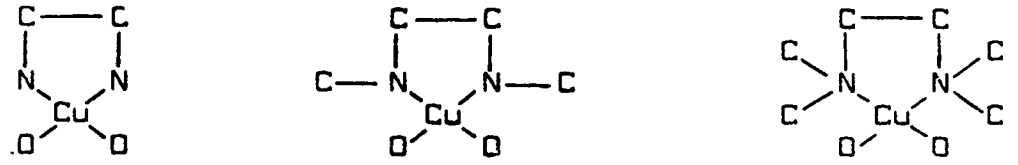

1b. $[Cu\ (EN)\ (H2O)_2]^{+2}$ 1c. $[Cu(DMEN)\ (H2O)_2]^{+2}$ 1d. $[Cu\ (TMEN)\ (H2O)_2]^{+2}$

Figure 1. Structures of Cu(II) Complexes. (Hydrogens are omitted.)

A starting geometry for Cu(II)-TMEN was obtained from X-ray data on a similar structure $[Cu(TMEN)OH]^{+2}_2$. In this crystal structure Cu(II) has a coordination number of four and a nearly square planar geometry. Starting geometries for Cu(II)-dimethylethylenediamine (DMEN) and Cu(II)-ethylenediamine (EN) were obtained from an optimized geometry of Cu(II)-TMEN. A starting geometry for the glucosamine moiety of Cu(II)-GA was obtained using X-ray data for N-acetylglucosamine and a square planar assumption in order to attach the Cu(II) moiety to the ring. Coordination sites were at the nitrogen and at the oxygen attached to carbon one of the glucosamine ring.

RESULTS

Geometry Optimization.

A comparison of calculated bond angles and lengths of Cu(II)-TMEN with the values from the X-ray data for $[Cu(TMEN)OH]^{+2}_2$ shown in Table 1.

TABLE 1. Comparison of Crystal Geometry of $[Cu(TMEN)OH]^{+2}_2$ and Calculated Geometry for Cu(II)-TMEN.

Bond	Crystal	Cu(II)-TMEN	Angle	Crystal	Cu(II)-TMEN
Cu-N	1.995A^{o}	1.9908A^{o}	N-Cu-N	87.8^{o}	90.46^{o}
Cu-N	2.033	2.0743	Cu-N-C	104.9	101.45
Cu-O	1.897	1.9628	N-C-C	115.9	114.07
Cu-O	1.931	1.9929	N-C-C	116.2	114.34
C-N(ring)	1.486	1.4418	Cu-N-C	106.4	103.39
C-N(ring)	1.470	1.4339	O-Cu-O	78.4	90.10
C-C	1.377	1.4970	N-Cu-O	96.3	84.18
C-N	1.467	1.4349	N-Cu-O	96.3	128.50
C-N	1.474	1.4424	C-N-C(methyl)	109.8	118.30
C-N	1.443	1.4279	C-N-C(methyl)	107.9	112.28
C-N	1.467	1.4285			

The coordination geometry in the crystal is almost planar, while the calculated Cu(II)-TMEN coordination is somewhat tetrahedrally distorted (versus square pyramid distorted). In addition, the two N-Cu-O bonds which are symmetric in the crystal structure lose this symmetry for the geometry optimized Cu(II)-TMEN complex.

Calculated coordination angles for the diamine complexes are compared in Table 2. The Cu(II)-EN structure has regained the symmetric N-Cu-O angles in contrast to the TMEN and DMEN structures.

Table 2. Comparison of Coordination Angles

Complex	N-Cu-N	O-Cu-O	O-Cu-N	O-Cu-N
Cu(II)-TMEN	90.5^{o}	90.4^{o}	84.2^{o}	128.5^{o}
Cu(II)-DMEN	94.3	98.7	116.3	139.4
Cu(II)-EN	94.0	94.0	101.4	101.5

Ground State Electronic Properties.

In order to gain insight into the quantum chemistry predictions it is instructive to relate the results to classical crystal field theory (CFT) and ligand field theory. Therefore, a small symmetrical model complex, tetraaquo copper(II) was examined using INDO/S theory. For a general case, according to CFT when no external electric field is present the five metal d orbitals are all degenerate. In the presence of six point charges arranged to produce an octahedral field at the metal ion the d orbitals are split into two degenerate energy levels separated by energy 10Dq. The lower energy orbitals are three fold degenerate and designated t2g (dxz,dxy,dyz) while the higher energy orbitals are two fold degenerate with the designation eg (dz2, d(x2-y2)). In the presence of a square planar environment, further splitting would occur. The exact details of this additional splitting depend upon the precise specification of the point charge environment.

What does INDO/S predict concerning the splitting of the Cu(II) d orbitals? Optimized bond lengths for the tetraaquo complex used for this calculation are Cu-O 1.8970 A and O-H 1.0240 A and for the bond angles values of O-Cu-O 90.0000 degrees and H-O-H 105.6700 degrees. Table 3 shows the nine highest occupied MOs. The nature of the MO, metal or ligand, is indicated in this table. MOs cannot always be readily classified as distinctly metal or ligand character so that these designations are guidelines Classically the HOMOs would be metal d orbitals. However, this is not the case here and the d orbitals are interspersed with ligand p orbitals. This appears to be a result obtained in many Hartree-Fock calculations (4). The d orbital eigenvalue ordering is dyz, dxz < dxy < dz2 < d(x2-y2) with a total splitting from the largest to the smallest eigenvalue of approximately 0.18 au. (Note the excess spin is alpha.) The dxz and dyz orbitals are degenerate as might be expected and the dxy orbital which is in the plane with the ligands has a higher energy due to electron-electron repulsion The dz2 orbital lies closer in energy to dxy than to d(x2-y2).

Table 3. Molecular Orbital Classification for Tetraaquo-Cu(II).

Orbital	Alpha		Beta	
	Character	Energy	Character	Energy
21	dx2-y2	-0.75011 a.u.	dx2-y2	-0.39324 a.u.
20	L(Pz), dxz	-0.81817	L(Pz), dxz	-0.80778
19	L(Pz), dyz	-0.81817	L(Pz), dyz	-0.80778
18	L(Pz)	-0.84204	dz2	-0.83485
17	dz2	-0.85980	L(Pz)	-0.83775
16	L(Pz)	-0.86533	L(Pz)	-0.86120
15	dxy	-0.90598	dxy	-0.89115
14	dxz	-0.92816	dxz	-0.90761
13	dyz	-0.92816	dyz	-0.90761

This type of molecular orbital classification is less clear for the Cu(II)-diamine complexes. For Cu(II)-EN, the highest eigenvalue is for an MO of d(x2-y2) nature with a dz2 and a dxy type MO following in the same order as for tetraaquo copper(II) complex. The energy splittings for these Cu(II)-EN MOs are 0.05 au between dxy and dz2 and 0.12au between dz2 and d(x2-y2). These values are very similar to those for the tetraaquo Cu(II) complex. For Cu(II)-TMEN the highest energy MO is still mostly d(x2-y2) in character. This is an indication that the Cu(II) environment is still of square planar nature, so that even though the initial square planar geometry is somewhat tetrahedrally distorted in the optimized TMEN geometry, the t2g and eg levels are not reversed as would be the case in a tetrahedral environment.

Calculated formal charges (Mulliken) for the Cu(II) portion of the diamine complexes and for Cu(II)-GA are given in Table 4.
Please refer to Figure 2 for the atomic numbering scheme.

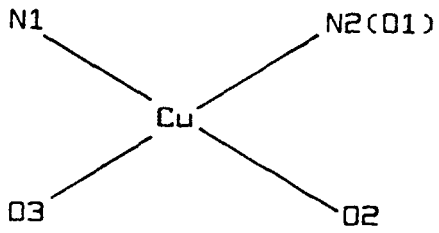

Figure 2. Numbering Scheme for Cu(II) Moiety of the Complexes

Table 4. Formal Charges (Mulliken) for Cu(II) Moiety

Complex	N1	N2(O1)	O2	O3	Cu
Cu(II)-EN	-0.35	-0.34	-0.45	-0.45	+0.99
Cu(II)-DMEN	-0.34	-0.21	-0.46	-0.48	+0.97
Cu(II)-TMEN	-0.32	-0.10	-0.47	-0.53	+0.92
Cu(II)-GA	-0.34	-0.44	-0.45	-0.45	+1.03

The formal charge of one of the nitrogens, N2, becomes less negative in progressing from the EN to the DMEN to the TMEN complexes. The charge on the other nitrogen has almost the same value for all of the complexes. For the oxygen and copper atoms, the results in Table 4 do not indicate as large a difference among these complexes when comparing charges for equivalent atoms as is predicted for the N2 of the diamines.

The calculated bond indices are given in Table 5.

Table 5. Bond Indices of Cu(II) Moiety of the Complexes

Complex	N1-Cu	N2(O1)-Cu	O2-Cu	O3-Cu
Cu(II)-EN	0.64	0.64	0.58	0.56
Cu(II)-DMEN	0.55	0.43	0.51	0.50
Cu(II)-TMEN	0.48	0.32	0.49	0.44
Cu(II)-GA	0.63	0.53	0.54	0.53

The nature of the bonds to the metal ion is changing from the EN to the DMEN to the TMEN complexes, becoming increasingly more ionic in character. The two N-Cu bonds within each individual complex not only show this tendency but also become progressively less equivalent in ionic/covalent nature within each individual structure.

Absorption Spectra.

In order to gain an insight into INDO/S predictions about the behavior of Cu(II) in a square planar environment calculations were performed on a small model complex tetraaquo Cu(II). (This small symmetric example can provide insight for the interpretation of spectral calculations of the diamine and GA complexes. This complex does not necessarily represent an experimentally observed absorber.) The results show four low energy electronic transitions for this structure. There is a doubly degenerate transition at 18426.9 cm-1. For each of these degenerate transitions there are two configurations which have large contributions. (Note that an ROHF wavefunction was used here and so this discussion does not precisely correspond to results given in Table 3 using a UHF wavefunction.) For one of the transitions, the contributing configurations are dxz --> d(x2-y2) and dxz,L(pz) --> d(x2-y2). For the other transition, the two largest contributing configurations are dyz --> d(x2-y2) and dyz,L(pz) --> d(x2-y2). Both of these transitions have a large d-d character but there is a ligand contribution. A third transition at 21033.8 cm-1 is essentially of a d-d type in the classical sense and is almost entirely dz2 --> d(x2-y2). The fourth transition at 21934.5 cm-1 is also of d-d type and results almost entirely from a dxy --> d(x2-y2) configuration.

CONCLUSION

The INDO/S scheme has been used for characterization of Cu(II) diamine complexes and Cu(II)-GA with respect to the nature of the MOs and eigenvalue ordering, metal orbital splitting due to the ligand field, prediction of formal charges and bond indices surrounding the metal ion and prediction of absorption spectra for a Cu(II) ion in a square planar environment.

These calculations indicate different coordination characteristics for the diamine complexes with respect to the optimized geometries, formal charges and bond indices. The catalytic effectiveness of the complexes with respect to detoxification of G-agents in solution is TMEN > DMEN > EN. In progressing from the TMEN to the EN complex, the coordination geometry becomes more symmetric as does the charge distribution and the ionic/covalent nature of the metal to ligand bonds.

ACKNOWLEDGEMENTS

The Molecular Modeling Analysis and Display software package supplied by Mr. George Famini and CRDEC was used for this work. Professor Zerner's permission to use INDO/S is gratefully acknowledged. The author expresses appreciation to Dr. David Remy for steadfast support and encouragement.

REFERENCES

1. Del Bene, J. and Jaffe, H.H., J. Chem. Phys., 48, 1807 (1968); 48, 4050 (1968).

2. Ridley, J. E. and Zerner, M. C., Theoret. Chim. Acta(Berl.), 32, 111(1973).

3. Arcus, C., Fivizzani, K. P. and Pavkovic, S. F., J. Inorg. Nucl. Chem., 39, 285 (1976).

4. Bacon, A. D. and Zerner, M. C., Theoret. Chim. Acta(Berl), 53, 21 (1979).

BLANK

MOLECULAR MODELING OF SELECTED ORGANOPHOSPHORUS COMPOUNDS

William E. White, George R. Famini, and Christopher J. Cramer

Chemometrics/Biometrics Modeling Branch
Chemical Research, Development and Engineering Center
Aberdeen Proving Ground, MD 21010-5423

ABSTRACT

Semiempirical methods have been used to calculate the molecular geometries and heats of formation for triphenylphosphine oxide and for triphenylphosphine sulfide. Both MNDO and the newer PM3 modification gave results that compare favorably with thermodynamic values obtained by calorimetry and with geometries obtained by x-ray crystalographic methods.

INTRODUCTION

Organophosphorus compounds containing oxygen and/or sulfur are used extensively because of their many desirable properties. Low melting points and high boiling

points coupled with solubility in a variety of liquids and polymers make them ideal plasticizers. Lack of flammability of phosphorus compounds particularly halogenated, has led to their use in fire extinguishers and as flame retardants in fabrics. The toxicity of some compounds has made them useful as pesticides and fungicides. The high thermal stability of sulfur containing isomers is proving valuable in the development of new lubricating fluids.

The wide range of properties results in part from the different valence and coordination states that phosphorus can assume. Tricoordinated phosphorus compounds are normally pyramidal with the lone pair of electrons occupying an sp^3 orbital on phosphorus. Common examples of this type of compound are phosphines [PR_3] in which the phosphorus has a valence state of -3, and phosphites [$P(OR)_3$] in which the phosphorus assumes a +3 valence state.

Closed-shell tetracoordinated compounds normally exist as tetrahedra or distorted tetrahedra with all four sp^3 hybridized orbitals involved in bonding. Neutral compounds of this type usually exist with phosphorus to sulfur, nitrogen, or oxygen double bonds. Physical and theoretical studies suggest that the bond is a dative bond with phosphorus acting as the donor atom.

Phosphines are trivalent phosphorous compounds with alkyl, aryl, or hydrogen substituents. They are pyramidal compounds with the lone pair in the apical position. Usually, the bond angles for phosphines are less than those for the corresponding amines. For example, the bond angles of PH_3 are 93° in contrast to 107° for NH_3. [1] Oxidation of phosphines yields the tetravalent phosphine oxide.

$$PEt_3 \longrightarrow P(O)Et_3$$

Triethyl phosphine Triethyl phosphine oxide

Molecular modeling or computational chemistry provides the tools for calculating molecular geometries, rotational barriers, energies of activation and other properties useful in deducing reaction mechanisms. These parameters provide data to predict where specific hydrolysis and oxidative reactions will occur. For our purposes, there has never been a thorough computational study of the effect of substituents (carbon, oxygen, and sulfur) on the electronic properties of phosphorus. Allen *et. al.* [2] have conducted an ab initio study on the ground and excited states of HP=PH and H_2P=P. They predicted the molecular geometry, energy, dipole moment, and vibrational frequencies of these compounds. As might be expected, the *trans* isomer of HP=PH was 3.5 kcal/mol more stable than the *cis*.

In an attempt to understand the binding of VX to acetylcholinesterase, Politzer *et al*[3] have conducted an ab initio study of O-methyl-S-2-dimethylaminoethyl methylphosphonothiolate, a VX analog containing five fewer methylene groups, using the Gaussian 82 program. Optimization at the STO-3G* level provided the molecular geometry for extended computations of the molecular electrostatic potential using an STO-5G basis set. Although ab initio methods provide the most accurate results, the computer time required becomes prohibitive for mechanistic studies on large systems. Semi-empirical methods such as MNDO rely on experimentally derived parameters to approximate certain one-electron integrals and therefore reduce the number of calculations. In the past, because of the unique bonding of the tetrahedral phosphorus, semi-empirical methods have typically failed to reproduce either molecular geome ries or energy. In an attempt to improve the calculations involving tetrahedral phosphorus, Stewart has recently developed the PM3 parameter set. Many of the property values were provided by the sophisticated estimation routines developed by Penski and Domalski.[4]

One of the major difficulties with modeling organophosphorus compounds is the absence of accurate experimental thermodynamic data. The computational methods rely on a systematic modification of the molecular geometry coupled with calculations of the corresponding heat of formation until a minimal energy is attained. If the input values are erroneous, then the resulting calculations may be wrong and the structure may converge to the incorrect geometry.

The data on heats of formation for triphenylphosphine oxide is typical of the confusion in the literature. Harrop and Head [5] report -27.9 kcal/mole, Bedford and Mortimer[6] report -15.5 kcal/mole, and Tsvetkov *et al* [7] report -24.2 kcal/mole. Recently Kirkland and Domalski[8] have completed a thorough study with more elaborate equipment than was previously available. They used a rotating bomb calorimeter to effect complete mixing of the products with water and thereby eliminate gradients of various phosphorus acids. Also detailed analysis of the reaction mixture permitted an accurate mass and energy balance. Their value of -27.2 kcal/mole is probably the most accurate currently reported and their results should have considerable impact on thermodynamic measurements of compounds that are difficult to oxidize.

The overall goal of the organophosphorus modeling program is to increase our theoretical understanding of the chemistry of the phosphorus-oxygen and phosphorus-sulfur bonds. The initial study centers on triphenylphosphine oxide and triphenylphosphine sulfide - two compounds whose thermodynamic properties and

solid phase geometry have been determined precisely by experimental methods. By comparing our computational results with experimental data, we can evaluate our results and predict the accuracy of future calculations.

EXPERIMENTAL

All computations analyses, and displays were performed on a Digital Equipment Co. microVax-II using the Molecular Modeling, Analysis, and Display System[9] (MMADS) developed at CRDEC. Semiempirical calculations were performed with the MNDO and MNDO-PM3 algorithms contained in the MOPAC 5.0 package of J.J.P. Stewart.

During the optimization process, the computational routine may trap the molecule in a local minimum well and fail to discover the global minimum. The result is a conformer whose total energy is greater than the most stable structure. Calculations with several modifications were performed to minimize the possibility that the final geometry the most stable conformation. Initially C_3 symmetry was imposed on the compounds to minimize calculation time and to produce a structure that was consistent with the assumed geometry for the compounds in the gas phase. All of the P-O and P-C bond lengths, bond angles, and torsional angles with the phenyl rings were allowed to optomize. The phenyl rings themselves were restricted to a planer geometry; however, the individual carbon atoms comprising the rings were allowed to optomize their bond lengths and angles within the plane. Subsequently, the C_3 symmetry restriction was removed thereby permitting each phenyl ring to rotate independently about its phosphorus carbon bond.

RESULTS

Table 1 compares theoretically derived heats of formation of triphenylphosphine and triphenylphosphine oxide with the experimentally derived values of Kirkland and Domalski. Molecular orbital calculations were performed on an isolated molecule which approximates the gas or vapor phase most closely. These values differ from the crystalline heat of formation by the heat of fusion.

Table 1. HEATS OF FORMATION (KCAL/MOLE)

COMPOUND	EXPERIMENTAL (VAPOR)	MNDO	PM3
Triphenylphosphine	76.78	56.0	91.9
Triphenylphosphine oxide	0.7	62.6	34.6
Triphenylphosphine sulfide	–	105.8	100.5

Crystals for the study by Bandoli[10] *et al* were recrystalyzed from ligroin as white orthorhombic prisms. In contrast, Spek[11] obtained his yellowish monoclinic crystals while attempting to recrystallize a palladium compound. Codding and Kerr[12] did not indicate how they prepared their triphenylphosphine sulfide crystals. They do report that that the asymmetric unit cell contains two molecules with slightly different geometries. Tables 2 and 3 show the results of our calculations and compare them to those reported from crystal data. Values in the column labeled MNDO were obtained using the original parameters of Dewer and Thiel[13] Those in the PM3 column were obtained with the modified parameters of Stewart.[14]

DISCUSSION

The PM3 parameters are superior to the original MNDO values for calculating the heats of formation. For triphenylphosphine oxide the PM3 value of 34.4 kcal/mole is much closer to the experimental value of 0.7 than the MNDO calculated value of 62.6 kcal/mole. For triphenylphosphine sulfide the PM3 value of 100.5 kcal/mole is probably more accurate than than the value of 105.8 kcal/mole; however, a final decision must await experimental measurements of the heat of combustion of triphenylphosphine sulfide.

The heat of formation calculated for benzene using the PM3 parameters differs from experimental values by 3.6 kcal mole.[15] Assuming this difference is the same for the phenyl rings in triphenylphosphine oxide, 10 kcal/mole error results from phenyl ring calculations and 20 kcal/mole from P-O and P-C calculations.

Table 2. TRIPHENYL PHOSPHINE OXIDE GEOMETRY

	Units	SPEK	BANDOLI et al	MNDO	PM3
P=O	Angstroms	1.484	1.46	1.519	1.477
P-C	Angstroms	1.798	1.77		
		1.804	1.77	1.772	1.827
		1.803	1.75		
O-P-C	Degrees	113.1	114.4		
		111.6	110.7	109.9	113.7
		112.1	110.1		
RING	Degrees	56.9	59.3		
TORSIONAL		21.4	24.7	37.6	27.9
		22.9	21.1		

Table 3. TRIPHENYL PHOSPHINE SULFIDE GEOMETRY

	UNITS	CODDING & KERR	MNDO	PM3
P=S	ANGSTROMS	1.950	1.944	1.956
P-C	ANGSTROMS	1.817	1.761	1.825
S-P-C	DEGREES	113.1	109.7	114.0
RING	DEGREES	50.3 50.0	37.8	28.7
TORSIONAL		55.2 57.5		
		10.6 12.2		

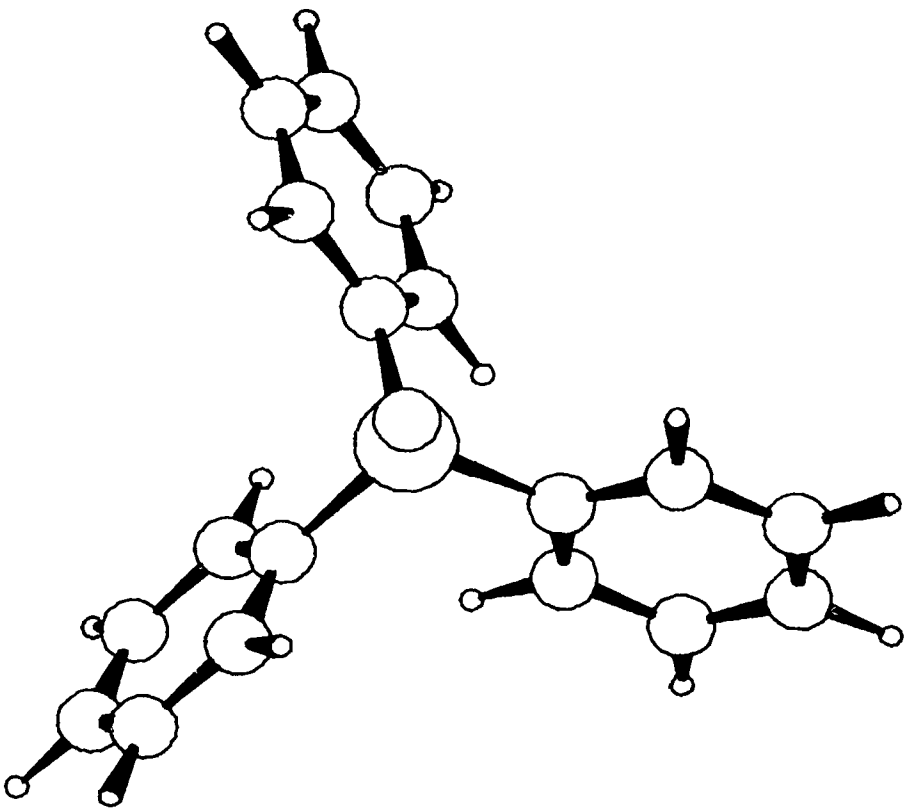

Because our semiempirical calculations were performed on an isolated molecule, structural data from microwave spectroscopy would most closely correlate with our results. Unfortunately, microwave data is unavailable for most organophosphorus compounds. Due to the low vapor pressure of triphenyl phosphine oxide and triphenyl phosphine sulfide it is unlikely that geometries obtained from microwave spectroscopy will be available soon. Therefore we have compared the geometries obtained by theoretical methods to those from x-ray crystalography.

Although it is difficult to draw unequivocal conclusions from theoretical and solid phase data, it is evident that the gross structural features are reasonably well reproduced. PM3 performs slightly better than MNDO for triphenyl phosphine sulfide and about equally well for triphenyl phosphine oxide. The ring torsional angles show no tendency to deviate from C_3 symmetry. When the optimized structure was reoptimized with the symmetry requirements removed, the molecule converged to essentially the same geometry.

The calculations indicate that the energy differences between the conformers with different torsional angles is small except when the torsional angles are near zero or 90 degrees. At zero degrees (C_{3v} symmetry with P-O bond in the plane of all three phenyl rings) the ortho hydrogens opposite the oxygen are occluded. At 90° (C_{3v} symmetry with all phenyl rings in the same plane) the neighboring ortho hydrogens interact. Calculations with the torsional angles set to the crystal structure gave energy values about 1 kcal/mole higher than the symmetrical propeller structure. Varying the pitch of the propeller (within limits) did not change the energy level significantly.

CONCLUSIONS

MNDO with the PM3 parameters is able to calculate heats of formation and geometries of organophosphorus compounds with a fair degree of accuracy. In the future the availability of accurate thermodynamic data will permit refinement of the semiempirical parameters and lead to inproved accuracy.

REFERENCES

1. Kirby, A.J. and Warren, S.G.; *The Organic Chemistry of Phosphorus* Elsevier Publishing Co., New York, 1967.
2. Allen, T.L.; Scheiner, A.C.; Yamaguchi, Y.; and Schaefer, H.F.; *J. Am. Chem. Soc.* Vol. 108, 7579-7588, (1986).
3. Politzer, P., Jayasuriya, K. and Lane, P.; *J. Mol Struc* Vol. 34, 259 (1987).
4. Penski, E.C. and Domalski, E.S.; CRDEC-TR-87063, 1987.
5. Harrop, D. and Head, A.J., *J. Chem Thermodynamics* Vol. 15, p 1067 (1977)
6. Bedford, A.F. and Mortimer, C.T. *J. Chem. Soc.*, 1622 (1960)
7. Tsvetkov, V.G.; Aleksandrov, Y.A., Glushakova, V.N., Skorodumova, N.A., and Kol'yakova, G.M.; *Zh. Obshch. Khim* Vol 50, 256 (1980).
8. Kirkland, D.R. and Domalski, E.S., *J. Chem. Thermodynamics* Vol 20, 743-754 (1988).
9. Leonard, J.M. and Famini, G.R. CRDEC-TR-030, 1989.
10. Bandoli, G.; Bortolozzo, G.; Clemente, D.A.; Croatto, U.; and Panattoni, C.; *J. Chem. Soc.(A)*, 2278-2280 (1970).
11. Spek, A.L., *Acta Cryst. C* Vol 43, 1233-1235 (1987).
12. Codding, P. and Kerr, K.A. *Acta Cryst. B* Vol 34, 3785-3787 (1978).
13. Dewer, M.J.S. and Thiel, W. *J. Amer. Chem. Soc.* 99, 4899 (1977).
14. Stewart, J.J.P., *J. Comp. Chem* Vol. 10, 209-220 (1989).
15. Stewart, J.J.P., *J. Comp. Chem.* Vol. 10, 221-264 (1989).

BLANK

III. FLUID DYNAMICS

BLANK

SOLVENT EFFECTS WHICH INFLUENCE THE RHEOLOGICAL BEHAVIOR OF POLYMER SOLUTIONS

Brian S. Ince and Wendel J. Shuely
U.S. Army Chemical Research, Development and Engineering Center
Aberdeen Proving Ground, MD 21010-5423

ABSTRACT

Research has been directed at the further study of the solvent effects influencing the rheological, breakup and antimisting behavior of semidilute polymer solutions. Recent measurements have allowed the classification of solvents into several sets, including: hydrogen bond donor, 82-100% comonomer soluble, 6-18% comonomer soluble and near theta-solvents. Concentration effects for these solvent sets were measured and compared. Rheological comparisons between toxic contaminants and model liquids are presented, to include: coil density estimates for chloroalkylsulfides, organophosphorus esters in the 6-18% comonomer-soluble solvent set, and theta solvents arising from different solubility classes.

INTRODUCTION

The study of solvent effects which influence the rheological behavior of polymer solutions was continued (1-3). Additional research has contributed to verifying different solvent effects for a defined concentration, temperature, shear rate or regime: (1 an increase in viscoelasticity with decreasing coil expansion for liquids soluble with 82-100% of the copolymer content and without specific interactions, (2) greater coil expansion and further decrease in viscoelasticity for proton donating liquids without competing, strong acceptor sites and, (3) an enhanced degree of viscoelasticity with decreasing coil expansion for liquids soluble with only 6-18% of the copolymer content, again without specific interactions.

Semidilute Regime. Variables held constant were polymer composition, molecular weight, molecular weight distribution, concentration and temperature. The concentration of 4.7 ± 0.1 g/dL resulted in coil density based on a concentration x limiting viscosity number (LVN) product of ca. 5-20, spanning the semidilute regime.

Characterization. Several physical, chemical and rheological characterization methods have been applied. Polymer Cohesion Phase Diagrams (PCPD) of the terpolymer (4) and homopolymer controls were employed to identify solvents with specific solution interactions. LVN or intrinsic viscosity measurements provided an estimate of coil expansion and degree of interaction (5). Linear Solvation Energy Relationship (LSER) scales were used to identify and quantify proton donating, weak or nonacceptor solvents (6). Straightforward solubility determinations, (ANSI/ASTM D 3132-72), were employed to classify solvent/nonsolvent interactions with homopolymer controls for each of the terpolymer repeat units. Rheological measurements provided a a characterization of viscous and viscoelastic properties: steady shear hysteresis, first normal stress difference (FNSD), apparent viscosity (AV) and critical shear rate for onset of FNSD are under evaluation. Dynamic and transient data have also been recorded for evaluation.

EXPERIMENTATION

LVN. The LVN was employed as a measure of the coil expansion of the polymer coil in the solvent. A poor solvent, approaching a theta solvent, has a low LVN relative to a good solvent, which has a high LVN. Procedures for obtaining the LVN from dilute solution extrapolations have been published (5). LVN measurements were determined by Springborn Laboratories, Enfield [illegible]r all solvents except GD and HD.

Rheology. Rheological measurements were performed using the Rheometrics Fluids Rheometer (RFR) Model 7800 with cone and plate geometry at a temperature of 25.0 ± 1.0 degrees C. The initial rheological data from the steady rate sweep experiment was further analyzed; FNSD versus shear rate squared was reduced to obtain FNSD coefficients and zero-shear FNSD. For many solvents, the onset of measurable FNSD occurred in or above the transition to the nonlinear region which has complicated data analysis. The linear region analyzed was defined as occurring above 1% full scale normal transducer output and included the linear data until the correlation coefficient dropped below 0.98.

RESULTS AND DISCUSSION

SOLUBILITY CLASSES. Preferential polymer-solvent interactions can be viewed in complexity as a range from a matrix of a homopolymer with a single solvent through a copolymer with cosolvents. The system investigated consists of a terpolymer with single solvents. The investigation was structured to qualitatively determine solvent-nonsolvent classes for each solvent with the three comonomeric components by independent determination of solubility with homopolymer analogs of the comonomers. For a terpolymer, this generates eight hypothetical classes. Based on the qualitative rheological results and the small number of solvents in several classes, these were collapsed into two classes as shown by the division in Table 1.

Polymer-solvent interactions were further evaluated according to a matrix of nonpolar, polar, and hydrogen-bond interactions. The poly (methyl methacrylate/ethyl acrylate/butyl acrylate), (Poly(MEB)), is a completely aprotic dipolar structure. The solvent sets are defined below.

TABLE 1

Formation of Solubility Classes by Permutation of Solubility (S) and Insolubility (I) of Component Homopolymers of the Terpolymer

Solubility Classes: Terpolymer Solubility		Homopolymer Solubility & mole fraction PMMA(M), 0.82	PEA(E), 0.12	PBA(B), 0.06
MEB Soluble	1)	S	S	S
ME Soluble	1)	S	S	I
MB Soluble	1)	S	I	S
M Soluble	1)	S	I	I
EB Soluble	2)	I	S	S
E Soluble	2)	I	S	I
B Soluble	2)	I	I	S
MEB Insoluble, (Not applicable)		I	I	I

1) Soluble with 0.82-1.00 of comonomer content, eg. M, MB, ME or MEB.
2) Soluble with 0.06-0.18 of comonomer content, eg. E or EB, labelled "Nonsolvent w/0.82+".

Aprotic Solvent Set. The majority of solvents were aprotic dipolar solvents, further classified by a nonsolvent/solvent determination for each terpolymer component, as described above (generally, group number 1 in Table 1).

Theta-Solvent Set. Solvents were identified that were theta or near theta-solvents and also belonged to the class demonstrating solubility with all three terpolymer components, that is, none of the homopolymer controls were insoluble with the terpolymer theta solvent.

Nonsolvent w/0.82+ Solvent Set. The term "Nonsolvent w/0.82+" defines an operational subset of solvents in which the solvent dissolves the terpolymer but was a nonsolvent for at least the majority 0.82 MMA fraction, based on a solubility determination with PMMA hompolymer (group number 2 in Table 1). A comparison of the rheological properties of "Nonsolvent w/0.82+" set with theta solvents was of interest since the low viscometric coil size estimates were similar but based on different physiochemical phenomena. The theta solvents appear to systematically extend the relationship of increasing FNSD and AV with decreasing LVN. The solvents that are in the "Nonsolvent w/0.82+" set display extremely high viscoelasticity as evidenced by FNSD, AV and dynamic properties. In general, hysteresis experiments do not demonstrate structure formation in these solvents although over 0.82 (PMMA) of the chain is nominally insoluble in the solvent.

Proton Donor Solvent Set. There are a select number of solvents with low to moderate proton donating strength, but even weaker acceptor strength (in most media); examples are chloroform, methylene chloride, pentachloroethane, trichloroethylene and pentachlorocyclopropane. These solvents should specifically interact with proton acceptor carbonyl and ester moieties of the polymer solute. All such solvents investigated showed enhanced coil expansion evidenced by LVN values clustered higher than any other "good" solvents and correspondingly low values for rheological properties.

Solubility Classification and LVN: Bis(2-chloroethyl) sulfide (HD). Homopolymer solubility control experiments, as previously described, were employed and they classified HD as MEB soluble. A LVN measurement was performed to estimate the degree of coil expansion of poly(MEB) in HD. The results are presented in Figure 1 and the equations are presented below, with x = concentration in g/dL and y = viscosity number and logarithmic viscosity number for equations 1 and 2 respectively. At zero concentration, (x = 0) in both equations, y is defined as the LVN with the values of 2.90 and 2.83 respectively. Extrapolation of both equations to their point of intersection produces a combined LVN of 2.86 dL/g. One can see that normal Kraemer and Huggins constants were obtained and that poly(MEB)/HD possesses a typical dilute solution viscometric relationship.

$$y = 2.08x + 2.90; \text{ for } x = 0,\ y = 2.90 \text{ dL/g} \quad \text{.....(1)}$$

$$y = -1.42x + 2.83; \text{ for } x = 0,\ y = 2.83 \text{ dL/g} \quad \text{.....(2)}$$

FIGURE 1

Viscosity Number and Logarithmic Viscosity Number vs Concentration Plots for Poly(methyl methacrylate/ethyl acrylate/butyl acrylate) in Bis (2-chloroethyl) Sulfide at 25.0 deg C

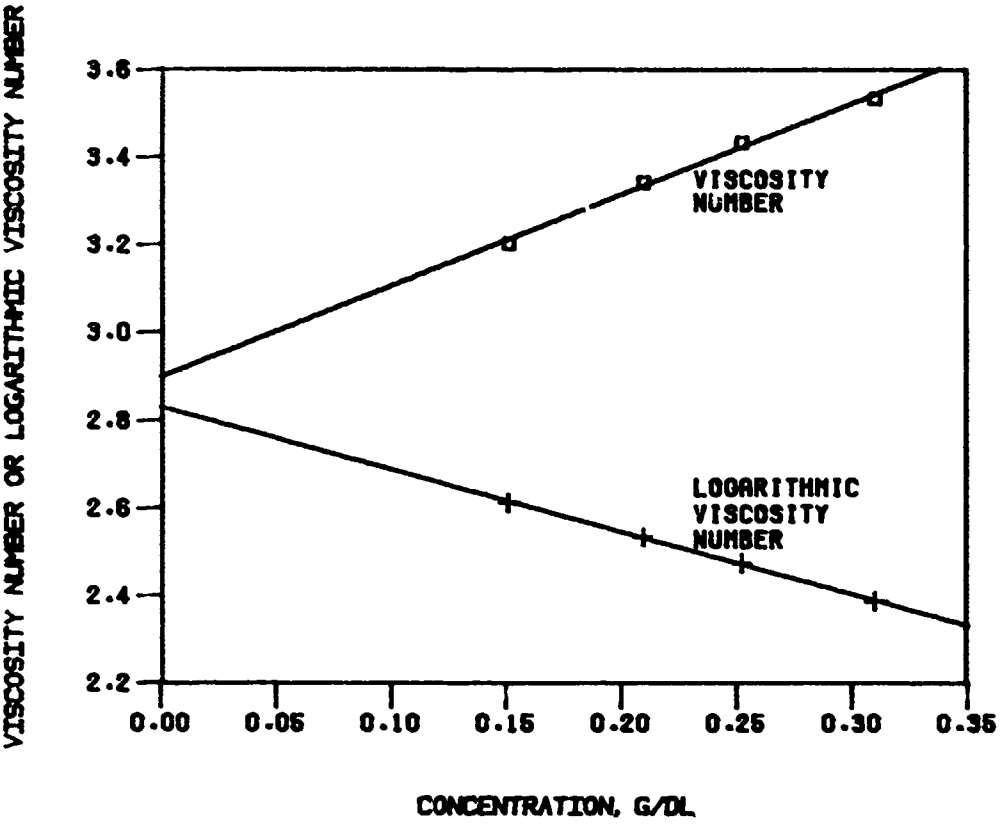

CORRELATIONS. Solvent Interaction Effect on FNSD. The range of solvent influence on FNSD can be viewed by inspection of Figure 2. FNSD vs shear

rate squared is graphed for examples of each solvent set. The full range of FNSD data is presented including high shear rate data well into the nonlinear region. Descriptions of solvent codes, solubility classes, solvent sets and LVN values are listed in Table 2.

FIGURE 2

First Normal Stress Difference vs Shear Rate Squared for Solutions of Poly(methyl methacrylate/ethyl acrylate/butyl acrylate) in Representative Solvents from each Solvent Set, at 25.0 ± 1.0 deg C and 4.7 ± 0.1 g/dL. (See Table 2 for Solvent Codes)

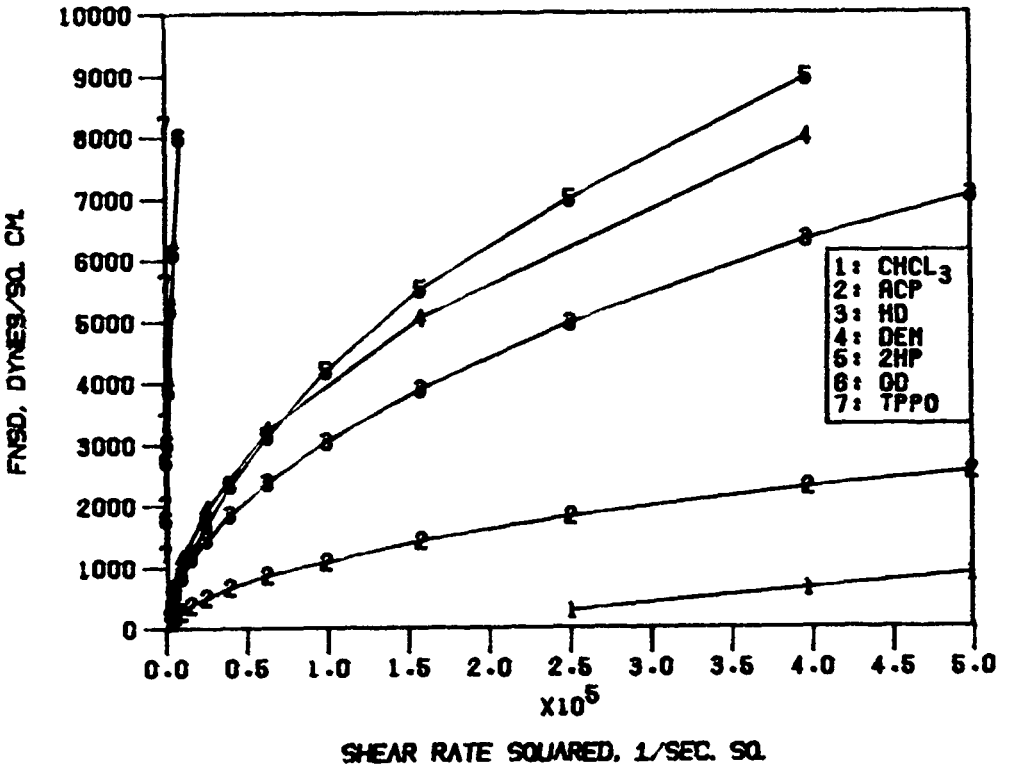

Figure 2 provides a format by which experimental data can display the full range of solvent effects on viscoelasticity. The lowest set values are from $CHCL_3$ as an example of a proton donating solvent. A typical good solvent is represented by ACP. The toxic HD is shown to be a moderate solvent, along with DEM. The poor solvent end of the normal spectrum is represented by 2HP. The remaining solvents, GD and TPPO, have exceptionally high FNSD values relative to their LVN and display partial solubility in the minority comonomer.

Figure 3 contains a plot of LVN vs First Normal Stress Difference (FNSD) for a moderately high shear rate of 400/sec. The LVN values provide a quantitative indication of degree of solvent interaction; the LVN values range from about 1.2 to 4.1 representing a low to high degree of coil expansion. One can note that certain solvent sets fall into limited LVN ranges. Only the proton donating solvents (MEB, plot symbol = 'X'; MB, plot symbol = 'star') have LVN values in the high range between 3.3 to 4.1. Even

the lowest values for a proton donating solvent were higher than the best 'good' solvent based on non-specific interactions.

TABLE 2

Codes, Solubility Classes, Solvent Sets and LVN Values for Representative Solvents (Figure 2)

No.	Codes	Solvent	LVN	Solubility Class	Solvent Set
1	$CHCL_3$	Chloroform	4.08	MEB	Proton donor
2	ACP	Acetophenone	3.03	MEB	Good, aprotic
3	HD	Bis(2-chloroethyl) sulfide	2.88	MEB	Moderate, aprotic
4	DEM	Diethyl malonate	2.40	MEB	Moderate, aprotic
5	2HP	2-heptanone	1.52	MEB	Near theta, aprotic
6	GD	Pinacolyl methyl-phosphonofluoridate	2.10	B	Nonsolvent w/0.82+
7	TPPO	Tripropyl phosphate	1.67	EB	Nonsolvent w/0.82+

FIGURE 3

First Normal Stress Difference at 400/sec vs Limiting Viscosity Number for Poly(methyl methacrylate/ethyl acrylate/butyl acrylate) in a Series of Solvents at 25.0 ± 1.0 deg C and 4.7 ± 0.1 g/dL.

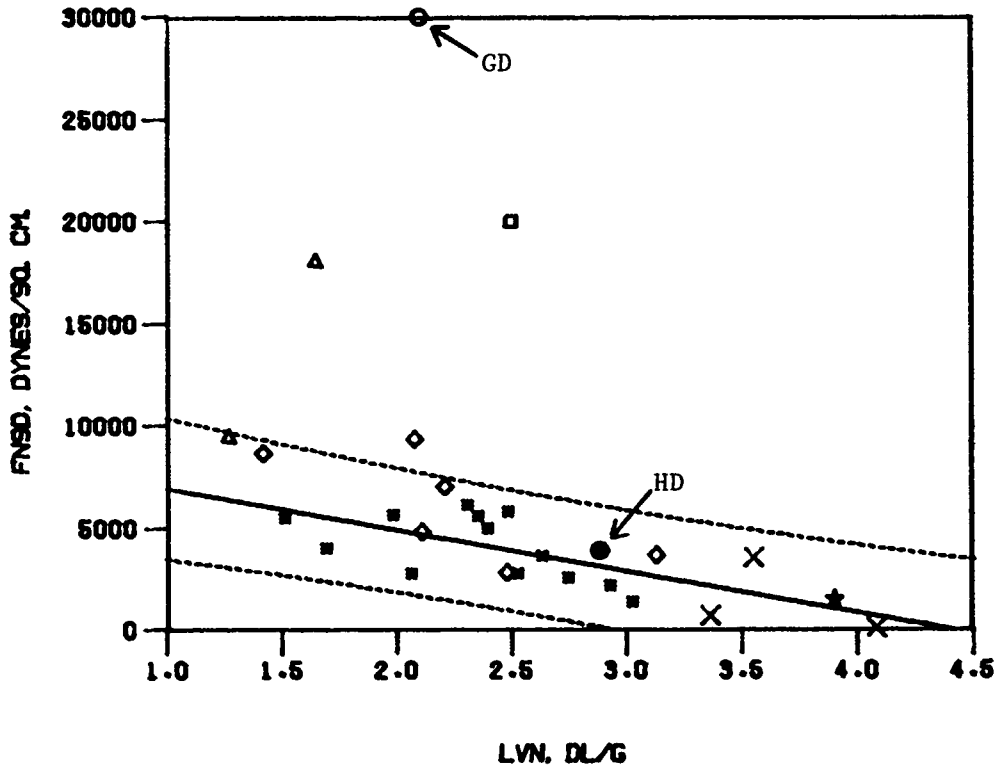

The LVN range from about 1.4 to 3.3 on the regression line in Figure 3 contains three solvent sets. The majority of the solvents are contained in the set defined as "soluble with all terpolymer components" (MEB, plot symbol = 'asterisk'). The solvent set consisting of solvents soluble with both PMMA and PEA are contained within this range (ME, plot symbol = 'diamond'). Qualitatively, the ME set, soluble with 0.94 of the terpolymer,

appears to be following the general trend of the 1.00 soluble MEB set. However, due to the limited data set, these have not been included in the regression in Figure 3.

The data point for an important contaminant, HD (MEB, plot symbol = 'circled asterisk'), was found to fall into this plot area and lies close to the regression line. This result is in agreement with the homopolymer solubility determinations and classification as 'MEB soluble'. HD then appears to behave as a typical moderately good solvent for this methacrylate copolymer. We have already shown that poly(MEB)/HD solutions display the absence of hysteresis, and typical pseudoplastic rheological behavior.

The LVN range between 1.5 to 2.0 appears quite complex, at first. The FNSD values seem to be rather randomly distributed between 3000 and 30,000 dynes/sq. cm., although some solvents lie upon the regression line. Actually, FNSD values range off-scale up to 900,000 dynes/sq. cm. (not plotted) within this 1.5 to 2.0 LVN range. One can begin to unravel the apparent random nature of the viscoelastic FNSD measurements by noting the solubility classifications and solvent data sets associated with the data points. For the 1.5 to 2.0 LVN range, no instance of anomalously high (defined as: above the regression line 95% confidence interval) FNSD measurements were recorded for solvents soluble with the 0.82 to 0.94 majority comonomer content. All solvents that were soluble with the 0.18 comonomer fraction (EB, plot symbol = 'triangle') have FNSD values at or above the regression 95% confidence interval; this includes several EB solvents that are off-scale at very high FNSD values. GD also appears at a FNSD value noticeably higher than the regression 95% confidence interval (B, plot symbol = 'circle').

FNSD coefficient can be independent of solvent effects for solutions of high MW-concentration products within the concentrated, network entangled regime. Within the semidilute regime for C x LVN = 5-20, and C x Mw = 7.1 g/dL megadalton, the FNSD increases with decreasing LVN as shown in Figure 3. The FNSD data has been analyzed as a function of specific shear rates of 100, 400, 1000/sec and as a function of FNSD coefficient at the onset of significant (>1% normal force transducer full scale) normal force response. The relationships at various shear rates are similar and data obtained to date can be summarized by the following equation. The equation represents 16 solvents and excludes preferential solvent effects due to "Nonsolvents w/0.82+", solubility classes EB or B.

$$FNSD\ (400/sec) = 8900 - (2000 \times LVN)$$

Range of Solvent Effects. The solvent effect range can be summarized in a manner analogous to concentration and MW effects (7). The ratio of high/low rheological values are listed in Table 3 for the example of a moderate coil density, within the semidilute regime of, C x Mw = 4.7 x 1.5 = 7.1 g/dL megadalton.

Two types of ranges are listed; 'within' a solvent class refers to the ratio between the highest/lowest values for a single class. 'Between' solvent classes refers to the ratio between the highest value of one class and the lowest of the other class. The properties listed in the first column

are LVN, apparent viscosity at low shear (10/sec), and first normal stress difference at a moderate shear (400/sec). The solvent sets defined in adjacent columns include: within MEB-soluble, within proton donor, within EB soluble and between proton donor and EB-soluble.

TABLE 3

Solvent Effect Ranges and Ratios for Rheological Properties of Polymer Solutions (See Table 1 for Abbreviations)

	Solvent Set			
Property	Within MEB	Within Proton Donor	Within EB	Between Proton Donor - EB
LVN	((3.03/1.27) = 2.4	(4.08/3.36) = 1.2	(2.12/1.27) = 1.7	(4.08/1.27) = 3.2
Apparent Viscosity @ 10/sec	((11.7/4.05) = 2.9	(16.1/2.52) = 6.4	(29.2/5.18) = 5.6	(29.2/2.52) = 11.6
First Normal Stress Difference @ 400/sec	((6800/1420) = 4.8	(6660/100.) = 67.	(900K/9400) = 96.	(900K/100.) = 9000.

The MEB-soluble solvent set provided a LVN ratio of 2.4, ranging from near theta-solvents to maximal values from non-specific interactions. The range of apparent viscosity and first normal stress values measured from this range is about 3X and 5X, respectively. The MEB-soluble solvent set of nonspecific interactions is bracketed at higher LVN values by the proton donor set and at lower LVN values by the preferential EB-soluble set. Both of these solvent sets have LVN ranges of about half of the 'regular' solution range, although the preferentially soluble solvent set and near theta-solvent LVN values overlap. Both of these solvent sets have wider ranges and larger ratios of apparent viscosity (about 6X) and first normal stress difference (67X - 96X) than the MEB-soluble set.

The last column records the measurement ranges and their ratios between the extremely high LVN and low rheological property values of the proton donor set and the high LVN and extremely high rheological property values of the preferentially EB-soluble set. The LVN range has been extended to 3.2X, the apparent viscosity ratio to 11.6X, and first normal stress difference to 9000X. Therefore, although the normal range of solvent influence on rheological properties between 'good' and theta-solvents is limited, the selection of polymer-solvent pairs can extend the viscous properties by about one decade and viscoelastic properties by over three decades.

CONCLUSIONS

A number of conclusions are provided below for the specific coil density investigated.

Copolymer solvents can be classified and experimentally sorted into "solubility classes" based on solubility/insolubility with homopolymer analogs of each comonomer. Copolymer solvents can be further sorted into 'solvent sets' based on the relationship between degree of coil expansion

and rheological properties. The relationship between polymer coil expansion and viscoelasticity (FNSD) was extended with additional model liquids and was interpreted in terms of these solubility classes and solvent sets.

Homopolymer solubility, coil expansion estimate and rheological viscoelastic properties for poly(MEB) in HD and GD were determined. The HD results indicate complete solubility, moderate interaction and normal, typical rheological behavior. The GD results indicate preferential solubility with the butyl acrylate fraction of poly(MEB), low overall interaction, and anomalously high viscoelastic properties. The identification of model compounds and test liquids for these hazardous contaminants can now be pursued based on these solubility classifications, solvent sets, coil densities and viscoelastic properties.

The range of solvent effects on rheological properties is significantly extended with proton-donating solvents and is greatly extended with preferentially soluble liquids.

REFERENCES

1. Shuely, Wendel J. and Ince, Brian S. CRDEC-SP-103. The Effects of Preferential Solubility and Hydrogen-Bond Interactions on the Rheological Behavior of Polymer Solutions. Proceedings of the 1988 U.S. Army Chemical Research, Development and Engineering Center Scientific Conference on Chemical Defense Research, 15-18 November 1988. August 1989. UNCLASSIFIED Report.

2. Shuely, Wendel J. and Ince, Brian S. CRDEC-SP-88013. The Effects of Polymer Concentration and Individual Monomer-Solvent Interactions on the Rheological Behavior of Polymer Solutions. Proceedings of the 1987 U.S. Army Chemical Research, Development and Engineering Center Scientific Conference on Chemical Defense Research, 17-20 November 1987. April 1988. UNCLASSIFIED Report.

3. Ince, Brian S. and Shuely, Wendel J. CRDEC-SP-87008. Investigation of Solvent Effects on Rheological Viscoelastic Properties and Application to Aerodynamic Breakup of Polymer Solutions in the Semidilute Regime: Rheological and Dilute Solution Measurements. Proceedings of the 1986 U.S. Army Chemical Research, Development and Engineering Center Scientific Conference on Chemical Defense Research, 18-21 November 1986. June 1987. UNCLASSIFIED Report.

4. Shuely, W. J. Proc. International Union of Pure and Applied Chemistry Symposium, 1986.

5. ANSI/ASTM D 2857-70 (Reapproved 1977)

6. Kamlet, M. J.; Abboud, J. L. M.; Abraham, M. H.; Taft, R. W.; J. Org. Chem. 1983, 48, 2877.

7. Vinogradov, G. V.; Malkin, A. Ya. Rheology of Polymers. Springer-Verlag, Berlin, Heidelberg, New York, Ed.; 1980.

BLANK

INFLUENCE OF TRACE AMOUNT OF ORGANIC ACIDS ON THE VISCOELASTIC PROPERTIES OF POLYMER SOLUTIONS

S.H. Hong, W. Limm and W.J. Shuely

Research Directorate
U.S. Army Chemical Research, Development and Engineering Center
Aberdeen Proving Ground, MD 21010-5423

Abstract

Research on the influence of trace components on the viscoelastic properties of certain polymer-liquid systems was continued. Measurements of FNSD, apparent viscosity, and dynamic viscoelastic properties were performed as a function of controlled addition of organic acids to the polymer solution. In addition, spectroscopic characterization methods such as UV-visible and FTIR were applied to study interaction between the polymer and additives or cosolvents and the consequent relationship between rheological properties and chemical structures of the polymer-liquid systems.

Introduction

Research on the viscoelastic properties of ultrahigh molecular weight polymer solutions inadvertantly led to a discovery of variation of rheological properties (1). The polymer solution exhibited a decrease in viscosity as a function of storage period and temperature, which might be explained in terms of kinetic dissolution processes. The polymer of interest is a copolymer of protic aminoalkyl methacrylate and aprotic alkyl methacrylate and the solvent system is a proprietary mixture of aliphatic alcohols and an aliphatic amine; therefore, complex hydrogen bonding interactions are possible between polymer and polymer as well as polymer and solvent.

A previous study of the polymer/solvent system indicated that there is little, if any, chemical change in the system, i.e., polymer degradation or chemical reaction between polymer and solvent system (2). The influence of processing and trace amount of various salts on the viscoelastic properties of the polymer solution was also studied (3). Rheological properties of

the filtered solution exhibited no apparent difference from those of the unfiltered reference solution. Also, rheological properties of the solutions with different organic salts showed no apparent change from those of the reference solution. However, solutions with inorganic salts such as LiCl, LiBr, and KOH resulted in an increase in both apparent viscosity and first normal stress difference (FNSD). A hypothetical mechanism suggested for this rheological property change is the possibility of a weak, dipole-dipole interaction type of cross-linking at carbonyl groups of the polymer.

In this study, a sample of the ultrahigh molecular weight polymer solution was treated with various organic acids including diacids and a polymeric acid, i.e., a copolymer of alkyl methacrylate and methacrylic acid. The investigation of the effect of trace acidic impurities completes an experimental survey on influence of a wide variety of chemical functionalities on rheological properties of the polymer solution. From a technological perspective, the objective was to determine if trace impurities might be associated with undesirable viscosity fluctuations as a function of time. The related rheological measurements with a polymeric acid additive, however, were directed toward exploiting the possibility of increasing polymer-polymer contacts and enhancing viscoelsticity. Also underway is the study of direct spectroscopic measurement of interaction between the polymer and the additive or solvents (4).

Experimentation

Rheological properties were measured by a Rheometrics Fluid Rheometer Model RFR 7800 with cone-and-plate fixture. The confirmation of existence of aromatic compounds such as benzoic acid and 2,6-naphthalene dicarboxylic acid in the solution was performed by Hewlett and Packard Model 8452A Diode Array Spectrophotometer.

The acid additives were obtained from ChemSources chemical kit and used without further purification. Ultrahigh molecular weight methacrylate copolymer and methacrylic acid copolymer were obtained from Rohm and Haas Company. The reference solutions were made from a stock solution of the copolymer in alcohols/amine (8 g/dL), which was prepared and equilibrated more than 18 months. Upon the completion of dilution, the reference solution was divided into small samples. An appropriate amount of acidic additives was introduced to each sample. Selection of the acid was based on the number of equivalents per molecule and the size. After the addition of the acids was completed, each sample was tumbled on a 3-dimensional motion Turbula mixer for at least 3 days to ensure complete mixing. The acidic additives were introduced so that their concentration was roughly an equal molar ratio to the concentration of amino units of the copolymer in the solution, except for the case of polymeric acid.

Results and Discussion

The rheological properties of the solutions with acidic additives were measured and compared to those of the reference solutions. Table 1 shows selected rheological properties of those solutions.

Table 1. Selected Rheological Properties of the Methacrylate Copolymer Solution with Acidic Additives.

Additive	% w/w of Additive	Molar Ratio[a]	Sol[b]	Apparent Viscosity @20/sec (poise)	FNSD[c] @100/sec (dyne/cm^2)
Monoacid					
Reference	-	-	-	6.833	372.2
				7.032	353.2
				7.167	392.7
Formic acid	5.59	1.13	S	7.264	928.7
Acetic acid	6.35	1.00	S	7.763	782.5
Propionic acid	7.65	1.01	S	7.381	673.4
n-Butyric acid	8.86	1.01	S	7.001	595.3
Isobutyric acid	9.08	1.02	S	7.450	678.5
n-Heptanoic acid	12.65	1.02	S	7.689	685.9
Cyclohexane carboxylic acid	12.06	1.00	S	7.033	564.6
Benzoic acid	?	?	I	7.167	262.2
Diacid					
Reference	-	-	-	18.12	1586
Adipic acid	2.02	1.2	I	18.78	1712
Sebacic acid	1.59	0.7	I	16.06	1709
Terephthalic acid	1.71	0.9	I	19.55	1555
2,6-Naphthalene dicarboxylic acid	2.36	0.9	I	17.84	1417

a. Molar ratio of the equivalent in the additive to the amino group content (normalized) of the copolymer in the solution.

b. Solubility - S means the solution was homogeneous and I means the solution still had solid phase after tumbling at least 3 days.

c. First Normal stress Difference.

1. Monoacids

The aliphtic acids introduced into the solution were in liquid state. When these additives were added to the sample, a white cloud was formed at the drop site. However, after tumbling, the cloudiness disappeared and the solution retained its clear, yellow color. One possible explanation for this phenomenon is salt formation by the acid additive and the amine component, probably from the solvent, rather than from the polymer; upon tumbling, this salt dissolved in the solvent to give clear liquid.

The rheological properties, especially FNSD, of the resulting solutions were quite different from those of the reference solution, as shown in Table 1 and Figure 1. The size of the acids apparently did not influence the change in rheological properties. One of the possible explanations for the change in rheological properties is somewhat weak hydrogen bond type interaction between the acid, and the polymer chains, either in free acid form or in clustered salt form. One might expect a stronger influence by the diacids, due to the fact that a diacid can form a bridge between polymer chains through both of the acidic functionalities.

The aromatic acid (benzoic acid), in its white crystalline form, was added. There was no apparent change upon addition and the mixture remained unchanged, i.e., liquid phase and solid phase, after tumbling. Whether this solid phase is in free acid form or in salt form was not determined. The UV spectrophotometer of the separated liquid phase showed presence of benzoic acid in the solution (Figure 2). However, the rheological properties of the separated liquid phase apparently showed no significant change (Figure 3). This might be due to the fact that there is not enough benzoic acid in the solution to influence the rheological properties of the solution. Although the solution is nominally saturated with benzoic acid, the ratio to protic aminoalkyl methacrylate functionality in the polymer should be well below equimolar.

2. Diacids

As shown in Table 1, several diacids of different chain length were employed, including aromatic acids (terephthalic acid and 2,6-naphthalene dicarboxylic acid). All the acids were in solid state. The results were similar to that of benzoic acid, i.e., no apparent change in either FNSD or apparent viscosity (Figure 4). This also can be explained in terms of low concentration of the acids in the polymer solution as in the case of benzoic acid.

3. Polymeric Acid

The polymeric acid employed is a copolymer of same alkyl methacrylate and methacrylic acid (9:1 molar ratio). The molecular weight of this copolymer is around 1 megadalton. A solution of this polymer in alcohols/amine mixture as well as mixture of alcohols without amine were prepared and mixed with appropriate ultrahigh molecular weight copolymer solutions so that the ratio of the two polymeric species became 4:1, 6:1 and 8:1. Rheological properties and the calculated concentration of total

polymers are given in Table 2. As shown in Figure 5 as well as Table 2, the polymeric acid altered the rheological properties, especially FNSD, significantly. A study with normalized polymer concentration is currently in progress in this laboratory.

Table 2. Selected Rheological Properties of the Methacrylate Copolymer in Alcohol Mixture with Polymeric Acid Additive.

Solution[a]	Total Polymer Concentration (g/dL)	Apparent Viscosity @100/sec (poise)	FNSD @100/sec (dyne/sq.cm)
Reference	4	11.10	2795
80/10 Mixture	3	11.54	6497
60/10 Mixture	2.8	8.95	5286
40/10 Mixture	2.5	10.53	7527

a. The ratios shown are Methacrylate copolymer/Polymeric acid.

Conclusion

Rheological properties, especially FNSD, of the polymer solutions with monoacid additives exhibited significant increase from those of the reference solutions. Also, rheological properties of the solutions with polymeric acid showed significant difference from those of the reference solution. However, apparent viscosity of the aforementioned solutions showed less change compared to FNSD. Solutions with additives of low solubility showed no apparent difference in rheological properties from the reference solutions.

An example of possible explanations of this change is a weak, hydrogen-bond type bond formation at carbonyl groups of the polymer. The polymeric acid additive should enhance this effect since they can create multiple polymer-polymer contact. Further studies with polymeric acid additive are in progress. Also, studies with soluble diacid additives are planned.

References

1. Hyttinen, L., Private communication.

2. Hong, S.H. and Beaudry, W.T., Proceedings of the U.S. Army Chemical Research, development and Engineering Center Scientific Conference on Chemical Defence Research, Nov 17-20, 1987. CRDEC-SP-88013.

3. Hong, S.H. and Shuely, W.J., Proceedings of the U.S. Army Chemical Research, development a d Engineering Center Scientific Conference on Chemical Defence Research, Nov 15-18, 1988. CRDEC-SP-013.

4. Limm, W. and Hong, S.H., Proceedings of the U.S. Army Chemical Research, development and Engineering Center Scientific Conference on Chemical Defence Research, Nov 14-17, 1989. In publication.

Figures

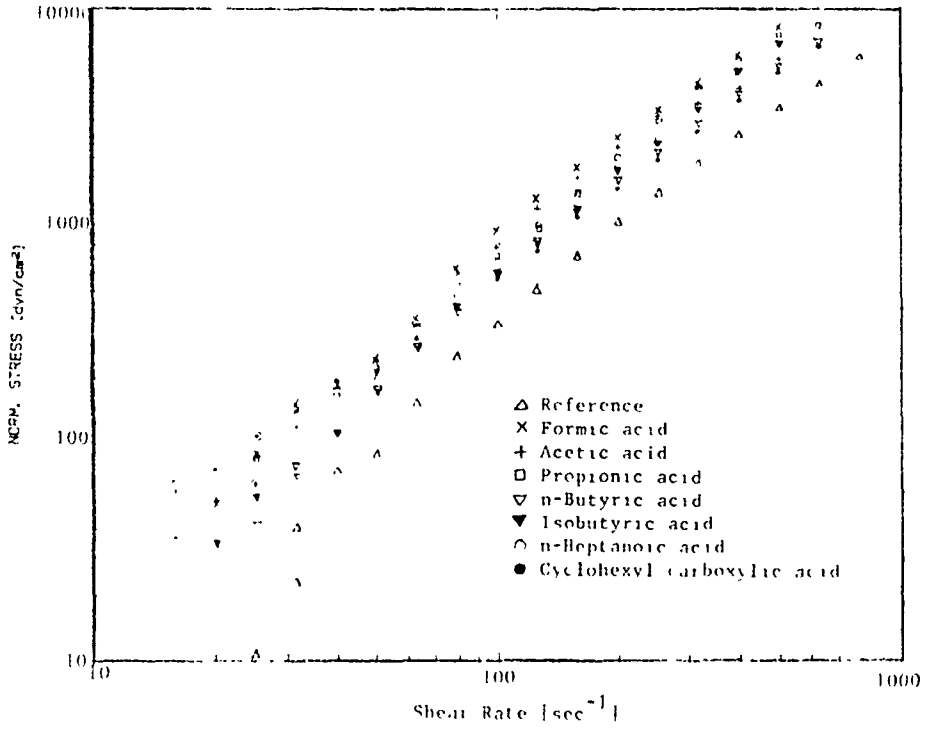

Figure 1. Rheological property (First Normal Stress Difference) of Polymer Solutions with Acid Additives.

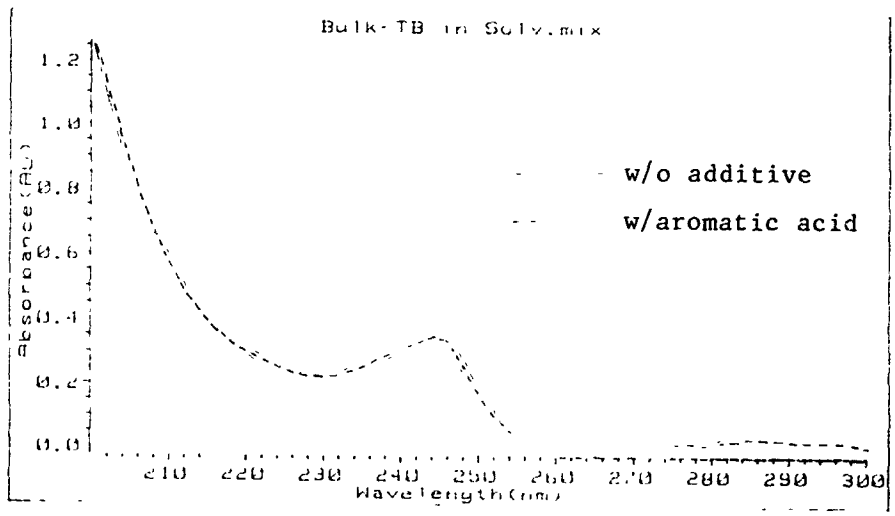

Figure 2. UV Spectra of Polymer Solutions with and without Aromatic Acid Additive (2,6-Naphthalene dicarboxylic acid).

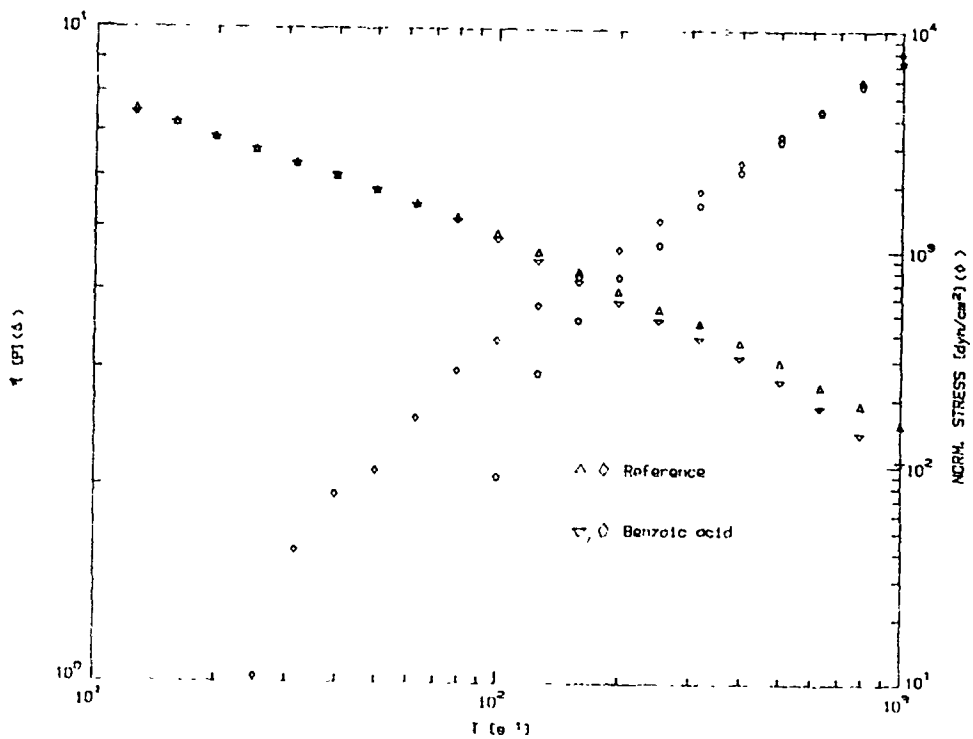

Figure 3. Rheological Properties (Apparent Viscosity and FNSD) of Polymer Solutions with and without Aromatic Acid Additive (Benzoic Acid).

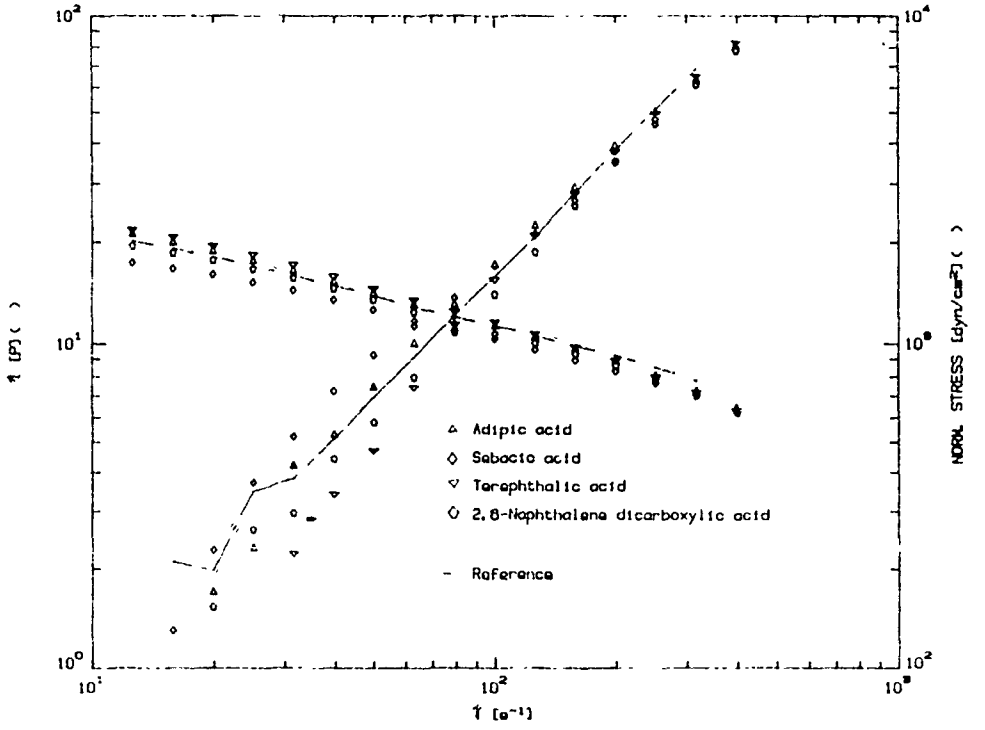

Figure 4. Rheological Properties (Apparent Viscosity and FNSD) of Polymer Solutions with Diacid Additives.

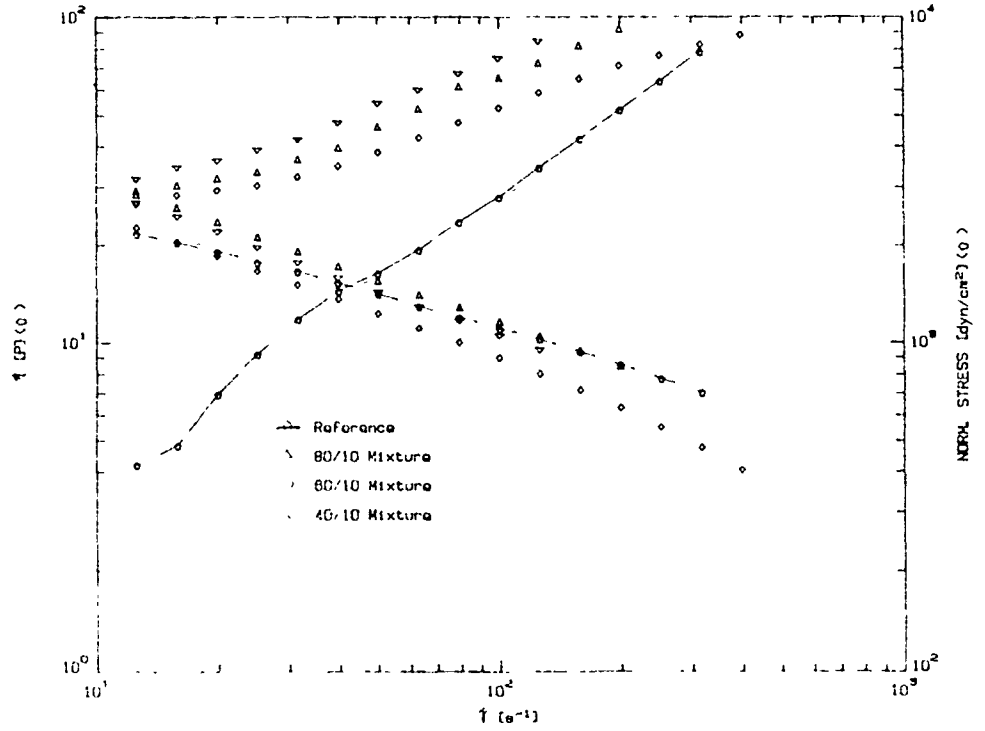

Figure 5. Rheological Properties (Apparent Viscosity and FNSD) of Polymer Solutions with Polymeric Acid Additive.

SOLUTION BEHAVIOR OF A RANDOM COPOLYMER OF POLY(ISOBUTYL METHACRYLATE-t-BUTYL AMINOETHYL METHACRYLATE). 1. LASER LIGHT SCATTERING STUDIES

Benjamin Chu,[1,2] Jian Wang[1] and Wendel J. Shuely[3]

1. Chemistry Department, State University of New York at Stony Brook Long Island, New York 11794-3400
2. Department of Materials Science and Engineering. State University of New York at Stony Brook, Long Island, New York 11794-2275
3. Research Division, Chemical Research, Development, and Engineering Center, Aberdeen Proving Ground, MD 21010-5423

ABSTRACT

Laser light scattering studies of solution behavior of a random copolymer of poly(isobutyl methacrylate-co-t-butyl aminoethyl methacrylate) in isopropylamine, N,N,N',N'-tetramethylethylenediamine (TMEDA), N,N-dimethyl formamide, N,N-dimethylacetamide, and a 0.4/0.6 (molar ratio) mixture of TMEDA and 3-heptanone are described. By taking advantage of the isorefractive property of poly(isobutyl methacrylate) [poly(iBMA)], poly(t-butyl aminoethyl methacrylate) [poly(t-BAEMA)] and poly(iBMA-tBAEMA), the light scattering intensity properties for the copolymer, poly(iBMA-tBAEMA) could be approximated as those of a homopolymer. Therefore, a distinguishing characteristic of the copolymer as a polymer additive which can influence the rheology of a large variety of fluids can be attributed to polymer aggregation by intra- and inter-molecular interactions.

I. INTRODUCTION

Acrylate or methacrylate polymers with pendant aminoalkyl groups have a wide range of applications, such as additives for lubricants, cosmatic preparations and coatings. Hong and McHugh have made extensive reviews on the preparation and properties of aminoalkyl acrylates and methacrylates[1] and of copolymers from aprotic (acrylic) monomers and protic (acrylic) monomers.[2] The presence of pendant aminoalkyl groups adds cationic characteristics to the copolymer and changes its solubility behavior.

Depending on the solvent nature, such copolymers have the potential to exhibit (pseudo) ionomer solution properties involving intramolecular and intermolecular interactions. One consequence of having aprotic/protic (or ionic) pendant groups present in a polymer chain is its ability to be soluble in both non-polar and polar solvents. The other property which makes ionomer-like copolymers with pendant aminoalkyl groups as useful polymer additives is their ability to change the viscosity of the fluids. In this article, we report laser light scattering (LLS) studies on the solution properties of poly(isobutyl methacrylate-co-t-butylaminoethylmethacrylate), abbreviated as poly(iBMA-tBAEMA), over a broad range of concentrations in several different solvents.

Light scattering (LS) has been used to determine the molecular weight of synthetic homopolymers for more than 40 years.[3] The theoretical treatment for light scattering by solutions of copolymers was developed by Stockmayer et al[4] and by Bushuk and Benoit[5] more than 30 years ago. However, only a handful of experiments have been reported since then.[6] For a copolymer with protic and aprotic pendant groups, such as poly(iBMA-tBAEMA), solution studies of intramolecular and intermolecular interactions would be very complex. Fortunately, homopolymers of poly(iBMA) and poly(t-BAEMA) have comparable refractive indices which are essentially the same within the experimental error limits. Thus, we were able to carry out light scattering studies by assuming the copolymer to be a "homopolymer" in terms of its scattering behavior; this isorefractive property of poly(iBMA), poly(t-BAEMA) and poly(iBMA-tBAEMA) permits us, for the first time to our knowledge, to investigate the intramolecular and intermolecular interactions of such systems by means of LLS.

In the following sections, we summarize the theoretical background in II, experimental methods in III, results and discussion in IV and conclusions in V.

II. THEORETICAL BACKGROUND

II.1. Static Light Scattering

The *excess* Rayleigh ratio R_{vv} for vertically polarized incident and scattered light due to a polydisperse homopolymer of uniform refractive index increment ν(= (dn/dC)) has the form:

$$\lim_{\substack{C\to 0 \\ \theta\to 0}} (H^* C/R_{vv}) = 1/(M_w \nu^2) \qquad (1)$$

where $H^* = 4\pi^2 n^2/(N_A \lambda_o^4)$ with n, N_A and λ_o being, respectively, the refractive index, the Avogadro number, and the incident wavelength in vacuo; C is the polymer concentration; M_w[= $\Sigma_i W_i M_i$ with W_i(= C_i/C) and M_i being, respectively, the weight fraction and the molecular weight of polymer species of chain length i] is the weight average molecular weight; and θ is the scattering angle. At finite scattering angles with $KR_g \lesssim 1$ and dilute concentrations, Eq. (1) becomes

$$\frac{HC}{R_{vv}(K)} \simeq \frac{1}{M_w}\left[1 + \frac{K^2 R_g^2(C)}{3}\right] + 2A_2C \qquad (2)$$

where $H = H^* \nu^2$, $K[= (4\pi/\lambda)\sin(\theta/2)$ with $\lambda = \lambda_o/n]$ and A_2 are, respectively, the magnitude of the momentum transfer vector and the second virial coefficient. $R_g^2(C)$ is an apparent radius of gyration at concentration C with $R_g^2[= \lim_{C\to 0} R_g^2(C)]$ being the mean square z-average radius of gyration.

II.2 Dynamic Light Scattering

The measured photoelectron count autocorrelation function $G^{(2)}(t)$ is related to the normalized electric field autocorrelation function $g^{(1)}(t)$ by the relation

$$G^{(2)}(t) = A(1 + b|g^{(1)}(t)|^2) \qquad (5)$$

where A is the background and b accounts for the non-ideal point detector. The net intensity autocorrelation function, $[G^{(2)}(t)/A]-1 = b|g^{(1)}(t)|^2$, can be related to monodisperse particle translational motions at dilute concentrations such that

$$b|g^{(1)}(t)|^2 = be^{-2\Gamma t} \qquad (6)$$

with $\Gamma = DK^2$ and D being the translational diffusion coefficient.

III. EXPERIMENTAL METHODS

Random copolymer, poly(iBMA-tBAEMA) (Lot# CM1-120) was prepared by emulsion polymerization and purchased from Polyscience. The homopolymer poly(tBAEMA) was prepared by solution polymerization of monomer tBAEMA (Polyscience, Inc.) in THF at a concentration of 10% and 70°C using 2,2'-azobisisobutyronitrile (Polyscience, Inc.) at 0.1% concentration as an initiator. The homopolymer of poly(iBMA) was purchased (Rohm and Haas Co.) after preparation by emulsion polymerization (lot 39015-23); the weight average molecular weight is approximately 1.7×10^6 g/mol by SEC and LS.

Refractive index increments (ν) were measured by means of a Brice Phoenix differential refractometer. The interpolated results (measured mostly to ±0.001) for the two homopolymers, poly(iBMA) and poly(tBAEMA), as well as the copolymer, poly(iBMA-tBAEMA), in different solvents are listed in Table 1.

A standard laboratory-built light-scattering spectrometer was used to measure the scattered intensity by photon counting and time correlation function by using a Brookhaven Instruments BI-2030 128-channel digital autocorrelator over an angular range of 15° and 135°.

TABLE 1
Molecular Parameters of Poly(iBMA-tBAEMA) in Different Solvents[a]

	IPA	TMEDA	DMF	DMAA	TMEDA/HTN[b]
ν_A	0.125	0.074	0.049	0.043	
ν_B	0.128	0.073	0.049	0.040	
ν	0.124	0.075	0.051	0.045	0.072
n_o	1.368	1.412	1.428	1.433	1.409
$M_w(10^6$ g/mol)	2.42	5.86	8.52	9.08	13.6
R_g(nm)	95	131	151	162	205
R_h(nm)	65	100	115	120	152
R_h/R_g	0.69	0.77	0.76	0.74	0.74
$10^3 C^*$ (g/mL)	4.69	4.33	4.11	3.55	

(a) Abbreviations: A: poly(iBMA); B: poly(tBAEMA); n_o = refractive index of solvent.
IPA: Isopropylamine
TMEDA: N,N,N',N'-Tetramethylethylenediamine
DMR: N,N-Dimethyl Formamide
DMAA: N,N-Dimethylacetamide
HTN: 3-Heptanone
Temperature: 30°C

(b) Compositions of TMEDA/HTN: mole ratio of TMEDA/HTN = 0.4/0.6

IV. RESULTS AND DISCUSSIONS

By taking advantage of the fact that the copolymer had essentially isorefractive components with *different* chemical properties, we could determine the *true* molar mass of the aggregates in the dilute solution regime. We also performed experiments at very dilute solution concentrations in order to show experimentally how the aggregates can be taken apart by dilution - like micelles and can be reduced to the unaggregated monomacromolecular state at very low concentrations.

Table 1 lists the refractive index increments of poly(iBMA), poly(tBAEMA) and poly(iBMA-tBAEMA) in isopropylamine (IPA); N,N,N',N'-tetramethyl ethylenediamine

(TMEDA); N,N-dimethyl formamide (DMF); N,N-dimethyl acetamide (DMAA); and a solvent mixture of TMEDA and 3-heptanone (HTN) with a mole ratio of [TMEDA]/[HTN] = 0.4/0.6 at λ_o = 488 nm and 30°C. A very important finding for this copolymer is that the two homopolymers (poly(iBMA) and poly(tBAEMA)) are essentially isorefractive with $\Delta \equiv \Delta\nu = \nu_A - \nu_B \simeq 0.003, 0.001, 0, 0.003$ in IPA, TMEDA, DMF and DMAA, respectively. The measured values of ν for the copolymer agree with the computed ones to within ~0.002, ~0.001, ~0.002, ~0.003 for poly(iBMA-tBAEMA) in IPA, TMEDA, DMF and DMAA, respectively. The isorefractive approximation of segments of iBMA and tBAEMA in poly(iBMA-tBAEMA) forms the key to interpreting the light scattering results of our interacting copolymer solutions, as we are no longer concerned with apparent molecular weight or apparent radius of gyration problems.

The macromolecular parameters determined by the Zimm plots are listed in Table 1. For each solvent, we have also computed the overlap concentration C* to show that the extrapolation to "infinite" dilution was performed at C << C*. The difference in M_w (or more precisely defined as the molar mass for the aggregated copolymer) from 2.42×10^6 to 1.36×10^7 g/mole suggests polymer aggregation properties in different solvents with no guarantee that $M_w \simeq 2.42 \times 10^6$ g/mol is the true molecular weight of the unaggregated poly(iBMA-tBAEMA) sample. The other values of M_w are all for poly(iBMA-tBAEMA) with different degrees of aggregation due to the nature of solvent quality for the two components of the copolymer and the composition/structure distribution of the two components within each copolymer chain of length i, i.e. the compositional drift of comonomer ratio as a function of molecular weight is characteristic of free radical copolymerization with comonomers of divergent reactivity ratios.

The light-scattering intensity study of dilute poly(iBMA-tBAEMA) solutions leads us to the concept that the random copolymer, poly(iBMA-tBAEMA), tends to form aggregates of varying degrees in most solvents. We could reach the above conclusion mainly because the copolymer had essentially isorefractive components (A = iBMA and B = tBAEMA).

From photon correlation measurements, the net intensity time correlation function, $b|g^{(1)}(\tau)|^2$, of the copolymer in IPA, TMEDA, DMF and DMAA, as illustrated in Fig. 1, shows an increase in the variance with an increase in the degree of aggregation (i.e., the molecular weight of associated polymers in solution, as listed in Table 1).

With our supposition of interacting copolymers to form relatively unentangled supramolecular aggregates in the solvents we have studied, we proceed to test this postulate by making laser light scattering measurements at very dilute concentrations. The idea is that if the copolymers, like micelles, form aggregates at dilute concentrations, we may be able to observe a breaking up of those aggregates at very low concentrations.

Figure 2 shows plots of excess scattered intensity of poly(iBMA-tBAEMA) at 30°C and after extrapolation to $\theta = 0$ in DMAA (inverted triangles) and in TMEDA (squares).

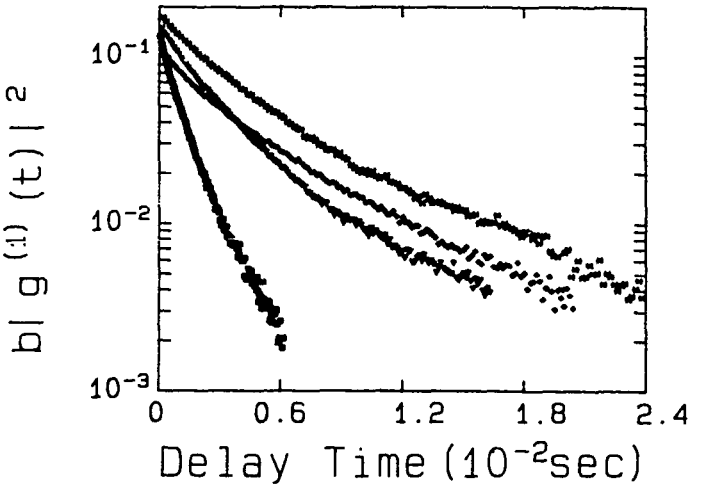

FIGURE 1. Semilog plots of net time correlation function for poly(iBMA-tBAEMA) in IPA (hollow squares), TMEDA (hollow triangles), DMF (hollow diamonds), and DMAA (stars) at 30°C.

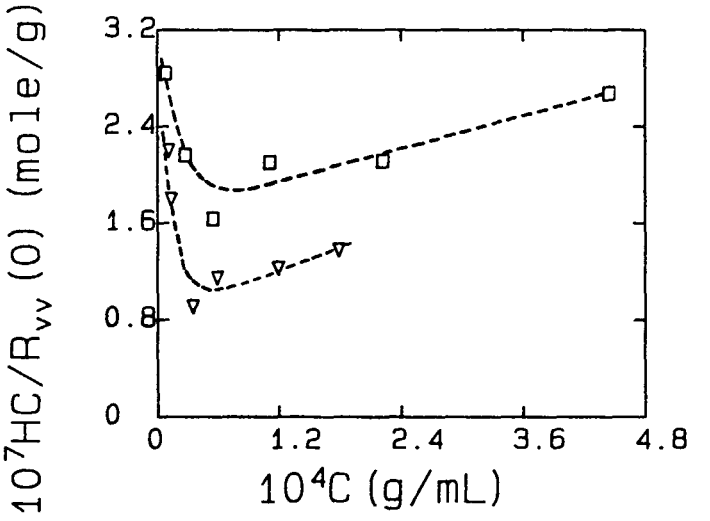

FIGURE 2. Dilution effect on excess scattered intensity of poly(iBMA-tBAEMA) at 30°C and after extrapolation to $\theta = 0°$ in DMAA (triangles) and in TMEDA (squares). The molecular weight could be estimated by extrapolation to infinite dilution from the upward curve and the downward curve, respectively. However, we could not establish a precise end point ($\lim_{C\to 0} HC/R_{vv}$) with the present data. It is clear that M_w should be ~ 2.4×10^6 g/mole.

Unfortunately, our light scattering intensity data at very dilute concentrations were not sufficiently precise to permit an unambiguous extrapolation for determination of the

copolymer weight-averaged molecular weight in its unaggregated state. A rough estimate by eye inspection would suggest $M_w \lesssim 2.4 \times 10^6$ g/mole.

V. CONCLUSIONS

Poly(iBMA-tBAEMA) forms supramolecular aggregates in most solvents, such as TMEDA, DMAA, etc. The aggregates enhance the effectiveness of the polymer additive because, in the presence of polymer aggregation, entangled polymer pseudo networks are formed at lower overlap concentrations. The non-Newtonian fluid behavior for the supramolecular polymer solution is responsible for such copolymers to be useful as effective additives.

By taking advantage of the almost isorefractive coincidence of poly(iBMA), poly(tBAEMA) and poly(iBMA-tBAEMA), we could ascertain the determination of the weight-averaged molar mass and the z-averaged radius of gyration for the supramolecular polymer solutions by light scattering intensity measurements. The aggregation phenomenon can be shown unambiguously by carrying out laser light scattering measurements at very dilute concentrations. A breakup of the aggregates clearly suggests that in the normal dilute solution regime, we estimate the molar mass of the aggregates (instead of the molecular weight of the copolymer).

ACKNOWLEDGEMENT

We gratefully acknowledge support of this work by the U.S. Army Research Office (DAAL0387K0136).

REFERENCES

1. Hong, S. H.; McHugh, V. M., "Review of polymerization and properties of aminoalkyl acrylates and aminoalkyl methacrylates", with 31 references, Gov't. Rpt., CRDEC-TR-88092, July, 1988.
2. Hong, S. H.; McHugh, V. M., "Review of preparation and properties of polymers from copolymerization of aprotic acrylic monomers with protic acrylic monomers," with 57 references, Gov't. Rpt., CRDEC-TR-88093, July 1988.
3. Debye, P. J. Phys. Colloid Chem. (1947) **51**, 18.
4. Stockmayer, W. H.; Moore, L. D., Jr.; Fixman, M.; Epstein, B. N. J. Polym. Sci. (1955) **16**, 517.
5. Bushuk, W.; Benoit, H. Can. J. Chem. (1958) **36**, 1616.
6. Chu, B.; Ying, Q.; Lee, D.; Wu, D. Macromolecules (1985) **18**, 1962; see references therein.

BLANK

LIQUID STRETCHING USING A FALLING CYLINDER

Joseph E. Matta and Raymond P. Tytus
U.S. Army Chemical Research, Development and Engineering Center
Aberdeen Proving Ground, MD 21010-5423

ABSTRACT

A novel free fall extensional device was developed, and its usefulness in measuring the elongational viscosity of both Newtonian and viscoelastic liquids was demonstrated. A small liquid quantity is inserted between the ends of two cylinders that are vertically oriented one above the other. The upper cylinder is held fixed while the lower cylinder, initially at rest, is allowed to fall and stretch the adhering sample. Time sequence photos of the stretching process are used to deduce the liquid deformation rate and ligament stress. The elongational viscosity is then determined from the stress/deformation rate ratio. Both Netwonian and viscoelastic solutions were tested. While Newtonian results are consistent with the Trouton expression, viscoelastic testing indices that the elongational viscosity increases with time and is significantly greater than that of a comparable viscous Newtonian liquid. Since only a small liquid quantity is required for testing and the apparatus can conveniently fit into a glove box, the elongational characterization of toxic chemical agents are now possible.

INTRODUCTION

Aerodynamic forces are often used to atomize liquids for various applications. However, when Newtonian liquids are subjected to relatively high air velocities, small particles normally result. To increase the drop size of the atomized fluid, polymers are often added. With this addition of polymer, non-Newtonian viscoelastic solutions are produced. Although the exact mechanisms of atomization are not well known, experimental studies[1-3] indicate that extensional rheological properties play a critical role in the breakup process and significantly influence the resultant drop sizes. Some theoretical arguments[4,5] indicate that nonlinear viscoelastic effects tend to stablize viscoelastic ligaments,

resulting in the formation of larger drops than those produced from a Newtonian fluid of similar viscosity. Thus, in order to develop a valid predictive drop size capability for viscoelastic breakup, an understanding of the extensional flow behavior of the fluid is required.

In steady extensional flow, the elongational viscosity, η_e, is the material function used to characterize the fluid. Elongational viscosity measurements on viscous polymer melts are normally made using a tensile testing machine[6] on which a rod-like sample is suspended in a silicone oil bath (to compensate gravity by buoyancy) and then stretched at a constant tensile stress or constant strain rate. However, polymer solutions typically have shear viscosities far too low to form a stable rod-like configuration. Other methods of characterizing the extensional flow behavior of a solution exist (e.g. tubeless syphon, impinging jets, and spin rheometer).[6] These methods, however, are not very suitable for use with toxic fluids since large liquid quantities are required. Also, since these methods all involve pre-shearing of the liquid, which is known to significantly affect the fluid rheology, the measurements are questionable. Extensional measurements of polymeric solutions are also possible using a falling drop experiment. Here a liquid sample is extruded vertically downward from a capillary until the drop forming at the capillary tip is no longer supported by surface tension. The falling drop stretches the connecting ligament. This method is limited since it is not possible to vary the extension rate nor insure that liquid does not flow into the drop during the stretching process. In addition, it is not possible to precisely initiate the moment of stretching since this is controlled largely by the surface tension of the liquid.

Thus, since no suitable methods exist to investigate the stretching behavior of toxic fluids at high rates of extension, a novel free fall stretching apparatus was developed. The device and its use with Newtonian and viscoelastic liquids is discussed here.

SIMPLE EXTENSION

Neglecting interfacial surface tension, one can easily show that, for a Newtonian fluid, the total stress T_{11} required to establish an elongational flow is:

$$T_{11} = 3\eta_0 \dot{\epsilon} \qquad (1)$$

where η_0 is the Newtonian shear viscosity, and $\dot{\epsilon}$, the elogation rate is defined as:

$$\dot{\epsilon} = -2V_r/r \qquad (2)$$

where r is the ligament radius with radial velocity V_r.

Since the elongational viscosity is defined as:

$$\eta_e = T_{11}/\dot{\epsilon} \qquad (3)$$

a simple relationship exists for a Newtonian fluid between the shear and

elongational viscosity, i.e., $\eta_e = 3\eta_o$ and is commonly referred to the Trouton expression.[7] However, if you include interfacial surface tension, as a source of stress on the ligament, then the total stress found necessary for simple extension is:

$$T_{11} = \eta_e \dot{\epsilon} + \sigma/r \qquad (4)$$

Thus, if a ligament is subjected to a simple extensional deformation, it must follow for a Newtonian fluid that the force F_L exerted on the cylinder by the ligament is:

$$F_L = T_{11} \pi r^2 = \pi \eta_e r^2 - \pi\sigma r \qquad (5)$$

Solving for the elongational viscosity, one obtains:

$$\eta_e = (F_L - \sigma\pi r)/\dot{\epsilon}\pi r^2 \qquad (6)$$

Therefore, simple extension is assumed to occur in the ligament stretched by a falling cylinder, if you measure F_L and observe using Equation 6 that the Trouton expression is satisfied.

To measure the ligament force, F_L, acting on the falling cylinder with mass, m, Newton's second law is applied, i.e.,

$$ma = mg - F_L - F_d \qquad (7)$$

where F_d is the drag force exerted on the cylinder, a is the acceleration, and g is gravitational constant. By rearranging Equation 7, one can then express the ligament force as,

$$F_L = m(g - a) - F_d \qquad (8)$$

EXPERIMENTAL METHODS

To generate an elongational flow, a novel free fall extensional device was developed. A small quantity of liquid ($\sim$ 30 mg) is inserted between the ends of two cylinders that are 6.35 mm in diameter and are vertically oriented one above the other. The upper cylider is held fixed, while the lower cylinder initially rests on top of an air piston. When activated, the piston quickly retracts downward, allowing the cylinder to fall and stretch the liquid sample adhering between the two cylinder end surfaces. High speed photographs ($\sim$ 1000 frames/sec) of the stretching process and the falling cylinder are used to deduce the liquid deformation rate and ligament stress, respectively. The elongational viscosity is then determined from the stress and deformation rate ratio (Equation 3).

Preliminary trials without liquid were conducted to determine the accuracy of the experiment and the significance of air drag on the free falling cylinder. From a least square fit of the measured fall velocity versus time for an 0.81-g cylinder, a constant acceleration of 960 cm/sec^2 was measured. Similar free fall trials using 2.15-g and 3.11-g cylinders without liquid all resulted in constant acceleration within 2% of the gravitational constant of 980 cm/sec^2. Thus, even if air drag is neglected,

the fall acceleration is measured with 2% accuracy.

NEWTONIAN RESULTS

Figure 1 is an example of a few selected frames taken of a standard ASTM Oil (S2000 Canon Instrument, Co.) being stretched by an 0.81-g cylinder that resulted in an elongation rate ranging from 45 to 58 sec^{-1}. Table 1 provides a summary of the measured cylinder acceleration, ligament radius and elongation rate, and the measured elongational viscosity obtained using Equation 6.

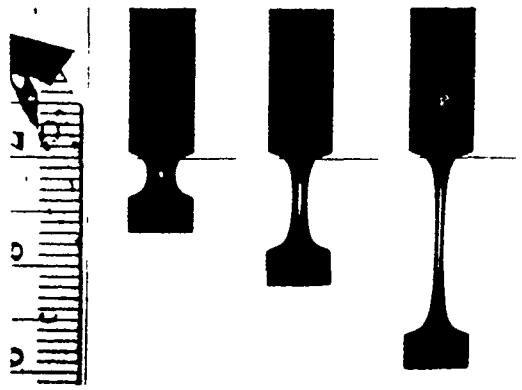

Figure 1. Time Photo of ASTM Oil Stretched by (0.81gm) Cylinder

Table 1. Results for a 33 Poise Newtonian Oil Stretched by a 0.81 gm Cylinder

Time(s)	$a(cm/s^2)$	r(cm)	$\dot{\epsilon}\ (s^{-1})$	η_e(poise)
.036	291	.203	34.4	123.6
.041	366	.186	39.3	114.3
.046	467	.169	45.1	100.8
.050	575	.151	47.1	95.4
.055	636	.134	51.0	94.8
.059	701	.122	52.3	90.3
.064	764	.107	54.6	86.1
.068	812	.093	57.6	83.1
.073	853	.081	56.3	84.3
.077	870	.073	58.4	87.3
.082	897	.066	50.1	92.7

The reported accelerations were graphically determined from slopes drawn to the velocity versus time curve. The elongation rate was similarly determined from the corresponding ligament radius versus time curve. Once the cylinder had fallen about 2 mm which occurred in about 0.05 sec, good agreement between the measured elongational viscosity and the Trouton prediction of 99 poise was observed.

Even better agreement was observed for the five other Newtonian trials conducted (Table 2). The reported elongational viscosities are the average values measured after the cylinder has fallen 2 mm. Prior to the 2-mm

displacement, the measured elongational viscosities were always greater than that predicted for simple extensional flow, indicating that the initial deformation is not merely simple extensional flow. The two trials performed with the heavier 2.15-g cylinder demonstrated how it is possible to increase the deformation rate of the stretching process.

Table 2. Newtonian Liquid Test Results

Fluid	Temp. (°F)	Cyl Mass (gm)	$\dot{\epsilon}$ (s^{-1})	η_e (poise)	$3\eta_o$ (poise)
ASTM Oil (S2000)	85	0.81	45-58	89	89
ASTM Oil (S2000)	77	2.15	65-68	146	150
ASTM Oil (S600)	85	0.81	73-90	29	27
Silicone Oil	85	0.81	56-70	104	99
Silicone Oil	85	2.15	68-77	99	99
Glycerol	83	0.81	92-105	12	12

VISCOELASTIC RESULTS

A 7.6-g/dL solution of K-124 diethylmalonate (DEM) was tested using the free falling cylinder device. K-125 is a copolymer of 80% polymethyl methacrylate and 20% poly (ethyl/butyl acrylate) with a molecular weight average of about 2 million. The shear viscosity and first normal stress difference was measured as a function of shear rate with a cone and plate viscometer and are reported elsewhere.[8]

Figure 2 is a plot of the fall velocity versus time measured to the 0.81 and 2.15-g cylinders. For the heavier cylinder, the initial 2-mm displacement occurred in about 0.02 seconds, while for the 0.81-g cylinder, it took about 0.05 seconds to fall the same distance. For both trials, shortly after the 2-mm distance, a constant fall acceleration was measured.

Figure 3 is a ln-ln plot, the ligament radius versus time for the two viscoelastic trials. A radius of about 0.13 cm corresponds to a 2-mm displacement of the falling cylinder. As observed by the good linear fit to the data, the radial time dependence is well approximated by a power law relationship. With this relationship, one can easily show that the elongation rate for both trials varies inversely with time.

Figures 4 and 5 show the measured elongational viscosities and deformation rates plotted versus time for the trials with 0.81-g and 2.15-g cylinders, respectively. The data clearly indicates that the elongational viscosity is much greater than that predicted for a Newtonian liquid. In addition, a comparison of the two figures shows that the rate at which the viscosity increases with time depends upon the rate at which the ligament is stressed. When the ligament is stressed at a higher rate

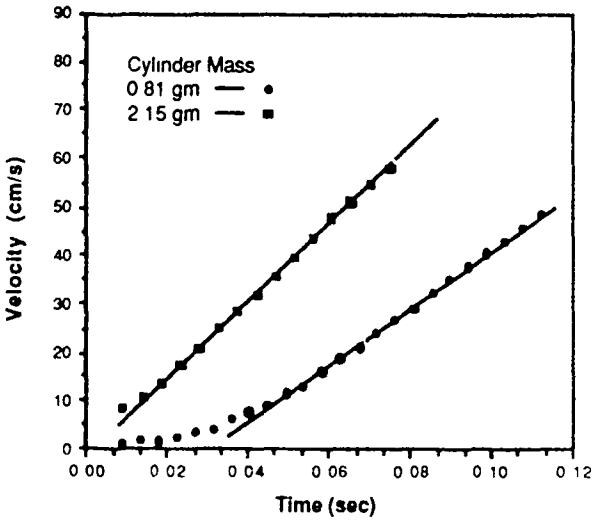

Figure 2. Fall Velocity versus Time for a K125/DEM Solution (7.6 g/dL) Stretched by a 0.81 and 2.15 gm Cylinder

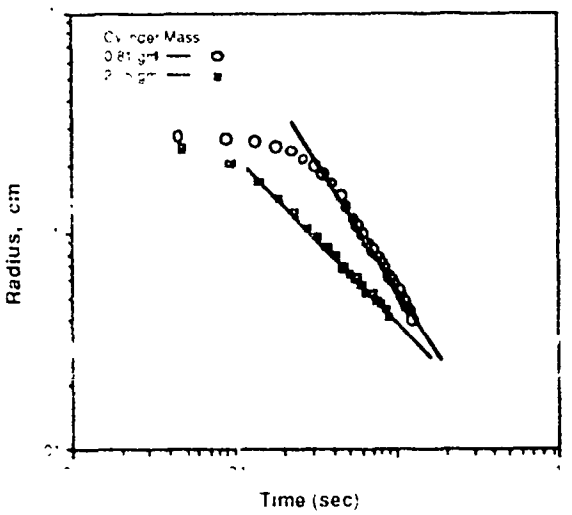

Figure 3. A Ln-Ln Plot of Radius versus Time for a Solution of K125/DEM Solution (7.6 g/dL) Stretched by a 0.81 and 2.15 gm Cylinder

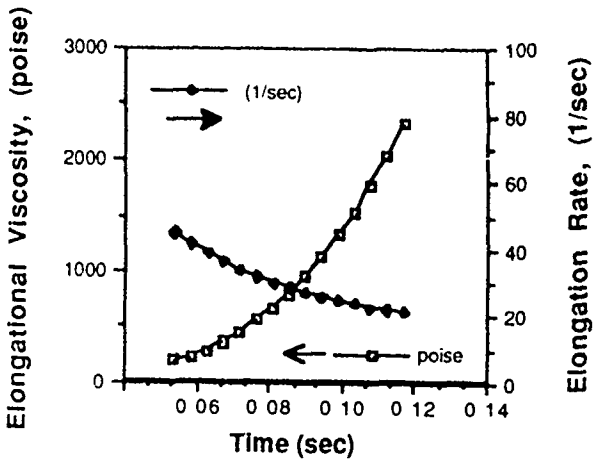

Figure 4. Elongational Viscosity and Deformation Rate Measured for a K125/DEM Solution (7.6 g/dL) Using a 0.81 gm Cylinder

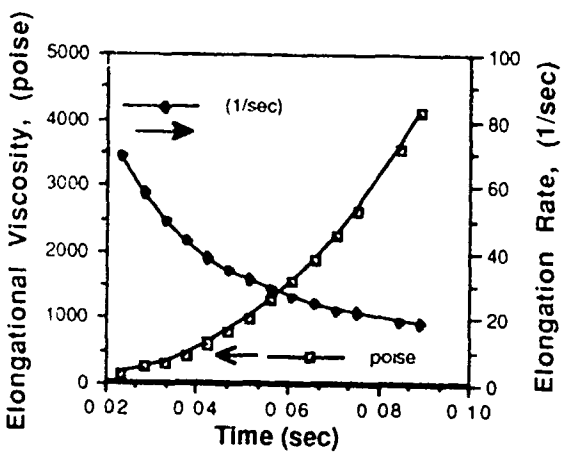

Figure 5. Elongational Viscosity and Deformation Rate Measured for a K125/DEM Solution (7.6 g/dL) Using a 2.15 Cylinder

by using the heavier cylinder, the elongational viscosity increases more rapidly with time.

CONCLUSION

A novel liquid-stretching device was successfully developed, and its usefulness in generating simple extensional flow fields with Newtonian liquids to measure the extensional viscosity was demonstrated. Viscoelastic liquids were tested with the device, and it is indicated that the elongational viscosity increases with time and is significantly greater than that of a comparable viscous Newtonian liquid. Since small liquid quantities are required for testing and the apparatus can fit conveniently into a glove box, the elongational characterization of toxic chemical agents are now possible.

REFERENCES

1. J.E. Matta and R.P. Tytus, "Viscoelastic Breakup in a High Velocity Airstream," J. Appl. Polymer Sci. Vol. 27, pp 397-405 (1982).

2. J.E. Matta, R.P. Tytus and J.L. Harris, "Aerodynamic Atomization of Polymeric Solutions," Chem. Eng. Com. Vol. 19, pp 192-204 (1983).

3. K.C. Chao, C.A. Child, E.A. Gren, and M.C. Williams, "The Anti-Misting Action of Polymer Additives in Jet Fuels," 53rd Annual Meeting of the Society of Rheology, KY, Oct 11-15, (1981).

4. M. Goldin, J. Yerushaimi, R. Pfeffer, and R. Shinnar, "The Stability of Viscoelastic Capillary Jets," J. Fluid Mech. Vol. 38, p 689 (1969).

5. S.L. Goren and M. Gottlieb, "Surface-Tension-Driven Breakup of Viscoelastic Threads," J. Fluid Mech. Vol. 120, pp 245-266 (1982).

6. C.J.S Petrie, Elongational Flows, Pitman Publishing Limited, London, England, 1979.

7. F.T. Trouton, Proc. Roy. Soc. Vol. A77, p 426 (1906).

8. J.E. Matta, "A Method of Ligament Stretching at High Extension Rates", CRDEC-SP-005, pp 11-17, (1989).

SILICONE FLUID RHEOGONIOMETER MEASUREMENTS AND THEIR APPLICATION TO DESPIN MOMENT STUDIES IN A SPINNING AND CONING CYLINDER

Raymond P. Tytus
U.S. Army Chemical Research, Development and Engineering Center
Aberdeen Proving Ground, MD 21010-5423

ABSTRACT

A Weissenberg Rheogoniometer was used to measure the viscosity and normal stress of a series of high viscosity silicone 200 fluids that were used in despin moment studies of a spinning and coning cylinder. The measurements indicated significant normal stress, and at the higher shear rates tested, viscosity shear thinning. The fluid rheology data was compared with two simple constitutive relationships and a suitable fit was found using a differential model. Possible model fluid parameters were applied to theoretical calculations of the despin moment for viscoelastic fluids contained in an infinitely long cylinder. Calculated despin moments were found to compare favorably with test results by proper choice of model constants.

INTRODUCTION

Recent liquid filled projectile instability studies by Miller and Weber[1] have confirmed that high viscosity liquids can produce significant despin moments which reduce the spin rate of the shell. Theoretical studies by Herbert[2] for newtonian liquids have established the variation in despin moment as a function of reynolds number. While test results obtained for the silicone fluids showed general agreement with theory for reynolds numbers above 30, anomalies were seen at lower reynolds number corresponding to the higher viscosity liquids. The liquids used by Miller in his test fixture were silicone 200 fluids manufactured by the Dow Chemical Company. These liquids are considered viscosity standards for many applications and can be obtained in specific viscosities and also blended to obtain a wide viscosity range. Based on studies by other workers[3,4], it has been

shown that the silicone fluids do exhibit elasticity and shear thinning is indicated at high shear rates. It was decided that accurate rheological measurements of the silicone fluids were necessary in order to determine if viscoelastic properties were significant and possibly responsible for the lack of agreement of experimental data with theory developed for newtonian fluids.

WEISSENBERG RHEOGONIOMETER

A model R18 Weissenberg Rheogoniometer was used to measure the rheological properties of the silicone fluids. The unit was used in the plate and cone steady rotational configuration where stress measurements can be obtained for both shear and normal stress at shear rates up to 5000 sec-1. In practice, however, the maximum shear rate at which one can obtain reliable data is much lower and is dependent on inertia and temperature effects of the liquid under test.

WEISSENBERG TEST RESULTS

Viscosity and normal stress test results for the silicone 200 fluids are shown in figure 1. Shear thinning is indicated at the highest shear rate for each fluid. For the higher viscosity fluids this occurred at shear rates between 10 and 100 sec-1. A normal stress was also measured for all fluid viscosities.

NON-NEWTONIAN EFFECTS ON DESPIN MOMENT

Early in the test program, the instability studies were extended to include the effect of viscoelastic liquid properties on the despin moment. Theoretical studies were made by Rosenblat[5], et al, which calculated the despin moment for simple viscoelastic models using two techniques. The more complex and accurate technique involved calculations using a finite element method. The other technique, which was used in this paper, involved calculations based on assuming an infinitely long cylinder. This technique was also used by Herbert for calculating theoretical despin moments for newtonian liquids. It should be pointed out that the results are only approximate and pertain only to small spin ratios (this was the case in Miller's test system).

In his report, Rosenblat indicated the difficulty in determining the model to use for describing non-newtonian flow. There is no constitutive relationship that can be applied to all flows of all non-newtonian liquids. On the other hand, a constitutive equation describing specific flows may be applicable for a wide range of fluids. Rosenblat also indicated that it is not known if shear thinning, normal stress, elongational viscosity, shear relaxation or some combination or all of these is significant in any real flow problem. He, therefore, restricted himself to testing and comparing simple consitutive relationships to experimental data.

Rosenblat selected two viscoelastic models to test, a second order fluid model and a differential model. In a second order fluid, shear thinning is not predicted but it does predict a normal stress (a quadratic function of shear rate). Two constants define this model, a zero shear

viscosity η_0 and a relaxation time constant λ . For the differential model, a modified version of the Oldroyd 8 constant model was proposed. Three constants define the model which exhibits both shear thinning and also normal stress behavior. A constant shear viscosity η_0, a relaxation time constant λ and a retardation time constant λ_r, where ϵ defines the λ_r/λ ratio. The zero shear viscosity is the same in both models and the relaxation time constant for ϵ=0 is the same relaxation time constant for a second order fluid.

A Basic Language computer program was written to calculate the three constants in the differential model for each of the silicone fluids tested. From above, this also calculates the constants for a second order fluid. The normal stress data was used to determine the relaxation time constant λ , for experimental values of normal stress, zero shear viscosity and shear rate as a function of ϵ =0, 0.2 and 0.4. Table 1 shows

TABLE 1

VISCOSITY	RELAXATION TIME		
KCS ϵ =	0	.2	.4
600	.0165	.0207	.0277
300	.0100	.0127	.0170
100	.0028	.0035	.0047
10	.0017	.0021	.0028

the results of these calculations. These fluid constants were then used to calculate the despin moment using the equation developed by Rosenblat for viscoelastic fluids.

DESPIN MOMENT CALCULATIONS

The despin moment equation calculated by Rosenblat is shown on page 34 of his final report. The equation was put into a Basic Language program for use on an Apple compatible computer for both the second order and differential model. The software was structured such that the required input parameters would be entered as input data on request by the program. The first required input is the fluid Deborah number which was an elastic parameter defined by Rosenblat in his report. This number is proportional to the product of fluid relaxation time constant and zero shear viscosity. If a zero is entered for the Deborah number of the liquid, the program then calculates the response for a newtonian fluid as a function of reynolds number. If a non-zero Deborah number is entered, the software then requests the reynolds number range for which to make the calculations. This was programmed as such because test data was obtained for each fluid viscosity over a limited range of reynolds number because of limitations in the spin rate of the test fixture. Thus, the calculated values of despin moment would cover only the actual range used in the test program.

DESPIN MOMENT RESULTS

Figure 2 shows the test results obtained by Miller and Weber for the

silicone 200 fluids. Included in the figure are the theoretical curves obtained by both Herbert and Rosenblat for the despin moments. The data points which deviate from the theoretical curve at the low reynolds numbers, although not noted as such, correspond to silicone viscosities of 600KCS, 300KCS and 100KCS going from left to right. If curves are drawn through the data points for each viscosity, a family of curves can be established for these three silicone viscosities at low reynolds numbers. The 10KCS data points appear to fall on the theoretical prediction of despin moment.

Figure 3 shows the calculated despin moments for both viscoelastic models using parameters shown in table 1. For the differential model, only the results for ϵ =0 is shown. Included in each figure is the despin moment response for a newtonian fluid. Results for the second order fluid model show very small despin moments at low reynolds number for the higher viscosity fluids. This does not agree with the test data. For the differential model the despin moment response for the 600KCS fluid rises sharply near a reynolds number of one and returns to approximately a value of 0.2 at a reynolds number of 3 (this range of 1-3 corresponds to the actual range used in the study). The 300KCS fluid has two peaks in the 2-8 reynolds number range, where as, the 100KCS fluid has one peak in the 5-20 reynolds number range. In all three cases the peaks extend well beyond the despin moment scale range of .6. These results agree with the trend in the experimental data which shows significant despin moments for the higher viscosity fluids while theory predicts very low values.

For the other two values of ϵ, the peaks noted above are significantly reduced but the resultant curves do not approach that of the test data especially for the 600KCS and 300KCS fluid viscosities which indicated higher experimental despin moments.

Based on the above analysis, the differential model predicts a significant increase in despin moment for the higher viscosity silicone fluids at low reynolds number compared to the theory for newtonian fluids. However, full agreement with test data is not indicated.

Much better agreement with test data can be found if one substitutes a Deborah number of 0.3 times the calculated value for ϵ=0 obtained using the differential model. Figure 4 shows the resultant despin moments for this condition. Also shown for comparison, is Miller's test data. We see that the 600KCS and 300KCS fluids show a sharp rise with reynolds number. The 100KCS fluid shows a rise and peak at about a reynolds number of 20 and the 10KCS shows a decreasing trend very close to the newtonian prediction. All of these fluids behave very similar to the actual test results.

CONCLUSIONS

A Weissenberg Rheogoniometer was used to measure the viscosity and normal stress for a series of silicone 200 test fluids. Results indicated non-newtonian behavior in the form of shear thinning and normal stress. Shear thinning occurred at the higher shear rates tested.

Using the Weissenberg data, parameters for two viscoelastic models were established. This was done in order to explain anomalies with theory developed for newtonian fluids in experimental despin moment test data for a spinning and coning cylinder. Using a theoretical predictive equation for calculating the despin moment for viscoelastic liquids, second order fluid model results did not agree with observed test data behavior. On the other hand, the differential model produced results which agreed with the general trends in the test data. Total agreement was not achieved. However, much better agreement with test data was found for a Deborah number equal to .3 times the calculated differential model value for ϵ=0. From this analysis, it appears that the discrepancies of despin moment test data with theory developed for newtonian fluids can be attributed to the viscoelastic properties of the higher viscosity silicone 200 fluids.

REFERENCES

1. M.C. Miller and D.J. Weber, "LIQUID INDUCED ROLLING AND YAWING MOMENT COEFFICIENTS FOR VISCOUS NEWTONIAN FLUIDS IN A SPINNING AND CONING CYLINDER," 1988 Proceedings of CRDEC Scientific Conference on Chemical Defense Research

2. T. Herbert, "FLUID MOTION IN A ROTATING AND NUTATING CONTAINER," CRDC-CR-84087, July 1984

3. D.V. Boger and R. Binnington, "SEPARATION OF ELASTIC AND SHEAR THINNING EFFECTS IN A CAPILLARY RHEOMETER," Transactions of the Society of Rheology, 21:4, 515-534, 1977

4. D.V. Boger and H. Nguyen, "A MODEL VISCOELASTIC FLUID," Polymer Engineering and Science, Vol. 18, No. 13, October 1978

5. S. Rosenblat, A. Goodling and M.S. Engleman, "FINITE ELEMENT CALCULATIONS OF VISCOELASTIC FLUID FLOW IN A SPINNING AND NUTATING CYLINDER," CRDEC-CR-87021, December 1986

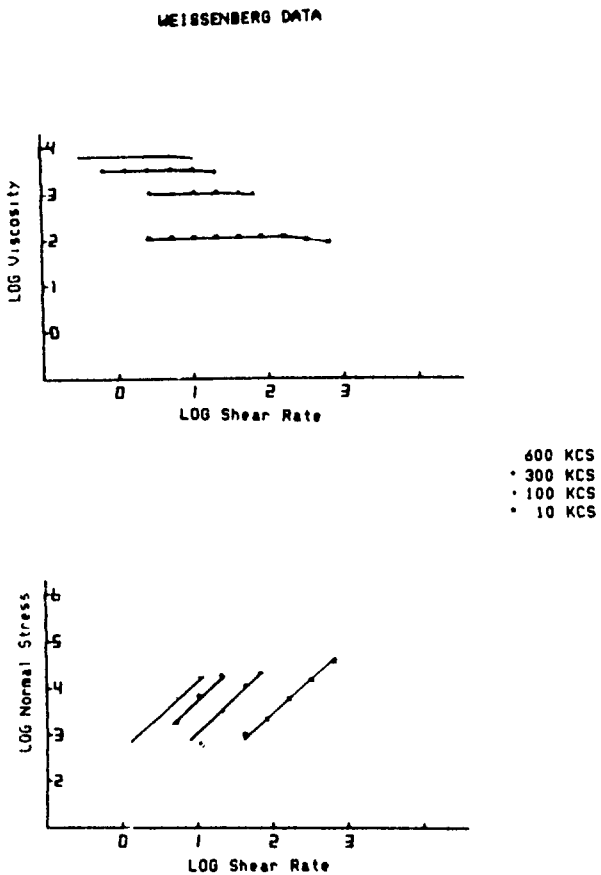

Figure 1

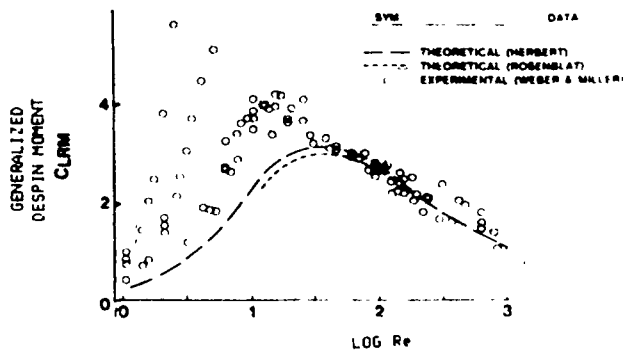

Figure 2

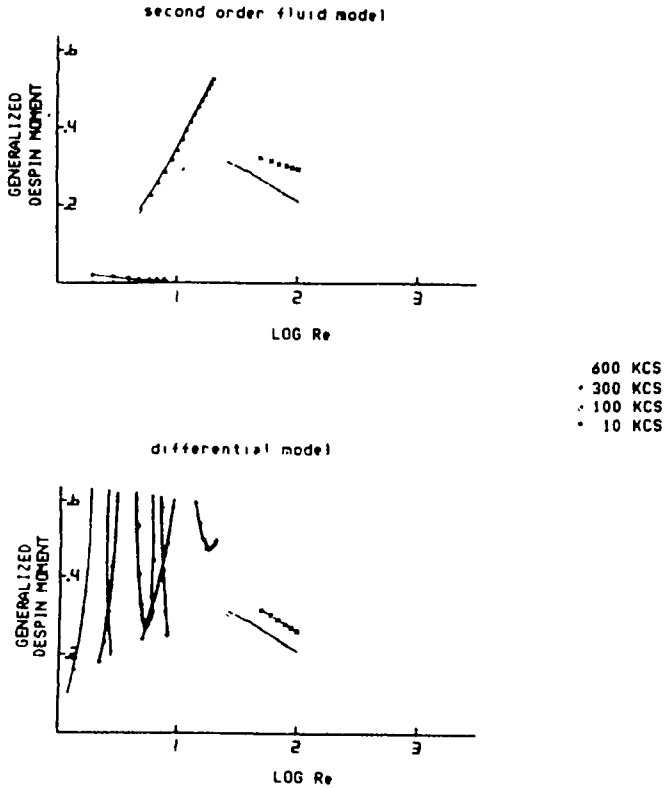

Figure 3

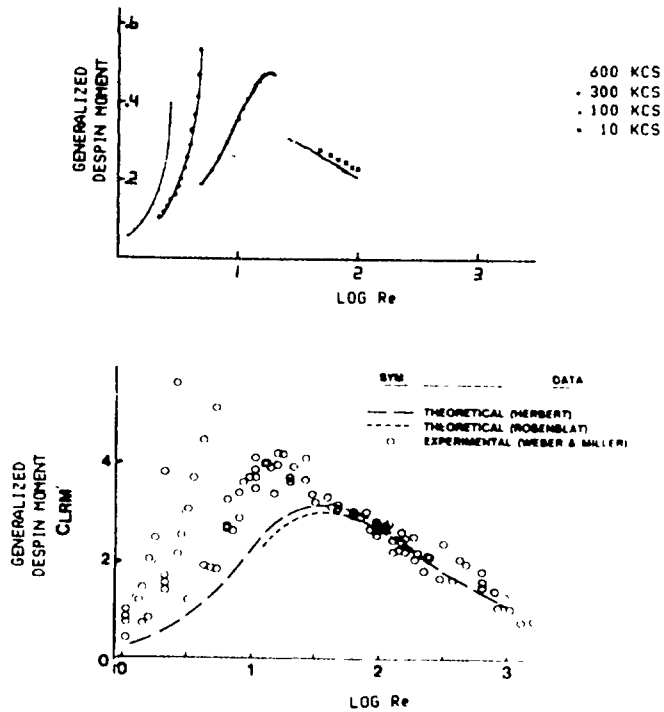

Figure 4

BLANK

COMPUTATIONAL FLUID DYNAMICS METHOD FOR LOW REYNOLDS NUMBER FLOW IN A PRECESSING/SPINNING LIQUID-FILLED CYLINDER WITH ROUNDED ENDCAPS

Michael J. Nusca

Launch and Flight Division
Ballistic Research Laboratory
Aberdeen Proving Ground, MD 21005

Abstract

The three-dimensional, steady, laminar, Navier-Stokes equations are solved using an implicit finite-difference scheme based on successive-over-relaxation. These numerical simulations are used to predict the behavior of incompressible liquids undergoing steady spin and steady precession at a fixed precession angle. The liquid is contained in a fully-filled cylinder with flat or rounded endcaps. These numerical simulations can predict steady viscous and pressure moments due to the liquid fill at low Reynolds number. These moments tend to increase the precession angle and reduce the spin rate of the container. Liquid-induced roll and side (yaw) moments are computed as functions of endcap height to cylinder radius ($0 \leq e/a \leq 1$), cylinder half-height to radius ($.5 \leq c/a \leq 4$), Reynolds number ($10 \leq \mathrm{Re} \leq 300$), ratio of precession to spin rate ($.05 \leq \tau \leq 95$), and precession angle ($\alpha_c = 2^\circ$). For a given cylinder, rounded endcaps can decrease the resonant liquid-induced moment by about 25% and shift the resonance to a smaller Reynolds number (for fixed coning frequency) Thus rounded endcaps can produce flight stability for some containers with highly viscous liquid payloads.

Introduction

The flight stability of liquid-filled, spin-stabilized projectiles has been considered for a wide variety of conditions. Originally, theories and experiments were centered about the case of large Reynolds number ($\mathrm{Re} = a^2\dot{\phi}/\nu$) for cylindrical payload containers.[1,2] Non-steady effects must be considered for practical applications and large Reynolds number, for example, spin-up. However, if the Reynolds number is small ($\mathrm{Re} < 500$), the effects of unsteady processes may be neglected. It is then possible to employ a steady finite-difference solution to the incompressible Navier-Stokes equations for a fixed precession angle and steady rates of spin and precession. This paper describes the steady-state finite-difference method of Strikwerda[3] that has been extensively investigated by Nusca[4] for fluid-filled cylindrical containers, and the extension of this code to non-cylindrical axisymmetric geometries. In particular, the case of a cylinder with rounded endcaps (see Figure 1) is investigated.

Background

Strikwerda and co-workers[3] have developed a steady-state, finite-difference, incompressible Navier-Stokes method for fully-filled cylindrical containers. The code employs an implicit, iterative, finite-difference method based on modified line successive-over-relaxation and a pressure update from the gradient of the velocity field. This code (denoted UWISC for University of Wisconsin) employs a non-uniform grid to resolve the velocity and pressure gradients near the cylinder walls, central finite-differences in the radial and axial directions, and pseudo-spectral differencing to represent the azimuthal dependence. Comparison of UWISC with other finite-difference codes, finite-element codes, and analytical methods is reported in Reference 4.

A spatial eigenvalue method has been developed by Hall, Sedney, and Gerber[5] (denoted HSG) for fully-filled cylindrical containers and constant-amplitude coning motion. Murphy et.al.[6] extended this method to partial-fill, fully-filled with central rod, two immiscible liquids, and slow changes to the amplitude of the coning motion. The Navier-Stokes equations are written in an inertial reference frame. They are then reduced to a set of linear partial differential equations based on small angle coning motion, and linear departures from solid body rotation are considered. No slip boundary conditions are imposed at the cylinder walls which makes all flow variables proportional to $e^{i(ft-\theta)}$ where f is the component of the projectile spin along the symmetry axis and t is time. A particular solution was employed which satisfies the axis and lateral wall boundary conditions but not endwall conditions. The eigenvalue problem is obtained using separation of variables from which an infinite sequence of complex eigenvalues is generated. The eigenvalues are determined by an iterative process for which sufficiently accurate initial estimates are required for convergence. The flow variables are expressed as eigenfunction expansions with the coefficients determined by satisfying the endwall boundary conditions. A least squares and collocation method have been used for this purpose. Comparisons of measured liquid moment coefficients with the spatial eigenvalue code (HSG) and UWISC results[4] have shown the consistency of both methods. However, since spatial eigenvalue methods yield results in significantly less computer run time, they are perhaps the preferred scheme for cylindrical containers.

A theory for non-cylindrical, axisymmetric, liquid-filled containers has been presented by Wedemeyer.[7] This theory is derived from the linearized, inviscid Navier-Stokes equations, thus $\mathrm{Re} = \infty$. Using this theory, the approximate eigen-frequencies of the liquid oscillations can be computed. Liquid moments occur whenever any of the eigen-frequencies fall within a certain bandwidth of the fast yaw (precessional) frequency of the projectile. Liquid-filled, non-cylindrical cavities can be examined where the radius of the cavity is a slowly varying function of the distance along the cavity axis (z-direction), $|da/dz| \ll 1$. For cylindrical cavities, the inviscid eigen-frequencies are computed exactly and given in Stewartson tables.[8] For small deviations from cylindrical shape, small changes of the eigen-frequencies must be expected. Karpov[9] showed experimentally that rounding the corners of the cylindrical cavity produced very little effect on the range of instability. However, considerable change resulted from modifications such as the conical reduction of one or both ends of the cavity. Wedemeyer's theory agreed favorably with Karpov's data.

Written at the U.S. Army Ballistic Research Laboratory (BRL), the present CFD code is a modified version of UWISC (denoted UWISC/BRL). Like the UWISC code, the UWISC/BRL code uses a finite-difference method for the non-linear, fully viscous Navier-Stokes equations. The computational algorithm is not efficient for flow Reynolds numbers above 300 (see **Results**). The contained flowfield and the liquid-induced moments are computed for axisymmetric containers of arbitrary shape. One application is for cylinders with rounded endcaps where $|da/dz| \geq 0$. The endcap is a circular arc where the cap height above the flat endwall, at the axis of the cylinder, is e/a. For a hemispherical endcap, $e/a = 1$ (see Figure 1).

Murphy[10] suggested the use of roll and side moment coefficients (C_{LRM} and C_{LSM}) for small, fixed precession angles (α_c) as defined below:

$$\text{Roll Moment} = m_l a^2 \dot{\phi}^2 [C_{\mathrm{LRM}_O} + \tau K_c^2 C_{\mathrm{LRM}}] \tag{1}$$

$$\text{Transverse Moment} = m_l a^2 \dot{\phi}^2 \tau [C_{\mathrm{LSM}} + iC_{\mathrm{LIM}}] K_c e^{i\phi_c} \tag{2}$$

where, m_l is the mass of liquid in a fully-filled cylindrical container ($2\pi\rho_l a^2 c$), τ is the ratio of coning rate to spin ($\dot{\phi}_c/\dot{\phi}$), C_{LRM_O} is the liquid roll moment coefficient due to transient liquid effects (i.e. spinup), C_{LIM} is

the liquid in-plane moment coefficient, K_c is $\sin\alpha_c$, α_c is the precession angle, and ϕ_c is the phase angle of the coning motion. Further, Reference 10 gives a relationship between the moment coefficients for the linearized, viscous Navier-Stokes equations. Hence, for small precession angles and independent of the Reynolds number $C_{LRM} = -C_{LSM}$. For arbitrary precession angles, Rosenblat[11] has shown that, $C_{LRM} = -C_{LSM}\tan\alpha_c$.

Computational Approach

In this section the implicit finite-difference method is described. The approach follows that of Strikwerda[3] for a cylindrical container. In certain aspects of the method basic changes were required for a non-cylindrical container (e.g. computational grid, grid stretching, boundary conditions). In particular the numerical code was originally written assuming cylindrical geometry throughout. Certain other aspects of the method are applicable to a non-cylindrical, axisymmetric container (e.g. psuedo-spectral differencing). These differences and similarities in the method are highlighted below.

Consider a fluid-filled container which is spinning about its geometric axis with spinrate Ω_s and about the coning axis with spinrate $\dot{\phi}_c$ (see Figure 1). The coning axis is fixed in the inertial (Earth-fixed) reference frame. The container axis is inclined to the coning axis by a fixed angle, α_c. The fluid velocity $\vec{V}$ and pressure p in the container are governed by the incompressible Navier-Stokes equations for constant viscosity (μ). These equations in an inertial, cartesian coordinate system are given by,

$$\rho\frac{D\vec{V}}{Dt} = -\nabla p + \mu\nabla^2\vec{V} \tag{3}$$

$$\nabla\cdot\vec{V} = 0 \tag{4}$$

These equations can be transformed to a non-inertial reference frame so that the fluid motion becomes steady and thus time derivatives are zero, $\partial/\partial t = 0$. This reference frame rotates with angular velocity $\dot{\phi}_c$ about the coning axis and was also used by Strikwerda.[3] Reference 3 gives the details of the transformation. In addition, the cylindrical coordinate system is used in which the radial, azimuthal, and axial directions are denoted r, ϕ, z with velocity components u, v, w. The cylindrical coordinate system is also used in the endcaps where the grid lines are not aligned with the r, z directions.

The equations and variables are non-dimensionalized by the maximum radius of the container (a) and with the inertial spinrate ($\dot{\phi} = \Omega_s + \dot{\phi}_c\cos\alpha_c$) and the container radius, as the velocity scale ($a\dot{\phi}$). Thus, the Reynolds number and the precessional frequency are defined as, $\mathrm{Re} = a^2\dot{\phi}/\nu$ and $\tau = \dot{\phi}_c/\dot{\phi}$, where the kinematic viscosity of the fluid is $\nu = \mu/\rho_l$. The solid-body rotation is subtracted from the velocity, and the pressure is redefined such that,

$$\vec{V} = \vec{V}_{\text{computed}} + \vec{V}_{\text{solid-body}} + \vec{\tau}\times\vec{r} \tag{5}$$

$$p = p_{\text{computed}} + \frac{r^2}{2} + r^2\tau\cos\alpha_c + \frac{\tau^2}{2}\left[(r\cos\phi\cos\alpha_c + z\sin\alpha_c)^2 + r^2\sin^2\alpha_c\right] \tag{6}$$

The resultant equations are given by Strikwerda[3] and Nusca[12].

The equations of motion are solved on a discrete grid that covers the entire flow domain. Figure 2 shows a typical grid for a cylinder of aspect ratio $c/a = 1.486$ with rounded endcaps of height, $e/a = 1$. Only the portion of the container bounded by $0 \le r/a \le 1, \phi = 0°, 0 \le z/a \le (c/a + e/a)$ is displayed in Figure 2. In this example there are 31 grid points in the r-direction, 81 grid points in the z-direction and 19 grid points in the endcaps (i.e. 5° spacing). The particular grid configuration was chosen for the endcap region to insure that grid cells are four-sided (in the ϕ = constant plane) except at the axis, $r/a = 0$. The axis grid line is a boundary, along which boundary conditions are prescribed, and is not part of the computational domain. Thus multiple grid points at this location are inconsequential. Grid stretching is used to insure adequate grid spacing at the walls so that boundary layers and viscous shear stresses are accurately resolved. This is accomplished using the transformations given in Reference 13.

The numerical method used to solve the equations of motion is based on the finite difference scheme of Strikwerda[14] and a psuedo-spectral method. Finite differences are used to approximate derivatives in the radial (r) and axial (z) directions and the psuedo-spectral method is used to approximate derivatives in the azimuthal direction (ϕ). See Reference 12 for further details. Use of the psuedo-spectral method is possible since the flow variables vary in a periodic fashion in the ϕ direction. Since the non-cylindrical geometry under consideration in this work is also axisymmetric, the periodicity in ϕ is preserved in the endcaps. This results in substantial savings in computer memory and execution time requirements. The boundary conditions on the container walls follow from the no-slip condition for velocity and extrapolation from the interior flow for the pressure. The boundary conditions on the container axis (z-axis) are obtained using interpolation from neighboring grid points. Variables at the grid points on the container axis at the interface between the cylinder and the endcaps ($r = 0, z = |c/a|$) are assigned equal values. These values are obtained using interpolation from neighboring grid points.

The system of non-linear equations is solved using a modified line successive-over-relaxation method (LSOR). The method is described by Strikwerda[15] for the case of linear finite difference equations. Because the psuedo-spectral method is used in the azimuthal direction, line relaxation is utilized. In this case each line contains the grid points in the azimuthal direction for each value of the radial and axial coordinates. This approach is unchanged for the non-cylindrical axisymmetric geometry. The coupling between the velocity components and the natural periodicity of the azimuthal coordinate leads to a periodic system of equations. Thus the system of equations that must be solved to determine the velocity updates for each radial and axial grid location is a block tridiagonal periodic linear system. After the velocity has been updated by one pass of the LSOR, the pressure is updated using,

$$p^{m+1} = p^m - \beta\left(\nabla \cdot \vec{V}^{m+1}\right) \tag{7}$$

where m is the iteration index and β is a parameter. Thus $\nabla \cdot \vec{V} = 0$ is not solved but rather $\nabla \cdot \vec{V} = \delta$ where δ is on the order of the truncation error for a second-order scheme.

Calculation of Liquid-Induced Moments

Conservation of angular momentum for the steady flow in a control volume $\mathbf{V}$ with surface $\mathbf{S}$ rotating with constant angular rate Ω about a fixed axis requires,

$$\vec{M} = \int_{\mathbf{S}} \left(\vec{r} \times \vec{F}\right) \mathrm{dS} = \int_{\mathbf{V}} \vec{r} \times \left(2\vec{\Omega} \times \vec{V}\right) \rho \mathrm{dV} + \int_{\mathbf{V}} \vec{r} \times \left[\vec{\Omega} \times \left(\vec{\Omega} \times \vec{r}\right)\right] \rho \mathrm{dV} + \int_{\mathbf{S}} \left(\vec{r} \times \vec{V}\right) \rho \vec{V} \cdot \mathrm{dS} \tag{8}$$

where the velocity $\vec{V}$ is measured relative to the non-inertial reference frame. In this equation, $\vec{M}$ and $\vec{F}$ are the resultant moment on the control volume and the stress acting on the walls of the fully-filled container, respectively. The last term on the right-hand side of the equation vanishes since $\vec{V} \cdot \mathrm{dS} \equiv 0$ on all boundaries. Thus the moment can be calculated using the "surface integral" approach or the "volume integral" approach. The moment can be expressed in terms of the cartesian components, $\vec{M} = (M_x, M_y, M_z)$, which denote the yaw, pitch and roll moments, respectively. The yaw and roll components correspond to the side and roll moment coefficients, C_{LSM} and C_{LRM}. Using the "volume integral" approach, Herbert[16] and Rosenblat[11] have shown that the non-dimensional yaw and roll moments (non-dimensionalized by $\rho_l a^5 \dot{\phi}_c^2$) for a cylindrical control volume can be expressed as,

$$M_x = \frac{2\cos\alpha_c}{\tau} \int_{-\eta}^{\eta} \int_0^{2\pi} \int_0^{r_{\max}} \left[w r^2 \cos\phi\right] \mathrm{d}r\mathrm{d}\phi\mathrm{d}z \tag{9}$$

$$M_z = -M_x \tan\alpha_c \tag{10}$$

thus,

$$C_{\mathrm{LSM}} = \frac{1}{\pi(c/a)\tan\alpha_c} \int_{-\eta}^{\eta} \int_0^{2\pi} \int_0^{r_{\max}} \left[w r^2 \cos\phi\right] \mathrm{d}r\mathrm{d}\phi\mathrm{d}z \tag{11}$$

$$C_{LRM} = -C_{LSM}\tan\alpha_c \tag{12}$$

where $\eta = c/a$ and $r_{max} = 1$. Murphy[6] has also derived and utilized the "volume integral" in the spatial-eigenvalue method for highly viscous liquids. For a control volume consisting of a cylinder with rounded endcaps, Equations 11 and 12 are used with $\eta = c/a + e/a$ and $r_{max} = r_{max}(z)$.

Results

In this section the effects of rounded endcaps, versus flat endwalls, on the liquid-induced side moment coefficient, C_{LSM}, is examined for a fully-filled cylindrical container. Results are shown for the original cylinder-only version of the finite-difference code, denoted UWISC, and the Hall-Sedney-Gerber spatial eigenvalue code, denoted HSG, for cylindrical geometries. For non-cylindrical geometries, results from the generalized axisymmetric geometry version of the finite-difference code, denoted UWISC/BRL, are presented. Moments were computed using both the "surface integral" and the "volume integral" approach. These methods yielded equivalent numerical results for all cases presented in this report. However, the "volume integral" approach requires less computational effort. Because the HSG code is formulated assuming a small coning angle, all of the UWISC and UWISC/BRL computations were performed for $\alpha_c = 2°$. All UWISC computations presented in this section were performed using the same grid dimensions with variable grid wall spacing All HSG computations were performed using 15 to 40 eigenvalues for Re 21.5 to 300. In some cases a cubic spline was used to join discrete data points in the following figures.

Variation of C_{LSM} with e/a.

Figure 3 shows the variation of C_{LSM} with endcap height, e/a, for a cylinder of aspect ratio, $c/a = 1.486$. The height of the endcap is measured at the cylinder axis (see Figure 1). For $e/a = 0$ the container is a cylinder with flat endwalls, and for $e/a = 1$ the endcaps are hemispherical. The same value of C_{LSM} for the cylindrical geometry is produced by the UWISC/BRL and HSG codes. The value of C_{LSM} decreases with increasing endcap height, and reaches a minimum for $e/a = 1$. This suggests that the liquid side moment can be reduced by as much as 20% by rounding the endwalls of a cylinder with aspect ratio $c/a = 1$ 486 at Re = 50. The value of the coning frequency used in this figure ($\tau = .0469$) is typical of ballistic projectiles with liquid payloads. Since an endcap height of 1 represents the limiting case, all subsequent calculations are for $e/a = 1$.

Variation of C_{LSM} with Re.

Figure 4 shows the variation of C_{LSM} with Reynolds number for endcap heights of 0 and 1, and a cylinder of aspect ratio of 1.486. For the cylindrical geometry, both the UWISC/BRL and HSG codes show the same variation of liquid side moment with Re, including a maximum, or resonance, at about Re = 75. Results using the UWISC/BRL code for the same cylinder with hemispherical endcaps show a resonant condition at about Re = 50. In addition, the value of C_{LSM} at resonance is about 22% smaller for the cylinder with rounded endcaps. For Re = 21.5 the liquid side moment is actually 12% smaller for the cylinder with flat endwalls. However, for Re greater than the resonance value, the addition of rounded endcaps has reduced the C_{LSM} by as much as 55%.

As noted in a previous study[4] the UWISC code becomes computationally inefficient for for Re $\geq$ 300. Figure 5 shows the variation of computer (CRAY X-MP/48) CPU time with Reynolds number. In each case the solution for a particular Re was used as a starting solution for the subsequent Re solution. Since the computer time required increases in an almost linear fashion with Re when scratch starts are used, the restart method results in a substantial savings in computer run time. For Re $\leq$ 100, solutions can be achieved in 2 to 4 hours using about 30,000 grid points for the cylindrical geometry, and 7000 additional grid points

for the rounded endcaps. These values are considered more than adequate for $c/a = 1.486$. In the previous study[4] with cylindrical containers, computer run times were slightly less than 2 hours for the same value of c/a since a smaller grid was used. The Re=100 solution for the cylindrical container required slightly more computer time than the cylinder with rounded endcaps. The data from Figure 4 indicate that the maximum C_{LSM} also occurs at about Re=100. This indicates that rounding the cylinder endcaps may promote faster solution convergence. For larger values of Re, the computer run time rapidly increases beyond 5 hours and approaches 12 hours for Re = 300. Some reduction in run time ($\leq$5%) can be realized by changing the value of β in Equation 7 (i.e. a converged solution would require fewer iterations) or relaxing the convergence tolerance. Partially-converged solutions (i.e. using relaxed convergence tolerance) for Reynolds Numbers around 10 can require $\leq$2 CPU hours using a mini-computer (e.g. VAX 8600) and be used for preliminary design applications. This technique (i.e. using partially-converged solutions) results in severe degradation of the accuracy of C_{LSM} values for Re greater than about 20.

Variation of C_{LSM} with τ.

Figure 6 shows the variation of C_{LSM} with coning frequency for Re = 50, endcap heights of 0 and 1, and a cylinder of aspect ratio of 1.486. For the cylindrical geometry, both the UWISC/BRL and HSG codes show the same variation of liquid side moment with τ, including a resonance at $\tau = .5$. Results using the UWISC/BRL code for the same cylinder with hemispherical endcaps show a resonant condition at $\tau = .65$, with a value of C_{LSM} about 20% larger than the C_{LSM} for a cylinder. For τ greater than about .35, the liquid side moment is actually 50% smaller for the cylinder with flat endwalls. However, for τ smaller than the resonance value, the addition of rounded endcaps has reduced the C_{LSM} by as much as 19%.

As noted in a previous study[4] the UWISC code cannot be run for $\tau \geq 1$ whereas the HSG code has been used for coning frequencies greater than the spin frequency. This condition can be resolved by reformulating the UWISC code and dividing the governing equations by τ.

Variation of C_{LSM} with c/a.

Figure 7 shows the variation of C_{LSM} with cylinder aspect ratio for Re = 50, $\tau = .0469$, and endcap heights of 0 and 1. For the cylindrical geometry, both the UWISC/BRL and HSG codes show the same variation of liquid side moment with c/a, including a resonance at $c/a = 1$ 2. Results using the UWISC/BRL code for the same cylinder with hemispherical endcaps show a resonant condition at $c/a = .6$, at about the same value of C_{LSM}. For c/a greater than 1.0 the liquid side moment is up to 19% smaller for the cylinder with rounded endcaps. For c/a greater than 2 the value of C_{LSM} is only 2% smaller for cylinders with rounded endcaps. The value of C_{LSM} approaches 0 as c/a approaches 0 for both the cylinder with flat endwalls and the cylinder with hemispherical endcaps. In the case of the hemispherical endcaps, for $c/a = 0$ the container is a sphere For a sphere, the integration of pressures over the symmetric interior geometry will not produce a contribution to C_{LSM}. Additionally, viscous shear stresses will be zero since, for a sphere, steady rotation and precession is simply rigid body rotation about a different axis.

Conclusions

The three-dimensional, steady, laminar, Navier-Stokes equations are solved using an implicit finite-difference scheme based on successive-over-relaxation. The method of Strikwerda, for fluid-filled cylindrical containers, has been extended to non-cylindrical axisymmetric geometries. The liquid side moment coefficient for a cylinder with rounded endcaps is investigated using this code for Reynolds number, $10 \leq Re \leq 300$. Rounded endcaps can decrease the liquid-induced moment by as much as 55% for some values of the Reynolds number, coning frequency, and cylinder aspect ratio.

Further modification of the code (e.g. ellipsoidal endcaps, partial-fill, etc.) could be accomplished. However, a computational fluid dynamics code for time-dependent, three-dimensional, incompressible flow in arbitrary geometries has been written by Chakravarthy et.al.[17]. This code is a generalized version of a previous code [18,19] that was used for fully-filled cylindrical containers in steady coning motion and flow Reynolds Numbers as high as 500,000. The new code by Chakravarthy uses the same numerical scheme as the previous code but includes a zonal grid scheme to facilitate grid generation in containers of arbitrary shape. The code requires modification of the boundary conditions, reference frame, and equations of motion in order to compute liquids in precessing/spinning containers. However, this code can be more easily modified than UWISC/BRL for free surface boundary conditions, multiple liquids, time-dependent container motion and other cases of interest.

References

1. Murphy, C.H., "Angular Motion of a Spinning Projectile with a Viscous Liquid Payload," ARBRL-MR-03194, U.S. Army Ballistic Research Laboratory, Aberdeen Proving Ground, Maryland, August 1982 (AD A118676). Also, AIAA Journal of Guidance, Control, and Dynamics, Vol. 6, No. 4, pp.280-286, July-August 1983.

2. Gerber, N. and Sedney, R. "Moment on a Liquid-Filled Spinning and Nutating Projectile: Solid Body Rotation," ARBRL-TR-02470, U.S. Army Ballistic Research Laboratory, Aberdeen Proving Ground, Maryland, February 1983 (AD A125332).

3. Strikwerda, J. C., and Nagel, Y. M., "A Numerical Method for the Incompressible Navier-Stokes Equations in Three-Dimensional Cylindrical Geometry," Journal of Computational Physics, Vol. 78, pp. 64-78, 1988. Also, Strikwerda, J. C., and Nagel, Y. M., "A Numerical Study of Flow in Spinning and Coning Cylinders," CRDC-SP-86007, Proceedings of the 1985 Scientific Conference on Chemical Defense Research, Aberdeen Proving Ground, Maryland, April 1986.

4. Nusca, M. J., "Computational Fluid Dynamics Methods for Low Reynolds Number Precessing/Spinning Incompressible Flows," ARBRL-MR-03657, U.S. Army Ballistic Research Laboratory, Aberdeen Proving Ground, Maryland, April 1988 (AD A193891).

5. Hall, P., Sedney, R., and Gerber, N., "Fluid Motion in Spinning, Coning Cylinder via Spatial Eigenfunction Expansions," ARBRL-TR-2813, U.S. Army Ballistic Research Laboratory, Aberdeen Proving Ground, Maryland, August 1987.

6. Murphy, C.H., Bradley, J.W., and Mermagen, W.H., "Liquid Side Moment Exerted by a Spinning, Coning, Highly Viscous Liquid Payload," U.S. Army Ballistic Research Laboratory, Aberdeen Proving Ground, Maryland, report in preparation.

7. Wedemeyer, E.H., "Dynamics of Liquid Filled Shell: Non-Cylindrical Cavity," BRL Report No. 1326, U.S. Army Ballistic Research Laboratory, Aberdeen Proving Ground, Maryland, August 1966.

8. Stewartson, K., "On The Stability of a Spinning Top Containing Liquid," Journal of Fluid Mechanics, Vol. 5, Pt. 4, 1959.

9. Karpov, B.G., "Dynamics of Liquid Filled Shell: Resonance in Modified Cylindrical Cavities," BRL Report No. 1332. U.S. Army Ballistic Research Laboratory, Aberdeen Proving Ground, Maryland, August 1966

10. Murphy, C. H., "A Relation Between Liquid Roll Moment and Liquid Side Moment," AIAA Journal of Guidance, Control and Dynamics, Vol. 8, No 2, pp. 287-288, March-April 1985. Also, ARBRL-MR-03347 U.S. Army Ballistic Research Laboratory, Aberdeen Proving Ground, Maryland, April 1984 (AD A140658).

11. Rosenblat, S., Gooding, A., and Engleman, M. S., "Finite Element Calculations of Viscoelastic Fluid Flow in a Spinning and Nutating Cylinder," CRDEC-CR-87021, U.S. Army Chemical Research, Development and Engineering Center, Aberdeen Proving Ground, Maryland, December 1986.

12. Nusca, M.J., "Computational Fluid Dynamics Method for Low Reynolds Number Flow in a Precessing/Spinning Liquid-Filled Cylinder with Rounded Endcaps," ARBRL-MR-03792, U.S. Army Ballistic Research Laboratory, Aberdeen Proving Ground, Maryland, December 1989.

13. Nusca, M.J., "Numerical Simulation of Unsteady Incompressible Flow in a Partially-Filled Rotating Cylinder," ARBRL-TR-02915, U.S. Army Ballistic Research Laboratory, Aberdeen Proving Ground, Maryland, June 1988 (AD A196001).

14. Strikwerda, J.C., "Finite Difference Methods for the Stokes and Navier-Stokes Equations," SIAM Journal of Scientific and Statistical Computing, Vol. 5, No. 1, March 1984.

15. Strikwerda, J C., "An Iterative Method for Solving Finite Difference Approximations to the Stokes Equations," SIAM Journal of Numerical Analysis, Vol. 21, No. 3, June, 1984.

16. Herbert, T , "On the Viscous Roll Moment in a Spinning and Nutating Cylinder," CRDC-SP-86007, Proceedings of the 1984 Scientific Conference on Chemical Defense Research, Aberdeen Proving Ground, Maryland, April 1985.

17. Pan, D., and Chakravarthy, S.R., "Unified Formulation for Incompressible Flows," AIAA-89-0122, Proceedings of the 27th AIAA Aerospace Sciences Meeting, Reno, NV. January 9-12, 1989.

18. Kwak, D., and Chakravarthy, S.R., "A Three-Dimensional Incompressible Navier-Stokes Flow Solver Using Primitive Variables," AIAA Journal, Vol. 24, No. 3, March 1986, pp. 390-396.

19. Nusca, M.J., and Cooper, G.R., "Computational Fluid Dynamics Method for Unsteady Incompressible Rotating Flow with Impulsive Coning Motion," CRDEC-SP-89005, Proceedings of the 1988 Scientific Conference on Chemical Defense Research, Aberdeen Proving Ground, Maryland, 1989.

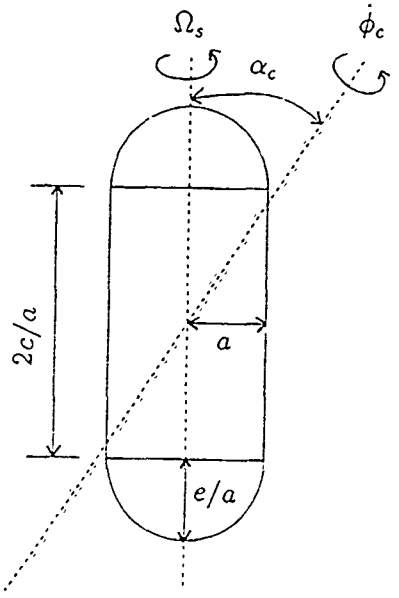

Fig. 1. Cylinder With Rounded Endcaps – Configuration and Nomenclature (Hemispherical Endcap Shown)

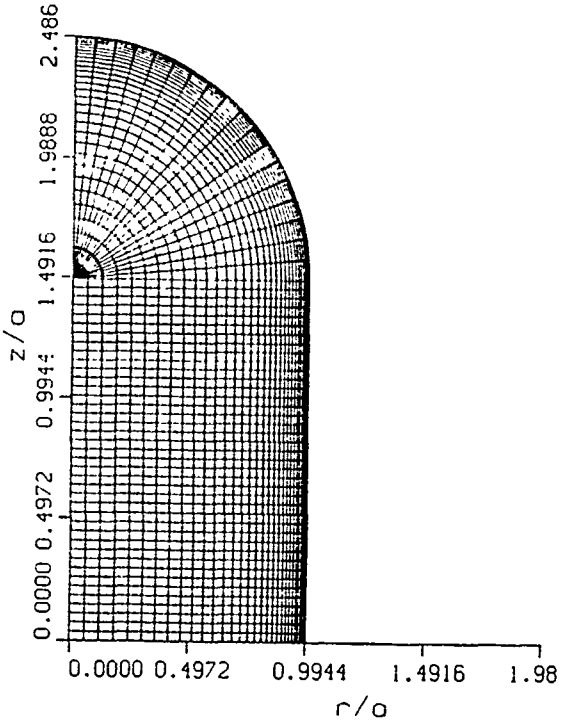

Fig. 2. Typical Computational Grid (Hemispherical Endcap Shown)

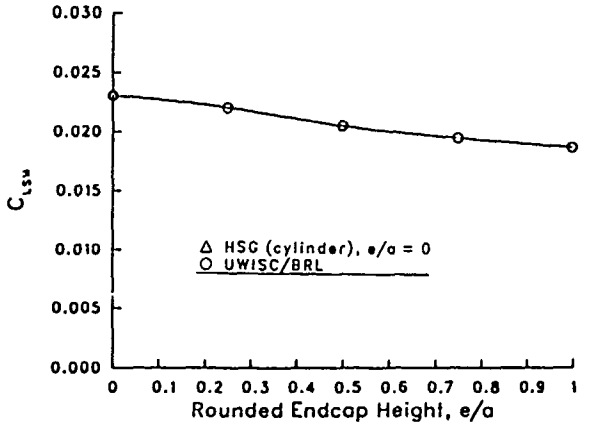

Fig. 3. Variation of Liquid-Induced Side Moment Coefficient with Rounded Endcap Height; Re = 50, τ = .0469, c/a = 1.486, $\alpha_c = 2°$

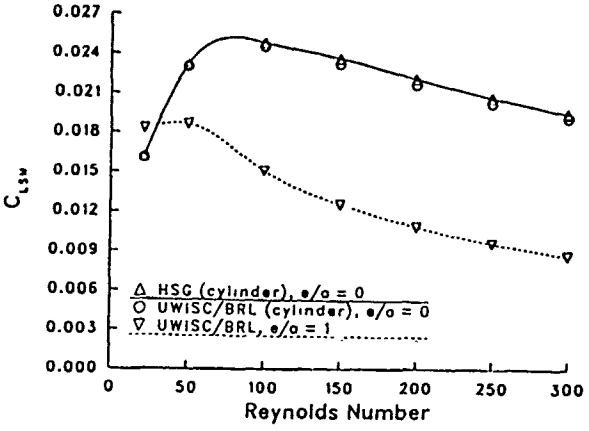

Fig. 4. Variation of Liquid-Induced Side Moment Coefficient with Reynolds Number; e/a = 0 and 1, τ = .0469, c/a = 1.486, $\alpha_c = 2°$

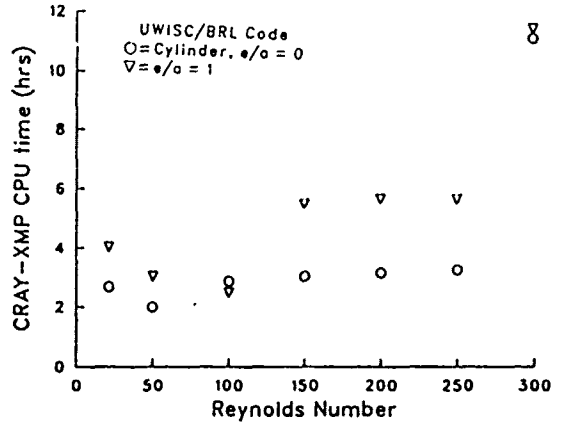

Fig. 5. Variation of CRAY X-MP/48 CPU Time with Reynolds Number; e/a = 0 and 1, τ = .0469, c/a = 1.486, $\alpha_c = 2°$

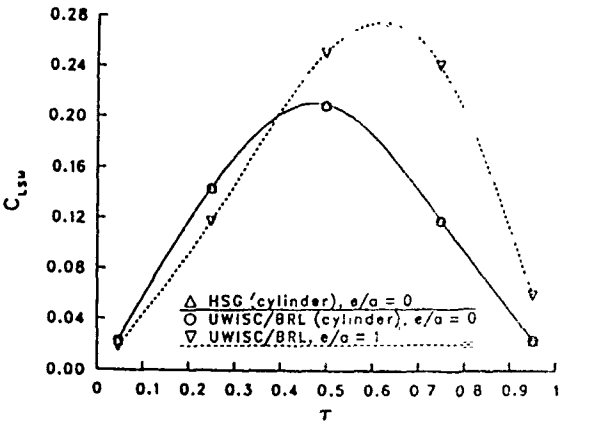

Fig. 6. Variation of Liquid-Induced Side Moment Coefficient with Coning Frequency, e/a = 0 and 1, Re = 50, c/a = 1.486, $\alpha_c = 2°$

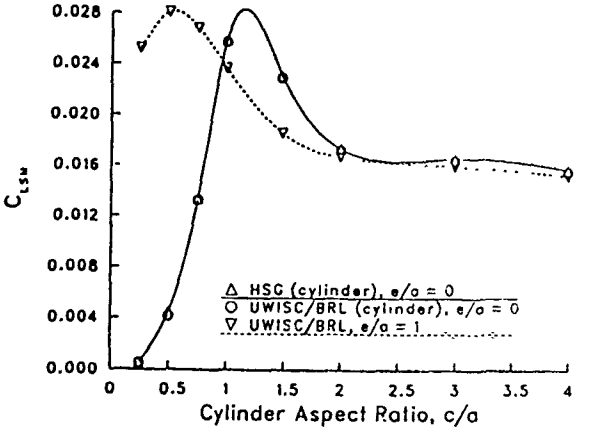

Fig. 7. Variation of Liquid-Induced Side Moment Coefficient with Cylinder Aspect Ratio; e/a = 0 and 1, Re = 50, τ = .0469, $\alpha_c = 2°$

BLANK

EFFECT OF PARTIAL-FILL ON DESTABILIZING MOMENT PRODUCED BY SPINNING AND CONING VISCOUS LIQUID

by

DANIEL J. WEBER
and
Miles C. Miller
U.S. Army Chemical Research, Development and Engineering Center
Aberdeen Proving Ground, Maryland 21010-5423

ABSTRACT

To date, the theories and experimental data related to flight instabilities produced by highly viscous liquid-fills have been limited to completely filled conditions (i.e., no void). This paper presents the results of a study to determine the effect of a partial-fill condition on the moments produced by a viscous liquid on a spinning and coning cylinder. The CRDEC Laboratory Test Fixture for Non-Rigid Payloads was used to measure the rolling moment produced by a representative, highly viscous, Newtonian fluid in a cylindrical container undergoing simultaneous spinning and coning motion. The fill ratio (i.e., ratio of liquid fill to total available volume) was varied incrementally from 0.2 to 1.0 and the resulting liquid induced moment measured at various motion conditions. The destabilizing moment was computed from the measured rolling moment data and presented in non-dimensional, general coefficient form as a function of Reynolds number and fill ratio. These results show that the destabilizing moment is relatively insensitive to fill ratio at the higher fill ratio values of interest.

ACKNOWLEDGEMENT

The authors would like to thank John W. Molnar, Research Directorate, for his assistance in the experimental and data analysis aspects of this study.

NOMENCLATURE

2a	canister inside diameter	I	axial moment of inertia
2c	canister inside length	M_{LRM}	liquid fill induced rolling moment
C_{LSM}'	generalized liquid side moment coefficient ($M_{LSM}/\Omega^2\ a^2\ m_L\ \tan\theta$)	M_{LSM}	liquid fill induced side moment
C_{LRM}'	generalized liquid rolling moment coefficient ($M_{LRM}/\Omega^2\ a^2\ m_L\ \tan^2\theta$)	m_L	total liquid mass
		V	empty canister internal volume ($2\pi a^2 c$)

V'	volume of liquid fill	τ	non-dimensional coning rate (Ω/ω')
$R_{e'}$	Reynolds number - $\omega' a^2/\nu$	Ω	canister coning rate
γ	specific mass of fluid	ω	canister spin rate (relative to coning reference frame)
θ	canister coning angle	ω'	canister absolute spin rate ($\omega + \Omega \cos \theta$)
ν	liquid fill kinematic viscosity		

I. INTRODUCTION

Considerable progress has been made recently in understanding and analyzing the flight dynamics of spinning projectiles having highly viscous liquid fills.[1] [2] These fills can create substantial liquid induced moments which cause the projectile to experience rapid yaw growth and despin with a consequent degradation in its range and accuracy.[4] [5] However these techniques and experimental moment measurements are limited to completely filled, right circular cylinders. This paper describes the laboratory measurement of the despin moment produced by a viscous liquid in a partially-filled cylindrical container undergoing simultaneous spinning and coning motion. The resulting data can be used to evolve and validate theoretical analyses involving a partial-fill condition.

II. Experimental Approach

A series of experiments were conducted using the Laboratory Test Fixture for Non-Rigid Payloads.[6] This apparatus forces a spinning, liquid-filled cylindrical container to undergo fixed-angle coning motion. Thus, the liquid-fill experiences the same basic dynamic environment it would have in a spinning and nutating projectile. The physical characteristics of the cylindrical container are summarized in Table 1. A silicone fluid was used to represent a homogeneous, highly viscous, liquid-fill. Its physical properties are also included in Table 1. The procedure was to fill the container up to the desired partial-fill condition defined as the ratio of the liquid volume (V_L) to the total cylinder internal volume (V).

The container was then mounted to the fixture frame at a coning angle of 20 degrees. All testing was conducted at this angle because it produces the largest moment and also represents a realistic flight condition. The container was spun about its longitudinal axis to a spin rate of about 8,000 RPM. The constant coning motion of the spinning container, which was held fixed during a particular test run, was produced by rotating the fixture frame about its vertical axis. At that point, the air turbine spinning the container was cut-off allowing the container and liquid-fill to despin under a constant coning angle and constant coning rate. The resulting data, container

spin rate versus time, were used to compute the total despin moment acting on the canister at the various spin rates. Subtracting out the contribution to the despin moment due to the bearing friction which had been previously determined from similar tests using an empty container, results in the despin moment induced by the liquid-fill. This is sometimes called the "liquid rolling moment" (M_{LRM}) and is directly related to the "liquid side moment" (M_{LSM}) which is a destabilizing yawing moment by the following:

$$M_{LSM} = \frac{M_{LRM}}{\tan \theta}$$

These terms are illustrated in Figure 1. Thus, from the easily measured liquid induced despin moment the destabilizing liquid yawing moment can be determined.

The canister was evaluated at fill ratios (V'/V) of 1.0, 0.99, 0.98, 0.95, 0.90, 0.80, 0.70, 0.60, 0.50, 0.40, 0.30 and 0.20 for coning rates of 200, 300, 400 and 500 rev/min with the canister coning angle constant at 20 degrees.

III. RESULTS AND DISCUSSION

Figure 2 shows the liquid rolling moment plotted against the canister spin rate for various fill-ratios under a constant coning angle and rate of 20 degrees and 500 RPM, respectively. This is the largest value of coning angle and rate evaluated and produced the largest moments. Also shown are the non-dimensional coning rates associated with these test conditions. Note the general clustering of the curves for fill ratios of 0.7 and above.

Using the liquid induced rolling moment for a fill ratio of 1.0 as a reference, the ratio of the liquid induced rolling moment for a particular fill ratio can be plotted versus fill ratio as shown in Figure 3. Data are presented for various constant values of non-dimensional coning rate. Note that for a given fill ratio, the moment ratio drops off with increasing non-dimensional coning rate. This is probably, due, in part, to the effect of the spin rate to centrifugally force the liquid to spread completely and evenly along the length of the canister. If this condition is attained, as with a low non-dimensional coning rate, the moment remains essentially large even down to fill ratios of 0.40. This leads to the surprising observation that for typical artillery projectile flight conditions (i.,e., $\tau \approx .1$), the liquid induced destabilizing moment is relatively insensitive to the amount of liquid fill present (around the condition of maximum liquid carried desired for a munition system). In fact, the large destabilizing moment present for the completely filled canister remains

at the same value even when as much as 60 percent of the liquid is removed!

Possibly, a certain fluid layer thickness must be present on the inside surface of the container to produce the moment. With a void, a low value of τ is necessary (high spin) to centritically force the liquid up the entire inside length of the container. If a sufficiently high spin rate is present, the liquid layer will have a uniform thickness which will depend on the percent of liquid fill in the container. The absolute thickness of this layer and its ratio with the radius for the container used in these experiments are summarized in Figure 4. Above a certain thickness of fluid, the addition of fluid does not increase the movement. However, the effect of the spin is reflected in the value of τ.

IV. NON-DIMENSIONAL COEFFICIENTS

The liquid-fill induced rolling moment can be expressed as a non-dimensional coefficient which is only a function of Reynolds number.[7] These coefficients are shown plotted against fill-ratio in Figure 5. Experimental data using liquids of 100,000 CS were selected to provide data in the Reynolds number range around ten thus, encompassing the peak moment value. Since the coefficients include a liquid mass term in the denominator, a reduction in liquid tends to increase the coefficient even though the moment produced might be the same. The effect of the liquid mass can be removed by multiplying the coefficient by the fill-ratio as shown in Figure 6 for constant values of Reynolds number. This plot illustrates the true effect of the partial fill induced moment. This plot shows that the maximum moment does not occur at the maximum fill condition, but at partial fill ratio just before the moment abruptly decreases to zero at a zero fill.

V. CONCLUSIONS

1. The destabilizing moment produced by a highly viscous liquid in a spinning and coning cylinder is relatively insensitive to the amount of liquid fill in the container at the high fill ratios of interest to munition applications.

2. The maximum moment does not occur at the maximum fill condition, but at a fill ratio just before the moment decreases to zero for the conditon of an empty container.

3. At Reynolds numbers where the maximum viscous liquid-fill destabilizing moments occur, the same large moment is present even if as much as 60% of the liquid fill is removed.

REFERENCES

1. Miller, M. C.; "Liquid Filled Projectiles New Problems - New Solutions"; Proceedings of the ADPA Ninth International Ballistics Symposium, England; 9 Apr - 1 May 86.

2. Miller, M. C.; "Liquid Filled Projectiles New Problem - New Solutions", Army Research, Development and Acquisition Magazine, Pp 24-27.

3. D'Amico, W. P. and Miller, M. C.; "Flight Instability Produced by a Rapidly Spinning and Highly Viscous Liquid," Journal of Spacecraft and Rockets, Vol 16, Jan-Feb 79, Pp 62-64.

4. Hall, P.; Sedney, R. and Gerber, N.; "Fluid Motion in a Spinning, Coning Cylinder via Spatial Eigenfunction Expansion," U.S. Army Ballistics Research Laboratory, Technical Report BRL-IMR-806, Apr 87.

5. Herbert, T. and Li, R.; "Numerical STudy of the Flow in a Spinning and Nutating Cylinder," AIAA 19th Fluid Dynamics, Plasma Dynamics and Lasers Conference, Paper 87-1445, Jun 87.

6. Miller, M. C.; "Laboratory Test Fixture for Non-Rigid Payloads," Proceedings of the 13th International Congress on Instrumentation on Aerospace Simulation Facilities (ICIASF)," Research Center; Gottingen, W. Germany; Pp 350-364, Sep 89.

8. Weber, D. J. and Miller, M. C.; "Liquid Induced Rolling and Yawing Moment Coefficients for Viscous Newtonian Fluids in a Spinning and Coning Cylinder," Proceedings of the 1988 U.S. Army Chemical Research, Development and Engineering Center Scientific Conference on Chemical Defense Research, CRDEC-SP-89019, Apr 89.

TABLE 1

PHYSICAL CHARACTERISTICS

Payload Container	Silicone Fluid
$2a = 11.07$ cm	$\nu = 100$ KCS
$2c = 49.81$	$\gamma = 0.98$
$c/a = 4.50$	
$I = 0.098$ Kg-m^2	

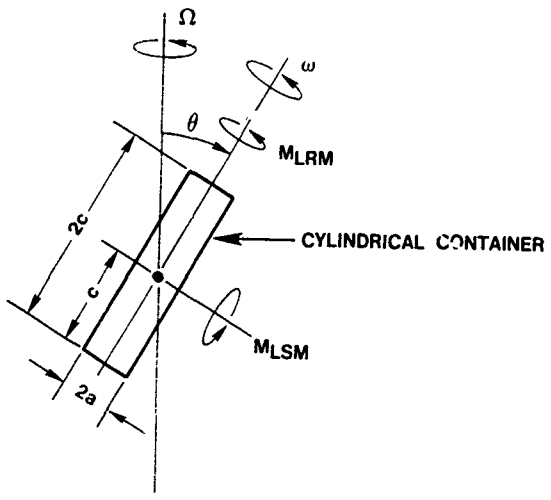

FIGURE 1 - Definition of Terms

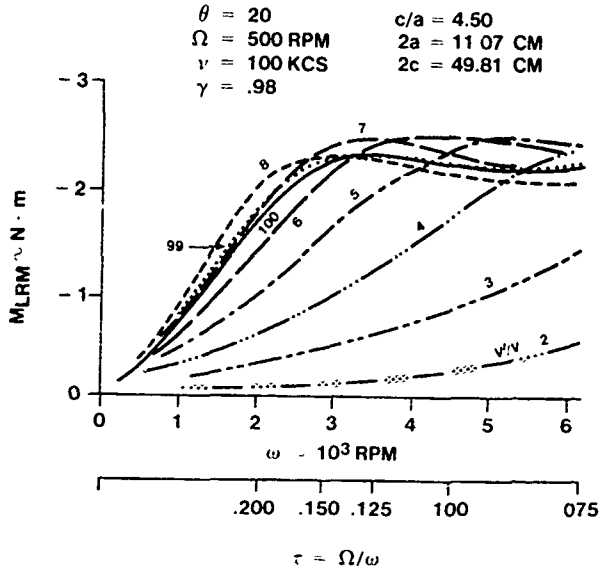

FIGURE 2 - Liquid Rolling Moment Versus Spin Rate for Various Fill Ratios

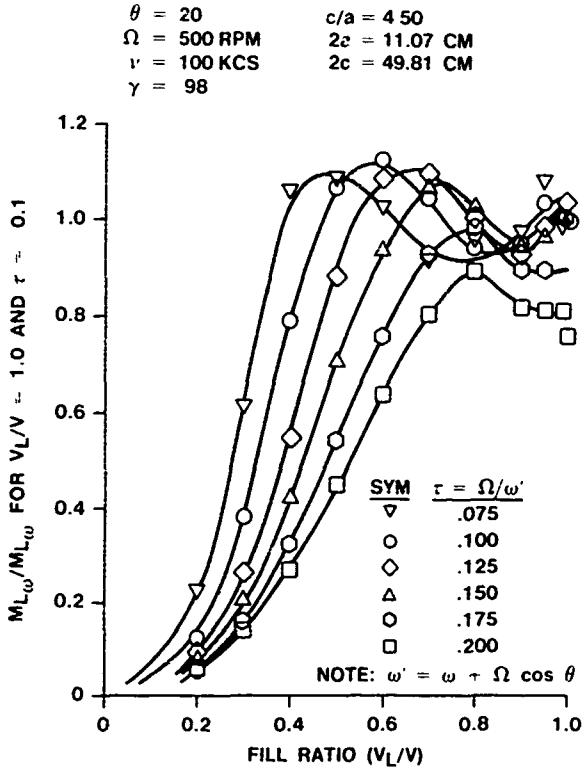

FIGURE 3 - Liquid Rolling Moment Versus Fill Ratio of $\tau = 0.1$ Condition

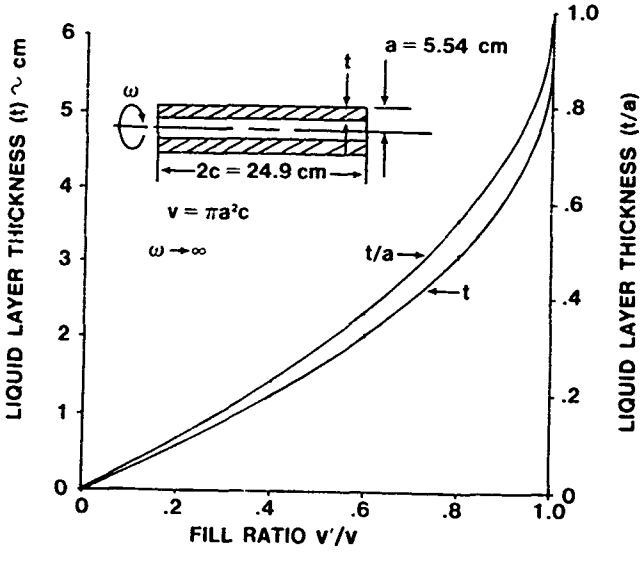

FIGURE 4 - Liquid Layer Thickness Versus Fill Ratio

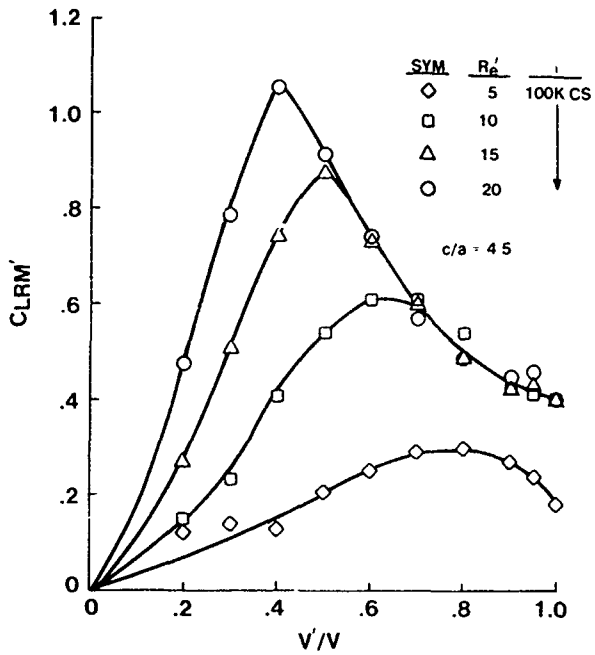

FIGURE 5 - Liquid Rolling Moment Coefficient Versus Fill Ratio for Various Reynolds Numbers

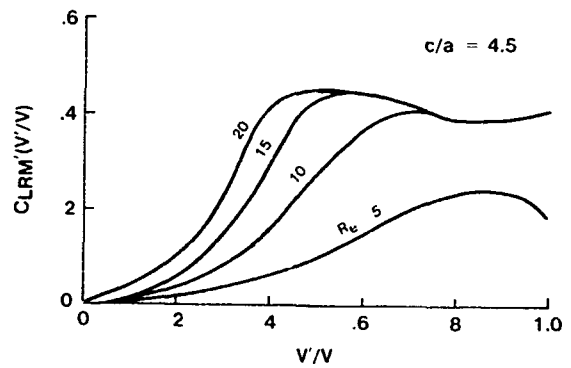

FIGURE 6 - Destabilizing Moment Effect Due to Partial-Fill

BLANK

ELIMINATION OF VISCOUS LIQUID-FILL FLIGHT INSTABILITY BY MEANS OF LOWER VISCOSITY, IMMISCIBLE LIQUID ADDITIVE

by

Miles C. Miller
U.S. Army Chemical Research, Development and Engineering Center
Aberdeen Proving Ground, Maryland 21010-5423

ABSTRACT

Highly viscous liquid-fills can create flight instabilities in spinning projectiles which are characterized by a rapid increase in yaw angle and decrease in spin rate. This paper presents experimental data which indicate that the liquid induced despin moment and associated destabilizing yawing moment produced by a viscous liquid in a spinning and coning cylinder can be reduced by a factor of 2 to 3 by the addition of a small amount (2% by volume) of an immiscible, low viscosity liquid. Studies were conducted on the CRDEC Laboratory Test Fixture for Non-Rigid Payloads to investigate the effect of relative viscosity, density and mixture amounts. The similarities between the immiscible, low viscosity additive in combination with a high viscosity liquid fill with that of a shear thinning, visco-elastic fluid are also evident.

ACKNOWLEDGEMENT

The author would like to thank John W. Molnar, Research Directorate, for his assistance in the experimental and data analysis aspects of this study.

NOMENCLATURE

$2a$	canister inside diameter	M_{LRM}	liquid fill induced rolling moment
$2c$	canister inside length	M_{LSM}	liquid fill induced side moment
C_{LSM}'	generalized liquid side moment coefficient ($M_{LSM}/\Omega^2\ a^2\ m_L \tan\theta$)	m_L	total liquid mass
C_{LRM}'	generalized liquid rolling moment coefficient ($M_{LRM}/\Omega^2\ a^2\ m_L \tan^2\theta$)	V	empty canister internal volume ($2\pi a^2 c$)
V_L	volume of low viscosity fluid	V_H	volume of high viscosity fluid
		τ	non-dimensional coning rate (Ω/ω')

$R_{e'}$	Reynolds number - $\omega' a^2/\nu$	Ω	canister coning rate
γ_H	specific mass of high viscosity fluid	ω	canister spin rate (relative to coning reference frame)
γ_L	specific mass of low viscosity fluid	ω'	canister absolute spin rate ($\omega + \Omega \cos \theta$)
θ	canister coning angle		
ν	liquid fill kinematic viscosity		

I. INTRODUCTION

Highly viscous liquid fills can create flight instabilities in spinning projectiles which are characterized by a rapid increase in yaw angle and decrease in spin rate.[1] [2] These projectile motions are the result of moments created by the internal liquid flow in response to the spin and nutation motion of the projectile and is termed a "forced motion" type of instability as opposed to the "resonance" type of instability present with low viscosity liquid fills. Considerable progress has been made in developing theoretical methods to understand and predict these liquid-fill induced moments.[3] [4] [5]

In the case of a low viscosity liquid, the familiar "resonance" type instability can be eliminated by minor changes in the aspect ratio of the internal payload compartment (i.e., length to diameter ratio). For the "forced motion" type instability associated with highly viscous liquids, changing the aspect ratio has little effect. Accordingly, alternate means are being considered to reduce or eliminate this latter type of instability. This paper presents laboratory data which demonstrate a significant reduction in the liquid-fill induced despin moment resulting from the addition of a small amount (1-2% by volume) of an immiscible, low viscosity fluid to the highly viscous liquid fill. The associated reduction in the liquid induced yawing moment would have a profound effect on the projectile flight stability.

This approach was first considered by the author after observing some experimental results of Dr. D. Joseph involving dynamic rollers immersed in two immiscible fluids of different viscosities.[6] His experiments demonstrated that the lower viscosity fluid migrated to the roller areas of highest shear stress and acted as a lubricant between the roller surface and the high viscosity liquid. From this, it was reasoned that, in the spinning and nutating projectile, a low viscosity, immiscible fluid might similarly migrate to the high shear rate area (on the inside surface of the payload container) and thereby reduce the destabilizing moment normally created by the highly viscous fluid.

II. Experimental Approach

A series of experiments were completed at the U.S. Army Chemical Research, Development and Engineering Center (CRDEC) on the Laboratory Test Fixture for Non-Rigid Payloads.[7] This apparatus forces a spinning, liquid-filled cylindrical container to undergo fixed-angle coning motion. Thus, the liquid-fill experiences the same basic dynamic environment it would have in a spinning and nutating projectile. A silicone fluid was used to represent a homogeneous, highly viscous, liquid-fill. The procedure was to mount the filled container to the fixture frame at a coning angle (θ) of 20 degrees. The container was spun about its longitudinal axis to a spin rate of about 8,000 RPM. The fixture frame was then rotated about a vertical axis until the spinning container assumed a coning motion at the fixed value desired for that particular test run. At that point, the container spin turbine air was cut-off allowing the container and liquid-fill to despin at a constant coning angle and constant coning rate. The resulting container spin rate versus time data were used to compute the net despin moment acting on the canister at the various spin rates.

Subtracting out the contribution to this moment due to the bearing friction (which had been previously determined with similar tests using an empty container), results in the despin moment induced by the liquid-fill. This is sometimes called the "liquid rolling moment" (M_{LRM}) and is directly related to an associated "liquid side moment" (M_{LSM}) which is described by the following simple expression:

$$M_{LSM} = M_{LSM}/\tan \theta$$

These terms are illustrated in Figure 1. Thus, the measured liquid induced despin moment is a measure of the destabilizing liquid yawing moment.

III. 100,000 CS NEWTONIAN LIQUID-FILL

All tests were conducted with a cylindrical container having an inside length of 49.83 cm and an inside diameter of 11.07 cm giving an aspect ratio of 4.50. The container was initially filled 98% by volume with a silicone fluid having a specific viscosity of 100,000 CS and a specific mass of .977. This particular viscosity was selected because it produces the maximum destabilizing moment (for the artillery projectile application) of any homogeneous, viscous liquid. The liquid fill induced despin moment was measured for the container spinning over the range from 8,000 to 0 RPM for coning rates of 200, 300, 400 and 500 RPM at coning angles of 10 and 20 degrees. This provided a reference fill condition to allow comparison with the influence of the lower viscosity, immiscible liquid additive.

Water was used as the low viscosity, immiscible liquid additive. In addition to being immiscible in the silicone fluid, it possesses a much lower specific viscosity (1 CS) and has a slightly larger specific density. The container of 100K CS fluid was evaluated with various amounts of water. The ratio of the volume of water (V_L) to the total fluid volume (i.e., $V_L + V_H$) was evaluated for values of 0, .01, .02, .05 and .10. The total volume of the two was held constant at the 98% fill ratio [i.e., $(V_L + V_H)/V$].

Figure 2 shows the liquid induced moment measured for the various percentages of water as a functior of the container spin rate for a specific value of coning rate and coning angle. Of particular interest, is the moment which occurs at a spin rate of 6,000 RPM. This condition relates to an actual artillery projectile transonic flight condition where the aerodynamic stability of the projectile is minimal and the liquid-fill induced moment can produce a flight instability. Note that, water amounts of .02 or larger result in a significant reduction in the despin moment and consequently, the destabilizing yawing moment.

The effect of the density of the low viscosity, immiscible additive was investigated by using alcohol in place of the water. The alcohol possesses the same viscosity as the water, but had a slightly lower density than that of the 100,000 CS fluid. Similar tests to those done with the water were conducted with the alcohol and the 100,000 CS silicone fluid in various amounts. This arrangement did not alter the liquid induced despin moment at all as shown in Figure 3. Evidently, the higher density water is centrifuged out to the inner surface of the container where it can act to reduce the moment whereas the lower density alcohol is centrifuged toward the center of the container where it is ineffectual. Thus, for the rotating container situation, the low viscosity additive must have a larger density than the main high viscosity payload because the centrifugal effect dominates the situation.

IV. 10,000 CS NEWTONIAN FLUID-FILL

The experiments were repeated using a 10,000 CS silicone fluid with water as the low viscosity additive. The 10,000 CS fluid does not produce as large as moment as the 100,000 CS fluid for identical motion conditions as illustrated in Figure 4. However, the fractional reduction in the moment due to various amounts of the low viscosity additive is similar as shown in Figure 5. Also, no appreciable change occurs for additive amounts above 2% for the higher spin rates of interest associated with the artillery projectile flight situation. Thus, the use of a low viscosity, immiscible fluid additive has the potential to decrease the liquid induced moment for a range of realistic liquid fills.

V. 600,000 CS NEWTONIAN FLUID-FILL

Similar tests to the 100,000 and 10,000 CS fluids were conducted with a 600,000 CS silicone fluid with water as the immiscible additive. These results are shown in Figure 6. As with the 100,000 CS fluid, the additive reduces the moment at high spin rates and increases the moment at low spin rates.

VI. DISCUSSION OF RESULTS

While, for a given viscous liquid fill, the addition of an immiscible, low viscosity fluid reduces the rolling moment at high spin rates associated with artillery projectile flight conditions, at lower spin rates, significant increases in the rolling moment result. Further, at these lower spin rates (i.e., lower Reynolds numbers) the moment is more sensitive to the amount of additive present. For example, in Figure 6, 5 percent of water added to a 600,000 CS fluid decreases the moment by a factor of 2 at a spin rate of 6,000 RPM, whereas it increases the moment by a factor of 6 at 2,000 RPM. It should be noted that the maximum rolling moment, for an additive situation, never exceeds the maximum value of the viscous fluid without any additive.

The immiscible, low viscosity liquid additive appears to have the same general effect in reducing the liquid induced moment as that observed with a shear thinning, viscoelastic fluid.[8] A typical comparison is shown in Figure 7.

The presentation of the liquid induced moment as a function of spin rate provides a measure of the various payload compositions on the flight stability of a typical artillery projectile. However, it is also of interest to show the data in a more general way which could apply to other dynamic situations. Accordingly, the data can be presented in the form of a non-dimensional moment coefficient.[9] In this case, a generalized moment coefficient is used which is only a function of Reynoilds number where the Reynolds number is based on the viscosity of the high viscosity fill. Figure 8 presents the data for the 100,000

and 10,000 CS fluids alone and in combination with 2% of the water additive. Note that while the water additive reduces the moment for certain Reynolds numbers, this effect goes away at lower Reynolds numbers. This behavior is, again, similar to that of a shear thinning viscoelastic fluid fill. For the 4.5 aspect ratio cylindrical container, 2% of an immiscible, low viscosity additive (water) with the 100K CS silicone fluid will reduce the destabilizing moment significantly (i.e., a factor of 2) for Reynolds numbers above 14 whereas for a 10K CS fluid, the same additive will reduce it above a Reynolds number of 80.

VII. CONCLUSIONS

1. The liquid-fill induced rolling moment and associated destabilizing yawing moment produced by a viscous liquid in a spinning and coning cylinder representative of projectile flight conditions can be significantly reduced by the addition of a small amount (2% by volume) of an immiscible, low viscosity liquid.

2. The immiscible, low viscosity additive must have a higher density than the basic viscous liquid fill in order to centrifuge to the cylindrical container inner surface under the spinning environment present.

3. Immiscible, low viscosity amounts between 1 and 2% by volume effectively reduce the viscous liquid induced moment by 50 to 75%. Increases beyond 2% (up to the maximum 10% evaluated in this study) do not result in any further effect.

4. At spin rates (Reynolds numbers) appreciably lower than projectile flight conditions, the immiscible additive acts to increase the liquid induced moments.

REFERENCES

1. Miller, M. C.; "Liquid Filled Projectiles New Problems - New Solutions"; Proceedings of the ADPA Ninth International Ballistics Symposium, England; 9 Apr - 1 May 86.

2. Miller, M. C.; "Liquid Filled Projectiles New Problem - New Solutions", Army Research, Development and Acquisition Magazine, Pp 24-27.

3. Murphy, C. H.; "Angular Motion of a Spinning Projectile With a Viscous Liquid Payload, "Journal of Guidance, Control, and Dynamics, Vol. 6, Jul-Aug 83, Pp 280-286.

4. Hall, P.; Sedney, R. and Gerber, N.; "Fluid Motion in a Spinning, Coning Cylinder via Spatial Eigenfunction Expansion," U.S. Army Ballistics Research Laboratory, Technical Report BRL-TR-02813, Aug 87.

5. Herbert, T., "Viscous Fluid Motion in a Spinning and Nutating Cylinder," CRDEC-CR86004, Nov 85.

6. Joseph, D. D. and Preziosi, L.; "Stability of Rigid Motions and Coating Films in Bicomponent Flows of Immiscible Liquids," Journal of Fluid Mechanics (1987), Vol. 185, Pp 323-351.

7. Miller, M. C.; "Laboratory Test Fixture for Non-Rigid Payloads," Proceedings of the 13th International Congress on Instrumentation on Aerospace Simulation Facilities (ICIASF)," Research Center; Gottingen, W. Germany; Pp 350-364, Sep 89.

8. Miller, M. C. and Weber, D. J.; "Destabilizing Moments Produced by a Viscoelastic Fluid in a Spinning and Coning Cylinder," Proceedings of 1988 U.S. Army Science Conference, Ft. Monroe, VA; Sep 88.

9. Weber, D. J. and Miller, M. C.; "Despin Moment Measurements for Viscous Liquids in a Spinning and Coning Cylinder," Proceedings of the 1987 CRDEC Scientific Conference on Chemical Defense Research, CRDEC-SP-89-006, Apr 89.

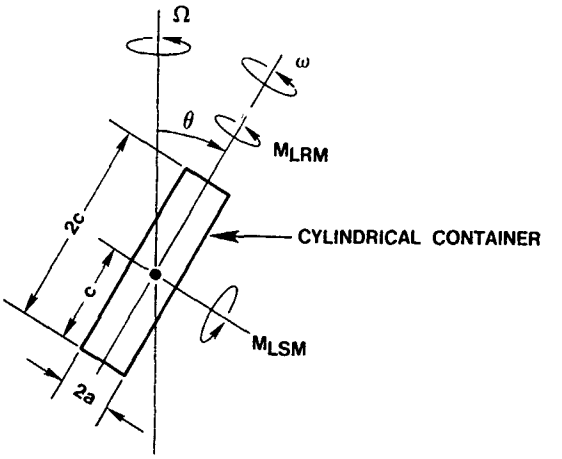

FIGURE 1 - Definition of Terms

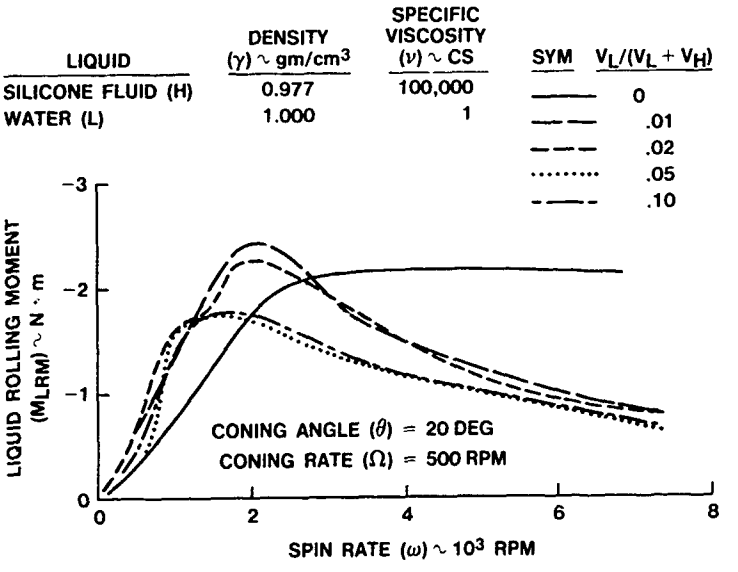

FIGURE 2 - Liquid Rolling Moment Versus Spin Rate for 100,000 CS Silicone Fluid With Water Additive

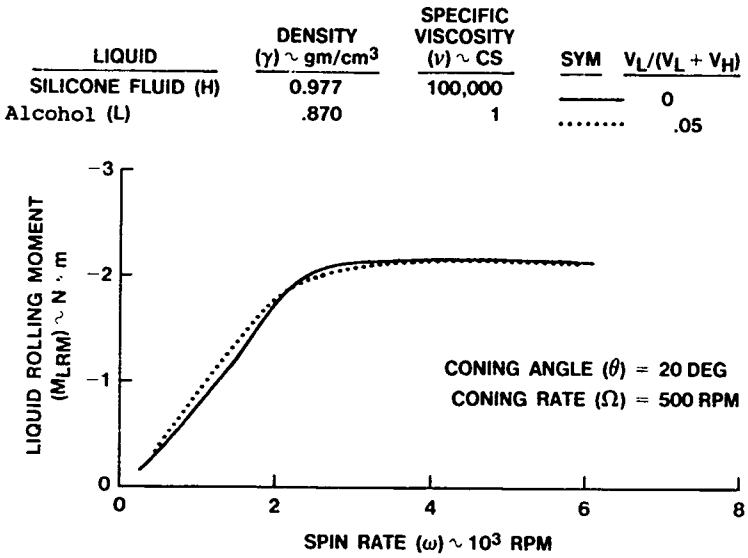

FIGURE 3 - Liquid Rolling Moment Versus Spin Rate for 100,000 CS Silicone Fluid With Alcohol Additive

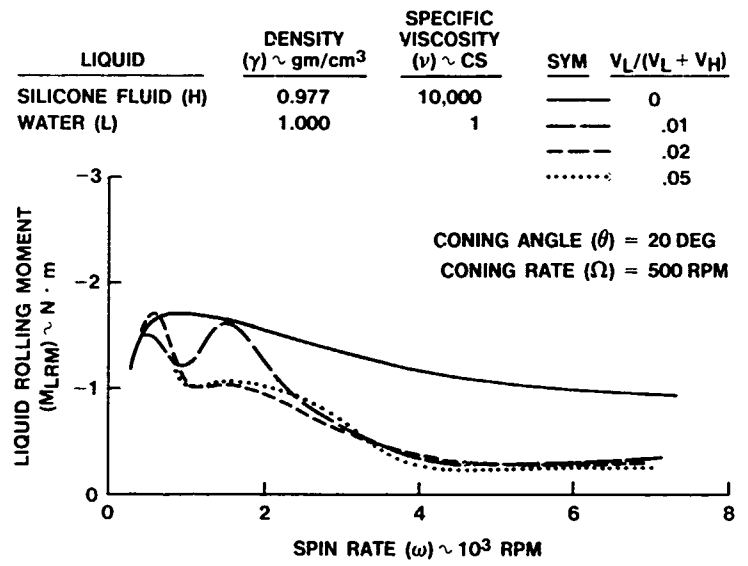

FIGURE 4 - Liquid Rolling Moment Versus Spin Rate for 10,000 CS Silicone Fluid With Water Additive

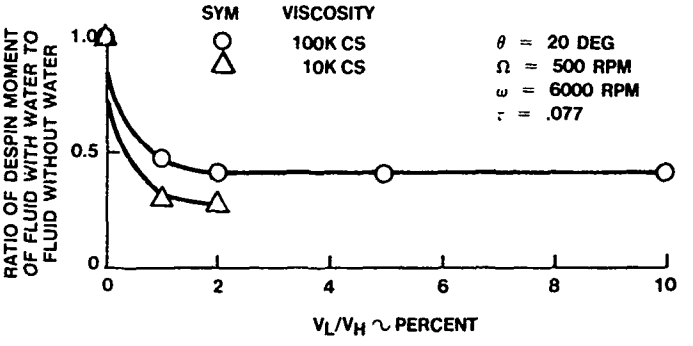

FIGURE 5 - Effect of Water Additive Amount on Liquid Rolling Moment for 100,000 and 10,000 Silicone Fluids

LIQUID	DENSITY (γ) ~ gm/cm^3	SPECIFIC VISCOSITY (ν) ~ CS
SILICONE FLUID (H)	0.977	600,000
WATER (L)	1.000	1

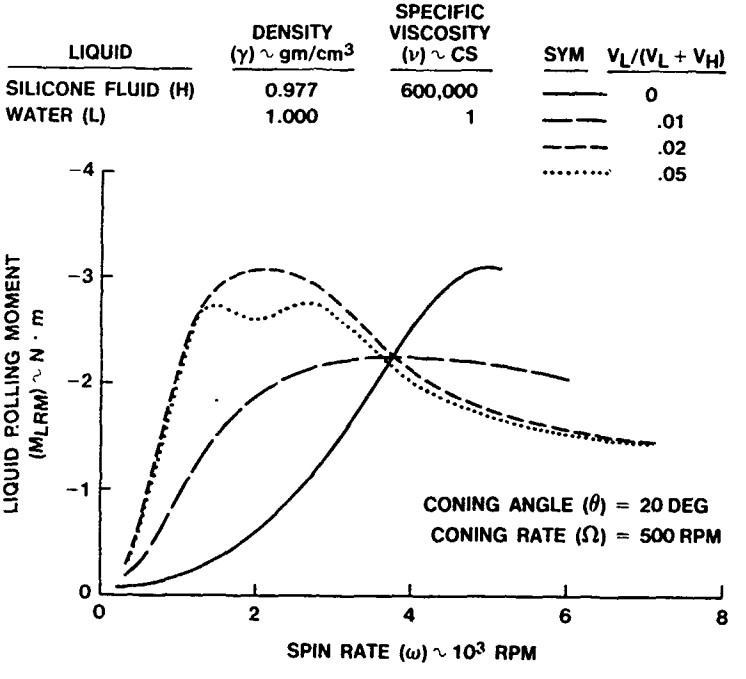

FIGURE 6 - Liquid Rolling Moment Versus Spin Rate for 600,000 CS Silicone Fluid With Water Additive

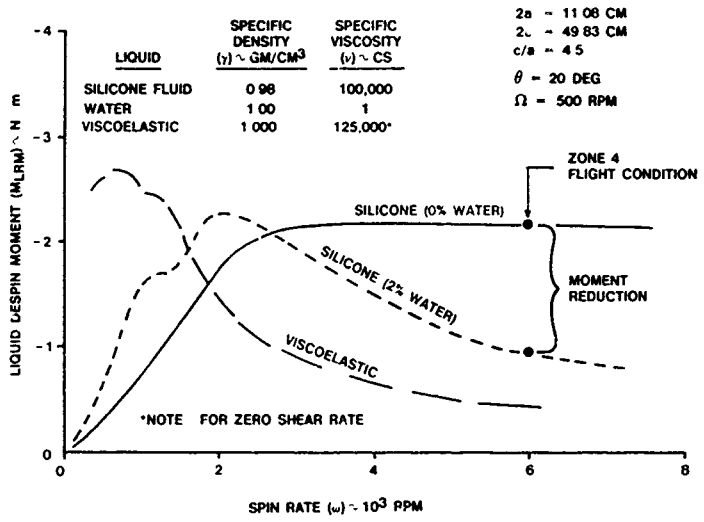

FIGURE 7 - Comparison of Viscous Liquid and Immiscible, Low Viscosity Additive With Viscoelastic Fluid

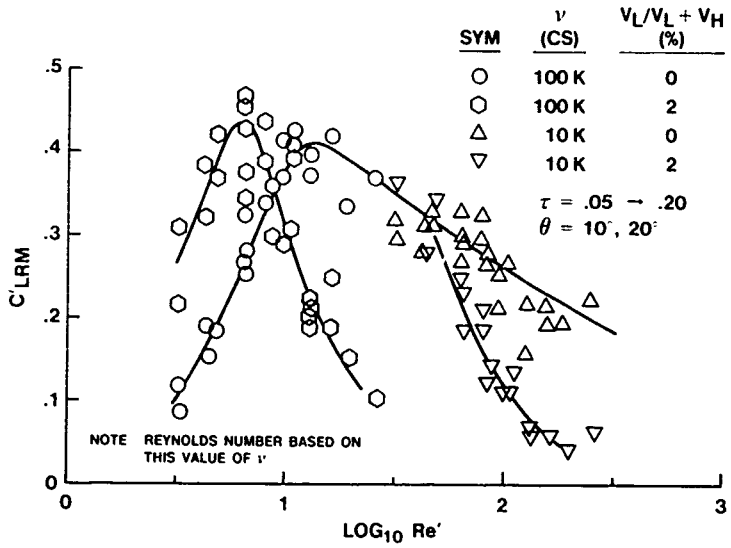

FIGURE 8 - Additive Effect in Terms of Non-Dimensional Moment Coefficients

TWO-FLUID FLOWS IN SPINNING AND NUTATING CYLINDERS

Mohamed Selmi
Department of Mechanical Engineering

Thorwald Herbert
Department of Mechanical Engineering and
Department of Aeronautical and Astronautical Engineering
The Ohio State University
Columbus, Ohio 43210

ABSTRACT

The moments exerted by viscous fluids in cylindrical payloads can cause severe flight instabilities of liquid filled projectiles. For cylinders completely filled with a homogeneous fluid, these moments can be estimated with analytical methods and analyzed with numerical methods based on spatial eigenfunction expansions (for the linearized problem) or spectral techniques (for the linear and nonlinear problem). Here we extend eigenfunction expansions to three cases of practical interest: (1) the flow in a cylinder with an inner rod that can affect motion and moments (Murphy 1989). (2) The flow in the presence of an inner void as it develops from a partial fill with a homogeneous fluid (Miller 1981, 1989). Even small percentages of air inclusion during production essentially modify the flow near the axis. (3) The flow of two fluids of different density and viscosity. Since a negative roll moment is caused by shear stresses at the cylinder wall, a heavy low-viscosity additive can reduce this moment (Miller 1989). We briefly describe the methods used, report some example results, and discuss characteristic changes in the moments.

1. Introduction

Liquid-filled projectiles are known to experience severe dynamical instabilities due to the motion of their liquid payloads. Two types of instabilities are currently understood for cylindrical containers completely filled with a homogeneous fluid. The first type is caused by resonance with inertial waves at critical coning frequencies (ratio of nutation rate to spinning rate). This instability is most pronounced for low-viscosity fluids and is known to strongly depend on the aspect ratio (ratio of length to diameter) of the payload cylinder. For a given frequency, the aspect ratio is usually properly chosen to avoid resonance. The second type of instability is related to the viscous stresses exerted by the fluid on the walls of the container. This type is associated with a rapid despin of the container and is most pronounced for high-viscosity fluids.

Theoretical and computational analysis of the flow in liquid-filled cylinders in the large range of relevant Reynolds numbers requires proper approximations. The boundary-layer approximation is the basis of the Stewartson-Wedemeyer theory (Stewartson 1959; Wedemeyer 1966). Since this approximation is only valid for flows at sufficiently large Reynolds numbers, the theory is primarily suited to predict the instability caused by inertial waves. Another common approximation is the linearization of the Navier-Stokes equations when the nutation angle is sufficiently small. This theory is of practical

interest since it can handle both types of instabilities. One approach to solving the linearized equations in terms of radial eigenfunctions was suggested by Hall et al. (1987). While this approach is successful for completely filled cylinders at moderate Reynolds numbers, the computational expense increases dramatically with the Reynolds number and for the configurations studied here.

When using the control volume approach for calculating the moments, these moments depend essentially on the axial velocity. Based on this observation, an alternative approach to solving the linearized equations was suggested by Li & Herbert (1989) who developed a sixth-order partial differential equation governing the axial velocity. The solution to this equation can be expanded in spatial eigenfunctions in the axial direction and Fourier series in the azimuthal direction, while the radial structure can be expressed in terms of Bessel functions. The expansion coefficients are found by satisfying the boundary conditions at the side walls using either collocation or least-square methods. This approach proves to be computationally efficient and flexible in treating other flows such as partial fill and two-fluid flows. Here, we apply this method to three related problems:

(A) The flow in a cylinder with a coaxial rod.

(B) The flow in a partially filled cylinder.

(C) The flow in a cylinder completely filled with two immiscible fluids of different densities and viscosities.

Our goal in studying these cases is gaining insight and analytical capabilities for the design of stable configurations. While a central rod or partial fill may serve to intentionally change liquid moments and resonant frequencies, partial fills are also frequent off-design products. Fills with two immiscible fluids, with a low-viscosity fluid in contact with the side wall, might lessen the viscous shear stresses and thereby reduce the despin rate.

2. Governing Equations

We consider the flow in a cylinder of radius a and length $2c$ containing one fluid of density ρ_1 and viscosity μ_1 and either a central rod of radius $a_0<a$, a void that originates from partial fill, or a less heavy fluid of density ρ_0 and viscosity μ_0. The cylinder rotates about its axis at the spin rate ω and rotates about a nutation axis through its center at the coning rate Ω. The angle between nutation axis and spin axis is denoted by θ. Under the influence of centrifugal forces, the heavy fluid accumulates at the side walls while the lighter fluid or the void surround the cylinder axis. For convenience, we adopt the notion of an inner region characterized by the index 0 and an outer region characterized by the index 1. While we need to solve for the inner solution in the case of the two-fluid flow, the inner solutions for the cases of a central rod or void are known, although the location of the interface between void and outer fluid needs to be determined.

For the moments, we use Cartesian coordinates x,y,z, where z is the spin axis and x is normal to z and coplanar with both the spin and nutation axes. However, the flow quantities are more conveniently expressed in cylindrical coordinates r,ϕ,z. We use the control volume approach to calculate the moments in the nutating coordinate system with the expressions given by Li & Herbert (1989). Here, however, the velocity vector of the deviation from rigid-body motion is

$$\mathbf{v} = (v_r, v_\phi, v_z) = \begin{cases} \mathbf{v}_0 = (v_r^0, v_\phi^0, v_z^0) & \text{if } 0 \le r \le r_f \\ \mathbf{v}_1 = (v_r^1, v_\phi^1, v_z^1) & \text{if } r_f \le r \le 1 \end{cases} \tag{1}$$

and the density is

$$\rho = \begin{cases} \rho_0 & \text{if } 0 \le r \le r_f \\ \rho_1 & \text{if } r_f \le r \le 1 \end{cases} \tag{2}$$

where r_f is the radial location of the interface. We write r_f in the form

$$r_f = r_0 + \zeta(\phi, z) \tag{3}$$

such that ζ is the deviation of the interface from the axisymmetric surface $r = r_0 = a_0/a$. For a slightly distorted interface, ζ is related to the radial velocity by

$$v_r(r_0, \phi, z) = \frac{\partial \zeta}{\partial \phi} \tag{4}$$

The linearized equation (linearized in $\varepsilon = (\Omega/\omega)\sin\theta$) governing the velocity field (Li & Herbert 1989) is given by

$$\frac{1}{\mathrm{Re}_\alpha^2}\nabla^6 \mathbf{v}_\alpha - \frac{2}{\mathrm{Re}_\alpha}\frac{\partial}{\partial \phi}\nabla^4 \mathbf{v}_\alpha + \frac{\partial^2}{\partial \phi^2}\nabla^2 \mathbf{v}_\alpha + t^2 \frac{\partial^2 \mathbf{v}_\alpha}{\partial z^2} = 0\,, \quad \alpha = 0, 1 \tag{5}$$

where $\mathrm{Re}_0 = \rho_0 \omega a^2/\mu_0$ and $\mathrm{Re}_1 = \rho_1 \omega a^2/\mu_1$ are the Reynolds numbers for the inner and outer flow, respectively, $t = 2(1+\tau_z)$, $\tau_z = (\Omega/\omega)\cos\theta$, and

$$\nabla^2 = \frac{\partial^2}{\partial r^2} + \frac{1}{r}\frac{\partial}{\partial r} + \frac{1}{r^2}\frac{\partial^2}{\partial \phi^2} + \frac{\partial^2}{\partial z^2} \tag{6}$$

We represent the velocities of both flows and the interface ζ by the Fourier series

$$\mathbf{v}_\alpha(r, \phi, z) = \sum_{n=-\infty}^{\infty} \mathbf{v}_n^\alpha(r, z) e^{in\phi}\,, \quad \mathbf{v}_n^\alpha = (u_n^\alpha, v_n^\alpha, w_n^\alpha)\,, \quad \alpha = 0, 1 \tag{7}$$

$$\zeta(\phi, z) = \sum_{n=-\infty}^{\infty} \zeta_n(z) e^{in\phi} \tag{8}$$

It is evident from the expressions for the moments that we need only consider the Fourier components w_1^α, v_0^α, $\alpha = 0, 1$ and ζ_1, provided ζ is small. Hence, if we introduce the scaled variables

$$w_1^\alpha = \varepsilon w_\alpha\,, \quad q_\alpha = (1+i)\sqrt{\mathrm{Re}_\alpha/2}\,, \quad \alpha = 0, 1 \tag{9}$$

$$(\tilde{r}, \tilde{z}) = \begin{cases} (r\, q_0, z\, q_0) & \text{if } 0 \le r \le r_f \\ (r\, q_1, z\, q_1) & \text{if } r_f \le r \le 1 \end{cases} \tag{10}$$

the fundamental components of the axial flow velocities are governed by

$$\tilde{\nabla}^2 w_\alpha - 2\,\tilde{\nabla}^4 w_\alpha + \tilde{\nabla}^6 w_\alpha - t^2 \frac{\partial^2 w_\alpha}{\partial \tilde{z}^2} = 0\,, \quad \alpha = 0, 1 \tag{11}$$

where

$$\tilde{\nabla}^2 = \frac{\partial^2}{\partial \tilde{r}^2} + \frac{1}{\tilde{r}}\frac{\partial}{\partial \tilde{r}} - \frac{1}{\tilde{r}^2} + \frac{\partial^2}{\partial \tilde{z}^2} \tag{12}$$

3. Boundary conditions

The boundary conditions at the end walls ($z = \pm\eta$, η is the aspect ratio) are independent of the type of flow considered:

$$w_\alpha = 0\,,\quad \frac{\partial w_\alpha}{\partial \tilde{z}} = 0\,,\quad -\frac{\partial^3 w_\alpha}{\partial \tilde{z}^3} + 2\tilde{\nabla}_1^2 \frac{\partial^3 w_\alpha}{\partial \tilde{z}^3} + \frac{\partial^5 w_\alpha}{\partial \tilde{z}^5} = 0\,,\quad \alpha = 0\,,1 \tag{13}$$

Similarly, the boundary conditions at the side wall ($r = 1$) apply only to the outer flow and are the same as given by Li & Herbert (1989) when w is replaced by w_1.

The remaining boundary conditions depend on the type of flow. For the cylinder with a central rod, the boundary conditions at the surface of the rod are the same as for the side walls except they are evaluated at $r = r_0$.

For the flow in a partially filled cylinder we require the shear and normal stresses across the fluid-void interface to vanish. These requirements provide the following conditions:

$$[-(1+t)\frac{1}{\tilde{r}}\tilde{\nabla}^2 + \frac{1}{\tilde{r}}\tilde{\nabla}^4 + \frac{t}{\tilde{r}} - 2\frac{t}{\tilde{r}}\frac{\partial^2}{\partial \tilde{z}^2} - \frac{t^3}{4}\frac{\partial}{\partial \tilde{r}}]w_1 = \frac{(2+t)t}{4iq_1} \tag{14}$$

$$[-t\frac{\partial}{\partial \tilde{r}}\tilde{\nabla}^2 - 2t\frac{\partial^3}{\partial \tilde{r}\partial \tilde{z}^2} + 2t\frac{\partial}{\partial \tilde{r}} - \frac{t}{2}\tilde{r}\,\tilde{\nabla}^2 + \frac{t}{2}\tilde{r}\,\tilde{\nabla}^4 - \frac{1}{\tilde{r}}\tilde{\nabla}^2 + \frac{1}{\tilde{r}}\tilde{\nabla}^4 - t^2\frac{\partial}{\partial \tilde{r}}]w_1 = \frac{t}{iq_1} \tag{15}$$

$$\begin{aligned}[-t(&\frac{1}{\tilde{r}}\tilde{\nabla}^2 + \frac{1}{\tilde{r}}\frac{\partial^2}{\partial \tilde{z}^2} - \frac{1}{\tilde{r}^2}\frac{\partial}{\partial \tilde{r}} - \frac{1}{\tilde{r}} - \frac{\partial}{\partial \tilde{r}} + \frac{\partial^3}{\partial \tilde{r}\partial \tilde{z}^2}) - \frac{\partial}{\partial \tilde{r}}\tilde{\nabla}^2 + \frac{\partial}{\partial \tilde{r}}\tilde{\nabla}^4 \\ &+ \frac{\tilde{r}}{2}\tilde{\nabla}^2 - \frac{\tilde{r}}{2}\tilde{\nabla}^2\frac{\partial^2}{\partial \tilde{z}^2} - \frac{\tilde{r}}{2}\tilde{\nabla}^4 + \frac{\tilde{r}}{2}\tilde{\nabla}^4\frac{\partial^2}{\partial \tilde{z}^2} - t^2\frac{\partial}{\partial \tilde{r}}]w_1 = \frac{t}{iq_1}\end{aligned} \tag{16}$$

In the case of two fluids, we require continuity of the velocity field and the stress state at the interface of both fluids which leads to six conditions of the form

$$L_k^0 w_0 - L_k^1 w_1 = C_k\,,\quad k = 1,6 \tag{17}$$

where L_k^α are interface boundary operators. The tedious derivation of the interface conditions and the lengthy operators and right-hand sides will be presented elsewhere.

4. Solution procedure

The governing equation for either the inner flow or the outer flow has homogeneous boundary conditions in the $\tilde{z}$ direction. This suggests the expansion of the solution in spatial eigenfunctions in the axial direction. For brevity we treat both the inner flow and the outer flow simultaneously, since for a given frequency, nutation angle, and aspect ratio, the eigenfunctions depend only on the Reynolds number. We let $q = q_\alpha$ and use the method of separation of variables to obtain the solution in the form

$$w_\alpha(\tilde{r}\,,\tilde{z}) = R(\tilde{r})Z(\tilde{z})\,, \tag{18}$$

and the radial function satisfies

$$\tilde{\nabla}_1^2 R = B\,R\,,\quad \tilde{\nabla}_1^2 = \frac{\partial^2}{\partial \tilde{r}^2} + \frac{1}{\tilde{r}}\frac{\partial}{\partial \tilde{r}} - \frac{1}{\tilde{r}^2}\,, \tag{19}$$

where B is a separation constant. Substituting equations (18) and (19) into (11) and (13) provides the eigenvalue problem

$$Z^{(6)} + (3B-2)Z^{(4)} + (3B^2 - 4B + 1 - t^2)Z'' + (B^3 - 2B^2 + B)Z = 0\,, \tag{20}$$

$$Z = 0\,,\quad Z' = 0\,,\quad Z^{(5)} + (2B-1)Z^{(3)} = 0 \quad \text{at} \quad \tilde{z} = q\,\eta\,, \tag{21}$$

where the prime denotes differentiation with respect to $\tilde{z}$. The solution to the above eigenvalue problem has been briefly discussed by Li & Herbert (1989), and a detailed discussion is given elsewhere. Let B_m^0 and B_m^1 be the eigenvalues of the above problem for $q = q_0, q_1$, respectively, and Z_m^0, Z_m^1 be the associated eigenfunctions, then the inner solution is given by

$$w_0 = \sum_{m=0}^{\infty} F_m^0 I_1(\sqrt{B_m^0}\tilde{r}) Z_m^0(\tilde{z}) \tag{22}$$

while the outer solution takes the form

$$w_1 = \sum_{m=0}^{\infty} [F_m^1 I_1(\sqrt{B_m^1}\tilde{r}) + G_m^1 K_1(\sqrt{B_m^1}\tilde{r})] Z_m^1(\tilde{z}) \tag{23}$$

The modified Bessel functions of the first and second kind, I_1 and K_1, are solutions to equation (19). The expansion coefficients F_m^α and G_m^1 are found by satisfying the radial boundary conditions at the side walls and/or interface, depending on the problem considered. Since the interface is not known a priori, the interface conditions are applied at the surface $r = r_0$. This is justified since the interface is only a small perturbation from this surface. This perturbation or interface amplitude ζ_1 can be found from relations relating the radial velocity to the axial velocity at the interface

$$\frac{d\zeta_1}{dz} = i \frac{\partial w_1^1}{\partial r}(r_0, z) \tag{24}$$

The integration of this equation is straightforward once w_1^1 is found.

5. Results

We have obtained detailed results for the three configurations in the Reynolds-number range up to $Re_1 = 10^4$, well overlapping with the region of validity of the boundary-layer approximation. Since the presentation and discussion of these results would exceed the page limit of this paper, we highlight only a few results and conclusions.

For a cylinder with partial fill, we show in figures 1a and 1b the shape of the interface for two cases of similar Reynolds number, nutating frequency, and aspect ratio but different nutating angles. The figures show that the distortion of the interface is negligible when the nutating angle is small but increases with increasing nutation angle. The fill ratio has a significant effect on the void distortion since the radial pressure gradient increases with r. For small fill ratios or large 'fill radius' r_0, a given normal force can be balanced by a small displacement of the interface. Also note in fig. 1a that the distortion for different fill ratios is qualitatively different. Other calculations show that the void distortion is small at low Reynolds numbers and increases with the Reynolds number, in agreement with the experimental results of Miller (1981).

Figure 2 presents our results for the nondimensional yaw moment as a function of the fill radius in comparison with data of Murphy et al. (1989) obtained with the KGS method. Murphy et al. (1989) present results of different approaches. In all cases, we find the best agreement with the results of the KGS method. The origin of the slight discrepancy shown in figure 2 is unclear. We have spent some efforts to convert correctly from their to our parameters. Therefore, we suspect the deviation is caused by the end-wall correction of the KGS approach at relatively low Reynolds numbers.

The remarkable maxima of the yaw moment in the neighborhood of certain 'critical' fill or rod radii have been found in all configurations. For cylinders with a central rod, figure 3 shows the roll

moment versus the rod radius for different values of the Reynolds numbers. While at low *Re* the moment monotonically decreases as the rod radius increases, maxima appear and become more pronounced at higher Reynolds numbers. The sharp peaks at certain critical values of the rod radius originate from resonance with inertial waves. We have verified these resonances analytically by an inviscid flow analysis for the different configurations. The inviscid resonance radii are shown by the dashed lines in fig. 2. A detailed discussion of the inviscid results will be presented elsewhere. We note, however, that such resonances occur for all configurations studied. Liquid payloads carefully designed by using criteria for complete fill may cause severe flight instabilities when partially filled. Since a 99% fill ratio has a fill radius $r_0 = 0.1$, even slight off-design conditions may be crucial.

Figure 4 shows the roll moment for a two-fluid configuration with 72% of highly viscous fluid (*Re* = 18.5) and 28% of a heavier, low-viscosity (high-Reynolds-number) additive. The effect of the low-viscosity additive is clearly to reduce the roll moment as the Reynolds number of the outer fluid increases, although the reduction is not monotonous. However, a word of caution is appropriate concerning the density ratio of the two fluids and the percentage of the low-viscosity additive. For small density differences, even small normal forces cause large deflections of the fluid interface. The theoretical artifact of an interface located outside the cylinder wall translates in reality to the highly viscous fluid breaking through the low-viscosity film at the wall. Only with sufficiently large density difference and thickness of the low-viscosity layer can the reduction in roll moment be fully achieved. If, on the other hand, the density of the inner fluid is much smaller, the configuration is more sensitive to resonance with inertial waves. Detailed parameter studies are currently performed to evaluate the full potential of two-fluid fills for stabilizing otherwise unstable payloads.

ACKNOWLEDGMENT

The assistance of Dr. Rihua Li in the analytical work is greatly appreciated. This work is supported by the U. S. Army AMCCOM under Contract DAAA15-89-K-0002.

REFERENCES

P. Hall, R. Sedney, and N. Gerber (1987) "Fluid motion in a spinning, coning cylinder via spatial eigenfunction expansion," Ballistic Research Laboratory, Technical Report BRL-TR-2813.

R. Li and Th. Herbert (1989) "High-Reynolds-number flows in a spinning and nutating cylinder," in *Proc. 1988 U.S. Army CRDEC Scientific Conference on Chemical Defense Research, Report CRDEC-SP-013*, ed. J. D. Williams and M. D. Rausa, pp. 497-504.

C. H. Murphy, J. W. Bradley, and W. H. Mermagen (1989) "Side moment exerted by a spinning, coning, highly viscous liquid payload," Ballistic Research Laboratory, Technical Report BRL-TR-3074.

M. C. Miller (1981) "Void characteristics of a liquid-filled cylinder undergoing spinning and coning motion," *J. Spacecraft Rockets*, Vol. 18, pp. 286-288.

M. C. Miller (1989) "Laboratory test fixture for non-rigid payloads," in *Proc. 13th Int. Cong. "Instrumentation on Aerospace Simulation Facilities," Göttingen, Germany, 1989.*

K. Stewartson (1956) "On the stability of a spinning top containing fluid," *J. Fluid Mech.*, Vol. 5, pp. 577-592.

E. H. Wedemeyer (1987) "Viscous correction to Stewartson's stability criterion," Ballistic Research Laboratory, Technical Report BRL-TR-2813.

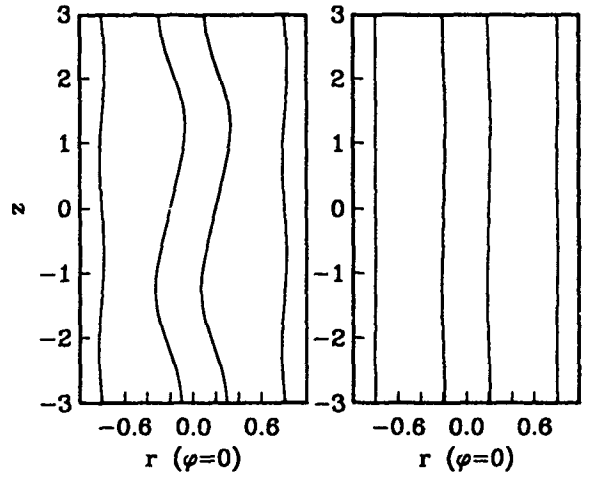

(a) (b)

Figure 1. Partial fill. Interface for $\eta=3$, $r_0=0.2$ and $r_0=0.8$. (a) $\theta=20^o$, $Re=453$, $\tau=0.11037$, (b) $\theta=2^o$, $Re=450$, $\tau=0.1111$.

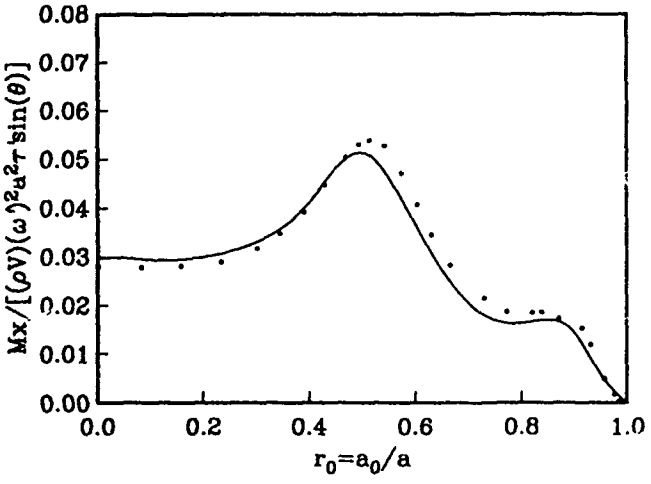

Figure 2. Partial Fill. Yaw moment vs. fill radius for $\eta=3$, $\theta=2^o$, $Re=450$, $\tau=0.1111$, (——) present results, (o) results of the KGS method (Murphy et al. 1989).

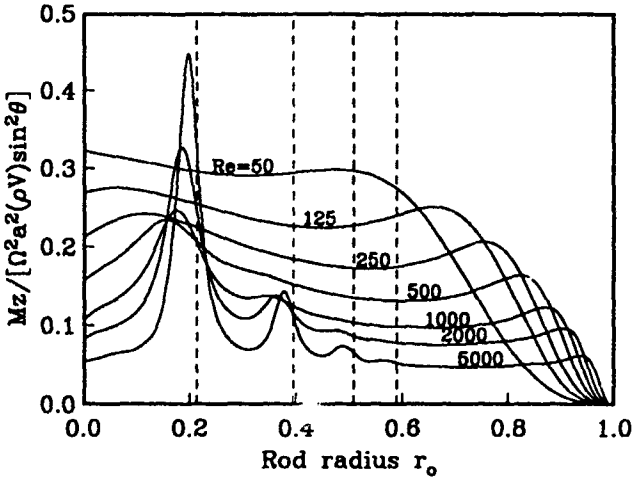

Figure 3. Central rod. Roll moment vs. rod radius for $\eta=4.5$, $\theta=20^o$, $\tau=0.08674$, and different Reynolds numbers.

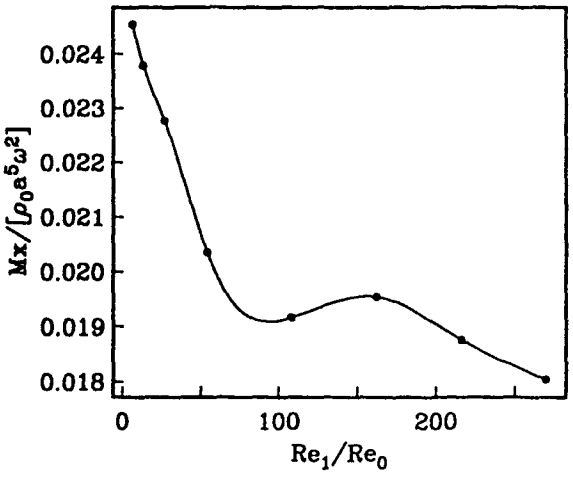

Figure 4. Two-fluid fill. Yaw moment vs. ratio of outer to inner Reynolds number for $\eta=4.5$, $\theta=20^o$, $Re_0=18.5$, $\tau=0.08674$, $r_0=0.85$, $\rho_0/\rho_1=0.9$.

BLANK

IV. SYNTHESIS AND PROPERTIES

NOTE: A paper with the following title was presented at the Conference but is not included in this document:

Formation of C-C Bonds by Rearrangements from Silicon to Carbon

BLANK

AN OVERVIEW OF THE SYNTHESIS OF ^{14}C RING-LABELED EA 4923

James W. King and Donald R. Bowie
U.S. Army Chemical Research, Development and Engineering Center
Aberdeen Proving Ground, Maryland 21010-5423

ABSTRACT

The distribution of a compound in a biological milieu is often most easily ascertained using a radiolabeled form of the material. For the purpose of determining the distribution of EA 4923 (1-methoxy-1,3,5-cycloheptatriene) in rats, the title compound was prepared by a known route starting with 1-methoxy-cyclohex-1-ene. Treatment of the latter with ethyl trichloro-acetate labeled with C-14 in the 2-position, in the presence of sodium methoxide in hexane, gave 7,7-dichloro(7-C-14)-1-methoxybicyclo(4.1.0)heptane in 59% chemical and 56% radio-chemical yield. The labeled bicyclic was then treated with a dehydrohalogenating agent and heat to give a crude mixture of methoxycycloheptatrienes. Acid catalyzed isomerization of the crude mixture followed by distillation gave ring-labeled EA 4923 in 14% chemical and 11.2% radiochemical yield.

INTRODUCTION

Sensory irritants have long been of interest to the Army either as chemical warfare agents, training or trialing agents, or as riot control agents in either military or civil disturbances. One of the earliest of these materials was DM or "Adamsite" (Figure 1), a tricyclic organoarsenic compound reported by the Germans prior to World War 1 but not used by either side. Very likely the Germans did not use it because of their success with chlorine and mustard, both of which would produce casualties that put more of a strain on medical resources than a sternutator (sneeze producer) and lachrymator such as DM. It was not used by the Allies as the necessary R&D efforts by the eminent Dr. Roger Adams (hence its name) were not complete until 1919. Furthermore, phosgene, which could be considered an irritant at low dose levels with more serious medical effects at higher exposures, had been successfully employed. During and subsequent to the 1920's, the classical "tear gas," alpha-chloroacetophenone (CN) was used as a riot control agent and as a "manouver" agent (in effect, a trialing agent) by the Army with chlorine being used as a training and mask discipline agent in gas chambers.

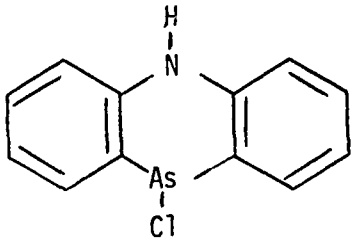

"Adamsite"
(DM)

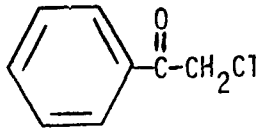

"Tear Gas"
(CN)

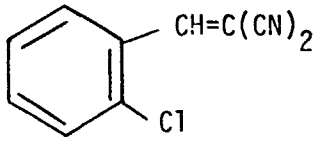

CS

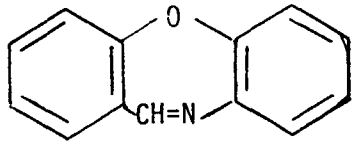

CR

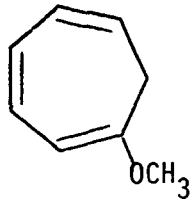

EA 4923

Figure 1. Structures of sensory irritants discussed in the text.

Other agents such as brombenzylcyanide (BBC) and capsaicin (the active ingredient in pepper) were among the topics of sensory irritant research during those years - and the latter still is, being the active ingredient in some commercially available mace (individual protection) units.

Research begun in the 1950's resulted in tear gas being largely supplanted by CS (o-chlorobenzalmalononitrile), a riot control agent currently in most police arsenals around the world. This material has also been used in military training scenarios, in mask discipline training, and in tunnel clearance operations in the Viet Nam war. It is more effective than CN and less toxic(1).

Another sensory irritant that has received study in recent years is dibenz[b,f][1,4]oxazepine (CR)(2). This compound is at least as potent as CS and has been most seriously considered as a riot control agent in British circles (3). However, it is not known if this material has been weaponized; it does tend to sensitize some individuals in cases of repeated exposures (4).

All of the compounds thus far noted are solids and present a challenge to dissemination methodology more confounding than do liquids. It was therefore of great interest in 1962, when attention was drawn to the irritant properties of what was subsequently identified as 1-methoxy-1,3,5-cycloheptatriene (EA 4923). This material was a liquid of moderate boiling point and a volatility approximating that of the nerve agent GB (isopropyl methylphosphonofluoridate). Subsequent research clarified and documented much of the chemistry and pharmacology of this compound but it ultimately became important to ascertain its distribution in an animal model. For this purpose a radiolabel was deemed most appropriate and EA 4923 with the sidechain methoxy group labeled with carbon 14 was synthesized (5) (Figure 2).

Although the methoxy-labeled compound proved to be suitable for its intended purpose (6), the possibility existed that distribution and other experimental results could be influenced by hepatic hydrolysis of the ether linkage (7). It was therefore of no little interest to synthesize EA 4923 with a ring label. The elegant and intellectually satisfying transetherification route used to prepare the sidechain-labeled compound would be of no utility in this case. But fortunately Australian investigators had devised a synthesis starting with cyclohexanone (8), and which, with minor modification proved suitable for the present purpose; it is detailed in Figure 3.

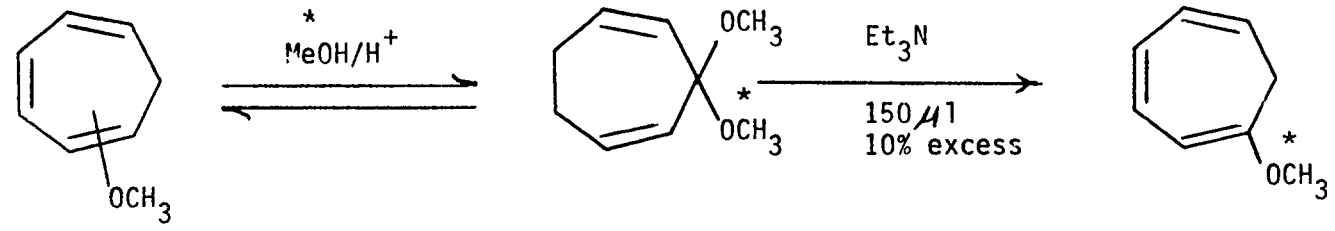

1- or 3-isomer
(3 ml)

MeOH - 1559 µCi
630 µl @ 2.475 Ci/µl
diluted to 3 ml

H^+ = 300 µl of
solution of
119 mg HCl/ml

48% yield
(65-69% usual)

1:3 isomer ratio ~ 97 mole%

1.405 g.

121.7 µCi/g. specific activity

Radiochemical yield: 10.9%

When sp.act 20-40 µCi/g:
chem. yield ~ 65%
rad. chem. yield ~ 15%

Figure 2. Synthesis of sidechain-labeled (^{14}C) EA 4923 (the asterisk indicates the position of the labeled atom).

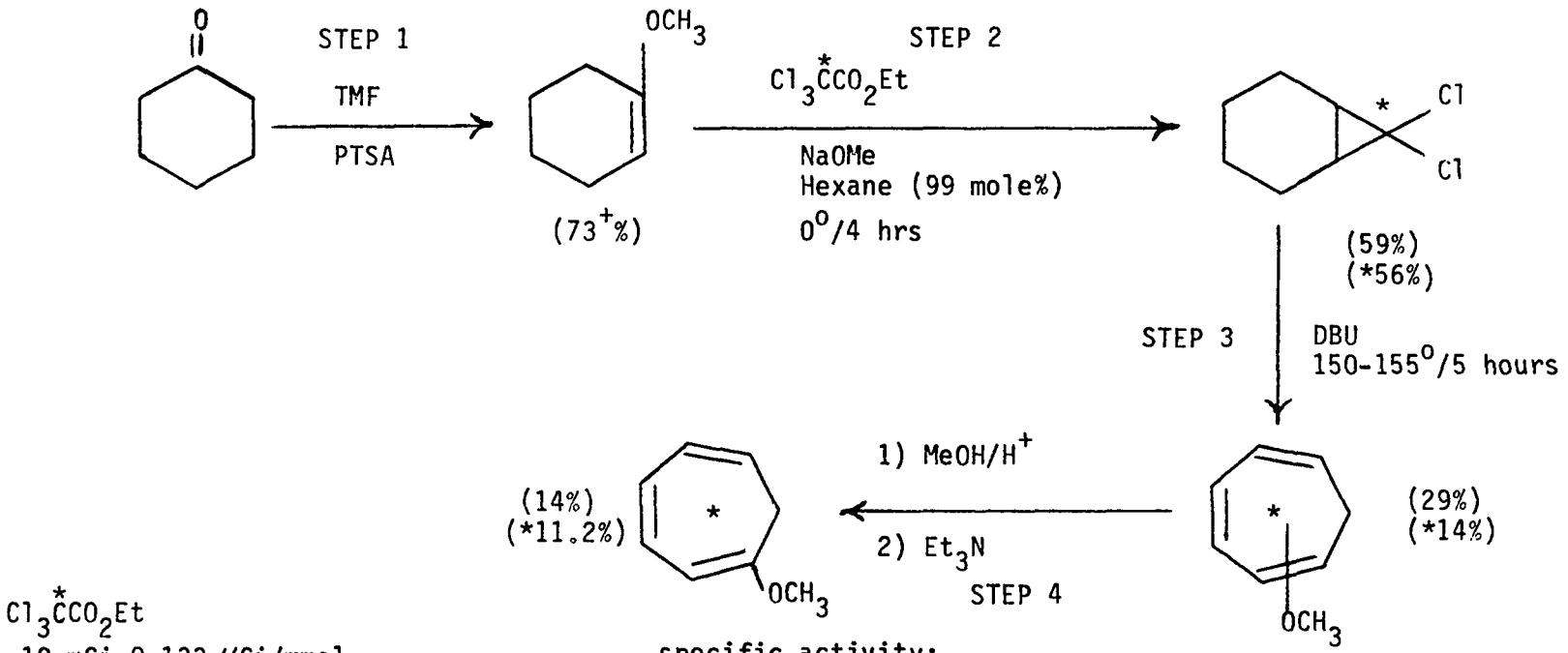

Figure 3. Synthesis of ring-labeled (^{14}C) EA 4923 (the asterisk indicates the position of the labeled atom or a radiochemical yield).

EXPERIMENTAL METHODOLOGY

The analytical methodology supporting this work has been described by King and colleagues (5). In the present instance, gas radiochromatography was again used as the principal tool for following the reactions. The precursor intermediates were also characterized initially by elemental and NMR analyses. Product purities and isomer rations paralleled those reported for the sidechain analog.

Inasmuch as the "cold" synthesis has been described as noted above and in further citations below, and in view of the fact that a detailed report on the "hot" synthesis is pending (9), only a general commentary on the reaction sequence will be presented here. Please refer to Figure 3 for the noted reaction steps.

STEP 1. Biffin and Paul referenced the preparation of 1-methoxycyclohex-1-ene by Lindsay and Reese (10). This reaction was optimized by Mr. T.C. Berenthien in his investigations of the entire process shown in Figure 3 (11).

STEP 2. In the previously cited synthesis of the bicyclic compound the reaction required chloroform as solvent and carbene precursor in the presence of aqueous base. For the "hot" synthesis, this step proved to be a convenient place to introduce the carbon 14. This was done with ethyl trichloroacetate labeled in the 2-position, in the presence of sodium methoxide and in hexane solvent.

STEP 3. Dehydrohalogenation of the bicyclic geminal dichloride has been accomplished with quinoline (8) as well as tri-n-butylamine (11). In our hands, quinoline was ineffective and the butylamine has been shown to present separation problems that could be solved for large "cold" preparations but were not easily adapted to a "hot" microscale synthesis. Alternatively, 1,8-diazabicyclo[5.4.0]undec-7-ene (DBU), available from Aldrich Chemical Co., Milwaukee, WI, and its analog, 1,5-diazabicyclo[4.3.0]non-5-ene (DBN) are well known reagents for this type reaction; DBU appeared to be the most effective in this synthesis.

STEP 4. The product from Step 3, a mixture of 1-, 2-, and 3-methoxycycloheptatrienes was not further purified prior to this acid-catalyzed isomerization/isomer enhancement reaction; reaction time in the acidulated methanol solvent was 70 minutes prior to neutralization with triethylamine. The resulting reaction mixture was distilled in vacuo at ambient temperature using a liquid nitrogen-cooled condenser in analogy to the purification of the sidechain-labeled material (5). Pressure was initially maintained at about 12 torr to remove the solvent. After clearance of the frozen solvent from the condenser (by warming) and recooling, maximum pump vacuum gave the product with the specific activity shown.

DISCUSSION

The modifications critical to the use of this reaction sequence for the synthesis of ring-labeled EA 4923 begin with Step 2. The use of labeled ethyl trichloroacetate as a carbene precursor required anhydrous conditions, an appropriate base, and a solvent. It is absolutely mandatory that the sodium methoxide be fresh or at least contain no hydrolyzed material. Several attempted preparations using material of unknown age and purity resulted in little or none of the bicyclic product being formed. It is no less important to use solvent free of unsaturated components; experimentation revealed that a technical grade of mixed hexanes also gave a reduced or no yield of the bicyclic product, the unsaturated components of the solvent apparently competing successfully for the carbene.

Step 3 is probably the most critical one of this procedure. The dichloride and the dehydrohalogenating agent, DBU, are mixed at 125°C and after a short induction period an exothermic reaction begins which carries the reaction temperature into the 170-200° range; as noted in Figure 3, the mixture is then held at 150-155° for 5 hours. Subsequent workup of the reaction mixture is somewhat complex, requiring aqueous acidulation to remove the DBU and then isolation of the product by extraction with organic solvents.

Step 4 is modeled on that reported by Biffin (11), and has been used to enhance the 1-isomer content of EA 4923 samples as well as to incorporate the C-14 methoxy group (5). The essential aspects of this step are to limit the isomerization/isomer enhancement period to 70 minutes and distill the product at ambient temperature; in both cases product quality is enhanced. Also, from a subjective viewpoint, the rate of radiolytic decomposition appears to be directly related to increasing specific activity of the preparations.

CONCLUSIONS

This study has demonstrated that ring-labeled EA 4923 with a reasonable specific activity can be prepared in modest yield with product purity and isomer ratios comparable to those obtained in the synthesis of the sidechain-labeled analog.

REFERENCES

1. T.C. Simmons, A. Singer, T.A. Koviak, W.J. Shuely, W.E. Sultan, and J.W. King. EC-TR-76018. Studies of Potential Irritant Agents. I. A Comprehensive Investigation of EA 4923. June 1976. UNCLASSIFIED Report.

2. A.W.H. Wardrop, G.L. Sainsbury, J.M. Harrison, and T.D. Inch. Preparation of Some Dibenz[b,f][1,4]oxazepines and Dibenz[b,e]azepines. J. Chem. Soc., Perkin I, 1279-1285 (1976).

3. Anomymous. Comments on CR. The Lancet, No. 7816, pp. 1370-1371. 16 June 1973.

4. Harry A. Brown, Jr. Personal communication.

5. J.W. King, D.R. Bowie, L.L. Szafraniec, and B.F. Truffa III. EC-TR-76083. Studies of Potential Irritant Agents. II. The Synthesis of Radiolabeled EA 4923. December 1976. UNCLASSIFIED Report.

6. B. Calesnick and A.M. Dinan. CRDC-CR-85002. Pharmacologic and Metabolic Studies of Selected Compounds. March 1985. UNCLASSIFIED Report. (The ring-labeled EA 4923 was also used by these investigators in a subsequent study. See Contract No. DAAK11-81-C-0029. Pharmacological and Catabolic Profiles of Selected Compounds).

7. J. Renson, H. Weissbach, and S. Udenfriend. On the Mechanism of Oxidative Cleavage of Aryl-Alkyl Ethers by Liver Microsomes. Mol. Pharmacol. 1, 145-148 (1965).

8. M.E.C. Biffin and D.B. Paul. Maribyrnong Report 461. Approaches to the Methoxycycloheptatrienes by Carbenoid Expansion of Six-Membered Ring Systems. August 1971. UNCLASSIFIED Report.

9. J.W. King and D.R. Bowie. Studies of Potential Irritant Agents. VI. The Synthesis of C-14 Ring-Labeled EA 4923. UNCLASSIFIED Report. In preparation.

10. D.G. Lindsay and C.B. Reese. Pyrolysis of 7,7-Dibromobicyclo[4.1.0]heptane and Derivatives. Tetrahedron 21, 1673-1680 (1965).

11. T.C. Berenthien, Munitions Directorate, U.S. Army Chemical Research, Development and Engineering Center, Aberdeen Proving Ground, MD. Mr. Berenthien later effectively supervised the scale-up of this process by a contractor (see J.T. Uchic, R.J. Dihu, R.H. Snow, W.D. Henline, and B.J. Jody. CRDC-CR-84016. Chemical and Mechanical Process Technology Development. Task B. Evaluation of Processes for Production of 1-Methoxycycloheptatriene (EA 4923). June 1984. UNCLASSIFIED Report).

12. M.E.C. Biffin. Maribyrnong Technical Note 242. The Acid Catalyzed Rearrangement of 3-Methoxycycloheptatriene Into Its 1-Methoxy Isomer. May 1972. UNCLASSIFIED Report.

Medetomidine Analogs as α-Adrenergic Agonists

Yoshiya Amemiya[1], Fulian Hsu[2], Gamal Shams[3], Dennis R. Feller[3], B. V. Venkataraman[3], Popat N. Patil[3], and Duane D. Miller[1]

ABSTRACT

There are two major classes of drugs that interact with adrenergic receptors. Recently, it has been reported that medetomidine is a new 4-substituted imidazole analog possessing selective and potent α_2-adrenergic properties. It has been shown that it reduces blood pressure, heart rate and saliva secretion. At the present time its sedative and hypotensive effects seem to be manifest in the same dose range. We have initiated a program to see if it is possible to separate these activities with analogs of medetomidine. The initial studies have been directed at procedures for the conversion of the imidazolines, a common structure of α-adrenergic drugs, to the corresponding imidazoles. It was found that 2-substituted and 2,4-disubstituted imidazolines can easily be converted into imidazoles using 10% Pd/C in refluxing toluene while in some instances there are some difficulties with the conversion of 4-substituted imidazolines to the imidazoles. The synthesis of 1- or 2-(2- or 4-imidazolylmethyl)naphthalene analogs of medetomidine will also be described.

INTRODUCTION

Although most potent α-adrenergic agonists are members of either the phenethanolamine or imidazoline class of chemical compounds, it has recently been shown the medetomidine (1), an imidazole analog, is a potent and selective α_2-adrenergic agonist. In order to gain a better understanding of the structural requirements of imidazole analogs for potent adrenergic activity, we have prepared two 4-substituted imidazoles, (2) and (3), along with a 2-substituted imidazole (4) for examination as α-adrenergic agonists.

Our initial approach in the synthesis of the analogs was to use a common synthetic scheme in which we would prepare imidazolines and carry out a dehydrogenation of the imidazolines to the desired imidazoles. There are several procedures reported [4-8] for the conversion of imidazolines to

FIGURE 1

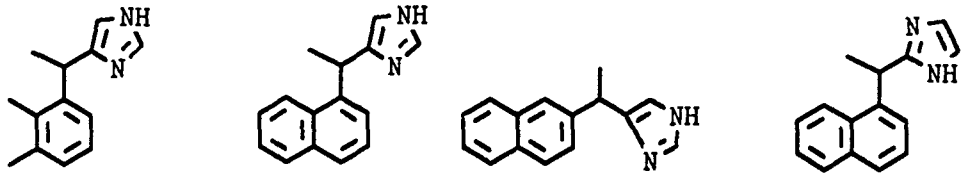

1 2 3 4

imidazoles. These conditions are normally harsh and include high reaction temperatures and the use of large amounts of oxidants.

FIGURE 2

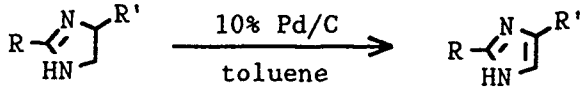

Our desire was to develop a mild oxidation for the conversion of imidazolines to imidazoles. We found that 2- and 2,4-disubstituted imidazolines could easily be converted to imidazoles using 10% Pd/C in refluxing toluene in high yield (Figure 2). A retrosynthetic procedure was devised for the synthesis of 2-substituted imidazoles as outlined in Figure 3.

FIGURE 3

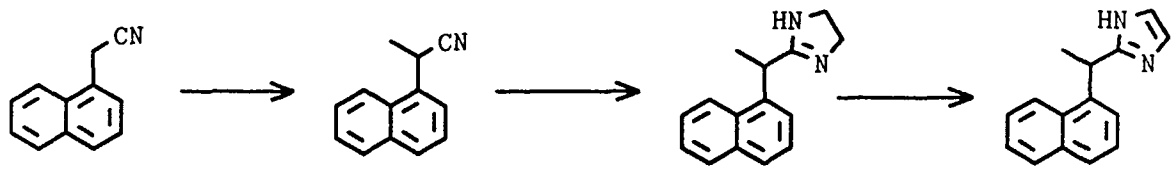

However, difficulties were encountered with the conversion of 4-substituted imidazolines to the respective imidazoles. Thus, we turned to another approach in the synthesis of 4-substituted imidazole analogs of medetomidine using TMS-imidazole in the presence of a benzylchloride as outlined in Figure 4.

FIGURE 4

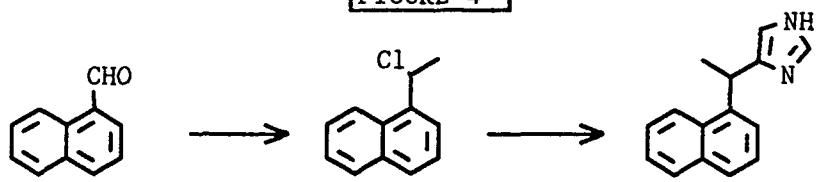

CHEMISTRY

1. Oxidation of Imidazolines to Imidazoles. We initiated our studies of the oxidation of imidazolines to imidazoles

with the conversion of 2-phenylimidazoline to the corresponding imidazole (85% yield) as shown in Figure 5.

FIGURE 5

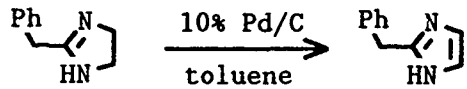

Next, we focused on the conditions of this new reaction and found that the nature of the 3,4-substituents on the 2-phenyl group had a major effect on the reaction as illustrated in Figure 6. Benzyl protecting groups seem to interfere with the

FIGURE 6

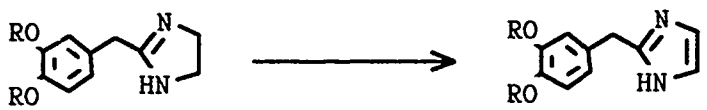

R	Cat	Reaction time	Yield
CH_2Ph	10% Pd/C	40h	0%
CH_3	10% Pd/C	40h	84%
CH_3	5% Pd/C	250h	69%

reaction. With the 3,4-dimethoxy groups the reaction worked best with 10% Pd/C as compared with 5% Pd/C. The use of 10% Pd/C allowed for shorter reaction times and gave higher yields in this specific instance. Also we found that 2,4-disubstituted imidazolines could also undergo the reaction in good yield (Figure 7). In the oxidation of 4-substituted

FIGURE 7

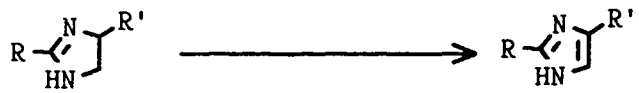

R	R'	Reaction time	Yield	M.P.
Ph	Ph	40h	85%	161-162
Ph	$PhCH_2$	40h	87%	168-169

imidazolines we obtained mixed results. The oxidation of 4-phenylimidazoline using 10% Pd/C gave the desired 4-phenylimidazole in 51% yield (Figure 8). However, when

FIGURE 8

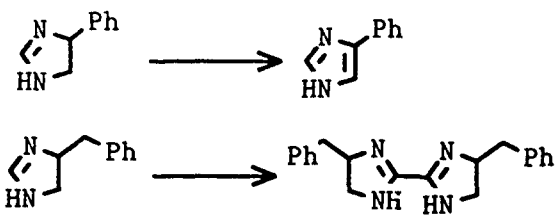

4-benzylimidazoline was treated with 10% Pd/C, we surprisingly obtained 2,2'-(4,4'-dibenzyl)diimidazoline (Figure 8). Thus,

we were not able to utilize this procedure in the preparation of the 4-substituted imidazoles as we had thought we might at the beginning of the project. Caution must be used when considering this oxidation procedure for the conversion of 4-substituted imidazolines to imidazoles.

2. Synthesis of 2-(1-naphthylethyl)imidazoline (4), using 10% Pd/C, as an analog of medetomidine (1) was carried out as outlined in the synthetic Scheme 1. 1-Naphthylacetonitrile was

SCHEME 1

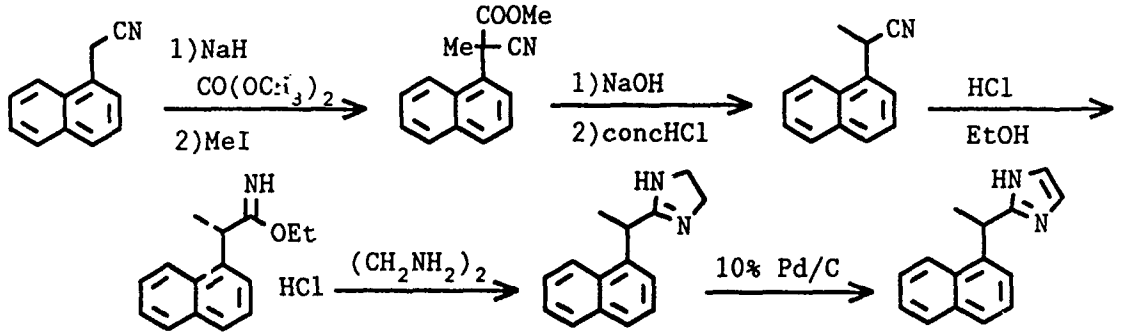

converted to the disubstituted methyl cyanoacetate derivative by the usual method [NaH and $CO(OCH_3)$], followed by treatment of MeI in DMF and toluene. The cyanoacetate derivative was hydrolyzed and decarboxylated to give the mono-substituted 1-naphthylacetonide derivative. The cyano compound was converted to the imido-ester and then to the 2-substituted imidazoline derivative. The imidazoline derivative was then oxidized using 10% Pd/C in refluxing toluene to give the desired imidazole (4) as a HCl salt in 89% yield.

3. Synthesis of the 4-substituted imidazole analogs 2 and 3 of medetomidine (1). Because of the difficulty in the oxidation of 4-substituted imidazoline analogs to imidazoles we utilized a different synthetic route as outlined in Scheme 2 for the synthesis of 2. 1-Formylnaphthalene was treated with

SCHEME 2

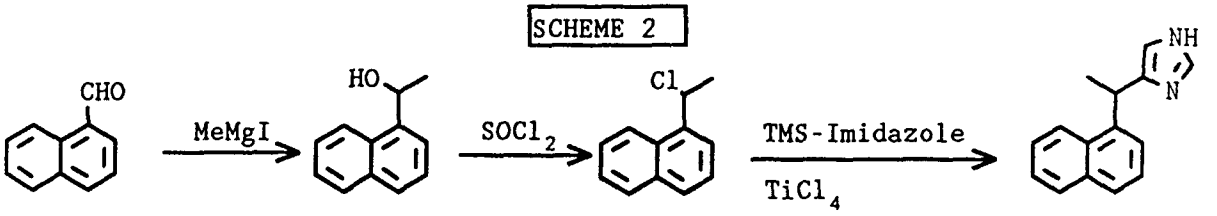

MeMgI to form an alcohol which was in turn treated with $SOCl_2$ to give a benzyl chloride. The chloride was then treated with TMS-imidazole in the presence of $TiCl_4$ using $CHCl_3$ as the solvent to give the desired 2. We have utilized a similar set of procedures starting with 2-formylnaphthalene to obtain the imidazole 3 (this sequence of reactions is not shown).

Compounds 2,3 and 4 have been examined for their α-adrenergic activity as inhibitors of platelet aggregation induced by epinephrine and compared to medetomidine (1), see Table 1. α-Adrenoceptor sites in human platelets are classified as an α_2- or α_{2A}-subtype and platelets are being

used as model system for the evaluation of the affinities of these compounds. Most imidazolines and imidazoles such as medetomidine possess inhibitory rather than stimulatory activities for platelet adrenergic receptors sites (α_2 subtype).

TABLE 1

Medetomidine and analogs mediated inhibition of primary [in presence of aspirin (1 mM)] and secondary phases of platelet aggregation induced by epinephrine (10-70 μM).

	pIC_{50}	
compound	with aspirin	without aspirin
1	5.48 ± 0.20	6.28 ± 0.17
2	5.47 ± 0.07	5.83 ± 0.16
3	3.92 ± 0.05	4.21 ± 0.03
4	3.58 ± 0.14	4.11 ± 0.01

CONCLUSIONS

We have developed a new mild and useful method for the conversion of imidazolines to imidazoles using 10% Pd/C in refluxing toluene. Using this procedure we have successfully synthesized a 2-substituted analog (4) of medetomidine (1). However, this procedure does not work with all 4-substituted imidazoline conversions to imidazoles. Thus, we turned to the use of TMS-imidazole with appropriate benzyl chlorides in the presence of $TiCl_4$ to prepare the imidazole analogs 2 and 3. Of the analogs prepared analog 2 was very similar in activity to medetomidine (1) as an inhibitor of platelet aggregation induced by epinephrine. Compounds 3 and 4 were much less potent as inhibitor in the same system.

ACKNOWLEDGMENTS

We thank the Department of the Army for partial support of this research project.

REFERENCES

1. Division of Medicinal Chemistry and Pharmacognosy, The Ohio State University, 500 West 12th Avenue, Columbus, Ohio 43210.

2. U.S.Army Chemical Research, Development and Engineering Center, Aberdeen Proving Ground, MD 21010-5423.

3. Division of Pharmacology, The Ohio State University, 500 West 12th Avenue, Columbus, Ohio 43210.

4. Grimmett, M.R., in Advances in Heterocyclic Chemistry; Katritzby, A.R., Boulton,A.J.,Eds., Academic press, New York, 1970, p. 129.

5. Chem. Abs., 64, 6412684h (1966).

6. Martin, K., Matthews, H.R., Rapoport, H., and Thyagarajan, G., J. Org. Chem., 33, 3758 (1968).

7. Hughey IV, J.L., Knapp, S., and Schugar, H., Synthesis, 1980, 489.

8. Zimmerman, S.C., Cramer, K.D., and Galan, A.A., J.Org.Chem., 54, 1256 (1989).

9. Hsu, F.,Hamada, A., Booher, M.E., Fuder, H., Patil P.N., and Miller, D.D., J. Med. Chem., 23, 1232 (1980).

RECENT DEVELOPMENTS IN THE PHYSICAL CHEMISTRY OF SIMULANT SELECTION

Elwin Penski, Donald Fielder, Ann Brozena, and Helen Walker
Physical Chemistry Branch, Chemical Division, Research Directorate
U.S. Army Chemical Research, Development, and Engineering Center
Aberdeen Proving Ground, Maryland 21010-5423

ABSTRACT

Since physical chemical properties are vital to the determination of many types of behavior of agents and their simulants, it is essential that accurate data for simulants be located and/or measured. A careful examination of the vapor pressure equations found in computerized data bases for several compounds including the common simulant, diethyl malonate, was performed. It shows that the data in the literature is frequently inadequate for the selection of chemicals to simulate the vapor pressure controlled properties of agents to within 100% or more inspite of impressive statistical correlations. Thermodynamic properties and Hildebrand parameters for the vesicant "mustard", its simulants, and 14 related compounds have been calculated and compared with values resulting from an extensive literature search. Good agreement between the few literature values available and calculated values was obtained. Recently measured vapor pressures, densities, and viscosities are referenced.

INTRODUCTION

Many types of system analysis and design calculations are based on the physical chemical properties of simulants. The physical chemical properties of the simulants involved in any practical endeavor are part of the foundation of data required in every stage of planning, development, or analysis. Often, delays and problems are a result of not having a solid data foundation in place before selecting a simulant.

In this report the usual definition of the word simulant is used, that is a relatively nonhazardous chemical with similiar properties (+/- 25%) as related to a given process of interest (such as skin decon training, explosive dissemination, or alkyd paint retention) for a hazardous chemical of interest.

For the reader who thinks that a few tenths of a Torr cannot be important, a calculation of the evaporation of a suspended

droplet of diethyl malonate at ambient conditions has been performed for illustrative purposes (1) with the largest and smallest vapor pressures found in the literature. Based on calculations using the U.S. Air Force Materials Data Base value of vapor pressure, it might be expected that DEM would be gone after five hours when according to Russian data about 48% is left. Vapor pressures have a major impact on many aspects of simulant behavior and are usually one of the most important factors in simulant selection. This report begins with a critical literature review of a few potential simulants.

REVIEW OF THE VAPOR PRESSURE LITERATJRE FOR N-AMYL ACETATE

Several vapor pressure values were found in the literature for n-amyl acetate. These are given in table 1.

TABLE 1. Summary of Vapor Pressure Data for n-Amyl Acetate

Source (Year)	Vapor Pressure at 25 °C, Torr	Vapor Pressure at 30 °C, Torr	Reference
Dykyl and Repas (1979)	5.2	7.2	2
Data from 1940			3
Timmermans (1950)	(Claimed that "There are no reliable data for n-amyl acetate.")		4
Scheflan and Jacobs (1953)		9.0	5
Jordan (1954)	4.0	5.5	6
DIPPR equation (1989)	3.5	4.8	7
Data from 1980			8
Riddick, Bunger and Sakano (1986)	9.7		9

Timmermans (4) claimed that "There are no reliable data for n-amyl acetate." He did not explain his statement, but it may have been made due to the fact that in the literature the words "n-amyl acetate" were found to often refer to mixtures with unspecified purities or only 85% n-amyl acetate (3,5).

The Design Institute for Physical Property Data (DIPPR) data file (7) gives the following equation for the dependence of n-amyl acetate vapor pressure on temperature:

$$\ln P = 75.753 - 8051.2 / T - 7.4786 \times \ln T + 8.0921 \times 10^{-18} \times T^{6}$$

where:

P = Vapor pressure (Pascal)
T = Temperature (Kelvin)

The DIPPR data file claims less than 3% error for the above equation in the range from -70.8 to 324.8 °C. The DIPPR equation is based on "data" from the Thermodynamics Research

Center, Data Project, Texas A&M University (8), a secondary source.

At this time it is necesary to be very skeptical of all n-amyl acetate data or equations for physical chemical properties for n-amyl acetate.

REVIEW OF THE VAPOR PRESSURE LITERATURE FOR ETHYL ACETOACETATE

Two sets of Antoine constants were found in the literature for ethylacetoacetate (6,10). These are given in table 2. All the data used to generate these equations came from Stull (11). The data Stull used to obtain his fit is given in table 3; most of the original data was published in 1884. Stull apparently fitted this data (Table 3) to the Clausius-Clapeyron Eq. with graphical methods. He then generated points at 1, 10, 40, 100, 200, 400, and 760 Torr. These points, "Stulls data," have been used as though they were experimental points by many workers to established vapor pressure-temperature equations.

Collins (12) has used the data in table 3 to obtain Antoine and Clausius-Clapeyron equation constants. This is all summarized in table 2.

TABLE 2. Summary of Vapor Pressure Equation Constants for Ethyl Acetoacetate Based on the Data Used by Stull

Antoine Constants			Vapor Pressure at 25 Celsius	Reference
A	B	C	Torr	
8.70805	2684.94	281.12	0.87	Jordan (6)
7.79115	2003.6	227.41	0.71	Czechs (10)
5.998	919.8	116.5	0.31	Collins fit to Antoine Eq.
8.814	2656	273.16 (13)	0.81	Collins (12)

TABLE 3. Source Vapor Pressure Data Used by Stull (11) for Ethyl Acetoacetate

Compound Name Used	Temperature Celsius	Vapor Pressure Torr	References
Acetessigsaure-aethylester	71.4	10	14 (1895)
	71.8	10	14
Acetessigather	54.3	5	15 (1884)
	65.9	10	15
	75.0	15	15, 16
	80.5	20	15, 16
	84.2	25	15
	95.1	50	15
	99.5	75	15
	181.0	760	15

The DIPPR data file (7) gives the following equation for the dependence of ethyl acetoacetate vapor pressure on temperature:

$$\ln P = 53.878 - 7499.7 / T - 4.2265 \times \ln T + 1.5175 \times 10^{-18} \times T^{6}$$

where

= Vapor pressure (Pascal)
T = Temperature (Kelvin)

The values calculated with it match "Stull's data." The data used to obtain this fit and all the statistics that go with it are "Stull's data." The CRC Handbook of Chemistry and Physics (17) only gives "Stull's data."

Pure ethyl acetoacetate does not exist (18). Ethyl acetoacetate is an excellent example of a tautomer. Tautomerism is the spontaneous equilibrium between chemical isomers that are in fact different compounds with the same atomic formula. The two ethyl acetoacetate isomers are given below:

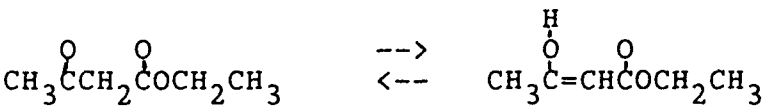

The alcohol form (enol form) is about 10% of the mixture at room temperature. The equilibrium should shift with temperature or solvent changes, but pure tautomer should have the same concentrations throughout its vapor pressure measurement due to the fact that equilbrium is restored in fractions of a minute. How this effects the vapor pressure is not known.

LITERATURE REVIEW OF DIETHYL MALONATE VAPOR PRESSURES

The vapor pressures of diethyl malonate are given by Jordan (6) and the CRC Handbook of Chemistry and Physics (17) (CRC) as specific values (Table 4) over the range from 40 to 198.9 C, the latter being the normal boiling point.

The above values were found to date as far back as 1895. Jordan obtained these values from Stull (11) who obtained the above data from fitting the 1895 data of Anschutz and Reitter (14), and the 1940 data of Hieber and Reindl (19). The data of Anschutz and Reitter, and Hieber and Reindl is also given in table 4. The data of Anschutz and Reitter was measured with a mercury manometer and the data of Hieber and Reindl was obtained with a glass spring manometer. Glass spring manometers were usually calibrated with a mercury manometer. Hieber and Reindl reported a plot of the logarithm of vapor pressures versus reciprocal of temperatures of their data to be quite linear.

TABLE 4. Diethyl Malonate Vapor Pressures from DIPPR, Jordan, the CRC Handbook and Their Sources

Temperature	Vapor Pressure			
	DIPPR	Jordan & CRC	Anschutz & Reitter	Hieber & Reindl
Celsius	Torr	Torr	Torr	Torr
40.0	0.82	1		
41.5				1.2
64.3				4.0
67.5	4.7	5		
81.3	10.0	10		
87.1			12	
92.5				16.5
94.8				18.3
95.9	20.7	20		
99.6				22.7
107.2				31.5
112.0				38.9
113.3	44.8	40		
115.6				45.4
118.7				51.2
121.7				58.0
123.0	66.7	60		
123.5				62.4
123.8				65.8
129.0				79.4
133.6				92.6
135.7				100.8
136.2	110.	100		
137.0				103.5
142.4				125.9
150.8				173.8
155.5	215.	200		
155.5				201.3
162.9				255.1
169.5				312.1
175.5				385.7
176.8	416.	400		
181.5				460.1
190.6				620.9
197.9			760	
198.9	766.	760		

A more recent Antoine equation for the range from 20 to 45 degree Celsius is provided by Stephenson and Malanowski (10) and is given below:

$$\text{Vapor Pressure (kPa)} = 10^{A - B/(T + C)}$$

where:

A = 9.1982 B = 3307 C = 273.15

t = Temperature in Celsius

At 40 °C the vapor pressure is 0.04346 kPa or 0.33 Torr compared to 1 Torr from Stull, CRC Handbook, and Jordan (One Torr is 0.13332 KPa). The Czech source (10) claims 1 to 5 degree accuracy in this range. Reference 10 is a survey that is nearly unknown outside of Eastern Europe. The above equation is from a Soviet report (20) and from effusion measurements.

It appears from table 5 that the standard handbooks are not in agreement with recent DEM data nor does the vapor pressure of GD (0.4 Torr at 25 deg. C.) match that of recent DEM measurements (21, 22).

TABLE 5. Comparison of Vapor Pressures at 25° and 40°C from Different Sources

Data Source	DEM Vapor Pressures Temperature 25°C Torr	Temperature 40° C Torr
Jordon (6), Data from Stull (11)	-	1.0
CRC Handbook of Chemistry & Physics, 1986 (17) from Stull	-	1.0
US Air Force Materials Data Base (Data source not given)	0.4	-
DIPPR, Same Data (7) as Jordan (6) and CRC Handbook (17)	0.27	0.82
Czech Handbook (10), Based on Soviet Data (20) (Effusion)	0.096	0.326
Irvin [Based on EPA standard method which measures evaporation from packed glass beads with GC (21)]	0.174	0.556
Fielder and Brozena [Effusion(22)]	0.223	0.695

Fielder and Brozena (23) have obtained the densities, viscosities, and vapor pressure data for other candidate GD simulants: isopropyl-t-butyl phosphonofluoridate, isobutyl-t-butyl phosphonofluoridate, and ethyl vinyl phosphonofluoridate.

HEATS OF FORMATION AND OTHER THERMODYNAMIC PROPERTIES OF MUSTARD, ITS SIMULANTS, AND RELATED COMPOUNDS

Recently values for the molar enthalpies of formation, enthalpies of vaporization, enthalpies of fusion, and Hildebrand parameters (solubility parameters) for the vesicant "mustard", its simulants and related compounds were estimated (24) from group contributions values provided by the National Institute of Standards and Technology. The compound names and abbreviations are given in table 6. The estimated values are given in table 7 and 8. Agreement with literature data was shown to be generally good (24). The report also compiled densities and molar volumes of the compounds listed in table 6.

TABLE 6. Compound Names and Abbreviations

1-Bromobutane (1-BB)
t-Butyl chloride; 2-chloro 2-methylpropane (TBC)
2-Chloroethyl n-butyl sulfide (CEBS)
2-Chloroethyl ethyl disulfide (CEED)
2-Chloroethyl ethyl sulfide (CEES)
2-Chloroethyl methyl sulfide (CEMS)
Di-(n-butyl) sulfide (DNBS)
Di-(2-chloroethyl) disulfide (DCED)
Di-(2-chloroethyl) sulfide (HD)
1,5-Dichloropentane (DCP)
Di-(3-chloropropyl) sulfide (DCPS)
Diethyl disulfide; 3,4-dithiahexane (DEDS)
Diethyl sulfide; 3-thiapentane (DES)
2-Hydroxyethyl 2-chloroethyl sulfide (HECES)
2-Hydroxyethyl ethyl sulfide (HEES)

TABLE 7. Molar Enthalpies of Formation at 25° Celsius

	Enthalpy of Formation Kcal/mole		
Chemical	Vapor	Liquid	Solid
1-BB	-25.6	-34.1	-37.1
TBC	-43.7	-50.3	-50.8
CEBS	-36.3	-50.3	-55.9
CEED	-26.6	-38.4	-42.4
CEES	-26.5	-38.0	-41.8
CEMS	-21.2	-31.7	-35.4
DNBS	-39.3	-52.9	-58.5
DCED	-33.5	-48.2	-53.8
HD	-33.4	-47.8	-53.3
DCP	-48.8	-60.7	-66.3
DCPS	-43.2	-60.1	-67.3
DEDS	-19.7	-28.7	-30.9
DES	-19.6	-28.3	-30.4
HECES	-62.0	-80.8	-85.4
HEES	-55.1	-71.0	-73.9

TABLE 8. Molar Enthalpies of Fusion and Vaporization, and Hildebrand Parameters at 25° Celsius

Chemical	Heats of Fusion	Heats of Vaporization	Hildebrand Parameter
	Kcal/mole	Kcal/mole	$(cal/cc)^{1/2}$
1-BB	3.0	8.5	8.6
TBC	0.5	6.6	7.4
CEBS	5.6	14.0	9.4
CEED	3.9	11.8	9.1
CEES	3.8	11.6	9.7
CEMS	3.7	10.5	10.0
DNBS	5.7	13.6	8.6
DCED	5.6	14.7	9.9
HD	5.5	14.4	10.5
DCP	5.6	11.9	9.4
DCPS	7.3	16.8	10.1
DEDS	2.3	9.0	8.2
DES	2.1	8.7	8.6
HECES	4.6	18.8	11.9
HEES	2.9	16.0	12.1

In addition, Fielder, Brozena, Beaudry, Rohrbaugh, Szafraniec, and McHugh (25) submitted a report for publication with selected physical and spectrometric properties of candidate mustard simulants DCED, DCPS, and CEED.

DISCUSSION AND CONCLUSIONS

One must be very skeptical of all vapor pressure data found in the literature and of elaborate statistical treatments of such data. The many fits of "Stull's data" found in the literature are worthless. They are not fits of data but fits of numbers generated by fits. To carry this necessary skepticism to its logical conclusion, one must wonder if even the raw data such as that of Kahlbaum (15)) did not undergo some modification before publication. In that case there may be three steps of fitting or smoothing of the data currently being used. Needless to say this introduces considerable error. Since so much data must be traced back so far to get to "real" data, special responsibilities are placed on librarians to maintain old journals, books, notebooks, and translations in a useable form.

A computerized literature search revealed little if any vapor pressure measurements of organic compounds with vapor pressures in the 0.001 to 1 Torr range having ever been performed in the United States except those at CRDEC and those measured for a few isolated or specialized applications. Some values in the 0.001 to 1 Torr range involve extrapolations of 40 to 80 degrees Celsius which may lead to errors of a few hundred percent. Such factors raise many questions about the physical chemical properties found in handbooks. For example most

solubility parameters are taken from heats of vaporization obtained from questionable vapor pressure data. Thus, it must be recognized that there are enormous knowledge gaps in simulant selection and use that cannot be eliminated without increased "quality" data gathering efforts. Low quality efforts only serve to impede progress in all programs by adding additional layers of misinformation and wasted resources.

Also, it has been found that documentation of vapor pressure measurement methodology varies from obscure to not mentioned. The criteria that a "knowledgeable scientist should be able to repeat the experiment" is rarely if ever met.

Clearly the ambient temperature vapor pressures of DEM in the standard handbooks are highly questionable. The experimental work of Brozena and Fielder covering the micron range up to the boiling point should be regarded as the best data available at this time (22). Recent DEM data does not appear to match GD data very well. As a result, DEM cannot be recommended as an evaporation simulant for GD.

REFERENCES

1. Penski, E.C. and Walker, H.M., U.S. Army Chemical Research, Development and Engineering Center, Aberdeen Proving Ground, MD, Private Communication, January 1989.
2. Dykyj, J., and Repas, M. Tlak Nasytenej Pary Organickych Zlucenin, Vydavatelstvo Slovenskej Akademie Vied, Bratislava, Czechoslovakia, Vol. I, 1979.
3. Qualye, O.R., and Norton, H.M., The Mechanism of Esterification of Strong Acids. The Esterification of Neopentyl Alcohol with Chloroacetic Acids, Journal of the American Chemical Society, Vol.62, 1170 (1940).
4. Timmermans, J., Physico-Chemical Constants of Pure Organic Compounds, Elsevier Publishing Company, Inc., New York, page 419, 1950.
5. Scheflan, L. and Jacobs, M.B., The Handbook of Solvents, D. Van Nostrand Company, Inc., New York, 1953.
6. Jordan, T.E., Vapor Pressure of Organic Compounds, Interscience Publishers, Inc., New York, 1954.
7. The Design Institute for Physical Property Data (DIPPR) data file was set up to contain data evaluated and verified by a project of the DIPPR of the American Institute of Chemical Engineers. The DIPPR Project staff are located at Pennsylvania State University. The only reference that they give as their data source for n-amyl actetate is reference 8.
8. Thermodynamics Research Center, Selected Values of Properties of Chemical Compounds, Data Project, Texas A&M University, College Station, Texas (Loose-leaf data sheets, extant, 1980). Dr. Ken Marsh of the Thermodynamics Research Center, Data Project, Texas A&M University, College Station, Texas has stated that Texas A&M has made no measurements.
9. Riddick, J.A., Bunger, W.B., and Sakano, T.K., Techniques of Chemistry Vol. II, Organic Solvents, Physical Properties and Methods of Purification, John Wiley & Sons, New York, 1986.

10. Stephenson, R.M. and Malanowski, S., Handbook of the Thermodynamics of Organic Compound, Elsevier, New York, p239, 1987. (Based on Dykyj, J., Repas, M. and Svoboda, J., Tlak Nasytenej Pary Organickych Zlucenin, Vydavatelstvo Slovenskej Akademie Vied, Bratislava, Czechoslovakia, Vol. I, 1979; Vol. II, 1984.)
11. Stull, D.R., Vapor Pressures of Pure Substances, Organic Compounds, Industrial and Engineering Chemistry, 39, 517 (1947).
12. Dr. Kenneth Collins, Physical Chemistry Branch, Cml Div, Rsch Dir, CRDEC, APG,MD
13. Data fit to Clausius-Clapeyron equation (C set at 273.16).
14. Anschutz, R., and Reitter, H., Die Distillation unter vermindertem Druck im Laboratorium, 2nd Edition, Verlag von Friedrich Cohen, Bonn, 1895.
15. Kahlbaum, G.W.A., Ueber die Abhangigkeit der Siedetemperatur vom Luftdruck, Chemische Berichte, 17,1245 (1884).
16. Repeated in reference 11.
17. Weast R.C., CRC Handbook of Chemistry and Physics, 66th Edition, The Chemical Rubber Company, 1986.
18. Noller, C.R., Textbook of Organic Chemistry, W.B. Saunders and Company, Philadelphia, 1958.
19. Hieber, V.W., and Reindl, E., Heats of Formation and the Constitution of Molecular Compounds of Tin Tetrachloride, Zeitschrift fuer Elektrochemie, 46, 559 (1940).
20. Lebedeva, N.D., Nazarova, L.F., and Katin, Yu.A., Enthalpies of Vaporization of a Series of Bi- and Polyfunctional Compounds, Termodinamika Organ. Sojedinenij (Gor'kij), No. 6, 72 (1977).
21. Irwin, K., Vapor Pressure of Diethyl Malonate, Technical Note for SRI Project 4900, SRI International, Jan 1989.
22. Brozena, A. and Fielder, D., Vapor Pressure of Diethyl Malonate Report submitted for publication in June 1989.
23. Fielder D., and Brozena, A., U.S. Army Chemical Research, Development and Engineering Center, Aberdeen Proving Ground, MD, Private communication, October 1989.
24. Penski, E.C., Estimation of Heats of Formations and Other Thermodynamic Properties III. Mustard, Its Simulants, and Related Compounds, CRDEC-TR-040, U.S. Army Chemical Research, Development and Engineering Center, Aberdeen Proving Ground, MD, January 1989, Unclassified Report.
25. Fielder D., Brozena, A., Beaudry, W.T., Rohrbaugh, D.K., Szafraniec, L.L., and McHugh, V.M., Selected Physical and Spectrometric Properties of Candidate Mustard (HD) Simulants EA 5957, EA 5983, and EA 5992, Report to be submitted for publication in October 1989.

USE OF PENTACOVALENT OXAPHOSPHORANE CHEMISTRY IN THE DEVELOPMENT OF NEW METHODOLOGY FOR THE SYNTHESIS OF NATURAL PRODUCTS

Cynthia K. McClure, Kang-Yeoun Jung, Christopher W. Grote
University of Delaware, Department of Chemistry and Biochemistry, Newark, De 19716

Abstract:

The "Ramirez" condensation between aldehydes and 2,2,2-trialkoxy-1,2λ^5-oxaphospholenes yielded β-hydroxy ketones (aldols) that contain an α-phosphonomethyl group in good to fair diastereomeric ratios. The *syn* diastereomer was the major product. Use of Lewis acids as catalysts allowed for lowered reaction temperatures, as well as shortened reaction times. The yields were also improved in some cases. The diastereomeric ratio of products changed in favor of the *anti* isomer when TMSOTf was the catalyst. Our results are contrary to the published results of Ramirez using 2,2,2-trialkoxy-1,3,2λ^5-dioxaphospholenes and various carbonyl compounds, where the *anti* isomer was the major product in uncatalyzed reactions. Our carbonyl condensation reaction has been applied to the syntheses of the antifungal compounds, *cis*- and *trans*-neocnidilide. Formation of chiral phosphorus in spirophosphoranes by arresting the pseudorotation around the phosphorus has been accomplished in 1,3,2λ^5-dioxaphospholenes with ephedrine as a bidentate ligand. The lack of pseudorotation has been demonstrated by variable temperature NMR studies.

Phosphonate containing compounds are of biological interest as antimetabolites and enzyme active-site probes, especially of pyrophosphatases, the glycolytic pathway, glycerol-related processes, and lipid processes.[1] They also have medicinal value as antivirals[2], antibiotics[3], antiacidosis agents[4], etc, as well as exhibiting herbicidal and insecticidal activities.[1a,b] Generally, the phosphonates initially developed are simple phosphonate analogues of the active phosphate-containing compounds. There are examples, however, of phosphonate-derived drugs that are not related structurally to other compounds with similar biological activities. For example, the phosphonate, Dimephosphon™ (dimethyl 1,1-dimethyl-3-oxobutylphosphonate), discovered during chemical and biological investigations of low-toxic organophosphorus compounds, is used in the treatment of acidosis.[4] In connection with our interest in synthesizing biologically active compounds containing phosphonate group(s), and also with synthetic endeavors in progress in our laboratories, we have investigated the use of the Ramirez carbonyl condensation reaction as a new method for the production of phosphonate-containing compounds.

In the late 1960's and early 1970's, Ramirez and coworkers reported their studies on the reactions of 1,3,2λ^5-dioxaphospholenes, **1a**.[5] New carbon-carbon bonds could be formed by condensation of **1a** with aldehydes and ketones to produce variously substituted α,β-dihydroxy carbonyl compounds (**3** and **4**). Since then, however, applications of these reactions have been few.[6] The use of 1,2λ^5-oxa-phospholenes[7], **1b**, in this carbonyl condensation reaction could produce various β-hydroxy carbonyl compounds, **5**, containing a phosphonate group. The presence of this phosphonate group makes these compounds, or derivatives thereof, possible candidates for screening as antimetabolites, antivirals, etc. For our synthetic targets, the presence of the phosphonate group in the "aldol" compound **5** makes it a very versatile intermediate: the phosphonate group can be eliminated[8,9] to give an α,β-unsaturated system now α-alkylated, or utilized in a Wadsworth-Emmons olefination reaction[9,10] (after suitable activation). **5** can also be alkylated α to the phosphorus[9] to produce more complex substitution patterns.

SCHEME 1

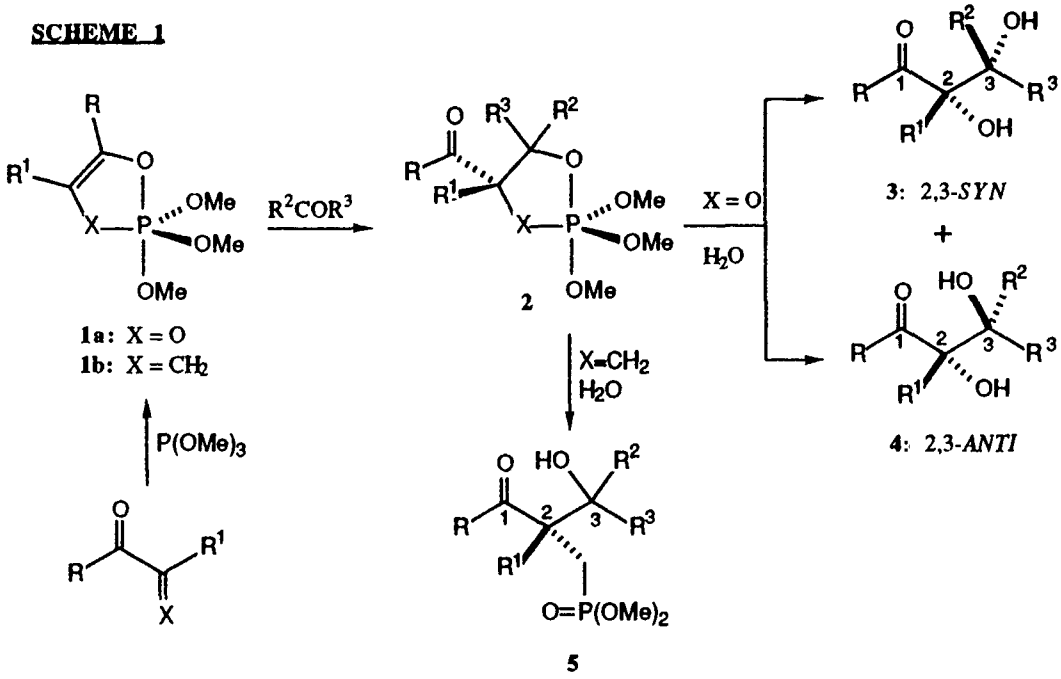

To our knowledge, only one reported attempt (unsuccessful) of this condensation reaction between a $1,2\lambda^5$-oxaphospholene (**1**: R = Me; R^1 = COMe; X = CHPh) and aliphatic aldehydes is documented.[11] The reasons for the failure of this reaction are not clear from the report, although the steric bulk imposed on the system by the phenyl group may be partly responsible. We now report our preliminary results on the successful condensations of various aldehydes with the $1,2\lambda^5$-oxaphospholenes, **6**, derived from methyl vinyl ketone and trialkyl phosphites.[7] We have been able to produce via this method the β-hydroxy α-phosphonomethyl compounds, **7** and **8**. The results to date are summarized in **Table 1**.[12] Correlation of the "aldol" stereochemistry in **7** and **8** was obtained by comparison with published spectral data on similar aldol compounds[13], as well as with the aldol-phosphonate compounds prepared independently via the reaction of the 9-BBN boron enolate of **9** with the aldehydes in question. This procedure is known to produce the *syn* aldol stereochemistry.[14]

The results in **Table 1** indicate that the best *syn* diastereoselectivities resulted from condensation between the bulkiest oxaphospholene (**6**: R = i-Pr) and either benzaldehyde (4.9:1.0 *syn:anti*) or isobutyraldehyde (3.5:1.0 *syn:anti*). Presumably, the steric bulk of the ligands on the phosphorus and/or around the aldehydes is influencing the stereoselectivity. We are presently investigating the effects of other R groups, as well as spiro P^V compounds, on the ratio of the condensation products.

Our initial condensation reactions were performed neat at room temperature according to the procedure used by Ramirez *et al.*, but the reaction times for the $1,2\lambda^5$-oxaphospholenes, **6**, ranged from 2-25 days. The effects of different solvents at various temperatures (THF, hexane, chloroform, dichloromethane, acetonitrile; 0° C, 20° C, 50° C) on the reaction of **6** (R = Me) with benzaldehyde were subsequently investigated. Heating under reflux in dichloromethane gave higher yields and more reasonable reaction times (20 hrs) when compared with the neat reaction conditions. Reactions of **6** with other aldehydes were also successfully performed in dichloromethane under reflux.

During the hydrolyses of the condensation products obtained from **6**, attention had to be paid to the pH of the solution. Retro-aldol occurred if the pH was very basic (≥ 10), with varying amounts of **9** and the aldehyde being isolated. Under these conditions, the ratios of the products **7** and **8** changed in favor of the *anti* isomer, indicating that the *syn* isomer undergoes retro-aldol in preference to the *anti* isomer. Hydrolysis with water resulted in a mixture of ≈ pH 3. Control experiments indicated no change in product composition at pH 1.5-7.0 for R = Et or i-Pr. However, the cyclic phosphonate, **10**, was isolated in varying amounts from the hydrolyses of the trimethoxy (R = OMe) cases at pH's 3, 5 and 10 leading to reduced yields of **7** and **8** for R = OMe.

SCHEME 2

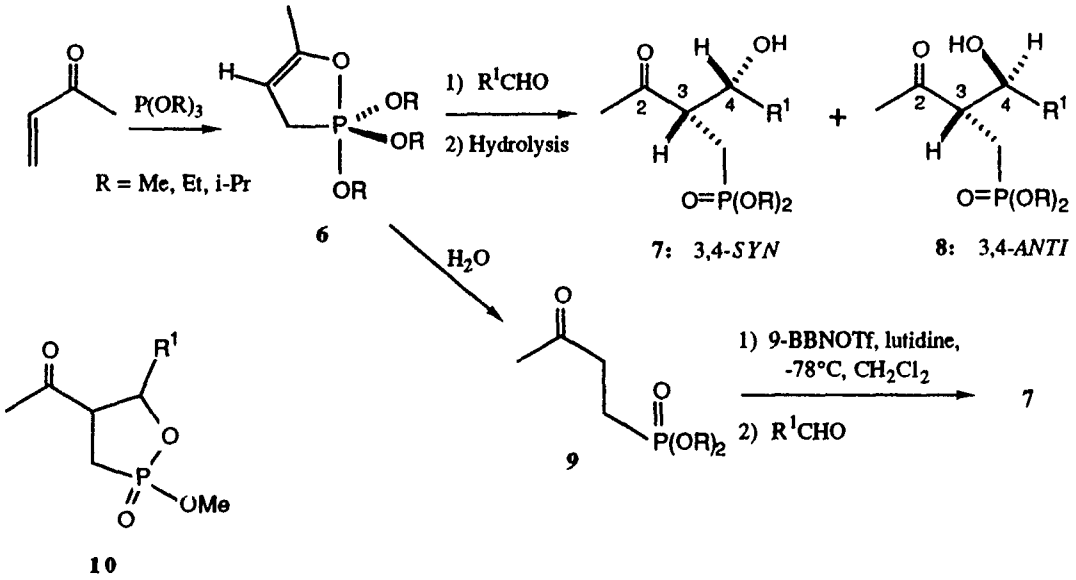

TABLE 1

Ratio of Diastereomers[a] **7:8** (% Isolated Yield)[b]

R'CHO	R=Me		R=Et		R=i-Pr	
	Neat, 20°C	CH_2Cl_2 40°C	Neat, 20°C	CH_2Cl_2 40°C	Neat, 20°C	CH_2Cl_2 40°C
MeCHO[c]	1.3:1.0 (58)		1.3:1.0 (61)		1.9:1.0 (70)	
n-PrCHO	1.5:1.0 (55)		1.4:1.0 (64)		1.7:1.0 (74)	
i-PrCHO	2.1:1.0 (51)		2.3:1.0 (59)	2.0:1.0 (65)	3.5:1.0 (69)	3.3:1.0 (68)
PhCHO	2.0:1.0 (62)[d]	1.4:1.0 (70)[e]	2.0:1.0 (78)[e]	1.2:1.0 (71)[e]	4.9:1.0 (69)	4.6:1.0 (82)[e]
CH_2=C(CH3)-CHO	1.6:1.0 (48)	2.0:1.0 (72)	1.6:1.0 (64)		1.6:1.0 (71)	

(a) Ratios were determined by the separation and isolation of the isomers by HPLC. (b) Yields were not optimized. Reactions were followed by NMR. (c) Condensations were performed at 0°C. (d) Ratios were determined by NMR integration and confirmed by HPLC isolation. (e) Ratios were determined by NMR integration.

The value of Lewis acids as catalysts in the promotion of the reactions of P^V organophosphorus compounds has been shown.[15] Preliminary results from the condensation of **6** with benzaldehyde in the presence of Lewis acids are presented in **Table 2**. The use of BF_3-OEt_2 produced the best overall yield, although the *syn/anti* isomer ratio was not improved when compared to the uncatalyzed reaction. The neat condensation reaction at various temperatures with trimethylsilyl triflate (TMSOTf) as catalyst yielded the greatest variation in *syn/anti* isomer ratios. At 20° C, a ratio of 4.5:1 in favor of the *anti* isomer, **8**, was produced, although the yield is lower than for the reactions performed at lower temperatures. The variation in ratio may be due to the selective decomposition of the *syn* isomer. We are currently investigating this possiblity.

TABLE 2

Lewis Acid Catalyzed Condensation Reactions of **6** (R = CH_2CH_3) with Benzaldehyde[a]: Ratio of **7**:**8**

Lewis Acid	Temperature	Reaction Time	7 : 8	% Yield
BF_3-OEt_2	0° C	14 hr	1.25:1.00	88
	-30° C	11 days	1.15:1.00	80
	-78° C	6 days	1.21:1.00	20% conversion
TMSOTf	40° C	10 hr	1.00:1.25 (@5 hr)	dec. after 10 hr
	20° C	10 hr	1.0:4.5	55
	0° C	14 hr	1.00:1.35	72
	-30° C	12 days	1.25:1.00	76
$SnCl_4$	0° C	14 hr	1.0:1.1	49
$TiCl_4$	0° C	14 hr	2.0:1.0	47
[b]$AlCl_3$	0° C	20 hr	1.35:1.00	64
[c]LiBr	0° C	20 hr	1.25:1.00	56

(a) Except as noted, reactions were performed neat. (b) Reaction in $CHCl_3$. (c) Reaction in 1:1 CH_2Cl_2:MeOH.

Ramirez reported that the condensation of 1,3,2λ^5-dioxaphospholenes with various aldehydes was stereoselective, producing exclusively the *anti* diols, **4**.[5a,16] As seen from our results, the condensation reactions of the 1,2λ^5-oxaphospholenes produced mixtures of the diastereomers **7** and **8**, with the *syn* isomer being the major in most cases. Our reinvestigation of the condensation reactions of the 1,3,2λ^5-dioxaphospholene **1a** (R = R^1 = Me) with various aldehydes indicated that while the degree of selectivity was not as high as was reported previously, the sense of selectivity did favor the *anti* diastereomer, **4**. In contrast to Ramirez's reported procedure, we did not distill the intermediate condensation products, **2a**, prior to hydrolysis, but analyzed the entire crude hydrolysis reaction mixture.

The nature of the mechanism of this condensation reaction has not been substantiated to date. Ramirez's proposed mechanism for the 1,3,2λ^5-dioxaphospholenes advocates prior coordination of the aldehyde to give a P^{VI} zwitterionic intermediate or transition state, followed by rupture of one of the endocyclic P-O bonds. Subsequent intramolecular attack of the resulting enolate onto the coordinated aldehyde yields the dioxaphospholanes, **2a**.[5a] It is possible that the condensation reactions of the 1,2λ^5-oxaphospholenes do not proceed via this mechanism. We are currently designing reactions to probe the mechanism(s) of this condensation reaction, as well as investigating the effects of other R groups and spiro P^V compounds on the ratio of the condensation products.

Chiral Spirophospholenes:

Asymmetric induction should also be possible in this condensation reaction by stopping the pseudorotation around the phosphorus, thus producing chirality *at phosphorus*. Formation of spirophosphoranes has been shown to slow down and in some cases to stop the pseudorotation around the phosphorus atom in pentacovalent compounds.[17] It is also known that the less apicophilic the groups are, the more restricted the pseudorotation. Therefore, by substituting ligands other than alkoxy groups on the phosphorus, ephedrine for example, we expect to form chiral phosphorus compounds. Use of these chiral spirophosphoranes in this carbonyl condensation reaction could result in chiral products. We have studied the spirophosphoranes **11**, **12** and **13** (prepared from **15** and the diketone), via variable temperature proton and phosphorus NMR[18]. It appears that pseudorotation is negligibly slow on the NMR timescale at 20° C. Cooling the samples to -75°C and following by ^{1}H NMR spectroscopy indicated little change. Slowly heating the samples up to 100°C produced another set of ^{1}H NMR signals, and indicated conversion to the other diastereomer. Upon cooling to room temperature again, this ratio did not change appreciably. These results indicate that epimerization does not occur until temperatures greater than 60 to 80°C are reached. See **Table 3**. Since variable temperature ^{31}P NMR did not indicate the formation of a phosphonium salt, we presume that this epimerization occurred via pseudorotation

and not bond rupture. Nuclear Overhauser Effect (NOE) NMR studies on the major diastereomer of **12a** indicates that it is isomer **I** and not **II**. The methyl vinyl ketone adduct, **14**, has been prepared, and is being studied via variable temperature NMR. These compounds are currently being investigated in the condensation reaction with simple aldehydes (with and without Lewis acid catalysis) to see what effect the spiro ligands have on the diastereomeric ratio of the products formed, and on the amount of asymmetric induction.

SCHEME 3

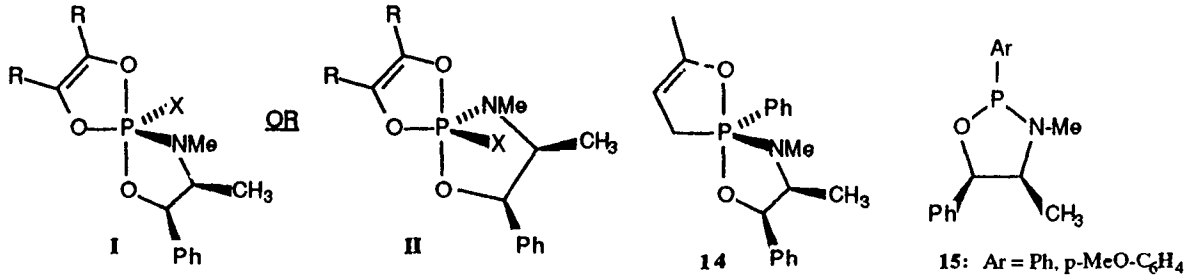

11: R = Me; X = Ph
12: R = Ph; X = Ph
13: R = Me; X = p-MeO-C_6H_4

TABLE 3:
High Temperature ^1H NMR Ratios[a] of the Diastereomers of **11**, **12** and **13**

Compound 11		Compound 12		Compound 13	
Temp. (°C)	Ratio	Temp. (°C)	Ratio	Temp. (°C)	Ratio
17	88/1	21	14.5/1	20	110/1
30	88/1	35	14.5/1	40	110/1
47	88/1	60	14.5/1	60	22/1
60	8/1	79	3/1	80	4.6/1
79	1.5/1	100	1.2/1	100	1.6/1
100	1.3/1	60	1.2/1	80	1.6/1
79	1.3/1	35	1.2/1	60	1.6/1
60	1.3/1	21	1.2/1	40	1.6/1
35	1.3/1			20	1.6/1
17	1.3/1				

(a) Determined by integration of the methine proton at C5.

Synthesis of *Cis*- and *Trans*-Neocnidilide:

The carbonyl condensation reaction of a suitable oxaphospholene with valeraldehyde forms the basis of a short and efficient synthesis of either *cis*- or *trans*-neocnidlide. These compounds are from the Umbelliferae family, and inhibit the growth and toxin production of mycotoxin-producing fungi .[19] We can produce *trans*-neocnidilide from the *syn* adduct, **18**, and *cis*-neocnidilide from the *anti* isomer, **19**. The synthesis commenced with the C4 unsubstituted oxaphospholene, **16**, and is shown in Scheme 4. The condensation of a model compound, **17**, (prepared from the known trans-ethyl 4-oxo-2-pentenoate[20] and trialkyl phosphite), with valeraldehyde has, to date, not produced any recognizable products due to the thermal instability of **17**. Condensation of **17** under Lewis acid catalyzed conditions is currently being examined. The ester, however, has successfully been introduced at a later stage in the synthesis by alkylating α to the phosphonate with ethyl chloroformate. The Scheme indicates the status of the synthesis. To date, the *syn* isomer, **18**, has been carried through the synthesis up to the last step, the Barton deoxygenation reaction. Work on the anti isomer, **19**, does not lag far behind.

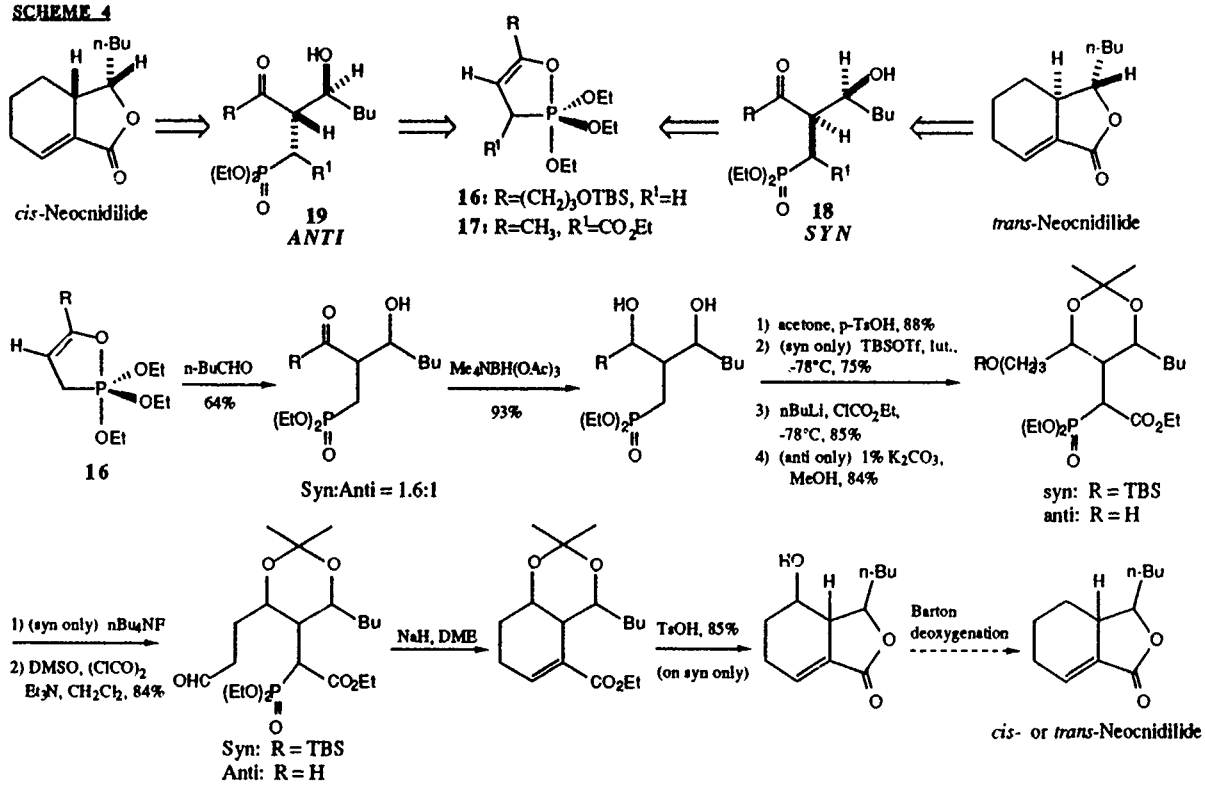

CONCLUSIONS:

We have been able to accomplish Ramirez's carbonyl condensation reaction between aldehydes and 1,2λ^5-oxaphospholenes. The products are potentially versatile intermediates for synthesis, as 2 or possibly 3 contiguous stereocenters are formed, and the phosphonate can be utilized in further carbon-carbon bond forming reactions. Some of the compounds produced via this method are also analogs of known antimetabolites of the glycolytic pathway[21], and will be examined for any potential biological activity. While we have laid the ground work on this condensation reaction, further study is necessary in order to improve the ratio of isomers formed and determine the full scope of this reaction.

ACKNOWLEDGMENT

We would like to thank the donors of the Petroleum Research Fund administered by the American Chemical Society, and the University of Delaware Research Foundation for support of this research.

REFERENCES:

(1) (a) Engel, R.; *Chem. Rev*, **1977**, *77*, 349. (b) Hilderbrand, R. L.; *The Role of Phosphonates in Living Systems*, CRC Press,Florida, 1983. (c) Knowles, J. R.; Orr, G. A.; *Biochem. J.* **1974**, *141*, 721. (d) Dixon, H. F. B.; Sparkes, M. J.; *ibid*, **1974**, *141*, 715.
(2) Hutchinson, D. W.; Cload, P. A.; Haugh, M. C.; *Phosphorus and Sulfur*, **1983**, *14*, 285.
(3) Hendlin, D.; Stapley, E. O.; Jackson, M.; Wallick, H.; Miller, A. K.; Wolf, F. J.; Miller, T.W.; Chaiet, L.; Kahan F. M.; Foltz, E. L.; Woodruff, H. B.; Mata, J. M.; Hernandez, S.; Mochales, S.; *Science*, **1969**,

166, 122.
(4) **(a)** Arbuzov, B. A.; Muslinkin, A. A.; Vizel, A. O.; Tarenko, Y. F.; Ivanovskaya, K. M.; *Otkrytiya Izobrt.*, **1986**, 285. Chem. Abstracts #106:P102557m. **(b)** Arbuzov, B. A.; Muslinkin, A. A.; Vizel, A. O.; Studentsova, I. A.; 11th International Conference on Phosphorus Chemistry, poster abstract #4-59.
(5) **(a)** Ramirez, F.; *Synthesis*, **1974**, 90. **(b)** Ramirez, F.; *Pure and Applied Chem.*, **1973**, *2*, 185. **(c)** *Ibid* **1964**, *9*, 337. **(d)** Ramirez, F.; Patwardhan, A. V.; Smith, C. P.; *J. Org. Chem.*, **1966**, *31*, 3159.
(6) **(a)** David, S., et al; *J. Chem, Soc. Chem. Comm.*, **1976**, 747. David, S.; *J. Chem. Soc. Perkin I*, **1980**, 1262. **(b)** Inouye, Y., et al; *Bull. Chem. Soc. Japan*, **1969**, *42*, 2948.
(7) **(a)** Westheimer, F.; *J. Am. Chem. Soc.*, **1970**, *92*, 634. **(b)** Voncken, W. G.; Buck, H. M.; *Recueil Trav. Chim. Pays-Bas*, **1974**, *93*, 14, 210. **(c)** Buono, G. J.; *J. Am. Chem. Soc.*, **1981**, *103*, 4532. **(d)** Arbuzov, B. A.; *Bull. Acad. Sci. USSR*, **1967**, *16*, 2185. **(e)** Voznesenskaya, A. Kh.; Razumova, N. A.; Petrov, A. A.; *J. Gen. Chem. USSR*, **1971**, *41*, 228.
(8) Zimmer, H.; *J. Org. Chem.*, **1980**, *45*, 3994.
(9) **(a)** Emsley, J.; Hall, C.; *The Chemistry of Phosphorus*, Harper and Row, New York, 1976. **(b)** Kosolapoff, G. M.; Maier, L., eds.; *Organic Phosphorus Compounds*, Wiley-Interscience. **(c)** Cadogen, J. I. G., ed., *Organophosphorus Reagents in Organic Synthesis*, Academic Press, New York, 1979. **(d)** Trippett, S., ed., *Organophosphorus Chemistry*, 1969-1979, vols. 1-11, Specialist Reports, Chemical Society, London. **(e)** Smith, D. J. H., in *Comprehensive Organic Chemistry*, Sutherland, I. O. ed., Pergamon Press, New York, **1979**, 2, ch. 10. **(f)** Gallagher, M. J.; Jenkins, I. D.; *Topics in Stereochemistry*, **1968**, *3*, 1.
(10) Thomas, R.; Boutagu, J.; *Chem. Rev.*, **1974**, *74*, 87.
(11) Ramirez, F.; Madan, O. P.; Heller, S. R.; *J. Am. Chem. Soc.*, **1965**, *87*, 731.
(12) General experimental procedure: To the oxaphospholene, **6**, (1 mmol) in a flame-dried flask under argon, was added the freshly distilled aldehyde (1.2-1.5 mmol). The reaction mixture was stirred at room temperature (0° C for the reactions with acetaldehyde) and monitored by ^{1}H NMR spectroscopy. For the reactions performed in a solvent, the oxaphospholene was diluted with solvent (see text) prior to addition of the aldehyde. The reaction mixture was then heated to 40° C, and monitored as above. After disappearance of the oxaphospholene, the reaction mixture was brought to rt, and water (10 mmol) was added. The mixture was allowed to stir for 6-10 hours, and the products were extracted with methylene chloride. The products were isolated via semi-preparative HPLC. Representative spectral data for the products from the condensation of **6** with benzaldehyde: **7**: (R = Me, R^1 = Ph); ^{1}H (250 MHz, $CDCl_3$, ppm) δ 7.31 (5H, m), 4.75 (1H, d, J = 6.0 Hz, CHPh), 3.60 (6H, d, J = 10.8 Hz, OCH_3), 3.30-3.15 (1H, m, CH_3COCH), 2.31-2.10 (2H, m, $CH_2PO(OMe)_2$), 1.97 (3H, s, CH_3CO). ^{13}C (62.86 MHz, $CDCl_3$, ppm) δ 210.0, 141.0, 126.2, 128.4, 128.7, 74.2 (d, J_{c-p} = 15 Hz), 53.8 (d, J_{c-p} = 4 Hz), 52.5 (d, J_{c-p} = 5.5 Hz), 52.3 (d, J_{c-p} = 5.8 Hz), 31.5 , 22.2 (d, J_{c-p} = 142 Hz); ^{31}P (101.3 MHz, $CDCl_3$) +34.1 ppm. IR (neat, cm^{-1}) 3343, 1713, 1262, 1237, 1043. MS: m/e (M^+) calcd 286.0965, obsd 286.0968, base m/e 57. **8**: (R = Me, R^1 = Ph); ^{1}H (250 MHz, $CDCl_3$, ppm) δ 7.31 (5H, m), 4.65 (1H, d, J = 7.7 Hz), 3.65 (6H, d, J = 10.8 Hz), 3.33 (1H, m), 3.00 (1H, bs, OH), 2.21 (3H, s), 2.16 - 1.49 (2 H, m); ^{13}C (62.86 MHz, $CDCl_3$, ppm) δ 211.1, 141.4, 128.7, 128.3, 126.3, 76.8 (d, J_{c-p} = 18.5 Hz), 52.4 (d, J_{c-p} = 3.8 Hz), 52.3 (d, J_{c-p} = 7.3 Hz), 52.2 (d, J_{c-p} = 6.8 Hz), 32.9, 24.1 (d, J_{c-p} = 142 Hz); ^{31}P (101.3 MHz, $CDCl_3$) +32.6 ppm.
(13) Heathcock, C. H.; Pirrung, M. C.; Sohn, J. E.; *J. Org. Chem.*, **1979**, *44*, 4294.
(14) Mukaiyama, T.; Inoue, T.; *Bull. Chem. Soc. Jpn*, **1980**, *53*, 174.
(15) Evans Jr., S. A., Murray, W. T.; *J. Org. Chem.*, **1989**, *54*, 2440.
(16) The intermediate dioxaphosphones (**2**) were distilled (spinning band) before being subjected to hydrolysis. See ref 5. Ramirez was not able to isolate the hydrolysis products from the condensation of benzaldehyde and dioxaphospholenes. Ramirez, F.; Patwardhan, A. V.; Ramanathan, N.; Desai, N. B.; Greco, C. V.; Heller, S. R.; *J. Am. Chem. Soc.*, **1965**, *87*, 543.
(17) Holmes, R. R., *Pentacoordinated Phosphorus , Vol. I,* ACS Monograph 175, Washington D.C., 1980. Koole, L. H.; van der Hofstad, W. J. M.; Buck, H. M.; *J. Org. Chem.*, 1985, **50**, 4381. Westheimer, F.; *J. Am. Chem. Soc.*, 1970, **92**, 634.
(18) McClure, C. K.; Grote C. W.; *Tetrahedron Letters*, 1989, **30**, 0000 (manuscript in preparation).
(19) Fischer, F. C.; Gijbels, J. M.; *Planta Medica*, 1987, 77. Suzuki, H.; Tanaka, A.; Yamashita, K.; *Agric. Biol. Chem.*, 1987, **51**, 3369.
(20) Bestmann, H. J.; Seng, F.; Shulz, H.; *Chem. Ber.*, 1963, **96**; 465.
(21) See for example: Blackburn, G. M., Rashid, A.; *J. Chem. Soc. Chem. Comm.*, 1988, 317.

BLANK

NEW APPROACHES TO THE SYNTHESIS OF FENTANYL DERIVATIVES

Harold D. Banks[1]

ABSTRACT

Methods have been developed for the chemoselective addition of organometallic reagents to the cyano function of aminonitrile, **1**, a key intermediate in the synthesis of fentanyl and its derivatives.

INTRODUCTION

Since the discovery of the potent synthetic opioid fentanyl by Janssen Pharmaceuticals in the early 1960's, many modifications of the structure of the parent molecule have been performed with a view to increasing the potency of the drug. Increased potency is due to the higher selectivity and affinity of the compound for the μ-receptor, which mediates analgesia, ideally, this increased selectivity results in minimal binding to those receptors that give rise to undesirable side effects such as respiratory depression, dependence and emesis. This search for the ideal analgesic has led to the preparation of a large number of fentanyl derivatives. Of these compounds, those that have been reported in the literature that are the most potent, are carfentanil and ohmefentanyl, having potencies of 27 and 28 times the potency of fentanyl respectively (using the rat tail-withdrawal method.)

In this investigation, alternative routes for synthesis of carfentanil have been investigated. The envisioned improvement focusses on the transformation of the key intermediate in the reaction, an α-aminonitrile, into an α-aminoester. The efficiency of individual steps[2,3] of the reported literature procedure has been significantly improved, providing an overall yield of over twenty times that reported in the literature.[4] Using a benzyl protecting group at the heterocyclic nitrogen, good to excellent yields of the corresponding α-aminoester could be obtained in two steps from the α-aminonitrile.[5] While this latter method has the versatility of allowing one to append different groups to the ring nitrogen position after removal of the benzyl protecting group, our synthesis of carfentanil would eliminate the deprotection and alkylation steps if the synthesis stated with 1-(2-phenylethyl)-α-aminonitrile, **1**.

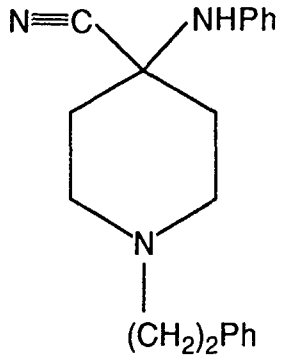

1

It was decided to choose an approach which did not depend on a hydrolysis sequence, which under the best conditions produced only a fair yield of the amide intermediate. A reduction-oxidation strategy was envisioned to represent a reasonable alternative.

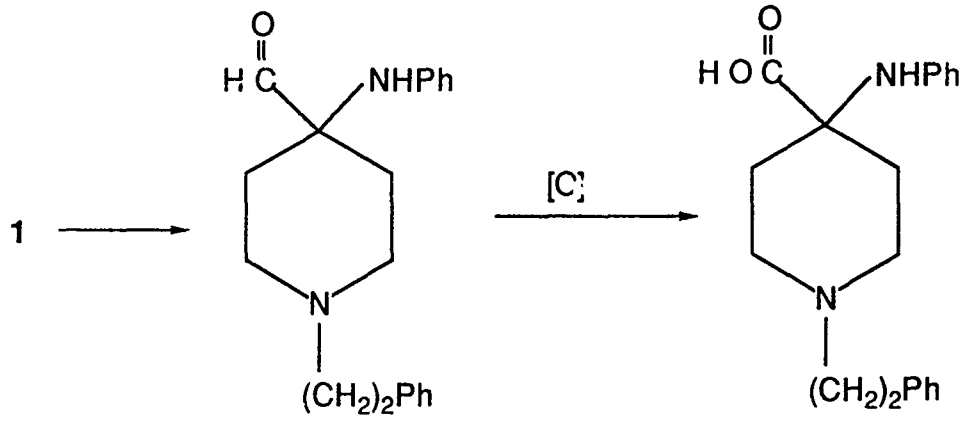

RESULTS AND DISCUSSION

The reduction step depicted above is complicated by the multiple functionalities present in **1**. Selective borohydride and aluminum hydride reducing agents are also basic. The anilino proton can be abstracted under these conditions to give rise to an imine, after expulsion of cyanide.

When **1** was treated with a equivalent quantity of sodium borohydride, Red-Al, Super-Hydride or L-Selectride the only product of the reaction was that resulting from the formal replacement of the cyano function by hydride. These results are in accord with those previously obtained for 3-methyl derivatives of **1**, demonstrating that the neighboring methyl group is not responsible for the observed chemoselection.[6]

It has been reported that the use of one equivalent of $LiAlH_4$ can be used for the partial reduction of nitriles to aldehydes[7]. When a solution of **1** in THF was slowly treated with a total of one equivalent of $LiAlH_4$ over a period of one hour, only primary amine resulting from the complete reduction of the cyano function in addition to unreacted α-aminonitrile could be detected.

A formal reduction can also be effected by addition of an organometallic reagent to the cyano function. This synthetic pathway is contrasted with the well-known Brulyants reaction which has been extensively employed for α-aminonitriles which do not bear an amino hydrogen, leading to displacement of the cyano function by the alkyl or aryl group of the organometallic. Using this strategy as a route to the carboxy function of carfentanil would require an easily oxidized carbon-carbon bond. Since methyl ketones are readily oxidized to carboxylic acids by means of the iodoform reaction, only methyl organometallics were considered. In previous studies, it was learned that the use of methyl Grignard reagents and methylithium gave rise to the imine resulting from the elimination of the elements of HCN. The chemistry of organocopper reagents had not been explored. It was hoped that the lower basicity and softer[8] nature of these organometallics would provide the required chemoselectivity for production of the desired methyl ketone. Support for this idea was provided by the recent results of Hall,[9] who reported good to excellent yields of ketimines in the reaction of nitriles with Grignard reagents in the presence of traces of Cu(I) salts.

When a solution of **1** in THF containing a trace of CuBr was treated slowly with excess CH_3MgCl in THF the corresponding methyl ketone could be obtained in good yield upon hydrolysis of the reaction mixture. It seems likely that the first step in the reaction is the abstraction of the anilino hydrogen which should not be unduly encumbered sterically. The expulsion of the cyano function to form a ketimine is apparently slow relative to attack of an organocopper species at the soft nitrile function. Additional experiments to define the scope of this reaction are planned.

EXPERIMENTAL

Into a 50 mL flask with septum port equipped with a reflux condenser and magnetic stirring bar was added under a dry nitrogen atmosphere, 5 mL of dry THF (distilled from benzophenone ketyl) and 100 mg (0.328 mmol) of 1-(2-phenylethyl)-4-cyano-4-phenylaminopiperidine. To this solution was added 5 mg of CuBr powder, followed by the dropwise addition of 1.0 mL of 2.0 M methylmagnesium chloride over a period of 10 min. The reaction mixture was monitored by TLC (silica gel GF, 95% $CHCl_3$/5% CH_3OH containing a trace of NH_4OH.) After stirring for 3 h at room temperature, the reaction mixture was refluxed for one hour and was then cooled in an ice-water bath. (Independent experiments established that refluxing for periods up to 8 h resulted in no increase in the reaction yield.) Dropwise addition of 3 mL of 6N HCl to dissolve the magnesium salts, was followed by 6 mL of concentrated NH_4OH. The reaction mixture was extracted with two 10 mL portions of, dried (Na_2SO_4) and concentrated on the rotary evaporator to give 0.95 g of a brown oil which solidified overnight at 0.1 torr. Recrystallization from diisopropyl ether gave 0.75 g of a white solid, mp 100 - 101° [lit[4] mp = 100.6°]. ^1H NMR (60 MHz, $CDCl_3$) δ 2.13 - 2.40 (m, 4 H), 2.45 - 2.98 (m, 8 H), 2.71 (s, 3 H), 6.96 - 7.13 (m, 10 H).

CONCLUSIONS

Reduction of aminonitrile, **1**, with a variety of borohydride and aluminum hydride reagents resulted in either displacement of the cyano function or complete reduction of the nitrile function to the aminomethyl group. Formal reduction by means of addition to the cyano function could be accomplished with CH_3MgCl in the presence of a trace of CuBr.

REFERENCES

1. U.S. Army Chemical Research, Development and Engineering Center, Aberdeen Proving Ground, MD 21010-5423.
2. H. D. Banks, P. P. Von Ostwalden and F-L. Hsu, Proceedings of the 1988 U.S. Army Chemical Research, Development and Engineering Center Scientific Conference on Chemical Defense Research, in press.
3. L. P. Reiff, unpublished observations.
4. Van Daele, P.G.H.; De Bruyn, M.F.L.; Boey, J.M.; Sanczuk, S.; Agten, J.T.M.; Janssen, P.A.J., Arnzeim.-Forsch. (Drug. Res.), **1976**, *26*, 1521 - 1531.
5. F-L. Hsu, L. P. Reiff and H. D. Banks, unpublished observations.
6. P. W. Von Ostwalden, F-L Hsu, H.D. Banks and C.P. Ferguson, CRDEC Technical Report (CRDEC-TR-038).
7. E. Mosettig, Org. Reactions, **1954**, *8*, 218 - 257.
8. T-L. Ho, Tetrahedron, **1985**, *41*, 1 - 86.
9. F. J. Welberth and S. S. Hall, J. Org. Chem., **1987**, *52*, 3901 - 3904.

THERMOCHEMISTRY OF HIGH ENERGY REACTIONS

Eugene S. Domalski and Thomas L. Jobe, Jr.
Chemical Thermodynamics Division
National Institute of Standards and Technology
Gaithersburg, MD 20899

ABSTRACT

Enthalpies of reaction at 298.15 K were calculated from evaluated data on the enthalpies of formation for combustion processes for selected hydrocarbons and chemical elements in both oxygen and in fluorine. A group of Thermite reactions were examined as well for exothermic characteristics. Some conclusions were derived from the study with respect to the reactions which possessed high exothermicity.

INTRODUCTION

Thermochemistry is that branch of physical chemistry which deals with reaction energetics. The enthalpy of a given reaction may be determined experimentally or it may be calculated if the enthalpies of formation of the reactants and products for the process are known. The typical equation for the calculation of the enthalpy of reaction for a given process is:

Enthalpy of reaction = Σ(enthalpies of formation of the products) - Σ(enthalpies of formation of the reactants).

It is common also for such reaction enthalpies to refer to a reference temperature of 298.15 K. Also, certain conventions have been adopted regarding exothermic and endothermic reactions. A reaction is designated as exothermic if heat must flow from an isolated system where the reaction occurs to the surroundings in order to restore the system to its initial state of thermal equilibrium. In this case, the heat is denoted as negative in sign. Similarly, a reaction is designated as endothermic if heat must flow to the system from the surroundings in order to restore the system to its initial state of thermal equilibrium. Here, the heat is denoted as positive in sign, but most often, in tables of data, for example, no sign is used.

In order to maximize the exothermicity for a process the enthalpies of formation of the reaction products should be large (negative) quantities and the enthalpies of formation of the reactants should be small (negative), or preferredly, large (positive) quantities. In addition, the composition and molecular structure of the reactants and products are important in determining and maximizing the exothermicity of the reaction.

The proper combination of fuel and oxidizer has been and is sought by combustion engineers, propulsion system designers, and munitions experts to deliver the maximum thrust, explosive power, or target destruction on impact.

Oxidation processes in general are exothermic and vary depending upon whether the oxidizing agent is fluorine, chlorine, bromine, or oxygen. Sometimes compounds of the latter four elements also serve as oxidizing

agents, such as: ClF_3, BrF_3, H_2O_2, $HClO_4$, and organic peroxides. Of the four chemical elements mentioned, fluorine is usually the superior oxidizing agent, however, the products of fluorination yield substances which are often environmentally undesirable or unacceptable, in particular HF. Oxygen has strong but reduced oxidative capabilities when compared with fluorine, however, its oxidation products are very acceptable from an environmental standpoint, namely, CO_2 and H_2O.

The choice of fuel is as important as the choice of the oxidizer. The fuel should be stable, nonvolatile, if possible, and burn at a slow steady rate in some instances and detonate with maximum force for other applications. Hydrocarbons have served as automotive and aircraft fuels for almost a century. Specific needs for space vehicles have required more exotic fuels.

PROJECT PLAN

The project plan in this work has been to review the literature for highly exothermic reactions as well as to search for fuels and oxidizers which when combined would constitute an array of highly exothermic reactions. Calculation would be carried out so that comparisons could be made regarding the quantitative exothermicity of one reaction versus another. A group of reaction classes were selected for examination with specific fuels (target materials) and oxidizers (reactive atmospheres).

The following classes of reaction were chosen for study and the enthalpies of reaction at 298.15 K were compiled:

(1) Oxygen combustion of organic and inorganic substances
(2) Fluorine combustion of organic and inorganic substances.
(3) Thermite reactions (metallic elements + oxides or nitrates)
(4) Hydrocarbons + inorganic oxidizers with available oxygen.
(5) Reaction of hydrogen peroxide and other peroxides.
(6) Reactions with elemental phosphorus or inorganic phosphorus compounds.
(7) Self-reaction processes.
(8) Reactions involving interhalogens or pseudohalogens.

DISCUSSION AND RESULTS

This paper is limited to the reporting of 130 enthalpies of reaction at 298.15 K for:

(a) oxygen combustion of 31 hydrocarbon compounds (Table 1)
(b) fluorine combustion of 31 hydrocarbon compounds (Table 2)
(c) combustion of 10 elements in oxygen and in fluorine (Table 3)
(d) 16 thermite reactions (Table 4).

TABLE 1.

Enthalpies of Combustion of Hydrocarbons in Oxygen at 298.15 K

C_xH_y + O_2(gas) = CO_2(gas) + H_2O(liq) Hydrocarbon	$\Delta_r H°$(kJ/g)	$\Delta_r H°$(kJ/cm^3)
Methane(gas),	-55.5	-0.036
Ethane(gas),	-51.9	-0.064
Ethylene(gas),	-50.3	-0.063
Acetylene(gas),	-50.0	-0.059
n-Pentane(gas),	-49.0	-0.200
n-Pentane(liq),	-48.6	-30.2
1-Pentene(gas),	-48.1	-0.197
1-Pentene(liq),	-47.8	-30.3
Cyclopropane(gas),	-49.7	-0.091
Cyclopropene(gas),	-50.7	-0.093
Cyclobutane(gas),	-48.9	-0.120
Cyclobutane(liq),	-48.5	-33.4
Cyclobutene(gas),	-47.9	-0.118
Cyclopentane(gas),	-47.3	-0.194
Cyclopentane(liq),	-46.9	-35.4
Cyclopentene(gas),	-46.2	-0.189
Cyclopentene(liq),	-45.7	-35.1
Cyclopentadiene(gas),	-44.8	-0.183
Cyclopentadiene(liq),	-44.3	-35.6
Spiropentane(gas),	-48.4	-0.198
Spiropentane(liq),	-48.0	-29.8
Cyclohexane(gas),	-47.0	-0.222
Cyclohexane(liq),	-46.6	-36.1
Cyclohexene(gas)	-46.1	-0.217
Cyclohexene(liq)	-45.7	-36.8
Cyclohexadiene(gas),	-45.1	-0.213
Cyclohexadiene(liq),	-44.7	-37.5
Benzene(gas),	-42.3	-0.210
Benzene(liq),	-41.8	-36.6
Cycloheptane(gas),	-47.2	-0.253
Cycloheptane(liq),	-46.8	-37.8
Cycloheptene(gas),	-46.5	-0.249
Cycloheptadiene(gas),	-45.4	-0.243
Cycloheptatriene(gas),	-44.3	-0.237
Cycloheptatriene(liq),	-43.9	-38.9
Cyclooctane(liq),	-46.9	-39.1
Cyclooctene(liq),	-46.1	-39.0
Cyclooctadiene(liq),	-45.5	-40.1
Bicyclo[2.2.2]octane(cr),	-45.4	-43.8
Cubane(cr),	-46.4	-55.7
Bicyclo[1.1.0]butane(gas),	-49.0	-0.120
Bicylco[1.1.0]butane(liq),	-48.5	-34.0
Bicyclo[3.1.0]hexane(liq),	-46.2	-35.6
Bicyclo[3.3.3]undecane(cr),	-46.2	-48.0
Adamantane(cr),	-44.2	-48.2
Hexacyclododecane(cr),	-42.8	-47.5

TABLE 2.

Enthalpies of Combustion of Hydrocarbons in Fluorine at 298.15 K

C_xH_y + F_2(gas) = CF_4(gas) + HF(gas)

Hydrocarbon	$\Delta_r H°$(kJ/g)	$\Delta_r H°$(kJ/cm^3)
Methane(gas),	-121.6	-0.078
Ethane(gas),	-113.8	-0.141
Ethylene(gas),	-107.4	-0.135
Acetylene(gas),	-101.4	-0.119
n-Pentane(gas),	-108.1	-0.442
n-Pentane(liq),	-107.7	-66.9
1-Pentene(gas),	-105.2	-0.430
1-Pentene(liq),	-104.8	-66.6
Cyclopropane(gas),	-106.8	-0.195
Cyclopropene(gas),	-104.1	-0.190
Cyclobutane(gas),	-106.0	-0.261
Cyclobutane(liq),	-105.6	-72.7
Cyclobutene(gas),	-102.2	-0.251
Cyclopentane(gas),	-104.4	-0.427
Cyclopentane(liq),	-104.0	-77.0
Cyclopentene(gas),	-101.1	-0.413
Cyclopentene(liq),	-100.7	-77.2
Cyclopentadiene(gas),	-97.4	-0.398
Cyclopentadiene(liq),	-97.0	-77.8
Spiropentane(gas),	-103.3	-0.423
Spiropentane(liq),	-102.9	-63.8
Cyclohexane(gas),	-104.0	-0.491
Cyclohexane(liq),	-103.6	-80.2
Cyclohexene(gas),	-101.4	-0.478
Cyclohexene(liq),	-101.0	-81.4
Cyclohexadiene(gas),	-98.5	-0.465
Cyclohexadiene(liq),	-98.1	-82.4
Benzene(gas),	-93.7	-0.469
Benzene(liq),	-93.3	-81.5
Cycloheptane(gas),	-104.3	-0.558
Cycloheptane(liq),	-103.9	-83.8
Cycloheptene(gas),	-101.	-0.545
Cycloheptadiene(gas),	-99.4	-0.532
Cycloheptatriene(gas),	-96.6	-0.517
Cycloheptatriene(liq),	-96.2	-85.4
Cyclooctane(liq),	-104.0	-86.5
Cyclooctene(liq),	-101.8	-86.2
Cyclooctadiene(liq),	-99.9	-88.1
Bicyclo[2.2.2]octane(cr),	-101.1	-97.5
Cubane(cr),	-97.9	-117.5
Bicyclo[1.1.0]butane(gas),	-103.4	-0.254
Bicyclo[1.1.0]butane(liq),	-102.	-72.0
Bicyclo[3.1.0]hexane(liq),	-101.5	-78.2
Bicyclo[3.3.3]undecane(cr),	-102.3	-106.4
Adamantane(cr),	-99	-108.1
Hexacyclododecane(cr),	-95.3	-105.7

TABLE 3.

Combustion of the Elements in Oxygen

Element + O_2 = Oxide

Enthalpy of combustion of the element in oxygen at 298.15 K
(based on unit mass or volume of the element reacted)

Oxide	$\Delta_f H°$ (kJ/g)	$\Delta_f H°$ (kJ/cm^3)
Al_2O_3 (cr, α-corundum)	-31.1	-83.9
B_2O_3 (cr)	-58.0	-135.7
BeO(cr)	-67.6	-125.0
CO_2 (gas)	-32.8	-65.5
H_2O(gas)	-119.9	-0.108
H_2O(liq)	-141.8	-0.128
MgO(cr)	-24.8	-43.0
P2O5(cr, hexagonal)	-24.2	-43.8
SO_3 (gas)	-12.3	-25.5
TiO_2 (cr, rutile)	-19.7	-89.5
ZrO_2 (cr, monoclinic)	-12.1	-78.5

Combustion of Elements in Fluorine

Element + F_2 = Fluoride

Enthalpy of combustion of the element in fluorine at 298.15 K
(based on unit mass or volume of the element reacted)

Fluoride	$\Delta_f H°$ (kJ/g)	$\Delta_f H°$ (kJ/cm^3)
AlF_3 (cr)	-56.0	-151.3
BF_3 (gas)	-105.1	-246.0
BeF_2 (cr)	-113.9	-210.6
CF_4 (gas)	-77.7	-155.4
HF(gas)	-135.6	-0.122
HF(liq)	-150.6	-0.136
MgF_2 (cr)	-46.3	-80.4
PF_5 (gas)	-51.5	-93.8
SF_6 (gas)	-38.1	-78.8
TiF_4 (solid, amorphous)	-34.4	-156.4
ZrF_4 (cr)	-21.0	-136.3

TABLE 4.

Enthalpies of Thermite Reactions at 298.15 K

(Homogeneous solid phase reactions)

The Thermite reaction consists of the displacement of a metallic oxide, halide, or nitrate by a metallic element of greater activity in the electrochemical series. For example,

$$Al(cr) + 0.5\ Fe_2O_3(cr) = Fe(cr) + 0.5\ Al_2O_3(cr)$$

Reactants	$\Delta_r H°$(kJ/g)	$\Delta_r H°$(kJ/cm^3)
Al + CoO	-17.8	-48.2
Al + Fe_2O_3	-15.8	-42.6
Al + PbF_2	-19.1	-51.5
Al + PbO_2	-23.3	-63.1
Al + SnO_2	-14.9	-40.3
Ba + SnO_2	-1.92	-6.73
Ca + $AgNO_3$	-17.2	-26.5
Ca + As_2O_3	-10.4	-16.1
Ca + $Pb(NO_3)_2$	-12.1	-18.7
Cu + Ag_2O	-1.08	-9.65
Mg + $Cu(NO_3)_2$	-20.1	-34.9
Mg + $Pb(NO_3)_2$	-13.9	-24.3
Mg + TiO_2	-5.42	-9.44
Mn + $PbCl_2$	-2.22	-16.0
Ni + $Cu(NO_3)_2$	-1.91	-17.0
Zn + $Pb(NO_3)_2$	-0.49	-3.473

SUMMARY AND CONCLUSIONS

Among the 130 reactions examined, the following observations and conclusions were made:

(1) The combustion of light elements in fluorine gives the highest values for the enthalpy of reaction at 298.15 K when based on either a mass or volumetric basis.

(2) The combustion of hydrocarbons in fluorine gives more than twice as much exothermicity as compared to combustion in oxygen.

(3) Hydrogen is the fuel which offers the largest exothermicity for combustion in either fluorine or oxygen on a mass basis. Methane, ethane, boron, and beryllium collectively form a second place grouping in this category.

(4) The combustion of elements: boron, beryllium, aluminum, titanium, or zirconium, in either fluorine or oxygen shows that maximum exothermicity can be achieved on a volumetric basis.

(5) Solid multi-cyclic organic compounds, like cubane and adamantane, that possess unique structural symmetry show promise as fuels which give high energy release in combustions with oxygen or fluorine.

(6) Thermite reactions in which elemental aluminum is a reactant show high exothermicity on a volumetric basis.

ACKNOWLEDGEMENT

Financial support for this work was provided by the U.S. Department of the Army, U.S. Army Chemical research, Development, and Engineering Center, Aberdeen Proving Ground, Maryland.

GENERAL REFERENCES

(1) Wagman, D.D., Evans, W.H., Parker, V.B., Schumm, R.H., Halow, I., Churney, K.L.,, and Nuttall, R.L., "NBS Tables of Chemical Thermodynamic Properties", J. Phys. & Chem. Ref. Data 11, Supplement No. 2 (1982).

(2) Marsh, K.N., et al., "Selected Values of Hydrocarbons and Related Compounds", Thermodynamics Research Center, Texas A & M University, College Station, TX (loose-leaf data sheets, extant 1989).

(3) Chase, M.W., Jr., Davies, C.A., Downey, J.R., Jr., Frurip, D.J., McDonald, R.A., and Syverud, A.N., "JANAF Thermochemical Tables, Third Edition", J. Phys. & Chem. Ref. Data 14, Supplement No. 1 (1985).

(4) Weast, R.C., Editor, "Handbook of Chemistry and Physics", 69th edition, CRC Press, Inc. Cleveland, OH, 1988-1989.

(5) Pedley, J.B., Naylor, R.D., and Kirby, S.P., "Thermochemical Data of Organic Compounds", Second Edition, (Chapman and Hall, London and New York, 1986).

(6) Cox, J.D., Wagman, D.D., and Medvedev, V.A., "CODATA Key Values for Thermodynamics", (Hemisphere Publishing Corp., New York, 1989).

BLANK

V. DETECTION

NOTE: A paper with the following title was presented at the Conference but is not included in this document:

Emerging Technologies in Field Screening Methods for Hazardous Waste Site Investigations

BLANK

LASER STAND-OFF DETECTION OF ATMOSPHERIC SPECIES UNDER THE CRDEC CO_2 LASER LIDAR FACILITY

Alan P. Force, Silvio L. Emery, Ronald B. Crosier, Francis M. D'Amico, and Felix L. Reyes
U.S. Army Chemical Research, Development and Engineering Center
Aberdeen Proving Ground, Maryland 21010-5423

Preliminary topographic lidar measurements with the CRDEC fixed-site lidar system indicated that there was a mismatch between the temporal profiles of the signals generated by the laser energy monitor and the lidar returns. It was feared that this mismatch would cause problems in normalizing both topographic and range-resolved lidar returns to the laser energy. A statistically designed experiment has been performed to determine the possible effects of the mismatch in the temporal profiles, and to determine if the signals must be integrated in order to use the peak area for normalization or if the height of the peak is sufficient for the measurements.

INTRODUCTION

The CRDEC fixed-site lidar facility was established to develop in-house capabilities and expertise in stand-off selection techniques. The research that is performed in the lidar facility is part of an effort to develop a laser sensor for the detection of chemical agents in the air and on the ground and other surfaces. Experiments being performed include the detection and measurement of trace ambient chemical compounds in the atmosphere and an analysis of topographic lidar returns from both hard and soft targets.

The main components in the lidar system are a pair of line-tunable CO_2 TEA lasers, steering mirrors to direct the laser radiation to targets outside the laboratory, an infrared telescope to collect the backscattered radiation and focus it onto the chip of a cooled HgCdTe detector (MCT), a room temperature MCT mounted in an integrating sphere used to monitor the laser output energy, and a PC based computer controlled data acquisition system. Signals from the two detectors are recorded by a pair of high-speed CAMAC (IEEE-583) transient recorders at digitization rates of up to 100 MHz. Preliminary measurements with the system revealed a mismatch in the temporal profiles of the peaks in the signals recorded from the two detectors. This mismatch results from the difference in the bandwidths of the room temperature a liquid N_2 cooled detectors; the room temperature MCT operates at 500 MHz while the cooled MCT operates at only 15 MHz. Therefore, the temporal profile of the lidar signal is longer with a wider and shorter gain switched spike and a much more prominent nitrogen tail than that of the temporal profile of the signal generated by the room temperature MCT.

The difference in the temporal profiles of the two signals raised concerns about the method used for normalizing the lidar returns to the laser energy.

In the past, the height of the signal peak from the laser energy monitor has been used as the measure of the laser pulse energy. This was done because the peak height can be easily measured with either a peak sensing analog-to-digital convertor (A/D) or with a peak sense and hold amplifier. However, high-speed digitizers and faster computers make it possible to record and analyze the entire laser pulse and measure all the energy in the pulse not just the peak energy. Since there is such a difference in the temporal profiles of the two detector signals and because the signal obtained from a range-resolved DIAL measurement is a function of all the energy in the laser pulse, we decided to design and run an experiment that would determine the best method of normalizaiton.

Experimental Design

A hard target at a range of about 550 meters was used to provide the topographic returns for the experiment. For each run both lasers were tuned to the same CO_2 laser transition and fired for 30 shots at a PRF of 3 Hz with a delay of 5 microseconds between the two lasers. Between runs the lasers were tuned to a different laser transition and power supply voltage. The laser transitions used were the 10(R20), 10R(18), 10R(12), 9P(14), and 9P (12). The power supply was set at 26, 28, or 30 kV. Two runs were performed at each laser transition-voltage combination for a total of 30 runs. The order of the runs was randomized using a statistical design to eliminate any bias from the experiment. Each signal was recorded at a digitization rate of 100 MHz and saved on the hard disk of the PC for analysis.

Data Analysis

Each experimental run was analyzed on a shot-to-shot basis. A C language program was used to calculate the peak height and peak area for each of the lidar returns and signals from the laser energy monitor. Peak heights were determined by calculating the maximum value for the signal that was found in a "window" area of the recorded signal that corresponded to the laser pulse. Peak areas were calculated by summing the values of all of the points found in each "window". Peak heights were then plotted again the peak areas for each laser and each detector. The resulting plots are linear, which indicates that the two methods should be equivalent.

Peak Goodness and Area Goodness were defined as

$$\text{Peak Goodness} = \ln[S1p/P1P/(S2p/P2p)]$$

and

$$\text{Area Goodness} = \ln[(S1a/P1a)/(S2a/P2a)]$$

or as the natural logarithm of the ratio of the normalized lidar returns using the peak method and area methods respectively. Since both lasers are tuned to the same line on each run, this is equivalent to performing a DIAL experiment with a differential absorption of zero. A plot of the Goodness against the run number should be linear with a value that is close to zero for every shot, because each pair of laser shots is separated by only 5 microseconds and "sees" the same atmosphere. The variation in the Area Goodness plot is greater than that in the Peak Goodness plot, but both

plots demonstrate the expected result.

A final check of the two methods was performed by plotting the lidar signal against the laser power producing a normalizaiton plot for each laser. Plots were made of the signal area normalized to the power area, tne signal peak normalized to the power peak, and the signal area normalized to the power peak; the three plots for each lasers are all but indistinguishable.

CONCLUSIONS

Since the two methods of normalization appear to be equivalent, there seems to be no advantage in using the peak area method of normalization. Data acquisition is much faster if a peak sensing A/D is used to obtain the data. The peak areas can also be very difficult to calculate if there is any noise in the signal, while no calculation is required to determine the peak height with the proper data acquisition equipment.

BLANK

STATISTICS FOR IDENTIFYING A CONTAMINATED ROUGH SURFACE BY POLARIZED IR SCATTERING: FULL WAVE APPROACH

S. Mark Haugland,[1] Ezekiel Bahar,[1] Arthur H. Carrieri[2]

Abstract. An optical technique to identify the presence of chemical coatings over rough surfaces is described. It is based on the selective use of the Mueller matrix elements which provide a complete characterization of scattered light from the surface. The Full Wave approach is used to compute the Mueller matrix elements as functions of backscattering angle and wavelength for coated terrestrial and fabricated rough surfaces. Statistical methods are developed to select initial values of backscatter angle and wavelength for the optimal detection of the optically thick contaminant layers. These parameters disencumber the experimental determination of the optimal values for backscatter angle and wavelength. Experimental data collected at the optimum values of incident angle and wavelength are inputs to the statistical algorithm that is used to identify, in near real time, the surface is coating (if any).

1. Introduction

The objective of this work is to develop an optical technique to identify the presence of a chemical coating (contaminant) over a rough surface that separates two semi infinite media. Multivariate statistical techniques that are widely used in remote sensing are usually based on spectral reflectance, emissivity, or pulse shape measurements. However, none of the above measurements provide a complete characterization of the scattered light from the surface. We propose to develop multivariate statistical algorithms for the detection of the coating that are based on the selective use of the (4 by 4) Mueller matrix data since it provides a complete characterization of the scattered light from the surface.

An analytical study based on the full wave approach[1] is used to develop an algorithm to select initial values of backscatter angles θ and wavelengths λ for the optimal identification of the coatings (characterized by their complex dielectric coefficients ϵ). In this phase of the investigation, it is assumed for simplicity that the coating material is optically thick and that both the coated and bare rough surfaces are characterized by the same statistical parameters. The initial values of θ and λ (obtained from the algorithm) are used to facilitate the efficient experimental determination of the optimal values for θ and λ for the identification of a specific coating over a rough surface. The algorithm for selecting the initial values for θ and λ can be upgraded by accounting for the finite thickness of the coating and the different statistical characterizations of the coated and bare surfaces.

Experimental data collected at these optimal combinations of θ and λ are used to develop a second algorithm to identify the specific coating material (if any) and the degree of confidence we have in the proper identification of the surface. This algorithm is based on Hotelling's T-squared method[2] and involves a principal axis transformation of the measured Mueller matrix elements used to identify

In section 2 an overview is presented of the full wave expressions used to compute the Mueller matrix elements. In section 3 the algorithm for the optimal selection of θ and λ is described and in section 4 the algorithm used to identify the specific coating (if any) is described.

2. Computation of the Mueller matrix elements using the full wave solutions

Electromagnetic waves incident upon and scattered from the (coated or bare) rough surface are characterized by the Stokes vectors $\vec{s}$ and $\vec{s}'$ respectively. In standard form the Stokes vector is given by[3]

$$\vec{s}=[I\ Q\ U\ V]^t \tag{1}$$

where

$$I=< |E_1|^2 + |E_2|^2 > \tag{2a}$$

$$Q=< |E_1|^2 - |E_2|^2 > \tag{2b}$$

$$U=2\ RE\ (< E_1E_2^* >) \tag{2c}$$

$$V=2\ IM\ (< E_1E_2^* >) \tag{2d}$$

in which the super t denotes transposition and E_1 and E_2 are two orthogonal components of the electric field in the plane normal to the wave vector $\vec{k}$ (in the direction of propagation). Typically E_1 and E_2 are the vertically and horizontally polarized components E^v and E^h respectively of the electric field. The symbol $*$ in (2) denotes the complex conjugate and $RE(\cdot)$ and $IM(\cdot)$ denote the real and imaginary parts of the argument.

The phase (Mueller) matrix M relates the scattered Stokes vector to the incident Stokes vector: Thus

$$\vec{s}' = M\vec{s}$$

For isotropic rough surfaces the normalized Mueller matrix (per unit area) for the backscattered Stokes vector reduces to the special form

$$M = \begin{bmatrix} M_{11} & M_{12} & 0 & 0 \\ M_{12} & M_{22} & 0 & 0 \\ 0 & 0 & M_{33} & M_{34} \\ 0 & 0 & -M_{34} & M_{44} \end{bmatrix} \tag{3}$$

where

$$F_{11}= .5\ (\ \sigma_{vv}^{vv} + 2\ \sigma_{hv}^{hv} + \sigma_{hh}^{hh}) \tag{4a}$$

$$F_{12} = .5\ (\ \sigma_{vv}^{vv} - \sigma_{hh}^{hh}) \tag{4b}$$

$$F_{22}= .5\ (\ \sigma_{vv}^{vv} - 2\ \sigma_{hv}^{hv} + \sigma_{hh}^{hh}) \tag{4c}$$

$$F_{33} = RE\ (\ \sigma_{vv}^{hh} + \sigma_{vh}^{hv}) \tag{4d}$$

$$F_{34} = -\ IM\ (\ \sigma_{vv}^{hh}\ ) \tag{4d}$$

$$F_{44} = RE\ (\ \sigma_{vv}^{hh} - \sigma_{vh}^{hv}) \tag{4d}$$

In which the full wave expressions for the Mueller matrix elements are[1] given by

$$\sigma_{RS}^{PQ} = Q(\vec{n}^f, \vec{n}^i, R)\, I_{RS}^{PQ}(\vec{n}^f, \vec{n}^i) \tag{5}$$

where

$$I_{RS}^{PQ} = \int \frac{D^{PQ*} D^{RS}}{(\vec{n}\cdot\vec{a}_y)^2} P_2(\vec{n}^f, \vec{n}^i|\vec{n}) p(\vec{n}) dh_x dh_z \tag{6}$$

$$Q = 2k_0^2 \int_0^\infty [\chi_2 - |\chi|^2]\, J_0(v_{xz} r_d) r_d dr_d \tag{7}$$

The unit vectors in the direction of the incident and scattered waves are $\vec{n}^i$ and $\vec{n}^f$ respectively. Thus for backscatter

$$\vec{n}^f = -\vec{n}^i = -\vec{a}_x \sin\theta + \vec{a}_y \cos\theta \tag{8}$$

$$\vec{v} = k_0(\vec{n}^f - \vec{n}^i) = 2k_0\vec{n}^f \tag{9}$$

where k_0 is the free space wave number. Thus

$$v_{xz} = \sqrt{v_x^2 + v_z^2} = 2k_0 \sin\theta, \quad v_y = 2k_0 \cos\theta \tag{10}$$

The unit vector normal to the rough surface y=h(x,z) (y=0 is the mean surface) is

$$\vec{n} = \frac{-\vec{a}_x h_x + \vec{a}_y - \vec{a}_z h_z}{\sqrt{1+h_x^2+h_z^2}} \tag{11a}$$

and

$$h_x = \frac{\partial h}{\partial x}, \; h_z = \frac{\partial h}{\partial z} \tag{11b}$$

The rough surface heights and slopes are assumed to be uncorrelated. The surface height characteristic function χ and joint characteristic function χ_2 for Gaussian surface height probability density functions are

$$\chi = \exp(-v_y^2 \langle h^2 \rangle / 2) \tag{12a}$$

$$\chi_2 = \exp[-v_y^2 \langle h^2 \rangle (1-R)] \tag{12b}$$

in which R is the normalized surface height auto correlation function. The slope probability density function $p(\vec{n})$ (also assumed Gaussian) is given by

$$p(\vec{n}) = \frac{1}{\pi \langle \sigma_s^2 \rangle} \exp[-(h_x^2 + h_z^2)/\langle \sigma_s^2 \rangle] \tag{13}$$

in which $\langle \sigma_s^2 \rangle = \langle \sigma_{sx}^2 \rangle + \langle \sigma_{sz}^2 \rangle$ is the total mean square slope for the isotropic surface. In (6) the rough surface scattering coefficients D^{PQ} depend on the polarization of the scattered wave (first superscript P=h(horizontal), P=v(vertical)) and incident wave (second superscript Q=h,v), the scattered and incident wave normals $\vec{n}^f$ and $\vec{n}^i$, the unit vector normal to the rough surface $\vec{n}$, and the electromagnetic parameters μ (permeability), ϵ (permittivity) of the media on both sides of the rough interface. Closed form expressions for the scattering coefficients have been derived.[4] For backscatter, $D^{PQ} = -D^{QP}$ $(P \neq Q)$ thus $\sigma_{vh}^{vh} = \sigma_{hv}^{hv}$ and $\sigma_{vh}^{hv} = \sigma_{hv}^{vh}$. Furthermore, for isotropic surfaces D^{PP} and

D^{PQ} ($P \neq Q$) are even and odd functions of $h_x h_z$ respectively. As a result eight terms of the backscatter Mueller matrix vanish. The shadow function P_2 is the probability that a point on the rough surface is both visible to the observer and illuminated by the source given the slope at that point.[5]

In (7) $J_0(v_{xz} r_d)$ is the Bessel function (first kind) of order zero and v_{xz} is given by (10). Implicit in (7) are the assumptions that the surface is both isotropic and homogenous. Thus the surface height autocorrelation function $\langle h(\vec{r})\, h(\vec{r}') \rangle = \langle h^2 \rangle\, R(r_d)$ is a function of the lateral distance

$$r_d = \sqrt{(x - x')^2 + (z - z')^2} \tag{14}$$

in this work R is also assumed to be Gaussian. In general it is the Fourier transform of the rough surface height spectral density function: Thus

$$R = \exp(-r_d^2 / l_c^2) \tag{15}$$

in which l_c is the correlation length. For the rough surface correlation function (15) l_c is related to the mean square height $\langle h^2 \rangle$ and the total mean square slope $\langle \sigma_s^2 \rangle$

$$l_c^2 = \frac{4\langle h^2 \rangle}{\langle \sigma_s^2 \rangle} \tag{16}$$

For isotropic surfaces the backscatter Mueller matrix has only 6 independent entries. However, when depolarization is negligible (relatively smooth surfaces), only four on these entries are independent.

3. Selection of incident angle and wavelength for optimal identification of the coating material

In this section, we describe the algorithm that is used to optimally select the backscatter angle and the wavelength of the excitation to identify different coating materials. The selection is done in two stages. The initial selection is made on the basis of the full wave analysis of light scattering from coated rough surfaces (section 2). The final selection of the backscatter angle θ and wavelength λ is made on the basis of an experimental mapping of the six independent Mueller matrix elements in a region ($\theta' \pm \delta\theta$ and $\lambda' \pm \delta\lambda$) around the initial values θ' and λ'. At this phase of our investigation, the coating is assumed to be optically thick and scattering at the lower interface of the coating material is neglected. The analysis can be upgraded to account for non-optically thick coatings.[6]

For the purpose of developing the algorithm to optimally select the initial values θ' and λ' we construct the vector $\vec{p}$ from the six independent Mueller matrix entries

$$\vec{p} = [p_1, p_2, p_3, p_4, p_5, p_6]^t = [F_{11}, F_{12}, F_{22}, F_{33}, F_{34}, F_{44}]^t \tag{17}$$

Let $\vec{p}^c$ and $\vec{p}^b$ denote the vector $\vec{p}$ for the rough surfaces with and without the coating respectively. These quantities are computed as functions of θ and λ (over the operating range of the experimental equipment) for given coated and uncoated random rough surfaces. For each θ, λ, and ϵ a set of realizations of $\vec{p}$ are computed for random selections of $\Delta\theta$, $\Delta\lambda$, $\Delta\epsilon$, $\Delta\langle h^2 \rangle$, $\Delta\langle \sigma_s^2 \rangle$, and Δl_c which represent the equipment tolerances, deviations in the medium parameters, and variations in the rough surface statistical parameters. For this set of realizations the mean values $\langle p_k \rangle$ and the standard deviations w_k of the elements of the vectors $\vec{p}^b$ and $\vec{p}^c$ are computed. The six components x_k (k=1, 2, 3, 4, 5, 6) of the normalized difference vector $\vec{x}$ are defined as follows

$$x_k = \frac{\langle p_k^c \rangle}{w_k^c} - \frac{\langle p_k^s \rangle}{w_k^s} \tag{18}$$

Thus the length of $\vec{x}$ is the distance between the normalized vectors $\vec{p}^b$ and $\vec{p}^c$ whose components have unit variance. The initial selection of the optimum values of backscatter angle and wavelength are chosen such that the length of the vector $\vec{x}$ given by

chosen such that the length of the vector $\vec{x}$ given by

$$\sqrt{\vec{x}^t\vec{x}} = x \tag{19}$$

is largest for a specific coating material. Different combinations of θ' and λ' are selected for different coating materials.

4. Identification of the coating material

The algorithm developed to identify the coating material (if any) is based on Hotelling's T-squared method.[2] This method involves the inversion of a covariance matrix. Thus to avoid problems associated with the inversion of matrices with very small determinants a principal axis transformation[7] (principal component analysis) is used to transform the average vectors $\langle\vec{p}\rangle$ into new vectors

$$\vec{z} = A\langle\vec{p}\rangle \tag{20}$$

where A is the transformation matrix. As a result the covariance matrix for $\vec{z}$ is the diagonal matrix Λ. It is related to the covariance matrix C of the vectors $\langle\vec{p}\rangle$ as follows

$$\Lambda = ACA^t \tag{21}$$

Since C is a real symmetric non-negative definite matrix, A is a unitary matrix ($A^{-1} = A^t$) and the elements of the diagonal matrix Λ are the real characteristic values λ_i ($\lambda_i \geq 0$) given by the characteristic equation

$$\det(C - I\lambda_i) = 0 \tag{22}$$

The i^{th} column of the matrix A^t is the characteristic vector A_i^t

$$CA_i^t = \lambda_i A_i^t \tag{23}$$

Those elements of the vector $\vec{z}$ corresponding to characteristic values λ_i that are sufficiently close to zero (to cause numerical instabilities) are extracted from the vector $\vec{z}$ to yield the truncated vector $\vec{\zeta}$ whose covariance matrix is assumed to be the corresponding truncated matrix Λ_0. Applying Hotelling's T-squared method to the truncated vector $\vec{\zeta}$, we define the quantity d^2 as follows

$$d^2 = (\vec{\zeta} - \vec{\zeta}^b)^t \Lambda_0^{-1} (\vec{\zeta} - \vec{\zeta}^b) = \sum_{i=1}^{N} \frac{(\zeta_i - \zeta_i^b)^2}{\lambda_i} \tag{24}$$

where $N \leq 6$. The quantity $\vec{\zeta}$ is measured for all the optimal combinations of θ and λ for which the corresponding values $\vec{\zeta}^b$ (for the bare surface) are pre-stored in an existing data bank. Thus the coating material for which d^2 is maximum is identified as the most likely coating being observed. The degree of assurance one has that this identification is correct depends on the magnitude of the positive real number d^2. This can be obtained experimentally or analytically[2] based on the statistical model used. If the degree of assurance one gets is not sufficient it is also necessary to conclude weather or not additional data may lead to better identification.

5. Conclusions

Six independent backscatter Mueller matrix elements completly characterize light scattering from isotropic coated and uncoated rough surfaces. Algorithms based on measurements of these matrix elements are developed to identify optically thick chemical coatings over rough surfaces. Our first task is to determine combinations wavelengths λ and backscatter angles θ that could be used optimally to identify the chemical coatings (if any). To make this task more tractable the six independant Mueller

matrix elements are evaluated numerically based on the full wave approach. The initial selection of λ and θ is made on the basis of these statistical computations. Once λ and θ are determined Hotelling's T-squared method is used to identify the coating material (if any) and to determine the degree of assurance one has on weather or not this identification is correct.

ACKNOWLEDGMENT

This work was sponsored by the CRDEC contract DAAD05-89-P-0427.

FOOTNOTES

1 Department of Electrical Engineering, University of Nebraska-Lincoln, Lincoln, NE 68588-0511
2 U.S. Army Chemical Research, Development, and Engineering Center, Aberdeen Proving Grounds, MD 21010-5423

REFERENCES

1 E. Bahar and M. A. Fitzwater, " Scattering and Depolarization of linearly polarized waves by finitely conducting particles, " J. Appl. Phys. 60, 15 Sept. 1986, pp 2123-2132.
2 Donald Morrison, Multivariate Statistical Methods, McGraw-Hill, 1967.
3 A Ishimaru, Wave Propagation and Scattering in Random Media (Academic, New York, 1978).
4 E. Bahar, "Full Wave Solutions for the Depolarization of the Scattered Radiation Fields by Rough Surfaces of Arbitrary Slope, " IEEE Trans. on Antennas and Propag. AP-29 no. 3, 1981, pp443-454.
5 M. I. Sancer, " Shadow-Corrected Electromagnetic Scattering from a Randomly Rough Surface," IEEE Trans. on Antennas and Propag. AP-17 no. 5, 1968, pp557-585.
6 Bahar and Fitzwater, " Physical Interpretation of the full wave solutions for the electromagnetic fields scattered from irregular stratified media, " Radio Science, Vol 23, no. 5, 1988, pp749-759.
7 Kendall, Multivariate Analysis, Charles Griffin and Cc. LTD, 1975.

LASER-INDUCED RESONANT TWO-PHOTON IONIZATION OF -NO_2 CONTAINING AROMATIC COMPOUNDS AT ATMOSPHERIC PRESSURE

Irit Sofer and David M. Lubman
Department of Chemistry
The University of Michigan
Ann Arbor, MI 48109

ABSTRACT

The laser-induced resonant two-photon ionization of various nitro-substituted aromatics is studied under atmospheric pressure conditions using 266 nm light. In general, relatively soft ionization is observed where either the molecular ion or $(M-NO)^+$ or $(M-OH)^+$ are detected as the dominant ion in the API/MS device.

Introduction

Atmospheric pressure ionization methods can provide a sensitive and rapid means of monitoring trace contaminants in the environment (1-12). The great sensitivity of this technique is based upon accomplishing ionization at atmospheric pressure under ambient conditions so that the actual concentration is directly examined during analysis. In addition, the ionization sources used at atmospheric pressure can often produce ionization with very high efficiency. These include the corona discharge and $^{63}Ni\beta$ source which utilize kiloelectronvolt electrons to ionize components in the air which then transfer charge through a series of ion/molecule reactions to the trace species of interest. Because of the large number of collisions at atmospheric pressure these methods may be nearly 100% efficient for molecules with high proton or electron affinities (6,12). The main drawbacks of this method are: (1) limited selectivity during the ionization process and; (2) background contaminants in the sample may result in a number of competing reactions and thus confusion can arise in the interpretation of the data.

An alternate means to achieve atmospheric pressure ionization is to use laser induced resonant two-photon ionization (R2PI) (8-10). In R2PI an ultraviolet photon excites a molecule to a real intermediate electronic state and a second photon ionizes the molecule. R2PI has been shown to be an efficient means of producing soft ionization under vacuum conditions, where only the molecular ion can be produced with little or no fragmentation at modest laser energies. More significantly, though, it has been shown that laser-induced R2PI under atmospheric pressure conditions produces soft ionization even at very high laser power ($>10^7$ W/cm^2) where only small fragments would otherwise be observed under vacuum conditions (10). In addition, another important advantage of R2PI as an atmospheric pressure ionization source is that it is a direct ionization method and thus may be less prone to competing ion/molecule reactions than the corona discharge or Niβ source. However, the most

unique aspect of this method is that selectivity can be obtained based upon the wavelength dependence of ionization in the R2PI process (9).

In the present work, R2PI is being explored as an ionization source for $-NO_2$ substituted aromatic compounds and other molecules with electron withdrawing groups on the aromatic ring under atmospheric pressure conditions. Previous work on R2PI has focused almost exclusively on aromatic molecules with electron-releasing substituent groups. These species generally have large absorption cross-sections and low ionization potentials and are thus ionized by R2PI in the near-UV very efficiently. However, $-NO_2$ substituted aromatics are an extremely important group of molecules since they include important explosives such as TNT and TNA. However, $-NO_2$ substituted aromatics tend to predissociate upon absorption of UV light and generally have relatively low cross-sections in electron impact ionization due to the electron-withdrawal of π electrons from the aromatic center by the $-NO_2$ substituent (7). Thus, we have explored the potential of R2PI as an atmospheric pressure ionization source for this important class of molecules. In particular, R2PI may serve as an important ionization source for detection of explosives in API/mass spectrometry or ion mobility spectrometry (IMS).

Experimental Section

The experimental set-up consists of a spectraEL™ atmospheric pressure ionization quadrupole mass spectrometer with an API cell modified for a laser ionization source. The API cell consists of a stainless steel cell 1.5 in. in diameter by 2.6 in. long in which ionization is produced by laser-induced R2PI. The ions are then biased to drift under the influence of an electric field toward a 30 μm orifice into the mass spectrometer. There are several 1/8" inlet SS tubes for the atmospheric pressure support gas to flow into and out of the cell. There are also several cajon ports for a discharge ionization source, sample probe, and for quartz windows to allow the UV laser ionization beam to pass through the cell. The cell was attached to the mass spectrometer via a teflon screw seal and teflon seals were used as needed in the cajon fittings and end plate to minimize air leakage into the cell. The end plate was biased at typically 350 V in the positive mode and -150 V in the negative mode in order to force the ions to drift toward the aperature. The sides of the cell were separately biased at 150 V positive or 50 V negative to prevent ions from being lost to the cell walls, while the aperture remained at ground potential. A constant flow of background gas was maintained through the cell at between 400 - 500 cc/min while the cell was kept at 150° - 230°C using cartridge heaters in order to keep the walls free from background contamination between samples. The flow passed in front of the orifice and exited at the opposite end of the cell in order to prevent sample and dust from reaching and blocking the orifice. The orifice was heated 10°C - 50°C higher than the cell to further prevent clogging.

The laser source was the fourth harmonic (266 nm) of a Quanta-Ray DCR-3 Nd:YAG laser. The laser was softly focused using a quartz lens (10 cm f.l.) within the API cell to produce a power density estimated at ~ 10^7 W/cm^2 in a 1 mm diameter spot. The focus could be varied to change the power density in order to study its effect upon the ionization process. The sample was introduced into the API cell using either diffusion tubes or a direct sample insertion probe as described in previous work (10,11). The concentrations that result are estimated to range from ~ 10 ppb for TNT to ~ 150 ppb for p-nitrophenol. The samples have been obtained from Aldrich Chemical Co. and have been used without further purification.

The SpectraEL™ mass spectrometer unit could be scanned to mass 1200 with a resolution of up to 1000. The present apparatus is set-up in the pulse-counting mode with a high-gain channeltron electron multiplier. The signal is accumulated using a PARC Model 4203 signal averager in the pulse counting mode and subsequently stored in a computer. The typical scan rate used was 50 amu/s over a range of 200-300 amu and the mass spectra were taken with unit resolution. The mass range was calibrated using either chlorine or bromine containing compounds in the negative mode or iodine to produce calibration peaks at m/z 127 and 254, respectively.

Results and Discussions

In figures 1a-c are shown atmospheric pressure ionization mass spectra of p-nitroaniline using various ionization methods. In figure 1a is a mass spectrum of p-nitroaniline taken using a discharge at ~ 0.9 kV (65-75 μamps) in helium background gas at 1 atm. In this case, the molecular ion MH^+ is observed as the dominant ion peak with a second small peak at $(M + H_2O)^+$. The other peaks are due to background. The estimated concentration of p-nitroaniline in figures 1a-c is between 10-20 ppb. In figure 1b is a laser-induced ionization spectrum of p-nitroaniline using 266 nm radiation in N_2 at 1 atm. One main peak is observed at relatively low laser energy at m/z 107 which is $(M-NO)^+$. The molecular ion peak was never observed. This result could be due to: (1) photodissociation followed by ionization; or (2) ionization by absorption of two photons which results in rapid dissociation; or (3) by ionization by two photons followed by absorption of additional photons which result in dissociation. A power dependence was undertaken to determine the number of photons absorbed. However, the result was n = 1 which may be due to a rate-limiting step. In figure 1c is shown direct photoionization by a 10.0 eV VUV lamp in He at 1 atm. The dominant peak here is also $(M-NO)^+$ which seems to indicate that dissociation follows ionization, rather than predissociation occurring upon absorption of one near-UV photon at 266 nm in Figure 1b. The two-photon energy of the 266 nm radiation is ~ 9.3 eV or similar to that of the VUV energy. Loss of NO has been observed as an important pathway in the EI and photodissociation (2.54 eV) mass spectrum of nitrotoluenes, although loss of $-NO_2$ is generally the major fragmentation pathway reported (14).

In figure 2 is shown a laser-induced mass spectrum of p-nitrophenol at 266 nm in 1 atm of N_2 in a concentration estimated at ~ 150 ppb. Once again, there is one dominant peak resulting which corresponds to $(M-OH)^+$. No molecular ion is observed under the conditions of mild focusing used in this experiment. The $(M-OH)^+$ fragmentation route is commonly observed in the EI mass spectra of nitroaromatic compounds (14), although it is not clear why this is the major product in this case as compared to elimination of -NO or $-NO_2$. In figure 3 is shown a laser-induced mass spectrum of o-nitrotoluene at an estimated concentration of 150 ppb. A slightly stronger focus is required for ionization in the $-CH_3$ substituted case as opposed to the $-NH_2$ or -OH substituted nitrobenzenes. $-CH_3$ is a more weakly electron-releasing group to the aromatic ring and is thus ionized less efficiently. In the case of o- and p-nitrotoluene the molecular ion, $M^{+}\cdot$, is observed. It may or may not be the base peak depending upon the power density. Other characteristic ion peaks are always observed, including $(M-OH)^+$ and $(M-NO)^+$ as well as $(M+OH)^+$ and $(M+NO)^+$ or the degree of fragmentation can be altered as the laser power is varied; however, purely soft ionization was not observed under the conditions used in these experiments.

CONCLUSIONS

In conclusion, laser R2PI at 266 nm can be used to produce relatively soft ionization of -NO_2 containing aromatic compounds. Although the molecular ion may not always be produced, characteristic ion peaks result with which these compounds may be easily identified. This method results in direct ionization and can be performed in 1 atm background gas of He, N_2, Ar or air with selective discrimination against small molecule background contaminants that are transparent to near-UV laser radiation.

ACKNOWLEDGMENTS

We thank HNU Systems, Inc. for the generous loan of VUV lamps for this study and Abe Berger of HNU for helpful suggestions during the course of this work.

CREDIT

This work has been funded by the Army Research Office under Grant No. DAAL03-88-k-0191 and by a generous gift from HNU Systems, Inc.

REFERENCES

1. Spangler, G. E.; Lawless, P. A. *Anal. Chem.* **1978**, *50*, 884-892.
2. Hill, H. H., Jr.; Baim, M. A. In *Plasma Chromatography*, Carr, T. W., Ed.; Plenum Press: New York, 1984; Chapter 5, pp 143-176.
3. Mitsui, Y.; Kambara, H.; Kojima, M.; Tomita, H.; Katoh, K.; Satoh, K. *Anal. Chem.* **1983**, *55*, 477-481.
4. Iribarne, J. V.; Dziedzic, P. J.; Thompson, B. A. *Int. J. Mass Spectrom. Ion Phys.* **1983**, *50*, 331-347.
5. Karasek, F. W.; Hill, H. H.; Kim, S. H. *J. Chromatogr.* **1976**, *117*, 327-336.
6. Carroll, D. I.; Dzidic, R. N.; Stillwell, M. G.; Horning, M. G.; Horning, E. C. *Anal. Chem.* **1974**, *46*, 706-710.
7. Crable, G. F.; Kearns, G. L.; Norris, M. S. *Anal. Chem.* **1960**, *32*, 13-17.
8. Lubman, D. M.; Kronick, M. N. *Anal. Chem.* **1982**, *54*, 1546-1551.
9. Lubman, D. M.; Kronick, M. N. *Anal. Chem.* **1982**, *54*, 2289-2291.
10. Kolaitis, L.; Lubman, D. M. *Anal. Chem.* **1986**, *58*, 1993.
11. Huang, S. D.; Kolaitis, L.; Lubman, D. M. *Appl. Spec.* **1987**, *41*, 1371.
12. Sciex, The API Book, Canada 1989.
13. Carroll, D. I.; Dzidic, I.; Horning, E. C.; Stillwell, R. N. *Appl. Spec. Rev.* **1981**, *17*, 337.
14. Yinon, J. *Mass Spec. Rev.* **1982**, *1*, 257.

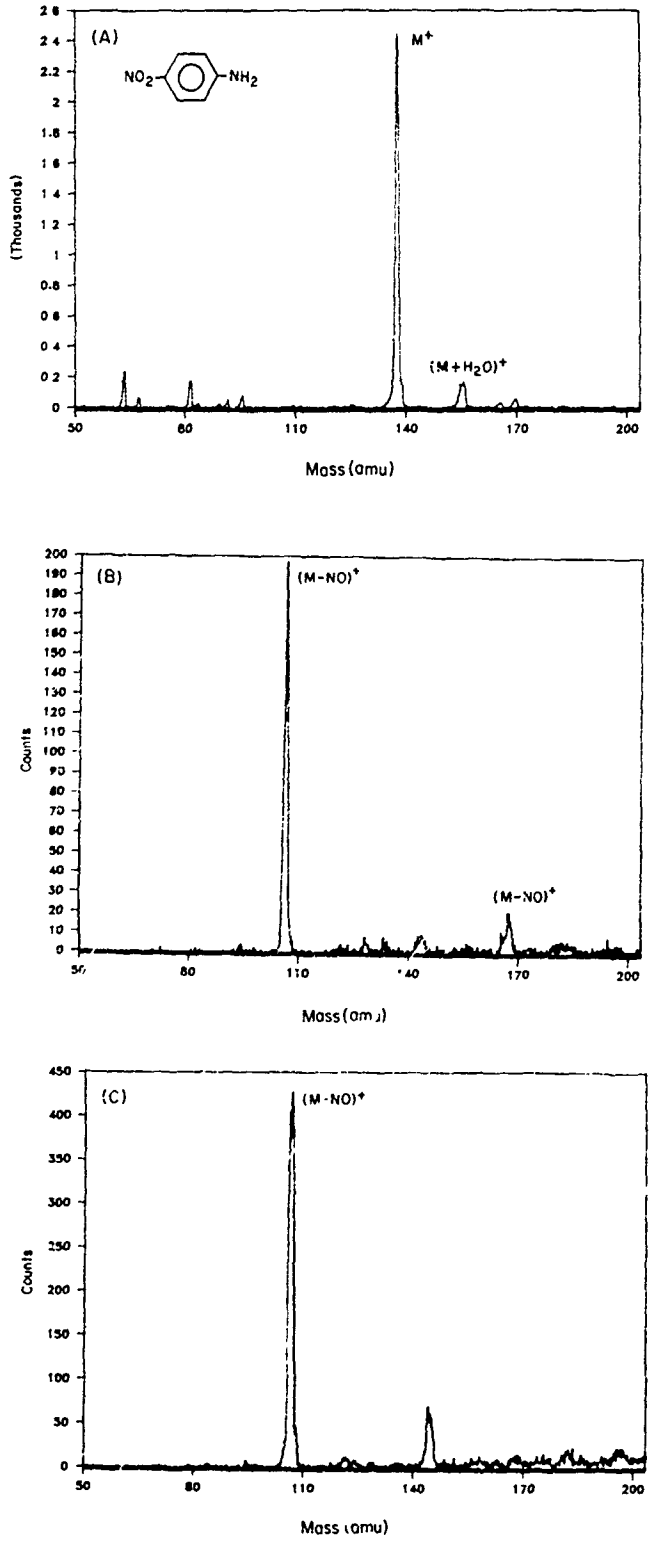

Figure 1. Atmospheric pressure ionization mass spectra of p-nitroaniline taken using (a) glow discharge in 1 atm. He; (b) resonant two-photon ionization at 266 nm in 1 atm of N_2; and (c) photoionization via a 10.0 eV VUV lamp in He at 1 atm.

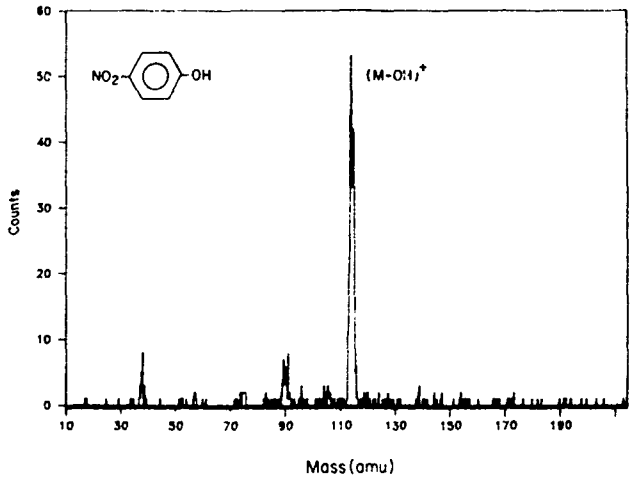

Figure 2. Laser-induced MPI mass spectrum of p-nitrophenol at 266 nm in 1 atm of N_2.

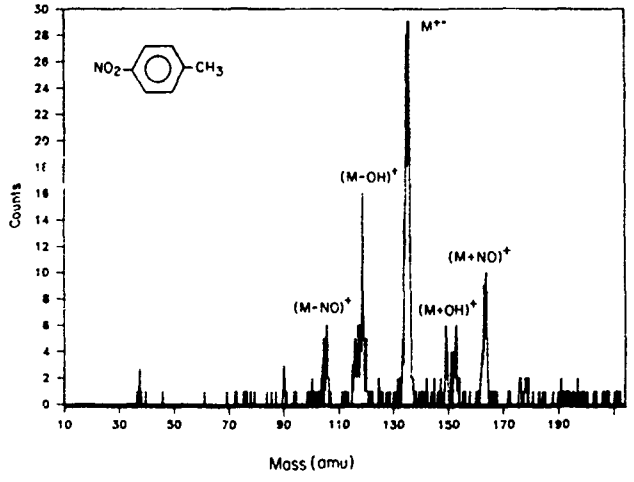

Figure 3. Laser induced MPI mass spectrum of o-nitrotoluene in 1 atm of N_2.

THE EFFECT OF CULTURAL CONDITIONS ON DEEP UV RESONANCE RAMAN SPECTRA OF BACTERIA

W.H. Nelson[1] and R. Manoharan[1], Department of Chemistry, and J.F. Sperry[2]
Department of Microbiology, University of Rhode Island, Kingston, R.I. 02881

Abstract. UV Resonance Raman spectra have been obtained for a series of Gram-negative and Gram-positive bacteria grown under varying cultural conditions. Spectra excited at 242 nm, a wavelength of sensitivity for DNA and RNA bases, do show major differences in RNA-related peak intensities as opposed to protein related features. Spectral differences between organisms grown on TSA(agar) as opposed to Davis minimal media have been found to be very substantial. Spectra of Gram-negative organisms reflected substantial differences in RNA content depending upon whether they were grown under aerobic or anaerobic conditions as well.

In stark contrast spectra obtained with 231 nm excitation, which reflect protein content primarily, show little or no dependence upon growth conditions. Spectra obtained with 222 nm excitation and which primarily result from interactions with cell wall constituents show only minor spectral features which are affected by cultural conditions. Spectra excited at either 222 or 231 nm show very characteristic features which are related to bacterial Gram type, but which are not culturally dependent. Spectra excited at 242 nm while showing major culturally-dependent differences in peaks reflecting relative amounts of proteins and nucleic acids, exhibit ratios of nucleic acid peak heights which are related to DNA base pair ratios.

INTRODUCTION

Previously we have demonstrated that bacteria give characteristic, fluorescence-free UV resonance Raman spectra when excited at 242 nm(1), that E. coli(2) produce characteristic spectra at 222, 231, 242 and 251 nm which change markedly with wavelength due to selective excitation of nucleic acid

[1] Department of Chemistry, University of Rhode Island, Kingston, RI 02881

[2] Department of Microbiology, University of Rhode Island, Kingston, RI 02881

and aromatic amino acids, and that dipicolinate can be selectively excited from bacterial spores(3). We have noted that so long as cultural conditions are kept constant the UV resonance Raman spectra are reproducible and characteristic for a wide range of organisms(3). We have shown using visible laser radiation that resonance Raman spectra of single chromobacterial cells can be obtained(4) and that spectra of single cells can be obtained from chromobacterial mixtures via micro-Raman experiments(5).

Bacterial UV Raman peaks can be attributed primarily to aromatic amino acids, nucleic acid bases and proline. Assignments have been made based on recent thorough studies of small molecules via deep UV Raman excitation. This work which has been done in several laboratories has produced substantial agreement regarding the nature of these nucleic and amino acid resonance Raman spectra(6-29). Various amide modes(6,16,19,27) have been studied also and then related to peptide and protein structure. Quinones(30) have been studied as well. It is now very clear that in the region(242-257nm) species such as nucleic acid bases, dipicolonate, quinones and to a limited extent tyrosine are selectively excited. With 220-230 nm excitation tyrosine and tryptophan are very strongly and selectively excited along with proline to a lesser extent. Below 220 nm a somewhat wider range of species are excited with amide modes especially increasing in intensity along with nucleic acid modes in the region 190-220 nm.

Our work has shown in detail that Raman scattering from bacteria can be interpreted as the contributions of proteins and nucleic acids especially. Because of the complex composition of bacteria, peaks are somewhat broader than those observed from solutions of small molecules, but spectra are still very detailed and appear to be very characteristic regardless of the UV wavelength used for excitation. Still UV Raman studies cannot be fully credible until they are able to reflect and account for the well-known phenotypic differences shown by bacteria. No attempt will be made to survey that literature or to enumerate all the various significant effects known to bacterial physiologists.

Certainly the variation of the RNA content of bacteria has been extensively documented and was reviewed over 25 years ago(31) by Neidhardt. It is clear that rapidly growing cultures usually contain much more ribosomal RNA than the slowly growing ones and that there are large differences in the RNA content depending upon cultural conditions. In contrast the amount of protein differs little from one physiological state to another although individual proteins can vary in concentration by orders of magnitude. In this study we have attempted to grow bacteria under cultural conditions which substantially effect rates of growth. It is expected that these changes will produce larger changes in nucleic acid peaks than protein peaks. It remains to be seen to what extent changes in RNA contributions will alter spectra at the various excitation wavelengths. It is doubted that changes in the amounts of lipids or polysaccharides will affect spectra since these materials do not absorb in the excited region and should be resonance-Raman silent.

RESULTS AND DISCUSSION

Figure 1 compares spectra of E. coli excited at 242 nm. The organisms studied were grown in three different ways. Culture 1(AERO) was grown aerobically on TSA(agar) while Culture 2(ANAERO) was grown anaerobically on

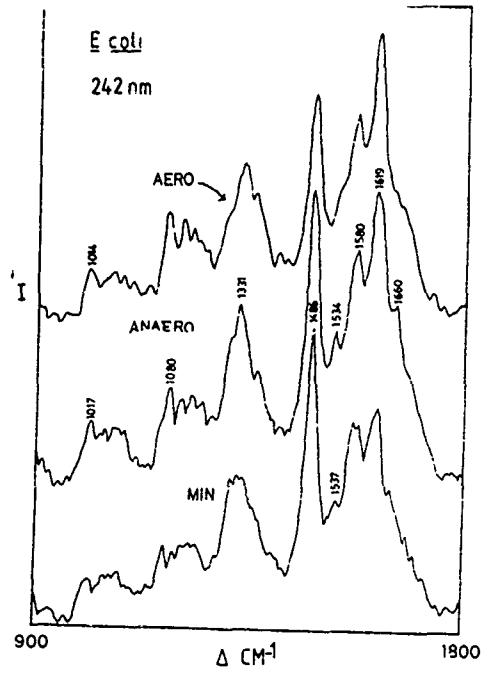

Figure 1. Resonance Raman Spectra (242 nm) Obtained from Three E. coli Cultures: AERO(TSA media grown aerobically), ANAERO(TSA media grown anaerobically), MIN(minimal media).

TSA. Culture 3(MIN) was grown on minimal growth media. It is clear that the spectra obtained at 242 nm show very substantial differences. Especially marked are the differences in the intensities of peaks associated with nucleic acid bases and protein tyrosine and to a limited extent protein tryptophan. Both ANAERO and MIN show much more intense adenine and guanine peaks at 1487 cm^{-1} and 1581 cm^{-1} than does the aerobically grown TSA culture, AERO. ANAERO and MIN show a more pronounced cytosine peak near 1530 cm^{-1} as well. The minimal media culture shows an especially weak protein tyrosine peak near 1620 cm^{-1} and at 1180 cm^{-1}. The anaerobically grown culture shows substantially lower tyrosine-protein/nucleic acid peak intensity ratios as well. It is suggested on the basis of these spectra that different relative amounts of RNA and protein produced under the different cultural conditions are the cause of the spectral differences. Apparently both the anaerobically-grown culture and the one grown in minimal media contain larger relative amounts of RNA. Figure 2 shows the part of Figure 1 obtained between 1300-1800 cm^{-1} at higher resolution to accentuate the differences. Figure 3 shows a spectrum of Torula yeast RNA obtained on the same scale as Figure 2. The similarity between the spectra of the RNA and parts of the bacterial spectra shown in Figure 2 aid in the identification of RNA-related peaks.

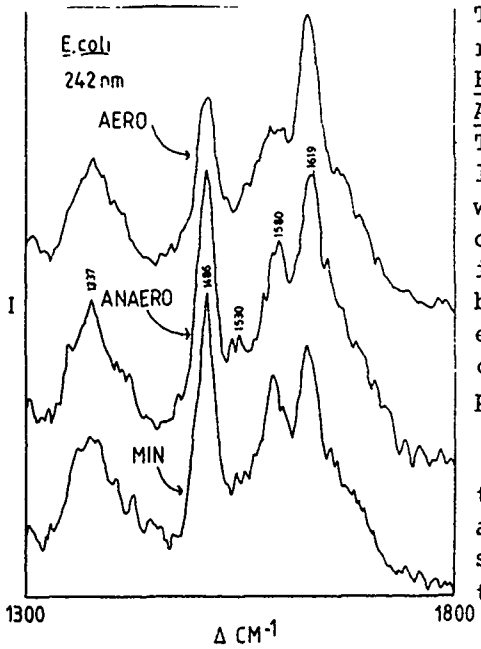

Figure 2. Resonance Raman Spectra of Figure 1 at Higher Resolution.

The experiments related to Figures 1 and 2 are repeated and very similar results obtained for Enterobacter cloacae, Enterobacter aerogenes, Aeromonas hydrophila and Pseudomonas aeruginosa. That is, peaks at 1340 cm^{-1}, 1490 cm^{-1} and 1580 cm^{-1} associated with adenine and guanine were relatively much more intense in the anaerobically-grown cultures and the cultures grown in minimal media while the culture grown aerobically on TSA(agar) had relatively much stronger protein tyrosine peaks at 1180 cm^{-1} and 1619 cm^{-1} and to a lesser extent protein tryptophan peaks at 1010 cm^{-1} and 1550 cm^{-1}.

In spite of the variation in the peak intensities associated with aromatic amino acid and nucleic acids there is an element of constancy in the nucleic acid peak height ratios taken from spectra of cultures grown in TSB (broth). Figure 4 shows a plot of (percent G+C in DNA) vs. the 1537 cm^{-1}/1484 cm^{-1} intensity ratio. It is assumed that the intensity of the 1537 cm^{-1} peak is proportional to the amount

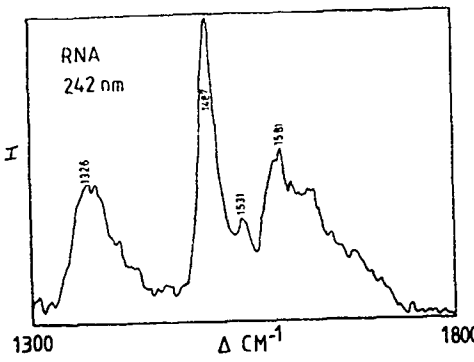

Figure 3. Spectra of Torula Yeast RNA Excited at 242 nm.

of cytosine present while the 1484 cm^{-1} peak will be roughly proportional to the amount of nucleic acid present. In Figure 4 eleven different organisms have been studied with percentages of G+C ranging from 32 to 71.4. The linearity of the plot seems to indicate that the nucleic acid base ratio varies much less than the protein-nucleic acid ratio.

Figure 5 shows spectra of two E. coli cultures excited with 231 nm light. These two samples were grown aerobically and anaerobically, respectively, on TSA(agar). The contrast between the spectra of Figures 1 and 5 is dramatic. While the spectra of Cultures 1 and 2 excited at 242 nm relfect strongly the differences in the RNA/protein ratio of these organisms, the spectra of these same cultures excited at 231 nm are essentially identical. Figure 6 which shows the two spectra of Figure 5 at high resolution indicates only the slightest differences and then only in the region around 1350 cm^{-1}. Similar observations have been made for 231 nm excitation of cultures of Enterobacter aerogenes and Enterobacter cloacae.

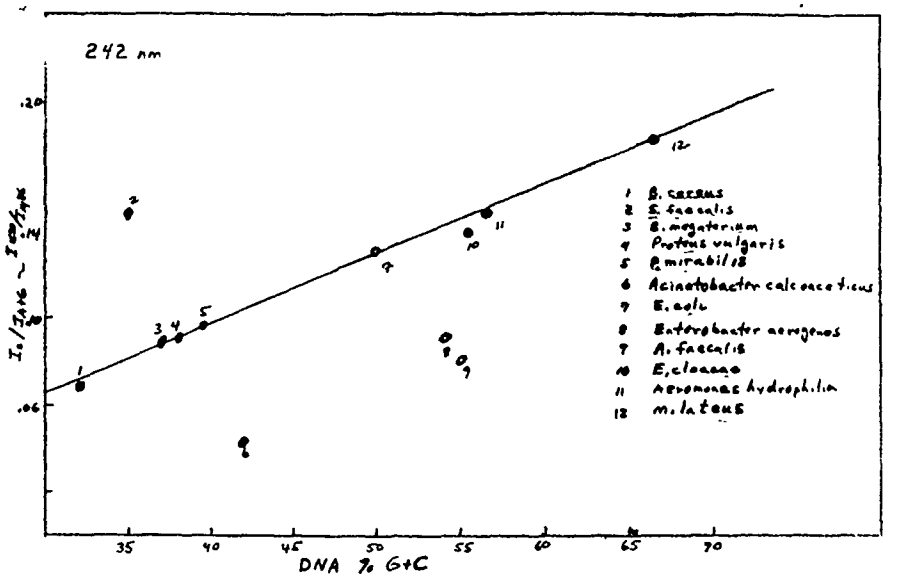

Figure 4. Plot of %(G+C) vs. I(1530)/I(1486).

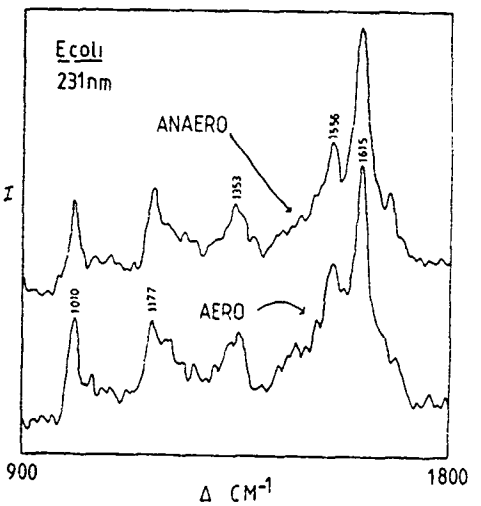

Figure 5. Spectra of AERO, ANAERO and MIN Excited at 321 nm.

Figures 7 and 8 show spectra E. coli cultures grown in the same ways as those investigated with 242 nm radiation. Once again we examine ANAERO, AERO and MIN only this time 222 nm excitation has been used. Like the spectra obtained with 231 nm excitation and unlike the results excited at 242 nm the spectra of all the cultures are markedly similar to one another even though they are substantially different from those of Figures 5 and 6. Like the spectra excited at 231 nm these are characterized by strong protein tyrosine peaks at 1615 cm^{-1} and 1180 cm^{-1} and strong tryptophan peaks at 1015 and 1556 cm^{-1}. Other features

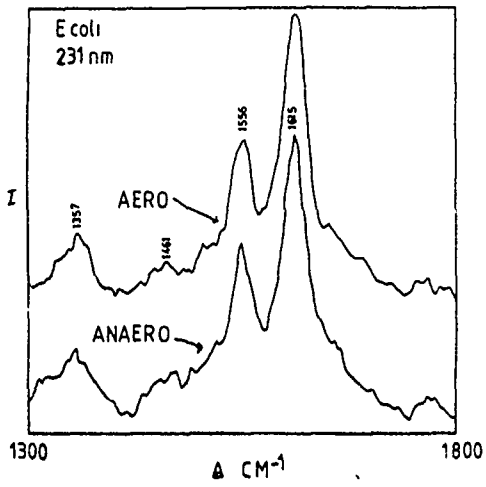

Figure 6. Spectra of Figure 5 at Higher Resolution.

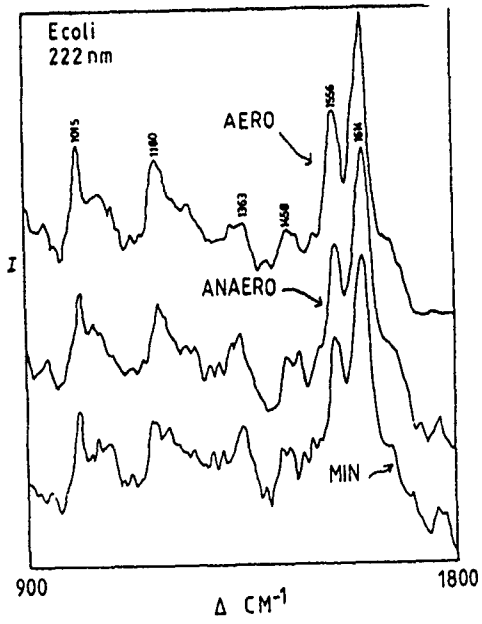

Figure 7. Spectra of AERO, ANAERC and Min Excited at 222 nm.

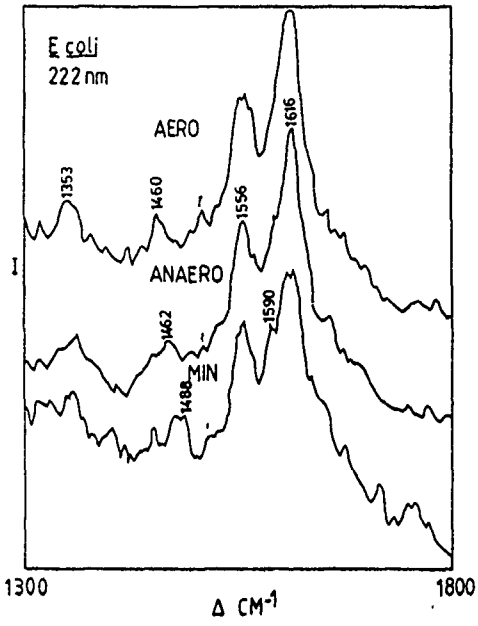

Figure 8. Spectra of Figure 7 at Higher Resolution.

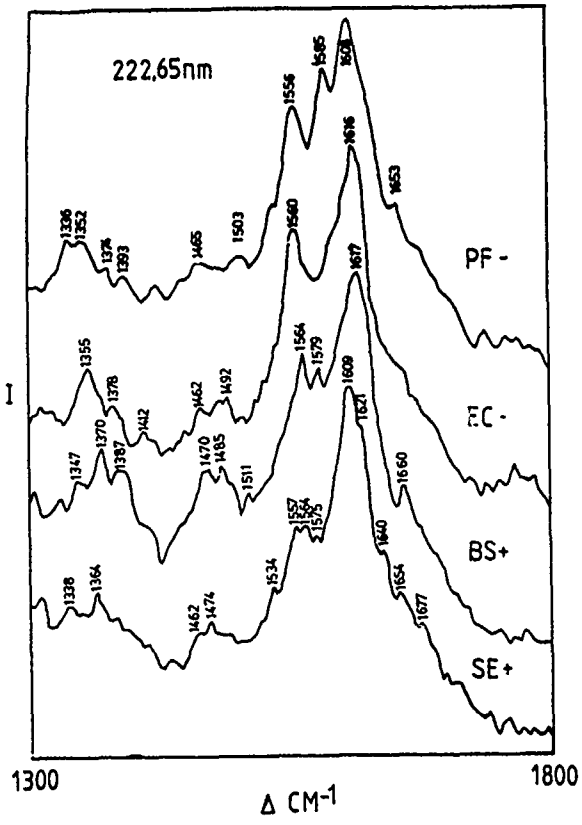

Figure 9. Resonance Raman Spectra 1300-1800 cm^{-1} of Staphylococcus epidermidis(SE), Enterobacter cloacae(EC), Bacillus subtilus(BS and Pseudomonas fluorescens(PF) excited at 222 nm.

such as those attributable to proline at 1460 cm^{-1} are remarkably similar too. Figure 8 shows several small but predictable spectral differences at higher resolution. From both ANAERO and MIN which are known from 242 nm spectra to have higher relative RNA content very weak A+G peaks can be seen at 1490 cm^{-1} and 1590 cm^{-1}. Otherwise spectra appear essentially identical within experimental error.

Figure 9 shows spectra excited at 222 nm cultured aerobically on TSA of Pseudomonas fluorescens, E. coli, Bacillus subtilus and Staphylococcus epidermidis. Differences in these spectra are substantial. Among these are substantial differences in the 1556 cm^{-1}(trp) peak and the 1613 cm^{-1}(tyr) peak intensities for the Gram-negative and the Gram-positive organisms. It is suggested that the stronger protein trp peaks associated with the spectra of the Gram-negative cells are due to the selective excitation of cell wall protein which is very different for the two Gram types.

It is concluded on the basis of this work that phenotypically related differences in bacterial cell components can be detected by UV resonance Raman spectra. It appears most likely that such differences will be observed most strongly in regions which excite both nucleic acid and protein spectra, such as the region between 240-260 nm. Below this wavelength region, however, it appears likely that because of increasing selectivity of cell wall protein components that spectra will be more characteristic of cell wall structural proteins, and, hence, will be much less sensitive to the effects of the cells' cultural environment. Because of the selectivity of resonance Raman excitation it appears likely that eventually it may be possible to assess both phenotypically and genotypically related features selectively via UV resonance Raman spectroscopy. Thus, with careful selection of exciting wavelengths identification of bacteria may be possible using deep UV resonance Raman spectroscopy.

REFERENCES

1. R.A. Dalterio, W.H. Nelson, D. Britt and J.F. Sperry, Appl. Spectrosc. 41, 417-422 (1987).

2. K.A. Britton, R.A. Dalterio, W.H. Nelson, D. Britt and J.F. Sperry, Appl. Spectrosc. 42, 782-788 (1988).

3. R. Manoharan, R.A. Dalterio, K.A. Britton, G. Ghiamati, W.H. Nelson and J.F. Sperry, J. Microbiol. Meth. (accepted for publication 1989).

4. R.A. Dalterio, W.H. Nelson, D. Britt, J.F. Sperry and F.J. Purcell, Appl. Spectrosc. 40, 271-272 (1986).

5. R.A. Dalterio, M. Baek, W.H. Nelson, D. Britt, J.F. Sperry and F.J. Purcell, Appl. Spectrosc. 41, 241-244 (1987).

6. J.M. Dudik, C R. Johnson and S.A. Asher, J. Phys. Chem. 89, 3805-3814 (1985).

7. S.A. Asher, M. Ludwig and C. Johnson, J. Am. Chem. Soc. 108, 3186-3197 (1986).

8. C.R. Johnson and S.A. Asher, J. Raman Spectrosc. 18, 345-349 (1987).

9. M. Ludwig and S.A. Asher, J. Am. Chem. Soc. 110, 1005-1011 (1988).

10. S.A. Asher, C.R. Johnson and J. Murtaugh, Rev. Sci. Instrum. 54, 1657-1662 (1983).

11. S.P.A. Fodor, C.A. Copeland, C.A. Grygon and T.G. Spiro, J. Am. Chem. Soc. 111, 5509-5518 (1989).

12. R.P. Rava and T.G. Spiro, J. Phys. Chem. 89, 1856-1861 (1985).

13. R.P. Rava and T.G. Spiro, J. Phys. Chem. 89, 1856-1861 (1985).

14. S.P.A. Fodor, R.P. Rava, T.R. Hays and T.G. Spiro, 107, 1520-1529 (1985).

15. S.P.A. Fodor, and T.G. Spiro, J. Am. Chem. Soc. 108, 3198-3205 (1986).

16. R.A. Copeland and T.G. Spiro, Biochem. 26, 2134-2139 (1987).

17. D.S. Caswell and T.G. Spiro, J. Am. Chem. Soc. 109, 2796-2800 (1987).

18. B. Hudson, Spectroscopy, 1, 22-30 (1986).

19. L.C. Mayne, L.D. Ziegler and B. Hudson, J. Physc. Chem. 89, 3395-3398 (1985).

20. E.G. Rogers and W.L. Peticolas, J. Raman Spectrosc. 9, 372-375 (1980).

21. W.L. Kubasek, B. Hudson and W.L. Peticolas, Proc. Natl. Acad. Sci, USA 82, 2369-2373 (1985).

22. L.D. Ziegler, B. Hudson, D.P. Strommen and W.L. Peticolas, Biopolymers 23, 2067-2081 (1984).

23. A.Y. Hirakawa, Y. Nishimura, T. Matsumoto, M. Nakanishi and M. Tsuboi, J. Raman Spectrosc. 7, 282-287 (1978).

24. S. Nocentini and L. Chinsky, J. Raman Spectrosc. 14, 9-10 (1983).

25. L. Chinsky, M. Hubert-Habart, A. Laigle and P.Y. Turpin, J. Raman Spectrosc. 14, 322-325 (1983).

26. B. Jolles, L. Chinsky and A. Laigle, J. Biomol. Stuct. and Dynam. 1, 1335-1346 (1984).

27. L. Chinsky, B. Jolles, A. Laigle and P.Y. Turpin, J. Raman Spectrosc. 16, 235-241 (1985).

28. L. Chinsky, B. Jolles and P.Y. Turpin, J. Raman Spectrosc. 18, 195-198 (1987).

29. M. Ghomi, R. Letellier, E. Tailander, L. Chinsky, A. Laigle and P.Y. Turpin, J. Raman Spectrosc. 17, 249-255 (1986).

30. M. Baek, W.H. Nelson and P.E. Hargraves, Appl. Spectrosc. 43, 159-162 (1989).

31. F. C. Niedhardt Ann. Rev. Microbiol. 17, 61-86 (1963).

PROGRESS IN CB DETECTION BY TRANSFER LINE GC/MS° USING A MINIATURIZED ION TRAP MASS SPECTROMETER

Henk L.C. Meuzelaar, Neil S. Arnold, William H. McClennen,
and A. Peter Snyder[1]
Center for Micro Analysis & Reaction Chemistry, University of Utah
214 EMRL, Salt Lake City, UT 84112

ABSTRACT

A novel direct vapor sampling inlet has been tested in combination with Transfer line Gas Chromatography/Mass spectrometry (TLGC/MS°) using the MINITMASS (Miniaturized Ion Trap Mass Spectrometer) system developed at the University of Utah. Typically, 0.2-0.5 s wide air pulses are injected into the 1 m long transfer line at 15-60 s intervals. Even with relatively complex mixtures of vapors, e.g., produced by desorption and combustion of model compounds in a laboratory-scale fixed bed reactor, sufficient GC separation may be obtained to allow positive identification of minor reaction products by direct library search and matching procedures. Moreover, the high sensitivity of the MINITMASS allows tandem MS analysis of subpicogram quantities of selected model compounds.

INTRODUCTION

Based on reports by Cramers *et al.*[1] and Trehy *et al.*[2], regarding the advantages of using short (3-5 m long) capillary GC columns under experimental conditions in which the column outlet is at vacuum pressures, e.g., in many GC/MS configurations, we undertook a series of experiments aimed at investigating the potentiality of short column GC/MS for CB detection applications. Results reported at the 1987 CRDEC Scientific Conference on Chemical Defense Research[3] demonstrated the feasibility of short column GC/MS analysis of underivatized trichothecene mycotoxins, including T2, using a Curie-point desorption injection method. Furthermore, highly characteristic biomarker signals were observed by means of Curie-point pyrolysis in combination with short column GC/MS. These included levoglucosan, amino acid "dimers" and diglycerides when analyzing glycogen, albumin and whole bacterial cells, respectively. Typical elution times varied from 25 seconds for levoglucosan to 300 seconds for diglycerides.

In subsequent experiments we eliminated the gas chromatograph altogether, using instead the 1 m long transfer line of the MINITMASS system as a chromatographic column. Preliminary results of aerosol and vapor sampling experiments using transfer line

[1]CRDEC, Aberdeen Proving Grounds, MD 21010

GC/MS^n were reported at the 1988 CRDEC Scientific Conference on Chemical Defense Research and demonstrated the capability of the TLGC/MS^n approach to monitor changes in vapor concentrations at 15-60 s intervals[4] while maintaining adequate chromatographic separation to enable positive identification of CB components and to reject interferent signals.

Aerosol analyses were performed by means of a novel inlet system consisting of a corona discharge region followed by electrostatic precipitation and Curie-point desorption/pyrolysis sections, respectively. Model aerosols, e.g., protein (albumin) particles, produced characteristic pyrolysis patterns from nanogram sample quantities collected directly on the pyrolysis filament by precipitation. A shortcoming of the aerosol inlet system, however, was the relatively low collection efficiency (2-5%) thought to be primarily due to incomplete optimization of flow, voltage and current parameters.

Vapor analyses were performed by means of a newly designed vapor sampling inlet capable of "injecting" a brief (2-4 s long) pulse of air into the transfer line. This enabled separation of compounds of interest away from air background gases while minimizing exposure of the transfer line GC column, as well as the ion source and the electron multiplier, to oxygen and water.

In order to enable field testing of these new aerosol and vapor sampling techniques as well as to demonstrate the feasibility of mobile Ion Trap MS we assembled a Miniaturized Ion Trap mass spectrometer (MINITMASS) capable of operating in EI, CI and MS^n modes at high sensitivity. In addition, we constructed a mobile laboratory module which could be readily transported on the bed of a regular 3/4 ton pick-up truck and enabled operation of the MINITMASS in remote, off-road locations as well as under harsh environmental conditions. Both the MINITMASS system and the mobile laboratory module were described at the 1988 CRDEC Scientific Conference on Chemical Defense Research[4].

In view of the highly promising operational characteristics of the vapor sampling technique for monitoring air as well as flue gases from toxic waste combustors and other reaction environments, we decided to concentrate first on the further development of the vapor sampling inlet for TLGC/MS^n and to continue further development of the aerosol sampling inlet after Jan 1, 1990. Results of the work on the vapor sampling inlet system performed over the past year will be reported here.

EXPERIMENTAL

Transfer line chromatography is performed using a 1 m fused silica capillary column which is contained and heated in the ITD* transfer line. The inlet of the column is at ambient pressure, while the exit is evacuated in the ion trap. Using a .18 mm ID column the carrier gas (helium) velocity is ~2.7 m sec^{-1} (at 4400 ft elevation), which is close to optimum[2] for the column length and pressure drop. We have used a DB-5 stationary phase with a .4 micron film (J&W Scientific) for the reported analyses.

The vapor sampling device is made from deactivated fused silica, quartz and glass (Figure 1) and the sample path contains no moving parts[5]. During inlet use, the atmosphere to be sampled is exposed to the column inlet for a controlled period of time (.5 to 2 sec in these studies), then a helium carrier gas flow is restored for the rest of the sampling cycle to allow for GC separation. The inlet is heated to prevent condensation of the compounds of interest.

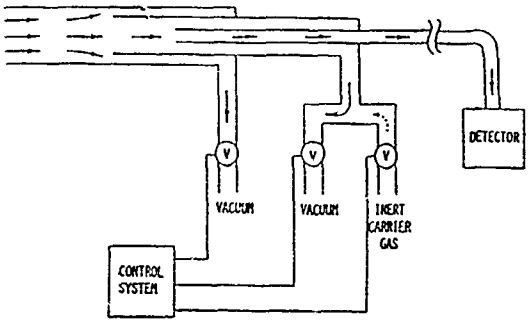

Figure 1. "Valveless" vapor inlet sampling technique for TLGC/MS.

All data presented here were obtained using an electron impact ionization scan function. Helium carrier gas flow into the ion trap was ~4 ml min^{-1}. The ion trap manifold was maintained at 100 C. Axial Modulation was used in all scan functions to provide approximately 1 order of magnitude increase in sensitivity[6]. For all but the MS/MS scan functions, an automatic gain control type scan function was used to control ionization time. Typical scan rates were 3 to 4 sec^{-1} scanning from m/z 50 to 200. Specific ion trap tuning parameters (e.g., multiplier voltage, emission current, etc.) varied from experiment to experiment.

Toxic waste combustion modeling data were obtained with the inlet at 160-175 C. Most runs were made with the column at 30 C. The sample time was ~2 sec and the sampling interval was 60 s. A glass lined stainless steel tube (1/8" OD) drew sample from the high temperature oven (536 C) to the inlet at ~12 ml min^{-1} (see Figure 2). Data are presented from the desorption of ~3 g of ethylbenzene from 600 g of soil in a 1/2 in thick bed. Air flow across the bed was 47 l s^{-1} and the sample was drawn 2 in. downstream from the bed.

RESULTS AND DISCUSSION

To obtain the highest possible chromatographic resolution in the short time available for each TLGC run it is necessary to minimize broadening due to the injection procedure. The shortest possible injection time necessary to obtain full peak height was found to be 0.1-0.2 sec. Preliminary calculations, however, indicate that reduction of vapor inlet dimensions in combination with the use of high speed miniature valves may eventually enable injection times in the 20-40 msec range[5]. The chromatographic resolution obtained with 0.2 s injections of a standard vapor mixture consisting of high ppb levels of toluene, ethylbenzene and xylene isomers is illustrated in Figure 3. Note that the width of the toluene peaks at half height is approx. 0.6 sec. The marked broadening of the later eluting peaks is due to the isothermal nature of the runs. Also note the high background of the TIC profile (Figure 3a) caused by the permanent residual gas background signals in the lower mass range. This background can be greatly reduced by increasing the starting mass settings to higher values and is absent in the m/z 91 ion

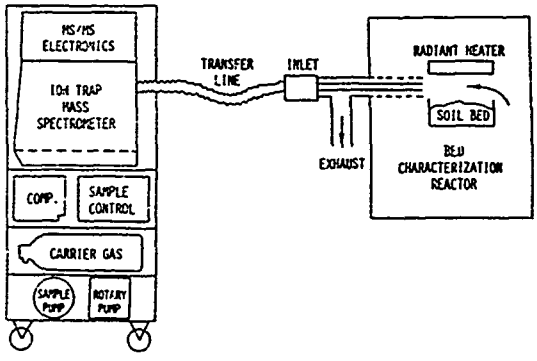

Figure 2. Experimental set-up for on-line TLGC/MS monitoring of fixed bed combustion reactor effluent gases.

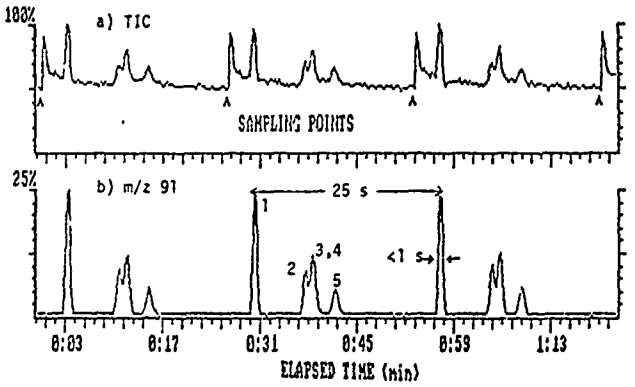

Figure 3. TLGC/MS profiles of alkylbenzene model compound mixture with 300 ppb toluene (peak 1) and 100 ppb each of ethylbenzene (peak 2), p-xylene + m-xylene (peaks 3,4) and o-xylene (peak 5).

chromatogram (Figure 3b) representing the common tropylium fragment ion of the alkylbenzenes.

The promising results obtained in the high ppb range encouraged us to prepare a more dilute mixture containing approx. 3.5 ppb of each alkylbenzene compound. As shown in Figure 4, this still produces a 10:1 S/N ratio at m/z 91 in spite of the fact that only approx. 200 femtograms of each component are present in each air sample "injected" into the transfer line. From these experiments the present limit of detection for relatively volatile, nonpolar compounds is estimated to be approx. 1 ppb. Although sub ppb concentrations of atmospheric vapors have been detected by other mass spectrometric techniques, e.g., by means of atmospheric pressure ionization (API)[7] or by trap and desorb methods[8], direct analysis of subpicogram quantities of aromatic compounds by means of electron ionization MS appears not to have been possible before.

These subpicogram detection levels can be credited to the unusually high sensitivity of Ion Trap MS systems, especially when equipped with axial modulation[6], in combination with the interferent rejection capabilities offered by transfer line GC. Figure 5 shows the near linear response of the vapor sampling system and MINITMASS over several orders of magnitude within the ppb concentration range. In case of extremely complex mixtures, it may be necessary to effect further separation, e.g., by means of tandem MS (MS^n) procedures. The feasibility of performing tandem MS on subpicogram sample quantities is illustrated in Figure 6.

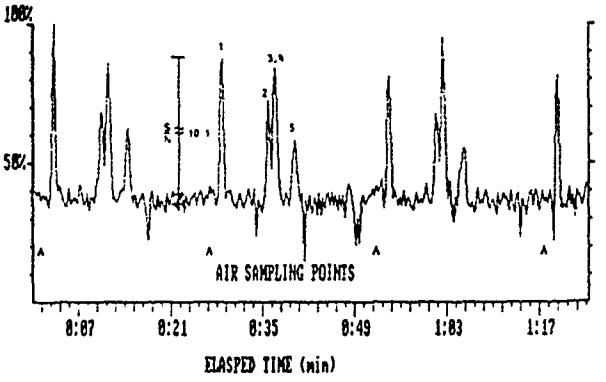

Figure 4. Total ion chromatogram showing a 10:1 S/N ratio for toluene at 4 ppb level. For peak numbers see Figure 3.

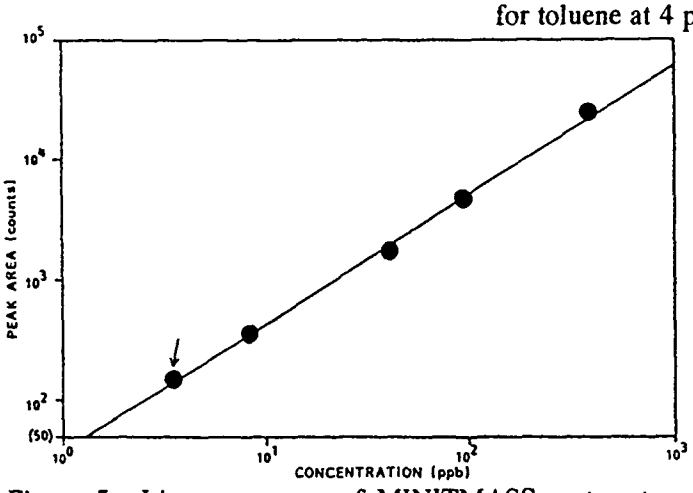

Figure 5. Linear response of MINITMASS system to trace levels of toluene in air over several orders of magnitude. Arrow points to 3.5 ppb (200 fg) sample.

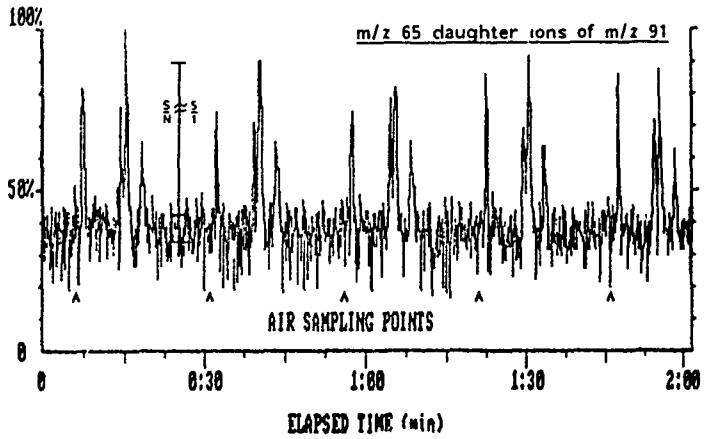

Figure 6. Daughter ions at m/z 65 obtained from tropylium ion at m/z 91, demonstrating feasibility of MS/MS at 4 ppb levels, equivalent to approx. 200 femtograms per compound.

Besides obvious applications in the area of CB detection and monitoring, as discussed last year[4], vapor sampling TLGC/MS techniques offer exciting potential for monitoring toxic waste combustion procedures, e.g., as part of chemical demilitarization programs as well as for treaty verification around and inside potential manufacturing and/or storage sites for CB agents. Use of the vapor sampling TL GC/MS technique for flue gas monitoring in laboratory-scale combustion experiments is described in more detail elsewhere[9]. Figure 2 shows the experimental setup whereas actual TLGC profiles obtained during test runs with ethylbenzene are shown in Figure 7. Note the useful degree of chromatographic separation obtained in spite of the very short (1 m long) isothermal capillary column and the short retention times of most compounds.

Further note the appearance of chlorinated reaction products, e.g., chloro-styrenes and chloro-ethylbenzenes, apparently generated as secondary reaction products due to matrix effects of the model soil bed. As shown in Figure 8, positive identification of these and other reaction products is readily possible using standard GC/MS library search procedures notwithstanding the low GC resolution of the transfer line column. Finally, it should be pointed out that the rapid repetition rate of TLGC/MS procedures allows investigation of reaction kinetics as well as of the underlying mechanisms, as illustrated in Figure 9.

Anticipated further improvements in the near future include combination with rapid trap

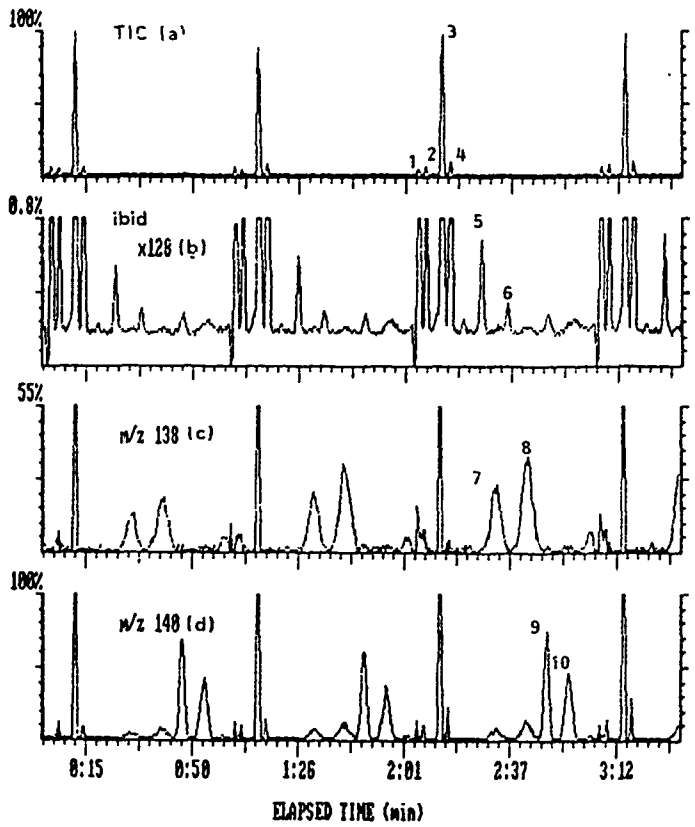

Figure 7. Data sample from fixed bed combustion charcterization study of ethylbenzene. (a) total ion chromatogram segment; (b) ibid x 128; (c) selected ion chromatogram of m/z 138, and (d) ibid of m/z 140.

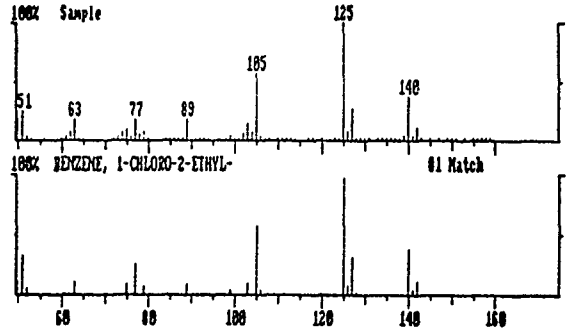

Figure 8. Library search example on chloroethylbenzene peak in Figure 7.

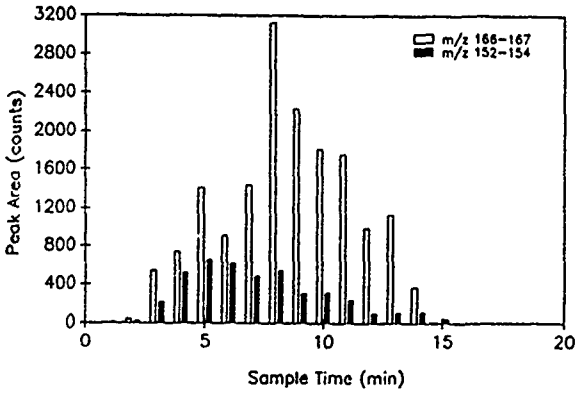

Figure 9. Evolution profiles of chlorobenzofuran (m/z 152-154) and 1,1 diphenylethane (m/z 166-167).

and desorb methods in order to achieve ppt sensitivity as well as the use of temperature programmed TLGC operation (at rates up to 60K/sec!) in order to extend the range of components which can be analyzed in a single TLGC run.

CONCLUSIONS

TLGC/MS using a special vapor sampling inlet in combination with a 1 m long capillary transfer line and a miniaturized Ion Trap MS system enables direct analysis of atmospheric vapors at low ppb levels (corresponding to subpicogram sample quantities) using regular electron ionization MS techniques. Even tandem MS operation is possible at these low levels. Combination with a laboratory scale combustion reactor enables positive identification of trace components in flue gas samples by direct library searching of transfer line GC/MS patterns as well as investigation of combustion kinetics. Future combination with trap and desorb techniques should enable operation in the ppt range. Further improvements envisaged for 1990 include rapid temperature programmed TLGC operation.

ACKNOWLEDGEMENTS

The expert advice and assistance of Wally Maswadeh, JoAnn Lighty, and Eric Lindgren is gratefully acknowledged. The research reported here was supported in part by the Advanced Combustion Engineering Research Center (funds for this Center are received from the National Science Foundation, the State of Utah, 23 industrial participants, and the U.S. Department of Energy); by the U.S. Army CRDEC (contract #DAAD05-89-M-P037) and by Finnigan MAT Corp.

REFERENCES

1. Cramers, C.A., LeClerc, P.A., CRC Reviews in Analytical Chemistry, 1988, 20, 117-147.

2. Trehy, M.L., Yost, R.A., Dorsey, J.G., "Short Open Tubular Columns in Gas Chromatography/Mass Spectrometry" Anal. Chem. 58, 14-19 (1986).

3. McClennen, W.H., Meuzelaar, H.L.C., Snyder, A.P., "Biomarker Detection by Curie-point Pyrolysis in Combination with an Ion Trap Mass Spectrometer", Proc. CRDEC Conference, Aberdeen Proving Grounds, MD, Vol. 1, 1987, 271-277.

4. Meuzelaar, H.L.C., McClennen, W.H., Arnold, N.S., Reynolds, T., Maswadeh, W., Jones, P.R., Urban, D.T., Snyder, P.A., "Development of a Mini-Tandem Mass Spectrometer for Rapid Detection and Identification of Vapors and Aerosols", Proc. CRDEC Conference, Aberdeen Proving Grounds, MD, Vol. 1, 1988, 147-153.

5. Arnold, N.S., McClennen, W.H., Meuzelaar, H.L.C., "Development of an On-line GC/MSn Sampling Method for Direct Atmospheric Vapor Analyses at Low PPB Levels", submitted to Analytical Chemistry, 1989.

6. Weber-Grabau, M., Kelley, P.E., Syka, J.E.P., Bradshaw, S.C., Brodbent, J.S., "Improved Ion Trap Performance with New CI and MS/MS Scan Functions", Proc. 35th ASMS Conf. Mass Spectrom. All. Topics, May 24-29, 1987, Denver, CO, pp. 1114-1115.

7. McLuckey, S.A., Dulak, J.G., Fite, W.L., Bucknes, J.D., Dheandhanoo, S. Anal. Chem. 1989, 61, 260-264.

8. Wise, M.B., Buchanan, M.V., Ilgner, R.H., Proc. 37th ASMS Conf. on Mass Spec. All Topics, Miami 1989, 80-81.

9. McClennen, W.H., Arnold, N.S., Lighty, J.S., Eddings, E.G., Lindgren, E.R., Roberts, K.A., Meuzelaar, H.L.C., "Monitoring the Evolution of Organic Compounds from the Thermal Treatment of Contaminated Soil Samples Using Short Column GC/MS", ACS Preprints, Div. of Fuel Chem., Miami, FL, Sept. 10-15, 1989, 34(4), 1028-1034.

BLANK

DEVELOPMENT OF A POINT DETECTOR FOR BIOLOGICAL AGENTS

Michael T. Goode[1], Brent R. Busey[1], Alan W. Zulich[1], Peter J. Stopa[1], J. Wallace Parce[2], Gregory L. Kirk[2], Stephen C. Alter[3], Mark E. Ballman[3], Mariann E. Lucas[4], Jeffrey M. Bolts[4], Francis J. Regina[4], and Marilyn F. Huntington[4]

Urease-linked enzyme immunoassay formats have been adapted to the light addressable potentiometric sensor (LAPS) for the detection of T2 toxin and Staphylococcal Enterotoxin B (SEB). T2 toxin was detected at a 2 ug level using a displacement assay procedure involving its analogue HT2. SEB could be detected down to 1 ng using a sandwich format. Both assays were within the detectable concentration level and assay time limit goals of the Bio-Chemical Detector. Each assay was performed in three steps: reagent/analyte reaction, filtration on nitrocellulose membranes to effect analyte complex capture, and quantitation using the LAPS.

Introduction

The Army has long required a system capable of detecting toxins and pathogens. To date, no such detection capability exists for these types of agents. In order to address this issue, the Bio-Chemical Detector development program was initiated in order to provide the Army with a man-portable, easy-to-operate, and rugged detector, for sensing threshold concentrations of chemical agents, toxins, and pathogens.

More specifically, the design criteria of the Bio-Chemical Detector calls for the detection of viruses; bacteria; rickettsia; and high, middle, and low molecular weight toxins at predetermined mass levels and within a two minute assay time. Early on, it was decided that in order to cope with the large number and diversity of potential threat materials, the Bio-Chemical Detector would have to employ antibody based recognition, capture, and quantitation protocols. Feasibility studies investigated a number of sensing technologies which supported the concept of antibody based detection. Extensive assay development and evaluation of these devices determined that the best sensor for inclusion into the Bio-Chemical Detector was the Light Addressable Potentiometric Sensor (LAPS) developed by Molecular Devices Corporation (Menlo Park, CA)

This paper will discuss the assays of two agents which have been successfully demonstrated within the Bio-Chemical Detector's concentration and time goals using the LAPS. The first, T2 toxin, is a low molecular weight (MW 462) non-protein toxin of the trichothecene subclass of mycotoxins. It is

commonly found in several types of crops (i.e., corn) as a secondary metabolite of the fungus Fusaria. The second, Staphylococcal Enterotoxin B (SEB) is a mid-range molecular weight (MW 30,000) protein toxin. It is of bacterial origin and is a major cause of food poisoning.

Light Addressable Potentiometric Sensor

The LAPS is a semiconductor based detector which monitors the change in pH over time due to the conversion of urea to ammonia by surface bound toxin/pathogen urease-antibody complex. In its current configuration (figure 1), the immunocomplex is first captured on a nitrocellulose membrane mounted on a plastic disposable dipstick (the filtration unit where capture takes place is not shown). This is followed by manual transfer of the dipstick to the reader where quantitation takes place. Figure 2 shows the design of the LAPS which will be used in the Bio-Chemical Detector. This system will be completely automated. The membranes will be mounted on a continuous tape which will be fed in turn to a filter station and a reader station.

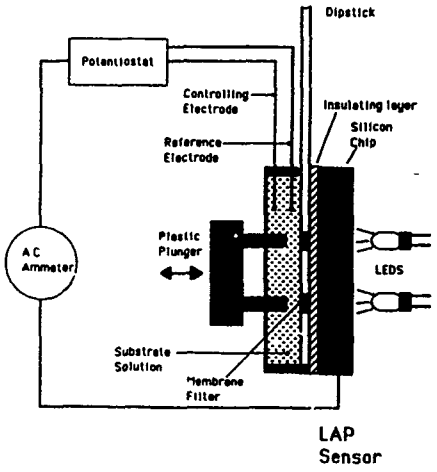

Figure 1. LAPS Manual Immunoassay Reader.

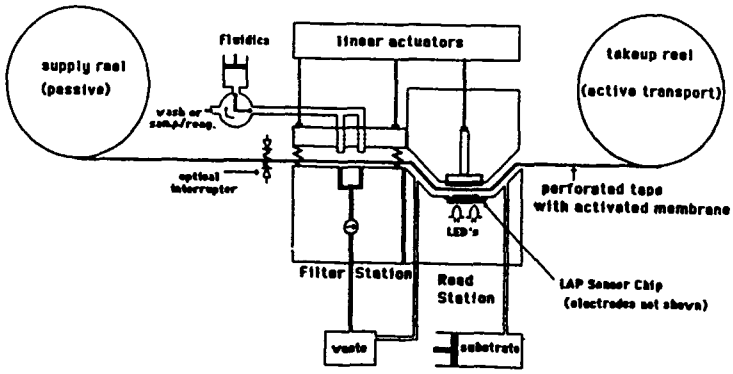

Figure 2. LAPS Automated Immunoassay Reader.

The LAPS assay involves three distinct steps: the reagent/target compound reaction phase, the membrane filtration phase to capture the target compound/reagent complex, and the reader based quantitation phase. Figure 3 displays the reaction and filtration steps for the SEB assay performed in this study. Stoichiometric amounts of SEB polyclonal antibody (Pab) labelled with either biotin (b) or urease (U), and free steptavidin (SA), are allowed to react with SEB. The resulting SA-bPab-SEB-(U-Pab) complex is then filtered through a biotinylated nitrocellulose membrane. The manual reader uses a dipstick with two membrane spots. The streptavidin binds to the surface biotin on the membrane resulting in the capture of the immunocomplex. The dipstick is then placed in the reader. Urea is allowed to react with the captured urease producing one CO_2 and two NH_3 molecules per urea. The pH change over time is noted in terms of a uV/sec response. This response is proportional to the concentration of the analyte.

The principles of operation of the LAPS are straight-forward (refer to figure 1). A 1000A insulating layer of silicon oxynitride is coated on one face of p or n type silicon. Electrolyte solution is allowed to make contact

with the insulated side but not the silicon. An electrode connected to a variable voltage source and an alternating current ammeter is immersed into the solution. A closed circuit is achieved by ohmic contact of the above with the silicon. The controlling electrode is set to the correct potential with respect to the bulk silicon in order to back bias the insulator-silicon junction, creating a depletion layer in the silicon at their interface. An array of infrared light emitting diodes (LEDs) focuses on the back side of the silicon. Excitation of each LED, in turn, at 10 kHz, produces electron-hole pairs in the silicon which is seen as an alternating current in the external circuit. The magnitude of this current is dependent on the local surface potential of the silicon chip (figures 4 and 5) immediately above the excited LED. Thus, the surface potential of several different areas of a small silicon chip can be probed independently at a fairly rapid rate. In our application, the controlling electrode potential is ramped about a particular set point, and the inflection point of the associated current response is plotted as a function of time. The slope of this plot is directly proportional (within certain other reaction constraints) to the activity of urease enzyme acting in the solution above the local silicon spot being probed.

The LAPS sensor exhibits a Nernstian response to changes in pH. The sensor's sensitivity advantage is in its good short and long range stability and in its adaptibility to monitoring microvolumes. In relation to the latter capability, the nitrocellulose membranes on which the immunocomplex is captured are pressed against the silicon by a high precision plunger, so that the substrate/buffer volume is less than 1 ul. This allows the rapid determination of very low amounts of enzyme conjugate (and hence analyte).

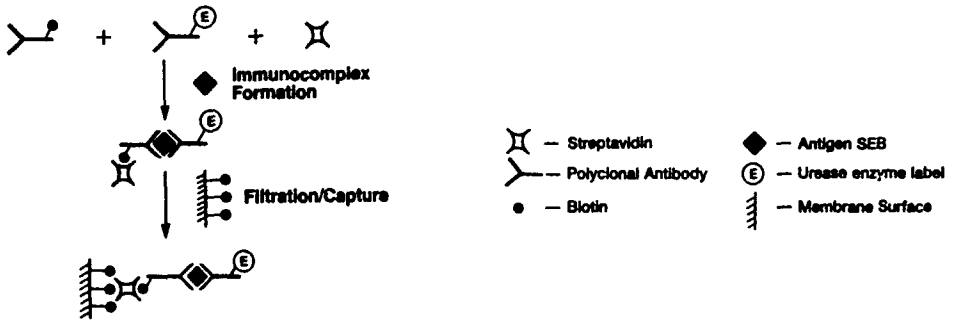

Figure 3. SEB Assay Configuration

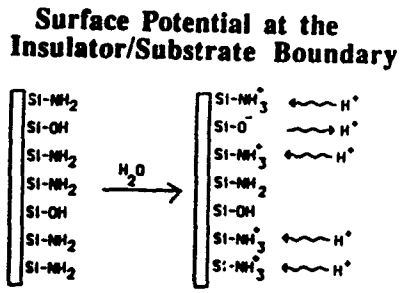

Figure 4. Proton-Silicon Oxynitride Interactions.

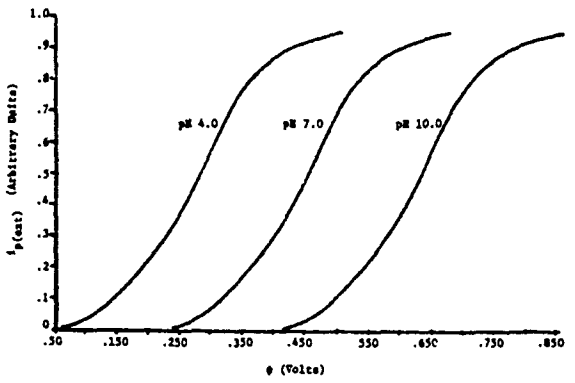

Figure 5. Response Curves For p-Type Silicon.

T2 Assay.

The T2 displacement assay configuration is shown in figure 6. Note that this assay is different from that shown in figure 3. HT2, an analogue of T2 which binds weakly to T2 monoclonal antibody (Mab), is formed into a SA-HT2-(U-Mab) complex. This is allowed to react with T2 which displaces the SA-HT2 to form T2-(U-Mab). Upon filtration, only the remaining SA-HT2-(U-Mab) and SA-HT2 will be captured. In this assay, signal intensity is inversely proportional to the analyte concentration, ie. the higher the signal, the lower the concentration of T2.

Figure 7 shows the dose response curve in terms of microvolts per second (uV/sec) versus micrograms (ug) of T2 applied. The plot shows a steady decrease in signal with increasing T2 concentration. The LAPS was able to detect 2 ug of T2 in a 100 ul sample in a total assay time of less than 3 minutes using this format.

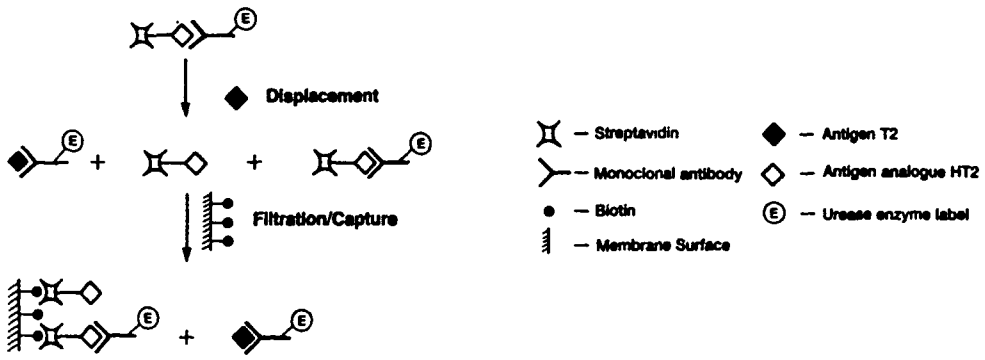

Figure 6. T2 Displacement Assay Configuration.

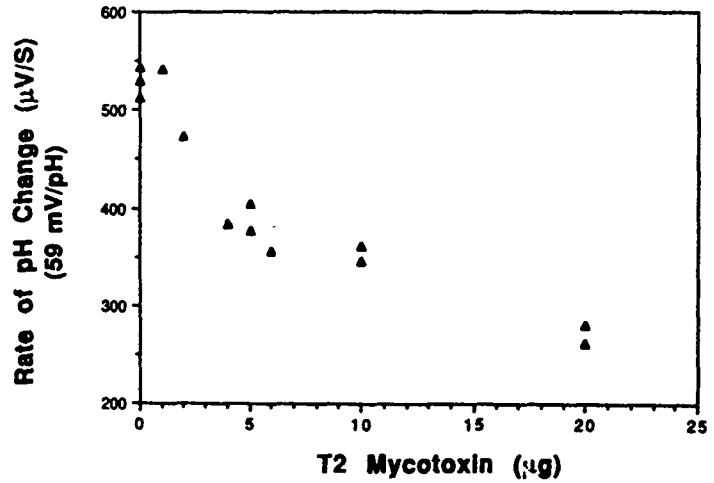

Figure 7. T2 Displacement Assay Results.

Staphylococcal Enterotoxin B

Figure 3 diagrams the assay configuration for SEB. Figure 8 shows a dose response curve in terms of microvolts per second (uV/sec) versus nanogram level antigen doses (ng). The curve is linear within the range of 0-10 ng of SEB. A dose of 0.5 ng in a 100 ul sample was discernable from backround in a total assay time of 3 minutes.

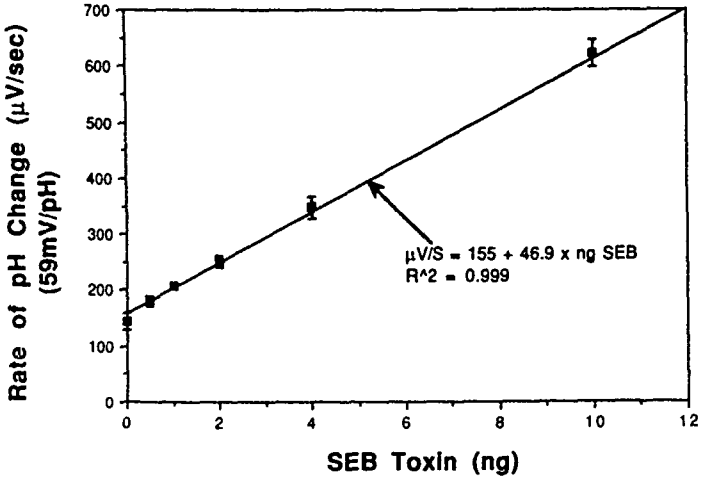

Figure 8. SEB Sandwich Assay Results.

CONCLUSIONS

The LAPS has proven to be capable of detecting two toxins of interest to the Bio-Chemical Detector program. A lower limit of 2 ug of T2 or 1 ng of SEB can be detected in 100 ul samples within 1 to 2 minutes. Both the sandwich assay configuration (for SEB) and the displacement assay configuration (for T2) have been used successfully with the LAPS. The Bio-Chemical Detector Program is progressing rapidly with ongoing development of LAPS-based assays for other analytes of interest as well as innovative engineering to automate the LAPS device.

REFERENCES

1. Detection Directorate, U.S. Army Chemical Research, Development and Engineering Center, Edgewood Area, APG, MD.

2. Molecular Devices Corporation, Menlo Park, CA.

3. Environmental Technologies Group, Inc., Baltimore, MD.

4. Allied-Signal Corporation, Morristown, NJ.

5. Dean G. Hafeman, J. Wallace Parce, and Harden M. McConnell., Science, 240, 1182, (1988).

MICRO-ELECTROCHEMICAL DETECTION SYSTEMS

Joseph R. Stetter, Transducer Research, Inc., Naperville, IL 60540

and

L. J. Luskus, USAF-SAM, Brooks AFB, Texas 78235

ABSTRACT

The low power, small size, and other logistical characteristics of electrochemical detectors make them an attractive technology for chemical warefare agent defense systems. While some commercial amperometric sensors are very successful, the current amperometric sensor technology suffers from a lack of sensitivity, selectivity, and stability in the most demanding field applications. Investigation of novel solid and film electrolytes and new alloy electrocatalysts coupled with a circuit on a single chip have produced encouraging results. The signal to noise for the alloy electrocatalyst was several hundred times better than some pure, noble metal materials.

INTRODUCTION

Electrochemical methods have been explored for the detection of blister and nerve agents for many years. Amperometric techniques have dominated but some potentiometric attempts have been made to construct useful detectors. In general, the electrochemical sensors have attractive logistic properties being light weight, low cost, self contained, small size, and real-time. Self-contained means that they required no external vacuum pumps or reagents to perform the detection operation. However, the nerve agents often require filter devices analysis filter devices for the conversion of analyte to another reactive species prior to analysis. Filter devices are still relatively simple devices when compared to sophisticated laboratory analytical equipment or even to portable laboratory instruments that have been engineered for field use.

The sensitivity of electroanalytical methods is often impressive. For example, a NO_2 sensor[1], even in a flowing gas stream, can detect about 4×10^{-12} G/sec and this corresponds to a detectable concentration of about 2 ppb in the 200 cc/min gas sample flowing through the electrochemical cell. The typical limit of detection in these systems is

not the detection of the reaction since the reaction produces significant electric currents even at low concentration. Rather, detection using electrochemical cells is limited by the ambient background currents, interferences, drift, and amplifier noise which all degrade the S/N (signal to noise ratio) of the analytical method.

Since the sensitivity can typically be engineered to be good for most applications, improvements in electrochemical cells should not be expected by increasing the magnitude of the analyte signal. Improvements, however, will be realized by designing sensors that reduce or eliminate background currents and by employing sensor systems that can distinguish the signal over the background, noise, and drift. In this paper, initial work has been performed to examine the potential for making substantial improvements in amperometric electrochemical agent detectors. All work was performed with simulants.

RESULTS

Compounds of Interest

Most industrial compounds are electrochemically active or can be made electroactive with only minor modification. The chemical warfare agents are not different in this respect. Electrochemical reactions are possible and have been proposed for all of the major classes of blister and nerve agents. Significant work remains to be performed in the characterization of the specific electrochemical reaction mechanisms to aid our understanding of the electroanalytical behavior of agents and some of the compounds used as agent simulants.

While the agents are our major concern, we confined these studies to simulants that were selected for their specific physical, chemical and electrochemical simularities to the agents. Chloroethylethylsulfide (CEES) was chosen as a simulant for the blister agents. CEES is known to react in a similar electrochemical manner to the agent 2,2'-dichlorodiethylsulfide (Mustard gas or HD). As a simulant for the nerve agents, dimethymethylphosphonate (DMMP) was chosen. To simulate a basic electrolytic electrochemical reaction, monomethyl hydrazine (MMH) was selected for its reactivity and interesting electrochemistry. The electrochemical reaction and measurement of methyl salicylate (oil of wintergreen or MES, o-$HOC_6H_4COOCH_3$) was studied because its physical properties are simiar to agents and it could be used in a complete evaluation program (perhaps involving human subjects). A sensitivie detector for this species would be useful and, therefore, this compound was investigated. Oxidation or reduction of the phenolic group or carbonyl group of MES could provide a simple and direct electroanalytical method.

Amperometric Sensor Design

The electrochemical cells have three major constituents: electrolyte, electrodes, and suitable housing materials. These three components are thoughtfully assembled in a very specific geometry. Geometry has a profound influence on the electrocatalytic event and on the ultimate performance of the electrochemical cell. The electrolyte consists of a solvent containing a material capable of ionic conduction. Typical examples are illustrated

in TABLE 1. To enhance the detection of agent, the electrolyte must solubilize the analyte in an appropriate form as well as be inert to the electrode and not cause corrosion currents to occur. For the solvent, it is important to consider the liquid range, vapor pressure, dielectric constant, viscosity, and spectroscopic properties (if a spectro-electrochemical experiment is planned). Low viscosity solvents produce electrolyte solutions with greater conductivity. Similarly, high dielectric constant solvents lead to electrolytes with high conductivity which in turn produces cells (sensors) with acceptable ohmic voltage loses and the potential for rapid response to gases. High vapor pressure leads to rapid solvent loss, changes in electrolyte composition and sensor drift. The solvent must be functional over the entire range of temperature, pressure, and relative humidity that the sensor is intended to operate. The supporting electrolyte should not be electroactive and should minimize migration currents by being present in excess making the double layer compact. In field detection, it is imperative that the electrolyte have long term stability and resist degradation and contamination from exposure to air and its ubiquitous pollutants. In some sensors, a semipermeable membrane is possible to maintain sensor integrity of response.

****

TABLE 1

COMMON ELECTROLYTES

AQUEOUS ELECTROLYTES	acid; sulfuric, perchloric, phosphoric base; NaOH, CsOH, LiOH, KOH neutral; KCl, LiCl, LiBr, $NaHCO_3$
NON-AQUEOUS	Solvents:Propylene carbonate, DMSO, DMF, Acetonitrile, ethylene glycol, Dichloromethane, (with salts for electrolyte)
	Electrolytes: perchlorate salts, LiCl,
SOLIDS, POLYMERS, and MIXTURES	Nafion, PEO*LiX, PVA/H_3PO_4, PVA/CsOH, $AgRb_4I_5$, AgI, ...

****

The sensor also contains a sensing (working), counter, and reference electrode. These are typically chosen from the noble metals such as Au, Pt, and composites like Pt/TFE. The electrode material must be compatible with the electrolyte. Silver and Nickel electrodes have been used in basic (and non-aqueous) electroyte systems and carbon electrodes are popular in acidic and basic media. The electrode material and the potential of operation are chosen to engineer sensitivity and selectivity into the detector.

Gas Detection Experiments with Electrochemical Cells

There is an integral and an important relationship among the materials of construction, the specific cell geometry, and the analytical performance of the sensor for a particular application. This can be appreciated by consideration of sensor response to specific analytes and the wide variety of sensor systems that are available commercially and that have been reported in the past. The essential components of a high volume electrolyte cell (Figure 1) and a planar cell with a polymer film electrolyte (Figure 2) are the same. However, the performance of these systems can be quite different. The polymer film electrode structure has produced reponse times in msec while the response of the liquid electrolyte cell is typically measured in seconds.

The effect of subtle alterations in the composition of the electrolyte cannot be overlooked. For example, in Figure 3 the signal is compared for the same sample (1 ppm NO_2 in air) in the same electrolyte (and same sensor). However, in experiment 3B, some HCl was added to the electrolyte. The presence of the CL^- ion, a very strong surface adsorbing ionic species, alters the rate of the electroreduction of NO_2 as well as the character of attainment of steady state. That means that the rate and extent of adsorption of the analyte at the electrode surface can often be influenced and sometimes controlled favorably by altering the electrolyte composition.

The CEES simulant provides an excellent example of direct detection of an agent. The agent, HD, will react very similarly to CEES which can be directly electrooxidized at a noble metal electrode. Using a sensor similar to Figure 1 in geometry, the response to high (21 ppm) and low (280 ppb) concentrations of CEES in air were measured with the result shown in Figure 4. The Au electrode was selected for its relatively inert character in most electrolytes and its insensitivity to many interfering analytes. In this case the Pt working electrode (Figure 4A), exhibits a much larger absolute signal but the S/N of the smaller Au electrode (Figure 4B) is better. The aqueous acid electrolyte was chosen for its resistance to cold temperature (battery acid freezes at about - 40 °C) and its excellent electrolytic conductivity.

The CEES response curves of Figure 4 illustrate the sensitivity of the electrochemical system for blister agent. Since these electrodes and electrolytes were prepared from ultra high purity materials, the background currents are very low. Yet, this sensor design allows the same amount of analyte, CEES, to reach the electrode as larger sensors. The result is that the observed signals of about 1 μA/ppm are comparable to industrial sensors with much larger electrodes. The Au electrode blister sensor is nearly linear over three orders of magnitude and this is very good performance for such sensor systems. From these data, the S/N at 280 ppb is conservatively estimated at 100:1 or about 2.5 ppb. The 280 ppb CEES corresponds to a concentration of about 1.5 μG/L and a lower detection limit of 0.015 μG/L. The response time is also good even at very low levels.

The detection of both MES and DMMP are illustrated in Figure 5 with sensors of geometry depicted in Figure 1. While one observes 1-2 μA/ppm for MES, only 0.05 μA/ppm are obtained for DMMP. The DMMP may not be a good simulant of nerve agent electrochemistry at all. The MES oxidation signal is very encouraging. It should be possible to construct an electrochemical sensors with good sensitivity to this substance.

We have examined the possibility of using a micro-chip potentiostat[2] together with a planar microsensor and film electrolyte. The potentiostat was contained on a single chip and mounted in a 40 pin DIP style housing. The CMOS chip together with a sensor is illustrated in Figure 6 and has been described in the literature[2]. The original chip potentiostat was used as a glucose sensor but herein we attempted to interface the chip to a planar gas sensor.

The planar sensor was designed as in Figure 2 and used a thin film Pt electrode. The electrode was covered with a polymer composite film (PVA/CsOH) that served as both the electrolyte and a gas barrier. A compound, MMH, that reacts well in basic solution was chosen to test the apparatus with the result given in Figure 7. Although the potentiostsat was limited to about 4 μA maximum current and allowed the reference potential to drift significantly during measurement, the observed signal is characteristic of much larger sensor systems and extremely encouraging. The use of planar structures for both the sensor and the electronics offers significant possibilities for the future instrument design. It may be possible to design and construct low cost sensors with all of the advantages of using silicon fabrication technology including increased reliability and improved analytical performance.

CONCLUDING REMARKS

The amperometric sensor is a complex and interacting system of metallic and non-metallic components. The entire device must be chosen as a system in order to obtain good analytical results in a specific application. The geometric design of the system is important as is the selection of appropriate materials. Our initial work indicates that some breakthroughs may be possible by taking a materials science based approach to the fabrication and the electrochemistry. Apparently, one can apply microfabrication techniques to agent gas/vapor sensors and electronics. We report herein the first reported signal from a micropotentiostat combined with a microfabricated amperometric gas sensor system for any gas or vapor.

The TRI sensor design demonstrated excellent S/N for the HD agent simulant CEES. Both liquid electrolytes and solid polymer electrolytes provided well behaved response for blister and nerve agent simulants (MMH, CEES, MES, and DMMP). Further work is warranted with both DC and variable potential (voltammetric and differential voltammetric) electroanalytical methods on these compounds. Development of the new materials for the electrode and electrolyte can produce sensors with improved analytical performance. The electrochemical systems should be studied for several reasons including: 1) to provide choices of materials for improved detector systems, 2) gain an understanding of the electrochemistry for the development of appropriate simulants, and 3) improve the sensitivity, selectivity, and logistical properties of electroanalytical systems.

REFERENCES

1. **Chang, S.C., and J.R. Stetter, Electroanalysis (1989); in Press.**

2. **Turner, R.B.F., D.J. Harrison, H.P. Bates,** "A CMOS Potentiostat for Amperometric Chemical Sensors," IEEE Journal of Solid-State Circuits, 22, 473, (1987).

ACKNOWLEDGEMENT

We acknowledge the support of USAF under contract F33615-87-C-0618. Further, the collaboration of Drs. Baltes, Harrison, and Turner of the University of Alberta at Edmonton are gratefully acknowledged for supplying the microchip potentiostat and helpful comments concerning its application.

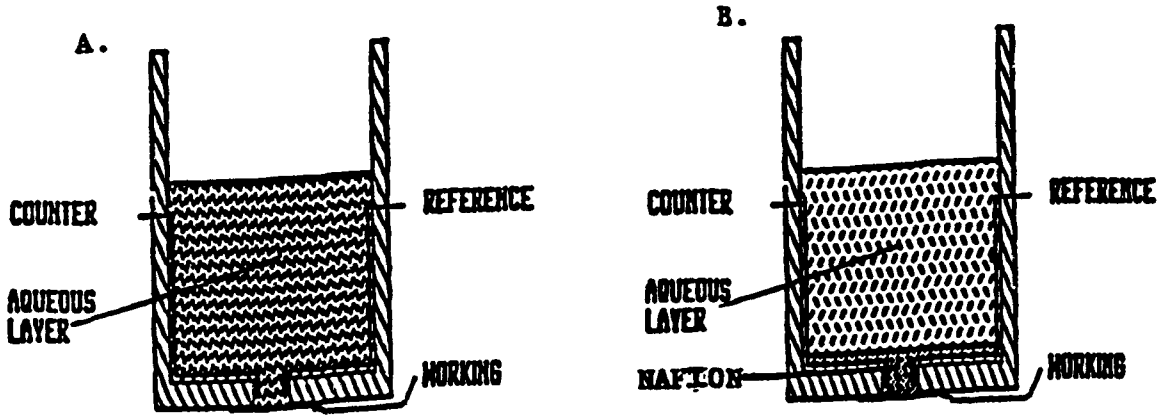

Figure 1. TRI Large Volume Electrolyte Geometry:
A) Aqueous Acid Electrolyte;
B) Nafion Solid Polymer Electrolyte

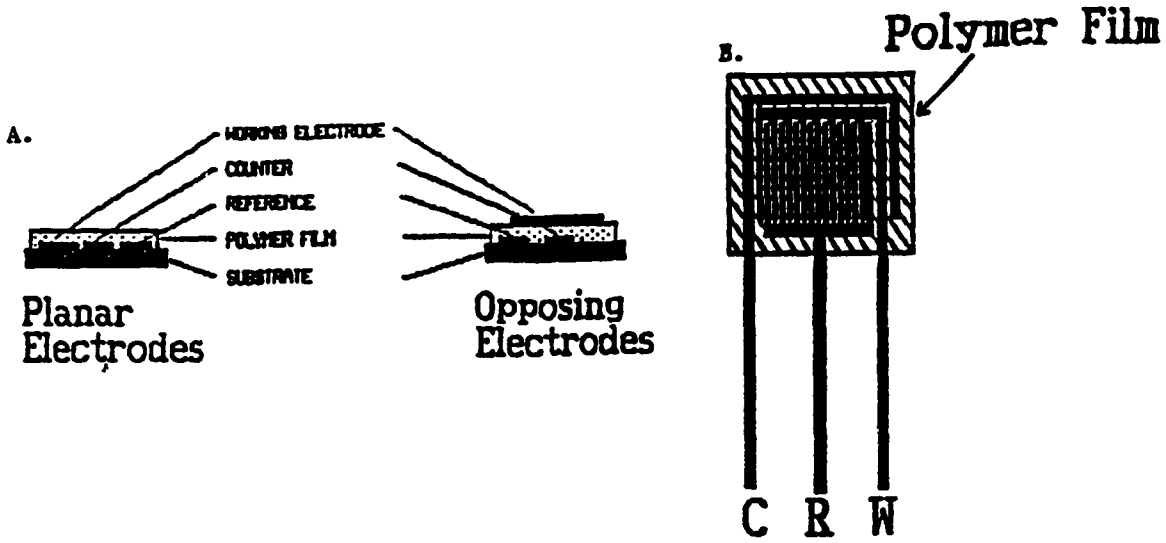

Figure 2. Cell Design for Planar Thin Film Amperometric Sensor:
A) Cross Section of Planar and Opposing Electrode Configuration;
B) Top View of Sensor

3A.

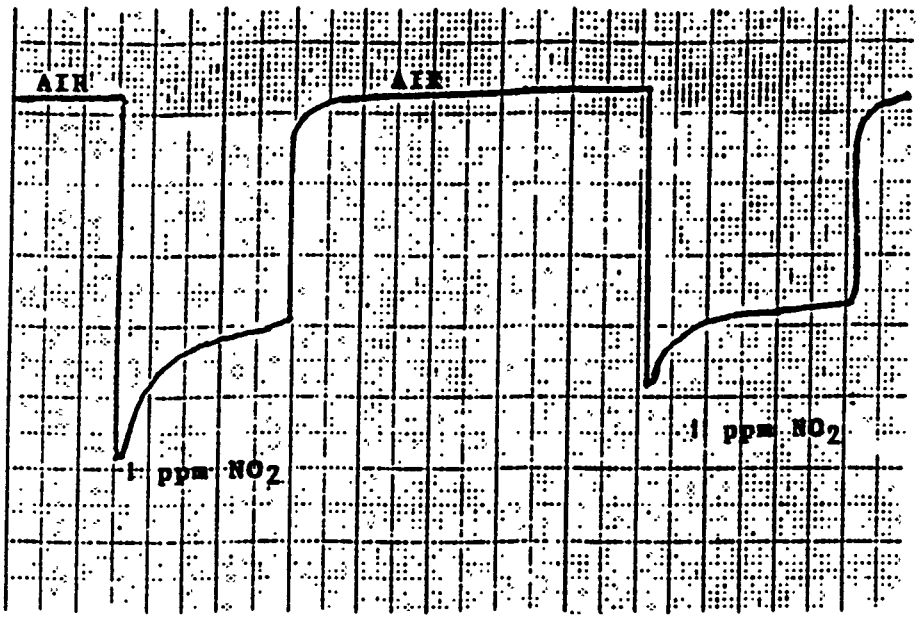

3B.

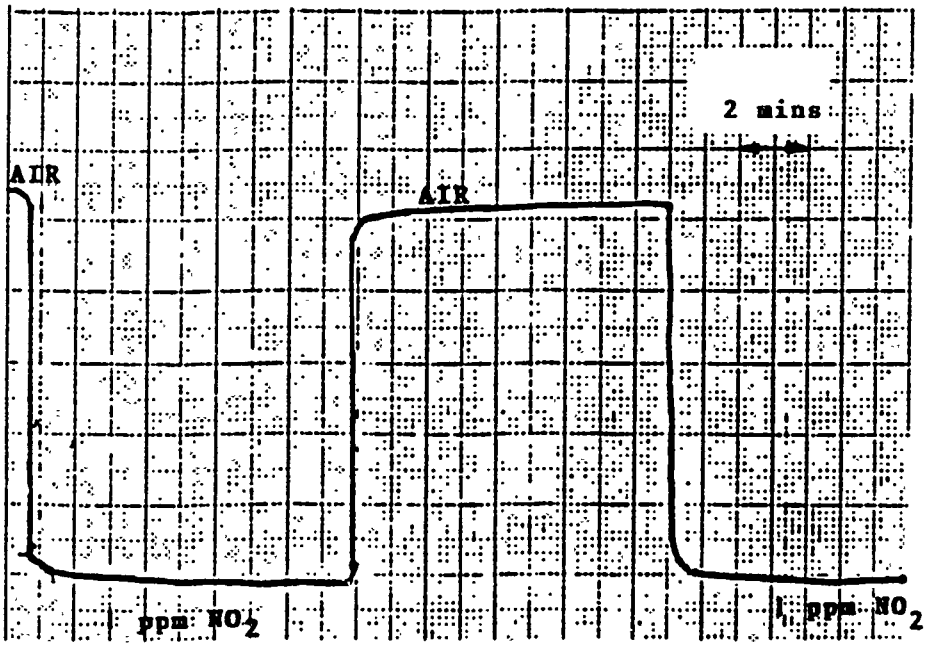

Figure 3. Effect of Electrolyte Composition on Sensor Response:
A) 4M H_2SO_4; Gas = 1 ppm NO_2; Bias = -100mV;
B) 2M H_2SO_4/0.1M HCl; Gas = 1 ppm NO_2;
Bias = -100 mV

4A.

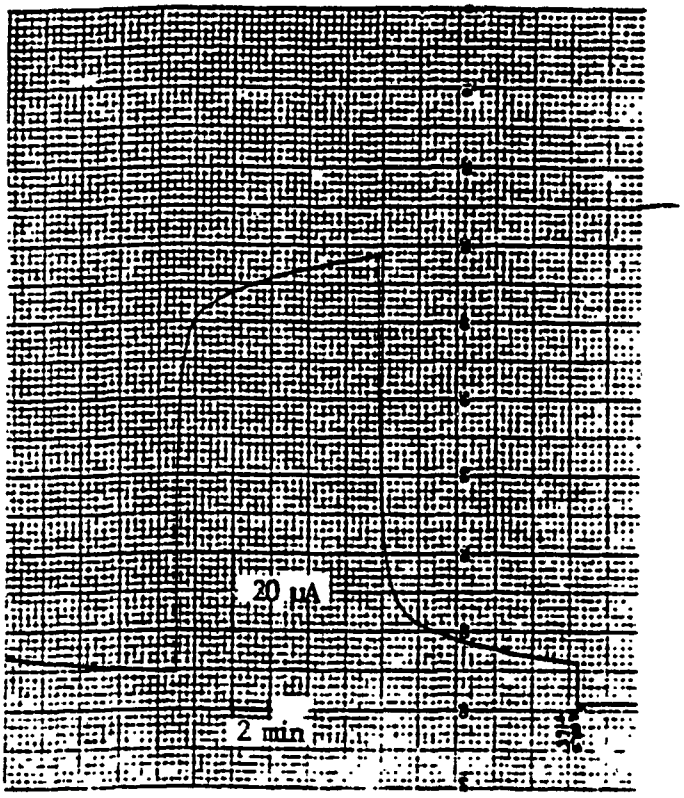

4B.

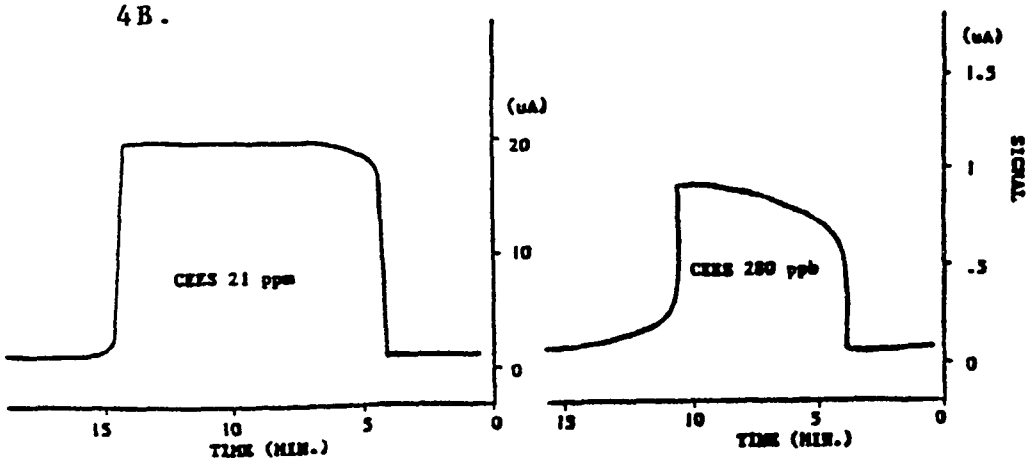

Figure 4. Sample Response to CEES from Several Acid Sensors Using the Design from Figure 1.
A) Pt Working Electrode (Bias = +400 mV); 21 ppm;
B) Gold Working Electrode (Bias = +200 mV)

5A.

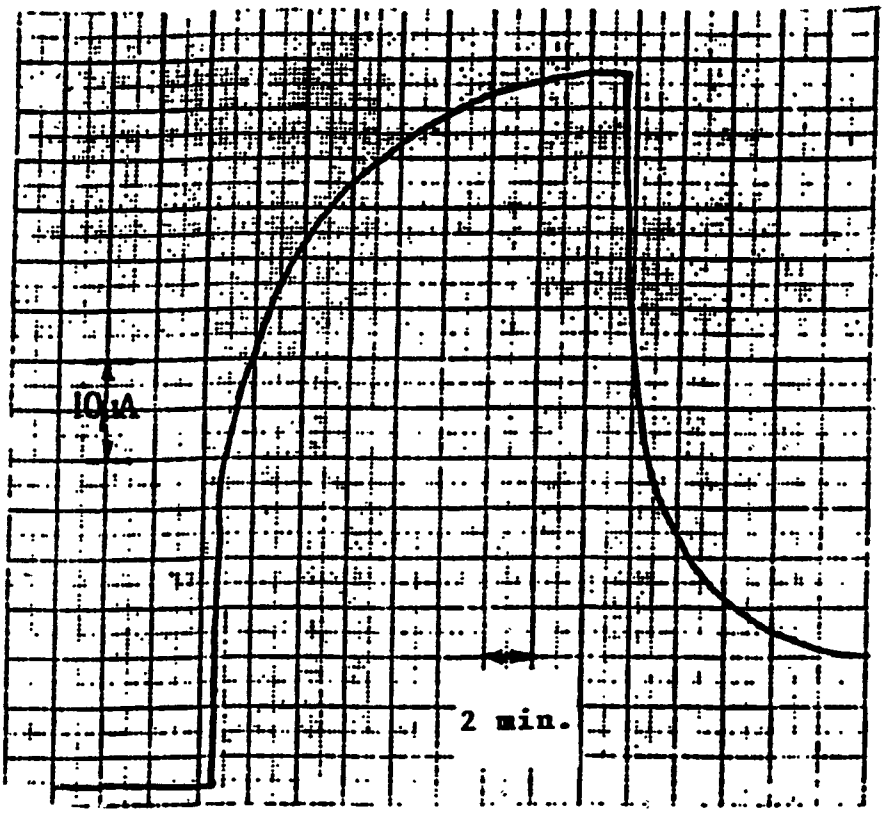

5B.

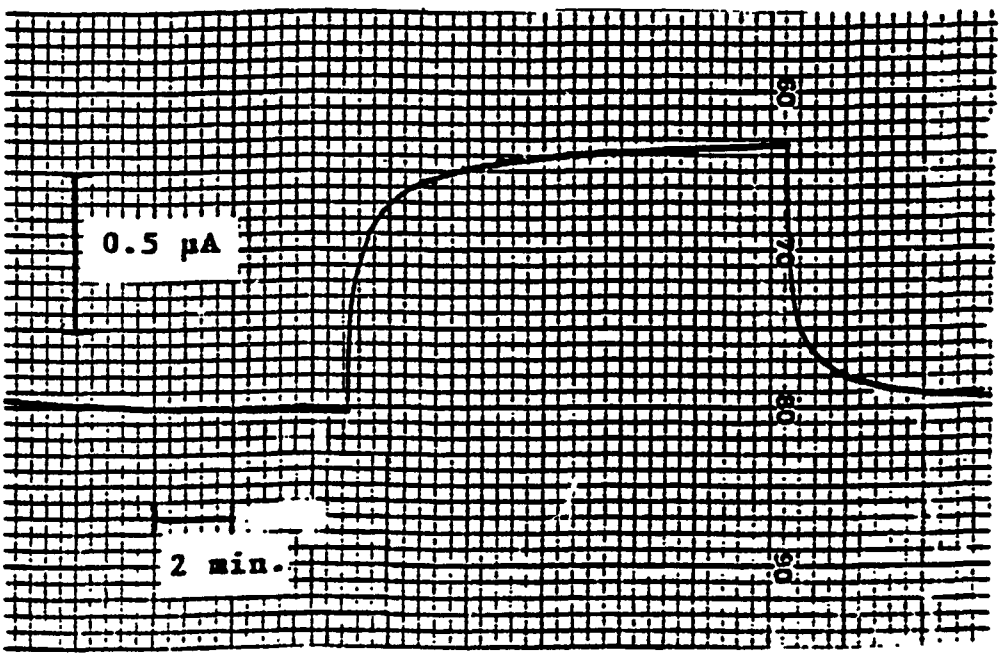

Figure 5. Signals of Simulants on a Gold Electrode:
A) 19.3 ppm MES
B) 15.2 ppm DMMP

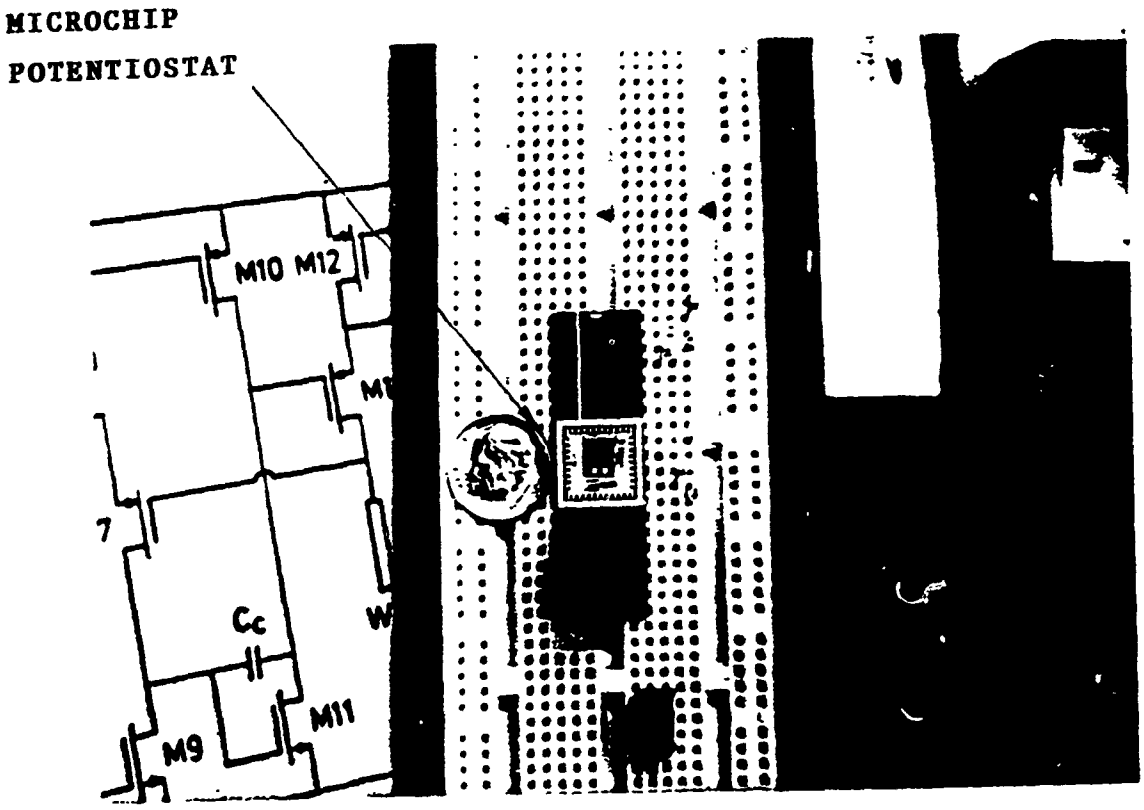

Figure 6. The Photograph of Micropotentiostat Chip Illustrating Actual Dimensions. The IC Chip contains 2 Potentiostat Circuits and can operate Two Amperometric Sensors

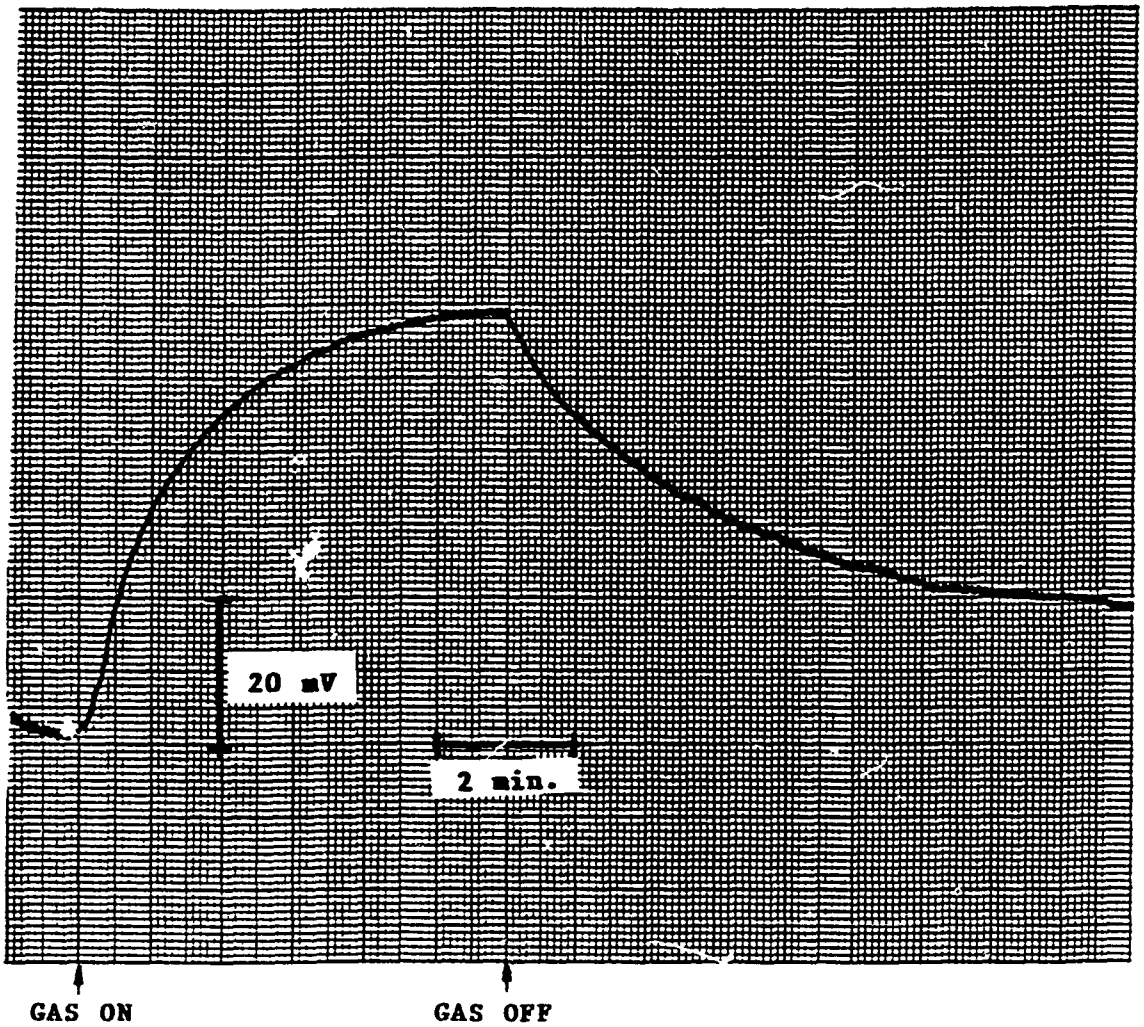

Figure 7. Response of the PVA/CsOH Electrolyte Film Sensor with a Planar Geometry to about 5 ppm Monomethyl hydrazine when operated with Micropotentiostat of Figure 6.

ACADA (XM22) AND CAM CW DETECTOR HARDWARE EMULATION FOR RESEARCH WITH SCPS SHELTERS

B.L. Houseman (a), L.A. Walker (a), L.J. Luskus (b), and W.C. Blanchard (c)

ABSTRACT

Modular Ion Mobility Spectrometers (M-IMS) can be used for research to emulate the CAM and ACADA if these items are unavailable or if a more general IMS sensor is desired. Both the ACADA and CAM use an IMS to sense the environment, then use a computer to evaluate a very similar signature and interface an alarm to the user. The CAM is a hand-held point CW sensor; the ACADA is a more versatile and 'smarter' area CW sensor with a secondary mission as a point sensor. The modular IMS can emulate the IMS signature-producing portion for either the CAM or the ACADA. Other chemistries, such as ammonia, were also researched for use in the SCPS shelter system using the M-IMS. The research measured the extent and limitations of the use of this hardware as an emulator of the ACADA and CAM in a SCPS environment.

INTRODUCTION

Ion mobility spectrometers (IMS) have proven to be effective monitors of the composition of the atmospheric environment, particularly for chemical warfare (CW) agents [1,2]. Their response time is short (approximately 5 seconds), sensitivity is high (low ppm for important CW agents), operation is relatively simple, and the equipment is portable. IMS units are strong candidates for monitoring the environment in USAF Survivable Collective Protective Shelters (SCPS-2), in which the background composition of the air is well known and external electric power is available.

Two IMS CW monitors are currently available for military use: the Chemical Agent Monitor (CAM) and the XM22 (ACADA). The CAM, a hand-held monitor which is particularly effective for scanning surfaces for contamination, uses beta particle impact on acetone vapor to create reactant ions ("acetone chemistry"). The ACADA, a slightly larger unit primarily for monitoring the surrounding atmosphere, uses beta particle impact on water vapor to create reactant ions ("water chemistry"). A third source of reactant ions, ammonia chemistry, is under development, with possible application for the ACADA.

The Modular Ion Mobility Spectrometer (M-IMS) [3], is a research device in which several parameters, including the reactant ion chemistry, can be changed. The physical parameters of the M-IMS are similar to both the basic IMS cells of the ACADA and CAM. That is:

- ---the sample inlets use membranes to transfer the gaseous chemicals of interest from the ambient air to the IMS cells.
- ---the samples, after entering the cells, are ionized using the same ionization source, beta emission from Ni-63.
- ---the physical dimensions and electric field intensities used in the ionization and drift regions are nearly identical.
- ---the mechanism of sampling the ions for detection, the Schroeder shutter grids, and the method for separation of these ions into their respective mobilities are identical.

The gas used inside the controlled environment of the cell of the M-IMS can be changed by externally inserting an appropriate diffusion tube into a

a. Goucher College, Towson, MD 21204 Correspondence to B.L. Houseman.
b. USAFSAM/VNC, Brooks AFB, TX 78235
c. Blanchard & Co., Phoenix, MD 21131

chamber, creating the possibility that it can emulate both the ACADA and the CAM.

EXPERIMENTAL

IMS signatures were obtained using the M-IMS unit in the SCPS system: signatures were taken with the SCPS-2 shelter in "clean" condition and with low levels of contamination with methyl salicylate (MeS), carried into the shelter on the clothing of human subjects. The M-IMS unit was operated with water chemistry, acetone chemistry, and ammonia chemistry. Cell temperature was 50 degrees Celsius.

Absolute values for MeS concentration were determined by the Sequential Impinger Sampler, a fluorimetric method in use in the SCPS program at Brooks AFB [4,5].

Both positive and negative signatures were obtained. They were compared with signatures of the CAM and the ACADA.

RESULTS

Ion mobility signatures for both positive and negative ions obtained with the M-IMS in the SCPS-2 shelter under clean conditions are shown using water chemistry (Figure 1), acetone chemistry (Figure 2), and ammonia chemistry (Figure 3). These shifts in relative position of the reactant ion are shown in Figure 4. Figure 5 shows the M-IMS signature in the negative mode in the SCPS-2 shelter when the MeS vapor concentration is 1.53 mg/M^3.

The signatures taken in the SCPS-2 under clean conditions show in each case a single, dominant peak due to the reactant ion. A comparison of the positive signatures shows a distinctive reactant ion signature for each of the three reactant ions. On the other hand, the negative reactant ion signatures are identical, within experimental limits, for all three reactant molecules. Similarly, the MeS peak appears in the negative signatures of all three of the reactant ions.

MeS is used as a simulant for CW blister agents. Blister agents are detected as negative ions in IMS. Although it is the negative signature of MeS that can be used to simulate blister agents, MeS can also be detected as a positive ion in water chemistry. The sensitivity in water chemistry to MeS is greater in the positive mode than in the negative mode.

DISCUSSION

The differences in the positive signatures and the similarities in the negative signatures can be explained by the relative stabilities of the ions which form and co-exist in equilibrium in the ionization chamber of the M-IMS. Figure 6 depicts the relative stabilities of the negative ion clusters associated with each compound; Figure 7 depicts relative stabilities of the positive ions.

It is evident that the similarity among the negative signatures of the three chemistries reflects the fact that, in the presence of water vapor, all three are operating on water chemistry, the negative ions of which are more stable than those of acetone or ammonia. It has been shown that in water chemistry the reactant ion is a hydrated O_2- ion [6]. Similarly, one can postulate that in all three negative signatures the MeS.O_2- ion is responsible for the MeS peak.

The postulated order of ion stability shown in Figures 6 and 7 leads to the prediction that, although the presence of ammonia in the SCPS shelter would have an effect on the positive signatures recorded by an IMS operating

on water chemistry, it would have no effect on the negative signatures.

Although simultaneous, direct comparisons of M-IMS signatures with those of ACADA and CAM under identical conditions were not obtained, available data for the ACADA [1] and for the CAM [7] show agreement with M-IMS signatures. Further, in all three instruments, the time-ratios of the positive reactant ion peaks to the negative reactant ion peaks are [8]:

--water chemistry: 1.07
--acetone chemistry: 1.22
--ammonia chemistry: 0.96

CONCLUSIONS

The Modular Ion Mobility Spectrometer can be used to emulate both the ACADA and the CAM in monitoring the composition of the ambient atmosphere to detect the presence of chemical warfare gases. It can be effectively used in the USAF Survivable Collective Protection Shelter in conjunction with methyl salicylate, a simulant for blister agents, to detect CW contamination of the shelter or of individuals entering the shelter.

ACKNOWLEDGMENT

Sponsor: USAF School of Aerospace Medicine, Human Systems Div. (AFSC), Brooks AFB, TX 78235-5301

REFERENCES

1. Blanchard, W.C., "Chemical Agent Sensor Testing in the Survivable Protection Shelter Environment," USAFSAM-TR-89-9, May 1988.

2. Blewett, W.K., Stickel, G.A., "Use of the Chemical Agent Monitor (CAM) With the M20 Collective Protection Equipment," CRDEC-TR-87057, July 1987.

3. Roehl, J.E., "Ion Mobility Spectrometry (IMS) - A Chemical Separation Technique using an Electrostatic Field," 24th IAS Annual Meeting, IEEE Industrial Applications Conf., October 1989, pp 1290-1295.

4. Conkle, J.P., Slate, A.R., Shaffstall, R.M., Kerch, J.H., Miranda, R.E., "Chemical Defense DON/DOFF Laboratory Procedures at the USAF School of Aerospace Medicine," USAFSAM-TP-85-5, December 1985.

5. Gause, E.M., "Conversion of Methyl Salicylate Fluorescence Assay Values to Vapor Concentrations," Internal Document of USAF ASFC/HSD Brooks AFB, TX, December 1986.

6. Nowak, D.M., "Mobility and Molecular Ions od Dimethyl Methyl Phosphate, Methyl Salicylate, and Acetone," U.S. Army ARCSL-TR-83056, June 1983.

7. Kilian, J.P., Private communication w/B.L. Houseman at Brooks AFB, TX, October 5, 1989.

8. Houseman, B.L., Walker, L.A., Blanchard, W.C., Project Final Report, DTIC Accession No. DF 306155, October 1989.

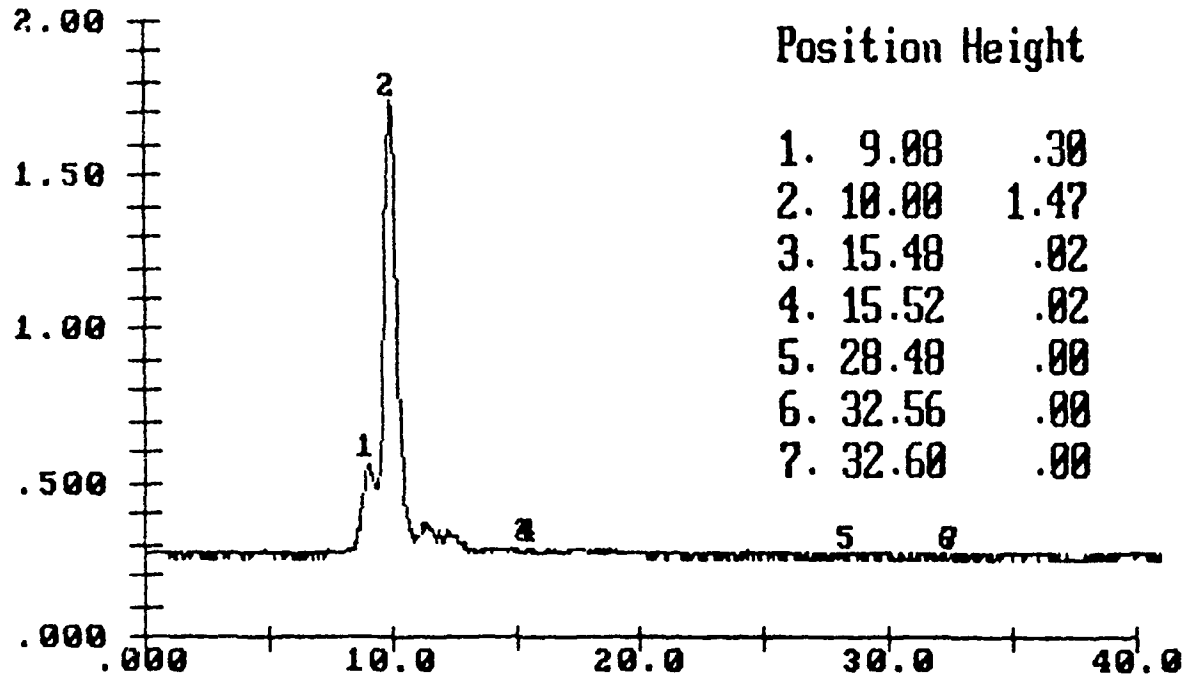

POSITIVE SIGNATURE

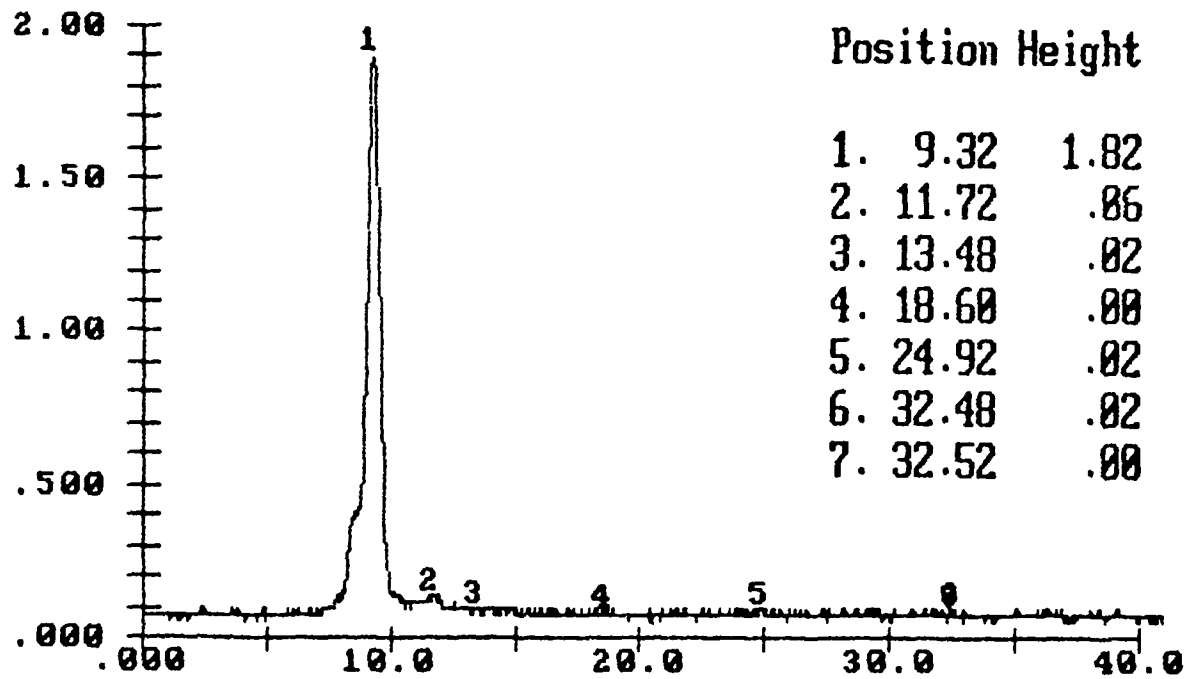

NEGATIVE SIGNATURE

Figure 1. Water Chemistry reference signature with the M-IMS, signal strength vs milliseconds.

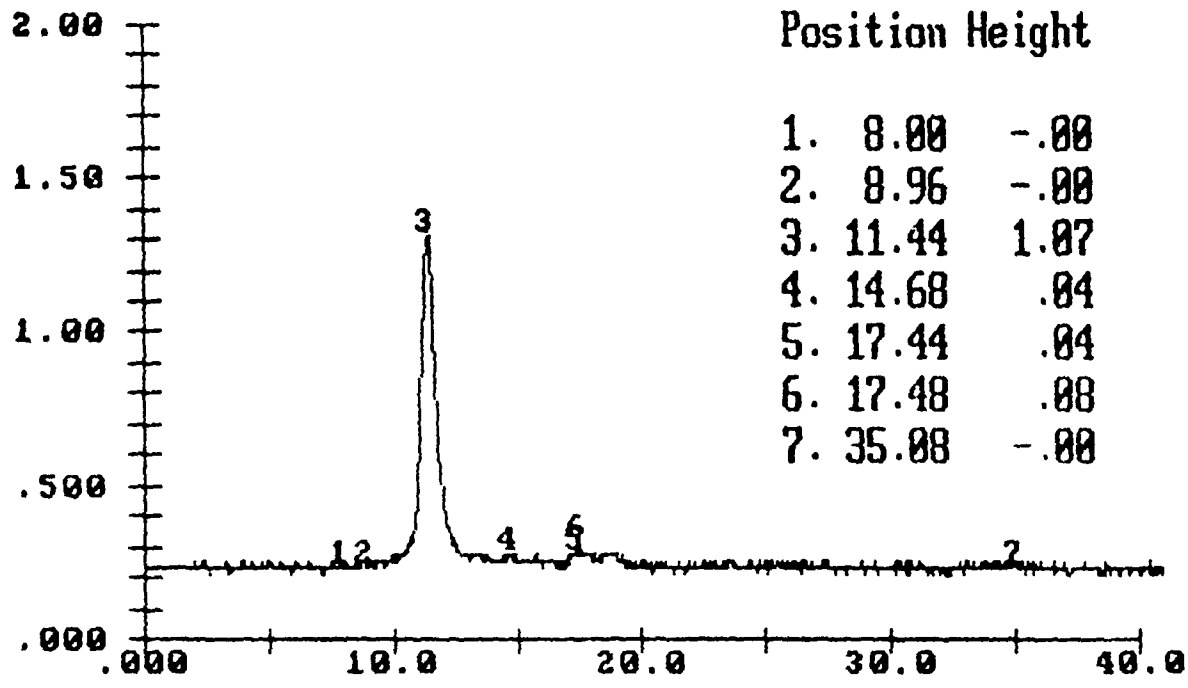

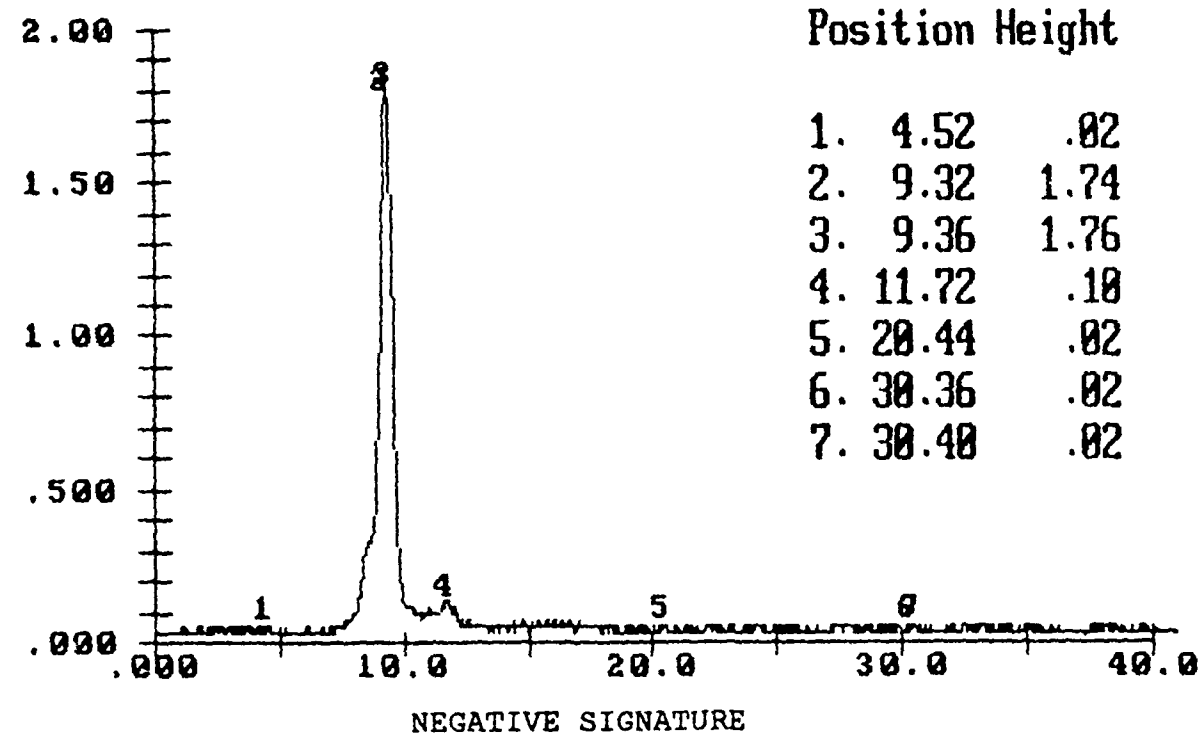

Figure 2. Acetone Chemistry reference signature with the M-IMS, signal strength vs milliseconds.

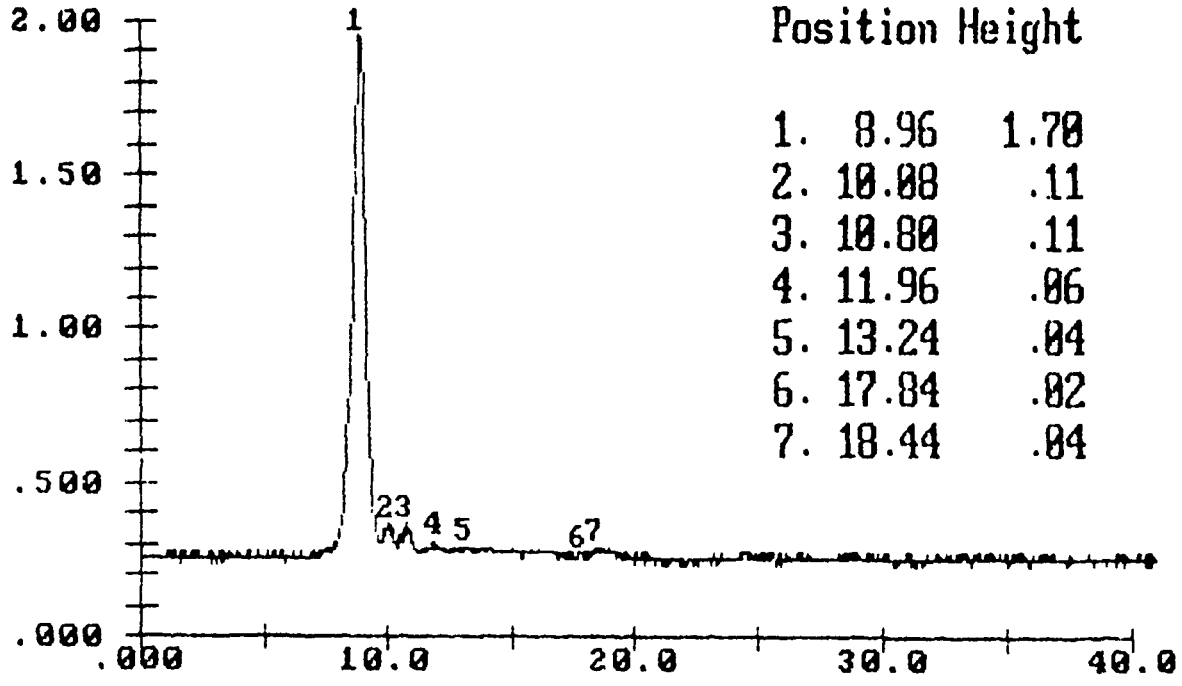

POSITIVE SIGNATURE

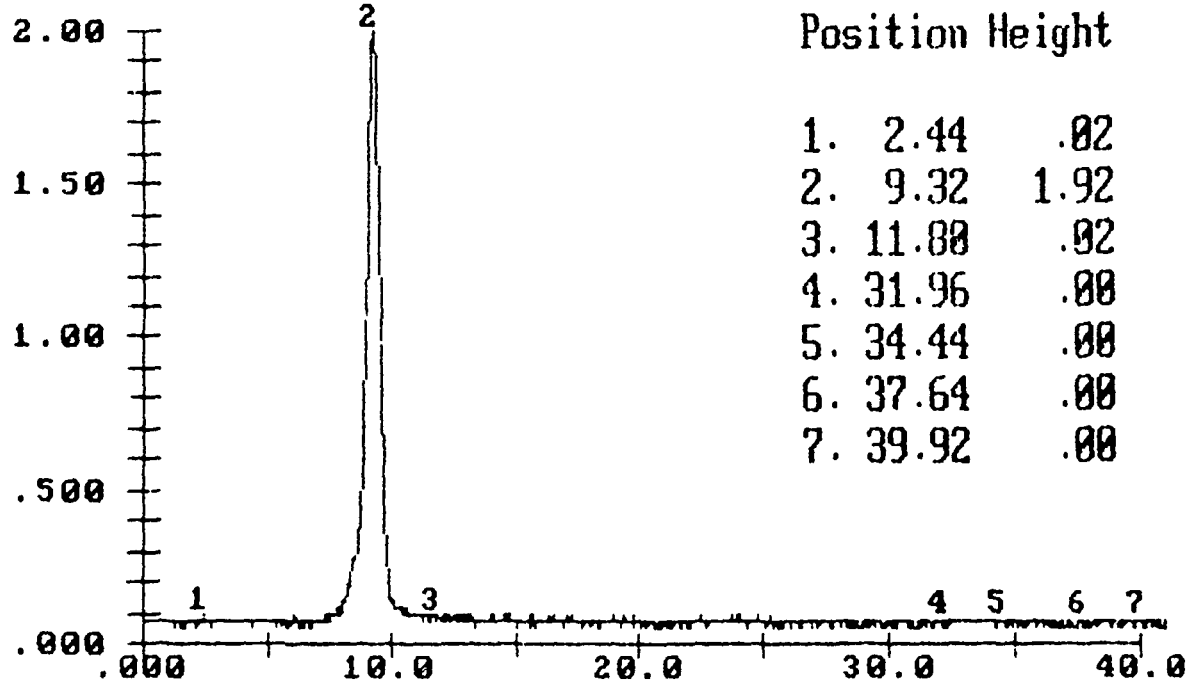

NEGATIVE SIGNATURE

Figure 3. Ammonia Chemistry reference signature with the M-IMS, signal strength vs milliseconds.

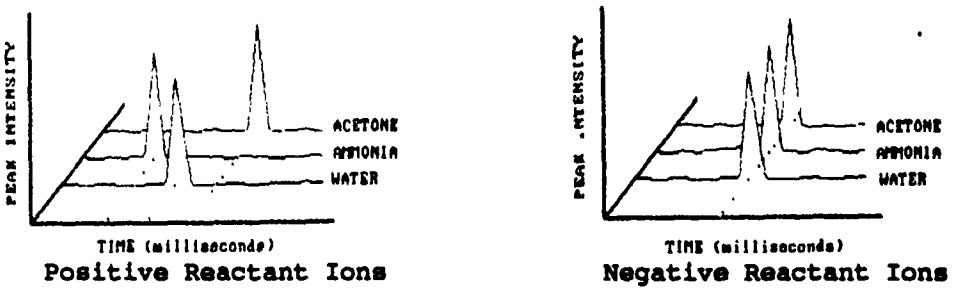

Figure 4. Relative position of reactant ions for water, ammonia, and acetone reactant ion chemistry.

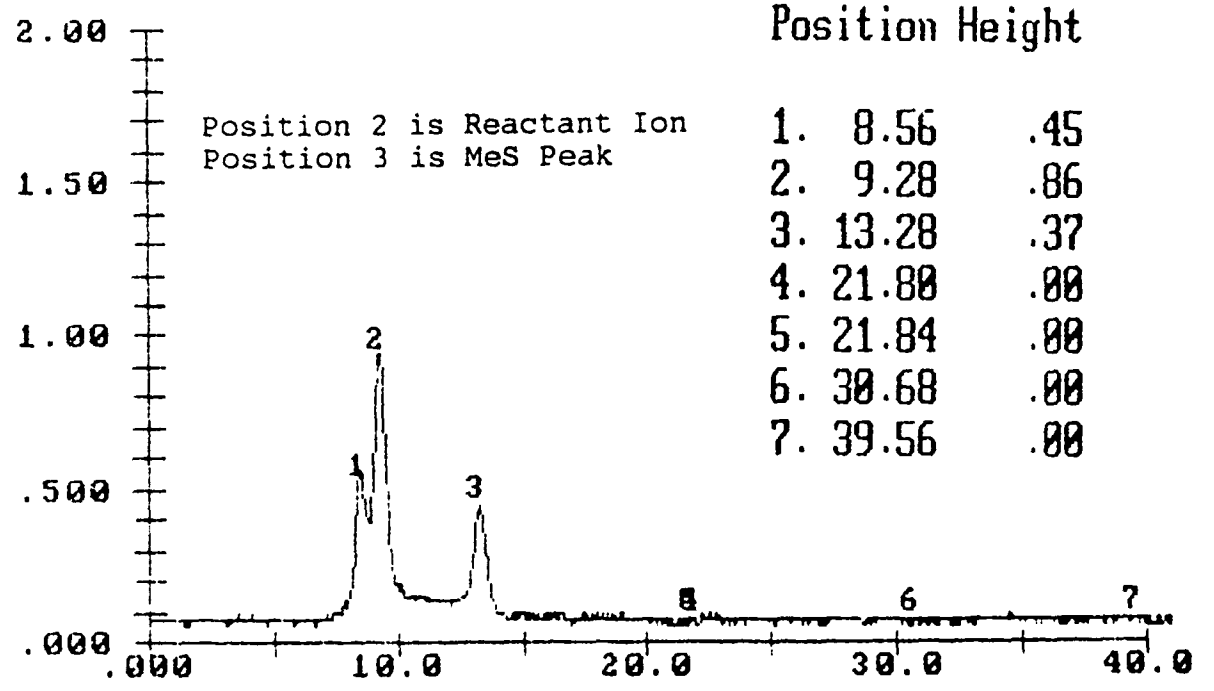

Figure 5. Negative mode signature for MeS at a concentration of 1.53 mg/M^3, signal strength vs milliseconds.

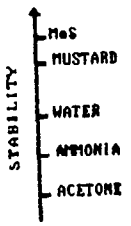

Figure 6. Relative stabilities of negative ions.

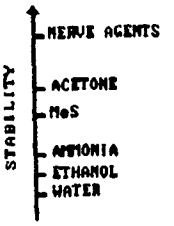

Figure 7. Relative stabilities of positive ions.

BLANK

DIGITAL SIGNAL PROCESSORS FOR REAL-TIME CHEMICAL ANALYSIS

John T. Ditillo, Robert T. Kroutil and Robert L. Gross

U.S. Army
Chemical Research, Development, and Engineering Center
ATTN: SMCCR-DDT
Aberdeen Proving Ground, MD 21010-5423

ABSTRACT

Real-time chemical analysis, using complex detection and pattern recognition algorithms, demands processor performance[1]. Real-time analysis, often using general purpose processors, has been severely limited until the recent emergence of a family of specialized processors known as the digital signal processors (DSP). These microprocessors have architectures optimized to perform the repetitive sum-of-products type calculations found in many signal processing algorithms such as the fast Fourier transform (FFT). Results, from the processing of FTIR data, show that a fifty to several hundred fold increase in performance is realized with a DSP. The digital signal processor, when embedded in chemical instrumentation, significantly improves the speed and sophistication of real-time chemical analysis.

INTRODUCTION

The modern day chemist demands rapid results from his chemical instrumentation, which often involves the use of sophisticated signal processing and pattern recognition algorithms. Much of today's instrumentation comes equipped with embedded processing modules or is accompanied by a stand-alone workstation which is used to perform this analysis. This hardware is often based on a general purpose processor due to their ease of use and familiarity to the designing engineer. Their performance is often adequate for laboratory data analysis. In instances where real-time analysis or large volumes of analysis are required, higher performance processing hardware is necessary.

Chemical analysis at the bench level has been severely limited until the recent emergence of a family of microprocessors known as digital signal processors (DSPs). These processors have

internal architectures which have been optimized to perform the repetitive sum-of-products type calculations found in many signal processing algorithms. These algorithms include finite impulse response (FIR) and infinite impulse response (IIR) filters, fast Fourier transforms (FFT), matrix manipulations and others. These processors often perform these mathematical manipulations hundreds of times faster than their general purpose counterparts. While their past use had been limited mainly to the telecommunication industry, in recent years they have been used in image, speech, sonar and radar applications. It will be shown that they can also be easily adapted to perform complex chemical data analysis.

DISCUSSION

Today's chemist is constantly inundated with computer jargon describing the latest in microprocessor architectures. This computer terminology includes CISC (Complex Instruction Set Computer), RISC (Reduced Instruction Set Computer) and DSP (Digital Signal Processor). This terminology describes the major classes of microprocessor technologies and often gives some indication of the processor's applicability for a given task. Recently, however, the distinction between the classes has begun to blur, making class generalizations difficult.

The most popular of these classes of microprocessors is the Complex Instruction Set Computer (CISC) or general-purpose processor. These processors are commonly found in desktop microcomputers and include Intel's 80x86 and Motorola's 680x0 families of processors. The CISC processor is capable of executing a very large instruction set which results in the processor's wide use for a variety of applications. This large instruction set, however, results in multiple machine cycles to execute even the simplest of instructions, thereby reducing performance. CISC processors are often based on a single internal data bus (von Neumann) architecture, requiring program instructions as well as data to flow over the same set of data lines. This coupled with a small set of internal registers can result in a bottleneck of information on the processor's data bus.

The second class of processors, which has gained popularity in recent years, is the Reduced Instruction Set Computer (RISC). Unlike their CISC counterparts, these processors are capable of executing a very limited instruction set. However, each of these instructions can be executed in a single machine cycle. In addition, these processors often contain large register sets and high speed memory caches, which keep the RISC's high performance processing units supplied with fresh instructions and data. Very often these processors are heavily pipelined, allowing multiple processor functions to be performed simultaneously. This high performance execution and limited instruction set makes the RISC ideal for specialized applications such as in engineering CAD/CAM

workstations.

The third class of processors and the focus of this paper is the digital signal processor (DSP). These processors have single instruction cycle execution speed similar to the RISCs, however, they are further optimized to perform the repetitive sum-of-products calculations commonly found in signal processing algorithms. Their increased performance is obtained through many of the same techniques employed by RISC designs including large register sets and pipelining. Additionally, hardware multipliers/accumulators and internal Harvard architecture is sometimes used to further improve the speed of complex computations.

The most unique of these features is the Harvard architecture. Unlike the von Neumann approach, Harvard architecture uses separate program and data memories, each having its own bus or buses. This allows simultaneous access of multiple pieces of information by the processing unit. The advantage of this feature is clearly evident in the performance of a finite impulse response (FIR) filter. Harvard architecture allows simultaneous access to a data point and its corresponding filter coefficient resulting in very efficient execution.

Digital signal processors come in a variety of forms ranging from the general purpose DSPs to custom or building block DSPs. This paper will limit its discussion to the single chip, floating point DSPs due to their combination of ease of use, flexibility, and applicability to chemical analysis. Two of the most popular of these are the AT&T DSP32C and the Texas Instrument TMS320C30. Both of these processors are equipped with a variety of features including high-speed on-chip memory, 16 Mbytes of external memory addressing, and direct memory access (DMA) controlled parallel and serial interfaces. The DSP32C is capable of 25 million floating-point operations per second (MFLOPS) while the TMS320C30 can achieve 33 MFLOPS performance.

How can these high performance processors benefit the bench-level chemist? To demonstrate these benefits, an IBM PC/AT compatible was outfitted with a 16MHz AT&T DSP32 (the predecessor to the more powerful DSP32C) digital signal processing module. The module functioned as a coprocessor to the AT's 80286/80287 host processors. In order for the module to operate on data which has been transferred to it, executable code must first be developed and stored within the card's on-board memory. This code can be developed, compiled and debugged on the host PC, using the DSP's native assembly language or "C" high-level language. Once developed, the code is transferred to the card's on-board memory through a series of "C" callable library functions provided with the board. Data can then be downloaded from the PC to the DSP, processed, and then uploaded back for display, storage, or further manipulation. When using the DSP as a coprocessor, one does pay a penalty for the transfer of data to and from the module as well as the time required for any

floating-point format changes which must be performed. Despite this overhead, a dramatic increase in performance can be realized.

Table 1 shows approximate execution times for several commonly used signal processing algorithms. The first of these benchmarks consists of a 1024 point complex FFT, followed by a power spectrum calculation. The second benchmark consisted of a 120 tap FIR filter being performed on a 75 point interferogram segment and the sum-of-the-squares of the resulting waveform being computed. The third and final benchmark consisted of a 6th order IIR filter performed on the same interferogram segment and the sum-of-the-squares calculated for the filtered waveform. Times were measured for an 8MHz PC/AT machine equipped with an 80287 numerics coprocessor. Execution times for the DSP are shown with and without transfer overhead, as this could be eliminated in an embedded application.

Benchmarking code for both the DSP32 and the PC/AT was written in "C", with no attempt at code optimization. The DSP code used supplied functions from the AT&T Application Support Library, which are optimized for the DSP32/DSP32C. The PC/AT code was designed to closely approximate the operation of these DSP functions. Times shown are in seconds and were calculated from the standard DOS clock functions. This limits the time resolution to approximately 55 milliseconds.

TABLE 1. Signal Processing Benchmarks

	8 MHz PC/AT	16 MHz DSP 32	16 MHz DSP 32 w/overhead
	*******	********	**********
1024 Point Complex FFT	2.31	0.05	0.11
120 Tap FIR Filter	1.59	0.05	0.05
6th Order IIR Filter	0.33	0.00	0.05

To fully utilize the tremendous processing power of these processors, chemical instrumentation must be designed to introduce data directly to the DSP. This would eliminate the performance robbing transfer overhead associated with its use as a coprocessor. Here, at the U.S. Army's Chemical Research,

Development and Engineering Center, a prototype module has been designed to interface directly to a fast scanning, commercial interferometer. The system demonstrates the possibility of designing a high speed interferometer capable of real-time chemical analysis for remote chemical plant monitoring or in-line chemical process control applications.

The prototype system (Figure 1) consists of an AT&T DSP32, 128 Kbytes of static random access memory (SRAM), a Burr-Brown ZPP1001 16 bit analog to digital module, signal conditioning electronics, and PC bus interface circuitry. The system is constructed as a PC coprocessor board, allowing the module to easily transfer processed information from the DSP to the host PC for storage or display.

Analog and digital signals from the interferometer are connected to the module via an external connector. The analog signal from the interferometer's detector preamplifier is first passed through a series of signal conditioning filters. The filters eliminate all unwanted noise which lies outside of the desired data range. This is accomplished with a combination of highpass and lowpass filters. The signal is first passed through a simple second order highpass Butterworth filter with a corner frequency of approximately 1000 Hz, thus eliminating low end noise. Next, the high frequency noise components are eliminated with a sharp roll-off lowpass filter with a jumper selectable cutoff frequency. The jumper allows for the easy adjustment for the dual scanning speed feature of the interferometer. The jumper settings adjust the cutoff frequency from 5000Hz to 28,000Hz for speeds of 5 and 40 scans per second respectively.

The conditioned interferogram signal is then connected to a Burr-Brown ZPP1001 Analog-to-Digital Module (ADM). The ADM is a single package module designed specifically for use with digital signal processors, including the DSP32 and the DSP32C. It includes a high speed sample and hold circuit, 150KHz 16 bit analog to digital converter, and all of the required timing, control, and interface circuitry necessary for the serial DSP input requirements. The ZPP1001 drastically reduces the complex circuitry previously required to interface the DSP32 to other parallel and serial output ADCs and therefore results in improved system reliability.

Once digitized, the detector signal is clocked into the DSP32's serial input port and stored in the onboard memory. This is accomplished either through software polling or by using the processor's DMA capability. Using the software polling technique allows the user to perform signal processing, such as filtering operations, on the data as it is being received. The more advanced DMA approach makes it possible to perform complex operations on one set of data while acquiring the next set. Once the DSP completes the desired data manipulation, the host PC is signaled to upload the results. This interprocessor handshaking is accomplished through the simple setting or clearing of a pre-

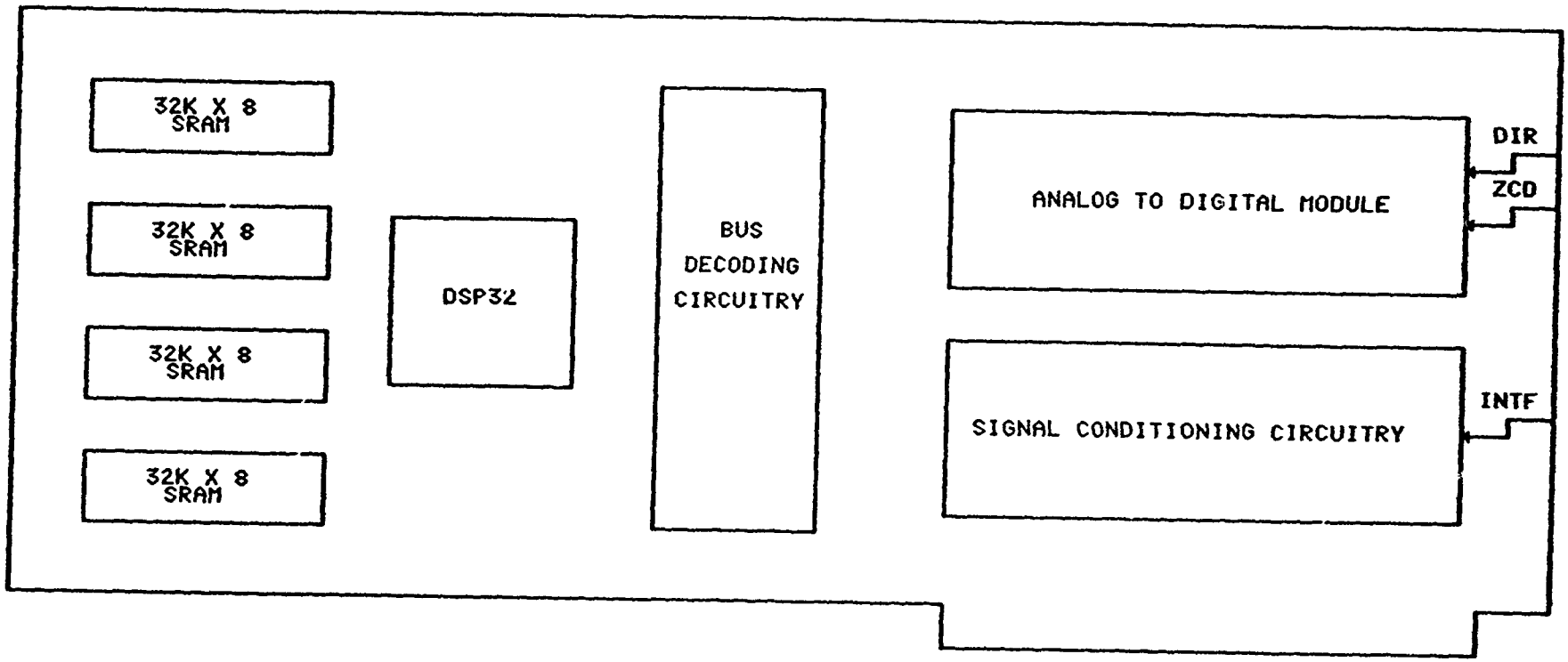

FIGURE 1.
DIGITAL SIGNAL PROCESSING
PROTOTYPE MODULE

specified memory location.

While our situation demanded the design of a specialized prototype DSP module, many applications can make use of commercially available products. Many of the processors are now available on PC or NUBUS plug-in cards resulting in a familiar development environment for the scientist. They are available in a wide variety of configurations with various input and output (I/O) interfaces and memory options. This allows the scientist to experiment with DSP technology either as an off-line data processor or as an on-line, real-time execution module. Prices for floating point implementations range from $700 to $10,000.

Ease of software development is a critical issue in the acceptance of DSP technology by the bench-level scientist. Many of the processor manufacturers have realized this and have developed a wide range of tools to simplify software design and testing. These tools include assemblers, compilers (mostly "C"), linkers, debuggers, and simulators. Also often included are libraries of hand-optimized signal processing algorithms commonly used by the scientist and engineer. In addition, third party vendors often include host/DSP utilities, signal acquisition and generation utilities, and custom environments to further insulate the user from the hardware details.

CONCLUSION

The tremendous processing performance of today's floating point digital signal processors make real-time complex chemical analysis a reality. However, a new generation of chemical instrumentation must be developed to take full advantage of these processor's capabilities. Until this instrumentation becomes widely available, scientists can begin to utilize this increased performance using commercially available digital signal processing hardware and software.

REFERENCES

(1) Kroutil,R.T.; Ditillo,J.T.; Small,G.W.; "Signal Processing Techniques for Chemical Detection" in Computer-Enhanced Analytical Spectroscopy, Plenum Press, New York, 1989, 71-111.

BLANK

VI. MATERIALS

NOTE: Papers with the following titles were presented at the Conference but are not included in this document:

An Experimental Test for Determining Resistance of Thin Polymeric Films to Penetration by Chemical Agents

Solubility Parameter of Poly (Methyl Methacrylate): An Inverse Gas Chromatography Study

BLANK

NON-ISOTHERMAL SORPTION OF TOLUENE VAPOR IN NATURAL RUBBER

Nathaniel S. Schneider and Lawrence S. Waksman
Polymer Research Branch,SLCMT-EMP, U.S. Army Materials Technology Laboratory
Watertown, MA 02172

ABSTRACT

Incremental vapor sorption measurements with toluene in natural rubber, carried out to determine the concentration dependence of the diffusion coefficient, showed slight "S" shaped curvature in the sorption curves, repesenting weight uptake against square-root of time. Application of an analysis developed by Armstrong and Stannett, indicated that heating effects were present, resulting in significant upward corrections to the diffusion coefficient. The "S" shaped sorption curves could be fitted using the full series solution for non-isothermal sorption provided by Lee and Ruthven, with parameters calculated from the Armstrong Stannett analysis. However, values of the heat transfer coefficient which gave the best fit were larger than could be accounted for on the basis of radiation and convection theory. Nonetheless, the results indicate that heating effects can take place in vapor sorption studies with highly swelling organic liquids in elastomers and that corrections to the diffusion constant will be required.

INTRODUCTION

A knowlege of the concentration dependence of the diffusion coefficient is important in modelling the permeation behavior of polymer barrier materials. A study was undertaken of toluene in natural rubber as a model system because of the importance of natural rubber and the availability of a considerable diffusion literature. During the course of the vapor sorption measurements on a series of samples with varying carbon black content (1), it was noted that the vapor sorption curves, above a moderate concentration were no longer strictly Fickian. The curves of fractional weight uptake plotted against the square root of time showed slight "S" shaped curvature which could not be explained as the result of problems in the experimental method. The data were first interpreted as a physical relaxation of the lightly crosslinked rubber network and the treatment of Joshi and Astarita (2) was employed to derive corrected diffusion coefficients. However, these data, when converted to solvent mobilities, failed to increase rapidly with concentration and to extrapolate to the self-diffusion coefficient of toluene at unit solvent volume fraction.

In seeking another explanation for the non-Fickian behavior the possiblity arose that temperature changes might be occurring during sorption. This paper describes the interpretation of the diffusion data in terms of these heating effects.

EXPERIMENTAL

Samples of natural rubber were prepared in 20 mil thickness containing 10 to 50 phr of two types of carbon black; N110, a fine particle black and N774, a large particle black. A crosslinked, unfilled sample and the N774 samples were used in the vapor sorption experiments. The vapor sorption measurements were carried out using a standard vacuum sorption system, thermostatted at 25°C, and a quartz helix spring balance with a sensitivity of about 10mg/cm. The samples were exposed to a series of approximately ten successive vapor pressure increments in the sorption cycle, followed by an equivalent desorption cycle and weight changes were determined by measuring the spring displacements to 0.01mm with a Gaertner cathetometer.

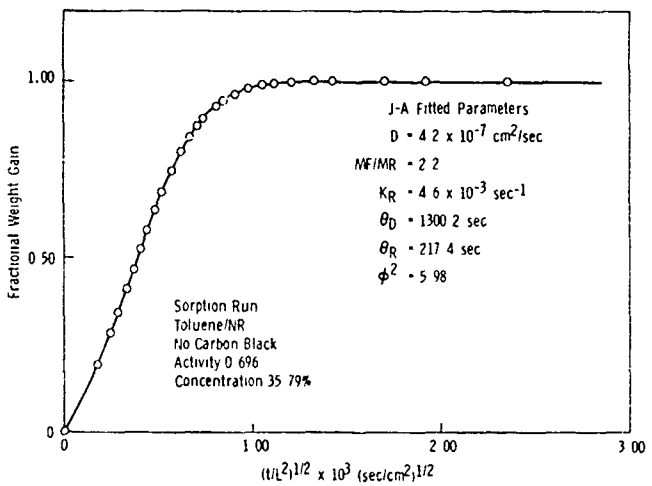

Figure 1. Vapor sorption curve at a_1 = 0.696, C = 35.8%, showing slight "S" Shape behavior. Open circles, experimental data; solid line, fit from Joshi Astarita analysis.

RESULTS AND DISCUSSION

An example of a vapor sorption curve displaying the mild "S" shaped curvature appears in Figure 1. Apparent diffusion constants were calculated from the relation (3):

$$D = 0.0492L^2/t_{1/2} \qquad (1)$$

where L is the sample thickness and $t_{1/2}$ is the time to reach one half the final weight gain. The results (see ref.1) go through a maximum in D with increasing concentration. As noted in the introduction, when these results were converted to solvent mobilities, by procedures described elsewhwere (1,4) they did not increase rapidly as expected with increasing concentration.

In searching for an explanation of the problems with the data,

consideration was given to the possible complication of heating effects accompanying vapor sorption. The influence of heating effects on the diffusion coefficent of water vapor in wool fibers and, later, in ethyl cellulose films was treated by Armstrong and Stannett (5,6). They showed that the resulting temperature increases could cause large reductions in the diffusion coefficient determined by the usual analysis. This is not ordinarily considered to be a problem for organic vapors due to the much lower heat of vaporization, eg. 102.5 cal/gm for toluene compared to 582 cal/gm for water.

In the analysis provided by Armstrong and Stannett, the diffusion coefficient is obtained from the limiting, long-time slope of the sorption-rate curve:

$$D = -1/\lambda_1^2 d\ln[(1 - M(t)/M(\infty)]/dt \qquad (2)$$

where λ_1 is the first eigenvalue in the solution of the differential equations governing the combined heat and mass-transfer. It might be noted that, in the absence of heating effects, this is the usual equation for determining D from the final rate of sorption with π replacing λ_1 (3). The parameter λ_1 is obtained from the following equation:

$$\frac{1}{H_v \omega}\left[\frac{H}{b\rho^* slope} - C\right] = \frac{\tan(\lambda_1 b)}{\lambda_1 b} \qquad (3)$$

where the various quantities are defined below. A figure is provided in their publications to assist in interpolating λ_1 from the right hand side of the above relation.

In applying the analysis to the present data the following values were used: latent heat of vaporization of toluene, H_v = 102.5 cal/gm; heat capacity, C = 0.437 and 0.357 cal/gm °C for the unfilled and 50 phr filled rubber, respectively; density of rubber, ρ = 0.9126 gm/cm^3; half thickness, b = 0.234 and 0.257 cm for the unfilled rubber and 50 phr N111 filled rubber, respectively. The temperature coefficient of weight gain, ω (g/g °C) was calculated from the sorption isotherm, rather than being measured directly, using the following relation:

$$\omega = \left(\frac{1}{1-\Phi_1}\right)^2 \frac{H_v}{RT^2}\left(\frac{\partial \Phi_1}{\partial \ln a_1}\right)_{T,P} \qquad (4)$$

The derivation of this relation will be treated in a future publication dealing more extensively with heating corrections to diffusion data. Since it was found that values of D obtained from the final rate of sorption using (2) with π replacing λ_1, were very close to the half-time or JA values, which varied in a more systematic manner with concentration, the final slope was computed from these values of D.

Calculations were run for three values of the heat transfer coefficient; H = 1.5×10^{-4} cal/cm^2 sec°C, the value obtained experimentally by Armstrong and Stannett, 3.0×10^{-4} and 7.5×10^{-4}. Lower values of the heat transfer coefficient will result in greater temperature increases and accompanying corrections to the diffusion coefficient. The results are recorded in Table 1 for the unfilled, crosslinked sample and for the sample with 50 phr N774 carbon black.

There are two problems with the analysis, for the present purpose, in the

way in which it has been implemented by Armstrong and Stannett. If all the required parameters are known, especially the value of the heat transfer coefficient, then a reliable estimate of the correction to the diffusion coefficient can be made by their method. If the value of the heat transfer coefficient is not known and is used as a variable parameter, there is no way of testing the reliability of the result. A second problem is that the approach does not give any information about the effect of the heating correction on the overall shape of the sorption curve.

Table 1

CORRECTED DIFFUSION COEFFICIENTS FOR VARIOUS HEAT TRANSFER COEFFICIENTS
Unfilled, crosslinked sample

		$H=1.5\times10^{-4}$		$H=3.0\times10^{-4}$		$H=7.5\times10^{-4}$	
Activ.	D orig. ($\times10^{-7}$)	D corr. ($\times10^{-7}$)	Error ($\times10^{-2}$)	D corr. ($\times10^{-7}$)	Error ($\times10^{-2}$)	D corr. ($\times10^{-7}$)	Error ($\times10^{-2}$)
0.09	1.22	N.C.		N.C.		N.C.	
0.19	1.91	N.C.		N.C.		N.C.	
0.30	2.65	2.91	0.189	N.C.		N.C.	
0.40	4.21	7.46	1.540	4.79	0.220	N.C.	
0.50	5.05	11.39	0.076	6.57	0.127	5.54	0.291
0.60	5.05	40.31	0.579	7.98	0.095	5.92	0.593
0.70	4.08	*		7.87	0.079	4.99	0.366
0.80	2.78	*		7.56	0.415	3.58	0.156
0.91	1.15	*		3.86	3.21	1.51	0.380

N.C. indicates that there is no change as the result of a heating correction.
* indicates that the sorption is completely controlled by the heating effect.

Ruthven and Lee (7) have derived equations relating the fractional mass uptake $M(t)/M(\infty)$ as a function of dimensionless time, $\tau = Dt/b^2$ for diffusion into a zeolite bed. Their equations are directly applicable to describing the nonisothermal diffusion of a solvent in a rubber sheet. The fractional weight uptake is given by the following series:

$$\frac{M(t)}{M(\infty)} = 1 - \sum_{n=0}^{\infty} \frac{2\exp(-p_n^2\tau)}{p_n^2 \cot^2 p_n (1+2/\beta) + p_n^2 + p_n \cot p_n} \qquad (5)$$

The values of p_n are given by the roots of:

$$\cot p_n = \frac{\beta p_n}{(\alpha - p_n^2)} \qquad (6)$$

The quantities α and β are defined as:

$$\alpha = \frac{Hb}{CD} \qquad \beta = \frac{H_v \omega}{C} \qquad (7)$$

where all variables have the same definition as that used in the discussion of Armstrong and Stannetts approach. Note that α contains the kinetic parameters, H and D, whereas β combines the various thermodynamic parameters. For given values of α and β, determined using the corrected diffusion coefficients from the Armstrong and Stannett analysis, sorption rate curves can be constructed

for comparison with the experimental curve. The calculations were carried out using a program which also computed an error as a test of the fit. A weighted root mean square error was calculated from the square of the deviations between experiment and theory divided by the experimental value at each point, in order to reflect the initial curvature. The unweighted root mean square error was also calculated. This quantity emphasizes the later time behavior. The error recorded in Table 1 is the square root of the product of these two quantities.

Consider first the results in Table 1 for the unfilled elastomer. For H = 1.5×10^{-4}, the corrected values of D increase very rapidly, reaching a value eight times larger than the original at an activity of 0.60, which corresponds to a concentration of 26%. At higher activities, the sorption rate is completely controlled by the relaxation of the increased sample temperature. For H = 3.0×10^{-4}, finite values of D are obtained over the entire range of activities. At an activity of 0.6, the corrected D is increased only by a factor of 1.6 and the fitting error is much lower than the comparable result for the lower value of H. However, the errors for the last two activities are much higher than the results obtained at these activities with H = 7.5×10^{-4}, shown in the next column. Thus, judged by the error values, the best fit is obtained for H = 3.0×10^{-4} up to an activity of 0.7 and H = 7.5×10^{-4} for the data at activities of 0.8 and 0.91. For the carbon black filled samples, the best fit was obtained with H = 7.5×10^{-4} throughout.

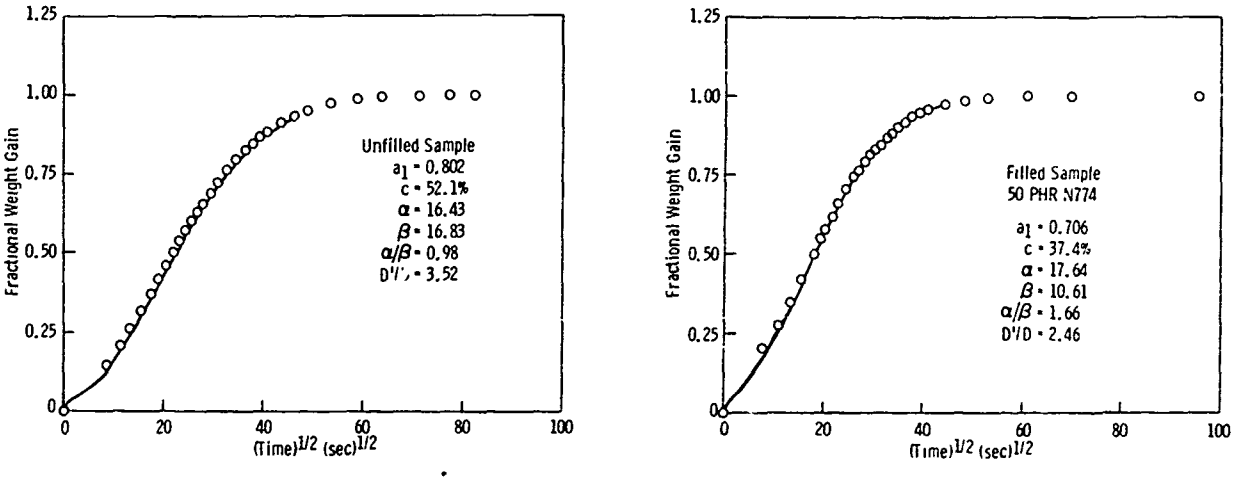

Figure 2 and Figure 3. Fit of Ruthven Lee analysis to unfilled crosslinked sample and carbon black filled samples, respectively. The parameters are defined in equation 7. The quantity D'/D represents the ratio of the heat corrected and the original diffusion coefficients.

Comparisons of the predicted and experimental sorption rate curves are shown in Figure 2 for the unfilled sample and in Figure 3 for the 50 phr N774 filled sample. The comparisons show that the theory is able to account for the "S" shape curvature reasonably well. However, it must be stated that the Joshi Astarita analysis frequently provides an even closer fit to the experimental data for the sorption rate curves at several activities.

Solvent mobilities, D_1, can be calculated from the heat corrected data to

determine whether the results are now capable of describing a reasonable extrapolation to the self diffusion coefficient for toluene. The resulting D_1 values are plotted against solvent volume fraction in Figure 3 and 4 for the unfilled and 50 phr N774 carbon black filled samples. The results in Figure 3 suggest that the heat corrected D values obtained with $H = 3.0x10^{-4}$ lead to D_1 values which rise above the suggested empirical extrapolation curve, while the final several D_1 values obtained with $H = 7.5x10^{-4}$ fall below this curve. The same trend is evident in the results for the 50 phr N774 sample of Figure 4, with the D_1 values obtained for $H = 3.0x10^{-4}$ clearly being much too high. Therefore, it appears possible, in this case, to obtain a consistent set of D_1 values by suitably adjusting the heat transfer coefficient within the range $H = 3.0x10^{-4}$ to $7.5x10^{-4}$.

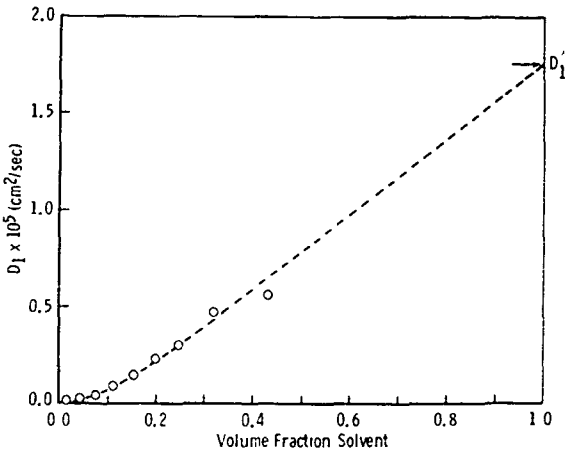

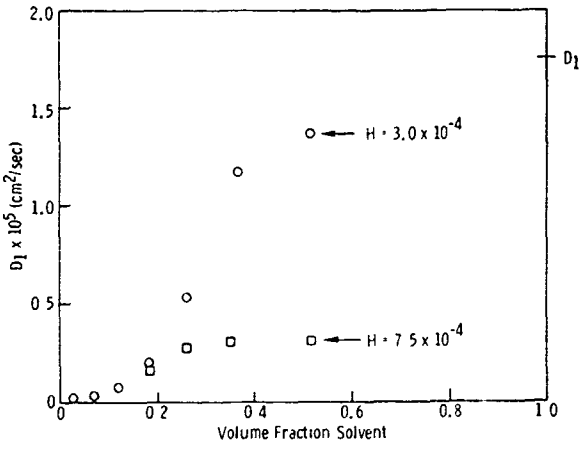

Figure 4 and Figure 5. Solvent mobilities D_1 versus volume fraction of solvent for the unfilled crosslinked sample and for the carbon black filled 50 phr N774 sample, respectively. Calculated results for different values of the heat transfer coefficient, H, are indicated. D_1 represents the self-diffusion coefficient of toluene.

CONCLUSIONS

In the preceeding analysis the heat transfer coefficient was treated as an adjustable parameter without regard to its physical origin. The maximum heat transfer coefficient due to radiation is $1.5x10^{-4}$ for a black body. This is the value used by Armstrong and Stannett in their studies with water vapor. It might be assumed that the higher values required to fit the present data are the result of convection. Indeed, the convection contribution to heat transfer with toluene vapor would be substantially higher than with water vapor, essentially in proportion to the ratio of the molecular weights. Howwever, the convection contribution calculated on the basis of circulation over a heated vertical surface, is an order of magnitude lower than the radiation contribution. It has not been possible to identify any external source of a large temperature gradient in the sample chamber which could contribute to covective heat loss. Thus, it appears that the higher values estimated from the Amstrong Stannett analysis and required for the Lee Ruthven fit cannot be accounted for. Efforts are underway to apply an improved fitting routine for

the Lee Ruthven analysis to obtain α and β parameters directly and to determine if these are consistent with the values calculated from the Armstrong Stannett approach. Nonetheless, the results indicate that heating effects can take place in vapor sorption studies with highly swelling organic liquids in elastomers and that correction to the diffusion coefficient will be required.

REFERENCES

1. L.S. Wacksman, and N.S. Schneider, ACS Symposium Series; Barrier Polymers and Barrier Structures, to be published.
2. S. Joshi and G. Astarita, Polymer, 20, 455 (1979).
3. J. Crank, "Mathematics of Diffusion", 2nd ed., Oxford University Press. London, 1975.
4. N.S. Schneider, C.F. Mee, R. Goydan and A.P. Angelopoulos, J. Polym. Sci.: Polym. Phys. Ed., 27, 939 (1989).
5. A.A. Armstrong, Jr., and V. Stannett, Macromol. Chemie, 90, 145 (1966).
6. A.A. Armstrong, Jr., J.D. Wellons and V. Stannett, Makromol. Chemie, 95, 78 (1966).
7. D.M. Ruthven and L.K. Lee, AICHE Journal, 27, 654 (1981).

BLANK

FLOODED CELL PERMEATION TESTING OF BUTYL RUBBER BARRIERS

Erik E. Engwall
U.S. Army Materials Technology Laboratory
Watertown, MA 02172

Abstract

Procedures for permeation testing of butyl glove material have been developed utilizing a Radian Microcell (Radian Corp.) and a Minicams chemical agent monitoring system (CMS Research Corp.). Permeation testing has been performed using dimethylmethyl-phosphonate (DMMP) as a G-agent simulant under fully flooded surface conditions. Test samples have been cut from 7 mil nominal gloves; the actual thickness varies widely depending on the portion of the glove from which the sample is cut. Flux and cumulative permeation data versus time are reported for testing at 25°C and 37°C.

Introduction

Current acceptance testing of chemical protective gloves is based on methods 206.1.2 and 204.1.1 of MIL-STD-282. These techniques yield single end point breakthrough times, based on fruit fly kill and congo red indicator paper for GB and HD respectivly. The detection methods for these tests preclude a precise conversion between breakthrough time and breakthrough amount. Simulant testing has been instituted to determine factors affecting the performance of butyl glove samples as barriers to liquid permeation. Testing is performed using a Radian Microcell to conduct flooded cell permeation testing using less liquid than the ASTM standard cell. The flooded cell enhances reproducibility by eliminating the time dependence of the challenge area. State of the art automated permeation testing instrumentation is used for continuous determination of permeant flux and cumulative permeation. This study will provide insights on the applicability of flooded cells and an automated analysis system to agent permeation testing in support of product acceptance.

Experimental

All the gloves used in testing were received from two sources. The first 3 pairs, received from NRDEC, were 7 mil nominal gloves (MIL-G-43976B, Type III). The second shipment was taken from stock at the mask issue point of the Aberdeen Proving Grounds at Edgewood, MD, and included 25 mil (Type I, same spec.) and 7 mil nominal gloves (five pairs each). Samples were cut from the gloves using a 1.75 inch circular die. Samples were designated according to a convention which indicates the type of glove, glove pair,

specific glove (right or left) and sample number (eg. B7-5R-3 indicates sample number 3, cut from the right-hand glove of the 5th pair of 7 mil nominal gloves). The thickness of the gloves tended to decrease from the palm and backhand to the cuff. The samples were cut from flat areas (no fingers) which showed little variation in thickness. Thickness measurments were made at 5 points, and the average was reported as sample thickness. Tests were performed on samples ranging from 7.5 mil to 11.0 mil. The cut samples were washed with distilled water, weighed and loaded into the test cell.

The cell assembly consisted of 5 cell components and 4 samples held in position by two bolted endplates. The challenge configuration is illustrated in Figure 1 which shows a crossection of two cell components with a sample. The assembly was placed in a cabinet maintained at 25°C or 37°C. The cell floods a 1 inch diameter circle on the sample surface with challenge liquid and requires 2.5 ml of liquid per compartment.[1] Excess liquid was required to insure the removal of trapped air from the flooded compartments. Challenge liquid was introduced from a common reservoir and overflow was stored in a second reservoir, the total volume of fluid used ranged from 30 to 40 ml. Samples were purged by 200 ml/min room air drawn through the cells and into stream selection system (SSS) by vacuum pump 1 as illustrated in Figure 2. Flow rates were monitored by Tylan linear mass flowmeters at the cell air purge inlets.

Analytical Procedure

The SSS (CMS Research) consists of a multi port G.C. valve housed in a heated oven. There are 12 sample ports with connections to a vacuum pump and to the Minicams chemical agent monitor (CMS Research). The valve is controlled by an IBM compatible personal computer and software, provided with the system. Actuation of the valve sequentially diverts each sample stream to the monitor. The timing and order of the sampling cycle are programmed by the operator prior to the start of an experiment. Analysis is based on solid state sorbent sample collection followed by thermal desorption and capillary gas chromatography. The monitor is controlled by the system computer from which the timing and temperatures for both the sorbent tube and G.C. column are set at the start of a run.

The sorbent tube is packed with a bed of Haysep-D porous polymer and organics are collected from the sample stream at 40°C. The collection period was one minute for the 25°C runs but was increased to 1.5 minutes for the 37°C runs. The sorbent tube is thermally desorbed for 30 seconds and purged with 30 ml/min nitrogen. The desorbed sample is focused onto the inlet of a capillary column which is heated to 200°C in a 90 second heating cycle. Peaks are eluted to a flame photometric detector and quantification is based on peak height. The peak height data is converted into permeant flux and cumulative permeation and stored. The monitor is calibrated by injection of known amounts of DMMP in a hexane solution. The response data, (nano amps) verses amount (ng), is curve fitted with a 3rd order polynomial using an engineering software package.

System Performance

During the course of this testing several system problems have been encountered which are worthy of mention. One problem is the retention of DMMP by the monitor (carry-over) following completion of the monitor cycle. Depending on the ammount of DMMP introduced, the residual DMMP can take up

Figure 1, Radian Microcell

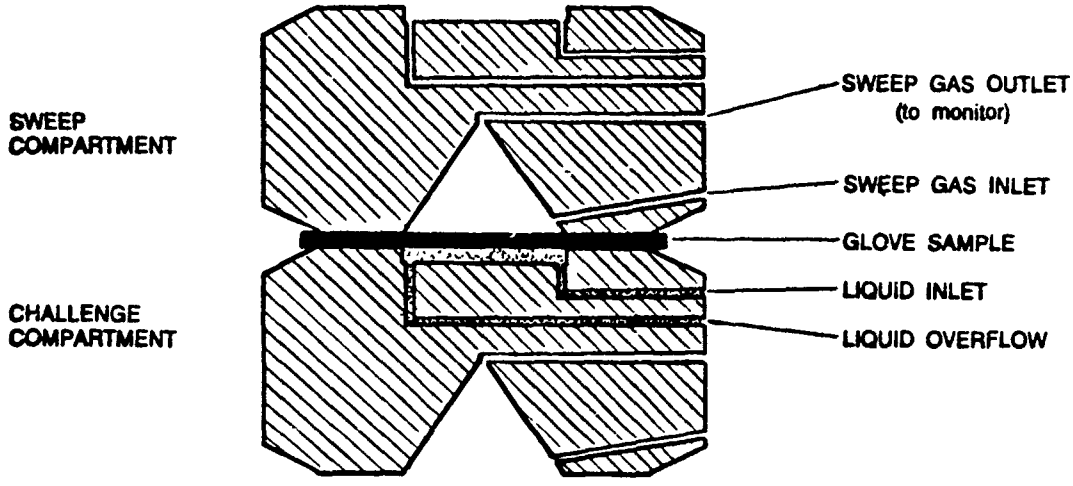

Figure 2, Permeation Testing System

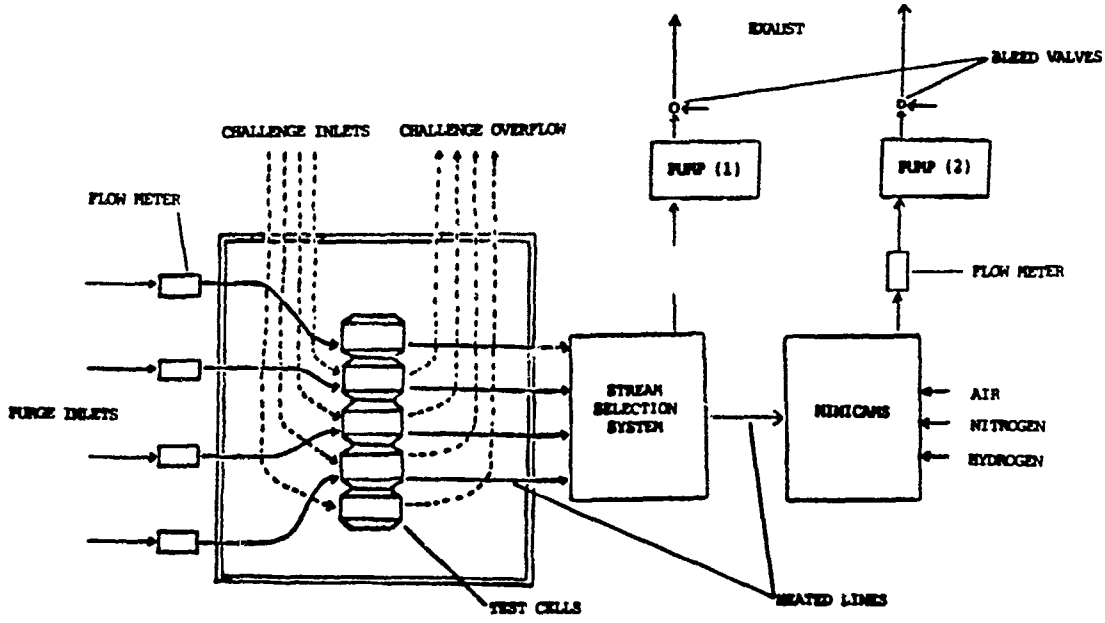

to 5 cycles to decay. The amount of carry-over is measured by the size of the peaks eluted from the column during blank monitor cycles following the initial (detection) peak. It is convenient to discuss carry-over in terms of a comparison between the initial and second peaks eluted following an injection or sampling. The second peak varies from 3 to 10 percent of the initial peak, depending on the amount DMMP introduced and the the manner of introduction. For large injections or samplings the amount of carry-over increases but the percentage relative to the first peak drops. In general, carry-over is significantly less for calibration injections than for the sampling of DMMP laden air. Attempts to increase the efficiency of sorbent tube desorption, by increasing temperature and the length of the desorption period, produce only a limited reduction in the amount of carry-over. The effects of these changes are visible in the permeation test results. The best strategy for the managment of carry-over seems to be the inclusion of blanks between samples.

There is also a problem with the control of the stream selection system. At random times throughout the testing of a set of samples, the stream selection valve will rotate past its assigned port and stop at port 1. The system remains at this port until the monitor cycle is complete, at which time it procedes to the next assignment. It is possible to determine when this has happened by review of the data file following a permeation test. The information for the port 1 samplings must be deleted prior to analysis of the data. In addition to the loss of a data point there is a drop in cell flowrates for all 4 cells from 200ml/min to 100ml/min. The missed assignments are completly random and occur with equal frequency in all portions of the sampling cycle. There appear to be no visible effects on the quality of the data following these missed assignments.

Initial Results

The first six samples were cut from the same glove and tested in 2 groups of 3 samples with a fourth unchallenged sample in each group used as a blank. The monitor sampled each cell consecutively for 1 minute. The cumulative permeation (ng/cm^2) and permeant flux ($ng/min/cm^2$) were ploted versus time (hrs) for each experiment.

In Figure 3a the cumulative permeation behavior is illustrated for the first six samples. The dashed curves are for samples B7-1L-3 and B7-1L-6 which followed the blanks in the sampling cycle. The remaining samples show that permeation follows an approximate relationship to the sample thickness. The lag in the data for B7-1L-3 and B7-1L-6, with respect to samples of similar thickness, is probably a carry-over effect. The blank runs acted as system purges reducing the amount of DMMP retained in the monitor. The detection of permeant for the samples which followed, was reduced due to the diminished carry-over. Figure 3b shows permeant flux versus time for three of the samples in Figure 3a and none has reached steady state at 48 hours. Some of the samples were run for 100 hours in an effort to reach equilibrium but even at these extended times none of the samples reached a clear steady state flux.

The long experimental times and failure to reach steady state at 25°C present unacceptable limitations on productivity. Raising the experimental temperature to 37°C reduced the time needed to reach steady state to less than 48 hours. The sampling cycle at this temperature included a blank between each challenged sample and the desorption temperature was raised to 225°C to minimize carry-over effects. The cumulative permeation and flux versus time curves, for three samples cut from the same glove, are ploted in

Figure 3a, Cumulative Permeation at 25°C

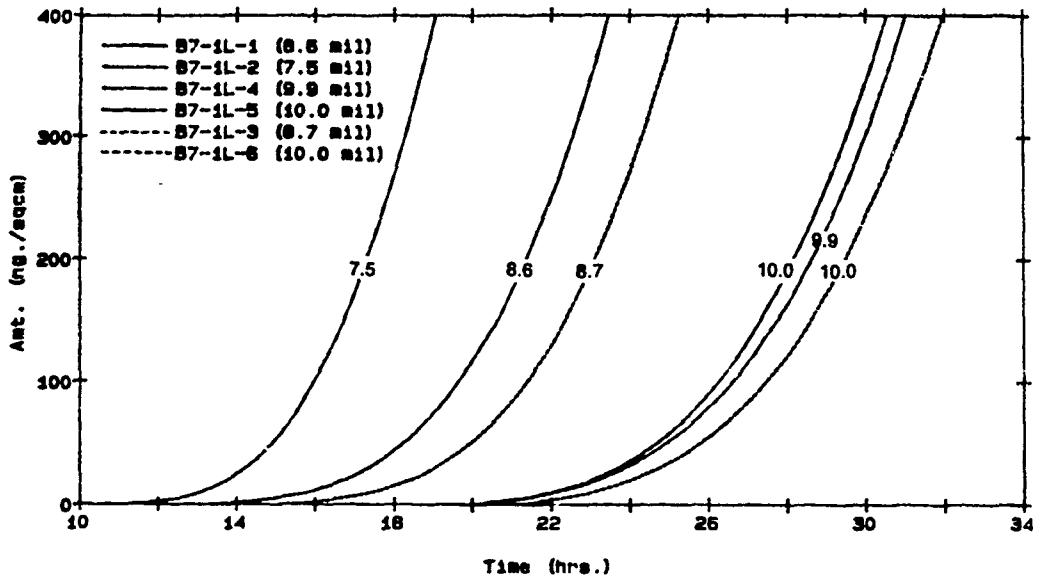

Figure 3b, Permeant Flux at 25°C

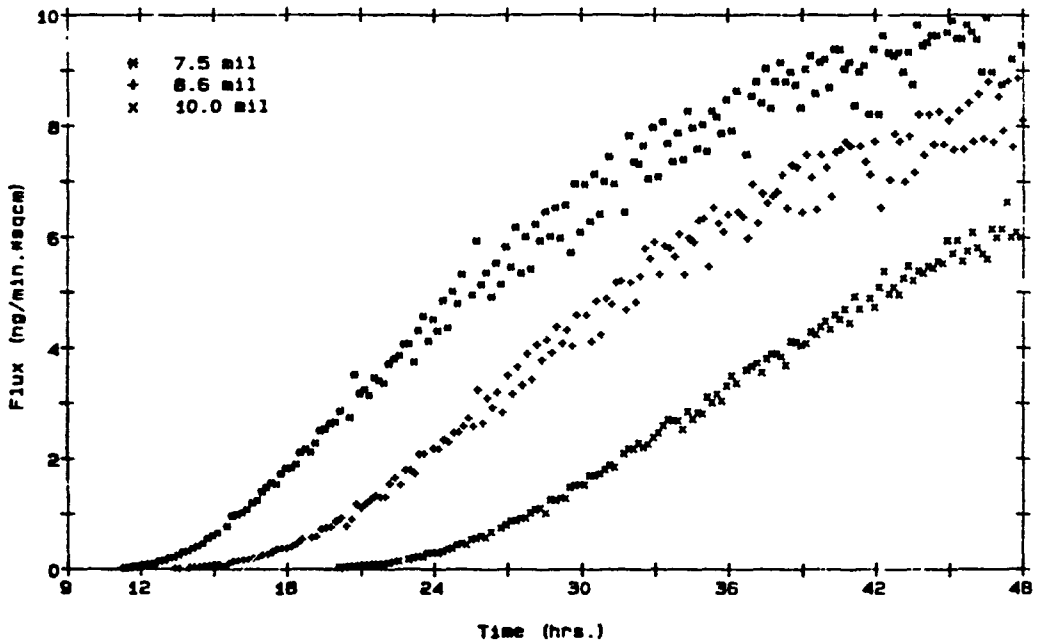

Figure 4a, Cumulative Permeation at 37°C

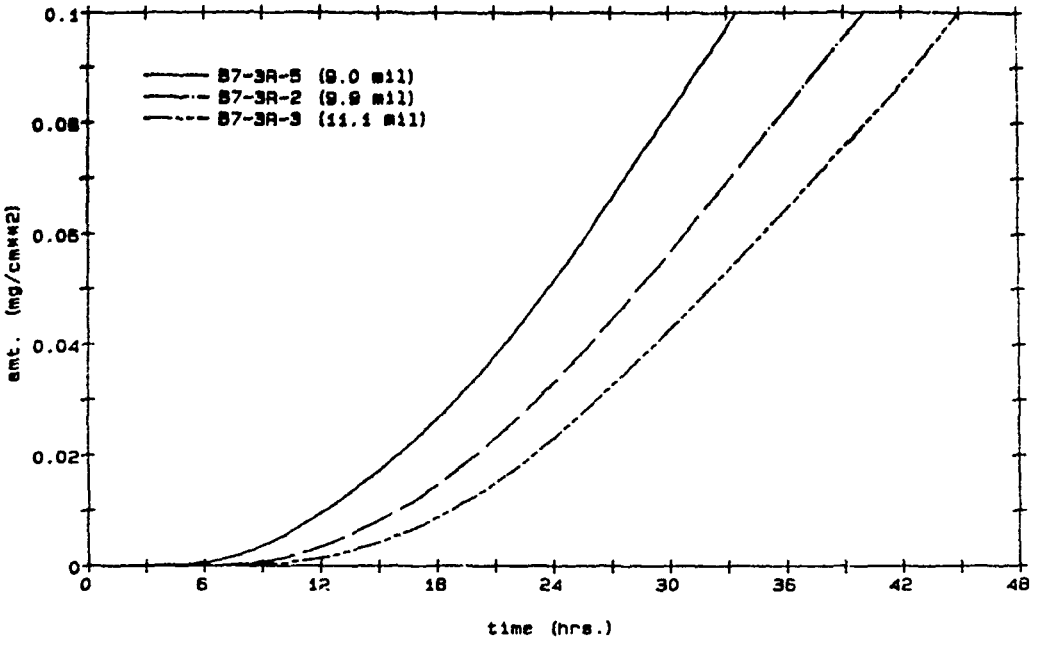

Figure 4b, Permeant Flux at 37°C

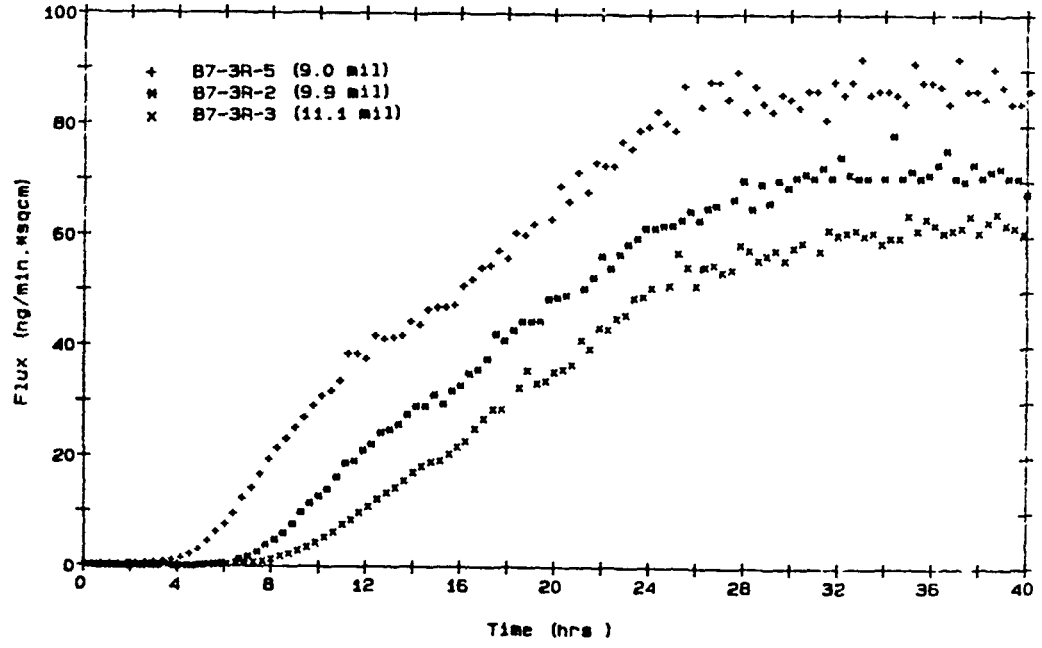

Figures 4a and 4b respectively. These results are qualitatively similar to the 25°C results in thickness dependence. The range of permeant flux increased by a factor of 10 and the time to the first detectable permeation decreased by a factor of three. The steady state permeant flux ranged from 87 to 60 ng/min/cm^2 for a sample thickness range of 9.0 to 11.1 mils and the time to reach steady state varied from approximately 26 to 32 hours.

Discussion

The experiments discussed above were conducted using a sample selection procedure by which we attempted to limit sample variability to only thickness differences. Samples were cut from lots which passed agent screening and comparisons were drawn between samples cut from the same glove to minimize the potential for variability in material properties. This approach was designed to provide the most favorable conditions for the establishment of experimental reproducibility, and the assessment of test methodology and system performance. The limited number of gloves tested, and progressive adaptations made in test parameters preclude a comparison of the test results for different gloves.

Comparison of results for differing thicknesses from the same glove show a dependence of permeation on sample thickness as expected. The first detectable permeation in the 10.0 mil sample lags the detection of permeation in the 7.5 mil sample by more than 8 hours (Figure 3a). There is less realitive separation of the cumulative permeation curves for 37°C (Figure 4a). This may be due in part to the smaller thickness range covered by these samples. The resolution of thickness dependence is limited by intra sample thickness variations. Single point thickness measurement variations of up to 20% have been found on a 1.75 inch diameter sample. In such a case early permeation would be controlled by the thinnest point. Samples with wide variations were avoided and with careful selection it was possible to find samples which vary by less then 0.5 mil from thinnest to thickest point. The thickness tolerances for type III gloves specify an acceptable range of 6 to 10 mil.[2] The results indicate that wide variations in barrier performance are possible within this range.

Future Work

In the future samples from glove lots which have failed product acceptance testing will be tested. Correlation of simulant permeation results with those obtained for agents will be necessary to show that factors affecting glove permeability are the same for each. The differences between our methodology and MIL-STD-282, methods 206.1.2 (GB test) and 204.1.1 (HD test) make quantitative determination of agent/simulant equivalence impractical. A qualitative comparison will be performed by testing fresh samples from gloves which have already been agent tested. Samples will be selected for agent testing based on material and physical property variations which are found to influence simulant permeation. Some of the simulant test samples will be solvent extracted for retesting. If reproducibility can be obtained for repeat testing then a group of these samples will be returned to PAD for agent testing. This will not determine sample failure as defined in MIL-G-43976B, however it will provide a direct comparison between MIL-STD-282 and our method for the same sample.

References

1. M. Conoley, Proceedings of the Workshop on Methodology for Testing of Materials with Agents and Decontaminants 9-11 July 1985, P. 409 (1986). CRDEC-SP-86016.

2. MIL-G-43976B, 30 June 1986, P. B3-B4

ANALYSIS OF CW LIQUID DROPLET PERMEATION TESTS PERFORMED WITH A SERIES OF RUBBER MATERIALS

Anthony F. Wilde
Polymer Research Branch
U.S. Army Materials Technology Laboratory
Watertown, MA 02172-0001

ABSTRACT

MTL has been analyzing test results derived from contractor-performed CW liquid droplet permeation through a series of rubber materials. The droplet breakthrough times exhibit a power-law dependence upon specimen thickness. The breakthrough times, normalized to a standard specimen thickness, increase with the glass transition temperature, Tg, of the rubber. The power-law exponent for thickness dependence tends to increase with Tg of the rubber and also appears to increase with the vapor pressure of the permeant liquid. Other permeation characteristics, such as the times of initial permeation and of maximum permeation rate, also may have a power-law dependence upon specimen thickness.

INTRODUCTION

There is a requirement to improve the resistance of Army materiel to contamination and permeation by chemical warfare agents[1]. For example, packaging materials, emergency shelters, and protective clothing should be lightweight, flexible, and nonflammable, and yet must resist permeation by toxic gases and liquids. Because of the lack of fundamental information regarding interaction of these agents with polymeric materials, especially those of complex formulation, the routes to be taken toward improved materials are not clear or obvious. Development of suitable new materials with improved permeation resistance must proceed instead from experimental permeation data that have been at least empirically correlated with geometric and materials parameters, such as thickness, compound formulation, and physical properties. This report describes continuing MTL analysis of contractor-performed agent and simulant droplet permeation through a series of rubber materials, and presents MTL empirical correlations of test results with materials and permeant parameters.

RUBBER MATERIALS, CW LIQUIDS, AND DROPLET PERMEATION TESTS

MTL has been working with a series of eleven compounded rubber materials, produced under contract for MTL in nominal thicknesses of 10, 20, and 40 mils by Smithers Scientific Services, Akron, Ohio[2]. Each rubber material was based upon a different type of elastomer and, in accordance with state-of-the-art practice, was formulated with many additional ingredients. Such ingredients typically provide rubbers for a variety of practical applications. These rubbers therefore constituted a series of materials of widely-ranging composition and properties, and are listed in Table 1.

For in-house immersion tests of the rubbers, MTL used two relatively innocuous simulants, identified in Figure 1 as DCP and DIMP. These are simulants for agents HD and GD, respectively. Under contract to MTL, Southern Research Institute (SRI), Birmingham, Alabama performed droplet permeation tests with the same series of rubbers[3]. In addition to DIMP, SRI employed two somewhat toxic simulants, identified in Figure 2 as CEES and DFP. These also are simulants for HD and GD, respectively. Furthermore, SRI used the two real agents, HD and GD, making a total of five liquids employed by them for the droplet permeation testing.

As described in the previous report[3], each SRI droplet permeation experiment involved the deposition of a 5μl droplet of liquid upon a rubber specimen of 10 cm^2 exposed area, with subsequent monitoring of the permeation rate for a period of 24 hours. The breakthrough time (t_b) refers to the time for cumulative permeation of a specified small amount of the liquid. For each experiment, SRI sent test results to MTL which consisted of a tabulation and plot of permeation rate as a function of time during the 24-hour test, plus the value of t_b. MTL has been analyzing these results in order to develop correlations with specimen thickness and with material properties.

For example, MTL has assembled three SRI permeation rate plots, as in Figure 3. Each plot depicts permeation of HD through Neoprene, and differs from the others only in the thickness of the specimen. It is evident that as the specimen thickness increased, the maximum permeation rate decreased, the time to maximum rate increased, and the t_b also increased. Other combinations of permeant and rubber exhibited similar trends with specimen thickness.

CONTINUED DATA ANALYSIS

Because characterization and qualification of protective materials are based almost entirely upon the value of t_b, the bulk of MTL's analyses has been devoted to this quantity. As stated above, increased specimen thickness leads to increased t_b. MTL has continued its empirical treatment of this thickness dependence. By analogy with one-dimensional diffusion, we have assumed that

$$t_b = k l^n \qquad \text{Equation 1}$$

where l is specimen thickness and k and n are constants. Reformulation of this power-law expression gives

$$\log t_b = \log k + n \log l \qquad \text{Equation 2}$$

If these equations are valid, a plot of log t_b versus log l will be linear and the slope will yield a value of n. Previous MTL plots of log t_b versus log l have generally exhibited straight-line behavior, thus indicating the applicability of this empirical treatment[3].

For later SRI droplet permeation tests, MTL has continued this kind of analysis by plotting the SRI data according to the logarithmic expression of Equation 2. Figures 4, 5, and 6 illustrate the MTL plots for three of the penetrant liquids. Each figure depicts the t_b data for one liquid with two or three rubbers. MTL used the method of least-squares to fit the logarithmic data to a straight line, plotted in the figures, and to provide a value for the slope or exponent, n, for each set of results.

The following observations can be made. Figure 4: Silicone was available only in the 40 mil thickness and showed a short t_b with HD. Figure 5: Because of the very rapid permeation by CEES, the relatively large scatter seen here is due to only small deviations in t_b. Figure 6: It was possible to estimate a t_b for DFP through Hypalon only by extrapolation of the SRI permeation rate data and only for the 10 mil specimens. In general, these and other recent logarithmic plots indicate good adherence to straight-line behavior. This continues to suggest the apparent power-law dependence of t_b upon specimen thickness in the range of 10 to 40 mils.

To compare breakthrough results among the various rubber materials, MTL defined a normalized value of t_b for each penetrant/rubber combination. This was chosen arbitrarily as the breakthrough time for a specimen thickness of 30 mils and was calculated from the least-squares linear fit of the logarithmic data, as exemplified in Figures 4, 5, and 6. These rubbers are not systematically related to each other in terms of composition or formulation. However, the glass transition temperature, T_g, is a fundamental material property of each rubber compound and is related to processes involving molecular motion, including diffusion of penetrant molecules through the rubber. For example, with the latest DIMP droplet permeation tests, a plot of normalized t_b versus T_g of the rubber appears in Figure 7. For the seven rubbers showing breakthrough, there is a general increase of t_b with increasing T_g, indicating that the more rigid rubber materials require longer time to allow permeation of the defined small amount of liquid. The Hypalon, Fluorocarbon, and Aflas might possibly undergo breakthrough at longer times and hence continue the same trend, but Butyl is clearly showing anomalous behavior. Similar trends have been noted for the other permeants, all leading to concave upward plots of this type.

ADDITIONAL CORRELATIONS

As mentioned above, one of the parameters involved in this data analysis is the power-law exponent, n, for the thickness dependence of breakthrough time. MTL least-squares analysis of the logarithmic data indicates that n has varied from about 1.3 to 5.0. With a given liquid, MTL has found that n tends to increase with increasing T_g of the rubber. This is shown in Figure 8 for the DFP permeant. (Here the value for Hydrin cannot be exactly determined from the experimental results, but it is greater than the point plotted here, as indicated by the upward-pointing arrow.) By the method of least-squares, these points were fitted arbitrarily to a straight line, also plotted in the figure. Similar trends are evident with the other permeant liquids. The reasons for the range of exponents are not well understood at the present time. MTL mathematical modeling studies indicate that droplet permeation is a complicated process[4]. The complexities include the unknown concentration-dependent diffusivity of the liquid in the rubber sheet, evaporation of liquid from the droplet, shrinking droplet size, changing contact angle, and possible polymer relaxation effects. All of these may affect the power-law exponent. Based upon the increase in t_b with T_g, as shown in Figure 7, the data in Figure 8 suggest the following: With higher T_g rubbers, the higher values of t_b permit more evaporation of liquid and hence more droplet depletion during the tests with all thicknesses. Apparently this increased depletion effect is relatively more pronounced with thicker specimens, thus leading to greater thickness dependence of t_b, hence a larger n.

With rubbers of high T_g, MTL has also observed that n appears to increase with increasing vapor pressure of the permeant liquid. This is illustrated in Figure 9 for two rubbers, Hydrin and Vamac. (The exponent could not be determined for GD permeation through Hydrin). In spite of some scatter, the general trend is evident. This underscores the importance of evaporative depletion of the droplet during the test. In contrast to droplets of low vapor pressure liquids, droplets of high vapor pressure liquids would tend to lose relatively more liquid during permeation of the thicker specimens, thus exhibiting a greater thickness dependence for t_b. Apparently this effect is most pronounced for those rubbers with inherently large values of t_b, namely, rubbers of high T_g, such as Hydrin and Vamac.

As a means of more completely characterizing the droplet permeation process, MTL has begun to examine other aspects of the SRI permeation rate curve, such as those depicted in Figure 3. In addition to the breakthrough time, one can determine a time of initial permeation, a time of maximum permeation rate, and the value of maximum permeation rate. These quantities are all dependent upon specimen thickness, as evident in Figure 3. For GD droplet permeation through Natural Rubber, MTL has made logarithmic plots of these characteristic times as a function of specimen thickness, as in Figure 10. A least-squares treatment was performed to fit each set of data to a straight line, also plotted in the figure. These lines express the data fairly well,

although some curvature of the data may be evident, as well as some instances of considerable scatter. For all thicknesses, breakthrough occurred considerably before the time of maximum permeation rate.

Figure 11 shows a logarithmic plot of maximum permeation rate versus thickness, as well as a repeat plot of the time of this maximum rate. The former quantity appears to drop linearly with thickness when plotted in this fashion. Thicker specimens, therefore, tend to change the permeation process by decreasing the maximum rate and shifting the time over which significant permeation occurs. Figures 10 and 11 help to quantify the apparent power-law thickness dependence of these permeation parameters.

CONCLUSIONS

The latest MTL analysis of contractor-performed agent and simulant droplet permeation tests with the series of rubber materials has continued to indicate a power-law dependence of droplet breakthrough time upon specimen thickness. The normalized breakthrough time and the power-law exponent for thickness dependence both tended to increase with the glass transition temperature of the rubber, demonstrating the effect of rubber flexibility upon the permeation process. The power-law exponent also appeared to increase with the vapor pressure of the permeant liquid, suggesting that evaporative depletion of the droplet has a significant effect upon the permeation rate of thicker specimens. The range of power-law exponents is surprisingly large and indicates the complexity and interplay of numerous factors that are involved in the permeation of small amounts of liquid from a droplet source. The times of initial permeation and of maximum permeation rate and the value of maximum permeation rate all appeared to suggest a power-law dependence upon specimen thickness, providing further information about the features of droplet permeation. All of these empirical correlations will help to characterize and to contrast the droplet permeation of a variety of CW liquids through a wide range of rubber materials.

REFERENCES

1. Army Regulation 70-71, Nuclear, Biological, and Chemical Contamination Survivability of Army Materiel, Dept. of the Army, Washington, DC, May 1984.

2. A. F. Wilde, Standard Rubbers for Chemical Defense Research, Vol. I: Formulation and Properties, MTL TR 89-5, Watertown, MA, January 1989.

3. A. F. Wilde, Chemical Agent and Simulant Interactions with Rubber Materials, Proc. 1987 CRDEC Sci. Conf. on Chem. Def. Rsch., CRDEC-SP-88013, Aberdeen Proving Ground, MD, April 1988.

4. A. P. Angelopoulos, N.S. Schneider, and J. H. Meldon, Numerical Simulation for the Permeation of Barrier Materials by Neat Liquid Droplets, MTL TR 88-35, Watertown, MA, October 1988.

Table 1. SERIES OF COMPOUNDED RUBBERS

Code No.	Rubber Compound (Elastomer Base)	Number of Components	Reinforcing Filler Content (phr*)	Plasticizer and Process Aid Content (phr*)	Shore A Hardness	Glass Temp. (^{o}K)
5	Neoprene	13	65	20	67	218
8	Hydrin	7	25	1	62	249
11	SBR	14	65	16	75	223
1	Butyl	14	75	17	72	208
7	Vamac	8	36	4	60	234
10	Nat. Rubber	11	75	20	70	204
2	Fluorocarbon	6	30	3	78	252
4	Nitrile	11	145	30	75	217
6	Hypalon	12	55	16	80	245
3	Silicone	>2†	†	†	54	149
9	Aflas	5	50	2	83	263

*Parts per 100 parts elastomer
†Proprietary compound obtained by Smithers from supplier

NAME	1,5-DICHLOROPENTANE	DIISOPROPYL METHYL PHOSPHONATE
ABREV	DCP	DIMP
STRUCTURE	Cl-CH_2-CH_2-CH_2-CH_2-CH_2-Cl	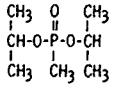
MOL WT.	141	180
MOLAR VOL., cm^3/MOLE	128	184
EST δ, $[J/cm^3]^{1/2}$	19 3	16 2

Figure 1

NAME	2-CHLOROETHYL ETHYL SULFIDE	DIISOPROPYL FLUORO PHOSPHATE
ABBREV	CEES	DFP
STRUCTURE	Cl-CH_2-CH_2-S-CH_2-CH_3	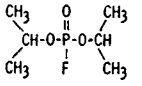
MOL WT	124	184
MOLAR VOL. cm^3/mole	116	167
EST δ $[J/cm^3]^{1/2}$	19.6	16.8

Figure 2

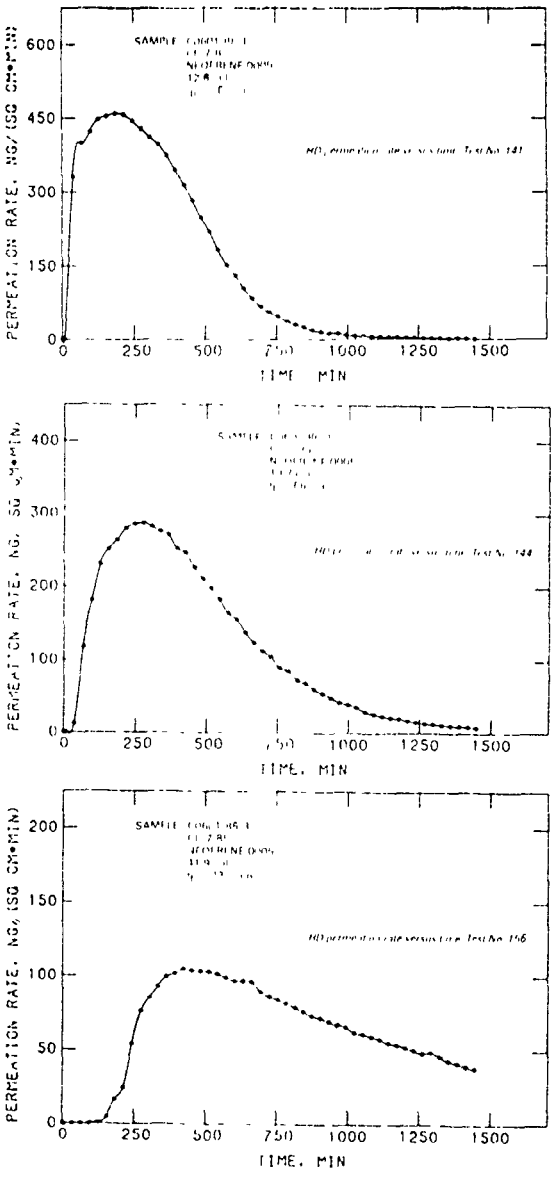

Figure 3

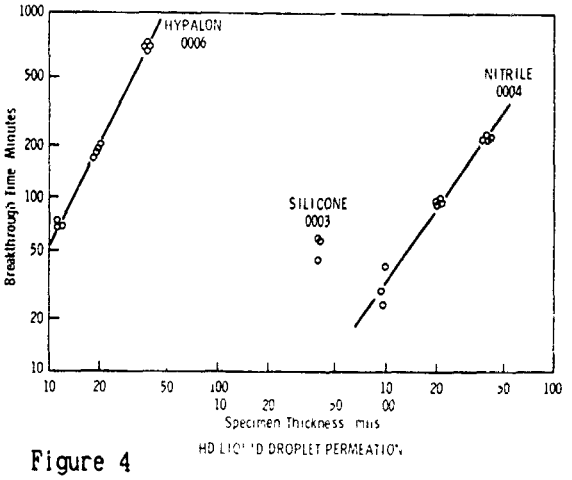

Figure 4

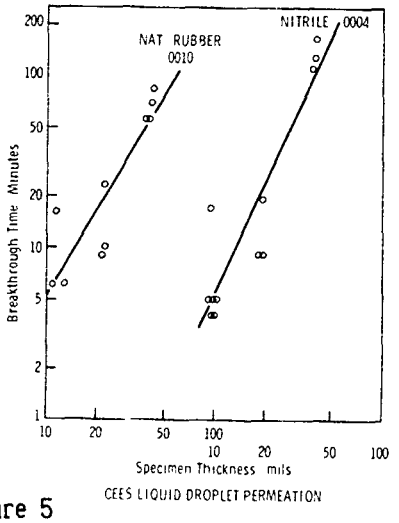

Figure 5

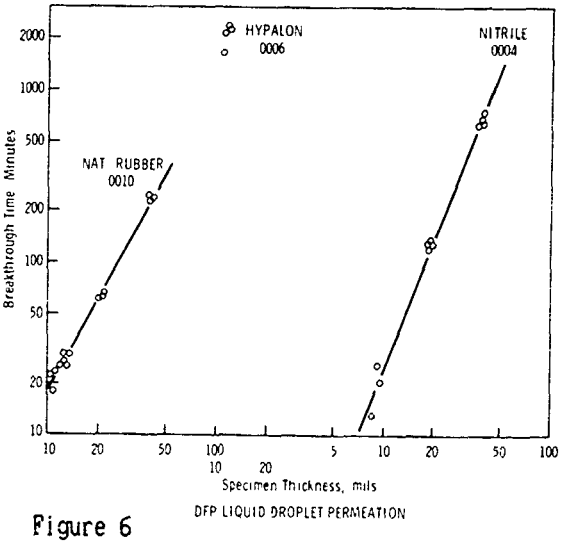

Figure 6

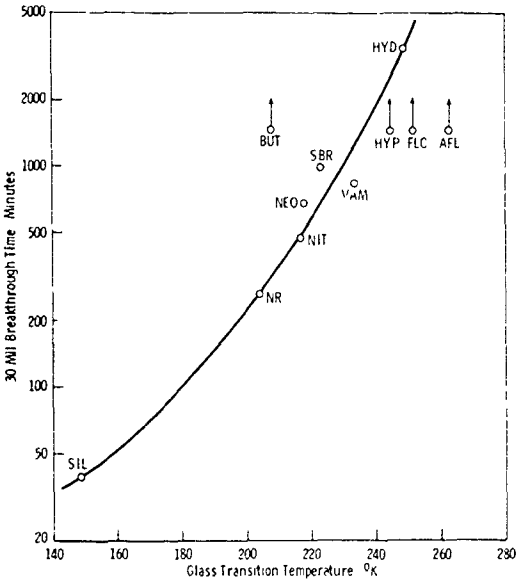

DIMP DROPLET PERMEATION WITH SMITHERS RUBBERS

Figure 7

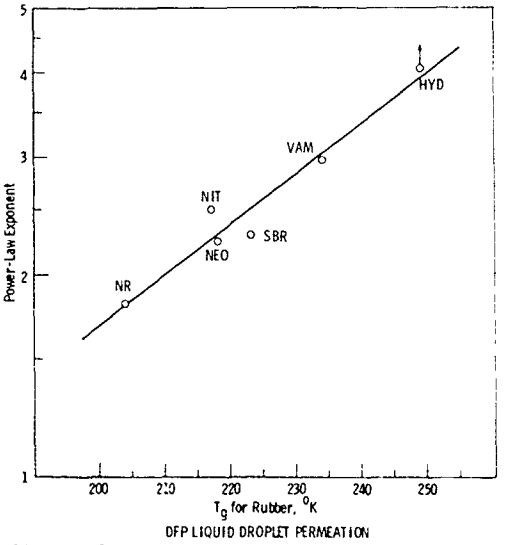

DFP LIQUID DROPLET PERMEATION

Figure 8

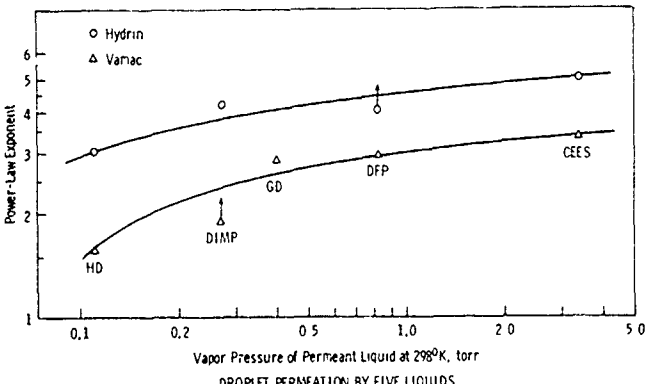

DROPLET PERMEATION BY FIVE LIQUIDS

Figure 9

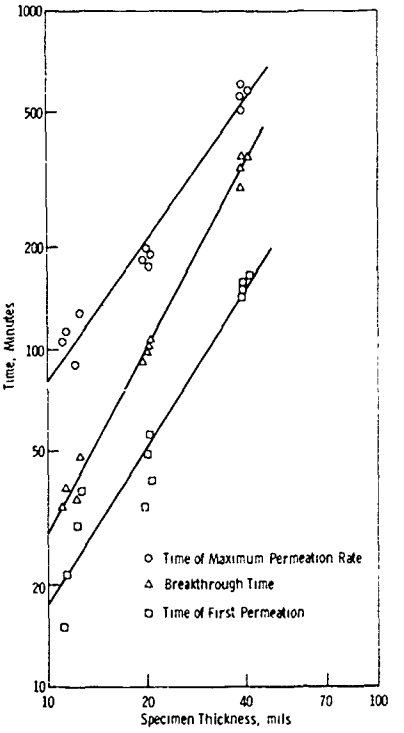

GD LIQUID DROPLET PERMEATION THROUGH NATURAL RUBBER

Figure 10

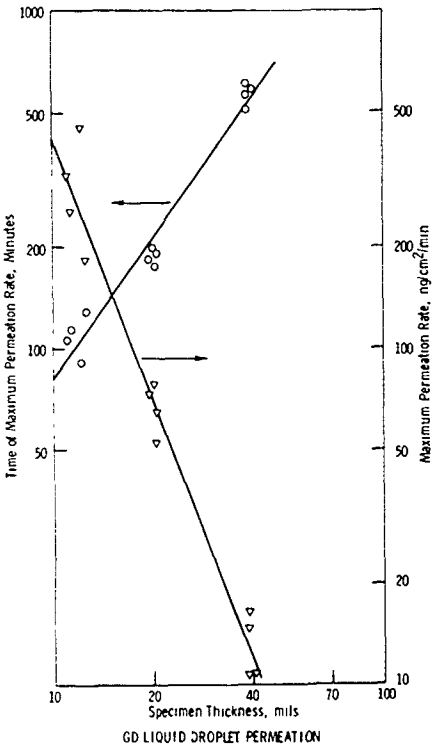

GD LIQUID DROPLET PERMEATION THROUGH NATURAL RUBBER

Figure 11

BLANK

LIQUID SORPTION AND DESORPTION OF CONTAMINANTS FROM CHEMICALLY RESISTANT AND PROTECTIVE POLYMERS

Brian S. Ince and Wendel J. Shuely
U.S. Army Chemical Research, Development and Engineering Center
Aberdeen Proving Ground, MD 21010-5423

ABSTRACT

Research progressed on the development and application of standardized methods for measuring equilibrium liquid or vapor sorption and desorption kinetics relevant to NBC survivable polymers. The liquids used were toxic contaminants and model liquids for solubility, diffusion and permeation processes. Equilibrium solubility and diffusion coefficients were calculated for the following comparative areas of interest: (1) microthermobalance sorption/desorption vs immersion/sorption method (2) vapor vs liquid solubility and (3) toxic contaminants vs model test liquids.

INTRODUCTION

Permeation, diffusion, solubility and extraction of migrants are all important processes for numerous applications. Several application areas of recent interest requiring permeation, diffusion, solubility and extraction data are listed below.

(1) Characterization of chemical resistance of materials and coatings.
(2) Development of protective clothing.
(3) Exposure evaluation to migrants in polymeric materials.
(4) Specification of protective clothing materials for safety data sheets and permit/registration of all new chemicals.
(5) Controlled release of active agricultural chemicals.

TEST METHODOLOGY DEVELOPMENT AND EVALUATION

An important goal is to anchor material-liquid interaction testing with selected standardized tests or experiments for "intrinsic" material properties. Intrinsic properties are those more fundamental properties whose values do not depend on the procedural aspects of the method or those properties that can be measured by two or more independent methods. Non-intrinsic tests are those technology-oriented measurements that are of relatively temporary utility and that yield values that depend on one or more arbitrary, convenience-oriented, or operational steps in the procedure.

In principle, one should be able to design experiments for permeation, diffusion coefficient and equilibrium solubility measurement that yield intrinsic properties. However the conversion of these experiments to tests that are standardized, transportable between laboratories, and safe with hazardous contaminants is challenging. In these studies we investigate the feasibility of obtaining (1) equilibrium solubility from vapor sorption and/or liquid immersion adjusted for extraction and (2) diffusion coefficient from the high concentration, Fickian region of a desorption experiment.

The computerized TGA method described for polymer/liquid interaction can be employed for measuring equilibrium solubility, fraction of extractables removed, and diffusion coefficient. Also, concentration dependent diffusion coefficients might be determined over a wide range of concentrations. In addition, permeation (P) of a liquid through a polymer is a function of solubility (S) and diffusivity (D): $P = DS$. Numerical and analytical models for permeation usually require diffusion and solubility values as input parameters.

COMPARATIVE EVALUATIONS WITH NEW TEST METHODOLOGY

STANDARDIZED MATERIAL-LIQUID PAIRS FOR TEST CALIBRATION AND TESTING VALIDATION. An objective is to evaluate the various material and model liquids for pairs that would serve as candidate standards. These test standards would serve, for example, to validate measurements at new test sites or diagnose testing problems.

INTRA-TEST CORRELATIONS. Many complex and pragmatic transport phenomena can be analyzed to consist of solubility, diffusion, permeation and partitioning components. An integrated series of tests for chemically resistant (survivable) and protective materials would be structured such that the output of one test provided input to a related test or model. Likewise, several intrinsic properties of material-liquid interaction should be combined into functions for correlations with non-intrinsic, operational tests.

LIQUID INTERACTION COMPARISONS. The standardized experiments for equilibrium solubility, extraction and diffusion coefficient can be employed to compare the interaction of two liquids; these are usually to survey and validate a model test liquid (simulant) for material(s). In the process of test development, several such comparisons were obtained and examples are provided.

MATERIAL COMPARISONS. An important application of standard equilibrium solubility and diffusion coefficient measurements is the screening, comparison and selection of candidate material compositions for resistance and protection.

NORMALIZING AND SCALING. Several characteristics of crosslinked, filled and plasticized elastomers complicate quantitative material comparisons. The effect of different filler content can be partially factored out by normalizing liquid to (pure) polymer content. Filler content can be estimated from knowledge of the formulation or from residual mass after a

pyrolitic or TGA experiment. Plasticizers functioning as a preswelling cosolvent for the test liquid can be factored out by pre-extraction of the sample followed by exhaustive vacuum devolatilization of extracting solvent. Alternatively, one might rationalize that the minor differences in plasticizer/additive content and composition between material samples places the materials compared in a nearly plateaued region for solubility diffusion effects. Crosslink density differences between otherwise identical compositions and formulations lead to higher swelling coefficient and equilibrium solubility in the more lightly crosslinked elastomer. The elastomers can be characterized by the effective crosslink concentration if the crosslinking formulation is known.

Specific regimes of high crosslink density and low interaction (and solubility) can lead to attenuated absolute solubilities, however, relative comparisons still cannot be obtained. A test strategy being pursued is the normalization or scaling of crosslink density and other effects to some extent by characterizing a crosslinked polymer with a (near) maximal solubility solvent. The maximal swelling liquid would define the upper limit of solubility and provide a nominal full scale index for each specimen. Identification of maximal solvents can be provided by handbook data on coil expansion coefficients, Flory interaction coefficients, relative LVN values, etc. For example, saturated model repeat units or small branched alkanes usually provided maximal swelling solvents for the usual polkyalkane elastomers.

EXPERIMENTATION

INSTRUMENTATION

A DuPont Model 951 TGA was used. The sample was suspended from a custom holder that was designed to suspend 10-40 mil thick circular sheet stock specimens and accomodate specimens that might swell to some variable new diameter. The computer system that supplements the DuPont Model 990 Controller is a dual PDP-11 system with one data acquisition/ control computer and another computational computer (1). The differential amplifiers have numerous offset and scaling functions which can be used, along with those built-in to the TGA electronics, to assist in various taring strategies.

MATERIALS AND PROCEDURES

The materials employed were those from a standard set of elastomers developed and characterized over the last 2-3 years at the Army Material Technology Laboratory, (MTL), Watertown, MA (2).

Immersion sorption rates with 2-3 solvents have been determined at MTL (3). The abbreviated names or codes for the elastomers are as follows: Butyl, isobutylene/isoprene; Fluorocarbon, vinylidene fluoride/hexafluoropropylene; Silicone, alkyl siloxane; Nitrile, acrylonitrile/butadiene; Neoprene, polychloroprene; Hypalon, chlorosulfonated polyethylene; Vamac, ethylene/methyl acrylate; Hydrin, polyepichlorohydrin; Aflas, tetrafluoroethylene/propylene; Natural Rubber, poly(cis-1,3-isoprene); SBR, styrene/

butadiene. The codes for the model aprotic dipolar liquids are as follows: DIMP, diisopropyl methylphosphonate; DFP, diisopropyl fluorophosphate; TCE, tetrachloroethylene; CEESS, 2-chloroethyl ethyldisulfide; DCP, 1,5-dichloropentane.

RESULTS

DATA REDUCTION EXAMPLE. A typical TGA desorption plot of HD and CEESS in Silicone elastomer is shown in Figure 1. The x-axis is time and the y-axis is residual mass fraction. An even higher data density was recorded in the typical isothermal TGA plot of weight vs time shown in Figure 1 and the number of points displayed is only a restriction of the graphics software. The data file contains a point every 2.5 seconds. The baseline is a nominal value and weight-taring input to the software calculates the fraction extracted. Total equilibrium solubility is determined from the weight at time-zero. A Fickian diffusion coefficient is calculated from the initial half of the weight vs time ** 0.5 relationship.

FIGURE 1

Comparison of Desorptive Diffusion (Mass vs Time) of HD and CEESS From Silicone Elastomer Employing a Computerized TGA Method

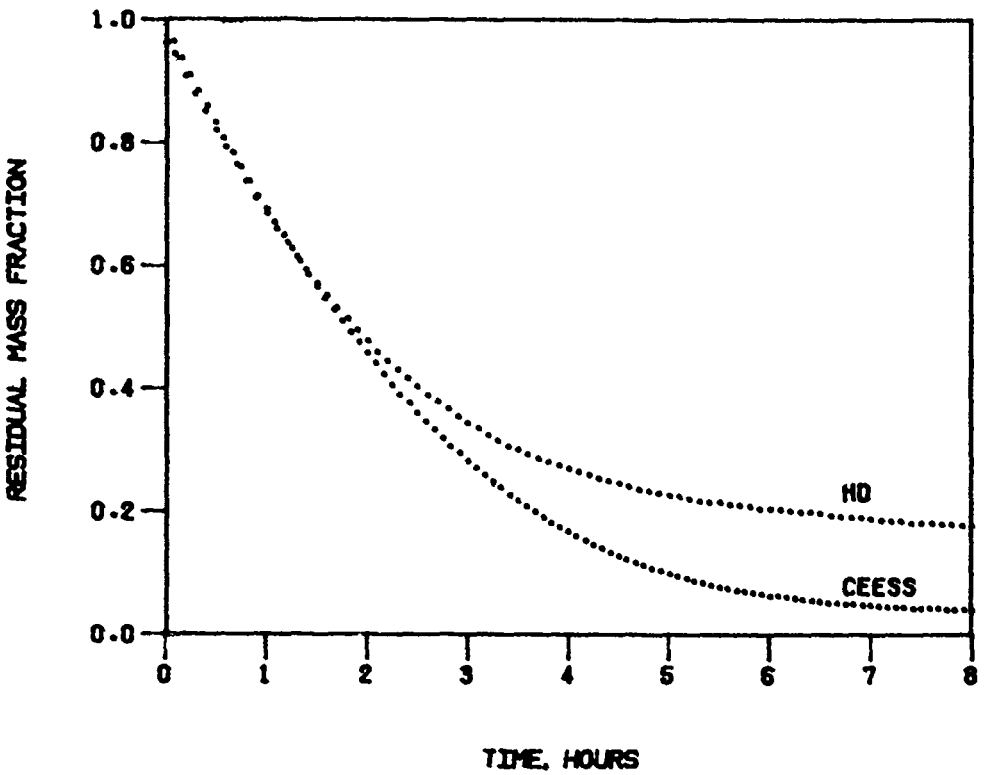

COMPARISONS OF TEST METHODS. Six immersion data sets were available for comparison and the same standard elastomers were measured by the TGA method with identical material lots and model liquids. A comparison of the

immersion and TGA methods for equilibrium solubility for these six constant elastomer/contaminant pairs is shown in Table 1. The total percent of liquid sorbed (Total Sorbed:TS) for both methods compares favorably. A paired t-test found no significant difference between the TGA and the ASTM immersion test as performed by MTL, for TS percent weight gain of liquid by an elastomer.

TABLE 1

Comparison of Equilibrium Solubility by Thermogravimetric Analysis (TGA) and Immersion Sorption (IS) Methods (TS: Maximum Percent wt gain, from Sorption process; EX: Total Percent extractables, from desorption process; TD: Maximum Percent wt gain, from desorption process)

Liquid:	Polymer	TS:TGA Percent		TS:IS Percent	EX:TGA Percent	EX:IS Percent	TD:TGA Percent	TD:IS Percent
DIMP:	Vamac	185	<	195	19	-	204	-
DIMP:	Nitrile	67	<	76	12	-	79	-
DIMP:	Silicone	40	>	39	3	-	43	-
DIMP:	SBR	28	<	33	11	-	39	-
TCE:	SBR	193	<	243	8	-	201	-
TCE:	Hydrin	38	>	36	2	-	40	-

The total percent of liquid desorbed (Total Desorbed:TD) obtained from the TGA method allows the determination of a value for percent extractables for each elastomer/contaminant pair. These values for percent extractables for the TGA method are compared in Table 2 with two other experimentally determined data sets and also to the calculated extractables based on the formulations of the individual elastomers. The macrobalance (MB) data were determined at MTL (4) and the values compare (within 1-2 wt% absolute) with the TGA data for each of the three same elastomer/contaminant pairs. The values for the TGA and MB methods fall within or exceed the calculated extraction. The sorption plateau (SP) values were obtained from liquid-immersion sorption kinetics plots (3). The large measured, compared to calculated, extractables for Vamac, from 2.9 to 50, could be indicating incomplete cure, uneven distribution of migratables in these specimens, or other inhomogeneity among the Vamac elastomer sample lot and should be further investigated. Nitrile and SBR values suggest that their lot homogeneity should also be studied.

TABLE 2

Comparison of Fraction Extracted (%) by a TGA Desorption and Macrobalance (MB) or Sorption Plateau (SP) Method

Liquid:	Polymer	Calculated Extraction	TGA	MB	SP
DIMP:	Vamac	2.9 - 7.8	19	17	50
DIMP:	Nitrile	8.7 - 10.9	12	13	6
DIMP:	Silicone	Unknown	3	4	5
DIMP:	SBR	8.1 - 9.6	11	-	16
TCE:	SBR	8.1 - 9.6	8	-	0
TCE:	Hydrin	0.7 - 2.2	2	-	2

Table 3 shows a comparison of the immersion sorption and TGA desorption methods for diffusion coefficients for the six elastomer/contaminant pairs. The TGA method generally gives lower values as expected since the desorption process is theoretically slower than the sorption process.

TABLE 3

Comparison of Diffusion Coefficients by a TGA Desorption and Immersion Sorption (IS) Methods ($D \times 10^8$)

Liquid:	Polymer	TGA		IS(3)	% Difference	Ratio
DIMP:	Vamac	0.49	<	7.4	1410	15.1
DIMP:	Nitrile	0.86	<	9.0	947	10.5
DIMP:	Silicone	8.90	<	37.0	316	4.2
DIMP:	SBR	1.9	<	6.3	232	3.3
TCE:	SBR	12.4	<	56.2	353	4.5
TCE:	Hydrin	4.2	>	2.9	31	0.7

Table 4 shows a comparison of the TGA and MB desorption methods for diffusion coefficients for the identical elastomer/contaminant pairs. Generally, the MB method produces nominally higher diffusion coefficients though the differences are not statistically significant by a paired t-test.

TABLE 4

Comparison of Diffusion Coefficients by a TGA and Macrobalance (MB) Desorption Methods ($D \times 10^8$)

Liquid:	Polymer	TGA	MB	% Difference	Ratio
DIMP:	Vamac	0.49	4.3	778	8.8
DIMP:	Nitrile	0.86	4.7	447	5.5
DIMP:	Silicone	8.90	9.7	9	1.1

COMPARISON OF VAPOR VS LIQUID SORPTION. Several polymer-liquid pairs have been equilibrated under both liquid immersion and saturated vapor conditions. The two examples for which both vapor and liquid comparisons are available are shown in Table 5. The differences range between 2 and 4 percent and are in different directions. The liquid sorption values compared include extractables replaced by sorbant. The results show that equilibrium solubility as measured by high activity vapor and liquid sorption were equivalent. Experimental procedures of concern which influence vapor-liquid comparison and which are under further study are: (1) immersion specimen: washing/blotting (2) vapor specimen: surface gloss removal and (3) experimental temperature.

TABLE 5

Comparison of Equilibrium Solubility Values (%) from Liquid and Vapor Sorption Experiments at 25 deg C

Liquid:	Polymer	Liquid	Vapor	Difference Relative %	Ratio
GD:	Nitrile	55.9	58.0	3.8	1.04
CEESS:	Silicone	23.4	22.9	2.2	0.98

COMPARISON OF CONTAMINANTS AND MODEL LIQUIDS. Diffusion coefficients and equilibrium solubility for GD and the two candidate model liquids DFP and

DIMP are shown in Table 6. These updated values on these polymer-liquid systems replaces previous data (5,6) which should be disregarded.

TABLE 6

Comparison of Diffusion Coefficient (D) (x 10^8) and Equilibrium Solubility (EqS) for Elastomers with Organophosphorus Liquids

Polymer		GD	DFP	RATIO	DIMP	RATIO
Silicone,	D:	20.	-	-	8.9	0.45
	EqS:	26.0	-	-	43.1	1.7
SBR,	D:	1.1	2.3	2.1	1.9	1.7
	EqS:	48.6	21.2	0.44	39.4	0.81
Nitrile,	D:	0.85	2.2	2.6	0.86	1.0
	EqS:	58.0	28.0	0.48	78.7	1.4
Vamac,	D:	0.47	-	-	0.49	1.0
	EqS:	83.9	-	-	204.	2.4

Three model liquids were designed and synthesized (in collaboration with R. Kassel, CRDEC and N. Schneider, MTL) as candidate material interaction test liquids for bis(2-chloroethyl) sulfide (HD): 2-chloroethyl ethyl disulfide (CEESS), bis(2-chloroethyl) disulfide (BCESS) and bis(3-chloropropyl) sulfide (BCPS) (7). The CEESS results are shown in Table 7 in which HD, CEESS and DCP solubility and diffusion coefficient measurements are compared.

For silicone rubber the HD and CEESS diffusion coefficients are very close while the DCP value is thirteen times larger. Both simulant solubility values are significantly higher. The remaining comparisons are for HD vs DCP in butyl and nitrile rubbers; diffusion coefficients differ by a factor of 6 to 156 and solubility by 0.8 to 4 times, and again (6) show DCP to be a very inaccurate simulant.

The solvent parameters and vapor pressure (7) of CEESS have been recently determined and compared with HD and both are in a range which suggest that CEESS is the most promising candidate as a HD test liquid.

TABLE 7

Comparison of Diffusion Coefficient (D) (x 10^8) and Equilibrium Solubility (EqS) for HD and HD Model Liquids in Elastomers

Polymer		HD	CEESS	RATIO	DCP	RATIO
Silicone	D	9.1	8.0	0.9	117.	13.
	EqS	6.0	22.9	3.8	26.	4.3
Butyl	D	0.60	-	-	4.1	6.7
	EqS	8.1	-	-	34.	4.2
Nitrile	D	0.17	-	-	26.	156.
	EqS	150.	-	-	121.	0.8

CONCLUSIONS

An instrumentation system, procedures and data reduction method have been developed which provides several advantages and improvements, among which are:

(1) The capability of measuring equilibrium solubility, diffusion coefficient and fraction-extracted on the identical material specimen,

(2) An extremely high data density throughout the desorptive diffusion process that allows the possibility of detection of non-Fickian processes and calculation of concentration dependent diffusion coefficients, and

(3) The method employs small samples and small hazardous contaminant volumes, requires minimal handling of hazardous materials, and can be conducted entirely in a fume hood.

The sorption/desorption/extracted-fraction methodology based on computerized TGA instrumentation was compared with a conventional immersion sorption method. A paired t-test of identical polymer-liquid pairs at alpha = 0.05 resulted in an inability to reject the hypothesis that the methods were equivalent. That is, no significant difference was found for the following comparisons:

(1) TGA desorption vs ASTM/MTL immersion method for equilibrium solubility and diffusion coefficient,

(2) TGA desorption vs macrobalance method for fraction extracted, and

(3) TGA vs macrobalance desorption for diffusion coefficient.

Comparisons were completed for two polymer-liquid pairs for equilibrium solubility by high activity vapor vs liquid sorption; both contaminant exposure methods were equivalent.

The capabilities of the computerized TGA with regard to providing comparisons of toxic contaminants with model test liquids were demonstrated by equilibrium solubility and diffusion coefficient measurements. GD and HD were compared with two model liquids each for an (incomplete) matrix of 4 and 3 polymers respectively. Interim conclusions based on partial results obtained to date suggest that the accuracy of (1) GD test liquids varied by material composition and experimental property and (2) HD test liquids were very poor for 1,5-dichloropentane (DCP) with respect to material composition and properties and was promising for 2-chloroethyl ethyldisulfide (CEESS).

Certain results and conclusions presented at the conference could not be included in the proceedings (due to space limitations) and these are summarized below.

The methodology was shown to be capable of measuring differences in diffusion coefficient and equilibrium solubility among similar formulations of the same generic silicone polymer.

GD and HD were compared to reveal which materials were resistant to both, only one, or neither liquid.

Polymer Cohesion Phase Diagram calculations of predicted GD solubility were completed and several comparisons were provided for measured equilibrium solubility vs predicted solubility.

REFERENCES

1. Shuely, Wendel J.; McHugh, Vincent M. and Ince, Brian S. CRDEC-TR-88054. Development of Computer-Controlled Thermogravimetric Instrumentation for Measurement of Environmental and High Temperature Volatilization and Desorption of Contaminants from Polymeric Materials. April 1988. UNCLASSIFIED Report.

2. Wilde, Anthony F. MTL-TR-89-5. Standard Rubbers for Chemical Defense Research, Volume I: Formulation and Properties. January 1989. UNCLASSIFIED Report.

3. Wilde, Anthony F. MTL-TR-89-48. Standard Rubbers for Chemical Defense Research, Volume II: MTL Immersion Tests with Decontaminants and Simulants. June 1989. UNCLASSIFIED Report.

4. Wilde, Anthony F. Private Communication. MTL, Watertown, MA.

5. Shuely, Wendel J. and Ince, Brian S. CRDEC-SP-013. Development of Procedures for the Measurement of Vapor Sorption followed by Desorption and Comparisons with Polymer Cohesion Parameter and Polymer Coil Expansion Values. Proceedings of the 1988 U.S. Army Chemical Research, Development and Engineering Center Scientific Conference on Chemical Defense Research, 15-18 November 1988. August 1989. UNCLASSIFIED Report.

6. Shuely, Wendel J.; Ince, Brian S. and McHugh, Vincent M. CRDEC-SP-89011 Material Interactions with Agents and Simulants. Proceedings of the Third International Simulant Workshop, U.S. Army Chemical Research, Development and Engineering Center, 7-9 March 1989. UNCLASSIFIED Report.

7. Fielder, Donald; Brozena, Ann; Beaudry, William T.; Rohrbaugh, Dennis K.; Szafraniec, Linda L. and McHugh, Vincent M. CRDEC-TR-xxx. Selected Physical and Spectrometric Properties of Candidate Mustard (HD) Simulants EA 5957, EA 5983 and EA 5992. In Preparation. UNCLASSIFIED Report.

BLANK

THE INTERPRETATION OF SORPTION AND PERMEATION MEASUREMENTS IN POLYMERS

Nathaniel S. Schneider and Anthony F. Wilde
Polymer Research Branch, SLCMT-EMP,
Army Materials Technology Laboratory, Watertown, MA 02172

ABSTRACT

Permeation measurements with a droplet source and with air flow over the droplet and membrane yield an empirical, field related, measure of barrier performance in terms of a breakthrough time, t_B. Alternative test methods offer the advantages of improved reproducibility and are better suited to obtaining values of the fundamental controlling parameters. A recent numerical solution to droplet permeation leads to a closed expression for t_B, which clarifies the dependence of t_B on transport and geometrical parameters. The approach, interpretation and some of the experimental precautions with the various experimental methods are discussed. Also, comparisons between experimental data and the predictions of the model are made which indicate some serious limitations of the model in accounting for the effect of thickness dependence and of air flow on t_B.

INTRODUCTION

The preferred method of assessing the performance of polymer barrier materials, involves some form of permeation testing, usually with a droplet challenge and air flow over the surface of the sample and the droplet. The rational for this approach is that it provides a reasonable simulation of the conditions of field exposure, in that the agent is delivered to the battle field in droplet form and evaporation of the droplet competes with permeation. The drawbacks include poor reproducibility and the difficulty of interpreting the results in terms of test conditions or fundamental parameters. It appears likely that the poor reproducibility is due to variability of the substrate surface which affects droplet wetting and spreading. To eliminate these effects, it has been proposed that permeation testing be conducted with a fully flooded surface. This offers the further advantage of a simple theoretical model for interpretation of the data. Fundamental studies of the interaction of liquids with polymer materials have favored the use of liquid or vapor sorption methods, where the barrier is exposed to a uniform, constant surface concentration, because the experimental results are directly

interpretable in terms of solubility and diffusion coefficients. A recently developed numerical solution to permeation from a droplet source, which takes account of the shrinking droplet radius, leads to a closed expression for t_B (1). This paper is concerned with the measurement and interpretation of the results from the different methods with emphasis on a comparison of the experimental results with the predictions of the droplet permeation model.

The Model of Droplet Permeation

A schematic representation of the droplet challenge is shown in Figure 1. The essential controlling parameters, include the diffusion constant, D, the solubility, C_o, and the contact angle, θ, which may be a function of time. In addition, evaporation from the droplet and the membrane surface, characterized by mass transfer coefficients, k_d and k_m, must be taken into account. The analysis, referred to above, treats the problem of diffusion from the shrinking droplet and computes the permeation rate, $\dot{Q}(t)$, and the droplet radius, R(t), as a function of time. The model also provides an explicit relation for the breakthrough time, which will be presented later.

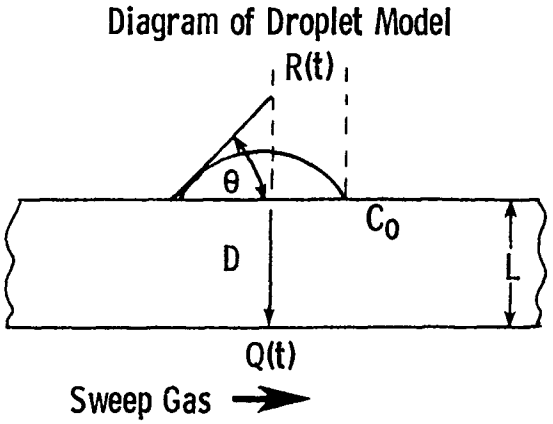

Figure 1. Schematic representation of a droplet challenge on a polymer membrane.

With a droplet challenge there is, ordinarily, no steady state. A typical permeation rate curve is shown in Figure 2, for diisopropyl methylphosphonate (DIMP) in a 22 mil Neoprene sample (2). The permeation resistance is usually characterized by a single parameter, the breakthrough time, t_B, as indicated in the figure.

Since the numerical model depends on a knowledge of the diffusion coefficient, D, and the solubility, C_o, it is of interest to examine how these parameters can be determined. With a fully flooded surface, the challenge concentration is both uniform and constant with time. The permeation rate, $\dot{Q}(t)$, increases monotonically and reaches a constant steady state value $\dot{Q}(\infty)$. Diffusion and solubility coefficients can be obtained from the following relations (3):

$$D = L^2/7.2t_{1/2} \qquad C_o = L\dot{Q}(\infty)/D \qquad (1)$$

where $t_{1/2}$ is the time to achieve one-half the maximum permeation rate and L is the thickness. Other methods of interpretation are available which, in the case of concentration dependent diffusion, provide different average values of the diffusion coefficient.

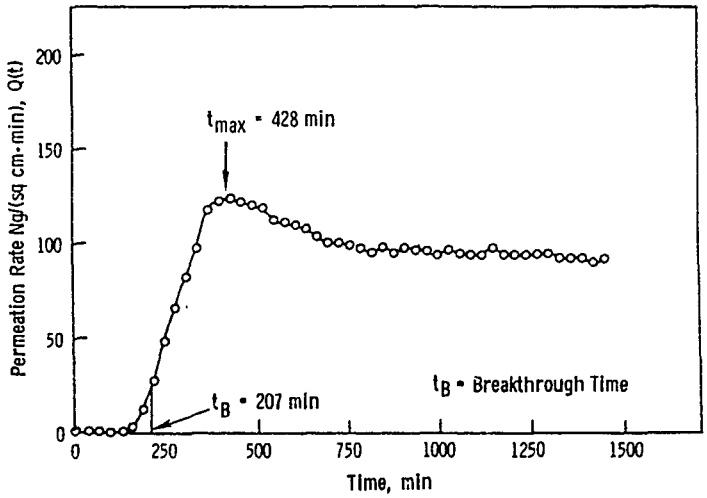

Figure 2. Permeation rate $\dot{Q}(t)$ versus time for a 5 microliter drop of diisopropyl methyl phosphonate on a 22 mil Neoprene sample, without air flow over the droplet and the upper surface of the membrane.

Sorption Measurements at Saturation

A common method of characterizing the interactions of a liquid with a polymer is to perform an immersion test, where the weight uptake is determined as a function of time until a constant value is obtained, indicating that equilibrium or saturation has occurred. If the behavior is Fickian, the uptake, plotted as a function of the square-root of time, is initially linear and through the origin. The diffusion coefficient can be obtained from the half-time, $t_{1/2}$, the time to reach one half the maximum weight gain (4):

$$D = 0.0492L^2/t_{1/2} \qquad (2)$$

and the solubility is directly the equilibrium weight gain. However, complications can occur, due to the fact that many samples of commercial interest contain a mixture of components, including plasticizers and processing aids, which are extractable. In such cases, there will be a maximum in the weight gain curve followed by a drop to a lower weight or possibly, continuing weight loss over an extended time, illustrated by the example in Figure 3,.

Because of the problems with extraction under immersion conditions, there has been interest in conducting experiments in the saturated vapor. The saturated vapor corresponds to unit activity and should give results indentical to the liquid, if the experiment is performed properly. the following is an example of problems which can arise in such a test. A small water jacketed chamber, 375 cc, was used to carry out vapor sorption runs using dichloropentane, p_o = 2.5 mm Hg at 34°C, with a natural rubber sample, weight 1.2 grams (5). Only 22% uptake occurred when the cell was thermostatted by water at 34°C. This increased to 45% when the cell was unheated and, at

longer times, to about 70%. The anomalous behavior was attributed to the circulation of vapor in the chamber, traveling up the ouside wall, cooling in contact with the unheated cap and flowing down over the heated sample, resulting in vapor which was undersaturated at the sample temperature. When the cell was placed in a 34°C oven, the uptake increased continuously to reach 90%, but the rate was much slower than in the liquid. With a low vapor pressure liquid the rate of uptake can be limited by the rate of evaporation. It was computed that it would require about 175 cell volumes of vapor to saturate the sample. Thus, under the properly controlled conditions, this vapor sorption method can be used to determine solubilities with low vapor pressure liquids but frequently will not give proper sorption rates for determining diffusion coefficients. An alternative approach is to first saturate the sample with vapor and then determine the desorption rate in flowing air with adequate thermostatting. However, if the diffusion coefficient is a strongly increasing function of concentration, the value determined on desorption will be appreciably lower than the value on sorption. In addition, the final stage of desorption will be extended to extremly long times.

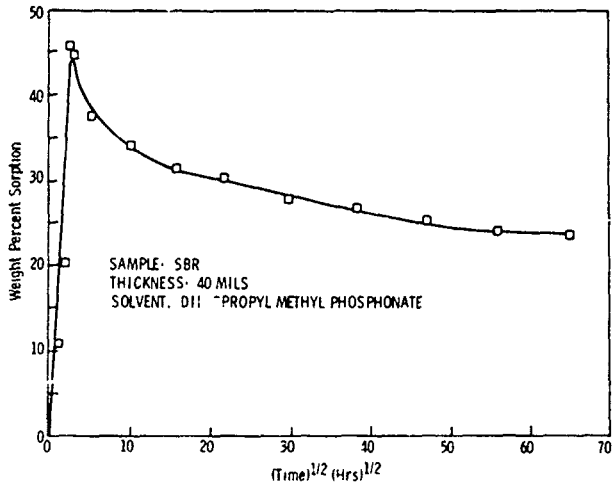

Figure 3. Immersion sorption-rate curve for diisopropyl methyl phosphonate in 40 mil SBR sample, showing a maximum in the weight gain related to the extraction of components in the formulation.

The Breakthrough Time

The breakthrough time, t_B, is defined in relation to the cumulative amount of agent which will first cause a physiological effect, usually normalized to the exposed membrane area. Typical values are; for HD, 1810 ng/cm^2 and for GD 540 ng/cm^2. Analysis of a considerable body of data on the droplet permeation of various elastomer samples has shown that the thickness dependence of t_B can be fitted by an exponential relation of the form (6):

$$t_B = kL^n \qquad (3)$$

where L is the film thickness. The exponent, n, is found to vary widely, ranging between 1.3 and 5.0, depending on the elastomer and challenge liquid.

A first approximation to a closed expression for the breakthrough time,

obtained by fitting the early time permeation rate curve obtained from the numerical model in dimensionless form, is as follows (1):

$$t_B = \frac{0.212}{D}\left(\frac{Q}{C_o R_o^2}\right)^{0.225} L^{1.775} \qquad (4)$$

where Q is the cumulative amount (gm) at break-through, L is the barrier thickness (cm), D is the diffusion coefficient (cm^2/sec), C_o is the solubility at saturation (gm/cc), and R_o is the radius (cm). The exponental dependence on thickness is consistent with experimental evidence. Also, t_B is inversly proportional to D, in common with the half-time relations (1) and (2). In contrast, t_B shows a weak dependence on the other parameters. If this expression holds, then t_B should not be sensitively dependent on R_o and, therefore, should not be unduely influenced by the variability of surface conditions.

This relation and results from the numerical modelling can also be used as a means of scaling test conditions for changes in cell geometry. Table 1 compares conditions used in testing by Southern Research (3) and by Battelle (8). The tests differ primarily in the size of the exposed sample surface. Battelle made some adjustments for the larger surface area of their cell in choosing the drop size and the definition of breakthrough. One conclusion of the numerical modelling is that there is no effect of the drop, beyond a distance of three times the initial radius. Therefore, the threefold larger sample area of the Battelle test cell should have not have required any adjustment in the test conditions.

TABLE 1

Comparison of Droplet Permeation Test Parameters

	Surface Area (cm^2)	Amt. HD Deposited*	HD Breakthrough Definition/Amount		HD Deposited / HD Brkthr.
SRI	10	6.35 mg (5μl)	1810 ng/cm_2	18.1μg	351
BCL	31.7	15.8 mg (12.4μl)	4000 ng/cm2	127 μg	125

*Corresponding to 5g/m^2

Limitations and Extensions of the Model for Droplet Permeation

The most obviously limitation of the above relation for t_B is the fixed value of the exponent in contrast to the widely varying experimental values. In addition, the relation lacks any dependence on a mass transfer coefficient, which would represent the effects of evaporation from the droplet and the membrane with air flow in the upper chamber. Table 2 summarizes the distribution of the droplet of HD in the permeation of a 10 mil Vamac elastomer sample, based on Battelle data (7), where the loss of agent to the air stream was determined by trapping, using a single bubbler for the six hour duration of the test. The amount of loss has been prorated based on the six hour test results, to arrive at the value used in the comparison at the 24 minute breakthrough time. A considerable portion of the total loss from the droplet is due

to evaporation, even at this early time. However, the depletion of the droplet is so small that evaporation should have no effect on the breakthrough at 24 minutes but could have a considerable effect on breakthrough for longer times. The problem is also evident in comparing permeation rate curves for DIMP in 20 mil Neoprene samples: without flow in the upper chamber, t_B = 210 minutes and t_{MAX} = 430 minutes, where t_{MAX} is the time to the maximum permeation rate; with 1 liter/min flow, t_B = 440 minutes and t_{MAX} = 1000 minutes.

Table 2

Agent Distribution in Droplet Permeation Test*
Note: Amounts in Micrograms

	24 min.	480 min.		
Amt. Permeated:	127	1920	Initial amt. of droplet:	15830
Amt. Evaporated:	137	2740	Evap. and perm.(24 min.):	2%
Total:	264	4660	Evap. and perm.(480 min.):	30%
% Evaporated:	52	60	% In membrane (480 min.):	70%

* Data from Battelle. Conditions: Vamac sample (10 mil), 12.5μl HD, 1 liter/min. air flow rate, breakthrough time 24 min. Percent in membrane assuming no surface liquid at 480 minutes.

It seems likely, on first consideration, that the variation in the thickness exponent and the effect of evaporation are coupled. This is reinforced by the fact that the exponent is greater for elastomers with lower diffusion coefficients and, therefore, longer breakthrough times. Also the exponent increases moderately with increasing vapor pressure of the challenge liquid. It is possible to modify the previous relation for t_B by incorporating an explicit dependence on mass transfer. An example is given by the following expression in dimensionless form:

$$\frac{t_B D_M}{L^2} = \left(\frac{Q}{CR_o^3}\right)^{\beta} \left(\frac{L}{R_o}\right)^{\gamma_1 + \gamma_2 H^{\gamma_3} \left(\frac{D_G MP^*}{D_M CRT}\right)^{\gamma_4}} \qquad (6)$$

Here H is a mass transfer coefficient which incorporate the air velocity, viscosity and diffusion coefficient in the sweep gas. P^* is the vapor pressure, M is the molecular weight of the challenge liquid and $D_G MP^*/D_M C$ represents the ratio of the mass transfer rate in stagnant air to that in the membrane. This modification reflects the observed increase in the thickness exponent for polymers of decreasing diffusion constant and with liquids of increasing vapor pressure. For consistency with the original version in equation 4, γ_1 must be negative and less than or equal to 0.225. It might be expected that with a sealed upper chamber, the thickness dependence would be very different. Data under this test condition is limited. However, it appears that the variation in the thickness exponent is similar to that with air flow in the upper chamber. This suggests that the effects of evaporation on the breakthrough time might not be the main factor contributing to the variation in the thickness exponent, as expressed in the above equation.

CONCLUSIONS

Several alternatives exist to droplet permeation testing to measure the barrier performance of polymer materials. These measurements, when properly performed, are also useful in obtaining values of the fundamental transport parameters needed for an understanding of the materials behavior. The results are also required in using the recently developed model for prediction or for correlation. However, comparison of the modelling and experimental results indicate that there are limitations in the numerical model for the prediction of the thickness effect on t_B and in taking account of the evaporation effects. There are two problems in achieving further advances. First there is the need for additional experimental data of high reliability to test the predictions of the theory in its current form. There is also the need for data to confirm and extend the empirical observations which are needed to establish a secure basis for further developments in the theory.

REFERENCES

1. "Numerical Simulation for the Permeation of Materials by Neat Liquid Droplets", A.P. Angelopoulos, N.S. Schneider, J.H. Meldon, MTL TR 88-45 (Oct. 1988).
2. "Immersion and Permeation Testing of Chemical Agent Polymers", Southern Research Institute, MTL TR 87-60.
3. R.M. Felder, J. Membr. Sci., 18, 15 (1978).
4. J. Crank, "Mathematics of Diffusion", 2nd ed., Oxford University Press, London, 1975.
5. A.F. Wilde, unpublished results.
6. "Interaction of CW Agents and Simulants with Rubber Materials", A.F. Wilde, MTL TR 89-103, (Nov. 1989).
7. Results reported by Battelle Columbus Laboratories, in work performed under contract DAAG 29-81-D-01000, (1986).

BLANK

A NEW METHOD OF ESTIMATING STRAIN TO FAILURE (CRACKING/CRAZING) OF POLYMERIC MATERIALS UNDER CHEMICAL STRESS

Larry M. Sturdivan, E. William Sarver, and Paul S. Grasso
U.S. Army Chemical Research, Development and Engineering Center
Aberdeen Proving Ground, Maryland 21010-5423

ABSTRACT

The traditional ASTM method of estimating a failure due to strain in a polymeric material identifies a "critical strain" at which the material will fail, given sufficient time. In the present situation, the strain is modified by the presence of chemicals. Given the variance in the properties of the material, the amount and placement of the chemical, and the interaction between them, the strain to failure is not well approximated as a deterministic quantity. The proposed method fits a probability distribution function to the strain versus failure data (where time to failure is terminated 30 minutes with a result of "no failure"). In this context, the critical strain could be taken as the strain at which 50% of the samples would fail. The first application of the results is to tests using transparent polymers in the presence of both chemical agents and simulants.

1. INTRODUCTION

ASTM method 790-80 is used to estimate a "critical strain" in a material, i.e., a value of strain at which the material would fail given a sufficient time. The apparatus called for in this method is the three-point rig depicted in Figure 1. A test strip of the polymer is held at each end and a strain is induced by raising the center support above a neutral plane. The strain is calculated from the following formula:

$$r = 6Dd/L^2 \tag{1}$$

where r = strain in the top layer

D = Displacement of the sample in the center

d = thickness of the sample

and L = Length of the support span (end to end).

2. PROCEDURE

The ASTM procedure was modified to allow the addition of a drop of solvent (chemical agent or simulant) to the top surface of the test strip in the center of the strip at a location just above the center support. If the material added is, indeed, a

solvent of the polymer being tested, the value of the critical strain is lowered by the addition of a chemical stress to the mechanical stress already present in the sample. In practice, the concept of a "critical strain" in this modified test cannot be realized. Variance in the homogeneity of the material, in the placement of the drop, in the size of the drop, and in the measurement of the thickness and displacement of the sample all lead to a different critical strain for each sample. Thus, it was necessary to modify the analysis of the data to allow for the concept of a mean strain to failure for each combination of material and challenge. This is accomplished by expressing the functional relation as a probability of failure (cracking or crazing) as a function of the strain on the surface exposed to the chemical. As it is expected that the standard deviation (square root of the total variance) would vary with the mean strain to failure, the data should be expressed as the logarithm of the strain. The function chosen for the analysis is the Logistic probability distribution function. If p is the probability of failure of the sample, the Logistic may be written

$$p = \frac{1}{1 + exp(-a - b\ ln(strain))} \tag{2}$$

where a and b are the parameters of the Logistic. The mean is $-a/b$ and the standard deviation is $\frac{\pi}{b\sqrt{3}}$.

There are several fitting routines that could be used to fit this function to data. Most standard statistical packages on mainframe computers (e.g. BMDP) will fit Maximum Likelihood Estimates for the Logistic. The routine of choice for obtaining the estimates at CRDEC is the in-house routine called Linearized Least Squares (Sturdivan and Jameson, reference 1). This routine fits approximate minimum χ^2 estimates to dose-response curves and is preferred because it is easily adapted to fitting a vector of parameters of arbitrary length in place of a and b of equation 2 (see below).

The data should be acquired with an experimental design that will give a good mix of failures and non-failures, such as the up-down method. The data may then be fitted to equation 2 to produce estimates of a and b. This will produce a reasonably good estimate of the mean strain (strain that would have a 50% chance of producing a failure) with a moderate number of samples, but would require a larger number of samples to produce an equally good estimate of the standard deviation. The components of variance, however, are additive. That is, variances from all the sources mentioned above will be cumulative. It is often feasible to assume, however, that the variance due to a particular combination of solvent and substrate is small compared to the other sources of variance. As these other components of variance will not change with the solvent used, one may, under that assumption, pool the data on different solvents used with a single substrate to fit for individual means with a common variance. This is easily achieved by fitting the following function:

$$p = \frac{1}{1 + exp(-\Sigma\ a_i - b\ ln(strain))} \tag{3}$$

To fit equation 3 to the pooled data, one uses "dummy" regressors that are have the value 1 for the first position for the first set and 0 for the others, 1 in the second

position for the second set, etc. If there are n sets, the result is a vector of n+1 parameters, i.e., $\{a_1, a_2, \cdots, a_n, b\}$. The common standard deviation may then be calculated from the estimate of b and the n means from the ratios $-a_i/b$.

If the data thus fitted include both agents and simulants, the method of picking the best simulant for a particular agent is simple; just pick the one which has a value of a closest to that of the agent.

3. CONCLUSIONS AND RECOMMENDATIONS

The above procedure is recommended for obtaining estimates of the mean failure stress of the various combinations of solvent and material, while developing a pooled estimate of the variance based on a much larger sample. This allows one to estimate stress levels for responses other that the usual 50% (mean) dose. I.e., one can obtain a predicted stress that would have any predetermined probability of producing a failure, such as 5% or 1% or even less. Because the data reduction is done on logs of the stress values, the tolerable levels of risk may be tabulated as a constant difference, in the log scale, from the estimated means. That is, the expression for a 5% probability of failure could be expressed as

$$\ln(5\%\ level) = -a/b - K(5\%)$$

A table of Ks for all desired risk levels could be developed. Note, however that the further the value is from the mean (50%), the less well determined it is. This is because of the greater difficulty in obtaining sufficiently large samples to pin down values far out in the tails of the distribution. Two sequential samples of 10,000 from the same population at a level that has a 0.0001 probability of producing a failure could result in no failures in one and several in the next, by chance alone. Furthermore, that eventuality is not a very low probability event.

For the future we will attempt to develop a test of significance of the difference between the agent and the closest simulant. The first step in this process is simple, as a measure of the variance of the parameters is easily calculated while doing the regression. The next part, however, is not quite as straightforward as it might seem at first, because one would be, in effect, making all possible pairwise comparisons between the magnitude of the a-parameter for the agent and the a_is of all the candidate simulants, yielding a substantial probability of finding an apparent match where one does not actually exist.

REFERENCE

1. Sturdivan, Larry. M. and Jameson, John. W., "Linearized Least Squares" in Proceedings of the 1976 Army Numerical Analysis and Computers Conference, ARO Report 76-3. US Army Research Office, PO Box 12211, Research Triangle Park, North Carolina.

He-Ne LASER CRAZING TEST

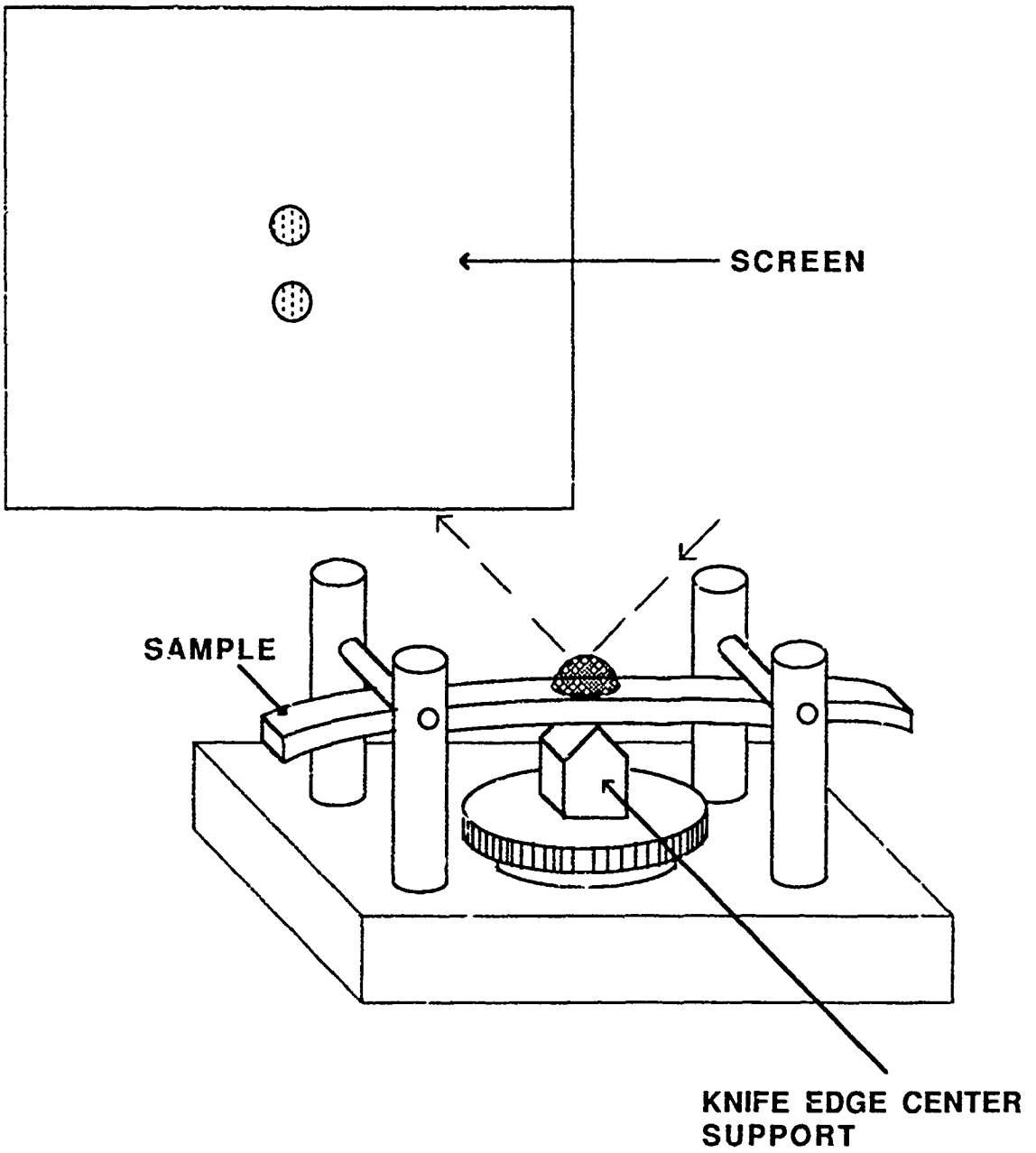

Figure 1: Schematic of Strain Test Rig.

STRESS CRAZING IN TRANSPARENT MATERIALS EXPOSED TO CHEMICAL AGENTS

P.S. Grasso, E.W. Sarver, L.M. Sturdivan
U.S. Army Chemical Research, Development and Engineering Center, Aberdeen Proving Ground, MD.

Abstract- A static bending system based on a modification of ASTM method D790-80, was used to test the crazing and cracking susceptibility of four transparent materials exposed to one of nine selected chemical agent simulants and chemical agent mustard (HD). A reflective He-Ne laser detection method was employed during these tests to improve sensitivity. Simulant selection was based on chemical/physical properties and prior use. The transparent materials selected were polycarbonate (PC), cast and stretched polymethylmethacrylate ((CP), (SP), and polyurethane (PU). Previously reported simulant test results were re-analyzed for mean critical strain and compared to HD. Curve variance was computed for each material type so that strains with lower failure probabilities could also be estimated. The best HD simulants were 2-Chloroethyl Methyl Sulfide (CEMS), and 2-Chloroethyl Ethyl Sulfide (CEES). The previously reported critical strain ranking of materials for simulants changed from: PC> CP> SP> PU, to CP> PC> SP> PU.

INTRODUCTION

This study was conducted as part of an ongoing effort at the U.S. Army Chemical, Research, Development and Engineering Center (CRDEC) to evaluate the survivability of transparent polymeric materials in a chemical agent environment. Earlier simulant test results generated under contract by GEO-CENTERS, INC.[9] were re-analyzed and compared to agent studies conducted at CRDEC.

Since chemical agents cannot be used without appropriate safety and surety procedures and apparatus in the laboratory , simulants must be selected and substituted for the chemical agents in many experimental environments. Using appropriate evaluation techniques, candidate chemicals can be selected to determine the best simulants to employ in a testing program.

Simulants employed in properly designed laboratory tests assist in evaluating the performance and behavior of challenged transparent polymeric materials. Subsequent modeling aids in predicting the performance of these polymeric materials under the realistic condition of chemical agent challenges. Also, the testing of transparent polymeric materials with simulants for GB, VX, and HD could be conducted at the polymer manufacturer's own facilities under non-surety conditions.

SIMULANT SELECTION

Because simulants are frequently substituted for agents, our experimental effort was to determine which of the nine previously tested simulants best matched the behavior of mustard (HD) in chemical stress crazing and cracking of transparent polymeric materials.

The test simulants utilized in these studies were carefully selected by comparing important physical and chemical parameters of the simulants to the same characteristics of the agents. These parameters included molecular weight, solubility, viscosity, melting and boiling points, density, vapor pressure, and reactivity.[1,2,3] The simulants were also selected not only for their chemical similarities to the agents but, also, for their molecular size similarities. Thus, we wish to develop or establish an envelope or region of comparable simulant and agent absorption into the various polymers being tested, as well as, similar reaction/behavior between the simulant or agent and the polymer.

Simulants selected for Isopropyl Methylphosphonofluoridate (GB) were Diisopropyl Methylphosphonate (DIMP), Diethyl Ethylphosphonate (DEEP), and Dimethyl Hydrogen-phosphonate (DMHP). The simulants used for 2,2'-Dichloroethyl Sulfide (HD) were 2-Chloroethyl Methyl Sulfide (CEMS), 2-Chloroethyl Ethyl Sulfide (CEES), and 1,5-Dichloro-pentane. VX(O-Ethyl-S-Diisopropylaminoethyl Methylphosphonothiolate) simulants used were O,S-Diethyl Ethlyphosphonothiolate (DEEPT), N,N-Diisopropylethylamine, and Diethyl(ethylthiomethyl) Phosphonate (DEETMP).

Even with extensive screening procedures used in simulant selection, actual agent test results are required to establish which chemical best simulates a given agent. As a result, all nine simulants were compared to HD test results.

EXPERIMENTAL METHOD

To determine stress crazing in transparent polymeric materials, a modified form of American Society of Testing and Materials method ASTM D790-80 was employed. ASTM D 790-80 determines the flexural properties of plastics in the form of rectangular bars molded directly or cut from sheets, plates, or molded shapes.[4] This ASTM procedure is generally applicable to rigid and semi-rigid materials but does not determine the flexural strength of materials that do not break or fail in their outer fibers.

The method employed for craze determination under static load for this series of tests employs a three-point loading system that utilizes center loading on a simply supported beam (Figure 1). The original procedure, developed for CRDEC by MTL, detected crazing visually.[5,6] However, the detection method employed for our tests was improved by employing a He-Ne laser to produce a reflection pattern. By recording the reflection patterns with a Sony U-Matic VCR and Sony Trinicon color camera equipped with a macro-zoom lens(Figure 2), the determination of the time of crazing is easily accomplished. The determination of the onset of crazing by changes in the reflection pattern is superior to the visual method because the reflection pattern enables minute crazing to be detected which are generally not apparent to the unaided eye.

The use of a He-Ne laser in conjunction with the three-point bend apparatus allows increased sensitivity in detecting the onset of crazing. The He-Ne laser reflection pattern is observed to change at the onset of crazing.[7,8] Figure 3 illustrates the various patterns observed with employment of the He-Ne laser to detect the onset of crazing. Figure 3a represents the normal pattern observed with no simulant present. When the simulant is added, some diffusion is noted in the pattern(i.e., the degree of diffusion depends upon the optical characteristics of the simulant)(figure 3b). As crazing occurs across the width of the sample, a horizontal line appears at the edges of the pattern, (the pattern changes from b to c). However, if a transition from crazing to cracking occurs, it progresses at 90 degrees from the initial craze, and results in a more intense vertical diffraction pattern (the pattern changes from c to d). Some materials solublize and yield at higher strains. For these cases, the onset of solublization is treated as the failure point.

Calibration tests for each three-point bend apparatus were determined prior to data collection. The reference test selected was polycarbonate challenged with HPLC grade diethylenetriamine. This procedure serves to bridge data collected by different testers at different times and sites.

A 1.0 microliter drop of challenge chemical is added at the center of the sample, where the laser beam intercepts the sample. The timer is started at the time of liquid addition and the reflection is recorded. The reflection pattern is carefully monitored. If the pattern begins to diffuse and develop horizontal lines, or the two initial points separate, crazing is occurring and the time is recorded. Extreme care is needed in determining the onset of crazing because evaporation of the simulant can distort the reflected pattern.

If crazing occurs at the strain (r) initially selected, this r value is divided by a factor of 1.2 and the new r value is used in the next test. If crazing does not occur within thirty minutes (1800 seconds), the r value initially selected is multiplied by a factor of 1.2 and this new r value used for the next sample. This process is repeated until a critical strain value can be estimated (about 10 points).

Strain in a polymer sample is calculated in the outer layers of the sample from the equation[4]:

$$r = 6Dd/L^2 \qquad (1)$$

where r=strain in upper layer; D=Displacement of sample at mid-span; L=support span length; d=thickness. Rearrangement of the equation for this series of experiments allows determination of the amount of displacement(D) for each sample via:

$$0.6667*(r/d)=D \qquad (2)$$

where 0.6667 is $L^2/6$(L=2 in.), r represents a selected percent strain value(%r) divided by 100 , and d is the thickness of the sample, measured for each sample.

Plots of strain versus time to the onset of crazing and cracking show an increase in crazing time as strain is reduced. Due to sample and test method variability, a transition zone can exist.Specimens subjected to strain values less than transition zone values do not craze within the 30 minute test period. Within the transition zone some samples craze quickly while others remain intact after 30 minutes. Thus no single critical strain value will represent the entire population of samples for a given material. As a result of this and the difficulty in locating the lower edge of the zone for all samples of a given material type, we selected the mid point of the transition zone, the 50% critical strain value, as the best single measure of critical strain, and this serves as a basis for comparison of agents to simulants. Estimates of variance for each material type was made to provide estimates of critical strains with lower probabilities of failure.

RESULTS AND DISCUSSION

The 50% critical strain values for the nine simulants and agent HD were computed and compared, within the limits of the experimental method, for the four transparent polymers selected. These results are shown in the critical strain table. An estimate of chemical susceptibility can be determined by noting the average critical strain for each material. The lower the strain average is, the more susceptible the material is. The average values were derived by adding the critical strains for each material and dividing by 10, even though true scores would be higher for the ">" values.

Using the total critical strain values as a basis for comparison, the chemical susceptibility is: PC>CP>SP>PU. As can be seen, PC and CP are about the same, SP is in the mid range and PU shows almost no effects from contact with chemicals.

Figures 4a-c depict the resulting sigmoids for each material type, with the mid point for each chemical shown at the 50% level. It was not possible to show curves for PU because the material did not fail. Greater then values were reported in place of mean values in this case. Analysis of the 50% critical strain values for each simulant compared to HD are shown under deviation in the critical strain table. This

column indicates the results of summing the ratio of the simulant critical strain deviation from HD, divided by the standard deviation for each material type. As can be seen, the best over-all simulants were CEMS and CEES. The best single material matches are also indicated in the critical strain table.

CONCLUSIONS

1. The two best simulants for agent HD were CEMS and CEES.

2. As can be seen from the critical strain table, one GD and one VX simulant compared well with HD, thus preliminary selection of simulants based on chemical and physical properties does not always identify the best simulants to use. Test verification is required.

3. Additional agent studies will be required to determine the best simulants for agents VX and GD.

4. This test method has matured sufficiently to transition it contractors for generating chemical agent data bases.

REFERENCES

1. U.S. Army Chemical Research, Development, and Engineering Center Data Management System, Edgewood Arsenal, Edgewood, MD.

2. "Military Chemistry and Chemical Compounds," Department of the Army, FM 3-9, October, 1975.

3. P.H. Howard, G.W. Sage, J.P. Robinson, J. Jackson, "Environmental Fate Assessments of Chemical Agent Simulants and Decontaminants," Chemical Research, Development, and Engineering Center, CRDC-CR-86016, 1986.

4. "Flexural Properties of Plastics and Electrical Insulating Materials," in Annual Book of ASTM Standards, American Society of Testing and Materials, ASTM D790-80, , 327, May 1980.

5. L.H. Lee, J.J. Vanselow, "Chemical Degradation and Stress Cracking of Polycarbonate in DS_2," MTL TR 87-46, Sept. 1987.

6. L.H. Lee, J.J. Vanselow, "Chemical Resistance of Coated Transparent Thermoplastics," MTL TR 87-6, Jan. 1987.

7. A. Cers, C.Y. Yuan Hsiao, C.C. Hsiao, "Laser Diffraction of Polymer Crazes," in Toughness and Brittleness of Plastics, **154**, 79, American Chemical Society, Washington, D.C., 1976.

8. C.C. Hsaio, *Appl. Phys. Lett.* , **23**, 20, 1973.

9. R.E.Lewis, S.A.Liebman, L.Isaacson, P.S.Grasso, E.W.Sarver, "CHEMICAL AGENT SIMULANTS FOR TESTING TRANSPARENT MATERIALS" Chemical Research, Development, and Engineering Center, CRDEC-CR-88069, May 1988.

FIGURE 1

He-Ne LASER CRAZING TEST

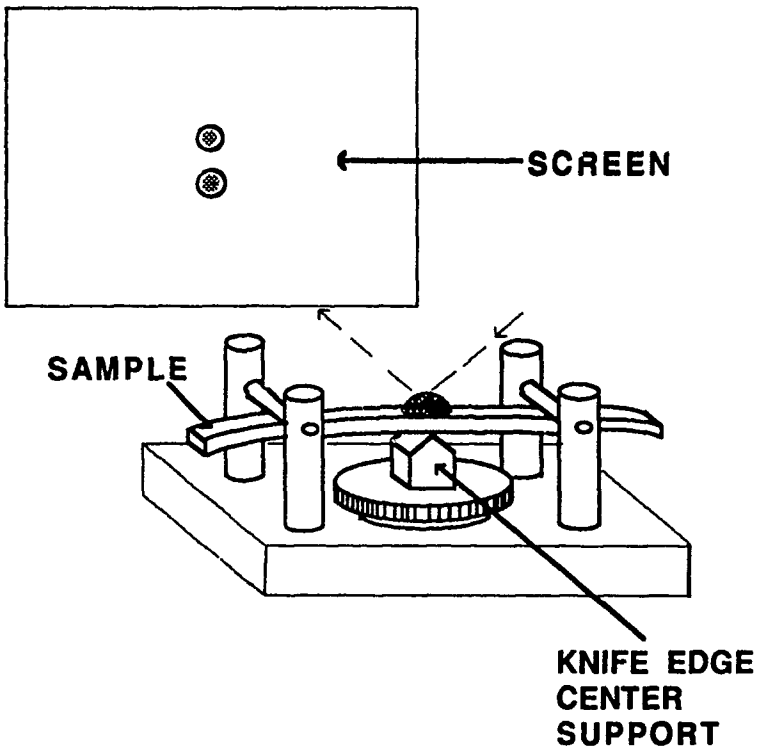

FIGURE 2

EQUIPMENT SCHEMATIC

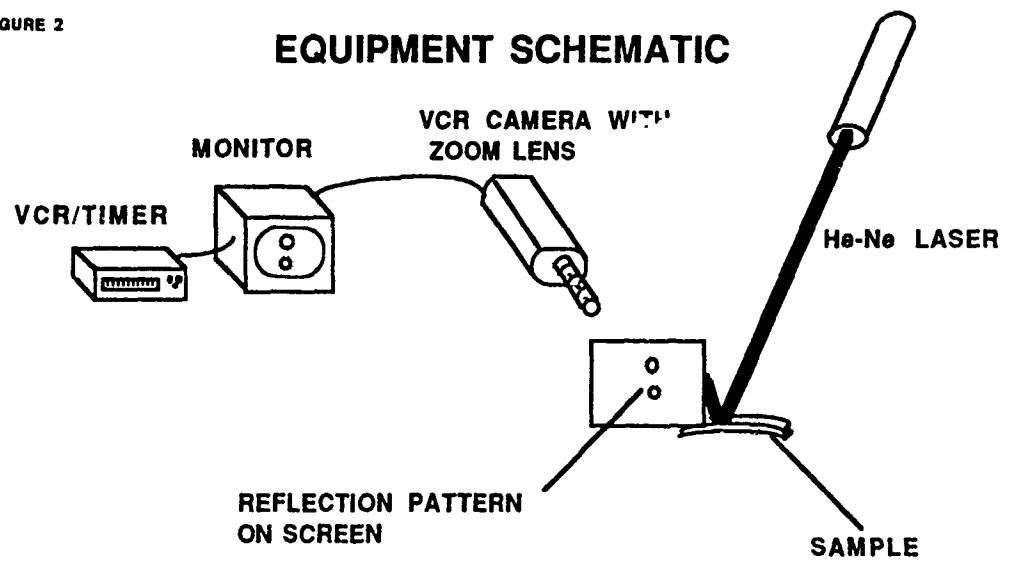

FIGURE 3

He-Ne LASER DIFFRACTION PATTERNS

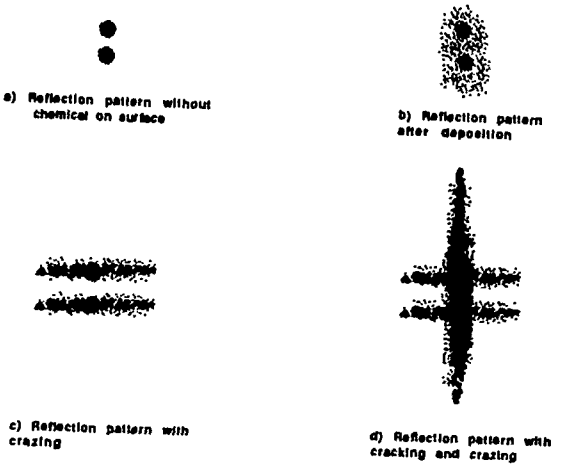

a) Reflection pattern without chemical on surface

b) Reflection pattern after deposition

c) Reflection pattern with crazing

d) Reflection pattern with cracking and crazing

TABLE

NOTES
* Best Mat Match
** Sig Evap

MATERIAL KEY	
PC	POLYCARBONATE
CP	CAST PMMA
SP	STRETCHED PMMA
PU	POLYURETHANE

MEAN % CRITICAL STRAIN X10						
SIMULANT		MATERIAL TYPE				DEV.
CLASS	SYMBOL	PC	CP	SP	PU	
GB	DMHP	* 9	9	11	> 26	17.4
	DEEP	6	10	* 15	> 26	14.1
	DIMP	* 7	9	* 15	24	12.0
VX	DEEPT	13	8	14	> 26	12.7
	DEETMP	5	8	28	> 26	22.9
	DIPEA	11	**>13	* 19	> 26	19.8
HD	CEES	3	5	11	> 26	11.3
	CEMS	11	* 4	10	20	10.3
	1,5 DCPT	11	5	8	> 26	14.8
AGENT HD		8	4	17	> 26	–
AVERAGE STRAIN		8.4	7.5	14.5	>25.2	–
STD. DEV.		3.61	.55	.74	–	–

FIGURE 4 (a-c)

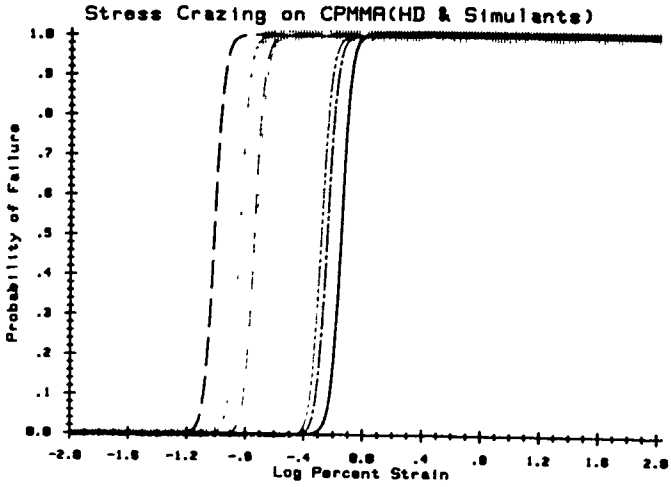

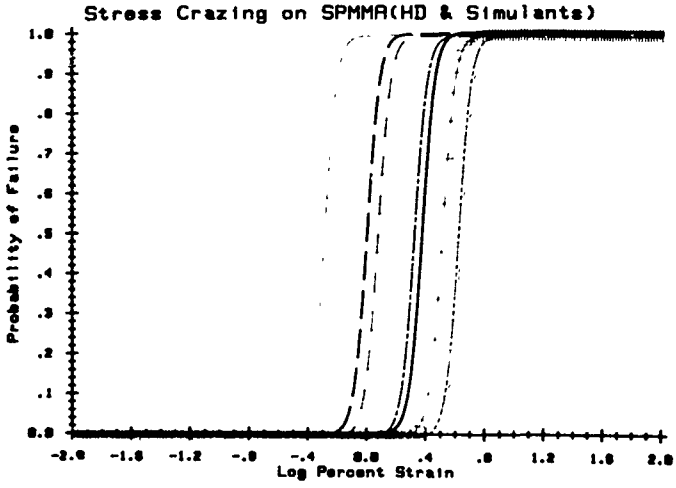

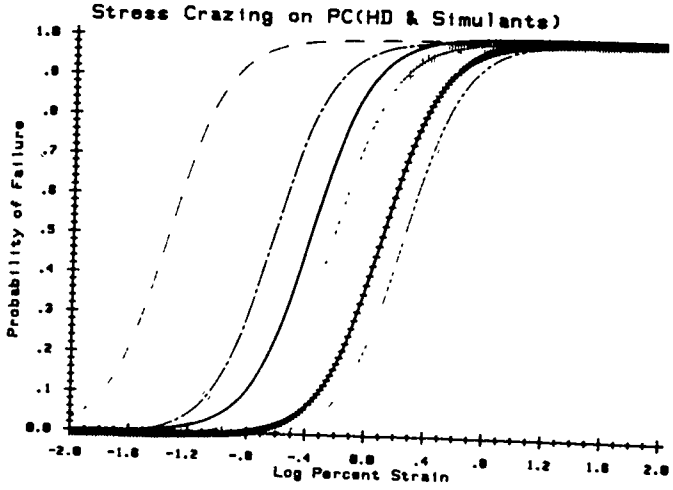

KEY	
CHEMICAL	SYMBOL
DIMP	
DEEP	
DMHP	
CEES	
CEMS	
1,5 DCPT	
DEETMP	
DEEPT	
DIPEA	
HD	

BLANK

VII. PROTECTION

NOTE: Papers with the following titles were presented at the Conference but are not included in this document:

An Examination of How Exposure to Humid Air Can Result in Changes in the Adsorption Properties of Activated Carbons

Catalytic Destruction of Hazardous Halogenated Organic Chemicals

Identification of a Species in a Silent Discharge Plasma

Updated Static Pulmonary Function Parameters for NBC Respirator Design

BLANK

THE EFFECTS OF AXIAL DISPERSION ON THE BREAKTHROUGH BEHAVIOR OF FREON 113

David K. Friday
GEO-CENTERS, INC.
10903 Indian Head Highway, Ft Washington, MD 20744

John J. Mahle
U. S. Army Chemical Research, Development, and Engineering Center, Aberdeen Proving Ground, MD 21010

Leonard C. Buettner
U. S. Army Chemical Research, Development, and Engineering Center, Aberdeen Proving Ground, MD 21010

ABSTRACT

Three methods are employed to identify axial dispersion and characterize it as an important phenomenon affecting filter performance. First, previous studies are cited where the investigators used bed depths, particle sizes, and velocities similar to those employed in military filter systems and found that axial dispersion was significant. Second, breakthrough curves for Freon 113 are measured using BPL and ASC carbons under dry and 80% RH conditions. The effect of velocity on the shape of the breakthrough curve verifies that axial dispersion must be considered as a primary mechanism. Finally, the predicted results of the Fixed-Bed Adsorptive Reactor model with reaction rates set to zero are compared to measured breakthrough data for the dry Freon 113-BPL system. Only when the number of stages is reduced to one or two, a strong indication that axial dispersion is important, does the model accurately reflect the system performance.

INTRODUCTION

A main objective of the work being performed at CRDEC in the Air Purification Branch is to understand and quantify the phenomena that determine the protection time of military filter systems. The information obtained as part of this effort may be used to; (1) evaluate the performance of existing and proposed military air purification systems, (2) optimize current systems and (3) design new systems. An integral part of achieving the objective is to develop a thorough understanding of the impact fixed-bed effects (axial dispersion and channeling) have on the protection time of a filter. The results presented here identify axial dispersion

as a primary mechanism and indicate the adverse effect it can have on filter performance.

BACKGROUND

There have been a number of papers that have identified axial dispersion as an important phenomenon governing the performance of an adsorption system. Sahimi et al.[1] modeled the dispersion of a non-adsorbing tracer gas using Monte Carlo simulations of flow through two and three dimensional porous networks. Coppola and Levan[2,3] studied the effect of axial dispersion on the breakthrough behavior of a favorably adsorbed vapor in shallow beds and deep beds. Levan and Vermeullen[4] analyzed radial and axial dispersion combined with channeling and developed a mathematical relationship to differentiate between channeling and dispersion. Others have investigated other approaches to model and understand the dispersion phenomena.[5,6,7] The results of these studies clearly show the significance of the dispersion effects and the need to understand how axial dispersion degrades the performance of military air purification systems.

A full mathematical development and in-depth discussion is beyond the scope of this short paper. Instead, an empirical analysis will be presented which both identifies axial dispersion as an important process and demonstrates its adverse effect on the breakthrough time.

EXPERIMENTAL

Experiments were performed using a test system with a bed bypass line to establish a constant challenge concentration prior to the start of the experiment. For the experiments at 80% relative humidity, a Miller-Nelson humidification unit was used to generate humid air. The humidity of the challenge air stream was verified using a EG&G Dewpoint Hygrometer. For the high humidity tests, an 80% relative humidity air stream was passed through the adsorbent for about 16 hours to insure the adsorbent was properly equilibrated. The challenge and effluent concentrations were each measured using a MIRAN 80 with a variable pathlength IR cell. The bed diameter used in all tests was 3.0 cm. The adsorbents used in this study were BPL 12x30 mesh, Lot# 1A9-B and ASC 12x30 mesh, Lot# 1535. The adsorbate for all experiments was (1,1,2) triclorotrifluoroethane from Matheson Inc.

RESULTS AND DISCUSSION

When a contaminant vapor challenges a clean bed, if the isotherm is favorable, the result is a concentration wave, called a shock or an abrupt transition, that forms in and is passed through the bed. Theory requires this shock to be infinitely sharp, that is, at the bed depth where the shock is located, the transition from zero concentration to the feed concentration takes place over an infinitesimal distance. However, in practice this is not observed because of the following mechanisms:

1. Axial dispersion and diffusion in the vapor phase
2. Diffusion from the vapor phase to the adsorbent
3. Diffusion within the pores of the adsorbent
4. Diffusion of adsorbed molecules along the surface of the adsorbent
5. Kinetic adsorption rate at the phase boundary

Shown in Figure 1 is a typical effluent concentration profile (breakthrough curve) for a constant concentration feed of a single, favorably adsorbed component. A "constant pattern" is achieved when area A and area B do not change as the wave is transmitted down the bed. If area A and area B increase with the passage downstream, then the slope at the stoichiometric center decreases and the wave is said to be "spreading". A "sharp" wave is one in which the areas A and B are relatively small.

If ary combination of the five rate mechanisms is significant, then the effluent concentration will be higher than expected before the stoichiometric time and lower than expected after the stoichiometric time. Since military systems require protection levels well below the stoichiometric center concentration, the overall effect of any of these mechanisms is a degradation in filter performance.

The breakthrough curves plotted in Figures 2 and 3 indicate that axial dispersion is an important phenomena controlling breakthrough behavior. The results are plotted as the effluent concentration versus time normalized by the time the stoichiometric center concentration exits the bed. The conditions for the experiments are given in the title of each figure. The significant result is that the slower velocity (6.1 cm/sec) does not produce a sharper breakthrough curve than the faster velocity (12.2 cm/sec) for either the BPL or the ASC carbon. If diffusion processes or the kinetic adsorption rate were important (mechanisms 2-5 above), then the slower velocity, thus a larger bed residence time, should result in a sharper breakthrough curve on a plot using the normalized time axis. This does not occur, in fact the higher velocity seems to be a little sharper. Therefore, one may

conclude from these results, a mechanism other than diffusion or the phase boundary adsorption rate causes the breakthrough curve to spread.

Figures 4 and 5 show the velocity dependence on the breakthrough shape at 80% RH conditions. At high relative humidities, one would might expect that an internal (inside the adsorbent particle) rate process (numbers 3 and 4 given above) may be rate-controlling, since Freon 113, a water insoluble compound, would have to diffuse through micropores almost filled with adsorbed water. Figures 4 and 5 indicate that a rate process (presumably internal) is important, since the slower velocity gives somewhat sharper breakthrough. However, these results do not show the strong velocity dependence one might expect, indicating that the effects of axial dispersion and internal diffusion may be of equal magnitudes. Further investigations of systems where several effects are important will be conducted.

Shown in Figure 6 are the measured effluent concentrations of Freon 113 using BPL under dry conditions compared to the predicted results of the Fixed-Bed Adsorptive Reactor (FBAR) model[8] using 1, 2, and 6 stages. The FBAR model uses parameter values obtained from other experimental measurements and standard chemical engineering correlations. The results shown in Figure 6 clearly show that the FBAR model is more accurate as the number of stages is reduced. If axial dispersion is not important, then model and data should agree only when a large number of stages is used. A small number of stages is a clear indication that dispersion is a major cause of the spreading of the breakthrough curve.

CONCLUSIONS

1. Axial dispersion is an important phenomena affecting the performance of military filters.

2. The effect of any "spreading" mechanism is to degrade the performance of a filter.

ACKNOWLEDGEMENTS

The authors would like to thank Elaine Neary, Al Barnes and Bernie Infiesto for their efforts in this work.

REFERENCES

1. Sahimi, M., Hughes, B.D., Scriven, L.E. and H.T. Davis, " Dispersion in Flow Through Porous Media - I. One Phase Flow," *Chem. Eng. Sci.*, 41, pp 2103-2122, 1986.

2. Coppola, A.P. and M.D. LeVan ," Adsorption with Axial Dispersion in Shallow Beds," *Chem. Eng. Sci.*, 38, pp 991-997, 1983.

3. Coppola, A.P. and M.D. LeVan ," Adsorption with Axial Dispersion in Deep Beds," *Chem. Eng. Sci.*, 36, pp 967-971, 1981.

4. LeVan M.D. and T. Vermeullen, " Channeling and Bed Diameter Effects in Fixed-Bed Adsorber Performance," *AIChE Symposium Series, Adsorption and Ion Exchange* , No 232, 80, pp 34-43, 1984.

5. Oliveros, G. and J.M. Smith , "Dynamic Studies of Dispersion and Channeling in Fixed-Beds," *AIChE J.*, 28 pp 751-759, 1982.

6. Tobis, J and D. Vortmeyer," The Near-Wall Channeling Effect on Isothermal Constant-Pattern Adsorption," *Chem. Eng. Sci.*, 43, pp 1363-1369, 1988.

7. Sundaresan, S. Amundson, N.R. and R. Aris, " Observations on Fixed-Bed Dispersion Models : The Role of the Interstitial Fluid," *AIChE J.*, 26, pp 530-536, 1980.

8. D.K. Friday, "The Breakthrough Behavior of a Light gas in a Fixed-Bed Adsorptive Reactor," *AIChE Symposium Series, Adsorption and Ion Exchange*, No. 264 , **84**, 89, 1988)

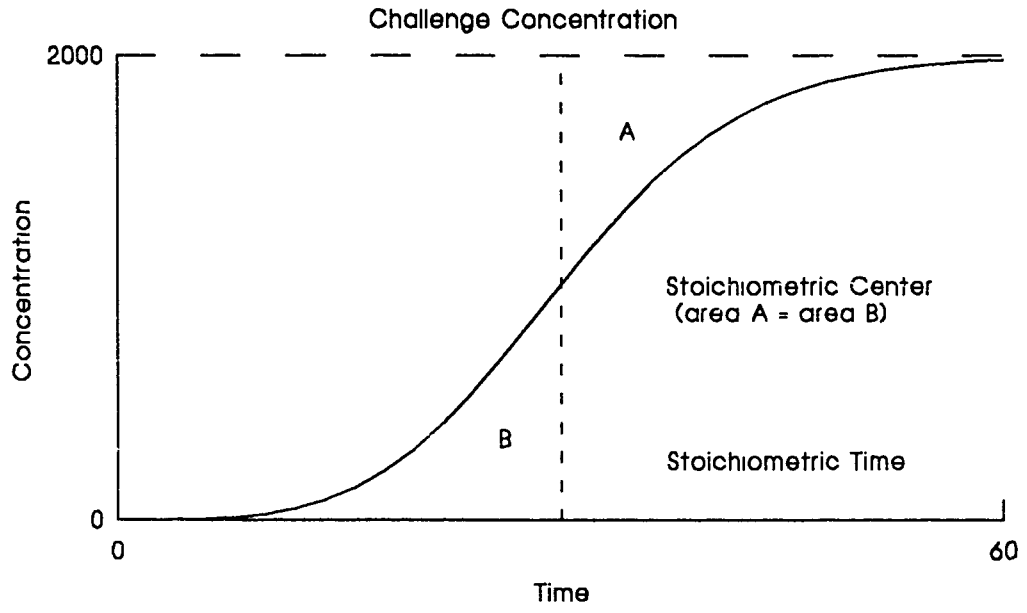

Figure 1. Breakthrough Curve with Term Definitions

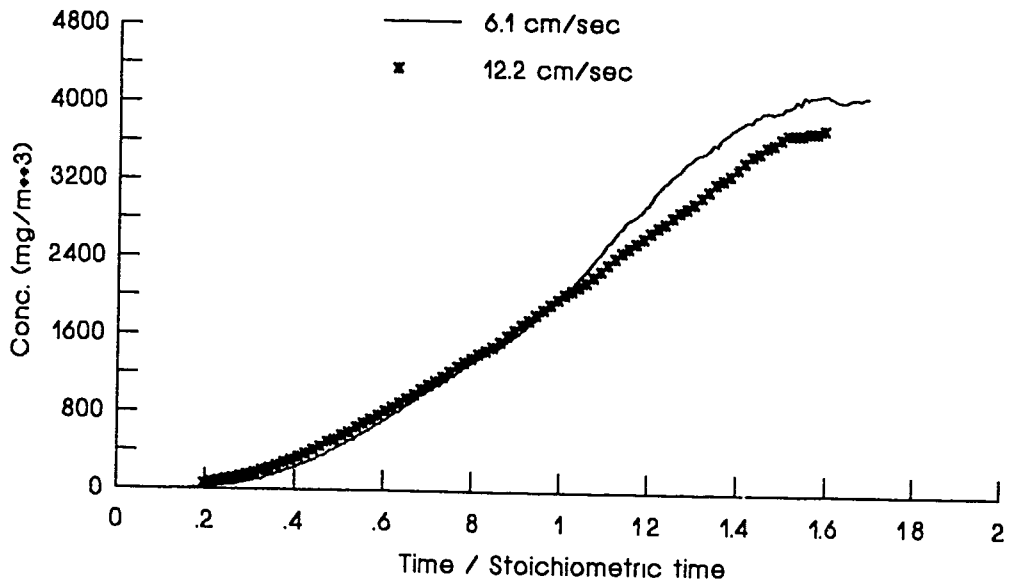

Figure 2. Normalized Breakthrough of Freon 113
on BPL Carbon under Dry Conditions
1 cm bed, 4 mg/lit challenge

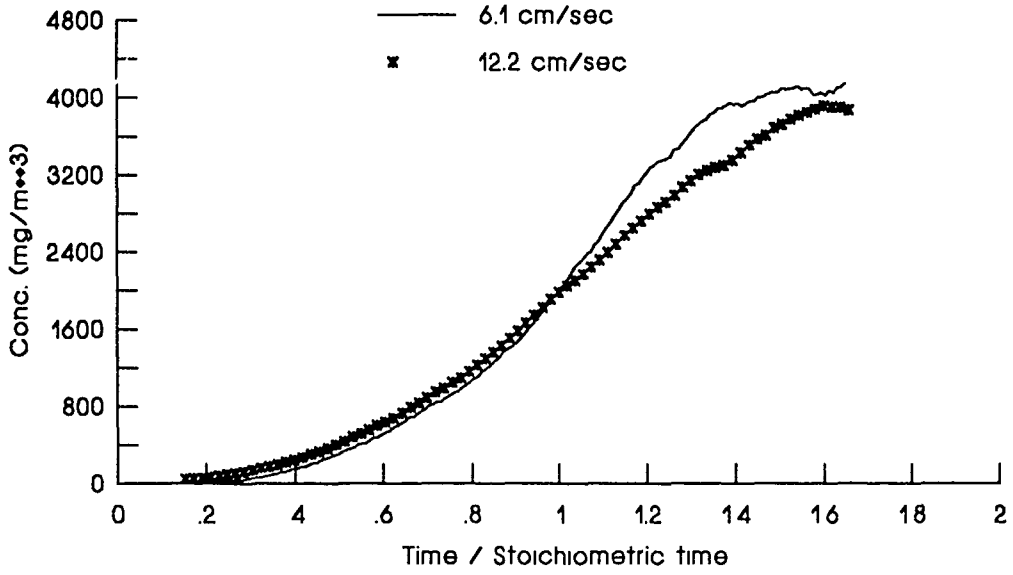

Figure 3. Normalized Breakthrough of Freon 113
on ASC Carbon under Dry Conditions
1 cm bed, 4 mg/lit challenge

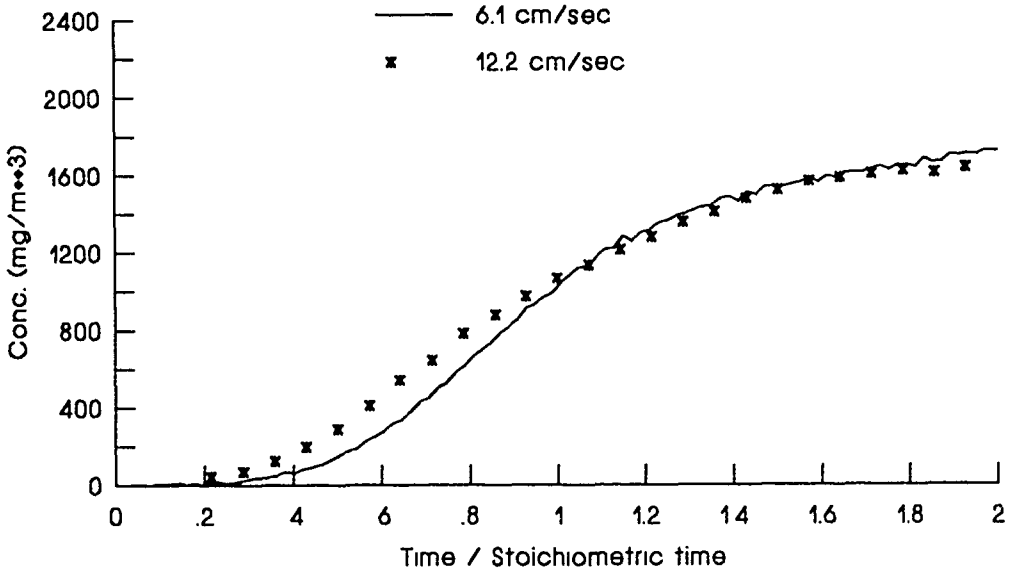

Figure 4. Normalized Breakthrough of Freon 113
on BPL Carbon under 80/80 Conditions
2 cm bed, 2 mg/lit challenge

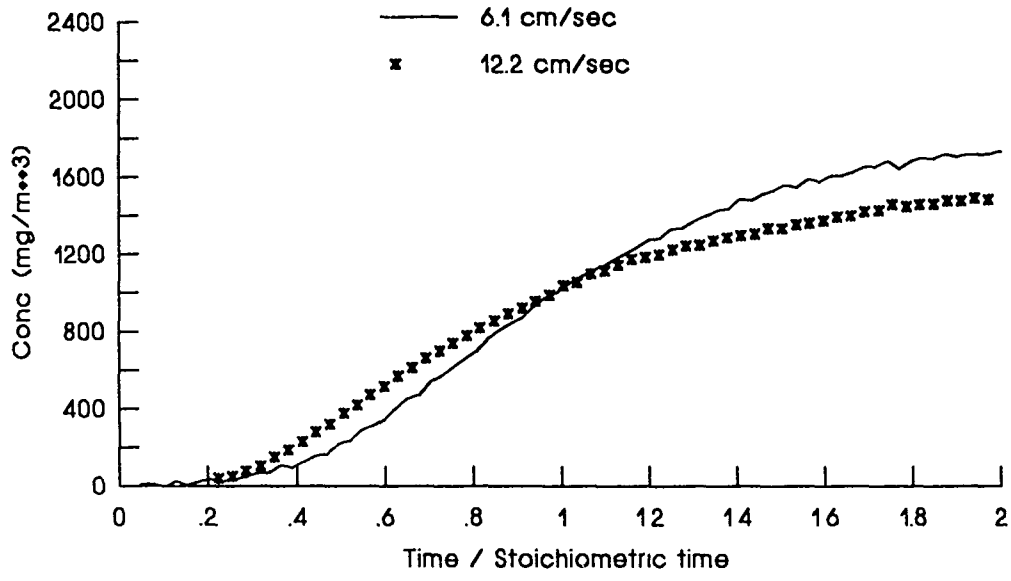

Figure 5. Normalized Breakthrough of Freon 113
on ASC Carbon under 80/80 Conditions
4 cm bed, 2 mg/lit challenge

Figure 6.
Fixed-Bed Adsorptive Reactor (FBAR) Results and Measured Data
For Freon 113, 1 cm bed, 6.1 cm/s, 4.0 mg/l challenge, Dry Conditions

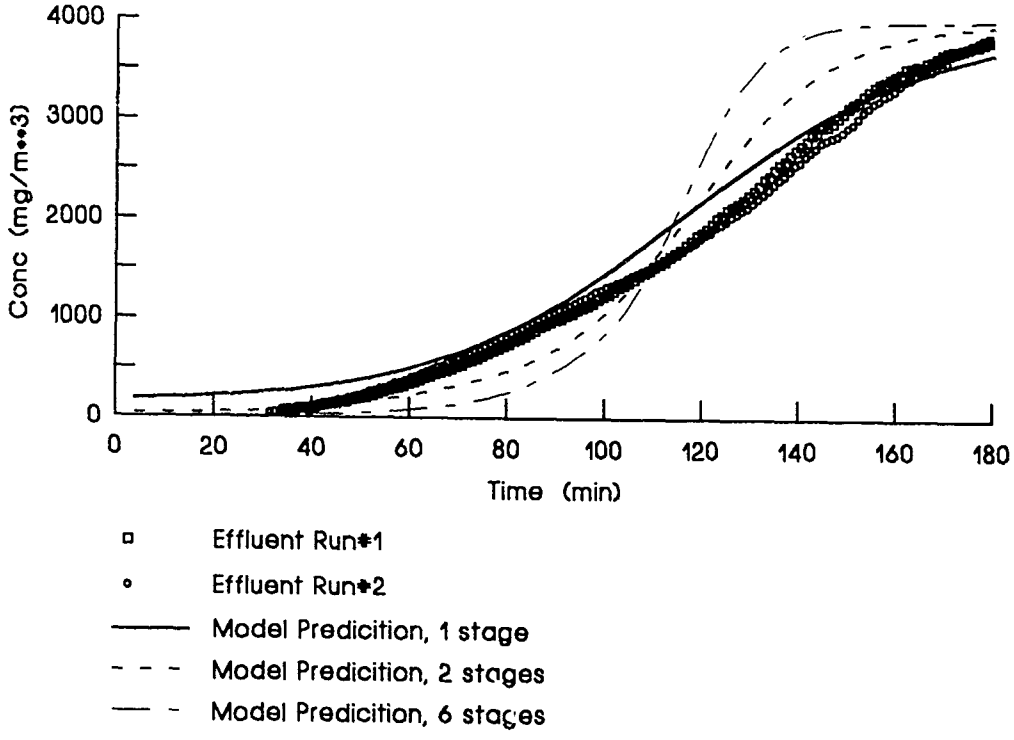

BATCH ADSORPTION: EQUILIBRIA AND RATE PROCESSES

John J. Mahle, Leonard C. Buettner C R D E C
David K. Friday GEO-CENTERS, Inc.

ABSTRACT

A batch adsorption system has been developed for the study of both adsorption equilibria and rate processes. This system has been used to obtain both single and multi-component isotherms. Adsorption equilibria results will be presented for Freon 113 adsorption on ASC- TEDA and BPL carbons under dry conditions and 80%RH at 25 C. A material balance to describe the dynamic behavior of the system will also be presented. The simulation will be compared to actual batch uptake curves.

1. INTRODUCTION

Batch adsorption systems are a standard means of studying adsorption processes[1]. They can be used for the determination of both equilibria and rate phenomena. A batch system has several advantages in a laboratory setting which have not previously been recognized by military researchers. The development and testing of novel adsorbent materials or threat vapors is usually carried out in small lots. These small amounts of material can be easily analyzed in a batch system using sample sizes on the order of a gram of adsorbent and several microliters of liquid compound. The reduced safety and environmental concerns associated with small samples are additional benefits along with the conservation of precious samples.

Batch adsorption systems have been described in the literature as powerful tools for the study of both equilibria and rate processes in adsorption systems. It is possible to obtain rapid evaluation of uptake curves using small quantities of both the chemical and the adsorbent. The same information that is currently obtained from filter tube testing can be obtained through accurate modeling of a batch system. This is information that would be used to assess the performance of various filter systems.

A batch adsorption system has been developed for application to military concerns. This system was conceived as a modification to the existing filter tube test system. Using such a system a material balance can be performed to provide adsorption equilibria data for both single and multicomponent systems. A material balance can also be written for the dynamic behavior for single component systems. This paper will describe a batch system used to study the equilibrium and dynamic adsorption behavior of Freon 113 on dry and humidified BPL and ASC-TEDA carbons.

2. THEORY

2.1 Isotherms

For compounds with high vapor pressures the influence of adsorbed water on adsorption can be dramatic. For this reason measurement of multicomponent data of organics and water must be considered in efforts to model filter performance. Substantial research has gone into the measurement of multicomponent adsorption mixtures for ideal systems of like compounds. However, there are only two references which discuss the measurement of non-ideal multicomponent adsorption systems characterized by water and organic components[2-4]. Both methods were found to be difficult to implement. In order to overcome these difficulties the batch adsorption system can be adapted for the measurement of adsorption equilibria with water and organics. Even with measured

equilibria data there is no well accepted theory to correlate it over a wide range of partial pressures for both the organic and water vapors. Short of this the data would be most useful if it were measured as isotherms of the organic at constant relative humidity. The latter relationship would be in keeping with typical vapor challenge scenarios that are conducted in the laboratory.

2.2 Material Balance

The intraparticle rate processes that influence the uptake in a batch system also occur in fixed bed processes. Therefore the ability to accurately model batch behavior should provide insight into the design of conventional filters. Earlier efforts to model fixed-bed adsorption processes is discussed by Friday and Mahle[8]. The material balance for a batch system can be written as:

$$\frac{\partial c}{\partial t} = -\frac{wt}{V}\frac{\partial q}{\partial t} - R_i(q,M) \tag{1}$$

A fluid film mass transfer resistance would take the following form

$$\rho_b \frac{\partial q}{\partial t} = k_v a(c-c^*) - R_i(q,M) \tag{2}$$

A solid film resistance can be written as a linear driving force:

$$\rho_b \frac{\partial q}{\partial t} = \rho_b k_p a(q^*-q) - R_i(q,M) \tag{3}$$

and the phase equilibria as

$$c^* = f(q^*) \tag{4}$$

This provides a set of coupled nonlinear ordinary differential equations such that given initial conditions for c, and q the equations can be solved as function of time.

3. EXPERIMENTAL

The principle components of the system are 1) an infrared detector with a large volume gas cell 2) the adsorbent sample tube and 3) a circulation pump. The system is operated such that the concentration is monitored as vapor either bypasses the adsorbent or contacts it.

The tubing was all stainless steel and the valves were stainless steel Whitey Ball valves. The flowrate was measured using a Tylan mass flow controller which was modified to perform as a flow meter. The circulating pump was manufactured by Metal Bellows Inc. The volume of the system, 5.89 l, was taken by summing the contribution made by the tubing and the gas cell from manufactures' specifications.

The adsorbent material was contained in a tube with a 1 cm inner diameter and 3 cm long. A screen was placed in the bottom of the tube and glass wool on top of the adsorbent. This formed a shallow

bed in the tube no more than one or two particle diameters deep.

The procedure for a typical run was as follows. The carbon sample was first dried overnight at 100 C. Next it was equilibrated to the desired RH. The humidified air was generated using a Miller-Nelson with the actual humidity tracked using an EG&G 911 Dew Point Hygrometer. The actual water loading on the carbon was verified by weighing the humidified sample before and after drying. The challenge concentration was established by first placing the system in the bypass mode and injecting a measured volume of Freon 113 through the septum. Once the bypass concentration was established the valve was rotated to circulate the vapor over the adsorbent.

Concentrations of Freon 113 greater that 4000 mg/m3 for the single component isotherms were measured using a HP 6880 gas chromatograph with a flame ionization detector. This was required because the sensitivity of the IR was reduced at higher concentrations. The temperature in the laboratory was controlled to 298 ± 3 K and the temperature in the loop was monitored using a thermocouple.

4. RESULTS

4.1 Isotherms

Measured uptake curves in the batch adsorption system provided both equilibria and rate data. The equilibrium loading was determined from the weight of carbon, the difference between the initial and final concentrations and the volume of system. The calculated loading corresponded to the final vapor phase concentration. The loading could be calculated for as many compounds as were monitored in the vapor phase. Both single and multicomponent isotherms were measured at ambient conditions 298 K. The single component isotherm for Freon 113 on BPL carbon is shown in Figures 1. The data was correlated to the LeVan isotherm expression [5]. The parameters for this correlation are presented in Table 1.

The adsorption equilibria measurements for Freon 113 and water have been presented in The Freon 113 data from the multicomponent case has been correlated to the LeVan isotherm as if the relative humidity and water loading remained constant. The validity of this assumption depends on how much the water loading actually changed. The water adsorption isotherms on BPL and ASC-TEDA carbons have been presented earlier[7]. At 80% RH the water loading on BPL and ASC-TEDA carbons are 0.320 and 0.290 g/g respectively. From the results it appears that over the range of partial pressures of Freon 113 that were measured the water loading did not change more than 10%.

4.2 Modeling Uptake Curves

Together with the isotherms from Table 1 the equations 1-4 were solved using a fourth order Runge-Kutta integration The results of the numerical simulation are compared to uptake data for two sample cases: dry BPL and ASC-TEDA previously equilibrated to 80%RH.

It has been noted previously that there is a strong influence from internal diffusion in the impregnated carbons. This is evident from the uptake curve for dry BPL in Figure 2(Dp=1.3E-6 cm^2/s). When the isotherm and diffusion parameters are used the model provides a good fit to the data.

The effect of internal diffusion resistance is even more pronounced with water loading corresponding

to 80%RH, Figure 3. In this case the diffusivity is decreased over that for dry carbon(Dp=0.8E-6 cm^2/s). It can also be seen that the assumption of constant humidity in the isotherm correlation has allowed for close fit of the uptake curve to the data.

5. CONCLUSIONS

The batch adsorption system can be a valuable tool to assess adsorption behavior of precious or highly toxic vapors. Both equilibria and rate data can be obtained using this system. This system has been used to measure multicomponent equilibria for water and organic vapors.

LITERATURE CITED

1. Rodriques, A., "Design Aspects of Fixed-Bed Adsorption Processes", in A. Rodrigues et al. (ed.) Adsorption: Science and Technology, NATO Advanced Study Institute on Adsorption--Science and Technology (1988 : Vimerio, Lisbon, Portugal) p. 239.

2. Okazaki, M., Tamon, H., and Toei, R., "Prediction of Binary Adsorption Equilibria Of Solvent And Water On Activated Carbon", Chemical Eng Journal of Japan, Vol. 11 No. 3 1978, p. 209.

3. Freeman, G. , and Reucroft, P., Adsorption of HCN and H_2O Vapor Mixtures By Activated And Impregnated Carbons", Carbon, 17, 313, 1979.

4. Reucroft, P., Rao, P., and Freeman, G., "Binary Vapor Adsorption By Activated Carbon", Carbon, 21, 171, 1983.

5. Hacskaylo, J. and LeVan, M.D., "Correlation of Adsorption Equilibrium Data Using A Modified Antoine Equation: A New Approach for Pore-Filling Models," Langmuir 1, 97, 1985.

7. Mahle, J., and Friday, D., "Water Adsorption Equilibria on Microporous Carbons", CRDEC-TR-018, 1988.

8. Friday, D., and Mahle, J., "Analysis of A Fixed-Bed Adsorptive Reactor Using The Cyanogen Chloride ASC System", CRDEC-TR-022, January, 1989.

Figure 1.

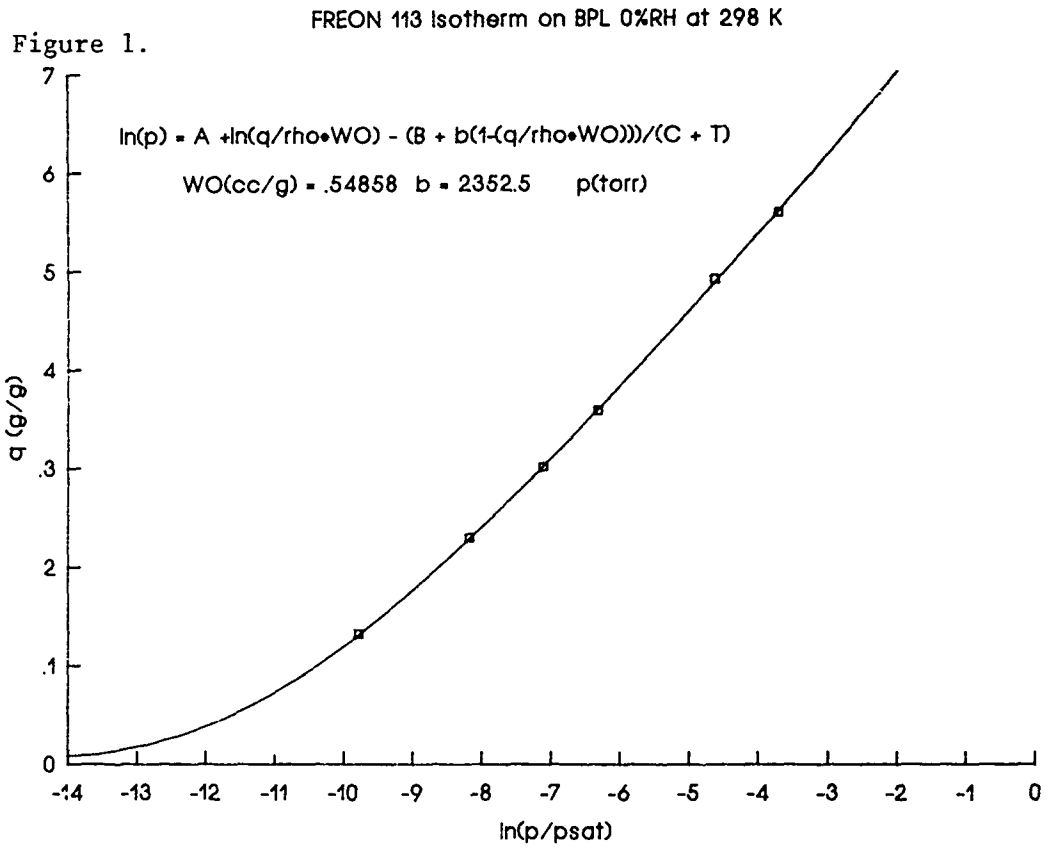

Table 1.

Equilibria Parameters

$$\ln(p) = A + \ln(\theta) - \frac{B + b(1-\theta)}{C + T} \qquad \theta = \frac{q}{\rho W_o}$$

	Conc Range (mg/M^3)	W_o (cc/g)	b*
BPL Dry	150 - 160,000	0.548	2350
BPL 80% RH	500 - 3300	0.220	1500
ASC-TEDA Dry	50 - 13,000	0.433	2150
ASC-TEDA 80% RH	150 - 8000	0.096	1250

Pressure - Torr

Figure 3. Batch Adsorption System
Freon 113 On BPL Dry

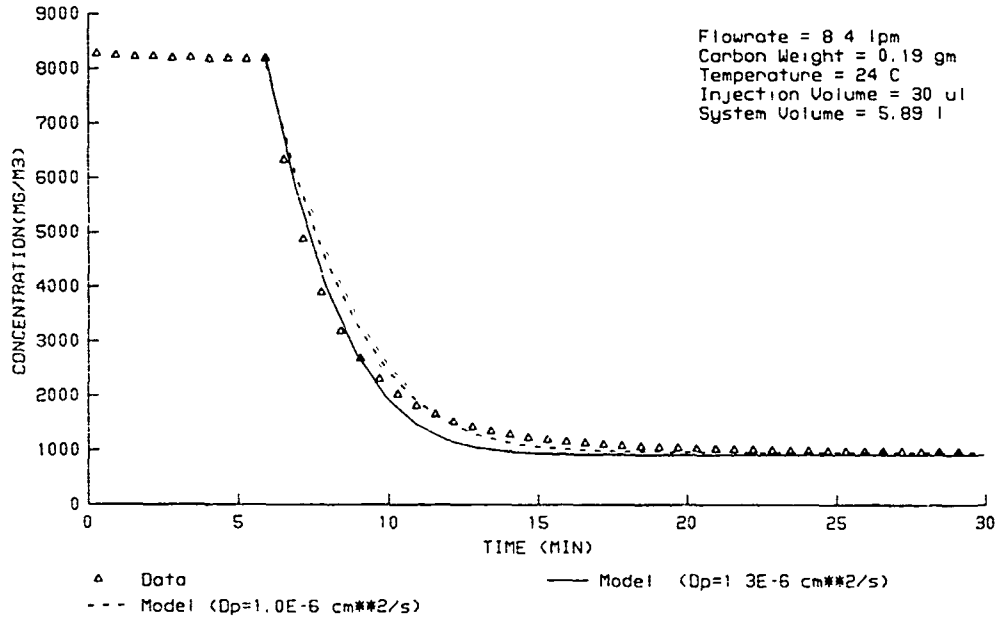

Figure 4. Batch Adsorption System
Freon 113 On ASC-TEDA 80%RH

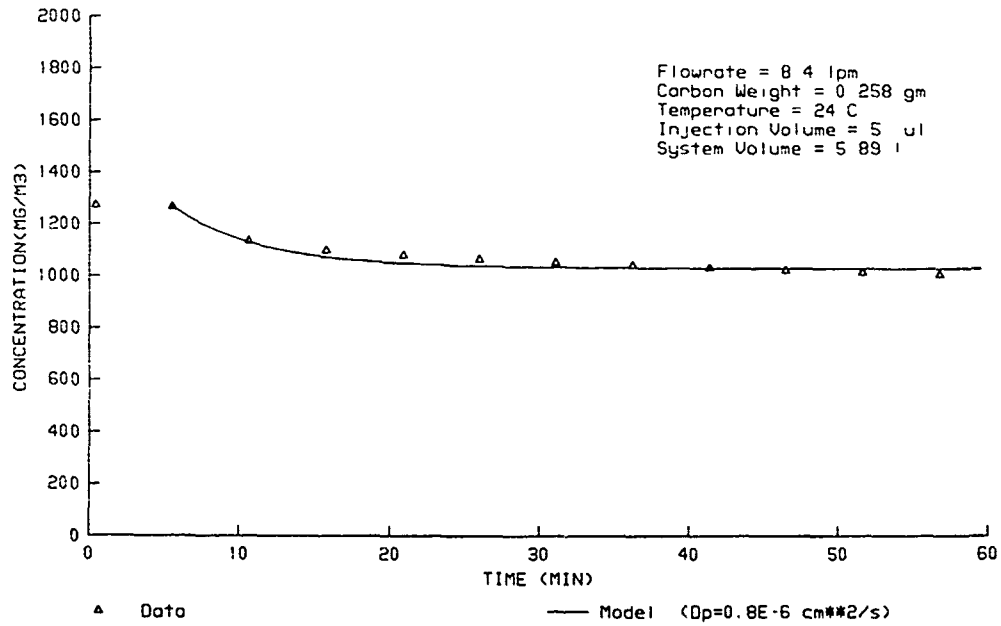

CHARACTERIZATION OF A WEATHERED CARBON DISPLAYING AGGLOMERATION TENDENCIES

Robert A. Lamontagne (1), Richard J. Colton (1), Henry A. Hoff (1), Richard A. Matuszko (2), Louis Isaacson (2), and Joseph Rossin (3)

ABSTRACT

An air purification carbon weathered in a marine environment for a period of 21 months has been characterized. This weathered carbon was divided into four fractions and analyzed for moisture, pH, DMMP capacity, organic loading and impregnated metal speciation (XPS, EDX, SEM). The physical and chemical character of the agglomerated portion will be compared with the character of the other fractions.

INTRODUCTION

At the present time, activated carbon is the medium of choice for use in single pass air filtration systems. This carbon can be used in the natural state or impregnated with a variety of materials to enhance its filtration efficiency or reactivity. Depending upon the weathering profile that the carbon experiences, its filtration efficiency will vary.

One environment that is extremely harsh is the marine environment. The presence of high relative humidities and associated marine atmospheric products presents unique problems not found in other air filtration environments and applications. To our knowledge, the effect of high relative humidities and environmentally produced marine materials on the impregnated metal species on the carbon has not been documented.

Impregnated carbons are presently being used in the Collective Protection Systems (CPS) onboard some Naval vessels. In addition to the marine environment, these carbons experience varied weathering regimes depending upon the mission of the ship. These in-service air purification carbons are routinely analyzed using a suite of analytical methods (4).

Upon retrieval of some of these carbons and subsequent downloading for analysis, it was noted that the carbon in the inlet portion of the carbon filter bed nearest to the metal retaining mesh had formed clumps. These clumps were easily broken with light pressure but still resistent to breaking with gentle handling. The present procedure for downloading the carbon filters is to apportion the carbon into three sections perpendicular

to the direction of air flow. These three fractions have been labeled inlet, center and outlet. In the situation where clumps were noticed, a fourth fraction was created and labeled "clump".

Upon drying the carbon for moisture content, it was noticed that the carbons from the filters which exhibited clumping displayed a whitish or grayish coating on the clumps and on a percentage of the loose carbon particles. This whitish coating had been observed previously on carbons which did not show/produce clumps. The percentage of non-clumped carbon particles which were coated was very small, usually less than 1% of the carbon present.

It was decided to view these clumps and some of the individual carbon particles that exhibited the whitish coating under a low power microscope. It was clear that some form of crystalline structure was present on the surface of the cabon particles. A decision was made to examine the carbon fractions with scanning electron microscopy (SEM), energy dispersive x-ray spectroscopy (EDX) and x-ray photoelectron spectroscopy (XPS) in addition to the standard characterization analyses normally performed.

This paper addresses the characterization results of one air purification carbon that has been weathered in a marine environment. It should be noted that a number of other carbon filters also show clumps or exhibit a tendency to produce clumps. This is deduced from carbon particles which produce a whitish coating upon drying. Isaacson et. al.(5) in a companion paper in the proceedings, will discuss the changes in metal impregnation in more detail.

EXPERIMENTAL

The characterization analyses usually performed on the carbon samples have been reported previously (4), but will be briefly reviewed:

WEIGHT LOSS: Samples are weighed, heated in a box type muffle furnace for three hours, cooled in a desiccator and reweighed.

pH MEASUREMENTS: Weighed carbon samples are placed in a known volume of doubled distilled water and the pH determined with a pencil combination 0-14 pH electrode.

ORGANIC LOADING: The atmospheric organic species adsorbed on the carbon during service were determined by extracting a weighed sample of carbon in a measured vloume of carbon disulfide then analyzed using a capillary gas chromatograph with a flame ionization detector.

DMMP CHALLENGE: Carbon samples are subjected to a DMMP vapor challenge and the effluent profile analyzed. The complete vapor generation system is detailed in the report by Matuszko and Little (6).

The surface analyses performed to characterize the surface of the carbons were:

1) The EDX experiments were performed with a Princeton-Gamma Tech (PGT) System 4 Plus windowless detector mounted on a Hitachi S 800 scanning electron micrograph. The SEM electron accelerating voltage was 10 kV. The carbon samples were placed on stainless steel mounts for analysis.

2) The XPS experiment was performed with a Surface Science Laboratory SSX 100-03 spectrometer using a monochromatized Al Kα x-ray source (1486.6 eV). The carbon clump was placed onto a piece of indium foil.

RESULTS AND DISCUSSION

The carbon being discussed has been weathered in a marine environment for a period of 21 months. Table 1 shows the weight loss for the inlet, center and outlet portions of the weathered carbon as well as for a reference carbon. Note that major weight loss occurs in all portions of the sample, with the center and outlet sections slightly exceeding the inlet section. This behavior is typical of most weathered carbons we have examined. The major weight loss is presently attributed to water with a portion also due to the low molecular weight organics present.

TABLE 1

WEIGHT LOSS

INLET	18 %
CENTER	21 %
OUTLET	23 %
REFERENCE	3 %

Figure 1 shows the degree of whitish coating appearing on the surface of the carbon particles in the inlet portion. The outlet portion does not exhibit carbon particles with the whitish coating. The center portion contains a few whitish particles which are probably due to contamination from the inlet portion during downloading from the filter. Other carbon filter samples in which a very small percentage of coated carbon particles was evident in inlet fraction after heating did not exhibit any evidence that there was intermixing between the fractions. This may very well be a case where the percentage of coated particles is too small to become identifiable in the center section. In no samples have any coated particles been found in the outlet portion.

Table 2 gives the results for pH, color of the water solution of the carbon and the surface area for each fraction of carbon (5). The several reference carbons (unweathered carbon from the same lots) used in the filters have pH's in the range 7.9 to 8.1. The reference carbon for this sample has a pH of 8.1. The clump carbon water extract is much more acidic than the other fractions. Note the progression from an acidic nature in the clump to a neutral condition or slightly alkaline condition in the outlet.

TABLE 2

pH ANALYSIS

SAMPLE	pH	COLOR	AREA (M2/GM)
CLUMP	3.9	BLUE/GREEN	37
INLET	4.7	CLEAR	241
CENTER	6.9	CLEAR	497
OUTLET	7.6	CLEAR	611
REFERENCE	8.1	YELLOW/GREEN	712

There is also a very dramatic color change for the water solutions of these carbon extracts. The reference carbon (unweathered) has the characteristic yellow/green color while the weathered carbons produce a clear solution which is consistent with the results from other weathered carbons. It has been found that a weathering time of four to six months produces a clear solution. Weathering times of less than four months produce degrees of the yellow/green color. The clump sample produces a blue/green color. This color is consistent with the preliminary XPS and EDX analysis.

The surface area results are given as additional evidence that there are very dramatic differences within the filter bed. The reference carbon exhibits an acceptable surface area for a TEDA impregnated carbon. The surface area decreases as the bed is traversed fom the outlet to the inlet. There is approximately a 75 % decrease in the surface area between the inlet and outlet. The clump sample represents a special case. It can be stated that this porion of the filter has little or no filtration capacity with a surface area of only 37 square meters per gram.

Figure 2 presents the gas chromatographic results from the organic loading analysis. The adsorbed species can normally be classified into four major chemical classes; namely, aliphatic hydrocarbons, aromatic hydrocarbons, halogenated alkanes/alkenes and substituted cyclohexanes/cyclohexenes. Previously published results (4) for other carbon samples show the same type of hydrocarbon distribution with the higher boiling materials located on the inlet portion of the bed such as aliphatic C10 to C16 hydrocarbons, and substituted aromatics. The outlet sample contains the more volatile materials such as toluene, xylene, chlorinated alkanes and some aliphatic (C9-C11) hydrocarbons. The center fraction represents a transition between the inlet and outlet in regard to the type of organic loadings identified.

Figure 3 compares the chromatogram of the inlet sample with the clump sample. There is a distinct difference in the hydrocarbon distributions on the two samples. The clump sample has predominately higher boiling compounds with much greater intensities than the inlet sample. The clump sample also exhibits a step series of hydrocarbon peaks starting with C10 and progressing to C16 (n-hexadecane). The inlet sample has C11 and C12 as its two most intense peaks. This distribution of hydrocarbons gives some indication of the types of changes that have taken place on the surface of

the carbon. The more volatile species (xylene, toluene, nonane) are not able to adsorb on to the inlet carbon surface because of the high boilers strongly adsorbed onto this portion of the carbon filter. This analysis is consistent with the smaller weight loss in the inlet portion with the assumption that those portions of the bed having a higher loading of adsorbed hydrocarbons should have less capacity to adsorb water vapor.

DMMP challenges are used to generate the breakthrough curves of figure 4. The reference carbon exhibits a breakthrough time of approximatrly 8 hours for the DMMP challenge used. The inlet sample has a much reduced capacity for DMMP as evident in the breakthrough time of approximately 3 hours. This is consistent with the organic loading results which indicate a high level of high boiling, strongly adsorbed organic materials on the carbon. The center and outlet samples have intermediate times consistent with the characterization results obtained. The center breakthrough time occurs slightly earlier than the outlet one.

Upon observing the clump samples under a low power microscope, small cyrstals were observed on the surface. These crystals appeared to dehydrate under the optic light of the microscope in about two hours and produced the whitish coating observed when the samples were dried in the oven. Preliminary XPS analysis indicated that the crystals on the surface were copper sulfate with five waters of hydration (Fig.5). SEM photographs coupled with (EDX) analysis are consistent with the presence of copper sulfate on the surface. The preliminary EDX analysis indicates that most of the surface of the carbon in the clump sample is covered with copper sulfate. No copper sulfate was found in the other portions of the bed. As expected, individual carbon particles with the whitish coating also had copper sulfate present on the surface.

The XPS and EDX analysis presents clear evidence that copper sulfate is present on the surface of the carbon in the clump samples. This is consistent when the clump samples are placed in water since the characteristic blue/green color of copper sulfate is observed. Surface area analysis indicates that there is minimum surface area available for adsorption to take place. The gas chromatograph results indicate a variable, but predictable organic distribution adsorbed onto the surface of the carbon. The organic species identified on the clumps and inlet portions represnt high boiling, strongly adsorbing hydrocarbons. The clump sample is different from the rest of the carbon in the bed. Weight loss and DMMP challenge have not been performed on the clumps because of the difficulty in obtaining a large enough quantity to perform the analysis. However, we believe that the results from these analyses would support the general consensus that the clump samples and those carbon samples that exhibit a whitish coating upon drying would be uniquely different from the bulk carbon.

How copper sulfate is produced on the surface of the carbon is speculative at the present time. Exposure to a marine environment with high relative humidities must be taken into consideration as well as the presence of acid rain as a source of sulfate for the clumping phenomena. Remote marine aerosol particles consist primarily of sulfates and sea salts (7). It is generally assumed that the sub-micron fraction of the sulfate particles are formed in a gas-to-particle conversion process by oxidation

of marine sulfur dioxide (8). There is sulfur present in the carbon, but the amount present is insufficient to produce the amount of copper sulfate present on the surface. The mechanism(s) which produce copper sulfate on the surface of the carbon is being investigated.

CONCLUSIONS

The results of the analyses for this carbon show: 1) copper sulfate is formed on the clump and inlet portion of the bed with subsequent loss of adsorption capacity and reactivity; 2) higher boiling, strongly adsorbing hydrocarbons keep water from adsorbing in the inlet region of the bed; 3) organic contaminants migrate non-uniformly within the carbon bed; 4) pH measurements show the inlet portion of the bed to be acidic while the outlet portion is in the neutral range.

The differences documented for the various fractions of the bed indicate that these changes can have a profound effect on the filter bed. The cumulative results effectively decrease the bed depth and overall efficiency of the filter. Characterizing the type, amount and distribution of the contaminants on weathered carbons is critical in evaluating and predicting residual filter life, carbon effectiveness and protection ability.

ACKNOWLEDGEMENT

This work was supported under Navy project element 63514N.

REFERENCES

1. Naval Research Laboratory, Washington, D.C. 20375

2. Geo-Centers Inc., Fort Washington, Md 20744

3. Chemical Reseach, Development and Engineering Center, Aberdeen Proving Ground, Md 21010

4. Lamontagne, R.A., L.Isaacson, R.A.Matuszko, "Characterization of Contaminated Air Purification Carbons," CRDEC-SP-013, November 1988.

5. Isaacson, L., R.A.Lamontagne, E.Riley, J.Rossin, "Effects of Environmental Weathering on the Properties of an ASC-TEDA Radial Flow Carbon Filter: Metal Impregnants," CRDEC Proceedings, November 1989.

6. Matuszko, R. and R.C.Little, "A System for Evaluating Sorbent Lifetimes," NRL Report No. 6052, September 1987.

7. Bates, T.S., R.J.Charlson, R.H.Gammon, "Evidence for the Role of Marine Biogenic Sulfur," Nature, Vol 329, No.6137, September 1987.

8. Bonsang,B., B.C.Nugyen, A.Gaudry, G.Lambert, "Sulfate Enrichment in Marine Aerosols Owing to Biogenic Gaseous Sulfur Compounds," J. Geophys. Res. 85, December 1980.

FIGURE 1

SAMPLE AFTER DRYING

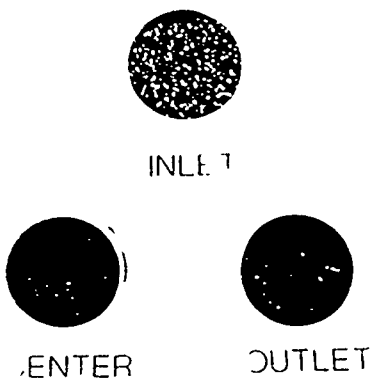

FIGURE 2

CHROMATOGRAM CF CARBON DISULFIDE EXTRACT OF CARBON SAMPLE

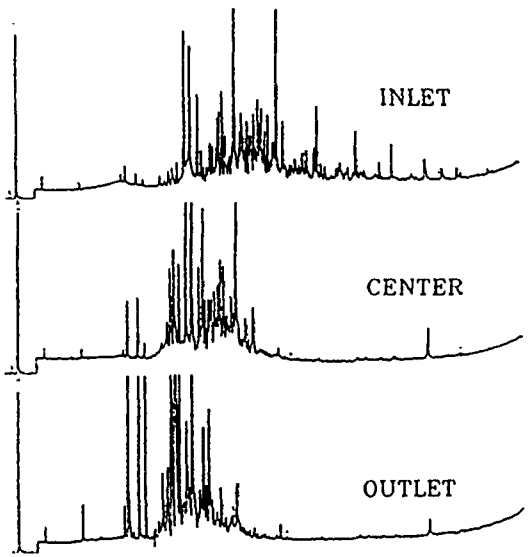

FIGURE 3

CHROMATOGRAM OF CARBON DISULFIDE EXTRACT OF CARBON SAMPLE

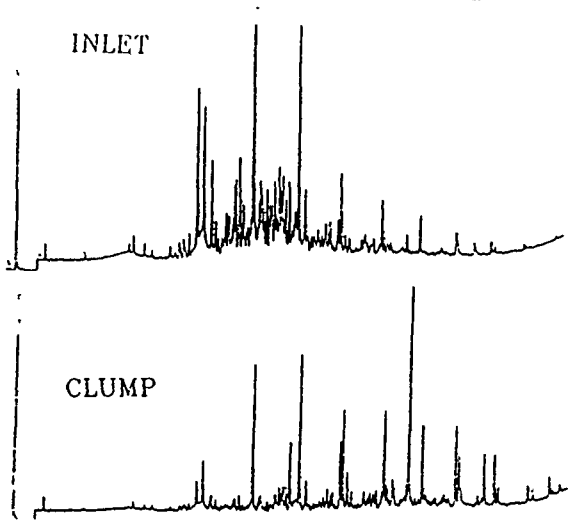

FIGURE 4

DMMP ON N-100 SERIES CARBON
350-370 PPM CHALLENGE

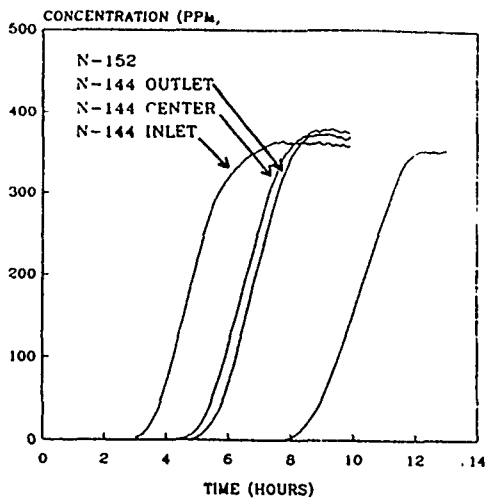

FIGURE 5

XPS SPECTRUM OF CLUMP

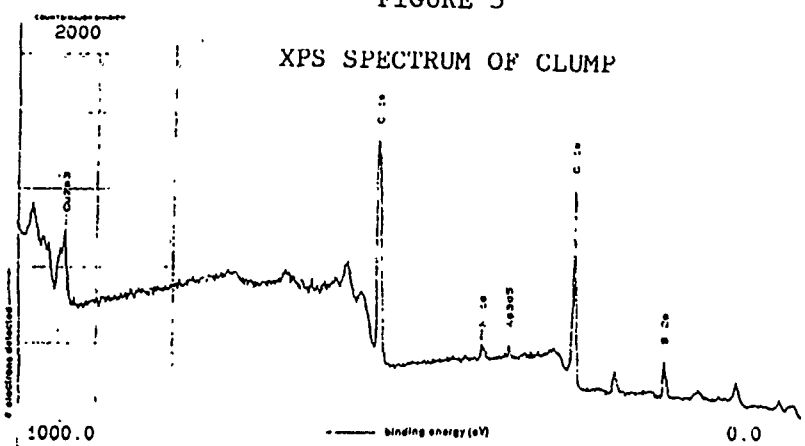

BLANK

Environmental Weathering of a Radial Flow Carbon Filter

Louis Isaacson; Geo-Centers, Inc., Suitland, MD 20744
Robert Lamontagne; Naval Research Laboratories,
Washington, DC 20375
Erica Riley; CRDEC, Aberdeen Proving Ground,
MD 21010
Joseph Rossin; CRDEC, Aberdeen Proving Ground,
MD 21010

Carbon samples from different locations within a radial flow filter exposed to a marine air stream for 21 months were analyzed using surface analysis methods. The effects of weathering resulted in the migration of the impregnants to the external surface of the granule and the formation of metal sulfates. The weathering effects were found to be most severe at the inlet region of the filter. Results pertaining to the chemical and physical changes of the impregnants will be discussed as a function of bed depth.

INTRODUCTION

Activated carbon provides protection against chemical agents by either adsorption of the agent within the micropores and/or chemical reaction with the copper/chromium/silver impregnants. The carbon filter employed on the modern day gas mask is sealed under vacuum and removed/installed only in the event of a chemical threat. In this manner, the filter is not exposed to the environment prior to the threat and loss of performance due to atmospheric weathering need not be taken into consideration. Unlike the gas mask filter, the filter employed for collective protection applications (e.g. fixed installations, armored vehicles, naval vessels, etc.) may be required to function continuously, whether or not a chemical threat exists. This results in the collective protection filter being continuously subjected to environmental contaminants which may reduce the filter performance against a chemical attack.

The objective of this study is to determine in detail the effects of environmental weathering on collective protection carbon filters. This work focuses on the changes in metal speciation and distribution within carbon granules removed from various locations within a radial flow carbon filter following 21 months of weathering in a marine environment. This study is part of an ongoing effort at CRDEC and NRL.

EXPERIMENTAL METHODS

Materials. ASC Whetlerite (Lot # 103) was obtained from Calgon Corporation as 12-30 mesh (U.S. Standard Sieve) granules. This sample contained 8% copper, 3% chromium, 0.05% silver and 2% tetraethylenediamine (TEDA) by weight. This sample will be referred to as ASC-TEDA.

Weathering of ASC-TEDA carbon. The weathered samples of ASC-TEDA carbon were obtained from a radial flow filter which had been exposed to a marine environment in an operational collective protection system. The collective protection filter is shown in Figure 1. This carbon filter was exposed to normal operating conditions representative of the sea going vessel.

Following weathering, carbon was removed from the radial flow filter and separated into four sections perpendicular to the direction of air flow. The four sections consisted of the inlet most portion of the filter (referred to as INLET throughout the text); a mixture of carbon from the filter inlet to a point extending one-third of the way into the bed (INLET 1/3); a mixture of carbon from a point one-third of the way into the bed to a point extending two-thirds of the way into the bed (CENTER 1/3); and a mixture of carbon from a point two-thirds of the way into the bed extending to the filter outlet (OUTLET 1/3). Samples removed from the inlet most region of the filter were clumped together, while samples removed from the other portions of the bed displayed no evidence of clumping.

Equipment. X-ray Photoelectron Spectroscopy (XPS) spectra were recorded using a Perkin-Elmer Phi 570 ESCA/SAM system employing MgK-α X-rays. Samples were analyzed for carbon, oxygen, copper, chromium and sulfur. No silver could be detected, likely due to the low quantity (0.05 wt%) associated with the sample. All binding energies reported are referenced to the carbon 1s photoelectron peak at 284.6 eV. The fraction of chromium(VI) was determined by subtracting the spectrum of chromate from that of the carbon granule[1]. Atomic ratios pertaining to elements of interest were determined by correcting peak areas using instrument supplied sensitivity factors.

Energy Dispersive X-ray Spectroscopy (EDS) was performed using a Tracor Northern 5700 EDS/WDS automation system interfaced with a JEOL 35CF scanning electron microscope. Cross sectional analysis was performed on single carbon granules bisected with a diamond knife. Analyses of the bisected carbon granules were performed by collecting spectra from a 100μm by 100μm square area stepped across the largest sample diameter.

Cyanogen Chloride Reactivity. The reactive properties of the unweathered and weathered samples of ASC-TEDA were determined by a cyanogen chloride (CK) breakthrough test. Approximately 18 g of carbon were placed into a glass bed and equilibrated with 80 % RH air at 80 °F overnight. The CK test was performed at 80 %RH, 80 °F with a CK feed concentration of 4 mg/l air and a linear bed velocity of 9.6 cm/s. The breakthrough time is defined as the time the effluent CK concentration exceeds 8μg/l.

Surface Area Determination. The surface areas of the unweathered and weathered samples of ASC-TEDA were determined using a Quantasorb Surface Area Analyzer. This instrument provides nitrogen BET surface areas using the desorption behavior of nitrogen from the carbon samples.

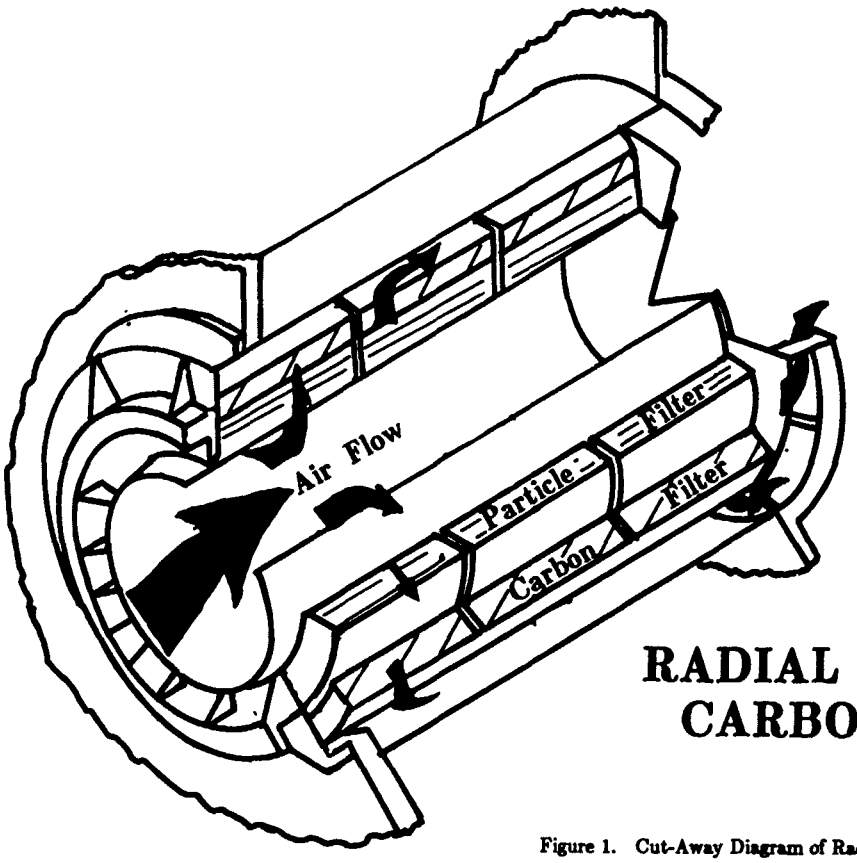

Figure 1. Cut-Away Diagram of Radial Flow Carbon Filter.

RESULTS

XPS analyses of the carbon samples are reported in Figures 2 and 3. In addition to carbon, copper, chromium and oxygen (as detected on the unweathered sample), a significant fraction of sulfur was detected on the samples from the filter INLET and INLET 1/3. Surprisingly, no sodium was detected, as one might expect due to the salt water environment. No silver was detected on either the unweathered or weathered sample, likely because the concentration of silver (about 0.05%) is below the detection limit of the instrument. Figure 2 compares the XPS spectra of the copper 2p photoelectron region of the weathered carbon granules from the different filter locations. The position of the copper $2p_{3/2}$ photoelectron peak corresponding to the unweathered sample is indicative of copper in the +2 oxidation state[1,2,3]. Figure 2 shows the position of the copper 2p peak to be shifted to a higher binding energy for carbons from the INLET and INLET 1/3 region of the filter relative to that of the unweathered sample. These peaks also appear broader than the peak corresponding to the unweathered sample. Note also the changes in the satellite shake-up region (about 939 to 947 eV) of the spectrum corresponding to the INLET sample. Spectra corresponding to the CENTER 1/3 and OUTLET 1/3 samples appear identical with that of the unweathered sample.

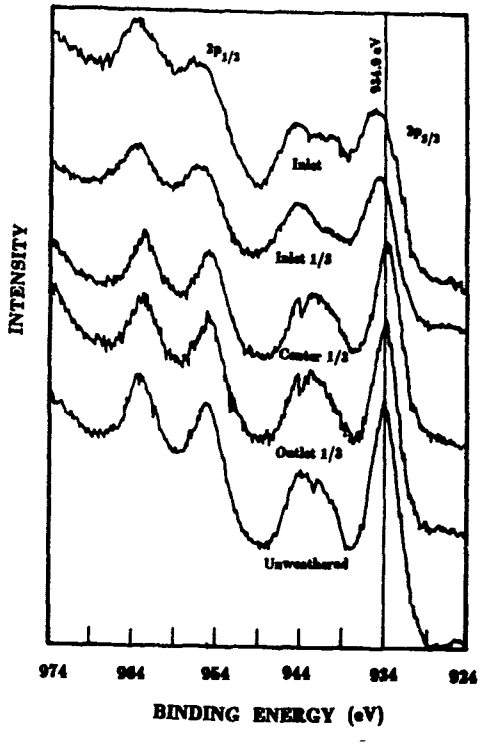

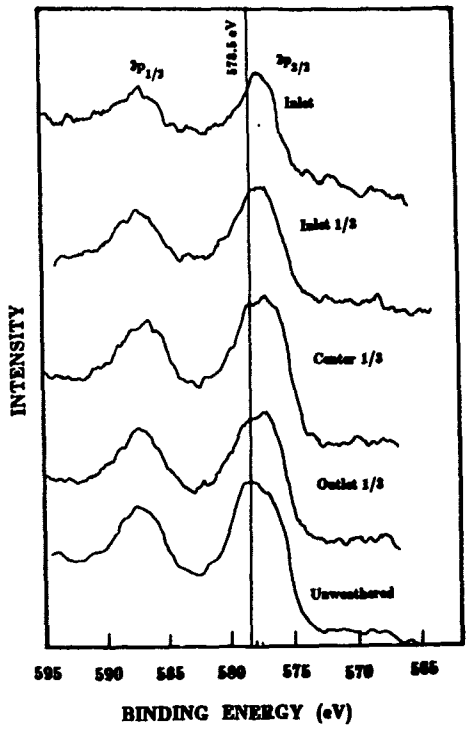

Figure 2. XPS Spectra of the Copper 2p Photoelectron Region for Fresh and Weathered Carbon Samples.

Figure 3. XPS Spectra of the Chromium 2p Photoelectron Region for Fresh and Weathered Carbon Samples. All samples analyzed as a powder.

Figure 3 compares the XPS spectra of the chromium 2p photoelectron region of the weathered carbon granules from the different filter locations. The spectrum corresponding to the unweathered carbon sample is shown for comparison. The position of the chromium $2p_{3/2}$ photoelectron peak corresponding to the unweathered sample is 578.5 eV, indicative of chromium in the +6 oxidation state[2,3,4]. The shoulder, present at about 576.5eV, is due to the presence of chromium(III) species. For the unweathered carbon sample, approximately 60% of the chromium associated with the sample was determined to be in the +6 oxidation state. The spectrum corresponding to the INLET carbon exhibits a $2p_{3/2}$ peak approximately 1.0 eV lower than that of the unweathered sample. Note also that the signal 578.5 eV is very weak, indicating that virtually no chromium is present in the +6 oxidation state. Moving further into the filter (INLET 1/3), the chromium $2p_{3/2}$ peak remains at a lower binding energy, but is much broader than that corresponding to the INLET sample. Moving still further into the filter (CENTER 1/3), the chromium $2p_{3/2}$ peak exhibits a strong shoulder at about 578.5 eV,

suggesting that a significant fraction of chromium(VI) is associated with this sample. The spectra from the CENTER 1/3 and OUTLET 1/3 are nearly identical. Approximately 40% of the chromium associated with each of these samples was determined to be in the +6 oxidation state.

Figure 4 shows a backscattered electron image (BEI) of a representative INLET carbon granule. The BEI is similar to an SEM; however, the BEI highlights high concentrations of metallic elements. Note from the figure that large regions of the weathered granule appear covered with an amorphous overlayer. EDS microbeam analysis of the amorphous overlayer revealed it to consist primarily of copper and sulfur; only a trace amount (<5%) of chromium was present.

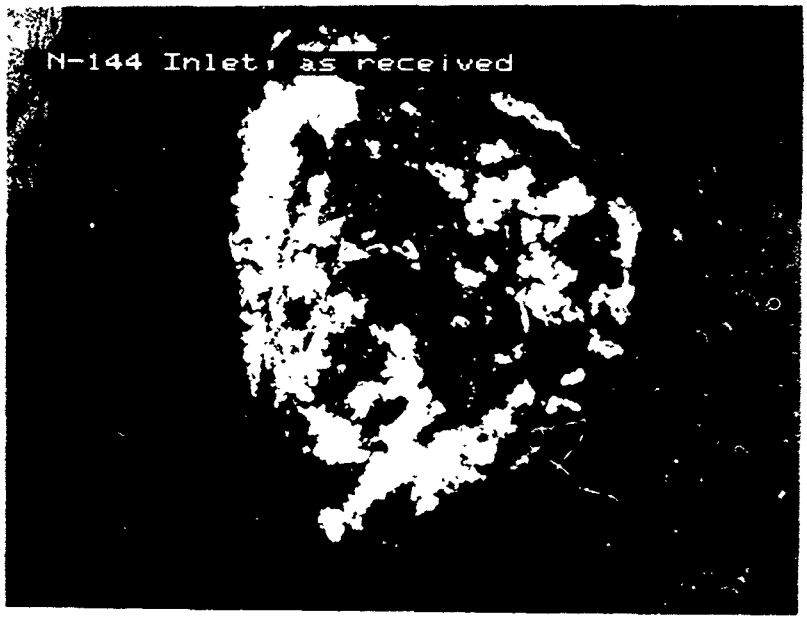

Figure 4. Backscattered Electron Image (BEI) of an ASC-TEDA Carbon Granule from the Filter Inlet following Weathering.

The surface area and CK breakthrough time of the unweathered and weathered samples are reported in Table 1. No CK data regarding the INLET sample was recorded, as there was not enough sample from the inlet most region of the carbon bed to perform the CK test.

DISCUSSION

The changes which have occurred in the carbon granules as a result of atmospheric weathering were found to be a function of location within the filter. Samples removed from the inlet region of the filter were much more severely affected by weathering than samples located further into the bed, similar to the observations of Deitz et al.[4]. Apparently, the inlet region of the filter rather effectively removes the airborne contaminants, preventing them from interacting with carbon further into the filter.

Table 1: Surface Area and CK Breakthrough Time for ASC-TEDA Samples From Different Filter Locations.

Sample	Surface Area (M^2/g)	CK Breakthrough Time (min)
INLET	37	-----
INLET 1/3	241	< 5.0
CENTER 1/3	497	24.2
OUTLET 1/3	611	24.6
Unweathered	712	37.8

Freshly prepared ASC Whetlerite is believed to contain copper-ammonium-chromium complexes[5]. These complexes possess chromium in the +6 oxidation state and are postulated to be responsible for the destruction of light gases; namely cyanogen chloride and hydrogen cyanide[2,5,6]. Changes in the impregnant speciation are expected to reduce the reactive properties of the carbon. It is evident from the data presented in Figures 2 and 3 that large scale changes in the copper and chromium speciation have occurred as a result of the marine weathering for samples located at the inlet region of the filter. The impregnants associated with carbon from the inlet regions of the filter have been transformed into metal sulfates as a result of weathering, based on the XPS analyses. Past the inlet third of the filter, virtually no sulfur was detected, suggesting that the airborne sulfates have been removed at the filter inlet. It was also evident that the impregnants associated with the inlet carbons have migrated from within the granule to the external surface (see Figure 4). EDS analysis of the bisected granule from the filter inlet revealed that virtually no impregnants were present within the granule.

EDS analyses of the CENTER 1/3 and OUTLET 1/3 samples indicated that metal migration did not occur to a significant extent. This suggested that leaching of metals was a result of sulfate formation and therefore confined to only the filter inlet. No change in the copper speciation was detected for samples located at the CENTER 1/3 and OUTLET 1/3 of the filter. However, a reduction of chromium(VI) to chromium(III) is evident. Quantitative XPS analysis of these samples indicates a decrease in the fraction of chromium(VI) from 60% to 40%, compared to the unweathered sample. The decrease in the fraction of chromium(VI) was expected to reduce the CK breakthrough time, as the chromium(VI) fraction has been linked to CK destruction.

Cyanogen chloride breakthrough times for the weathered carbon samples were recorded in an effort to determine the reactive properties of the weathered carbon from the different bed locations. These data are reported in Table 1. The INLET 1/3 sample possessed a small fraction of chromium in the +6 oxidation state. The cyanogen chloride breakthrough time indicated that carbon from this region of the filter provided virtually no protection against light gases. The breakthrough time for carbon located at the center and outlet of the filter were identical. Note that both samples possess approximately 40% of the chromium in the +6 oxidation state. Breakthrough times for both these samples, however, were about 35% less than that of the unweathered sample. It is interesting to note that the decrease in the chromium(VI) fraction (about one-third) corresponds to a proportional decrease in the CK breakthrough time. This is consistent with recent studies which have linked CK reactivity to the chromium(VI) content of the carbon sample[2,7]

CONCLUSIONS

1) The inlet portion of the filter was severely affected by weathering.

2) Weathering resulted in the formation of metal sulfates at the filter inlet. These sulfates leached impregnants to the external surface of the granule. No sulfates were detected past the inlet third of the filter.

3) Past the inlet third of the filter, approximately one-third of the chromium(VI) fraction had been reduced to chromium(III) species.

4) Weathering reduced the effectiveness of the filter against removal of light gases by approximately 50%.

Acknowledgements: One of us (J.A.R.) wishes to thank the National Research Council for financial support on this project. R.A.L and L.I. thank NAVSEA for financial support. The authors wish to thank J. Rehrmann for providing the surface area measurements and R. Grue for providing the CK data.

LITERATURE CITED

1) Rossin, J. A., "XPS Surface Studies of Activated Carbon," *Carbon* Vol. 27, p.611 (1989).

2) Ross, M. M., Colton, M. M. and Deitz, V. R., "The Study of Whetlerite Surfaces by X-ray Photoelectron Spectroscopy," *Carbon* Vol. 27, p. 426 (1989).

3) Hammarstrom, J. L. and Sacco, A., "Investigation of Deactivation Mechanisms of ASC Whetlerite Charcoal," *J. Catal.* Vol. 112, p. 267 (1988).

4) Deitz, V. R., Puhala, R. J., Stroup, D. B. and Dickey, G. F., *"Influence of Atmospheric Weathering on the Performance of Whetlerite"*, Naval Research Laboratory Memo. Report No. 4752, Washington, D.C. (1982).

5) Pytlewski, L. L., *"Studies of ASC Whetlerite Reactivity,"* Report ARCSL-CR-79008, U.S. Army Chemical Systems Laboratory, Aberdeen Proving Ground, Maryland, Nov. 1979, UNCLASSIFIED Report.

6) Krishnan, P. N., Katz, S. A., Birenzvige, A. and Salem, H., "The Role of Chromium in ASC Whetlerite," *Carbon* Vol. 26, p.914 (1988).

SINGLE AND BINARY ADSORPTION OF n-NONANE AND XYLENE ON BPL CARBON

Richard A. Matuszko[1], David K. Friday[1], Louis Isaacson[1],
and Robert A. Lamontagne[2]

ABSTRACT

Single component isotherms are measured for n-nonane and xylene on BPL carbon using an automated, static adsorption apparatus. The isotherm data are correlated using a modified Antoine equation. A Binary adsorption isotherm relationship is produced from the single component correlations using the Ideal Adsorbed Solution Theory (IAST). Breakthrough curves are measured for single vapor and selected binary mixture feeds. A computer stage model, integrating the correlated single isotherms and IAST binary isotherm, is used to predict both the single and binary component breakthrough curves. The model predictions are compared with the measured breakthrough data.

Single component breakthrough data show that xylene breaks through later than nonane under identical test conditions. However, measured binary breakthrough data with equimolar feeds show a roll-up of xylene. The stage model predicts this xylene roll-up. The phenomenon of roll-up and the concept of selectivity reversal for a binary system is investigated.

INTRODUCTION

For many years, researchers have sought to unlock the secrets of multi-component equilibria. Because of the difficulties involved with measuring multi-component data, research has centered on creating adequate predictive models using information obtained from single component data. Langmuir's extended isotherm[3] was the first of the multi-component, predictive isotherm models. It suffered, however, from its very limited applicability due to its poor fit of even the single component data.

In 1965, Myers and Prausnitz[4] developed the Ideal Adsorbed Solution Theory (IAST) which allowed the use of any single component isotherm equation to predict multi-component isotherms. In 1980, Suwanayuen and Danner[5] introduced the Vacancy Solution Theory (VST) which correlated single component data into their single component isotherm model and extended it to a multi-component isotherm. Both theories were effective in predicting isotherms for selected multi-component systems, but began to lose appeal when their limitations were investigated. The VST was not thermodynamically consistent, and forced the user to use a specific single component isotherm

model. The IAST was thermodynamically consistent and allowed any single component isotherm equation to be used, but suffered from its inability to predict systems where the adsorbed phase was non-ideal.

To address the imperfections of the IAST, modifications were performed using binary data to calculate mixing parameters such as activity coefficients. Although these modifications improved the accuracy of the multi-component isotherm fits, and have great utility in many applications, they stray from the original purpose of the predictive model. The IAST was originally proposed to avoid the tedious task of measuring multi-component data and provide an adequate engineering approximation of the multi-component adsorption isotherm.

Some attempts to modify IAST have, in fact, led to erroneous applications of mixing parameters. Assumptions that non-idealities of mixing are the answer to imperfect multi-component fits of the IAST have led to the incorrect calculation of activity coefficients. Myers[6] shows that failure of the IAST to accurately predict multi-component isotherms in a number of systems is not due to non-unity activity coefficients, but due to the inadequacy of the single component isotherm model employed.

It has been further claimed that IAST does not, and in fact can not, predict irregular isotherm behavior such as the formation of azeotropes. Hyun and Danner[7] and Coroyannakis[8] each state that IAST can not predict an adsorption azeotrope and selectivity reversal. Myers, with his Heterogenous IAST[9], shows that a selectivity reversal can be predicted with the IAST if the correct single component isotherm model is employed.

This paper proposes that using the modified Antoine equation first proposed by Hacskaylo and LeVan[10] to correlate single component isotherm data, IAST can and will predict a selectivity reversal for a binary system. The adsorbate pair of xylene and n-nonane on BPL carbon is investigated and shown to yield a selectivity reversal. IAST is applied and yields a qualitative prediction of the selectivity reversal.

THEORY

First, isotherm data are correlated using a modified Antoine equation first proposed by Hacskaylo and LeVan[10]. The equation has the form:

$$\ln(P_i) = A_i + \ln(\theta_i) - \frac{B_i + b_i(1 - \theta_i)}{C_i + T} \qquad (1)$$

The Antoine coefficients are readily found in the literature. The parameters b and the normalizing factor for θ_i ($n_{0,i}$) are fit using a Newton-Raphson routine to minimize the function:

$$\text{Error} = \Sigma(|\ln(P_{calculated}) - \ln(P_{experimental})|) \qquad (2)$$

Binary isotherms are generated using the Ideal Adsorbed Solution Theory (IAST) with the LeVan isotherm equations for each component. It should be noted that the IAST can be readily extended to more than two

components. However, for this paper, we are confining the analysis to two components. Details of the IAST are given in reference 4.

The LeVan isotherm is particularly well suited for adaptation into the IAST because it reduces to Henry's law at low coverage. In addition, for computer programs that use values of n_i to calculate values of P_i, the IAST-LeVan isotherm system reduces to easily calculable explicit functions. The IAST spreading pressure integral,

$$f_i(\pi) = \int_0^{n^\circ_i} \frac{d\ln P}{d\ln n}\, dn \qquad (3)$$

when combined with equation (1), reduces to the form:

$$f_i(\pi) = n^\circ_i + \frac{b_i {n^\circ_i}^2}{2n_{0,i}(C_i + T)} \qquad (4)$$

The spreading pressure functions of equation (4) are then set equal for each component yielding:

$$n^\circ_1 + \frac{b_1 {n^\circ_1}^2}{2n_{0,1}(C_1 + T)} = n^\circ_2 + \frac{b_2 {n^\circ_2}^2}{2n_{0,2}(C_2 + T)} \qquad (5)$$

Equation (5) is solved simultaneously with the IAST requirement that there is no change in the area/molecule on mixing:

$$\frac{1}{n_1 + n_2} = \frac{x_1}{n^\circ_1} + \frac{x_2}{n^\circ_2} \qquad (6)$$

to yield explicit solutions for n°_1 and n°_2 as functions of n_1 and n_2. Corresponding values of P°_1 and P°_2 are readily obtained using equation (1) substituting n°_1 and n°_2 for n_i for each single component isotherm. Finally, using the IAST vapor phase - adsorbed phase equilibrium expression:

$$P_i = x_i P^\circ_i \qquad (7)$$

the vapor phase concentrations P_1 and P_2 are obtained.

Breakthrough curve predictions are generated using a stage model similar to that employed by Friday and LeVan[11]. It is assumed that the system is isothermal with no axial dispersion and negligible vapor phase accumulation. An external film resistance is employed using a linear driving force approximation.

SELECTIVITY REVERSAL

The spreading pressure integral in equation (3) is equivalent to the area under an isotherm curve from 0 to P°_i plotted as n vs lnP as shown in Figure 1. An equilibrium requirement of the IAST is that the spreading pressures, and thus the areas under the isotherm curves bounded by 0 and

P°_i, be equal. Since the isotherm equations are fixed for each system, areas under the curves are varied by selecting values of P°_i such that the spreading pressure integrals for each component are equal.

In certain binary adsorption systems, the Henry's law slope for component 1 is greater than that of component 2 while the molar saturation capacity, $n_{0,i}$, is greater for component 2 than for component 1. In these situations, the single component isotherms cross. In selected cases, to achieve equal areas under the n vs ln(P) curve as required by the IAST, the relative values of P°_1 and P°_2 must reverse. Myers and Prausnitz define a selectivity[4], $s_{1,2}$:

$$s_{1,2} = \frac{x_1/y_1}{x_2/y_2} = \frac{P^\circ_2}{P^\circ_1} \qquad (8)$$

From this definition, it follows that a reversal in the relative magnitudes of P°_1 and P°_2 results in a reversal of the selectivity $s_{1,2}$ (i.e. $s_{1,2} > 1$ to $s_{1,2} < 1$).

EXPERIMENTAL

MATERIALS

The adsorbent used for these experiments was a 12-30 mesh BPL carbon obtained from Calgon corp. The carbon was prepared prior to use by heating in a drying oven for 3 hours at 150 degrees C. The adsorbates selected for the experiments were n-nonane (Phillips 66, 99% purity) and a xylene mixture containing meta, para, and ortho isomers (Fisher Scientific, A.C.S. certified grade). These adsorbates were used without further purification.

DATA COLLECTION

The experimental apparatus for collecting isotherm data consisted of a Cahn micro-balance integrated with a vacuum pump and a computerized data acquisition and control system. Details of the system and operating procedure can be found in reference 12.

A computer controlled system was employed to generate and test vapor challenges to a fixed bed of the BPL adsorbent. The amount of carbon added was standardized at a bed depth of 1 cm. Details of the system and operating procedure can be found in reference 13.

RESULTS AND DISCUSSION

A prediction of the isotherm behavior for the xylene/nonane system was generated using the IAST-LeVan binary isotherm model. Figure 2 is a plot of the prediction which shows that the IAST predicts a selectivity reversal for the binary pair. The line in Figure 6 represents the concentrations of xylene and nonane where the selectivity is one. According to this prediction, if a breakthrough experiment was performed using feed concentrations on the left side of the unity selectivity line, xylene should roll-up. If, however, the feed concentrations were to the right of the unity selectivity line, nonane should roll-up.

In an attempt to confirm the predicted selectivity reversal, breakthrough experiments were run using feed conditions on either side of the line of equal selectivity. Figure 3 gives the results of the first the binary challenge experiments. The stage model prediction using the is also shown on the plot. Xylene and nonane at 200 ppm each were fed simultaneously to a clean bed of BPL carbon. According to the IAST isotherm prediction, the data should exhibit a roll-up of xylene. It can be seen that both the data and the stage model show a roll-up of xylene. Important features such as time of initial breakthrough of the toe of each wave as well as the qualitative features of the roll-up phenomenon are predicted by the stage model.

Breakthrough experiments were then run with very high feed concentrations to confirm that a selectivity reversal would indeed occur. Figure 4 gives the results of a breakthrough experiment with an equimolar feed of xylene and nonane of 3000 ppm. As the IAST isotherm predicts, the selectivity has reversed and the nonane is rolled-up by the xylene.

The failure of the IAST-LeVan isotherm to predict exact breakthrough behavior of a binary pair that demonstrates the non-idealities found in the nonane/xylene system does not in any way reflect poorly on the theory as a whole. Considering that the isotherm prediction uses no fitted binary parameters, is considered ideal, and uses no low coverage isotherm data, the ability to qualitatively predict binary breakthrough behavior when combined with the stage model is quite remarkable.

CONCLUSIONS

1. The IAST can predict selectivity reversals if the proper single component isotherm model is used.

2. For a selectivity reversal to occur in the IAST, the single component isotherms must cross in a plot of moles/mass carbon versus partial pressure.

3. Engineering predictions of binary component breakthrough behavior can be performed using single component isotherm data.

NOTATION

A_i, B_i, C_i	=	Appropriate Antoine coefficients for component i
b_i	=	LeVan equation fitting parameter for component i
$f_i(\pi)$	=	spreading pressure function for component i
n_i	=	number of moles of component i in adsorbed phase per unit mass of adsorbent in equilibrium with P_i
$n_{0,i}$	=	saturation capacity of adsorbent for component i per unit mass of adsorbent
n°_i	=	number of moles of component i in adsorbed phase per unit mass of adsorbent in equilibrium with P°_i
P_i	=	partial pressure of component i

P°_i = pressure of pure component i corresponding to spreading pressure π in equilibrium with n°_i

$s_{1,2}$ = selectivity coefficient for component 1 relative to component 2

x_i = mole fraction of component i in adsorbed phase

y_i = mole fraction of component i in gas phase

π = spreading pressure

θ_i = $n_i/n_{0,i}$ - fractional surface coverage

REFERENCES

1. Geo-Centers, Inc., 10903 Indian Head Highway, Fort Washinton, MD 20744.

2. Naval Research Laboratory, Code 6180, 4555 Overlook Avenue, Washington DC 20375.

3. "Principles of Adsorption and Adsorption Processes", Ruthven, D. M., John Wiley & Sons, New York, p. 106, 1984.

4. Myers, A. L. and Prausnitz, J. M., "Thermodynamics of Mixed-Gas Adsorption," AIChE J., 11, 121 (1965).

5. Suwanayuen, S. and Danner, R. P., "Vacancy Solution Theory of Adsorption from Gas Mixtures," AIChE J., 26, 76 (1980).

6. Myers, A. L., "Activity Coefficients of Mixtures Adsorbed on Heterogenous Surfaces," AIChE J., 29, 691 (1983).

7. Hyun, S. H. and Danner, R. P., "Equilibrium Adsorption of Ethane, Ethylene, Isobutane, Carbon Dioxide, and Their Binary Mixtures on 13X Molecular Sieves," J. Chem. Eng. Data, 27, 196 (1982).

8. Coroyannakis, P., "Studies on Isotherm Multi-Component Sorption Using Equilibrium Theory," PhD dissertation for the Department of Chemical Engineering and Applied Chemistry, University of Toronto, 1987.

9. Myers, A. L., "Molecular Thermodynamics of Adsorption of Gas and Liquid Mixtures," Proceedings of the Second Engineering Foundation Conference on Fundamentals of Adsorption, May 4-9, 1986, Santa Barbara, CA, p. 3.

10. Hacskaylo, J. J. and LeVan, M. D., "Correlation of Adsorption Equilibrium Data Using a Modified Antoine Equation: A New Approach for Pore-Filling Models," Langmuir, 1, No. 1, 97, (1985).

11. Friday, D. K. and LeVan, M. D., "Solute Condensation in Adsorption Beds During Thermal Regeneration," AIChE J., 28, 86 (1982).

12. Matuszko, R. A., Dedrick, J. M., Lamontagne, R. A. and Isaacson, L., "A System for Generating Adsorption Isotherms," NRL Memorandum Report in preparation, Naval Research Laboratory, Washington DC 20375, 1989.

13. Matuszko, R., and Little, R., "A System for Evaluating Sorbent Lifetimes," NRL Memorandum Report No. 6052, September 1987.

EVALUATION OF SPREADING PRESSURE

MOLES/Kg CARBON vs LOG PARTIAL PRESSURE

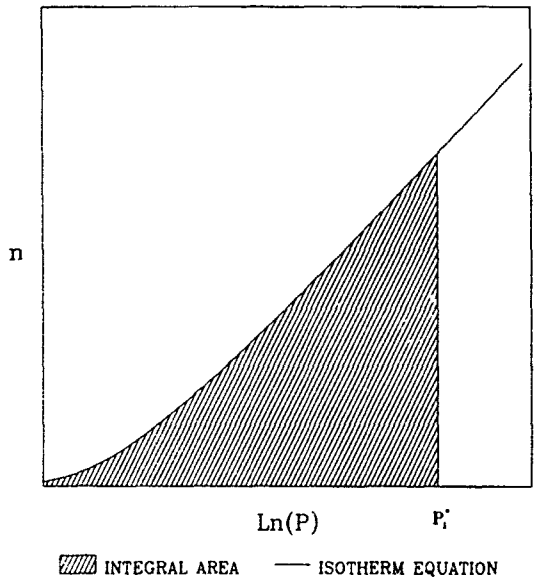

FIGURE 1

SELECTIVITY OF XYLENE AND NONANE ON BPL CARBON

25 deg C

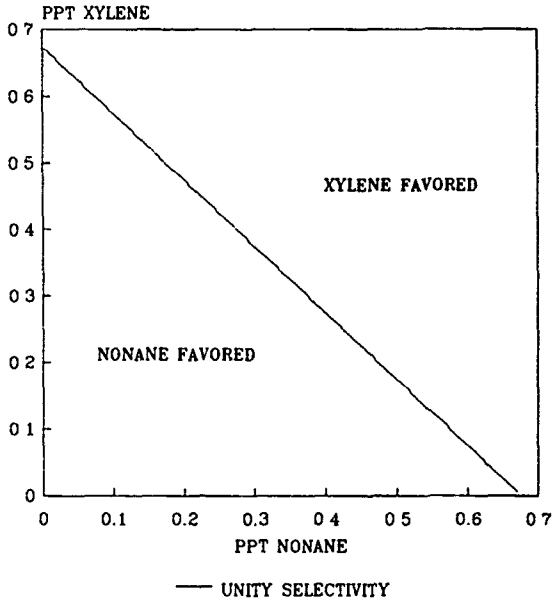

FIGURE 2

XYLENE AND NONANE ON BPL CARBON

200 PPM CHALLENGE

25 7 deg C

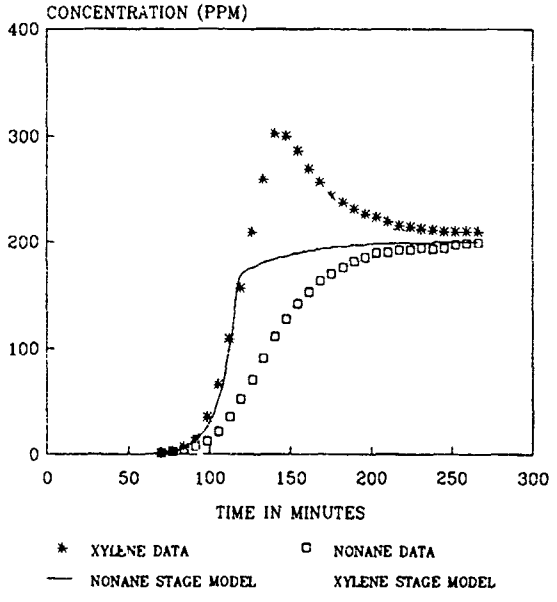

FIGURE 3

XYLENE AND NONANE ON BPL CARBON

3000 PPM CHALLENGE

24.3 deg C

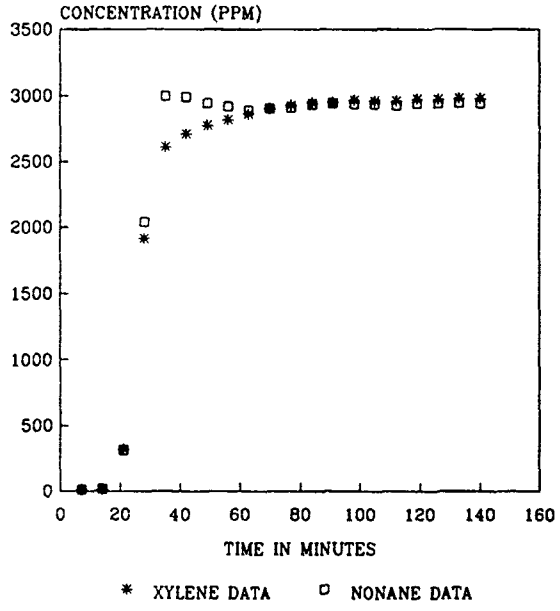

FIGURE 4

BLANK

ADSORPTION BED BREAKTHROUGH CURVE DATA FITTING

Gerry O. Wood
Los Alamos National Laboratory
Industrial Hygiene Group, MS-K486
Los Alamos, New Mexico 87545

ABSTRACT

Carbon filter beds used in gas mask canisters and collective protection systems have limited service lives. Gas breakthrough curves are measured in the laboratory for quality control and to predict performance under field conditions. If these breakthrough curves can be fitted to mathematical models, more information can be derived for extrapolation to other situations (e.g., different allowable penetrations, lower challenge concentrations, or higher humidities). The simple two parameter Reaction Kinetic Model and its special case, the Wheeler equation, often do not adequately describe these curves well. A four parameter equation has now been developed which meets the following criteria: 1) It is flexible enough to fit quite asymmetric curves. 2) It reduces to the Reaction Kinetic and Wheeler equations as special cases. 3) Its parameters can be assigned physical significance. 4) It has the proper range and limits. 5) And it provides a good fit of experimental breakthrough curve data, particularly at the more important low penetrations.

INTRODUCTION

As carbon adsorber beds become loaded with the contaminant(s) they are removing from flowing air, they lose their efficiency. The penetration of a contaminant increases with time of bed use until it reaches a predefined unacceptable level. The time at which this occurs is called the service life of the canister or other carbon bed. Service life measurements are often made in manufacturer, user, and research laboratories to characterize and compare performance of carbon beds with minimum standards. Service life times are dependent on both equilibrium bed capacities and dynamic mass transfer rates, which can be sorted out by making multiple service life measurements at different bed depths.[1]

Less often, entire or parts of breakthrough curves (penetration fraction vs. time) are measured. This usually requires little more effort than measuring a service life, which is but one point on the breakthrough curve. The breakthrough curve contains much information on the equilibrium and kinetic processes occurring in the bed, if it can be properly analyzed.

One approach to the analysis of breakthrough curves is to measure or estimate equilibrium and kinetic processes and parameters, and then calculate breakthrough curves for comparisons with experiment ones.[2] Assumptions are modified, if necessary, to obtain a match with experimental breakthrough curves.

A complementary procedure is to extract information directly from breakthrough curves by fitting them to mathematical models. If the model fits the data well, it can be used for 1) interpolation between measured points on a breakthrough curve or 2) smoothing and averaging of replicate breakthrough curve measurements. Figure 1 shows an example of breakthrough curves run in triplicate, where such smoothing and averaging has been done.

If the model parameters can be assigned physical meaning, they become system descriptive parameters that can be used to 1) show trends in service life and adsorption processes as environmental and use parameters are varied and 2) indicate possible improvements in design, components, and use procedures. Also, there is the potential of deriving such physical parameters from simpler, independent measurements or calculations.

Several approaches to breakthrough curve fitting have been reported.[3] Linear combinations of statistical moments have been used. Rate limited, constant pattern solutions based on the Langmuir isotherm have been developed, including the Reaction Kinetic (RK) solution.[4] The RK equation can be considered the "ideal" solution, useful for describing symmetrical breakthrough curves. In terms usually associated with the Wheeler/Jonas equation, the RK equation is:

$$t = \frac{W_e W}{C_o Q} - \frac{W_e \rho_B}{C_c k_v} \ln\left(\frac{C_o - C}{C}\right) \qquad (1)$$

where t = time from start of challenge,
C_o = constant challenge concentration,
C = effluent vapor concentration,
Q = constant air flow rate,
ρ_B = carbon bed packing density,
W = weight of activated carbon,
W_e = bed equilibrium capacity at C_o, and
k_v = first order rate coefficient for adsorption.

In terms of adjustable curve fit parameters A and B and penetration fraction
$P = C/C_o$, this becomes:

$$t = A - B \ln[(1-P)/P] \qquad (2)$$

or

$$P = \frac{\exp[(t-A)/B]}{1 + \exp[(t-A)/B]} \qquad (3)$$

The Jonas modification of the Wheeler equation is widely used for correlating service life measurements.[1] It is actually a special case of the RK, limited to $P < 0.1$, where approximately $P = \exp[(t-A)/B]$. It is not useful for curve fitting, since it deviates widely from data above $P = 0.1$ and predicts no limit to adsorption capacity.

Yoon and Nelson have developed a two-parameter equation, which has the same form as the RK, and a three-parameter equation (YN) for nonideal breakthrough curves:[5]

$$P = (1+\exp[A-k''\ln(W_a+t)])^{-1} \qquad (4)$$

The three curve fit parameters in the YN equation (A, k", and W_a) are empirical, without reasonable physical meanings. Furthermore, this function is undefined for $t < -W_a$ (W_a usually negative).

It was apparent that a better breakthrough curve equation was needed, particularly for the more common case of asymmetric breakthrough curves. Certain desirable characteristics of such an equation were identified. An equation meeting these requirements was developed and tested against experimental breakthrough curve data.

NEW BREAKTHROUGH CURVE EQUATION

Six requirements for a breakthrough curve equation were identified:

1. Reduce to the RK as a special case.
2. $P = f(t)$ for for easy integration.
3. $0 \leq P \leq 1$ (proper range).
4. $P \rightarrow 1$ as $t \rightarrow \infty$ (proper limit).
5. Good fit of data over entire curve.
6. Parameters have physical meaning.

Three observations provided additional input to the equation derived: 1) Some data showed the apparent adsorption rate coefficient (k_v in Eq. 1 above) increasing linearly with -ln P for $P < 0.2$. 2) The rate limiting solutions for various rate limiting mechanisms[4] can be summarized by replacing (C_o-C) in the natural logarithm term of Eq. 1 by $(C_o-C)^n$, where n is a parameter of the system. 3) A very important point on the breakthrough curve, corresponding to a point W_e on the equilibrium adsorption isotherm of the system, is the stoichiometric time:

$$t_s = \int_o^\infty (1 - P)\, dt \qquad (5)$$

and its corresponding stoichiometric penetration fraction P_s.

The breakthrough curve equation developed on the basis of these requirements and observations is:

$$P = \frac{\exp\left[\dfrac{t-A}{B+G(t-A)}\right]}{\exp\left[\dfrac{t-A}{B+G(t-A)}\right] + \left(\dfrac{1-P_s}{P_s}\right)\exp\left[\dfrac{-H(t-A)}{B}\right]} \qquad (6)$$

where A, B, G, and H are curve fit parameters (not the same as in above equations). For brevity the derivation of this equation will not be given here. This equation (W) reduces to the ideal RK equation as G and H go to zero. Therefore, it will fit breakthrough curve data at least as well as the RK. It has the form of $P = f(t)$ so that Eq. 6 can be easily integrated numerically to give t_s and P_s. This equation has the proper range and limits. At time $t = A$, $P = P_s$, so that A also has the physical meaning of t_s, the stoichiometic time. The curve fit parameter B is inversely related to the adsorption rate coefficient at the stoichiometric point by $B = W_e \rho_B / C_o k_v$. The parameter G represents the linear increase of k_v with $\ln[(1-P)/P]$. The parameter H is less well defined at this point, but from the derivation is related to the n parameter discussed above, and describes some of the asymmetry of the breakthrough curve.

EQUATION FITTING COMPARISONS

Since Eq. 6 is proposed as a better alternative to the RK and YN equations, the fits of all three of these equations to experimental data were compared. The breakthrough curve data used for these comparisons are those generated by Gary Nelson, et al., of the Lawrence Livermore National Laboratory.[6] Respirator canister breakthrough curves were measured using carbon tetrachloride and benzene vapors at several preconditioning and testing relative humidities.

Three parameter (A, B, and G) nonlinear regression fits were done using a BASIC computer program on an IBM PC-XT. The parameter H was varied systematically and P_s was obtained from t_s determined by Eq. 5 until a minimum in the sum of squares of residuals (SSR) was found. The residuals are differences in experimental P values and those calculated from the fit curve. The minimum SSR values were used as the quantitative basis for comparing fits of the three equations.

RESULTS AND DISCUSSION

Figures 2-4 show sample comparisons of the curve fitting results for the RK, YN, and W equations. The resultant values of 100xSSR are given in the legends. Figure 2 shows a nearly ideal case, i.e., where the RK fits the data quite well over all the curve (100xSSR = 0.34). The YN overall fit is not as good (0.64), while the W equation fit is slightly better (0.33). At the lowest penetrations the RK and Wood fits are best. Figure 3 shows a very unsymmetrical breakthrough curve, where the RK provides a very poor data fit overall (32.01) and at low penetrations. The YN fit is much better (1.63), particularly at low penetration fractions, and the W equation is again best overall (0.45). Figure 4 shows an unusual breakthrough curve that is practically linear over its midrange. The W equation provides a much better fit overall (2.26) and at low penetrations than either the RK (3.86) or the YN (5.76).

The summaries of fits results for benzene in Tables 1 and 2 show that the comparisons in Figs. 2-4 are typical. All of the breakthrough curves had overall fits by the W equation significantly better than by the other two equations. First breakthrough times were also fit most consistently by the W equation. Times calculated by the W equation were higher than experimental ones by only 3-9 minutes, which could be at least partially explained by including axial dispersion in the model.[4]

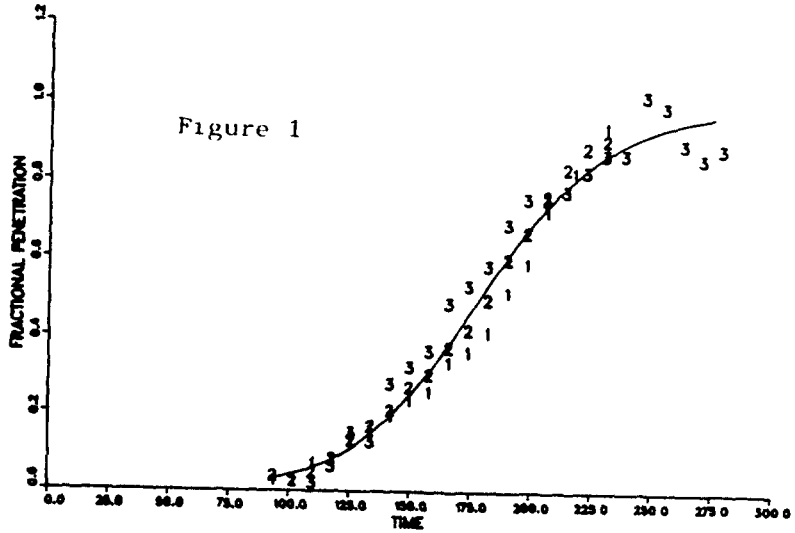

Figure 1

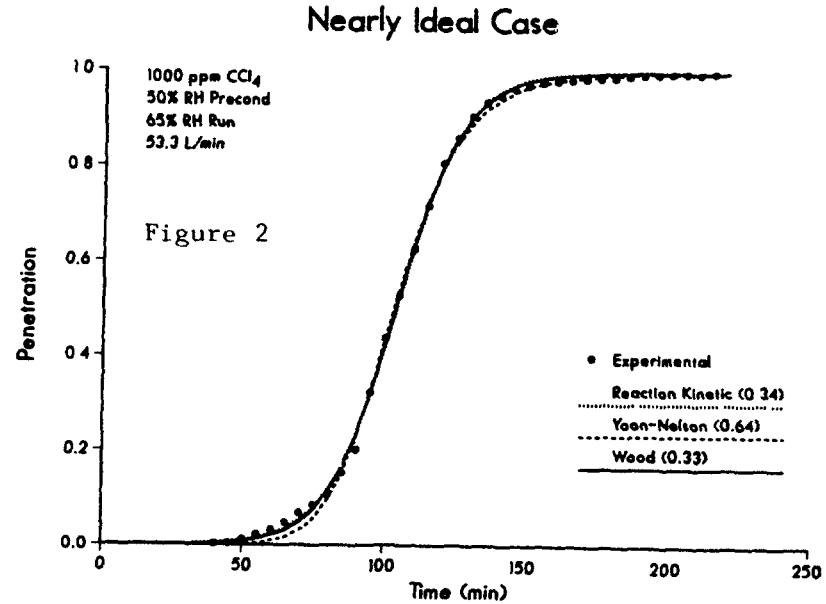

Figure 2

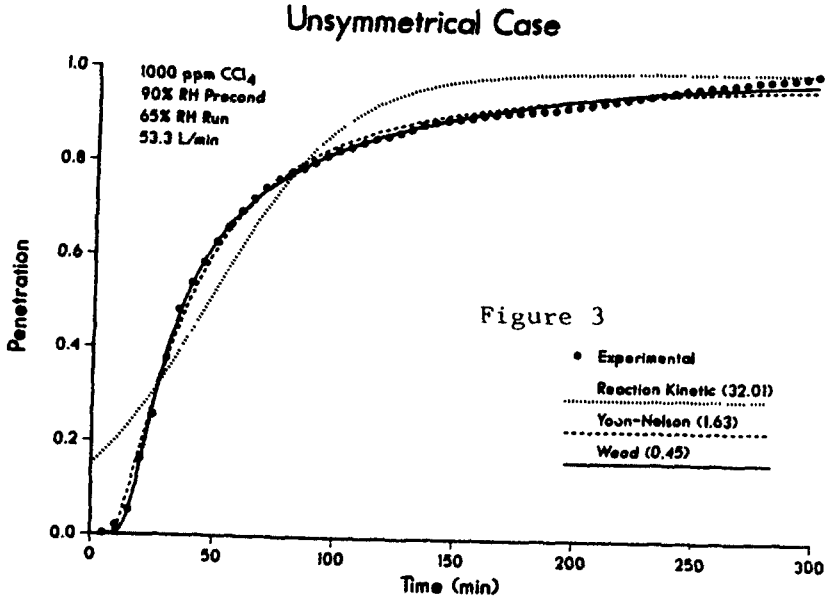

Figure 3

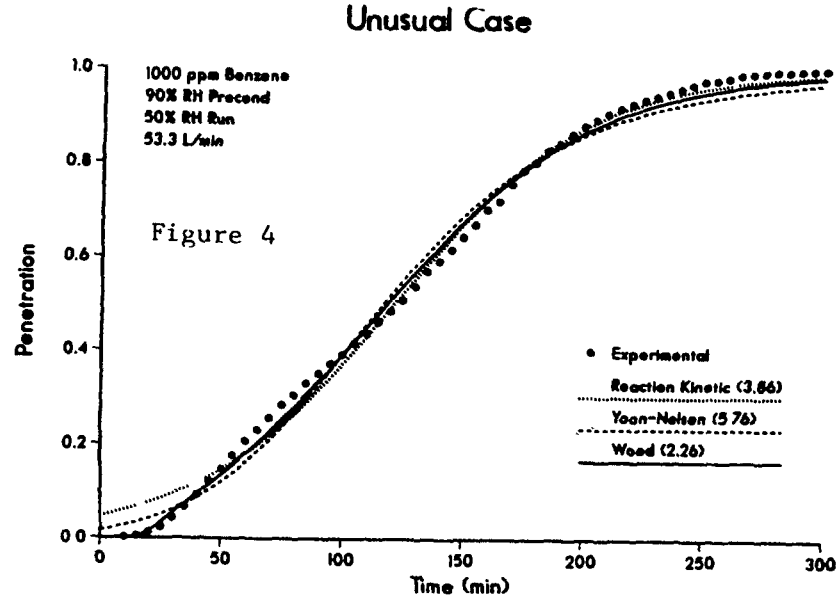

Figure 4

Table 1. Comparisons of Breakthrough Curve Fits

% Relative Humidity		Sum of Squares of Residuals x100		
Precond	Run	RK	Y-N	W
None	20	12.10	1.78	1.22
50	20	9.55	0.91	0.53
80	20	11.60	0.85	0.57
None	50	13.50	1.66	1.08
50	50	12.21	1.50	0.88
80	50	3.47	0.91	0.22
90	50	3.86	5.76	2.26
None	80	7.95	0.51	0.03
50	80	7.84	0.43	0.06
80	80	13.51	1.76	0.06
90	80	17.54	2.10	0.93

Table 2. Comparisons of First Breakthrough Times

Exp	Penetration	Experimental	Calculated Times (min)		
#	Fraction	Time (min)	RK	Y-N	W
1195	0.001	85	12	92	93
1197	0.001	85	15	89	91
1201	0.001	80	3	83	83
1203	0.001	85	20	92	94
1205	0.001	85	13	90	92
1207	0.001	60	-50	29	64
1217	0.001	10	-158	-46	15
1215	0.001	75	-3	74	80
1213	0.001	70	-5	71	76
1211	0.001	40	-104	33	44
1209	0.002	5	-142	2	9

CONCLUSIONS

The newly proposed Eq. 6 provides improved fits of breakthrough curve data compared with the ideal Reaction Kinetic equation and the three parameter Yoon-Nelson equation. It has the other desirable characteristics that make it useful for interpreting laboratory experiments. Once physically meaningful parameters are derived, they can be used to correlate and extrapolate to various environmental and use conditions of various bed designs.

REFERENCES

1. Jonas, L.A., and Rehrmann, J.A., "Predictive Equations in Gas Adsorption Kinetics," Carbon 11, 59-64 (1973) and "The Rate of Gas Adsorption by Activated Carbon," Carbon 12, 95-101 (1974).

2. Friday, D.K., and Mahle, J.J., "The Breakthrough Behavior of Cyanogen Chloride on ASC Carbon at 80% Relative Humidity," in Proceedings of the 1988 U.S. Army Chemical Research, Development and Engineering Center Scientific Conference on Chemical Defense Research, CRDEC-SP-013, 269-275 (1989).

3. Grubner, O., and Burgess, W.A., "Calculation of Adsorption Breakthrough Curves in Air Cleaning and Sampling Devices," Environ. Sci. Technol. 15, 1346-1351 (1981).

4. Vermeulen, T., LeVan, M.D., Hiester, N.K., and Klein, G., "Adsorption and Ion Exchange," in Chemical Engineers Handbook, 6th Edition, McGraw-Hill, New York, Section 16 (1984).

5. Yoon, H.Y., and Nelson, J.H., "A Theoretical Study of the Effect of Humidity on Respirator Cartridge Service Life," Am. Ind. Hyg. Assoc. J. 49, 325-332 (1988).

6. Nelson, G.O., and Correia, N., "Respirator Cartridge Efficiency Studies: VIII. Summary and Conclusions," Am. Ind. Hyg. Assoc. J. 37, 514-525 (1976).

ACKNOWLEDGMENTS

This work was sponsored jointly by the U.S. Department of the Army and the U.S. Department of Energy. Some of the computer computations were performed by Travis Weaver, a high school coop student sponsored by the Department of Energy.

BLANK

CK BREAKTHROUGH TIMES AND BET SURFACE AREA OF ASC WHETLERITE AS A FUNCTION OF PARTICLE DENSITY AND PARTICLE SIZE

Victor R. Deitz[1] and Joseph A. Rehrmann[2]

Abstract

Whetlerite is a heterogeneous mixture of particles ranging in density and size (12-30 mesh). In order to study the influence of these two parameters, a whetlerite (Lot 794) was separated into six fractions by passage over a triangular inclined vibrating table and by collection of the fractions exiting on the edge opposite to the inlet. Also, the material in the original Lot 794 was sieved into four fractions: 14-16, 16-18, 18-20, and 20-30. Each sieve fraction was then separated into six density fractions. The bulk density, surface area and CK performance were measured. The 20-30 fractions of the mixture had a CK activity about twice that of the larger size fractions when evaluated at a constant test volume. The use of a distribution matrix is a helpful procedure to study the properties of the heterogeneous mixture of particles in whetlerites; the trend in properties is thus made readily apparent.

[1]Naval Research Laboratory, Code 6170, Washington, DC 20375-5000

[2]Chemical Research Development and Engineering Center, SMCCR-RSC-A, Aberdeen Proving Ground, MD 21010-5423

1. Introduction

Whetlerite is an impregnated granular activated carbon having a nominal particle size distribution within the openings of 12-30 U.S. Standard Sieves. Bulk density measurements by a given test procedure can vary due to source and manufacturing variations. As a consequence of these independent parameters, the removal of test fractions from a given supply of whetlerite can be sensitive to the sampling procedures, despite the fact that there are thousands of particles per gram of sample. The influence of these parameters on both physical and chemical adsorptive properties of whetlerite is the subject of the present studies.

The BET surface area (physical adsorption), bulk density, and the penetration of ClCN (chemisorption) have been determined for the sieve and density fractions obtained from ASC Whetlerite, Lot 794. Some interesting correlations will be presented.

2. Experimental

2.1 Particle Fractionation

An ample supply of whetlerite (Lot 794) was sieved into five fractions, namely, 12-14, 14-16, 16-18, 18-20, and 20-30.

The original supply was also separated into density fractions by passage over a triangular inclined vibrating table (Whippet Specific Gravity Table) and the collection of six fractions at equal distances on the opposite edge to the inlet corner. Each sieve fraction was then separated into six density fractions (Figure 1). Altogether, including the initial supply, 35 fractions were obtained. The 35 fractions define a matrix of test samples for the proposed analyses (Table 1). The results for any one property form a "distribution matrix."

The distribution matrix for the weight-percent (dry weight) in the various fractions from whetlerite, Lot 794, is given in Table 2. The amounts of the 12-14 sieve fraction (approximately 1%) was not enough to follow up with a density separation.

FIGURE 1
Procedures Used to Separate Original Whetlerite (Lot 794) into Density Fractions, Sieve Fractions, and into Pre-Sieved Density Fractions

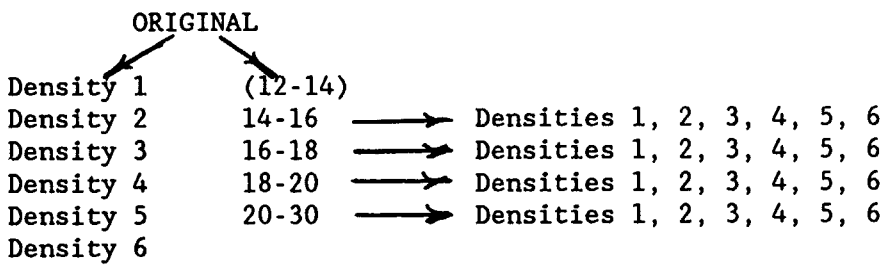

TABLE 1
Distribution Matrix for ASC Whetlerite, Lot 794

Sieve Fraction	Density Fractions (100% of each Sieve Fraction)					
Original	1	2	3	4	5	6
14-16	1	2	3	4	5	6
16-18	1	2	3	4	5	6
18-20	1	2	3	4	5	6
20-30	1	2	3	4	5	6

TABLE 2
Distribution Matrix of Weight-Percent for ASC Whetlerite, Lot 794, all entries are percentage of the original sample

Sieve Fraction		Density Fractions 1	2	3	4	5	6
Original	100%	7.5	14.8	20.1	19.1	26.2	12.3
14-16	12.3	.418%	1.02	1.81	2.61	3.91	2.53
16-18	25.1	.628%	3.04	4.69	6.05	7.05	3.64
18-20	30.2	.423%	2.75	5.47	7.25	9.48	4.80
20-30	27.2	1.22%	4.84	5.96	5.03	5.90	3.29

The problem of duplication in the fractionations was recognized early in this study[3]. Four sieve analyses of the original Whetlerite were made with the reproducibility shown in Table 3. The mean and standard deviation are given to illustrate the magnitudes involved. Seven additional sieving determinations were also made by an independent operator for the same whetlerite, Lot 794; these results are also given in Table 3.

Data were obtained (Table 4) for the reproducibility of a density fractionation for the 14-16 sieve fraction. The critical adjustment in the procedure is to maintain a uniform flow of particles across the vibrating table and along the discharge edge of the table.

[3]V.R. Deitz and J.V. Pistritto, "Influence of Particle Size and Bulk Density of Whetlerite on CK Performance," Proc. 1984 Scientific Conference on Chemical Defense Research, pp 397-404, CRDC-SP-85006, June 1985.

TABLE 3
Sieve Analyses (dry weight) of the Original ASC Whetlerite, Lot 794

Sieve Fraction	Detns	Wt.% Mean	Std. Dev.	Detns	Wt.% Mean	Std. Dev.
		Operator 1			Operator 2	
12-14	4	1.8	0.23	7	2.0	0.14
14-16	4	12.3	0.99	7	13.0	0.75
16-18	4	25.1	1.73	7	26.1	0.74
18-20	4	30.2	0.98	7	28.6	0.44
20-30	4	27.2	1.44	7	27.8	1.35

TABLE 4
Reproducibility of Bulk Density (free fall) Determinations
Based on the 14-16 Data from Each Density Fractionation

Density Fraction	Trial 1	Trial 2	Trial 3	Mean Density	Standard Deviation
1	.473	.500	.517	.497	.018
2	.522	.567	.553	.544	.016
3	.577	.588	.586	.584	.0048
4	.602	.618	.629	.616	.011
5	.660	.672	.671	.668	.0054
6	.717	.717	.732	.722	.0071

The bulk densities of each of 35 fractions separated from ASC Whetlerite, Lot 794, are given in Table 5. The sieve fraction 12-14 was not present in sufficient quantity for the density fractionation, being less than 2 wt.% in the original sample. The bulk density was determined by free fall into a graduated cylinder from a height of 30 inches.

TABLE 5
Distribution Matrix for Bulk Densities of the Fractions Separated from ASC Whetlerite, Lot 794

Sieve Fractions		Density Fractions 1	2	3	4	5	6
Original	0.526	.527	.559	.570	.598	.637	.693
14-16	0.620	.497	.544	.584	.616	.668	.722
16-18	0.612	.500	.535	.577	.620	.684	.723
18-20	0.602	.460	.539	.579	.589	.620	.676
20-30	0.604	.507	.560	.590	.599	.619	.666

For comparison purposes a sample of a base charcoal, CWS, was sieved into the same size fractions as the whetlerite. The results (Table 6) for bulk density show little difference among the various sieve fractions. In this respect the CWS sample was rather uniform in particle density when compared to ASC Whetlerite (Table 5).

TABLE 6
Sieve Analysis and Bulk Density of CWS Base Charcoal (dry weight)

Sieve Fraction	Run 1		Run 2		Mean		Standard Deviation
	wt.%	Bulk Density	wt.%	Bulk Density	wt.%	Bulk Density	
12-14	0.72	0.7	0.97	0.7	0.84	0.7	
14-16	12.28	.595	13.48	.582	12.88	.589	.0065
16-18	22.25	.564	23.03	.578	22.64	.571	.0070
18-20	31.28	.552	30.63	.565	30.96	.559	.0065
20-30	33.29	.542	29.89	.553	31.59	.548	.0055

2.2 Distribution Matrix for the Penetration of ClCN Through Fractions of Lot 794

All samples for the ClCN penetration measurements were made with the same kinetic parameters listed below. The breakthrough times (minutes) are denoted by t_b.

Bed Depth	3 cm
Bed Diameter	2.5 cm
Air Flow	1.63 L/min
Temperature	23-24°C
Dose Concentration	4 mg/liter
Prehumidified	80% RH overnight

TABLE 7
Distribution Matrix of Breakthrough Times (t_b, minutes)
for the Penetration of CK through ASC Whetlerite, Lot 794

Sieve Fractions		Density Fractions					
		1	2	3	4	5	6
Original	76,63,69	105,115	81	84,83	66	58,79	67,53
12-14	20,18	--	--	--	--	--	--
14-16	43	27	--	35	31	45	28
16-18	53	--	53	55	56	40	64
18-20	82	--	74	89	80	55	91
20-30	90	83	107	98	110	106	78

2.3 Nitrogen BET Surface Area (m^2/g)

The BET surface area of the various fractions from ASC whetlerite, Lot 794, have been determined. The measurements were made with the Quantasorb Surface Area Analyzer.

TABLE 8
Distribution Matrix of BET Nitrogen Surface Areas (m^2/g)

Sieve Fractions		Density Fractions 1	2	3	4	5	6
Original	820	900	796	740	740	630	570
12-14	750						
14-16	880	850	890	650	640	610	495
16-18	850	870	860	750	760	503	527
18-20	710	840	890	800	790	750	560
20-30	680	802	823	765	763	606	665

3. Discussion

It has been shown that whetlerite, nominally a 12-30 sieve designation, is actually a heterogeneous mixture of intermediate particle sizes and particle densities. For a given density fraction, for example #6, by actual count there are approximately 550 particles/g for 14-16 sieve fraction and 2700 particles/g for 20-30 sieve fraction. For a given sieve fraction the bulk density is additive among the different density fractions:

$$\delta_{exptl} = \sum_{1}^{6} w_i \, \delta_i$$

where w_i = fractional weight of i th density fraction, δ_i = density of i th fraction. The additivity is shown (Table 9) for the four sieve fractions from Lot 794.

TABLE 9
Additivity of Bulk Density (g/cm^3) among Density Fractions From a Given Sieve Fraction

Sieve Fractions	Bulk Density (g/cm^3) Observed	Calculated
14-16	0.620	0.622
16-18	0.612	0.632
18-20	0.602	0.604
20-30	0.604	0.598

The distribution matrix for the CK penetration times, t_b(minutes), for whetlerite (Table 7) shows a definite dependence on particle size and little dependence on particle density. However, the distribution matrix for bulk density (Table 5) show a definite dependence on density fractionation and little dependence on sieve fraction, i.e. particle size. The CK penetration for the base charcoal, CWS, was too rapid to determine under the same kinetic parameters used for whetlerite.

One explanation for the above results may reside in the original impregnation procedure. The contact time of the dry base charcoal with the whetlerizing solution is quite short[4] and during this interval the rate of adsorption is more rapid on the smaller particles. In a continuous process and a short time interval between wetting and drying, the surface coverage of the smaller particles is more complete. Actually, the BET nitrogen coverage is smaller for whetlerite than that for the base CWS charcoal. While the distribution matrix, for the BET surface area (Table 8) is not as yet complete, there is indication that both high density fractions and 20-30 sieve fractions have the smaller surface areas.

The CK retention by whetlerite is the result of the chemical reactivity with the impregnated chemical species. Analyses for total copper and total chromium have been made and the distribution matrix of these metals has been determined (Table 10). The results do indicate an enrichment of both metals in both small particles and in high density fractions.

TABLE 10
Distribution Matrix for Total Copper and Chromium Contents (wt-% of metal)

Sieve Fraction	Metal	Density Fractions 1	2	3	4	5	6
Original							
14-16	Cu			6.24	6.39		
	Cr			2.13	2.09		
16-18	Cu	7.76		7.04			8.44
	Cr	2.59		2.33			2.65
18-20	Cu		7.20		7.28		7.59
	Cr		2.33		2.42		2.48
20-30	Cu		7.77	7.51	8.57		
	Cr		2.53	2.47	2.84		

[4]Communications from Dr. Norman J. Wagner, Calgon Corp.

CONCLUSIONS

The use of a distribution matrix is a helpful procedure to study the properties of the heterogeneous mixture of particles in whetlerite; the trend in properties is thus made readily apparent. Bulk density, surface area, penetration of cyanogen chloride have been determined. The breakthrough times for cyanogen chloride were linearly dependent on particle size with a correlation coefficient of 0.989. No dependence on BET surface area was found since the breakthrough time is determined by a chemisorption process and the BET area is determined by physical adsorption of nitrogen. Chemical analyses indicated an enrichment of both Cu and Cr in small particles and the breakthrough times were linearly dependent on the total amounts of both metals. The short duration of the impregnation process, wherein the whetlerizing solution is contacted with the base charcoal, could lead directly to a built-in heterogeneity in the final product. The above analysis should be useful in the development of new impregnations and the establishment of efficient impregnation procedures.

EFFECT OF IMPREGNATION LOADING ON THE ADSORPTION CAPACITY OF ACTIVATED CARBONS

Christopher J. Karwacki
John J. Mahle
David K. Friday

Chemical Research Development and Engineering Center
Physical Protection Directorate
Aberdeen Proving Ground, Maryland 21010-5423

ABSTRACT

Impregnated carbons are needed to protect against volatile toxic vapors. Increased impregnant loadings can improve reactivity but at the expense of adsorption capacity. This investigation examines the sensitivity of the adsorption capacity of Freon-113 and water as a function of impregnant loadings on activated carbon. Adsorption capacities of samples with impregnant loadings from 0 to .31 g/g of carbon were measured. Adsorption capacities of component systems were evaluated: (1) Water concentrations at 80 and near 100% RH, (2) Single component Freon 113 loadings between 50 and 500 ppm (3) Freon 113 loadings between 50 and 500 ppm on carbons equilibrated to 80% RH.

INTRODUCTION

In recent years trends in new sorbent development have shown an increased interest in sorbents possessing higher overall chemical activity. Although this presents exciting challenges for development of these materials, there are serious concerns regarding the combined affects to adsorption equilibria, material balances and kinetics in achieving a higher chemically active sorbent.

To achieve superior filtration performance for any protective system, industrial or military, the chemical and adsorptive processes between the vapor and adsorbent must be well characterized. In this paper the objective will be to obtain information on adsorption equilibria by conducting a sensitivity analysis on the effects of adsorption capacity resulting from changes in impregnant loading.

To date, little has been reported regarding investigations into the effects of changes in adsorbate capacities on carbons containing various amounts of impregnants (1,2). Although numerous investigations have determined isotherms for many single and multi-component vapors most were constrained to a single loading level of impregnants on the sorbents.

Typically, determination of changes in net availible pore space are made by dynamic breakthrough tests of a vapor of interest under a constant set of test conditions. Changes in the breakthrough time are noted and correlated with changes in the sorbents net availible pore space (3). The difficulty with a dynamic breakthrough test, in estimating adsorption equilibria capacities, lies in

the interpretation of the results. Since, adsorption equilibria and rate processes are occurring simultaneously it is difficult to distinguish between the two, unless of course one or the other is fixed. Pore size distribution, impregnant quantity, particle size and moisture loading affect adsorption equilibria or rate processes. If the effect of these parameters are not well understood conclusions drawn would be in error.

In this investigation equilibria capacity values (q_{eq}) were measured using a novel instrumental design by Mahle and Buettner (4). By exposing a known amount of carbon in a circulation loop containing a given amount of Freon 113, a reduction in initial vapor phase concentration was obtained. Isotherms for each sorbent-sorbate pair were plotted using a modified Antoine equation proposed by Hacskaylo and LeVan (5). This method has demonstrated to be most powerful for low vapor phase concentrations. Differences in q between each impregnation level for a given vapor phase concentration were evaluated to show the effect of changes in physical adsorption as a function of changes in impregnant loading.

THEORY

The Modified Antoine equation developed by Hacskaylo and LeVan is a correlation of adsorption equilibria data for porous adsorbents to the pure component vapor pressures of saturated liquids. The constants that are correlated depend on the loading of the vapor into the microporous region of the sorbent. This model was derived to provide a function which is continuous at $\theta = 1$ and has a linear region at very low partial pressures (Henry's law).

In one form the expression is written in terms of p, θ and T

$$\ln p = A' - B'/(C + T) \qquad (1)$$

where,

$$A' = A + \ln \theta$$

$$B' = B + b(1-\theta)$$

and,

p = partial pressure of vapor
θ = fraction of pores filled by the liquid vapor, W/Wo
T = temperature of vapor
b1 = sorbate-sorbent affinity parameter
A,B,C = Antoine constants for the pure component vapor

The application of equation 1 to the experimental'y measured values of q and p is performed by a least squares regression of b1 and Wo, (the equilibrated capacity at saturation). The Freon 113 concentrations evaluated in this investigation were all below 0.1%.

EXPERIMENTAL

Four carbons were evaluated in this investigation and are shown in Table 1. Sample 01 is an

unimpregnated activated carbon substrate typically used in the preparation of ASC whetlerite carbon. Samples 02 through 04 are of a whetlerite type and range in total impregnant loadirg from 9.5 - 31.4 percent by weight on carbon. Loadings were determined by taking the difference between the impregnated and unimpregnated densities and dividing by the density of the impregnated carbon sample.

Table 1. Impregnant Loadings of Carbons Evaluated for Adsorption Equilibria Capacities Using Freon 113 and Water.

SAMPLE I.D.	IMPREGNANT LOADING %
01	0
02	9.5
03	16.5
04	31.4

Adsorption equilibria capacities were measured for samples 01 through 04 using single component water and Freon 113 and multi-component Freon 113 with water at 80-80 RH conditions. The matrix of adsorbate conditions are shown in Table 2.

Table 2. Adsorbate Conditions for Freon 113 and Water.

Adsorbate	Concentration
Water	0.8 p_{sat}
Freon 113 (dry)	50 and 500 ppm
Freon 113 (80-80 RH)	50 and 500 ppm

Samples were evaluated in a test system similar to the schematic shown in Figure 1. Sample weights between 0.15 to 1.5 g are loaded into the test holder and the bed is placed in a by-passed mode. Changes in vapor phase concentration were measured by an infrared gas analyzer. Figure 2 shows a sample output.

Equilibrated capacity values (q_{eq}) were obtained at concentrations above and below the target values of 50 and 500 ppm (50 ppm = 0.384 mg/l). Adsorbate loadings were determined by taking the difference between the initial and final concentration and multiplying by the system volume. The quantity of gas adsorbed divided by the initial sample weight determined $q_{eq}/g_{sorbent}$. A gravimetric weighing of the sample was made after the test to verify the analytical determinations. Although the weigh method was less accurate better than 10% agreement was observed.

Figure 1. Schematic of Isotherm Apparatus

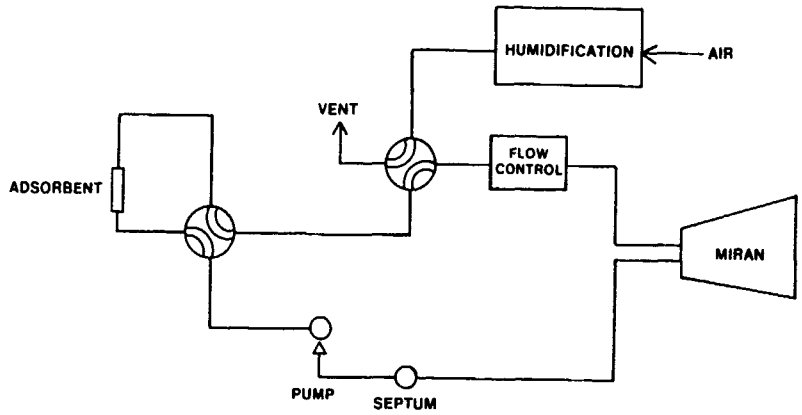

Figure 2. Plot of Vapor Phase Concentration Before and After Exposure to Sorbent Sample

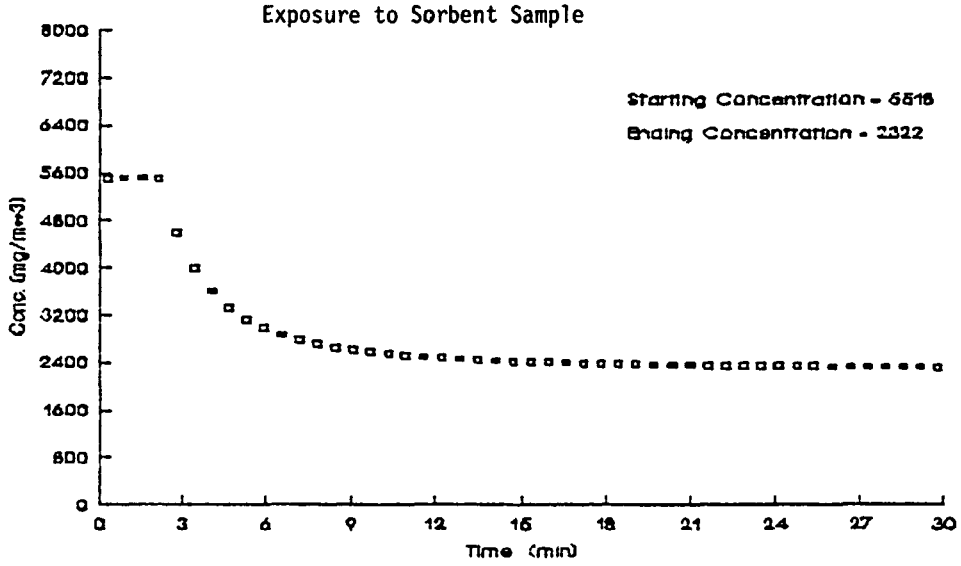

RESULTS AND DISCUSSION

The experimental data collected was used to fit a least squares regression of b_1 and w_o in the form shown in equation 1. Figures 3 and 4 show the isotherm plots derived from the experimental data for the dry-dry and 80-80 RH conditions.

It is interesting to note the magnitude of change in adsorbed phase loading between the unimpregnated sample 01 and sample 04 at 31.4 percent impregnant loading. The percent reduction between samples 01 and 04 for the 50 and 500 ppm concentrations under dry conditions was approximately 65 and 47%, respectively. For the Freon 113 loadings run at 80-80 RH, the reductions at 50 and 500 ppm were 71 and 69%, respectively. Table 3 shows the adsorbed phase concentrations in g_{freon}/g_{carbon} determined for 50 and 500 ppm concentrations under dry and 80 RH conditions.

Table 3. $Q_{(g/g)}$ For Carbons Evaluated At 50 and 500 ppm of Freon 113 Under Dry Conditions.

	Adsorbed Phase Concentration (Q)			
SAMPLE I.D.	FREON 113 CONCENTRATIONS (DRY-DRY)		(80-80)	
	50	500	50	500
01	0.17	0.34	0.007	0.039
02	0.12	0.30	0.006	0.032
03	0.08	0.20	0.003	0.023
04	0.06	0.18	0.002	0.012

Closer inspection of the data shows a dominating effect on adsorbed phase concentration to changes in impregnant loading above 9.5%. Between 9.5% and 16.5% impregnant loading the largest changes occurred. For samples 02 and 03, a 50% reduction in adsorbed phase capacity resulted for the 50 ppm and 80-80 RH conditions. Under dry conditions the effect was less, resulting in a 33% reduction. Figures 5 and 6 show graphically this relationship.

A hypothetical case can be demonstrated where a filter's gas life will change as a result of changes in the adsorbed phase capacity. To be valid, a constant pattern must develop and no change in the rate processes (i.e., internal/external diffusion, axial dispersion) can occurr. The analysis is valid only for adsorption capacity.

Shown in Table 4 is an estimate of changes in gas life based on the equilibria capacity values measured and given in Table 3.

Figure 3 Freon 113 Isotherm on Dry Carbons

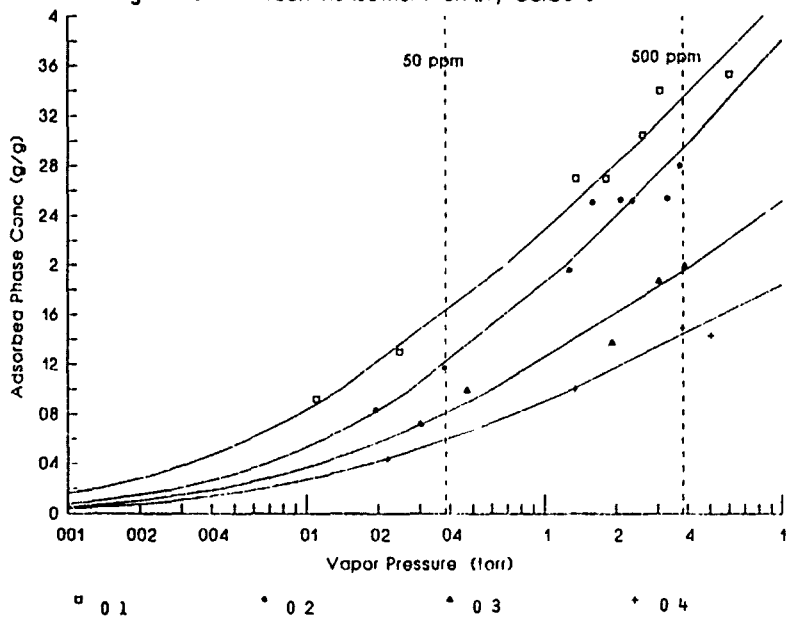

Figure 4 Freon 113 Isotherm on Carbons Humidified At 80%RH

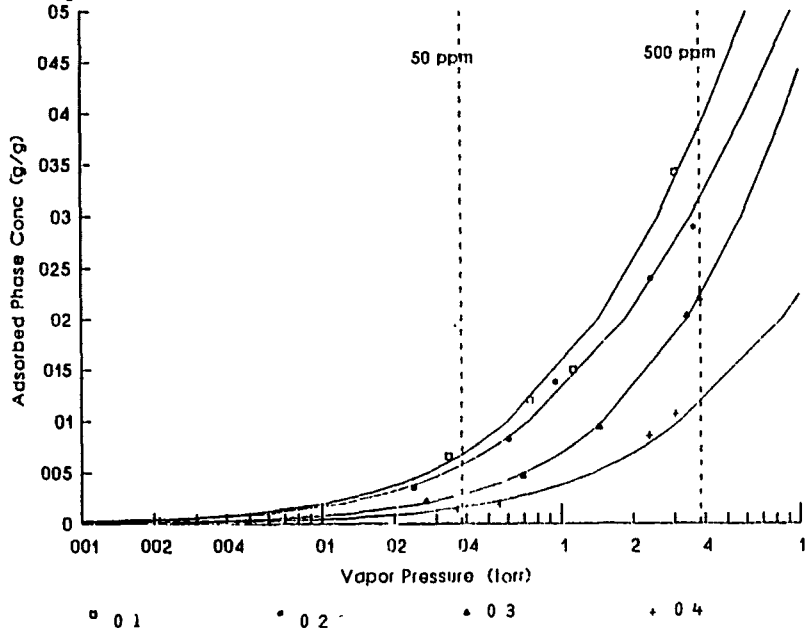

Figure 5 – Change in Adsorbate Loading of Freon 113 at 50 and 500 PPM Due to Changes In Impregnant Loading On Carbon Under Dry Conditions

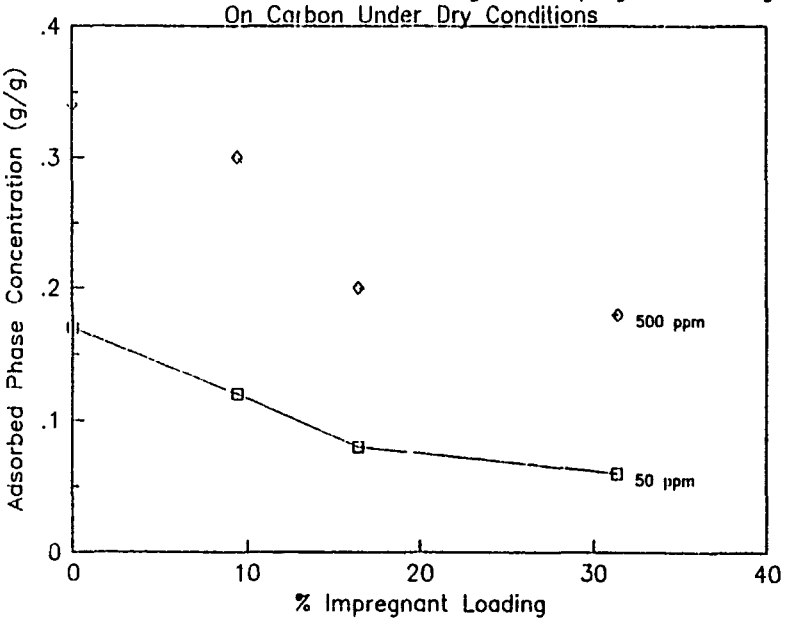

Figure 6 – Change in Adsorbate Loading of Freon 113 at 50 and 500 PPM Due to Changes In Impregnant Loading On Carbon Under 80/80 RH Conditions

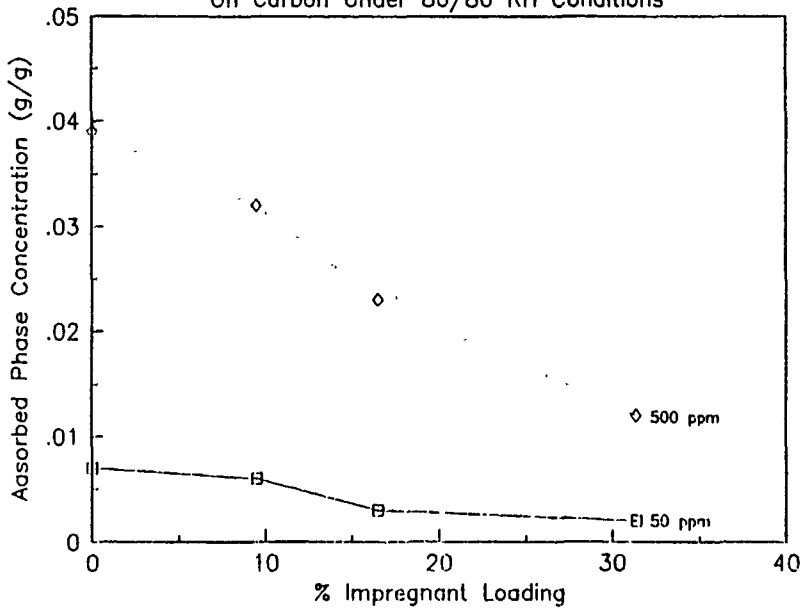

Table 4. Estimated Change in Filter Gas Life with Increasing Impregnant and Moisture Loading.

Sample I.D.	Gas Life in Minutes Freon 113 Concentrations (Dry-Dry) 50	(Dry-Dry) 500	(80-80) 50	(80-80) 500
01	1000	200	41	23
02	706	176	35	19
03	471	118	18	14
04	353	106	12	7

For sample 01 at 50 ppm (dry) a filter life of 1000 minutes was arbitrarily selected. Fractions of that time resulted due to either a decrease in adsorbed phase capacity or increase in challenge concentration. Note the dramatic decrease in estimated gas life from sample 01 to sample 04 at 500 ppm (80RH) with 7 minutes of filter life.

CONCLUSIONS

1. The sensitivity of adsorbed phase concentrations to changes in impregnant loading is most significant between 9.5 and 16.5%, resulting in a 47 to 71% decrease in capacity.

2. Changes in percentage of adsorbed phase capacity is approximately equivalent for dry and 80-80 RH conditions. Although, the highest reductions occured for the 80-80 RH conditions at 69 and 71%.

3. Estimates of filter gas life decrease proportionately with decreasing adsorbed phase concentration. For the samples and conditions evaluated estimated filter gas life decreased from 1000 to 7 minutes of protection.

REFERENCES

1. Reucroft, P.J. and Chiou,C.T., Adsorption of Cyanogen Chloride and Hydrogen Cyanide by Activated and Impregnated Carbons, Carbon 15, vol. 15 pp. 285-290, 1977.

2. Kloubek J., Investigation of Impregnant Deposition in Activated Carbon. Carbon, 19, No. 4, pp 303-308, 1981.

3. Tolles, E.D., Improved Charcoal Impregnation Technology, Final Comprehensive Report, CRDEC-CR-86066, 1986.

4. Mahle J., Batch Adsorption Equlibria and Rate Apparatus, Proceedings of The 1989 U.S. Army Chemical Research Development and Engineering Center Scientific Conference on Chemical Defense Research, Nov. 1989.

5. Hacskaylo, J.J., and M.D. LeVan, 1985. Correlation of Adsorption Equilibrium Data Using a Modified Antoine Equation : A New Approach for Pore-Filling Models, Langmuir 1, 97.

THE DEVELOPMENT OF A NEW CHROMIUM-FREE WHETLERITE CARBON FOR ADSORPTION OF TOXIC GASES

David T. Doughty and Norman J. Wagner
Calgon Carbon Corporation
P.O. Box 717
Pittsburgh, Pennsylvania

R. W. Morrison and R. J. Puhala
U. S. Army Chemical Research Development
and Engineering Center
Aberdeen Proving Ground, Maryland

ABSTRACT

A new chromium-free filter carbon has been developed for the removal of toxic vapors from air. A formulation containing 6% Cu, 6% Zn, 0.05% Ag and 3% TEDA provides good balanced protection against AC, CK, and other chemical vapors, and is resistant to aging. Long term evaluation of preliminary production quantities of this material is in progress.

INTRODUCTION

Recently, concern has developed about possible adverse health and environmental effects related to the presence of hexavalent chromium in type ASC Whetlerite. The desire to eliminate chromium from the formulation has led to a research and development program funded by CRDEC. The objective of the program was the development of a low-toxicity chromium-free activated carbon material to replace ASC Whetlerite in toxic gas filters.

This three-year program has led to the development of a product containing copper, silver, zinc, and triethylene- diamine. This material provides good balanced protection against a broad spectrum of toxic chemical vapors.

RESULTS AND DISCUSSION

The program for development of a chromium- free impregnated carbon was divided into three stages. In Phase I, a literature search was conducted to determine gases for which the presence of Cr was believed to be important in the protection afforded by ASC. It was concluded that chromium only played a significant role for the cyanide gases: hydrogen cyanide (AC), cyanogen $(CN)_2$, and cyanogen chloride (CK). Potential methods to remove these gases were then specifically targeted in a second literature review. Toxicity screening removed a number of possible impregnants from further consideration. Where necessary, materials were screened by AC and CK testing to determine the five most promising candidates.

Phase II development consisted of formulation optimization for each of the five candidate formulations. The goal of the optimization procedure was to determine the formulation of impregnant loadings which would provide the maximum degree of protection against AC and CK. At the same time, many toxic gases are removed by physical adsorption, which can be expected to deteriorate at higher impregnant loadings[1]. In an effort to balance these two demands, attempts were made to limit metal impregnants to 12%, and to minimize the use of organic impregnants. Of the materials studied in Phase II, the best balanced performance was obtained by formulations containing copper, zinc, silver and TEDA. This formulation was chosen for Phase III scale-up and long term aging studies, which are currently in progress.

Optimization of the Cu, Zn, Ag, TEDA formulation in Phase II was carried out using the principles of statistical experimental design. Using this procedure, a set of experiments was designed to explore the practical range of impregnant loadings. AC and CK were chosen as the primary responses, as these gases are most affected by the absence of Cr. After preparation of the necessary samples and determination of AC and CK lives, regression equations were developed to satisfactorily model the AC and CK response surfaces. These equations were then analyzed for predictions of optimum AC and CK performance. Performance in the optimum region was subsequently verified experimentally.

Figure 1 illustrates that the maximum AC performance consistent with relatively low impregnant loadings is obtained with a formulation containing 6% Cu and 6% Zn. Figure 2 indicates that this level of performance is relatively unaffected by increased loadings of TEDA and that the best AC performance is once again predicted for compositions containing 6% Cu and 6% Zn. Note, however, that impregnant loadings can be reduced if a lower level of AC protection can be tolerated. In this case, best performance would still be predicted for compositions containing equal amounts of copper and zinc.

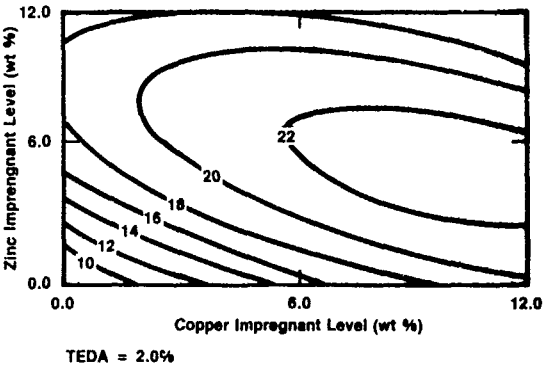

FIGURE 1: AC Life of Cu-Zn Samples with 2% TEDA

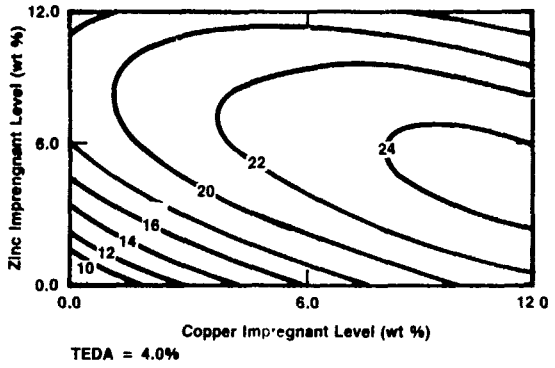

FIGURE 2: AC Life of Cu-Zn Samples with 4% TEDA

In contrast to the AC results, CK performance of samples containing copper and zinc is quite dependent on TEDA. Figure 3 shows that for samples with 2% TEDA, best performance is obtained with mixtures of 6% Cu and 6% Zn. At higher TEDA levels (Figure 4) a 6%

Cu, 6% Zn formulation remains a good choice for those with 12% metals, but improved performance is predicted for higher metal loadings. Arguments based on pore filling models, however, indicate that these higher impregnant levels will likely decrease capacity for physically adsorbed materials[1]. Similarly, increased levels of TEDA will improve CK performance, but physical adsorption capacity will decrease. Figure 5 illustrates that TEDA cannot be removed from the formulation, as essentially no CK protection is provided in its absence. Similarly, TEDA affords very little CK protection in the absence of copper and zinc (Figure 6).

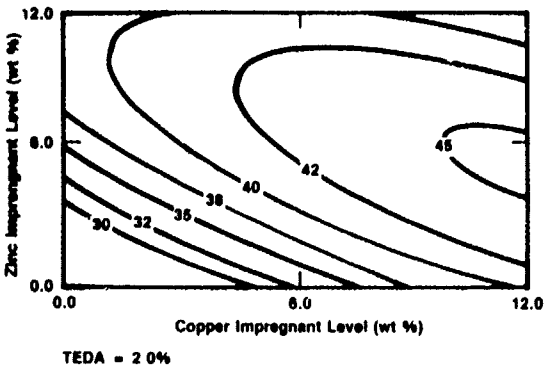

FIGURE 3: CK Life of Cu-Zn Samples with 2% TEDA

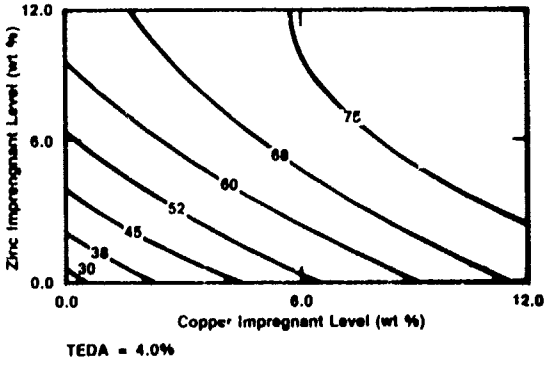

FIGURE 4: CK Life of Cu-Zn Samples with 4% TEDA

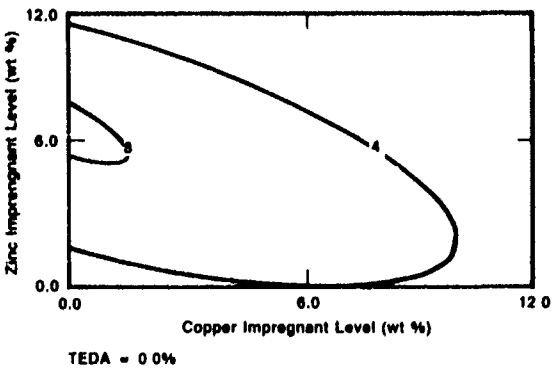

FIGURE 5: CK Life of Samples with 0% TEDA

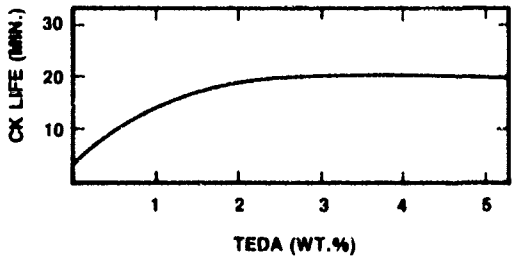

FIGURE 6: Effect of TEDA on CK Life in Absence of Metals

Consistent with the goals of optimizing AC and CK performance without resorting to overly high impregnant loadings, the optimum formulation contains 6% Cu and 6% Zn. A TEDA loading of 3% provides adequate CK protection. Metal levels can be reduced if lower AC performance can be tolerated. Similarly, CK performance can be adjusted by increasing or decreasing metal or TEDA levels. Gains in CK performance obtained by increasing TEDA will, however, likely cause a reduction in capacity for physisorbed materials such as DMMP.

Demonstration quantities of this material were prepared and subjected to accelerated aging testing. The results of CK testing

are shown in Table 1. No change in test lives were observed over the period of the test for the Cu-Zn-Ag-TEDA (ASZ-TEDA) composition, while the CK life of the ASC comparison sample, as expected, decreased by 30%.

TABLE 1

CK Performance of Demonstration Sample

	CK Life (min)	
	Fresh	Aged*
ASZ-4% TEDA	58	57
ASC	69	46

* 7 days 45°C, 85% RH

After review, it was concluded that the TEDA level could be reduced to 3% with little loss of CK performance. A preliminary production quantity of this material has been prepared, and is currently the subject of long-term aging studies at CCC and CRDEC. The composition of the product is 6% Cu, 6% Zn, 0.05% Ag, and 3% TEDA. Initial product performance is in good agreement with predictions, and is shown in Table 2.

TABLE 2

AC & CK Performance of Pilot-Scale Sample

Composition	AC Life (min)	CK Life (min)
ASZ-3% TEDA	23	51

EXPERIMENTAL

Sample Preparation: Samples were prepared by impregnation of 12x30 mesh coal-based granular activated carbon with ammoniacal solutions of copper and zinc. Silver was omitted during the optimization procedure, but included on all final product samples. TEDA was incorporated using established procedures[2].

Testing: Samples were tested for AC and CK removal effectiveness using procedures similar to current U.S. Mil Spec methods[3]. All tests were conducted in glass tubes under constant flow. Determination of AC life was based on detection of either HCN or $(CN)_2$ at the specified breakthrough level. Accelerated aging testing was performed by equilibrating samples under air flow at 25°C and 80% RH, followed by storage at 45°C and 85% RH for seven days. After re-equilibration at 25° and 80% RH, the samples were tested normally.

SUMMARY

A chromium-free filter carbon impregnated with copper, zinc, silver and triethylenediamine has been developed for the removal of toxic vapors from air. A formulation containing 6% Cu, 6% Zn, 0.05% Ag, and 3% TEDA provides good balanced protection against chemical vapors, and is resistant to aging. The combination of 6% Cu and 6% Zn provides optimum AC performance. Increases in total metal levels provide no additional benefit. Protection afforded against CK is good with these metal levels and 3% TEDA. Additional TEDA will improve CK protection, but protection against vapors removed by physical adsorption will suffer. Silver was retained in the formulation at the current specification level of >0.03% to provide protection against arsine. Long term evaluation of preliminary production quantities of this material is in progress.

ACKNOWLEDGEMENT

This work was supported by the U.S. Army Chemical Research Development and Engineering Center, Aberdeen, Maryland, under contract DAAA15-86-C-0030.

REFERENCES

1. Kloubek, J., Medek, J.; Tomanova, D.; Porous Structure of Active Carbons and ASC Whetlerite Produced Therefrom; Carbon 22 1984, pp. 163-167.

2. Groose, J. E.; Liu, P. K. T.; Sublimation of Amine Compounds on Activated Carbon Pore Surfaces; U.S. Patent #4531953, July 30, 1985.

3. Mil. Spec. Mil-C-0013724C (EA)

BLANK

SURFACE CHARACTERIZATION OF CHROMIUM-FREE IMPREGNATED CARBONS

Chen C. Hsu

U.S. Army Chemical Research, Development and Engineering Center,
Aberdeen Proving Ground, MD 21010-5423

ABSTRACT

A comparative study of three chromium-free carbon samples was conducted using surface spectroscopic techniques. The samples include ASZ carbon (Z = zinc), ASZ-tartaric Acid, and ASZ-tartaric acid-TEDA. The results indicate the existence of Zn, Cu, C, O, and P. For Zn and Cu, they are in the oxide form - Zn(II) and Cu (II). To verify the source of P in these three samples, a base carbon (CWS) was analyzed. The result shows no P in CWS carbon, indicating that P in the samples was possibly due to the contamination in the process for producing chromium-free carbons. The findings from Auger elemental maps for Zn, Cu, C, O, Si, Al, and P have shown (1) tartaric acid does help disperse active metals on carbon surfaces and (2) the distribution of active metals on carbon internal surfaces appears to be fairly uniform. The SEM micrographs show the detailed morphology of carbon surfaces in terms of micro-, meso-, macro-pores, voids, channels, and cracks.

INTRODUCTION

ASC whetlerite carbons were developed for use in gas masks during World War II [1]. Recently, one of the active ingredients, chromium, was identified through laboratory tests as a carcinogen. Efforts have been directed toward the development of a chromium-free carbon to replace ASC whetlerite carbons [2]. A number of formulations were evaluated for chromium replacement and zinc was determined to be the most desirable element. To further improve the distribution of active impregnants on carbon surfaces, thus better performance, tartaric acid was added in the preparation step [2]. Additionally, it was also found that TEDA (triethylenediamine) is a necessary additive in the preparation process to improve the carbon life under tropical weather condition (high temperature and high humidity environment). Although laboratory tests have proven its effectiveness in the measurements of AC and CK lives of chromium-free carbons (ASZ carbons), questions such as (1) what is the distribution of active metals (Cu, and Zn) on carbon surfaces; (2) does tartaric acid indeed help active metals distribution; (3) what are the oxidation states of Cu and Zn; and (4) what is the chemical effect due

to TEDA; need to be answered. Surface characterization was undertaken to address these questions for which SAM (scanning Auger microprobe) and XPS (X-ray photoelectron spectroscopy) were used.

EXPERIMENTAL

Three fresh ASZ carbon samples, ASZ carbon (ASZ), ASZ + 10% tartaric acid carbon (ASZ+TA), and ASZ + 10% tartaric acid + 1% TEDA carbon (ASZ+TA+TEDA), base carbon (CWS carbon), and basic $CuCO_3$, were received from Calgon Carbon Corporation. ASZ carbon samples were dried at 110°-120° C in a vacuum oven for five hours. During which period, ASZ, ASZ+TA, and ASZ+TA+TEDA carbons lost weight by 0.06, 0.07, and 0.71%, respectively. The samples were later stored in a desiccator box before they were loaded into the test chamber. Basic $CuCO_3$ and CWS carbon were used as received.

For SAM and XPS techniques, Perkin-Elmer PHI Model 570 Surface Analysis System was used. The general operational procedures and parameters were described previously [3]. Briefly, for SAM analysis, normally 3kV and 10 nA electron beam was used. For XPS analysis, we used 14 kV and 300 W Mg K_{alpha} X-ray source (1253.6 eV) with 100 and 50 eV passing energies for XPS survey and multiplex runs, respectively. The test chamber is routinely maintained at 3.0x10E-10 torr. The system energy calibration is based on the binding energies of Cu(2p) and Cu(3p) after pure Cu metal was sputtered for 15 minutes with argon ion gun (15 A/min sputtering rate). In calculating the atomic concentration of each identified elements, the elemental detection sensitivity factors were taken into account. For Auger elemental maps, a SEM micrographs was taken and a matrix of 160x160 was defined for scanning. The result was reproduced on the 10x13 cm Polaroid films. A sharp razor blade was used to cut through a carbon granule slowly for Auger mapping of carbon internal surfaces.

RESULTS AND DISCUSSION

XPS Result. XPS survey runs were conducted for ASZ, ASZ+TA, ASZ+TA+TEDA carbons from which the elements on carbon surfaces were identified. They were Zn, Cu, C, O, and P, shown in Figure 1. The finding of P was unexpected in ASZ carbons. In order to verify the result, an XPS analysis was performed on the base carbon, the raw material from which the impregnated activated carbon was prepared. The elements identified on CWS carbon were C, O, S, Al, and Si, Figure 1. No P was observed indicating that P might be introduced during the impregnation process. Multiplex runs were also performed to determine the oxidation states of Cu and Zn and the concentrations of the identified elements. These results are shown in Tables 1-4. The binding energy of $Zn(2p_{3/2})$ remained fairly constant among three ASZ carbons except ASZ+TA+TEDA carbon being the least at 1023.04 eV. On the other

Table 1.
RESULTS OF XPS ANALYSIS ON ASZ NON-TARTARIC ACID

ELEMENT	APPARENT BINDING ENERGY eV	CORRECTED BINDING ENERGY eV	ATOMIC CONCENTRATION %
Zn ($2p_{1/2}$)	1047.70	1047.03	12.2
Zn ($2p_{3/2}$)	1024.11	1023.44	
Cu ($2p_{1/2}$)	956.51	955.84	3.3
Cu ($2p_{3/2}$)	935.69	935.02	
C (1s)	285.27	284.60	62.0
O (1s)	532.08	531.41	18.8
P (2p)	141.54	140.87	2.6

Table 2.
RESULTS OF XPS ANALYSIS ON ASZ + 10% TARTARIC ACID

ELEMENT	APPARENT BINDING ENERGY eV	CORRECTED BINDING ENERGY eV	ATOMIC CONCENTRATION %
Zn ($2p_{1/2}$)	1049.28	1047.22	11.5
Zn ($2p_{3/2}$)	1025.50	1023.44	
Cu ($2p_{1/2}$)	958.09	956.03	4.8
Cu ($2p_{3/2}$)	936.49	934.43	
C (1s)	286.66	284.60	58.7
O (1s)	533.66	531.60	18.1
P (2p)	143.33	141.27	5.8

Table 3.
RESULTS OF XPS ANALYSIS ON ASZ + 10% TARTARIC ACID + 4% TEDA*

ELEMENT	APPARENT BINDING ENERGY eV	CORRECTED BINDING ENERGY eV	ATOMIC CONCENTRATION %
Zn ($2p_{1/2}$)	1048.49	1046.83	16.4
Zn ($2p_{3/2}$)	1024.70	1023.04	
Cu ($2p_{1/2}$)	956.90	955.24	1.2
Cu ($2p_{3/2}$)	935.89	934.23	
C (1s)	286.26	284.60	61.7
O (1s)	533.07	531.41	16.0
P (2p)	141.94	140.28	0.5

*Lot # 2754-76. 6% Cu, 6% Zn, 0.05% Ag, and 4% TEDA.

Table 4.
RESULTS OF XPS ANALYSIS ON CWS BASE CARBON

ELEMENT	APPARENT BINDING ENERGY eV	CORRECTED BINDING ENERGY eV	ATOMIC CONCENTRATION %
C (1s)	283.48	284.60	87.3
O (1s)	531.88	533.00	10.2
Si (2p)	101.30	102.42	1.3
Al (2p)	74.14	75.26	0.6
S (2p)	153.24	154.36	0.4

hand, the binding energy of $Cu(2p_{3/2})$ had shown decreasing in the order of ASZ, ASZ+TA, and ASZ+TA+TEDA. It appears that the addition of TEDA reduced the binding energies of Cu and Zn. Based on the binding energies, the Auger electron kinetic energies, and the shape of the XPS spectra, it was determined that the oxidation states of Cu and Zn were at 2+ state, possibly in the oxide form [4]. A comparison of the binding energies of $Cu(2p_{1/2})$, $Cu(2p_{3/2})$, $Zn(2p_{1/2})$, $Zn(2p_{3/2})$, and O(1s) were shown in Table 5. For O(1s), ASZ carbons have smaller binding energy than that of CWS carbon.

Table 5.
BINDING ENERGIES FOR THE ATOMS OF Cu, Zn, AND O OF VARIOUS CARBONS

CARBON	BINDING ENERGY, eV				
	$Cu(2p_{1/2})$	$Cu(2p_{3/2})$	$Zn(2p_{1/2})$	$Zn(2p_{3/2})$	O(1s)
ASZ	955.84	935.02	1047.03	1023.44	531.41
ASZ-TA	956.03	934.43	1047.22	1023.44	531.60
ASZ-TA-TEDA	955.24	934.23	1046.83	1023.04	531.41
CWS	-	-	-	-	533.00

In order to address the question as to whether basic copper carbonate, the source material of copper for impregnation, still exists on ASZ carbon surfaces, XPS analysis was carried out and the results are shown in Table 6. On average, the binding energies of $Cu(2p_{3/2})$, C(1s), and O(1s) are about 5 eV higher than that of ASZ carbons. The XPS multiplex spectrum of $Cu(2p_{3/2})$ showed two split peaks, one at 939.80 eV and the other at 946.80 eV, Figure 2. In a study of the passive behavior of copper in weak acid and alkaline solutions, Strehblow and Titze observed the second peak at higher energy than the original copper peak and assigned to copper II oxide or hydroxide [5]. Additionally, in the CRC Handbook of Spectroscopy [6], the binding energy of $Cu(OH)_2$ has relatively lower than $CuCO_3$. This leads us to assign the binding energies of 939.80 and 946.80 eV to $Cu(OH)_2$ and $CuCO_3$, respectively. The binding energy of C(1s) at 289.40 eV for $CuCO_3$ shown in Table 6, is consistent with the value reported in the literature [7]. The binding energy of O(1s) at 537.80 eV for basic $CuCO_3$, however, is about 7 eV higher than the value of carbonate moiety. This difference may be due to the combination of oxygen from carbonate and hydroxide of basic $CuCO_3$. In comparison with the binding energy of $Cu(2p_{3/2})$ of ASZ carbons, it is obvious that basic copper carbonate was transformed into oxide during the preparation process.

Table 6.
RESULTS OF XPS ANALYSIS ON BASIC $CuCO_3$

ELEMENT	APPARENT BINDING ENERGY eV	CORRECTED BINDING ENERGY eV	ATOMIC CONCENTRATION %
Cu ($2p_{1/2}$)	961.00	961.40	21.9
Cu ($2p_{3/2}$)	939.40	939.80	
C (1s)	289.00	289.40	17.8
O (1s)	537.40	537.80	60.0

SAM Results. SEM micrographs were obtained initially to define the area for Auger elemental mapping. The Auger mapping was conducted for the those elements identified on the surfaces of ASZ carbons. Figures 3-5 show the SEM micrographs of the internal surfaces and the Auger elemental maps of ASZ, ASZ+TA, and ASZ+TA+TEDA carbons, respectively. In general, the distribution of active metals on ASZ carbons, manifested as the bright spots, are fairly uniform across the cross section of carbon granule. A detailed comparison between ASZ, ASZ+TA, and ASZ+TA+TEDA carbons showed the positive effect of tartaric acid on Cu and Zn distribution on carbon surfaces, Figures 3 and 4. For C maps of ASZ carbons, they all show a large bright area as expected. The morphology of carbon surfaces in terms of micro-, meso-, macro-pores, voids, channels, and cracks is quite visible from these SEM micrographs, Figure 6.

SUMMARY

1. THREE KINDS OF CHROMIUM-FREE CARBONS - ASZ WITHOUT TARTARIC ACID (TA), ASZ WITH TA, AND ASZ WITH TA AND TEDA - ALONG WITH CWS CARBON AND BASIC $CuCO_3$ WERE ANALYZED SURFACE SPECTROSCOPICALLY.

2. ELEMENTS OF Cu, Zn, O, C, AND P WERE DETECTED IN THESE FRESH ASZ CARBON SAMPLES. THE OXIDATION STATES OF Cu AND Zn WERE DETERMINED TO BE 2+. THE OXIDATION STATE OF Cu OF BASIC $CuCO_3$, THE PRECURSOR OF Cu IMPREGNANT, WAS ALSO FOUND TO BE 2+, BUT WITH RELATIVELY HIGHER BINDING ENERGY THAN THAT OF ASZ, ASZ+TA, AND ASZ+TA+TEDA CARBONS. P WAS NOT DETECTED IN CWS CARBON. THE FACT THAT PHOSPHORUS WAS IDENTIFIED IN ALL THREE ASZ CARBON SAMPLES MAY BE DUE TO THE CONTAMINATION IN MANUFACTURING PROCESSES.

3. **TEDA APPEARS TO REDUCE THE BINDING ENERGIES OF Cu AND Zn.**

4. **SEM MICROGRAPHS AND AUGER ELEMENTAL MAPS WERE OBTAINED FOR THE IDENTIFIED ELEMENTS. THE DISTRIBUTION OF Cu AND Zn ON CARBON SURFACES APPEARS TO BE MORE UNIFORM WITH THE USE OF TARTARIC ACID IN THE PREPARATION OF ASZ CARBONS.**

ACKNOWLEDGEMENTS

Dr. David E. Tevault and Mr. Robert W. Morrison of Army CRDEC and Dr. David T. Doughty and Mr. Matthew J. Smith of Calgon Carbon Corporation are gratefully acknowledged for providing the samples used in this study and for helpful discussion.

REFERENCES

[1] W. A. Noyes, Jr., "Summary Technical Report of the National Defense Research Committee, Division 10," Volume 1, Washington, D.C.,(1946).

[2] D. T. Doughty, "Development of a Chromium-Free Impregnated Carbon for Absorption of Toxic Agents. Final Report - Phase II." Calgon Carbon Corporation, Pittsburgh, PA (1989).

[3] C. C. Hsu, "Surface Spectroscopic Analysis of Fresh and Spent Oxidation Catalysts," Proceedings of U.S. Army CRDEC Scientific Conference on Chemical Defense Research, CRDEC-SP-013, Vol. 1, 407-417 (1989).

[4] C. D. Wagner, W. M. Riggs, L. E. Davis, J. F. Moulder, Handbook of X-Ray Photoelectron Spectroscopy, Perkin-Elmer Corporation, Minnesota (1978).

[5] H.-H. Strehblow and B. Titze, "The Investigation of the Passive Behavior of Copper in Weak Acid and the Examination of the Passive Film by ESCA and ISS," Electrochimica ACTA, 25(1980)839-850.

[6] CRC Handbook of Spectroscopy, ed., J. W. Robinson, Vol. 1, 573-578, CRC Press (1974).

[7] G. Marlettsa, "Cation Dependence of the Chemical Modification Induced by Low Energy Particle Bombardment on Inorganic Salts: An XPS Study," Nuclear Instruments and Methods in Physics Research, B32(1988)204-210.

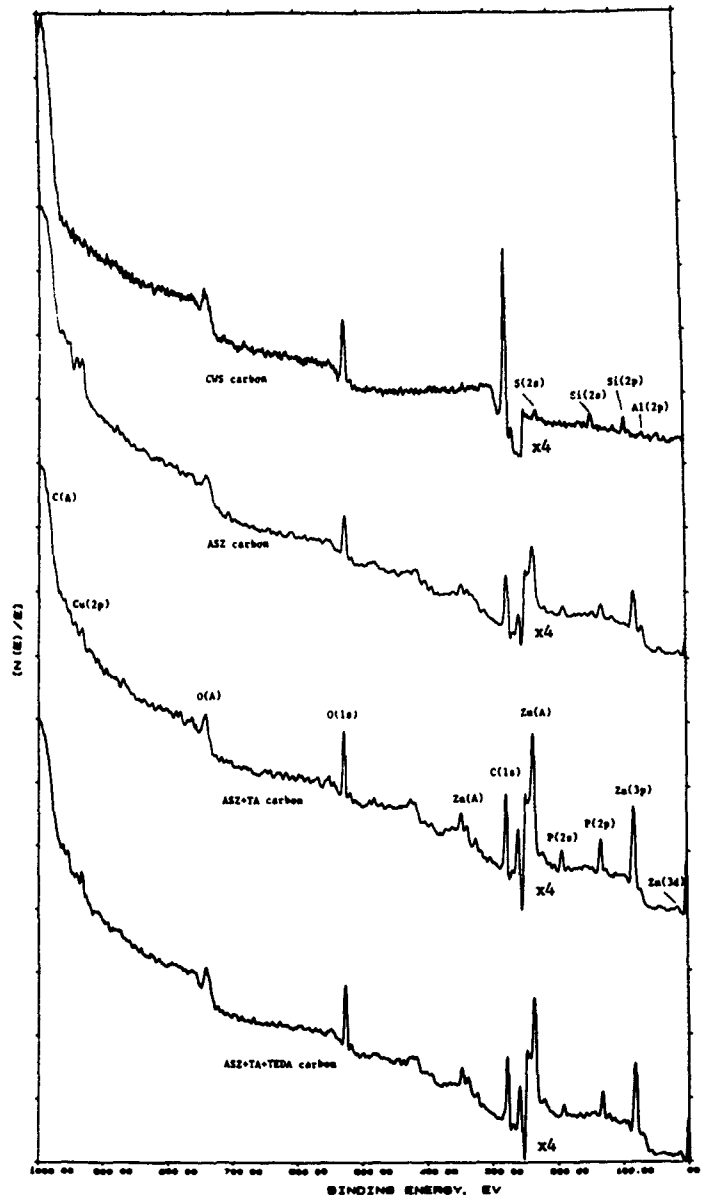

Figure 1. XPS survey spectra of CWS, ASZ, ASZ+TA, and ASZ+TA+TEDA carbons.

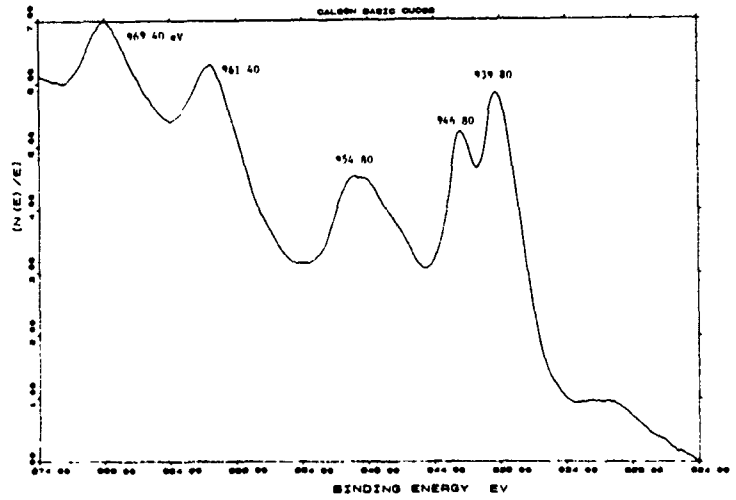

Figure 2. XPS spectrum of Cu of basic $CuCO_3$.

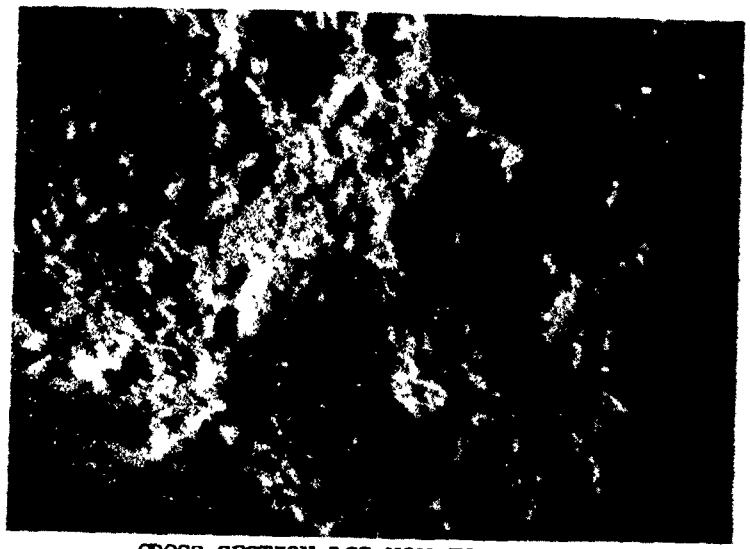

Figure 3. SEM micrograph and Auger elemental maps of Cu, Zn, and O of ASZ-NON-TA carbon, 225X.

CROSS SECTION ASZ-TA 200X

CROSS SECTION ASZ-TA 200X Cu MAP

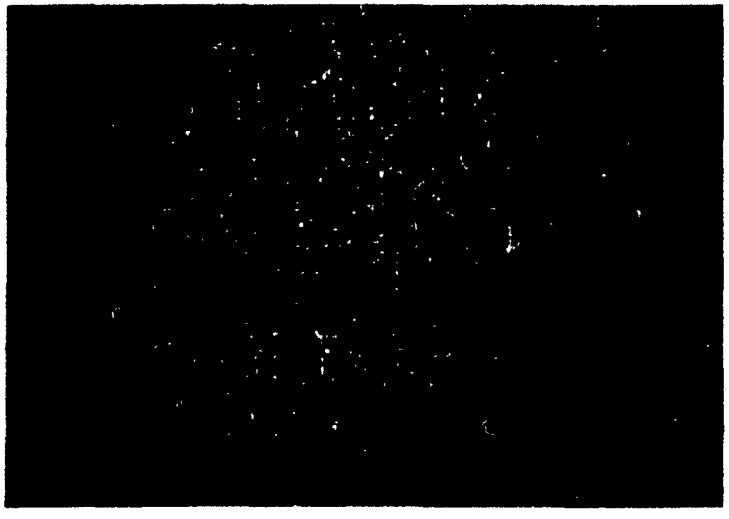

CROSS SECTION ASZ-TA 200X Zn MAP

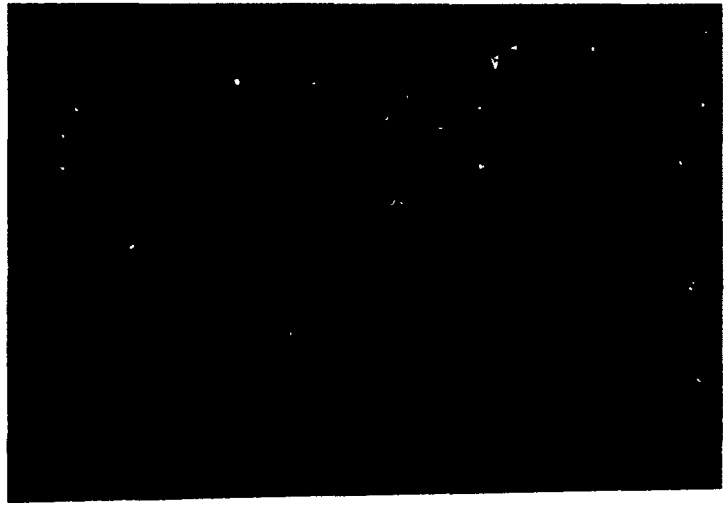

CROSS SECTION ASZ-TA 200X C MAP

Figure 4. SEM micrograph and Auger elemental maps of Cu, Zn, and O of ASZ-TA carbon, 200X.

CROSS SECTION ASZ-TA-TEDA 200X

CROSS SECTION ASZ-TA-TEDA 200X C MAP

CROSS SECTION ASZ-TA-TEDA 200X Cu MAP

CROSS SECTION ASZ-TA-TEDA 200X Zn MAP

Figure 5. SEM micrograph and Auger elemental maps of Cu, Zn, and O of ASZ-TA-TEDA carbon, 200X.

CROSS SECTION ASZ-NON-TA 64X

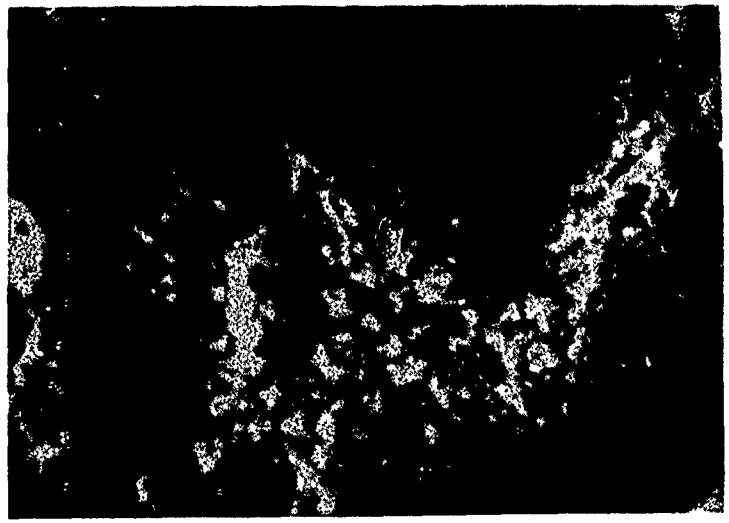

CROSS SECTION ASZ-NON-TA 125X

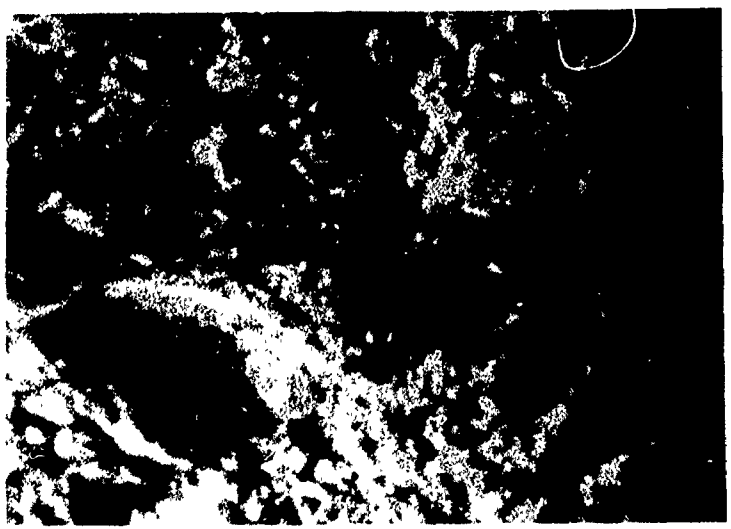

CROSS SECTION ASZ-NON-TA 250X

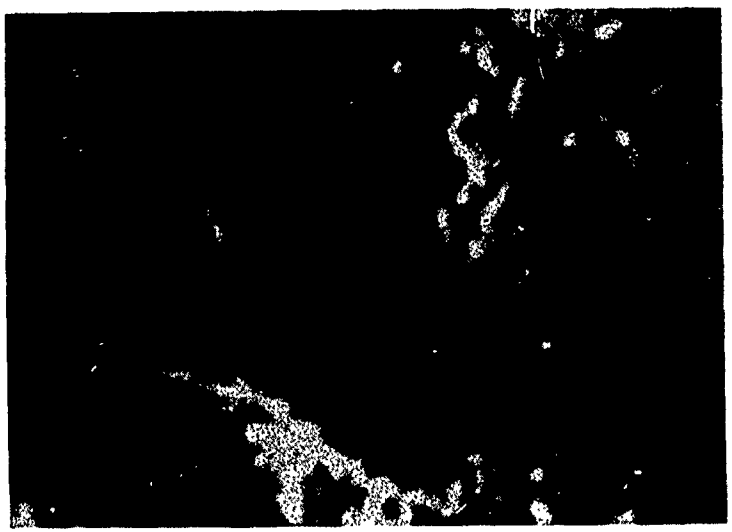

CROSS SECTION ASZ-NON-TA 300X

Figure 6. SEM micrograph of ASZ-NON-TA carbon at 64X, 125X, 250X, and 300X.

SYNCHROTRON X-RAY ABSORPTION STUDY OF CR AND OTHER METALS IN ACTIVATED CHARCOAL FILTERS

W. T. Elam.
Naval Research Laboratory, Washington, DC 20375

Research Funded by NSWC, CRDEC

ABSTRACT

X-ray absorption provides a method of studying the valence and local bonding environment of a specific metallic atom in a complex sample. This technique has been used to measure the Cr oxidation state in activated charcoal. A specific spectral feature is particularly valuable in that it is associated with the +6 oxidation state. It has been possible to make quantitative measurements of the amount of Cr+6 remaining after aging for various periods. These measurements have also confirmed the suspected relation between amount of remaining Cr+6 and breakthrough times.

The increasing availability of synchrotron x-ray sources has made x-ray absorption spectroscopy a viable technique for studying metals in relatively low concentrations, such as those present in carbon filters. This study was undertaken to demonstrate the feasibility of using XAS to study transition metals adsorbed on carbons and to see what information was available. The technique should yield information useful in studying the chemistry of systems adsorbed on carbons and might yield insights relevant to protection chemistry.

The experimental setup is shown in figure 1 below.

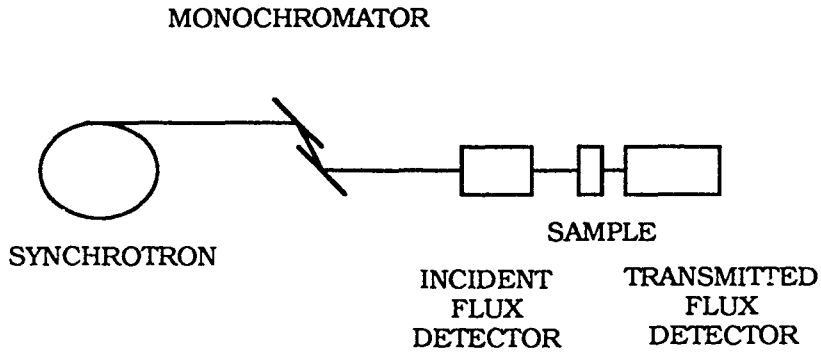

X-ray Absorption Experimental Setup
Figure 1

X-rays from a synchrotron source are monochromatized and passed through a sample. The absorption is measured by monitoring incident and transmitted flux. Varying the x-ray energy gives a spectrum near the absorption edge of any element of choice. Since carbon is relatively transparent to x-rays, compared to metals, spectra can be obtained relatively easily for metals adsorbed on carbon, in situ. The metal need not be chemically reacted or otherwise disturbed.

Figure 2 shows a typical x-ray absorption spectrum.

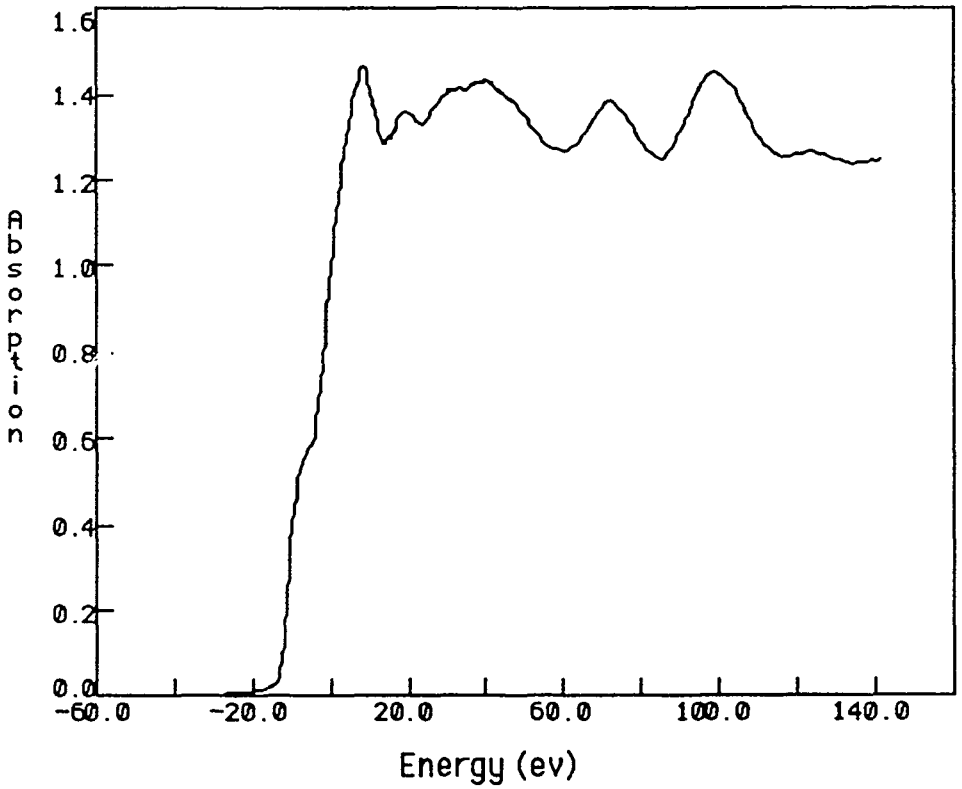

X-ray absorption spectrum of chromium metal
Figure 2

The plot is absorption vs. x-ray energy around the energy of the K-edge of Cr. (The absorption is measured on a per-atom basis, corrected for the exponential dependence of transmitted flux on absorption.) The edge is the abrupt increase in absorption in the left half of the figure. Its position and shape give information about the oxidation state of the Cr. The structure above the edge is the EXAFS (Extended X-ray Absorption Fine Structure). It depends upon the type, distance, and ordering of the nearby atoms, and can be analyzed to give information about the local atomic structure of the metal atoms.

Determination of the oxidation state of the chromium atom depends on both the position and shape of the absorption edge. Chromium in the +3 and +6 oxidation states (as found in chromium oxide and in sodium chromate) were measured to determine the sensitivity of the technique to these valences, and to provide quantitative calibration. The two spectra are shown in figure 3.

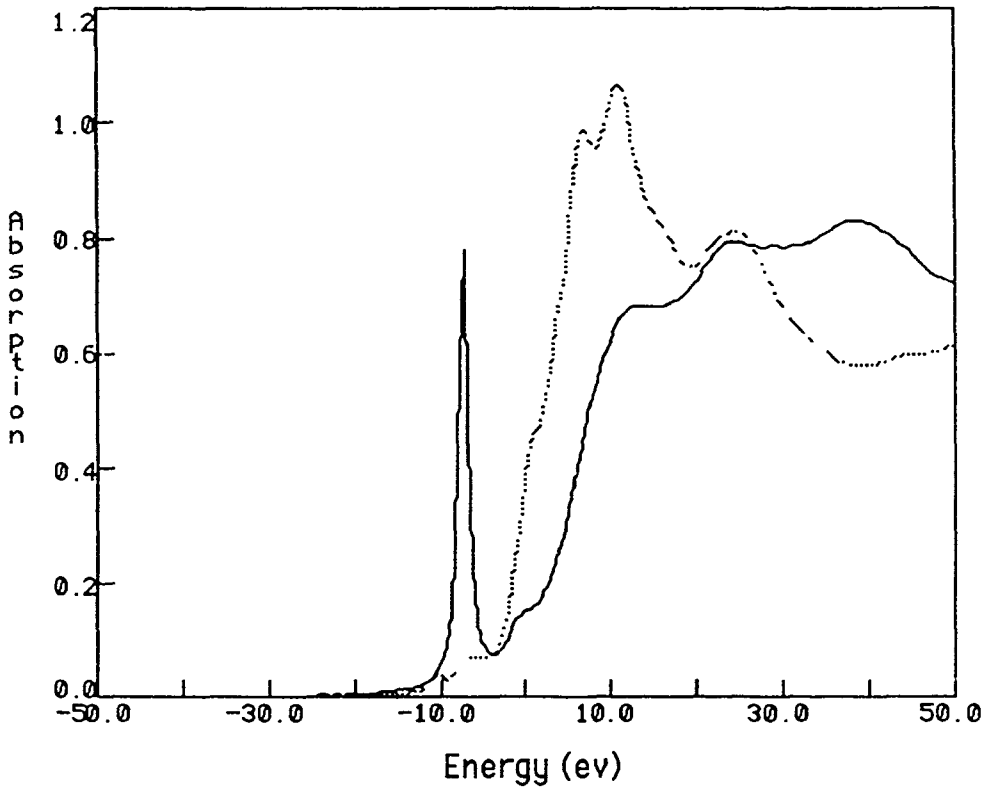

Sodium Chromate (solid, Cr+6) and Chromium Oxide (dashed, Cr+3)

Figure 3

The solid line is a spectrum of Cr in the +6 oxidation state (from sodium chromate). The dashed line is a similar spectrum for Cr in the +3 oxidation state (from chromium oxide, Cr_2O_3). As the oxidation state increases, the edge shifts to the right by an amount easily visible in the figure.

Specific to 3d transition metals (Sc through Ni) is a pre-edge peak characteristic of metal ions in high oxidation states and low-symmetry sites. This feature is visible in the spectrum as the sharp peak just below the edge in the solid curve. The Cr ion in sodium chromate is in the +6 valence state and sits in a tetrahedral site, surrounded by 4 oxygen atoms. This peak provides a convenient indicator, since it is particularly associated with the +6 oxidation state of Cr.

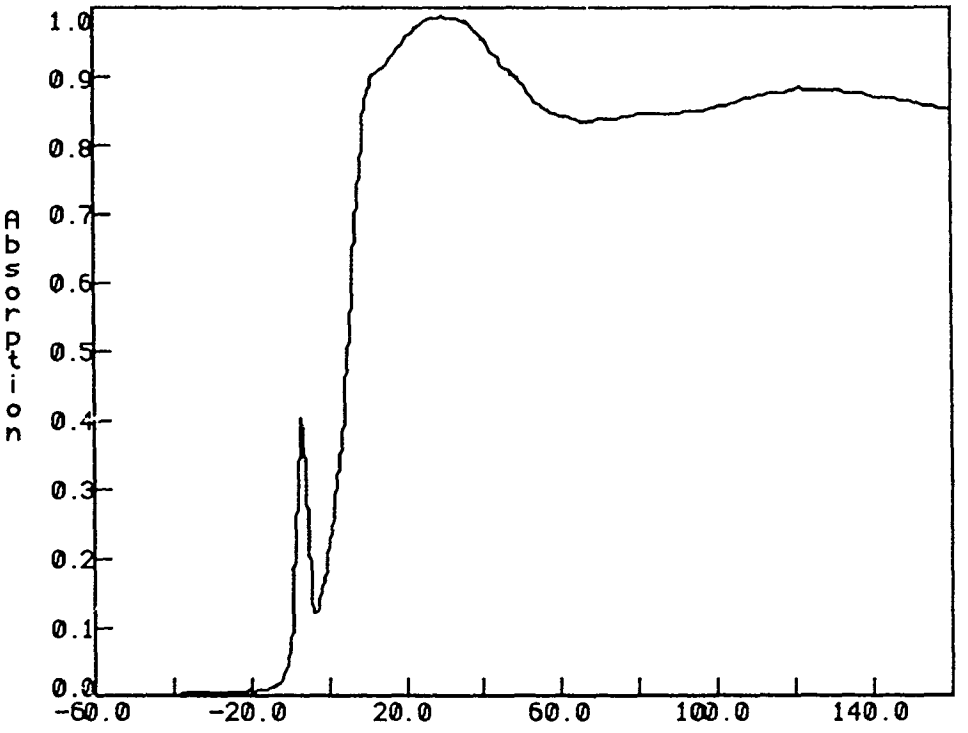

Cr in lab. standard Whetlerite

Figure 4

The spectrum in figure 4 was taken on a Calgon Laboratory Standard carbon at the Cr edge energy. The presence of the Cr+6 peak can be easily seen. Quantitative measurements of the amount of Cr+6 were made by comparing the height of the pre-edge peak to the total edge height.

This method was tested by measuring samples with known amounts of Cr in the different oxidation states. The errors were unacceptably large, sometimes as much as 50%. The problem arises because of the vastly different shape of the spectra from Cr+6 and Cr+3. As can be seen in figure 3, the shape of the spectrum above the absorption edge is very different for Cr in the two different oxidation

states. The height of the absorption edge, which represents the signal from all of the chromium atoms, is difficult to measure reliably as its shape changes with the changes in relative amounts of +6 vs. +3. Quantitative measurement of the relative amounts of Cr in the different oxidation states depends on the ratio of the height of the pre-edge peak to the total absorption.

In spite of the errors in the first attempts at measuring relative oxidation states, some useful trends were observed. A series of samples which had been aged for different times and whose effectiveness had been subsequently measured was obtained from V. R. Deitz at NRL (for more information, see his quarterly report of Jan.-March 1987, available from NRL Code 6170, ref. # 6170-187).

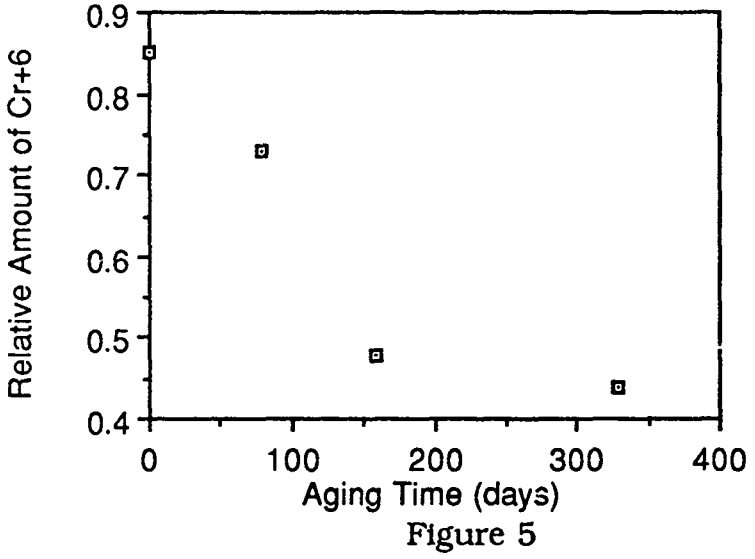

Figure 5

The plot in figure 5 shows the relative amount of Cr+6 in the four samples (as measured by the method described above) plotted vs. the time the sample was aged. The amount of Cr+6 decreases dramatically with age.

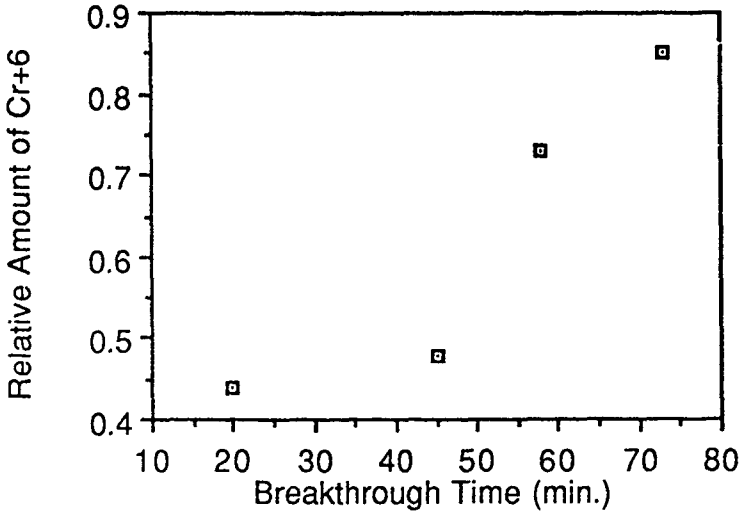

Figure 6

The plot in figure 6 shows the same relative oxidation state data plotted vs. the CK breakthrough time measured for the samples. Again, the trends are clear in spite of the large scatter in the data.

Since the x-ray absorption process is linear, the problem of the complex spectrum shape can be overcome by combining reference spectra in known relative amounts. More reliable quantitative information can be obtained if the result can be matched to the spectrum of the unknown. The quality of such simulated mixed-oxidation-state spectra is shown in figure 7.

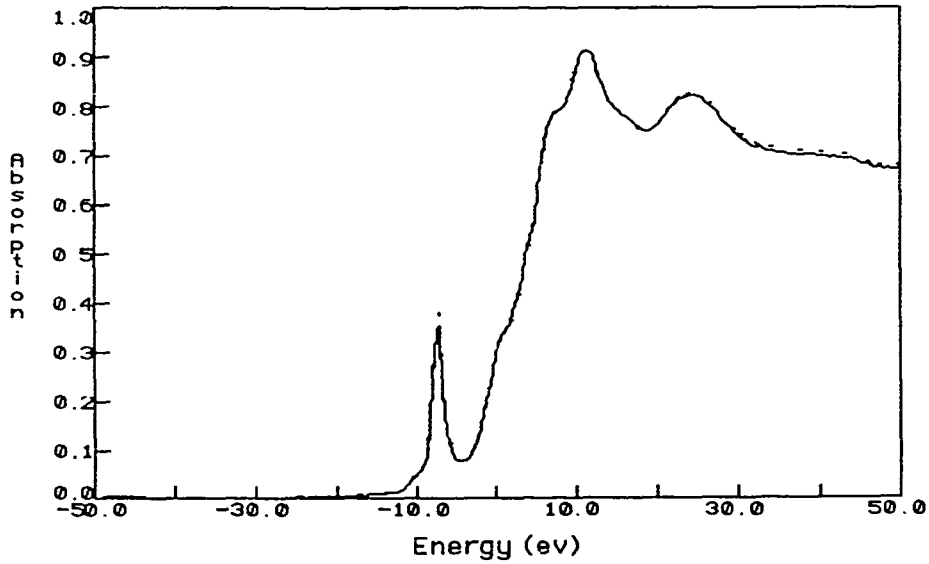

46% Cr+3 + 54% Cr+6 (solid)
Simulation (56% Cr+3 + 44% Cr+6) (dashed)

Figure 7

The solid line is a spectrum taken on a sample with a known mixture of Cr+6 and Cr+3. The dashed line is a simulated spectrum produced by mathematically adding the spectra from pure Cr+6 and pure Cr+3 in the proportions shown at the top of the figure. The measurement of the relative amounts of Cr in the two oxidation states is correct to within a few percent, and the reproduction of the spectral shape is excellent. The process was repeated for different relative amounts of Cr in the different oxidation states, with similar results. Using least-squares fitting techniques should reduce the errors to about 1%. Since the carbon spectral shape is slightly different from the chromium oxides used here, the errors will be higher for actual carbon samples. This can be overcome by using organic compounds for reference spectra (perhaps even fresh vs. fully depleted carbons).

Similar measurements to those shown for chromium were performed for copper. The Cu is in the +2 oxidation state, and no change could be detected on aging.

CONCLUSIONS

In conclusion, various metals were studied while adsorbed on carbon using x-ray absorption spectroscopy. Quantitative measurements of the amount of metal ions in the different oxidation states were obtained with accuracies of a few percent. Changes in both the oxidation state and in the local geometry of chromium were observed with aging of the samples. Copper was not observed to change significantly in oxidation state. Changes in the chromium oxidation state correlated well with the decrease in breakthrough times of the aged samples.

BLANK

Complete Catalytic Oxidation of Diethyl Sulfide Over a 1% Pt/Al_2O_3 Catalyst Effects of Mass Transfer on Reactivity

Joseph A. Rossin
Air Purification Branch
U.S. Army CRDEC
Aberdeen Proving Ground, MD 21010

Abstract

The effects of intraparticle mass transfer on the complete oxidation of diethyl sulfide over a 1% Pt/Al_2O_3 was investigated using a fixed bed catalytic reactor. Reaction rates were recorded at temperatures between 225 ° C and 300 ° C, diethyl sulfide concentrations between 5 and 250 ppm (v/v) and one atmosphere pressure. The reaction rate expression was determined in the absence of mass transfer resistances using below 70 mesh catalyst particles. The oxidation kinetics of diethyl sulfide was determined to be zeroth order over the range of process conditions studied. Mass transfer resistances were observed at temperatures above 250 ° C when employing 35/65 mesh catalyst particles. In these cases, data could be correlated using a diffusion and reaction model which accounted for intraparticle gradients. At low sulfide concentrations, as will be encountered in catalytic systems designed for removal of CW agents, mass transfer resistances are highly significant.

INTRODUCTION

Complete catalytic oxidation of chemical warfare (CW) agents is an alternative to adsorption as a means of collective protection. While activated carbon systems are presently used to remove CW agents, these systems have shortcomings in that they do not function well in moist climates over extended periods of usage. They also are limited in their capacity for agents which are removed by reaction and those which are weakly adsorbed. Complete catalytic oxidation is an effective method of air purification, as has been demonstrated by the automotive industry[1-5]. In addition, recent studies have indicated that catalytic oxidation is a promising alternative means of collective protection[6].

Catalytic systems designed for the removal of CW agents from streams of air will be different than those designed for industrial and automotive applications. This is because when dealing with CW agents, effluent concentrations on the order of parts per billion (ppb) are required due to the potential high toxicity of the various agents [7]. This compares with the requirement of 5,000 parts per million (ppm) for carbon monoxide in automobile exhaust. When dealing with low concentrations such as the case with CW agents, mass transfer resistances will strongly reduce the intrinsic catalytic activity. Baier et al.[8] performed the initial feasibility studies pertaining to the catalytic oxidation of CW agents. In their study strong intraparticle diffusion resistances were noted but no attempt was undertaken to develop a model which would account for these resistances.

At the ultra high conversions required for removal of CW agents, mass transfer resistances are expected to be severe. The first objective of this study is to first determine the reaction kinetics of a mustard simulant (diethyl sulfide). The second objective is to determine the intraparticle mass transfer resistances of the simulant. The approach taken was to first determine the reaction kinetics for the oxidation of diethyl sulfide free of mass transport effects. The reaction kinetics will then be incorporated into a design equation aimed at determining the intraparticle mass transfer resistances.

DIFFUSION-REACTION MODEL

The oxidation of diethyl sulfide over Pt/Al_2O_3 was determined to be zeroth order over the conditions employed in this study[29]. This section deals with the development of a mathematical model which accounts for intrapartical diffusion and zeroth order chemical reaction.

Development of Diffusion-Reaction Model.

The zeroth order rate expression was incorporated into the development of the diffusion-reaction model. The model developed below employs Thiele's concept of effectiveness factor, where the effectiveness factor, η, is a proportionality constant relating the observed reaction rate to the true reaction rate[10-14]:

$$\eta = \frac{\text{Observed reaction rate}}{\text{True reaction rate}} \tag{1}$$

For a fixed bed catalytic reactor, the conversion for a zeroth order reaction may be determined from:

$$\frac{dX}{dW} = \frac{\eta K_0}{F} \tag{2}$$

Where X is the fractional conversion, W is the catalyst weight, F is the reactant molar flow rate, and K_0 is the zeroth order rate constant. η must be evaluated at the local conditions (along the reactor length). The solution to this equation involves simultaneously determining η and solving equation 2 at the desired operating conditions. The derivation of the diffusion-reaction model begins with solving the problem for a single pellet. The solution for the catalyst pellet is then incorporated into the design equation for the fixed bed catalytic reactor.

The catalyst particle is represented by a sphere of radius R. R is defined to be zero at the center of the sphere. For a zeroth order reaction, anywhere within the pellet where reactant is present, regardless of its concentration, the reaction rate will be constant. R_m is defined as the radial point within the particle at which the reactant concentration is zero. The observed reaction rate will equal the rate constant integrated over the catalyst volume where the concentration of reactant is greater than zero (from $r = R_m$ to $r = R$). Knowing R_m the effectiveness factor is then determined from:

$$\eta = \frac{4\pi K_0 \int_{r=R_m}^{r=R} Rr^2 dr}{4\pi K_0 \int_{r=0}^{r=R} r^2 dr} = \left(1 - \frac{R_m^3}{R^3}\right) \quad (3)$$

R_m is unknown and must be determined in order to calculate η. Solving the material balance equation for the catalyst particle, R_m may be determined from:

$$1 - \frac{\Phi^2}{6}(1 - r_m^2) + \frac{\Phi^2}{3} r_m^2 (1 - r_m) = 0 \quad (4)$$

Where: $\Phi = R \left(\frac{K_0}{D_e C_a^0}\right)^{1/2}$ and $r_m = \frac{R_m}{R}$

D_e is the effective diffusivity and C_a^0 is the reactant feed concentration. Details of this derivation have been reported elsewhere[15].

3. EXPERIMENTAL METHODS

Materials: Diethyl sulfide (reagent grade) was obtained from Eastman-Kodak and was used as received. The 1% $Pt/\gamma\text{-}Al_2O_3$ catalyst employed in this study was obtained from Houdry. The support has a nominal BET surface area of 100 m^2/g as reported by the manufacturer.

Catalyst Preparation: The catalyst used in this study was pretreated by calcining in flowing air at 425 °C in a quartz tube furnace. This pretreatment procedure was found to yield a highly reactive catalyst[16].

Process Conditions: A detailed description of the equipment and procedure are presented elsewhere[15]. In order to evaluate the rate expression, two sets of experiments were performed. The first set involved varying the diethyl sulfide flow rate while maintaining a constant air flow rate. In this manner, the contact time of the reactant was held constant. This allowed for simultaneously studying the effects of concentration and flow rate of diethyl sulfide at a constant air space velocity. The second set of experiments involved maintaining a constant flow rate of diethyl sulfide and varying the flow rate of air. Because only trace quantities of diethyl sulfide were employed, varying the air flow rate did not affect the concentration of oxygen. This allowed for the study of the effects of diethyl sulfide concentration at a constant diethyl sulfide flow rate.

Kinetics studies were performed at 225 °C, 250 °C, 275 °C and 300 °C at approximately 1.25 atmospheres total pressure using catalyst particles crushed to below 70 mesh (U.S. Sieve Series). The diethyl sulfide concentration was varied between 6 and 250 ppm (v/v) in dry air, with air flow rates ranging between 0.20 and 2.0 Nl/min. Process conditions were maintained a minimum of 8 hr in order to assure steady state. In addition, a fresh catalyst bed was employed at each reaction temperature.

The effects of mass transfer on catalytic activity was studied using 35/65 mesh catalyst particles. Reactant sulfide and air flow rates were varied in a manner similar to that employed in the study of the <70 mesh catalyst particles. Runs

were conducted at 250 °C, 275 °C and 300 °C at about 1.25 atmospheres total pressure. Diethyl sulfide concentrations were varied between 5.0 and 250 ppm (v/v) in dry air. All process conditions were maintained for a minimum of 8 hr.

4. RESULTS

No partial oxidation products were detected during any of the runs. SO_2 was the only sulfur containing product present in the effluent. Sulfur balances were performed at each set of process conditions. Balances were typically between 85% and 95%. Discrepancies in the sulfur balances were attributed to the formation of SO_3, which could not be analyzed (SO_3 will combine with product water to form sulfuric acid).

Figure 1 illustrates the effect of diethyl sulfide concentration on conversion at 250 °C and 300 °C at constant values of W/F for less than 70 mesh catalyst particles. As the figure shows, the concentration of diethyl sulfide has no effect on sulfide conversion over the range of conditions reported here.

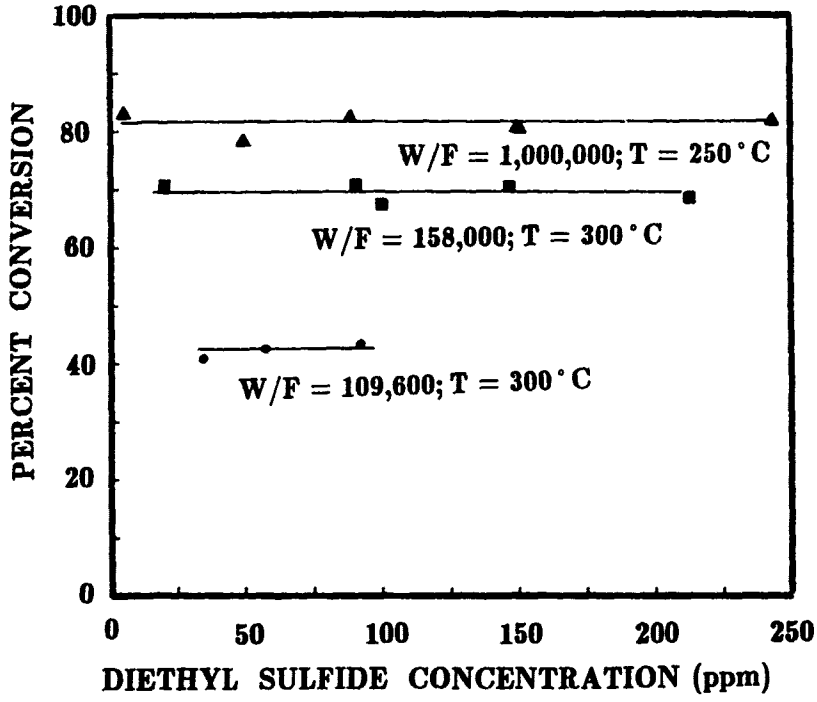

Figure 1: Effect of Diethyl Sulfide Concentration on Conversion at Constant Values of W/F at 250 °C and 300 °C (<70 Mesh Catalyst Particles).

The reaction rate expression was determined to be independent of the feed concentration and the temperature dependence of the zeroth order rate constant, K_0, is illustrated in Figure 2 for the less than 70 mesh catalyst particles. Data were fit using an Arrhenius type relation, with the log of the rate constant being proportional to reciprocal temperature. The rate constant was calculated to be 78.8 exp (-19,100/RT) mols/sec-g-cat. The units of activation energy are cals/mol, and T is in kelvins.

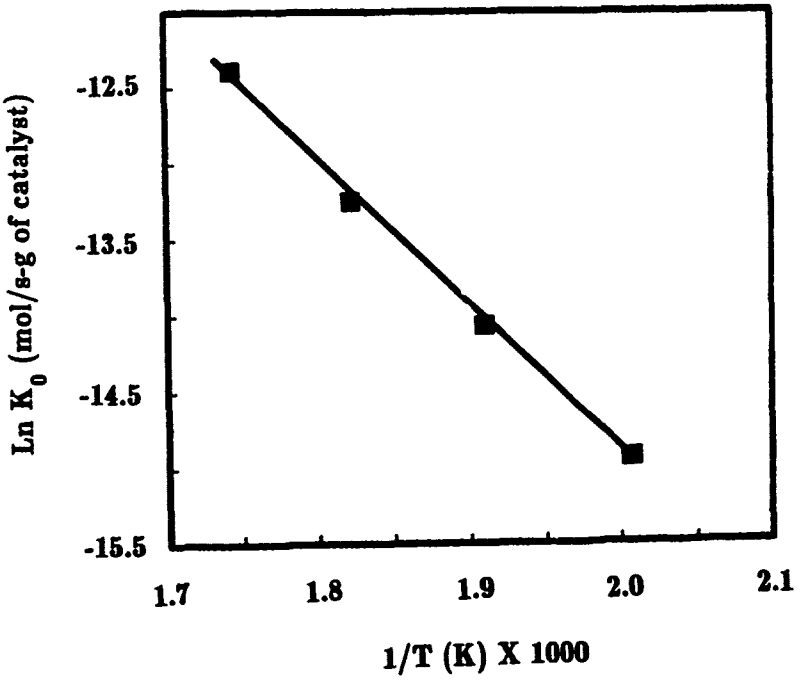

Figure 2: Arrhenius Plot of the Zeroth Order Rate Constant for <70 Mesh Catalyst Particles. [K_0 = 78.8 exp (-19,100/RT) mols Et_2S/s-g-cat; r^2 = 0.9992.]

Figure 3 reports conversion as a function of diethyl sulfide feed concentration at constant values of W/F at 250 °C employing the 35/65 mesh catalyst particles. As the figure indicates, the diethyl sulfide feed concentration has a strong influence on conversion (at constant W/F). The solid line through the points represents the conversion as predicted by the diffusion-reaction model employing an effective diffusivity (D_e) of 0.015 cm^2/sec.

Figures 4 and 5 report conversion as a function of diethyl sulfide feed concentration at 275 °C and 300 °C for constant values of W/F employing the 35/65 mesh catalyst particles. Again, note that unlike the less than 70 mesh particles, conversion increases with an increase in diethyl sulfide feed concentration (at a constant value of W/F). In both cases, conversions obtained are much less those obtained using the smaller catalyst particles. The solid lines in the figures represent conversions predicted employing the diffusion-reaction model with D_e equal to 0.0165 and 0.015 cm^2/sec, respectively. As the figure indicates, the model accurately describes the data over the range of process conditions employed in this study.

DISCUSSION

In developing the diffusion reaction model, it was necessary to first determine the reaction kinetics free of transport effects. A sample of these data are reported in Figures 1 and 2. As Figure 1 indicates, changing the feed concentration of diethyl sulfide (constant W/F) does not affect the conversion. The activation energy, as obtained from data reported in Figure 2, is consistent with that reported for oxidation organic compounds. A detailed discussion of the oxidation kinetics of diethyl sulfide has been reported elsewhere[9].

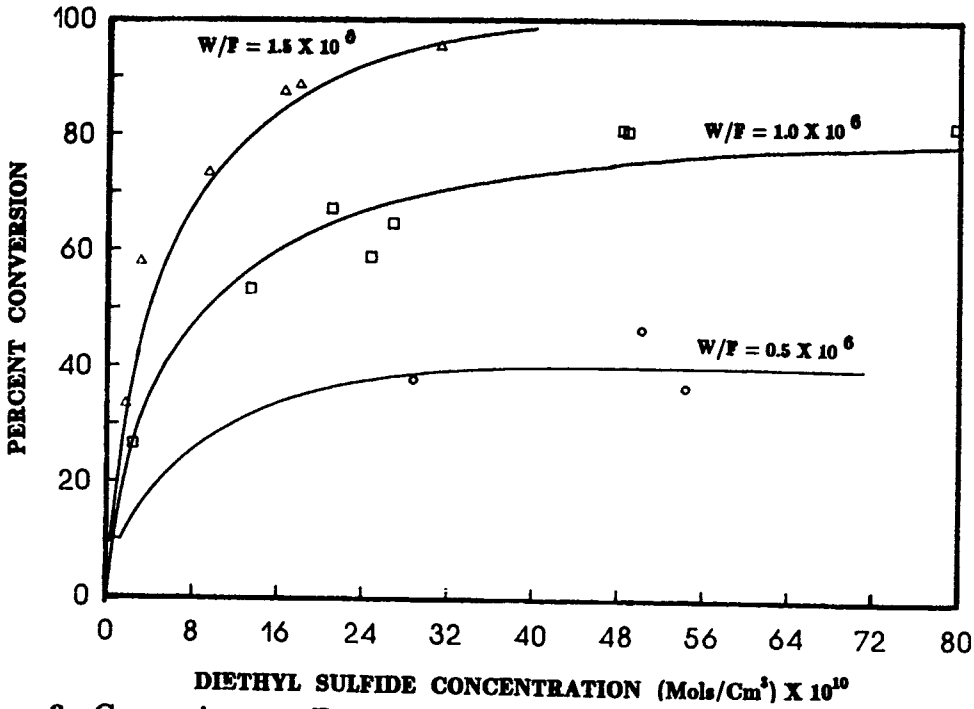

Figure 3: Conversion as a Function of Diethyl Sulfide Feed Concentration for 35/65 Mesh Catalyst Particles at 250 ° C.

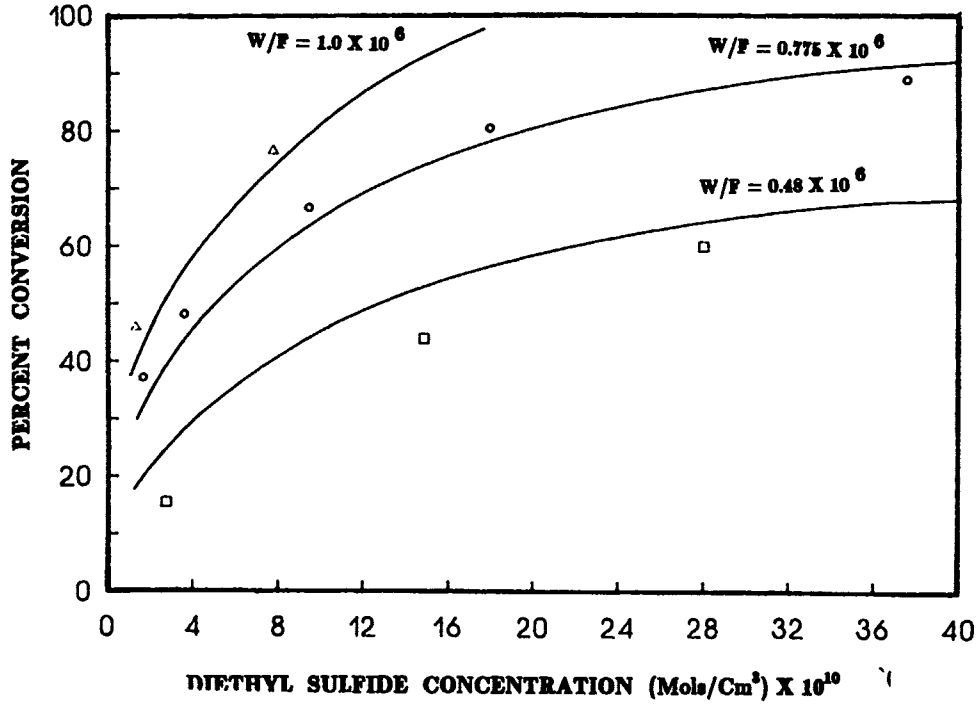

Figure 4: Conversion as a Function of Diethyl Sulfide Feed Concentration for 35/65 Mesh Catalyst Particles at 275 ° C.

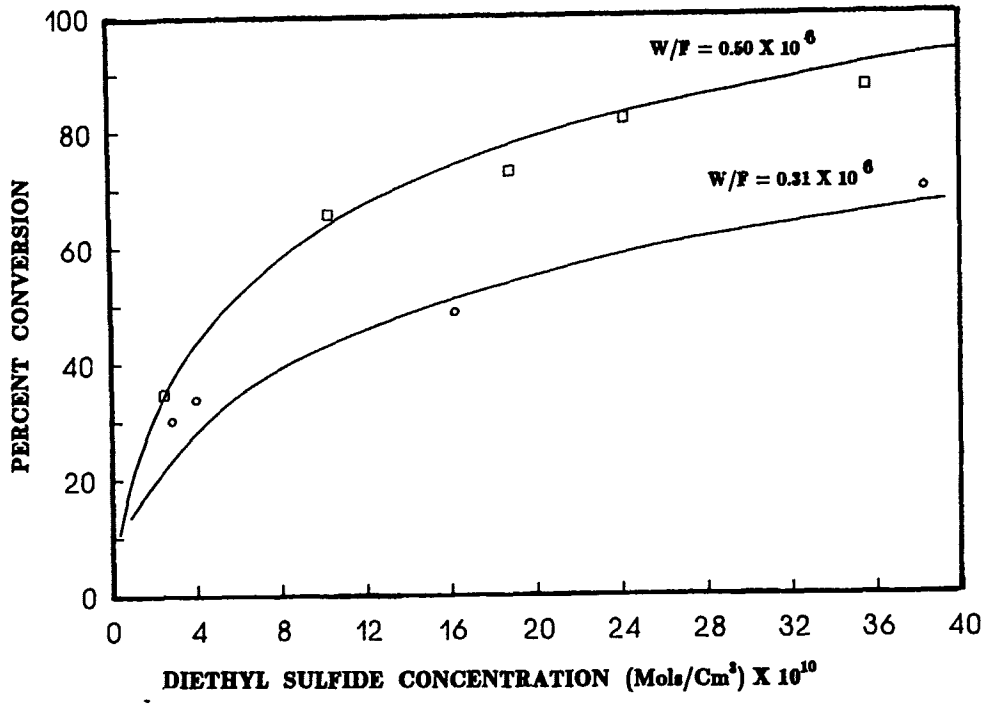

Figure 5: Conversion as a Function of Diethyl Sulfide Feed Concentration for 35/65 Mesh Catalyst Particles at 300 ° C.

The behavior of the 35/65 mesh catalyst particles was different from the <70 mesh particles in that the feed concentration did influence conversion (at a constant W/F) and the catalytic activity was reduced. The physical properties of the the two materials are identical (assuming the metal distribution to be radially uniform), so it is likely that the decreased catalytic performance of the 35/65 mesh particles was due to diffusional resistances. The diffusion-reaction model was written to account for only intraparticle mass transfer resistances. As illustrated in Figures 10 through 12, the model accurately describes the data. Therefore, external resistances were not incorporated into the model. An average particle radius of r = 0.020 cm was employed in solving the model, and feed concentrations were calculated at reaction temperature and pressure.

Figure 3 illustrates the effect of diethyl sulfide concentration on conversion at 250 ° C (W/F = 1.5 x 10^6, 1.0 x 10^6 and 0.5 x 10^6 g-cat-sec/mole sulfide). The solid line in the figure represents the curve-of-best-fit as determined from the diffusion-reaction model with D_e equal to 0.015 cm^2/sec. As illustrated in Figure 3, the diffusion-reaction model may be used to describe the data over a wide range of concentrations at different values of W/F. At high concentrations of diethyl sulfide ($[Et_2S] > 40 \times 10^{-10}$), diffusion does not significantly influence the observed reaction rate, as the catalyst activity was similar to that obtained with the <70 mesh particles. This curve is rather important, as the reactant concentration is varied between regions where the reaction is controlled by the kinetics (no mass transfer resistances evident) and regions where both mass transfer and kinetics contribute to the observed reactivity. Despite the transition between the two regions, the diffusion-reaction model accurately describes the catalytic behavior. Figures 4 and 5 report conversion as a function of the diethyl sulfide concentration at 275 ° C and

300 ° C, respectively, at different values of W/F. In both cases, data are well correlated by the diffusion-reaction model employing D_e equal to 0.0165 and 0.015 cm^2/sec, respectively.

All effective diffusivities determined by solving the diffusion-reaction model were similar in magnitude. This was to be expected, as pore diffusion in the Knudsen region is a weak function of temperature[17,18]. Intraparticle diffusion coefficients are reported to increase with increasing temperature proportional[18] to $T^{1/2}$. (Assuming D_e to be proportional to $T^{1/2}$, only a 5% increase in D_e would be expected over the 50 ° C temperature range studied here. The range of temperatures studied here was not sufficient to allow for observing any temperature dependence of D_e.)

CONCLUSIONS

1) The reaction of diethyl sulfide over a platinum alumina catalyst is zeroth order over the range of concentrations and temperatures employed in this study.

2) Intraparticle diffusion resistances were found to be significant in evaluation of catalyst particles greater than 400 microns.

3) These diffusion resistances can be accounted for using the diffusion-reaction model presented in this text.

LITERATURE CITED

1) Cho, B. K., "Performance of Pt/Al2O3 catalysts in Automobile Engine Exhaust with Oscillatory Air/Fuel Ratios," *Ind. Eng. Chem. Res.* Vol. 27, p 30 (1988).

2) Kummer, J. T., "Laboratory Experiments Evaluating the Effects of S and Cu on a Pt/Al2O3 Auto Exhaust Catalyst," *J. Catal.* Vol. 38 p 166 (1975).

3) Shelef, M., Otto, K. and Otto, N. C., "Poisoning of Automotive Catalysts", *Adv. Catal.* Vol. 27, p 311 (1978).

4) Wei, J, "Catalysis for Motor Vehicle Emissions," *Adv. Catal.* Vol. 25, p 57 (1975).

5) Williamson, W. B., Stepien, H. K. and Gandhi, H. S., "Poisoning of Platinum- Rhodium Automotive Three-Way Catalysts: Behavior of Single Component Catalysts and Effects of Sulfur and Phosphorus," *Env. Sci. Tech.* Vol. 14, p 319 (1980).

6) Hart, J. M., Ruder, J. M., and Tom, R., "*Phase I Interim Technical Report: Chemical and Biological Agents Protection System (CABAPS),*" Air Force Contract F33615-86-C-3409, AiResearch, Los Angeles, CA, (1988).

7) Hart, J. M., Ruder, J. M., and Tom, R., "*Phase I Interim Technical Report: Chemical and Biological Agents Protection System (CABAPS),*" Air Force Contract F33615-86-C-3409, AiResearch, Los Angeles, CA, p 1-7 (1988).

8) Baier, R. W., Graren, W. M., Linhardt, H. D., Oliver, R. C., Peters, D. L., and Weller, S. W., "*Final Report: Feasibility Study of Catalytic Methods of Air Purification,*" U.S. Army CRDEC Publication No. C-2767, Aberdeen Proving Ground, MD, 1964.

9) Rossin, J. A., "Complete Catalytic Oxidation of Diethyl Sulfide over a 1% Pt/Al2O3 Catalyst," *Ind. Eng. Chem. Res.* Vol. 28, p 1562 (1989).

10) Bird, R. B., Stewart, W. E., and Lightfoot, E. N. "*Transport Phenomena,*" John Wiley, New York, NY, p 542-546 (1960).

11) Wheeler, A., "Reaction Rates and Selectivity in Catalysts Pores," *Adv. Catal.* Vol. 3, p 249 (1951).

12) Bischoff, K. B., "An Extension of the General Criterion for Importance of Pore Diffusion with Chemical Reaction," *Chem. Eng. Sci.* Vol. 22, p 525 (1967).

13) Froment, G. F., and Bischoff, K. B., "*Chemical Reactor Analysis and Design,*" John Wiley, New York, NY, p 178-200 (1979).

14) Smith, J. M., "*Chemical Engineering Kinetics,*" McGraw-Hill, New York, NY, p 478-507 (1981).

15) Rossin, J. A., "lComplete Catalytic Oxidation of Diethyl Sulfide over a 1% Pt/Al2O3 Catalyst: Effects of Mass Transfer on Reactivity" Report CRDEC-TR-091, U.S. Army CRDEC, Aberdeen Proving Ground, MD, 1989, UNCLASSIFIED Report.

16) Rossin, J. A., "Effects of Pretreatment Conditions on the Activity of a 1% Pt/Al2O3 Catalyst," *J. Mol. Catal.*, in press (1989).

17) Satterfield, C. N., "**Hetrogeneous Catalysis in Practice,**" McGraw-Hill, New York, NY, p 318-344 (1980).

18) Froment, G. F., and Bischoff, K. B., "*Chemical Reactor Analysis and Design,*" John Wiley, New York, NY, p 163-177 (1979).

BLANK

CATALYTIC OXIDATION OF PERFLUOROPROPENE OVER A MONOLITHIC Pt/TiO_2 OXIDATION CATALYST

P. Nazario-Gonzalez and D.S.Y. Hsu
Code 6170H, Chemistry Division
Naval Research Laboratory
Washington, DC 20375-5000

ABSTRACT

The catalytic oxidation of perfluoropropene (C_3F_6) over a monolithic Pt/TiO_2 catalyst (Allied Signal) was studied by electron ionization mass spectrometry. The data suggested that at least two different oxidation processes were involved, depending on the temperature range -- one in which direct oxidation of C_3F_6 took place and another in which "residues" (or reaction products built up on the catalyst) underwent oxidation. The temperature at which complete destruction of PFP occurred was 800K. In the absence of H_2O additive to the reaction mixture, CO_2 accounted for about 98% of all observed products,and HF and COF_2 made up for the rest. When H_2O was added to the reaction mixture a large increase in HF production and a severe inhibition of the reaction were observed. However, complete destruction of PFP was obtained at 875K.

INTRODUCTION

There have been only a few studies on the catalytic oxidation of fluoro-olefins.[1-4] Some of these deal with liquid suspensions of solid catalysts. We are primarily interested in the oxidation of gas phase fluoro-olefins over dry catalysts, for which mechanistic information is even more scarce. The mechanisms of oxidation and combustion of perfluoropropene (PFP) can be expected to be different from that of propene because one of the final main products for the latter is the stable H_2O molecule (even at high temperatures) whereas the would-be counterpart F_2O molecule for the former is not stable at elevated temperatures and is not produced in a similar mechanistic step. The effects of fluorine (from the decomposition of fluorocarbons) and moisture on the catalyst surface and the catalytic reactions are also virtually unknown.

In this work, we have employed the electron ionization mass spectrometry technique to investigate the products resulting from the catalytic oxidation of perfluoropropene (PFP) over a monolithic Pt/TiO_2 catalyst -- SRC-2000, made by Allied Signal Corp. The effects of temperature and moisture on the product distribution and on the surface reactivity were also investigated. These kinetic data should provide important data base information for unraveling the mechanisms of the catalytic oxidation of perfluoro-olefins and halocarbons.

EXPERIMENTAL

The experimental apparatus used in this work has been previously described in detail.[5,6] Briefly, products exiting the quartz catalytic reactor were detected by a quadrupole mass spectrometer (Extranuclear). The reactor was located about 1 cm above the skimmer which separated the upper chamber which contained the catalytic reactor from the differentially-pumped mass spectrometer chamber. The catalyst was activated prior to each experiment by heating it in O_2 at 945K followed by reduction in H_2 at 425K. The reactants were prepared as a 760 Torr gas premixture of PFP and oxygen with a 43:1 PFP:O_2 ratio (2.2% PFP) in a stainless steel bulb. The temperature of the catalyst was monitored by a chromel-alumel thermocouple with digital readout. The typical pressure in the upper chamber was in the 10^{-5} Torr range, as measured by an ionization gauge.

A separate experiment was carried out to determine the effect of water on the catalyst and the catalytic reaction. A separate 3.1% H_2O in O_2 mixture was added to the PFP/O_2 mixture upstream to the catalyst so that the total pressure was 2.3×10^{-5} Torr with the H_2O to PFP ratio of 3.2. Simultaneous data acquisition of ion signals of PFP, CO_2, HF, and COF_2 and data processing were handled by a microcomputer using a program developed at NRL.

RESULTS AND DISCUSSION

Figure 1 shows the temperature dependences of the PFP parent and the CO_2 product mass ion signals when the PFP/O_2 gas mixture was flowed through the catalyst bed. Each of the curves exhibits: (A) a strong temperature dependence in the lower temperature range (rapid decrease for PFP and rapid increase for CO_2), (B) followed by a change in the opposite direction (indicating a retardation of the reactions), and (C) a weaker temperature dependence in the original direction. Behavior (A) suggests a fast catalytic oxidation of PFP to yield the main product CO_2. In each of the curves, behavior (B) occurs at about the same temperature for PFP consumption and the corresponding CO_2 production; namely, at this temperature a mechanism sets in to slow down the catalytic oxidation of PFP and the consequent production of CO_2. This mechanism could be due to catalyst poisoning processes by "residues" such as metal fluorides, fluorocarbon products tightly bonded to the catalyst surface,

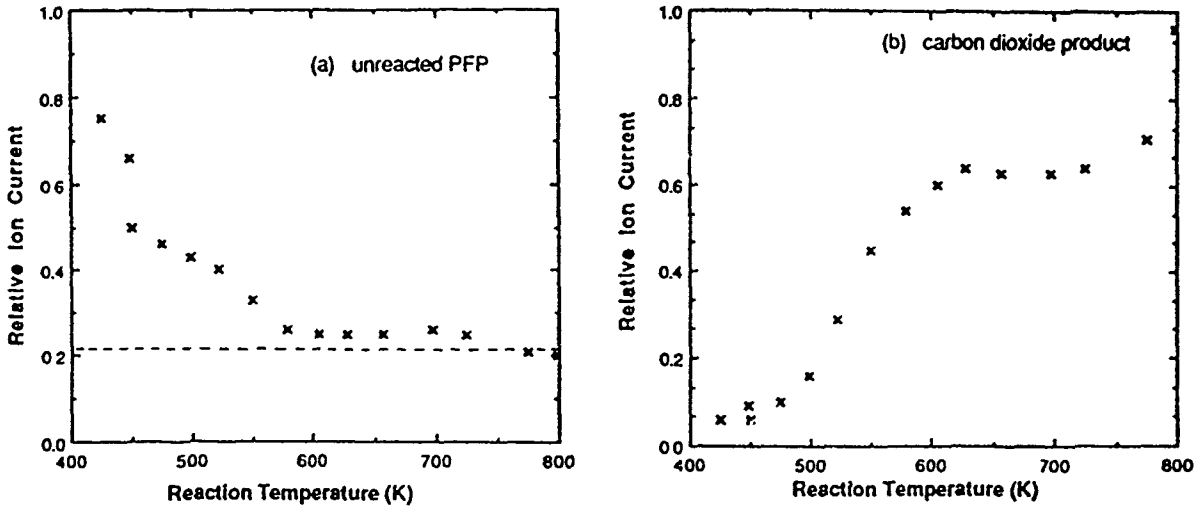

Fig. 1. Mass spectrometer relative ion signal as a function of catalyst temperature for (a) unreacted PFP and (b) carbon dioxide product. The dashed line in (a) represents the background signal of mass 150 (PFP) with no PFP in the system.

fluorocarbon polymers formed in the pyrolysis, or even by carbon deposits. At higher temperatures some of these "residues" can undergo catalytic combustion and free up surface sites for catalytic reaction of PFP, as reflected by a further but slower decrease in the PFP signal and increase in the CO_2 signal (behavior (C)). At 800K complete destruction of PFP was achieved as shown by comparison with the dashed line (in Figures 1a) which represents the background signal level at the PFP mass with no PFP in the system. The continued rise in CO_2 signal at the highest temperature could be due to the continued catalytic combustion of the "residues" on the catalyst and not so much due to the same initial mechanism of catalytic oxidation of PFP to CO_2.

Figure 2 shows the Arrhenius plots for rates of PFP disappearance and the corresponding rates of CO_2production in the lower temperature range. The parameter R is the ratio of signal

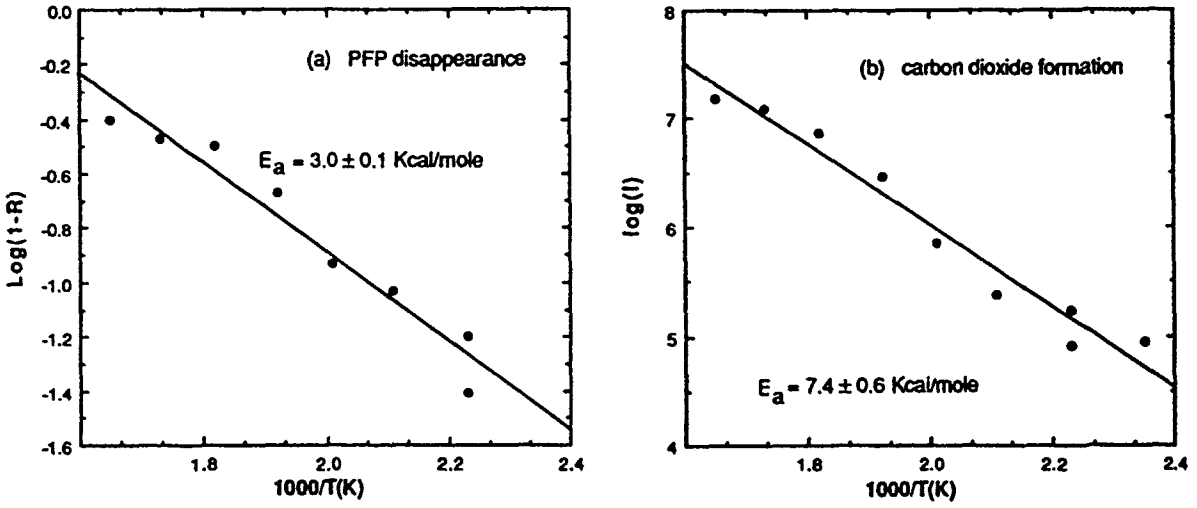

Fig. 2. Arrhenius plots for the lower temperature range rates of (a) PFP disappearance and (b) carbon dioxide formation.

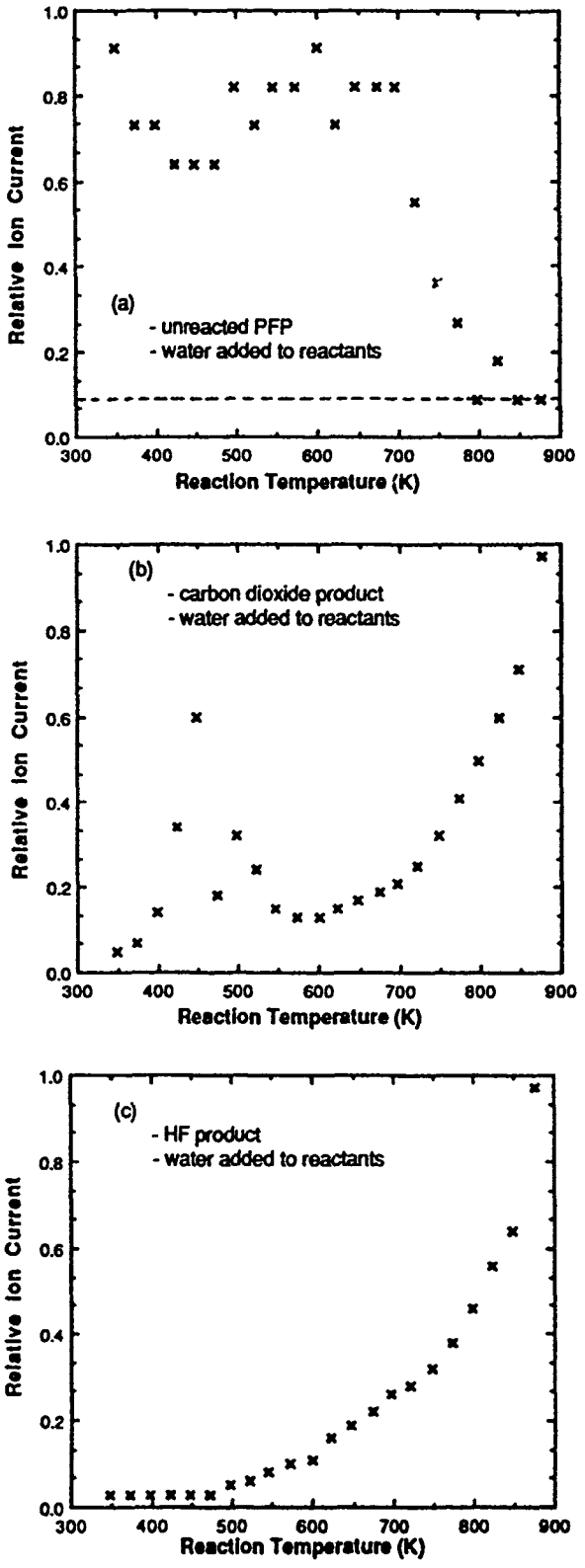

Fig. 3. Mass spectrometer relative ion signals as a function of catalyst temperature for (a) unreacted PFP, (b) carbon dioxide product and (c) HF product with water added to the reactants. The dashed line in (a) represents the background signal of mass 150 (PFP) with no PFP in the system.

of PFP at temperature T to the signal of PFP at room temperature at which there is no reaction. The apparent activation energies for PFP disappearance and CO_2 production are 3 and 7 kcal/mole respectively.

The only other observed reaction products were COF_2 and HF, each at about 1% of the total product signals at the highest temperature studied in the experiment.

Figure 3 shows the temperature dependence of the PFP, CO_2, and HF product mass ion signals when water was added to the PFP/O_2 gas mixture. The partial pressures were 2.2×10^{-7} Torr of PFP, 7.1×10^{-7} Torr of H_2O and 2.2×10^{-5} Torr of O_2. The behaviors of PFP disappearance and CO_2 production are very different from the case without the water additive (compare with Fig. 1). In the presence of added H_2O, significant decrease in the unreacted PFP begins only at temperatures above 700K, whereas in the absence of H_2O, the destruction of PFP is nearly complete at 700K. There is a steep decrease in the CO_2 signal between 450 and 600K shown in Fig. 3b compared to the fast rise in CO_2 signal in the same temperature range in Fig. 1. H_2O appears to have introduced a severe inhibition effect on the catalyst in the temperature range below 700K. At 875K the HF signal is about 22% of the total product. In the case of absence of water, the HF fraction at 800K was about 1% of the total products compared to 20% HF at 800K in the case of added water. Thus the effect of added water was to increase dramatically the fractional HF distribution. Figure 4 shows

the Arrhenius plot for the HF production with water as an additive. The overall apparent activation energy of HF formation was about 6.2 kcal/mole. Possible mechanisms for HF production will be discussed below. In contrast to HF, COF_2 production remained at a low level, i.e. <0.5% throughout the temperature range studied.

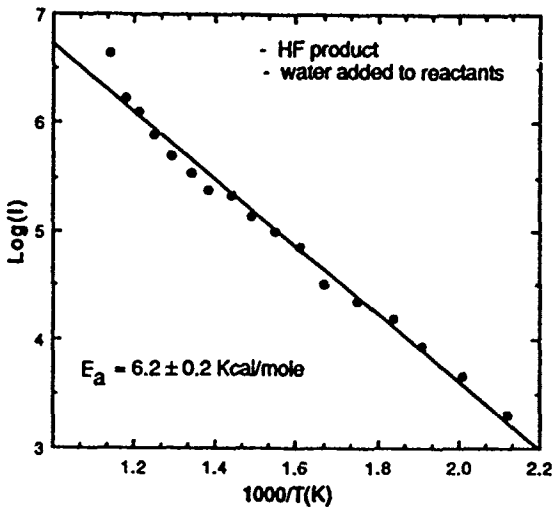

Fig. 4. Arrhenius plot for the HF production rate with water added to the reactants.

It appears that water and its reaction products such as HF, CF_3-CFOH-COF, etc. (see below) could block a large number of active sites reducing the rate of disappearence of PFP below 700K and therefore limiting the CO_2 production rate. As temperature increases above 700K, surface concentration of adsorbed water becomes negligible and the concentration of its reaction products decreases due to their increased desorption rate resulting in the increase of available active sites. Consequently we observed an increase in the rate of catalytic reaction of PFP with the corresponding increase in CO_2 production. Total destruction of PFP was observed at around 875K (Figure 3a) compared to 800K for the case without water as an additive. The increase in temperature can be directly attributed to the partial blocking of active sites by reaction products derived from water even at these high temperatures.

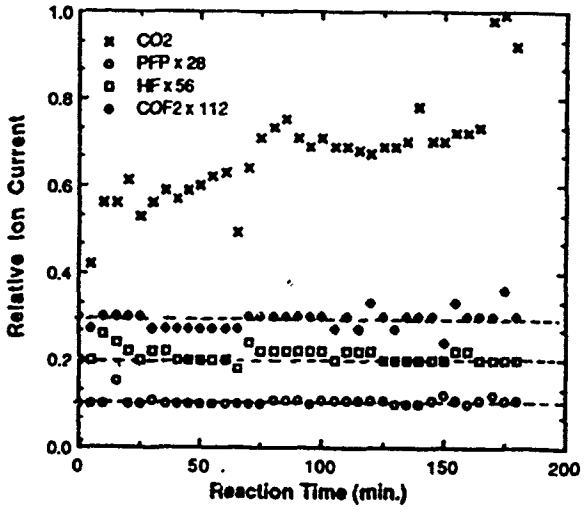

Fig. 5. Mass spectrometer ion signals at 803K as a function of reaction time for CO2, COF2 and HF products, and unreacted PFP. Dashed lines represents the background signal for PFP, HF, and COF2 respectively.

Figure 5 shows the oxidation of PFP in the absence of H_2O reactant at the constant temperature of 803K in continuous operation for three hours. The data showed complete destruction of PFP and no significant catalyst deactivation. Only formation of CO_2 and traces of HF and COF_2 were observed.

Perfluoro-olefin epoxides have been formed by reactions of perfluoro-olefins with liquid oxidizers (such as H_2O_2)[7-9] and with O_2 under ultra-violet light.[10,11] We propose that one possible route in the catalytic oxidation of perfluoropropene is the formation of the perfluoropropene epoxide:

$$CF_3\text{-}CF{=}CF_2(ad) + O(ad) \longrightarrow CF_3\text{-}FC\overset{O}{\diagdown\diagup}CF_2(ad) \quad (1)$$

where (ad) indicates "adsorbed". Over a Lewis acid catalyst such as Al_2O_3 at about 373K perfluoropropene epoxide is known to produce hexafluoroacetone (CF_3COCF_3) with high yield.[7,12,13] One of the base materials in our catalyst is Al_2O_3. Hexafluoroacetone is known to decompose to CO and 2 CF_3 at higher than 573K in the gas phase. On the catalyst, the temperature could be much lower. CO_2 can be produced from the catalytic oxidation of CO:

$$CO(ad) + O(ad) \longrightarrow CO_2(ad) \longrightarrow CO_2(g) \quad (2)$$

The CF_3 surface radicals can react with excess surface oxygen to form CF_3O which can decompose to COF_2 and subsequent decomposition products:

$$CF_3(ad) + O(ad) \longrightarrow CF_3O(ad) \longrightarrow COF_2(ad) + F(ad) \quad (3)$$

$$COF_2(ad) \longrightarrow COF_2(g) \quad (4)$$

$$COF_2(ad) \longrightarrow CO(ad) + 2F(ad) \quad (5)$$

The CO(ad) produced in the last reaction can then be catalytically oxidized to CO_2. In the presence of moisture, COF_2 undergoes hydrolysis to give CO_2 and HF:

$$COF_2 + H_2O \longrightarrow CO_2 + 2HF \quad (6)$$

However, in the presence of moisture, the perfluoropropene epoxide can react with H_2O to form CF_3-CFOH-COF and HF. In two additional reactions with H_2O, CF_3-CFOH-COF can be converted into the stable trifluoropyruvic acid hydrate $CF_3\text{-}C(OH)_2\text{-}COOH$ with the production of two additional molecules of HF.[7,14] These reaction steps, as well as reaction (6), can help explain the mechanism for the observed increase in HF production when H_2O has been added to the reaction mixture. At high temperatures the trifluoropyruvic acid hydrate may decompose to give CO_2 and H_2O. At lower temperatures it may act as a catalyst poison, producing the observed retardation of the reactions. It is also known that thermally stable polymers (one having average formula $(C_3F_6O_{1.05})_{15}$ and the other having composition $(CF_2O)_n$)[11] have been produced in the photo-oxidation of perfluoropropene.[11] It is conceivable that polymers such as these have also been produced in the present system. These can also act as catalyst poisons until they have been "burned" off in catalytic combustion reactions at high temperatures.

Another possible route for the catalytic oxidation of PFP could start with the initial breakdown of PFP into smaller groups on the catalyst surface. These could then be oxidized to CO and CO_2 via steps such as reactions (3), (5), and (2).

There is no clear reason why HF was found in much smaller quantities compared to CO_2 in the experiment with H_2O as an additive. The low yield of COF_2 could be explained by reactions (5) and (6). The electron impact ionization cross sections for HF is unknown. However, HCl has even a larger electron impact ionization cross section than CO_2.[15] Assuming that HF does not have much smaller ionization cross sections than CO_2, the only plausible explanation for its observed low concentration is that stable fluorinated compounds are formed on the catalyst surface and do not desorb appreciably at the temperatures studied.

CONCLUSIONS

Our results on the catalytic oxidation of PFP on the monolithic Pt/TiO_2 catalyst show that complete destruction of PFP is possible at a catalyst temperature of 800K in the absence of water vapor as suggested by Figure 1a. Inhibition of catalytic reaction has been observed but are compensatable by high temperature oxidation removal of the adsorbed inhibitors. Added water increases HF production, severely inhibits the catalytic reaction of PFP below 700K, and shifts the temperature for complete destruction of PFP to about 75 degrees higher in comparison to the case without water as an additive. However, at 875K, the addition of water does not seem to decrease the catalytic activity significantly. Pretreatment of the catalyst by first heating it at high temperatures in O_2 to remove carbon-containing species and other impurities, followed by reduction by H_2, appears to be a satisfactory catalyst regeneration process. Continuous operation of the catalyst in the absence of moisture at the optimum temperature (for complete destruction of PFP) for three hours showed no decrease in catalyst activity or poison effects due to accumulation of undesirable decomposition products. Future directions are to prepare and test different catalysts, to extend these experiments to other halocarbon systems such as freons, and to carry out experiments at much higher pressure and flow conditions. It is worthwhile to note that the catalyst temperatures required for the complete destruction of DMMP over the Pt/TiO_2 monolithic catalyst are the same (namely 250C) for the low pressure (<0.1 Torr, nearly identical to ours)[5] and the high pressure (1 atm)[16,17] experiments.

ACKNOWLEDGEMENTS

The authors thank Dr. D. Venezky for his supportiveness and encouragement in this research and Drs. C.C. Hsu and D. Tevault (CRDEC) for their interest and for supplying the catalyst.

REFERENCES

1. C. Guizard, H. Cheradame, Y. Brunel and C. G. Beguin, J. Fluorine Chem. 13, 175 (1979).

2. A. Battais, B. Boutevin, Y. Pietrasanta, and P. Sierra, J. Fluorine Chem. 19, 35 (1981/1982).

3. Daikin Kogyo Co., Ltd. Jpn Kokai Tokkyo Koho, Jpn patent 80,130,928 (1980).

4. Daikin Kogyo Co., Ltd. Jpn Kokai Tokkyo Koho, Jpn patent 81,32,426 (1981).

5. C.C. Hsu, C.S. Dulcey, J.S. Horwitz and M.C. Lin, Proc. 1987 CRDEC Scientific Conference on Chemical Defense Research, p. 1121, CRDEC, Aberdeen, MD (1987).

6. C. S. Dulcey, M. C. Lin, and C.C. Hsu, Chem. Phys. Lett., 115, 481 (1985).

7. R. E. Banks, Fluorocarbons and Their Derivatives, MacDonald & Co. (Publishers) Ltd., London, 1970.

8. W.A. Sheppard and C. M. Sharts, Organic Fluorine Chemistry, W.A. Benjamin, Inc., New York, 1969.

9. E.I. Du Pont de Nemours and Co., U.S. patent 904877 (1962).

10. E.I. Du Pont de Nemours and Co. U.S. patent 931587 (1963).

11. D. Sianesi, A. Pasetti and C. Corti, Die Makromolekulare Chemie 86, 308 (1965).

12. E.P. Moore and A. Milian, British patent 1019788 (1966).

13. E.P. Moore and A Milian, U.S. patent 3321515 (1967).

14. D. Sianesi, A. Pasetti and F. Tarli, J. Org. Chem 31, 2312 (1966).

15. R.I. Reed, Ion Production by Electron Impact, Academic Press, London, New York, 1962.

16. G.R. Lester and R.E. Marinangel, Proc. 1986 CRDEC Scientific Conference on Chemical Defense Research, p. 193, CRDEC, Aberdeen, MD (Nov. 1986).

17. G.R. Lester and G.C. Joy, Proc. 1988 CRDEC Scientific Conference on Chemical Defense Research, p. 373, CRDEC, Aberdeen, MD (Nov. 1988).

REMOVAL OF TOXIC CATALYTIC OXIDATION PRODUCTS VIA ADSORPTION †

In-Won Kim, Glenn D. Munkvold and Joseph J. Beaman [1]
Won W. Choi and A. J. Hitt III

CRDEC Scientific Conference on Chemical Defense Research
Aberdeen Proving Ground, Maryland
November 17, 1989

ABSTRACT

The Air Force is currently developing thermal/catalytic processes to destroy Chemical and Biological Warfare agents in aircraft Environmental Control Systems. However, there remains an uncertainty that toxic combustion products, particularly acidic chemical species, will be reduced sufficiently to provide safe and breathable air. This study is being conducted to select candidate filtration/separation technologies as a downstream treatment to augment catalytic oxidation. A number of potential sorbents have been screened, including alumina, rare earth compounds and various zeolites. Adsorption experiments were conducted using both gravimetric and chromatographic methods with selected adsorbents and simulated combustion gas mixtures. Performance tests with some selected adsorbents were done as single bed breakthrough experiments. Among the adsorbents investigated magnesium oxide magnesium oxide from the chemistry department of Kansas State University showed the hightest capacity and stability in contact with these gases.

INTRODUCTION

The performance of tactical aircraft missions in a Chemical Warfare (CW) environment places new and demanding survivability requirements on aircraft Environmental Control systems. The basic problem is to protect the aircrew and vital electronic systems from the effects of CW agents.

One of the proposed solutions is to incorporate agent decomposition/removal devices into the aircraft environmental control system (ECS). Such devices could provide critical protection to aircrew in the event of chemical or biological attack. Reduction or elimination of agent contamination internal to the aircraft should result in a major reduction in the supportability/maintainability burden for aircraft operations in a CW environment.

---

† Export Authority: 22CFR125-4(b) (13)

For aircraft applications, thermal decomposition and catalytic oxidation have been determined to be effective means of sterilizing biological agents and decomposing chemical agents into much less toxic chemical forms. Agent breakdown products, however, may be present in the effluent from thermal/catalytic processes [1]. Effluent air from thermal/catalytic reactors may still be far from being usable as breathing air. The removal of the still-toxic agent oxidation products may require additional treatment by filtration and separation. Therefore, it is necessary to assess and select filtration/separation technologies that can effectively remove combustion product in the effluent from the thermal/catalytic oxidation process.

The purpose of this work is to generate basic experimental and analytical data required to assess gas separation and purification technologies. The primary objectives are to evaluate the adsorption of contaminants by various sorbents, and to determine the performance characteristics of those sorbents that appear to be viable candidates for aircraft applications.

SIMULATION OF COMBUSTION GASES

The compositions of combustion product gases were simulated based on the agent oxidation reactions (Equations (1) to (3)) in a catalytic oxidization/thermal decomposition device given the maximum concentrations in Table 1; results for CK and Freon-12 mixture are summarized in Table 2. These maximums are somewhat arbitrary. Actual filter design needs to be based on realistic threat concentrations, but the approach and data presented in this paper can be used directly for this design. The these initial studies have focused on acid gas removal. As a consequence, complete oxidation has been assumed. Similar analysis has been performed for the other agents separately.

$$CK + \frac{7}{4}O_2 + \frac{1}{2}H_2O \text{ ---> } CO_2 + NO_2 + HCl \quad (1)$$

$$HD + \frac{13}{2}O_2 \text{ ---> } 4\,CO_2 + SO_2 + 2\,HCl + 3\,H_2O \quad (2)$$

$$GD + 11\,O_2 \text{ ---> } 7\,CO_2 + HF + H_3PO_4 + 6\,H_2O \quad (3)$$

TABLE 1
Agent inlet concentration to the catalytic decomposition device

Code	Formula	M.W.	Concentration mg/m^3	Chemical name
GD	$C_7H_{16}O_2FP$	182.2	4000	Pinacolyl methyl phosphonofluoridate
HD	$(ClCH_2CH_2)_2S$	159.1	1000	Bis(2-chloroethyl) sulfide
CK	ClCN	61.5	6000	Cyanogen chrolide
Freon-12	CCl_2F_2	121	4000	Dichloro-difluoromethane

*Source: MCAIR Engineering Statement of Work, WS-AD-2877, July 11, 1988.

TABLE 2
Combustion product gas composition for CK at 50% relative humidity

Gas	concentration gmol/m^3 dry air	mole fraction	ppm
O_2	9.2043	0.2051	206176
N_2	34.8214	0.7758	780000
Ar	0.4464	0.0099	10000
H_2O	0.0843	0.0019	1888
CO_2	0.0976	0.0022	2185
HCl	0.0976	0.0022	2185
NO_2	0.0976	0.0022	2185
Freon-12	0.0331	0.0007	740
Total	44.8821	1	1005360

SORBENT SCREENING

For the removal of water vapor, NOx , SOx and CO_2, a crystalline molecular sieve material, a silica adsorbent, an improved zeolite molecular sieve Y (which has a high degree of ionic character coupled with a high degree of acid stability), and clinoptilolite (which is an acid treated natural zeolite) have been used. The main characteristics of these adsorbents are high SiO_2/Al_2O_3 ratio and a high degree of acid stability.

It is known that zeolite materials are decomposed by acids, many of them with the subsequent formation of gels. The rule generally followed is that zeolites with a framework structure having a silicon/aluminum ratio of 1.5 or less will gelatinize. Zeolite A, for example, is readily decomposed by HCl and precipitates a clear gel.

Most zeolites are not stable in the presence of acids and the amount of apparent decomposition in anhydrous HCl gas depends on temperature and silica content. Usually the extent of decomposition increases with rising temperature and diminishing silica content.

Thus the adsorbents were carefully selected based on acid stability and the adsorption capacity of contaminants.

EXPERIMENTAL

The gravimetric method was chosen for the preliminary screening of the adsorbents. The amount of adsorption of gas mixtures on adsorbents were measured using a micro balance (Cahn 1100 balance). Initially adsorbent samples were activated under vacuum for at least 24 hours at a temperature less than the maximum temperature dictated by the dehydration behavior of adsorbents. The total mass adsorbed was monitored on an IBM-XT.

To confirm the performance of adsorbents at the actual operating condition, breakthrough experiments were carried out with adsorbents selected using the results from the gravimetric experiments. One inch outside diameter beds were packed with the adsorbents and a contaminant mixture was injected to the bed at a given pressure and temperature. The outlet concentration of the gas mixture were analyzed by a mass selective detector, MSD (Hewllet Packard model 5970).

RESULTS AND DISCUSSION

HCl adsorption experiments by the gravimetric method

HCl gas is an important contaminant to be removed in the air filtration processes, because the water removal unit in front of adsorption beds may not remove all HCl gas from the combustion gas from the oxidation device.

The amount of adsorption of HCl gas was measured by Cahn-1100 balance on several different adsorbents (in Table 3). These measurement were done at high pressures instead of the actual operating pressure, 30-60 psia, because of the slow achievement of equilibrium processes of HCl on these adsorbents.As shown in Figure 3, the magnitude of adsorption is in order of MgO> Activated carbon> Silicalite> Na-mordenite> H-mordenite > Silica gel > Clinoptilolite> Selexsorb-HCl> Zeolon 900-Na.

TABLE 3
Adsorbents tested for the adsorption of HCl

Adsorbent	Activation Temp.	Size	Supplier Brand name
MgO	350°C	slice	Kansas State U.
Activated carbon	150°C	50-200 mesh	Allied
Silicalite	350°C	1/16" extrudate	Union Carbide S-115
Na-Mordenite	350°C	1/16" extrudate	Union Carbide LZM-5
H-Mordenite	350°C	1/16" extrudate	Union Carbide LZM-8
Silica gel	176°C	40/60 mesh	Alltech Assoc. Inc.
Clinoptilolite	350°C	granular	Zeotech Corp. Kitty Crystals
Selexsorb-HCl	230°C	1/8" bead	Alcoa
Zeolon 900-Na	350°C	1/16" extrudate	PQ corp.

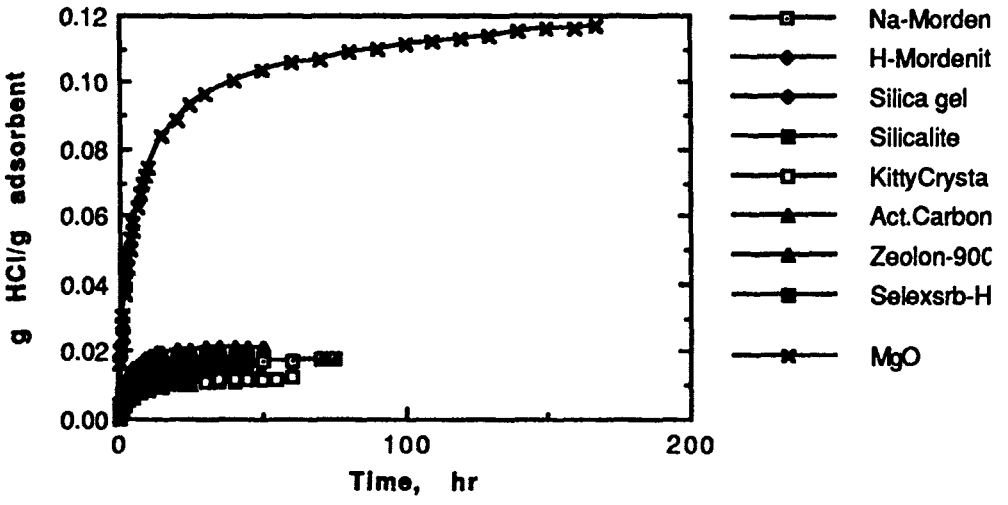

FIGURE 3

HCl adsorption at 24°C and 175 psia, 504 ppm HCL in He

HCl breakthrough experiment on Selexsorb-SPCL

Because the suitable amount and form of MgO was not available, the breakthrough experiment of HCl on Selexsorb-SPCL, activated alumina from Alcoa, was carried out to confirm the gravimetric predictions of the performance of adsorption units at actual operating conditions. The operating conditions are given in Table 4. After 2 hours, HCl was not detected at all from the outlet of the bed . After over 4 hour run, the experiment had to be stopped because of the limited memory space of the MSD for data acquisition. The abundance from MSD for 504 ppm HCl was 12500, so the fraction of the abundances over this number gives the appropriate ppm of HCl at the outlet.

The amount of HCl removed in the bed could be calculated by integration of the area of upper side of the breakthrough curve. Though 260 minutes actual experimental data were used to calculate the amount removed, but after that time the data were extrapolated to the saturation point, shown in Figure 4. Thus the calculated amount of HCl gas removed by Selexsorb-HPCl was approximately 1.69 gram , i.e., 4.05 wt %.
This amount calculated by the chromatographic method is in good agreement with the gravimetric method at the same low pressures.

TABLE 4
Operating conditions for HCl breakthrough experiment

Adsorbate	:	HCl 504 ppm in Helium
Adsorbent	:	Selexsorb-SPCL from ALCOA
Sample weight	:	41.67 gr
Bed	:	1" O.D. stainless steel
Analyzer	:	Mass Selective Detector, HP 5970
Temperature	:	24 °C
Pressure	:	29 psia
Flow rate	:	6.3 slpm

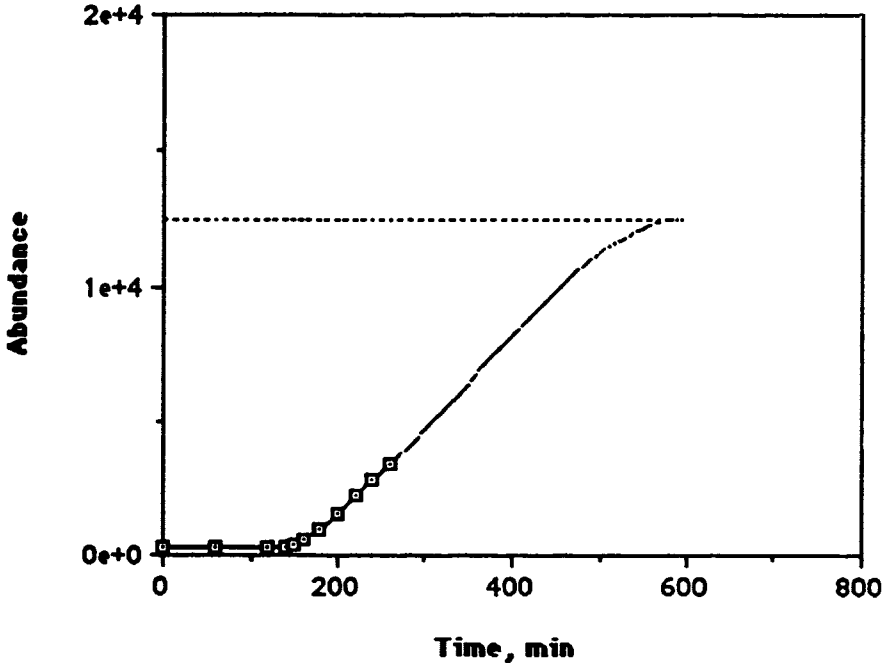

FIGURE 4
Breakthrough curve of HCl on Selexsorb-HPCL at 24 °C and 29 psia

Calculation of the weight of adsorbent for air purification

The sorption capacity results have been used to perform preliminary sizing studies for a catalytic reactor post-filter. The calculations presented here are based on the following assumptions: a) Each gas is allowed to be adsorbed without interaction between gases; b) HCl, HF, NO_2 and SO_2 should be removed completely because of their threshold limit values (TLV) and the importance of unimpared aircrew vision; c) CO_2 should be removed to approximately 3000 ppm; d) the effect of prior exposure of sorbent to water is neglected; and e) complete oxidation reaction.

These sizing estimates, as an example, are based on the maximum challenge concentrations of agents specified in Table 1. The amount of MgO to be loaded for the removal of HCl in CK combustion product gas was calculated at operating conditions given in Table 5 and was 6.5 kgs MgO/hr. At low operating pressures, the amount of adsorbent

will increase. For actual operating conditions and agent concetrations, the weight of adsorption bed might be smaller.

TABLE 5
Operating conditions of air filtration unit

Air flow	:	4.54 kgs/min (10 lbs/min)
Pressure	:	174.7 psia
Temperature	:	24 °C
HCl Mole fraction	:	0.0022
Adsorbent	:	MgO
Adsorption capacity	:	116 mg HCl/g MgO
HCl to be removed from air	:	12.6 grams HCl/min

CONCLUSIONS

The requirement for a catalytic post-filter is a function of the aircraft threat and operational scenarios. For ECS systems designed to operate in low level threat environments, the size of the post filter could be greatly reduced.

The amount of sorbent that will be required for HCl gas removal from CK combustion product gas is up to 7 kgs/hr for an exmple maximum agent concentrations in Table 1. This value, which does not include the weight of the catalytic reactor itself, is an unacceptably high weight penalty for aircraft ECS when compared to alternative concepts, specifically high pressure carbon [2]. For actual operating conditions and agent concetrations, the weight of adsorption bed might be substantially smaller.

Depending on system applications, the use of solid sorbent catalytic post-filters may be attractive in some high level threat environments. The replacement and disposal of acid contaminated MgO should be less hazardous than the handling of conventional filters contaminated with agents. In addition, the consequences of bed saturation and contaminant breakthrough are substantially less catastrophic for catalytic post-filters than for conventional filters.

More experiments for MgO, including adsorption breakthroughs, are planned, provided suitable amount and form of MgO becomes available.

ACKNOWLEDGMENT

This work was supported by McDonnell Douglas Corporation.

REFERENCES

[1] MCAIR Engineering Statement of Work, WS-AD-2877, 11 July, 1988.
[2] Cleays, H. M. and Smisek, R. F., Nuclear, Biological, and Chemical (NBC) Contamination Avoidance Concepts for Aircraft Applications, Report No. AFWAL-TR-86-3005 (1986).

1 University of Texas at Austin
Department of Mechanical Engineering
Austin, TX 78712

BLANK

MODEL OF AEROSOL PROTECTION OFFERED BY PERMEABLE PROTECTIVE GARMENTS

Paul D. Fedele [1], James T. Hanley [2],
Douglas W. VanOsdell [3], and David S. Ensor [4]

ABSTRACT

Advances in aerosol technology have resulted in increasing hazards presented by aerosols on the battle field. Continued improvements to individual protective systems must be sought to defend against these hazards. With appropriate representations of clothing geometry, hydrodynamic pressure distributions, aerosol penetration efficiencies and aerosol deposition velocities, protective clothing performance has been successfully modeled. Combining described representations of each of these factors with a generalized representation of aerosol penetration of fabrics, we can determine the protective characteristics of general permeable protective ensembles. The presented modeling capability offers valuable guidance in optimizing the protective performance of permeable ensembles and in determining the limits of protection achievable through the use of permeable protective materials.

I BACKGROUND

Driven by increasing concerns regarding aerosol hazards in the field, CRDEC initiated studies of the aerosol protection capacity of permeable protective clothing. Experimental studies were conducted to measure aerosol deposition and penetration associated with permeable protective systems [5] and modeling was performed to identify physical mechanisms involved [6]. Through the modeling effort, we have produced a physical, predictive model for the aerosol penetration and deposition associated with full-scale, permeable garment systems. The model has successfully reproduced the levels and characteristics of experimentally measured aerosol penetration and deposition and provides the ability to estimate the amount of aerosol protection offered by current systems. It also indicates approaches and limits for improvements in aerosol protection.

II MODEL DESCRIPTION

Using an appropriate geometry, the model calculates the air flow through the permeable fabrics. The aerosol penetration is determined using the aerosol penetration efficiency of the fabric. The aerosol penetration and the flow under the fabric are used to determine the amount of aerosol deposition on the solid surface beneath the fabric system, providing an assessment of the protection offered by the fabric system.

The model geometry is illustrated in Figure 1. This geometry allows flow into and out of the fabric, as occurs in real, permeable clothing systems.

The clothing material is specified by a permeability and an aerosol penetration efficiency. The permeability is the ratio of the velocity of air entering the fabric (face-velocity), to the pressure drop across the fabric. The permeability is constant, with units of CM^2 SEC/GR.

The aerosol penetration efficiency is the aerosol concentration penetrating the fabric divided by the aerosol concentration entering the fabric. A semi-empirical aerosol penetration expression, including modifications to account for inertial impaction, has been applied to illustrate the principles of the clothing model. This expression was developed by K. Lee and B.Y.H. Liu [7]. In Figure 2, the aerosol penetration efficiency is shown for two fiber beds of the same permeability. The illustrated aerosol penetration efficiency applies to randomly oriented fiber beds. Empirical modifications (not presented in this paper) have been developed to allow an accurate assessments for woven fabric systems.

The challenge aerosol is assumed to have a log-normal size distribution characterized by a mass median diameter and a geometric standard deviation.

Wind causes pressures which force air to flow through the permeable fabric system. Although pumping is not considered in the model, an effective windspeed can be used to produce air flows associated with pumping. Turbulence effects are included by using an appropriate external pressure distribution to calculate the induced air flow through the fabric. The external pressure distribution consists of two parts: one simulates the steady, aerodynamic drag force and another simulates the time-dependent alternating lift force. The external pressure distribution is shown in Figure 3. The external pressure distribution is not intended to exactly reproduce the aerodynamic forces acting on the body; it simply produces flow conditions which are adequate for the aerosol transport assessment. The magnitude of the total pressure distribution has been adjusted so that rates of air flow through the fabric correspond with measurements. Expressions for continuity, flow through permeable fabrics, and pressure drops in channel flow are solved by an iterative first-order Taylor series method to obtain the internal pressure shown in Figure 3, where the free-stream wind speed is 20 MPH.

From the difference between the external and the internal pressure, the air flow through the fabric is determined. Figure 4 shows the calculated air flow through a fabric of permeability 2.0E-3, CM^2 SEC/GR, in a wind of 20 MPH. The external pressure distribution is such that flow out occurs primarily on other side of the cylinder.

III AEROSOL PENETRATION

For the fabrics with penetration efficiencies shown in Figure 2, aerosol penetration is shown in Figure 5. The wind speed is 20 MPH and the air gap between the clothing and the surface of the body is 0.4 CM. The aerosol penetration is illustrated by the ratio of the internal aerosol number concentration to the external aerosol number concentration. It is emphasized that Fabric 2 shows much less penetration, even though it has the same permeability as Fabric 1.

IV AEROSOL DEPOSITION VELOCITY

Aerosol deposition processes are quantitatively expressed by the aerosol deposition velocity. The aerosol deposition velocity is the speed with which an aerosol concentration moves onto a surface. Only aerosol motion, not air flow, is needed in a deposition process. The aerosol deposition velocity is obtained by dividing the mass deposition per unit area, by the product of the external aerosol mass concentration and the time of the exposure.

Comparison with measured depositions indicates that turbulent deposition occurs under permeable garments. To model the turbulent deposition process, we have applied expressions describing deposition from turbulent flow in pipes [8]. Figure 6 shows the aerosol deposition velocity for four average values of turbulent flow in pipes.

V AEROSOL DEPOSITION VELOCITY ON FABRIC AND CYLINDER SURFACES

Aerosol retention in the fabric is used to calculate the aerosol deposition velocity in the fabric, while the air flow beneath the fabric and the deposition velocity for turbulent pipe flow are used to calculate the maximum expected aerosol deposition velocity on the suface of the cylinder. In Figure 7, aerosol deposition velocities on Fabric 1 and on the surface beneath Fabric 1 are shown for wind speeds of 20 MPH and 5 MPH, as indicated. The decrease in deposition on the fabric at 5 MPH indicates that larger, more massive, particles penetrate the fabric more efficiently at the lower wind speed. Even though larger particles penetrate the garment more efficiently, the aerosol deposition velocity on the cylinder is smaller because the rate of air movement under the fabric is lower at the lower wind speed. Reducing the rate of air flow between the fabric and the cylinder reduces the aerosol deposition on the surface.

Figure 8 shows fabric and surface aerosol deposition velocities for a wind speed of 20 MPH, for Fabric 1 and 2. These fabrics have the same air flow characteristics, however, the aerosol deposition on Fabric 2 is much

greater because Fabric 2 has a much lower aerosol penetration efficiency. The lower penetration efficiency of Fabric 2 reduces the internal aerosol concentration, causing a reduction in the aerosol deposition velocity on the surface. It is emphasized that a reduced penetration efficiency does not necessarily mean a reduced permeability.

VI APPLICATION OF DEPOSITION VELOCITY TO HAZARD ASSESSMENT

With the assumption that the total mass of aerosol deposited on the surface of a body determines the probability of a casualty, the aerosol deposition velocity calculated by this model can be applied to hazard assessments. A simple example is used to illustrate the application.

Consider a cloud with a uniform and constant total mass concentration, C, moving with speed V, past a cylinder of radius R and height, H. The cloud passes the cylinder in time interval, T, so the cloud has a width, VT. On the surface of the cylinder, the aerosol deposition velocity is V_m, so the total mass collected on the surface of the cylinder is the product $2\pi RHV_mCT$, neglecting the ends.

Alternately, some wish to consider the area dose method, in which one considers the amount of aerosol intercepted by the cross section of the cylinder. The total mass that would pass through the frame is 2RHVTC. Only a fraction, f, of this aerosol is retained on the body, thus, the total mass collection is 2RHVTCf, again, neglecting the ends. Rearranging the terms, one has 2RHfVCT.

As can be seen, V_m is simply, and very nearly, the fraction, f, of the cloud velocity. Since the deposition velocity is defined using the total surface area of a body, and the area dose fraction is defined using the cross section of the body, the V_m differs from fV by only the ratio of the cross section to the total surface of the cylinder, or π. However, application of the areal dose method becomes difficult when the cross section of the body becomes very small, as for a thin, flat plate held parallel to the free stream velocity. In such cases, the fraction of aerosol collected can become larger than unity, giving the mistaken indication that more aerosol deposits on the plate than is contained in the free stream. This difficulty is avoided using the total surface area to define the areal dose. Doing this, however, makes the velocity fraction used in the areal dose method exactly equal to the deposition velocity.

VII CONCLUSIONS

Aerosol protection from permeable materials can be analysed on basis of established processes. Application of these processes can be used to estimate aerosol hazards and to guide development of improved aerosol protective systems, while retaining advantages of permeability.

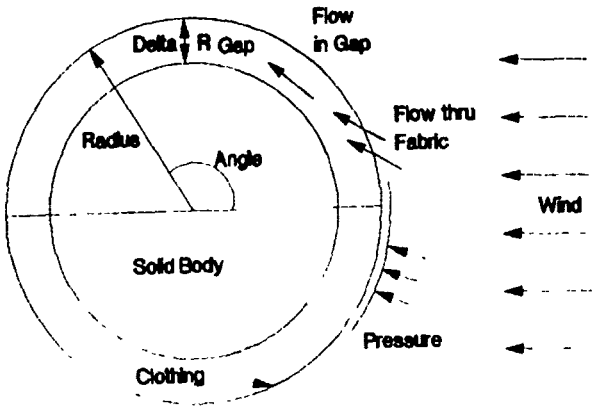

Figure 1 MODEL GEOMETRY.
The body is represented by a solid cylinder. Clothing is wrapped around the cylinder a uniform distance from the surface, leaving an air gap between the fabric and the cylinder. On the surface of the fabric, winds create pressures which cause air to flow through the permeable fabrics, and between the fabric and the cylinder surface. Flow through the fabric is a function of angle around the fabric surface.

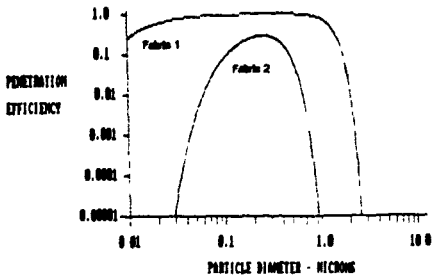

Fabric 1		Fabric 2	
Fiber Diameter	0.04 cm	Fiber Diameter	0.0004 cm
Packing Fraction	0.80	Packing Fraction	0.15
Bed Depth	0.17 cm	Bed Depth	0.084 cm

Both Fabrics; Permeability 2.0E-3 cm^2 sec/gr

Figure 2 AEROSOL PENETRATION EFFICIENCY.
The aerosol penetration efficiency is a function of the aerosol particle size and mass, the air flow face velocity, the fabric fiber diameter, the fabric thickness and the ratio of the volume of solids in the fabric to the overall fabric volume (packing fraction). The illustrated empirical expressions represent the aerosol penetration efficiency for filter media with fibers uniformly distributed and randomly oriented, perpendicular to the air flow. The face velocity is 5 CM/SEC. Although both fabrics have the same permeability, Fabric 2 allows much less aerosol penetration.

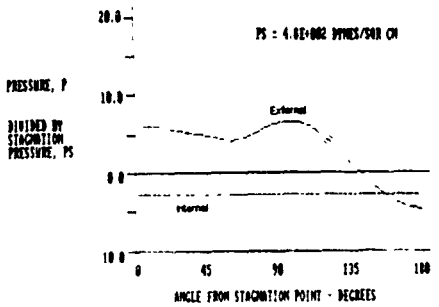

Figure 3 EXTERNAL AND INTERNAL PRESSURE DISTRIBUTIONS.
The external pressure distribution consists of two parts: one part represents the pressures that contribute to drag forces and another represents the pressures that contribute to fluctuating lift forces. The time-average lift force is zero because the pressure alternates from side to side around the cylinder. However, the peak pressure value can be greater than the stagnation pressure. The lift force pressure distribution is maximum at 90 degrees from the forward stagnation point. Although not shown, the lift force pressure is negative at 270 degrees, so that the average internal pressure equals the average external pressure, as required by the continuity equation. The air gap between the fabric and the cylinder is 0.4 CM.

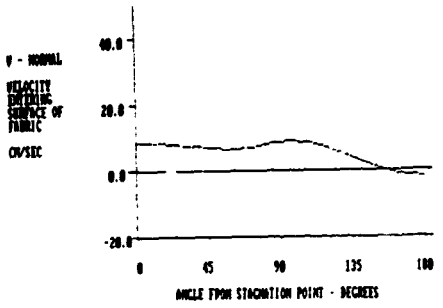

Figure 4 AIR FACE VELOCITY INTO FABRIC.
The illustrated air velocity is induced through the fabric, by the pressure distribution shown in Figure 3. The fabric permeability is 2.0E-3, CM^2 SEC/GR, the wind speed is 20 MPH and the air gap is 0.4 CM. Note that flow out, which does not influence penetration, occurs largely between angles of 180 and 360 degrees, and is not shown. The face velocity is combined with the aerosol penetration efficiency (shown in Figure 2), to determine the overall aerosol penetration.

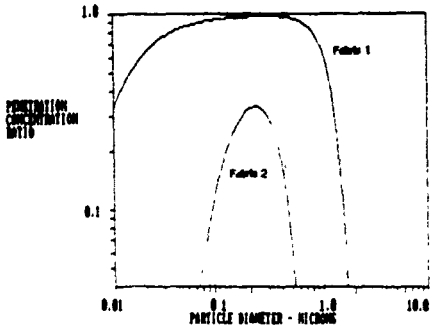

Figure 5 AEROSOL PENETRATION FOR TWO FABRICS.
The aerosol penetration is illustrated by the ratio of the internal aerosol number concentration to the external aerosol number concentration. A value of unity implies complete penetration. For both fabric representations, peak penetration occurs for particles with diameters of about 0.2 microns. The small fiber diameter in Fabric 2 allows considerably less aerosol penetration. The wind speed is 20 MPH and the air gap is 0.4 CM.

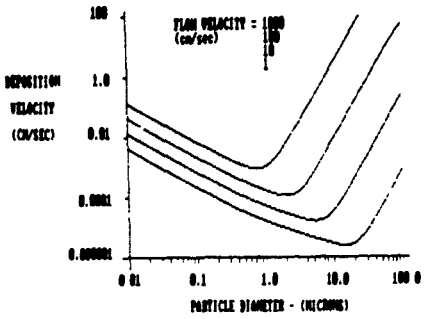

Figure 6 AEROSOL DEPOSITION FROM TURBULENT FLOW IN PIPES.
Illustrated are aerosol deposition velocities for turbulent flow in pipes. Increasing levels of turbulent velocity fluctuations decrease the thickness of the boundary layer, increasing the overall rates of aerosol deposition. The turbulent velocity fluctuations fling large particles across the boundary layer, increasing deposition, while smaller particles diffuse more rapidly across the boundary layer, also resulting in increases in the deposition velocity.

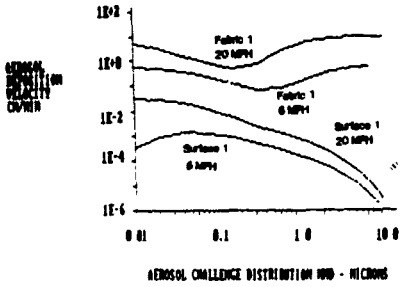

Figure 7 AEROSOL DEPOSITION VELOCITY AT TWO WIND SPEEDS.
Aerosol Deposition Velocities are shown on Fabric 1 and on the surface beneath Fabric 1, at 20 and 5 MPH. Geometric standard deviations of the aerosol challenge distributions are 2.0. Lower deposition on the fabric implies more aerosol penetration. However, because the deposition velocity on the surface depends on the overall air flow rate, the surface deposition does not increase at the lower wind speed

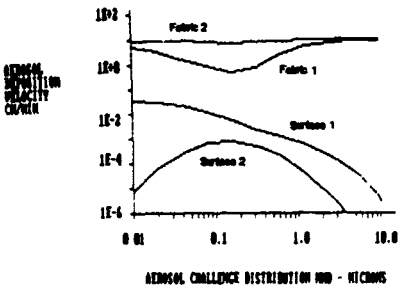

Figure 8 AEROSOL DEPOSITION VELOCITY FOR 2 FABRICS.
Higher deposition in Fabric 2 indicates less penetration. Since the fabrics have the same permeability, the air flows are the same, and the reductions in aerosol deposition on the surfaces are due to reduced internal aerosol concentrations. Increasing reductions in surface deposition occur as the challenge aerosol mass median diameter becomes larger, or smaller than about 0.2 microns.

REFERENCES

[1] U.S. Army Chemical Research Development anbd Engineering Center, Attn: SMCCR-RSP-P, Aberdeen Proving Ground, Maryland 21010-5423.

[2] Research Triangle Institute, Post Office Box 12194, Research Triangle Park, North Carolina 27709-2194.

[3] Same as Mr. Hanley.

[4] Same as Mr. Hanley.

[5] Hanley, J.T., "Aerosol Challenge of The Individual Protective Ensemble: First Annual Progress Report", CRDEC-CR-88040, February 1988; Hanley, J.T., VanOsdell, D.W., and Fedele, P.D., "Methodologies for Testing Permeable Chemical Protective Fabrics and Garments Against an Aerosol Threat", Proceedings of the 1988 USACRDEC Sci. Conf. on CD Research, Page 347, August 1989, Hanley, J.T., and Fedele, P.D., "Wind Tunnel Study of Aerosol Penetration Through Protective Overgarments", Proceedings of the 1987 USACRDEC Sci. Conf. on CD Research, Page 444, August 1988.

[6] Fedele, P.D., Bergman, W., McCallen, R., and Sutton, S., "Hydrodynamically Induced Aerosol Transport Through Clothing", Proceedings of the 1986 US Army Science Conference, 1987, Bergman, W., Fedele, P.D., McCallen, R., and Sutton, S., "Hydrodynamically Induced Aerosol Transport", Proceedings of the 1985 USACRDEC Sci. Conf., August 1986.

[7] Lee, K.W., and Liu, B.Y.H., "Theoretical Study of Aerosol Filtration By Fibrous Filters", Aerosol Science and Technology, 1:147-161, 1982.

[8] Fissan, H., and Schwientek, G., "Sampling and Transport of Aerosols", TSI Journal of Particle Instrumentation, Vol.2-2, July-December, 1987.

BLANK

RECENT ADVANCES IN AUTOMATED PERMEATION TESTING OF CHEMICAL DEFENSE FABRICS

Daniel R. Coleman, J. Todd Brown,
Gary D. Sides, and Thomas G. Thomas

INTRODUCTION

With the continuous development of new protective garments for use by the military in chemical-warfare environments, there is a need for the reliable and cost-effective evaluation of these new garments and their materials of construction. A critical component of evaluating protective clothing materials is measuring the permeation of chemical agents and simulants through the protective fabric. CMS Research Corporation has recently developed a MINICAMS®-based, permeation-testing system that automatically measures the permeation of chemical agents and simulants through protective fabrics. It consists of the following components: the MINICAMS sampling-and-analytical system; one or two 12-port, stream-selection systems; and the permeation cells. A photograph of the permeation-testing system is shown in Figure 1.

PERFORMANCE CHARACTERISTICS

Because both the chemical analyses and the data reduction are performed automatically, the MINICAMS-based, permeation-testing system is capable of generating large amounts of useful permeation data with relatively little labor. The system can determine the permeation, penetration, or evaporation of chemical agents and simulants. Also, the design of the system and the operating procedures ensure the containment of toxic compounds during a test and ensure the safe operation of the system.

Specifically, the permeation-testing system has the following features:

- Sequential sampling of up to 24 gas streams containing the compound of interest.
- Sampling each gas stream usually every 60 to 120 min.

CMS Research Corporation, 1075 South 13th Street, Birmingham, Alabama 35205; Telephone: 205-934-9151.

- Efficient collection and desorption of chemical agents and simulants on the solid-sorbent preconcentrator tube.
- Detecting chemical agents and simulants over a wide range of concentrations.
- Calibration of the sampling-and-analytical system over the entire detectable range using dilute standard solutions. (Calibration using a vapor generator is not necessary.)
- Computing real-time, curve-fit parameters on calibration data.
- Computing agent or simulant concentrations and storing these data on a hard disk on a PC.
- Performing regression analyses and other data reduction to calculate calibration curves, permeation rates, breakthrough times, etc.

DESCRIPTION OF THE SYSTEM

The three critical components of the permeation-testing system are the permeation cells, the stream-selection system, and the sampling-and-analysis system. Other peripheral equipment can be used optionally. A diagram of the system is shown in Figure 2. A typical configuration within a multichamber test cell is shown in Figure 3. If a vapor challenge of the protective fabric is used, the upper portion of the chamber is connected to a vapor generator. The outlet may be sampled to verify the proper operation of the vapor generator. If a liquid challenge is used, the upper portion of the chamber is flushed with air or nitrogen and the evaporation rate of the chemical agent or simulant deposited on the fabric can be determined by sampling the effluent.

Up to 24 evaporation and permeation inlets may be sequentially sampled and analyzed. Concentrations ranging from less than 0.00001 to greater than 1.0 mg/m^3 may be sampled and analyzed directly from the permeation inlets. By using a sample loop or by diluting the gas stream, concentrations greater than 1000 mg/m^3 may be determined from the evaporation inlets.

The stream-selection system consists of a multiport valve, inlet fittings connected to test cells, and a common inlet that is connected to MINICAMS. Each stream is sequentially sampled by actuation of a multiport stream-selection valve. The operation of this valve is controlled by the MINICAMS PC computer and

software package. The multiport valve is mounted in a temperature-controlled oven. The temperature is usually maintained at about 100°C to minimize condensation or absorption of the compound of interest on surfaces. Heated Teflon sample lines are used between the stream-selection system and MINICAMS and between the permeation cells and the stream-selection system.

The sampling-and-analytical system -- MINICAMS -- is based on concentration of the chemical agent or simulant on solid sorbents, separation by capillary-column gas chromatography, and detection by a flame-ionization (FID) or a flame-photometric detector (FPD). The FPD is used to detect agents or simulants containing sulfur or phosphorus atoms, whereas, the FID detects a much wider range of compounds such as methyl salicylate or diethyl malonate..

Additional features of the MINICAMS-based, permeation-testing system include the capability of calibrating the system over the entire concentration range by injecting standard solutions into the sampling line leading to the MINICAMS and into any of the ports of the stream-selection system. Also, all of the operating parameters of the permeation-testing system can be displayed on the computer screen including concentration, elapsed time in the permeation test, stream-selection system port number, and identity of the compound being determined. The user can change operating parameters through the keyboard and observe the operating parameters and the status of the permeation-testing system through the computer's video screen.

The PC computer and software package associated with the permeation-testing system are capable of performing regression analyses of the calibration data. Simple first-order or more complex log-log, third-order curve fits can be performed on the calibration data. During an actual test, concentrations, amounts permeating or evaporating, evaporation or permeation rates, cumulative amounts permeating or evaporating, and breakthrough times can also be calculated. Typical computer screens that illustrate the calibration and setup features are shown in Figure 4 and 5. A series of chromatograms from the calibration challenges listed in Figure 5 are shown in Figure 6. A simulated profile of desorption rate versus time for GB (O-isopropylmethyl-phosphonofluoridate) is shown in Figure 8. Simulated cumulative desorption versus time is shown on Figure 9.

OTHER APPLICATIONS

MINICAMS used with one or two stream selection systems in a configuration similar to the permeation-testing system can also be used as a multipoint sampling-and-analytical system for chemical agents or simulants. Air can be sampled through as many as 24 sample lines sequentially to determine agent or simulant concentrations at up to 24 locations. Each sample line can be as long as 50 ft. This multipoint monitoring system can be used in

test-and-evaluation sites, agent laboratories, and storage sites where multipoint monitoring is required. The permeation-testing software package described above can be readily setup to support multipoint monitoring operations.

Also, by using the MINI-NET™ distributed network as shown in Figure 10, up to 50 multipoint monitoring systems can be linked to a single central computer located up to 5000 ft away. This central computer can then be used to log automatically concentration and status reports around-the-clock for each monitoring system.

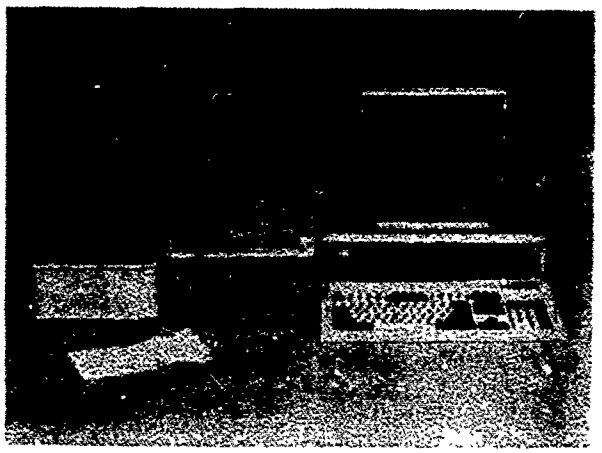

Figure 1. Permeation-testing system showing MINICAMS and one 12-port stream-selection system.

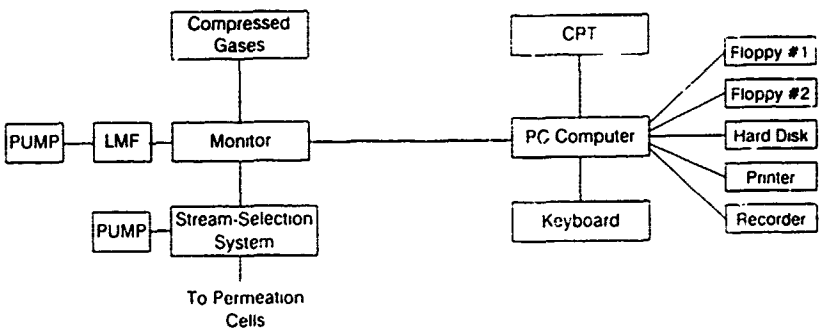

Figure 2. Diagram of the permeation-testing system.

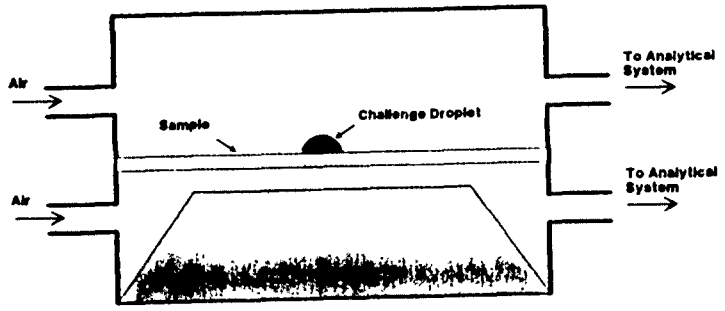

Figure 3. Experimental configuration of a permeation cell.

Groups Params Methods Record Setup Calib Test F5=Ignite F9=Ht/Area F10=Exit

AGENT: GB — MINICAMS CALIBRATION DATA — MODIFY INFO

GROUP: 1 TEST. 1 PROJECT: 9941

	INJ NO.	SSS NO.	POR NO	STD NO	VOL uL	INJ ng	PEAK nA	CAL ng
1. CONCN: 1.00 ng/uL	1	A	1	1	0.1	0.10	2.21	0.10
DOC. NO. -	2	A	1	1	0.2	0.20	6.42	0.23
AGENT NO: -	3	A	1	1	0.4	0.40	11.97	0.40
	4	A	1	1	0.6	0.60	18.61	0.60
2: CONCN: 0.00 ng/uL	5	A	1	1	0.8	0.80	21.42	0.69
DOC. NO: -	6	A	1	1	1.0	1.00	33.51	1.07
AGENT NO -	7	A	1	1	2.0	2.00	63.34	1.96
	8	A	1	1	4.0	4.00	127.39	4.19
3: CONCN: 0.00 ng/uL	9	A	1	1	6.0	6.00	170.57	5.69
DOC. NO -	10	A	1	1	8.0	8.00	249.46	8.48
AGENT N: -	11	A	1	1	10.0	10.00	294.23	10.10
	12	A	1	1	20.0	20.00	548.07	19.38

CURVE FIT: LOG-LOG, 3RD ORDER — LAST CALIBRATION. 10/27/88

A=-4.901e-003 B=8.003e-002 C=6.163e-001 D=-2.876e+000 R=0.999149

F1 = Start Acquisition F2 = Save Data

MINICAMS, CMS Research Corporation, Birmingham, AL, Copyright 1988, 1989 19

Figure 4. Computer screen showing data from a series of calibration challenges.

Groups Params Methods Record Setup Calib Test F5=Ignite F9=Ht/Area F10=Exit

MINICAMS TEST CONFIGURATION — MODIFY INFO

GROUP:	1	PROJECT: 9862	TEST NO 1	NO. OF POINTS:	1
METHOD:	GB	ANALYST: THR	AGENT: GB	BREAK (ng/cm^2):	10
POINT NO:	1	SAMPLE DESCRIPTION			Carbon fabric
SSS NO:	A	SAMPLE NO:			1
PORT NO:	1	COMMENTS:			Aged sample
TEMP (°F):	70				
RH (%):	50				
CELL NO:	1	TEST TYPE (E,D,P).	D	VAPOR CONCN (ug/L)	0.1
CHAMBER NO:	1	FLOW RATE (ccm):	200	NO OF DROPS:	0
COMPARTMENT:	U	SAMPLE DIAM (mm):	100	DROP SIZE (mm):	0
		SAMPLE THICK (mm):	1.0	DROP VOLUME (uL).	0

F1 = Save Data

MINICAMS, CMS Research Corporation, Birmingham, AL, Copyright 1988, 1989 127

Figure 5. Computer screen used to setup a permeation test.

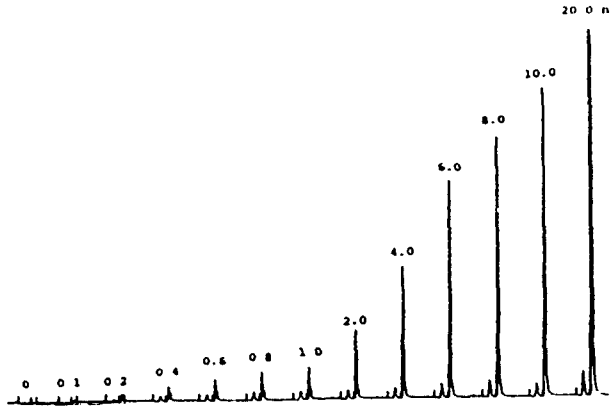

Figure 6. A series of GB chromatograms of the calibration challenges shown in Figure 4.

GROUP:	1	ANALYST:	TMR
PROJECT:	9862	AGENT:	GB
TEST:	2	DATE:	10/27/88
METHOD:	GB	TIME:	14:06
NO OF RUNS:	1	BREAK (ng):	1000

ELAPSED TIME	RUN NO.	SSS NO.	PORT NO.	TEST TYPE	FLOW ccm	VOL cc	PEAK nA	QTY ng	RATE ng/min	CUM AMT ng
0:01:35	1	A	1	D	143	143	908.09	32.65	45.35	35.90
0:04:35	1	A	1	D	143	143	503.41	17.73	24.64	140.30
0:07:35	1	A	1	D	143	143	326.43	11.27	15.67	200.43
0:10:35	1	A	1	D	143	143	213.23	7.20	10.02	238.75
0:13:35	1	A	1	D	143	143	140.52	4.65	6.46	263.33
0:16:35	1	A	1	D	143	143	91.00	2.95	4.11	279.10
0:19:35	1	A	1	D	143	143	66.23	2.13	2.96	289.64
0:22:35	1	A	1	D	143	143	47.47	1.51	2.10	297.19
0:25:35	1	A	1	D	143	143	31.12	0.99	1.38	302.32
0:28:35	1	A	1	D	143	143	24.33	0.78	1.08	305.99
0:31:35	1	A	1	D	143	143	18.42	0.59	0.83	308.84
0:34:35	1	A	1	D	143	143	15.20	0.49	0.69	311.10
0:37:35	1	A	1	D	143	143	11.67	0.39	0.54	312.93
0:40:35	1	A	1	D	143	143	9.64	0.32	0.45	314.41
0:43:35	1	A	1	D	143	143	7.99	0.27	0.38	315.65
0:46:35	1	A	1	D	143	143	6.95	0.24	0.34	316.71
0:49:35	1	A	1	D	143	143	6.51	0.23	0.32	317.71
0:52:35	1	A	1	D	143	143	6.08	0.22	0.30	318.63
0:55:35	1	A	1	D	143	143	5.37	0.19	0.27	319.48
0:58:35	1	A	1	D	143	143	5.40	0.20	0.27	320.29
1:01:35	1	A	1	D	143	143	4.60	0.17	0.24	321.06
1:04:35	1	A	1	D	143	143	4.55	0.17	0.24	321.77
1:07:35	1	A	1	D	143	143	4.23	0.16	0.22	322.48
1:10:35	1	A	1	D	143	143	4.27	0.16	0.22	323.12
1.13:35	1	A	1	D	143	143	3.84	0.15	0 21	323.76

Figure 7. Computer screen showing GB desorption data (simulated using a vapor generator).

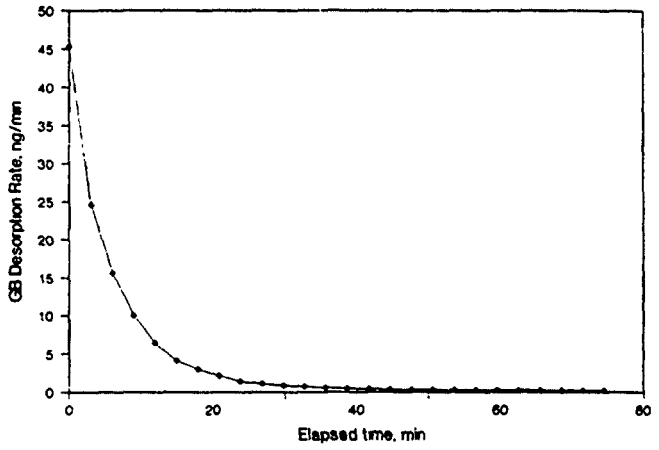

Figure 8. Plot of simulated GB desorption rate from data shown in Figure 7.

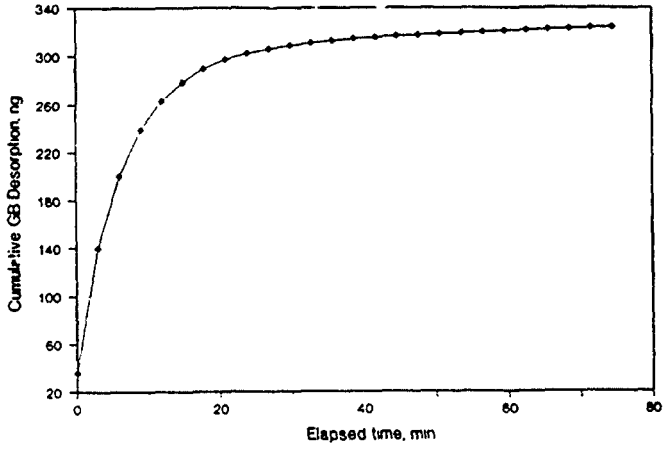

Figure 9. Plot of simulated cumulative GB desorption from data shown in Figure 7.

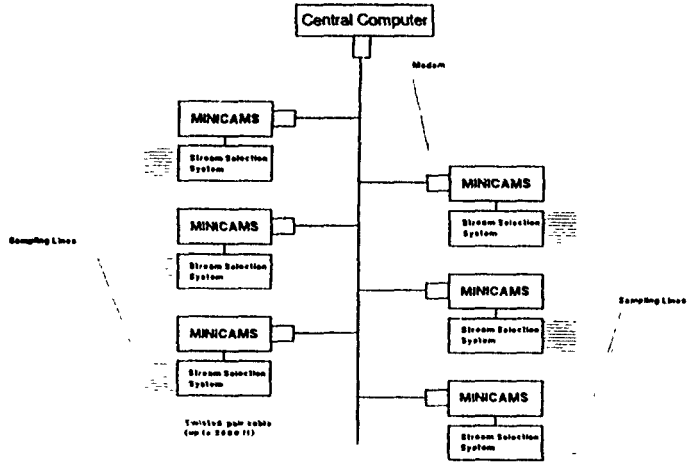

Figure 10. Diagram of MINI-NET™ distributed monitoring network.

VIII. TOXICOLOGICAL AND ENVIRONMENTAL STUDIES

NOTE: Papers with the following titles were presented at the Conference but are not included in this document:

Microbial Populations in Soil Maintained Under Anaerobic Conditions

Use of Open-Top Chambers to Assess the Toxicity of Chemicals to Plants

A Charcoal Filter Test System Using a Combination of Chemical and Toxicological Detectors to Assess Performance

Potentiation of Perfluoroisobutylene-Induced Lung Injury by Exercise

The following paper presented at the Conference was received too late to be included in this section; it is contained in Appendix C.

Growth Characteristics of Commercial Normal Human Abdominal Keratinocytes

BLANK

REMOVAL OF HAZARDOUS SUBSTANCES FROM CONTAMINATED SOIL BY EXTRACTION AND WASHING USING FLOW-THROUGH COLUMN SYSTEM

Vijay S. Rajput[1] Mark E. Singley, Andrew J. Higgins
Peter F. Strom

Abstract

A study was conducted to investigate decontamination of soil contaminated with 1, 2, 4 trichlorobenzene, aniline, phenol and 2,4 dichlorophenol, by extraction and washing under stationary condition. Extractive agents used were surface active agents (surfactant) and deionized water. an aqueous solution of surfactant and water alone were allowed to gravity flow through the Teflon made column filled with a contaminated soil. The nonionic surfactant at 2% aqueous concentration efficiently solubilized 1, 2, 4, trichlorobenzene under stationary condition. The hydrophillic compounds tested were removed efficiently by deionized water alone.

Introduction

The effects of hazardous organic compounds released into the soil can be severely damaging to the local environment. The problem of environmental contamination can be aggravated if contaminantes are not removed from the soil as they may percolate to groundwater source or flow to a surface water body by surface run off. The sources of surface and subsurface soil contaminantes need to be removed if public health is to be protected. Removal and clean up of the spilled material on land could be easier. Once the contaminant migrates into groundwater, removal becomes much more difficult and expensive.

One of the viable alternatives for the cleanup of soils contaminated with hazardous organic compounds may be to excavate and treat the contaminated soils on-site using a combination of extraction and washing and biodegradation. In order to investigate potential of such a decontamination technology, an extensive research work was designed and conducted (2,3). A summary of results obtained from the experiments on the removal of different pure organic compounds from the soil by extraction with surfactants under equilibrium condition (shaker table) and biodegradability of different organic compounds at their different concentrations determined by a microcalorimeter, was presented at the 1987 CRDEC conference(4).

The main purpose of this paper is to present a summary of the results obtained on removal of organic contaminantes under flow-through conditions both by surfactant and deionized water. Detailed experimental data are available elsewhere (2,3).

Materials and Methods

Test Soil: All experiments were conducted using a sandy loam soil. It was brought from a nearby field where grab samples were collected from a depth of 0 to 60 cm.

Organic Compounds: Organic compounds selected for this study were 1, 2, 4, trichlorobenzene, phenol, 2, 4 dichlorophenol and aniline. All of them were purchased either from Fisher or Aldrich Co., at a purity from 97% to 99%.

Surfactants: Surfactants selected for the study were Adsee 799, witconol NP-100 and witconol NS-500K. All are the products of Witco Chemical Corporations.

Experimental Set-Up and Procedure: Figure 1 shows a typical gravity flow through column system. The columns used were made of Teflon, 36 cm. (14.17 inch) in height and 5 cm. (1.97 inch) in diameter. All the experiments used 120 g of air dried, sandy loam soil. The height of soil in the column was 7 cm. (2.76 inch) before treatment. The soil was underlain by pure sand, a thin layer of glass wool, and glass beads. The extraction liquid was poured from the top. A total of six washes was applied. Each wash consisted of 200 ml of extraction liquid. The samples of leachate were collected at the end of every individual wash and analyzed for the contaminant concentrations and pH. The soil was analyzed only at the end of the six washes.

Analytical Techniques: Organic compounds from aqueous leachate samples were extracted using the liquid - liquid extraction where as soxhlet extraction was used for soil samples. All the above extractions were performed using methylene chloride as a solvent. Gas chromatography was performed on the extracts of soil and aqueous leachate samples using Hewlett Packard model 5730 series equipped with a dual flame ionization detector. Quantitization was obtained using a Hewlett Packard model 3390 A reporting integrator.

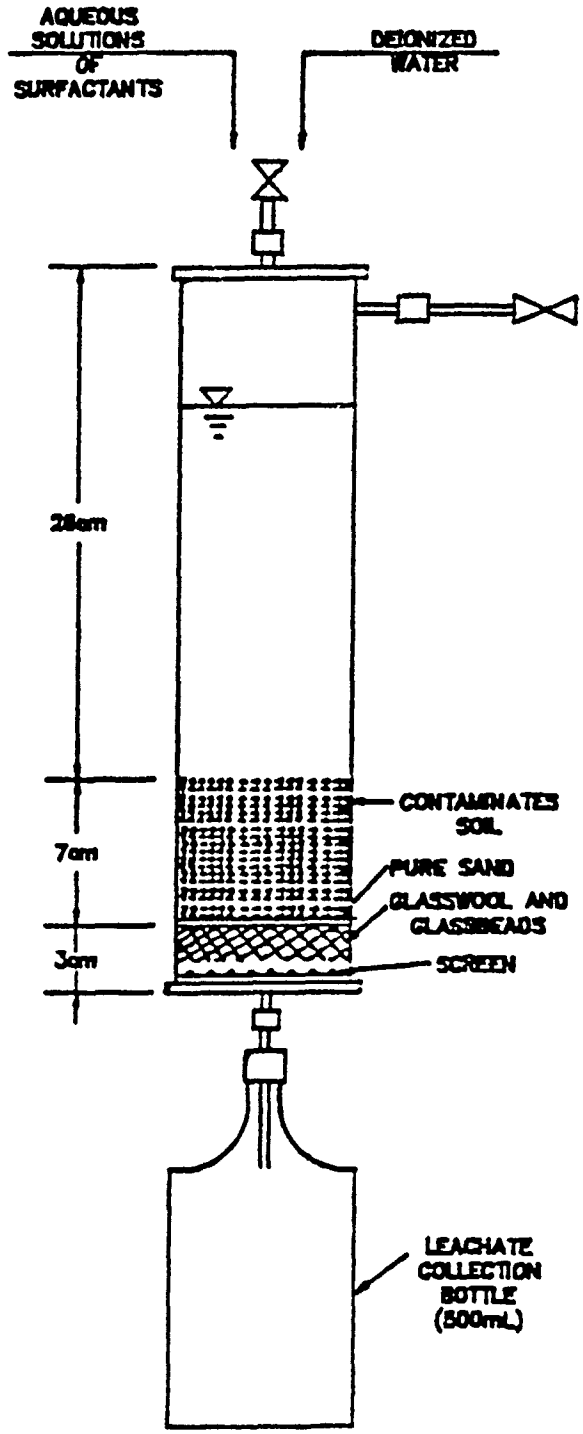

FIGURE 1: FLOW THROUGH COLUMN EXPERIMENTAL SET UP FOR WASHING CONTAMINATED SOIL

Results and Discussion

The model field soil used during the present study belongs to the freehold series and is classified as a sandy loam soil based on its particle size distribution. The soil consisted of 72% sand, 16% silt and 12% clay. The pH, total nitrogen and carbon content were 6.0, 0.1% and 1.0% (range 1.0 - 3), respectively.

The constant head percolation rate of both water and surfactants through the sandy loam soil decreased as more volume of the liquid was passed due to progressive consolidation of the soil mass. The percolation rates of deionized water, a mixture of 2% adsee plus 2% witconol NP-100 and 2% witconol NS-500K were 0.05 inch/day, 0.92 inch/day, and 1.63 inch/day, respectively. The mixture of 2% adsee plus 2% witconol NP-100, which was observed to be very effective in removing 1, 2,4 trichlorobenzene during the shaker table experiments, was found to be very ineffective in the flow through column condition. Instead witconol NS-500K surfactant at 2% aqueous solution was found to be very effective.

The removal of 1, 2, 4 trichlorobenzene was observed to depend on the concentration of witconol NS-500K surfactant. The surfactant was less effective at the concentration of 1% when compared with that at 2% concentration (Figure 2). It can also be seen from Figure 2 that very little removal of the 2, 3, 4 trichlorobenzene was obtained by washing with water alone. This could be attributed to the hydrophobic nature of the compound.

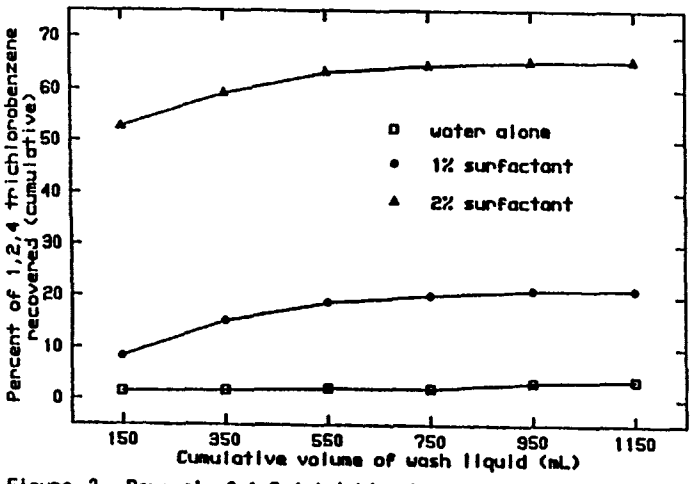

Figure 2 Removal of 1,2,4 trichlorobenzene from soil by washing with water, 1% and 2% aqueous solutions of Witconol NS-500K. Gravity flow-through column experiments.

Figure 3 shows the removal of 1,2,4 trichlorobenzene, aniline, phenol and 2,4 dichlorophenol by washing with a 2% aqueous solutions of witconol NS-500K and rinsing with deionized water. Figure 4 shows the removals of 1,2,4 trichlorobenzene, aniline, phenol, and 2,4, dichlorophenol by washing with deionized water alone. As appears from these two figures, except for 1,2, 4 trichlorobenzene, all three remaining hydrophillic compounds were efficiently removed from the soil by washing with water alone. Six water washes alone yielded a total of 99.1%, 99.99% and 96.5% removals of aniline, phenol and 2, 4 dichlorophenol, respectively. The total removals of 98.0%, 97.1% and 96.7% and 97.8% of 1,2,4 trichlorobenzene, aniline, phenol, and 2,4 dichlorophenol were obtained, respectively, when the contaminated soil was washed three times with 2% aqueous solution of the surfactant plus three water rinses. It is evident from these results that the surfactant washing has no advantage over washing with water alone.

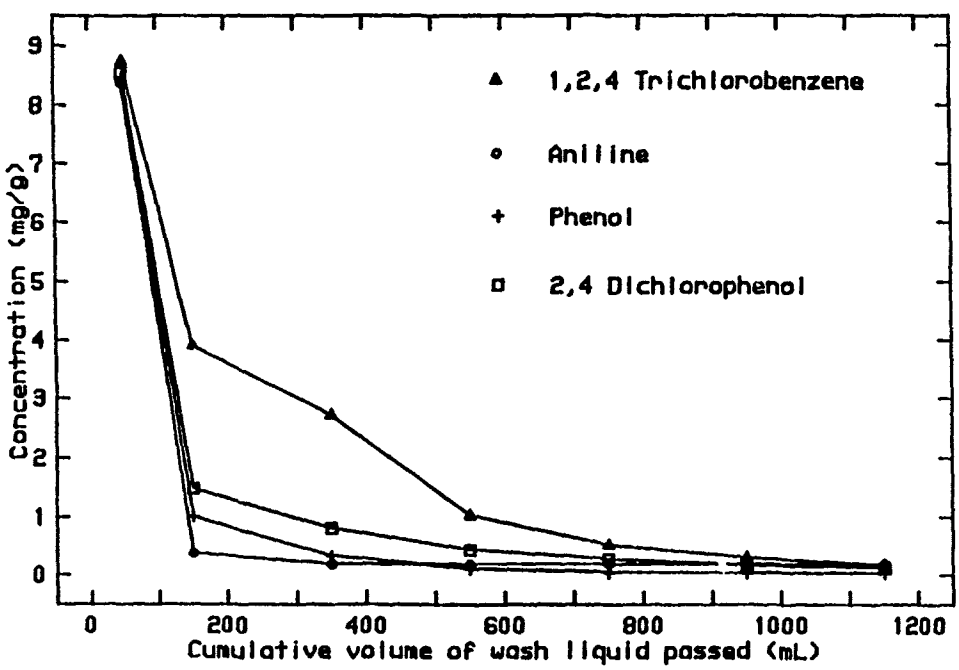

Figure 3 Removal of organic compounds from soil by washing with 2% Witconol NS-500K and water using gravity flow-through column system.

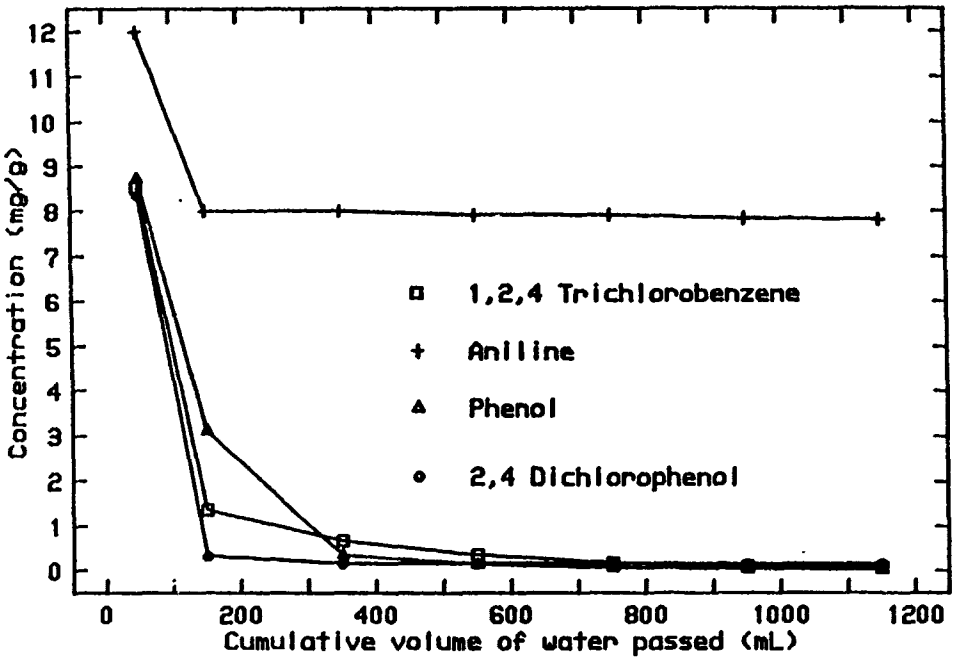

Figure 4 Removal of organic compounds from soil by washing with water. Gravity flow through column experiments

CONCLUSIONS

The sandy loam soil contaminated with the hydrophillic organic compounds such as aniline, phenol and 2, 4, dichlorophenol can effectively be cleaned by water washing alone under stationary or flow-through conditions. The soil contaminated with the hydrophobic compounds such as 1,2,4 trichlorobenzen can be cleaned by a combination of washes and rinses with the surfactant and water, respectively. However, a much longer time will be required for cleanup under stationary conditions then under dynamic conditions. The results of this study also show that soil contaminated with the compounds studied can be cleaned by in-situ flushing using a 2% aqueous solution of witconol NS-500K and water depending upon the contaminant type.

ACKNOWLEDGMENTS

This research was supported as a project of the National Science Foundation Industry/University Cooperative Center for Research in Hazardous and Toxic Substances, at New Jersey Institute of Technology, and Advanced Technology Center of the New Jersey Commission on Science and Technology. The research was conducted at the Department of Biological and Agricultural Engineering, Rutgers, the State University of New Jersey, New Brunswick, New Jersey.

REFERENCES

1. Unitech Engineers, Inc., 654 N. Woodbourne Road, Langhorne, Pa. 19047

2. Rajput, V.S., S.C. Pilapitiya, M.E. Singley, and A. J. Higgins. 2988. "Biotechnology for the Treatment of Hazardous Waste Contaminated Soils and Residues", Final Report submitted to the National Science Foundation Industry/Co-operative Center for Research in Hazardous and Toxic Substances, NJIT, Newark, New Jersey.

3. Rajput, V.S. 2988. "Treatment of Hazardous Waste Contaminated Soils by Extraction and Washing", Phd. Dissertation, Graduate School, Rutgers, The State University of New Jersey, New Brunswick, NJ 08903.

4. Rajput, V. S., S.C. Pilapitiya, M. E. Singley, and A. J. Higgins. 2987. "Biotechnology for the Treatment of Hazardous Waste Contaminated Soils and Residues, "Proceedings of the 1987 U. S. Army CRDEC Conference prepared by Michael D. Rausa, Vol. 2, pp. 785-791, U. S. Army Armament, Munitions and Chemical Command, Aberdeen Proving Ground Maryland 21010-5423.

BLANK

THE PHARMACOKINETICS OF VOLATILE ANESTHETICS - A BRIEF INTRODUCTION

James W. King
U.S. Army Chemical Research, Development & Engineering Center
Aberdeen Proving Ground, Maryland 21010-5423

ABSTRACT

The potential of inhalation anesthetics as a basis for the design of compounds for consideration as reversible incapacitants places a particular emphasis on how they are acted upon by the body. Inasmuch as pharmacokinetic modeling techniques provide succinct methods for describing the behavior of compounds in vivo, the literature related to volatile anesthetic pharmacokinetics has been monitored. Recent evidence that these compounds act through specific rather than nonspecific mechanisms presents an opportunity to formulate enhanced models to assist in the design of new and more potent volatile anesthetics.

INTRODUCTION

Because of their effect on the central nervous system, volatile anesthetics are worthy of consideration as potential incapacitating agents. The liabilities associated with their employment in this manner are their relatively small therapeutic index (safety ratio) and their lack of potency on a molar basis.[1] In respect to the former, their use in the medical arena is under highly controlled conditions by experts monitoring a patient with sophisticated instrumentation, and thus, the chances for overdosage and possible lethal effects are minimized. In the latter event, the medical community apparently does not see a requirement for greater potency even though such compounds should minimize the psychotomimetic side effects of depression and hallucinations suffered by some patients during recovery from an anesthetic as commonly used as halothane.[2]

The increase in potency that is needed in order for volatile anesthetics to be considered for military use is about three orders of magnitude (1000 times).[1] If such should prove possible, the candidate anesthetic would approach the nerve agent GB (isopropyl methylphosphonofluoridate) in potency - but, of course, not as to type of pharmacology.

In any study that attempts to establish a basis for the design of compounds with increased potency, it is a first requirement to know two things. Initially, one needs to know the pharmacological responses induced by administration of compound(s) of interest; this is termed pharmacodynamics - the effect of compound(s) on the body. Just as imperitive is a knowledge of the body's action on the compound(s); this is termed pharmacokinetics, and takes into consideration rates of administration, distribution, metabolism, excretion (by fecal, urinary, or respiratory processes), and someimes, storage in a tissue depot. As an aside, it is necessary to distinguish between pharmacokinetic models which are based on considering the body as composed of one or more compartments (typically, not more than three), and physicolgically based models in which there may be many compartments, each representing some body organ or system. The latter are flow-limited and require large amounts of data but are useful in some situations. The former are kinetically based and as previously noted give a picture of the body's action on a compound; they usually require less initial data. Also, any number of pharmacokinetic models may be envisioned and mathematically structured a priori, awaiting only blood level data on a compound to begin fitting trials. The particular compartment model that best accomodates experimental data can often provide insights on compound behavior, e.g., whether there is a significant peripheral compartment(s) in addition to the central compartment. Such information may indicate whether a tissue depot is likely or not.

Before reviewing the applicable literature, it is pertinent to consider the general types of models used in pharmacokinetics; these are seen in Figure 1. The mammillalry system or, more likely, abbreviated versions of it are probably the most common seen in the literature. Models based on the catenary paradigm are certainly possible but most often seen in physiologically-based systems.

LITERATURE REVIEW

After monitoring the literature for several years and acquiring an impression as to the general direction of reported work, one is, nevertheless, somewhat surprised to eventually find only a few papers strictly applicable to the subject topic. Perhaps this should not be too surprising in that anesthesia can be induced by a number of other methods, e.g.[3], by intravenous administration of large doses of analgesics. Also, the use of closed-circuit inhalation apparatus is often favored in clinical practice and such systems can result in multicompartment models for description - six tissue compartments for example.[4,5,6] Whether such extensive systems are of practical value in the design of super anesthetics remains to be seen.

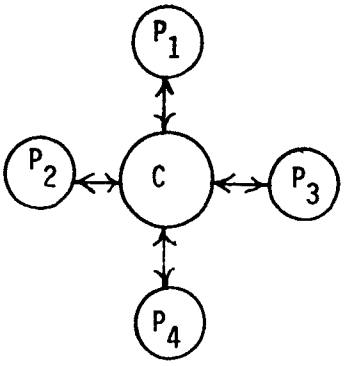

Mammillary Model

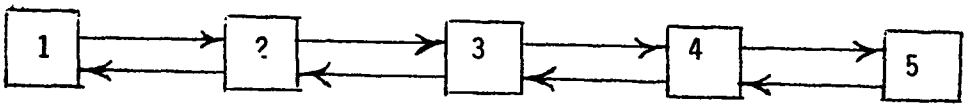

Catenary Model

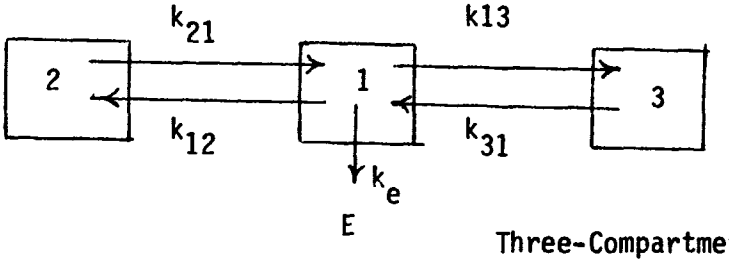

Three-Compartment Model

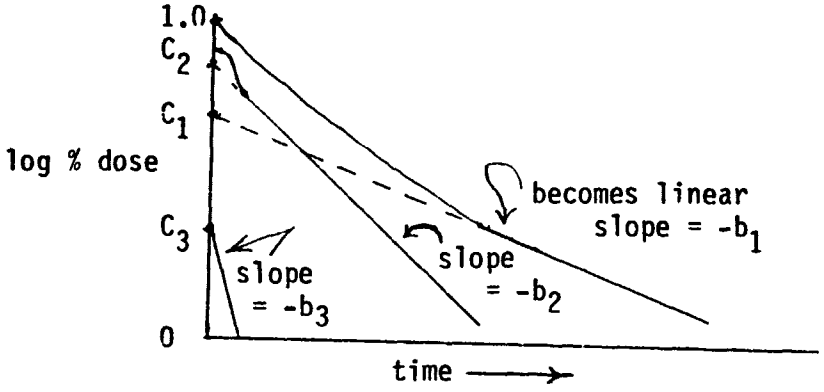

Typical Plot for a Three-Compartment Model

$$\frac{X_1}{(X_1)_0} = C_1e^{-b_1t} + C_2e^{-b_2t} + C_3e^{-b_3t}$$

Equation for a Three-Compartment Model

Figure 1. The pharmacokinetic "milieu."

The work of Finegold and Holaday[7] is likely to be more useful to the drug designer. They considered in some detail the pharmacokinetics of metabolism of inhalation anesthetics using both a linear and a non-linear whole-body compartmental model. Their finding that both models show that significant metbolism takes place for several days following administration is of importance, but of more import, they concluded that the quantity of anesthetic metabolized is directly dependent on tissue solubilities of the anesthetic. In a similar study, Cahalan and his colleagues found that halothane clearance was a combination of linear clearance to depots and saturable metabolism, the former proportional to the clearance of a marker (unmetabolized isoflurane), and the latter attributable to a Michaelis-Menten process. Using this combination as the basis for a model resulted in a significantly better data fit than if either was used to the exculsion of the other.[8]

One of the more interesting, and probably useful, models is the three-compartment model of Tanner.[9] Their central compartment (analagous to compartment 1 of the three-compartment model shown in Figure 1) represented lung gas, pulmonary venous blood, and arterial blood. A "fast" peripheral compartment represented a vessel rich or visceral group, while the third was a "slow" or muscle group compartment. This study used only the solubilities in water and oil to predict the uptake (alveolar-to-inspired concentration ratio) of several volatile anesthetics. An unexpected delight in this work is that only a programmable calculator is needed to provide rapid solutions to the input data and these are available almost instantaneously if calculated constants have been stored in memory. Also, as noted previously, comparisons of a priori structured models can easily be made as Tanner did in evaluating Kety's two-compartment model for the same data.[10] In this case the three-compartment model provided a better fit to the data. But such is not always the case since, as with any mathematical treatment of data, complex models may not offer a conceptual or accuracy advantage over their less sophisticated counterparts. And one should also note that, generally, the more complex the model, the more accurate the data needed.

DISCUSSION

The papers cited above certainly are not all that are to be found relating to the pharmacokinetics of volatile anesthetics. Buth they are critical general entries to a literature that diverges into many specific areas. There are, for instance, many papers relating to the tissue absorption of halogenated ethers and hydrocarbons. These must be viewed, to some extent, in the context of the mechanistic theories of anesthesia that were extant at the time the papers were written. One of the theories was that the anesthetics functioned by virtue of increasing the volume of the lipid bilayer into which they were absorbed. Therefore, tissue solubility of the compounds became an area for investigation.

Of more probable current importance for the compounds at hand is their propensity (or lack of it) for complexation with proteins - particularly serum proteins inasmuch as the anesthetics must be transported from the lungs by the general circulation; the development of binding constant data would be most appropriate now since most specific agents are considered to bind at proteinaceous receptors. This area has become more important due to the increasing weight of evidence that some of the volatile anesthetics bind to specific anesthetic sites in the brain and do not act by nonspecific membrane effects.[11] Recent structure-activity studies support this premise, in that the inert gases and small compounds are likely non-specific in their action but the larger halogenated ethers and halocarbons probably act at potentially identifiable receptors.[12] Further support has also been found in studies of high pressure and anesthetic effects.[13] The significance of this specificity is that new and more appropriate pharmacokinetic models can be formulated and evaluated.

From this viewpoint one must also look at metabolic processes. Although the literature is fairly strong in respect to volatile anesthetic metabolism, the data generated has not, with the exceptions noted above, usually been included in the pharmacokinetic models. Rather, the emphasis, as previously noted, has been on tissue deposition. For a greater understanding of the body's treatment of volatile anesthetics, perhaps it is not premature to suggest that a metabolic model be formulated. At the very least, a "black box metabolizer" could generate rate data on known and new compounds that could be fed, on a comparative basis, into new pharmacokinetic models.

CONCLUSIONS

Pharmacokinetic modeling can provide the framework for an increased understanding of compound behavior in the biological milieu. Enhanced models, based on new evidence of specific receptors for volatile anesthetics, should provide the knowledge to design compounds or prodrugs that are transported to their site of action in the most facile manner, be highly site-specific when they arrive, and resist catabolic body processes for specified periods of time.

ACKNOWLEDGMENT

The author is forever indebted to Professor James Leslie of the University of Maryland, Baltimore, for introducing him to the magnificient conceptual edifice that is pharmacokinetics. It is a pleasure to note the long-term support and encouragement of Mr. C. Parker Ferguson, Chief of the Organic Chemistry Branch, Chemical Division, Research Directorate. The author is grateful also for the interest and efforts of Dr. John F. Weimaster in the promotion of this work.

REFERENCES

1. J.P. Cleveland. Memorandum for Chief, Research Division. Subject: Preliminary Considerations on the Relationship of Volatile Anesthetic MAC Values and Equivalent Field Concentrations. 24 March 1980.

2. P.S. Magee. Personal communication.

3. M.M. Ghoneim and K. Korttila. Pharmacokinetics of Intravenous Anaesthetics: Implications for Clinical Use. Clinical Pharmacokinetics 2, 344-372 (1977) [Chem. Abstr. 90, 114745k (1979)].

4. I.S. Goldberg, J.W. Mostert, E.F. Lanzl, and H.J. Lowe. A Pharmacokinetic Model of Closed-Circuit Inhalation Anesthesia. Annals of Biomedical Engineering 6, 231-249, (1978) [Chem. Abstr. 90, 97312x (1979)].

5. W.W. Mapleson. Pharmacokinetics of Inhalation Anaesthetics. Int. Congr. Ser. - Excerpta Med. 538, 405-408 (1981) [Chem. Abstr. 95, 143674r (1981)].

6. J.W. Mostert. A Pharmacokinetic Model of Closed-Circuit Inhalation Anesthesia. Int. Congr. Ser. - Excerpta Med. 538, 422-425 (1981) [Chem. Abstr. 95, 143816t (1981)].

7. A. Feingold and D.A. Holaday. The Pharmacokinetics of Metabolism of Inhalation Anaesthetics. Br. J. Anaesth. 49, 155 (1977) [Chem. Abstr. 86, 150300n (1977)].

8. M.K. Cahalan, et al. A Noninvasive In Vivo Method of Assessing the Kinetics of Halothane Metabolism in Humans. Anesthesiology 57, 298-302 (1982) [Chem. Abstr. 97, 192722j (1982)].

9. G. Tanner. Pharmacokinetics of Inhalation Anesthetics: A Three-Compartment Linear Model. Anesth. Analg. (Cleveland) 61(7), 587-594 (1982) [Chem. Abstr. 97, 65985x (1982)].

10. S.S. Kety. The Theory and Applications of the Exchange of Inert Gas at the Lungs and Tissues. Pharmacol. Rev. 3, 1-41 (1951).

11. A.S. Evers, B.A. Berkowitz, and D.A. d'Avignon. Correlation Between the Anaesthetic Effect of Halothane and Saturable Binding in Brain. Nature 328, 157-160 (1987).

12. J.W. King, P.S. Magee, J.H. Block, L.B. Kier, and C-c. Tsai. Unpublished proceedings of the Volatile Anesthetics Project Workshop. 22-25 September 1989. Vallejo, CA. Sponsored by the U.S. Army Chemical Research, Development & Engineering Center, Aberdeen Proving Ground, MD.

13. M.J. Halsey, A.F. Mott, C.C. Spicer, and B. Wardley-Smith. A Mathematical Analysis of High Pressure and Anesthetic Effects. Underwater Physiology 7, 661-665 (1981) [Chem. Abstr. 95, 143726p (1981).

BLANK

A SINGLE EXPOSURE TO A CHEMICAL CARCINOGEN CAN CAUSE CANCER: DOCUMENTATION, LIMITATIONS AND IMPLICATIONS FOR RISK ASSESSMENT

Edward J. Calabrese
Environmental Health Sciences Program
School of Public Health
University of Massachusetts
Amherst, MA 01003

ABSTRACT

A single exposure to 32 chemical carcinogens representing 12 chemical classes has been found to cause cancer in mammalian models. This phenomenon has been reported in 28 mouse strains, 14 rat strains as well as in other less frequently used models such as hamsters, gerbils, guinea pigs and rabbits. Similarly, this phenomenon is not restricted to a given tumor type, a specific age, or sex nor is it limited to extremely high doses as judged by percentage of the LD_{50}.

INTRODUCTION

Tumor formation as a result of a brief or limited exposure to a carcinogen is an important public health question because exposure patterns within the human population are highly variable in which transitory or episodic exposures to elevated pollutant levels occur. This may be true as a result of one's occupation, hobbies, spills and their clean up, exposure to certain medicines and medicinal treatments and numerous other experiences in which one is inadvertently exposed to a relatively large dose of a carcinogenic agent for a brief period of time.

The paper provides a preliminary in-progress summary of an ongoing study which is designed to identify and assess the published literature where animal models developed cancer when administered but a single exposure to a carcinogenic agent without the assistance of a promotional agent, such as croton oil or its derivatives (as in the case of the two-stage model of carcinogenesis). Due to limitations in space this report will be restricted to data on mammalian models

with findings from fish species and epidemiologic studies not included. Finally, the assessment of the relevance of these findings to the risk assessment process will not be included in the present analysis.

IDENTIFICATION OF AGENTS CAUSING CANCER WITH A SINGLE DOSE

This study has revealed that at least 32 chemical carcinogenic agents cause tumorigenesis in mammalian models with but a single exposure. These agents represent 12 different chemical classes (Table 1). While most of these agents are believed to be genotoxic carcinogens, requiring bioactivation to an ultimate carcinogenic form, some are thought to be direct acting genotoxic carcinogens while the sole apparent epigenetic carcinogen possibly acting via hormone modification is DES.

TABLE 1
Agents Causing Cancer With One Exposure Dose In Mammalian Models

Chemical Classes of Carcinogens Studied

1. Alkyl Hydrazines
   - 1,2 - dimethylhydrazine (DMH)
   - 1,2 - diethylhydrazine (DEH)
   - cycasin

2. Carbamates
   - urethane

3. Nitrosamines
   - dimethylnitrosamine (DMN)
   - diethylnitrosamine (DEN)
   - N-nitrobis (2-oxypropyl) amine (BOP)
   - N-bis (2-hydroxypropyl) amine (BHP)

4. Nitrosoureas
   - methylnitrosourea (MNU)
   - ethylnitrosourea (ENU)
   - methylnitrosobiuret (MNB)

5. Polycyclic Aromatic Hydrocarbons
   - 7,12 - dimethylbenzanthracene (7,12 - DMBA)
   - 9,10 - dimethylbenzanthracene (9,10 - DMBA)
   - 7-methylbenz(a)anthracene
   - 7-bromomethyl-12-methylben(a)anthracene
   - benzanthracene (BA)
   - benzpyrene (BP)

6. Aromatic Amines
   - 2-naphthylhydroxylamine (NHA)

TABLE 1 (Continued)

7. Azo Dye
   ortho-aminoazotoluene (AAT)

8. Sulphonates
   ethyl methane sulphonate (EMS)

9. Inorganics
   beryllium
   cadmium chloride
   cadmium oxide
   cadmium sulphide
   nickel sulfide
   nickel oxide

   cobalt sulfide
   cobalt oxide

10. Mycotoxins
    aflatoxin B_1 (AFB_1)

11. Alkaloids
    retrosine

12. Miscellaneous
    diethylstilbesterol (DES)
    metallurgical powder of multiple metals including copper, nickel cobalt, ferric, silicon compounds.

INFLUENCE OF DOSE

Of relevance to this discussion is that the claim may be made that it is not surprising that a single exposure of a carcinogen could cause cancer if the dose were sufficiently high. The implicit assumption in such a statement is that the single dose used must be exceeding high and approach acute toxicity by itself. A review of the positive studies indicates that this assumption is not generally valid. For example, it has been shown that a single dose of MCA as low as 1/1000 of the LD_{50} caused fibrosarcomas in neonatal albino mice (O'Gara et al., 1965). In addition, DMBA at 1/600 of the LD_{50} dose caused increases in skin cancer in two reports (Terricini et al., 1960; Turusov et al., 1971). Other investigators have revealed that a single dose of 1/120 LD_{50} for DMN (Cardesa et al., 1974), 1/200 the LD_{50} for DEN (Li et al., 1979), and 1/48 the LD_{50} for ENU (Druckrey, 1973) produced cancer in animal models. In fact, in the case of the 1/48 LD_{50} for ENU, the single dose caused cancer in about 90% of the animals exposed (Stoica and Koestner, 1984). This suggests that amuch lower dose could have been used and still cause cancer in the animal model. These examples illustrate that single doses of these agents some two and three orders of magnitude below the LD_{50}, have caused cancer in the respective animal models.

Layton et al. (1987) have shown that the ratio of chronic oral NOEL to oral LD_{50} for a large number of agents approximate 0.015 -0.02 using the geometric mean as the measure of central tendency. This suggests that the unit of exposure, based on the examples noted above, needed to cause cancer from a single exposure may at least for some agents approxiamte the chronic NOEL.

ROLE OF SPECIES/STRAIN SUSCEPTIBILITY

One of the most striking aspects of this review is that single exposures to carcinogens have been shown to cause cancer in numerous species and/or strains of animal models. More specifically, positive studies have been reported in six different species (mice, rats, hamsters, gerbils, rabbits, and guinea pigs). As for rats, positive findings have been reported in 14 strains, while in mice 28 strains have revealed positive findings. Such similarities in cross-species, cross-strain responses support the premise that susceptibility to a single carcinogen exposure may be a generalizable phenomenon and suggest that humans are likely to respond in a comparable fashion.

Another way to consider the breath of the available data base is to determine how many different species/strains have been involved in the evaluation of a particular agent. Of the 32 agents for which there are positive findings in mammals, DMBA was tested positively for cancer with a single exposure in 15 different species/strains followed by DMN, ENU, and MCA, each with nine.

ARE ONLY THE MOST POTENT CARCINOGENS RELEVANT?

It is a reasonable assumption that if an agent can cause cancer with but a single dose at an exposure level considerably below the LD_{50} and in fact approaching the chronic NOEL, the agent must be a very potent carcinogen. Of the 32 agents with evidence that they cause cancer in mammalian models with but a single dose some have been ranked for both cancer and mutagenic potency. For example, Stoner and Shinkin (1985) developed a relative quantitative potency ranking for a large number of carcinogens for lung tumor formation in the strain A mouse. Some of the agents identified in the present search were ranked by Stoner and Shinkin (1985). MCA was determined to be the most potent carcinogen in the Strain A model and was assigned a reference value of 1; DMBA was 7-fold less potent than MCA, AFB, was 20-fold less potent than MCA. Benzo (a) pyrene was 31-fold less potent than MCA, N -Nitrosomethylurea - 243-fold less potent than MCA, and urethane was 1963-fold less potent than MCA. These findings indicate that the relative potency can markedly vary - over more than three orders of magnitude.

ROLE OF AGE

Age has been reported to be an important factor affecting susceptibility to chemically induced cancer following a single exposure (Calabrese, 1986). The present assessment of mammalian studies has revealed that some of the studies involved transplacental exposures, while others involved exposure to neonates, yet many investigators utilized adults in their studies. In fact, the number of agents tested and the number of species/strains used were clearly

greater for adults followed by neonates and then the transplacental exposures. Thus, the data base is not predominantly comprised of exposure situations likely to present conditions of greatest susceptibility, if fact, the reverse is the case.

DOSE-RESPONSE DATA

A number of experiments were conducted in which a wide range of single exposure doses were administered to the animal models (Cardesa et al, 1974; Ii et al, 1979; O'Gara et al, 1965). The dose response relationships frequently indicated that a single exposure was effective in producing tumors over a wide range of doses often in a dose-dependent fashion. The shape of such multiple dose response curves appear consistent with other dose-response curves observed in routine bioassays when daily exposures are administered using multiple dose levels. Of significance to the present evaluation is that the responses observed indicate that cancer caused by a single dose exposure was not a random event nor one that happened exclusively at the highest levels of exposure. The data clearly support the occurrence of normal sigmoidal dose response curves.

ROUTE OF ADMINISTRATION

A wide variety of routes of administration have been employed in the studies reviewed here for the single exposure to carcinogens. These include IV, IP, SC, IM, Oral, intracolonic, intratracheal and catheter to the bladder. The most frequently emphasized routes were the SC (N=37) followed by IP (N=25), oral (N=20), IV (N=16), and dermal (N=15).

QUALITY OF DATA BASE

Given the controversial nature of this topic it is important to assess the quality of the data using both indirect and direct approaches for evaluating the original data base. An analysis of the animal model studies cited in this report assessed these papers with respect to sample size, adequacy of control groups, number and range of dose levels and nature of statistical analyses of the data. These analyses revealed that 73% of the studies had $\geq$25 animals per treatment group and 30% had $\geq$50 animals per treatment group. Seventy percent of the studies had standard concurrent controls, 10% used historic control while 15% did not report any mention of a reference or control group. Fifty-seven per cent of the studies used at least two treatment groups in addition to a control group. Thirty-four percent of the strains had $\geq$3 treatment groups. The type of statistical analysis varied markedly amongst the studies with a majority of reports (i.e. about 75%) indicating only the percentage of animals with tumors as opposed to controls. The remaining articles used significance testing in the analysis of the data.

DISCUSSION/CONCLUSION

It is difficult to make generalizations about the entire data base since each study was designed for the testing of a specific hypothesis unique to the investigators. In general, these were not studies that were designed for routine rodent cancer bioassays within the framework of NTP Bioassays. Nonetheless, while being cognizant of the above noted limitations these studies were of generally adequate size, had concurrent controls and used multiple dosage schemes. Perhaps the greatest overall limitation was the widespread lack of significance testing; this concern may be more apparent than real since consideration of the data presented in these reports with limited statistical analysis generally reveal that the carcinogenic responses observed were usually strikingly apparent Thus, it would be extremely unlikely that the application of more vigorous statistical analysis to those reports limited in statistical aspects would alter the original interpretations of the authors. In fact, it is more likely to considerably strengthen such initial conclusions.

The principal issue is whether the collective data base allows one to properly judge whether a single exposure to a chemical carcinogen causes cancer in an animal model. A careful consideration of these data indicate that in over 80 peer reviewed studies in multiple animal models, routes of exposure, with different chemical agents this phenomenon occurred. While one may question legitimately the adequacy of selected individual studies because of sample size, lack of concurrent controls, and lack of multiples doses, the bulk of the studies remain, and, when taken collectively represent a strong data base for assessment of the hypothesis that a single exposure can cause cancer in animal models.

ACKNOWLEDGMENT

I would like to acknowledge the assistance of Judith Sanders and David Gordon in the development of the data base and initial summarization of the findings.

REFERENCES

Calabrese, E.J. (1986). Age and Susceptibility to Toxic Substances. John Wiley and Sons, New York.

Cardesa, A., Pour, P., Althoff, J., and Mohr, U. (1974). Comparative studies of neoplastic response to a single dose of nitroso compounds. Journal of Cancer Research and Clinical Oncology, 81:229-233.

Druckrey, H. (1973). Chemical structure and action in transplacental carcinogenesis and teratogenesis. International Agency for Research on Cancer, 4:45-58.

Ii, Y., Pour, P., and Althoff, J. (1979). Comparative studies of neoplastic response to a single dose of nitroso compounds. Journal of Cancer Research and Clinical Oncology, 94:1-5.

Layton, D.W., Mallon, B.J., Rosenblatt, D.H., and Small, M.J. (1987). Deriving allowable daily intakes for systemic toxicants lacking chronic toxicity data. Reg. Tox. Pharm., 7:96-112.

O'Gara, R.W., Kelley, M.G., Brown, J., and Mantel, N. (1965). Induction of tumors in mice given a minute single dose of dibenza[a,h]anthracene or 3-methylcholanthrene as newborns. A dose-response study. Journal of the National Cancer Institute, 35:1027-1042.

Stoica, G., and Koestner, A. (1984). Diverse spectrum of tumors in male Sprague-Dawley rats following single high doses of n-ethyl-n-nitrosourea (ENU). American Journal of Pathology, 116:319-326.

Stoner, G.D.. and Shimkin, M.B. (1985). Lung tumors in strain A mice as a bioassay for carcinogenicity. In: Handbook of Carcinogen Testing. H.A. Millman and E.K. Weisburger. Noyes Publishers, Park Ridge, New Jersey, pp. 179-214.

Terracini, B., Shubik, P., Della and Porta, G. (1960). A study of skin carcinogenesis in the mouse with single applications of 9,10-dimethyl-1,2-benzanthracene at different dosages. Cancer Research, 20:1538-1542.

BLANK

IX. BIOTECHNOLOGY

NOTE: Papers with the following titles were presented at the Conference but are not included in this document:

Modification of the Ditam (Diffusion Through a Membrane) Assay and Apparatus for the Detection of Small Molecular Weight Substances

Partial Purification and Characterization of a High Affinity Ca^{2+} Channel Receptor from Porcine Brain

A Nicotinic Receptor Optical Biosensor

Functional Reconstitution of Olfactory Receptor for Analytical Application

The following paper presented at the Conference was received too late to be included in this section; it is contained in Appendix C.

Induction of Enhanced Strains of a Thermophile That Synthesizes an OPA Anhydrase Effective in Detoxifying Soman

BLANK

PURIFICATION PROCEDURES FOR OPA ANHYDRASE-2 FROM HALOPHILE JD6.5

Tu-chen Cheng, Rebekah A. Deas, Joseph J. DeFrank and Ilya Elashvili

Biotechnology Division, U.S. Army Chemical Research, Development and Engineering Center, Aberdeen Proving Ground, MD, 21010.

ABSTRACT

The obligate halophilic isolate, JD6.5 (tentatively identified as a species of *Alteromonas*), possesses several DFP-hydrolyzing Organophosphorus acid (OPA) Anhydrases. The predominant one, designated OPA Anhydrase-2, has been purified to homogeneity by $(NH_4)_2SO_4$ fractionation, DEAE-Sephacel and Hydroxyapatite chromatography, gel permeation HPLC and non-denaturing polyacrylamide gel electrophoresis. The purified enzyme gave a single band with a molecular weight of 60,000 on SDS-PAGE in the presence or absence of DTT, indicating that the enzyme is a single polypeptide chain. The final enzyme preparation had a specific activity of approximately 300 μmoles DFP hydrolyzed/min/mg protein in the presence of Mn^{++}, representing a greater than 1000 fold purification. The purified OPA Anhydrase-2 has also been found to react with rat anti-serum and monoclonal antibody prepared against the enzyme.

INTRODUCTION

Organophosphorus Acid (OPA) Anhydrases are enzymes that are able to hydrolyze a wide variety of organophosphates including fluoride containing agents, acetylcholinesterase inhibitors and pesticides. Diisopropylfluorophosphate (DFP) is a common substrate used to screen for OPA anhydrase activity. OPA anhydrases were found in different sources both in procaryotic and eukaryotic organisms (1-9). In the past, these enzymes were called DFPases, somanases, paraoxonases or parathion hydrolases, based on their substrate specificity. The given name was selected during First DFPase Workshop (Marine Biological Laboratory, Woods Hole, MA, June 1987) for their basic activity. So far, nothing is known either about their natural substrate or function.

The obligate halophilic isolate JD6.5 was isolated from Grantsville Warm Springs (Utah) by Dr. Joseph DeFrank in 1985. This isolate posseses several DFP-hydrolyzing OPA anhydrase activities. The present paper describes the isolation and purification procedures for OPA anhydrase-2, the predominate enzyme from JD6.5.

EXPERIMENTAL

Organism and cultivation. Isolate JD6.5 was isolated from Grantsville Warm Springs, which is located approximately 30 miles west of Salt Lake City, Utah, and south of the Great Salt Lake. Cultures were grown in a medium consisting of (grams per liter): NaCl, 50; $MgSO_4.7H_2O$, 10; proteose peptone (Difco), 10; yeast extract, 6; casamino acid, 5; and HEPES, 2.5 (pH6.8). Inoculated flasks (4 or 6 liter) containing

1-1.5 liters of medium were incubated at 37 ° C, on a rotary shaker at 240 rpm, for 18-24 hours. Cell were then harvested by centrifugation (7,500xg) and stored -20 ° C.

Enzyme assay. OPA Anhydrase activity was routinely assayed by monitoring fluoride release by an ion-specific electrode as has been described numerous times in the literature (7). The reaction medium contained, 500 mM NaCl, 50 mM Bis-Tris Propane, pH 7.2, 3 mM DFP (in isopropanol), 1 mM $MnCl_2$ and 10-50 ul of enzyme solution in a total volume of 2.5 ml. Assays were routinely run at 25 ° C in a thermostatically controlled vessel with stirring. The enzyme sample was preincubated in the reaction medium for 3 minutes before reaction was initiated by the addition of the DFP. The reaction was monitored for 4 minutes and the rate of fluoride release corrected for spontaneous DFP hydrolysis. One unit of OPA Anhydrase activity catalyzes the release of 1.0 μmole of F^- per min at 25 ° C. Specitic activity is expressed as units per milligram of protein.

Enzyme purification. All procedures were conducted at 4 ° C, and all centrifugations were at 46,000xg for 30 min.

Frozen or freshly harvested cells were respended in 10BM buffer (10 mM Bis-Tris Propane, 0.1 mM $MnCl_2$, pH 7.2) at a ratio of 1 g of cells for each 3 ml of buffer. The cells were disrupted by passage through a French Pressure cell (SLM Aminco) at 16,000 psi. Cellular debris was removed by centrifugation. The crude cell supernatant which contained OPA anhydrase activity, was treated with 20% protamine sulfate to final concentration of 2%. After centrifugation, the supernatant was then fractionated with solid $(NH_4)_2SO_4$ to give the 30-65% (saturation) precipitate. The pellet was resuspended in a minimal volume of 10 BM buffer and dialyzed against several changes of 20 volumes of the same buffer.

The dialyzed sample was applied to a DEAE-Sephacel (Pharmacia) column (5x20 cm) previously equilibrated with 10 BM buffer. The column was washed to remove non-binding proteins followed by 200 mM NaCl in 10 BM. The enzyme fraction was eluted with a 4-liter linear gradient of 200 to 600 mM NaCl. Active fractions were pooled, concentrated by precipitation at 65% $(NH_4)_2SO_4$ and the pellet dissolved in 10 BM supplemented with 100 mM NaCl. The solution was dialyzed overnight against this buffer.

The enzyme solution was loaded onto a Hydroxyapatite (HA) Ultrogel (IBF Biotechnics) column (2.6x14 cm) previously equilibrated with the the same buffer described above. After non-binding protein was eluted, elution was carried out with a linear gradient of 5 to 150 mM KH_2PO_4. Enzyme fractions were pooled and concentrated by 65 % $(NH_4)_2SO_4$. After centrifugation, the pellet was redissolved in 10 BM supplemented with 100 mM NaCl and dialyzed against the same buffer.

The enzyme solution was further purified on HPLC-GTi system (LKB) using two sequencial GF-250 column (0.94x25 cm) (DuPont) and run with the same buffer at a flowrate of 0.5 ml fraction/min. The pooled enzyme fraction was concentrated with Centricon-30 concentrator (Amicon) and loaded on 7 % polyacrylamide gel. Electrophoresis was performed accoding to Laemmli (10) but without SDS and DTT. Immediately after the electrophoresis, the bands containing enzyme activity were cut out of the gel and eluted in the same electrophoresis with Extraphor Electrophoretic Concentrator (LKB).

SDS-PAGE and Protein Determination. Sodium dodecylsulfate polyacrylamide gel electrophoresis (SDS-PAGE) was performed according to Laemmli (10). The protein bands were visualized with the Gelcode Silver Stain Kit (Pierce). The Coomassie Protein Assay Reagent (Pierce) was used for protein determination with bovine serum albumin as the standard.

Preparation of polyclonal and monoclonal antibodies. The polyclonal antiserum to OPA anhydrase-2 was prepared by immunizing a rat (Spraque-Dawley) with the HPLC-purified enzyme fraction. Rat spleen cells were fused with mouse myeloma cell line SP2/OAg 14 (11). The hybridoma cell clone was detected by ELISA assay using microtiter plates coated with crude enzyme preparation. Biotinylated rabbit anti-rat

IgG conjugated to horseradish peroxidase (Sigma Rat Extravidin Staining Kit) was used for detection of antibodies against OPA anhydrase-2. For Western blot analysis (11), the same detection kit was used in immunobinding assay.

RESULTS

Halophile JD6.5 is a gram-negative, aerobic, short rod. requiring at least 2% NaCl and 1% $MgSO_4$ for growth. Fatty acid analysis (Microbial ID, Newark, DE) tentatively identified it as a species of *Alteromonas*. OPA anhydrase-2 is stimulated by Mn^{++} and hydrolyzes DFP, soman, paraxon and several chromogenic substrates (detailed in next paper).

Isolate JD6.5 was routinely grown at 37 °C with vigorous agitation. The effects of Mn^{++} and mutiple metal ions (Wolin salts solution) and OPA anhydrase activity on cell growth is shown in Table 1. While cell growth increase over 40% in growth medium supplemented with Mn^{++}, a slight loss of enzyme activity in crude extract was observed. However, total activity recovered from cells (U/g cells) was greatly reduced when assayed in the presence of Mn^{++}. In contrast, there was a slight increase of OPA anhydrase activity, both in crude extract and total activity, from cell growth in the presence of Wolin salts solution. The possible effects of Mn^{++} and multiple metal additions have not yet been examined.

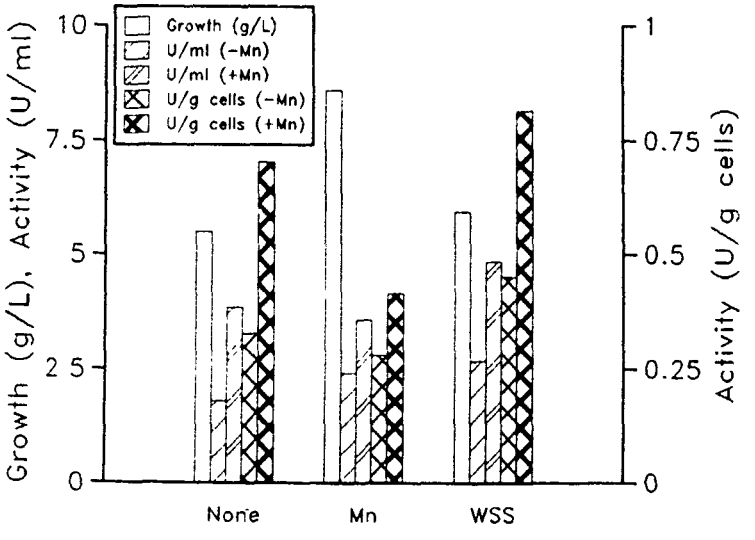

Fig. 1. Requirement of Metals in Growth Media. Regular JD6.5 cultures were grown in a medium as described in *"Experimental Procedures"*. In similar growth conditions, the standard medium was supplemented with either Mn (1 mM) or WSS (Wolin Salts Solution).

A summary of the OPA anhydrase-2 purification is shown in Table 2. After the initial crude enzyme extract was obtained from French Pressure Cell, the supernatant was first treated with 2% protamine sulfate to remove nucleic acids prior to $(NH_4)_2SO_4$ fractionation. The ammonium sulfate fractionation step (30-65%) served to concentrate the enzyme while giving ~3 fold purification over the supernatant with ~124 % recovery.

TABLE 1. Purification of OPAA-2 from JD6.5

Procedure	Total Volume (ml)	Total Protein (mg)	Total Activity (u)*	Specific Activity (u/mg)*	Purification (fold)	Yield (%)
Crude Extract	306	3005	801	0.267	-	100
0 2% Protamine Sulfate	328	2938	853	0 290	1.09	106 5
30-65% Ammonium Sulfate	145	1167	992	0 850	3.18	123.8
DEAE-Sephacel Chromatography (conc)**	19	19.4	570	29 38	110 0	71.2
Hydroxyapatite Chromatography (conc)**	1 3	0 79	205	259.49	971 89	25 6
HPLC-GF 250 (Du Pont)	2 0	0.40	143	357 50	1337.08	17 9
Polyacrylamide Gel Electrophoresis***	4	0.094	26.8	285 11	1067 82	3.3

*Enzyme Unit (u)= μmole/min/ml

**Pooled protein fractions concentrated by 65% ammonium sulfate.

*** Protein concentration was estimated from silver-stained gel (SDS-PAGE) using BSA as a standard.

When the enzyme from the $(NH_4)_2SO_4$ fractionation was applied to a DEAE-Sephacel column equilibrated with 10BM buffer, the enzyme remained bound to the column while the bulk of the non-binding protein passed through. As shown in Fig. 2, a small enzyme fraction (OPA anhydrase-1) was eluted by increasing the NaCl concentration in buffer to 0.2 M. The bulk of enzyme activity (>90% of the total activity), designated OPA Anhydrase-2, eluted with a 0.2 to 0.6 M NaCl gradient in the same buffer. Enzyme activity from this second peak was pooled, concentrated by 65% $(NH_4)_2SO_4$, and used for next step. This chromatographic step resulted in a ~110 fold purification and an overall recovery of ~71%.

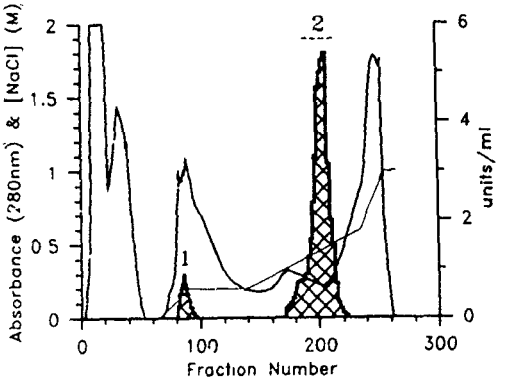

Fig. 2. Fraction of OPA Anhydrases on DEAE-Sephacel.

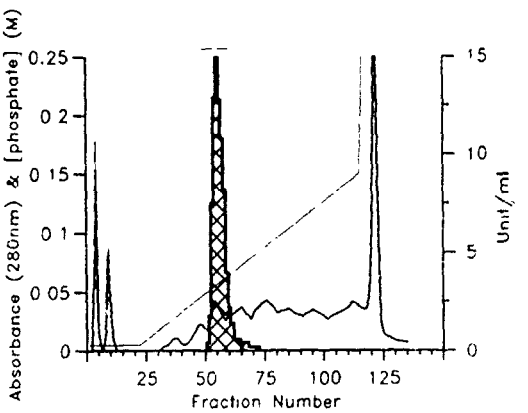

Fig. 3. Purification of OPA Anhydrase-2 on HA column.

Fig. 3 shows that when the enzyme solution from the DEAE-Sephacel was applied to a Hydroxyapatite Ultrogel column equilibrated with 10 mM Bis-tris propane (pH 7.2) containing 100 mM NaCl and 5 mM K_2HPO_4, the enzyme was retained in the column. When a gradient of 5-150 mM K_2HPO_4 was passed through the column, the enzyme eluted in a single peak in early fraction. The pooled enzyme fractions with activity over 1 U/ml were concentration by $(NH_4)_2SO_4$ fractionation. This column gave a ~972 fold purification with an overall recovery of ~26%.

The enzyme solution was further purified through HPLC on GF-250 (gel filtration column). As shown in Fig. 4, the majority of enzyme activity eluted as a sharp peak in fractions 36 and 37. The concentrated enzyme solution was furthe purified on a 7% non-denaturing polyacrylamide gel. After electrophoresis, the gel slices that contained enzyme protein were detected by Fast-stain (Zoion Research Inc. MA) and eluted by an electroelution procedure with an Extraphor Electrophoretic Concentrator

(Pharmacia LKB). This final enzyme preparation had a specific activity of ~300 μmoles DFP hydrolyzed/min/mg protein, representing an overall ~1000 fold purification and ~3% recovery.

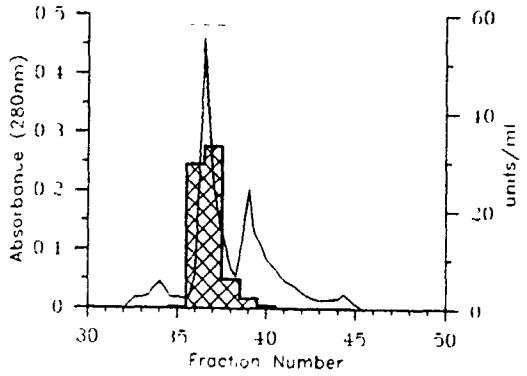

Fig. 4. HPLC chromatograms of OPA Anhydrase-2.

The enzyme preparation at different purification steps was analysed by SDS-PAGE (Fig. 5). A single band with a molecular weight of approximately 60,000 was identified by silver staining. In another gel analysis (Fig. 6A), no difference was observed in the electrophoretical mobility of purified OPA anhydrase-2 under non-reducing condition. The NaOH treatment, which cleaves O-linked glycosylation by beta-elimination, also resulted in no change in molecular weight of the purified enzyme (Fig. 6B) under reducing condition. The results strongly suggest that the final purified enzyme is a cellular protein containing a single polypeptide.

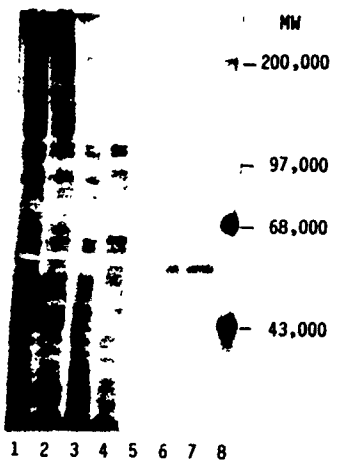

Fig. 5. Analysis of various purified OPA Anhydrase fractions from JD6.5 cells by SDS-PAGE. The protein fractions were identified on 7% SDS-PAGE by silver-stain. Lane 1, crude extract 2 μg. Lane 2, proteins after protamine treatment 2 μg. Lane 3, 30-65% ammonium sulfate fractionate 2 μg. Lane 4, fraction-2 from DEAE-Sephacel step 1 μg. Lane 5, pooled fractions from HA-column 250 ng. Lane 6, pooled fractions from HPLC on GF-250 125 ng. Lane 7, gel purified OPA Anhydrase-2 125 ng. Lane 8, molecular weight markers.

Fig. 6. SDS-PAGE analysis of purified OPA Anhydrase-2. (A) The purified OPA Anhydrase-2 (100 ng) was analyzed by SDS-PAGE under reducing (2) and non-reducing (3) conditions. (B) The purified OPA Anhydrase-2 was incubated with 0.1 N NaOH overnight at 37°C and analyzed by SDS-PAGE. Lane 2 and 3, before and after NaOH treatment. Lane 1 (A and B), molecular weight markers.

The purified OPA anhydrase-2, compared with pooled fractions 1 and 2 from the DEAE-Sephacel step and crude extract, were also analysed by Western blotting after SDS-PAGE. The blots were analysed with either monoclonal antibody, MAb#6 (A) or anti-serum (B). As shown in Fig. 7, a single band of purified OPA anhydrase-2 was detected on both blots (A-5 & B-1). To characterize the anti-serum in term of biological activity, the enzyme activity of purified OPA anhydrase-2 after immunoprecipitation was performed. At a 250 fold dilution of anti-serum, a 50% inhibition of enzyme activity was observed (data not shown). The monoclonal antibody was shown to react with 2 protein bands (MW 78,000 and 74,000) in pooled fraction-1 and crude extract (A-1 & 3). In blot reacted with anti-serum, these two bands and a third band with an estimated molecular weight of 53,000 was also detected (B-2 &4). The results suggest that these three protein bands are fractionated by DEAE-Sephacel chromatography. In addition, in pooled fraction-2 and crude extract (B-3 & 4), a stronger signal of OPA anhydrase-2 and a minor band with molecular weight approximately 170,000 was also observed (B-3). These Western blotting analysis further confirm the purification of OPA anhydrase-2.

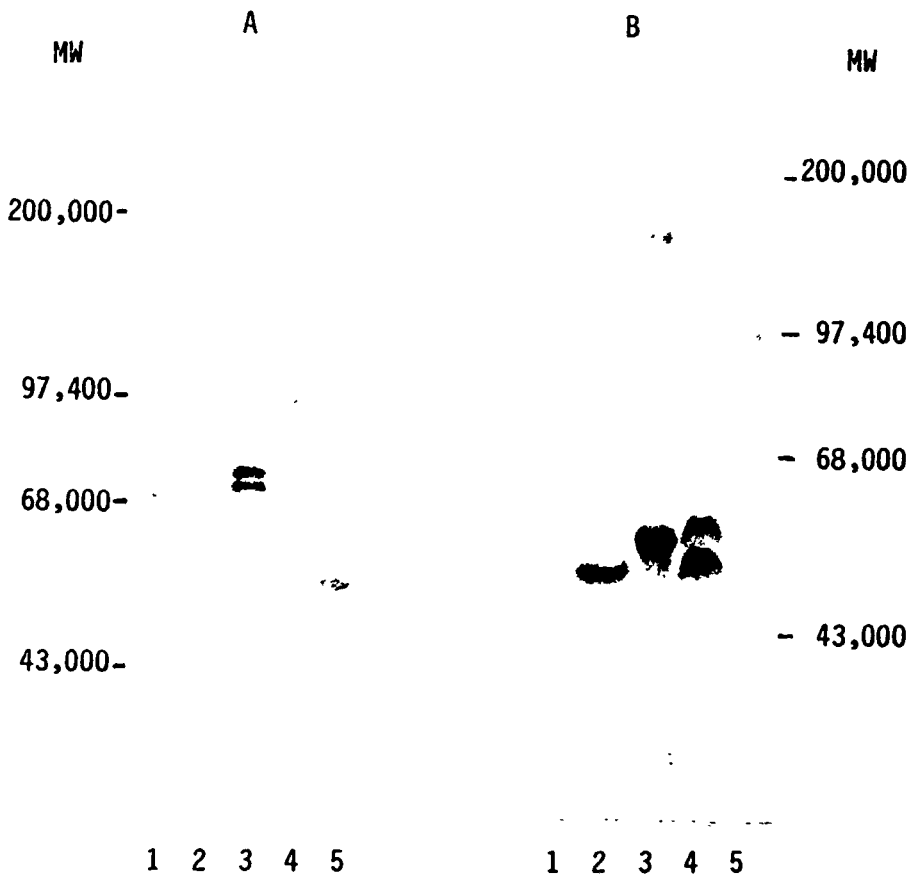

Fig. 7. SDS-PAGE and Western blotting analysis of various OPA Anhydrase fractions. SDS-polyacrylamide gels (7%) were run and blotted onto nitrocellulose membrane and probed with either (A) monoclonal antibody or (B) anti-serum. Lane 1 (A) and 2 (B), 25 μg fraction-1 from DEAE-Sephacel step. Lane 2 (A) and 3 (B), 10 μg fraction-2 from DEAE-Sephacel step. Lane 3 (A) and 4 (B), 25 μg crude enzyme extract. Lane 5 (A) and 1 (B), 20 ng purified OPA Anhydrase-2. Lane 4 (A) and 5 (B), pre-stained molecular weight markers.

CONCLUSION

Halophile JD6.5 requires multiple metal ions in growth media to recover highest OPA Anhydrase activities. The possible effect of multiple additions or different concentrations have not as yet been investigated. Halophile JD6.5 possesses several OPA Anhydrase activities. Among all the OPA Anhydrases of different sources that are able to hydrolyze DFP, the JD6.5 enzyme is known to have highest activity. The predominant enzyme, OPA Anhydrase-2, can be separated from OPA Anhydrase-1 by DEAE-Sephacel chromatography. Using DEAE-Sephacel with a pH gradient in the presence of high salt, OPA Anhydrase-1 was found to contain at least two DFP hydrolyzing activities.

By following the purification procedures described above, OPA Anhydrase-2 has been purified to homogeneity with a greater than 1000 fold purification. SDS-PAGE indicates that the enzyme is composed of single polypeptide with a molecular weight of 60,000 which corresponding well with the apparant molecular weight obtained from Sephacel S-200 chromatography (data not shown). Since several attempts to purify OPA Anhydrase-2 on a PBA-60 column failed to eluate the functional enzyme under non-ionic condition, the behavior suggested that the enzyme molecule is highly hydrophobic.

Protein sequences of the OPA Anhydrase-2 is now in progress at NRL. The polyclonal anti-serum and monclonal antibody against this enzyme have been prepared. The presence and purity of OPA Anhydrase-2 have been determined by Western blotting analysis using these antibodies. Preliminary results also showed that these antibodies can react with various OPA Anhydrases from other halophiles and thermophiles by immunoblotting. These antibodies should therefore facilitate the identification and purification of functionally similar enzymes from other sources even though these enzymes may differ from JD6.5 enzyme in terms of charge, size etc.

The genomic library for JD6.5 has already been prepared with Lambda gt 10 and 11 vectors. With these antibodies and knowledge of protein sequence of purified OPA Anhydrase-2 to prepare DNA probes, they will provide a powerful tool to sceen the genomic libraries.

ACKNOWLEDGEMENT

We are grateful to Dr. Sammy Liu and Ms. Maryalice Miller for the preparation of rat polyclonal anti-serum and monoclonal antibody respectively.

REFERENCES

1. Mazur, A. An Enzyme in Animal Tissue capable of Hydrolyzing the Phosphorus-fluorine bond of Alkyl Fluorophosphates. *J. Biol. Chem.* 164: 271 (1946)

2. Mounter, L. A., Baxter, R. F., and Chautin, A. Dialkylfluorophosphatases of Microorganisms. *J. Biol. Chem.* 215: 699 (1955)

3. Hoskin, F. C. G. and Long, R. J. Purification of a DFP-hydrolyzing Enzyme from Squid Head Ganglion. *Arch Biochem. Biophys.* 150: 548 (1972)

4. Zech, R. and Wigand, K. D. Organophosphate-detoxifying Enzymes in *E. coli*; Gel Filtration and Isoelectric Focusing of DFPase, Paroxonase, and Unspecified Phosphohydrolases. *Experientia* 31: 157 (1975)

5. Landis, W. G., Savage, R. E. Jr., and Hoskin, F. C. G. An Organofluorophosphate-hydrolyzing Activity in *Tetrahymena thermophila*. *J. Protozool.* 32: 517 (1985)

6. Anderson, R. S., Durst, H. D. and Landis, W. G. Initial Characterization of a OPA Anhydrase in the Clam, *Rangia cuneata. Comp. Biochem. Physiol.* 91, 575 (1988)

7. Hoskin, F. C. G. Inhibition of a Soman and Diisopropyl Phosphorofluoridate (DFP)-hydrolyzing Enzyme by Mipafox. *Biochem. Pharmacol.*, 34: 2069 (1986)

8. Chettur, G., DeFrank, J. J., Gallo, B. J., Hoskin, F. C. G., Mainer, S., Robbins, F. M., Steinmann, K. E. and Walker, J. E. Soman Hydrolyzing and Detixifying Properties of an Enzyme from a Thermophilic Bacterium. *Fund. Appl. Tox.* 11, 127 (1988)

9. Chemnitius, J. M., Losch, H., Losch, K. and Zech, R. Organophosphate Detoxicating Hydrolases in Different Vertebrate Species. *Comp. Biochem. Physiol.*, 76: 85 (1983)

10. Laemmli, U. Cleavage of Structural Proteins During the Assembly of the Head of Bacteriophate T4. *Nature (London)*, 227: 680 (1970)

11. Harlow, E. and Lane D. In *Antibodies; A Laboratory Manual. Cold Spring Harbor Laboratory*, Cold Spring Harbor, New York, p141-243 (1988)

12. Davis, L. G., Dibner, M. D. and Battey, J. F. In *Basic Methods in Molecular Biology.* Elsevier, New York, p311-314 (1986)

PROPERTIES OF OPA ANHYDRASE-2 FROM HALOPHILE JD6.5

Tu-chen Cheng, Rebekah A. Deas and Joseph J. DeFrank

Biotechnology Division, Research Directorate
U.S. Army Chemical Research, Development & Engineering Center
Aberdeen Proving Ground, Maryland 21010-5423

ABSTRACT

Several of the physical/chemical properties of the predominant DFP-hydrolyzing Organophosphorus Acid Anhydrase (OPAA-2) from the halophilic bacterial isolate JD6.5, have been determined. In addition to DFP, substrates hydrolyzed include diethyl-*p*-nitrophenyl phosphate (paraoxon), *p*-nitrophenyl ethyl(phenyl) phosphinate (NPEPP), *p*-nitrophenyl methyl(phenyl) phosphinate (NPMPP) and *O*-1,2,2-trimethylpropyl methylphosphonofluoridate (Soman). An analog of DFP, Mipafox (N,N'-diisopropyl phosphorodiamidofluoridate) is a non-metabolized, competitive inhibitor of the enzyme. Common substrates for esterases, phosphatases, phosphodiesterases, and phospholipases are not hydrolyzed by this enzyme. OPAA-2 is stimulated by manganese and cobalt, has a pH optimum of ~8.5 and a temperature optimum of ~50° C. The addition of reducing agents has a stimulatory and stabilizing effect on the enzyme.

INTRODUCTION

As described in the previous paper[1], the halophilic bacterial isolate JD6.5 contains a Diisopropylfluorophosphate (DFP) hydrolyzing Organophosphorus Acid Anhydrase (OPAA-2), that may have significant applications in the enzymatic decontamination of G-type chemical warfare agents. The potential utility of enzymes of this type for decontamination purposes has been recognized since their discovery by Mazur[2] in 1946, and has been reviewed by Mounter[3] in 1963 and Landis[4] in 1989.

Preliminary characterization of the properties of OPAA-2 was presented at the 1988 Scientific Conference on Chemical Defense Research[5]. However, the earlier studies were conducted with enzyme that was only partially purified. The results reported in this paper were obtained with enzyme purified to homogeneity as described previously[1].

EXPERIMENTAL

ORGANISM

Bacterial isolate JD6.5 is an obligately halophilic, Gram-negative rod, which was obtained from Grantsville Warm Springs, Utah[6]. Based on analysis of its fatty acids (Microbial ID, Inc., Newark, DE) it has tentatively been identified as a strain of *Alteromonas*. Growth of the organism and purification of the enzyme has been described previously[1,5].

ENZYME ASSAYS

OPA Anhydrase activity was assayed by monitoring fluoride release by ion-specific electrode as has been described numerous times in the literature[7,8]. The reaction medium contained (unless otherwise noted) 500 mM NaCl, 50 mM Bis-Tris Propane, pH 7.2, and ±1 mM $MnCl_2$ in a total volume of 2.5 ml. The enzyme sample (5-25 μl) was preincubated in the reaction medium for one minute before the addition of DFP (25 μl of 300 mM in isopropanol) to 3 mM. After the initial 2 minutes, the fluoride release was monitored for 4 minutes. All reported rates of fluoride release are corrected for spontaneous hydrolysis under identical conditions. One unit of OPA Anhydrase activity is defined as that amount of enzyme that catalyzes the release of 1.0 μmole F^-/minute.

Hydrolysis of chromogenic substrates was conducted in an identical reaction mixture as above, with a reduction in substrate concentration to 5-100 μM. Activity was monitored by following the increase in absorbance at 405 nm (for *p*-nitrophenol) and units expressed as 1.0 μmole *p*-nitrophenol released/minute. The concentration of *p*-nitrophenol was determined from a standard curve with authentic material.

RESULTS

SUBSTRATE SPECIFICITY

The specific activity of OPAA-2 against a variety of substrates is illustrated in Fig. 1. As can be seen, of all the substrates tested, the highest activity was with DFP. The blank bar for GD (Soman), EBU (2-ethylbutyl methylphosphonofluoridate), and Dimebu (3,3-dimethylbutyl methylphosphonofluoridate) is because that while preliminary studies with partially purified enzyme showed activity with the first two compounds, difficulties in scheduling assays with the purified OPAA-2 prevented the acquisition of this data. From the preliminary studies it is expected that the activity with these compounds will be between 50-80% that of DFP.

FIGURE 1

Substrate Specificity of JD6.5 OPAA-2

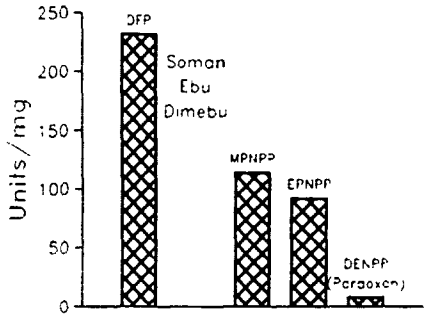

FIGURE 2

Inhibition of JD6.5 OPAA-2 by Mipafox

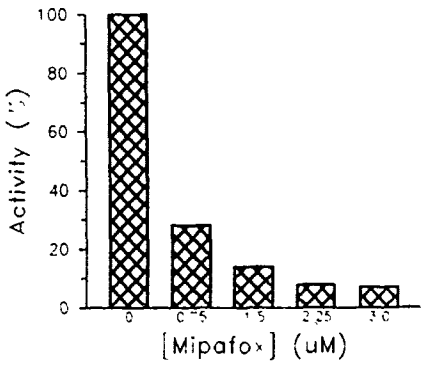

In addition to these compounds, a variety of potential substrates for esterases, phosphatases, phosphodiesterases, phosphotriesterases, and phospholipases were examined as summarized in Table 1. Three analogs of G-agents were also tested. These compounds showed little or no activity with OPAA-2. Only Mipafox, of the compounds tested, showed more than minimal activity, but for Mipafox the more interesting feature is its high level of inhibition of the enzyme for the hydrolysis of DFP.

Figure 2 shows the effect of incubation of OPAA-2 with micromolar levels of Mipafox. The Mipafox was added to the enzyme during the one minute preincubation before the addition of DFP. At 3.0 μM Mipafox the DFP hydrolysis is inhibited to greater than 90%. However, the inhibition is completely reversible. If the inhibited enzyme is dialyzed overnight against buffer, all the activity against DFP is

restored (data not shown).

TABLE 1

Compounds Not Hydrolyzed by JD6.5 OPAA-2

Esterase Substrates	**Phosphotriesterase Substrates**
p-Nitrophenyl acetate	Tris(*p*-nitrophenyl)phosphate*
Phosphatase Substrates	**Phosphodiesterase Substrates**
p-Nitrophenyl phosphate α-Naphthyl phosphate β-Naphthyl phosphate Indolyl phosphate 5-Bromo-4-chloro-3-indolyl phosphate (BCIP)	Bis(*p*-nitrophenyl)phosphate* *p*-Nitrophenyl phenyl phosphonate β-Naphthyl phenyl phosphonate
Phospholipase C Substrates	**G-Agent Analogs**
p-Nitrophenyl phosphorylcholine	*O*-Isopropyl-*t*-butyl phosphonofluoridate* *O*-Isobutyl-*t*-butyl phosphonofluoridate Diisopropylphosphorodiamidofluoridate (Mipafox)†

* Substrates showing low activity (<0.5% of DFP)
† Activity <5.0% of DFP

EFFECT OF pH AND TEMPERATURE

With DFP as substrate, the effect of pH on the activity of OPAA-2 was examined. In addition, the kinetic parameters were determined at each pH value. These parameters are plotted in Fig. 3. The K_{cat} is the catalytic constant or turnover number for the enzyme. It represents the number of substrate molecules converted to products per active site per unit time[9]. In this instance the units for K_{cat} are molecules of DFP hydrolyzed per second and was calculated by multiplying the Specific Activity of the enzyme by its molecular weight in thousands and dividing by 60. Since the molecular weight of OPAA-2 is 60,000 Daltons, the number value for K_{cat} (s^{-1}) is the same as the Specific Activity.

The K_M is the dissociation constant of the enzyme-substrate and is plotted as [mM]. The parameter K_{cat}/K_M is sometimes referred to as the "specificity constant" or "catalytic efficiency." The units for K_{cat}/K_M are ($s^{-1}M^{-1}$). Since the diffusion-controlled encounter frequency of an enzyme and a substrate should be about 10^9 $s^{-1}M^{-1}$ this represents the upper limit for K_{cat}/K_M. A "perfect" enzyme should have a $K_{cat}/K_M \simeq 10^8$ - 10^9 and a K_M significantly greater that the concentration of substrate normally encountered.

Unlike previous studies with partially purified enzyme, the observed pH optimum for OPAA-2 was found to be ~8.5. Earlier experiments suggested an optimum of 7.5. The highest level of catalytic efficiency (K_{cat}/K_M) was seen at pH 6.8. This value may give insight into the pK_a of the enzyme and the identity of ionizing groups in the active site or on the surface. From these preliminary studies the presence of a histidine or a cysteine is suggested.

The effect of temperature on the reaction rate of the hydrolysis of DFP by OPAA-2 is shown in Figure 4. The initial reaction rate of the enzyme with 3 mM DFP reached its maximum at 50 ° C at pH 7.2 in the presence of 1 mM $MnCl_2$. Although significant levels of activity were still being observed, the reaction was not followed at temperatures higher than 55 ° C to prevent damage to the fluoride electrode.

FIGURE 3

pH Profile of JD6.5 OPAA-2 with DFP

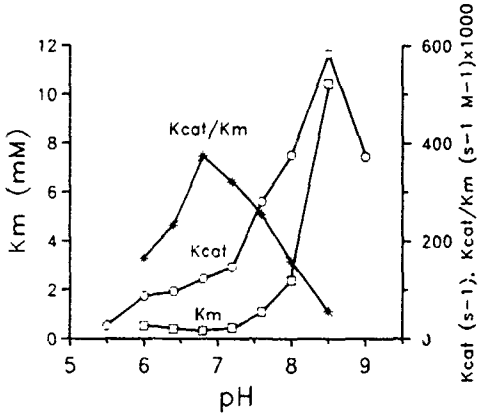

FIGURE 4

Temperature Profile of JD6.5 OPAA-2

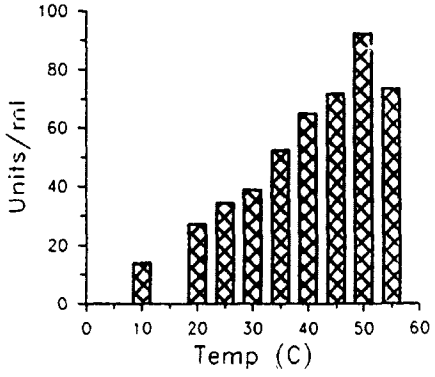

Although detailed stability studies have yet to be carried out, some preliminary information was obtained with samples treated with a variety of "protective" compounds and stored at -70° C. Figure 5 shows that over the course of six months the presence of glycerol had no apparent stabilizing effect, whereas dithiothreitol (DTT) not only improved stability but appeared to stimulate activity. This is in line with the possible presence of an active sulfhydryl group (suggested by the pH studies).

To confirm the stimulation of OPAA-2 activity by reducing agents, enzyme samples were incubated at 4° C in the presence of 0.1 or 1.0 mM DTT or β-mercaptoethanol (BME). Figure 6 shows the result of this study. Both reducing agents gave a stimulation to the enzyme samples over the course of the experiment with DTT causing the greatest increase. During the 18 hours of the experiment, the untreated enzyme remained at constant activity.

FIGURE 5

Storage Stability of JD6.5 OPAA-2 at -70° C.

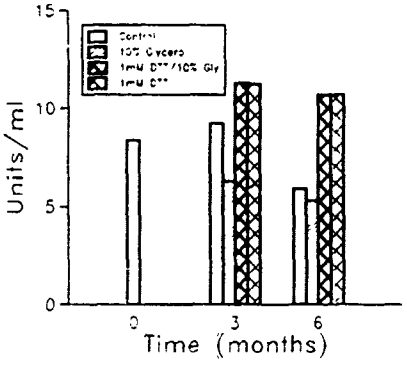

FIGURE 6

Effect of Reducing Agents on DFP Hydrolysis

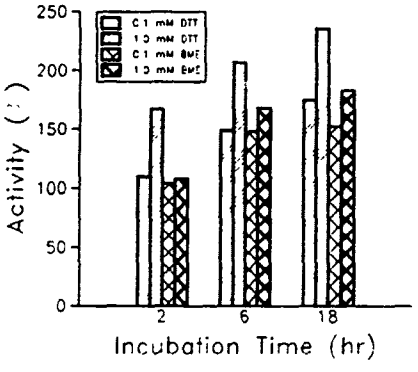

EFFECT OF INHIBITORS

To determine whether OPAA-2 does have a sulfhydryl group in its active site, the effect of several sulfhydryl-specific inhibitors was examined. The inhibitors, *p*-chloromercuribenzoate (PCMB), iodoacetic acid (IAA), and N-ethylmaleimide (NEM) were added to the enzyme at 0.1, 1.0 and 5.0 mM and preincubated for 1 hour at 4° C. As illustrated in Figure 7, all the reagents caused an inhibition of activity of OPAA-2 against DFP, with NEM having the greatest effect. Although these results suggest the involvement of a sulfhydryl group in the activity of the enzyme, they do not eliminate the possibility of a reaction with a group distant from the active site, but important for enzyme stability or three-dimensional configuration.

EFFECT OF METALS

The implication of metal ions in the stabilization and stimulation of OPA Anhydrase activity has recently received much greater attention[10,11]. It had been known from previous studies that manganese caused a stimulation of the partially purified OPAA-2 from JD6.5. Earlier attempts to inhibit the enzyme with EDTA showed only a slight effect[5]. The inhibitory effect of EGTA was examined owing to its stronger binding of divalent metals. In Figure 8, it can be observed that incubation of the enzyme with 0.1 mM EGTA resulted in a nearly complete inhibition of activity against DFP. Surprisingly, on addition of manganese (0.4 mM) to the reaction mixture, the level of activity rose to levels considerably higher than that seen with the original enzyme sample. This effect varies from one preparation of enzyme to another. A possible explanation of this phenomenon is that the native enzyme when synthesized becomes partially loaded with metal ions that are not optimal for activity. The removal of these metals would allow complete loading with manganese. In growth conditions where higher levels of manganese may be present, the enzyme may be more completely loaded and this increase in activity would not be observed.

FIGURE 7

Inhibition of JD6.5 OPAA-2 by Sulfhydryl Reagents

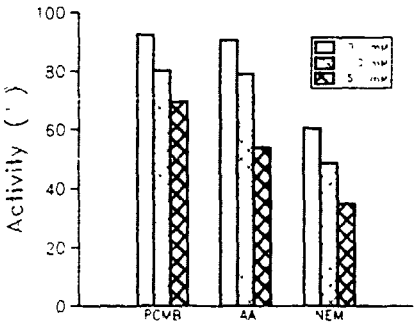

FIGURE 8

Effect of EGTA on DFP Hydrolysis

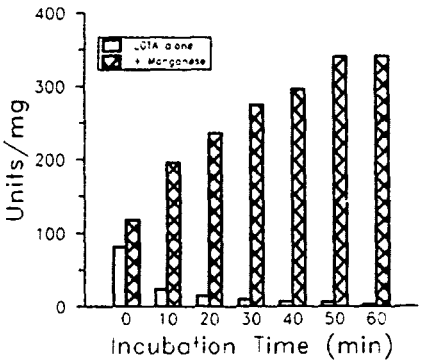

The scenario described above may explain the results summarized in Figures 9-11. The treatment of the enzyme preparation with EGTA and readdition of manganese does not result in a higher level of activity. The experiments summarized in these figures were conducted in the following manner. The enzyme sample was initially tested, as is, with the various metals shown. The result is shown by the first bar in the cluster (average of two or more assays). A separate sample of enzyme was incubated with 0.1 mM EGTA for 60 minutes at room temperature and then assayed for activity with DFP. The EGTA-inhibited activity is represented by the second bar. At that time the metal being tested was added to the reaction mixture (at 0.4 mM) and the activity monitored after two minutes. The third bar shows this result. Finally, manganese was added to the reaction to determine if any additional stimulation would be

observed. The fourth bar of the cluster gives the results of this addition.

Three types of reactions were observed. In Figure 9, the activity of the starting material (purified OPAA-2 with no added metals), as well as manganese and cobalt addition is illustrated. Both of these metals show nearly complete reactivation of the enzyme with no additional stimulation by manganese.

In Figure 10, the metals tested (Cs, Cu, Fe, Mg, and Ni) showed little or no reactivation of the enzyme, but also did not block reactivation by manganese addition.

FIGURE 9

Metal/EGTA-Treatment - Group 1

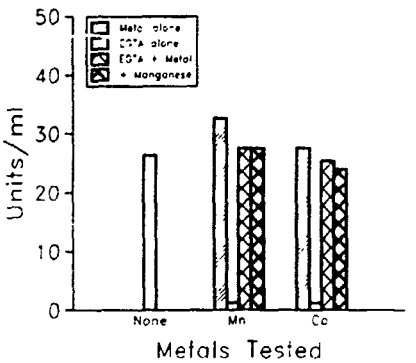

FIGURE 10

Metal/EGTA Treatment - Group 2

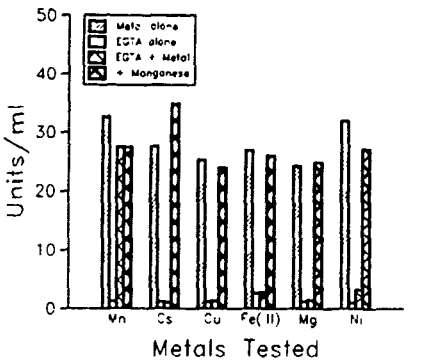

The third group of metals (calcium and zinc) not only inhibited the enzyme to varying degrees, but also prevented reactivation by manganese. Zinc, in particular, showed significant inhibitory action against the OPAA-2, both as an exogenous inhibitor as well as blocking its reactivation. The results shown in Figure 11 would suggest that if the hypothesis proposed for the results observed in Figure 8 is correct, then the native enzyme contained significant levels of calcium or zinc that rendered it inactive. Growth of JD6.5 in the presence of sufficiently high levels of manganese should help remedy this situation.

FIGURE 11

Metal/EGTA Treatment - Group 3

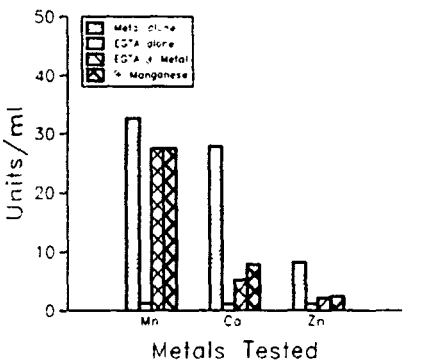

CONCLUSIONS

The G-agent degrading enzyme OPAA-2 from halophilic isolate JD6.5 has been shown to possess high activity with several toxic organophosphorus compounds. Studies with the purified enzyme have shown a pH optimum of 8.5 and a temperature optimum of 50 ° C. Under these conditions the calculated turnover number for the enzyme would be ~96,000 molecules of DFP hydrolyzed/min/enzyme molecule. At room temperature the turnover number is still a respectable 35,660 min^{-1}.

The enzyme is strongly, but reversibly inhibited by both Mipafox and EGTA. Stimulation and

stabilization of the enzyme is observed with reducing agents such as DTT and by the metals manganese and cobalt. The presence of an active sulfhydryl group was suggested by the inhibition of enzyme activity by PCMB, IAA, and NEM.

Although considerable work remains to be done in the determination of the optimum conditions for storage, stabilization and/or immobilization of OPAA-2, it appears to be an excellent candidate for incorporation into an enzyme-based decontamination system.

REFERENCES

1. Cheng, T.-c., R.A. Deas, J.J. DeFrank, and I. Elashvili. 1989. Purification Procedures for OPA Anhydrase-2 from Halophile JD6.5. In *Proceedings of 1989 Scientific Conference on Chemical Defense Research.* (in press)

2. Mazur, A. 1946. An Enzyme in Animal Tissue Capable of Hydrolyzing the Phosphorus-Fluorine Bond of Alkyl Fluorophosphates. *J. Biol. Chem.,* **164**: 271-289.

3. Mounter, L.A. 1963. Metabolism of Organophosphorus Anticholinesterase Agents. In *Hanbuch de Experimentellen Pharmakologie: Cholinesterases and Anticholinesterase Agents,* Kolle, G.B. Eds., Springer-Verlag, Berlin, 486-504.

4. Landis, W.G. and H.D. Durst. 1989. Distribution, Nature and Utility of Organophosphate Acid Anhydrases. CRDEC Technical Report. (in press)

5. DeFrank, J.J., T.-c. Cheng, and R.A. Deas. 1989. Purification and Properties of OPAA II from Halophile #6-5. In *Proceedings of 1988 Scientific Conference on Chemical Defense Research,* CRDEC-SP-013, 703-711.

6. DeFrank, J.J., R.A. Deas, and B.L. DeVivo. 1989. Preliminary Screening of Halophilic Bacteria for G-Agent Degrading Enzyme Activity. CRDEC-TR-080.

7. Hoskin, F.C.G., and A.H. Roush. 1982. Hydrolysis of Nerve Gas by Squid Type Diisopropylphosphorofluoridate Hydrolyzing Enzyme on Agarose Resin. *Science,* **215**: 1255-1257.

8. Landis, W.G., M.V. Haley, and D.W. Johnson. 1986. Kinetics of the DFPase Activity in *Tetrahymena thermophila. J. Protozool.,* **33**: 216-218.

9. Fersht, A. 1985. *Enzyme Structure and Mechanism.* W.H. Freeman and Company, New York.

10. Hoskin, F.C.G., G. Chettur, S. Mainer, K.E. Steinmann, J.J. DeFrank, B.J. Gallo, F.M. Robbins, and J.E. Walker. 1989. Soman Hydrolysis and Detoxication by a Thermophilic Bacterial Enzyme. In *Enzymes Hydrolyzing Organophosphorus Compounds* (E. Reiner, W.N. Aldridge, and F.C.G. Hoskin, eds), Ellis Horwood, Ltd., Chichester, England (John Wiley, American distributors), 53-64.

11. Hoskin, F.C.G., J.J. DeFrank, B.J. Gallo, and J.E. Walker. 1989. Isomers of Soman as Research Tools for the Study of Organophosphorus Acid (OPA) Anhydrases (formerly DFPases). In *Proceedings of the Third International Symposium on Protection Against Chemical Warfare Agents* (Swedish Defense Research Establishment, Umea, Sweden, editors and publishers), 187-194.

BLANK

MOLECULAR TOPOGRAPHY OF SQUID OPA ANHYDRASE (EC 3.1.8.1) AS REVEALED BY SPECTROSCOPIC STUDIES

John E. Walker, James J. Connolly, and Diane M. Steeves
U.S. Army Natick Research, Development and Engineering Center
Natick, Massachusetts 01760-5020

Francis C. G. Hoskin and Krishma S. Rajan
Illinois Institute of Technology
Chicago, Illinois 60616

ABSTRACT

An enzyme (EC 3.1.8.1) isolated from nerve, hepatopancreas and saliva of squid (Loligo Pealei) has been shown to hydrolyze the P-F bond of G-agents, resulting in the detoxification of the nerve agent. The molecular weight of the enzyme is 26K and amino acid analysis shows that the protein contains 6 tryptophans and 11 cysteine residues. Studies involving the quenching of tryptophan fluorescence revealed that in the native enzyme 2 tryptophans are exposed on the molecular surface and 4 residues are buried. Titration with 5,5'dithio bis-(2-nitro benzoic acid), DINB, showed one available -SH and 5 S-S bridges. Ca^{+2} is required for enzymatic activity, but the enzymes' resistance to denaturation (6M urea) and disulfide reduction (dithiothreitol) indicates that maintenance of secondary and tertiary protein structure is not needed for active site functionality. A model is postulated in which Ca^{+2} forms an intramolecular bridge in the region near the enzymes' active site and is uneffected by changes in secondary or tertiary protein structure.

INTRODUCTION

Squid OPA Anhydrase EC 3.1.8.1 (formerly Squid DFPase) is a single chain protein of molecular weight 26,000 (1) and an isoelectric point of 5.5 (2). In a series of papers from 1965 to 1983, F.C.G. Hoskin and coworkers established that the enzyme is found in all tissues of cephalopods and not in members of other phyla, or even in other classes of this same phylum

(3,4,5,6). The enzyme was found to hydrolyze the nerve agents Soman (1,2,2-trimethyl propylmethylphosphonofluoridate) and Sarin (isopropyl methylphosphonofluridate) and could be covalently attached to agarose without loss of its catalytic activity (7). Military applications of the squid enzyme in a decon formulation to detoxify G-agents have been investigated by K.S. Rajan and coworkers at the Illinois Institute of Technology Research Institute (IITRI). They have shown that a phosphate buffered solution of the enzyme (100 units in 100 mls) could decontaminate 200-250 mg Soman/square inch material surface. The enzyme retained > 96% of its initial activity after each decontamination experiment, indicating its recovery and reuse potential (8). The stability characteristics of the enzyme indicate plausible field deployment (9).

In this paper we report on studies of the secondary and tertiary structure of squid OPA anhydrase relating to the enzymes' stability.

MATERIALS AND METHODS

Isolation of Squid OPA Anhydrase from the Hepatopancreas of Squid.

The procedure followed was that of Garden et al (2) as modified by Rajan (10). The molecular weight of the purified OPA anhydrase was determined by SDS polyacrylamide gel electrophoresis using the discontinuous buffer method of Laemelli (12).

Assay for Enzyme Activity.

Squid OPA anhydrase activity was assayed using diisopropyl fluorophosphate (DFP) as the substrate (1). The release of F-ion was monitored with a fluoride sensitive electrode (11) and monitored with an Orion Research Microprocessor ion analyzer 901 (Orion Research).

Circular Dichroism.

Circular dichroism spectra of the purified OPA anhydrase were recorded in the wavelength range of 240 to 190 NM on an AVIV 61DS solid-state instrument (AVIV Associates, Lakewood, NJ). The instrument is equipped with a 50 kH_z photoelastic modulator and an end-on photomultiplier. The instrument is interfaced with an AT&T computer which is used for all mathematical calculations. Secondary structure determinations were made using the computer method of Yang (13) which was supplied with the AVIV 61DS.

Fluorescence Quenching.

Fluorescence measurements were performed using an SLM 4800S spectrofluorometer (SLM Instruments). Quenching experiments were carried out according to the method of Holmes and Robbins (14). Solutions were excited at 305 NM and the emission spectra recorded from 320 NM to 450 NM. The quenchers were reagent grade and were used without further purification; acrylamide (Eastman), N-methyl nicotinamide chloride (Sigma), and potassium iodide (Eastman). The calculations were performed by the method of Lehrer (15).

Interfilter effects were corrected by the method of Lakowicz (16).

Amino Acid Analysis.

Amino acid analyses were performed by the Pico-Tag method (Waters) (17).

Determination of Free SH Groups.

The method of Potter et al (18) was used.

FLUORESCENCE QUENCHING OF TRYPTOPHENYL RESIDUES IN SQUID OPA ANHYDRASE

- Quenchers: N'-Methylnicotinamide Chloride, Acrylamide, and Potassium Iodide
- Calculations:

$$F_0/F = 1 + K_Q[Q]$$

with $K_Q = k^* \tau$

$$F_0/\Delta F = 1/[Q] f_a K_Q = 1/f_a$$

where F_0 and F are the fluorescent intensities in the absence and presence of quencher. K_Q is the Stern-Volmer quenching constant, K^* is the biomolecular rate constant for quenching, τ is the average fluorescent life time in the absence of quencher. [Q] is the concentration of the quencher, f_a is the fractional accessibility of tryptophyl residues, and k_Q is their effective quenching constant.

Addition of Metal ions and Metal ion Chelators to Squid OPA Anhydrase.

Metal ions and chelators were made up in 25 mM HEPES buffer pH 7.2 at 100 mM concentrations. Suitable additions were made to the enzyme solutions to give a range of concentrations from 1 mM to 0.1 mM. The reaction proceeded at room temperature for 30 minutes and changes in OPA anhydrase were monitored using the DFP assay method.

RESULTS

The amino acid analysis of squid OPA anhydrase is given in Table 1.

TABLE 1

AMINO ACID COMPOSITIONAL ANAYSIS OF SQUID HEPATOPANCREASE OPAAase

amino acid	average pmol	mole percent	percent SD	residue number
cys acid	169.51	5.39	.53	10 8 (11.0)
asx	409 78	13.03	46	26.0
thru	257.06	8.12	.73	16 0
ser	118.82	3.75	53	7.0
glx	353 87	10.93	1.07	21.8 (22.0)
pro	121 4	3.84	.32	7.6 (8.0)
gly	373.27	11.85	.95	23.2 (23.0)
ala	224 63	6.74	1.12	13 4 (13.0)
val	230 25	7.38	.35	14.8 (15.0)
met	3.20	0.07	.11	0.02 (0.0)
ile	142.41	4.58	.28	9.0
leu	203 67	6.35	.25	12.8 (13.0)
tyr	32 48	0.94	.99	1.8 (2.0)
phe	5.27	5.27	1.81	10.4 (10.0)
his	73.79	2.41	.27	4.8 (5.0)
lys	171.40	5.50	.39	11.0
arg	130 92	4.09	.27	8.2 (8.0)
trp	nd	nd	nd	(6.0)*

*calculated from extinction coefficient and number of tyrosines

Ellman reagent titration for reactive -SH groups by Potter's method (18) gave 0.7 mole SH/mole of enzyme indicating that all but one of the 11 cysteine residues in the protein exist in disulfide bridging.

The effect of N-methylnicotinamide chloride (NMNCL) on tryptophan fluorescence of squid OPA anhydrase in the presence and absence of quanidine hydrochloride (GdHCL) is shown in Figure 1. The fluorescence data is plotted by the Stern-Volmer relationship as modified by Lehrer (15). Quenching data for acrylamide and KI obeyed the Stern-Volmer relationship (data not shown). The accessibility of the tryptophyl residues of the native protein was estimated by comparing the K_q value to that of the K_q value for a model compound in the presence of N-acetyl-L-tryptophan ethylester NATEE (data not shown). The quenching constants (K_q) were obtained from the slope of the Stern-Volmer plots. The k_q values determined in this manner are apparently a function of the

FIGURE 1

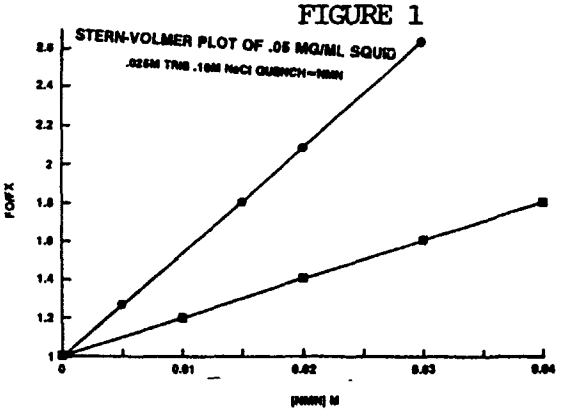

accessibility of the tryptophyl residues in the protein. The number of tryptophyl residues for the squid enzyme that are accessible was calculated from the expression

$$\frac{K_q(\text{enzyme})}{K_q(\text{NATEE})} \times N_p = N_E$$

where N_p is the number of tryptophans in the enzyme and N_E is the number of exposed tryptophans. The results show that of the 6 tryptophans only 2 are accessible in the native squid enzyme. The effects of metal ions and chelators on OPA anhydrase is given in Tables 2 and 3.

TABLE 2

EFFECTS OF 10^{-4} M CHELATORS ON OPA ANHYDRASES (% STIMULATION [+] OR INHIBITION [-])

Chelator	Squid Enzyme (Purified or Axoplasm) (DFP or Soman)
EDTA	-92
EGTA	-75
1, 10-o-Phenanthroline	-5
8-OHQ-5-SA	-2

TABLE 3

RECOVERY OF SQUID-TYPE OPA ANHYDRASE ACTIVITY AFTER CHELATOR INHIBITION

First Treatment Chelator (Conc., Time)	Followed By Cation (Conc., Time)	% Recovery (±Std. dev., n)
EGTA (10^{-4}M, 30 min.)	Ca^{2+} (10^{-3}M, 30 min.)	84 (±20, 8)
EGTA (10^{-4}M, 30 min.)	Mg^{2+} (10^{-3}M, 30 min.)	20 (±10, 8)

The results in Table 3 indicate that squid OPA anhydrase may have a Ca^{+2} requirement. Addition of Ca^{+2} in millimolar quantities to the enzyme without prior treatment of EDTA or EGTA is slightly inhibitory (data not shown). At this time no conclusions can be made as to whether or not Ca^{+2} functions as a cofactor.

Secondary structure changes in squid OPA anhydrase in the presence or absence of EDTA are shown in Figures 2 and 3.

FIGURE 2

FAR UV CD SPECTRA OF SQUID OPA ANHYDRASE IN THE PRESENCE OF EDTA

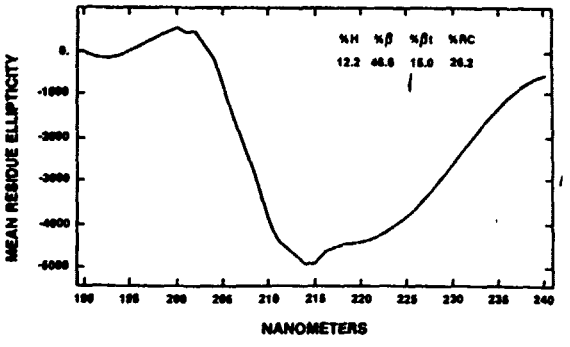

FIGURE 3

FAR UV CD SPECTRA OF SQUID OPA ANHYDRASE

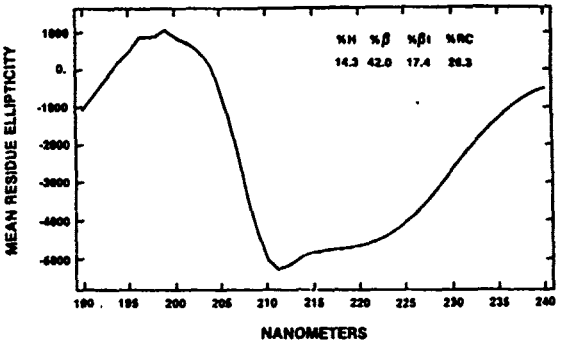

The results shown in Figures 2 and 3 indicate that there is no change in the enzyme's secondary structure when Ca^{+2} is removed.

At unexpected result was obtained when squid OPA anhydrase was denatured by urea and then the disulfide bridges were reduced by dithiothreitol (DTT). As is shown in Table 4, the enzyme retained 85% of its activity.

In 4M quanidine hydrochloride (Gu-HCL) there was complete loss of enzymatic activity indicating that hydrogen bonding may be essential for active site stability. The fluorescence spectra for tryptophan in the presence of urea or quanidine hydrochloride is shown in Figure 4.

TABLE 4

EFFECTS OF DENATURANTS ON SQUID OPA ANHYDRASE

Denaturant	% Loss of Activity
6M UREA	10
6M UREA & DTT	15
4M Gu-HCL	100

FIGURE 4

TRYPTOPHAN FLUORESCENCE OF SQUID OPA ANHYDRASE

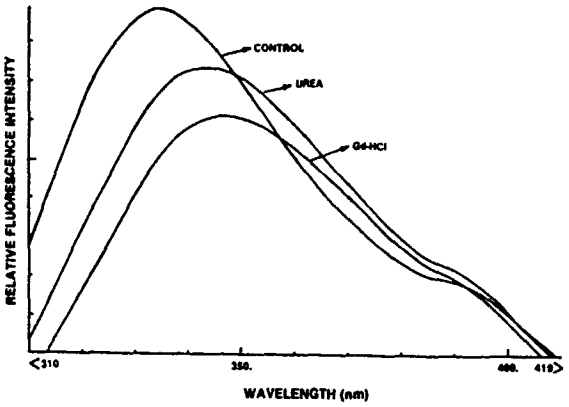

The shifting of the tryptophan fluorescence emission to higher wavelengths indicates an opening up (denaturation) of the enzyme structure (18).

DISCUSSION

Table 5 gives the properties of squid OPA Anhydrase.

TABLE 5

PHYSICO-CHEMICAL PROPERTIES OF SQUID OPA ANHYDRASE

- Narrow Distribution; Squid nerve, saliva, hepatopancreas
- Molecular Weight; 30,000
- Isoelectric Point, 5.5
- Soman/DFP = 0.25
- Km 2.5 x 10^{-3}M
- Hydrolyzes all isomers of Soman
- Ca^{+2} requiring, not Ca^{+2} stimulated. Ca^{+2} may be involved in intramolecular bonding
- Mipafox indifferent
- E_M^{280} = 38,500
- Disulfide bridges not essential for enzyme activity
- 2 of the 6 TRP residues are exposed to the microenvironment

Our results show that a certain degree of secondary and tertiary structure disruption can be tolerated by the enzyme (e.g. retention of activity in 8M urea under reducing conditions), but that a divalent cation, probably CA^{+2}, is an essential requirement. Finally, disulfide bridging may not be in the active site domain of the enzyme. A possible model for the enzyme is shown in Figure 5.

FIGURE 5

SQUID OPA ANHYDRASE

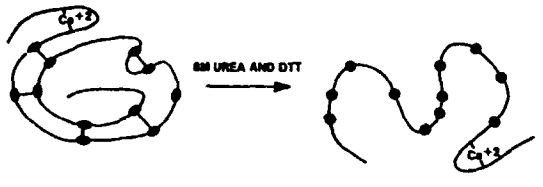

Ca^{+2} may be envisioned as intramolecularly binding two portions of the peptide chain and possibly configuring the active site by interacting with glutamic acid and aspartic residues. In addition to two folds of the peptide chain being linked by Ca^{+2}, intramolecular hydrogen bonds

may play an active role since enzymatic activity is lost on exposure to 4M quanidine hydrochloride. Such a model is likened to the Ca^{+2} binding region (EF-hand) of troponin C (20), but no sequencing of the squid OPA anhydrase has been reported to support such a binding region near the active site.

CONCLUSIONS

Squid OPA anhydrase is the first "decon" enzyme that has been demonstrated to have both specificity toward CW agent (Soman and Sarin) and good stability characteristics. Research on this enzyme should be extended toward isolating the peptide region containing the active site. Since the molecular weight of the native enzyme is low (26,000 daltons), the resulting 'active site' peptide may be of such a size that it could be synthesized.

REFERENCES

1. Steinmann, K.E., "Purification and Properties of an Organophosphorous Hydrolyzing Enzyme from Squid", Ph.D. Thesis, Illinois Institute of Technology, 1989.

2. Garden, J.M., Hause, S.K., Hoskin, F.C.G., and Roush, A.H., "Comparison of DFP Hydrolyzing Enzyme Purified from Head Ganglia and Hepatopancreas of Squid (Loligo pealei) by Means of Isoelectric Focusing", Comp. Biochem. Physiol., 52C:95-98, 1975.

3. Hoskin, F.C.G., Rosenberg, P., and Brzin, M., "Re-examination of the Effect of DFP on Electrical and Cholinesterase Activity of Squid Giant Axon", Proc. Nat. Acad. Sci. USA, 55:1231-1235, 1966.

4. Hoskin, F.C.G., and Long, R.J., "Purification of a DFP-hydrolyzing Enzyme from Squid Head Ganlion", Arch. Biochem. Biophys. 150:548-555, 1972.

5. Hoskin, F.C.G., and Brande, M., "An Improved Sulfur Assay Applied to a Problem of Isethionate Metabolism in Squid Axon and Other Nerves", J. Neurochem. 20:1317-1327, 1973.

6. Hoskin, F.C.G., and Prusch, R.D., "Characterization of a DFP-hydrolyzing Enzyme in Squid Posterior Salivary Glan by Use of Soman, DFP, and Manganous Ion", Comp. Biochem. Physiol. 75C:17-20, 1983.

7. Hoskin, F.C.G., and Roush, "Hydrolysis of Nerve Gas by Squid Type Diisopropylphosphosphorofluoridate Hydrolyzing Enzyme on Agarose Resin", Science 215:1255-1257, 1982.

8. Rajan, K.S., Mainer, S., Steinmann, K.E., and Hoskin, F.C.G., "Stability of Squid-Type DFPase and Its Recovery in CW-Agent Decontamination Application", Proceedings of the U.S. Army CRDEC Scientific Conference on Chemical Defense Research, Aberdeen Proving Ground, Maryland, Nov 15-18, 1988.

9. Rajan, K.S., "Enzymatic Detoxification of CW Agents: Immobilization of the Enzymes on Material Surfaces", Contract NO. N0014-85-K-0054-ONR.

10. Rajan, K.S., Mainer, S., Steinmann, K.E., and Hoskin, F.C.G., "The Purification and Characterization of DFPases for Detoxifying Organophosphate-Type AChE Inhibitors", Pharmacol. 29:179, 1987.

11. Frank, M.S., and Ross, J.W., Jr., "Electrode for Sensing Fluoride Ion Activity in Solution", Science 154:1553-1555, 1966.

12. Laemmli, U.K., "Cleavage of Structural Proteins During the Assembly of the Head of Bacteriophase T4", Nature 227:680-685, 1970.

13. Yang, J.T., Wu, C-S, and Martinez, H.M., "Calculation of Protein Conformation from Circular Dichroism", Methods in Enzymology 130:PtK, 208-269, 1986.

14. Holmes, L.G., and Robbins, F.M., "Quenching of Tryptophyl Fluorescence in Proteins by N'-Methylnicotinamide Chloride", Photochem. Photobiology 19:361-366, 1974.

15. Lehrer, S.S., "Solute Perturbation of Protein Fluorescence", Bioch. 10:3254-3263, 1971.

16. Lakowicz, J.R., "Principles of Fluorescence Spectroscopy", Plenum Press, New York, 1983.

17. Cohen, S.A., Meys, M., and Tarvin, T.L., "The Pico-Tag Method: A Manual for Advanced Techniques for Amino Acid Analysis", Waters Co. Tech Bulletin WM02, Rev 1, 1988.

18. Potter, J.D. Seidel, J.C., Leavis, P., Lehrer, S.S., and Gerely, J., "Effect of Ca^{+2} Binding on Troponin C", J. Biol. Chem 251:7551-7556, 1976.

19. Kronman, M.J., and Holmes, L.G., "The Fluorescence of Native, Denatured and Reduced-Denatured Proteins", PhotoChem. Photobiol. 14:113-134, 1971.

20. Zot, A.S., and Potter, J.D., "Structural Aspects of Troponin-Tropomyosin Regulation of Skeletal Muscle Contraction", Ann. Rev. Biophys. Biophy. Chem. 16:535-559, 1987.

BLANK

REMOVAL OF CRUDE OIL FROM VALDEZ, ALASKA ROCK SAMPLES WITH A MICROBIALLY-PRODUCED BIOSURFACTANT

Steve Harvey*, Ilya Elashvili and James J. Valdes
Research Directorate, Biotechnology Division
U.S. Army Chemical Research, Development and Engineering Center

Daphne Kamely
Scientific Advisor for Biotechnology
U.S. Army Chemical Research, Development and Engineering Center

A.M. Chakrabarty
University of Illinois at Chicago, Department of Microbiology/Immunology

ABSTRACT

Clean-up methods for the Exxon Valdez oil spill in Valdes, Alaska have focused on the use of high temperature pressurized water to remove oil from the beaches. We have tested a non-toxic, biodegradable surfactant from Pseudomonas aeruginosa for its ability to remove oil from oil-contaminated Alaskan gravel. Gravel samples were first washed with water, surfactant and/or xanthan gum solutions. The wash and the residual oil on the gravel were subsequently extracted with organic solvent and the oil contents were determined spectrophotometrically. The results clearly demonstrate the ability of the microbial surfactant to release oil from Alaskan gravel to a much greater extent than water alone.

INTRODUCTION

The recent oil spill from the Exxon Valdez tanker and its associated clean-up effort illustrated the difficulties and the cost of removing oil from seawater and the surrounding shoreline. Although oil spills are not exclusively a recent phenomenon, the fact that this one occurred in such a pristine environment as the Prince William Sound magnified many of the usual ecological and aesthetic problems. The oil proved to be particularly difficult to remove from the beaches because it had to first be washed back into the sound using pressurized hot water. This was a very costly

and time-consuming task. Additionally, the use of hot water can itself cause damage to the sensitive ecology of the beach. Chemical dispersants, which have been widely used in distant ocean spills, are believed to cause major pollution problems in shallow coastal waters because of their toxicity and persistence in nature[1]. Apart from the type of scrubbing operation mounted by Exxon then, microbial degradation is often the only means by which oil can be removed from beaches or shallow waters. Indeed, application of oleophilic fertilizers, which provide nitrogen and phosphorus nutrients to indigenous microorganisms to enhance the rate of in situ biodegradation, appears to have greatly facilitated the removal of oil from the Alaskan beaches[2]. Although genetically improved microorganisms capable of rapid growth on crude oil have been constructed[3], their ability to remove oil from a spill has never been tested because of the debate concerning the release of genetically engineered microorganisms in an open environment[4]. Thus, in the case of the Valdez oil spill, Exxon has devoted considerable resources to the physical removal of oil from the beaches using hot, pressurized water. Many oil-utilizing microorganisms produce potent surface active compounds that can emulsify oil in water and thereby facilitate its removal. We have demonstrated the production of a glycolipid emulsifier by a strain of Pseudomonas aeruginosa that reduces the surface or interfacial tension of an oil-water interface very effectively and acts as a potent dispersant of oil in water[5]. Unlike the chemical dispersants, the microbial emulsifier is non-toxic and biodegradable. Thus, use of such a natural microbial dispersant could be an effective means to remove the adherent oil from Alaskan beaches without the attendant hazard to the ecology.

MATERIALS AND METHODS

Isolation and Characterization of the Surfactant

Detailed methods on the nature and characterization of the surfactant have been described previously[5]. The surfactant used in this work was kindly supplied by Dr. Santi Bannerjee of Petrogen, Inc., Arlington Heights, Illinois.

Removal of Oil from Alaskan Gravel

Oil-covered gravel from Valdez, Alaska was sorted to exclude stones larger than approximately 5 mm in diameter. 25 g samples of gravel were loaded into 50 ml polypropylene centrifuge tubes and equilibrated to temperature. 25 ml samples of the appropriate wash solutions were equilibrated separately. In order to remove the oil, wash solutions were added to the tubes containing the gravel and the mixtures were inverted end-over-end at 23 rpm at constant temperature for 1 min. The wash was poured off immediately, and after equilibration to room temperature, both the wash and the residual oil on the gravel were extracted twice with 10 ml chloroform. Chloroform:oil volumes were normalized to 20 ml and the oil content was determined spectrophotometrically on a Gilford 2600 spectrophotometer at 254 nm. Blanks were chloroform extractions of

identical dilutions of clean wash solutions. This provided a control for any change in absorbance caused by surfactant or xanthan gum partitioning into the organic phase during extraction. Surfactant solutions were initially made at 1% concentration by warming slightly to dissolve the surfactant. Other surfactant solutions were dilutions of the initial 1% solution. Xanthan gum (Xanvis, Kelco Oil Field Group, Inc.) was dissolved at 0.05%. This concentration produced a noticeable increase in viscosity without the solution becoming so viscous that it could not be cleanly separated from the gravel.

RESULTS AND DISCUSSION

Isolation and Characterization of Surfactant

We have previously described the isolation of a strain (SB30) of Pseudomonas aeruginosa that produces a glycolipid surfactant (EM) which greatly reduces the surface and interfacial tension between oil and water. The emulsification of the oil in water is essential for oil-utilization by this microorganism since a mutant incapable of producing the surfactant is also incapable of utilizing liquid normal alkanes or oil as carbon sources. Addition of the surfactant to the growth medium will subsequently restore the growth of the mutant cells in oil.

Removal of Exxon Valdez-Spilled Oil from Alaskan Gravel

Since the Valdez oil spill, considerable discussions have been held about the potential impact of the spill on the environment of the Prince William Sound area[6,7]. A great deal of criticism has been leveled at the parties involved in the clean-up for the apparent slow pace with which the efforts began. Of particular concern has been the fact that evaporation and weathering of the oil made it too viscous to be removed by chemical dispersants.[1]

We sought to determine if a microbial surfactant, which unlike most synthetic chemical dispersants, is non-toxic and highly biodegradable, is capable of removing oil from weathered (collected 4 to 5 months after the spill) oil-contaminated gravel. Oil-covered gravel from Alaska was washed by water as well as by a 1% solution of the P. aeruginosa SB30 surfactant at different temperatures. The results in Fig. 1 clearly suggest that the surfactant enhances the release of oil from the gravel. At 10 to 20 C the effect of the surfactant is not dramatic but it removes at least 2.8 times more oil than water alone. From 30 to 50 C, the difference between the effect of the surfactant and the water is more pronounced and it can be seen that the surfactant is removing from 3.3 (30 C) to 2.4 (50 C) times more oil than the water alone. At 60 C, the water removes 41.52% of the oil whereas the surfactant removes 69.67%. Above 60 C, this degree of difference remains fairly constant. Fig. 2 shows the appearances of the water and surfactant solutions after each is used to wash 25 g of oil-covered gravel at 40 C.

FIGURE 1

Ability of water alone and a 1% surfactant solution to remove crude oil from Alaskan gravel at various temperatures.

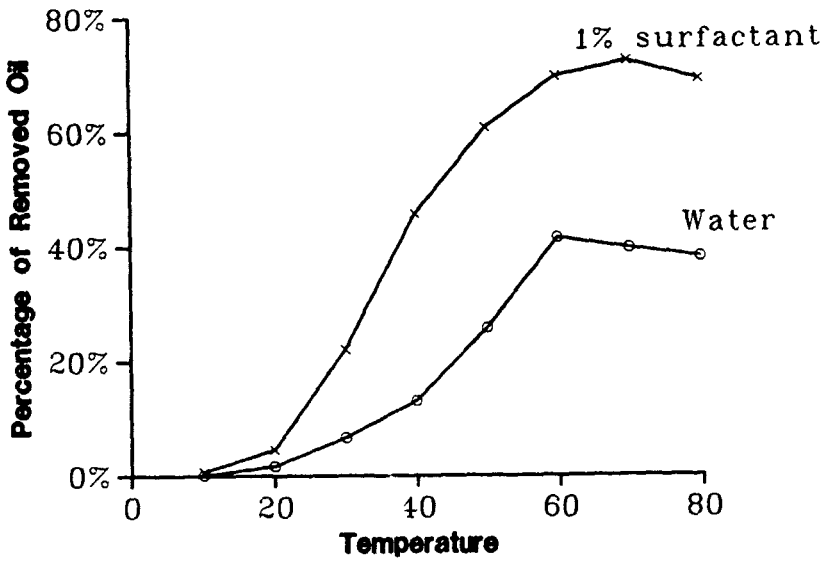

FIGURE 2

Water (left) and 1% surfactant solution (right) after being used to wash 25 g gravel at 40 C.

Since Exxon presently uses fire hoses to wash off oil with warm water jets[2], the time of contact between the water and the oil on the gravel is important. As shown in Fig. 3, the difference between the results achieved with surfactant versus water is most pronounced at the shortest time period (1 min). The water achieves its maximum effect at 1.5 min and then levels off. The surfactant achieves its maximum effect at 1 min and then levels off (50 C) or even decreaes (30C). The difference between surfactant and water at even shorter time periods might have been interesting to observe but times shorter than 1 min would have been very difficult to quantitate under the conditions of these experiments. Clearly, though, the surfactant allows increased removal of oil with a minimal time of contact.

FIGURE 3

The effect of contact time on the amount of oil released by the surfactant and water alone at 30 C and 50 C.

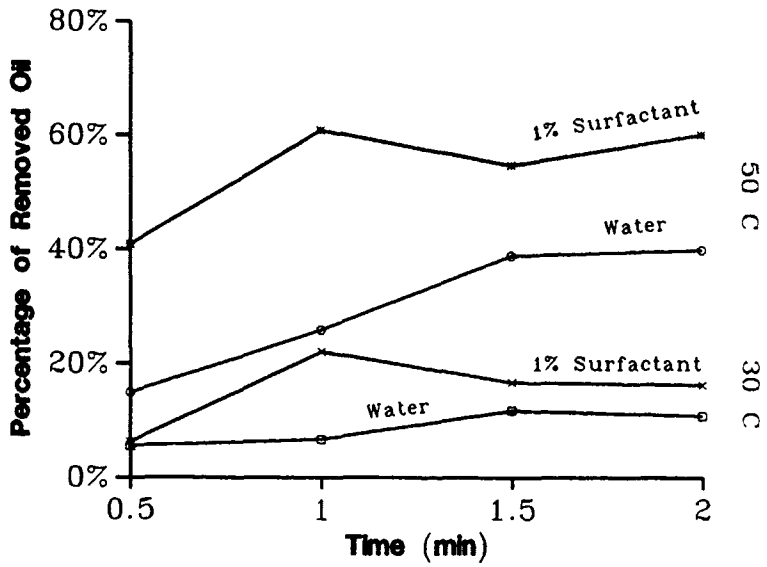

Since the surfactant is a glycolipid,[5] it is sparingly soluble in water and a certain amount of heat is needed to prepare a 1% solution. We determined the effects of varying concentrations of the surfactant on its ability to release oil from the gravel (Fig.4). The increased effect with increased surfactant concentration was more pronounced at 50 C than at 30 C.

FIGURE 4

The effect of varying concentrations of surfactant on release of oil from Alaskan gravel at 30 C and 50 C.

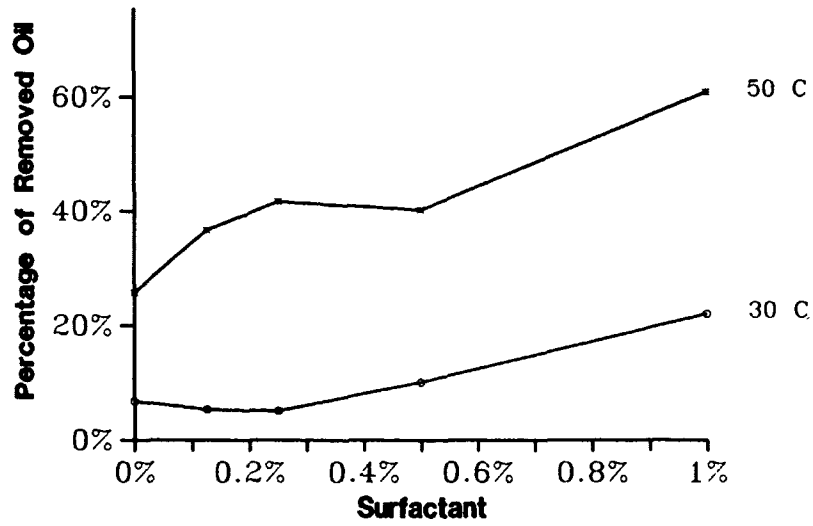

When oil is washed from the beach it, of course tends to flow back to the water where it can still be a problem. Viscofiers such as xanthan gum are often added to flood water during oil recovery to control the mobility of the oil. We were therefore interested in determining what effect the addition of xanthan gum to the surfactant solution would have in releasing the oil, both at 30 C and at 50 C. The results in Fig. 5 show that while 0.05% xanthan gum had little effect on the release of oil by water alone at either temperature, it inhibited the extent of oil released by the surfactant at both 30 C and 50 C. Higher concentrations of xanthan gum produced too viscous a solution to be effectively pumped. Thus addition of xanthan gum appears to be of little practical value in the enhanced release of oil by the microbial surfacant.

FIGURE 5

Release of oil by water alone and 1% surfactant
in the presence and absence of 0.05% xanthan gum

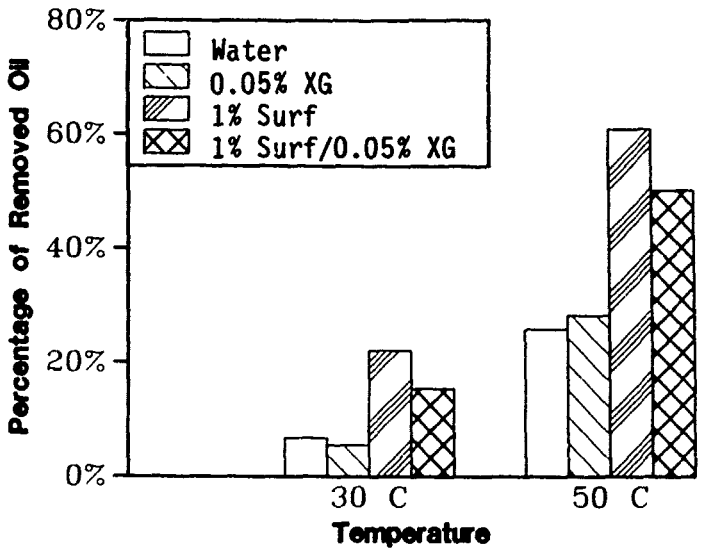

CONCLUSIONS

We have demonstrated that a microbial surfactant greatly enhances the removal of oil from Alaskan gravel. This may have important implications or potential applications for future oil spill clean-up efforts. Apart from Exxon's efforts to wash the beach with hot water jets, the Environmental Protection Agency has conducted extensive *in situ* bioremediation experiments which appear to suggest that indigenous microorganisms may digest much of the oil if appropriate amounts of nitrogen and phosphate nutrients are provided. It should be emphasized that many species of natural microflora produce surface active compounds to facilitate cellular uptake of the oil. Bioremediation experiments then, may encourage the production of such surface-active agents *in situ* to

solubilize some of the oil. Because bioremediation is a slow process, another alternative is to use isolated surface active compounds, such as the present surfactant, to emulsify the oil, thereby not only removing the bulk of the oil from the contaminated sites, but at the same time enhancing natural degradation of the remaining oil by facilitating the uptake of the released oil by the indigenous microflora.

This work demonstrates the potential utility of biosurfactants for the solubilization of organic compounds. This, or other similar biosurfactants may have important military applications where it would be desirable to have a non-toxic, non-corrosive, biodegradable surfactant for the decontamination of toxic chemicals from surfaces of vehicles or equipment.

ACKNOWLEDGEMENTS

This work was supported under an IPA contract between the U.S. Army CRDEC and the University of Illinois. We are grateful to Dr. Santi Bannerjee of Petrogen Inc. for the supply of the surfactant.

*SMCCR-RSB E3220 Aberdeen Proving Grounds, MD 21010-5423

REFERENCES

1. McIntosh, H. Oil Spill Dispersants: Good or Bad for the Environment? NRC News Report 39: 13-15. 1989.

2. Fox, J.L. Native Microbes' Role in Alaskan Clean-up. Biotechnology 7: 852. 1989.

3. Friello, D.A., Mylroie, J.R. and Chakrabarty, A. M. Use of Genetically-Engineered Multi-Plasmid Microorganisms for the Degradation of Fuel Hydrocarbons, p.205-214. In: Proceedings of 3rd International Biodegradation Symposium. Sharpely, J.M. (Ed.) Applied Science Publications, Essex, England. 1976

4. National Research Council. Field Testing Genetically Modified Organisms. p. 1-170. National Academy Press, Washington D.C. 1989.

5. Chakrabarty, A.M. Genetically-manipulated Microorganisms and their Products in the Oil Service Industries. Trends in Biotechnol. 3: 32-38. 1985.

6. Fogle, S. Scientific Community Unprepared for Oil Spill. J. NIH Research 1: 65-69. 1989.

7. Baringa, M. Alaskan Oil Spill: Health Risks Uncovered. Science 245: 463. 1989.

BLANK

ENZYME-AMPLIFIED RECEPTOR ASSAY SCREENING TEST FOR CHLORPROMAZINE, TRIFLUOPERAZINE, AND PCP

Susan F. Hallowell [a] and Garry A. Rechnitz [b]

Abstract: A new receptor based assay is described for the determination of classes of drugs that have high affinities for the acetylcholine receptor channel binding site. The method is based upon the inhibition of the enzyme activity of an enzyme-drug conjugate by the binding to the receptor protein, and competition between free drugs and the enzyme-drug conjugate for a limited number of receptor sites. The activity of the enzyme marker system, glucose-6-phosphate dehydrogenase covalently conjugated to desipramine, is monitored by colorimetric detection of the rate for NADH formation at 340 nm. The procedure proposed is designed to provide a simple drug screen which can be done in a minimally equipped laboratory while achieving the required sensitivity. The technique is illustrated for three acetylcholine channel binding compounds: the hallucinogen PCP and the antipsychotic agents chlorpromazine and trifluoperazine. The procedure yields calibration curves with detection limits at nanomolar levels of drug. Aspecific binding responses of unlabeled enzyme to drug or receptor to compounds with low affinity for the receptor are shown to have minimal effect on the assay.

INTRODUCTION

Receptors are by nature extremely efficient detectors. Radioreceptor assay (RRA) exploits this phenomenon and has been routinely utilized by pharmacologists to determine pharmacological potency of compounds. Although the use of antibody/antigen and biocatalyst-based biosensor systems has emerged in the last 15 years, the use of isolated receptors as the molecular recognition element in a detector system is a fairly recent innovation. This concept appears to be very viable. Research done by Chemical Research Development and Engineering Center (CRDEC) has demonstrated the ability to use receptor based technology for the determination of acetylcholine agonists and antagonist compounds using both capacitance sensors and fiber optic fluorosensor devices using fluorescent labeled bungarotoxin probes (1,2). These systems have the unique characteristic of pharmacological recognition of toxins at the level of toxicity, unlike immunogenic systems. The notion of coupling a receptor with other transducer-detection systems is limited only by the ability of the detector to sense the toxin binding reaction either directly or indirectly. This is done by the development of a physical or chemical environment which is both altered by the toxin binding reaction, and sensed by the detector. For instance, a new type of acetylcholine sensor was recently described using an Ion Sensitive Field Effect Transistor (ISFET) with an acetylcholine receptor which exploits the natural ion gating function of the receptor moiety as the signal producing event (3). Yet another receptor based sensor has been developed by incorporating receptors into the surface of a polymeric membrane cast onto the surface of an electrode, by which capacitance changes of the membrane were monitored as charged target compounds bound to the membrane's surface (4). The use of an enzyme marker system with a receptor recognition element has been shown to be an attractive, inherently sensitive system. The toxin binding reaction to the receptor is indirectly determined by its competition with an enzyme-labeled drug probe.

a. Analytical Division, Chemical Research Development and Engineering Center, APG, MD.
b. Department of Chemistry, University of Hawaii, 2545 The Mall, Honolulu, Hawaii, 96822

The enzyme's activity is decreased by the binding of the drug attached to it as it binds to the receptor. Thus, the toxin binding reaction, which occurs at the nanomolar level, is catalytically enhanced by the presence of the enzyme, and the signal detected is that of the amount of enzyme activity, determined by the measurement of the amount of conversion of substrate to product. Because the enzyme's activity has been linked to the amount of toxin present, and since it amplified this reaction by a factor of approximately 100,000 fold, this system does not rely on an ultrasensitive detection systems (such as the capacitance sensor) which can be subject to drift, reproducibility, and precision problems. A conventional detector can be used which is chosen to measure the signal created by the appearance of enzyme product . We have recently demonstrated the viability of this concept in our laboratory, and determined the theoretical limits of this assay (5,6). Last year, we developed and optimized a prototype Enzyme-Amplified Receptor Assay (ERA) system using the acetylcholine receptor and the drug desipramine, a channel binding compound, labeled with the enzyme glucose-6-phosphate dehydrogenase (7). The objectives of this present study were to determine to analytical characteristics of this technique with respect to the analysis of channel binding drugs.

METHODS

Reagents

Trifluoperazine (TFP, T8516) chlorpromazine hydrochloride (CHL, C8138) nicotinamide adenine dinucleotide (NAD, N7004), glucose-6-phosphate disodium salt (G6P, G7250, and carbamylcholine chloride (CARB, C4382) were all purchased from Sigma Chemical company. The NAD, CARB and G6P were reconstituted with a tris based buffer (54 mM NaCl, 50 mM Tris and 1mM EDTA) at pH 7.4. The CHL and TRI were reconstituted in warmed, distilled, deionized water, and standards were prepared in the working buffer. The NAD, CARB and G6P were reconstituted with a tris based buffer (54 mM NaCl, 50mM Tris and 1mM EDTA) at pH 7.4. Dr. Roy Thompson, Chemical Research, Development and Engineering Center (CRDEC) at Aberdeen Proving Ground, Md., kindly provided us with the phencyclidine. The glucose-6-phosphate dehydrogenase conjugated with desipramine (G6PD-DES, which is not to be taken as a 1:1 stoichiometric conjugate) was purchased from Syva Co. (3J019) as a part of EMIT tricyclic antidepressant assay kit (7C319, reagent B), and was reconstituted according to the manufacturer's specifications in distilled, deionized water. No information was available on the enzyme activity or the DES concentration of this conjugate (Under assay conditions comparable to unconjugated enzyme, the G6PD-DES was estimated to be 1.2 units/mL.) Buffer was made with Sigma Trizma Base (T-1503, tris(hydroxymethyl)aminomethane) and adjusted to pH 7.4 with HCl. Sodium chloride (NaCl, S271-500), disodium phosphate, (Na_2HPO_4, 3828-1), and disodium ethylenediamineetraacetate (EDTA, S-311) were all purchased from Fisher Scientific. Distilled, deionized water was used throughout, and all reagents were stored at 4 ^{o}C when not in use.

Instruments

Centrifugations were carried out with an IET-HT centrifuge at 4^{o}C. Acetylcholine receptors were homogenized using a Polytron (Brinkman Instruments) setting at 5 (50% power). Reactions were carried out in 1.5 mL microcentrifuge tubes at room temperature (22^{o}C). Enzymatic activity of the G6PD and G6PD-DES was monitored in quartz cuvettes with the spectrophotometer at 340 nM at room temperature. Measurements were made with a Hitachi model 100-60 spectrophotometer. Responses were followed on a Heath strip chart recorder and initial rates calculated manually from recorder tracings.

Preparation of the Acetylcholine Receptor

Torpedo nobiliana was prepared as described elsewhere (7). This procedure yields receptors prepared as vesicles at an average protein concentration of about 5 mg/mL. The acetylcholine

receptors were assayed with respect to total protein concentration by the method of Bradford (8)

Calibration Curves of Trifluoperazine, Chlorpromazine, and PCP

Working standard solutions of chlorpromazine, trifluoperazine and PCP were prepared using Torpedo buffer without Na_2HPO_4. Concentrations typically ranged from 0.2μM to 10 μM, which resulted in final concentrations of analytes in the reaction vials of about 5 nM to 500 nM. A 8 μL quantity of 1 mM CARB was first added to vials containing 150 μL of receptor protein or Torpedo buffer (as blank) and were allowed to stand for 2 minutes. Standard solutions of analytes (7 μL) were then introduced and the mixtures were mixed thoroughly. Two different kinds of blanks were run. One set contained no drug while the other set contained no receptor protein, some with and without the analyte. After allowing these mixtures containing the drug and receptor to preincubate for about 5 minutes, 15 μL aliquots of G6PD-DES enzyme was added. All vials were then incubated for a minimum of 30 minutes at room temperature.

After an incubation period, the vials were centrifuged at 3000 X g (8,000 rpm) for 10 minutes at 4°C. After centrifugation, 50 μL of supernatant from each vial were added to 750 μL of substrate containing 1mM G6P and NAD in a quartz cuvette and this was immediately followed by measurement of enzyme activity.

In most experiments, the data were normalized to indicate the percentage of initial enzyme activity remaining (or the percentage inhibition of enzyme activity) as a function of the toxin concentration.

RESULTS

The general principle of ERA is shown in figure 1. The specific scheme for the ERA technique as it applies here is shown in equations 1-3. Equation 3 shows the overall reactions involved in the analytical method. As previous determined, the binding of a specific drug or toxin is mainly dependent on the affinity equilibria in the first reaction. The assay employs commercially available G6PD, which has a ligand (desipramine) attached to it known to bind to the channel site. When the enzyme-labeled drug is complexed with the acetylcholine receptor, the enzyme is rendered inactive. The exact mechanism for the enzyme inactivation is postulated to involve the steric exclusion of the enzyme substrate from the enzyme active site. In the presence of free drugs which have high affinities for the channel site region on the receptor protein, the enzyme drug conjugate and free drug compete for receptor binding sites. Thus, the presence of free drug causes some of the enzyme labeled conjugate to remain uncomplexed and enzymatically active. The level of enzyme activity is directly related to the concentration of free drug introduced.

$$\text{AChR} + \text{Analyte} \rightleftharpoons \text{AChR:Analyte} \qquad [1]$$

$$\underset{\text{(active)}}{\text{AChR} + \text{Analyte} + \text{G6PD-ligand}} \rightleftharpoons \underset{\text{(inactive)}}{\text{AchR:Analyte} + \text{AChR:G6PD-ligand}} \qquad [2]$$

$$\text{G6P} + \text{NAD} \xrightarrow{\text{G6PD-ligand (active)}} \text{6-phosphoglucono-d-lactone} + \text{NADH} + \text{H}^+ \qquad [3]$$

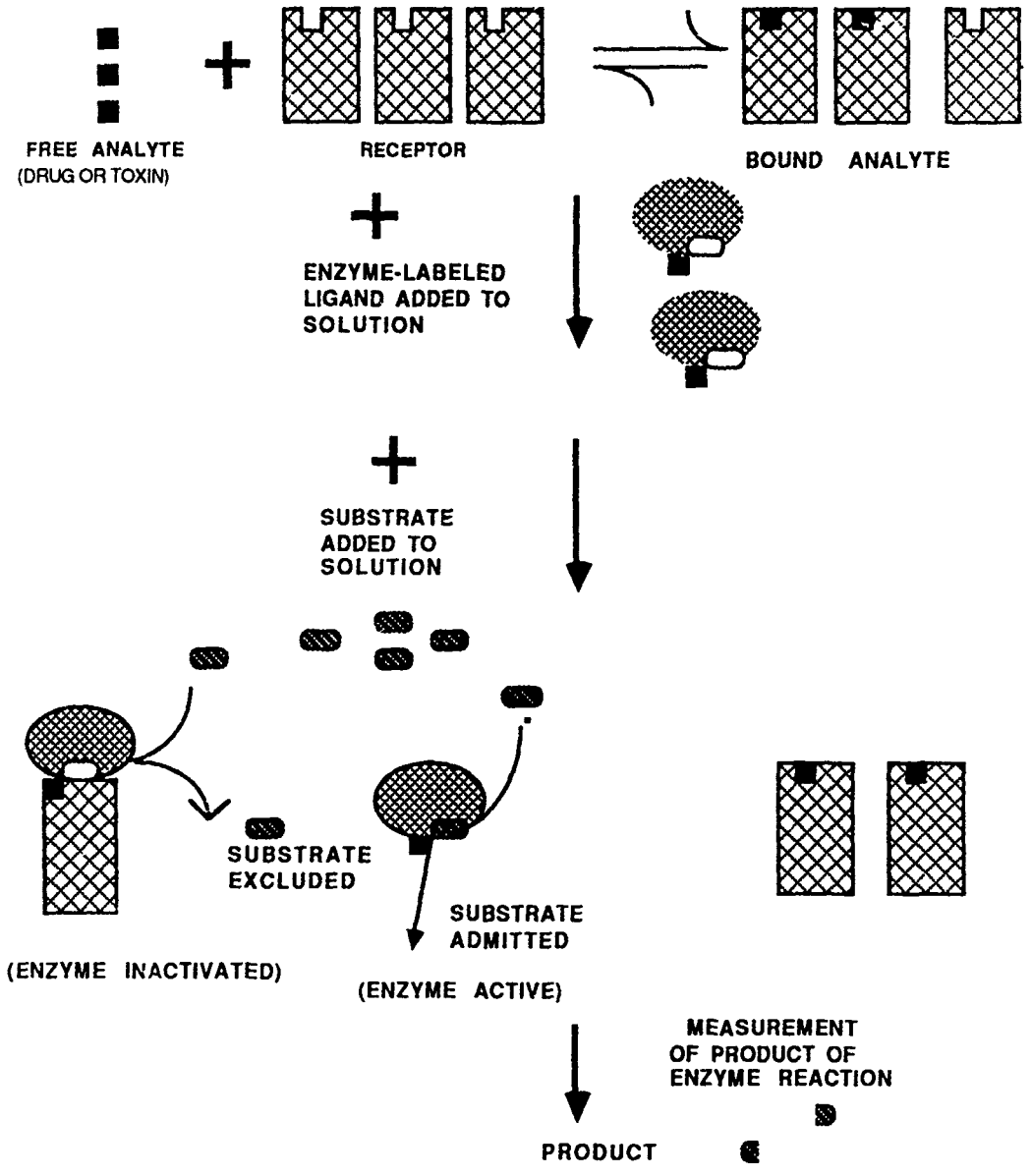

Figure 1: ERA principle. The analyte (drug or toxin) to be assayed is contained in solution. Receptors are added to solution, along with enzyme labeled with a ligand having a high affinity for the receptor. Competition for the receptor binding sites occurs between the free drug in the sample and the enzyme-labeled drug. When the enzyme-labeled drug binds to the receptor, the enzymatic activity is reduced. Only the free enzyme-labeled drug can act on the substrate which converts it to product. The amount of product is measured, and is proportional to the enzyme concentration (activity). Enzyme activity is directly proportional to the free analyte concentration.

In most cases, the receptor protein was removed from solution prior to analysis and, as a consequence, the enzyme inactivation is not actually employed in this study. The G6PD activity is followed by the change in absorbance produced by the conversion of NAD to NADH which exhibits absorbance at 340 nm, or oxidation at an anode set at a polarizing voltage of +700 mV. The rate of formation of NADH is proportional to the amount of enzyme (or to the free drug) present.

Last year, we established the theoretical limits of the ERA experiment, and determined how the sensitivity and range of the assay could be modulated by varying the concentrations of receptor and or the enzyme label. The experimental protocol was fixed using the procedures described above, and standard response curves for several channel binding drugs were prepared, including desipramine, imipramine, phencyclidine, chlorpromazine, trifluoperazine, nortriptyline, and amitriptyline. Concentration ranges of analyte typically ranged from 100 nM to 10 µM which resulted in solution concentrations of approximately 5 nM to 500 nM of PCP. The raw data collected was in the form of the rate of formation of NADH: this was determined by measuring the slope of the strip chart output that showed the absorbance as a function of time. Figure 2 shows a strip chart output with the increasing activity of the G6PD-DES as a function of increasing PCP concentration. When the rate of NADH formation is plotted as a function of the log of the concentration of analyte, a standard curve is observed which appoximates linearity. Figures 3 and 4 show standard curves for chlorpromazine and trifluoperazine using the log transform and enzyme activity normalization procedures described, with an average of three measurements per point, with the precision of each point indicated by the error bars shown

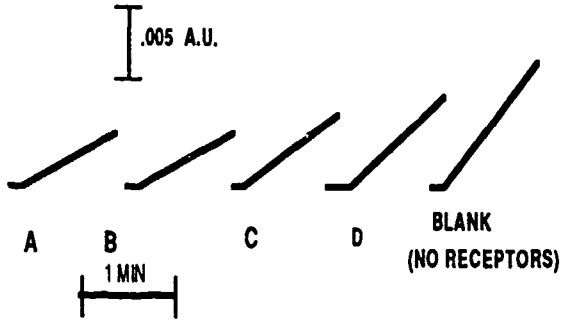

Figure 2: Dependence of enzyme activity on increasing PCP concentration. (a) 0 nM PCP, (b) 5 nM PCP (c) 50 nM PCP (d) 500 nM PCP, (e) Blank (no receptor protein).

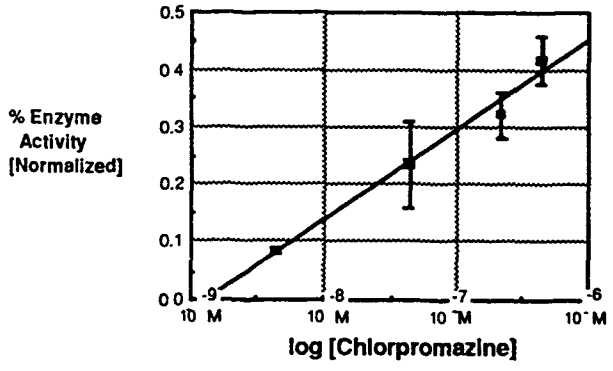

Figure 3: Standard calibration curve of chlorpromazine using ERA. Receptor concentration is 4.8 µg/mL, carb is 4.4 X 10 -5 M, enzyme concentrations is .097 units/ mL, 50 µL of sample solution was added to 750 uL of substrate containing 10 -3 M G6P, NAD in Tris buffer.

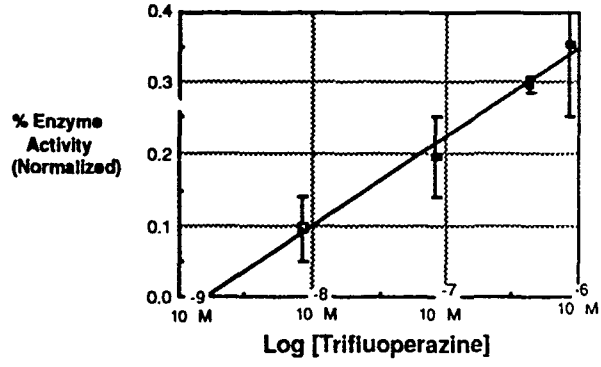

Figure 4: Standard calibration curve of trifluoperazine using ERA. Receptor concentration is 4.8 µg/mL, carb is 4.4 X 10 -5 M, enzyme concentrations is .097 units/ mL, 50 µL of sample solution was added to 750 uL of substrate containing 10 -3 M G6P, NAD in Tris buffer.

Table 1: Response Characteristics of PCP, Trifluoperazine, and Chlorpromazine using ERA.

Parameter	PCP	CHL	TRI
slope (Enzyme Activity Normalized/ (log C)	.174	.157	.126
correlation coefficient (r)	.983	.991	.992
intercept, (normalized response)	-.0394	-.0214	-.0306
lower limit of linear range (lowest standard)	5 nM	4.4 nM	8.6 nM

From least squares analyses of at least four concentrations done in triplicate.

at ± 1 standard deviation. A summary of the response characteristics of the PCP, chlorpromazine, and trifluoperazine assays is shown in table 1. The correlation coefficient exceeded .95 in all standard curves. The sensitivity of the assays, as indicated by the relative slopes of the regression curves correlated with the relative values of the dissociation constants for these compounds for the channel site.

Discussion

The development of a receptor based assay using a labeled enzyme probe has been demonstrated to be feasible. Here, we have developed a homogeneous assay technique which can be used to screen for substances that are pharmacologically active due to their interaction with the acetylcholine receptor system. This assay is unique in it's use of a channel probe as the marker compound, which can detect the presence of substances binding at two separate active sites on the receptor compound. Others have used primarily bungarotoxin probes to demonstrate feasibility of receptor based systems since it has such a high affinity for the receptor moiety. However, this approach is limited in its ability to detect one class of compounds (antagonists) and since bungarotoxin binds irreversibly, is not ammenable for the development of a reversible sensor. It is notable that our demonstrated system produces analytical results: although the channel probe used (desipramine) has a much lower receptor affinity (kd = 10^{-6}) than the bungarotoxin (kd=10^{-10} -10^{-12}), this probe can be successfully used in conjunction with the enzyme amplification feature. The enzyme-amplifier used in this assay was taken from a commercially available EMIT kit. We compared the ERA procedure as used for the analysis of PCP or imipramine to the commercially available EMIT (antibody) kits which are typically used by clinicians for the screening of these substances in biological fluids, and demonstrated that our receptor based assay has as good as or even better precision than the EMIT, by which it can be inferred that the use of receptors rather than antibodies did not introduce additional imprecision into the assay due to nonhomogeneous effects of the receptor preparation. Because we were using the same enzyme probe as the EMIT kits, it can also be inferred that that interferences with the EMIT assay due to interaction with the enzyme will also appear in the ERA assay. These are minimal when using biological matrices. Although we did not observe significant interference problems, the judicious use of blanks is highly recommended when using this assay. Our receptor based system performed adequately using a UV-VIS spectrophotometer detector.

The greatest significance of this study is the demonstration of the general feasibility of using receptor systems with enzyme amplification. This should prove to be a powerful general procedure, both for the clinician and for those interested in fabricating receptor based biosensors. Presumably, one can select a receptor system appropriate for a category of drugs or toxins, and then choose an enzyme system which will produce a signal compatible with the desired detection scheme, whether it be colorimetric, potentiometric, or electrochemical. Table 2 indicates some enzymes, the products they produce, and the detectors which can be used with these enzymes, which may be useful in the development of other ERA methods. The ERA technique should be suitable for transition to a number of different physical systems. For instance, the chemistry presented above should be directly transferable

Table 2: Candidate Enzyme Labels for ERA

Enzyme (MW)	Source	pH optimum	Specific activity at 37°C/units mg-1	Km	Detection Method
Acetylcholinesterase MW= 54,000	Electrophorus electricus	7-8	1,400	90 µM	pH electrode or spectrophotometric
Adenosine deaminase	Calf intestine	7.5-9	200	60 µM	ammonia gas-sensing electrode
Alkaline phosphatase MW = 100,000	calf intestine	8-10	1,000	0.2 mM	spectrophotometric or fluorimetric
Catalase MW = 250,000	calf liver	6-8	40,000	•	UV absorbance or thermometry
B-Galactosidase MW = 540,000	Escherichia coli	6-8	600	1 mM	spectrophotometric or fluorimetric
Glucose oxidase MW = 186,000	Aspergillus niger	4-7	200	33 mM	peroxide combines with chromogen
Peroxidase MW = 40,000	Horseradish	5-7	4,500	0.2 mM	peroxide combines with chromogen
Urease MW = 483,000	Jack beans	6.5-7.5	10,000	10 mM	ammonia reacts with chromogen or gas sensing electrode

to the fiber optic system currently under development at CRDEC since NADH is fluorescent, assuming that the immoblization procedures for the receptor allows the functional recognition of channel binding compounds to the acetylcholine receptor, and the receptor density is sufficiently high to meet the previous established criteria for this procedure. If receptor technology can mature to the stage than receptors can be immobilized onto to paper tab, a ERA technique could be developed into a quick visual indicator kit, similar to commercially available home pregnancy kits, which employ antibody recognition in conjunction with enzyme amplification. Our ERA procedure could be developed into field kit configuration by the synthesis of a probe using an enzyme which results either directly or indirectly in a colored product, with the "detector" being the human eye.

ACKNOWLEDGEMENT: This work was funded by CRDEC through the ILIR program in FY 89.

REFERENCES

1. Eldefrawi, M.E., Sherby, S.M., Andreou, A., Nansour, N.A., Annau, Z., Blum, N.A. and Valdes, J.J. (1988) Anlyt. Lett. 21, 1665-1680.

2. Rogers, K.R., and Eldefrawi, M.E., Accepted to Analytical Biochemistry 7/18/89

3. Gotoh, M., Tarniya, E., Momoi, M., Kagawa, Y. and Karube, I. (1987) Analyt. Lett. 20. 857.

4. Taylor, R.F., Marenchic, I.G. and Cook, E.J. (1988) Analyt. Chim. Acta. 213, 131-138.

5. Hallowell, S.F. and Rechnitz, G.A.,(1987) Anal. Lett., 20 (12) 1929.

6. Hallowell, S.F. and Rechnitz, G.A.,(1988) Anal. Lett., 22 (1) .

7.Hallowell, S.F. and Rechnitz, G.A. (1989) CRDEC-SP-005, 23.

8. Bradford, M.M. (1976). Anal. Biochem., 72, 255.

BLANK

RECENT HARDWARE ADVANCES IN EVANESCENT WAVE FIBER OPTIC BIOSENSORS

Myron J. Block, Steve J. Lackie, Thomas R. Glass
ORD, Incorporated, 334 North Main Street, P.O. Box 148 N. Salem, NH 03073

A recent advance in evanescent wave fiber optic biosensors is the injection molded polystyrene fiber optic assembly. It has several advantages over the quartz fiber, it's injection molded, (easily mass produced), the integrally molded lens relaxes alignment tolerances, and it provides the sample chamber with a pressure tight front seal. A more fundamental advance is the simultaneous multichannel assay. Multichannel can be more beneficial than simultaneously assaying analytes. It can monitor nonspecific binding and other correlatable parameters, on the same fiber and sample simultaneously with the analyte - reducing or eliminating effects that limit the sensitivity and specificity.

For those of you who do not know of the evanescent wave I will use two heuristic descriptions so that its properties will seem more reasonable. First, consider total internal refection. How does the light know that the less dense medium is there, if it doesn't enter it? It probes the medium with a feeler and says "oh oh I can't enter". What about the feeler? It cannot extend as far as a wavelength because having made one wavelength it knows all it needs, the rest is repetition, to continue on its way. Therefore, the penetration will be less than a wavelength.

Second, consider the fluorescence excited by the evanescent wave. It is not an ordinary fluorescent photon, because before it can propagate a full wavelength, it senses the boundary and the boundary conditions become established. As a result, the radiation pattern is not a sphere, but is greater in the evanescent directions enabling it to enter and be trapped in the fiber and thus be transmitted out the ends.

Now that you understand the fundamentals of evanescence, let me briefly remind you of some of the characteristics of our system: Figure 1 is to remind you that we are not talking about an optrode; Figure 2 is to show that the fluorescent photon is an evanescent photon; Figure 3 shows the sub-wavelength thickness of the evanescent zone; Figure 4 shows an often ignored fact that evanescent excitation and fluorescence is approximately an order of magnitude more efficient than other excitation and fluorescence methods; and Figure 5 shows that the system can be miniaturized.

Now for some data that you may not have seen. Figure 6 shows that immunoassay can be performed on raw whole blood (a difficult sample). Figures 7 through 10 were obtained by Ciba-Corning one of our licensees. Figure 7 shows a good fit with and greater dynamic range than RIA. Figure 8 shows that an assay can be performed in 25 seconds. Figures 9 and 10 show a sensitivity adequate to assay for digoxin in the clinical range. The digoxin assay is the rite of passage for clinical application. To be topical Figure 11 shows some results on an AIDS assay. We have just licensed Fujirebio in Japan for AIDS testing and all blood bank applications.

Figure 12 shows the remarkably strong dependance of signal on NA and serves as a basis for the design considerations of our new fiber-sample

chamber system. Figure 13 shows the extreme ray in our injection molded polystyrene fiber optic assembly, which includes an integral lens. The injection molded polystyrene fiber assembly has several advantages over the quartz fiber we previously used. The fact that it is an injection molded polystyrene assembly means it is more economical to produce in mass quantities. The fact that it has an integrally molded lens means that the alignment tolerances are relaxed for the user and it provides the sample chamber with a pressure tight front seal. The extreme ray can be seen to be well inside of the mounting edge. This means that we do not suffer any loss in NA which was difficult to accomplish when holding a cylindrical fiber (rod). Figure 14 are photographs of our fiber (rod) and the capillary chamber that holds it. The chamber may be used as a flow cell or as a one-shot disposable having capillary fill.

Figure 15 summarizes the characteristics of our method. Item 6 is multiplex the promised revelation of what I believe to be a common characteristics of the next generation of biosensors. Multiplex means the ability to make different and correlatable measurements on the same sample, at the same location in the same microenvironment, on the same immobilized phase, at the same time. It is not merely adding additional sensors in the same sample. Figure 16 is a first guess at a list of what multiplex will do. The first item can be accomplished with parallel sensors. The second item is obvious The third item needs multiplex and is a new way to increase confidence. It is to simultaneously and correlatably measure more than one aspect of the analyte, thus increasing reliability of detection. The importance of this in military applications is obvious. The item is illustrated for AIDS detection. It is also illustrated by M.J. Khosravi and R. Sudsbury (8) who obtained "ultraspecificity" in a assay for lutropin, by selecting for that assay an optimum pair of monoclonal antibodies out of 36 combinations. This was an elementary (2 component) multiplex procedure which enabled the rejection of cross reactivity with choriogonaotropin.

The fourth item is brand new capability. Every immunochemist will tell you that non-specific binding limits ultimate sensitivity in sandwich assays. Correcting for non-specific binding therefore increases the sensitivity limit beyond that achievable in any other system. We do this by using an irrelevant antibody tagged differently than the analyte antibody and by measuring its non-specific binding. Which can be related to the non-specific binding of the analyte antibody. Item 5 is my invitation to you to invent new correlations.

Item 6 Labelling the Immobilized Phase, yields the ratio analyte Ab^{*}/immobilized Ab^{**}. This solves QC problems for the manufacturer. It also is a new way of automatically providing a reusable sensor. Here, instead of breaking the Ag-Ab bond and removing the analyte, one can strip the used immobilized Ab^{*} and automatically flow through and adsorb fresh Ab^{*}.

However perhaps the most interesting potential application of tagging the immobilized phase would be to serve as a basis for the development of reagentless biosensors having the high sensitivity of fluorescent tag and the great specificity of a direct characterizable ligand binding assay.

This might be accomplished by choosing the tag on the immobilized phase molecule properly. That is, so that its fluorescence would be modified by conformational changes of the immobilized phase molecule to which it is attached. The conformational changes would be produced by the binding event of analyte to the immobilized phase molecule.

CONCLUSIONS

The advantages of multiplexing will become the featured subject of many meetings to come. It provides greater sensitivity and specificity than can any single chanel system.

ACKNOWLEDGMENT

This work is supported by U.S. Army under contract # DAAA15-88-C-0026

REFERENCES

1) T.R. Glass, S. Lackie and T. Hirschfeld, "Effect of Numerical Aperture on the Signal Level in Cylindrical Waveguide Evanescent Fluorosensors" Applied Optics Vol. 26, No. 11, 1 June 1987 p2181.
2) US Patent 4,447,546
3) US Patent 4,558,014
4) US Patent 4,582,809
5) US Patent 4,654,532
6) US Patent 4,716,121
7) US Patent 4,844,869
8) M.J. Khosravi and R. Sudsbury "Ultra-specific Time Resolved Immunofluorometric Assay of Lutropin in Serum" Clin. Chem. 1989; 35:2251.

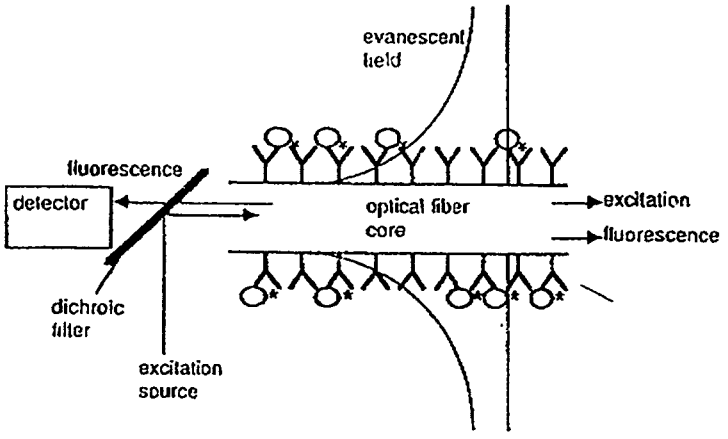

FIGURE 1 Schematic illustration of a fiber optic fluoroimmunosensor. This figure is a general guide, and actual systems may vary in detector placement, filter arrangement, light source, and assay method.

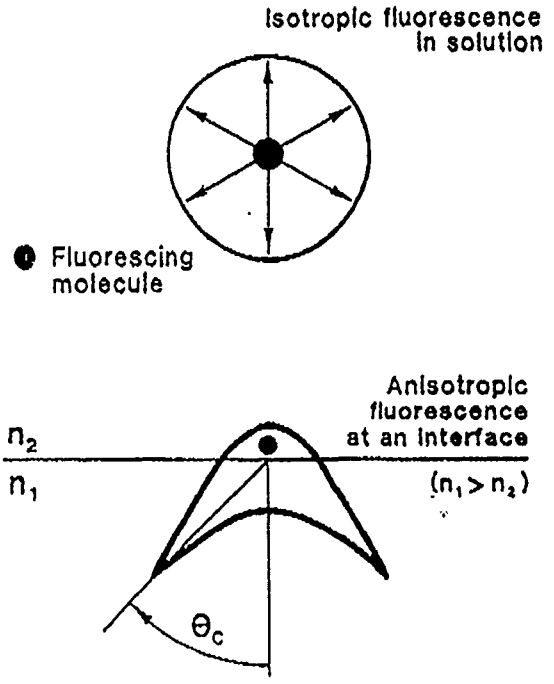

FIGURE 2

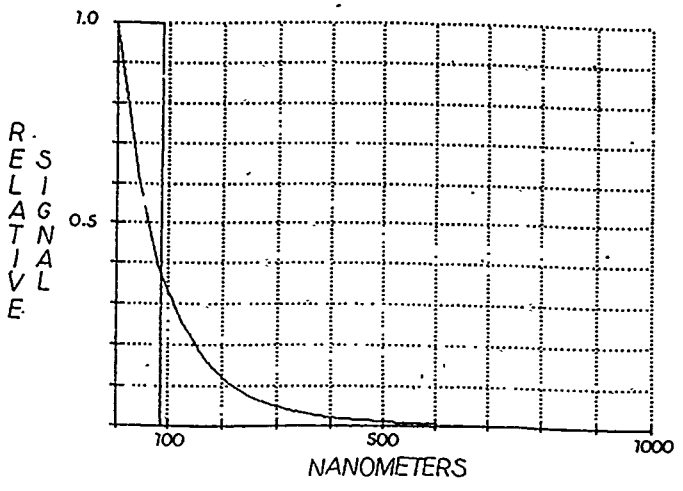

FIGURE 3

The ratios of signal level to volume sensed for each of the three methods indicate relative signal per molecule, as shown in the following table.

Method	Vol. (microliters)	Sensitivity (Molar)	Relative Signal (per molecule)
Evanescent	0.01	$4.26*10^{-11}$	1.0
HNG	50.2	$9.20*10^{-14}$	0.09
End On	1.0. (max. vol.)	$3.42*10^{-12}$	0.12

As expected the HNG and End On methods give equivalent signals per molecule while the evanescent sensor gives about 10 times the signal per molecule.

FIGURE 4

POSTER SESSIONS

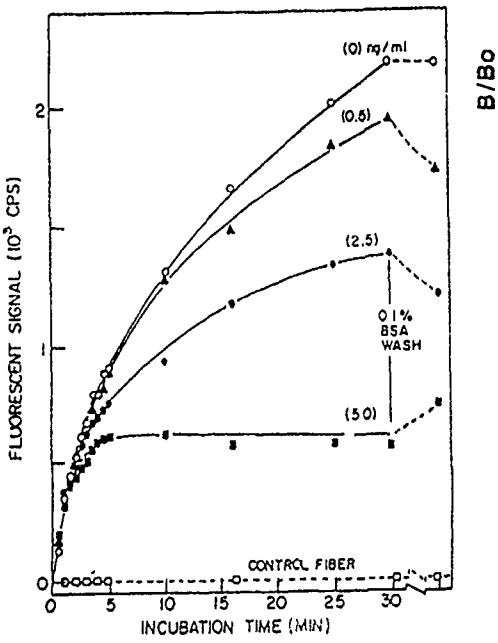

FIGURE 9

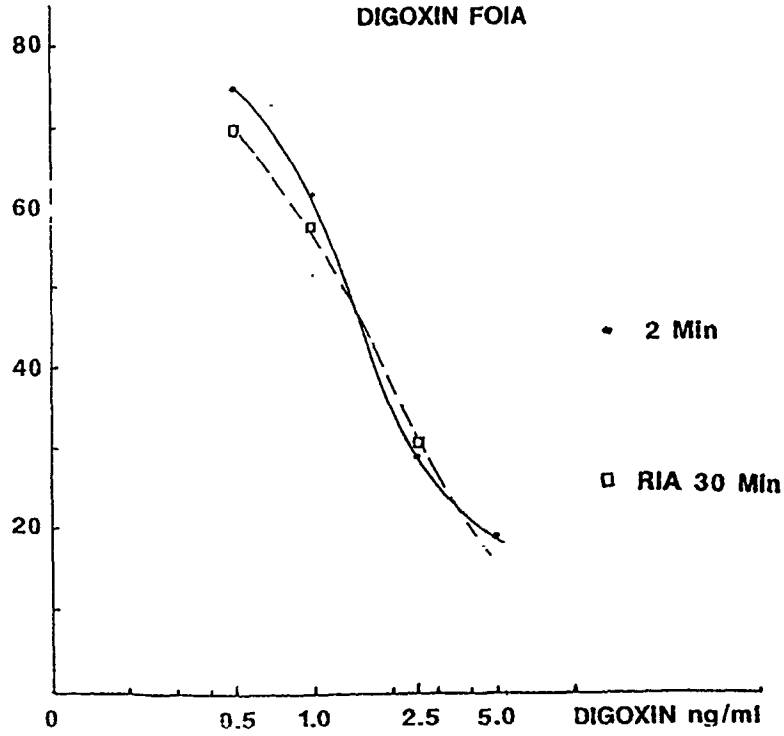

FIGURE 10

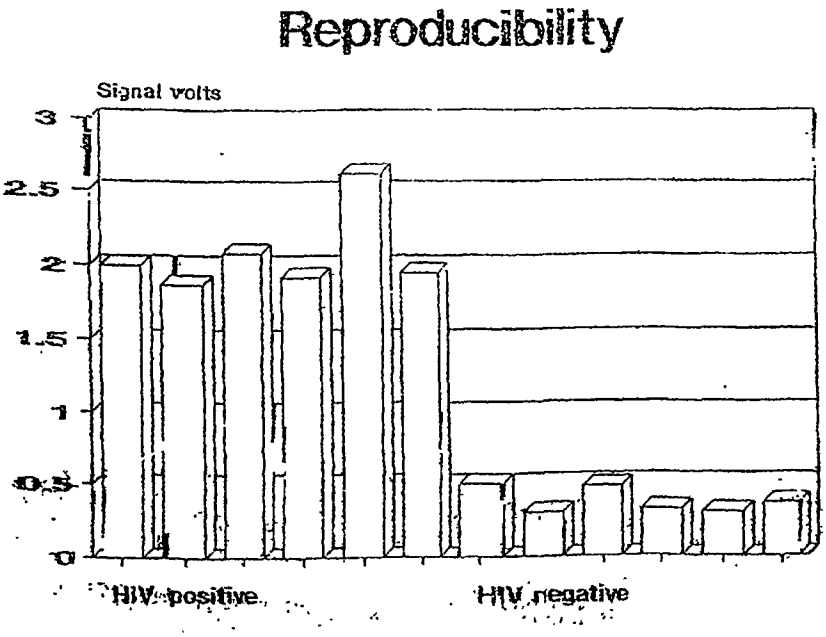

FIGURE 11

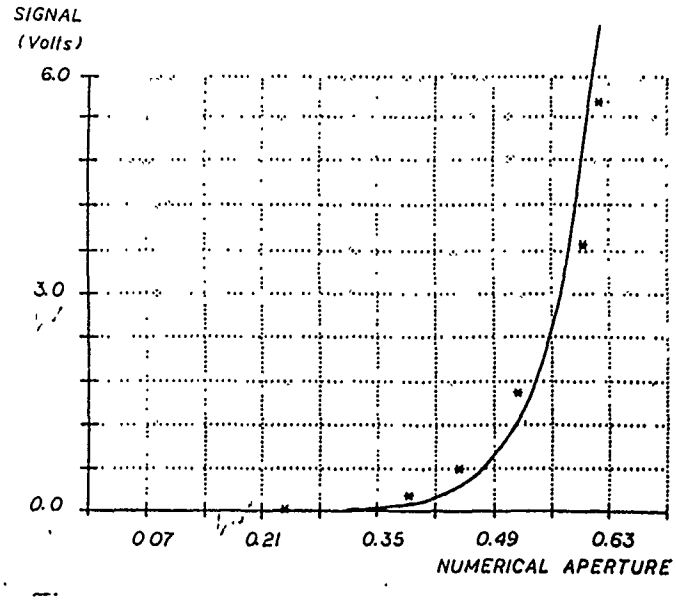

FIGURE 12

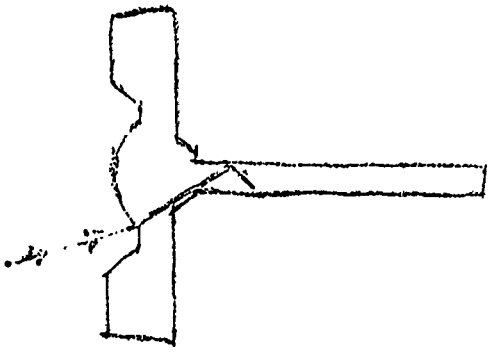

FIGURE 13

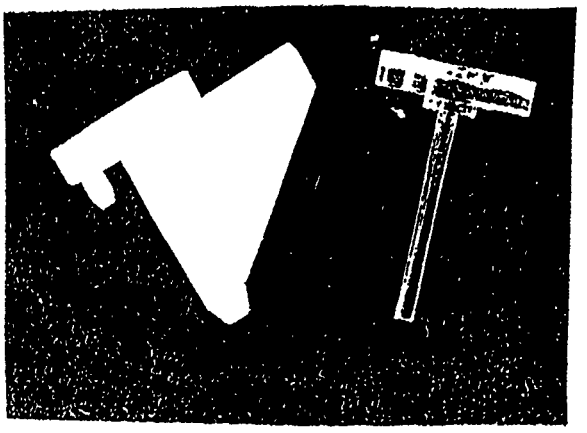

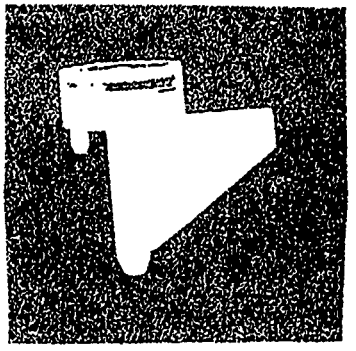

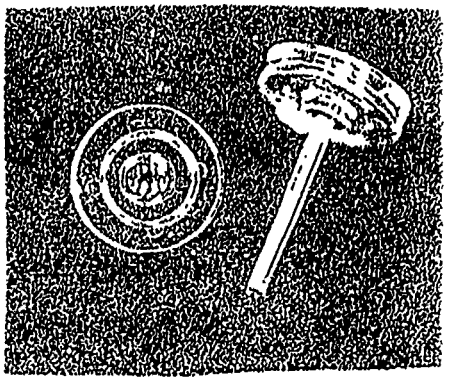

FIGURE 14

CHARACTERISTICS OF THE ORD BIOSENSOR

1) NO VOLUME MEASUREMENT FOR QUANTITATION
2) PSEUDO-HOMOGENEOUS ASSAY SYSTEM
3) HIGH SENSITIVITY - 10^{-12}m OR LESS
4) RAPID ASSAY TIME ~ SECONDS
5) ADAPTABLE TO AUTOMATION
6) MULTIPLEX

FIGURE 15

MULTIPLEX ADVANTAGES

* MULTIPLE ANALYTES
* INTERNAL REFERENCES AND STANDARDS
* INCREASE CONFIDENCE (P24* P41**)
* CORRECT NON-SPECIFIC BINDING
* CORRELATE MEASURES OF CHOICE
* LABELED IMMOBILIZING PHASE
    1. ANALYTE AB*/IMMOBILIZED AB**
    2. REAGENTLESS SENSOR

FIGURE 16

BLANK

POSTER SESSIONS

BLANK

POSTER SESSIONS

X. DECONTAMINATION POSTERS

NOTE: A paper with the following title was presented at the Conference but is not included in this document:

Studies on the Reformulation of Agent Decontaminant DS-2

BLANK

MECHANISMS OF VX OXIDATION
II. OXIDATION BY CHLORINE-BASED OXIDANTS

Yu-Chu Yang*, Linda L. Szafraniec, William T. Beaudry and Dennis K. Rohrbaugh

Physical Protection* and Research Directorates,
U.S. Army Chemical Research, Development and Engineering Center,
Aberdeen Proving Ground, MD 21010-5423

abstract

The oxidation stoichiometries of VX and a phosphonothiolate derivative by a range of chlorine-based compounds were examined in t-butanol, t-butanol-water and water systems at 18-20°C. The phosphonothiolate which does not contain a nitrogen atom reacted with all of the oxidants examined. VX did not react with chloramine-B but reacted instantaneously with Fichlor in both water and t-butanol-water. Three equivalents of active chlorine were required to produce the corresponding phosphonic and sulfonic acids. In the absence of water or a nucleophile, oxidation at the sulfur atoms of both substrates by t-butyl hypochlorite was observed.

INTRODUCTION

Laboratory detoxification of the nerve agent, VX, (**1a**, S-(diisopropylamino)-ethyl O-ethyl methylphosphonothiolate) has been commonly accomplished by house-hold bleach (typically contains 0.5-0.7 M NaOCl). The products were identified as the phosphonic (**1b**) and sulfonic acids (**2a**) shown in Equation(1) when the reaction mixture was kept at low pH.[1]

1a **1b** **2a**

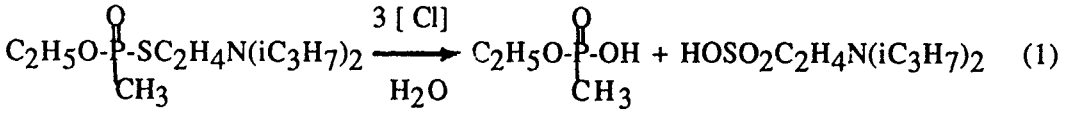

(1)

As the solution becomes more basic, greater amounts of active chlorine were consumed.[1] Presumably the unprotonated nitrogen is oxidatively more reactive at high pH and was quickly oxidized to a series of products of higher oxidation states.

Furthermore, since VX has a small solubility in basic solutions, the reaction mixture at relatively high VX concentrations could be of two-phases initially. The sulfonic acid produced might be able to facilitate the decomposition of hypochlorite to chlorine gas in the heterogeneous solution. Thus, the oxidant was deactivated by the reaction product, and excess bleach will be required for the complete cconversion of VX. The products from VX-hypochlorite reaction in neutral or basic solutions, however, have not been completely identified.

It is the purpose of this study to determine the mechanism by which VX reacts with hypochlorite. The approach was to first identify the reaction products of VX with three chlorine-based oxidants in basic and neutral solvents over a range of polarities. Based on a separate study,[2] the nitrogen in VX was a more reactive site for the oxidation by a peroxygen in the same solutions. In order to determine the effect of the nitrogen on a chlorine-based oxidant, a simple phosphonothiolate derivative of VX (**1c,** see Equation(4)) was investigated under identical conditions for comparison. Each of the reactions was monitored by ^{31}P NMR. Both ^{13}C NMR and GC/MS were used subsquently to further identify the reaction products. For GC/MS analyses of aqueous samples, the organic components were extracted into CH_2Cl_2, while the ionic products were identified by Direct Exposure Probe (DEP) Mass Spectrometry. The active oxygen content was quantitatively determined for each oxidant with a standard thiosulfate solution in an iodometric titration. The active chlorine or oxygen content was 0.865 moles per mole chloramine-B, and 1.825 moles per mole Fichlor. The t-butyl hypochlorite was kindly prepared by Dr. Leonard Shiff of CRDEC. Detailed experimental methods and peak assignments will be reported in a future publication.

RESULTS AND DISCUSSION

1. t-BuOCl in t-BuOH and in t-BuOH-Water

In an equal-molar mixture of VX (0.04 M) and t-BuOCl in t-butanol, about 5% of the VX reacted immediately, but the reaction was stopped after the first 2 to 5 minutes. A product at ^{31}P NMR δ 26.4 ppm was observed, and was different from **1b**. When a large excess of t-BuOCl was subsequently added to the above reaction mixture, about 65% of the VX further reacted before the reaction stopped again in a few minutes.

1a **1d** (δ 26.4 ppm)

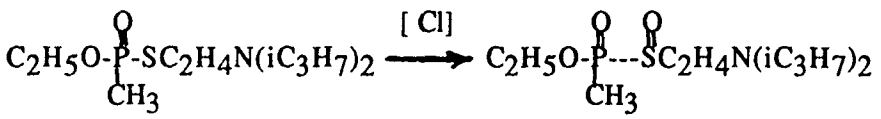

(2)

1e (δ 41.0 ppm) **2b**

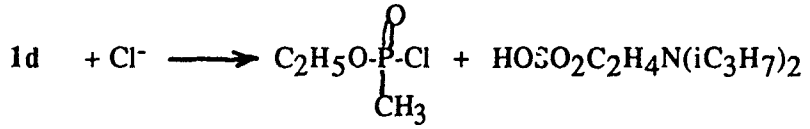

(3)

The ^{31}P NMR spectrum of the final reaction mixture showed about 50 mole% of the same product at δ26.4 ppm and 20 mole% of another product at δ 41.0 ppm, 30% of the VX was left unreacted. The reactions leading to the two products were tentatively represented in Equations (2) and (3). The reaction mixture began to turn yellow at about 20 minutes after mixing, suggesting that chlorine gas might be produced as a result of the production of a strong acid(**2d**). In the presence of excess oxidant, **2b** is likely to be oxidized further and decomposes at the N-C bonds.[2] After about 24 hous, the pyrophosphate **1e** was produced. This compound was frequently identified as a degradation product from VX and other organophosphorus compounds at both room and elevated temperatures.[3]

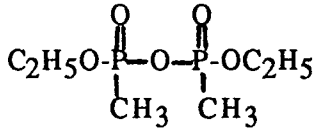

1f

Under the same conditions, the reaction of **1c** and tBuOCl in t-BuOH also produced a stable product and intermediate, tentatively assigned as the sulfoxide, **1g** (δ 27.2). This compound subsquently reacted with a trace amount of water in the solvent to produce **1b**. Unlike VX, the reaction did not stop, but seemed to have reached completion slowly. After a few days, the final reaction mixture still contained 2-3 mole% of **1g**, 18% **1b** and 80% unreacted **1c**. The structure of the intermediate(**1d**) and its subsequent hydrolysis are proposed in the following equations.

1c **1g**

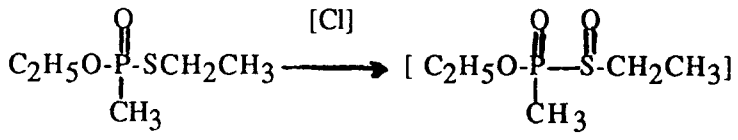

(4)

In the presence of a trace amount of water, **1g** was hydrolyzed to **1b**. The sulfenic acid **2c** was not detected as it is expected to oxidize immediately to **2d**.

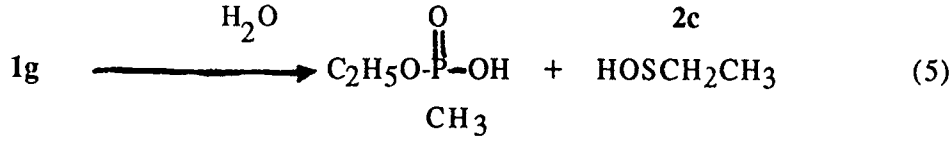

(5)

2d

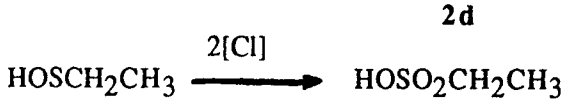

(6)

In an equal molar mixture of VX and tBuOCl in 50 vol% t-butanol, 20% of the VX reacted instantaneously to produce **1b**. No sulfoxide, **1d**, was detected. About 4-5 equivalents of active chlorine was consumed per equivalent of VX. The solution remained colorless. In the same solvent, compound **1c** also reacted with t-BuOCl to produce **1b** in less than 2 minutes. However, **1g** was present in small concentrations of about 2%. About 3 to 4 equivalents of tBuOCl were consumed per equivalent of **1c** reacted. It is proposed that most of the **1c** was oxidized directly

according to Equation(7). A comparison of the observed reactions of **1c** in t-BuOH with that in t-BuOH-water systems indicated that in the absence of water the first step of reaction shown in Equation(4) was a fast equilibrium between the substrate and **1g**. Whereas in the presence of a large amount of water as in 50% t-butanol, the reaction was driven to completion quickly as shown in Equation(7). **1g**, once produced, was immediately hydrolyzed to **1b** and only a small amount of **1g** was detected.

1c **1b** **2d**

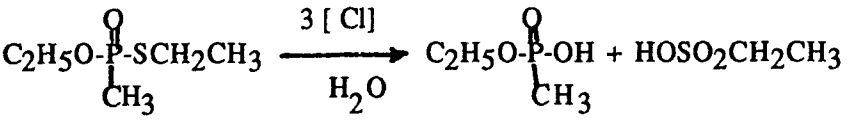

(7)

VX probably reacted in a similar manner as **1c**. In t-BuOH, an oxidation equilibrium (shown in Equation(2)) could also be present. However, since **1b** was not produced, the limited amount of water must have been consumed to produce the hypochlorite anion from tBuOCl to act as the reactive oxidizing component in the system. Apparently, the formation of **1d** was more difficult and required a larger amount of hypochlorite than the formation of **1g**. In 50% t-butanol or in the presence of a nucleophile such as the chloride ion, the intermediate was quickly converted to the observed product. Thus the conversion of VX was increased by the nucleophilic displacement reactions of **1d** in the second step. The chlorophosphonate, **1e**, was not found in the aqueous solution since it formes less quickly than **1b** but hydrolyzes quickly to **1b**. Therefore, the presence of water was essential in the oxidation of VX by an active chlorine. The oxidation of VX by tBuOCl in 50% t-butanol is proposed to be the same as in Equation(1).

2. Chloramine-B($C_6H_5SO_2N(Cl)Na$) in t-BuOH-Water and in Water

VX did not react with chloramine-B in either of the above solvents. This is consistent with a previous study in which no reaction could be detected even when a 30 fold excess chloramine-B was used to oxidize VX in an ethanol-water mixture at room temperature.[4] After 24 hours, a small amount of VX was hydrolyzed. In an equal molar mixture, 94% of the VX was left in 50 vol% t-BuOH; and 74% of the VX was left in pure water. The hydrolysis in pure water was found to have proceeded by simultaneous P-O and P-S bond cleavages.[5]

On the contrary, **1c** reacted with chloramine-B to form identical but complicated products in water (quickly) and in 50 vol% t-butanol (less quickly). In addition to the phosphonic and sulfonic acids, a series of oxidation products consisting of S-S, S-N, S=O and S=N groups were identified by NMR and/or by GC/MS. Their structures are shown below, in which the sulfur atoms are present in different oxidation states. It is believed that these compounds were reaction intermediates which would be oxidized and hydrolyzed to **2g** first and finally to the ethylsulfonic acid(**2d**) completely in the presence of sufficient oxidant. The reaction mechanism seems to be the electrophilic attack of the nitrogen in chloramine-B on the sulfur in **2c**, followed by hydrolysis. If this is true, the reaction is similar to that of regular sulfides reported in the literature.[6] Since the sulfur in VX has been found to be more difficult to oxidize than that in **1c**,[2] the

nitrogen in the chloramine-B is perhaps too weak to react with the sulfur as an electrophile in the first step of oxidation. Since the reaction was completely different from that of tBuOCl, little or no hypochlorite was expected to be present in the reaction mixture.

2e

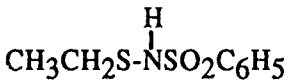

2g

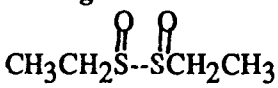

2i

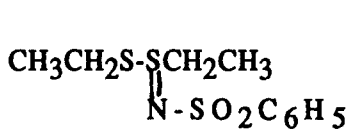

2f

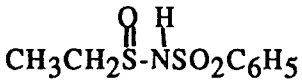

2h

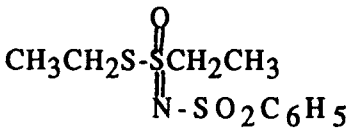

3. Fichlor(Sodium Dichloroisocyanurate, $C_3O_3N_3Cl_2Na$) in Water and in t-BuOH-Water

VX reacted with Fichlor instantaneously in water and in an aqueous solution containing 33 vol% t-butanol. The reaction was complete in less than 2 minutes in each solvent system. **1c** also reacted in an identical manner as VX. The stoichiometry was the same as that in Equation(1) or (7) above using tBuOCl in 50% t-butanol. The products shown in these Equations were positively identified by both ^{31}P and ^{13}C NMR and by GC/MS. This indicated that the Fichlor, unlike the chloramine-B discussed above, was completely converted to hypochlorite anion in the above solutions. Only three equivalents of active chlorine were required per equivalent of **1c** or VX, indicating that the nitrogen in VX was not oxidized before all of the VX was reacted. Therefore, the oxidation of sulfur was much faster than the nitrogen in VX. The sulfur must be more reactive towards a hypochlorite anion than a peroxygen which was found to oxidize the nitrogen first.[2] The hypochlorite anion must have also functioned as a nucleophile and attacked the phosphorus to assist the cleavage of the P-S bond. The sulfur atom, then, becomes a more reactive site for oxidation.

SUMMARY

The stoichiometry and products of the oxidation of VX by Fichlor, a chloramine, have been determined for the first time in pure water and in a less polar solvent containing 33% t-butanol by volume. The reaction at about 20°C was instantaneous. Phosphonic and sulfonic acids were produced and three equivalents of active chlorine were required per equivalent of VX. A VX derivative, which does not have the diisopropylamino group, was oxidized in the same manner. It is believed that all of the Fichlor was converted to the hypochlorite anion, because the same rate and stoichiometry were observed for t-butyl hypochlorite in a water-t-butanol mixture. In pure t-butanol, only a small fraction of the VX and its derivative reacted with t-butyl hypochlorite to produce a sulfoxide. No oxidation of the

nitrogen in VX to an N-oxide prior to the oxidation of the sulfur was ever detected by ^{31}P NMR in any of the above reaction mixtures.

VX was unreactive towards chloramine-B. The phosphonothiolate derivative of VX reacted with chloamine-B by the same mechanism as that of a regular sulfide. The reaction mechanism is the electrophilic attack on the sulfur by the nitrogen in the chloamine-B followed by hydrolysis, and is completely different from that of the hypochlorite. It is believed that little or no hypochlorite was generated from the chloramine-B. In the absence of the neighboring amino group, the sulfur in a phosphonothiolate is apparently more reactive than that in VX.

REFERENCES

1. Private communications with Mr. Joseph W. Hovanec, Research Directorate, CRDEC.

2. Yang, Y.-C.; Szafraniec, L. L.; Beaudry, W. T.; and Rohrbaugh, D. K., Mechanisms of VX Oxidation I. The Oxidation by Peroxides and OXONE; in Proceedings of the CRDEC Scientific Conference on Chemical Defense, Aberdeen Proving Ground, MD, November, 1989.

3. D'Agostino, P. A.; Provost, L. R.; Visentini, J., J. Chromatgr. (1987) 402, 221-232

4. Szafraniec, L. L.; Beaudry, W. T.; Rohrbaugh, D. K.; Ward, J. R.; Stoichiometry of Reaction of GA, GB, VX and HD in Mixed Aqueous Solution, in Preceedings of the CRDEC Scientific Conference on Chemical Defense, Aberdeen Proving Ground, MD, November, 1988

5. Szafraniec, L. J., Szafraniec, L. L., Beaudry, W. T., and Ward J. R., On the Stoichiometry of Phosphonothiolate Ester Hydrolysis, in Preceedings of the CRDEC Scientific Conference on Chemical Defense, Aberdeen Proving Ground, MD, November. 1988

6. Campbell, M. M.; Johnson, G.; Chem. Rev. (1978) 78, 65

THE EFFECT OF BIOLOGICAL MEDIA ON THE HYDROLYSIS OF MUSTARD SIMULANTS

Lawrence C. Cerny and Elaine L. Cerny
Utica College of Syracuse University
Utica, N.Y. 13502

The hydrolysis kinetics of three mustard simulants, 2-chloroethyl ethyl, 2-chloroethyl methyl and 2-bromoethyl phenyl sulfide (CEES, CEMS, AND BEPS) were studied in a variety of aqueous biological media at 25 C. Previously, a very rapid rate of hydrolysis in dilute gelatin solutions was observed. This work has been extended to include rat tail collagen in its native state, a rod-like triple helical structure; the dissociated components of the triple helix and shorter random coils of gelatin. As a potential non-corrosive oxidant, methemoglobin was added. The rate constants were determined by conductivity of the reaction mixture. The formation of sulfhemoglobin was followed spectrophotometrically. It appears possible that a decontaminant could consist of a freeze-dried mixture of collagen (gelatin), methemoglobin and selected salts.

INTRODUCTION

Preliminary investigations using a variety of biological substances have shown that these materials may be a viable decontaminant for mustard (1).

These studies have indicated that an approach to this problem could be a material which is a combination of gelatin, sea water and methemoglobin. The rationale for the choice of these three substances is as follows: Gelatin is a common household product readily available and well-characterized. Depending upon its concentration, it can be a dilute solution or a gel. It is a suitable vehicle for the decontamination process. The ions in the sea water are useful in maintaining the ionic strength and pH of the solution. Specific ion catalysis may

play an important role in the hydrolysis of the mustard. Finally, decontamination does not proceed by hydrolysis alone, oxidation also plays an important role. A biological molecule available in almost unlimited quantities is bovine hemoglobin. The ferric state of the iron provides a natural oxidizing reagent. Initial experiments using these three substances merit an in-depth investigation.

There are approximately ten billion units of bovine blood discarded each year. Since New York State is one of the leaders in the dairy industry in the United States, this source of hemoglobin (Hgb) was tapped. The procedure for processing this compound has been reported (2). This method takes special care to maintain the iron in its reduced state (Fe^{+2}). However, exposure to air for twenty-four hours is adequate to form methemoglobin, Met, with the oxidized iron (Fe^{+3}).

Two sources and forms of gelatin are available. The first can be obtained commercially such as Knox gelatin. This is a degraded collagen product with a low molecular weight, random coil configuration and moderate intrinsic viscosity. It is readily available and very uniform in its composition. The second type is native collagen. This is readily available from the tendons of rat tails. It has been shown that this form has a high molecular weight, is an extended triple helix with a high intrinsic viscosity (3). Also there is a third variable. The biopolymer has some variations depending upon the age of the rat from which it is extracted.

EXPERIMENTAL

Chemicals and Materials

The bromo phenyl ethyl sulfide, chloro ethyl ethyl sulfide and chloro ethyl methyl sulfide were obtained from the Fairfield Chemical Company. They were used without any further purification. The gelatin was purchased as KNOX Gelatin, a commercially available household item. The native collagen was extracted from rat tails. This technique has previously been described (3). This material was denatured into the random coil form by heating at 48 C for three hours. A significant lowering of the viscosity indicated that the process was completed. The concentration of the collagen was determined by dry weight measurements. The extraction, purification and characterization of the hemoglobin (Hgb) are well-documented procedures (2).

Equipment

The kinetic studies were followed by the increase in the rate of conductivity of the HCl in the reaction mixture. Accurate measurements were made with a YS 1 Model 35 Conductance Meter and monitored by a Heath Strip Chart Recorder using calibrated conductivity cells. The rate constants were determined using a non-linear regression analysis (4).

The non-Newtonian flow properties of the solvents were determined with a Well-Brookfield micro-cone plate viscometer (5).

All measurements were made at 25 ± 0.1 C.

An ANALECT ATC-753 FTIR DATA System was used for the spectroscopic investigations.

The concentrations were made by weight. Each substrate was dissolved in freshly distilled acetronitrile at a concentration of 10%. The initial concentration for all kinetic studies were less than 8 x 10^{-4} M.

RESULTS

The results of the kinetic studies presented in Table 1 follow the normal first order rate equations (1,6,7). However the data given in Table 2 could not be used in the standard first-order kinetic forms.

TABLE 1

Summary of Results at 25 C with Conductance Cell

SOLVENT	SUBSTRATE	K_1 (1/min)
0.025 Mole Fract Acetone(1)	phenyl-Br	1.10 x 10^{-2}
0.5% Gelatin in H_2O(1)	phenyl-Br	2.25 x 10^{-2}
0.068% Collagen (Random Coil)	phenyl-Br	1.09 x 10^{-2}
7.5% Hgb	phenyl-Br	3.82 x 10^{-2}
0.068% Native Collagen + 7.5% Hgb (1:1)	phenyl-Br	3.53 x 10^{-2}
0.068% Collagen (Random Coil) + 7.5% Hgb (1:1)	phenyl-Br	3.19 x 10^{-2}
7.5% Hgb + H_2O (1:1)	phenyl-Br	3.74 x 10^{-2}
0.068% Native Collagen + 7.5% Hgb (1:1)	CEES	4.11 x 10^{-1}
0.068% Native Collagen + 5.6% Met (1:1)	CEES	3.81 x 10^{-1}
0.068% Native Collagen + H_2O (1:1)	CEES	1.05 x 10^{-2}

TABLE 2

SUMMARY OF RESULTS at 25 C
with CONDUCTANCE CELL
(Complex rate equations, not first order)

SOLVENT	SUBSTRATE
0.068% Native Collagen	phenyl-Br
0.068% Native Collagen + H_2O (1:1)	phenyl-Br
0.068% Native Collagen + 0.068% Random Coils(1:1)	phenyl-Br
0.068% Native Collagen	CEES
0.068% Native Collagen	CEMS

This is shown graphically in Fig. 1. Perhaps one of the contributing factors is the structure of the native collagen. The rigid triple helix structure and the random coil denatured form appear in Fig. 2.

Fig. 1

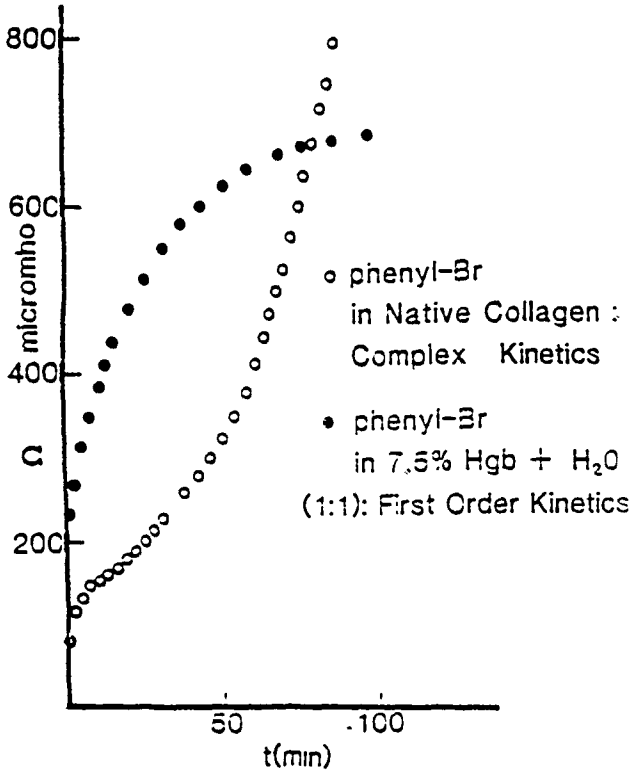

Fig.2

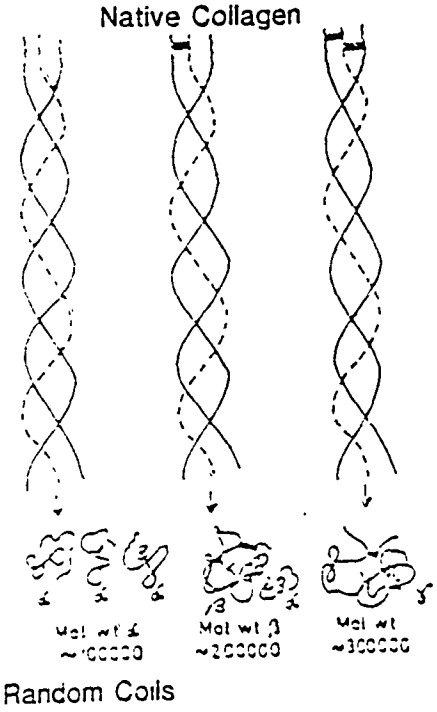

The viscosity of the various solvents certainly play an important role in the kinetic mechanism. The non-Newtonian flow measurements were determined in a cone-plate viscometer. The data were evaluated using the Casson equation (8)

$$\tau^{\frac{1}{2}} = \tau_y^{\frac{1}{2}} + (b\,\dot{\gamma})^{\frac{1}{2}} \qquad (1)$$

The important term in Eq. 1 is τ_y, the yield stress. This is the minimum stress value in order for the system to start to flow. It can be evaluated from a graph of $\tau^{\frac{1}{2}}$, the shear stress, versus $\dot{\gamma}$, the shear rate. The intercept of this linear relationship is $\tau_y^{\frac{1}{2}}$. The parameter b relates to the Newtonian flow behavior of the system. The values of τ_y for three solvents are given in Fig. 3. The viscometric behavior of three systems in the presence of a substrate at the completion of a reaction is presented in Fig. 4.

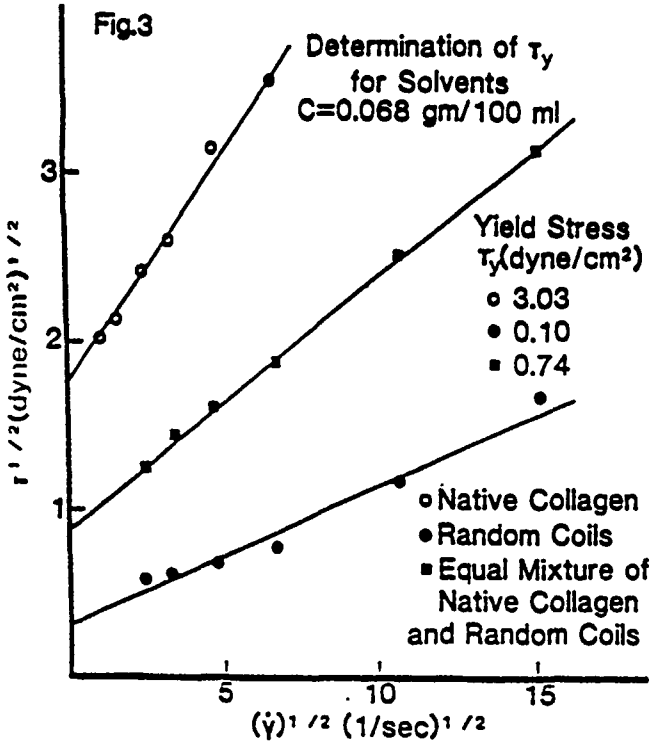

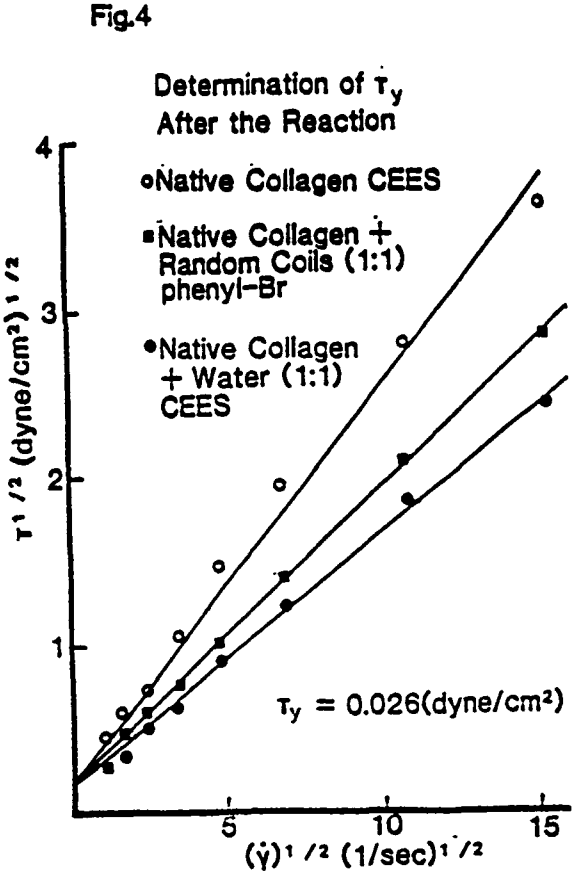

As a means of trying to evaluate the role of the Hgb in the reaction mechanism, some of the reaction mixtures were observed spectrophotometrically. It was anticipated that sulfhemoglobin may be formed in the reactions. In Fig. 5a, the spectrograph for the reaction mixture of native collagen and hemoglobin is presented. The two spectrographs in Fig. 5b after the completion of the reaction in the presence of the substrate, phenyl-Br, do show a peak at 630 nm which could be attributed to sulfhemoglobin (9).

Fig.5a

Native Collagen + 7.5% Hgb (1:1)

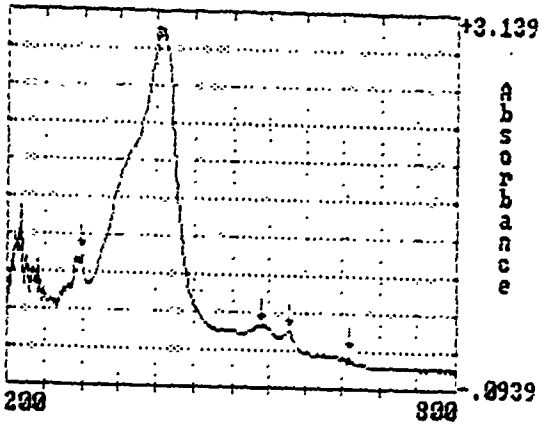

Fig.5b 7.5% Hgb phenyl - Br

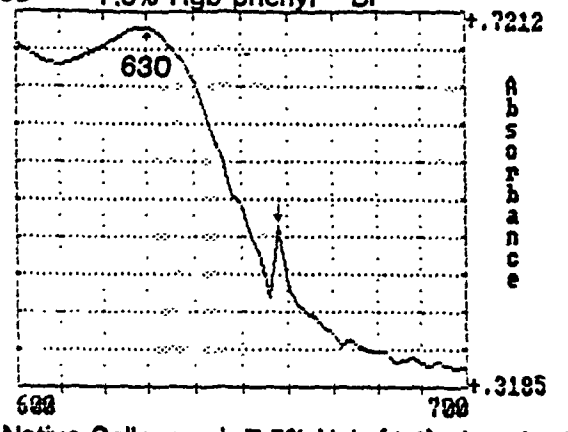

Native Collagen + 7.5% Hgb (1:1) phenyl - Br

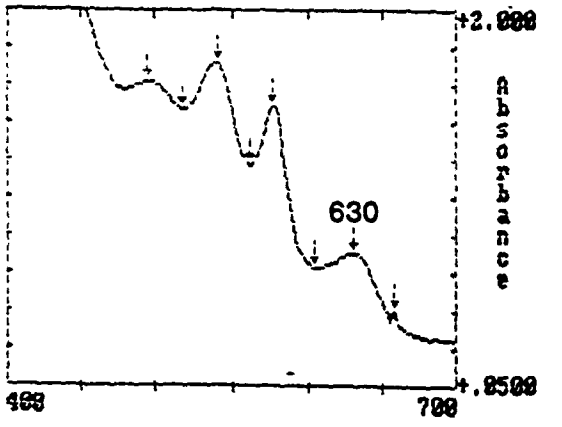

CONCLUSIONS

This preliminary investigation indicates that a possible decontaminant for mustard simulants could be a combination of collagen, hemoglobin and sea water. The interesting conclusions of this study are:

1) In the presence of the collagen molecule, the kinetics of the hydrolysis do not follow a simple first order rate equation;

2) There is strong evidence that the simulant reacts with the native collagen, denaturing it to random coils in the same manner as heating;

3) Spectrographs indicate that sulfhemoglobin may be formed between the hemoglobin and the mustard simulant.

REFERENCES

1) Cerny, L.C., Yang, Y.-C. and Ward, J.R. Proc. U.S. Army CRDE Sci.Conf. on Chem. Def. Res. 1:75-81, 1989.

2) Cerny, L.C., Stasiw, D., Cerny, E.L., Baldwin, J.E. and Gill, B. Clin. Hemorheology 2:355-365, 1982.

3) Cerny, L.C., Grauz, D. and James, H. Biorheology 6:161-168, 1970.

4) Physical Chemistry on a Microcomputer J. H. Noggle, Little, Brown and Co. Boston, 1985, p.145.

5) Cerny, L.C., Stasiw, D. and Tinelli, W. Biorheology 10:565-575, 1973.

6) Yang, Yu-Chu and Fayles, T.H. J. Am. Chem. Soc. 103:5849-54, 1981.

7) Yang, Yu-Chu, Ward, J.R. and Lutern, T. J. Org. Chem. 51: 2756-60, 1986.

8) Cerny, L.C. and Cerny, E.L. Mat. Res. Soc. 110:107-112, 1989.

9) Dijkhuizen, P, Boursma, A., Gerding, A.M. and Zijlstra, W.G., Clin. Chem. Acta 78:479-487, 1977.

BLANK

C-AGENT EVAPORATION AND WEATHERING ON SURFACES: EFFECT OF SURFACE TEMPERATURE

Hugh R. Carlon
Research Directorate
U.S. Army Chemical Research, Development and Engineering Center
Aberdeen Proving Ground, Maryland 21010-5423

ABSTRACT

Previously we reported in CRDEC-TR-017, November 1988, that surface temperature is the critical parameter determining the speed and efficiency of decontamination by surface heating. More recent research, reported here, studied time/temperature data in the literature to learn how the speed of decontamination varies with measured surface temperature between ambient temperatures and 121 °C, the "critical" surface temperature found earlier to decontaminate VX, THD and TGD to residual levels of one percent of less in a matter of seconds. The study was hampered by the lack of published data reporting measured surface temperatures, as opposed to other parameters, in chemical decontamination trials. But it was possible to reach several conclusions and recommendations for future work. It was also found that Bis (2-ethylhexyl) phosphonate ("BIS") is a poor simulant for VX in surface-heating decontamination studies.

INTRODUCTION

A recent study[1] showed that surface decontamination of VX, THD and TGD to residual levels of one percent or less can be achieved by bringing the surface temperature, even momentarily, to 250 °F (121 °C) or more. The mechanisms involved have not been studied, but it is clear that at higher temperatures physical properties of liquids and surfaces are complex and interactive. Simple evaporation as a function of vapor pressure with temperature no longer dominates as it often does at ambient or moderate temperatures.

It is immaterial how this "critical" surface temperature (250 °F) is attained, but decontamination by hot air impingement in the open atmosphere is inherently a very energy-inefficient process. Thus alternative methods to heat surfaces more efficiently need to be studied. The study[1] showed that surface temperature was the only significant parameter in experiments in which the parameters varied included hot air temperature, air (jet) velocity, standoff distance, heating time, sample size, substrate (surface) material and the C-agent or simulant being evaluated. Similar results were found by workers using infrared radiation rather than hot air to heat contaminated surfaces.[2]

These observations led us to undertake an extensive literature search. The specific purpose of this search was to locate existing experimental data relating C-agent evaporation rates to surface temperatures and times of heating. Weathering data were known to exist from many studies conducted under typical ambient conditions, but the data sought were those for temperatures between ambient ones, and 250 °F or more that our study had identified as the critical surface temperature for virtually complete C-agent decontamination in a matter of seconds (the time required to heat the surface to 250 °F).

The literature search produced only six references containing data of the kind sought. Other references were less valuable for a variety of reasons, but most commonly because quantitative elapsed times and surface temperatures were not reported along with residual contamination levels. The data from Ref. 1 were found to be far more complete and reliable in this respect than any other located in the literature search.

EXPERIMENTAL

Figures 1, 2 and 3 show pulse-jet data[1] for C-agents VX, THD and TGD, respectively, for samples that were prepared and then heated immediately by the jet with exposure times ranging from 10 to 90 seconds. These exposure times, combined with several jet nozzle-to-surface standoff distances, yielded a wide range of surface temperatures.

The key shows that both alkyd- and urethane-painted metal plates were used. The sample plates were chemically extracted for analysis immediately before and after jet exposure. The percent residuals of each agent thus determined after heating are shown by the ordinate scales. Note that regardless of the paint type or jet exposure time (and other attendant variables including jet standoff distance and resulting gas temperature at the sample surface), only the surface temperature is clearly significant. At surface temperatures of up to about 150 °F, there is almost no evaporation of VX (Figure 1). At slightly higher temperatures, there is a precipitous increase in VX evaporation from the surface which is reflected as a nearly step-function drop in VX residual on the plate (which includes VX sorbed in the paint).

By the time the surface temperature has reached about 250 °F, the VX residual has fallen to one percent (1%) or less of the original contamination density. At still higher surface temperatures, the residuals are below 1% and, in most cases, are too small to be detected by the analytical techniques used (points in parentheses).

This same behavior is observed for agent THD, except that a 1% residual is reached at a lower surface temperature than for VX (about 230 °F, Figure 2). Agent TGD behaves similarly, but at a still lower temperature (about 200 °F, Figure 3). Although a range of jet exposure times was used, it was found in practice[1] that at surface temperatures above about 250 °F all three C-agents were evaporated to residuals of about 1% or less within several seconds.

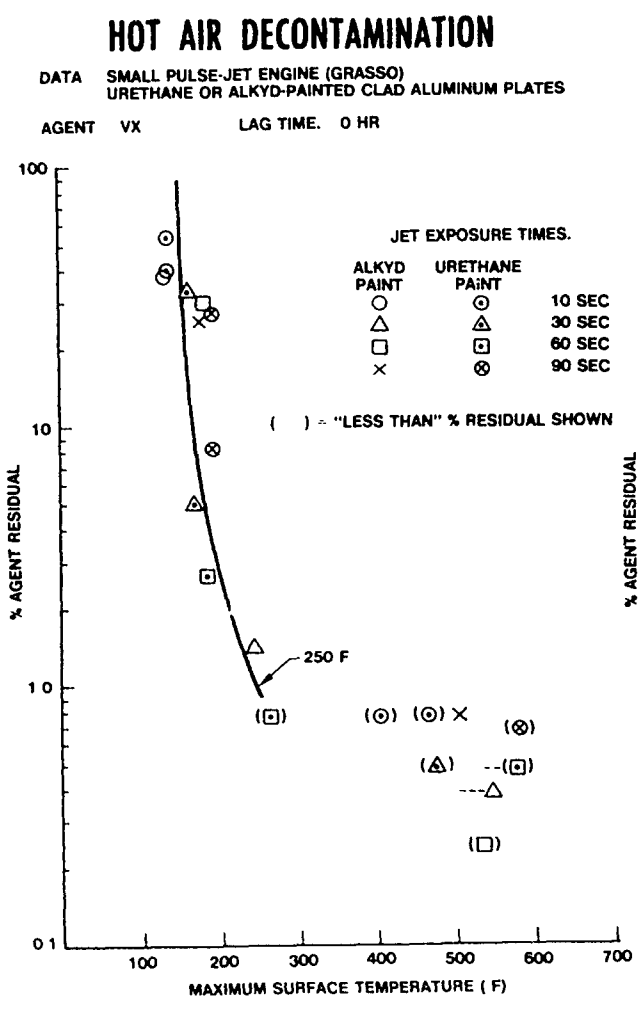

Figure 1. Surface-Heating Data for Decontamination of Agent VX; Lag or Weathering Time: 0 Hours.

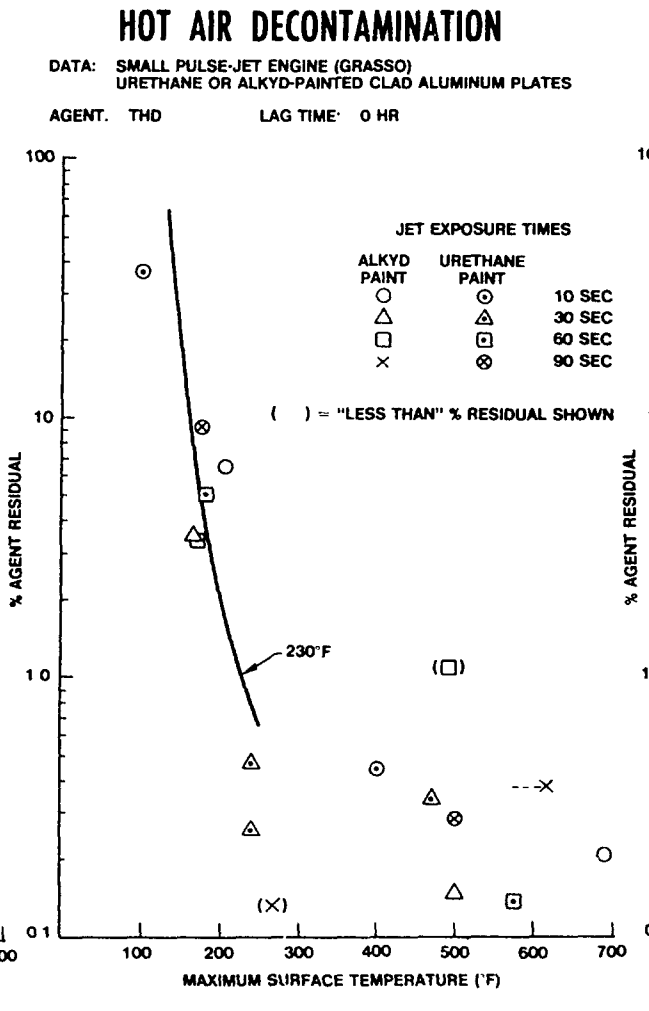

Figure 2. Surface-Heating Data for Decontamination of Agent THD; Lag or Weathering Time: 0 Hours.

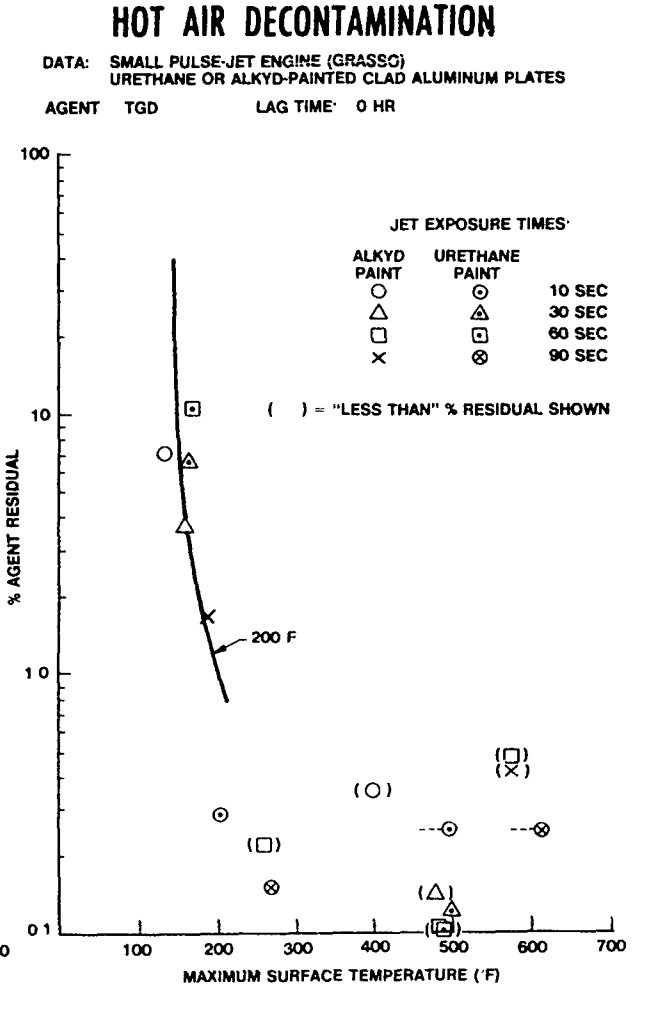

Figure 3. Surface-Heating Data for Decontamination of Agent TGD; Lag or Weathering Time: 0 Hours.

Since VX (Figure 1) requires the highest surface temperature for evaporative decontamination of the three agents tested, it could be considered a "standard" or worst-case agent. Thus a 250 °F (121 °C) surface temperature is critical for the evaporative decontamination of the agents discussed here within a few seconds. Penkov[2] also found that a surface temperature of 120 °C could be reached in seconds by infrared radiant heating, and was all that was required for complete vaporization of a toxic chemical agent from a contaminated surface.

When test samples[1] were permitted to weather or age for several hours before being heated and decontaminated by the pulse-jet exhaust gases, complications were introduced. Some agents on some substrates spread rapidly and reached the edges of the 1" x 1 7/16" rectangular metal plates, where they were partially protected from the jet by the sample holder. Evaporation of THD and specially of TGD became significant at room temperature, although VX was little affected. The agents penetrated paint layers (especially alkyd paint). Thickeners separated from agents in some cases. But the most important results obtained for the zero-weathered samples were substantially borne out for the weathered ones. A surface temperature of 250 °F was still found, after weathering, to be approximately the critical surface temperature for evaporative decontamination to residual levels of about 1% or less.

This is demonstrated in Figures 4-6, which show data for the three test C-agents in the same sequence as Figures 1-3: VX, THD and TGD. The data for VX in Figure 1 are repeated in Figure 4, where the abscissa scale is expanded. Similarly, the data for THD in Figure 2 are repeated in Figure 5, and the data for TGD in Figure 3 are repeated in Figure 6. But Figures 4-6 also include all available data[1] for 4 and 24 hour lag (aging) or weathering times.

In Figure 4, note that for VX at temperatures above 200 °F the agent residuals for aged or unaged samples were all a few percent or less, and that these residuals fell to about 1% or less (or to immeasurable values) as the surface temperature reached the "critical" value of 250 °F.

In Figure 5, note that for THD most residuals for aged or unaged samples were about 1% or less as the surface temperature reached 240 °F. The exceptions are a few data points for alkyd-painted substrates. But alkyd paints are notorious for their C-agent sorption, and are presently being replaced by urethane paints on military equipment.

In Figure 6, note that for TGD the residuals for aged or unaged samples were at or below 1% (except for one alkyd-painted substrate) at a surface temperature of less than 210 °F, and that they fell below 1% (or to immeasurable levels) for slightly hotter surfaces.

Figure 7 presents composite data[1,3] for several weathering or lag times between 0 and 4 hours for agent TGD, in a somewhat different way (for details, refer to Reference 3). TGD is the most volatile of the three C-agents considered here, and its evaporation even during a period of four hours or less under moderate to warm ambient conditions at temperatures of 75 °F, 100 °F and 125 °F can be considerable. Figure 7 demonstrates that, while evaporation due to weathering alone can significantly

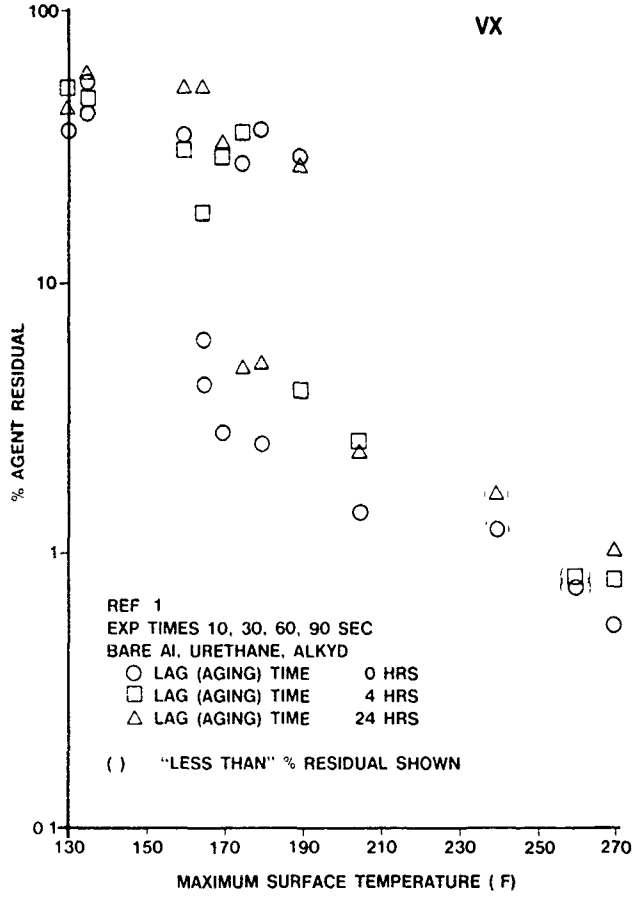

Figure 4. (Top Left) Weathering and Surface-Heating Data for Decontamination of Agent VX; Lag or Weathering Times: 0, 4, and 24 Hours.

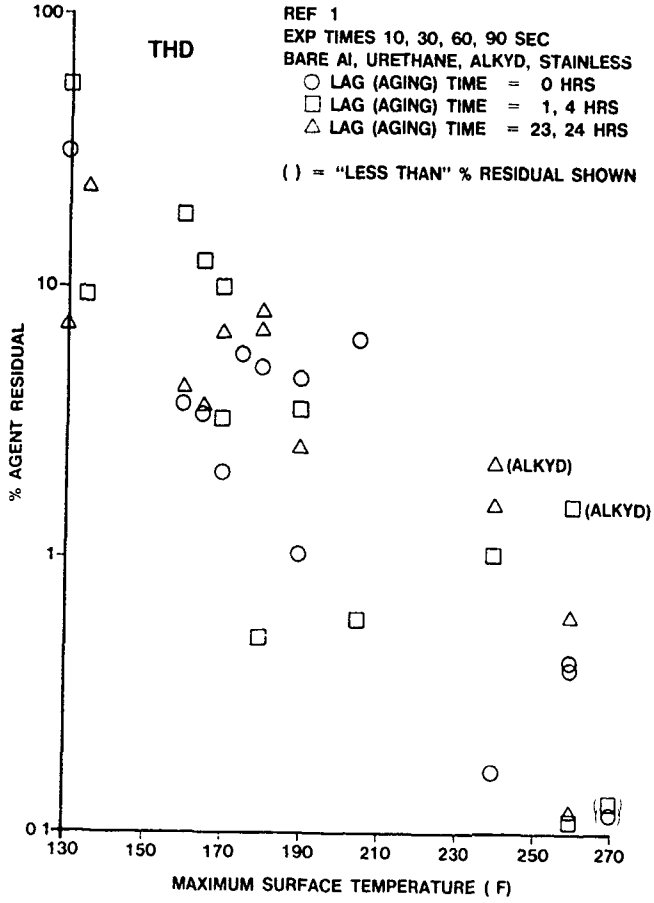

Figure 5. (Top Right) Weathering and Surface-Heating Data for Decontamination of Agent THD; Lag or Weathering Times: 0, 4, and 24 Hours.

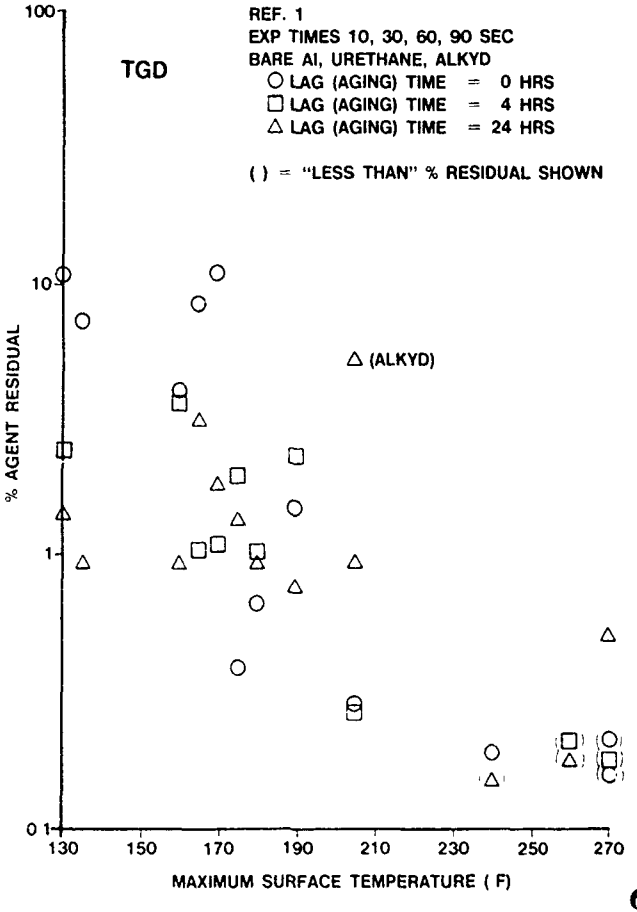

Figure 6. (Left) Weathering and Surface-Heating Data for Decontamination of Agent TGD; Lag or Weathering Times: 0, 4, and 24 Hours.

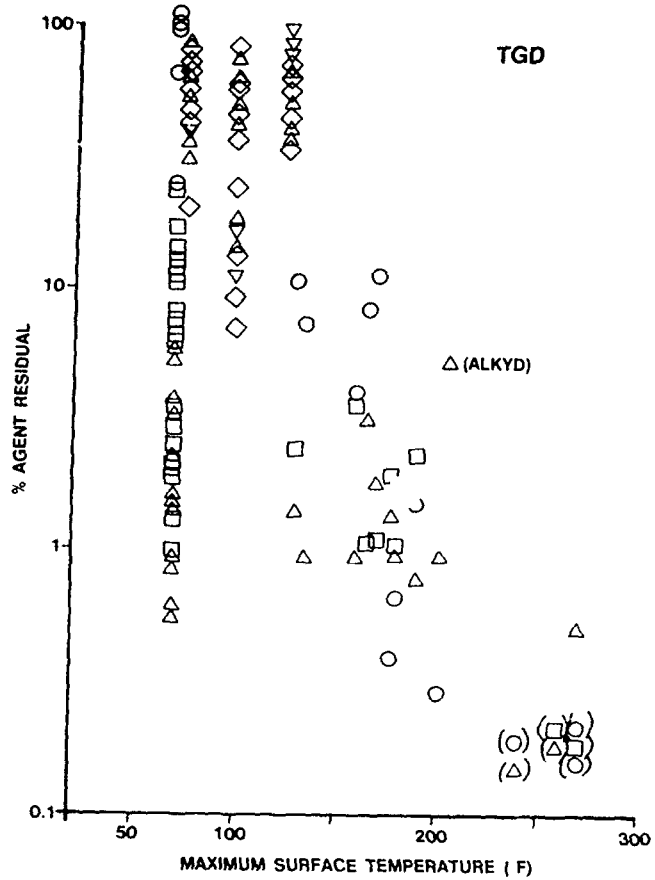

Figure 7. Weathering Data[3] at 75 °F, 100 °F and 125 °F and Surface-Heating Data[1] for Decontamination of Agent TGD; for Several Lag or Weathering Times Between 0 and 4 Hours.

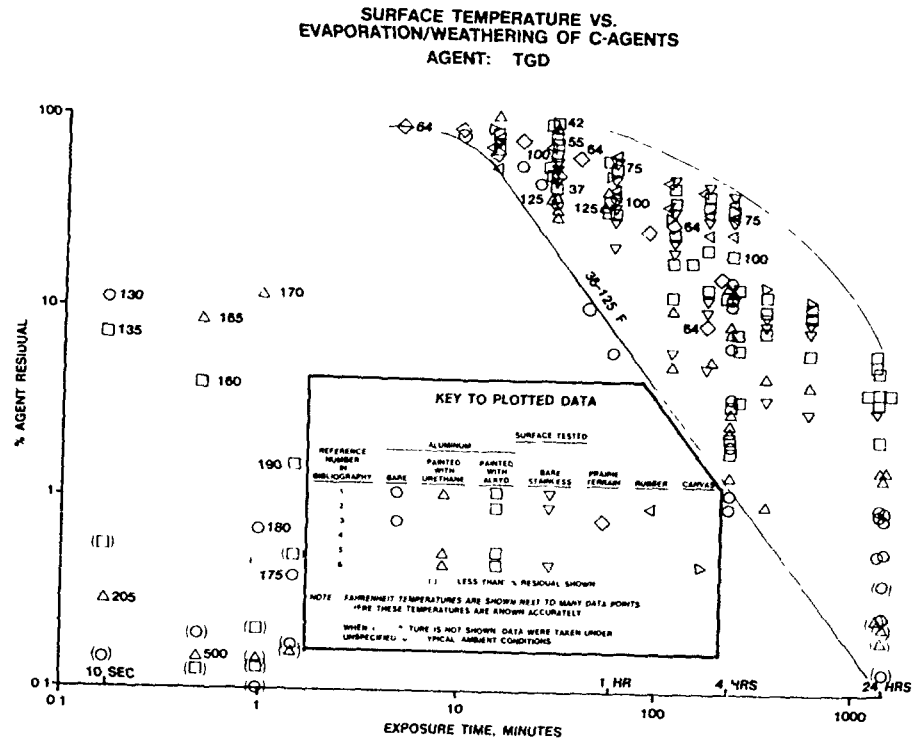

Figure 8. Surface Temperature Versus Evaporation/Weathering of C-Agents; Agent: TGD.

"decontaminate" TGD from a surface in a period of a few hours or less, the application of surface heating (in this case using a hot gas jet) can complete the job in a matter of seconds.

Figures 4-7 show quite clearly that, despite the complications of weathering, a surface temperature of about 250 °F (121 °C) is the "critical" temperature for the evaporative decontamination of C-agents from surfaces to residual levels of about 1% or less, in seconds.

DISCUSSION

While our results[1] include some weathering data at ambient temperatures, and a great many at elevated temperatures, they are comparatively lacking in data for surface temperatures between ambient and the critical value of 250°F. Very few references are available that contain results in this temperature range; some of these are discussed in Ref. 4.

Some of the data in Ref. 4 were taken over a range of temperatures thought to be likely to occur on battlefields in temperate regions. Some were taken in desert terrain, where summer surface temperatures can reach those in the range of interest for the present study; but these temperatures were measured incidentally, and not precisely, compared to other parameters.

In Figure 8, many of the data from Refs. 1 and 4 are summarized. To the left of Figure 8 are plotted our data[1] for agent TGD heated to the surface temperatures shown next to the data points. These are included to indicate the very brief exposure times that are required for substantial evaporative decontamination at surface temperatures higher than those that are normally encountered in natural weathering situations.

To the right of Figure 8, a great many data points are plotted between two solid boundary curves, the lower one of which is labeled "36-125 °F". This indicates that all of the data points between the curves were taken for surface temperatures that were, as nearly as could be determined, between 36 °F and 125 °F. Where space permits, some of the surface temperatures are shown next to their corresponding points. No significant correlation could be found between evaporation rates, percent agent residuals, and surface temperatures for the data in this temperature range.

Note that exposure times of 4 to 24 hours are required for natural weathering to lower TGD residuals to levels of several percent or less, as compared to about one minute or less for surface temperatures beginning only several degrees above 125 °F. Some individual data points can, of course, be erratic especially if the surface temperature was not accurately known as was often the case for data in Ref. 4.

Surface-heating data were obtained in our experiments[1] for simulants as well as for agents. A separate report will discuss the simulant data[5] and observations that can be made from their analysis. However, it is worth mentioning here that while our simulants for THD (thickened methyl salicylate (TMS)), and for TGD (triethyl phosphate (TEP)) performed well,

our simulant for VX (Bis (2-ethylhexyl) phosphonate (BIS)) did not. BIS residuals were consistently higher than those of VX for a given surface temperature, and surface temperatures far above 250 °F (121 °C) were required to decontaminate BIS to residuals of 1% or less. Thus use of BIS would lead to the indication that decontamination is less effective than actually is the case for VX, possibly leading to overdesign of equipment. Data are shown in Figure 9.

CONCLUSIONS AND RECOMMENDATIONS

It is risky to infer too much from the data shown here, but some generalized conclusions can be reached. For surface temperatures up to about 125 °F, little enhancement of TGD evaporation can be demonstrated within the limits of experimental error, even for exposure times of several hours. For surface temperatures between about 130 °F and 190 °F, evaporation times for TGD are reduced from hours to minutes to reach residual levels of from 10% to 1% or less, but many results are erratic. Insufficient data are available for VX and THD over these temperature ranges to prepare plots like Figure 8 for them for surface temperatures below 200 °F. Above surface temperatures of about 200 °F, agents VX, THD and TGD all show enhanced evaporation with increasing temperature, and times to reach residual levels of 1% or less are reduced from minutes to seconds, but erratic results still are sometimes observed.

The data support the view that a surface temperature of about 250 °F really is "critical" for C-agent evaporation to residuals of about one percent or less within a few seconds. But unless carefully-performed new C-agent experiments are carried out over the surface temperature range 130 °F to 250 °F, it will never be possible to quantify the time/temperature evaporation characteristics of each C-agent in decontamination studies of various surfaces; only the crudest empirical estimates will be possible. It is strongly recommended that these C-agent studies be initiated as soon as possible to provide an essential data source for designers and developers of evaporative decontamination systems, such as hot-air or infrared radiative systems for vehicles.

REFERENCES

1. Carlon, H.R., and Grasso, P.S., Surface Temperature: The Critical Parameter in Decontamination by Forced Hot Air and Other Surface-Heating Methods, CRDEC-TR-017, U.S. Army Chemical Research, Development and Engineering Center, Aberdeen Proving Ground, MD, November 1988, UNCLASSIFIED Report. (AD B128 933)

2. Penkov, M., Chemical Decontamination of Military Equipment Using Infrared Rays, Voenna Tekhnika (Bulgaria), No. 11, pp 17-18, 1970; FSTC-1021-77, Report No. AST-1620I-029-77, U.S. Army Foreign Science and Technology Center, Charlottesville, VA, November 1977, UNCLASSIFIED Report. (AD B026 239)

3. Chinn, K.S.K., The Effect of Time and Temperature on Evaporation and Transfer of Thickened GD and Thickened GD Simulants, DPG-FR-C120A, U.S. Army Dugway Proving Ground, Dugway, Utah 84022, January 1979. (AD B034 430)

4. Carlon, H.R., C-Agent Evaporation and Weathering on Surfaces: Effect of Surface Temperature, CRDEC-TR-024, U.S. Army Chemical Research, Development and Engineering Center, Aberdeen Proving Ground, MD, January 1989, UNCLASSIFIED Report. (B128 742L)

5. Carlon, H.R., Performance Evaluation of Simulants for VX, THD and TGD in Surface-Heating Decontamination Studies, CRDEC Technical Report, in preparation, U.S. Army Chemical Research, Development and Engineering Center, Aberdeen Proving Ground, MD, 1989, UNCLASSIFIED Report.

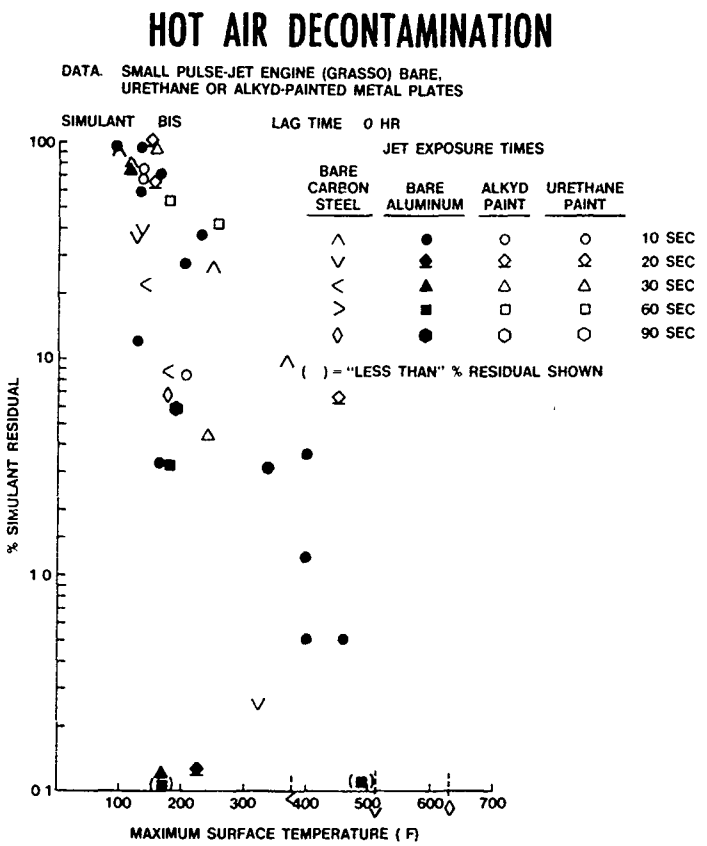

Figure 9. Data From Reference 5; Bare and Painted Metal Plates, Weathering Time Zero Hours, Simulant (for VX): BIS.

BLANK

A COMPARISON OF *o*-IODOSOBENZOIC ACID DERIVATIVES IN THE CATALYTIC HYDROLYSIS OF PNDP

Charles A. Panetta,[1] Stephanie M. Garlick,[3] H. D. Durst,[2]
Keith G. Haddaway,[3] Frederick R. Longo[2,4]

[1] NRC-CRDEC Research Associate,
University of Mississippi, Oxford, MISS 38677

[2] U. S. Army Chemical Research, Development, and Engineering Center.
Aberdeen Proving Ground, MD 21010-5423

[3] Geo-Centers, Inc.
Fort Washington, MD 20744

[4] Drexel University
Philadelphia, PA 19104

Abstract

We have measured second order rate constants for the catalyzed hydrolysis of *p*-nitrophenyldiphenyl phosphate (PNDP) in microemulsion media by 4-alkyl substituted *o*-iodosobenzoic acid (IBA) derivatives. We compare these results with published rate constants.[1-9] The synthesis of 4-alkyl-2-iodosobenzoate derivatives is outlined.

Introduction

Moss originally described IBA as a turnover catalyst, and proposed that its catalytic activity arose from the fact that IBA exists in solution as a cyclized valence tautomer, 1-hydroxy-1,2-benziodoxolin-3-one.[2,8,10-12] Since the pK_a of IBA is 7.02,[8] the oxygen of the iodoso group is negatively charged in mildly basic solutions. The nucleophile IBA easily displaces a labile group on a phosphate ester by attack at the electron deficient phosphorus atom with the simultaneous loss of p-nitrophenoxide (PNP). Hydroxide ion then attacks the IBA-diphenylphosphate intermediate at the iodine atom to give the diphenylphosphate anion and IBA.[3,8,13-16] IBA is regenerated in the

reaction sequence, therefore, it is considered a turnover catalyst.[2,4,8,11] Since this reaction releases a chromophore, the kinetics can conveniently be followed spectrophotometrically. PNP is an excellent spectrophotometric indicator since its molar absorptivity is ~18,000 $M^{-1}cm^{-1}$ at 402 nm.[17] Longo, Knier, Mackay, and Durst[8] has studied the IBA catalyzed hydrolysis of PNDP in CTAB/1-butanol/ hexadecane/ water microemulsions. PNDP decomposition proceeds according to Eq 1.

$$\text{rate} = k_{hyd}[\text{PNDP}] + k_{OH}[\text{OH}][\text{PNDP}] + k_{IBA}[\text{IBA}][\text{PNDP}] \quad \text{(Eq 1)}$$

$$\text{rate} = (k_{hyd} + k_{OH}[\text{OH}] + k_{IBA}[\text{IBA}])[\text{PNDP}] \quad \text{(Eq 2)}$$

k_{hyd} is the pseudo first order rate constant for the background hydrolysis of PNDP in the medium. k_{OH} and k_{IBA} are the second order rate constants for the hydroxide and IBA dependent hydrolysis of PNDP. Since IBA is a turnover catalyst, and the media is buffered, [IBA] and [OH] are constant, and,

$$\text{rate} = k_{obsd}[\text{PNDP}] \quad \text{(Eq 3)}$$

$$\text{where } k_{obsd} = k_{hyd} + k_{OH}[OH^-] + k_{IBA}[IBA^-] \quad \text{(Eq 4)}$$

Anionic forms of 2-iodoso (**1**) and 2-iodoxy (**1a**) benzoic acid are indicated in Figure 1.

FIGURE 1

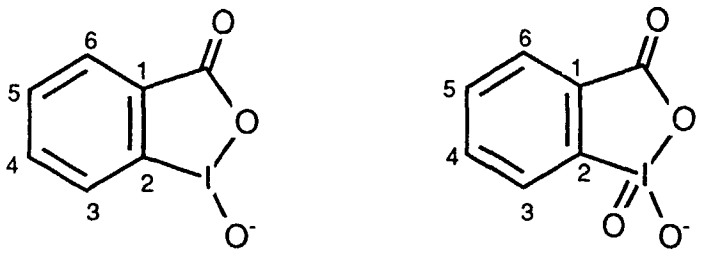

1 **1a**

Previous work has documented IBA/IBX and their derivatives as catalysts in the hydrolysis of phosphate esters.[1,2-4,6-9,18] Of the derivatives that have been tested as catalysts, only a few are substituted in the 4-position. For the most part, 4-substituents have included only carboxy and nitro groups. With the exception of 4-methyl-2-iodoxy benzoate,[1,5] no IBA/IBX derivatives containing lipophilic groups in the 4-position have been tested. The 4-alkyl-IBA derivatives have therefore been synthesized and evaluated as catalysts.

Materials

All chemicals used in the syntheses of the 4-alkyl-2-iodosobenzoates were purchased from Aldrich and used as received as was cetyltrimethylammonium bromide (CTAB) and toluene (TOL). The cosurfactant, 1-methyl-2-pyrrolidinone (MP), was supplied from BASF Corp. Buffer solution, 0.03 M in sodium tetraborate decahydrate, pH 9.2, was prepared using glass distilled water. IBA was obtained from Sigma, converted to the sodium salt, and dissolved in borate buffer prior to use. PNDP was prepared as a custom synthesis by Biomol Research Labs, Inc.

Experimental Procedure

The same synthetic procedure (Figure 2) was followed for 4-methyl (**2**), 4-ethyl (**3**), 4-*n* -propyl (**4**), 4-*n* -pentyl (**5**), and 4-*n* -octyl (**6**) 2-iodosobenzoic acid. The starting material for the syntheses was the corresponding 4-alkyl-benzyl alcohol **8**. Attempts to

synthesize 2-iodoso-4-*n* -butylbenzoic acid and 2-iodoso-4-*n* -hexylbenzoic acid were unsuccessful.

A. Preparation of 4-alkyl-benzyl alcohols, **8**

The 4-methylbenzyl alcohol was purchased, and the other alcohols were prepared as follows. A solution consisting of 0.92 mL of 2 N NaOH, 8.3 mL of water, and 0.63 g (0.017 mol) of sodium borohydride ($NaBH_4$) was added dropwise, over a 10 minute period, to a stirred solution containing 0.04 mol of the corresponding 4-alkylbenzaldehyde,**7**, in 50 mL of methanol. The temperature of the reaction mixture was maintained at 18-24 °C during the addition. This mixture was stirred for 35 minutes at room temperature, and the methanol was removed by distillation. The residue was diluted 1:1 with a saturated potassium chloride solution, and extracted with benzene. The organic layer was washed with water, dried, and concentrated to a colorless oil. If thin layer chromatography (TLC; hexane:ethyl acetate,70:30) could not adequately separate the product **8**, column chromatography (silica gel; E. Merck # 9385) was used.

B. Preparation of 4-alkyl-2-iodobenzyl alcohols, **9**

The procedure of Meyer and Seebach[19] was followed to prepare the 4-alkyl-2-iodobenzyl alcohols, **9**. 0.035 mol of the corresponding 4-alkyl-benzyl alcohol was dried over 4 Å molecular sieves, and added to 72 mL of petroleum ether, 10.93 mL (0.072 mol) of tetramethylethylenediamine ($Me_2NCH_2CH_2NMe_2$). A volume of 48.05 mL of a 1.5 M solution of *n* -butyllithium in hexane was added with stirring in two portions over a 10 minute period. The reaction mixture was kept between 30 - 60 °C under a nitrogen atmosphere. The mixture was then refluxed for 11 hours and stirred at room temperature for 13 hours. After the reaction mixture was cooled to -78 °C, 0.0247 mol of iodine was added. The solution was stirred and warmed to room temperature for 1 hour. A volume of 53 mL of 10 % H_2SO_4 was added, and the aqueous layer was separated and extracted with ether two times. The ether layers were combined, washed with water, and dried. The organic solvents were then removed under reduced pressure. The dark oil that remained was chromatographed (100 g silica gel; E. Merck # 9385) by elution with hexane:ethyl acetate, 95:5. The middle column fractions were pooled and evaporated. The solid residue, **9**, was recrystallized from low-boiling petroleum ether or from hexane.

C. Preparation of 4-alkyl-2-iodobenzoic acids,**10**

The 4-alkyl-2-iodobenzoic acids were prepared using the procedure of Herriott and Picker.[20] Since their oxidation scheme was applied to benzyl alcohol, minor modifications were necessary here. A mixture of 0.03 mol of potassium permanganate ($KMnO_4$) and 50 mL of water was stirred vigorously for 10 minutes and cooled. This was followed by the sequential addition of 0.011 mol of the corresponding 4-alkyl-2-iodobenzyl alcohols, **9**, 30 mL of benzene, and 0.0016 mol of tetrabutyl ammonmium bromide (**2**) or tetrabutylphosphonium chloride, (*n* -butyl)$_4$PCl, (**3, 4, 5, 6**) as the phase-transfer agent. The mixture was stirred for at 25 °C. After 3 (**2,4,5,6**) or 4 (**3**) hours, some sodium bisulfite was added to discharge the residual permanganate color. An 80 mL volume of ether was added, and the mixture was acidified with 50 % H_2SO_4 and filtered through Celite. The aqueous layer was then extracted 3 times with ether. The organic washes were combined, washed with a saturated KCl solution, and dried. The solvent was evaporated under reduced pressure. The mixture of residual oil

FIGURE 2

SYNTHETIC SCHEME FOR 4-ALKYL-2-IODOSOBENZOIC ACIDS

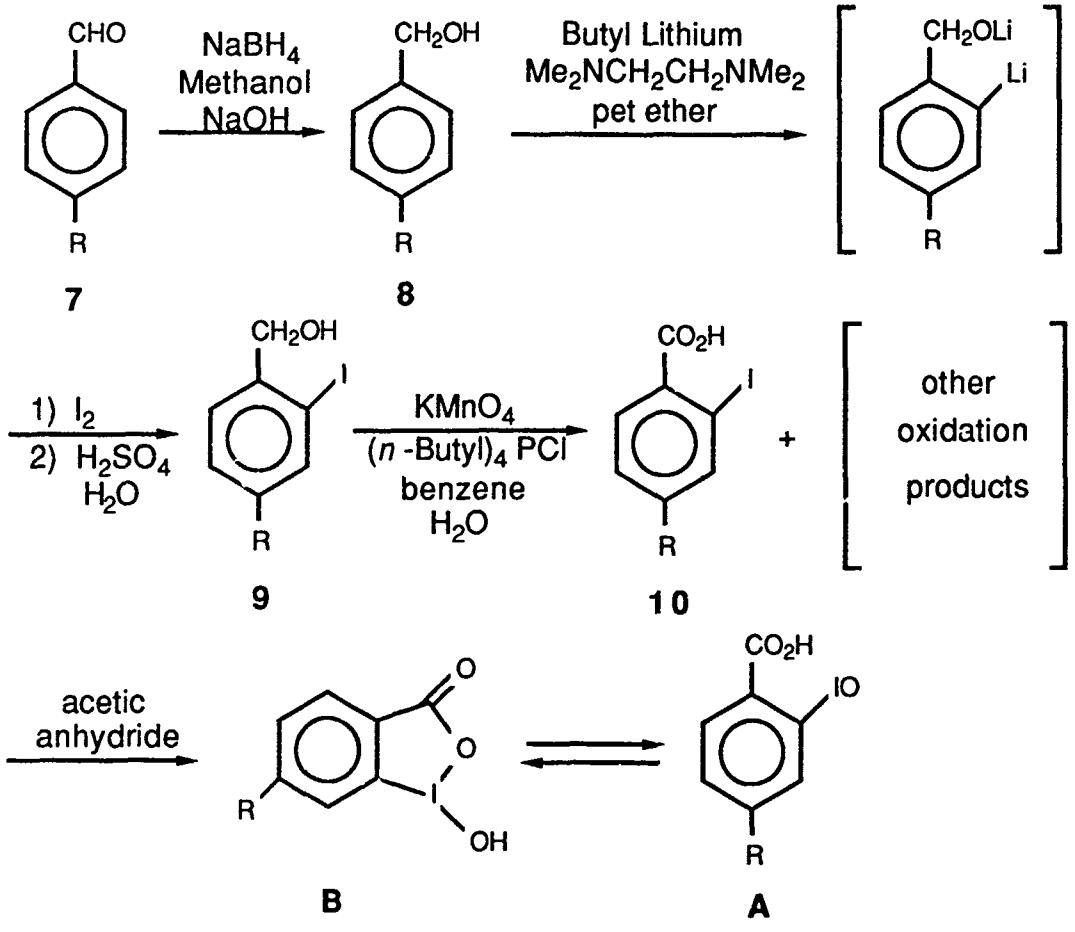

and solid was chromatographed (90 g silica gel; E. Merck # 9385) by elution with a solvent gradient of hexane:ethyl acetate: acetic acid, 79:20:1 to ethyl acetate:acetic acid, 95:5. The corresponding 4-alkyl-2-iodobenzoic acid was separated as follows:

a) 2-iodo-4-methylbenzoic acid

The product mixture contained 3 components. In the order of increasing R_f values, the compounds were 2-iodo-4-methylbenzaldehyde (64 %), 2-iodo-4-methylbenzoic acid (24 %), and a third unidentified compound. The synthesis was repeated with tetrabutyl- phosphonium chloride. The starting material was completely oxidized, and the yield of 2-iodo-4-methylbenzoic acid increased to 39 %. The synthesis of 2-iodo-4-methylbenzoic acid has been reported[21] only one other time in the literature.

b) 4-ethyl-2-iodobenzoic acid

The product mixture contained 3 components. In order of increasing R_f value, the compounds were 4-ethyl-2-iodobenzaldehyde (12 %), 4-ethyl-2-iodobenzoic acid (37 %), and a third compound (44 %) partially identifiable as 2-iodoterephthalic acid.

c) 2-iodo-4-*n*-propylbenzoic acid and 2-iodo-4-*n* -pentylbenzoic acid

Only a trace of the starting material remained in either product mixture. The mixtures

contained, respectively, 2-iodo-4-*n* -propylbenzoic acid (44 %) and 2-iodo-4-*n* -pentylbenzoic acid (63 %). Since the desired products had the same R_f value as their starting materials, both product mixtures were recrystallized from hot aqueous ethanol and rechromatographed. The third compound in the product mixtures was either 2-iodoso-4-*n* -propylbenzoic acid or 2-iodoso-4-*n* -pentyl benzoic acid.

d) 2-iodo-4-*n* -octylbenzoic acid

The product mixture contained 3 components. In order of increasing R_f value, the compounds were 2-iodo-4-*n* -octylbenzaldehyde (trace), 2-iodo-4-*n* -octylbenzoic acid (55 %), and a third compound that was not identified. The desired product was recrystallized from warm petroleum ether (30-60 °C).

D. Preparation of 4-alkyl-2-iodosobenzoic acids, **A, B**

The procedure of Katritsky, et al.[6] was followed to prepare the 4-alkyl-2-iodoso benzoic acid derivatives. Acetic anhydride (Ac_2O; 9.6 mL) and 2.4 mL of 30 % hydrogen peroxide (H_2O_2)were stirred for 4 hours at 40 °C. The correspondinding 4-alkyl-2-iodobenzoic acid (0.0048 mol) was then added. The temperature was maintained at 40 °C. The solution became turbid almost immediately and a white solid precipitated. The mixture was heated at 60 °C for 20 hours. Water (96 mL) was added, and the solution was stirred at room temperature for 1 hour. The mixture was filtered, and the white solid was washed with water and dried. The products were recrystallized from hot ethanol (**2,3,4,6**) or from hot acetone (**5**). Two TLC spots were obtained for **4** and for **5.** One spot from each mixture chromatographed similarly to one of the spots from the product mixture in the synthesis of 2-iodo-4-*n* -propylbenzoic acid and of 2-iodo-4-*n* -pentyl benzoic acid. Since the elemental analysis results of both TLC spots were identical for each respective product, it was concluded that the spots corresponded to the **A** and **B** forms of each product.

Kinetics Studies

Known weights of the 4-alkyl-2-iodosobenzoic acid derivatives were added to 4 mL of distilled water. A molar equivalent of standard 0.2 N NaOH solution was added. The solutions were allowed to stand until conversion to the sodium salt was complete. A small volume, usually ≤ 100 µL, was added to 5 mL of a control microemulsion consisting of 8 %CTAB/ 8 %MP/ 4 %TOL/ 80 %AQ. The acquisition and analysis of rate data and the determination of k_{IBA} and k_{OH} have been described in great detail.[1-5] The computer programs used to collect the rate data, and to calculate the rate constants, were written by Dr. B. L. Knier.[22] Results (Table 1) are compared to the measured rate constant for unsubstituted IBA, **1**.

TABLE 1

VALUES OF k_{IBA} FOR 4-ALKYL-2-IODOSOBENZOIC ACID DERIVATIVES

Catalyst	k_{IBA} ($s^{-1}M^{-1}$)
1	12.4 ± 0.55
2	18.6 ± 0.36
3	22.9 ± 0.38
4	0.013 ± 0.005
5	0.026 ± 0.010
6	---

CONCLUSIONS

The IBA derivatives with the smaller alkyl substituents (**2,3**) are significantly better catalysts than those with larger alkyl substituents, and even better than unsubstituted IBA (**1**). The *n* -propyl (**3**) and the *n* -pentyl (**4**) derivatives exhibited poor catalysis possibly due to their incorporation into the interface of the microemulsion aggregates. The alkyl substituent in **6** was too lipophilic to permit the sodium salt to be prepared in water. The increase in the rate constant for the 4-alkyl derivative relative to unsubstituted IBA can be explained by the electron releasing properties of the alkyl groups. In the 4- or 5-alkyl derivatives, the nucleophilicity of the oxygen atom increases as the iodine assumes a partial negative charge.

Several additional trends are indicated from reported rate constants.[1-9] The order of decreasing catalytic effectiveness of IBA / IBX derivatives is: 5-(*n* -butoxy)-2-iodoxybenzoate (BXIBA) ≈ 5-(*n*-octyloxy)-2-iodosobenzoate(OXIBA) ≈ 5-(*n* -dodecyloxy)-2-iodoso benzoate(DDXIBA) ≈ 5-(*n* -butoxy)-2-iodoxybenzoate(BXIBX) ≈ 5-(*n* -octyloxy)-2-iodoxybenzoate(OXIBX) ≈ 5-(*n* -dodecyloxy)-2-iodoxybenzoate(DDXIBX) > 4-nitro-2-iodosobenzoate(NIBA) ≈ 4-nitro-2-iodoxybenzoate(NIBX) > 5-methyl-2-iodoso benzoate(MIBA) ≈ 5-methyl-2-iodoxybenzoate(MIBX) > 5-nitro-2-iodosobenzoate ≈ 5-nitro-2-iodoxybenzoate > IBA > 4-carboxy-2-iodosobenzoate(CXIBA) in CTAC micelles,[6] and 4-NIBA > IBA > 4-MIBX > 5-OXIBA > 5-CXIBA in CTAC/Adogen/HEX/AQ microemulsion media.[5] Valence bond canonical structures can be drawn for 5-NIBA /NIBX that cannot be drawn for 4-NIBA/NIBX. These structures explain the relative magnitude of the rate constants reported for 4- and 5- NIBA/NIBX.[5] A carboxyl group in the 4 or 5 position of IBA (4-CXIBA, 5-CXIBA) exhibits a negative mesomeric effect that decreases the nucleophilicity of the iodoso oxygen by diminishing its negative charge.[5,6] Rate constants reported for 5-BXIBA, 5-OXIBA, 5-DDXIBA and for 5-BXIBX, 5-OXIBX, 5-DDXIBX in micellar media[6] are comparable. We may infer that the size of the 5-alkoxy (OR) substituent has little effect on the rate constant. No resonance structures can be drawn for 4-RO-IBA/IBX or 5-RO-IBA/IBX.

ACKNOWLEDGMENT

Financial assistance for this project was provided by Geocenters, Inc., and the U. S. Army Chemical Research, Development, and Engineering Center.

REFERENCES

1. Burnside, B. A. *The Hydrolysis of p-Nitrophenyl Diphenyl Phosphate Ester in Microemulsion Media;* PhD Thesis, Drexel University: Philadelphia, PA. 1987.

2. Moss, R. A.; Alwis, K. W.; Shin, J-S. *J. Am Chem. Soc.* **1984,***106,* 2651.

3. Knier, B. L.; Durst, H. D.; Burnside, B. A.; Mackay, R. A.; Longo, F. R. *J. Soln. Chem.* **1988,** *17,* 77.

4. Moss, R. A.; Kin, K. W.; Swarup, S. *J. Am. Chem. Soc.* **1986,** *108,* 788.

5. Burnside, B. A.; Knier, B. L.; Mackay, R. A.; Durst, H. D.; Longo, F. R. *J. Phys. Chem.* **1988,** *92,* 4505.

6. Katritzky, A. R.; Duell, B. L.; Durst, H. D.; Knier, B. L. *J. Org. Chem.* **1988,** *53,* 3972.

7. Moss, R. A.; Chatterjee, S.; Wilk, B. *J. Org. Chem.* **1986,** *51,* 4303.

8. Mackay, R. A.; Longo, F. R.; Knier, B. L.; Durst, H. D. *J. Phys. Chem.* **1987,** *91,* 861.

9. Moss, R. A.; Alwis, K. W.; Bizzigotti, G. O. *J. Am. Chem. Soc.* **1984,***105,* 1681.

10. Shefter, E; Wolf, W. *Nature (London)* **1964,** *203,* 512.

11. Moss, R. A.; Alwis, K. W.; Bizzigotti, G. O. *J. Am. Chem. Soc.* **1984,***105,* 1681.

12. Moss, R. A.; Scrimin, P.; Rosen, R. T. *Tetr. Lett.* **1987,** *28,* 251.

13. Hermansky, C. G. *Reactions In and Characterization of Oil in Water Microemulsions;* PhD Thesis, Drexel University: Philadelphia, PA, 1980.

14. Mackay, R. A.; Hermansky, C. *J. Phys. Chem.* **1981,** *85,* 739.

15. Bunton, C. A.; De Buzzaccarini, F.; Hamed, F. H. *J. Org. Chem.* **1983,***48,* 2457.

16. Burnside, B. A.; Szafraniec, L. L.; Knier, B. L.; Durst, H. D.; Mackay, R. A.; Longo, F. R. *J. Org. Chem.* **1988,** *53,* 2009.

17. Experimentally determined value; personal observation.

18. Hammond, P. S.; Forster, J. S.; Lieske, C. N.; Durst, H. D. *J. Am. Chem. Soc.* **1989,** *111,* 7860.

19. Meyer, N.; Seebach, D. *Angew. Chem. Int. Ed. Engl.* **1978,** *17,* 521.

20. Herriott, A. W.; Picker, D. *Tetr. Lett.* **1974,** *16,* 1511.

21. Carruthers, W.; Pooranamoorthy, R. *J. Chem. Soc. Perkin Trans.* **1974,** 2405.

22. EAI Corporation, P.O. Box 764, Toele, UT. 84074

BLANK

THE PHOTOOXIDATION OF MUSTARD AND VX IN SOLUTIONS AND ON TITANIA SURFACES

James H. Buchanan, Dennis K. Rohrbaugh, Linda L. Szafraniec, William T. Beaudry and Yu-Chu Yang*

Physical Protection* and Research Directorates,
U.S. Army Chemical Research, Development and Engineering Center,
Aberdeen Proving Ground, MD 21010-5423

Abstract

The photodegradation of chemical agents mustard (2, 2'- dichlorodiethyl sulfide) and VX (O-ethyl S-(diisopropylamino)ethyl methylphosphonothiolate) was investigated in 0.01 M solutions in acetonitrile, acetonitrile-water, and cyclohexane at ambient conditions. The photocatalytic activity of titanium(IV) dioxide powder suspended in each of the above solvents and irradiated at 350 nm was determined for the potential application as a catalytic decontamination method. Mustard sulfoxide was produced from photooxidation both in the presence and in the absence of titania by two different mechanisms. No apparent oxidation was observed for VX. Instead, VX was quickly degraded by the light energy via S-C bond cleavage to form thiopyrophosphate, pyrophosphate, thioic acid, and diisopropylethylamine. The overall observed quantum efficiency was 1-5% for mustard and its simulants, and about 9% for VX.

INTRODUCTION

As a result of solar energy research, a number of semiconductor oxides have been identified as photocatalysts which produce electron-hole pairs upon photoactivation. Organic molecules containing electron-donating functional groups could be oxidized by oxygen on the surfaces of these oxides by an interfacial electron-transfer process.[1] ARO-sponsored researchers M. Gratzel and M. A. Fox showed that irradiated titanium(IV) oxide (titania, TiO_2) could convert oxygen adsorbed on the surface to reactive superoxide anion. The hydrolysis of a G-agent simulant[2] was catalyzed by photoactivated titania powders. It is the purpose of this study to examine the photooxidation of mustard (HD) and VX using titania as a photocatalyst. The photooxidation of VX is expected to be more difficult than that of mustard, as the sulfur adjacent to the phosphoryl group in VX may be

less nucleophilic. However, in photocatalytic oxidation, the superoxide anion generated on the TiO_2 surface could also act as a nucleophile to attack the phosphorus. A displacement reaction shown in the proposed Scheme 1, particularly in the presence of water, will follow. The combined displacement-oxidation reactions should therefore increase the possibility of the photodegradation of VX.

SCHEME 1

PROPOSED SCHEME FOR PHOTOCATALYTIC OXIDATION/HYDROLYSIS OF H, G AND V AGENTS

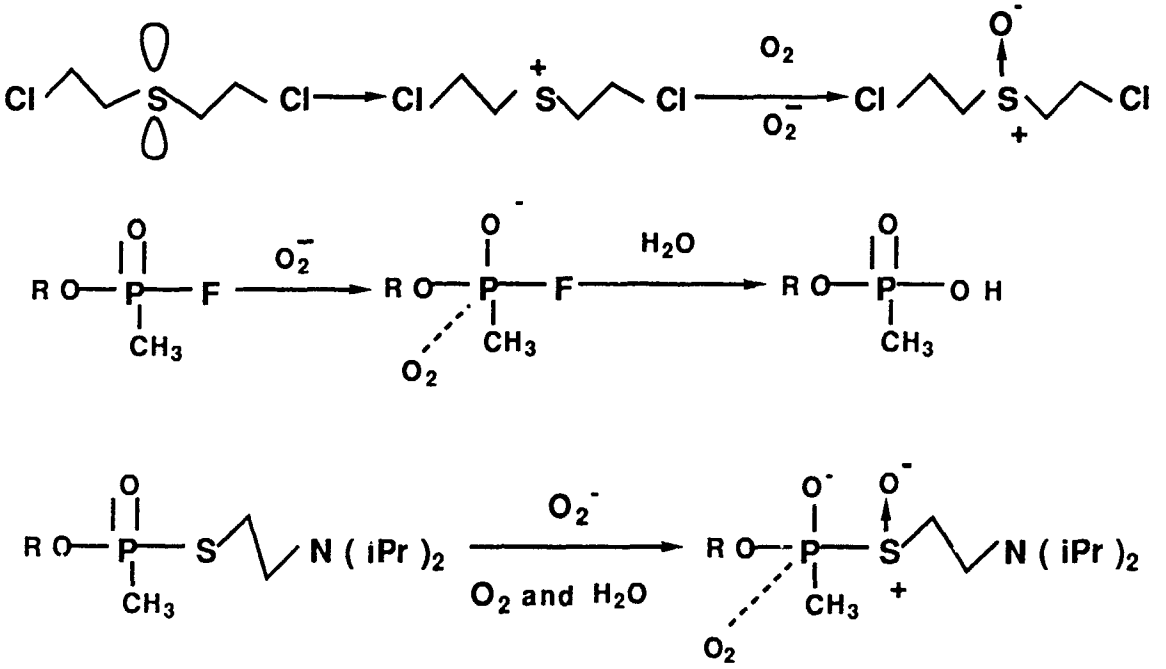

EXPERIMENTAL

Materials

Mustard and VX were obtained from the Chemical Agent Standard Analytical Reference Material (CASARM) Program of CRDEC, and were greater than 95% pure by ^{13}C and ^{31}P NMR respectively. The C-13 enriched simulant, $^{13}CH_3SC_2H_4Cl$, was kindly prepared by Dr. Sankar Lal of Drexel University. Mustard sulfoxide was prepared by adding mustard dropwise to an excess of 38% nitric acid. The sulfoxide was obtained as a white crystalline solid after all the liquid was evaporated at room tem-perature. Gold-labelled titanium(IV) oxide (TiO_2) at 99.99% purity was obtained from Aldrich Chemical Company. The TiO_2 catalyst was characterized by B.E.T. surface area and pore distributions to have an average particle size of 36 micron. More than 95% of the titania was an Anatase based on X-ray analysis. X-ray Photoelectron Spectroscopy(XPS) was used to analyze the surface compositions of the catalyst before and after the photodegradation reactions.

Photooxidation Experiments:

A Rayonet Photochemical Chamber Reactor (Model RPR-100) was used for the photooxidation study. The reactor was equipped with sixteen "black light" lamps of 24 watts. More than 90% of the intensity of the irradiated light was at 350 nm. At the center of the reactor chamber where the pyrex reactor tube was placed the black light irradiation was about 9200 microwatts/cm^2. An air-driven magnetic stirrer is installed in the reactor chamber base. An internal cooling fan was supposed to control the chamber temperature to 39-40°C range when all the lamps are turned on. However, the temperature profiles recorded were higher. In acetonitrile and cyclohexane, the average chamber temperature was 55°C, but in acetonitrile-water mixtures, the average temperature was only about 43°C. The conversion of mustard, its simulants, and VX has been measured as a function of light irradiation and solvent property. The major reaction products were identified and quantified by GC, NMR and further verified by GC/MS. An external standard, n-octane, was used for GC quantitation. Detailed experimental procedures and instrumentation can be found in References 3 and 4.

RESULTS AND DISCUSSION

1. PHOTOOXIDATION OF MUSTARD

Based on quantitative GC analyses, the simultaneous disappearance of mustard (HD, present as a 0.01 M solution in acetonitrile) and appearance of mustard sulfoxide (HD=O) as a function of irradiation time at 350 nm are illustrated in FIGURE 1. During the first 12 hours only a trace amount of sulfoxide was produced. But after 24 hours of irradiation half of the initial mustard was reacted to form primarily sulfoxide. Beyond 36 hours of irradiation, the yield of sulfoxide was reduced and additional products were observed.

FIGURE 1

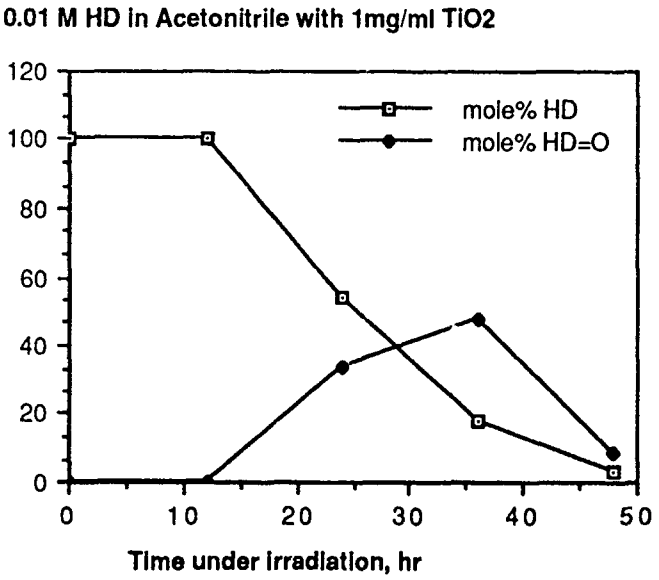

The GC/MS identifications of compounds found in a sample after 24 hours irradiation are listed in TABLE 1. Different from reports in the literature, mustard sulfone, $(ClCH_2CH_2)_2SO_2$, was not found in any significant amount, perhaps due to the lack of excess oxygen in solution. Instead, mustard disulfide, $(ClCH_2CH_2)_2S_2$, was positively identified by comparison with the GC/MS characteristics of a pure standard. The disulfide was produced apparently from photolysis of the S-C bonds. These results suggest that both photocatalysis and photolysis reaction paths were present.

TABLE 1

PHOTOOXIDATION OF MUSTARD ON TiO_2 SURFACE IN CH_3CN AFTER 24 HOURS OF IRRADIATION AT 350 nm

Compound	GC/MS-CI, area%
MW=59 (HSCN ?)	11.3
$ClCH_2CH_2SCH_2CH_2Cl$ (mustard)	41.2
$NCCH_2SCH_2CH_2Cl$	1.6
$Cl_2C_2H_3SCH_2CH_2Cl$ (chloro-mustard)	4.6
$ClCH_2CH_2S\text{-}SCH_2CH_2Cl$ (mustard disulfide)	9.0
$NCCH_2S\text{-}SCH_2CH_2Cl$	2.5
$ClCH_2CH_2\overset{O}{\overset{\|}{S}}CH_2CH_2Cl$ (mustard sulfoxide)	17.4

FIGURE 2

PHOTODEGRADATION OF MUSTARD ON TIO2

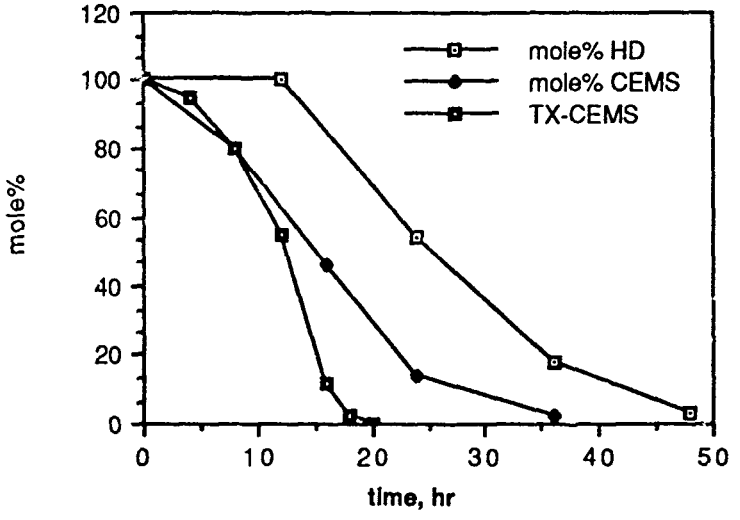

Another titania sample containing 2% Pd was used under identical conditions. The efficiency was improved by about 16% during the first 12 hours, but the activity became identical with the normal titania at 24 hours of irradiation. It was possible that the surface of the Pd-doped titania was poisoned by some of the reaction products. This was consistent with the results from M. A. Fox of the University of Texas. Based on her study, Pt or Pd-doped titania only increased the efficiency moderately.[5]

To verify the mustard result, a comparative study using the simulants, 2-chloroethyl ethyl sulfide(CEES) and 2-chloroethyl methyl sulfide(CEMS) was performed as a Contract effort at the University of Texas.[5] In addition, the photooxidation of a ^{13}C-enriched CEMS (or $CE^{13}MS$) was investigated under identical conditions, but the sample analysis was independently accomplished by ^{13}C NMR. Based on the NMR result(see reference 3 for detailed data), the simulant reacted faster than HD, but the product pattern was similar. This is consistent with the previous observation that the oxidation rate of a sulfide molecule increased with the nucleophilicity of the sulfur atom:[6] There are two electron-withdrawing chloroethyl groups in mustard, resulting in a lower nucleophilicity of the sulfur atom than that in CEMS. Therefore, CEMS oxidized faster than HD. In photooxidation apparently the same trend has been observed. The conversions of HD by GC and of $CE^{13}MS$ by ^{13}C NMR are compared with that of CEMS by GC from the University of Texas. As shown in FIGURE 2, the conversions of CEMS from both Laboratories were close initially; but after about 12 hours of irradiation, the reaction rate obtained at Texas was faster. Perhaps because their experiments were made in acetonitrile solutions saturated with pure oxygen. For the same reason, a greater yield of the sulfoxide was also found at the University of Texas.[5]

The effect of water on photooxidation was examined using an aqueous solvent system of 50 vol% CH_3CN. $CE^{13}MS$ had to be used for NMR analysis because GC methods are not appropriate for aqueous samples. Photooxidation was significantly retarded by water, which might have absorbed photons. A minimum of 10^oC decrease in reaction temperature in the aqueous solution relative to that in acetonitrile also resulted in a decrease in observed conversion. In addition, the TiO_2 suspensions were less stable in aqueous solutions. At each sampling interval, all of the titanium oxide powders had precipitated, leaving a clear solution in the test tube. This demonstrated that the titanium oxide powders were not exposed to light for any significant period of time. However, it is interesting to find that hydrolysis was almost completely prevented by light irradiation at 350 nm. This is perhaps due to the fact that photo-generated radicals formed faster than the cyclic ethylenesulfonium ion, produced in the first and rate-determining step in hydrolysis.[7] At identical conditions in the absence of light, hydrolysis did occur and the dimer product,[9] $(^{13}CH_3SCH_2CH_2)S^+(^{13}CH_3)(CH_2CH_2X)$ where X=Cl or OH, with a second $^{13}CH_3S$ peak at *14.5ppm*) was positively identified at 36 hours after mixing.

2. THE PHOTODEGRADATION OF VX

VX was photodegraded at a faster rate than mustard. After 9 hours of irradiation at 350 nm, about 95% of the VX present as a 0.01 M solution in acetonitrile was converted to products. As summarized in TABLE 2, the same products were obtained both in the absence and in the presence of titania. Although the yield of the thiopyrophosphates(S-PYRO) was greater in the presence of titania. The major phosphorus-containing products were identified by ^{31}P NMR and are listed in TABLE 2. It seems that these products were produced from the breaking of the S-C bond by the light energy. Diisopropylethyl amine was the only additional non-phosphorus product identified by GC/MS. While the thioic acid(S-acid) is non-toxic, both the S-PYRO and the pyrophosphate(PYRO) are toxic. Since 2 moles of VX were required to form 1 mole of the S-PYRO or the PYRO products, the composition in

TABLE 2 is expressed in AREA% by ^{31}P NMR, which is based on the %conversion per mole of the initial VX. As no oxidation products were observed (see discussions on VX oxidation products in the latter part of this report), it is believed that neither the molecular oxygen nor the superoxide anion were strong enough to oxidize VX. This is the first time the photolysis products of VX at controlled conditions were ever identified. Since VX was photodegraded relatively quickly at 350 nm, these products are expected to be present in VX samples exposed to light.

TABLE 2

THE PHOTODEGRADATION PRODUCTS OF 0.01 M VX IN ACETONITRILE

		AREA% by ^{31}P NMR			
		TiO_2 / CH_3CN		CH_3CN	
IRRADIATION TIME, hr.		4 hr	8 hr	4 hr	8 hr
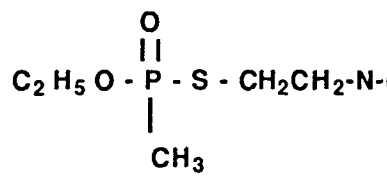	(VX)	49.4	5.1	56.3	4.7
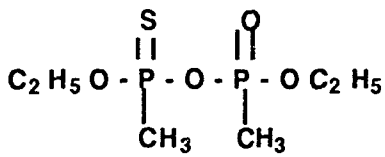	(S-PYRO)	16.1	40.4	9.3	18.7
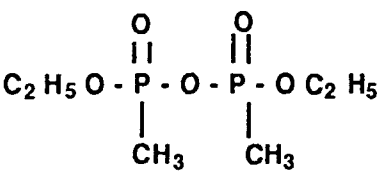	(PYRO)	9.5	17.1	16.0	25.1
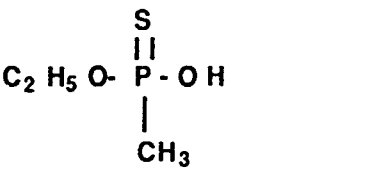	(S-acid)	17.0	24.8	11.6	27.8

As shown in TABLE 3, the rate and product of the photodegradation of VX were close in both acetonitrile and cyclohexane. As was observed for mustard, the photodegradtion of VX was retarded by the presence of water in acetonitrile. The S-C bond in VX was cleaved by light, followed by hydrolysis to produce the thioic acid (S-acid) as tne only photolysis product in water. No additional products similar to those in pure acetonitrile were ever found over an irradiation period of 36 hours. The ethyl methylphosphonic acid(P-acid) was produced from hydrolysis alone and was present in the control sample as well. As reported previously, VX hydrolyzes via multiple paths in pure water.[8] The observed single hydrolysis path via the P-S bond cleavage should be further investigated. The rates of the photodegradation,

measured by the conversions of VX by ^{31}P NMR with time, was plotted in FIGURE 2 for the three solvent systems for comparison.

TABLE 3

SOLVENT EFFECT IN THE PHOTODEGRADATION OF 0.01 M VX AT 350 nm

Composition, AREA% by ^{31}P NMR

Solvent	C_6H_6	CH_3CN	H_2O-CH_3CN		
Time after mixing, hr.	8	8	8	8	0
Time of Irradiation, hr.	8	8	8	0	0
VX	25.7	4.7	83	91.8	97.4
(S-PYRO)	27.9	18.7	0	0	0
(PYRO)	13.1	25.1	0	0	0
(S-acid)	29.3	27.8	9.3	0	0
(P-acid)	0	0	6.1	6.4	2.6

FIGURE 2

PHOTODECOMPOSITION OF VX AT 350 nm

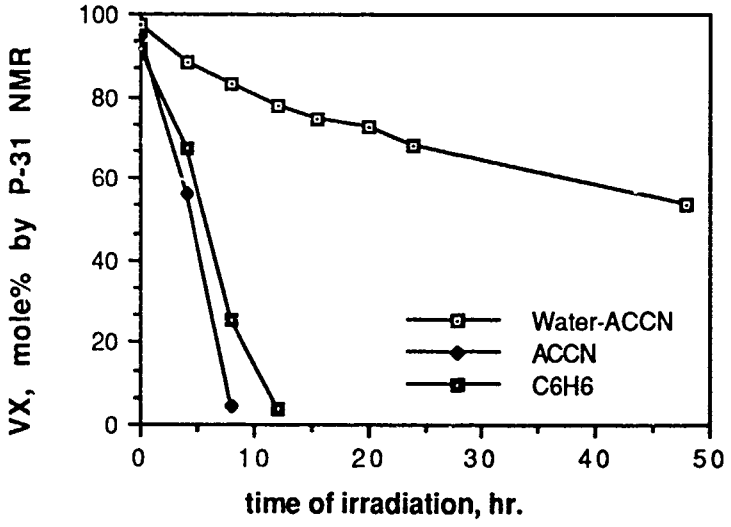

Very little information on the oxidation of VX could be found in the literature.[4] The oxidation products of VX were identified for the first time using a range of peroxides and chlorine-based oxidants to determine if any of the products observed in TABLE 2 were from photooxidation. As discussed in detail in two recent papers in references 9 and 10, a small amount of the PYRO compound was produced after the sulfur was oxidized by a peroxybenzoic acid in t-butanol. However, the PYRO could also be found in aged VX, particularly at elevated temperatures. The S-PYRO was not detected from the oxidation of VX, and was thermally unstable. The typical oxidation products of VX such as the amine oxides, and the sulfoxides and sulfones[9,10] were not found in the photodegradation processes, either in the presence or in the absence of TiO_2. It is therefore believed that the S-PYRO is the

major product from photolysis, and that VX was not oxidized by air in the presence of photoactivated TiO_2.

ACKNOWLEDGEMENT

The authors are grateful to Dr. Joseph Rossin (Chemical Div., Research Dir.) for the XPS characterizations; to Mr. Gary Russo (Eastman Kodak Corp.) for a sample of Pd-doped titania as well as X-ray and surface area determinations; and to Mr. Tony Perry (Collective Protection Div., Physical Protection Dir.) for the B.E.T. surface area determinations of the titania catalyst samples.

REFERENCES

1 Fox, M. A., Organic Heterogeneous Photocatalysis: Chemical Conversions Sensitized by Irradiated Semiconductors, Accts. Chem. Res., 1983, 16, 314-321

2. Gratzel, C. K.; Jirousek, M.; and Gratzel, M., Accelerated Decomposition of Active Phosphates on TiC_2 Surfaces, J. Mole. Catalysis, 1987, 39, 347-353

3. Yang, Y.-C.; Photocatalytic Oxidation of Mustard Using Semiconductor Oxides, in Final ILIR Report FY88, CRDEC-SP-005, April, 1989

4. Yang, Y.-C.; Buchanan, J. H.; Rohrbaugh, D. K.; Szafraniec, L. L.; Beaudry, W. T.; Photocatalytic Air Oxidation of Mustard and VX, in Final ILIR Report FY89, in press.

5. Fox, M. A.; Investigation of the Photocatalytic Degradation Reactions of Mustard Simulants, A Final Report of STAS Contract Number SSP88-14 (COR: Yang, Y.-C.); under ARO Contract DAAL03-86-0-001 with Battelle; June 1989.

6. Yang, Y.-C.; Szafraniec, L. L.; Beaudry, W. T.; and Davis, F. A.; On Simulating the Oxidation Reactivities of Mustard and VX; in Proceedings of the CRDEC Scientific Conference on Chemical Defense, Aberdeen Proving Ground, MD, November, 1988.

7. Yang, Y.-C.; Szafraniec, L. L.; Beaudry, W. T.; and Ward J. R., Kinetics and Mechanism of the Hydrolysis of 2-Chloroethyl Sulfides, J. Org. Chem. 1988, 53, 3293-3297

8. Szafraniec, L. J., Szafraniec, L. L., Beaudry, W. T., and Ward J. R., On the Stoichiometry of Phosphonothiolate Ester Hydrolysis, in Preceedings of the CRDEC Scientific Conference on Chemical Defense, Aberdeen Proving Ground, MD, November. 1988

9. Yang, Y.-C.; Szafraniec, L. L.; Beaudry, W. T.; and Rohrbaugh, D. K., Mechanisms of VX Oxidation I. The Oxidation by Peroxides and OXONE; in Proceedings of the CRDEC Scientific Conference on Chemical Defense, Aberdeen Proving Ground, MD, November, 1989.

10. Yang, Y.-C.; Szafraniec, L. L.; Beaudry, W. T.; and Rohrbaugh, D. K.; Mechanisms of VX Oxidation II. The Oxidation by Chlorine-Based Oxidants; in Proceedings of the CRDEC Scientific Conference on Chemical Defense, Aberdeen Proving Ground, MD, November, 1989.

INHIBITION OF ORGANOPHOSPHOROUS ACID ANHYDRASE FROM SQUID HEPATOPANCREAS BY SPECIFIC ALKYLATING REAGENTS

Karla Kopec-Smyth[1], Lawrence D. Loomis[2], Jeffrey R. Deschamps[1], and Keith B. Ward[1]

[1] Code 6030, Naval Research Laboratory, Washington, DC 20375

[2]Div. of Retrovirology, Walter Reed Army Inst. of Research, Washington, DC 20307

Elucidating the structure and mechanism of enzymes capable of degrading organophosphate compounds is essential to our understanding and effective utilization of these proteins as tools for decontamination. Specific alkylating reagents have been used to determine amino acid residues which are essential to activity and metal binding. Diethyl-pyrocarbonate (DPC) inhibited 85% of the original activity of squid hepatopancreas organophosphorous acid (OPA) anhydrase after a 30 minute incubation. Inhibition by DPC, which can alkylate histidine, tyrosine and primary amines, was rapid and reversible in the presence of base. Amino acid analysis of DPC-treated enzyme showed a decrease in free histidine. These results indicate that histidine is an essential residue in the degradation of organophosphate compounds by this enzyme. We have demonstrated that zinc is present in equimolar amounts in purified enzyme. Contrary to our expectations, we have shown that cysteines do not participate in zinc binding, but instead are involved in disulfide bonding. The moieties which bind the essential metal are still unclear, but these residues can be alkylated by N-ethyl maleimide, and to a much lesser extent, by iodoacetic acid.

INTRODUCTION

The organophosphorous acid (OPA) anhydrases consist of several classes of enzymes capable of degrading organophosphorous compounds. These organophosphorous compounds include various nerve poisons, such as diisopropylfluorophosphate (DFP) and Soman, and certain insecticides, such as parathion and paraoxon. The OPA anhydrase from the hepatopancreas of the squid *Loligo pealei* has a molecular weight of 26,000 daltons (1) and can hydrolyze diisopropylfluorophosphate. Squid hepatopancreas OPA anhydrase also hydrolyzes the agents Tabun, Sarin and Soman, although the K_m's are higher for these substrates than for DFP (2,3). While many physical characteristics of this enzyme are known (Table 1), little is known about the enzymic mechanism for the degradation of organophosphorous compounds. Functional groups necessary for catalysis can be identified by chemical modification of specific residues. Our approach was to use two types of alkylating reagents. N-ethyl maleimide (NEM) and iodoacetic acid (IAA) were used to alkylate and quantify cysteine residues; diethyl pyrocarbonate (DEP) was used to alkylate histidine residues. By observing the loss of activity

after incubation with the modifying reagent and quantifying the modified residues, a relationship could be drawn between these residues and their function in the enzyme

TABLE 1

Summary of physical characteristics of OPA anhydrase from squid hepatopancreas. Apparent molecular weight as determined by [a]HPLC gel filtration and from [b]amino acid compositional analysis.

pI	5.08
molecular weight (apparent)	23,600[a] 26,000[b]
e	72,046 L/mol cm
$E^{1\%}$	27.7 cm -1
metals	zinc
specific activity	315 U/mg
pH optimum	8.0

MATERIALS AND METHODS

Assay for OPA anhydrase activity

A fluoride sensitive electrode was used to monitor the release of fluoride from DFP, and the rate of increase of $[F^-]$ was recorded on a strip chart recorder. In a continuously stirred reaction vessel, 0.8 ml of 62 mM DFP was added to 8.4 ml of buffer (0.05 M Tris, 0.4M KCl, 0.05 M NaCl, pH 8.0). Autohydrolysis rate was determined and subtracted from assays run in the presence of enzyme. Total assay volume was 10 ml. The electrode was calibrated with fluoride standards (Fisher Scientific) in the range of 0.1 M to 1 mM.

Amino Acid Analysis

Quantitative amino acid analyses was accomplished on a Beckman 6300 amino acid analyzer with a Hewlett Packard integrator. Five hundred picomoles of denatured, reduced and alkylated enzyme were added to clean prescored ampules (Fisher) or to acid washed ignition tubes. Constant boiling hydrochloric acid (Pierce) was added to the tubes, which were then evacuated, sealed, and incubated for 22 hours at 110° C. The sample tubes were opened and the contents rotoevaporated to dryness. The acid hydrolyzed samples were dissolved in buffer and applied to the analyzer. Denaturation, reduction and alkylation for the protection of cysteine residues in the enzyme was performed as described elsewhere (5).

RESULTS AND DISCUSSION

The activity of hepatopancreas OPA anhydrase was measured as a function of pH prior to the alkylation experiments, in order to ascertain the type and number of ionizable residues involved either in catalysis or in maintaining the active conformation of the enzyme. OPA anhydrase shows maximum activity at pH 8.0 (Figure 1A). A plot of the log of activity vs pH (Figure 2B) shows only one inflexion point at approximately pH 7.0. This type of curve indicates that activity depends on the ionization of one amino acid residue in its basic form. These facts implicate a histidine as the residue involved in the enzymatic degradation of DFP.

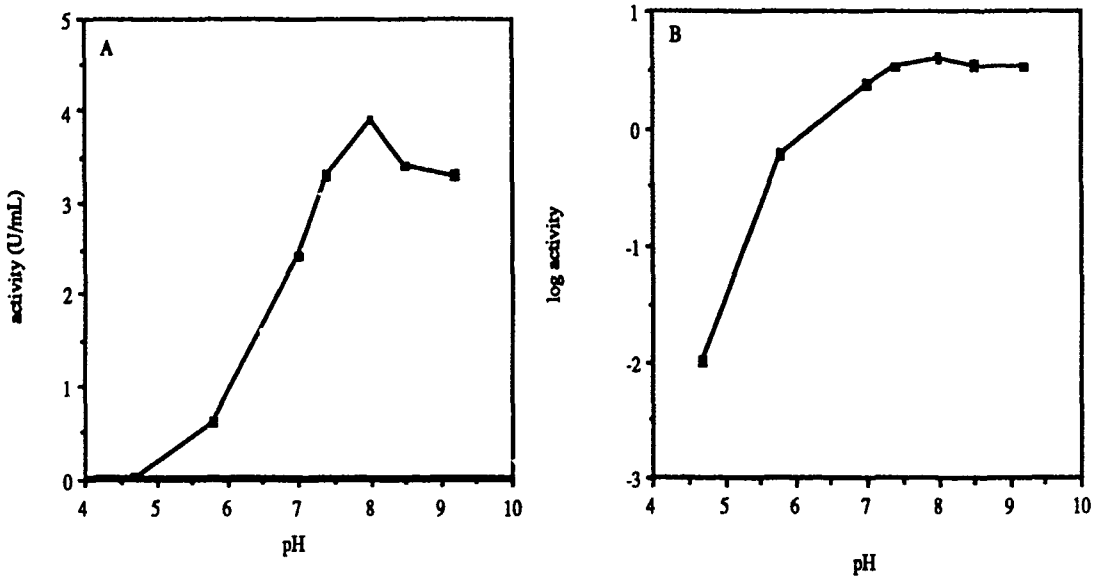

Figure 1. Effect of pH on the activity of squid hepatopancreas OPA anhydrase. Buffers used in the assays were acetate (pH 4.7 and 5.8), phosphate (pH 7.0, and 7.4), Tris (pH 8.0 and 8.5), and borate (pH 9.2). All buffers were at 0.05 M concentration with 0.4 M KCl and 0.05 M NaCl. Autohydrolysis rates varied with pH, and were measured and subtracted for each pH individually. A. Activity (U/mL) vs. pH. B. Log of activity (U/mL) vs. pH.

An attempt was made to inhibit OPA anhydrase activity by alkylation of histidine residues with diethylpyrocarbonate (DEP). Figure 2 shows the time course of inhibition with DEP. Activity was completely inhibited by two minutes, with gradually increasing activity after two minutes. This is probably due to dealkylation of the modified histidine residue to yield free histidine, and thus, active enzyme. Addition of fresh DEP to the incubation mix at 45 minutes again resulted in an almost complete loss of activity. Addition of hydroxylamine to DEP-inhibited enzyme resulted in regeneration of 80% of the original activity. DEP modification of histidine residues is reversible in the presence of neutral hydroxylamine (4). DEP has been documented to modify tyrosine and primary amines as well as histidine, and this reaction is favored at higher pH. However, modified primary amino groups are stable to hydroxylamine reactivation. Therefore, because activity could be regenerated with hydroxylamine, it is unlikely that DEP modified primary amino groups in OPA anhydrase. Amino acid analysis of DEP-treated OPA anhydrase produced a decrease of 1.31 histidine residues as compared to native

enzyme (Table 2). No change in tyrosine was detected. These results show that histidine is an essential residue in the catalytic degradation of DFP by OPA anhydrase.

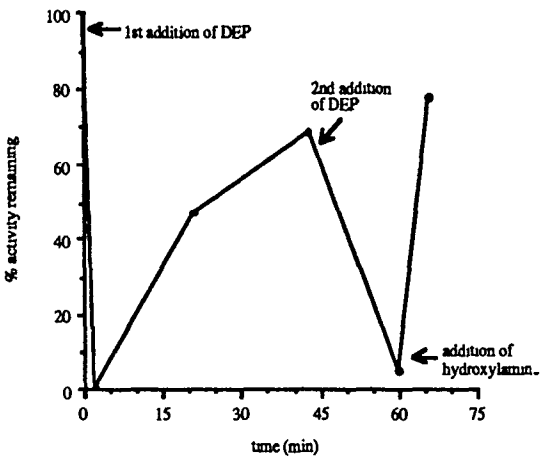

Figure 2. Time course for the inhibition of OPA anhydrase by diethylpyrocarbonate (DEP). 20 mM DEP was added to 0.03 units of enzyme in buffer (17 mM sodium phosphate, 17 mM sodium chloride, 130 mM potassium chloride, pH 6.25) and incubated for the times shown. To regenerate OPA anhydrase activity after DEP inhibition, 40 mM hydroxylamine was directly added to the assay mix.

TABLE 2

Amino acid analyses of native and DEP-treated enzyme. DEP was added to 2 μg of OPA anhydrase in 0.05 M sodium phosphate, pH 6.25, prior to acid hydrolysis of the samples.

	Native	DEP-treated
Histidine	3.99 ± 0.08	2.68 ± 0.07
Tyrosine	4.29 ± 0.9	4.28± 0.12

The OPA anhydrase from squid hepatopancreas has been shown to require metal for activity, and zinc has been identified by atomic absorption in digests of highly purified, native enzyme (1). We performed a series of experiments to determine if the cysteines in OPA anhydrase were present as free cysteines, disulfide bridges, or were responsible for binding metal to the

enzyme. Incubation of native OPA anhydrase with 1 mM NEM showed no significant decrease in activity as compared to the control (Table 3). Amino acid analyses of the enzyme after this treatment showed no modification of cysteine residues. Therefore, there are no solvent accessible, free cysteine residues in OPA anhydrase. However, when NEM was added to EDTA-treated enzyme, no more than 22% of the original activity was recovered upon reactivation by the addition of metal cations. Under the same conditions, addition of metal cations to EDTA-treated enzyme without NEM treatment restored 70% of the original activity. These results suggested that cysteine residues might be involved in binding the zinc cations necessary for activity.

TABLE 3

Amino acid analyses and activity of differentially labelled OPA anhydrase samples. Cysteine residues were quantified as carboxymethyl cysteine due to modification with iodoacetic acid. Samples taken for activity measurements were treated as indicated, while samples for amino acid analyses were treated as indicated followed by denaturation, reduction and alkylation with iodoacetic acid. Any successful alkylation by NEM would be seen as a reduction in carboxylmethyl cysteine. EDTA-treated samples were incubated in 2 mM EDTA and activity was restored by the addition of 10 mM $CaCl_2$.

treatment	Cys residues modified	% activity remaining
Untreated	3.9 ± 0.18	100 %
NEM only	3.5 ± 0.09	100 %
EDTA + $CaCl_2$	ND	70.0 ± 9%
EDTA + NEM + $CaCl_2$	3.6 ± 0.06	23.1 ± 6%

However, subsequent amino acid analysis of EDTA-treated and alkylated OPA anhydrase did not support the conclusion that cysteine residues were responsible for binding metal. No decrease in carboxymethyl cysteine could be seen for EDTA- and NEM-treated enzyme (Figure 5). The only successful modification of cysteine was to first denature and reduce prior to alkylation with IAA. This treatment yields 4 carboxymethyl cysteine residues. There was a large difference in the effect of these modifications on activity. NEM could not alter activity of native enzyme. Only EDTA treatment followed by modification with NEM could prevent restoration of activity with metal ions.

The amino acid analysis and activity data both support the idea that there are no solvent accessible, free sulfhydral groups in OPA anhydrase. While NEM has a strong effect on the capacity to regenerate EDTA-treated enzyme, it could not be demonstrated that the site of alkylation was at cysteine residues. Since alkylation was successful only if the sample was reduced prior to alkylation, we conclude that the four cysteines are present in the form of two disulfide bonds (2 cystines).

CONCLUSIONS

1. Histidine is an essential residue in the catalytic degradation of DFP, and appears to be the only ionizable residue critical for catalysis.

2. The four cysteines observed in the amino acid analysis of hepatopancreas OPA anhydrase occur as two cystines in the native enzyme.

REFERENCES

1. Kopec-Smyth, K., Deschamps, J.R., Loomis, L.D., Miller-Ihle, N., and Ward, K.B. The biochemical characterization of organophosphorous acid anhydrase from squid hepatopancreas. Manuscript in preparation.

2. Hoskin, F.C.G. (1971) Diisopropylphosphorofluoridate and Tabun: Enzymatic hydrolysis and nerve function. *Science* **172**, 1243-1245.

3. Hoskin, F.C.G. and Long, R.J. (1972) Purification of a Diisopropylphosphorofluoridate-hydrolyzing enzyme from squid head ganglion. *Arch. of Biochem. and Biophys.* **150**, 548-555.

4. Lundblad, R. L. and Noyes, C.M. Chemical Reagents for Protein Modification: Volume 1 CRC Press, Inc. Boca Raton, Florida. page 109.

5. Elder, J.H. and Alexander, S. (1982) *Proc. Natl. Acad. Sci. U.S.A.* **79**, 4540-4544

FRACTIONAL FACTORIAL TEST MATRIX DESIGNED TO EVALUATE A NEW CHEMICAL DECONTAMINANT AGAINST TWO EXISTING DECONTAMINANTS

Brian K. MacIver[1], Larry M. Sturdivan[2] and Joseph H. Thompson[1]

Physical Protection Directorate[1]
Research Directorate[2]
U.S. Army Chemical Research, Development and Engineering Center
Aberdeen Proving Ground, Maryland 21010-5423

ABSTRACT

The Multipurpose Chemical/Biological Decontaminant (MCBD) is being developed to replace DS2 as the new deliberate decontaminant. Prior to the start of full scale development a screening evaluation was required to determine decontamination efficacy against controls, DS2 and C8 Emulsion. A fractional factorial design was used to screen a large number of parameters with very few tests. Seven parameters were selected to model the possible conditions under which the decontaminant might be used in the field. The design allows estimates of the main effects, such as MCBD versus the controls, as well as two-way and, in some cases, three-way interactions of the parameters.

INTRODUCTION

The Multipurpose Chemical/Biological Decontaminant (MCBD) is being developed to replace DS2 as the new deliberate decontaminant. The development effort through the Chemical Research, Development and Engineering Center (CRDEC) follows a contractual investigation executed by the Southern Research Institute (SoRI). This study investigated various decontaminant concepts based on the efficacy of decontamination and evaluations of materials compatibility.[1] The outcome from the study suggested that a high surfactant aqueous system (microemulsion) using a hypochlorite as the reactive component, was the best approach to meet the requirements specified by the U.S. Army Chemical School for a new decontaminant. The Chemical School has indicated that the replacement decontaminant will replace DS2 with reduced corrosive properties while lessening logistic burdens and maintain the same or better rate of decontamination efficacy.

The proposed microemulsion system was designed with two reactants incorporated, sodium N,N-dichloroisocyanuric acid (fichlor) and 2-iodoxybenzoate (IBX). Fichlor is intended to replace the classic use of HTH as the hypochlorite source due to

its slower release of chlorine. IBX originated as a more stable form of 2-iodosobenzoate (IBA) to catalyze the hydrolysis of G-agents. Previous work has indicated the decontamination efficacy of MCBD with reactants in glassware tests.[2] Unpublished data indicates that surface testing yields results, in some instances, varying from the same experiments performed in glassware. Therefore, panel tests were needed to account for the differing interactions which may result due to increased surface area and the possible interference of the paint itself. Additionally, panel tests create an environment more depictive of field conditions.

MCBD is a oil in water cationic microemulsion developed at CRDEC. Prior to full scale development MCBD needed an extensive testing report showing its ability to decontaminate surfaces (panels) under a variety of conditions (parameters). The parameters were selected to show similarities to conditions which may be found when decontaminants are applied during a battle or training situation. Seven initial parameters were selected to include: a water rinse option, a scrubbing option, paint type, panel orientation, number of applications, capacity and controls (C8 Emulsion and DS2).

The demand on resources has dictated a need for an expeditious test evaluation. When there is a large number of factors (parameters) it becomes difficult to organize an experiment involving these treatments. A simple replication of a 2^7 factorial will provide estimates of the main effects and all but the highest order interaction. To further simplify the design and reduce size, cost and time a fraction of the factorial design can be used to obtain an estimate of the main effects,[3] such as MCBD versus the controls, as well as two-way interactions of the parameters.

EXPERIMENTAL

Table I shows the partial matrix design for the fractional factorial test scheme. Four agents were used to screen MCBD against the parameters versus controls (DS2 and C8 Emulsion). This particular study has been set up in two phases. During Phase I the seven described parameters were used for evaluation of VX and THD. The matrix consisted of sixty four total tests for each agent, excluding controls. Under these conditions a quarter replicate of a 2^8 ($2^{8-1} = 2^6$) design is used. Estimates of the main effects from this design can be obtained with reasonable accuracy.

Following the evaluation of the results from Phase I, it was determined that certain parameters had little or no influence in the outcome of the experiment. With this information two parameters were eliminated from the matrix and one additional added, contact time. This redesign allowed evaluation with a half replicate at 2^{7-1} for neat HD.

The remaining agent, TGD, needed evaluation from an additional

Table I: Matrix Test Design

Run	Paint	Angle	Capacity	Rinse	Brush	Appl.	Decontaminant	
1	-1 Alkyd	-1 Hor	-1 Small	-1 None	-1 None	1 Two	1 Control	-1 C8
2	1 CARC	1 45^0	1 Large	-1 None	1 Yes	-1 One	-1 MCBD	0
3	1 CARC	-1 Hor	1 Large	1 Yes	1 Yes	-1 One	-1 MCBD	0 0
4	1 CARC	1 45^0	1 Large	1 Yes	1 Yes	1 Two	1 Control	1 DS2
5	-1 Alkyd	-1 Hor	-1 Small	-1 None	1 Yes	1 Two	1 Control	1 DS2
6	1 CARC	-1 Hor	-1 Small	-1 None	1 Yes	1 Two	-1 MCBD	0
. . . 64								

parameter, IBX. IBX is a catalyst being tested for its ability to catalyze the hydrolysis reaction of TGD. In tests with the first three agents, half of the design incorporated MCBD while the remaining half was split equally between the two controls, C8 Emulsion and DS2. For the TGD test the MCBD factor was split into half containing IBX and half without. Thus, the size of the test, 2^{7-1}, remained the same.

Tables II through V show the analysis of the raw data. Using a randomized test matrix (Table I) data was obtained using a standard extraction technique followed by the appropriate analysis method. The use of each parameter was carefully thought out and pretested to determine the consistency of the results that would be obtained. The data acquired was fitted into the regression program on Minitab. The t-ratio delivered an estimate from the main effects of the parameters and the degrees of freedom corresponding to that particular agent analysis. The degrees of freedom indicated the appropriate confidence levels yielding those parameters which showed significance.

Table II: VX Data

Predictor	Coef.	StDev.	tRatio
Constant	3.72	0.20	18.97
Paint	-.03	0.20	-1.76
Angle	0.85	0.20	4.32
Capacity	-1.42	0.20	-7.22
Rinse	-0.08	0.20	-0.40
Brush	-0.49	0.20	-2.51
Application	-0.08	0.20	-0.35
Decon (MCBD)	-0.17	0.20	-0.88
Control	0.89	0.20	3.20
Significant Two-way Interactions			
Ang*Brush	0.30	0.20	1.52
Ang*Control	0.43	0.28	1.57
Cap*Rinse	0.29	0.20	1.46
Cap*Decon	-0.24	0.20	-1.25
Cap*Control	0.54	0.28	1.95
Rinse*Brush	0.26	0.20	1.32

Confidence
99% = 2.76
95% = 2.05

Table III: THD Data

Predictor	Coef.	StDev.	tRatio
Constant	4.64	0.16	28.97
Paint	-0.33	0.16	-2.10
Angle	1.26	0.15	8.03
Capacity	-0.34	0.16	-2.16
Rinse	0.21	0.16	1.32
Brush	-0.42	0.16	-2.67
Application	0.06	0.16	0.37
Decon (MCBD)	0.30	0.16	1.90
Control	0.30	0.21	1.42
Significant Two-way Interactions			
Paint*Ang	0.46	0.16	2.93
Paint*Cap	0.45	0.15	2.90
Paint*Decon	-0.36	0.16	-2.32
Ang*Rinse	-0.46	0.15	-2.97
Ang*Decon	-0.34	0.15	-2.16
Rinse*Decon	-0.35	0.15	-2.20

Confidence
99% = 2.76
95% = 2.05

Table IV: TGD Data

Predictor	Coef.	StDev.	tRatio
Constant	6.54	0.06	107.96
Angle	0.18	0.06	3.07
Brush	-0.56	0.06	-9.25
Contact t	-0.28	0.06	-4.77
Decon (MCBD)	-0.26	0.06	-4.37
Control	-0.31	0.08	-3.66
Significant Two-way Interactions			
Ang*Brush	-0.13	0.06	-2.21
Ang*Brush	-0.24	0.06	-4.07
Cap*Decon	-0.23	0.06	-3.76
IBX*Rinse	-0.17	0.06	-2.04

Confidence
99% = 2.68
95% = 2.01

Table V: HD Data

Predictor	Coef.	StDev.	tRatio
Constant	3.95	0.17	23.59
Angle	0.39	0.17	2.37
Capacity	-1.0	0.17	-0.60
Rinse	0.10	0.17	0.61
Brush	0.36	0.17	2.13
Contact t	-0.23	0.17	-1.37
Decon (MCBD)	0.94	0.17	5.61
Control	-0.09	0.24	-0.39
Significant Two-way Interactions			
Ang*Cap	0.44	0.17	2.59
Cap*Brush	-0.44	0.17	-2.67
Rinse*Brush	0.36	0.17	2.16
Brush*Decon	-0.37	0.17	-2.18

Confidence
99% = 2.72
95% = 2.02

CONCLUSION

Several areas of emphasis were targeted for observation prior to the creation of this testing. A quick method for determining the effectiveness of several materials and their capacity to produce a desired effect can be accomplished through the use of a factorial design. To further reduce the size of the experiment a fraction of the factorial design can reduce the inherit hazard and logistic problems that might occur when working with chemical agents. In addition, non-experimental types of errors may crop up while planning and conducting a large experiment. For example, the treatment labelling may be interchanged, the plot numbers may be wrongly noted and similar other things may happen. For this reason the fractional factorial testing matrix is valid in creating a screening profile for agent studies, while estimates of the main effects show the significant individual parameters and the two-way interactions of the parameters.

The second area of emphasis concluded from this experiment is the effect of MCBD as a decontaminant and if IBX will improve the hydrolysis rate of TGD. From the results of the regression there is indication that MCBD has decontaminant efficacy statistically similar to DS2 and C8 Emulsion. Results can be displayed isolating the effects that individual parameters have on efficiency of MCBD acting as a decontaminant. Also, there is no statistical benefit offered from IBX to catalyze the hydrolysis rate of TGD.

REFERENCES

1. D. W. Mason, D. R. Coleman, R. B. Spafford and T. E. Lawler, Development of a Multipurpose Chemical/Biological Decontaminant, Technical Report CRDEC-CR-87025 (February 1987).

2. J. W. Hovanec, Unpublished Interim Report: MCBD 6.2 Effort (May 1988).

3. G. Box, W. Hunter and J. Hunter, Statistics For Experimenters, p. 374 ff. John Wiley & Sons, Inc. New York, NY 1978.

Electrochemical Studies in Microemulsions

Paul L. Cannon Jr[a], Stephanie M. Garlick[a,c] and Frederick R. Longo[a,b]

a. U. S. Army Chemical Research, Development, and Engineering Center
Aberdeen Proving Ground, MD 21010-5423

b. Drexel University
Philadelphia, PA 19104

c. Geo-Centers, Inc.
10903 Indian Head Highway
Ft. Washington, MD 20744

Abstract

We have developed a broad plan for the investigation of the aggregate structure of microemulsions using various physical techniques. Recently, we initiated a study of the electrochemical oxidation of ferrocene in several cationic microemulsions. We have probed the mechanism of the electrochemical process and the nature of the microemulsion media employing cyclic voltammetry and chronopotentiometry. The results of our electrochemical studies will be related to our kinetics data and to our luminescence investigations in these systems.

1. Introduction

During the last quarter century there have been an increasing number of investigations of the effects of surfactants on the rates and mechanisms of chemical reactions.[1,2] Surfactant systems have also been employed as media for organic synthesis and as models for enzymatic action.[3-8] These studies have been primarily concerned with the influence of normal micelles in aqueous solution, although processes in reversed micelles, lyotropic liquid crystalline phases, vesicles, and monolayers have also been examined. Common to all these systems is the presence of the microscopic oil/water interface.

In spite of the advantages relatively few studies of chemical reactions in

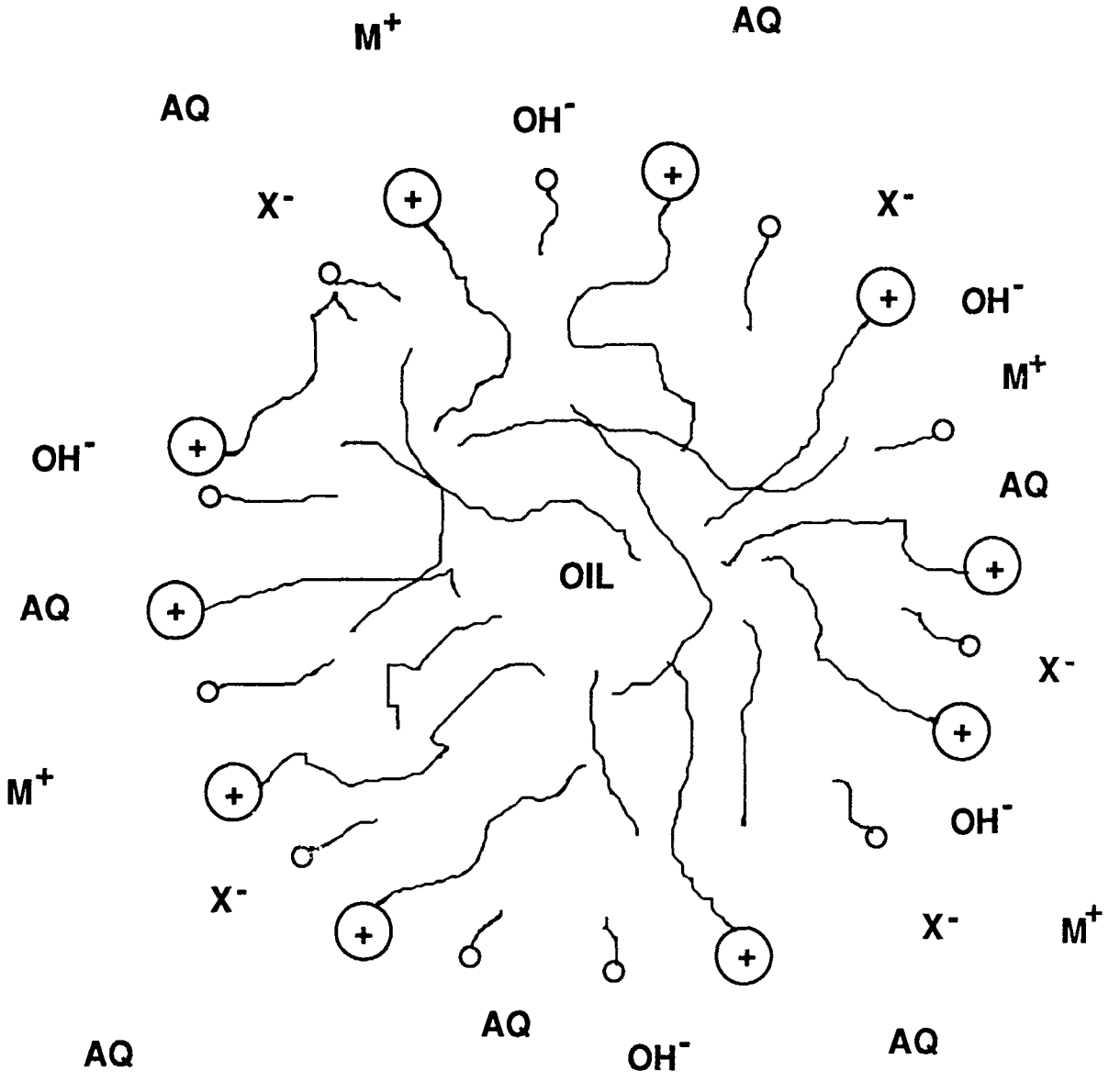

Figure 1. An Oil Microdroplet Stabilized in an Aqueous Continuum by a Cationic Surfactant and a Cosurfactant.

microemulsions have been reported. Microemulsions are capable of dissolving large amounts of a great variety of solutes due to the presence of different phases, including the oil, the aqueous, and the unique interphase, over which there is a gradient in the dielectric constant ranging from ~2 to ~78. Very nonpolar solutes will be located in the oily core of the microemulsion droplet, whereas more polar substances will be distributed throughout the interphase and aqueous regions. Thus, the microemulsion medium makes it is possible to bring nonpolar oil-soluble (lipids) and polar, water-soluble reagents into contact.

2. The Nature of Microemulsions

There is no universal agreement concerning the nature of the fluids which have variously been referred to as microemulsions,[9-12] solubilized micellar solutions, [13] and micellar emulsions.[14] These systems are translucent or transparent dispersions of oil-in-water (o/w) or water-in-oil (w/o) which contain one or more amphiphilic compounds and are mechanically stable. There are some systems which are demonstrably only kinetically stable, [15-18] while many others[19-25] appear to be thermodynamically stable. It is often difficult to prove thermodynamic stability in these systems of complex composition; the important criteria for this determination include spontaneous formation and physical properties independent of order of addition of components. Furthermore, after subjected to a "pulse" perturbation (ΔT, ΔpH, etc.) which causes phase separation, a microemulsion identical with the original must reform. Accounts of earlier work on thermodynamic stability and microstructure are presented in reviews by Shinoda and Friberg [26] and Prince.[27]

Microemulsions are believed to consist of a dispersion of oil microdroplets in a water continuum or vice-versa. The volume occupied by the dispersed phase (phase volume) can be high (20 to 80%). The droplet diameter is on the order of 100 to 600 Å. In this size range the droplets appear to be monodisperse,[10,12,29,30] although more recent work has provided evidence for a more complex structure in some systems.[31,32] Conceptually, the droplet may be divided into two regions: the oil or water core and the surface or interphase region. Essentially all of the surfactant and part of the cosurfactant are located in the interphase region. A model of an o/w microemulsion is shown in Figure 1. Under appropriate conditions, a third phase which appears to be oil and water continuous may be detected. This phase has been called the middle or surfactant phase.[25,26] It has variously been suggested that this surfactant phase consists of bicontinuous structures, [33] lamellae of oil and water,[31] or molecularly dispersed solutions.[35]

All aspects of surfactant systems are more recently reviewed in the six volumes representing the proceedings from the 4th and 5th Symposia on Surfactants in Solution;[37] in particular, Volume 6, Part VII is entirely devoted to microemulsions (structure, stability and composition) and chemical reactions in microemusions.1

3. Electrochemistry: Voltammetric Experiments

When a potential is applied to a solution containing an electroactive material, the measured current is proportional to the rate of the electrochemical reaction. For diffusion controlled reactions an examination of the dependence of the current on the applied potential (voltammetry) can yield the diffusion coefficient of the electroactive reagent . When a microemulsion is doped with an electroactive species, soluble only in the oily interior of the microdroplet, the measured current depends on the rate at which the microdroplet "vehicles" move to the electrode surface. Hence, the diffusion coefficient and the hydrodynamic radius of the microdroplet can be determined from voltammetry experiments.

Using a polarographic method, Mackay obtained microdroplet radii (in anionic and cationic micremulsions) comparable to to those obtained from small angle x-ray scattering, quasi-elastic light scattering and luminescense quenching.[38] Qutubuddin has recently reported that reasonable values of diffusion coeffients and microdroplet radii can be obtained from cyclic and rotating disc voltammetry experiments in CTAB/1-butanol microemulsions.[39]

In cyclic voltammetry the peak current, i_p, is given by the Randles-Sevcik Equation:

$$i_p = 0.4463nF AC_0(nF /RT)^{1/2}D^{1/2}v^{1/2} \qquad \text{Eq 1}$$

where A, D, and v are the electrode area, the diffusion coefficient and the potential scan rate, respectively. A study of the variation of i_p with v yields the diffusion coefficient.

In the chronopotentiomtric technique a constant current or current step is applied to the electrode and the induced potential is recorded as a function of time. The Sands Equation applies to the process:

$$\tau^{1/2} = (\pi^{1/2}nFAD^{1/2}C)/(2i) \qquad \text{Eq 2}$$

where i is the current, τ is the transition time, F is the faraday, A is the electrode area, D is the diffusion coefficient and C is the concentration of the electroactive species. The transition time is the length of the period beginning with the initiation of electrolysis to the point at which the potential begins to change rapidly; this represents the depletion of the most readily reduced (or oxidized) electroactive species in the region near the electrode. The value of τ depends on the value of the applied constant current. As indicated by Eq 2, a plot of $\tau^{1/2}$ versus i^{-1} yields a straight line whose slope is proportional to $D^{1/2}$.

Choosing the correct electroactive probe is the key to obtaining meaningful data. Qutubuddin has recently discussed this problem.[39] The electroactive probe must not cause changes in the nature of the microemulsion; it must undergo diffusion controlled charge transfer at the electrode surface; it must be non-polar, preferentially oil soluble and exhibit insignificant adsorption at the electrode surface. Of course, it must be electrochemically reactive within the potential range governed by the electrode material and the microemulsion medium. Ferrocene meets these requirements in many microemulsions and we have employed it as a probe in our studies.

4. Materials and Procedures

Cetyltrimethyl ammonium bromide was purchased from Aldrich (95 %) or Sigma (98%) and used as received. Toluene (100%) was obtained from Baker. Sodium tetraborate decahydrate ($Na_2B_4O_7 \cdot 10H_2O$) was purchased from Fisher. [Aqueous solutions of borate buffer (0.03 M) are designated as AQ.] The cosurfactant N,N-diethyl formamide (DEF, 99%) was obtained from Aldrich.

Microemulsions, (4.5% CTAB, 4.5% DEF, 1.0% TOL and 90.0% AQ) doped with 4.46 or 7.9 mM ferrocene, i. e., bis(cyclopentadienyl) iron II, were prepared for the study at 26°. A Bioanalytical Systems (BAS) C-1A electrochemical cell stand and electrode holder were employed in conjunction with an MF2012 3.2 mm diameter glassy carbon electrode, an RE-1 Ag/AgCl reference electrode and an M4130 platinum auxiliary electrode.

The effective cross sectional area of the glassy carbon electrode was determined was determined to be 0.082 cm^2 by chronopotentiomtry of a 4.0 mM potassium ferrocyanide/1.0 M potassium chloride solution.

Potentiostatic and galvanostatic controls were maintained with an Apple //e Computer employing EG&G PAR Model 276, Volume I Software. The computer was connected by an IEEE 488 interface bus to an EG&G PAR Model 276 Interface Module in a Model 173D Potentiostat/Galvanostat. Cyclic voltammetric scan rates were 10 to 200 mV/s with no IR compensation. Chrnopotentiometric anodic currents of -10, -12 and -15 μA were employed.

5. Results and Discusion

We have obtained cyclic voltammograms and chronopotentiograms in CTAB microemusions (4.5% CTAB, 4.5% DEF, 1.0% TOL and 90.0% AQ) doped with ferrocene at concentrations of 4.46 mM and 7.9 mM. Voltammograms were obtained in 7.9 mM ferrocene at potential sweep rates of 10, 20, 50, 100 and 200 mV/s; the voltammogram obtained at 10 mV/s is shown in Figure 2. The peak currents obtained from these graphs were plotted versus potential sweep rate; this plot is presented in Figure 3. The slope of this plot at 7.9 mM ferrocene was determined to be 6.51×10^{-5}

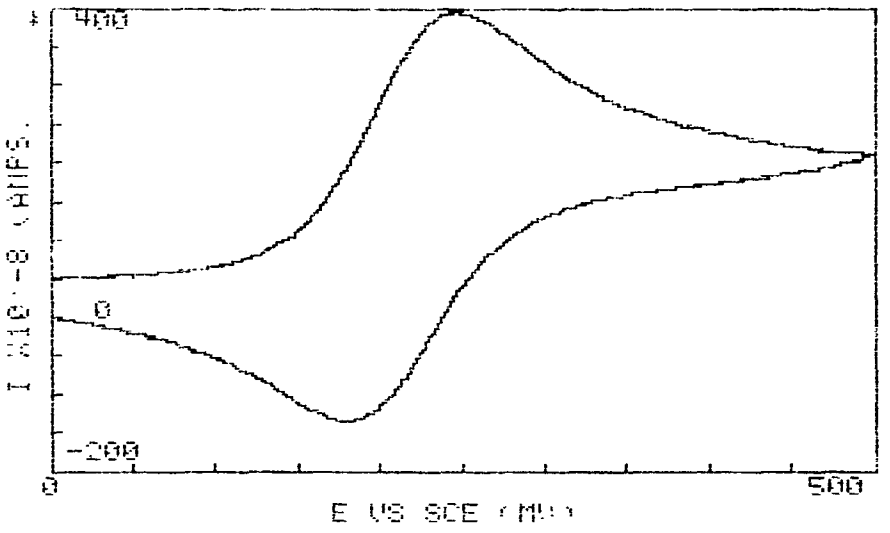

Figure 2. The cyclic voltammogram for ferrocene at 7.9 mM in a μE at a potential sweep rate 10 mV/s. The initial and final potentials were 0.0 mV and the vertex potential was 500 mV. The reference electrode was Ag/AgCl. Perfect reversibility of the ferrocene to ferricinium cation was not obtained as determined from the ratio anodic to cathodic currents.

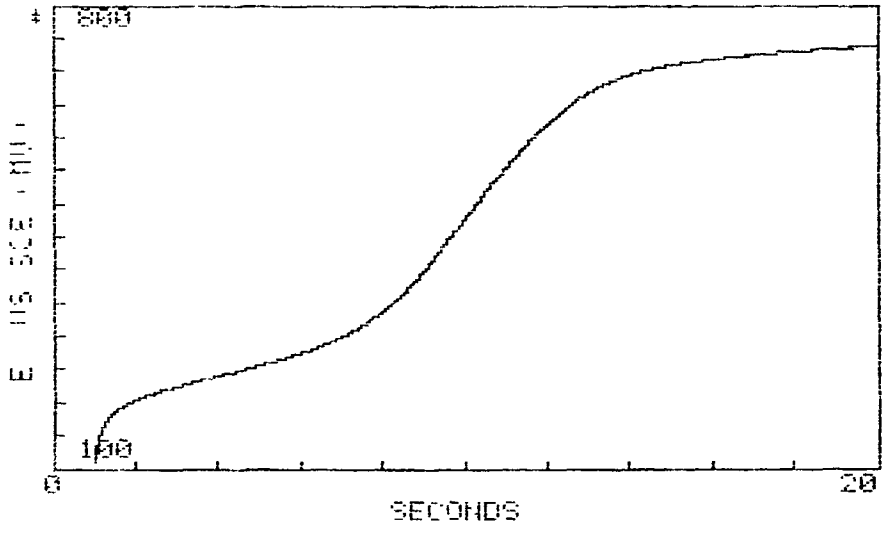

Figure 4. The chronopotentiogram for ferrocene in a μE ot an applied current of 10 μA. Our equipment did not permit us to do current reversal chronopotentiometric studies.

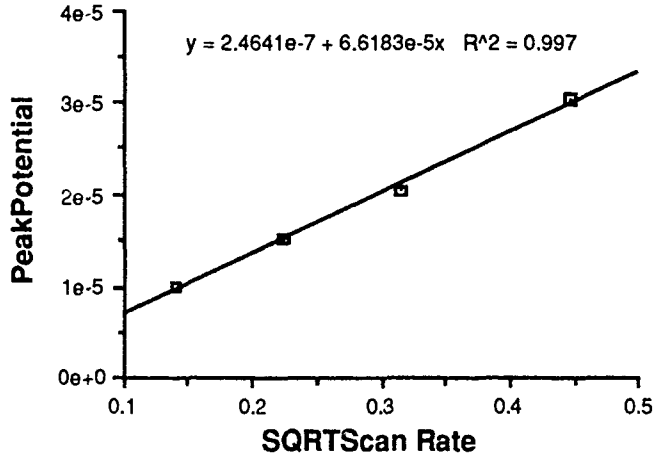

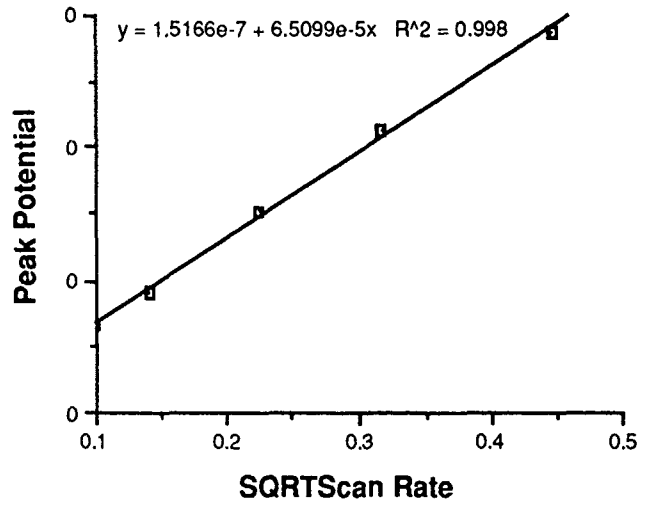

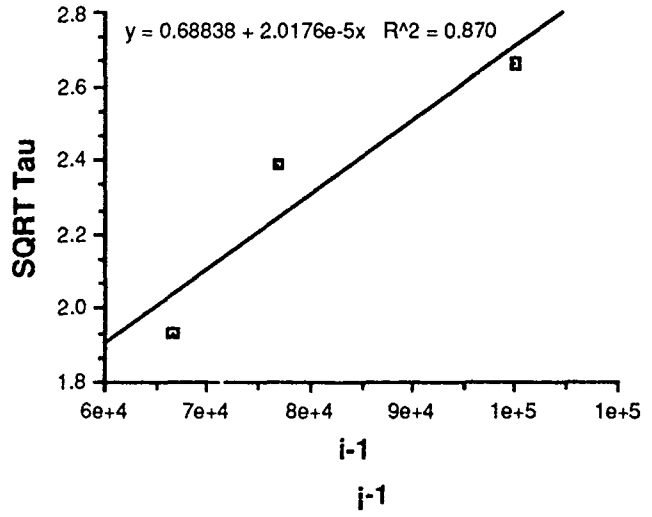

Figure 3. Analyses of CV and CP According to Equations 1 & 2.

from which, by application of Equation 1, we obtained a diffusion coefficient of 1.35×10^{-11} m^2/s and (by application of the Stokes Einstein Equation) an aggregate diameter of 324 Å. The cyclic voltammetric data obtained at 4.46 mM ferrocene were treated in the same manner and the results are presented in Figure 3 and in Table 1.

Chronopotentiograms were obtained in the 7.9 mM ferrocene system. The graph for the case of i = 10 μA is shown as an example in Figure 4. A plot of the square root of the transition times versus the inverse of the current is presented in Figure 3. The slope of this plot was determined to be 2.02×10^{-5} from which, by application of Equation 2, we obtained a diffusion coeficient of 1.32×10^{-11} m^2/s and, by application of the Stokes Einstein Equation, a diameter of 332 Å.

As can be seen, by examination of Table 1, the CV and CP results seem to be in very good agreement. This is fortuitous since the correlation function for the CP data is very low.

The large difference in the values of the diffusion coefficients obtained at 4.46 mM and 7.9 mM ferrocene is difficult to explain. We had anticipated little effect of the probe molecule on the diffusion of the aggregate. In addition, we might have anticipated the opposite observation; i. e., an apparent increase in the diffusion cefficient with increase in probe concentration. This would be tantamount to considering an aggregate bound to n probe molecules as representing a unit carrying n electrochemical equivalents.

We plan to continue these electrochemical investigations in order to gain a better understanding of the structure of microemulsion aggregates and to explain the anomalous probe concentration effect on the measured diffusion coefficients.

Table 1. Summary of CV and CP determination of the difussion coefficient and the diameters of aggregates in mE's composed of 4.5% cetyltrimethyl ammonium bromide (CTAB), 4.5% N,N-diethylformamide (DEF) 1.00% toluene (TOL) and 0.03M borate buffer (AQ). The electroactive probe is ferrocene.

Method	[Ferrocene]	D(m^2/s)	d/Å
CV	4.46 mM	4.4E-11	100
CV	7.9 mM	1.35E-11	324
CP	7.9 mM	1.32E-11	332

6. LITERATURE CITED

1. Cordes, E.H., and Dunlop, R.B., "Kinetics of Organic Reactions in Micellar Systems," *Accts. Chem. Res.* Vol. 2, p 329 **(1969).**

2. Fendler, E.J., and Fendler, S.N., "Reactions in Micellar Media," *Phys. Org. Chem.* Vol. 8, p 271 **(1970).**

3. Fendler, J.H., and Fendler, E.J. *Catalysis in Micellar and Macromolecular Systems*, Academic Press, New York, New York, 1975.

4. Rijnbout, J.B., "Stokes Principle of Reversion and the Optical Measurement of Soap Film Thickness," *J. Phys. Chem.* Vol. 75, p 2001 **(1971).**

5. Kitahara, A., "Solubilization and Catalysis in Reversed Micelles ," *Adv. Colloid Int. Sci.* Vol. 12, p 109 **(1980).**

6. Ahmad, S.I., and Friberg, S., "Catalysis in Micellar and Liquid Crystalline Phases. I. The System Water-Hexadecyltrimethyl Ammonium Bromide-Hexanol," *J. Am. Chem. Soc.* Vol. 94, p 5196 **(1972).**

7. Fendler, J.H., "Surfactant Vesicles as Membrane Mimetic Agents: Characterization and Utilization," *Acct. Chem. Res.* Vol. 13, p 7 **(1980).**

8. Davis, J.T., "Structure of Organized Media," *Adv. Catalysis* Vol. 6, p 1 **(1954).**

9. Hoar, T.P., and Schulman, H.H., "Transparent Water-in-Oil Dispersions: the Oleopathic Hydro-Micelle," *Nature* (London) Vol. 152, p 102 **(1943).**

10. Schulman, J.H., Matalon, R., and Cohen, M., "The Role of the Cosurfactant," *Discuss Faraday Soc.* Vol. 11, p 117 **(1951).**

11. Schulman, J.H., Stockenius, W., and Prince, L.M., "Mechanism of Formation and Structure of Microemulsions by Electron Microscopy," *J. Phys. Chem.* Vol. 63, p 1677 **(1959).**

12. Stockenius, W., Schulman, J.H., and Prince, L.M., "The Structure of Myelin Figures and Microemulsions as Observed with the Electron Microscope," *Kolloid. Z.* Vol. 169 , p 170 **(1960).**

13. Shinoda, K., and Kunieda, H., "Conditions to Produce So-called Microemulsions: Factors to Increase Mutual Solubility of Oil and Water by Solubilizer," *J. Colloid. Interface Sci.* Vol. 42, p 381 **(1973).**

14. Adamson, A.W., "A Model for Micellar Emulsions," *J. Colloid. Interface Sci.* Vol. 29, p 261 **(1969).**

15. Clausse, M., Sherman, P., and Hebd, C.R., "Theory of Luminescence Quenching," *Seanc. Acad. Sci., Ser C* Vol. 279, p 919 **(1974).**

16. Clausse, M., Sherman, P., and Sheppard, R.J., "Dielectric Properties of Benzene-in-Water Microemulsions in the Frequency Range 100 kHz - 5 MHz," *J. Colloid. and Interface Sci.* Vol. 56 , p 123 **(1976).**

17. Hermansky, C., and Mackay, R.A., *Solution Chemistry of Surfactants,* pp 723-730, K. L. Mittal, Ed., Plenum Press, New York, NY, **(1979).**

18. Rosano, H.L., Lan, T., Weiss, A., Gerbacia, W.E.F., and Whittan, J.H., "Transparent Dispersions: An Investigation of Some of the Variables Affecting Their Formation," *J. Colloid. Interface Sci.* Vol. 72 , p 233 **(1979).**

19. Letts, K., and Mackay, R.A., "Reactions in Microemulsions. I. Metal Ion Incorporation by Tetraphenylporphin," *Inorg. Chem.* Vol. 14, p 2990 **(1975).**

20. Letts, K., and Mackay, R.A., "Reactions in Microemulsions. II. Solubilization of Intermediates," *Inorg. Chem.* Vol. 14 , p 2993 **(1975).**

21. Smith, G.D., Garrett, B.B., Holt, S.L., and Barden, R.E., "The Interaction of Copper(II) and N^{α}-Acyl-L-Histidinol at the Interface of an Oil Continuous Microemulsion," *J. Phys. Chem.* Vol. 80, p 1708 **(1976).**

22. Smith, G.D., Garrett, B.B., Holt, S.L., and Barden, R.E., "Properties of Metal Complexes in the Interphase of an Oil Continuous Microemulsion. 2. Interaction of Copper(II) with the Side Chains of Lysine, Glutamine, and Methionine," *Inorg. Chem.* Vol. 16, p 558 **(1977).**

23. Mackay, R.A., Dixit, N.S., Hermansky, C., and Kertes, A.S., "Conductivity and Diffusion Measurements in Micellar and O/W Microemulsion Systems. A Comparative Study," *Colloids and Surfaces* Vol. 21, pp 27-39 **(1986).**

24. Mackay, R.A., and Agarwal, R., "Electrochemical Studies in Nonionic Microemulsions," *J. Colloid Interface Science* Vol. 65, p 225 **(1978).**

25. Reed, R.L., and Healy, R.N., *Improved Oil Recovery by Surfactant and Polymer Flooding*, Academic Press, New York, NY, 1977.

26. Shinoda, K., and Friberg, S., "Microemulsions: Colloidal Aspects," *Adv. Colloid Interface Sci.* Vol. 4, p 281 **(1975).**

27. Prince, L.M., "Emulsions and Emulsion Technology, Part I," p 125, Lissant, K.J., Ed., Marcel Decker, Inc., New York, NY, 1974.

28. Prince, L.M., "Microemulsions," Ed, Academic Press, New York, NY, 1977.

29. Tosch, W.C., Jones, S.C., and Adamson, A.W., "Distribution Equilibria in a Micellar Solution System," *J. Colloid Sci.* Vol. 31 , p 297 **(1969).**

30. Cook, C.E., and Schulman, J.H., "Surface Chemistry," p 231, Munksgaard, Copenhagen, 1965.

31. Tricot, Y., Kiwi, J., Niederberger, W., and Gratzel, M., "Application ^{13}C NMR, Fluorescence, and Light Scattering Techniques for Structural Studies of Oil-in-Water Microemulsions," *J. Phys. Chem.* Vol. 85, p 862 **(1981).**

32. Gulari, E., Bedwell, B., and Alkafaji, S., "Quasi-Elastic Light-Scattering Investigation of Microemulsions," *J. Colloid Interface Sci.* Vol. 77, p 202 **(1980).**

33. Scriven, L., *Micellization, Solubilization and Microemulsions*, Vol. 2, p 877, Mittal, K.L., Ed., Plenum Press, New York, NY, 1977.

34. Friberg, S., Lapizynska, I., and Gillberg, G., "Microemulsions Containing Nonionic Surfactants - The Importance of the PIT Value," *J. Colliod Interface Sci.* Vol. 56, p 19 **(1976).**

35. Shah, D.O., Walker Jr., R.D., Hsieh, W.C., Shad, N.J., Dwivedi, S., Nelander, J., Pexinsky, R., and Deamer, D.W., SPE 5815, In *Proceedings of the Improved Oil Recovery Symposium of Soc. Pet. Eng. of AIME*, Tulsa, OK March 1976.

36. Holt, S.L., Microemulsions: A Contemporary Overview *J. Dispersion Sci. and Tech.* Vol. 1, p 423 **(1980).**

37. a. Mittal, K.L., and Lindman, B., Ed., "Surfactants in Solution. II," In *Volumes 1 to 3, 4th International Symposium*, Lund, Sweden, 1982; Mittal, K.L., and Bothorel, P., Ed., "Surfactants in Solution. II," In *Volumes 4 to 6, 5th International Symposium*, Bordeaux, France, **1984.**

38. Mackay, R. A., Dixit, N. S., Hermansky, C. and Kertes, A. S.; "Conductivity and Diffusion Measurements in Micellar and Oil/Water Microemulsion Systems. A Comparative Study." *Colloids and Surfaces.* Vol 21, p 27-39 (**1986**)

39. Kalpesh, C., Qutubuddin, S. and Hussan,A.; "Electrochemical Investigation of Microemulsions". *J Colloid and Interface Science*, **1989**, in press.

BLANK

POLYESTER CARRIERS FOR CATALYTIC REACTANTS

Nolan Tillman, Lois M. Speaker,[1] and Gary M. Russo

This program explored the feasibility of producing sorptive, self-decontaminating solid coatings from AQ29, a member of the Eastman AQ™ family of ionic polyesters. Sample coatings of AQ29 loaded with various stoichiometric and catalytic reagents for CW agent destruction were fabricated and challenged with simulants. By analysis of solvent extracts after challenge, we determined the degree of simulant destruction within the matrix of the loaded films. It was demonstrated that these composite films retained reagent activity towards several simulants. Examples included stoichiometric oxidation of chloroethyl ethyl sulfide (CEES) by chloramine-T (CAT), and promotion of the hydrolysis of *p*-nitrophenyl diphenyl phosphate (PNPDPP) and *p*-nitrophenyl hexanoate (PNPH) by sodium iodosobenzoate (NaIBA). In preliminary experiments, most metal oxides did not show significant activity in promoting photo-oxidation of 1,1-diphenyl ethene (DPE), with the exception of iron (III) oxide.

Introduction

Exposure of vehicles and other equipment to chemically-contaminated conditions can result in absorption of the toxic agent by equipment components. The contaminated materiel can then serve as a secondary source of agent by slowly desorbing the agent even after the equipment has been removed from the contaminated environment.

The development of a coating which can self-decontaminate the treated surface would represent a significant enhancement of the capability of units to function in a chemically-contaminated environment. We are attempting to address this need by formulating polyester coating materials loaded with compounds that detoxify agents and simulants.

We have been working with the AQ™ family of Kodak-produced polyesters. These AQ polyesters are linear copolymers of sulfonate-containing monomers and aliphatic or cycloaliphatic

glycols with $M_n \approx 15,000$. Varieties are available with glass transition temperatures ranging from 29°C (AQ29) to 55°C (AQ55). They are water dispersible without the aid of cosolvents or surfactants. They can be used as sealants, adhesives, or coating materials with good bonding to a variety of surfaces, including metals, plastics, wood, and glass. They are available in either water-dispersed or solid form.

The presence of hydrophilic and hydrophobic groups is believed to confer an "emulsion-like" structure in the water-dispersed form. AQ polyesters have been used to form aqueous dispersions containing a variety of hydrophobic materials, including paraffins, silicon oils, and various other plasticizers, tackifiers, oils and waxes. These properties suggest that AQ polyester films may serve as excellent carriers of decontaminating reagents.

This approach differs from previous, extensive work performed by others that has been developing polystyrene-based, strong acid/base functionalized resins for skin decontamination and sorptive coatings,[2,3] as well as from other recent work that covalently bonds decontaminating reagents to polymer chains for catalytic hydrolysis and oxidation.[4,5] AQ polyesters should provide a general material that can be loaded with a variety materials for decontamination of many different types of agents, as well as for decontaminating effectiveness against multiple agent threats.

General Experimental Methodology

AQ29 dispersions were cast into films using a doctor blade and drying at 120 °F. Control samples were prepared using AQ29 alone, and loaded films were prepared using 24% chloramine-T hydrate (CAT), 1-3% sodium iodosobenzoate (NaIBA)/1.3% anhydrous sodium tetraborate, 3% iron (III) oxide, 3% zinc oxide, and 3-15% titanium dioxide (anatase). Weight percents are based on the amount of AQ solids in the dried films. Films containing reactants were prepared by using ~15% aqueous AQ29 dispersions with a calculated amount of the additive dissolved in the dispersion. Dispersions containing ~30% AQ29 plus the additive were tried, but they tended to form an insoluble precipitate with ionic components, although they were suitable for loading with metal oxides. Better quality films were prepared using an automatic, rotating drum-coating apparatus. Dried film thickness was measured using a digital micrometer. The formulation could be adjusted to prepare coatings of thickness 15-200 μm.

Coatings were applied on either an ESTAR™ polyethyleneterephthalate film, or on a silicone release layer-coated polyethylene film and stripped after drying to form a "freestanding" film. An initial layer of 36% unloaded

AQ29 was applied to the silicone layer to form such freestanding films and allowed to dry (thickness ca. 15 μm) prior to fabrication of the "working" film. This proved necessary because 15% AQ29 dispersions did not wet the silicone surface.

The dried coatings were challenged with appropriate simulants. After standing for a period of time, each film was extracted with a suitable solvent and the extract was analyzed by GLC, HPLC, or UV-vis spectroscopy.

Challenge of CAT-Loaded Films With Mustard Simulants

For experiments using CAT-loaded films, simulant (such as CEES) was dropped onto the CAT-loaded surface of coupons of 120 ± 10 μm thick freestanding films of AQ29. The films were formulated to contain 24% CAT by weight. The challenged films were allowed to stand overnight; presumably this represents more than sufficient time for reaction to occur.

Samples were prepared and qualitative analysis, using the KI-starch test, was performed to follow the disappearance of CAT from the film. The complete consumption of CAT was indicated by a negative KI test when a drop of a 5% aqueous KI solution was applied to the simulant-treated surface. In this procedure, film coupons were challenged with a complete excess of simulant (ca. 10 drops/in^2). The results indicated that CAT in the films was completely reacted when challenged with mustard simulants such as CEES and thiodiglycol, but not with inert materials such as chloroform, nonane, and, surprisingly, butyl sulfide. Since AQ29 is generally soluble in halogenated solvents such as chloroform, methylene chloride and insoluble in nonpolar, inert materials such as n-alkanes, the result for butyl sulfide may be the result of poor mutual solubility of the AQ polymer and the sulfide. Good solubility may be necessary to promote intimate mixing and efficient reaction.

Quantitative analysis of the CAT(AQ)-CEES reaction was performed by challenging one cm^2 coupons with 2.0 μL of CEES. The films were extracted with several milliliters of diethyl ether. A known amount of nonane was added by microliter syringe as an internal standard and the samples were analyzed by capillary GLC, using a nonpolar column (DB-5, polydimethylsiloxane with 5% phenyl groups). Peak areas for the ether extracts were measured by electronic integration of the peaks. The amount of simulant recovered was calculated using FID response factors for the simulant relative to the internal standard, determined from standard solutions.

The results of this procedure are presented graphically in Figure 1, which shows the yield of CEES recovered from CAT-loaded and unloaded films in two separate determinations (experiments 1 and 2). Each bar in Figure 1 represents the average of 3-5 independent samples. From the average of the two runs, it can be seen that the amount of CEES recovered is

decreased by over 60% by loading of the film with CAT. Although the complete fate of the CEES has not been quantitatively accounted for, traces of *p*-toluene sulfonamide and 2-chloroethyl ethyl sulfoxide were found by GLC, and HPLC analysis of a THF extract of a challenged films showed there to be a large peak identified by retention time and UV spectrum to be 2-chloroethyl ethyl sulfine p-toluene sulfonylimine. These are expected products based on known reactions of chloramine-T and alkyl sulfides.[6,7]

FIGURE 1

Recovery of CEES From Unloaded AQ29 Films and From Films Containing 24% Chloramine-T Hydrate

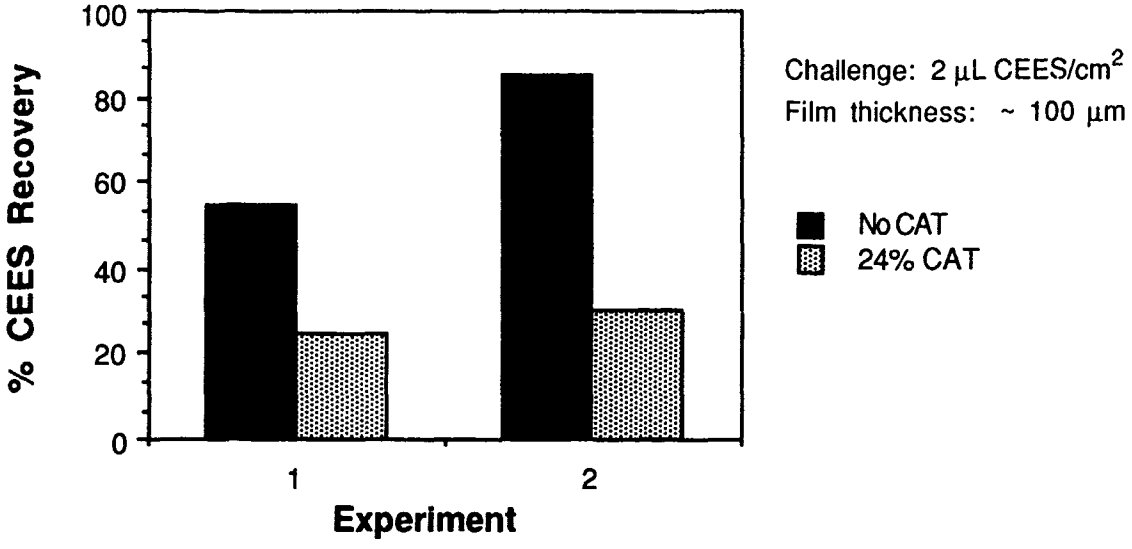

Challenge of NaIBA-Loaded Films With PNPH

Challenges of NaIBA-loaded films with the G-agent simulant PNPH were done using Estar-backed films with an AQ29 layer thickness of 45 ± 10 µm (weight of AQ layer: 7 ± 1 mg). The AQ layer contained 2.7% NaIBA and 1.3% sodium tetraborate. One-cm^2 coupons were challenged with 10 µL of a 0.14 M solution of PNPH in acetonitrile (total challenge: 1.4 µmol). After the samples had stood for one hour, they were extracted with 2.0 mL of diethyl ether. To this solution was added 2.0 µmol of diethyl malonate as an internal standard, and the mixture was quantitatively analyzed by GLC against a calibration curve prepared from standard solutions. The column employed was a polymethyl/5% phenyl siloxane on fused silica capillary column.

The results of this procedure are depicted in Figure 2. Each bar in Figure 2 represents the average of three samples. These results show that the yield of recovered PNPH was

decreased by an average of 24% (from 56 ± 7% to 32 ± 4%, 0.34 µmol) with loading of the film with NaIBA. This result does not show catalytic turnover of the NaIBA, because the amount of NaIBA is estimated to be ca. 0.7 µmol, but it does show that the NaIBA at least *promotes* the hydrolysis reaction. Since the films were extracted with a nonaqueous solvent prior to analysis, the reaction definitely occurs within the matrix of the solid, loaded AQ film.

Extraction of the PNPH-challenged films with acetonitrile and analysis by UV-visible spectroscopy showed that p-nitrophenol was formed as a reaction product, which is expected for the known NaIBA-catalyzed hydrolysis of PNPH and similar simulants in microemulsion media.[8,9] Other work using p-nitrophenyl diphenyl phosphate in acetonitrile, with film extraction by aqueous borate buffer solution and UV-vis analysis, gave similar results.

FIGURE 2

Recovery of PNPH From AQ29 Films Challenged With PNPH in Acetonitrile, Measured by GLC

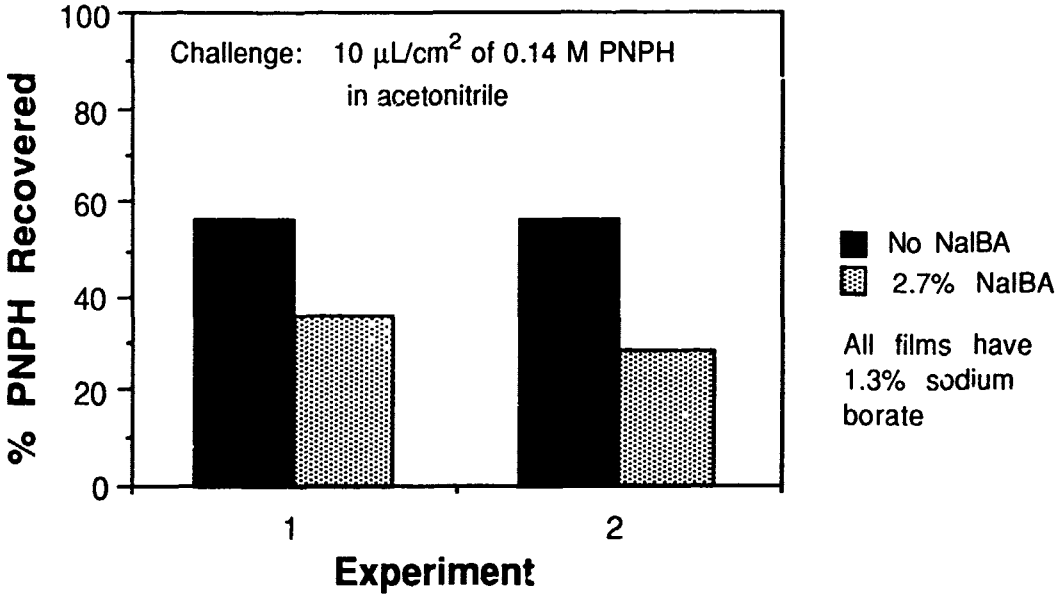

Photo-oxidation Catalyzed by Metal Oxides

Since it is known from the literature that various metal oxide semiconductors sensitize the photo-oxidation of organic compounds,[10,11] we decided to test whether such materials, loaded into AQ29 films, would promote photodegradation of an appropriate simulant. Because of its extensive prior use in the literature, we chose diphenyl ethene (DPE) as a useful probe. DPE is known to be oxidized my molecular oxygen to benzophenone and several minor products upon UV-vis

irradiation,[10,12] in a reaction catalyzed by anatase titanium dioxide.

Freestanding films of ca. 150 μm thickness were prepared that were loaded with one of the following: 3-15% anatase titanium dioxide, 3% palladium-doped titanium dioxide, 3% iron (III) oxide, or 3% zinc oxide. The samples were challenged with neat DPE simulant (2.0 μL per one-cm^2 film coupon) or 10% v/v DPE in acetonitrile. They were then photolyzed for 0.5 hour with a 1000 W Oriel UV-visible light source, filtered through pyrex. After photolysis the films were extracted with diethyl ether and quantitatively analyzed for DPE recovery by GLC. A polymethyl/5% phenyl siloxane on fused silica capillary column, using diethyl malonate as internal standard, was employed for GLC determinations.

The effect of added metal oxide proved, in general, to insignificantly effect DPE recovery, with the exception of films containing 3% iron (III) oxide.[11] For the DPE/acetonitrile challenge, the DPE recovery was only 17 ± 4% from the photolyzed, iron oxide-loaded film, compared with 41 ± 4% for an unloaded, photolyzed film and 59 ± 2% from an iron oxide-loaded film that was not photolyzed. These values represent averages of from 5-9 samples.

CONCLUSIONS

This work has shown that:

--Kodak anionic polyester AQ29 readily forms 15-200 μm-thick films that can incorporate several different types of decontaminating reagents;
--CAT significantly decontaminates neat CEES when loaded in AQ29 films;
--Hydrolysis of PNPH and PNPDPP, applied in dilute acetonitrile solution, is promoted by films containing 1-3% NaIBA;
--Anatase titanium dioxide, palladium-doped titanium dioxide, and zinc oxide loaded in AQ29 films did not sensitize the photo-oxidation of DPE, but the effect of 3% iron (III) oxide was significant.

ACKNOWLEDGEMENT

The sponsorship of CRDEC under Contract DAAA15-88-C-0014 (James A. Richmond, COR) is gratefully acknowleged.

REFERENCES

(1) Advanced Chemical Technologies Group, Federal Systems Division, Eastman Kodak Company, Rochester, NY 14650-2156.

(2) Shuely, W. J.; McHugh, V. M. "Development of Decontaminating Coatings Employing Sulfonic Acid Catalysts Bonded to Macroreticular Sorbent Particles", U.S. Army Chemical Research, Development and Engineering Center Technical Report (CRDEC-TR-88113), Aberdeen Proving Ground MD, July 1988. UNCLASSIFIED Report.

(3) Maroldo, S. G.; Holy, N.; Kaufell, L. A.; Langenmayr, E. J.; Smith, R. L. "High Surface Area Ion Exchange Resins as Adsorbents for Air Purification", Proceedings of the 1987 U.S. Army Chemical Research, Development and Engineering Center Scientific Conference on Chemical Defense Research, November 17-20 1987.

(4) Moss, R.A.; Bolikal, D.; Durst, H. D.; Hovanec, J. W. "Polymer-Bound Iodosobenzoate Reagents for the Cleavage of Reactive Phosphates", *Tet. Lett. 29*, 2433 (1988).

(5) Menger, F. M.; Tsuno, T. "Organic Reactions Catalyzed by Copper-Loaded Polymers. Reactivity vs Polymer Structure", *J. Am. Chem. Soc. 111*, 4903 (1989).

(6) Campbell, M. M.; Johnson, G. "Chloramine T and Related N-Halogeno-N-metallo Reagents", *Chem. Rev. 78*, 65 (1978)

(7) Tsujihara, K.; Furukawa, N.; Qae, K.; Oae, S. "Sulfilimine. I. Synthesis and Formation Mechanism", *Bull. Chem. Soc. Jpn. 42*, 2631 (1969).

(8) Moss, R. A.; Wilk, B.; Krogh-Jespersen, K.; Blair, J. T.; Westbrook, J. D. "Organoiodinane Reagents for Phosphate Cleavage: Experimental and Computational Studies", *J. Am. Chem. Soc. 111*, 250 (1989).

(9) Mackay, R. A.; Longo, F. R.; Knier, B. L.; Durst, H. D. "Iodosobenzoate Catalyzed Hydrolysis of 4-Nitrophenyl Diphenyl Phosphate in a CTAB Microemulsion", *J. Phys. Chem. 91*, 861 (1987).

(10) Fox, M. A."Organic Heterogeneous Photocatalysis: Chemical Conversions Sensitized by Irradiated Semiconductors", *Accts. Chem. Res. 16*, 314 (1983).

(11) Bard, A. J. "Photoelectrochemistry", *Science 207*, 4427 (1980).

(12) Fox, M. A.; Chen, C.-C. "Mechanistic Features of the Semiconductor Photocatalyzed Olefin-to-Carbonyl Oxidative Cleavage", *J. Am. Chem. Soc. 103*, 6757 (1981).

BLANK

A QUANTITATIVE DESCRIPTION OF THE EFFECT OF MICELLIZED CTAB ON THE *o*-IODOSOBENZOATE CATALYZED HYDROLYSIS OF G-AGENTS

D.R. LESLIE and S. PANTELIDIS

Materials Research Laboratory, Melbourne,
Defence Science and Technology Organization, Australia.

ABSTRACT

The *o*-iodosobenzoate (*o*-IBA) catalyzed hydrolysis of active esters and related compounds is known to be enhanced by micellized cationic detergents. Profiles of apparent second order rate constants against detergent (ctab) concentration for reaction of *o*-IBA with G agents, *p*-nitrophenyl acetete (PNPA), and *p*-nitrophenyl diphenyl phosphate (PNPDPP) are analyzed according to a phase seperation model. Thus, second-order rate constants for reactions in the micellar phase and micelle-reactant binding constants are obtained. Increasing the binding of the catalyst (*o*-IBA) to the micelles is predicted to provide only a small increase to the maximum micellar enhancement for its reaction with G agents.

INTRODUCTION

In recent years *o*-iodosbenzoic acid (*o*-IBA) and aryl substituted analogues have been investigated as nucleophilic catalysts for ester hydrolysis and their potential as a basis for decontamination of nerve agents, in particular the G agents has been recognised.[1-3] Even so, in aqueous solution *o*-IBA's are unremarkable in their role as hydrolysis catalysts.

For example, the half life of PNPDPP in pH 9.2 buffer at 25° C is 8.5 hours. A 0.1 mM solution of *o*-IBA in the same buffer reduces the half life to ~80 minutes. However, addition of a cationic detergent, such as cetyltrimethylammonium bromide (ctab), to this solution reduces the half life to 3.5 seconds; a 1300 fold rate enhancement over that observed in the absence of detergent. With PNPA as substrate a similar pattern is observed. The half-life in buffer is about 45 minutes; in 0.1 mM *o*-IBA this reduces to 25 minutes, but addition of ctab can reduce this to 20 seconds. In this case the rate enhancement provided by the detergent is only about 75 fold.

Clearly the detergent plays a crucial role in the hydrolysis of esters by *o*-IBA, and its ability to enhance reaction rates is not the same for different substrates. This is not unexpected as it has been recognised for many years that the rate acceleration afforded to bimolecular reactions by micellized surfactants is inextricably related to the binding, or partitioning, of rectants by the micellar phase.[4,5] For organic species, partitioning into micelles is a function of their hydrophobicity. It is possible that a larger second order rate constant for the rection in the micellar phase compared with that in the bulk aqueous phase may also contribute to any rate enhancement observed.[4,5]

Insofar as the G agents are concerned, the relative importance of these two effects is not known. In this work, the hydrolysis of GA, GB and GD, as well as that of the models or simulants PNPDPP and PNPA, catalysed by *o*-IBA are examined as a function of detergent concentration.

EXPERIMENTAL

Substrates were available within the laboratory from a previous study.[6] The ctab (Fluka) was purified as described by Mukerjee and Mysels.[7] The *o*-iodosobenzoic acids were prepared from the corresponding *o*-iodo-compounds by reaction with peracetic acid.[6] Pseudo first order rate constants (k_ψ) were obtained from reactions monitored by the pH-stat method or spectrophotometrically. The standard conditions for pH-stat reactions were: 0.02 M NaCl, pH 9.2, 25.0 $\pm$ 0.5° C, [substrate] = 0.9 to 1.1 x 10^{-4} M, [catalyst] = 0.9 to 1.1 x 10^{-4}; and for reactions monitored spectrophotometrically: 0.01 M $Na_2B_4O_7$ buffer, pH 9.2, 25.0 $\pm$ 0.5°C, [substrate] = 1.0 x 10^{-5}, [catalyst] = 1.0 to 1.1 x 10^{-4} M. Apparent second order rate constants ($k_{2(app)}$) were calculated according to:

$$k_{2(app)} = (k_{\psi(mc)} - k_{\psi(m)})/[o\text{-IBA}] \qquad (1)$$

where $k_{\psi(mc)}$ is the observed first order rate constant in the presence of detergent and catalyst, $k_{\psi(m)}$ the rate constant in the presence of detergent only, and [*o*-IBA] is the concentration of *o*-IBA catalyst.

RESULTS AND DISCUSSION

Profiles of apparent second-order rate constants against detergent (ctab) concentration for reaction of *o*-IBA with PNPA, GB, GD and GD in 0.02 M NaCl maintained at pH 9.2 by titration with 0.01 M NaOH are given in Figure 1. In each instance $k_{2(app)}$ values initially increase sharply with detergent concetration, level off, then eventually decrease. These profiles are typical for micellar enhanced reactions. The maximum rate enhancement provided by the detergent, i.e $(k_{2(app)}/k_{2w})_{max}$, for the G agents range from 7 (GB) to 50 (GD) and are less than observed for PNPA

(100). Similar profiles are obtained for the reaction of *o*-IBA with PNPDPP and PNPA in 0.01 M borax buffer at pH 9.2 (Figure 2). However, the maximum enhancement for PNPDPP is 1600, much larger than observed for PNPA (160) in this medium. The enhancements for the G agents are extremely modest in comparison to that for PNPDPP.

Analysis of the profiles to provide a quantitative description of the processes which result in the enhancements can be performed using the phase seperation model for micellar catalysis developed by Berezin.[8] In this model, the micellar solution is assumed to consist of two distinct phases, the bulk aqueous phase and the micellar phase. The reactants are assumed to partition between these two phases and the observed rection rate is the weighted average of the rates in each phase. Thus the apparent second-order rate constant is given by:

$$k_{2(app)} = (\bar{k}_{2m} K_A K_B + k_{2w})/[(1 + K_A C_m)(1 + K_B C_m)] \qquad (2)$$

in which $\bar{k}_{2m}$ is the second order rate constant for reaction in the micellar phase divided by an effective molar volume for the detergent. k_{2w} is the rate constant measured for the reaction in the aqueous phase, C_m is the detergent concentration less the critical micelle concentration (cmc) and K_A and K_B are binding constants for formation of a micelle/reactant complex according to:

$$M + R \overset{K_i}{\rightleftharpoons} MR \qquad (3)$$

The experimental reaction priofiles were fitted to the model using a least squares procedure with $\bar{k}_{2m}$, K_A, K_B and the cmc treated as variable parameters. The validity of the model regarding its application to these reactions is demonstrated by the excellent agreement between the experimental and calculated profiles obtained for each substrate. The continuous lines in the Figures are the calculated profiles.

Apart from the agreement between the experimental and calculated profiles, the validity of the phase seperation model in analyzing the rate data is supported by the values of the fitted parameters (Table 1). There are a number of favorable comparisons which may be made between parameters calculated from different profiles and also with reported data.

The ratio of the second order rate constants for reactions in the micellar (k_{2m}) and aqueous(k_{2w}) phases of each substrate are included in Table 1. In each case, the ratio is close to unity. This is generally found to be the case for bimolecular substitution reactions in micellar solutions.[5] Thus the rate enhancement provided by the micellized detergent does not arise from an increase in the inherent reactivity of the components upon partitioning into the micellar phase. It is in fact, simply a function of reactant concentration in the micellar phase.

This is demonstrated by the constants for reactant/micelle binding (Table 1). For reactions of the model compounds, PNPDPP and PNPA in 0.01 M $Na_2B_4O_7$ the binding constant for *o*-IBA is similar for both reaction profiles. This is reassuring as the phase seperation model assumes that solutes partition independently. Furthermore, the values are similar to that reported by Bunton, who obtained a value of 700 litres per mole.[9] The binding constants of the substrates are, however, very different; 7500 for PNPDPP and 62 for PNPA. These compare favorably with literature values of 10000-16000 for PNPDPP[10] and 35 for PNPA.[11] Herein lies the explaination for the different maximum rate enhancements. The phase seperation model predicts the maximum enhancement to be given by:[8]

$$(k_{2(app)}/k_{2w}) = (k_{2m}/k_{2w})\{K_A.K_B/[V_m(K_A^{1/2} + K_B^{1/2})^2]\} \quad (4)$$

Given that the ratio of the rate constants is about 1, the enhancement is reduced to a function of the binding constants:- the stronger the binding, which is a measure of substrate hydrophobicity, the greater the enhancement.

For the G agents, the binding constants are smaller than for PNPA and very much less than for PNPDPP. Thus, the modest rate enhancements obtained for these organophosphorus species are understandable. Note that the binding constants increase in the order; GB is less than GA is less than GD. This reflects the increasing hydrophobicity of the substituents on the central phosphorus atom. Reactions of the G agents were monitored in a solution of a different ionic composition than for PNPDPP, and the binding of the catalyst (*o*-IBA) which is anionic is seen to differ between the two reaction media. This probably reflects a change in the electrostatic potential of the micelles. The binding of PNPA, a neutral species, and therefore less affected by such a change is similar in both reaction media.

The binding constants are particularly valuable for assessing the potential of other *o*-IBA catalysts for hydrolysing G agents in micellar solutions. For example, 5-octyloxy-*o*-IBA is reported to be about 16 times more effective than *o*-IBA at catalysing the hydrolysis of PNPDPP in micellar ctab.[2] Because substitution of the aromatic nucleus is known to have little effect on the nucleophilicity of the anion the increased effectiveness can be attributed to the stronger binding of the octyloxy derivative to the micelles than that of *o*-IBA itself.[12] Consideration of the $K_A.K_B/[V_m(K_A^{1/2} + K_B^{1/2})^2]$ term in equation (4) reveals that the strategy of enhancing $k_{2(app)}$ by increasing K_A will not be successful when the binding of the catalyst to the micelle is already much stronger than that of the substrate. One would therefore predict that the increase in the maximum rate enhancement effected by replacing *o*-IBA with the 5-octyloxy derivative will be much less for the G agents than found for PNPDPP.

Profiles of apparent second order rate constants against detergent concentration were obtained for the reaction of the octyloxy analogue

with the G agents and the maximum enhancements determined under the same conditions used for the parent compound . The superiority of the octyloxy derivative expressed as the ratio of the $(k_{2m}/k_{2w})_{max}$ values obtained for the octyloxy and parent compounds is given in Table 1. For the G agents the octyloxy derivative is only about twice as effective as the parent compound and does not approach the impressive increase obtained for PNPDPP. The practical significance of this is that the extra effort required to synthesize the octyloxy compound does not provide a proportionate increase in reactivity.

CONCLUSIONS

1. The reactivity of *o*-IBA towards the G agents, PNPA and PNPDPP is the same in the micellar and aqueous phases (i.e. $k_{2m} = k_{2w}$).

2. The enhancement provided by the micellized detergent is attributable to the sequestering of reactants into the reduced volume of the micellar phase.

3. Only modest enhancements are available for the G agents because of their unfavorable partitioning between the micellar and aqueous phases.

4. Effectiveness of micellar systems will reach a limit that is dependent on the partitioning of the agent.

5. Because the critical parameter in determining the efficiency of the micellar systems is the partitioning of the substrates (a function of hydrophobicity) the selection of simulants to use for studies in multiphase systems is even more difficult than for reactions in truly homogeneous systems.

REFERENCES

1. Moss, R.A., Alwis, K.W., and Bizzigotti, G.O., *J. Am. Chem. Soc.*, 1983, **105**, 681; Moss, R.A., Kim, K.Y., and Swarup, S., *J. Am. Chem. Soc.*, 1986, **108**, 788.

2. Moss, R.A., Alwis, K.W., and Shin, J S., *J. Am. Chem. Soc.*, 1984, **106**, 2651.

3. Katritzky, A.R., Duell, B.L., Durst, H.D., and Knier, B.L. in "Proceedings of the 1987 U.S. Army Chemical Research, Development and Engineering Center Scientific Conference on Chemical Defense", Rousa, M.D., Ed., CRDEC-SP-88013, p 3., Burnside, B.A., Knier,B.L., Mackay, R.A., Durst, H.D., and Longo,F.R., *ibid*, p 57.

4. Fendler, E.J., and Fendler, J.H., *Adv. Phys. Org. Chem.*, 1970, **8**, 271.

5. Bunton, C.A., and Savelli, G., *Adv. Phys. Org. Chem.*, 1986, **22**, 213.

6. Leslie, D.R., Report MRL-R-1134, DSTO Materials Research Laboratory, Melbourne, Australia.

7. Mukerjee, P., and Mysels, K.J., *J. Am. Chem. Soc.*, 1955, **77**, 2937.

8. Berezin, I.V., Martinek, K., and Yatsimirskii, A.K., *Russ. Chem. Rev. (Engl. Transl.)* 1973, **42**, 787.

9. Bunton, C.A., Mhala, M.M., and Moffatt, J.R., in "Proceedings of the 1987 U.S. Army Chemical Research, Development and Engineering Center Scientific Conference on Chemical Defense", Rousa, M. D., Ed., CRDEC-SP-88013, p 75.

10. Bunton, C.A., Cerichelli, G., Ihara, Y., and Sepulveda, L., *J. Am. Chem. Soc.*, 1979, **101**, 2429; Bunton, C.A., Gan, L-H., Moffatt, J.R., Romsted, L.S., and Savelli, G., *J. Phys. Chem.*, 1981, **88**, 4118.

11. Romsted,L.R., and Cordes, E. H., *J. Am. Chem. Soc.*, 1968, **90**, 4404; Yatsimirski, A.K., Martinek, K., and Berezin, I. V., *Tetrahedron*, 1971, **27**, 2855.

12. Moss, R.A., Chatterjee, S., and Wilk, B., *J. Org. Chem.*, 1986, **51**, 4303.

TABLE 1. Parameters Describing The Reaction of *o*-IBA with Substrates in Micellar CTAB Solution.

Substrate	$\bar{k}_{2m}$	K_A[c]	K_B[d]	k_{2m}/k_{2w}[e]	$(k_{(oct)}/k_{(parent)})_{max}$
GA[a]	15	325	6	0.9	1.7
GB[a]	15	304	2.6	0.7	2.0
GD[a]	9	380	23	0.8	2.4
PNPA[a]	7	190	84	0.8	2.6
PNPA[b]	9	830	62	1.2	-
PNPDPP[b]	4.5	690	7450	0.9	16.5

[a] Reaction in 0.02 M NaCl, [b] Reaction in 0.01 M $Na_2B_4O_7$, [c] Binding constant for *o*-IBA, [d] Binding constant for substrate, [e] Calculated using $V_m = 0.25\ l.mol^{-1}$.

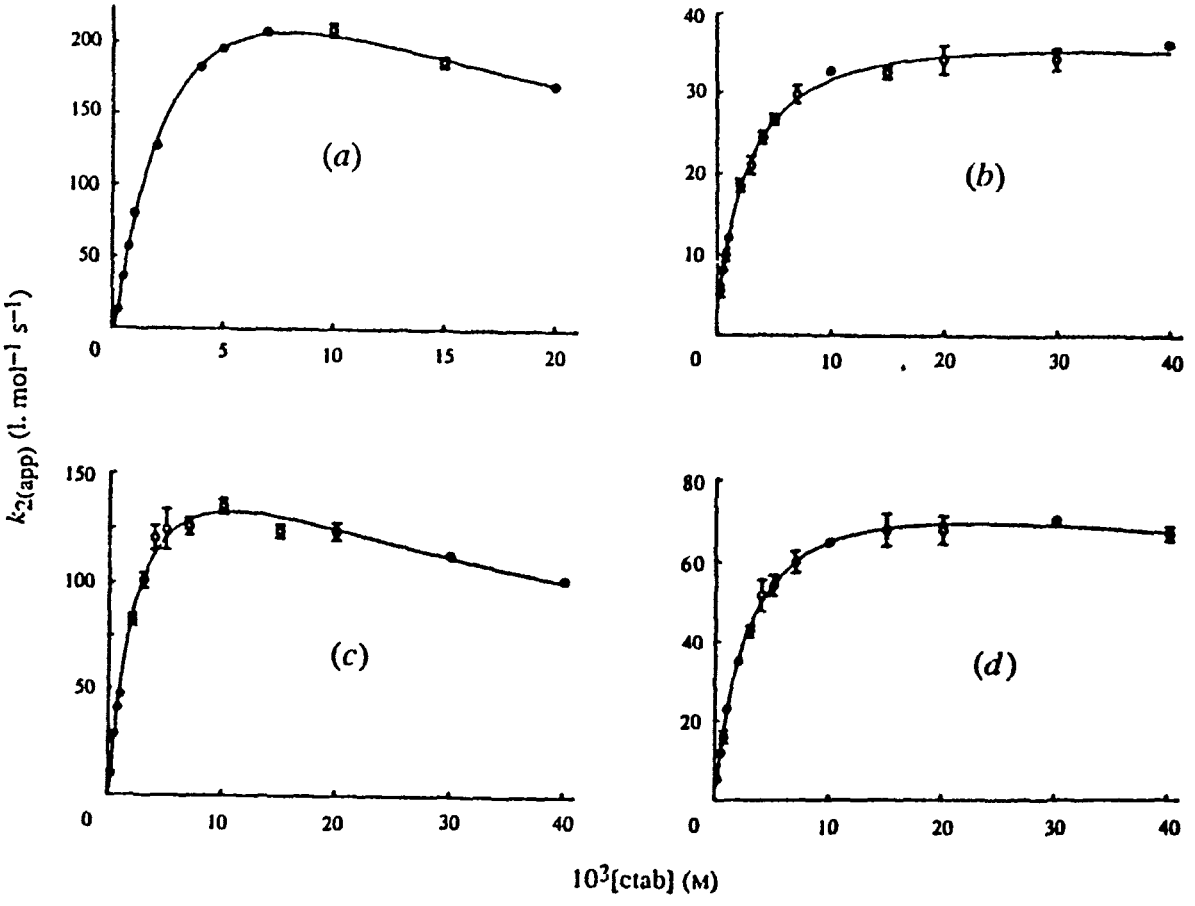

Figure 1. Dependence of $k_{2(app)}$ on [CTAB] for reaction of *o*-iodosobenzoate in 0.02 M NaCl with: (*a*) PNPA; (*b*) GB; (*c*) GD; (*d*) GA.

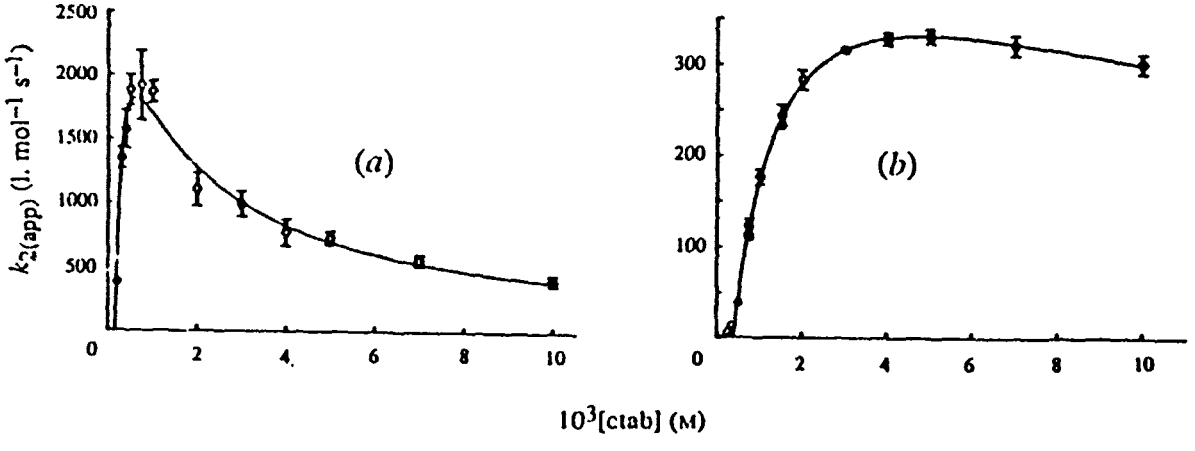

Figure 2. Dependence of $k_{2(app)}$ on [CTAB] for reaction of *o*-iodosobenzoate in 0.01 M $Na_2B_4O_7$ with: (*a*) PNPDPP; (*b*) PNPA.

XI. COMPUTATIONAL CHEMISTRY POSTERS

NOTE: Papers with the following titles were presented at the Conference but are not included in this document:

Molecular Modeling of Anatoxin and Selected Analogs

Theoretical Investigation of the Reactivity and Reaction Mechanisms of Perfluoroisobutene (PFIB)

Accurate Calculations for Hydrogen Bonded Systems Using Molecular Mechanics Methods

BLANK

A COMPUTATIONAL COMPARISON OF THE ELECTRONIC PROPERTIES OF G AGENTS WITH SELECTED REACTION SIMULANTS

George R. Famini

1. Introduction

1.1 Computational Chemistry

Computational chemistry is being used extensively in the examination of chemical, physical and biological properties of chemical compounds. While several computational techniques have been used successfully to correlate and predict these types of properties, examining reactivity and predicting reaction related properties has been less successful. [1-3] Theoretical procedures allow for the facile computation of numerous electronic properties of molecules that can be used to infer reactivity or can be used to compute reaction related properties. [4]

Three recent advances that have facilitated the acceptance of more widespread use of computational methods are 1) the development of more user-friendly software; 2) the ability of the computers to handle larger molecules; and 3) the development of molecular graphics techniques to permit visualization of molecular properties. These three factors allow computations on more realistic chemical compounds and systems, that is, compounds and systems the experimental chemist is interested in, and allow for a more natural method for displaying many of the results. The Chemometric/Biometric Modeling Branch (CBM) of the U. S. Army Chemical Research, Development and Engineering Center (CRDEC) has developed and integrated softaware package, the Molecular Modeling, Analysis and Display System (MMADS), which has been used for the computation and display of molecular structures and molecular properties. [5,6]

1.2 Reaction Simulants

Simulants are being used with ever increasing regularity in place of experiments with chemical agents. Because of the constraints placed upon the use of chemical agents, the use of simulants have become vital for timely testing of procedures, new methods, and equipment. The Chemical Agent Simulant Data Center (CASDC) was established in order to meet the needs of selecting simulants by matching physical properties with those of the agent(s) in question.[7] Difficulty has arisen, however, in selecting simulants that will mimic various chemical reactivities of the agents. Matching the standard physical properties that are contained in the CASDC is not sufficient for selecting a reaction simulant. In a presentation at the 3rd Annual Simulant Workshop, Durst described the current experimental efforts in this area, and which simulants were most commonly used.[8] In particular, a thrust has been in the area of hydrolysis of G agents, a selecting simulants for that reaction. The hydrolysis reaction is shown in figure 1.

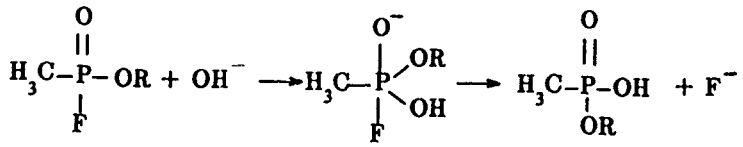

Figure 1. Hydrolysis of G Agents

The chemical structures for Sarin (GB) and Soman (GD) are shown in figures 2 and 3. Durst also described several chemical compounds that are currently being used in one fashion or another as reaction simulants (compounds 1-5, shown in figures 4-8).

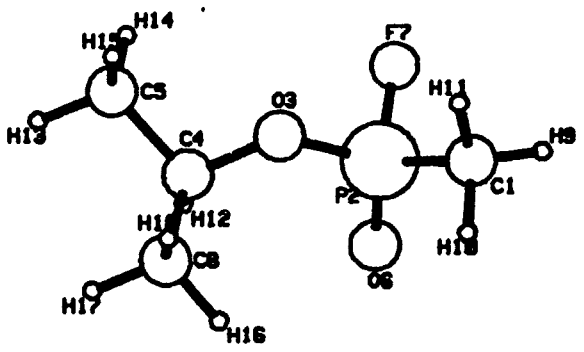

Figure 2. Sarin (GB)

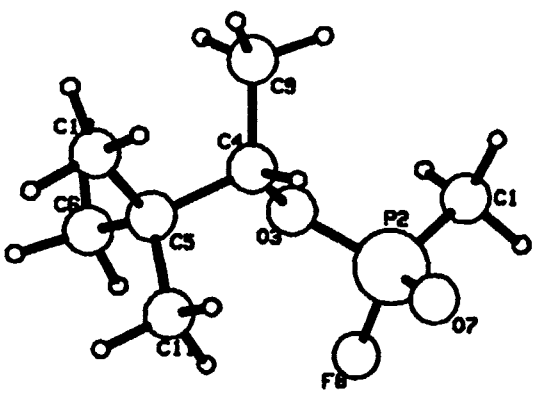

Figure 3. Soman (GD)

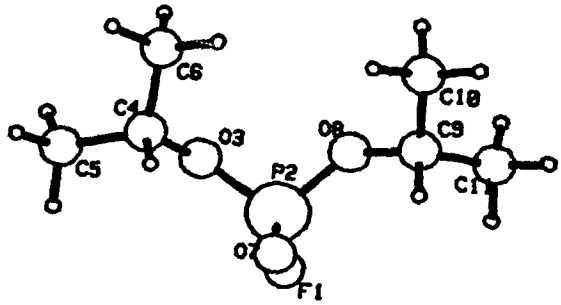

Figure 4. Di-i-propyl fluorophosphate (DFP) (1)

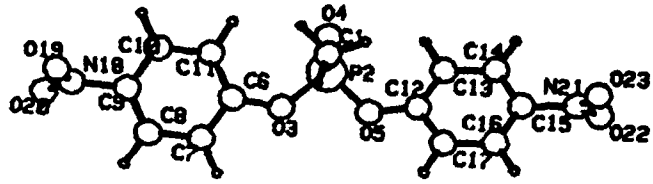

Figure 5. Di(p-nitrophenyl) Methylphosphonate (2)

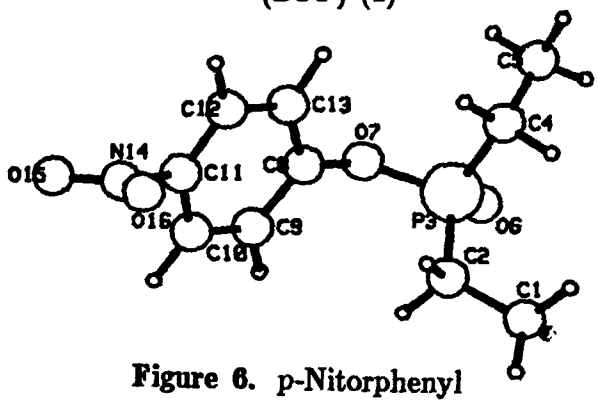

Figure 6. p-Nitorphenyl Diethylphosphinate (3)

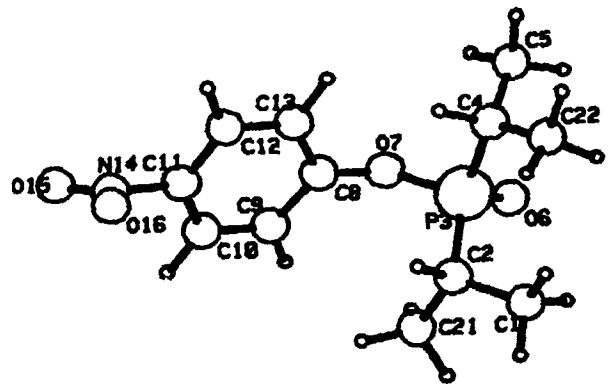

Figure 7. p-Nitorphenyl Di-i-propylphosphinate (4)

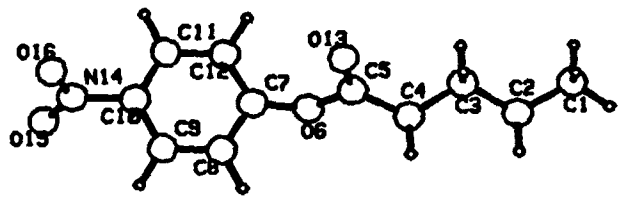

Figure 8. p-Nitrophenyl Hexanoate (5)

Hierarchical clustering techniques have been used successfully with physical and chemical data from the CASDC as an aid to selecting the compounds that best match the *critical* properties for a given experiment.[9,10] These methods treat all properties simultaneously result in a numerical rating of how close each compound is to the target compound. Crosier has shown this to be superior to the sequential searching algorithms currently in most databases.

A number of researchers have shown that electronic properties generated from theoretical calculations often correlate highly with and can be used to predict specific reactivity. In addition, Politzer has shown that electrostatic potentials can be used to qualitatively assess the reactivity of a substrate.[11] This paper will examine how hierarchical clustering and computational chemistry techniques can be used in tandem to aid the selecting of G agent hydrolysis simulants.

2. Calculational Procedures

All geometry optimizations and calculations of electronic properties have been carried out using the MNDO algorithm in MOPAC v3.0.[12,13] Graphical display of structures and electrostatic potentials were accomplished using CBM Branch's Molecular Modeling, Analysis and Display System (MMADS).[5] The pattern recognition package ARTHUR was used to perform the hierarchical clustering of the electronic properties, using Euclidean distance criteria.

3. Results and Discussion

Two methods were employed to attempt to determine if theoretical and computational methods could be useful in assisting the selection of reaction simulants. If the *important* properties that determine the reactivity of the G Agents could be adequately matched by a potential simulant, then it is likely that the reactivities would be similar. It is not intuitively clear, however, what the *important* properties would be in hydrolysis. Seven theoretically determined electronic properties have been calculated and used to attempt to model this reactivity (described in the next section). Using pattern recognition methods, it is possible to determine which of the simulants best match all of the properties of the agent (GB). The second approach used to examine the likelihood of reactivities is the electrostatic potential. Both will be described in the appropriate sections.

3.1 Hierarchical Clustering

Seven properties determined from the MNDO calculations were selected as being likely in influencing chemical reactivity. These properties and the values for the five simulants chosen and the agents Sarin (GB) and Soman (GD) are shown in Table 1.

TABLE 1: MNDO ELECTRONIC PROPERTIES

Compound	ΔH_f	E_{HOMO}	E_{LUMO}	Charge E	Charge L	Charge =O	Dip. Mom.
GE	-153.3564	-10.9851	-1.22459	1.195	-0.369	-0.645	3.795
GD	-148.8808	-10.9773	-1.25655	1.208	-0.361	-0.648	4.088
1	-210.8512	-11.6226	-1.16226	1.458	-0.346	-0.648	3.146
2	-49.21210	-9.9386	-1.73475	0.887	-0.406	-0.602	4.186
3	-37.52280	-10.1458	-2.21286	1.146	-0.420	-0.624	3.864
4	-44.27794	-9.8177	-1.83152	0.874	-0.422	-0.608	4.600
5	-57.53538	-10.2054	-1.10599	0.363	-0.499	-0.332	6.166

ΔH_f	=	Heat of Formation
E_{HOMO}	=	Energy of the Highest Occupied Molecular Orbital
E_{LUMO}	=	Energy of the Lowest Unoccupied Molecular Orbital
Charge E	=	Charge on the Electrophilic Site (either P or C)
Charge L	=	Charge on the Leaving Group (either F or -O-)
Charge =O	=	Charge on the Double Bonded Oxygen
Dip. Mom.	=	Dipole Moment

Using the hierarchical clustering algorithm within the pattern recognition package ARTHUR, simulants that best match the properties of the G agents can be identified. The output of the hierarchical clustering algorithm yields a dendrogram, with the best fits being the farthest to the left (indicating a 100% overlap or perfect fit). Figure 9 shows the dendrogram for the simulants and GB and GD for all seven electronic properties. The simulant that matches theses properties most closely is compound 1, methyl difluorophosphate.

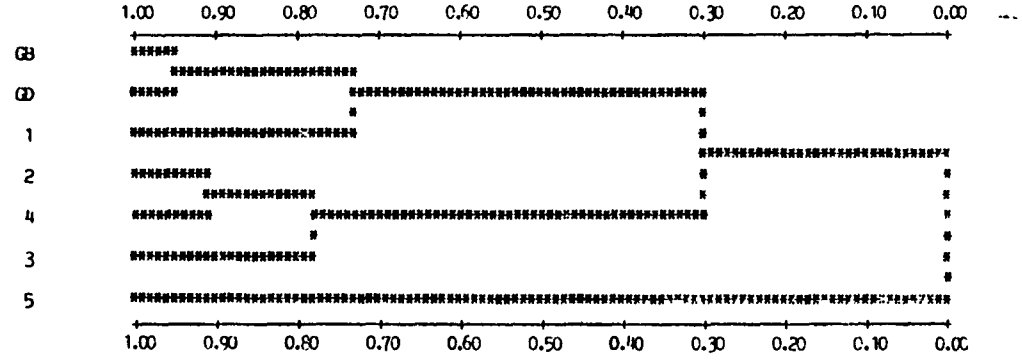

Figure 9. Dendrogram for 7 Electronic Properties

Looking at the hydrolysis of an organophosphate as a simple S_N2 reaction, the attack of a nucleophile followed by expulsion of the leaving group, Frontier Molecular Orbital Theory indicates that the lowest unoccupied molecular orbital (LUMO) should be the most significant of the electronic properties, and hydrolsyis rates should be dependent in some way on the energy of the LUMO (E_{LUMO}). Figure 10 shows the dendrogram for GB, GD and the five simulants using E_{LUMO} as the only property. Both compounds 1 (DFP) and 5 (p-Nitrophenyl Pentanoate) match the E_{LUMO} of the agents the best.

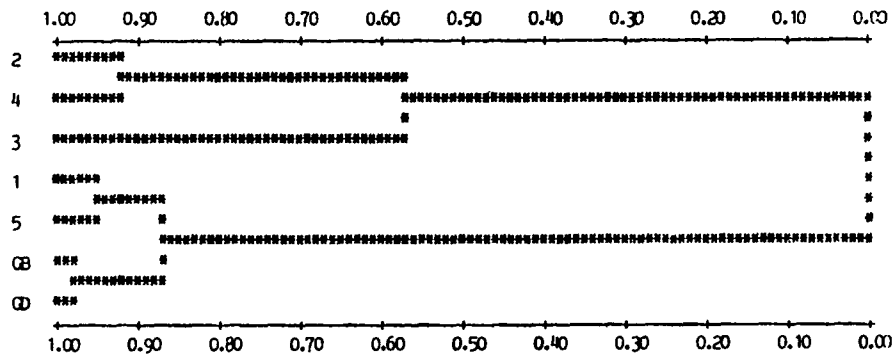

Figure 10. Dendrogram for E_{LUMO}

3.2 Electrostatic Potentials

Several previous investigations have shown that FMO approaches can lead to faulty results. Electrostatic potentials have been shown to indicate relative regions of attraction and repulsion to point charges. Equation 1 shows the form for the exact electrostatic potential.

$$V(\vec{r}) = \sum_A \frac{Z_A}{|\vec{R}_A - \vec{r}|} - \int \frac{\rho(\vec{r}\,')d\vec{r}\,'}{|\vec{r}\,' - \vec{r}|} \qquad (1)$$

where Z_A is the nuclear charge on atom A, located at position $\vec{R}$, representing the nuclear contribution. The second term in equation 1 represents the electronic

contribution, with $\rho(\vec{r}')$ being the electron density at point $\vec{r}'$. The potential, $V(\vec{r})$ represents the electrostatic potential observed at point $\vec{r}$.

Computation of the electrostatic potential using equation 1 is extremely time consuming. If multiple potential surfaces are required, then the computation time can be prohibitive. An approximate method for the calculation of the electrostatic potential using a modified Coulombic expression is shown is equation 2.

$$V_{app}(\vec{r}) = \sum_{A} \frac{FC(A)}{\vec{R}_A - \vec{r}} \tag{2}$$

where FC (A) is the formal charge on atom A, and $\vec{R}_A$ and $\vec{r}$ are as in equation 1. The advantage of equation 2 is that the computation of the electrostatic surface is extremely rapid. The major disadvantage is that the electron density around each atom is smeared over the entire volume of the atom, and not localized in orbital positions. If the latter constraints are kept in mind, then the V_{app} can be a useful and rapid method for determining electrostatic potentials.

Using the method described in equation 2, the electrostatic potentials for GB and the 5 simulants have been computed (figures 11-16). In each figure, the phosphorus, double bonded oxygen and the leaving group determined the plane to be displayed. In this way, the region 180 degrees to the leaving group can be shown and can be compared between potentials. The solid contour lines represent positive potential regions (attractive to a negative charge) and dashed contours represent negative potential regions (attractive to a positive point charge).

To an incoming nucleophile attacking the phosphorus (or carbon in simulant 5), the region opposite the leaving group should have the most direct influence on reactivity and consequently, hydrolysis. In order to select an appropriate simulant for GB (or GD) that will have similar reactivity, this region should be similar in shape and magnitude. In order to simplify the comparison of the electrostatic potential maps, an algorithm was developed that displays the difference between two potentials. Figures 17-21 display these difference plots for GB and each of the simulants. A small lobe opposite the leaving group(s) indicate high similarity between GB and a given simulant.

The simulant with the best overlap of electrostatic potentials with GB is simulant 5, p-nitrophenyl pentanoate, as shown by the difference plot in figure 21.

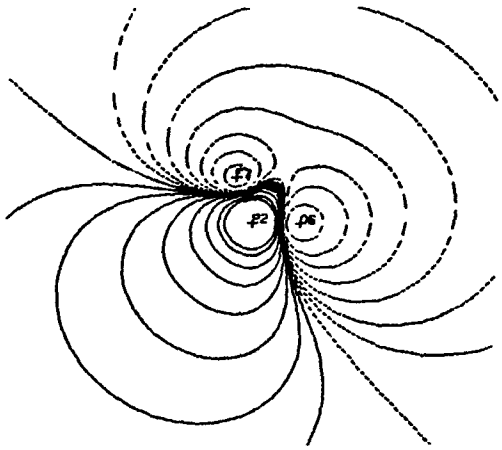

Figure 11. Electrostatic Potential for GB

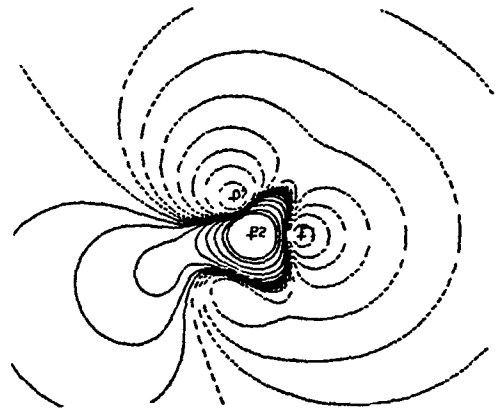

Figure 12. Electrostatic Potential for Simulant 1

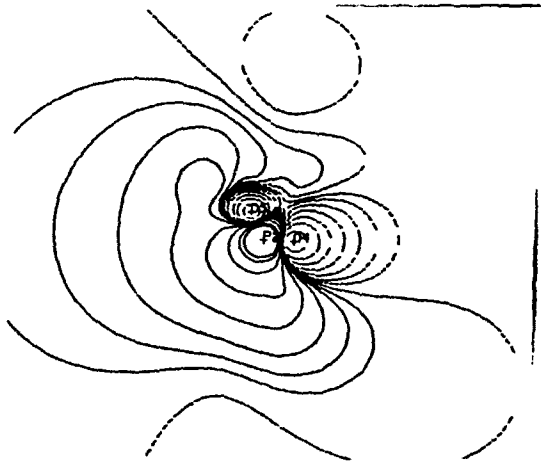

Figure 13. Electrostatic Potential for Simulant 2

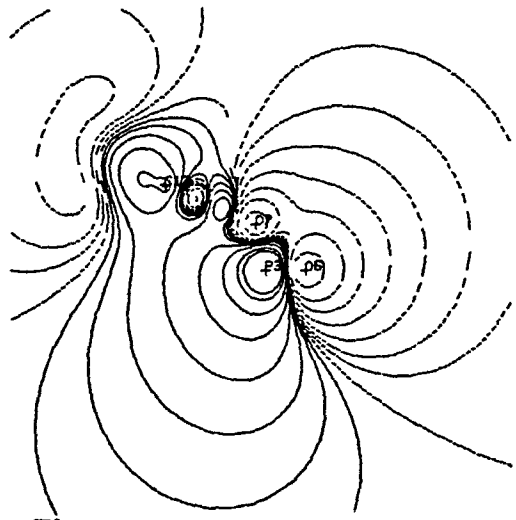

Figure 14. Electrostatic Potential for Simulant 3

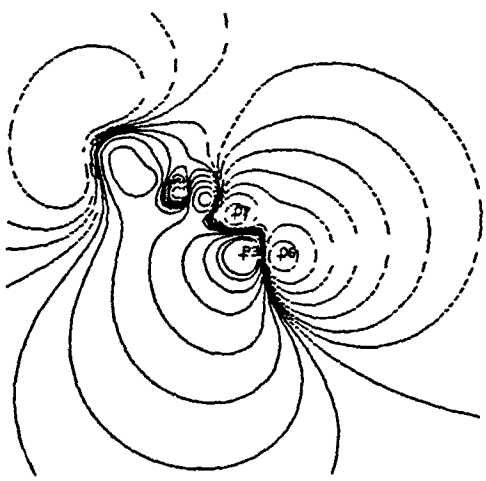

Figure 15. Electrostatic Potential for Simulant 4

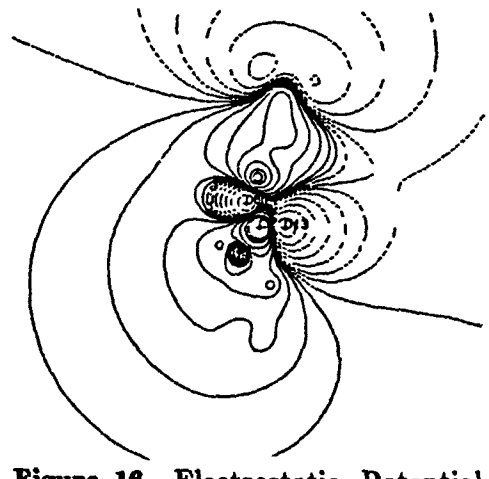

Figure 16. Electrostatic Potential for Simulant 5

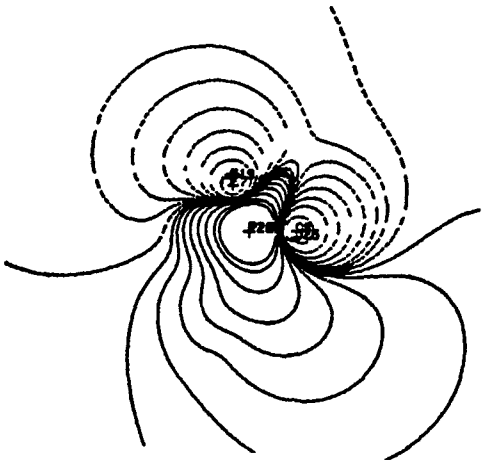

Figure 17. Difference Plot for GB and Simulant 1

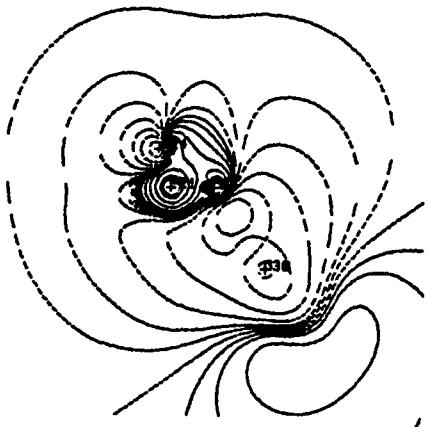

Figure 18. Difference Plot for GB and Simulant 2

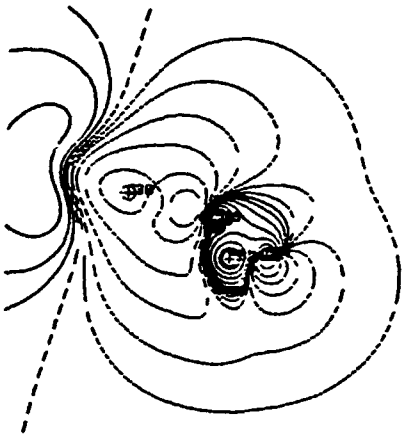

Figure 19. Difference Plot for GB and Simulant 3

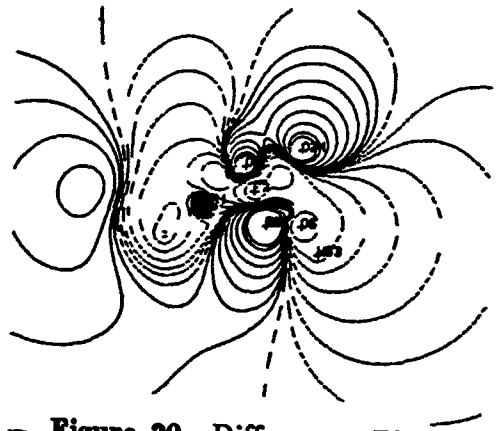

Figure 20. Difference Plot for GB and Simulant 4

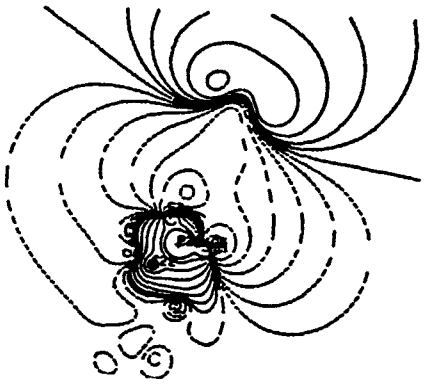

Figure 21. Difference Plot for GB and Simulant 5

Simulants 2,3, and 4 yield difference maps that would also indicate reasonable similarity, although these do not indicate as much similarity as simulant 5. The difference map for GB and simulant 1, DFP, indicates that DFP should be much less reactive than GB toward nucleophilic attack. This is evident both from the electrostatic potential of DFP (figure 12) where the positive lobe is significantly smaller than that of GB (figure 11), and in the difference plot (figure 17) where the large region surrounded by solid lines indicate where the GB potential is much more positive (more likely for nucleophilic attack) than DFP.

4. Summary

From both the hierarchical clustering and the electrostatic potentials, recommendations can be drawn as to the best simulant to mimic the hydrolysis reactivity of GB. Both studies indicate that p-nitrophenyl pentanoate would make a likely candidate. DFP is also selected by hierarchical clustering, but the electrostatic maps tend to indicate it will be much less reactive than GB.

5. References

1. Kamlet, M.J, Taft R.W., *Acta Chem. Scand.*, Vol B39, pp611-628 (1985).
2. Hansch, C. and Leo, A.,
3. Famini, G.R., "Using Theoretical Descriptors in Structure Activity Relationships V. A Review of the Theoretical Parameters", CRDEC-TR-085, U.S. Army Chemical Research, Development and Engineering Center, Aberdeen Proving Ground, MD, July 1989, UNCLASSIFIED Report.
4. Hehre, W.J., Radom, L., Schleyer, P. v.R., Pople, J.A., *Ab Initio Molecula Orbital Theory*, John Wiley and Sons, NY, 1985.
5. Leonard, J.M., Famini, G.R., "A User's Guide to the Molecular Modeling, Analysis and Display System (MMADS)", CRDEC-TR-030, U.S. Army Chemical Research, Development and Engineering Center, Aberdeen Proving Ground, MD, January 1989, UNCLASSIFIED Report.
6. Famini, G.R, "Applying Computational CHemistry Techniques to Simulant Technology", in White, W.E., ed. "Proceedings of the Second International Simulant WOrkshop", CRDEC-SP-002, U.S. Army Chemical Research, Development and Engineering Center, Aberdeen Proving Ground, MD, December 1988, UNCLASSIFIED Report.
7. Coon, P.A., Famini, G.R., White, W.E., Thornton, R.C., "Database User's Guide for the Chemical Agent SImulant Data Center", CRDEC-SP-88032, U.S. Army Chemical Research, Development and Engineering Center,

Aberdeen Proving Ground, MD, November 1988, UNCLASSIFIED Report.

8. Durst, H.D., presented at the Third International Simulant Workshop, U.S. Army Chemical Research, Development and Engineering Center, Aberdeen Proving Ground, MD, March 1989.

9. Famini, G.R., Coon, P.A., "A Systematic Mathematical Approach for the Selection of Chemical Warfare Agent Simulants", CRDC-TR-84044, U.S. Army Chemical Systems Laboratory, January 1985, UNCLASSIFIED Report.

10. Crosier, R.B., "Methods for the Selection of Chemicals for Simulantion of Chemical Warfare Agent Experiments", CRDEC-TR-88105, U.S. Army Chemical Research, Development and Engineering Center, Aberdeen Proving Ground, MD, March 1989, UNCLASSIFIED Report.

11. Politzer, P. and Truhlar, D., *Chemical Applications of Molecular Electrostatic Potentials*, Plenum Press, NY, 1981.

12. Dewar, M.J.K, and Thiel, W., *JACS*, Vol 99, p 4899 (1977).

13. Stewart, J.J.P., "MOPAC: A General Molecular Orbital Package", FJSRL-TR-86-0003, Frank J. Seiler Research Lab, U.S. Air Force Academy, CO, June 1986, UNCLASSIFIED Report.

BLANK

MOLECULAR AND TOPOLOGICAL TRANSFORMS IN MOLECULAR SIMILARITY ANALYSIS

James W. King[1] and Belinda B. King[2]

ABSTRACT

Until recently the comparison of compounds as to their molecular and/or physicochemical similarity was essentially qualitative and, while largely almost a reflexive exercise by most chemists, the results depended on one's background, training, viewpoint, and current project objectives. However, methodology is being developed by many investigators to enable quantitative comparisons. One of these methods is the molecular transform. In essence this procedure generates a binary descriptor for individual molecules; the descriptors may then be compared by means of decision rules derived from pattern recognition considerations. A related procedure, the topological molecular transform, generates a single number indicator of similarity known as the "topological difference." At first glance the mathematics for these techniques appears formidable and this has likely precluded wide use of the methodology. These techniques are reviewed in an attempt to demystify the concepts.

INTRODUCTION

The comparison of molecules, usually in a pairwise fashion, is virtually as old as chemistry itself and reflects the chemist's desire, nay, obsession to understand the similarities between molecules that are reflected in their physicochemical and pharmacological manifestations. The comparisons may be oriented toward similarities or differences in structure, properties, reactivities, or classification schemes based on these attributes and often incorporate graphical or matrix representations of the molecules.

Representations of molecules may be regarded as being at two levels, i.e., the 2-dimensional (topological) and the 3-dimensional (topographical). The inherent nature of chemistry and the way it is taught has led chemists to document chemical structures graphically in two dimensions but to think about the structures in terms of their three dimensional actuality. There is a crossover in this process in that the third dimesion is almost always implied, even in two dimensional representations and certainly in the matrix formulations necessary for computerized manipulation of structures. However, the problem that eventually surfaces in comparison trials is how to quantitate structural similarity. This is of great import because compounds that are close together in structure space will be close together in property

space - and of even more impact, in pharmacological space. This is not to say that discontinuities (or catastrophes, in the latest parlance) do not exist, but their extent or means to span such space is somewhat beyond the objectives of this report (and also perhaps beyond the methodology currently available).

Nevertheless, attempts to establish the basis for quantitative comparisons based on topological considerations is reflected in the work of Balaban and his colleagues,[3] as well as others not cited in this reference. More recently, the senior author has shown that essential chemical character, as represented by atomic number, can be integrated into a topological molecular representation to increase its value in structure-activity correlations.[4] In effect, this method is another means of spanning the 2-D/3-D space representation of molecules.

Another means of spanning representational space was suggested in a 1976 communication by Soltzberg and Wilkins.[5] In this instance they defined the methodology of molecular transforms as utilized to generate binary patterns which were then compared by classification schemes[6] which included an error-correction feedback mechanism. The molecular transform in this case was a simplified Fourier transform of 3-D cartesian coordidnates, a methodology used in X-ray diffraction studies and tracable to Wierl's work on the derivation of molecular structure from electron diffraction data.[7] Soltzberg and Wilkins followed their initial communication with a paper that left no doubt as to the value of this methodology in chemical structure-pharmacological activity relationship studies.[8]

Because 2-D matrix (i.e., graph theoretic) representations of molecules approximate (in a rough way) 3-D coordinates, it is possible to apply Fourier methodology to such representations. Gabanyi and his colleagues developed this concept by transforming molecular adjacency and distance matrices with the Fourier formalism and then went a step further to define a "topological difference," an abstract distance between the topological molecular transforms of two molecules[9] (this may be thought of as the difference between the integrated transforms of the two molecules). The latter permits the establishment of "minimum topological difference" criteria for comparison of molecules within series (and perhaps outside of series). Náray-Szabó has since tried to integrate electrostatic potential and molecular transform methodologies;[10] the potential in this case is geared to the design of new bioactive compounds and analogs and it will be of interest to follow future developments.

Finally, it is our objective to effect a summary review of the Soltzberg-Wilkins methodology (molecular transforms) as well as the Náray-Szabó contribution of the topological molecular transform used as the basis for the "topological difference."

METHODOLOGY REVIEW

Beginning with the paper by Soltzberg and Wilkins,[5] we have an equation for the molecular transform of a given molecule. The form was originally proposed by Wierl:[7]

$$I(s) = K\sum_{i=2}^{N}\sum_{j=1}^{i-1} f_i f_j \int_0^{\infty} P_{ij}(r)\frac{\sin sr}{sr}\,dr$$

Notation:

I(s) is the intensity of the scattered radiation
s is the independent variable measuring the scattering angle[11];

$$s = \frac{4\pi \sin(\theta/2)}{\lambda}$$

where θ is the scattering angle and λ is the wavelength of the electron beam
r represents the interatomic distance
$P_{ij}(r)$ is the probability distribution describing the vibrational variation in the distance between atoms i and j
f_i and f_j are the form factors for atoms i and j
K is a collection of experimental constants
N is the number of atoms in the molecule

To obtain the simplified transform in [5], the following simplifications can be made:

$$K = 1 \quad (1)$$
$$f_i = Z_i \quad (2)$$
$$P_{ij}(r) = \delta(r - r_{ij}) \quad (3)$$

Equation 1 sets the experimental constants to unity. Equation 2 assumes that the atoms are point scatterers which allows replacement of the form factors by the atomic numbers of the atoms. Equation 3 assumes the molecule is rigid and so replaces the vibrational distribution of distances with a δ-function peaking at the average interatomic distance r_{ij}.[12]
These simplifications lead to the equation:

$$I(s) = \sum_{i=2}^{N}\sum_{j=1}^{i-1} Z_i Z_j \int_0^{\infty} \delta(r - r_{ij})\frac{\sin sr}{sr}\,dr$$

By noting the property of δ-functions that

$$\int_0^{\infty} \delta(x - x^*) f(x)\,dx = f(x^*)$$

where f(x) is any function and x* is a specific value of x we see that

$$\int_0^{\infty} \delta(r - r_{ij})\frac{\sin sr}{sr}\,dr = \frac{\sin sr_{ij}}{sr_{ij}}$$

which leads to the form of the transform given in [5],

$$I(s) = \sum_{i=2}^{N}\sum_{j=1}^{i-1} Z_i Z_j \frac{\sin sr_{ij}}{sr_{ij}}\,.$$

In this equation,

Z_i and Z_j represent the atomic number of the i^{th} and j^{th} atoms

r_{ij} is the distance between atoms i and j

and the other symbols are as above.

To apply this formula to specific problems, we perform a numerical approximation to the function I(s) by taking 200 equally spaced values for s ranging from $1Å^{-1}$ to $31Å^{-1}$ and computing the corresponding I(s) value. The 200 points obtained, (s, I(s)), are then plotted, and a curve is sketched through these points (this can be done by hand or using a commercially manufactured graphics packages like MatLab GraphPak).

Once this numerical calculation is complete, the range $1Å^{-1}$ to $31Å^{-1}$ is divided into 100 intervals. Each of these 100 intervals which contains a "zero crossing", i.e., the value of I(s) is zero for some point in the interval receives a value of "1". All other intervals receive a value of "0". This reduces the transform I(s) to a binary pattern or code which can be used for molecular classification.

This method established, a variation presented by Gabanyi, et.al.[9] can be considered. There appear to be two differences in this variation; the first is that the molecular transform I(s) now includes a constant, C, which makes it dimensionless, i.e., it has no units. The second is that the topological distance between atoms D_{ij} is used instead of the bond distance r_{ij} ($D_{ij} = 1$ for directly bound atom pairs, 2 for second neighbors, etc.). The authors call this transform the "topological" molecular transform. The equation obtained through these modifications for the "topological molecular transform is:

$$I_t(s) = C^{-1} \sum_{i=2}^{N} \sum_{j=1}^{i-1} Z_i Z_j \frac{\sin sD_{ij}}{sD_{ij}}$$

$$C^2 = \sum_{i=2}^{N} \sum_{j=1}^{i-1} \sum_{l=2}^{N} \sum_{m=1}^{l-1} \frac{\pi Z_i Z_j Z_l Z_m}{2D_{ij} D_{lm}} \min (D_{ij}, D_{lm})$$

Note that the authors do not include the indices of summation; these are mathematically compatible with the previous derivations. The computations for this case are clearly more complicated though a straightforward program can be written to perform the job as in the previous case.

Now, the authors define an abstract distance between topological molecular transforms of molecules a and b, t_{ab}, which can be used as a basis for comparison of pharmacological activity:

$$t_{ab}^2 = \int_0^{\infty} \left[I_t^a(s) - I_t^b(s) \right]^2 ds$$

This would be applied by comparing each compound a, b, c, ... in a series to a lead compound m by computing t_{am}, t_{bm}, t_{cm}, etc. Molecules a and b can be regarded as similar if $t_{ab} \leq .05$. This method has the advantage of requiring only the molecular formula and not the bond lengths, though the computations are more lengthy.

DISCUSSION

The detailed derivation of the molecular transform and the topological molecular transform has been presented in order to clarify the origin of the techniques and present in a straightforward manner the simplifying assumptions that permit the modified Wierl formalism to be aplied in structure similarity analyses. Even so, it is not yet clear as to the physical meaning of transforming a set of molecular cartesian coordinates from a time domain to a frequency domain; nor is it more enlightening when, rather can cartesian coordinates, one

transforms molecular adjacency or distance (graph theoretic parametrics) matrices. Further complicating these considerations is Náray-Szabó's "topological distance" construct, in which the difference between the transforms of two molecules is an index that, indeed, permits a quantitative pairwise evaluation of molecular similarity. Perhaps it is somewhat premature to expect a complete understanding of the basis of the methodology; after all, scientific progress has often preceeded a firm theoretical basis for concepts that could be used with great effect. Too, as new promising methodologies are utilized for the solution of practical problems their advantages and limitations usually become quite obvious, and nowhere are the constraints more well-defined than in similarity analysis, e.g., the problem of geometric and optical isomerism - these have yet to be addressed with the current formalism. But the very nature of the transform technique would lead one to confidently expect that these barriers can and will be overcome.

On a more speculative note, it would seem that the binary patterns emerging from the molecular transform of Soltzberg and Wilkins could be used in classification schemes. An example of such would be a chemical inventory stored in a computer file as a list of binary descriptors; searching such a list with a known descriptor would be extremely rapid - and probably even more rapid if the binary descriptors had been subjected to data compression techniques. As with any molecular coding (this one included) the most difficult problem is the generation of a structure from the code, but for many purposes this would not preclude use of the methodology.

CONCLUSIONS

This review has demonstrated that the mathematical infrastructure of molecular and topological transforms is shrouded neither in mystery nor incomprehensible terminology. Further, the potential of these methods to generate useful molecular comparison indices as well as simple, and perhaps unambiguous, molecular codes, is enormous. Further utilization of these methods can reasonably be expected to have a very significant impact on organic and biomedical chemistry in general and more specifically, on the design of new compounds for many purposes.

ACKNOWLEDGMENT

The authors are indebted to Drs. Cliff R. King and Gábor Náray-Szabó for helpful discussions.

REFERENCES

1. U.S. Army Chemical Research, Development and Engineering Center, Aberdeen Proving Ground, Maryland 21010-5423.

2. Department of Mathematics, Clemson University, Clemson, SC 29632.

3. A.T. Balaban, I. Motoc, D. Bonchev, and O. Mekenyan. Topological Indices for Structure-Activity Correlations. Topics in Current Chemistry 114, 21-25 (1983).

4. J.W. King. A Z-Modified Information Content Index. Int. J. Quant. Chem.: Quant. Biol. Symp. 1989. In press.

5. L.J. Soltzberg and C.L. Wilkins. Computer Recognition of Activity Class from Molecular Transforms. J. Am. Chem. Soc. 98, 4006 (1976).

6. L.J. Soltzberg, C.L. Wilkins, S.L. Kaberline, T.F. Lam, and T.R. Brunner. Evaluation and Comparison of Pattern Classifiers for Chemical Applications. J. Am. Chem. Soc. 98 (23), 7139-7144 (1976).

7. R. Wierl. Electron Diffraction and Molecular Structure. Ann. Phys. (Leipzig) 8, 521-564 (1931)(Ger.)[Chem. Abstr. 25, 2886 (1931)].

8. L.J. Soltzberg and C.L. Wilkins. Molecular Transforms: A Potential Tool for Structure-Activity Studies. J. Am. Chem. Soc. 99, 439-443 (1977).

9. Z. Gabanyi, P. Surjan, and G. Náray-Szabó. Application of Topological Molecular Transforms to Rational Drug Design. Eur. J. Med. Chem. - Chim. Ther. 17 (4), 307-311 (1982).

10. G. Náray-Szabó. Similarity Analysis of Bioactive Molecules: Electrostatic Lock-and-Key Model and Topological Molecular Transforms for Trypsin Inhibitors. J. Mol. Struct. (Theochem) 134, 401-409 (1986).

11. Note that s is not the scattering angle; it measures the scattering angle. S has units of 1/distance. See A. Guinier. X-Ray Diffraction. W.H. Freeman and Co., San Francisco and London. 1963.

12. A delta function has the property that it vanishes for $r \neq r_{ij}$, i.e., $(r-r_{ij}) = 0$ if $r \neq r_{ij}$. Also $\int_0^\infty \delta(r-r_{ij})\,dr = 1$

DEUTERIUM ELECTRIC FIELD GRADIENTS OF DIATOMICS BY VARIATION-PERTURBATION METHOD: COMPARISON OF RESULTS BASED ON SLATER AND GAUSSIAN BASIS SETS

Hae-Won Kim[1]
Penn State Ogontz, Abington, PA

James O. Jensen
U.S. Army Chemical Research, Development and Engineering Center
Aberdeen Proving Ground, MD

Hendrik F. Hameka
University of Pennsylvania, Philadelphia, PA

We Present calculations of deuterium electric field gradients in the HD and LiD molecules that were obtained by using Gaussian atomic orbitals. The differences between the theoretical and corresponding experimental values are 2% for both basis sets. We conclude that the accuracy of the variation-perturbation method using Gaussians is comparable to the accuracy of the results using Slater orbitals.

I. Introduction

In a recent series of papers we reported calculations of the deuterium electric field gradients (EFG) on the HD molecule[2], the LiD molecule[3] and the DF molecule[4]. We also computed the vibrational dependence of the field gradient in the HD molecule[5]. The above calculations were all based on the use of Slater atomic orbitals using a variation-perturbation method[6]. Since we wish to extend the scope of our calculations beyond diatomics it is necessary to make use of Gaussian atomic orbitals. In order to judge the accuracy of EFG calculations based on Gaussians we present a study on the HD and LiD molecules and compare the result to that of the calculation based on Slater basis sets.

II. Method

We start our calculations with an approximate molecular function Ψ_o, an SCF molecular wave function which is an antisymmetrized product of molecular orbitals Φ_i. The molecular orbitals Φ_i are linear combinations of Dunning-Hay contracted Gaussian orbitals[7]. The expectation value q_D^o of the EFG at the deuterium position is then given by

$$q_D^o(el) = \langle \Psi_o | V_{zz}(el) | \Psi_o \rangle$$

$$= 2\Sigma_k \langle \Phi_k | V_{zz}(el) | \Phi_k \rangle \quad (1)$$

summed over all occupied molecular orbitals where

$$V_{zz}(el) = \Sigma_i V_{zz}(i)$$

$$= (r_{Di}^2 - 3z_{Di}^2)/r_{Di}^5 \quad (2)$$

summed over all electrons.

The next step in the calculations is the derivation of a function F by minimizing the functional

$$\langle F | H-E_o | F \rangle + \langle F | V_{zz}(el) | \Psi_o \rangle + \langle \Psi_o | V_{zz}(el) | F \rangle \quad (3)$$

subject to the condition

$$\langle F | \Psi_o \rangle = 0 \quad (4)$$

The correction term to $q_D^o(el)$, $q_D'(el)$, is given by

$$q_D'(el) = \langle F | H-E_o | \Psi_o \rangle + \langle \Psi_o | H-E_o | F \rangle \quad (5)$$

and the corrected EFG value $q_D(el)$ is

$$q_D(el) = q_D^o(el) + q_D'(el) \quad (6)$$

Most of the calculations were performed on a PC clone. Integrals over the Hamiltonian operator were calculated with a program GOTHLAND which was made available to us by J. R. de la Vega of Villanova University, PA. The atomic integrals over the EFG operator were evaluated with a slight variation to a procedure reported by McMurchie and Davidson[8].

III. Application

For the calculations based on Gaussians, we perform one calculation for HD at R = 1.4 a.u. and two calculations for LiD at R = 3.015 a.u. The HD basis set is a Dunning-Hay [2s] hydrogen set

plus a polarization function(ζ_p= 1.0) for both centers. The first LiD basis set(I) is a Dunning-Hay [3s] contracted basis set for Li with a [2s] hydrogen set. The second LiD basis set(II) is a Dunning-Hay [3s2p] contracted basis set for Li with a [2s] hydrogen set plus a polarization function(ζ_p= 1.0) for H. For both molecules we also use two 3d orbitals centered on deuterium with orbital exponents 6.14092 and 0.69436. For the calculations based on Slater basis sets, we used the LCAO MO SCF function proposed by Ransil[9] for LiD at R = 3.015 a.u. For HD, we used a single configuration LCAO MO wavefunction at R = 1.4 a.u. by Fraga and Ransil[10]. For both molecules we also use two 3d orbitals centered on deuterium with orbital exponents of 7 and 7/3.

TABLE 1

Results of deuterium EFG calculations for HD and LiD using Gaussians. Results based on Slater orbitals and experimental values are listed for comparison. All values are in atomic units.

	HD	LiD(I)	LiD(II)
Energy(a.u.)	-1.131198	-7.967622	-7.981163
q_D^o(el)	-0.368041	-0.141584	-0.149818
q_D'(el)	-0.014427	-0.020230	-0.015966
q_D(el)	-0.382468	-0.161814	-0.165784
$q_D(el)_{Slater}$	-0.38305	-	-0.16438
$q_D(el)_{Sundholm}$	-	-	-0.168
$q_D(el)_{exp}$[11,12]	-0.39094	-	-0.169

IV. Results

In the accompanying table we compare our results with experiment and the best theoretical values. For LiD we list the experimental value which we derived from the measurements by Wharton, Gold and Klemperer[11]. In the case of HD we list the most

precise theoretical value derived by Bishop and Cheung[12] for a fixed internuclear distance R=1.4. We believe that this value is more accurate for our purpose than the experimental value since the latter includes the vibrational motion.

From our results we may conclude that the Gaussian results are comparable in accuracy with the Slater results based on the variation-perturbation method. In the case of HD the difference between the two sets of theoretical results is only 0.15% and the difference between the Gaussian result and the "exact" value of Bishop and Cheung[12] is 2.17%. In the case of LiD the result from our Gaussian Calculation II is significantly better than the result from Gaussian calculation I. This indicates that it is desirable to include 2p atomic orbitals in the deuterium basis set. The difference between the Gaussian II result and the experimental result[11] is 1.9% and the difference between the Slater result[3] and the experimental value[11] is 2.7%. It should be noted though that the Gaussian II basis set includes a $2p_z$ orbital on deuterium and that the Slater basis set[3] contains only s atomic Slater orbitals on deuterium.

It may be instructive to compare our result for the deuterium EFG value in LiD with that obtained by Sundholm et al[13]. In reference [3] we presented the experimental value of $q_D(el)$ derived from the measurements of Wharton, Gold and Klemperer[11] as q_D=-0.169+ 0.0015. Our value is q_D=-0.166 and the value presented by Sundholm et al[13] is q_D=-0.168. It should be noted though that this slightly better result requires 993 configuration in a CI treatment whereas our value requires only 16 correction terms.

CONCLUSIONS

We may conclude from our present results that the determination of deuterium EFG based on the variation-perturbation method can just as effectively be calculated from Gaussian atomic orbitals as from Slater atomic orbitals. We also conclude that our variation-perturbation method seems to be more effective than the other procedures since the slight decrease in accuracy is more than compensated by decrease in computational effort. We will therefore proceed to calculate deuterium EFG in some larger systems by using Gaussian atomic orbitals in the GOTHLAND program.

REFERENCES

1. Hae-Won Kim, Penn State Ogontz, Abington, PA,19001

2. Zamani-Khamiri O, and Hameka HF (1981) J. Chem. Phys. 75:781 and (1982) J. Chem. Phys.77:2218

3. Pietrovito AJ, Hameka HF, Zeroka D (1982) J. Chem. Phys. 81:1960

4. Kim HW, Hameka HF, Zeroka D (1986) J. Chem. Phys. 84:5639

5. Kim HW, Hameka HF, Zeroka D (1988) J. Chem. Phys. 88:3159

6. Hameka HF, Svendsen EN (1976) Int. J. Quantum Chem. 10:249

7. Dunning TH Jr., Hay PJ (1977) Electronic Structure Theory, Schaefer HF III.(ed), vol. 3 Plenum Press, New York, N.Y., Page 1

8. McMurchie LE, Davidson ER (1978) J. Comp. Phys. 26:218

9. Ransil BJ (1960) Rev. Mod. Phys. 32:245

10. Fraga s, Ransil BJ (1967) J. Chem. Phys. 35:1967; (1969) J. Chem. Phys. 50:572

11. Wharton L, Gold LP, Klemperer W (1962) J. Chem. Phys. 37:2149

12. Bishop DM, Cheung LM (1979) Phys. Rev. A20:381

13. Sundholm D, Pyykko P, Laaksonen L, Sadlej AJ (1984) Chem. Phys. Lett 112:1

BLANK

MOLECULAR MODELING OF SOME ALPHA-2 ADRENERGIC COMPOUNDS

Alexander P. Mickiewicz and William P. Ashman
Chemometric/Biometric Modeling Branch
Physics Division, Research Directorate
Chemical Research Development and Engineering Center
Aberdeen Proving Ground, Maryland 21010-5423

ABSTRACT

Adrenergic compounds can activate the alpha-2 adrenoreceptors in the central nervous system, producing sedation without respiratory depression. The Chemical Research Development and Engineering Center's Molecular Modeling Analysis and Display System (MMADS) was used to compare the three dimensional structures of various classes of alpha-2 adrenergic compounds. A pharmacophore model for use in compound/adrenergic receptor interaction studies was developed. The model is based on common geometric dimensions and common substructural physicochemical features of the compounds.

INTRODUCTION

Ruffolo (1) has developed structure-activity relationships and defined stereochemical requirements (2) for the interaction of compounds with the alpha-2 adrenergic receptor. Reviews by Timmermans (3) and Savola (4) have discussed the classification and mechanisms of action of the various subtypes of adrenergic receptors. A molecular modeling study (1) has been done on antagonists of the alpha-2 adrenergic receptor.

Various classes of compounds have been developed that have been shown to interact with the alpha-2 adrenergic receptor. The major therapeutic goal of the developers of these compounds has been their use as antihypertensive drugs. Sedation has been a major undesirable side effect of these adrenergics so that the major goal of the design of new adrenergic compounds is to produce antihypertensive activity without sedation.

Bloor (5), Scheinin (6), and Maze (7) have investigated various adrenergic compounds for their sedative and anesthetic activity. The reason for this research is that most anesthetics in medical use today have a major unwanted side effect in that they cause respiratory depression that requires medical assistance to help the patient breathe during their use.

In animal studies, alpha-2 adrenergic compounds have been used in combination with anesthetics and have produced the same anesthetic effect but have reduced the unwanted respiratory and hemodynamic side effects. This has resulted in research to study various classes of alpha-2 adrenergic compounds to define the mechanisms involved with their sedative and anesthetic activity, to define the structure- adrenoreceptor interaction relationships for these compounds, and to identify compounds that will provide anesthesia free of the unwanted side effects.

This paper describes a molecular modeling study to develop a pharamacophore environment of the alpha-2 adrenergic receptor. A proposed topography of the active region of the receptor environment is described.

COMPOUNDS

Eight compounds that are known to be selective as agonists for the alpha-2 adrenergic receptor were selected for analysis. Figure 1 illustrates their 2 dimensional representation. The compounds analyzed are Noradrenaline; Alpha methyl norepinephrine (1R,2S); Alpha methyl norepinephrine (1S, 2R); BHT920; BHT933; A62033; Dexmedetomidine (r form of medetomidine); and UK-14304.

METHODOLOGY

MMADS was used to incorporate the structures of the selected alpha-2 adrenergic compounds and to perform a computer assisted optimization to determine the minimum energy conformation using Allinger's MM2 (molecular mechanics) algorithm. This procedure resulted in a three dimensional configuration for each compound.

The compounds were then superimposed over each other in order to define physicochemical, functional group (phenyl rings, nitrogen atoms, oxygen atoms), and geometric orientations most common to all. This molecular modeling analysis was performed using the Tektronics 4105 Graphics Terminal and the Adage 3000 Color Graphics System.

A three dimensional pharmacophore model was then designed based on the common geometric and physicochemical characteristics of the eight alpha-2 adrenergic compounds. This model represents a description of compound/ adrenergic receptor interaction environment.

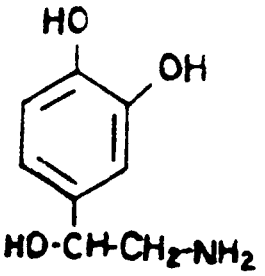

Noradrenaline

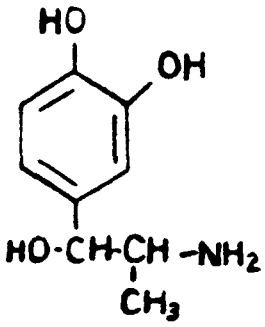

α Methyl Norepinephrine 1R,2S

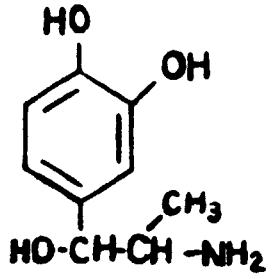

α Methyl Norepinephrine 1S,2R

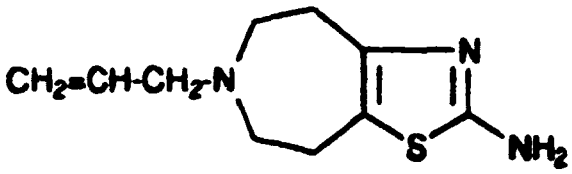

B-HT 920
(Thomae, FDR)

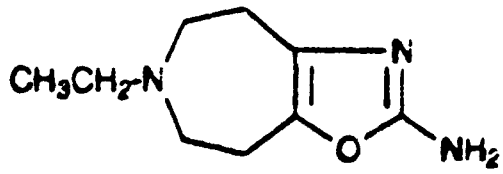

Azepexole (B-HT 933)
(Thomae, FDR)

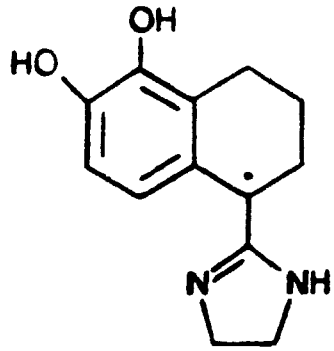

A62033 (*R* Isomer)
(Abbot, USA)

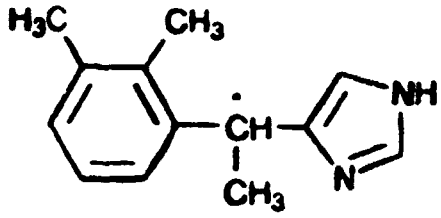

Dexmed
(Farmos, Finland)

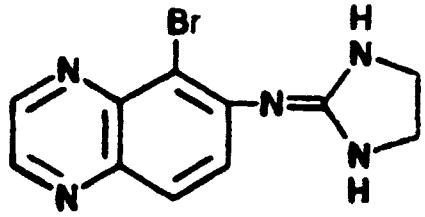

UK-14304
(Pfizer, USA)

FIGURE 1 ALPHA-2 ADRENOCEPTOR AGONISTS

RESULTS AND DISCUSSION

Figures 2 and 3 are the results of overlapping the 8 alpha-2 adrenergic compounds at their similar function regions.

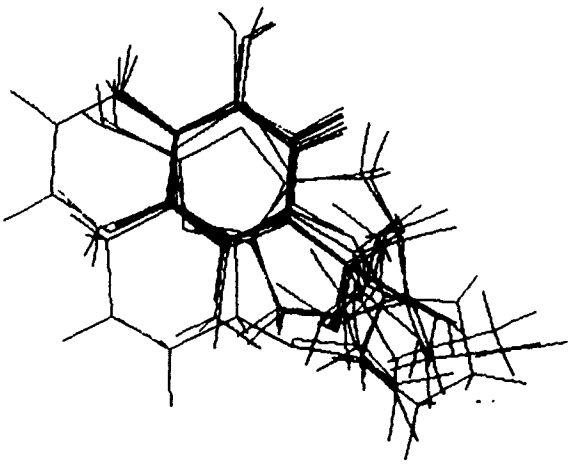

FIGURE 2 TOP VIEW: OVERLAP OF 8 ALPHA-2 ADRENERGIC AGONISTS

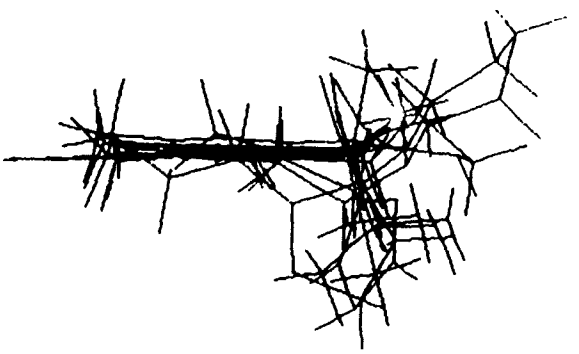

FIGURE 3 SIDE VIEW: OVERLAP OF 8 ALPHA-2 ADRENERGIC AGONISTS

A pharmacophore of the environment of the alpha-2 adrenergic receptor is illustrated in Figures 4 and 5. The proposed compound/receptor interaction environment is composed of a planar pi-pi or lipophilic interaction area surrounded by various regions for either hydrogen bonding, Coulombic, or hydrophobic interactions. The spacial relationship of the regions to each other is illustrated.

The area designated A is a proposed anionic area on the receptor that will bind the corresponding positive charged region of the compound. As illustrated, it is located nearly perpendicular to the plane of the proposed pi-pi interaction area. Compounds that are alpha-2 adrenergic agonists must contain a pi-pi planar region and a region that contains a nitrogen for possible charge-charge (Coulombic) interaction with A.

Additionally, it is proposed that the receptor environment may contain an area (Area B) for hydrogen bonding and another area (Area C) for charge-charge interaction. The hydrophobic cleft area represents an area that either allows for hydrophobic interaction or represents an opening to the receptor active site. Additional analysis is planned for this proposed hydrophobic area.

COORDINATES

Area
A – (1.8,-1.4,-0.9)
B – (-1.0,4.0,.1568)
C – (-3.5,2.0,0.0)

π-π Region
(-0.108,0.624,0.378)
(-0.014,1.964,0.278)
(-1.105,2.740,0.236)
(-2.316,2.174,0.300)
(-2.439,0.839,0.400)
(-1.336,0.550,0.439)

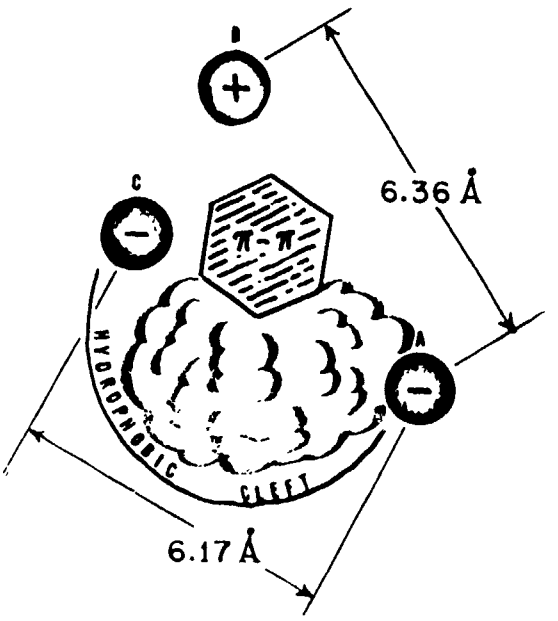

FIGURE 4 TOP VIEW: PHARMACOPHORE MODEL OF ALPHA-2 ADRENERGIC RECEPTOR ENVIRONMENT

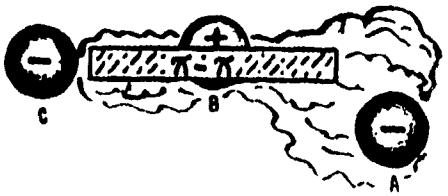

FIGURE 5 SIDE VIEW: PHARMACOPHORE MODEL OF ALPHA-2 ADRENERGIC ENVIRONMENT

CONCLUSIONS

A pharmacophore model of the alpha-2 adrenergic receptor active region that defines the geometric and physicochemical features for compound-receptor interaction has been developed. The model can be used to design new compounds having activity desired by the researcher; and also as a guide to help explain the activities of known adrenergic compounds.

REFERENCES

1. Ruffolo, Robert R., Jr., De Marinis, Robert, M., Wise, Margaret, and Hieble, J. Paul. Chapter 4. Structure-Activity Relationships for Alpha-2 Adrenergic Receptor Agonists and Antagonists. The Alpha-2 Adrenergic Receptors. Edited by Lee E. Limbird. Humana Press. Clifton, New Jersey, 1988, 115-187.

2. Ruffolo, Robert R., Jr., Stereochemical Requirements for Activation and Blockade of Alpha-1 and Alpha-2 Adrenoreceptors. Trends In Pharamaceutical Science (TIPS), April 1984, 160-164.

3. Timmermans, Pierre B., and van Zwie, Pieter. Alpha-2 Adrenoceptors: Classification, Localization, Mechanisms, and Targets for Drug Action. Journal of Medicinal Chemistry, Volume 25, Number 12, December 1982, 1389-1401.

4. Savola, Juha-Matti, Cardiovascular and Sedative Effects of Novel Detomidine-like Arylalkyl Imidazoles and Related Derivatives, Thesis Paper, Acta Universitatis Ouluensis, Series D, Medica No. 147, Pharmacologica Et Physiologica No. 25, 1986.

5. Bloor, Byron, and Flacke, W.E., Reduction in Halothane Anesthetic Requirement by Clonidine, An Alpha Adrenergic Agonist. Anesth Analg 41, 1982, 741-745.

6. Scheinin, Mika, Kallio, Antero, Koulu, Markku, Viikari, Jorma, and Scheinin, H. Sedative and Cardiovascular Effects of Medetomidine, a Novel Alpha-2 Adrenoreceptor Agonist in Healthy Volunteers. British Journal of Clinical Pharmacology, 24, 1987, 443-451.

7. Maze, M., Vickery, R.G., Merlone, S.M., and Gaba, D.M. MAC for Isoflurane is Profoundly Reduced by Azepexole (BHT 933), An Alpha-2 Adrenergic Agonist, Anesthesiology, V 67, No. 3A, Sept 1987.

BLANK

XII. DETECTION POSTERS

NOTE: Papers with the following titles were presented at the Conference but are not included in this document:

Distributed Air-Monitoring Network for Multipoint Determination of Chemical Agents

Raman Spectroscopy for Contamination Monitoring

Analysis of Fatty Acids in Bacteria by Pyrolysis/Tandem Mass Spectrometry

BLANK

DETECTION AND IDENTIFICATION OF QL DEGRADATION PRODUCTS BY CHEMICAL IONIZATION MASS SPECTROMETRY

Dennis K. Rohrbaugh
Research Directorate
U.S. Army Chemical Research, Development and Engineering Center
Aberdeen Proving Ground, MD 21010-5423

ABSTRACT

Methane chemical ionization (CI) capillary column gas chromatography/ mass spectrometry (GC/MS) has been used to identify ten degradation products produced during storage of QL [O-(2-diisopropylaminoethyl) O'-ethyl methylphosphonite]. Products resulting from disproportionation, hydrolysis, oxidation and Michaelis-Arbusov rearrangement reactions were observed. Methane chemical ionization provides valuable molecular ion and fragmentation information not provided by conventional electron ionization techniques to aid in the identification of this class of compounds.

INTRODUCTION

The objective of this study was to develop a method for the detection and identification of products produced during the degradation of O-(2-diisopropylaminoethyl) O'-ethyl methylphosphonite (QL), which is one of the components used to produce the nerve agent O-ethyl S-(2-diisopropylaminoethyl) methylphosphonothioate (VX). This information is of interest from both an environmental and a safety standpoint. Identification of phosphonites and other organophosphorus compounds containing the 2-diisopropylaminoethyl group by conventional electron impact (EI) mass spectrometry is difficult because little or no molecular ion information is available. Extensive fragmentation occurs predominantly to $(iPr)_2N{=}CH_2^+$ at m/z 114, resulting in similar spectra for compounds containing this group. In this study we apply methane CI capillary GC/MS to identify ten QL degradation products produced during storage. Methane CI (soft ionization) provides the molecular ion and fragmentation pattern information necessary for identification of these compounds.

METHODS

The product was characterized using a Finnigan model 5100 GC/MS equipped with a fused silica 15 m x 0.25 mm ID SE-54 capillary column (J&W Scientific). Injection temperature was 220°C, GC/MS interface temperature was 220°C and the oven was programmed from 60°C to 260°C at 10°C/min. 0.01 µl of sample was injected with a split ratio of 25:1. The CI reagent gas was methane with an internal source pressure of 0.6 Torr. The mass range was scanned from 60 to 450 amu at a rate of 1 scan per second.

RESULTS AND DISCUSSION

Figure 1 illustrates the GC/MS CI total ion chromatogram obtained for a stored sample of QL. Ten compounds were observed. The identification of each of these compounds is listed in Table 1. Characteristic CI fragmentation ions observed are shown in Table 2.

Figure 1

GC/MS Chromatogram of a Stored QL Sample

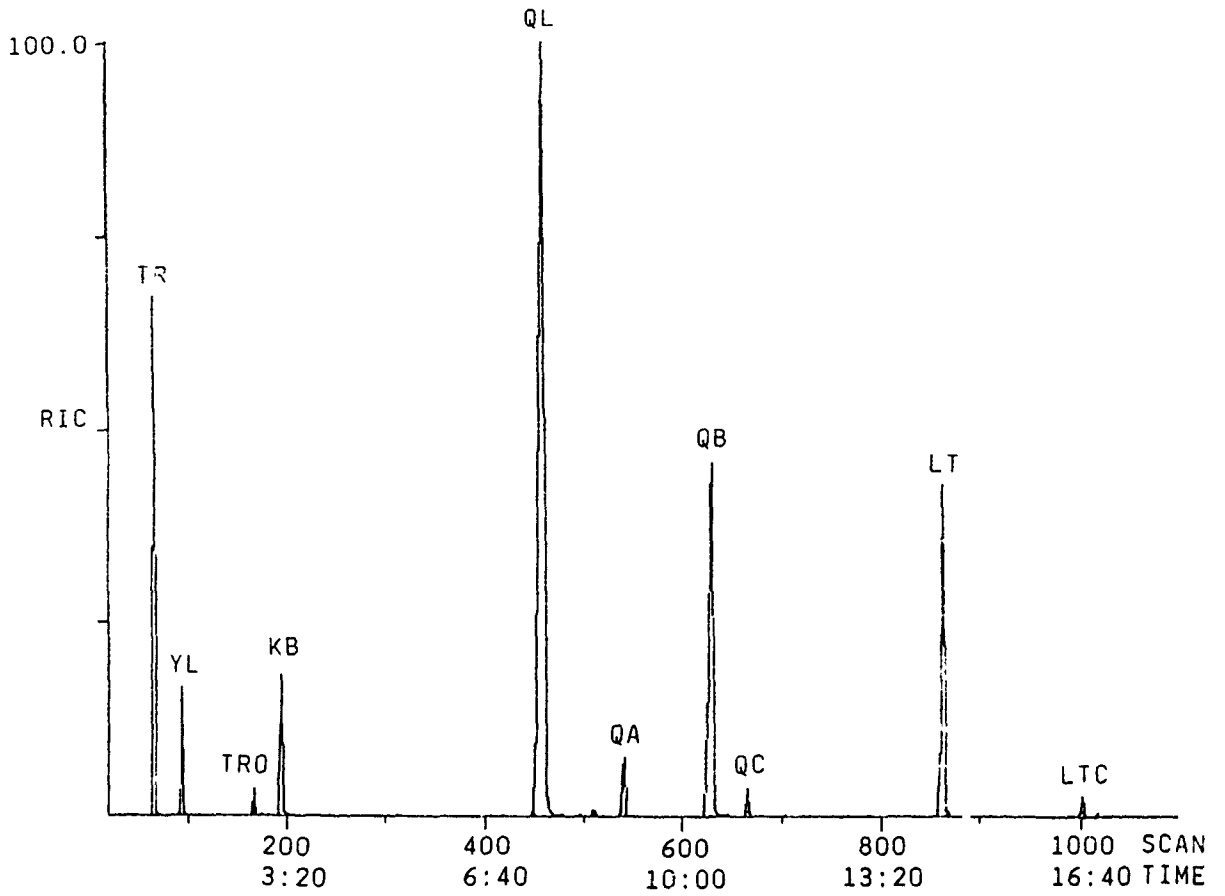

Table 1. Compounds Identified in a Stored Sample of QL

R.T. (min)	Mol Wt	Symbol	Name	Structure
1.1	136	TR	O,O'-Diethyl Methylphosphonite	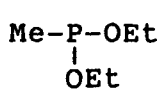
1.6	108	YL	O-Ethyl Methylphosphinate	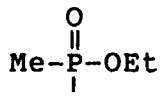
2.8	152	TRO	O,O'-Diethyl Methylphosphonate	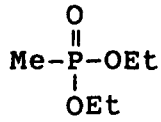
3.3	145	KB	2-Diisopropylaminoethanol	$HOCH_2CH_2N(iPr)_2$
7.7	235	QL	O-(2-Diisopropylamino-ethyl) O'-Ethyl Methylphosphonite	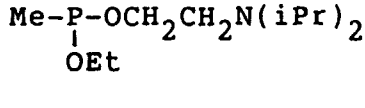
9.0	207	QA	O-(2-Diisopropylamino-ethyl) Methylphosphinate	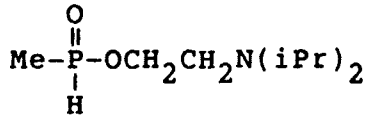
10.5	251	QB	O-(2-Diisopropylamino-ethyl) O'-Ethyl Methylphosphonate	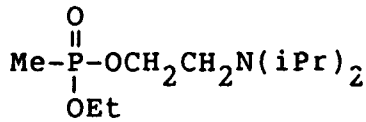
11.1	235	QC	O-Ethyl 2-Diisopropyl-aminoethylmethyl-phosphinate	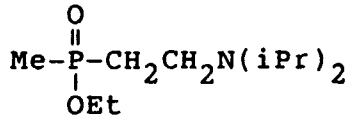
			O-(2-Diisopropylamino-ethyl) Ethylmethyl-phosphinate	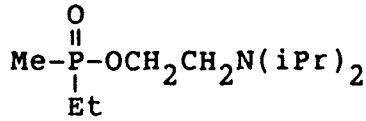
14.4	334	LT	O,O'-Bis(2-Diisopropyl-aminoethyl) Methylphosphonite	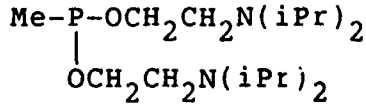
16.7	334	LTC	O-(2-Diisopropylamino-ethyl) 2-Diisopropylamino-ethylmethylphosphinate	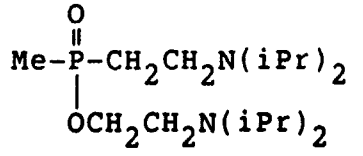

Table 2. CI Fragmentation Observed for QL Decomposition Products

M/Z	Proposed Structure	Relative Intensity (% of Base Peak)									
		TR	YL	TRO	KB	QL	QA	QB	QC	LT	LTC
M+1	$(M+H)^+$	100	100	100	100	1	62	63	100		10
M-1	$(M-H)^+$	11			7	13	3	4	8	2	2
M+29	$(M+C_2H_5)^+$	6	4	10	9	1		1	19	1	
M+41	$(M+C_3H_5)^+$	12	4	4	3				6		
M-15	$(M-CH_3)^+$	51		1	8	23	7	8	14		4
81	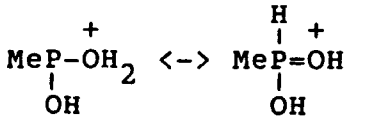	35	28								
91	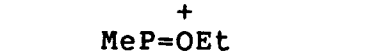	92									
97	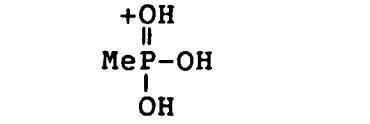			2							
109	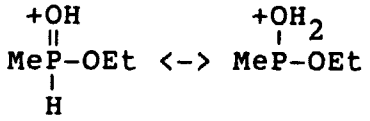	66				7					
114	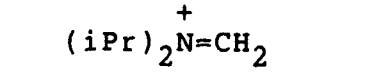				5	8	4	4	12	3	1
125	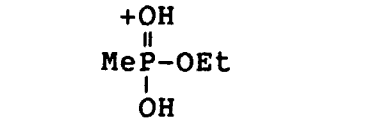			9							
128	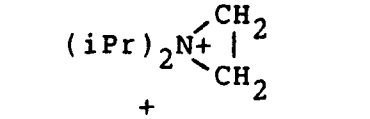				13	100	100	100		100	100
146	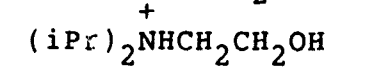				(100)		8			2	1
190	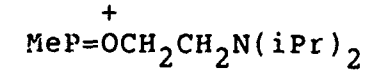					33				9	
192	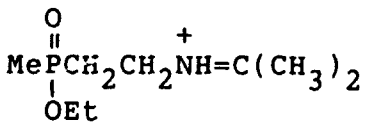								17		

Identification of phosphonites and other organophosphorus compounds containing the 2-diisopropylaminoethyl group is difficult on the basis of EI information alone because the spectra are similar and little or no molecular ion information is available. No molecular ion is observed for QL, QA, QB, QC, LT or LTC. The fragment ion formed by loss of a methyl group is observed only at trace levels in the EI spectra of QL, QA and QB and is absent in the spectra of LT and LTC. The EI spectra of compounds containing the 2-diisopropylaminoethyl group are dominated by characteristic fragment ions resulting from this group that may be represented as $(iPr)_2\overset{+}{N}=CH_2$ at m/z 114 (67 to 100% of base peak), $C_4H_8N^+$ at m/z 70 (34 to 100% of base peak), $(iPr)\overset{+}{N}H=CH_2$ at m/z 72 (30 to 69% of base peak), $C_5H_{10}N^+$ at m/z 84 (22 to 73 % of base peak), $[(iPr)_2N-CH=CH_2]^+$ at m/z 127 (12 to 33% of base peak) and $(iPr)_2N^+=\overset{CH_2}{\underset{CH_2}{|}}$ at m/z 128 (0 to 85% of base peak).

Methane chemical ionization provides the valuable molecular ion information as well as significant fragment ion information to confirm the identification assignments of these compounds, as illustrated in Table 2. Pseudomolecular ions were observed for all ten compounds. The phosphonites containing the 2-diisopropylaminoethyl group are unusual in that the formation of the $(M-1)^+$ ions were observed rather than the usual $(M+H)^+$ ions. The CI mass spectra of QL, QA, QB, LT and LTC are dominated by a peak at m/z 128 (base peak in all cases). The absence of this ion and increased protonated molecular ion formation for QC suggests that the Michaelis-Arbusov rearrangement product is primarily MeP(O)(OEt)(R) and not MeP(O)(Et)(OR), where R = 2-diisopropylaminoethyl, because of the increased thermodynamic stability of the P-R bond relative to the P-OR bond.

A comparison of the EI and methane CI mass spectra of QL is shown in Figure 2. A CI fragmentation scheme for QL is provided below.

Scheme. QL Fragmentation under Methane CI Conditions

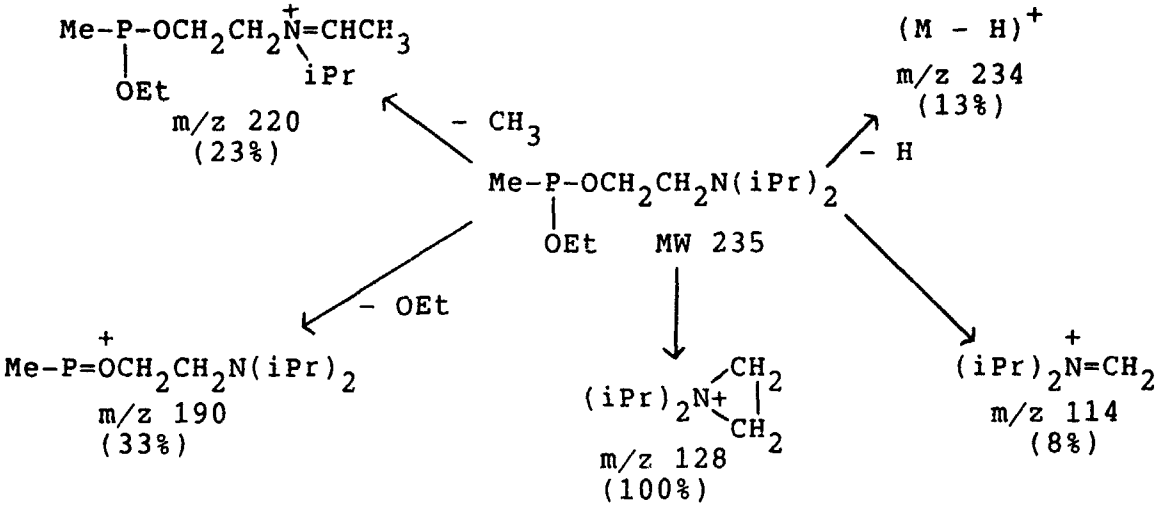

Figure 2. EI and CI Mass Spectra of QL

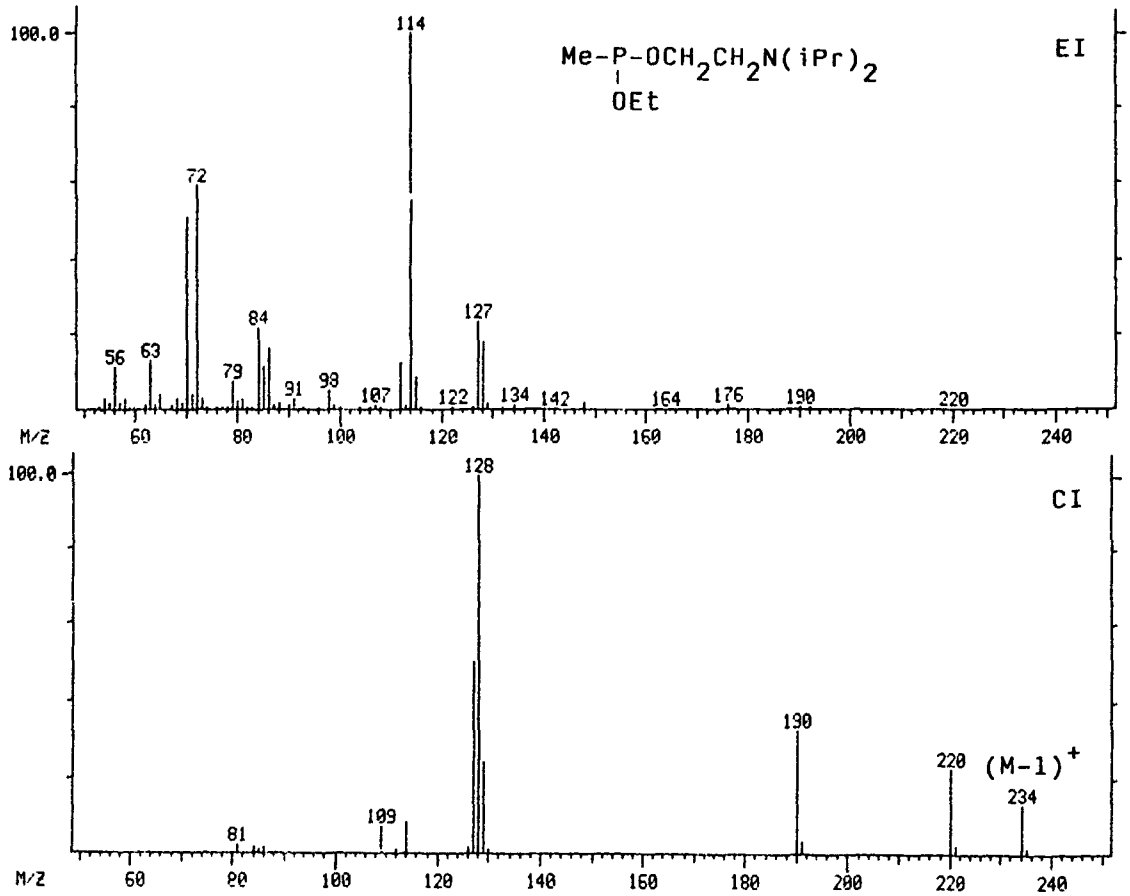

CONCLUSIONS

Methane chemical ionization GC/MS is an excellent technique for the identification of QL decomposition products. Unlike electron ionization methods, where many of the compounds have similar spectra with no molecular ion information, chemical ionization provides both molecular ion and fragmentation information to aid in compound identification. Ten compounds were identified in a stored sample of QL. These compounds resulted from QL disproportionation, hydrolysis, oxidation and Michaelis-Arbusov rearrangement reactions.

2-NAPHTHALENETHIOLATE ION AS A FLUOROGENIC REAGENT FOR DETECTION OF THE BLISTER AGENT SIMULANT 2-CHLOROETHYLETHYLSULFIDE

Thaddeus J. Novak[1]

U.S. Army Chemical Research, Development and Engineering Center
Aberdeen Proving Ground, MD 21010-5423

and

Paul M. Davis

GEO-CENTERS, Inc.,
10903 Indian Head Highway
Ft. Washington, MD 20774

ABSTRACT

Fluorescence properties of 2-naphthalenethiol, 2-naphthalenethiolate ion, and the product of the reaction of 2-naphthalenethiolate ion with 2-chloroethylethylsulfide (CEES) are described. The fluorescence of the latter is used as the basis for a new detection method for CEES. This detection method, which has been optimized for future studies as a candidate system for detecting blister agents, is capable of detecting CEES at levels down to 0.2 micrograms per milliliter. If the detection procedure is successfully extended in follow up studies to include detection of blister agents, the method may be useful in extending the chemical agent detection capability of a flow cell fiber-optic waveguide detector that has recently been developed for detection of toxins and nerve agents.

INTRODUCTION

Except for a recently developed method for detecting liquid mustard on surfaces[2] fluorogenic methods for detection of blister agents are not available. Consequently, there do not appear to be any sensitive candidate fluorogenic methods that can be studied for possible application for blister agent detection in fiber-optic waveguide detectors such as the flow cell FOWG detector that has been developed at CRDEC for detection of toxins and nerve agents[3].

Since blister agents are known to react with nucleophiles (e.g. mustard reacts with 4-(4'-nitrobenzyl)-pyridine and lewisite reacts with 1,3-dithio-2-propanol) it was considered of interest at this time to investigate the strongly nucleophilic 2-naphthalenethiolate ion as a candidate fluorogenic reagent for detecting blister agents. With the ultimate goal of develop-

ing a detection method for blister agents applicable to fiber-optic waveguide detectors, preliminary studies were undertaken using the blister agent simulant 2-chloroethylethylsulfide (CEES) as the analyte. This report summaries the results of the preliminary study.

EXPERIMENTAL

Equipment

Studies were carried out using a Perkin-Elmer MPF-66 spectrophotofluorometer. Excitation and emission slits were 5.0 nm.

Reagents and Solutions

Solvents were spectroquality and/or showed no significant fluoresence when excited at 254 nm or 282 nm. Aqueous solutions were made with distilled water. 2-Naphthalenethiol (99+%) (2-NPT) and 2-chloroethylethylsulfide (99+%) (CEES) were from Aldrich Chemical Co. Buffers were from usual laboratory supply sources.

General Procedure for the Fluorescence Studies

The effect of parameters such as reagent concentration, buffer type and pH, and reaction solvent were studied. Stock solutions of 2-naphthalenethiol were prepared by dissolving the required quantity of 2-naphthalenethiol in methanol. The stock solution was diluted 1:10 with methanol and the resulting solution was further diluted 1:25 with either water or methanol as desired to make the working solution. The working solution (3.0 ml) was placed in a 1-cm pathlength quartz fluorescence cell and aqueous buffer solution (0.3 ml) as required for the experiment was added. When CEES was used, it was added in acetonitrile solution (10 microliters). After adding CEES the cell was capped and inverted several times to mix the components. Incubation with CEES was for 15 minutes. All studies were carried out in the thermostatted cell compartment of the spectrophotofluorometer at 25^{o} C.

Spectral Characteristics of 2-Naphthalenethiol Ion Detection System

FIG. 1 shows the excitation spectra (emission wavelength 374 nm) and FIG. 2 shows the emission spectra (excitation wavelength 254 nm) for 2-naphthalenethiolate ion in aqueous CHES buffer containing 4% methanol before and after incubation with CEES. The emission spectrum of the reagent blank (FIG. 2, curve A) shows no significant peaks in the range 350-400 nm while the incubated mixture (FIG. 2, curve B) has a prominent emission maximum at 374 nm. The excitation maxima for the blank (FIG. 1, curve A) at 238 nm and 275 nm are weak while the excitation maxima for the 2-naphthalenethiolate ion solution incubated with CEES (FIG. 1, curve B) at 233 nm, 254 nm, and 287.5 nm are prominent.

Interference Tests

Each candidate interferent (50 micrograms in 10 microliters of acetonitrile) was added to the fluorescence cell containing 2-naphthalenethiol solution (4.22×10^{-5} M; 3.0 ml) to which 1M CHES buffer (pH 9.75; 0.3 ml) had been added. After adding CEES, the cell was capped and inverted several times to mix the components. The solution was then incubated at 25^{o} C. With the excitation wavelength set at 254 nm, the emission intensity at 374 nm was read before and after a 15-min incubation with CEES. The net intensity was found by subtracting the initial (blank) reading from the final reading.

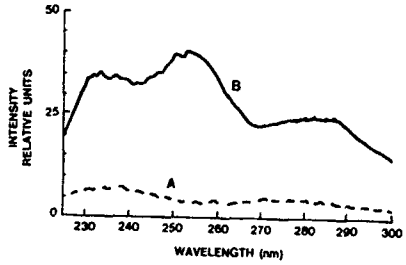

FIGURE 1 EXCITATION SPECTRA (EMISSION WAVELENGTH 374 nm) FOR 2-NAPHTHALENETHIOLATE ION IN AQUEOUS CHES BUFFER CONTAINING 4% METHANOL BEFORE (CURVE A) AND AFTER (CURVE B) INCUBATION WITH CEES

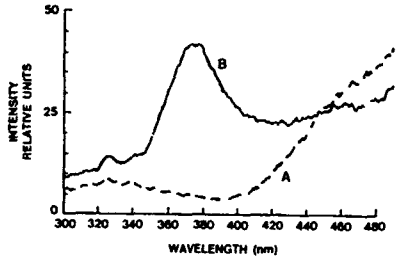

FIGURE 2 EMISSION SPECTRA (EXCITATION WAVELENGTH 254 nm) FOR 2-NAPHTHALENETHIOLATE ION IN AQUEOUS CHES BUFFER CONTAINING 4% METHANOL BEFORE (CURVE A) AND AFTER (CURVE B) INCUBATION WITH CEES

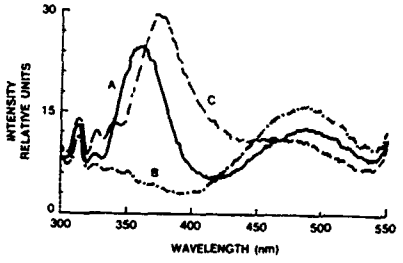

FIGURE 3 EMISSION SPECTRA WITH EXCITATION WAVELENGTH 282 nm OF NAPHTHALENETHIOL (CURVE A), 2-NAPHTHALENETHIOLATE ION (CURVE B) AND THE PRODUCT OF THE REACTION OF 2-NAPHTHALENETHIOLATE ION WITH CEES (CURVE C)

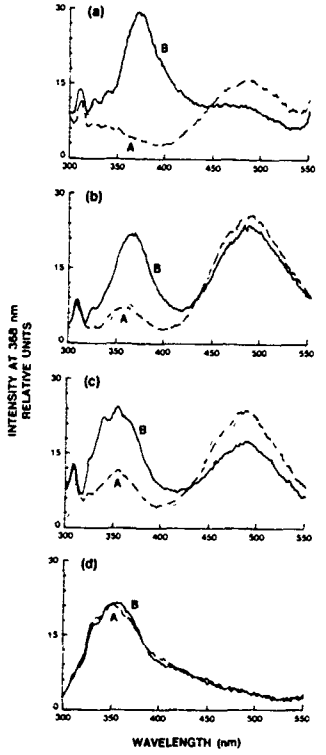

FIGURE 4 EFFECT OF ORGANIC/AQUEOUS COMPOSITION OF THE SOLVENT ON SPECTRA OF 2-NAPHTHALENETHIOLATE ION TAKEN BEFORE (CURVE A) AND AFTER (CURVE B) INCUBATION WITH CEES. EXCITATION WAVELENGTH WAS 282 nm. SOLVENT SYSTEMS ARE (a) METHANOL.WATER (1·25), (b) METHANOL WATER (9 1), (c) 2-METHOXYETHANOL WATER (9·1), AND (d) HEXYLENE GLYCOL.WATER (9 1)

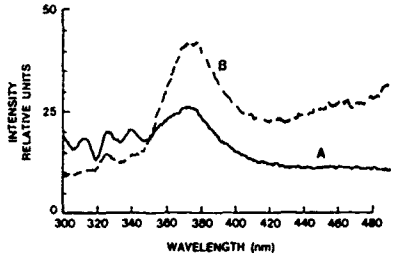

FIGURE 5. EMISSION SPECTRA WITH EXCITATION WAVELENGTH AT 282 nm (CURVE A) AND WITH EXCITATION WAVELENGTH 254 nm (CURVE B) OF PRODUCT OF REACTION OF 2-NAPHTHALENETHIOLATE ION WITH CEES IN AQUEOUS CHES BUFFER CONTAINING 4% METHANOL.

RESULTS AND DISCUSSION

Reaction of CEES with 2-Naphthalenethiolate Ion

Spectra of 2-naphthalenethiol; 2-naphthalenethiolate ion; and the product of the reaction of 2-naphthalenethiolate ion with CEES obtained with the excitation wavelength at 282 nm are shown in FIG. 3. A methanolic solution of 2-naphthalenethiol displays a strong peak with a maximum at 359 nm (FIG. 3, curve A) and a weaker peak with a maximum at 489 nm. Quenching of the 359 nm emission occurs at alkaline pH (FIG. 3, curve B) due to ionization of the -SH group. The ionized species is only very weakly fluorescent in the wavelength region 350-400 nm. Reaction with CEES causes the strong emission band to return but at a wavelength maximum of 374 nm (FIG. 3, curve C), bathochromically shifted 15 nm relative to 2-naphthalenethiol in methanol.

Effect of 2-Naphthalenethiol Concentration

The effect of the reagent concentration on the fluorescence intensity of solutions containing a constant CEES concentration (2.5 micrograms per 3.3 ml) was studied under conditions similar to the recommended method. The essential differences were the excitation wavelength (282 nm instead of 254 nm) and the solvent contained a higher percentage of methanol (90% instead of 4%). Results are in table 1. The fluorescence intensity at the emission maximum (368 nm) increased up to 4.22×10^{-5} M and then decreased above this concentration. In accordance with this, a 4.22×10^{-5} M concentration was chosen as optimum.

Table 1

Effect of Concentration of 2-Naphthalenethiolate Ion on the Strength of the Response to 2-Chloroethylethylsulfide

2-Naphthalenethiolate Ion Concentration ($M \times 10^5$)	Net Change in Intensity* at 368 nm (Relative Units)
1.06	5.84
2.11	6.52
4.22	7.34
8.45	3.62
12.67	2.67

* 15 minute reaction at 25° C with 2.5 micrograms CEES per 3.3 ml.

Effect of Buffer Type, pH, and Concentration

The effect of several different buffers and the pH of CHES buffer on the response of the detection method to CEES is shown in table 2. The data show that the chemical composition of the buffer is not critical to production of the fluorescence emission near 370 nm upon reaction with CEES. In addition, tests with CHES at pH 9.19, 9.75, and 10.58 indicate that a pH range 9.75-10.58 is desireable. The responses obtained at pH 9.75 and 10.58 were nearly identical.

Table 2

Effect of Buffer Type and Buffer pH on the Strength of the Response of the 2-Naphthalenethiolate Ion Detection System to 2-Chloroethylethylsulfide

Buffer*	Adjusted pH Value	Net Change in Intensity** at 368 nm
TAPS	8.86	3.77
BIS-TRIS PROPANE	8.59	2.56
TES	7.74	3.18
BICINE	8.37	1.24
CHES	9.19	2.52
CHES	9.75	4.86
CHES	10.58	4.82

* Buffer codes: TAPS = (N-tris[hydroxymethyl)methyl-3-aminopropanesulfonic acid; BIS-TRIS PROPANE = bis[tris(hydroxymethyl)methylaminopropane; TES = (N-tris-[hydroxymethyl]methyl-2-aminoethanesulfonic acid; BICINE = (N,N-bis[2-hydroxy-ethyl]glycine; CHES = (2-[N-cyclohexylamino]ethanesulfonic acid.

** 15-min reaction at 25° C with 2.5 micrograms CEES per 3.3 ml. Excitation wavelength was 282 nm. Methanol content of solvent was 90%.

A variable even more important than the chemical compositon and the pH of the buffer is the ability of the buffering system to negate the effect of acidic impurities in the analyte. An initial study conducted with 2-naphthalenethiol in methanol showed that HCl is a serious interferent; when sufficient HCl was added to unbuffered or weakly buffered reagent solution, the solution was unable to respond to CEES. Since HCl is produced upon hydrolysis of blister agents, and since acidic pollutants in the atmosphere can accumulate in the sample when it is collected, it is essential that the detection system be buffered at an alkaline pH. Studies of the effect of concentration of CHES buffer, which is added one part in ten to the 2-naphthalenethiol working solution, showed that 1 M is the optimum concentration. Quenching occurred when the molarity of the added buffer was increased to 3.3 M; concurrently, the fluorescence response decreased to about two-thirds of that obtained with the 1 M buffer. Addition of 700 micrograms of HCl to the 3.3 ml sample caused the pH to drop only ca. 0.7 units (to pH 9.05). Thus the detection method will tolerate an acid content in the analyte which is far in excess of the expected levels.

Effect of Solvent

The spectrum of the product of 2-naphthalenethiolate ion with CEES excited at 282 nm (FIG. 4a, curve B) shows a characteristic peak with a wavelength maximum at 374 nm and three much weaker peaks with wavelength maxima at 313 nm, 337 nm, and 341 nm. It also displays a weak broad shoulder near 490 nm. The wavelength maximum for the strong emission shifted from 374 nm to 368 nm (FIGS. 4a-d) as the solvent composition was changed from methanol-water (1:25) to methanol-water (9:1) to 2-methoxyethanol-water (9:1) and finally to hexylene glycol-water (9:1). Concomitantly, the weaker maxima became less prominent or disappeared, and with the exception of the solution that contained hexylene glycol, the shoulder evolved into a strong peak with a wavelength maximum of 489 nm. The most relevant change was that between 300 nm and 400 nm the shape of the spectrum of the 2-naphthalenethiolate ion blank more closely resembled that of the product of the reaction of 2-naphthalenethiolate ion with CEES as the polarity of the solvent system decreased. Consequently, for identical reaction times with a constant amount of CEES, there was a smaller net change in the intensity

of fluoresence at the emission maximum as the polarity of the solvent system was decreased. Thus, the solvent system containing 96% water was selected as optimum.

Effect of Excitation Wavelength

FIG. 5 contains a comparison of the effect of exciting the sample at 254 nm and at 282 nm on the emission spectra obtained for the product of the reaction of 2-naphthalenethiolate ion with CEES. Since the emission intensity at 374 nm was nearly twice as strong when the excitation wavelength was 254 nm, in this preliminary study it was judged to be optimum. However, the final decision on the choice of the optimum excitation wavelength will also be affected by stability requirements.

Recommended Detection Method

Prepare 2-naphthalenethiol stock solution in a 100-ml volumetric flask by dissolving 2-naphthalenethiol (99+%, 169.2 mg) in methanol and adding methanol to the mark. Dilute the stock solution 1:10 with methanol. Prepare working solution by diluting the stock solution 1:25 with distilled water. Place the working solution (3.0 ml) in a 1-cm quartz fluoresence cell and add 0.3 ml of aqueous CHES buffer (1M; pH 9.75). Bring the temperature of the solution in the fluorescence cell to 25° C. With the excitation wavelength at 254 nm and the emission wavelength at 374 nm read the fluoresence intensity for a reagent blank. Add the CEES sample dissolved (collected) in acetonitrile (10 microliters) to the solution in the cell. Cap the cell and mix the sample by inverting the cell several times. Incubate the sample at 25° C for 15 minutes. With the excitation wavelength at 254 nm and the emission wavelength at 374 nm read the fluorescence intensity for the sample. Calculate the net fluorescence intensity for the sample by subtracting the blank reading from the sample reading.

This detection method when used in combination with a Perkin-Elmer MPF-66 spectrophotofluorometer with excitation and emission slits at 5.0 nm is capable of detecting CEES at final concentrations down to 0.2 micrograms per milliliter. The reaction profile for the reaction of 2-naphthalenethiolate ion with CEES under the recommended detection conditions is shown in FIG 6. The data show that the reaction is complete in ca. 10 minutes. By comparison, increasing the methanol content of the reagent solution to 90 % increases the time required to complete the reaction to ca. 60 minutes.

Stability Considerations

As of this writing, stability studies have not been completed. Preliminary data, however, indicate that the 254 nm excitation can probably be tolerated if the buffered reagent solution is not continuously irradiated. The data also suggest that the working solution containing 1 M CHES pH 9.75 buffer is subject to oxidation but probably can perform adequately for 1-2 days if contact with air is restricted.

Interferences

Table 3 contains the responses of seven candidate interferents on the detection method. Only dimethylsulfate, a strong alkylating agent, produced a measureable response. A noteworthy negative result is the one obained with bis-(2-hydroxyethyl)sulfide, which is a hydrolysis product of mustard. The latter result indicates that an impurity likely to be found in mustard, its hydrolysis product, is not an interferent.

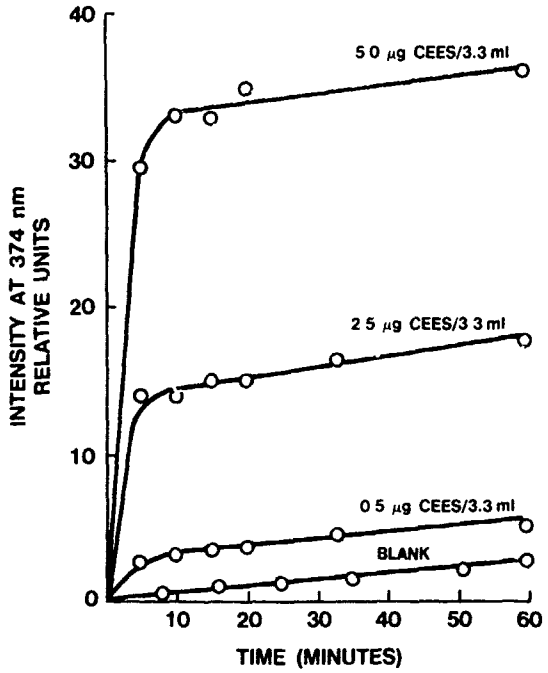

FIGURE 6. REACTION PROFILE FOR REACTION AT 25°C OF 2-NAPHTHALENETHIOLATE ION IN AQUEOUS CHES BUFFER CONTAINING 4% METHANOL WITH THREE DIFFERENT LEVELS OF CEES. EXCITATION WAVELENGTH IS 254 nm.

Table 3

Effect of Candidate Interferents on the 2-Naphthalenethiolate Ion Detection Method

Compound	Net Change in Fluorescence Emission at 374 nm With Excitation at 254 nm (Relative Units)
Bis(2-hydroxyethyl)sulfide	0
2-Chloroethylethylether	0
Bis(2-chloroethyl)ether	0
Methylethylketone	0
Butyl Iodide	0
Ethyl Iodide	0
Dimethyl Sulfate	16.6

Mechanism of the Reaction of 2-Naphthalenethiolate Ion with CEES

While the mechanism of the reaction of 2-naphthalenethiolate ion with CEES has not yet been studied, the positive response obtained with dimethylsulfate coupled with the observation that unionized 2-naphthalenethiol fluoresces strongly near 370 nm while 2-naphthalenethiolate ion does not, suggests that alkylation of the thiolate ion is responsible for the fluorescence response obtained with CEES. This mechanism is also consistent with the strong nucleophilicity of the 2-naphthalenethiolate ion.

CONCLUSIONS

The proposed detection method employing the 2-naphthalenethiol ion for detection of mustard is simple and sensitive. The only interferent is dimethylsulfate, a strong alkylating agent, which is also an interferent in the preferred (frequently used) chromogenic detection method for mustard which uses 4-(4'-nitrobenzyl)-pyridine as the analytical reagent. The proposed detection method, however, has an important advantage over the detection method based on 4-(4'-nitrobenzyl)pyridine because detection is achieved without the requirement for adding a reagent following the incubation with analyte. Also, this detection method, if successfully extended to detection of blister agents, may be suitable for use in the flow cell fiber-optic waveguide detector that has recently been developed for detection of toxins and nerve agents, and may thereby extend its capability.

REFERENCES

1. U.S. Army CRDEC, Research Directorate, Chemical Division, APG, MD 21010-5423.

2. (a) Krieger, W., Rossmann, K., and Diehl, W., German Patent No. 3,344,700, 20 June 1985. (b) Krieger, W., Rossman, K., and Diehl, W., Canadian Patent No. 1,231,634, 19 January 1988. (c) Diehl, W., Detection and Survey of Chemical Warfare Agents Based on Fluorescence Analysis, Proceedings of the Second International Symposium Against Chemical Warfare Agents, Stockholm Sweden, 15-19 June 1986, pp. 173-179.

3. Busey, B.R., Bauldauf, F.C., and Thames, K.E., Fluorometric Detection of Acetylcholinesterase Inhibitors Using a Fiber Optic Waveguide. Proceedings of the 1987 Scientific Conference on Chemical Defense Research, Aberdeen Proving Ground, MD, pp. 329-335, and references therein.

NOVEL GC/FT-IR AND GC/MS TECHNIQUES IN THE ANALYSES OF LASER-INDUCED REACTIONS OF ALCOHOLS

Robert A. Johnson
Research Directorate, AMSMI-RD-RE-QP
Research, Development, and Engineering Center
U.S. Army Missile Command
Redstone Arsenal, AL 35898-5248

ABSTRACT

The objective of this investigation was to utilize the complementary techniques of gas chromatography coupled with Fourier transform infrared (GC/FT-IR) and mass spectroscopy (GC/MS) to analyze the laser-induced reaction of some alcohols. Lightpipe modifications and novel techniques were developed for the GC/FT-IR instruments that enabled the isolation and identification of the resultant reaction product, methoxymethanol. GC/MS data complemented and confirmed the infrared analysis.

INTRODUCTION

In the past this research laboratory investigated the laser-induced dissociation of chemical agent simulants[1-4]. These studies included the laser induced reactions of some alcohols and used Fourier transform infrared spectroscopy to analyze the reactants and products. An interesting consecutive reaction occurred spontaneously between the formaldehyde produced and excess methanol to produce methoxymethanol. The infrared spectra of this ensuing reaction showed the combined absorption bands of methoxymethanol and methanol. Conventional GC/FT-IR techniques produced reconstructed chromatograms with separation between the methanol and methoxymethanol peaks but the infrared spectra of the methoxymethanol was obscured by bands due to formaldehyde and methanol, suggesting the methoxymethanol was decomposing. Through modifications to the commercially available lightpipe and use of new techniques, the infrared spectra of methoxymethanol was recorded.

EXPERIMENTAL

Infrared laser excitation was provided by a Coherent Radiation model 41 continuous wave, tunable, carbon dioxide laser. The laser was operated in a single line mode at various selected wavelengths and powers, depending on the alcohol. Only gas phase reactions were investigated. Product/reactant separation was accomplished using Hewlett-Packard model 5890 gas chromatographs. A Mattson Sirius 100 Fourier transform infrared spectrometer with their gold

coated LYRA lightpipe coupled to the chromatograph was used to record the infrared spectra. A Hewlett-Packard model 5970 mass selective detector interfaced to the chromatograph was utilized to obtain mass spectra. All were commercially obtained. Reactions were conducted in a stainless steel sample cell with dimensions 10 x 6 x 6 cm with an optical pathlength of 9.5 cm.

Modifications to both GC instruments included installation of a Valco 6-port gas sampling valve for the introduction of samples. The lightpipe compartment was modified to allow a coolant reservoir to contact and cool the lightpipe without affecting the nitrogen-purged environment. Also the interface between the lightpipe and chromatograph was externally cooled. Coolant used in this investigation was DRY ICE.

RESULTS AND DISCUSSION

This laboratory successfully demonstrated the laser-induced destruction of alcohols as reported in reference 1. The alcohols investigated were methanol, ethanol, 1-propanol and 2-propanol. The study on methanol reactions was extensive in itself and will be reported in the next paragraph. The other three alcohols all produced similar results, each yielding methane, acetylene and ethylene. The primary alcohols produced acetaldehyde while 2-propanol produced acetone. There was no evidence of any consecutive reactions occurring. Figure 1 shows the infrared spectra of ethanol before (A) and after (B) laser irradiation. The new bands at 1746, 1306, and 949 cm^{-1} are the products acetaldehyde, methane, and ethylene, respectively. Mass spectral data obtained from the GC/MS analysis supported these findings. A typical representation of data of the mass spectra (A) and chromatogram (B) is shown in Figure 2, which is the chromatogram of the laser-induced reaction of 1-propanol and the mass spectra of the acetaldehyde peak.

The laser-induced reaction of methanol produced formaldehyde, as well as methane and carbon monoxide. The interesting difference in this reaction was the ensuing reaction of formaldehyde with excess methanol to yield methoxymethanol. The infrared spectra obtained by this author in the past was that with combined absorption bands due to both methanol and methoxymethanol, these bands in the fingerprint region overlapped and made it impossible to identify all the methoxymethanol bands.

The challenge to record the infrared spectra of just methoxymethanol led to further investigations utilizing GC/FT-IR instrumentation and techniques. These conventional techniques did present a reconstructed chromatogram with baseline separation between the methanol and methoxymethanol peaks. However, upon investigation of the infrared spectra of that methoxymethanol peak, only bands due to methanol and formaldehyde were identified. This suggested the decomposition of methoxymethanol, yielding methanol and formaldehyde (Figure 3).

Lowering the temperature of the lightpipe initially made little difference in the decomposition. It appeared that sub-ambient temperature might be worth trying, so this author modified the lightpipe compartment to allow access to the lightpipe to place a coolant tray directly onto the lightpipe to allow sub-ambient cooling, yet maintain the nitrogen-purged environment of the lightpipe. DRY ICE was the coolant used in this particular study and the temperature was below -18°C. This, combined with an ambient temperature injection port and the cryogenically controlled oven at 0° or 10°C produced successful results. The interface columns between the gas chromatograph and the lightpipe were cooled to -16°C with DRY ICE also. Figure 4 shows

the infrared spectrum of the methoxymethanol peak at a resolution of 4 cm^{-1}. There was no significant decomposition noticed.

CONCLUSION

This low temperature lightpipe technique has afforded this laboratory the ability to record the infrared spectra of an elusive and unstable reaction product. The cryogenic chromatograph oven and this GC/FT-IR technique are quite complementary and should be useful for many applications. The analyses of the higher resolution spectra of the normal and deuterated modifications will be the subject of another article.

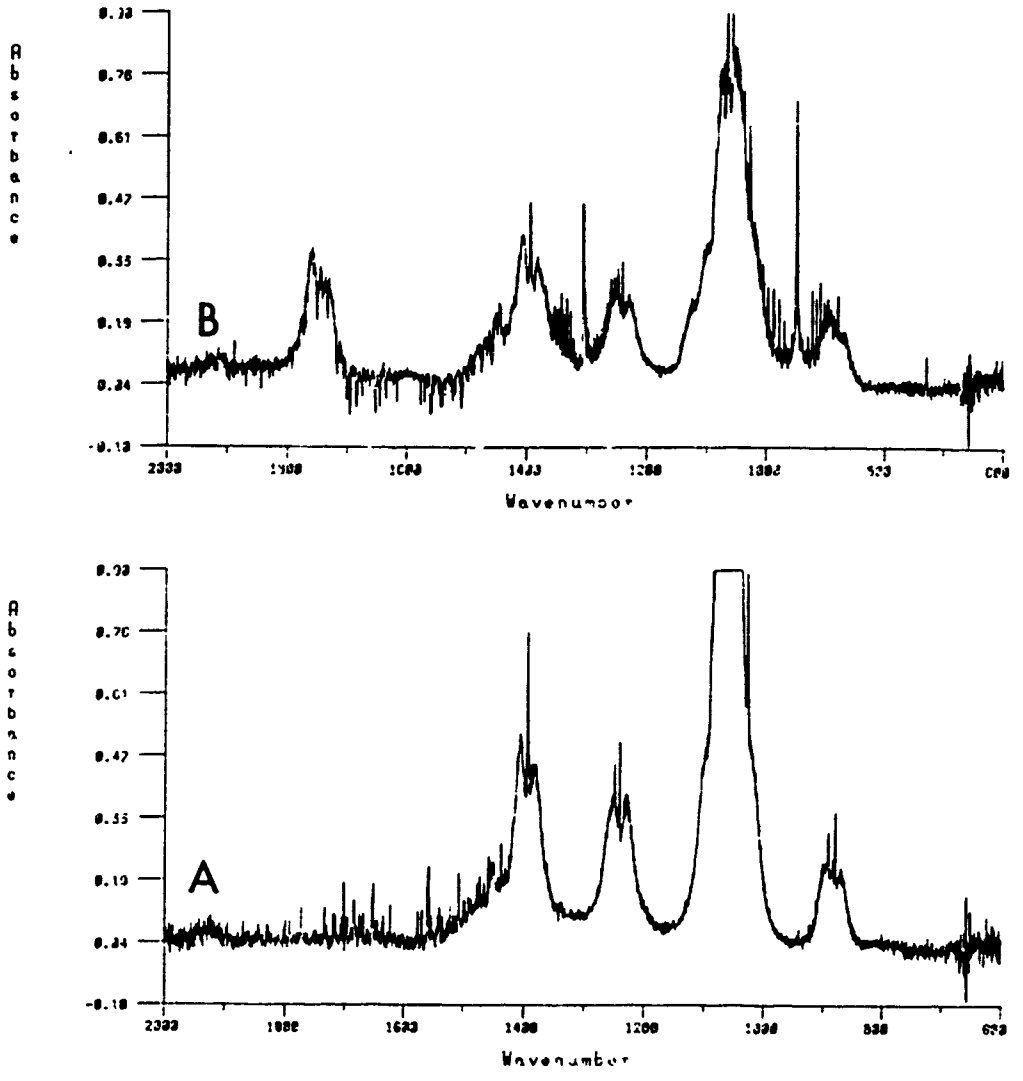

Fig. 1. Infrared spectra of ethanol, before (A) and after (B) laser irradiation.

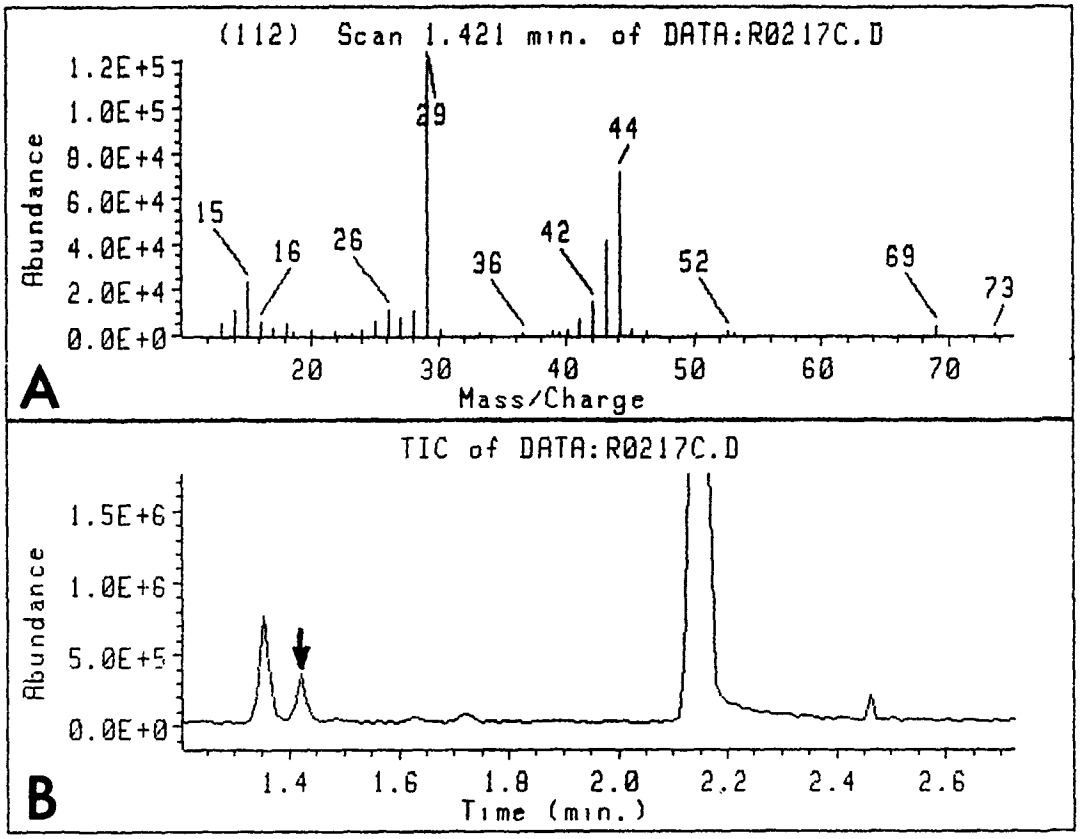

Fig. 2. GC/MS of the laser-induced reaction of 1-propanol.

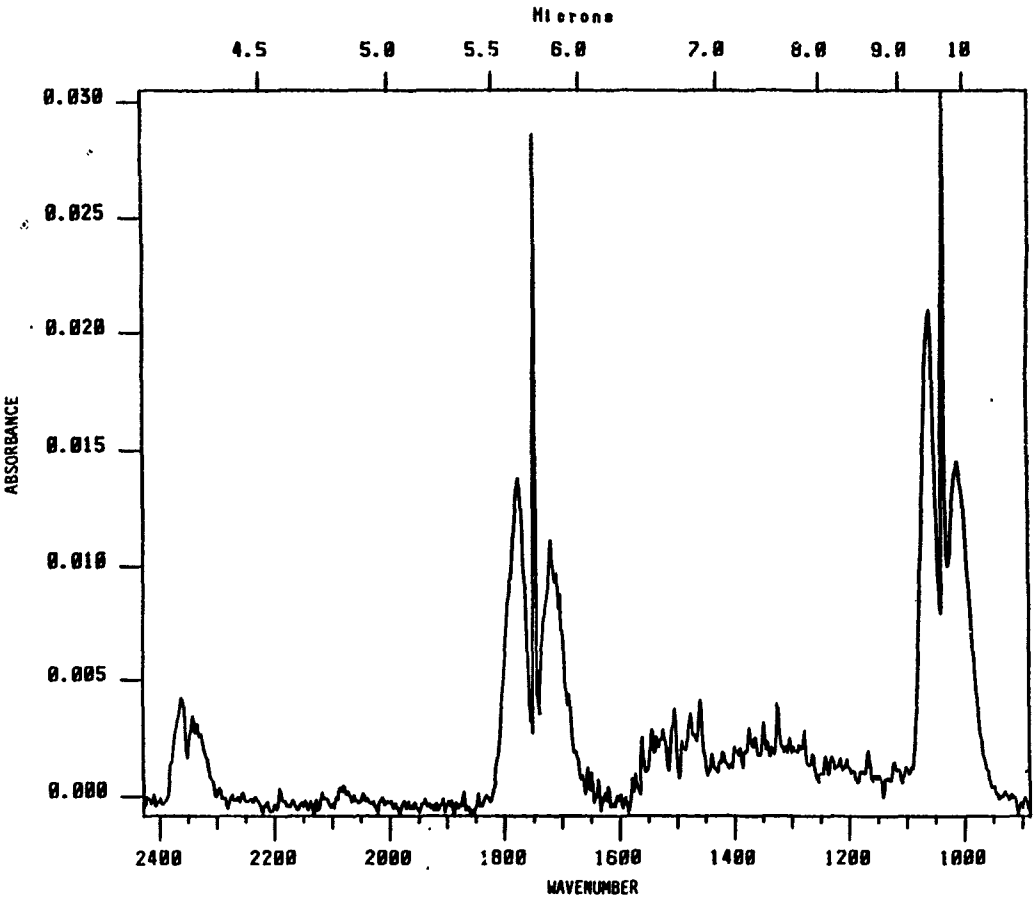

Fig. 3. Infrared spectra of the methoxymethanol peak, lightpipe at 125°C.

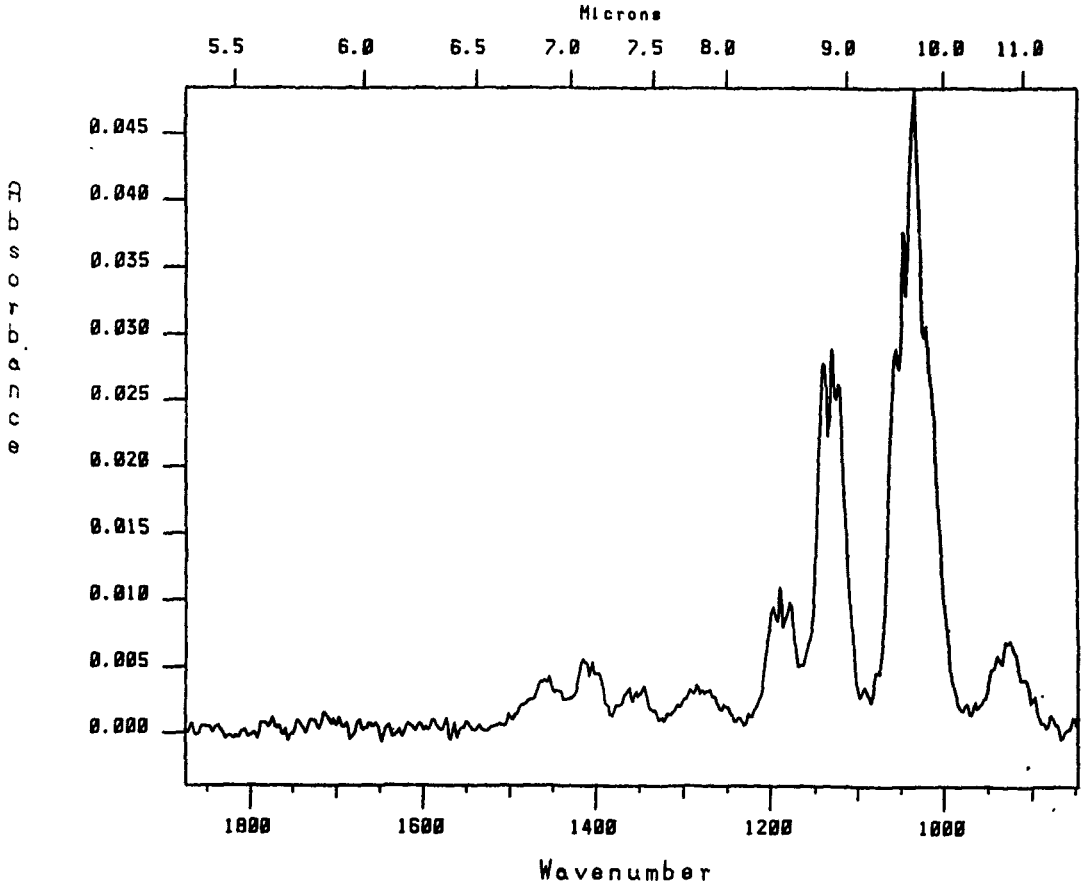

Fig. 4. Infrared spectra of the methoxymethanol peak, lightpipe at -16°C.

REFERENCES

1. Johnson, R. A. and Stanley, A. E., *Laser-Induced Destruction of Some Chemical Agent Simulants: The Alcohols*, Technical Report RD-RE-87-2, U.S. Army Missile Command, Redstone Arsenal, AL, February 1987.

2. Johnson, R. A. and Stanley, A. E., *Laser-Induced Photochemical Reactions of Methanol, Ethanol, 1-Propanol, and 2-Propanol*, Appl. Spectrosc. 42, 1268 (1988).

3. Stanley, A. E., *Laser-Induced Destruction of Some Chemical Agent Simulants: Dimethylmethylphosphonate, Di-Isopropylmethylphosphonate and Trimethylphosphate*, Technical Report RE-86-13, U.S. Army Missile Command, Redstone Arsenal, AL, September 1986.

4. Stanley, A. E., *Laser-Induced Chemistry of the Chemical Agent Simulant: Methylphosphonic Difluoride*, Technical Report RE-86-15, U.S. Army Missile Command, Redstone Arsenal, AL, November 1986.

DETERMINATION OF THE FRAGMENTATION MECHANISMS OF ORGANOPHOSPHORUS IONS BY H_2O AND D_2O ATMOSPHERIC PRESSURE IONIZATION TANDEM MASS SPECTROMETRY

A. Peter Snyder and Charles S. Harden
U.S. Army Chemical Research, Development and Engineering Center
SMCCR-RSL, Aberdeen Proving Ground, MD 21010-5423

ABSTRACT

Dimethylphosphonate (DMMP), dimethylphosphite (DMPI), trimethylphosphite (TMPI) and trimethylphosphate (TMP) were investigated with H_2O and D_2O atmospheric pressure ionization tandem mass spectrometry. All daughter ions could be explained by one or a successive number of stable molecule losses as opposed to radical losses such as the hydride, methyl and methoxy species. Methanol and dimethylether neutral losses and protonated methanol and formaldehyde ions were observed from all four organophosphorus pseudomolecular ions. The DMMP and DMPI MH^+ pseudomolecular ions produced the C_2H_6 and water neutral losses, respectively. Formaldehyde loss was not observed for the MH^+ ions, however, it was well represented in the decomposition pathways of daughter ions. The D_2O reagent gas highlighted the role of the ionizing proton/deuteron in the various daughter ions including m/z 95, 79, 65, 49, 33, 31 and 47. The latter ion was found to be isobaric in that m/z 47 and 48 both appeared with similar abundances in the D_2O-API daughter ion mass spectra of TMPI and TMP.

INTRODUCTION

Organophosphorus compounds are an important commodity in the industrial and commercial economic sectors. Their detection and identification, particularly at trace levels, are high priority concerns within various regulatory and consumer protection agencies. Foodstuff, water and soil contamination by agricultural use of organophosphorus pesticides are issues that have mobilized and coalesced laboratory-based research, environmental monitoring and trace detection and identification efforts in a number of scientific areas. Tandem mass spectrometry techniques (MS/MS) offer advantages in detection and identification because they are characterized by a relatively high degree of sensitivity, selectivity and speed of analysis.[1]

Relatively few daughter ion analyses have been reported on the electron ionization (EI) of the most basic organophosphorus compounds such as dimethylmethylphosphonate (DMMP),[2] dimethylphosphite (DMPI)[3,4] and trimethylphosphite (TMPI).[2] Decomposition of the molecular ions (M^+) under collision-induced dissociation (CID) proceeded by the loss of radicals such as hydride, methyl and methoxy groups. Formaldehyde loss was also observed from the ionized molecular ions. Isobutane chemical ionization (CI)-MS/MS analyses were conducted with DMMP and TMPI and radical losses as well as formaldehyde and methanol stable molecule losses were used to explain the observed daughter ions.[2]

An important adjunct in CI-MS analyses in a series of papers by Hunt et al.[5-7] was the comparison of reagent gases and their deuterated analogues (e.g. D_2O, EtOD or ND_3) in the determination of acidic protons in organic compounds with a variety of acidic functional groups. Harrison and Ichikawa[8] used the H_2, D_2 and CH_4, CD_4 reagent gases in CI-MS with olefinic esters in a determination of their fragmentation pathways. Zitrin[9] used CD_4

and iso-C_4D_{10} in the determination of decomposition mechanisms and identification of ion structures from the cyclotrimethylenetrinitramine (RDX) energetic material.

With the exception of dimethylmorpholinophosphoramidate[10], daughter ion mass spectra of the pseudomolecular ions of organophosphorus compounds have not been reported in the literature under atmospheric pressure ionization (API) conditions. A high degree of sensitivity characterizes the formation of organophosphorus pseudomolecular ion species under API conditions which allow for convenient detection characteristics.[11-13] The present report focuses on the investigations of DMMP, DMPI, TMPI and trimethylphosphate (TMP) for their API-MS/MS response and pseudomolecular ion CID fragmentation pathways. A comparison of H_2O- and D_2O-API daughter ion mass spectra revealed insights with respect to the role of the ionizing proton in the individual daughter ions and in the presence of isobaric daughter ions.

EXPERIMENTAL

A TAGA 6000 API triple quadrupole mass spectrometer system (Sciex, Thornhill, Ontario, Canada, L3T 1P2) was used for analyses of the organophosphorus compounds. General operating procedures for the API-MS/MS system can be found elsewhere[10,13,14] and a schematic of the ion source and ion lens assembly has been published.[15,16] The specific voltage conditions for the present study are as follows: potential difference between the point (needle) and plane (interface), 2400V; lens 1, 80V; lens 2, 64V. The remaining computer-controlled parameters were as follows: ion lenses were (L3) 52V, (L4) 35V, (L5) -250V, (L6) 25V, (L10) 100V; quadrupole 1, 2, and 3 rod offsets were +45, 0 and auto adjust, respectively, quadrupole 1 and 3 resolution values were both 130V. Normal operating pressure in the MS mode was 2.5 - 3.0 x 10^{-6} Torr and all daughter ion analyses were obtained with a collision gas target thickness of 6.1 x 10^{14} molecules cm^{-2} (equivalent pressure 1.2 x 10^{-3} Torr) with ultra-high purity argon collision gas. For analyte and D_2O delivery into the API source, a glass tube was stoppered on one end and the open end was inserted into the five liter ion source canister. Two sidearms extended from the glass tube. One was for D_2O delivery and the other was used for the placement of a vial with the organophosphorus compound. The vial-sidearm tube was sealed with Parafilm (American Can Co., Greenwich, CT 06830) and the exhaust motor of the ion source was turned on to facilitate analyte and D_2O entry into the ion source. Ultra-high purity nitrogen (Matheson Gas Products, Dorsey, MD 21227) was bubbled through approximately 10 mL of D_2O (Alfa Products, Danvers, MA 01923) with a Chemical Data Systems Model 330 Sample Concentrator Sparger assembly (Oxford, PA 19363), and the D_2O vapor was directed into the glass tube sidearm via a short piece of plastic tubing. DMPI and TMP were purchased from Aldrich Chemical Co., Inc., Milwaukee, WI 53233. DMMP and TMPI were obtained from Alfa Products, Danvers, MA 01923 and Fluka Chemical Corporation, Ronkonkoma, NY 11779, respectively.

MH^+ and MD^+ daughter ion mass spectra were obtained for the four organophosphorus compounds. Because of the 1 u proximity of the MH^+/MD^+ species, their ion profiles were adjusted such that a less than 10% overlap occurred with a peak width at half-height of less than 0.6 u.

RESULTS AND DISCUSSION

Water vapor is an ubiquitous constituent in an APCI source; in the positive ion mode, it is the main reagent ion. The m/z 19, 37, 55 and 73

reagent ions representing $(H_2O)_nH^+$, n = 1-4, were readily apparent. After approximately 2 hr of conditioning the APCI source with D_2O, a typical reagent ion distribution was as follows (m/z, percent abundance): 19(79), 20(58), 21(25), 22(6), 37(100), 38(75), 39(29), 40(6), 55(8), 56(12), 57(17), 58(6) and 59(8). It required approximately 8 hr of D_2O conditioning in order to shift the proton hydrate ion distribution to the following: 19(5), 20(24), 21(38), 22(17), 37(7), 38(33), 39(81), 40(100), 41(59), 42(17), 55(0), 56(5), 57(24), 58(24), 59(31), 60(26), 61(9) and 62(2). In practice, however, it was found that within 10 min of introducing the sample into the D_2O vapor stream under either of the H_2O/D_2O reagent ion distribution conditions, similar intensities were observed for the MH^+ and MD^+ species.

DMPI. Figure 1 presents the MH^+ and MD^+ daughter ion mass spectra of DMPI and Scheme 1 depicts the CID fragmentation pathways of the m/z 111/112 parent ions. The notation m/z 111/112 indicates that m/z 111 is observed in the MH^+ daughter ion mass spectrum while m/z 112 is observed in the MD^+ daughter ion mass spectrum and the asterisk denotes an ion source proton and deuteron in the MH^+ and MD^+ daughter ion mass spectra, respectively. DMPI can exist as the phosphite species as well as the dimethyl hydrogen phosphonate isomer. In a series of papers, Cooks et al.[3,4] illustrated that under multiple collision conditions in the MS/MS mode, the DMPI isomer was the preferred structural isomer. The 6.1×10^{14} molecules cm^{-2} CID gas target thickness of the present study ensures that multiple collision conditions predominate for a DMPI analysis. The ion source proton can protonate both the hydroxyl and methoxy oxygen atoms. HOH^* loss (Scheme 1) can lead to m/z 93, however, this pathway is a low probability decomposition pathway due to the ion's relatively low intensity as observed in Fig. 1. A dimethylether loss from the parent ion can lead to the m/z 65/66 species and a proposed mechanism for the loss of the ether compound is presented in Scheme 1. An interesting occurrence in the MH^* daughter ion mass spectra of DMPI is that m/z 79 is present in the MH^+ case, however, both m/z 79 and 80 are present in the MD^+ daughter ion mass spectrum. This strongly suggests that there are two m/z 79 species, one containing a source proton and the other that does not have the source proton. Scheme 1 offers an explanation of this phenomenon in terms of which acidic proton on the parent ion is found on the methanol leaving group. The intensities of m/z 79 and 80 in the MD^+ daughter ion mass spectrum are approximately the same which infers an almost equal probability of either CH_3OH or CH_3OH^* as the leaving group in the formation of the m/z 79 and 80 species. This is a reasonable assumption because DMPI contains two acidic protons and two methoxy groups. Either hydrogen can occupy either of the two methoxy oxygen atoms. PO^+, m/z 47, can be formed by a number of neutral loss decomposition pathways, and the formation of the m/z 33/34 ions are particularly important for DMPI as compared to DMMP, TMPI, and TMP (Fig. 1). Other ions that are found in the MH^+/MD^+ daughter ion mass spectra of DMPI are m/z 63, 49/50, 31/32 and 15. m/z 63, although minor in intensity, appears to be formed by a formaldehyde loss from m/z 93 (Scheme 1). The m/z 79/80 species containing the source proton can lose CH_2O to form the m/z 49/50 ions $[H^*P(O)H]^+$, respectively, and m/z 79 which does not contain the source proton, can lose a formaldehyde molecule to yield m/z 49, $[H_2PO]^+$ (Table 1). $[H_2PO]^+$ is present in both the MH^+ and MD^+ daughter ion mass spectra. The initial impression of the m/z 31 daughter ion from the MH^+ ion of DMPI is that it can be interpreted as the methoxy ion. However, the corresponding MD^+

daughter ion mass spectrum contains both m/z 31 and 32 and the latter ion indicates the presence of the source deuteron. Therefore m/z 31 and 32 most likely represent the methoxy and deuterated formaldehyde isomer ions, respectively. Thus it appears feasible to expose and identify certain isomeric ions under D_2O APCI-MS/MS conditions.

DMMP. Scheme 2 presents the major stable molecule losses and resulting ions from the CID of the MH^* species of DMMP. There are three primary decomposition pathways for DMMP and involve the loss of dimethylether, methanol and either an ethane or two methyl radicals. Note in particular that in order to produce m/z 93, the acidic proton on the methanol leaving group must originate from the ion source because the MD^+ daughter ion mass spectrum of DMMP in Fig. 1 displays m/z 93 and not m/z 94. This comparison between the MH^+ and MD^+ daughter ion mass spectra of DMMP indicates that the ion source proton is absent from m/z 93. Both m/z 79 and 95 daughter ions retain the ion source proton because they shift to m/z 80 and 96, respectively, in the m/z 126 daughter ion mass spectrum of DMMP. The DMMP decomposition pathway that produces dimethylether appears to involve the migration of the P-CH_3 methyl moiety to one of the methoxy groups. Had a methyl on one methoxy group migrated to the other methoxy group in the formation of the dimethylether, the $[H_3CP(O)OH^*]^+$ species would have resulted. An internal methyl rearrangement in this species prior to a formaldehyde loss would be necessary in order to produce the m/z 49/50 ion, while only a hydrogen migration with a subsequent formaldehyde loss is required in order to form the m/z 49/50 species as outlined in Scheme 2. The formation of the m/z 95/96 ions must occur by a loss of 30 u from the respective MH^+/MD^+ parent and the source proton must be retained on the ions. A formaldehyde loss was postulated and is presented in Scheme 3. An m/z 95/96 structure would result with two acidic protons. These hydrogens would be expected to interconvert and the resulting methanol loss would be expected to yield m/z 64 in addition to m/z 63 (Scheme 3). That both acidic hydrogens would be expected to rapidly exchange with each other has some support from DMPI as noted in Scheme 1. The presence of m/z 79 and m/z 79/80 strongly suggests that both the inherent proton and ionizing deuteron are particularly labile about the deuterated DMPI ion. The MD^+ daughter ion mass spectrum of DMMP in Fig. 1 does not show an m/z 64 ion and thus a formaldehyde loss from the parent DMMP ion was considered unlikely. It is interesting to note that the DMPI and TMP phosphoryl species as well as TMPI do not show a 30 u neutral loss from their respective MH^+/MD^+ ions (Figure 1). An alternative explanation for the 30 u loss from DMMP appears to be an ethane neutral loss, and a decomposition pathway is proposed in Scheme 2. Note that the structure of m/z 95/96 resulting from the ethane neutral loss in Scheme 2 is not an isomer of the postulated isobar in Scheme 3. A methyl loss is not observed from DMMP (Fig. 1) and Scheme 2 shows the ethane loss to occur from the PCH_3 and an OCH_3 group. If the ethane originated from the methyl groups on both methoxy functionalities, the $[H_3CPO_3H^*]^+$ would be produced as the m/z 95/96 ion. In an analogous situation with m/z 79/80, formation of m/z 65/66 would require an internal methyl migration prior to the loss of formaldehyde as opposed to the straightforward hydrogen migration and subsequent loss of CH_2O from m/z 95/96 to form m/z 65/66 (Scheme 2). This tends to argue against the $[H_3CPO_3H^*]^+$ structure for m/z 95/96. This line of reasoning for the phosphoryl methyl loss has found support from several previous investigations. Holtzclaw *et al.*[2] presented evidence that indeed the phosphoryl methyl is lost under EI-MS because

$^{13}CH_3$-P labeled DMMP exhibited an m/z 109 ion while no m/z 110 species was observed. The bond dissociation energy of the P-C and C-O bonds are 65 and 84 kcal $mole^{-1}$, respectively. Using the P-C bond dissociation energy in their calculations, Bafus et al.[17] found that the calculated value of the ionization potential for the m/z 109 ion fragment from DMMP was more similar to their experimentally observed value than that of using the C-O bond dissociation value. Scheme 2 outlines further neutral losses from m/z 93, 79/80 and 65/66 to form the m/z 47 PO^+ species.

Other ions that are observed in the MH^* daughter ion mass spectra of DMMP are m/z 63, 45, 33/34, 31/32 and 15. m/z 63 appears to be generated by a formaldehyde loss from m/z 93 and a proposed mechanism for this decomposition is presented in Scheme 2. m/z 45 can be formed by a loss of water from m/z 63 to yield the $[H_2C{=}P]^+$ ion. This, however, is in contrast to the high resolution EI-MS result[17] in which m/z 45 was due to $C_2H_5O^+$ as opposed to PCH_2^+. m/z 31/32 can be the protonated formaldehyde species, i.e. $[H_2C{=}OH^*]^+$. This latter ion can be produced directly from the parent MH^+/MD^+ and/or from m/z 79/80. Furthermore, in the MD^+ daughter ion mass spectrum of DMMP, a small amount of m/z 31 was observed, which appeared to be the methoxy ion isomer of protonated formaldehyde. Protonated methanol appears to represent the m/z 33/34 species and can be formed directly from the MH^* ion.

TMP. Figure 1 presents the MH^* daughter ion mass spectra of TMP and its CID decomposition pathways are illustrated in Scheme 4. The formation of m/z 109 from m/z 141/142 is a favored pathway because the ion is the base peak in the daughter ion mass spectrum. The m/z 109 ion can be formed by the loss of a CH_3OH^* molecule. m/z 109 can subsequently lose a dimethylether molecule to form m/z 63. The formation of m/z 95/96 from the MH^+ and MD^+ ions can occur from a dimethylether loss and this pair of ions can subsequently lose a CH_3OH^* or a CH_2O molecule to form m/z 63 or m/z 65/66, respectively. TMP displays a similar phenomenon with DMPI in the MH^+/MD^+ daughter ion mass spectra with respect to the m/z 79/80 pair (Fig. 1). However, a comparison of Schemes 4 and 1 shows their formation pathways to be quite different. m/z 79 can be formed from a formaldehyde loss from m/z 109, however, it appears that the formation of m/z 79/80 can only be explained by either successive methoxy losses or by the loss of a dimethylperoxide species from the parent ion. To the best of the authors' knowledge, the latter postulate is unprecedented in organophosphate chemistry and a single methoxy loss is not observed in the TMP mass spectra (Fig. 1), i.e. - m/z 110 is not observed. Therefore it appears that the D_2O reagent ion uncovered the possibility that m/z 79 can be formed by two fragmentation pathways from TMP. One is characterized as a relatively low energy process (CH_3OH^* and OCH_2 losses) and the other appears to be a relatively higher energy process of methoxy losses. Furthermore, m/z 93, even though of minor intensity, can be postulated to arise from either a successive loss of a methoxy and a hydroxyl group or the loss of methylperoxide where both mechanisms include the loss of the source proton (Scheme 4). As with the case of m/z 79/80, the postulated peroxide and/or methoxy loss fragmentation mechanisms yielding m/z 93 are also unprecedented in that structural considerations of TMP lead one to these conclusions. It is unlikely that m/z 93 represents an impurity because it would have to originate as a daughter ion fragment from a compound with a protonated molecular weight of 141. This compound must also have a relatively high proton affinity which is a characteristic of TMP in order to compete for

available protons. It is known that phosphoryl-containing compounds as a class have relatively high proton affinities.[18] m/z 93 can subsequently lose dimethylether to form PO^+ and might lose formaldehyde to form $[HPOCH_3]^+$.

The PO^+ species can be formed from a number of neutral loss pathways as observed in Scheme 4, and the MD^+ daughter ion mass spectrum (Fig. 1) of TMP also shows the presence of an m/z 48. This species cannot represent the protonated PO^+ species, therefore, possible compounds that contain the ion source proton could be either protonated dimethylether and/or the $[H_3CPH^*]^+$ species, the latter of which has not been observed in the alkylorganophosphorus literature to the best of the authors' knowledge. To shed more light on this problem, water chemical ionization of TMP was performed with an in-house designed and constructed Fourier Transform mass spectrometer (FT-MS) system[19] with accurate mass measurements (AMM). An accurate mass determination of PO, PCH_4 and C_2H_7O are 46.969, 47.005 and 47.049. Under H_2O-CI conditions in the FT-MS intensities were observed at AMM of m/z 46.979 and m/z 47.015 which appear to represent the PO^+ and $[H_3CPH^*]^+$ species, respectively. It is unclear as to the mechanism of formation of the latter species and the TMP ion does not contain an inherent P-CH_3 or P-H bond. It is interesting to note that even though DMMP has an inherent P-CH_3 bond, an m/z 48 ion is not observed in its MD^+ daughter ion mass spectrum (Fig. 1).

Other ions that are observed in the daughter ion mass spectra of TMP are m/z 33/34, 31/32 and 15. m/z 33/34 is the protonated methanol species and m/z 31/32 and m/z 31 in the MD^+ spectrum (Fig. 1) appear to originate in a manner similar to that of DMPI.

TMPI. The MH^+ and MD^+ daughter ion mass spectra of TMPI are presented in Fig. 1 and proposed decomposition pathways that yield the CID ion products are shown in Scheme 5. A CH_3OH^* loss can lead to m/z 93 and a dimethylether loss from the MH^+/MD^+ ions can produce m/z 79/80. As with DMPI and TMP, TMPI also has an m/z 79 ion in its MD^+ daughter ion mass spectrum in addition to m/z 80. The mechanism of formation of m/z 79 which does not contain the ion source proton in the MD^+ spectrum is uncertain. Formaldehyde losses from m/z 79/80 and 93 yield m/z 49/50 and 63, respectively (Scheme 5). PO^+ can be formed from both m/z 79/80 and 93 by CH_3OH^* and dimethylether losses, respectively. As with TMP, the MD^+ daughter ion mass spectrum shows an m/z 48 ion and this feature is tentatively identified as the $[H_3CPH^*]^+$ ion pending AMM FT-MS studies. As with TMP, the mechanism of formation of m/z 48 remains uncertain. m/z 31/32, 33/34 and 15 are also observed in the daughter ion mass spectra of TMPI. m/z 33/34 can be produced by the formation of protonated methanol from the parent ion, and m/z 31/32 and m/z 31 in the MD^+ daughter ion mass spectrum appear to be formed in a fashion analogous to DMPI.

Diagnostic Aids for Methylphosphoryl-based Compounds. The daughter ion mass spectra of DMPI, DMMP, TMP, and TMPI show similarities and differences and with the aid of the D_2O reagent ion, certain criteria can be proposed that lend themselves to the analytical investigation of organophosphorus compounds in various matrices. The use of tandem mass spectrometry is certainly attractive in terms of isolating a specific pseudomolecular ion of interest. Key fragment ions that are generally found (Fig. 1) are m/z 15, 63 and 93. The presence of these ions can provide a first impression in terms of the possible presence of a methylphosphoryl moiety. m/z 65 can be recognized generally as the hypophosphite ion, $(PH_2O_2^+)$. With the inclusion of D_2O as the reagent ion the potential of a more selective set of criteria

is introduced. For example, the presence of m/z 47 and 48 in an APCI-daughter ion mass spectrum can indicate a methylphosphorus-based compound, and the presence of m/z 79 and 80 in the same MS/MS mass spectrum can signify a methylhypophosphite moiety. Along with the pseudomolecular ion, the multiplicity of daughter ion fragment markers can provide clues as to the presence of the organophosphorus compounds in a diverse array of matrices. It appears that D_2O as the reagent gas can provide a relative degree of specificity that is not available with H_2O alone.

CONCLUSIONS

Information-rich daughter ion mass spectra were produced from DMPI, DMMP, TMPI and TMP when these compounds were processed under API conditions. Virtually all daughter ions could be explained as a result of stable molecule losses as opposed to neutral radical losses which are commonplace under EI as well as isobutane CI conditions[2]. Formaldehyde losses were not observed from the pseudomolecular ions, however, methanol and dimethylether neutral losses and protonated methanol and formaldehyde ions were observed to occur from the MH^+/MD^+ ions of the four organophosphorus compounds. Water and ethane neutral losses appeared to occur from the DMPI and DMMP pseudomolecular ions, respectively. D_2O proved particularly useful as a reagent gas in that the role of the ionizing proton could be clearly observed with respect to its occurrence in certain of the daughter ions. Moreover, D_2O uncovered the fact that two ions were formed with a nominal mass of m/z 47 for TMPI and TMP. AMM with an FT-MS for TMP showed that the two masses were the expected PO^+ ion and the unexpected $[H_3CPH^*]^+$ species. All four compounds could yield the m/z 63 PO_2^+ and $[H_3COP]H^+$ or $[H_3CPO]H^+$ ion structures by plausible decomposition pathways and work is continuing on AMM FT-MS studies to test these assumptions.

ACKNOWLEDGEMENTS

The authors wish to thank C.C. Chou for the Fourier Transform MS/MS analyses and Ms. Linda Jarvis for the preparation and editing of the manuscript, figures and the schematic decomposition pathways.

REFERENCES

1. J. Johnson and R. Yost, Anal. Chem. 57, 758A (1985).
2. J.R. Holtzclaw, J.R. Wyatt and J.E. Campana, Org. Mass Spectrom. 20, 90 (1985).
3. H.I. Kenttamaa and R.G. Cooks, J. Am. Chem. Soc. 107, 1881 (1985).
4. J.S. Brodbelt, H.I. Kenttamaa and R.G. Cooks, Org. Mass Spectrom. 23, 6 (1988).
5. D.F. Hunt, C.N. McEwen and R.A. Upham, Tetrahedron Lett. 4539 (1971).
6. D.F. Hunt, C.N. McEwen and R.A. Upham, Anal. Chem. 44, 1292 (1972).
7. D.F. Hunt and S.K. Sethl, J. Am. Chem. Soc. 102, 6953 (1980).
8. A.G. Harrison and H. Ichikawa, Org. Mass Spectrom. 15, 24[illegible] (1980).
9. S. Zitrin, Org. Mass Spectrom. 17, 74 (1982).
10. P.H. Dawson, J.B. French, J.A. Buckley, D.J. Douglas, and D. Simmons, Org. Mass Spectrom., 17, 212 (1982).
11. J.P. Carrico, A.W. Davis, D.N. Campbell J.E. Roehl, G.R. Sima, G.E. Spangler, K.N. Vora and R.J. White, Am. Lab. 18, 152 (1986).
12. S.N. Ketkar, J.G. Dulak, W.L. Fite, J.D. Buchner and S. Dheandhanoo, Anal. Chem. 61, 260 (1989).

13. P.H. Dawson, J.B. French, J.A. Buckley, D.J. Douglas and D. Simmons, Org. Mass Spectrom., 17, 205 (1982).
14. V.J. Caldecourt, D. Zakett and J.C. Tou, Int. J. Mass Spectrom. Ion Phys. 49, 233 (1983).
15. A.P. Snyder, J.H. Kremer, H.L.C. Meuzelaar, W. Windig and K. Taghizadeh, Anal. Chem. 59, 1945 (1987).
16. S.A. Liebman, A.P. Snyder, J.H. Kremer, D.J. Reutter, M.A. Schroeder and R.A. Fifer, J. Anal. Appl. Pyrolysis 12, 83 (1987).
17. D.A. Bafus, E.J. Gallegos and R.W. Kiser, J. Phys. Chem. 70, 2614 (1966).
18. R.V. Hodges, T.J. McDonnell and J.L. Beauchamp, J. Am. Chem. Soc. 102, 1327 (1980).
19. C.C. Chou, Int. J. Mass Spectrom. Ion Processes, submitted for publication.

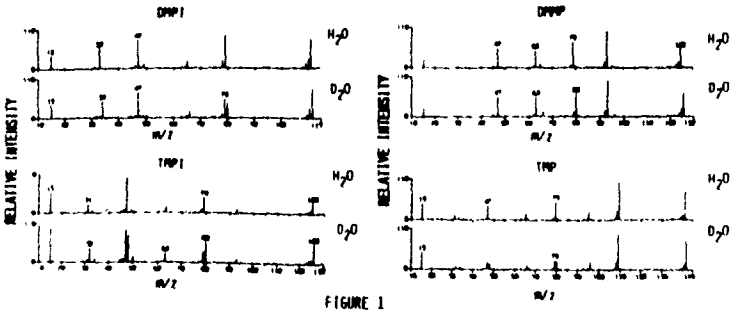

FIGURE 1

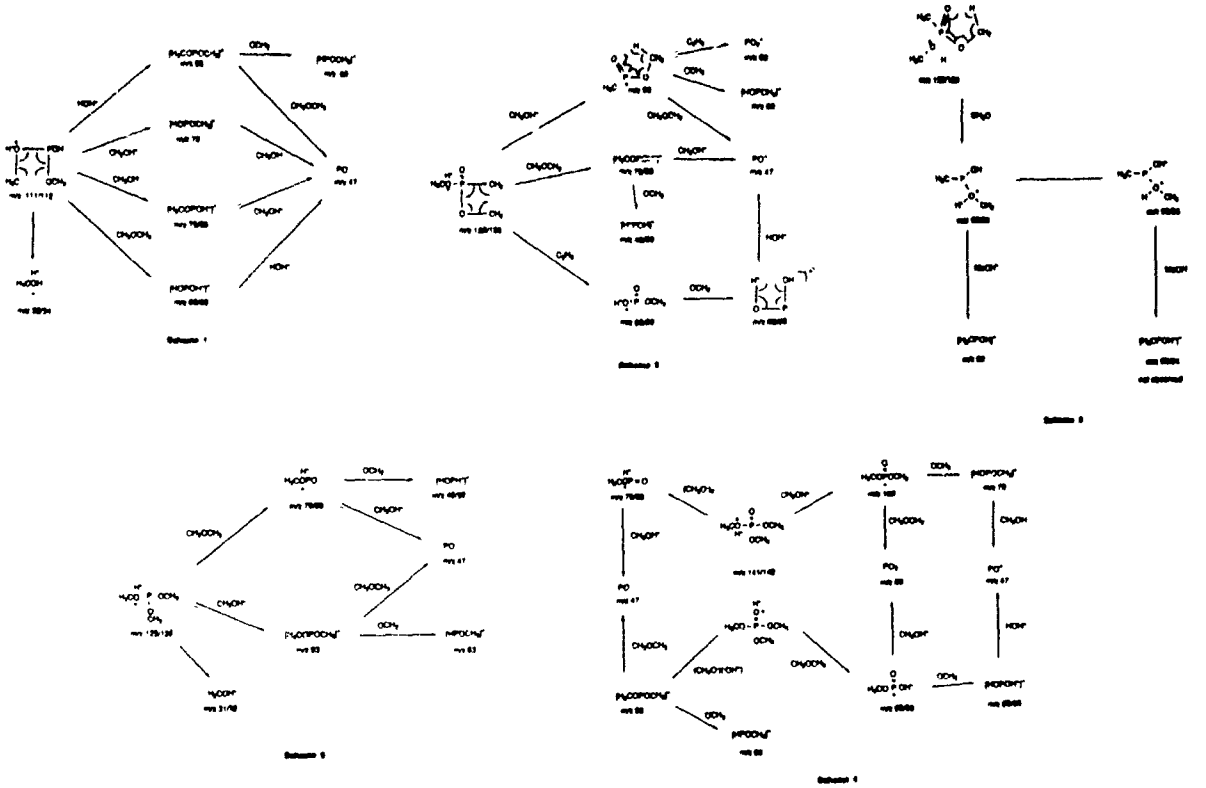

SURFACE ACOUSTIC WAVE AND CHEMIRESISTOR RESPONSES TO VAPOR CHALLENGES USING ARYLPHOSPHONIC ACIDS, SALTS, AND ESTERS AS MICROSENSOR COATINGS

Alan R. Katritzky, G. Paul Savage, Rick J. Offerman, and Boguslaw Pilarski*

Department of Chemistry, University of Florida
Gainesville, FL 32611

Research Funded by: CRDEC

ABSTRACT: New coatings for surface acoustic wave and chemiresistor devices were investigated to maximize the selective detection and reversible monitoring of two chemical warfare agent simulants.

A variety of phosphonic acids, phosphonate esters and cyclohexylammonium phosphonic salts were spray-coated onto surface acoustic wave (SAW) devices and exposed in turn to vapor challenges of chloroethyl ethyl sulfide (CEES), dimethyl methylphosphonate (DMMP), and water. Changes in the resonant frequency of the device or the resistance of the coating were monitored by computer controlled data acquisition.

Two of the esters showed major potential for reversible and selective CEES detection, and one of the acids displayed similar behavior for DMMP. One salt gave a large reversible chemiresistor response (from 200 GΩ to 500 kΩ) to water vapor.

INTRODUCTION

The relatively new field of chemical microsensors is concerned with detection devices whose selectivity and sensitivity rely on various properties of a thin coating of an organic or inorganic film. Ideally the coating should selectively and reversibly absorb a given contaminant so as to cause a measurable change in some physical property of the device. A number of existing devices currently exploit this technology including surface acoustic wave (SAW), chemiresistor, and optical waveguide devices.[1-3]

Both SAW and chemiresistor devices are manufactured from piezoelectric quartz and have a gold interdigital electrode array which is lithographically fabricated onto the surface of the quartz crystal.[4,5] The chemiresistor device experiences a change in the resistance between the interdigital electrodes on the surface of the device upon exposure of a thin film of semiconducting coating to a vapor challenge. In a SAW device, changes in the resonant frequency of the device are monitored upon vapor exposure.[4-8] This frequency variation is essentially related to the mass uptake of the coating on the surface of the device. The characteristic resonant frequency of the device is dependent on the electrode geometry, and is sensitive to small mass changes on the surface which are readily observed as a shift in this resonant frequency. The mode of operation of these devices has been described in detail elsewhere.[8]

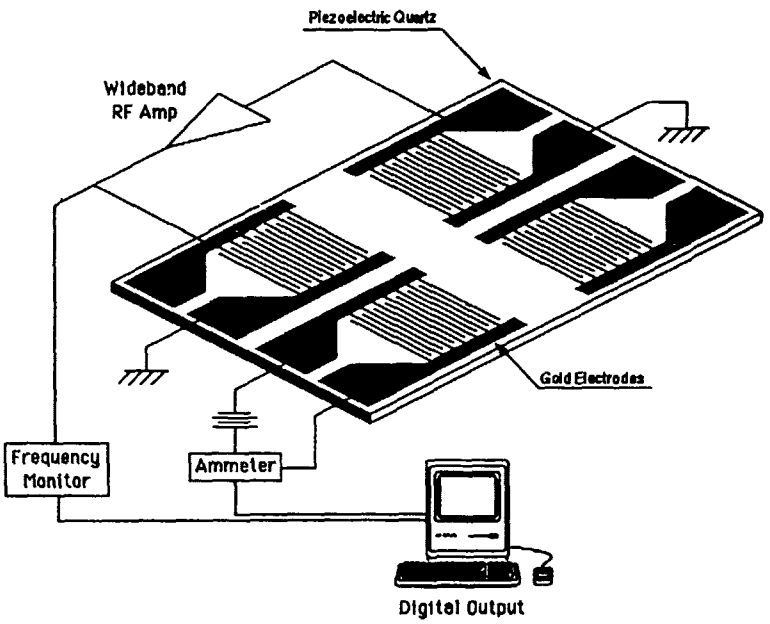

SAW devices are similar to bulk wave piezoelectric quartz crystal sensors[9,10] but are more sensitive due to their higher operating frequencies. They are also of smaller size, easier to coat and are more rugged. Unlike a chemiresistor device which can only be used for resistance measurements, a SAW device with the appropriate electronics allows resistance and frequency measurements to be conducted simultaneously (Figure 1).

There are two basic areas to be addressed in the development of chemical microsensors. One involves the interface or surface problems associated with the effective and reproducible application of the coating materials to small electronic devices to take maximum advantage of the chemical properties of the coating. The second is the planning, synthesis, and

characterization of new coating materials that conform with the requirements of the former area. These requirements include chemical stability for the anticipated operational lifetime of the chemical sensor.

A variety of compounds have been employed as coatings for SAW and bulk piezoelectric devices.[11] Many of these materials however, have not been adequately characterized in the open literature and therefore remain of an ill-defined nature. For this reason it is still difficult to use literature precedent to predict coatings of high selectivity and sensitivity. To date, no systematic approach has been taken for the identification or development of new microsensor coatings and the primary criterion for selection of coatings for SAW devices appears to be the perceived solubility of the vapor to be detected in the coating.[12] Chemiresistors have been investigated for many years, however, reports on the use of *selective* coatings for chemiresistor devices are few in number.[5,6,13] It is this lack of adequate coating materials that has impeded the successful development and utilization of chemical microsensors.

Our interests lie in the synthesis and testing of novel organic compounds that may be suitable coatings for the sensitive and selective detection of CEES (a sulfur mustard simulant), and DMMP (a nerve agent simulant) vapors. Previous work[1] in our Laboratory on microsensor coatings was focused on utilizing pyridinium compounds (pyridine 1-oxides, pyridinium salts and betaines), and met with some success. As mentioned, the mass uptake on the surface of the device seems to be associated with the solubility of the vapor challenge in the coating material:[12] therefore, phosphonate esters and phosphonic acids are promising candidates for such coatings, as the solubility of DMMP in such materials is expected to be high. For the same reason it was envisaged that such coatings would show good discrimination between DMMP and a given interferent (e.g. water). To that end we prepared and characterized a number of phenylphosphonate esters, the corresponding acids (if stable), and their cyclohexylammonium salts, together with some diethyl benzylphosphonates and benzylphosphonic acids. These compounds, along with various commercially available benzyl- and phenyl-phosphonic acid derivatives which were also tested in this study, are shown in Figure 2.

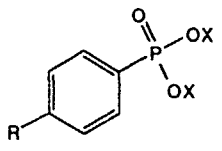

1

a R = H, X = H
b R = NH_2, X = H
c. R = NMe_2, X = cy-$C_6H_{11}NH_3$
d. R = H, X = p-NO_2Ph
e. R = H, X = Et
f R = NMe_2, X = Et
g. R = CN, X = Et
h R = CO_2H, X = H
i R = H, X = $^nC_8H_{17}$

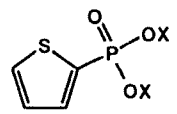

2

a. X = Et
b X = cy-$C_6H_{11}NH_3$

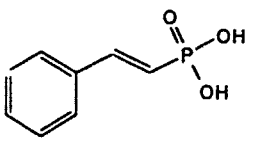

3

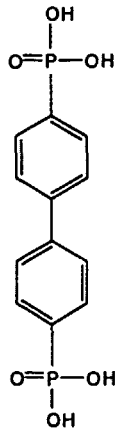

4

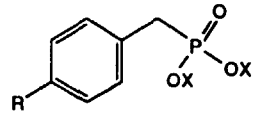

5

a. R = Me, X = Et
b. R = Me, X = H
c. R = NO_2, X = Et
d. R = NO_2, X = H
e. R = H, X = Et
f R = H, X = H
g R = Cl, X = H
h. R = OMe, X = H
i R = ^{t}Bu, X = H

FIGURE 2

A number of methods are routinely used to apply coatings to microsensor devices and the choice of a particular coating technique can sometimes influence the choice of a coating and vice versa. Among these techniques are sublimation,[14] spin coating,[14] spray coating[6] and the Langmuir-Blodgett technique.[5,14-16] The L-B technique applies the coating to the device in ordered monolayers;[15] however, sophisticated equipment is required for this method.

The present work utilized the spray coating method. The material to be applied was dissolved in a suitable volatile organic solvent and aspirated, with an air brush, onto the surface of the SAW device. After deposition of the fine aerosol, a drying period was allowed (depending on the volatility of the solvent) before the commencement of measurements. Most coatings can be applied by this fast, reproducible, and versatile technique.

EXPERIMENTAL SECTION

Simultaneous chemiresistor and SAW measurements were performed while exposing the device (in turn) to DMMP, CEES and water vapors. The dual 52 MHz surface acoustic wave apparatus used (Microsensor Systems, Inc.), has been described in detail previously.[11] The quartz device was coated after placing it in a machined teflon housing, in which provision had been made for pressure clip connections to the interdigital electrodes. The original pressure clips, supplied with the apparatus, were replaced by new clips, fabricated from 0.2 mm platinum wire, to avoid the surface corrosion that leads to poor electrical contact.

The resonant frequency was monitored with a digital frequency counter, Phillips Model PM 6674 universal frequency counter (550 MHz). The conductivity measurements were made by the application of a 1-V bias to either of the two remaining electrodes, and measurement of the current. The precision current to voltage converter used consisted of an operational amplifier and a switch selectable feedback resistor.

The coatings were dissolved in a volatile organic solvent, typically spectroscopic grade dichloromethane, and the device was spray-coated with an air brush using dry nitrogen as the propellent. The coating thickness was monitored via the frequency counter until a frequency shift of *ca* 50 kHz was obtained. The frequency shifts caused by the coating were recorded as an indication of coating thickness. Vapor challenges were generated by passing a regulated flow of nitrogen through the neat liquid at 0 °C, in a vapor bubbler equipped with a gas dispersion tube. The flow rate over the device was controlled with a flow meter and was determined to be 7.5 ml/min using a bubble meter. The vapor pressures of the liquids at 0 °C were calculated using the following formula:

$$\log P = 2.8808 - \frac{\Phi \Delta t}{T - 0.15 \Delta t}$$

where T = temperature (Kelvin) at which P is to be calculated, P = vapor pressure (mmHg) at temperature T, Φ = entropy of vaporization at 760 mmHg, and Δt = boiling point of liquid (at 760 mmHg) – T.

Assuming the Ideal Gas Law holds, at 0 °C, the vapor concentration of DMMP is 5 gm^{-3}, the vapor concentration of CEES is 33 gm^{-3}, and the vapor concentration of water is 4 gm^{-3}.

Initially the system was purged with nitrogen for 5 min to establish a baseline curve. The device was then exposed to the vapor for 40 min and this was followed by a nitrogen purge for 50-60 min. If a response was irreversible, the SAW device was cleaned and recoated before exposure to the next vapor challenge. The SAW devices were rinsed between runs with acetone, and this was followed by ultrasonic cleaning for 10 min in spectroscopic grade isopropanol.

All compounds, including those commercially obtained, were characterized by their ^{1}H n.m.r. and ^{13}C n.m.r spectra, and by their melting points for the solids. Correct elemental analyses were obtained for all the novel compounds synthesized.

RESULTS AND DISCUSSION

Responses of the various coatings to vapor challenges are recorded in Table 1. The frequency shifts were calculated by subtracting the lowest frequency recorded during vapor exposure from the initial (baseline) frequency. Resistance changes were calculated by dividing the initial, baseline resistance (usually in the order of 10^{10} Ω) by the lowest resistance recorded during exposure to the vapor challenge. Thus, for the resistance factors, a value close to unity essentially denotes no change. Values marked with an asterisk indicate responses that were irreversible. Results were reproducible to ± 5%.

As can be seen from Table 1, diethyl 4-(N,N-dimethylamino)phenylphosphonate **1f** gave a frequency shift of 77 kHz upon exposure to CEES, and showed satisfactory discrimination, with shifts of only 14 kHz and 21 kHz to water and to DMMP, respectively. Diethyl 2-thienylphosphonate **2a** also showed a large response to CEES vapor (66 kHz), and importantly displayed excellent discriminating power with negligible responses to either water or DMMP.

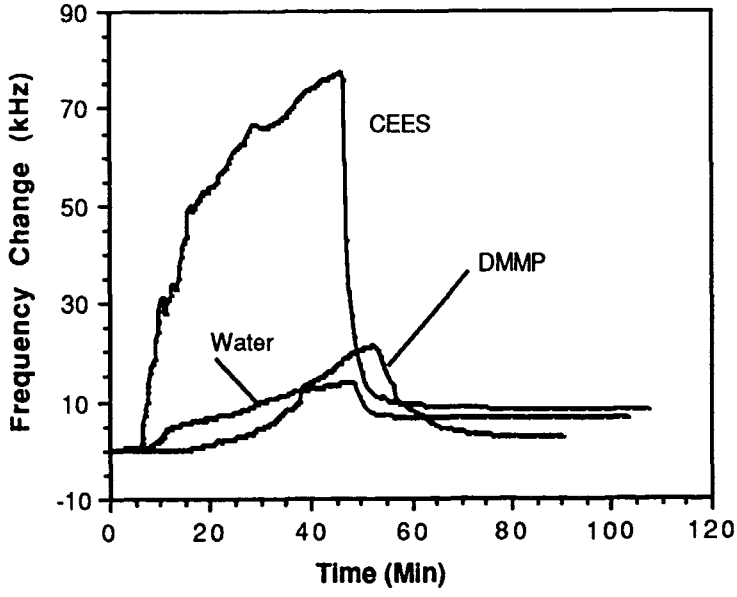

Figure 3. Frequency response of diethyl 4-dimethylaminophenylphosphonate (1f) versus time for vapor exposure (vapor on t= 5 min, off t = 46 min).

Figure 3 shows the frequency response against time of diethyl 4-dimethylaminophenylphosphonate **1f** to CEES, DMMP and water. It can be seen that the frequency change occurs very rapidly upon exposure to the CEES vapor challenge and rapidly

Table 1. Response of Aryl Phosphonic Acids and Aryl Phosphonate Esters to Vapor Challenges.

Cmpd.	Coating	Resistance Change (Factor)			Frequency Shift (kHz)			Compound Characterization			
	(kHz)	DMMP	CEES	H2O	DMMP	CEES	H2O	m.p. or b.p.	Lit.	Ref.	Source
1a	55	1	1	142	0	0	25	162-164	162.5-163	17	c
1b	47	1	2	2	0	15	3	205-8/1	185-7/0.3	Aldrich	c
1c	47	5	33	a	0	1	32	264(dec)	--	--	d
1d	58	1	1	25	0	3	0	99-100	99-101	Alpha	e
1e	49	1	2	67	0	23	0.5	130-4/3	121-3/2	Alpha	e
1f	52	3	10	2	21	77	14	201-5/4[f]	--	--	d
1g	48	5	2	13	0	5	4	31-33	31-33	18	d
1h	54	32	4	24	1	3	1	>300	>300	17	d
2a	47	1	103*	1	0	66	0	136-9/4	106-10/0.2	18	d
2b	47	40	5	b	16	3	41*	280(dec)[f]	--	--	d
3	51	11	6	3	33	4	3	154-156	154.5-155	19	d
4	52	4	1	17	1	0.5	3	254-258[f]	192-193	17	d
5a	47	1	1	1	0	21	1.5	142-4/3	130-3/2	20	d
5b	54	608*	4	1	74	0	0	185-187	185-186	20	d
5c	51	3	6	4	0	24	2	184-8/4	148-53/0.1	21	d
5d	48	321*	5	84	75*	0	4	234-236	232-234	21	d
5e	55	65	1440*	9	8	0.5	0	162-6/16	160-4/15	21	d
5f	53	1	2	1	0	7	0	172-174	173-175	21	d
5g	49	165*	1	32	3	0	0	165-166	302-6 °F	22	d
5h	52	1	3	1	1	0.5	0	204-205	204-206	23	d
5i	54	0.5	15	4	0	0.5	0	193-194[f]	--	--	d

(a) 5.6 Orders of magnitude (357000 fold) reversible change. (b) Resistance went to nil, irreversibly. (c) Purchased from Aldrich Chemical Company, Inc. (d) A. R. Katritzky and B. Pilarski, unpublished results. (e) Purchased from Alfa Products, Thiokol. (f) Correct C and H analysis were obtained.

returns to almost baseline levels when the vapor is removed. This coating also shows good discrimination to DMMP and water vapors. Sequential exposure of **1f** to CEES vapor did not result in saturation and a reasonable return to the baseline frequency occurred after the vapor challenge was removed.

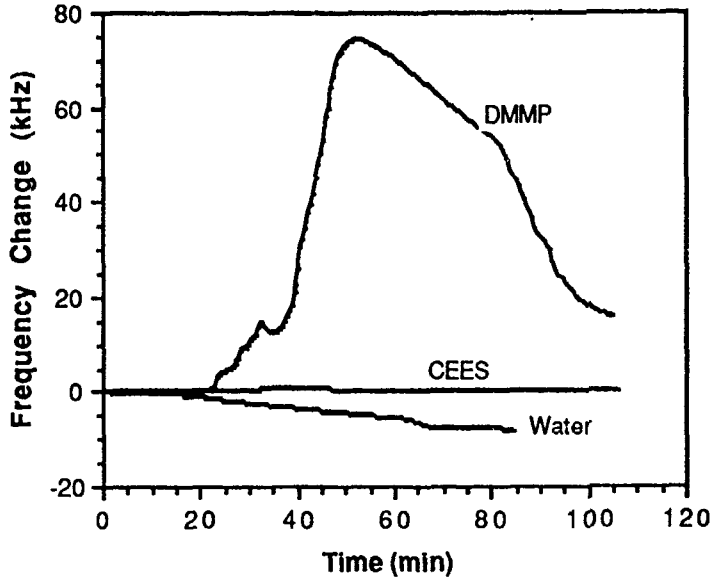

Figure 4. Frequency response of 4-methylbenzylphosphonic acid (5b) versus time for vapor exposure (vapor on t = 5 min, off t = 46 min)

The greatest reversible frequency response to DMMP vapor was observed with 4-methylbenzylphosphonic acid **5b** (74 kHz, Figure 4). This coating also showed excellent discrimination with little to no response to water or CEES vapors. The styrylphosphonic acid **3** also gave a major response to DMMP vapor (33 kHz) with good discrimination against water (3 kHz) and CEES (4 kHz).

None of the phenylphosphonic acids or esters gave exceptional responses as chemiresistors. Diethyl 2-thienylphosphonate **2a** gave a significant, though irreversible, chemiresistor response to CEES. The benzylphosphonic acids **5b**, **5d**, and **5g** gave large, but irreversible resistance responses to DMMP. Diethyl benzylphosphonate **5e** exhibited a large reversible chemiresistor response (65 fold) to DMMP, but gave a still larger, irreversible response to CEES vapor.

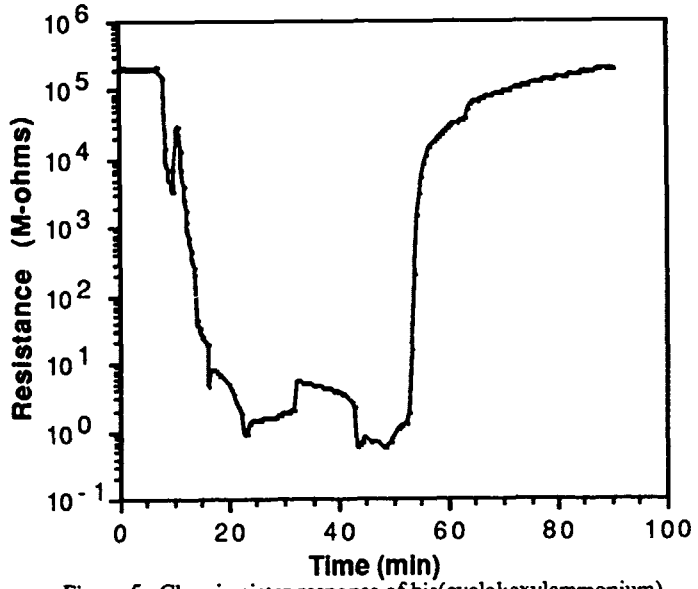

Figure 5. Chemiresistor response of bis(cyclohexylammonium)-4-dimethylaminophenylphosphonate (1c) versus time for water vapor exposure (vapor on t = 6 min, off t = 45 min)

With the salts tested, it was not surprising to observe in many cases a large irreversible increase in conductivity upon water vapor exposure as these salts are somewhat hygroscopic. It is interesting to note, however, that the bis(cyclohexylammonium) salt of 4-dimethylaminophenylphosphonic acid **1c** gave a large (from 200 GΩ to 500 kΩ) reversible response to water vapor (Figure 5). This means that such a

coating on a chemiresistor device essentially constitutes a chemical switch for the detection of water vapor. This has potential application in such areas as humidity control.

All of the diethyl phosphonates tested in this work are non-volatile, photochemically stable compounds. Heating the esters under reflux in concentrated hydrochloric acid for 24 h resulted in minimal hydrolysis. The acids are also stable and have an indefinite shelf life at ambient conditions while the salts were generally found to be slightly hygroscopic.

Thus, diethyl 4-(N,N-dimethylamino)phenylphosphonate **1f** and diethyl 2-thienylphosphonate **2a** appear to be excellent candidates for CEES detection, as both gave reversible and selective SAW responses to this vapor. 4-Methylbenzylphosphonic acid **5b** likewise gave an excellent SAW response of 74 kHz to DMMP vapor (*cf* a PEM coating under the same conditions gave a 23 kHz response) with good selectivity and fair reversibility. 4-dimethylaminophenylphosphonic acid **1c** is an excellent chemiresistor coating for the detection of water vapor.

REFERENCES

1. Katritzky, A. R.; Offerman, R. J.; Wang, Z., *Langmuir*, **1989**, 5, 1087.
2. Solid State Chemical Sensors; Janata, J.; Huber, R. J., Eds.; Academic Press: Orlando, **1985**.
3. Fundamentals and Applications of Chemical Sensors; Schuetzle, D.; Hammerle, R., Eds.; *ACS Symposium Series 309*; American Chemical Society: Washington, DC, **1984**.
4. Barendsz, A. W.; Van Beest, C. A.; Wittgen, P. P. M. M. *Proceedings of the 1981 Scientific Conference on Chemical Defense Research*; ARCSL-SP-83026; June, **1983**, pp 35-41.
5. Wohltjen, H.; Barger, W. R.; Snow, A. W.; Jarvis, N. L. *IEEE Trans. Elect. Dev.* **1985**, 32(7), 1170.
6. Snow, A. W.; Barger, W. R.; Klusty, M.; Wohltjen, H.; Jarvis, N. L. *Langmuir* **1986**, 2, 513.
7. Barger, W. R.; Wohltjen, H.; Snow, A. W.; Lint, J.; Jarvis, N. L. in *Fundamentals and Applications of Chemical Sensors*, Schuetzle, D. and Hammerle, R., Eds., ACS Symposium Series 309; American Chemical Society: Washington, DC, **1986**, pp 155-165.
8. Wohltjen, H. *Sensors and Actuators* **1984**, 5, 307.
9. Hlavay, J.; Guilbault, G. G. *Anal. Chem.* **1977**, 49(13), 1890.
10. King, W. H., Jr. *Anal. Chem.* **1964**, 36, 1735.
11. Katritzky, A. R.; Offerman, R. J., CRC *"Critical Reviews in Analytical Chemistry,"* in press.
12. Kamlet, M. J.; Doherty, R. M.; Abraham, M. H.; Taft, R. W. *Proceedings of the 1984 Scientific Conference on Chemical Defense Research*; CRDC-SP-85006; June, **1985**; pp 601-606.
13. Guilbault, G. G.; Kristoff, J.; Owen, D. *Anal. Chem.* **1985**, 57(8), 1754.
14. Snow, A. W.; Jarvis, N. L. *J. Am. Chem. Soc.* **1984**, 106, 4706.
15. *Thin Solid Films* **1983**, 99, (1-3), entire issue.
16. Gaines, G. L., Jr. *Insoluble Monolayers at Liquid-Gas Interfaces*; Wiley Interscience: New York, **1966**.
17. Doak, G. O.; Freedman, L. D. *J. Am. Chem. Soc.* **1951**, 73, 5658.
18. Tavs, P. *Ber. Deutsh Chem. Ges.* **1970**, 103, 2428.
19. Kosolapoff, G. M.; Huber, W. F. *J. Am. Chem. Soc.* **1946**, 68, 2540.
20. Lugovkin, B. P.; Arbuzov, B. A. *Izvest. Akad. Nauk S.S.S.R., Otdel Khim. Nauk* **1950**, 56.
21. Kagan, F.; Birkenmeyer, R. D.; Strube, R. E. *J. Am. Chem. Soc.* **1959**, 81, 3026.
22. Jensen, W.; Clayton, J. O.; *U.S. Patent 2,795,609* Through Chemical Abstracts 51:16535c.
23. Williams, A.; Naylor, R. A.; Collyer, S. G. *J. Chem. Soc. Perkin Trans. II* **1973**, 25.

THERMAL CATALYSIS OF TOXIC VAPORS AND ITS APPLICATION FOR CHEMICAL ANALYSIS

William J. Buttner[1], Chen Hsu[2], and Paul Doskey[1]

[1]Environmental Research Division, Argonne National Laboratory Argonne, IL 60439, [2]U.S. Army CRDEC, Aberdeen Proving Ground, MD 21010.

Abstract

Catalytic degradation of hazardous chemicals has been used both for the detoxification of dangerous environments and for use in chemical detection instrumentation. Such technology had been applied in a toxic vapor monitor that was developed at Argonne National Laboratory in which samples were treated by heated noble metal filaments to convert them from electrochemically inactive compounds into products which are readily detectable by electrochemical sensors. However, there are no detailed investigations into the thermal degradation process, and the identity of the products is frequently unknown. In order to optimize the efficiency of such processes, we have initiated a series of experiments to identify the mechanism of thermal catalysis which occurs when selected chemicals are exposed to heated filaments. Several classes of environmentally important pollutants (e.g., toluene, trichloroethylene, etc.) have been analyzed thus far by FTIR and other analytical methods.

Introduction

The Environmental Research Division at Argonne National Laboratory has developed a versatile portable instrument for the on-site analysis of toxic vapors. This instrument, the Chemical Parameter Spectrometer (CPS-100), was designed for use in the field as a means for detection of hazardous compounds. It uses four electrochemical sensors which respond with different selectivity to various vapors. The analyte is pretreated by four sequential processes (thermal catalysis over a platinum filament heated to 900° C, a rhodium filament heated to 750 ° C, a rhodium filament heated to 1000° C, and no pretreatment). The output of the four sensors in response to the pretreatment products produces 16 signals or chemical parameters. Analysis is based upon comparing response patterns of unknown vapors to the response patterns of previously measured standards using a Euclidian distance algorithm (1,2). Thus, in addition to providing additional signals for the unambiguous identification of an unknown, the derivation of the analyte by the heated noble metal filaments also transforms electrochemically inactive compounds, hence undetectable, into electroactive products. The use of thermal catalysis to transform undetectable compounds into products which can then be monitored has been applied to other sensor systems (3). We have previously determined that compounds which have similar electrochemical and physical properties (e.g., trichloroethylene and tetrachloroethylene, toluene and benzene) tend to exhibit similar responses with the sensor array used in the CPS-100. To

understand the electrochemical reactions and mechanism which control the response of the sensors, it is first necessary to identify the products which are formed as a result of the thermal degradation.

Methodology

Vapor samples were prepared by evaporating known volumes of reagent grade solvents into standard 2.5 liter air sample bags. The initial survey of the thermal degradation products was performed on an FTIR (Nicolet model 60SX) equipped with a gas flow cell (4,5). The classes of organic vapors analyzed were: hydrocarbons (toluene), sulfur organics (carbon disulfide), chlorinated hydrocarbons (trichloroethylene and dichloromethane), nitriles (acrylonitrile), and oxygenated organics (acetone and methanol). Typically, spectra were generated with of 32 scans. Thermal catalysis of the vapor was achieved using heated noble metal filaments with the filament temperature controlled by external, custom-built circuitry. Spectra were obtained for the untreated vapor and for the vapor following exposure to the heated filaments. The four filament modes which were used in this study were: a rhodium filament (0.13 mm diameter and 0.8 cm in length) heated to 750° C and 1000° C, and a platinum filament (0.13 mm diameter, 1.0 cm in length) heated to 750° C and 1000 ° C. Identification of the degradation products was performed by comparison to IR spectra compiled in handbooks (6,7). Electrochemical measurements were performed with the CPS-100 (1,8).

Results and Discussions

It had been previously determined that the response patterns generated from the electrochemical sensors are similar for related compounds (8). Thus selected compounds could be chosen to serve as models for certain classes of chemicals which have been monitored by the CPS-100. Representative IR spectra of selected compounds are shown in Figures 1-4 along with the IR spectra of the analytes following thermal catalysis by a 1000 ° C platinum filament.

Most unsubstituted organics vapors tend to exhibit nearly identical behavior with the CPS-100 (8), indicating that the catalytic degradation products were similar. For these experiments, toluene served as a model for the hydrocarbons. For unsubstituted organic compounds, complete catalytic oxidation should generate water and CO_2 with the formation of CO representing incomplete oxidation. The generation of CO was evidenced by the response of electrochemical sensors with a platinum working electrode (Table 1). Hydrocarbons are electrochemically inactive, but following catalytic treatment, products are generated which are electrodetectable. Since CO_2 is also electrochemically inert under the sensors operating conditions, the electroactive species is probably CO. This was substantiated by a large response with a platinum electrochemical sensor in contrast to a negligible response induced on a gold sensor; the selectivity factor of CO on a platinum electrode relative to a gold electrode is over 10^2 (9). Electrochemical measurements alone, however, do not provide an indication of the efficiency of thermal catalysis. For example, based upon the electrochemical measurements listed in Table 1, the rhodium filament generated more CO than the platinum filament, but this provides no data relating to the efficiency of the catalatic process. The FTIR analysis of the degradation products of toluene

provides a direct measure of the products which are formed and the efficiency of the catalytic breakdown of toluene. Figure 1 depicts the FTIR spectra for toluene and for the thermal degradation products generated by a 1000° C platinum filament. The results for the untreated vapor along with the vapor treated by three other filament modes are also summarized in Table 1. To provide a quantitative measure of relative concentration, the major IR bands associated with the identified products are listed as absorbances in Table 1. The FTIR analysis verified not only that a higher amount of CO is generated by the rhodium filament than that of the platinum filament, but also demonstrates that the catalytic breakdown of hydrocarbons on platinum filament tends to go to completion (e.g., to CO_2 and water). Moreover, a much larger portion of the total toluene which was present was destroyed by the platinum filament. These observations demonstrate that the platinum filament is more active catalytically than the rhodium filament, but that the rhodium filament generates more CO. Identical catalytic breakdown efficiencies and product profiles were observed for nonaromatic hydrocarbons (10).

TABLE 1
Toluene (Hydrocarbons)

mode	toluene[1] (1738 cm-) (IR)	CO_2[1] (2360 cm-) (IR)	CO[1] (2170 cm-) (IR)	Pt Sensor[2] (0 mV) (electrochemical)
no filament	0.3058	0	0	0
Rh = 750°	0.1855	0.5628	0.0132	4.12 μA
Rh = 1000°	0.2358	0.6980	0.0242	9.83 μA
Pt = 750°	0.1493	1.5590	0.0144	----
Pt = 1000°	0.0660	1.4450	0.0177	8.60 μA

1. Major IR bands for the indicated compounds and treatment, measured in absorption units, for 0.5% toluene vapor in air.
2. Current induced on a electrochemical sensor with a platinum working electrode by 100 ppm toluene for the indicated treatment.

Substituted organic compounds generated multiple products which were observed in the FTIR spectra. This is illustrated in Figures 2-4 in which the FTIR spectra for trichloroethylene (TCE), acrylonitrile, and carbon disulfide respectively are depicted. These results also are summarized in Tables 2-4.

An inspection of Figure 2 and Table 2 indicates that thermal catalysis of the chlorinated hydrocarbons proceeds with a much lower efficiency than that of the hydrocarbons, but that a broader range of products is generated. In addition to CO_2, and CO, we were able to identify IR peaks which correspond to HCl and carbonyl chloride ($COCl_2$--phosgene). Whereas the amount of HCl seems to be controlled primarily by the temperature of the filament and not by the choice of material, the generation of phosgene was significantly greater for the platinum filament. This effect was more pronounced for dichloromethane (10). The chlorinated hydrocarbons were unique in that they exhibited maximum electrochemical activity on a gold electrode. This indicates that the major electroactive product generated was not CO (9). Furthermore, the generation of the electrodetectable species was controlled by

the temperature of the filament (11). We have previously observed that the chlorinated hydrocarbons exhibited a unique electrochemical response. Figure 5 depicts the current-time plot of a gold sensor in response to tetrachloroethylene (PCE), a compound analogous to TCE, passing over a rhodium filament heated to 1250° C. For comparison, the current-time plot of a platinum sensor in response to xylene passing over a platinum filament is also shown. Whereas the response induced by xylene quickly reached a steady-state level, the signals for chlorinated hydrocarbons continued to increase throughout the exposure period. Although the xylene degradation products (CO) are undergoing a purely electrocatalytic reaction at the electrode surface, a chemical reaction is occurring between the gold surface of the electrode and the decomposition products of the chlorinated hydrocarbons. It had been previously postulated that HCl is formed during thermal catalysis which then corrodes the working electrode surface, ostensibly through the formation of a soluble gold chloride (11). From these FTIR measurements, we have verified that HCl is indeed formed.

Figure 3 and 4 depict the FTIR spectra for acrylonitrile and carbon disulfide. For acrylonitrile, thermal catalysis generated products which are active on both gold and platinum electrodes. From the FTIR measurements, we determined that in addition to CO, NO_x is formed, probably as NO which is electroactive on both platinum and gold. It is of interest that the generation of NO by thermal catalysis was highly specific to the platinum filament.

Alternatively, carbon disulfide exhibits low intrinsic electroactivity, but following thermal catalysis, products generated are selectively active on a platinum electrode. From the IR analysis, the major product was determined to be SO_2 with some CO, and SO_2 is electroactive on platinum (8). In addition, there were two bands at 2069 cm^{-1} and 1540 cm^{-1} associated with the catalytic degradation products whose origins have not yet been determined. The lower concentration of thermal degradation products listed in Table 4 for the 1000° C platinum filament was due to a depletion of vapor sample during the course of the measurements and therefore do not allow for a quantitative comparison of efficiencies of the thermal degradation process between the different filament modes.

Similar FTIR measurements were performed on the thermal degradation products of oxygenated organics (i.e., methanol and acetone) (10). Essentially, the major products in all cases were water, CO_2 and CO.

Conclusions

The thermal catalytic reactions of several classes of organic compounds were investigated by FTIR and electrochemical methods. The major catalytic reaction products were identified by FTIR. As expected, the catalytic reaction products were CO_2 and a small amount of CO, with the platinum filament being more active catalytically. For enhancing electroanalytical sensitivity of the hydrocarbons and related compounds, CO generation should be maximized. For CO generation, the rhodium filament was more efficient than that of platinum. Finally, in the case of substituted organics, thermal catalysis generated additional products which controlled the electrochemical reactions (e.g., HCl from TCE, NO from acrylonitrile, and SO_2 from carbon disulfide).

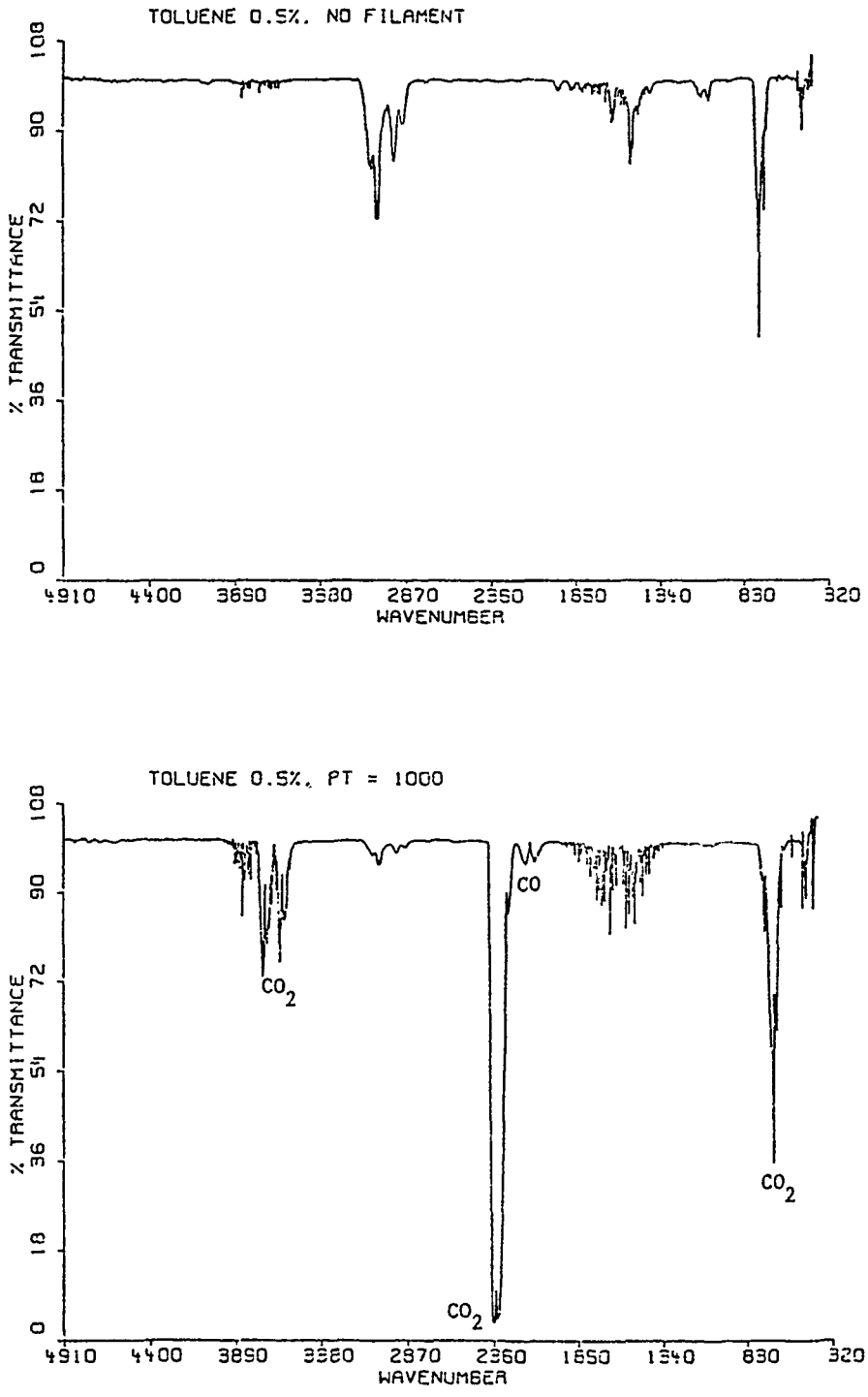

Figure 1: FTIR spectra for toluene and for the thermal degradation of toluene generated by a platinum filament heated to 1000° C.

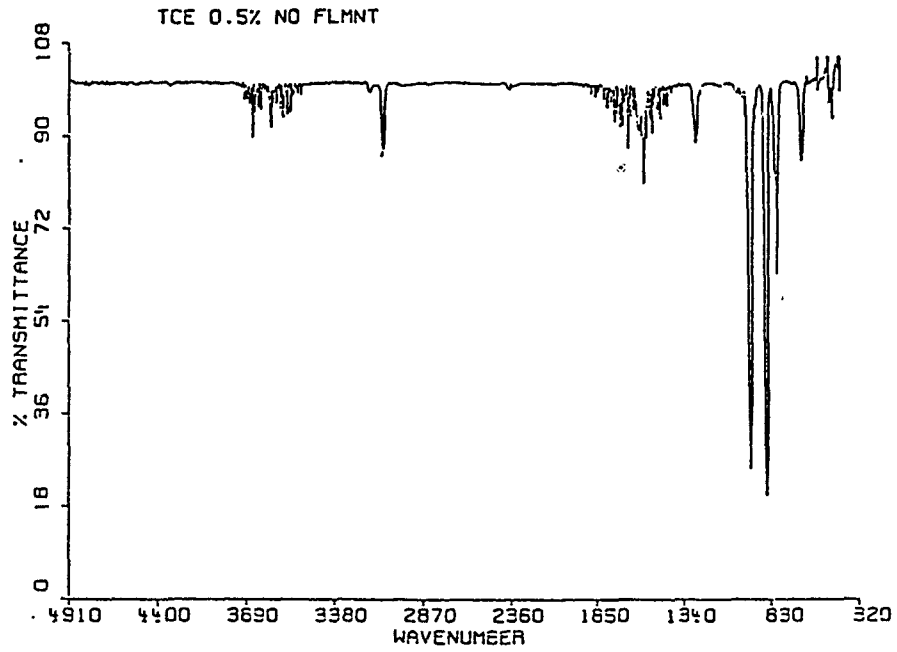

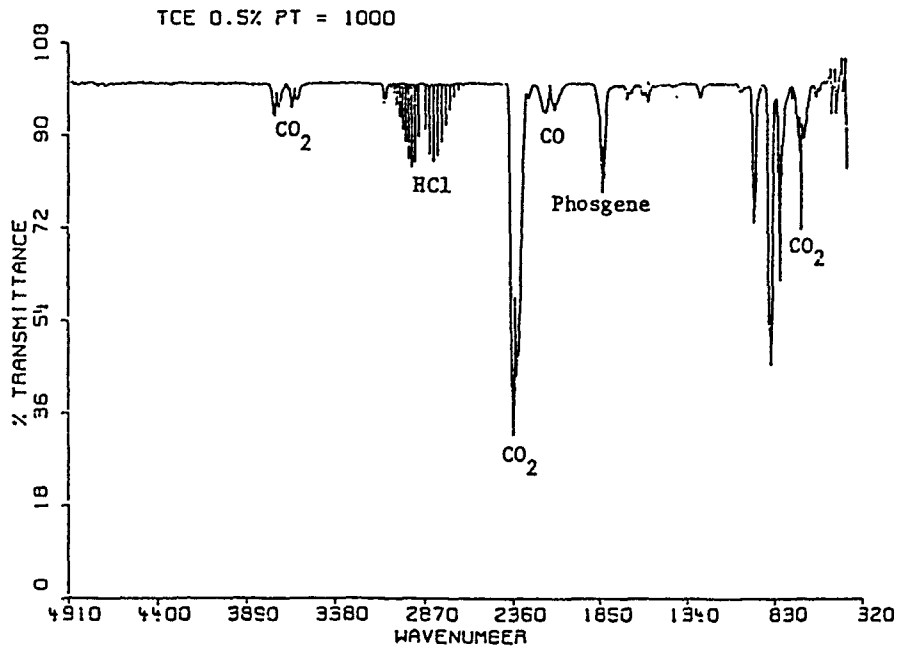

Figure 2: FTIR spectra for TCE and for the thermal degradation of TCE generated by a platinum filament heated to 1000° C.

TABLE 2
Trichloroethylene (Chlorinated Hydrocarbons)

mode	TCE[1] 851 cm- (IR)	CO_2[1] 2360 cm- (IR)	CO[1] 2170 cm- (IR)	HCl[1] 2944 cm- (IR)	$COCl_2$ 1834 cm- (IR)	Pt[2] (0 mV) (electrochemical)	Au[2] (+300 mV) (electrochemical)
no filmnt	0.6858	0	0	0	0	0	0
Rh = 750°	0.5067	0.4658	0.0237	0.0594	0.0836	3.15 µA	26.09 µA
Rh = 1000°	0.4138	0.6310	0.0239	0.0760	0.0862	4.72 µA	29.77 µA
Pt = 750°	0.6240	0.1510	0.0300	0.0344	0.1142	----	----
Pt = 1000°	0.3289	0.5005	0.0256	0.0681	0.0990	4.40 µA	31.60 µA

1. Major IR bands for the indicated compounds and treatment, measured in absorption units, for 0.5% TCE vapor in air.
2. Current induced on a electrochemical sensor by 100 ppm TCE for the indicated treatment.

TABLE 3
Acrylonitrile (nitriles)

mode	acrylonitrile[1] (851 cm-) (IR)	CO_2[1] (2360 cm-) (IR)	CO[1] (2170 cm-) (IR)	NO_x[1] (1630 cm-) (IR)	Pt[2] (0 mV) electrochemical	Au[2] (+300 mV) electrochemical
no filament	0.1958	0	0	0	0	0
Rh = 750°	0.1354	0.8388	0.0094	0.0	31.30 µA	13.2(µA
Rh = 1000°	0.0810	1.0372	^ 0092	0.0	28.68 µA	11.11 µA
Pt = 750°	0.0243	1.0811	0.0.72	0.1919	----	----
Pt = 1000°	0.0183	0.9548	0.0303	0.0702	41.70 µA	20.04 µA

1. Major IR bands for the indicated compounds and treatment, measured in absorption units, for 0.35% acrylonitrile vapor in air.
2. Current induced on a electrochemical sensor by 100 ppm acrylonitrile for the indicated treatment.

TABLE 4
Carbon Disulfide (Sulfur organics)

mode	CS_2[1] (1539 cm-) (IR)	CO_2[1] (2360 cm-) (IR)	CO[1] (2170 cm-) (IR)	SO_2[1] (1375 cm-) (IR)	Pt[2] (0 mV) electrochemical
no filament	2.1358	0	0	0	10.00 µA
Rh = 750°	0.4730	0.1055	0.0331	0.5468	80.19 µA
Rh = 1000°	0.1854	0.1516	0.0317	0.7507	101.54 µA
Pt = 750°	0.0842	0.3171	0.0125	0.6489	----
Pt = 1000°	0.0217	0.2140	0.0037	0.4295	141.60 µA

1. Major IR bands for the indicated compounds and treatment, measured in absorption units, for 0.25% carbon disulfide vapor in air.
2. Current induced on a electrochemical sensor by 100 ppm CS_2.

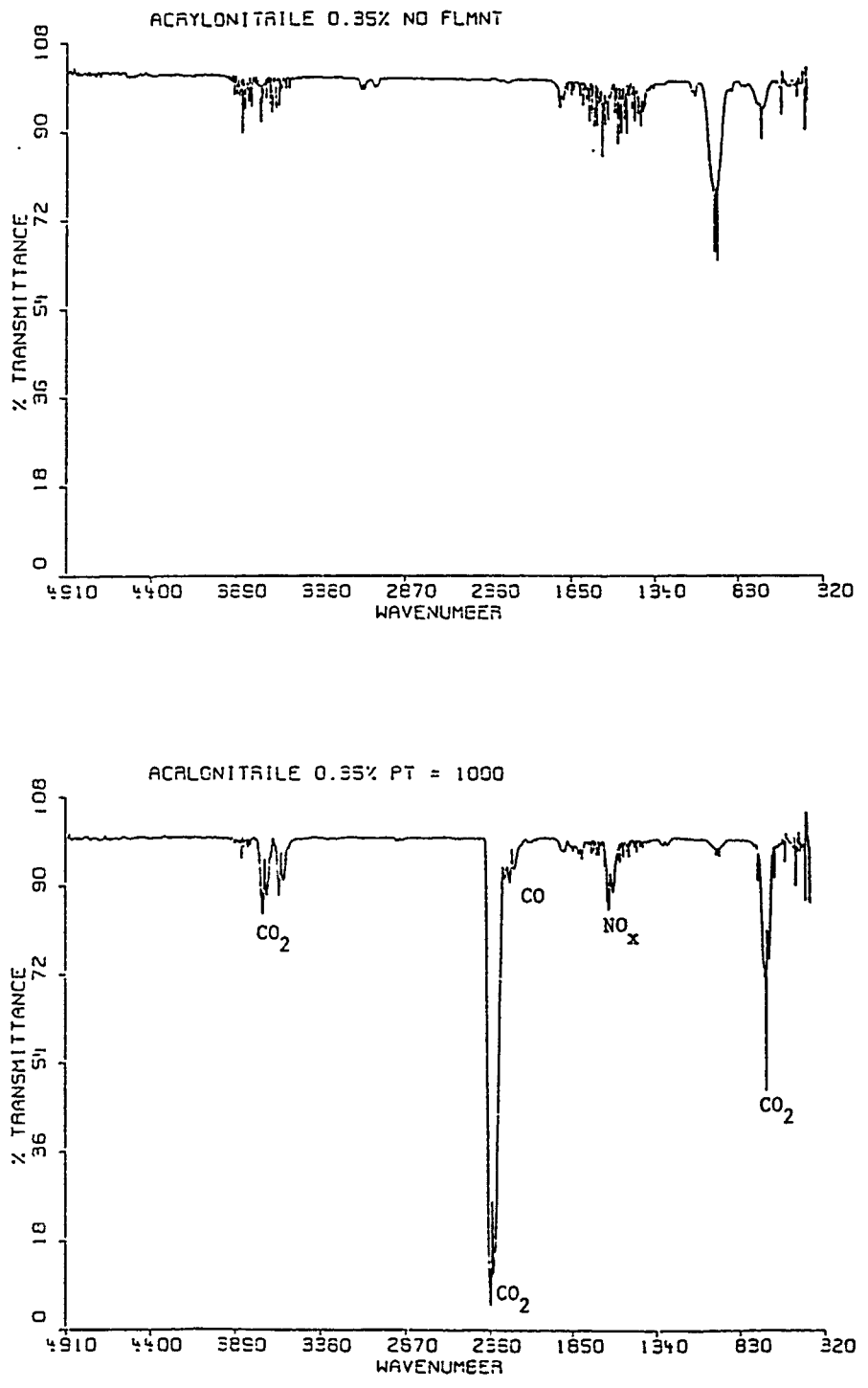

Figure 3: FTIR spectra for acrylonitrile and for the thermal degradation of acrylonitrile generated by a platinum filament heated to 1000° C.

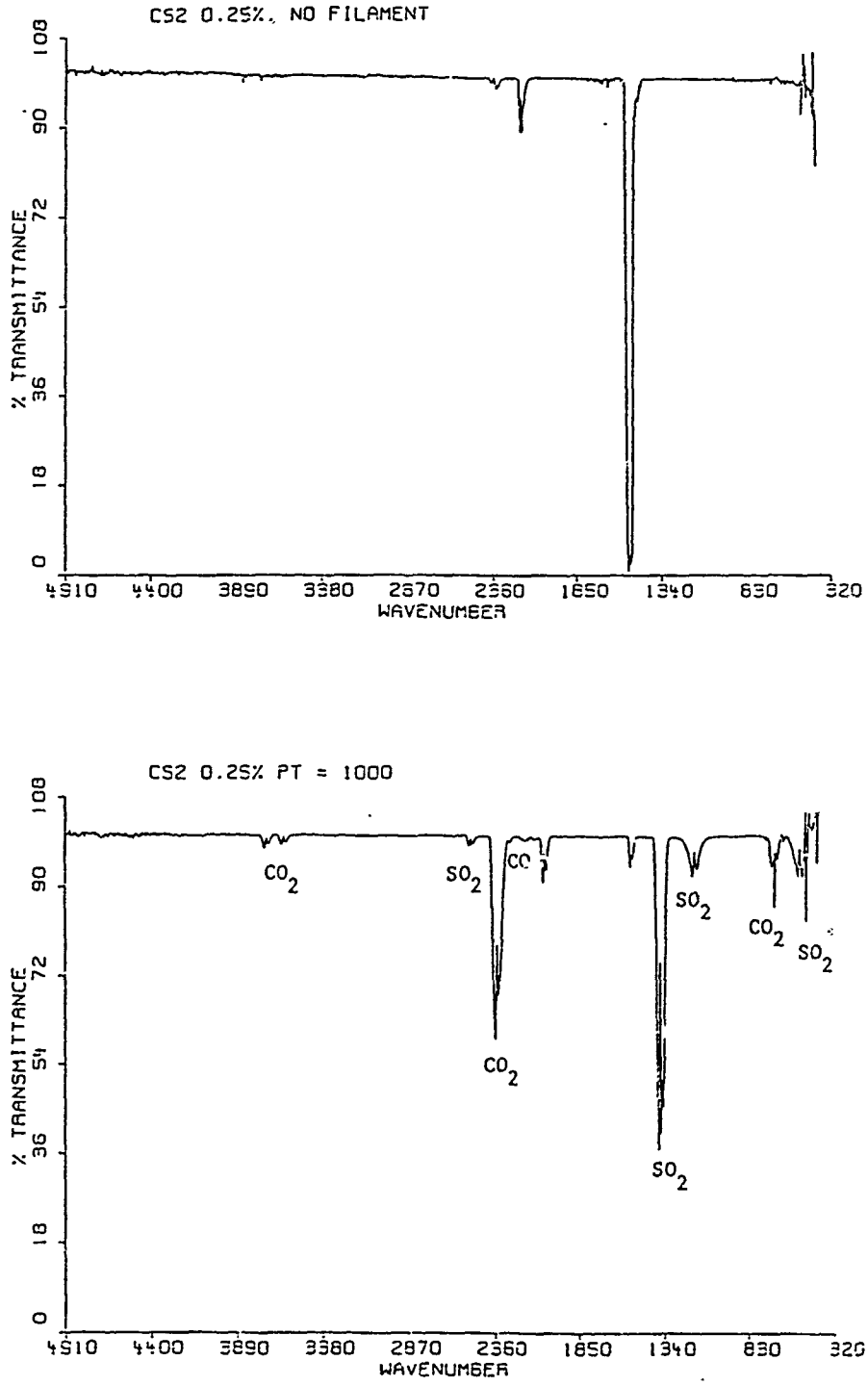

Figure 4: FTIR spectra for carbon sulfide and for the thermal degradation of carbon disulfide generated by a platinum filament heated to 1000° C.

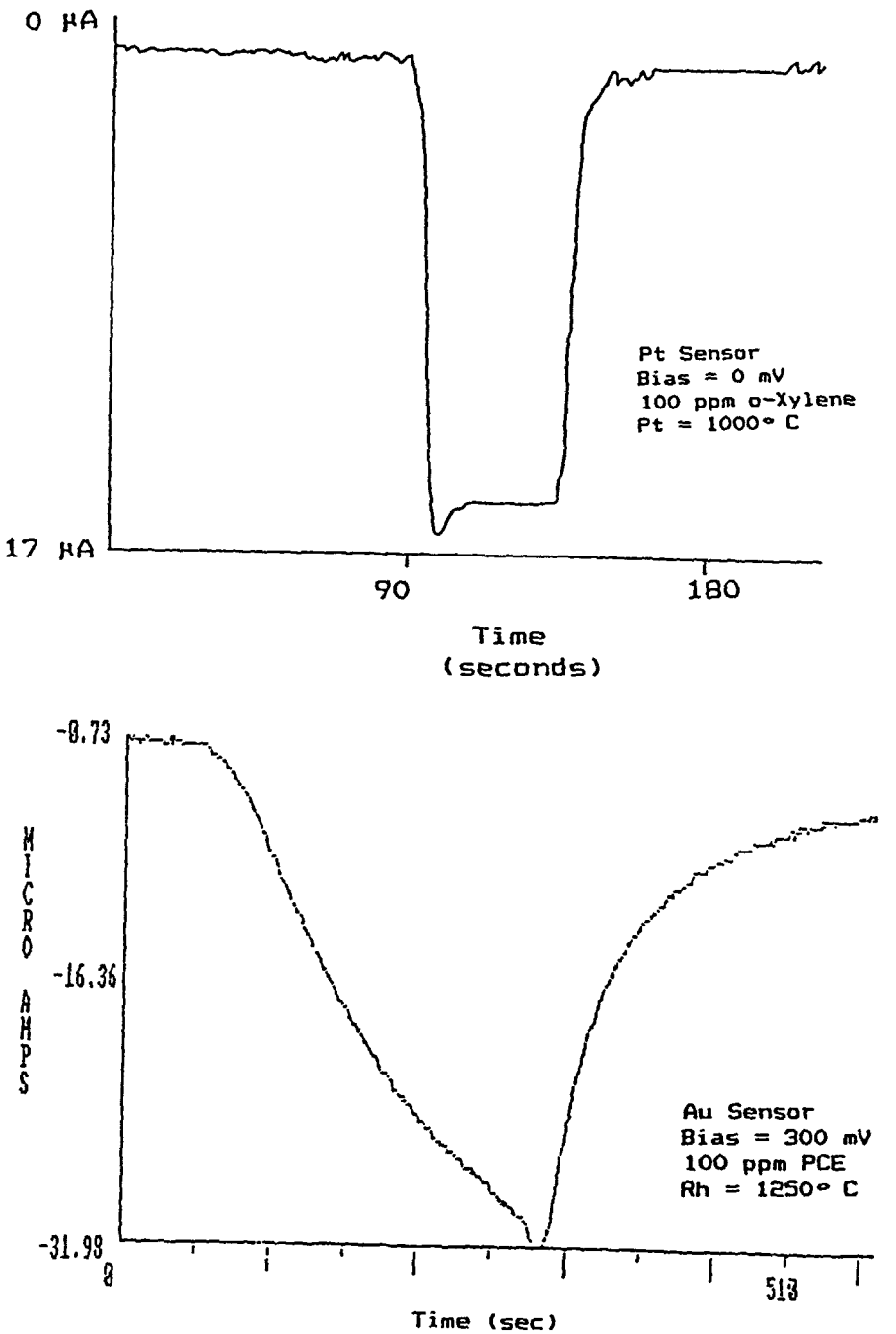

Figure 5: Current-time profiles for the indicated electrode induced by thermal degradation products of the indicated compound. In the top figure, 100 ppm of o-xylene was exposed to a platinum filament heated to 1000° from 90 to 135 seconds. In the bottom figure, 100 ppm of PCE was heated over a rhodium filament from 30 to 270 seconds.

References

1. J. R. Stetter, W. R. Penrose, S. Zaromb, D. Christian, D. M. Hampton, M. Nolan, M. W. Billings, C. Steinke, T. Otagawa, and J. O. Stull, Proceedings of the Second Annual Technical Seminar on Chemical Spills, Toronto, Canada, Minister of Supply and Services Canada, Ottawa, Ontario, Canada, (February, 1985) 332-343.

2. J. R. Stetter, P.C. Jurs, and S.L. Rose, Anal. Chem. 58 (1986) 860.

3. J. R. Stetter and Z. Cao, Anal. Chem., in press (1989).

4. C. C. Hsu, ACS Symposium Series 411, ed., S A. Bradley, M. J. Bottuso, R.J. Berolacini, Chapter 22, 234-242 (1989).

5. C. C. Hsu and M. A. Yeh, Proceedings of the 1988 U.S. Army CRDEC Scientific Conference on Chemical Defense, 931-938 (1989).

6. Gases and Vapors High Resolution Infrared Spectra, Sadtler Research Laboratories, Inc., (1972).

7. J. R. Dryer, Applications of Absorption Spectroscopy of Organic Compounds, Prentice-Hall, Inc. Englewood Cliffs, NJ (1965).

8. W. J. Buttner, R. Battin, C. Gentry, V. C. Stamoudis, J. R. Stetter, and S. Zaromb, Proceedings of the 5th Technical Seminar on Chemical Spills, Environment Canada, Montreal (February, 1989) 245-252.

9. J. M. Sedlak and K. F. Blurton, J. Eletrochem. Soc., 1976, 123, 1476.

10. Unpublished data.

11. W. J. Buttner, J. Carrillo, and G. M. Flanagan, Final Report of Savannah River Plant Order No. AX 0798811: "Development of a Real-Time Chlorohydrocarbon Monitor for Savannah River Air Stripper Effluents", (1988).

BLANK

CHEMICAL AGENT DETECTION WITH AMPLIFYING BIORESPONSE SIMULATOR

George D. Case <a>, Marilyn M. Howton <a><b>, Diana S. Beattie <b>, Jennings F. Worley III <c>, Spyros N. Agathos <d>, and Leonard J. Luskus <e>.

<a> Resource Technologies Group, Inc., Morgantown, WV 26505; <b> Department of Biochemistry, and <c> Department of Pharmacology and Toxicology, West Virginia University, Morgantown, WV 26506; <d> Department of Chemical and Biochemical Engineering, Rutgers University, Piscataway, NJ 08854; <e> U.S. Air Force School of Aerospace Medicine, Brooks AFB, TX 78235.

Abstract

Recently, we have demonstrated an amplifying bioresponse simulator for chemical agent exposure, which relies on AChE inhibition to trigger a physical-chemical cascade. In a film badge configuration, AChE inhibitor (CW) simulants initiate an oxidative reaction detected as a color change. The same reactions are also designed to generate a highly sensitive electrochemical response. Poised system color control was attained at mediator concentrations sufficiently low to permit a <1 min response time. Of the system constituents, only AChE was found to be significantly sensitive to CW simulants. Rapid responses were detected for oxidative cycle colorimetric reactions following exposure to DFP and PMSF in an integrated system, in vitro and in film badges. Potential electrochemical readouts are being evaluated.

Introduction

With the use of chemical agents ever a threat in future battlefield or terrorism situations, development of simple, inexpensive, rapid portable dosimeters for personnel exposure is needed. Biosensor based detection [1] of chemical agents combines the fidelity of physiological target simulation for chemical agent effects, with a transducing output to alert personnel. Unlike physical chemical methods [2],[3],[4],[5] which detect specific agents, chemical agent biosensors measure the inactivation of a key biological target such as acetylcholinesterase (AChE) [6],[7] or acetylcholine receptors (AChR) [8],[9],[10].

Appropriately coupled biosensor modules can, in principle, be adapted for a broad range of military, medical, environmental and occupational applications. Modular capabilities offer the added advantage of a common signal processing and readout system applied to the detection of a wide array of chemical or biological agents limited only by the coupling mechanism -- a "biochemical switch." Figure 1 shows a schematic of an amplifying chemical agent detector for AChE inhibitors as described in a previous report [11]. The "bioresponse simulator" serves as the recognition element of detector, and generates as a by-product an inhibitory substance

which modulates the "biochemical switch." A unique characteristic of the Figure 1 design is the biochemical equivalent of an electrical relay switch: The detection system is actuated by a break in the bioresponse simulator, similar to the mechanism of a burglar alarm.

We have previously demonstrated the feasibility of effective switch control by the inhibitory modulating agent, and primary and secondary colorimetric detection of triggering events in this system [11]. The "transducer" of Figure 1 converts the products of the biochemical switch reactions into amplified chemical and/or electrical responses. For the colorimetric chemical response, an amplification factor of at least 3-10 fold has been observed [11]. Xerographic images of "poised" and "exposed" film badges are shown to the right of the respective schematics in Figure 1. Amplification gain with the electrical response can be several orders of magnitude greater. The present report describes the results of experimental work on triggering reaction mechanisms in the bioresponse simulator, switch control, and verification of electrical transducing mechanisms.

Experimental

Tests of individual components and tandem combinations of the bioresponse simulator and biochemical switch modules were performed both in vitro by established procedures [11] and in film badge configurations as described elsewhere [12]. Assays of bioresponse simulator constituents were performed according to methods of Hestrin [13] and O'Brien [14]. Electrochemical measurements pertaining to the transducer module were carried out using bilayer membrane tests systems described previously [15],[16].

Results

Figure 2 shows a typical time course for in vitro DCIP reduction by the switch reaction [11], before and after addition of the inhibitor trigger substance. Initiation of the reaction gives an optical density decrease with time (negative slope immediately following the first addition event) which is stopped by the addition of 1mM inhibitor (nearly flat curve, following the second event).

Figure 3 shows comparable film badge tests of switch reaction control by the the inhibitor substance. A gel layer containing switch reaction substrates and either 1mM or 5mM inhibitor was deposited onto a clear plastic sheet, and overlaid with an addition switch enzyme at time = 0. The theoretical rate for uncontrolled bleaching is given by the sloped solid line. Spontaneous bleaching of film spots was observed to a partial extent at the lower inhibitor concentrations, but none was detected at 5mM or above. These measurements are equivalent to current leakage around a switch. Thus, complete effective control of the biochemical switch is demonstrated at an inhibitor concentration which is feasible for rapid chemical agent detection.

The purpose of the chemical reaction tests of bioresponse simulator constituents in tandem was to determine their sensitivities relative to AChE to nerve type chemical agents. Specific experimental tests included assays of acetylcholine, ACh, hydrolysis and regeneration and determinations of simulant effects on the regeneration cycle relative to AChE.

Figure 1. Amplifying Chemical Agent Detector

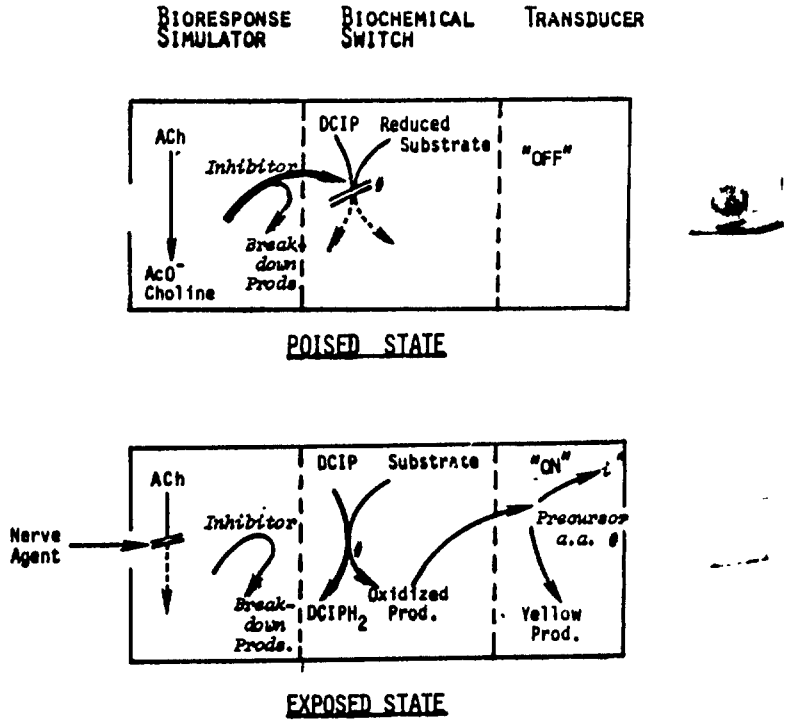

*: Electrical (current) output.

#: Switch reaction of bioamplifier.

θ: Basic amino acid, precursor for electrical output and/or colorimetric indicator reaction.

Figure 2. Typical Time Course for Switch Reaction

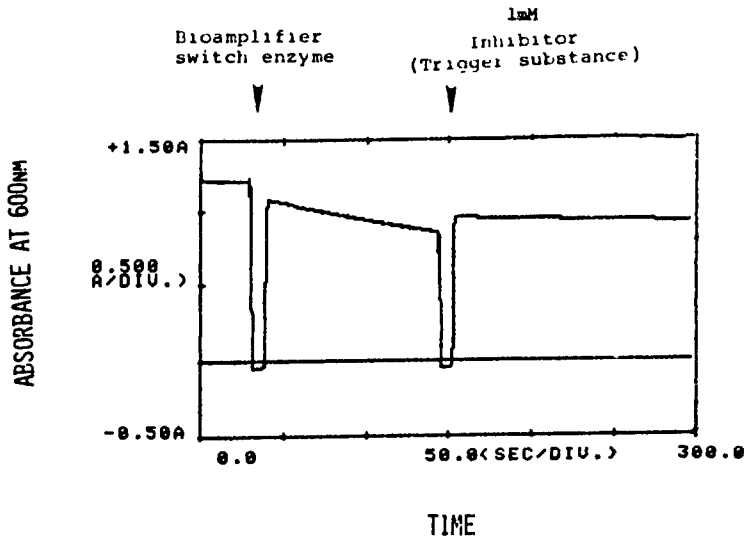

Figure 4 shows inhibition curves for AChE and the inhibitor breakdown enzyme [11] as a function of nominal concentration of the simulant phenylmethanesulfonylflouride (PMSF). AChE is half-maximally blocked at a nominal PMSF concentration corresponding roughly to a 40-50 fold molar excess over the enzyme. The high excess ratio reflects a combination of partial hydrolysis of the simulant during preparation and assay, and its relatively weaker affinity for AChE (hence, its greater safety) than CW agents. The Figure 4 results clearly show that the inhibitor breakdown enzyme is considerably less sensitive to PMSF than is AChE (For comparative discussion of other CW agent sensitive enzymes, see Ellin [17]). Comparable experiments with other system enzymes have, likewise, revealed no inhibition due to PMSF.

The purpose of the integration tests of bioresponse simulator and biochemical switch components was to demonstrate detection of chemical agent simulants directly by the coupled reactions of the biochemical switch. These tests were carried out both in vitro (as in Figure 2, above) and in colorimetric film badge configuration (as in Figure 3, above). The in vitro experiments (Figure 5, below) were designed to quantify the response of the combined constituents to chemical agent simulant as a function of time. The film badge tests (Table 1) were designed to verify such a response by visual detection in an actual film badge configuration.

Figure 5 shows in vitro time courses for shutdown of the biochemical switch reaction (Upper half) and switch inhibitor production (Lower half) resulting from the cyclic hydrolysis and regeneration of ACh, with and without an addition of the simulants DFP and PMSF. In these tests, positive exposure to an AChE inhibitor is reflected by a time delay in the shutdown of the switch reaction (Figure 5, Upper half) accompanied by a shutdown of inhibitor production (Figure 5, Lower half).

AChE poisoning by DFP and PMSF depressed the buildup of inhibitor and retarded the inhibition of switch reaction activity. Subsequent addition of agricultural grade malathion to a partially blocked system knocked out switch reaction activity, without significantly increasing the inhibitor concentration in the system. This result suggests a different mechanism of attack which may permit effective discrimination of pesticides from nerve agents in a chemical agent detector.

Table 1 shows the results of film badge tests of the combined bioresponse simulator and biochemical switch components. The switch reaction (same as Figure 5, Upper half) served as the colorimetric indicator for exposure to a mixture of the simulants DFP and PMSF. Six replicates for each condition were used. Significantly enhanced and accelerated bleaching of test spots was observed following exposure, compared to unexposed controls, for freshly prepared badges and for badges which had been stored at room temperature for one day. While fresh badges gave faster response, the day-old preparations exhibited better switch control (less current leakage in the intact system).

Initial tests of the transducer module components are shown in Figure 6. Changes in membrane conductance, measured as an amino acid triggered electric current flow, are shown for a -30 mV stimulus voltage. The inset shows typical current time courses at -30mV and at base potential (0-3mV,

Figure 3. Film Badge Tests of Switch Reaction Inhibition

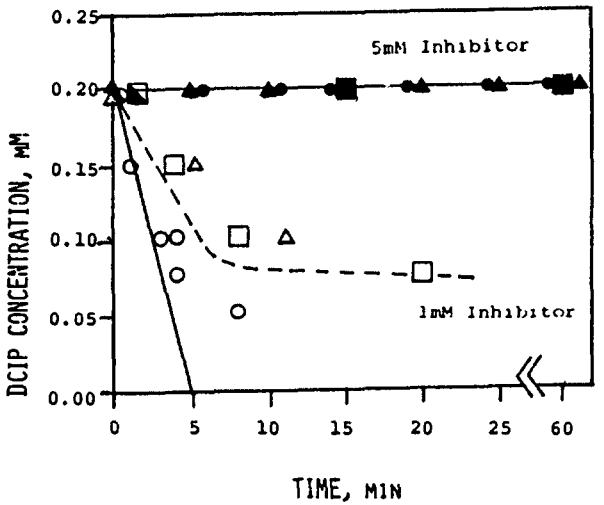

Table 1. AChE Poisoning Triggers Switch Reaction in Film Badges.

	DCIP BLEACHING FOLLOWING EXPOSURE			
	INTACT AChE		POISONED AChE	
	Extent	Time (min)	Extent	Time (min)
Fresh Badges	50% ; 100%	0.5 ; ∞	100%	0.1
	50% ; 100%	2.0 ; 1000	100%	1.0
	50% ; 100%	2.0 ; ∞	100%	1.0
	50% ; 100%	60 ; ∞	100%	20
	50% ; 100%	1000 ; ∞	50%	60
	50% ; 100%	1000 ; ∞	50%	1000
1-Day Old Badges	50%	20.	70%	15.
	50%	120.	50%	15.
	50%	30.	50%	15.
	0%	∞	50%	30.
	0%	∞	90%	10.
	0%	∞	90%	5.

Figure 4. Sensitivities of AChE and Inhibitor Breakdown Enzyme to Chemical Agent Simulants

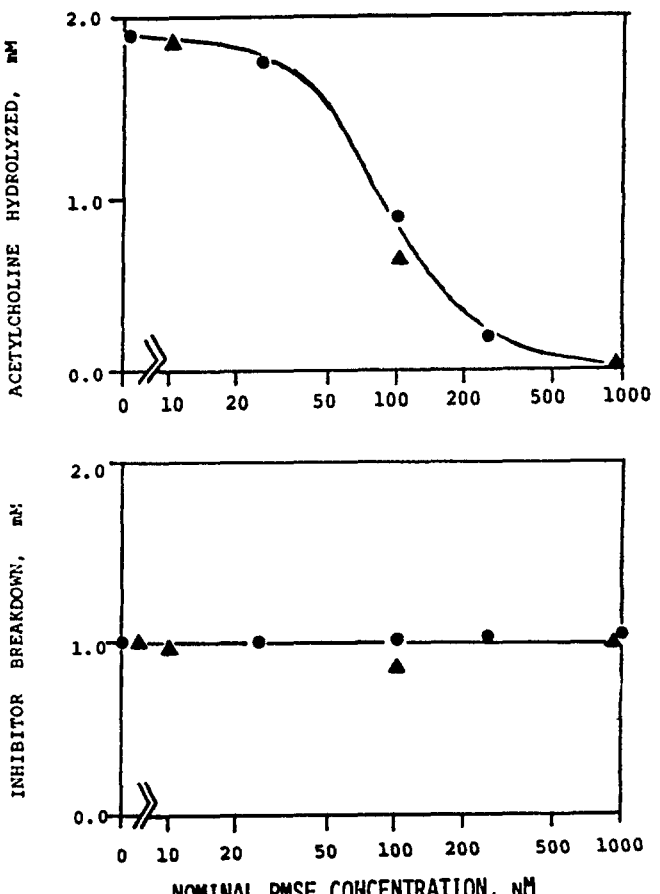

Figure 5. AChE Poisoning Triggers the Switch Reaction.

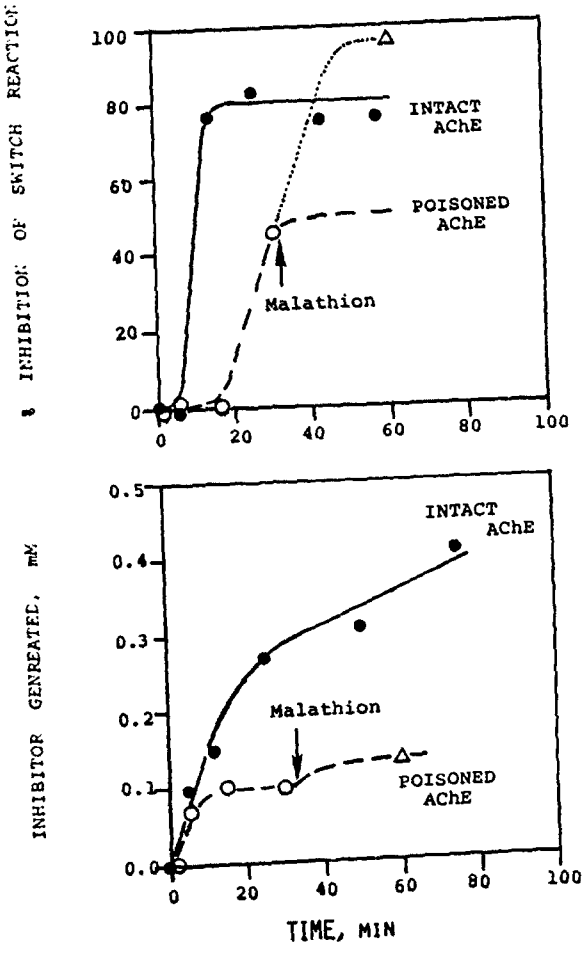

Figure 6. Inhibitor Prevents Electrical Conductance in Membrane

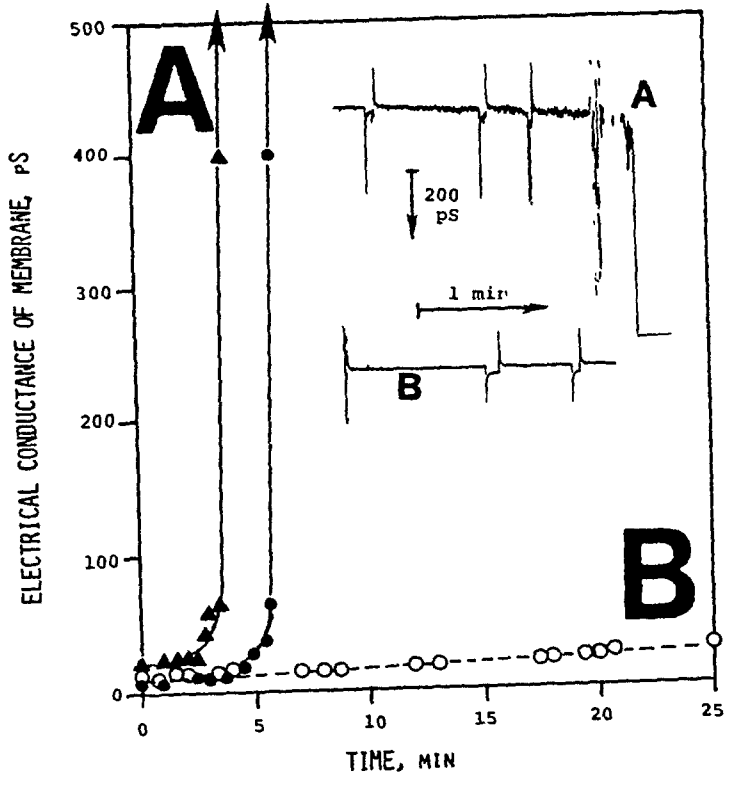

"A:" Complete, active test system, with inhibitor (trigger substance) absent.

"B:" Test system, with 10mM inhibitor present.

intermittent test spikes to verify membrane integrity). In the presence of inhibitor substance ("B", in Figure 6), no significant current flow develops. With inhibitor substance absent, the trigger elicits a catastrophic electric current surge within 3-5 minutes or less ("A," in Figure 6). These results show that a triggered electrical response can be effectively modulated by the outputs of either or both the bioresponse simulator and/or the biochemical switch modules (Figure 1).

Discussion

The present research has shown that the bioresponse simulator components (Figure 1) operate near their nominal design specifications with respect to enzymatic activities and product turnover. Implicit in this result is that sensitivity of AChE to nerve-type chemical agent simulants approaches the theoretical physiological threshold. Response amplification in the downstream detection components, both the colorimetric film badge responses of the biochemical switch module and the electrical response of the transducer module, ensues from the physiological sensitivity of AChE. Both configurations embody a "relay switch" design, turning "on" only after an AChE poisoning trigger event. Amplification serves to accelerate the speed of a measurable response, and to simplify the detection system design. Further improvements in switch control, and integration into an operational detector, remain for future research and development.

Acknowledgements

This work was supported under contract number F33615-88-C-0639, by the USAF School of Aerospace Medicine, Human Systems Division (AFSC), U.S. Air Force, Brooks AFB, Texas 78235-5301.

Literature Cited

1. Rechnitz, G.A. (1988) Chem. Eng. New [illegible] ,38).

2. Blanchard, W.C. (1987) "USAF SCPS-2 Enhancements Resulting from XM22 ACADA Type Sensors," Proc. U.S. Army Chem. Res. Dev. Engin. Center Sci. Conf. on Chemical Defense Res. (M.D. Rausa, ed.) pp. 1077-1084, U.S. Army CRDEC: Aberdeen Proving Ground, MD.

3. Hull, R.J., D.G. Biron, S. Marcus, and J.H. Shapiro (1983) "Coherent Laser Remote Sensing," Final Report, Contract No. F19628-80-C-0002, U.S. Department of the Air Force.

4. Fritsche, U. (1980) Anal. Chim. Acta 118: 179-183.

5. Diehl, W. (1986) "Detection and Survey of Chemical Warfare Against Based on Fluorescence Analysis," Proc. 2nd Int. Symp. Protection Against Chem. Warfare Agents, pp. 173-179: Stockholm, Sweden.

6. Koelle, G.B. (1970) "Anticholinesterase Agents," in The Pharmacological Basis of Therapeutics (L.S. Goodman and A. Gilman, eds.) 4th Ed., MacMillan: New York, NY.

7. Busey, B.R., F.C. Bauldauf, and K.E. Thames (1987) "Fluorimetric Detection of Acetylcholinesterase Inhibitors Using a Fiber Optic Waveguide," Proc. U.S. Army Chem. Res. Dev. Engin. Center Sci. Conf. on Chemical Defense Res. (M.D. Rausa, ed.) pp. 329-335, U.S. Army CRDEC: Aberdeen Proving Ground, MD.

8. Hallowell, S.F., and G.A. Rechnitz (1988) "Optimization and Demonstration of an Enzyme Amplified Receptor Based Assay (ERA)," Proc. U.S. Army Chem. Res. Dev. Engin. Center Sci. Conf. on Chemical Defense Res. (J.D. Williams and M.D. Rausa, eds.) pp. 655-664, U.S. Army CRDEC: Aberdeen Proving Ground, MD.

9. Eldefrawi, M. (1988) "Acetylcholine Receptor-Based Biosensor," presented at U.S. Army Chem. Res. Dev. Engin. Center Sci. Conf. on Chemical Defense Res. (J.D. Williams and M.D. Rausa, eds.) p. 1209, U.S. Army CRDEC: Aberdeen Proving Ground, MD.

10. Taylor, R.F., and I.G. Marenchic (1988) "Receptor-Based Biosensors for CBW Agent Detection," Proc. U.S. Army Chem. Res. Dev. Engin. Center Sci. Conf. on Chemical Defense Res. (J.D. Williams and M.D. Rausa, eds.) pp. 665-671, U.S. Army CRDEC: Aberdeen Proving Ground, MD.

11. Case, G.D., M.M. Howton, D.S. Beattie, and L.J. Luskus (1988) "Bioamplifier for Chemical Agent Detection," Proc. U.S. Army Chem. Res. Dev. Engin. Center Sci. Conf. on Chemical Defense Res. (J.D. Williams and M.D. Rausa, eds.) pp. 1221-1227, U.S. Army CRDEC: Aberdeen Proving Ground, MD.

12. Case, G.D., P.J. Bekowies, and P.R. Miles (1986) "Direct Passive Monitor for Toxic Activity of Chemical Agents," Final Report, Grant No. 1-R43-ES-OH-03807-01, National Institute of Environmental Health Sciences, PHS, USDHHS: Research Triangle Park, NC.

13. Hestrin, S. (1949) J. Biol. Chem. 180: 249.

14. O'Brien, W. (1976) Anal. Biochem. 76: 423.

15. Krueger, B.K., J. F. Worley, and R.J. French (1986) Ann. N.Y. Acad. Sci. 479: 257-268.

16. Case, G.D., J.F. Worley, and B.K. Krueger (1988) "Biochemically Coupled Membrane Electrode," Final Report, Grant No. ISI87-60728, National Science Foundation: Washington, DC.

17. Ellin, R.J. (1982) General Pharmacol. 13: 457-466.

AN EXPERT SYSTEM FOR INTERPRETING IR SPECTRA OF ORGANOPHOSPHORUS COMPOUNDS

Lynn D. Hoffland[1], Ronald Piffath[1],
Barry J. Wythoff[2] and Sterling A. Tomellini[2]

A system has been developed for computer-assisted interpretation of IR spectra of mixtures. The goal was to develop a system to assist in the determination of the likelihood of the presence of specific organophosphorus compounds. This work is based on PAIRS (the Program for the Analysis of IR Spectra) and PAWMI (the Program for Automated Waste Mixture Interpretation). Interpretation rules have been written and tested for over 130 organophosphorus compounds. The present capabilities and limitations of the system and rules will be presented.

Introduction

Determining the likely components in a mixture of chemicals based on the mixture's infrared spectrum is often a difficult task. Using typical spectral matching techniques employing the infrared spectra of the suspected components often proves to be unsatisfactory. The reasons for the failure of spectral matching arises from the presence of infrared bands from other components of the mixture, band shifting due to matrix effects and masking of absorption bands of a suspected component by stronger absorptions due to the presence of other components having higher absorptivities or which are present in higher concentrations.

Puskar et al. (3,4) developed an alternate approach to determining which compounds are likely to be present in an unknown mixture based on the expert system, PAIRS, the Program for the Analysis of Infrared Spectra (5). A schematic diagram of the rule-based expert system, PAIRS, is given in Figure 1. These researchers were interested in determining the presence of specific solvents in hazardous waste solutions. They developed interpretation rules, based on the spectra of the pure compounds, which were designed to account for spectral shifting due to matrix effects, band overlap, etc. This was accomplished by assigning a given level of importance to finding a band in the mixture spectrum which appears to correspond to an absorption band in the spectrum of the pure compound. Each absorption band in the spectrum of the pure compound was assigned an equivalent value. Rules were then written using three window regions about each peak, (+/-10 cm^{-1}, +/- 5 cm^{-1}, and +/- 3 cm^{-1}) with sublevels of importance being given to finding a peak within the specified region. Puskar et al. decided to allocate 20% of the value of the peak in the pure compound spectrum for a corresponding peak in the mixture spectrum within the 10 cm^{-1} region. Likewise, 30% of the value of the peak in the pure compound

spectrum for a corresponding peak in the mixture spectrum within the +/-5 cm^{-1} region and 50% of the value

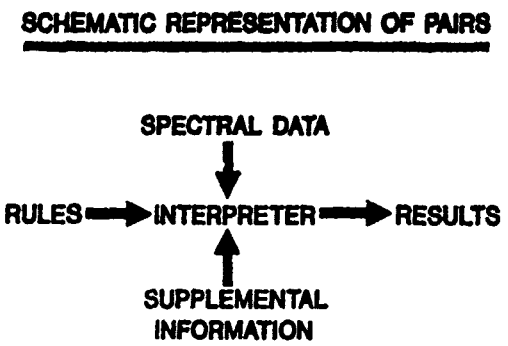

Figure 1.

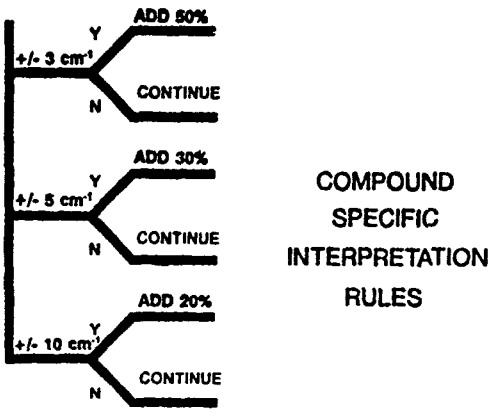

Figure 2.

of the peak in the pure compound spectrum for a peak in the spectrum of the mixture which is within the +/- 3 cm^{-1} region. An example of a partial decision tree for the resulting rules is given in Figure 2.

One of the limitations of the approach used by Levine et al. in PAWMI was that the interpretation rules were produced manually. Thus, a great deal of time was required to produce or modify a rule base. For this reason, it was decided to develop a program capable of generating the interpretation rules in an automated manner based on the peak data from the pure compound spectra (6). Using this rule generator, a rule base can be created, tested and modified with much greater efficiency. Additional improvements included developing a microcomputer version of both the interpreter (7) and rule generation programs. This is especially important since FTIR instruments are increasingly microcomputer based.

Rule Development for Organophosphorus Compounds

Once the automated rule generator and interpreter programs were in place, rules were created for over 130 organophosphorus compounds. These organophosphorus compounds and their degradation products are of special interest to scientists at CRDEC. Spectra of these compounds were processed to determine the positions and relative intensities of the absorption peaks in the pure compound spectra. All spectra were peak picked using a Nicolet 640 minicomputer and Nicolet DX software. Peaks having intensities less than approximately 15% of the largest peak in the spectrum were not included in the peak listings since such peaks are not expected to be observed in mixtures due to their low intensities. These raw peak tables were transferred from the Nicolet 640 to a PC compatible microcomputer via a DEC VAX 8820. Once peak tables were acquired for all the organophosphorus compounds to be included in the rule base, the peak table for each compound was manually evaluated to determine the peaks to be used for rules for that particular compound. Rules

were generated for only the ten largest peaks of a compound, when possible. Generating rules for more than ten peaks for a given compound reduces the importance of any given peak to generally insignificant levels. An additional goal of this manual, time intensive step, is to eliminate peak picking errors such as detecting noise or base line shifts in the spectra. Using the rule generator on the microcomputer,interpretation rules were created using the entire modified peak list (i.e., generally containing the ten most intense peaks) for all organophosphorus compounds in this data set. The windows used to generate these rules were: +/- 10 cm^{-1}, +/- 5 cm^{-1} and +/- 3 cm^{-1} with the allotment for each region being 20%, 30% and 50% of the peak value,

Table 1.

Expectation Value	Spectrum	Compound
0.99	SMX 3707	Ethyl 2-diisopropylaminoethylmethylphosphonite, Liquid, CF/CSI
0.85	SMX 8003	Bis(2-diisopropylaminoethyl)methylphosphonite, Liquid, CF/KBr
0.76	SMX 4101	Diethylmethylphosphonite, Liquid, CF/KBr
0.57	SMX 2823	Ethyl 2-(diisopropylamino)ethylmethylphosphonate, Liquid, CF/CSI

respectively. To facilitate rapid interpretations, rules for a maximum of 30 compounds were placed in a single file and five separate rule files were created. The non-modified, peak lists for the pure compounds were then interpreted using the rules created. The non-modified peak lists were used for rule evaluation since they represent the peak data which is likely to be provided by the peak picking routines for an unknown spectrum. An example of the interpretation results using these rules for the compound ethyl 2-diisopropylaminoethyl methylphosphonite are given in Table 1. The results of an interpretation are a numerical indication of the likelihood of presence for a given compound ranging from a low of 0.01 to a high of 0.99. The compounds having a numerical likelihood of presence greater than 0.50 are given here. The results are encouraging since the other compounds with high likelihoods are closely related to ethyl 2-diisopropylaminoethylmethyl-phosphonite. For example, the expectation value for bis(2-diisopropyl aminoethyl) methylphosphonite, was found to be 0.85. The spectrum for this compound closely resembles that of ethyl 2-diisopropylaminoethyl methylphosphonite, as expected. It was postulated that generating interpretation rules using only the more intense bands in the spectrum of the pure compound would provide better interpretation results. The reason for this is that it is expected that only the most intense bands from a compound will be observed in complex mixtures. One disadvantage of using such interpretation rules is that each band is more heavily weighted, thus missing any band for a compound will seriously affect the final expectation value for that compound. Further, if a compound has only a few large peaks which are weighted heavily, the expectation value for the compound will be high if any of these peaks are observed in a spectrum being interpreted.

A second set of interpretation rules were created using only those peaks having an intensity of 5 or greater. The peak data for the compound ethyl 2-diisopropylaminoethyl methylphosphonite were interpreted using these intensity 5 or greater rules and the interpretation results are presented in Table 2.

Table 2.

Expectation Value	Spectrum	Compound
0.99	SMX 3025	Isopropyl methylphosphonic acid, Liquid, CF/KBr
0.99	SMX 3502	Triethyl phosphate, Liquid, CF/CSI
0.99	SMX 3707	Ethyl 2-diisopropylaminoethyl methylphosphonite, Liquid, CF/CSI
0.85	SMX 8003	Bis(2-diisopropylaminoethyl)methyl-phosphonite, Liquid, CF/KBr
0.75	SMX 8903	methyl di-n-butylphosphinite
0.75	SMX 8901	methyl di-t-butylphosphinite, Liquid, CF/KBr
0.68	SMX 4024	Diethylmethylphosphonothionate, Liquid, CF/KBr
0.68	SMX 4101	Diethyl methylphosphonite, Liquid, CF/KBr
0.64	SMX 4213	2-(Diisopropylaminoethyl) ethylmethyl-phosphonothiolate, Liquid, CF/CSI
0.60	SMX 2816	Bis(ethyl n,n-dimethylphosphoramidic)anhydride, Liquid, CF/CSI
0.51	SMX 2823	Ethyl 2-(diisopropylamino)ethylmethylphosphonate, Liquid, CF/CSI

While one may at first question why the compound, triethyl phosphate, has an expectation value of 0.99, viewing the spectrum of this compound serves to clear up any confusion. The spectrum for triethyl phosphate is given in Figure 3.

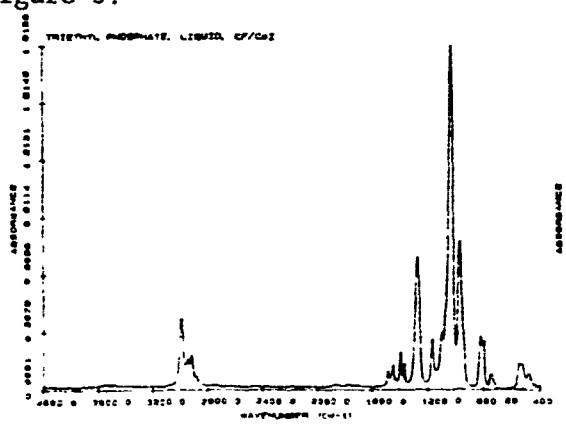

Figure 3.

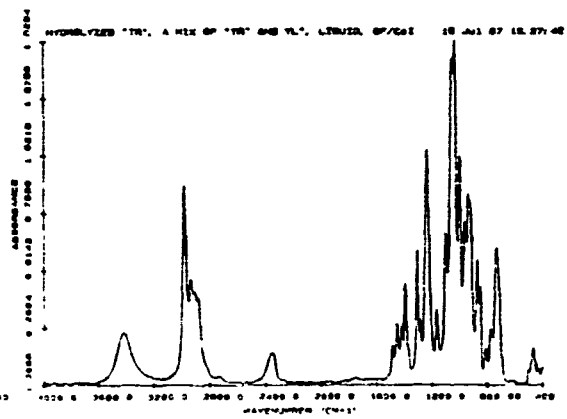

Figure 4.

It clearly has a large absorption peak at 1035 cm^{-1} and no other peaks with an intensity of 5 or greater in the spectrum. Thus, finding a corresponding absorption in the spectrum being interpreted is weighted very heavily. While this may at first appear to be a flaw in the interpretation rules, it should be noted that one cannot discount the presence of this compound in a mixture if a peak in the region of 1035 cm^{-1} exists.

Interpretation of mixtures of organophosphorus compounds.

The interpretation of mixtures containing organophosphorus compounds will be demonstrated using a binary and a ternary mixture. The first example is a hydrolyzed sample of diethyl methylphosphonite, "TR", which contains both "TR" and ethyl hydrogenmethylphosphinate, "YL". The spectrum for this mixture is given in Figure 4. The spectrum was peak picked with the resulting peak data

being interpreted. Table 3 presents the interpretation results using the rules written for all absorptions greater than 1 in the spectra of the pure compounds. The interpretation results obtained when using the rules written only for those bands in the pure compound spectra which have intensities greater than 5 are presented in Table 4. Only compounds with expectation values greater than 0.50 are listed in either case. It is encouraging to note that both sets of rules result in high expectation values for "YL" and "TR",

Table 3.

Expectation Value	Spectrum	Compound
0.99	SMX 4101	Diethyl methyl phosphonite, Liquid, CF/KBr 'TR'
0.73	SMX 2423	Ethyl hydrogenmethylphosphinate, Liquid, CF/KBr 'YL'
0.69	SMX 8911	Diethyl ethylphosphonite, Liquid, CF/KBr
0.56	SMX 7911	Diethyl dithiophosphate 90%, Liquid, CF/KBr
0.56	SMX 4024	Diethyl methylphosphonothionate, Liquid, CF/KBr
0.56	SMX 3707	Ethyl-2-diisopropyl aminoethyl phosphonite
0.52	SMX 3313	2-diisopropyl

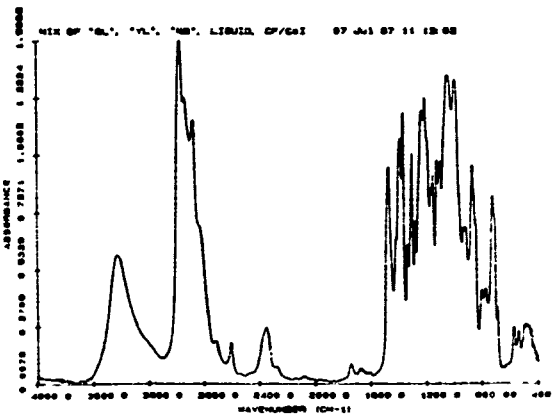

Figure 5.

the compounds actually present in the mixture. Further, the interpretation results suggest to the user other possible explanations for the absorptions present in the spectrum of the mixture.

The results for the interpretation of a three component mixture of ethyl 2-diisopropylaminoethyl methylphosphonite, "QL"; ethyl hydrogenmethylphosphinate, "YL", and 2-(diisopropylamino)ethanol, "KB", are somewhat more intriguing. The spectrum for this three component mixture is given in Figure 5. The spectrum was peak picked using the Nicolet peak picking routines. The interpretation results using the intensity greater than 1 rules and the intensity greater than 5 rules are given in Tables 4 and 5, respectively. Again, only those compounds with expectation values greater than 0.50 are listed. It is interesting to note that using those rules which include the lower intensity absorptions resulted in both "QL" and "YL" having expectation values greater than 0.50, though the actual values (0.63 for "YL" and 0.51 for "QL") are still somewhat low. The compound, "KB", does not contain phosphorous and is, therefore, not included in either rule set.

The interpretation results when using the intensity 5 or greater rules are somewhat less pleasing at first glance. While the expectation value for "YL" has decreased to 0.60, it is still above the 0.50 threshold chosen arbitrarily as a cutoff. The expectation value for "QL" fell below 0.50 threshold. Upon further investigation the reason for the low expectation value for "QL" using these rules was ascertained. The spectrum of pure "QL" contains only 4 peaks

Table 4. Interpretation results using intensity 5 or greater rules.

Expectation Value	Spectrum	Compound
0.99	SMX 7803	Diethylchlorophosphate(diethylphosphorochloridate), Liquid, CF/KBr
0.99	SMX 7410	Triisopropyl phosphinite 90%, Liquid, CF/KBr
0.99	SMX 6824	Triethylphosphine sulfide, Solid, KBr pellet
0.99	**SMX 4101**	**Diethylmethylphosphonite, Liquid, CF/KBr 'TR'**
0.99	SMX 4024	Diethyl methylphosphonothionate, Liquid, CF/KBr
0.99	SMX 3908	Monosodium salt of methylphosphonic acid, Solid, KBr Pellet
0.99	SMX 3502	Triethylphosphate, Liquid, CF/CSI
0.85	SMX 7603	Trimethylphosphate, Liquid, CF/KBr
0.84	**SMX 2423**	**Ethyl hydrogen methylphosphinate, Liquid, CF/KBr 'YL'**
0.75	SMX 5223	Diisopropyl methylphosphonite, Liquid, CF/KBr
0.75	SMX 1025	S-(2-Diisopropylaminoethyl) ethylmethylphosphonothiolate, Liquid, CF/CSI
0.68	SMX 8003	Bis(2-diisopropyl aminoethyl) methyl phosphonite, Liquid, CF/KBr
0.65	SMX 8911	Diethylethylphosphonite, Liquid, CF/KBr
0.60	EA 0620	Ethylmethylphosphonothionic acid, Liquid, CF/KBr
0.56	SMX 7305	Methyl methylphosphonofluoridate, Liquid, CF/KBr
0.55	SMX 3707	Ethyl 2-diisopropylaminoethylphosphonite, Liquid, CF/CSI
0.51	SMX 3814	S-(2-Dimethylaminoethyl) ethylmethylphosphonothiolate, Liquid, CF/KBr
0.51	SMX 2823	Ethyl 2-(diisopropylamino) ethylmethylphosphonate, Liquid, CF/CSI

Table 5.

Expectation Value	Spectrum	Compound
0.87	SMX 3313	2-Diisopropylaminoethylmethylphosphinate Liquid, CF/KBr
0.85	SMX 8003	Bis(2-diisopropylaminoethyl)methylphosphonite, Liquid, CF/KBr
0.65	SMX 3525	2-(2-Diisopropyl)aminoethylhydrogenmethylphosphonothiolate, Solid, KBr Pellet
0.63	**SMX 2423**	**Ethylhydrogenmethylphosphinate, Liquid, CF/KBr 'YL'**
0.55	SMX 8911	Ethyl ethylphosphonite, Liquid, CF/KBr
0.55	SMX 6824	Triethyl phosphine sulfide, Solid, KBr Pellet
0.54	SMX 4101	Diethyl methylphosphonite, Liquid, CF/KBr
0.52	SMX 2717	Bis(2-ethylhexyl)2-ethylhexyl phosphonate Liquid, CF/CSI
0.52	SDX 1743	(+/-)-1-Aminoethylphosphonic acid 96%, solid between KBr Disks
0.51	SMX 8711	(+/-) Butylphosphonic difluoride, Liquid, CF/KBr
0.51	SMX 3707	Ethyl 2-diisopropylaminoethylmethylphosphonite, Liquid, CF/CSI 'QL'
0.50	SMX 4622	Pinacolylmethylphosphonic acid,Liquid, CF/CSI

which are of intensity 5 or greater. They are 1020 cm^{-1} (intensity = 6), 1032 cm^{-1} (intensity =7), 1053 cm^{-1} (intensity = 7) and 2970 cm^{-1} (intensity = 10). Each of these four absorption bands was allotted 25% of the total expectation value for the compound, or 0.25. The percentage of the 0.25 given for any peak in the mixture is based on the position of the actual band in the mixture and whether the peak is within the +/- 10 cm^{-1} (worth 20% of 0.25), +/- 5 cm^{-1} (worth 30% of 0.25) or +/- 3 cm^{-1} (worth 50%) of 0.25) region windows centered around each peak in the spectrum of the pure compound. In the case of this

mixture, only the bands at 1046 and 2966 are within the specified position regions for "QL" which explains the low expectation value.

CONCLUSION

Two preliminary sets of interpretation rules have been developed for 130 organophosphorus compounds. The rules are based on the absorption spectra of the pure compounds. One set of rules includes absorption bands which are greater than intensity 1. A more restrictive set of rules was also developed which includes only those bands with intensities greater than 5. Initial testing of these rules sets indicates they have reasonable discriminating power among the organophosphorus compounds included in the sets. Work continues to improve the discriminating power of the rules for the interpretation of mixtures of organophosphorus compounds. The ultimate goal being to develop a system capable of providing the user with assistance in establishing the likelihood of presence for a particular organophosphorus compound in a complex mixture.

REFERENCES

1.) CRDEC, Aberdeen Proving Ground, MD 21010

2.) Department of Chemistry, University of New Hampshire, Durham, NH 03824

3.) M.A. Puskar, S.P. Levine and S.R. Lowry, Anal. Chem. 1986, 58, 1156.

4.) M.A. Puskar, S.P. Levine and S.R. Lowry, Anal. Chem. 1986, 58, 1981.

5.) H.B. Woodruff and G.M. Smith, Anal. Chem. 1980, 52, 2321.

6.) S.A. Tomellini, R.R. Smardzewski, D.R. Reutter, J.M. Leonard, R.A. Fifer and S.A. Liebman, "Advanced PAIRS Expert System for Mixture Analysis Within the EXMAT System", Proceedings of the U.S. Army Chemical Research, Development, and Engineering Conference on Chemical Defense Research. U.S. Armament Munitions & Chemical Command, Aberdeen Proving Ground, MD, April, 1988.

7.) B.J. Wythoff, C.F. Buck and S.A. Tomellini, Anal. Chim. Acta 1989, 217, 203.

BLANK

XIII. MATERIALS POSTERS

NOTE: A paper with the following title was presented at the Conference but is not included in this document:

A Novel Interaction of Acrylic Polymers with Protic Solvents: An FTIR Study

BLANK

OPTICAL PROPERTIES OF INORGANIC POLYMERS

KIM F. FERRIS AND STEVEN M. RISSER
Pacific Northwest Laboratory, Materials and Chemical Sciences Center, Richland, WA 99352

ABSTRACT

The electronic structure of organic and inorganic polymeric systems are well described by their molecular symmetry, even with the large bond polarity shown by such systems as polyphosphazenes. We have performed calculations using semi-empirical Hamiltonians to determine the electronic structure and optical nonlinearities for a series of model phosphonitrilic and organic compounds. The optical transition energies for phosphonitrilic compounds are greater than their organic counterparts as a result of in-plane π' bonding interactions, and are modulated by the electronegativity of the substituent groups on the phosphorus atoms. We report values for the vertical ionization energy and electronic absorption wavelengths, and use molecular orbital contour analysis to show the effects of ligand electronegativity on the π' network. Hyperpolarizabilities were calculated from third order perturbation theory for a series of phosphonitrilic compounds, $(X_2P\text{-}N)_n$, as a function of bond length alternation and ligand substitution. In contrast to organic polyenes, the difference in π orbital energy between phosphorus and nitrogen is critical to determining the onset of saturation and the magnitude of the hyperpolarizability.

INTRODUCTION

The chemical bonding of the P-N subunits in phosphonitrilic compounds gives rise to a unique set of properties making these compounds potential candidates for optical applications. The chemical bonding in these species is characterized by polarized chemical bonds between N and P, which can be attributed to the large electronegativity difference between first and second row elements. There are two π bonding type networks in these species, the traditional out-of-plane π bonding, and an in-plane π' bonding network[1]. The presence of the π' bonding network is largely responsible for the large increase in optical transition energies, keeping the polymer transparent in the visible region[2]. The conjugation of these π networks is also responsible for the large non-linear optical properties recently observed and calculated for these polymers[3]. Other important properties stem from the ease with which substituent groups on the phosphorus may be altered, resulting in markedly different physical characteristics[4].

Molecular models of polymers and their constituent fragments are often representations of the monomeric species comprising their repeat units. As such, species such as pyridine and ethylpyridine have provided valuable information for polyvinylpyridine[5]. Examples for inorganic polymeric systems have only recently been explored, mainly in the ceramic and mineral fields where silicate work has dominated research. Because of the large number of heavy atoms in the inorganic polymers, investigations have tended to focus on small molecule models. In previous electronic structure investigations, we have compared the value of small cyclic molecules and linear oligomers for the polyphosphonitrilic system [1]. Termination effects both distort the electron distribution and cause bond length alternation for a small number of repeat units. Trinquier[6] has provided an excellent

review using ab initio methods correlating monomer, dimer and trimer properties.

The optical properties of organically based systems have been the subject of numerous investigations. Although inorganic systems have many chemical bonding attributes in common with organics, the presence of the π' network in inorganics often prevents direct analogies with the electronic structure of organic systems. In this paper, we report the results of electronic structure calculations on a series of phosphonitrilic systems ($(F_2PN)_3$, $(F_2PN)_4$ and $F_2PN)_5$) and organic systems ($C_3H_3N_3$) in order to compare orbital interactions, electronic transitions, and nonlinear optical properties in these materials.

METHODS

Semiempirical valence electron molecular orbital methods were used to evaluate the electronic structure of ($(F_2PN)_3$, $(F_2PN)_4$, C_5H_5N and $C_3H_3N_3$) and were compared to *ab initio* results[1] where applicable. Coulomb integrals were evaluated using the Mataga-Nishimoto interpolation formula[7], and the Pople-Segal formalism[8] was used for core Hamiltonian matrix terms. The nonlinear optical properties of inorganic polymers have substantials contributions by π and π' bonding electrons, allowing them to be treated by a tight-binding π electron Hamiltonian (Huckel) for the determination of their hyperpolarizabilities[9]. The third order hyperpolarizability were determined from these wavefunctions using perturbation theory to calculate the coefficients of the Taylor expansion[3,9] of the energy. Ligand group effects at the phosphorus sites were modelled by variations in the π orbital energy ($\Delta\alpha$) between the nitrogen and phosphorus centers; bond alternation effects through changes in the off diagonal hopping term β_{ij} ($0.00\beta_{PN}$=no bond alternation). Structural parameters for the polyphosphazenes were taken from recent *ab initio* calculations for $(F_2PN)_4$. Further details on the electronic structure method are available in ref [2,10].

RESULTS AND DISCUSSION

While the electronic structures of organic and inorganic polymers are well characterized by their molecular symmetry, the in-plane π'bonding interactions in the inorganic systems endow unusual characteristics on their molecular spectroscopy. The electronic absorption of π bonded molecules are typically described by their π-π^* transitions for hydrocarbons, and n-π^* for systems involving heteroatoms. The energy level assignments corresponding to molecular orbitals using Koopman's theorem are often defined through an electronic spectroscopy technique such as photoelectron spectroscopy (PES). However, the assignment of electronic energies through PES spectroscopy and the interpretation of electronic absorption transition becomes considerably more complicated by the presence of this additional π' bonding network.

The vertical ionization potentials for the phosphonitrilic trimer and triazene are given in Table 1 and show good agreement with experimental values[11]. Photoelectron spectra were simulated by the superposition of gaussian energy distributions centered at the one electron orbital eigenvalues. Given the orthogonality of the π and π' networks, simple molecular symmetry arguments determine the orbital pattern of the uppermost occupied molecular orbitals. For example, the first ionization potential for triazene corresponds the doubly degenerate e'(σ,n) linear combination from the interaction of the nitrogen lone pairs. The resulting electronic absorption predictions were n-π^* transitions for pyridine and triazene occur at 256 and 278 nm respectively, both in good agreement with experimental values.

However, the first ionization potential for the cyclic phosphonitrilic trimer corresponds to the pair of doubly degenerate orbitals (e' and e"), one of which contains the in-plane π' interactions, the other, the out-of-plane π orbital. These out-of plane interactions are nearly the same strength as the interaction energy of the π' system, resulting in degenerate or nearly degenerate orbital energy levels lying near the top of the the occupied orbital manifold. Thus, the PES spectra which often plays an critical role in defining the electronic structure of molecules, becomes unresolvable given the finite linewidths seen with normal experimental measurements by the presence of an additional π network. Higher ionization potentials arise from singly degenerate π and π' interactions, and the P-N σ network respectively[12].

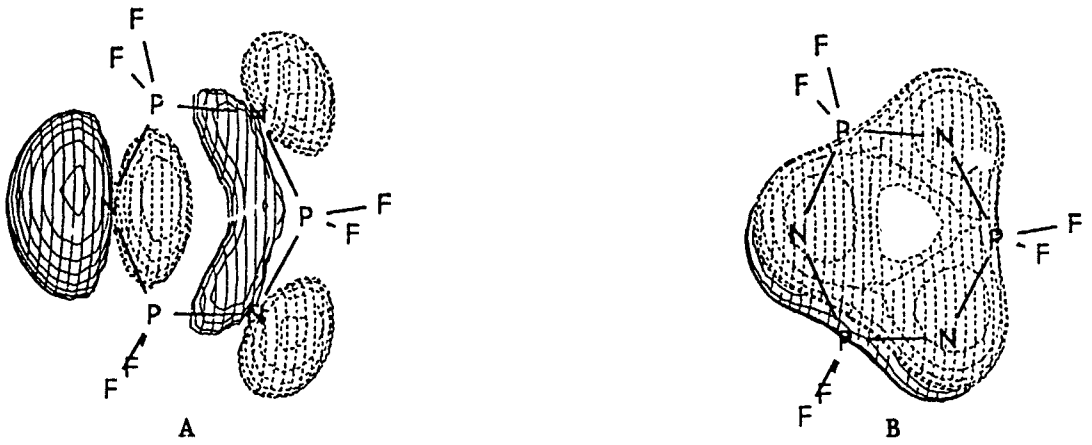

Figure 1 - Orbital contour for (a) π' and (b) π interactions in $(F_2PN)_3$. Ligand orbital contributions omitted for clarity.

Table 1 - Vertical ionization potentials (eV) for $(NPF_2)_3$, and $C_3H_3N_3$.

$P_3N_3F_6$		$C_3N_3H_3$	
Calculated	Expt'l[13]	Calculated	Expt'l [11]
11.4	11.4	10.37	10.37
13.0	13.1	11.82	11.67
14.8	15.4	13.97	13.2

Such effects are carried over into interpretations of the electronic absorption transitions. As one does not have an unambiguous assignment of the orbital ordering for the inorganic species, it becomes difficult to accurately predict and interpret the likely electronic transitions by electron spectroscopy alone. Thus, one of the simplest optical properties, electronic absorption becomes a multivariate problem since the orbital ordering cannot be a priori defined by a straightforward one to one correspondence with the PES spectra. These type of constraints extract a high premium on the use of corroborating data for imposing additional restraints on an otherwise underdetermined problem. In our case we used ab initio electronic structural information for the orbital ordering and ligand electronegativity

effects. Previous investigations on the electronic structure of phosphonitrilic systems have shown the importance of the nitrogen lone pair interactions, and the strength of these interactions relative to the out-of-plane π bonding.

Using this approach, we assigned the uppermost orbital ordering to π'-e"(σ,n), π-e'(π) and a' orbitals. Combined with the reported ionization energies and ordering we were able to predict the lowest electronic transitions for the phosphonitrilic systems as given in Table 2. This transition can be described as a charge transfer process between the π orbital localized mostly on the nitrogen sites, and the ligands. The energetics of these transitions are particularly sensitive to ligand electronegativity [4]. Previous work[1] has shown that the uppermost π orbitals in the occupied orbital manifold becomes higher in energy with decreased ligand electronegativity, while at the same time the π' orbital interactions become less pronounced.

Table 2 - Electronic absorption wavelengths (nm) for $(NPF_2)_n$

	Calculated	Experimental [14]
$(NPF_2)_3$	149	149
$(NPF_2)_4$	162	148
$(NPF_2)_5$	155	---

While there are a number of similarities in the electronic properties between the organic and inorganic systems, one of the significant differences is the charge distribution along the polymer backbone. Large electronegativity differences between phosphorus and nitrogen may affect the hyperpolarizabilities by restricting the delocalization of the π bonding electrons, while the electron drawing power of the substituent groups may also affect the delocalization in the π' network. We evaluated the effects of substituent groups on the hyperpolarizability of model polyphosphazenes through variations in the energy of a p_z electron on the phosphorus atoms in the molecule. Figure 2 shows the normalized

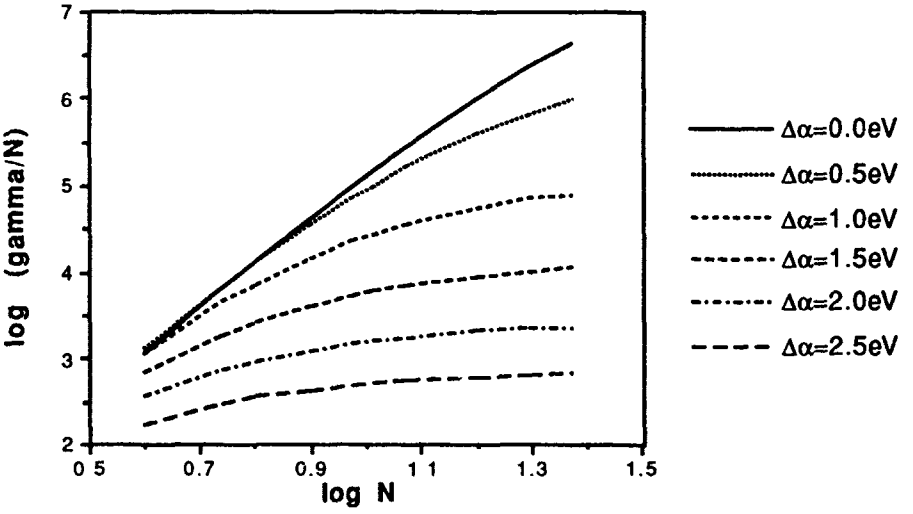

Figure 2. Hyperpolarizability per repeat unit of cis-trans conformation polyphosphazene vs. number of repeat units for various energy differences between p_z orbitals on nitrogen and phosphorus. The bond alternation is held at $0.04\beta_{PN}$.

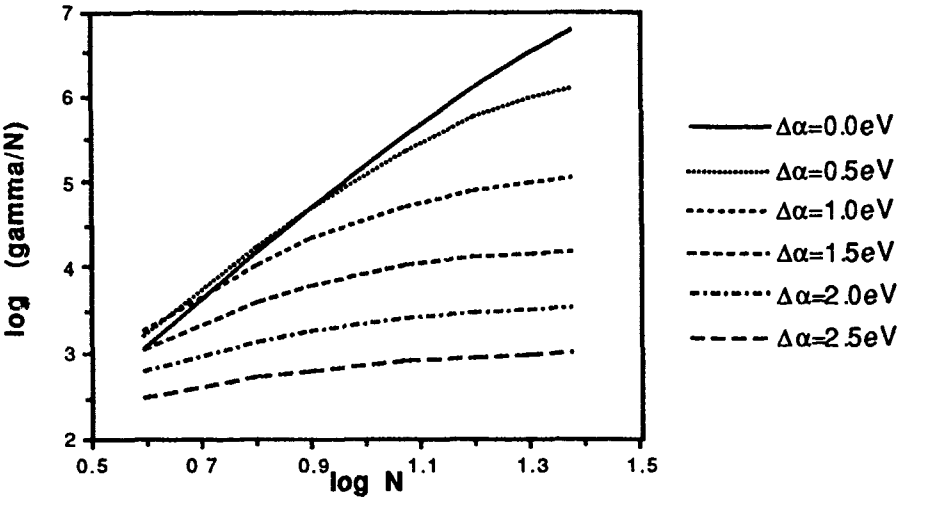

Figure 3. Hyperpolarizability per repeat unit of trans conformation polyphosphazene vs. number of repeat units for various energy differences between p_z orbitals on nitrogen and phosphorus. The bond alternation is held at $0.04\beta_{PN}$.

hyperpolarizability plotted against the number of repeat units for a series of energy differences ($\Delta\alpha$) between the nitrogen and phosphorus p_z orbitals. The bond alternation was held at a value of $0.04\beta_{PN}$. Conformational effects were investigated by performing similar calculations on the all-trans conformation of the polyphosphazene and are presented in Figure 3.

The overall appearance of these figures is very similar with the exception for very small number of repeat units, where the zero energy difference($\Delta\alpha$=0.0eV) curve for the trans conformation drops noticeably below the $\Delta\alpha$=0.5 eV curve for the cis-trans conformation. Previous calculations of the hyperpolarizability of trans and cis polyenes have shown that the length of the conjugated system is of primary importance in determining the magnitude of the hyperpolarizability. For the polyenes, the magnitudes of the hyperpolarizability for the two conformations are almost exactly identical per unit length of the primary axis of the molecule. The similarity of these figures for large number of repeat units reaffirms the concept that the length of the conjugated inorganic polymer network is of primary importance in determining the magnitude of the third order hyperpolarizability for inorganic system as well.

Within the limits of Huckel theory, Figures 2 and 3 also provide insight for synthetic directions of polyphosphazenes to maximize their nonlinear optical properties. In order to reach higher hyperpolarizabilities, our results indicate that the energy of the p_z orbitals on the nitrogen and phosphorus should be equivalent. Such conditions are best achieved by weak electron drawing and large polarizable groups at the phosphorus sites. Decreasing $\Delta\alpha$ not only causes the magnitude of the hyperpolarizability to dramatically increase, but also delays the onset of saturation, with the $\Delta\alpha$=0.0 curve showing no sign of saturation even at 60 repeat units. Preliminary measurements of second order hyperpolarizabilities have indeed shown that -SCN and -aminophenyl substitutions increase the hyperpolarizability over the chlorine substitution, and demonstrate a correlation with ^{31}P chemical shifts[15].

CONCLUSIONS

The optical properties of both organic and inorganic materials are a direct function of their electronic structure, and can be related to structural, conformational and ligand electronegativity effects. While the electronic structure of both systems can be well described by their molecular symmetry, the large electronegativity differences possible with inorganic systems complicates simple interpretations of their electronic structure. The major difference between organic and inorganic systems is the extent of orbital interaction in the π' bonding networks which are modulated by ligand electronegativity, and its effect on electronic transition energies. Substituent electronegativity effects also play a major role in determining the hyperpolarizability of the phosphonitrilic system, with the largest magnitudes arising from weakly electron accepting groups.

REFERENCES

[1] K.F. Ferris, P. Friedman, and D.M. Friedrich, Int. J. Quant. Chem. S22, 207, (1988); K.F. Ferris and C.B. Duke, Int. J. Quant. Chem. S23, 397, (1989).

[2] K.F. Ferris, S.M. Risser, A.K. Hanson, Proc. Mat. Res. Soc.: Electrical, Optical and Magnetic Properties of Organic Solid State Materials, ed. C. Liang, in press.

[3] S.M. Risser and K.F. Ferris, Laser Induced Damage in Optical Materials: 1989, NBS Spec. Publ., in press.

[4] H.R. Allcock in "Phosphorus-Nitrogen Compounds" New York: Academic Press (1972).

[5] C.B. Duke, W.R. Salaneck, T.J. Fabish, J.J. Ritsko, H.R. Thomas, and A. Paton, Phys. Rev. B 18, 5717, (1978).

[6] G.J. Trinquier, J. Amer. Chem. Soc. 108, 568 (1986).

[7] N. Mataga and K. Nishimoto, Z. Phys. Chem. 13, 140, (1957).

[8] J.A. Pople and G.A. Segal, J. Chem. Phys. 43, 5136, (1965).

[9] S.M. Risser, S. Klemm, D.W. Allender and Michael A. Lee, Mol. Cryst. Liq. Cryst., 150b, 631 (1987).

[10] C.B. Duke, K.L. Yip, G.P. Ceasar, A.W. Potts, and D.G. Streets, J. Chem. Phys. 66, 256, (1977).

[11] R. Gleiter, E. Heilbronner, and V. Hornung, Helv. Chim. Acta 55, 255, (1972).

[12] H.R. Allcock in "Phosphorus-Nitrogen Compounds" New York: Academic Press (1972).

[13] G.R. Branton, C.E. Brion, D.C. Frost, K.A.R. Mitchell, and N.L. Paddock, J. Chem. Soc. A, 151, (1970).

[14] B. Lakatos, A. Hesz, Z. Vetessy, and G. Horvath, Acta Chim. Acad. Sci. Hung. 60, 309, (1969).

[15] G.J. Exarhos and K. Crosby, Laser Induced Damage in Optical Materials: 1989, NBS Spec. Publ., in press.

DILUTE SOLUTION CHARACTERIZATION OF POLY(IBMA-CO-TBAEMA)

Marie Kayser Potts
Polymer Research Branch, U.S. Army Materials Technology Laboratory
Watertown, MA 02172-0001

Dilute solution techniques (laser light scattering and dilute solution viscometry) were utilized to study a random copolymer of poly(isobutylmethacrylate-co-t-butylaminoethylmethacrylate) in isopropyl alcohol, methyl ethyl ketone, tetrahydrofuran and dichloromethane. The experimentally determined solvent-dependent molecular weights are proposed to be caused by some type of polymer aggregation in solution. Of the four solvents studied, methyl ethyl ketone was determined to be the best solvent for the copolymer.

INTRODUCTION

Laser light scattering in the static mode may be utilized to obtain the absolute (solvent independent) weight-average molecular weight (Mw), the z-average radius of gyration (Rg), and the second virial coefficient (A_2) of a polymer, the latter two quantities being solvent-dependent properties. The ability to determine these polymer properties in any given solvent depends on the magnitude of the refractive index increment (dn/dC) between the solvent and the (dilute) polymer solution, which determines the intensity of the scattered laser light. In copolymers, since there are two distinct chemical species present, each will have its own dn/dC value in a given solvent, and every molecule with a different ratio of the same comomoners will have a slightly different dn/dC. Since synthetic copolymers will always have a chemical composition distribution, a macroscopically determined dn/dC value will reflect the average composition of the copolymer; however, during the light scattering experiment, the molecule that is at the scattering center at any given time will undoubtedly have a composition different from that of the average composition, and therefore a unique dn/dC value. This discrepancy between the average dn/dC value used in the calculation of the molecular weight, and the instantaneous dn/dC value which determines the scattered light intensity yields molecular weights which are solvent dependent, and usually increase as the refractive index of the solvent approaches that of the polymer. These molecular weights are usually regarded as apparent (Mw,app)

molecular weights as opposed to absolute (Mw) molecular weights. A similar type of analysis applies to the Rg value of a copolymer; however, unless the copolymer is very "blocky", the apparent Rg values do not vary much from the actual values.[1]

EXPERIMENTAL

Materials. Poly(iBMA-co-tBAEMA) of approximate molar ratio 77:23 was obtained from Polyscience (Lot # CM1-120). The molecular weight from light scattering [2] and aqueous SEC [3] is estimated to be approximately 2.7 million.

2-propanol (glass distilled) from Burdick & Jackson Laboratories, Ltd. was used as received. Methyl ethyl ketone, tetrahydrofuran (unpreserved), and dichloromethane (all distilled in glass) were obtained from Caledon Laboratories, Ltd. and used as received. Toluene from EM Science (glass distilled) was used as received.

Equipment. Light scattering intensity measurements were made on a Brookhaven Instruments 200SM goniometer and analzed with a BI2030AT correlator/computer. The light source was a Melles-Griot 5 mW helium-neon laser operating at 633 nm. All measurements were made at 25 $\pm$ 0.1^{0} C. The angular range was typically 30^{0} - 135^{0}. Toluene was used as the reference liquid with a Rayleigh ratio [4] of 1.40 x 10^{-5} cm^{-1}. Solvents were filtered through 0.25 micron PTFE filters and polymer solutions (concentrations < 10^{-3} g/mL) were filtered through 5 micron filters (twice) to remove dust. (Filters of 0.45 and 1 micron porosity clogged almost immediately when used to filter solutions.)

Refractive index increments were calculated [5] according to (dn/dC) = 1.3238 - 0.8923n, where n is the refractive index of the solvent.

Intrinsic viscosity (or limiting viscosity number, LVN) measurements were made with Cannon Ubbelohde dilution viscometers at 25 $\pm$ 0.05^{0} C. Solvents were filtered through 1 micron and polymer solutions (concentrations < 5 x 10^{-3} g/mL) throught 10 micron PTFE filters to remove gross particulates.

RESULTS AND DISCUSSION

Light scattering results were analyzed via Zimm Plots, Fig. 1, and the results are tabulated in Table 1, from highest to lowest apparent molecular weights. Except for isopropyl alcohol, this trend of decreasing Mw parallels the refractive index. The second virial coefficients in Table 1 are all negative, except for methyl ethyl ketone. THF, in particular, has a large negative A_2 value, indicating a rather poor solvent. Isopropyl alcohol has a slightly negative second virial coefficient, probably indicative of a theta solvent, and indeed, isopropyl alcohol is a theta solvent for poly(iBMA) at room temperature [6].

There is a large variation in the apparent molecular weights for the copolymer in these solvents, and this would normally be attributed to compositional differences in the copolymer sample, as discussed in the Introduction. From measurements made in our laboratory [2] and elsewhere [7], the dn/dc values determined in several solvents for the copolymer poly(iBMA-co-tBAEMA) and its two constituent homopolymers did not vary by more than about 10% for any given solvent. This leads one to conclude that the two components of the copolymer have nearly identical refractive indices, and

indeed, the similarity in their chemical structure supports this theory. Thus, any compositional heterogeneity in the copolymer sample would have little effect on the dn/dC values. This implies that the differences in molecular weights determined from light scattering are not due to compositional differences as previously suspected [2,8,9], but must be due to some type of aggregation in solution, caused by polymer/polymer or polymer/solvent interactions.

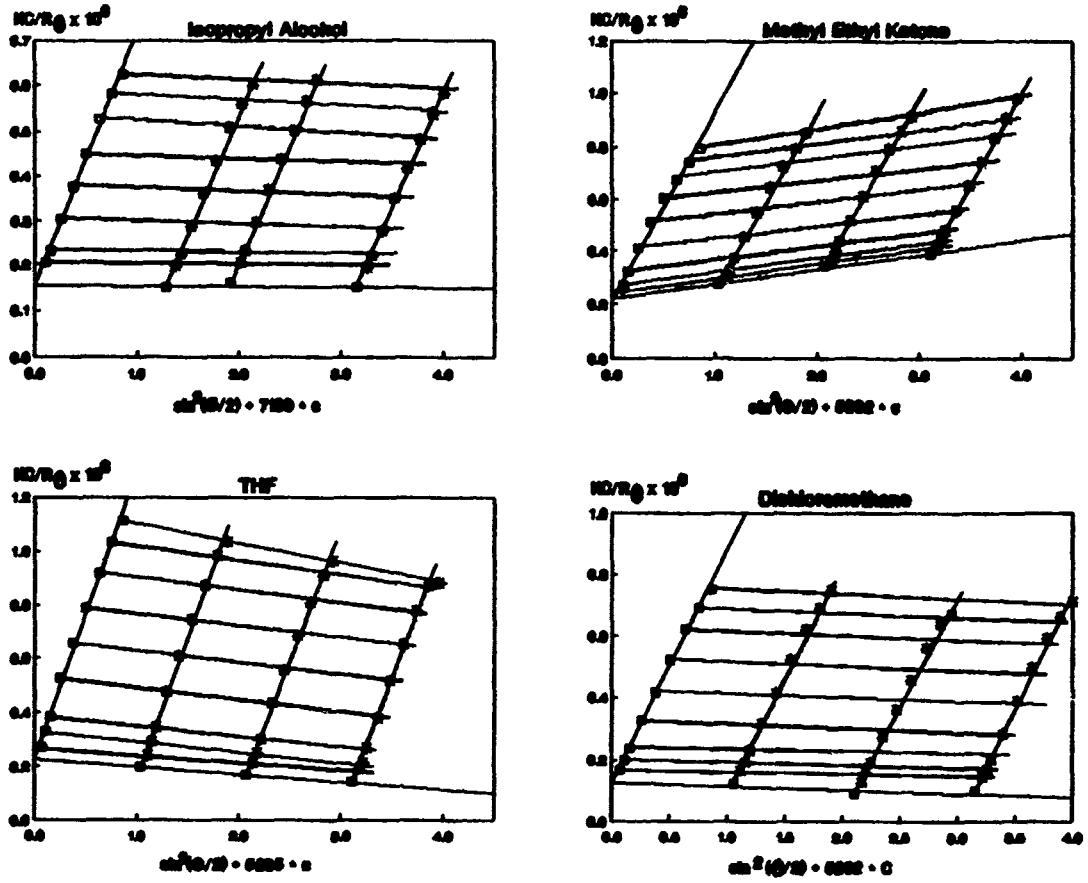

Fig. 1. Zimm Plots of poly(iBMA-co-tBAEMA)

TABLE 1

Light Scattering Results

Solvent	n	dn/dC mL/g	Mw,app x 10^6	Rg nm	A_2 x 10^4 mL-mol/g^2
$MeCl_2$	1.420	0.057	7.72	148	-0.368
iPrOH	1.374	0.097	6.12	122	-0.059
THF	1.404	0.071	5.05	142	-2.07
MEK	1.375	0.097	4.30	107	1.95

LVN data were analyzed via Huggins plots ($[\eta/\eta_o - 1]/C$ vs. C) and Kraemer plots ($\ln [\eta/\eta_o]/C$ vs. C), Fig. 2, and tabulated in Table 2, in order of

decreasing LVN value. This order parallels that of decreasing molecular weight from Table 1, except for isopropyl alcohol which, again, is anomalous. The constants k' and k" are determined from the slopes of the Huggins and Kraemer plots, respectively, and should be in the ranges $0 < k" < 0.15$, and $0.15 < k' < 0.35$, with the sum of the two constants approximately 0.5, for a thermodynamically good solvent. From Table 2, methyl ethyl ketone appears to exhibit the best solution behavior, based on the values of the two constants.

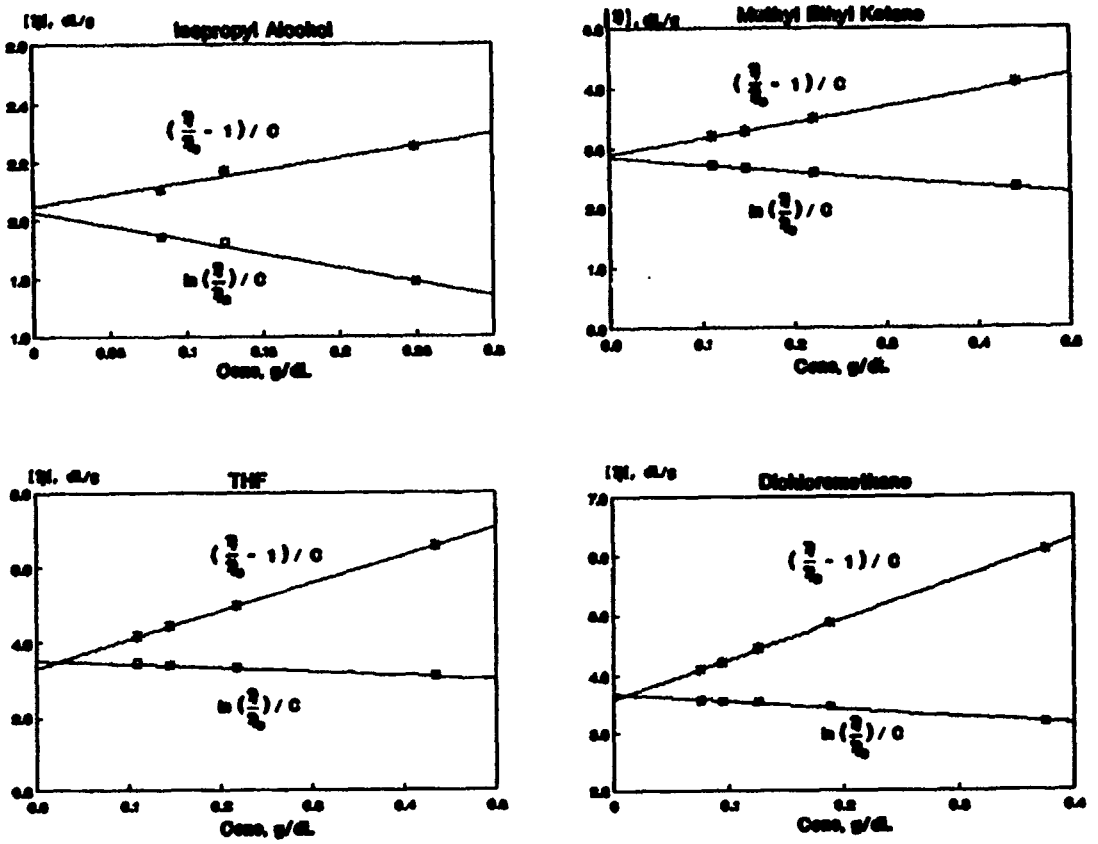

Fig. 2. Huggins and Kraemer plots of poly(iBMA-co-tBAEMA)

TABLE 2

Limiting Viscosity Number Results

Solvent	LVN dL/g	k'	k"	k'+k"
$MeCl_2$	3.644	0.516	0.099	0.615
THF	3.455	0.662	0.081	0.743
MEK	2.878	0.321	0.146	0.467
iPrOH	2.040	0.194	0.233	0.427

Usually, one would associate the solvent with the highest LVN value as having the highest solvating power for the polymer, and thus the thermodynamically best solvent. Under the present assumption of copolymer aggregation in solution, however, it appears that the higher LVN values may represent the

viscosity of larger copolymer aggregates, and not single coils.

CONCLUSIONS

Based on the light scattering and LVN analysis of the four solvents studied, methyl ethyl ketone appears to exhibit the best solution behavior for poly(iBMA-co-tBAEMA). The other solvents appear to be thermodynamically poor solvents, based on the second virial coefficients determined from light scattering measurements. Isopropyl alcohol may be a theta or near-theta solvent for the copolymer at room temperature.

Since the differences in refractive index between the two constituent homopolymers, poly(iBMA) and poly(tBAEMA), and the copolymer are very small, one can assume that small compositional differences in the bulk copolymer sample have little effect on the overall (dn/dc) value. This implies that differences in molecular weights determined in different solvents are not due to compositional differences in the copolymer, but to some type of interaction occuring under different solvent conditions. If this is the case, the lower molecular weights may indicate that fewer interactions are occuring, and may be closer to the true molecular weight.

By a similar analysis, the higher LVN values may be indicative of aggregation in solution, and as long as the Huggins and Kraemer constants are in the range for good solution behavior, the solvents with the lower LVN values will generally be preferred.

REFERENCES

1. H. Morawetz, "Macromolecules in Solution", Interscience Publishers, New York, 1965, Chap. 5.

2. M.K. Potts, G.L. Hagnauer, D.A. Dunn, Proceedings of the 1988 Scientific Conference on Chemical Defense Research (1989).

3. V.M. McHugh, Appendix A of CRDEC Technical Report (in press; MS-581).

4. W. Kaye, J B. McDaniel, Applied Optics 13, 1934 (1974).

5. J.C. Galin, Institut Charles Sadron, Strasbourg, France; private communication.

6. J. Brandup, E.H. Immergut, Eds. Polymer Handbook, John Wiley & Sons, New York, 1975; pp. IV-162, IV-244.

7. B. Chu; private communication.

8. B. Chu, R. Hilfiker, J. Shook, J. Wang, Proceedings of the 1988 Scientific Conference on Chemical Defense Research (1989).

9. J.C. Galin, "Report on Copolymers CM, K-125 E and K-125 G", Institut Charles Sadron, Strasbourg, France; internal publication.

BLANK

XIV. PROTECTION POSTER

NOTE: Papers with the following titles were presented at the Conference but are not included in this document:

Rapid Three-Dimensional Anthropometric and Mold Measurement for Mask Design

Improved Method for Investigating NBC Respirator Communication Capability

Respirator Lens Configuration for Optical Coupling to Sighting Systems

BLANK

AES AND XPS ANALYSES OF PLASTIC WELDS

Chen C. Hsu and Janice A. Fritz

U.S. Army Chemical Research, Development and Engineering Center, Aberdeen Proving Ground, MD 21010-5423

ABSTRACT

A total of twelve plastic samples were analyzed using Auger electron spectroscopy (AES) and X-ray photoelectron spectroscopy (XPS) techniques. The samples include plastic raw material, virgin plastic sheet, scratched virgin plastic, failed thin and thick plastic welds, the center of the failed plastic disks and the failed plastic welds from the contractor. Since the plastic material is polyethylene, so carbon was detected. Additionally, sulfur, oxygen, chlorine, phosphorus, and silicon were identified. It turns out that sulfur is due to the anti-oxidant additive in the plastics and chlorine is due to the cleaner used in the shop - trichloroethane. The weld's bonding pattern of the failed plastic welds shown in the SEM micrographs can be attributed to the insufficient bonding between the plastic pipe and the disk which may be due to contaminants and non-uniform heating before welding.

INTRODUCTION

Polyethylene plastics were selected for the fabrication of chemical containment. It requires two components, one from a section of plastic pipe with 4 3/4 inches in diameter and 1/4 inch thick and the other with a disk with the same diameter and 1/16 inch thick stamped from a plastic sheet. Both components were heated before they were pressed together to form a weld. The welding protocol requires the welding operator to clean the area where both components join with a spray cleaner. The spray cleaner used in the shop contains trichloroethane. Pressure tests were conducted to make sure that the weld holds a minimum pressure of 125 lbs. Recently, however, for unknown reasons that several plastic welds failed the pressure test. The surface spectroscopic analysis (XPS and SAM) was conducted on the failed plastic samples to address the questions as to why the plastic welds failed.

EXPERIMENTAL

A one centimeter square sample of the failed plastic welds was taken from the failed spot by using a shearer. The sample consisting of the plastic disk and the pipe section were separately mounted on two sample mounts with the weld surface facing up for analysis. Copper-backed conducting tapes were used for the sample mounting to reduce the possible charging on the sample. This is the only one step for sample preparation. The sample was initially evacuated to 10^{-6} torr in the sample introduction port before it was introduced into the test chamber which is routinely maintained at 3.0x10E-10 torr.

For SAM and XPS analyses, Perkin-Elmer PHI Model 570 Surface Analysis System was used. The general operational procedures and parameters were described previously [1]. Briefly, for SAM analysis, normally 3kV and 10 nA electron beam was used. For XPS analysis, we used 14 kV and 200 W Mg K_{alpha} X-ray source (1253.6 eV) with 100 and 50 eV passing energies for XPS survey and multiplex runs, respectively. The system energy calibration is based on the binding energies of Cu(2p) and Cu(3p) after pure Cu metal was sputtered for 15 minutes with argon ion gun (15 A/min sputtering rate). In calculating the atomic concentration of each identified elements, the elemental detection sensitivity factors were taken into account. For Auger elemental maps, a SEM micrograph was taken and a matrix of 160x160 was defined for scanning. The result was reproduced on the 10x13 cm Polaroid films.

RESULTS AND DISCUSSION

XPS Results. The XPS survey was conducted to identify the elements on sample surfaces followed by multiplex runs for the identified elements. The multiplex results provides the accurate binding energy of the identified elements from which the oxidation state of an element is determined. Additionally, the integration of the peak area gives the atomic concentration of the element of interest. The results of XPS analysis of the plastic samples are shown in Tables 1-12. The elements identified are C, O, S, Cl, Si, and P. The finding of C, S, and O is expected [2] since the plastics was made of polyethylene, butene-1, and antioxidant, 4,4'-thiobis(2-t-butyl-5-methylphenol), which has the following structure:

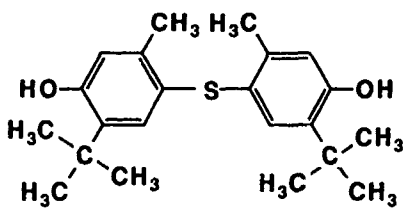

The finding of Cl, Si, and P were somewhat unexpected. It was later found that Cl was attributed to trichloroethane, the spread cleaner used in the shop for cleaning the plastic components before welding. The source of Si and P is possibly from air contaminants.

SAM Results. Auger elemental maps were obtained from the area defined by the SEM micrographs of the plastic samples of interest. Figure 1 shows the relatively smooth surface of the plastic weld sample M2 which failed at 80 lbs of pressure test (the specification requires 125 lbs to pass the test) [2]. The bonding pattern is rather sporadic. This strongly suggested that the plastic components were not heated uniformly before welding. It is reported that the melting point of the copolymer of ethylene and butene-1 is 125° C with a density range of 0.941-0.945 g/cm^3 [2]. These values are considered reasonable in comparison with the values reported in the literature for high density polyethylene, 130-135° C with densities in the range of 0.945-0.965 g/cm^3 [3]. With 4 wt% of butene-1 in the blend, the melting point of the copolymer is reduced by about 5° C. It is conceivable that the heat plates for the welding of the plastic disk and pipe either did not reach to 125° C or did reach to 125° C but without sufficient contact time at the spots where the weld failed the pressure test.

On the contrary, Figure 2 shows the continuous bonding pattern of the plastic weld which indeed passed the pressure test and ultimately failed at 129 lbs. Auger mapping was also conducted to find the distribution of those contaminants and the results are shown in Figure 3. It reveals that the contaminants locate around the area of failure where the plastic disk separated from the plastic pipe.

SUMMARY

1. **Twelve plastic samples were analyzed surface spectroscopically.**

2. **XPS results indicate the presence of the elements of Cl, S, O, P, and Si in addition to C, the major constituent of the polyethylene plastics. S and O were due to plastic antioxidant, 4,4'-thiobis[2-t-butylphenol], and Cl due to trichloroethane, while Si and P were due to air contaminants.**

3. **SEM micrographs show the sporadic bonding patterns, due possibly to non-uniform heating, for those failed plastic welds as opposed to dense and continuous bonding pattern for those passed the pressure test at 129 lbs.**

4. **Auger elemental maps reveal the distribution of contaminants which seem localize in the area of failure.**

5. **It may be concluded that the causes of failure of plastic welds are due to contaminants and non-uniform heating before welding.**

REFERENCES

[1] C. C. Hsu, "Surface Spectroscopic Analysis of Fresh and Spent Oxidation Catalysts," Proceedings of U.S. Army CRDEC Scientific Conference on Chemical Defense Research, CRDEC-SP-013, Vol. 1, 407-417 (1989).

[2] Military Specification, Plastic Molding and Extrusion Material, Polyethylene Butene-1 Copolymer, High Density, MIL-P-51431(EA), 22 February 1977.

[3] A. W. Birley, R. J. Heath, and M. J. Scott, "Plastic Materials, Properties and Applications," 2nd edition, Chapman and Hall (1988).

TABLE 1.

RESULTS OF XPS ANALYSIS ON PLASTIC SAMPLE 128 (THIN SIDE)

ELEMENT	APPARENT BINDING ENERGY eV	CORRECTED BINDING ENERGY eV	ATOMIC CONCENTRATION %
C (1s)	285.66	284.60	89.6
O (1s)	533.27	532.21	8.1
Si (2p)	101.90	100.84	0.9
S (2p)	164.54	163.48	0.6
Cl (2p)	197.45	196.39	0.3
P (2p)	129.65	128.59	0.2

TABLE 2.

RESULTS OF XPS ANALYSIS ON PLASTIC SAMPLE 128 (THICK SIDE)

ELEMENT	APPARENT BINDING ENERGY eV	CORRECTED BINDING ENERGY eV	ATOMIC CONCENTRATION %
C (1s)	286.26	284.60	95.4
O (1s)	533.86	532.20	3.0
Si (2p)	102.89	101.23	0.6
P (2p)	134.01	132.35	0.3
S (2p)	164.94	164.28	0.2
Cl (2p)	199.63	197.97	0.2

TABLE 3.

RESULTS OF XPS ANALYSIS ON PLASTIC SAMPLE 140 (THICK SIDE)

ELEMENT	APPARENT BINDING ENERGY eV	CORRECTED BINDING ENERGY eV	ATOMIC CONCENTRATION %
C (1s)	286.26	284.60	95.0
O (1s)	533.66	532.00	3.6
Si (2p)	102.29	100.63	0.8
S (2p)	153.64	151.98	0.2
P (2p)	130.24	128.58	0.1

TABLE 4.

RESULTS OF XPS ANALYSIS ON PLASTIC SAMPLE 140 (THIN SIDE)

ELEMENT	APPARENT BINDING ENERGY eV	CORRECTED BINDING ENERGY eV	ATOMIC CONCENTRATION %
C (1s)	285.66	284.60	76.2
O (1s)	532.87	531.81	19.6
Si (2p)	102.09	101.03	3.2
Cl (2p)	197.65	196.59	0.5
P (2p)	135.00	133.94	0.2
S (2p)	164.54	163.48	0.1

TABLE 5.

RESULTS OF XPS ANALYSIS ON RAW PLASTIC SAMPLE MATERIAL M445

ELEMENT	APPARENT BINDING ENERGY eV	CORRECTED BINDING ENERGY eV	ATOMIC CONCENTRATION %
C (1s)	285.47	284.60	94.6
O (1s)	533.27	532.40	3.9
S (2p)	163.94	163.07	0.8
Si (2p)	102.09	101.22	0.5

TABLE 6.

RESULTS OF XPS ANALYSIS ON PLASTIC SAMPLE MATERIAL M2 (THIN SIDE)

ELEMENT	APPARENT BINDING ENERGY eV	CORRECTED BINDING ENERGY eV	ATOMIC CONCENTRATION %
C (1s)	285.86	284.60	95.8
S (2p)	165.33	164.07	2.9
O (1s)	533.66	532.40	1.1

TABLE 7.

RESULTS OF XPS ANALYSIS ON PLASTIC SAMPLE MATERIAL M2 (THICK SIDE)

ELEMENT	APPARENT BINDING ENERGY eV	CORRECTED BINDING ENERGY eV	ATOMIC CONCENTRATION %
C (1s)	286.06	284.60	88.8
O (1s)	533.86	532.40	10.1
Si (2p)	102.89	101.43	0.9
Cl (2p)	200.42	198.96	0.1

TABLE 8.

RESULTS OF XPS ANALYSIS ON PLASTIC SAMPLE MATERIAL M2 (CENTER)

ELEMENT	APPARENT BINDING ENERGY eV	CORRECTED BINDING ENERGY eV	ATOMIC CONCENTRATION %
C (1s)	286.06	284.60	92.2
O (1s)	533.27	531.81	5.8
Si (2p)	102.09	100.63	1.3
S (2p)	153.44	151.98	0.5

TABLE 9.

RESULTS OF XPS ANALYSIS ON PLASTIC SAMPLE MATERIAL M14 (CENTER)

ELEMENT	APPARENT BINDING ENERGY eV	CORRECTED BINDING ENERGY eV	ATOMIC CONCENTRATION %
C (1s)	286.06	284.60	93.2
O (1s)	533.46	532.00	5.9
Si (2p)	102.29	100.83	0.5
S (2p)	163.33	163.87	0.2

TABLE 10.

RESULTS OF XPS ANALYSIS ON PLASTIC SAMPLE MATERIAL M14 (THIN SIDE)

ELEMENT	APPARENT BINDING ENERGY eV	CORRECTED BINDING ENERGY eV	ATOMIC CONCENTRATION %
C (1s)	285.86	284.60	93.0
O (1s)	533.27	532.01	6.0
Si (2p)	102.49	101.23	0.5
S (2p)	164.54	163.28	0.3
Cl (2p)	200.02	198.76	0.1

TABLE 11.

RESULTS OF XPS ANALYSIS ON THE SCRATCHED VIRGIN PLASTIC SAMPLE

ELEMENT	APPARENT BINDING ENERGY eV	CORRECTED BINDING ENERGY eV	ATOMIC CONCENTRATION %
C (1s)	285.47	284.60	88.7
O (1s)	533.66	532.79	8.7
Si (2p)	102.29	101.42	2.0
S (2p)	164.14	163.27	0.4

TABLE 12.

RESULTS OF XPS ANALYSIS ON THE VIRGIN PLASTIC SAMPLE

ELEMENT	APPARENT BINDING ENERGY eV	CORRECTED BINDING ENERGY eV	ATOMIC CONCENTRATION %
C (1s)	285.47	284.60	80.3
O (1s)	532.87	532.00	12.2
Si (2p)	102.09	101.22	6.1
Cl (2p)	197.64	196.77	0.6
S (2p)	164.74	163.87	0.5

M14 SAMPLE (THICK SIDE), 20X

M14 SAMPLE (THICK SIDE), 100X

Figure 1. SEM micrographs of M14 sample which passed the pressure test at 129 lbs.

M2 SAMPLE (THICK SIDE), 20X

M2 SAMPLE (THICK SIDE), 100X

Figure 2. SEM micrographs of M2 sample which failed the pressure test at 80 lbs.

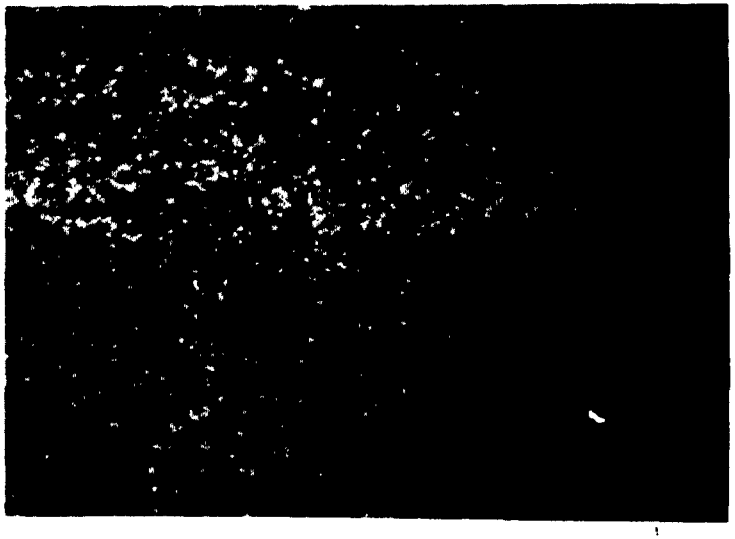

M2 SAMPLE (THICK SIDE), 100X, C MAP

M2 SAMPLE (THICK SIDE), 100X, O MAP

M2 SAMPLE (THICK SIDE), 100X, Cl MAP

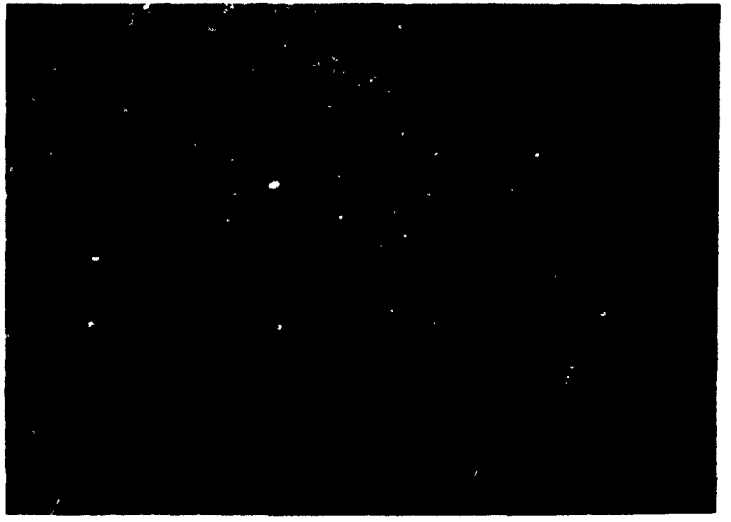

M2 SAMPLE (THICK SIDE), 100X, Si MAP

Figure 3. Auger elemental maps of carbon, oxygen, chlorine, and silicon of M2 sample. The bright spots on the maps are the location of elements.

BLANK

XV. TOXICOLOGICAL AND ENVIRONMENTAL STUDIES POSTERS

BLANK

SOLVENT–WATER PARTITIONING AND EXTRACTION OF PHOSPHONATES

Daniel C. Leggett

U.S. Army Cold Regions Research and Engineering Laboratory
72 Lyme Road
Hanover, New Hampshire 03755-1290

ABSTRACT

Phosphonates are used as G-agent simulants in a number of applications. Partitioning of dimethyl methylphosphonate (DMMP) between water and various solvents was examined with a view toward optimization of solvent extraction methods for this class of compounds. The results of these partitioning experiments indicate that the best solvents for extraction of DMMP from water are H-donors, suggesting H-bonding as the principal mechanism. Advantage was also taken of the universal salting-out effect; saturating the aqueous phase with NaCl increased the partition coefficient of DMMP six-fold (0.78 log units), irrespective of the solvent. By analogy, similar results may be expected for other low molecular weight phosphonates, phosphites, phosphates and phosphonofluoridates.

INTRODUCTION

Dimethyl methylphosphonate (DMMP) and other phosphonates are used as nontoxic simulants for G-agents by the U.S. Army and its contractors. In addition DMMP and several other phosphonates are used as commercial flame retardants and viscosity suppressants,[2] although accurate production figures were not available. Reported neutral hydrolysis half-lives for DMMP vary from 13 to 88 years,[1,3] while its stability in soil appears to be on the order of days to months.[1] Acids and bases both catalyze its hydrolysis, so its persistence in different soil/water environments will vary. The most frequently used predictor of organic contaminant mobility in soil is the octanol/water partition coefficient,[4] P_{oct}. A measured value for P_{oct} of DMMP was 0.074,[5] which suggests high soil-water mobility.

Military and commercial use of phosphonates requires development of suitable methods for their determination in a variety of matrices. Methods that have been used for these and related compounds in aqueous samples include direct injection-gas chromatography (GC)[5] and solvent extraction with chloroform followed by GC[6,7,8] on packed columns using either flame ionization (FID) or flame photometric (FPD) detectors. The sensitivity of FPD is about 100 times that of FID for these compounds.[8] Chloroform extraction methods all included addition of sodium chloride (0.2 g/mL), presumably to increase extraction efficiency. Even so only 50% of the agent sarin (GB) was extracted when a 1:100 solvent–water ratio was used.[7] In their later method Shih and Ellin[8] employed a 1:10 solvent–water ratio. Since DMMP is even more hydrophilic than GB,[5] linear free energy

relationships (LFERS) among solvents[9] tell us that its chloroform/water partition coefficient, and hence its extractability, will also be lower than that of GB.

The idea of using salting-out to separate miscible solvents from water for the purpose of extracting polar organics has recently been exploited.[10,11] Not only are the partition coefficients of analytes increased by salting but the polarity range of solvents that can be used for extraction of water is greatly expanded. It was of interest to examine the partitioning of DMMP into various solvents with a view toward optimization of extractive preconcentration of these compounds. Also, the expanded range of solvents made available by the addition of salt permits the clearer evaluation of the role of polar interactions in solvent extraction.

METHODOLOGY

Solvents were obtained from various suppliers and used without further purification. DMMP and diethyl methylphosphonate (DEMP) were obtained from Aldrich. Diethyl ethylphosphonate (DEEP) was obtained from Pfaltz and Bauer. Diisopropyl methylphosphonate (DIMP) was a standard analytical reference material (SARM) obained from the Toxic and Hazardous Materials Agency (THAMA).

A 500-mg/L stock solution of DMMP was prepared in house-distilled water; 5-mL aliquots of this solution were transferred to glass vials followed by an equal volume of each of the solvents. The vials were capped and shaken manually for a few minutes and the phases allowed to separate. The DMMP concentration in both phases was determined by direct injection GC-FID on a 180-cm × 0.18-cm i.d. 10% SP-1000 column (Supelco) at a temperature of 115°C and a carrier flow rate of 20 mL/minute. The carrier gas was zero-grade nitrogen (Air Products) purified with an in-line oxygen trap (J&W). The injector temperature was 200°C. The retention time under these conditions was 8.0 ±0.1 minutes. Data were taken with a digital integrator (H-P 3390).

To each of the vials was added an excess of sodium chloride (Baker) and the equilibration and analyses repeated. Obviously, for the water-miscible solvents, data were only taken after addition of salt. The partition coefficients were calculated from the ratio of relative chromatographic responses in the two phases when the same volumes were injected (2.00 µL).

The partition coefficient of DMMP between water and hexafluoroisopropanol (HFIP) could not be measured in this way because the aqueous phase concentration was undetectable. An alternate method was used to measure the HFIP/salt-water partition coefficients of four phosphonate esters. An aqueous stock containing 500 mg/L each of DMMP, DEMP, DIMP and DEEP was prepared — 35 mL of this solution, 11.0 g NaCl and 1.00 mL of HFIP were mixed on a vortex mixer until no more salt would dissolve. Aqueous phase concentrations of the four compounds were determined before and after extraction and the HFIP concentration was determined as the difference multiplied by the ratio of final water to solvent volumes, which were 39.0 and 0.85 mL, respectively.

Analyses for this part of the experimental work were performed on a 10% SP-1200/1% H_3PO_4 column, as the SP-1000 column did not completely resolve the four compounds. A comparable separation was obtained on a 15-m DB-wax megabore column at 70°C, which was used for GC-FPD analysis.

RESULTS AND DISCUSSION

Since part of the rationale for this work was to examine a range of water-miscible solvents not normally used for solvent extraction, some initial testing was done to see which solvents could be salted out using the experimental protocol. Table 1 is a list of only those solvents actually tested and is not intended to include all those possible.

TABLE 1
Solvents Subjected to Salting with Saturated NaCl

Salted Out	Not Salted Out
acetone	dimethylformamide
acetonitrile	ethanol
hexafluoroisopropanol	ethylene glycol
isopropanol	ethyl cellosolve
n-propanol	methanol
tetrahydrofuran	
trifluoroethanol	

The results of DMMP partitioning experiments in the absence and presence of saturated NaCl are shown in Table 2. In addition to those shown, several, unfortunately, could not be analyzed because of interferences during GC analysis; these were toluene, benzyl alcohol, and nitrobenzene.

The solvents were chosen to cover a range of polar functional groups: ethers, alcohols, ketones, nitriles, carbonates, aldehydes, nitroalkanes, and esters. The relative extraction efficiencies of the different solvents are similar to those reported earlier for several phosphonofluoridates.[12] The highest partition coefficients are with known H-donor solvents, alcohols, haloforms, and nitroalkanes, and the relative partitioning appears to be consistent with substituent electron-withdrawing effects on H-donicity. Ethers, ketones, esters, and nitriles are electron-pair donors like DMMP and had lower partition coefficients, reflecting their relatively weak H-donor properties. Weakest of all were compounds with negligible or no H-donor properties, hexane, carbon disulfide, carbon tetrachloride. Compounds such as benzene and benzonitrile may behave as weak, electron-pair accepting Lewis acids, even though they have negligible H-donor properties. Heats of mixing of DMMP with chloroform, HFIP and probably TFE as well are greater than with water,[13] which suggests stronger H-bond formation with these solvents. The ability of DMMP and related organophosphorus compounds to form H-bond complexes has been firmly established.[14-18]

Saturation of the aqueous phase with NaCl increased the partition coefficients six-fold on average. Even with salting, however, chloroform extracted only 90% of the DMMP at a 1:1 solvent to water ratio. At a 1:10 ratio the recovery would be 48% and at 1:100, 8.5%. Thus preconcentration with chloroform would require evaporation of the solvent to achieve an appreciable preconcentration of DMMP. In contrast TFE is 16 times better and HFIP 129 times better than chloroform. Thus 92% recovery of DMMP is, in principle, achievable at an HFIP/water ratio of 100:1, obviating the need for evaporative preconcentration in many applications.

TABLE 2
Partitioning of DMMP between Water and Various Solvents

Solvent	P_{sw}	P_{sw}^{salt}	r[a]
hexane	b	0.0035	
carbon disulfide	0.0026	0.033	12.7
carbon tetrachloride	0.011	0.10	9.1
diethyl ether	0.032	0.19	5.9
1,1,1-trichloroethane	b	0.20	
benzene	0.069	0.21	3.0
trichloroethylene	0.053	0.47	8.9
tetrahydrofuran	c	0.59	
n-octanol	0.074	b	
methyl ethyl ketone	0.19	0.83	4.4
benzonitrile	0.15	1.0	6.7
acetone	c	1.0	
benzyl nitrile	0.30	1.2	4.0
propylene carbonate	0.36	1.2	3.3
propanal	0.55	1.3	2.4
nitroethane	0.32	1.5	4.7
ethyl acetate	0.17	1.7	10.0
isopropanol	c	2.5	
acetonitrile	c	2.6	
1,1,2-trichloroethane	0.49	3.0	6.1
nitromethane	0.56	3.1	5.5
isobutanol	0.74	3.2	4.3
bromoform	0.46	3.3	7.2
n-propanol	c	3.5	
methylene chloride	0.66	4.6	7.0
chloroform	1.5	9.3	6.2
trifluoroethanol	c	150	
hexafluoroisopropanol	c	1200	

a—r is the ratio P_{sw}^{salt}/P_{sw}; b—no data; c—miscible.

The HFIP/water partition coefficients of four phosphonates were determined as described in the METHODOLOGY section. The results shown in Table 3 indicate that extractive preconcentration of other phosphonates is even more efficient than for DMMP. This was anticipated since they also have higher octanol/water partition coefficients. By use of P_{oct} values derived from earlier work[5], a correlation of P_{HFIP} with P_{oct} was given by the equation $\log P_{HFIP} = 3.438 + 0.297 \log P_{oct}$ with a correlation coefficient of 0.977. Using the protocol for measuring these partition coefficients as a preconcentration method for phosphonates theoretically gives a concentration factor of 35/0.85 or 41, with recoveries of 99% for DEMP, DIMP, and DEEP and 97% for DMMP. Provided this correlation holds for phosphonofluoridates, recoveries of sarin and soman would also be ≥99%. Thus, preconcentration factors of 100 or more do seem feasible for these compounds, as indicated earlier.

TABLE 3
Partition Coefficients of Four Phosphonates Between HFIP and Salt-Saturated Water

Compound	P_{sw}^{salt}
DMMP	1200
DEMP	3060
DEEP	3390
DIMP	4440

FIGURE 1
Separation of Phosphonate Esters in HFIP Extract on a
SP1200/H_3PO_4 Column

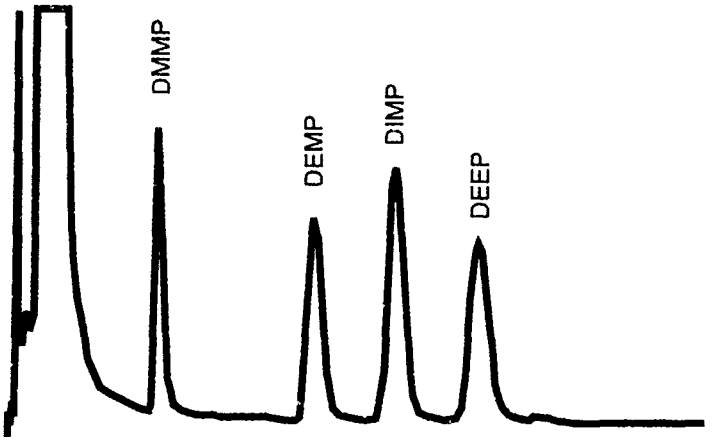

Finally, in anticipation of future analytical method development for phosphonates and related compounds, some preliminary experiments were conducted using the same protocol as for the partition coefficient determination. Figure 1 shows the separation of the same four phosphonate esters after extraction from salt-saturated water into HFIP. This work was done on the GC-FID with an SP-1200/H_3PO_4 column. An equally good separation was achieved on a 15-m, DB-wax megabore column at 70°C. With the FID the DMMP peak elutes on the tail of the HFIP solvent peak, and may interfere with determination of DMMP at low concentration. HFIP response was much less on the FPD, which would be required for the most sensitive analyses in any case.

CONCLUSIONS

Phosphonates and like compounds are extracted from water by H-bond donor solvents, including halogenated methanes and the fluorinated alcohols, trifluoroethanol and hexafluoroisopropanol. Presaturating the water with sodium chloride increases the solvent/water partition coefficient by a factor of six on average and makes possible the use of solvents not normally used for solvent extraction. Extractive preconcentration with HFIP can be used to increase the sensitivity of analytical methods 100-fold or more, a better than ten-fold improvement over older methods employing chloroform as the extracting solvent.

ACKNOWLEDGEMENTS

I would like to express my thanks to Mr. Alan Hewitt and Dr. Thomas Jenkins for providing helpful comments on the manuscript.

REFERENCES

1. Bennett, S.R., J.M. Bane, P.J. Benford and R.L. Pyatt (1984) Environmental hazards of chemical agent simulants. Aberdeen Proving Ground, Maryland: Chemical Research and Development Center, CRDC-TR-84055.

2. Howard, P.H., G.W. Sage, J.P. Robinson and J. Jackson (1986) Environmental fate assessments of chemical agent simulants and decontaminants. Aberdeen Proving Ground, Maryland: Chemical Research and Development Center, CR-86016 (AD-B101095).

3. Mabey, T. Mill (1978) Critical review of hydolysis of organic compounds in water under environmental conditions. J. Phys. Chem. Ref. Data, 7(2):383–414.

4. Lyman, W.J. (1982) Adsorption coefficients for soils and sediments. Chapter 4 in: Handbook of Chemical Property Estimation Methods, Environmental Behavior of Organic Compounds. New York: McGraw Hill.

5. Leggett, D.C. (1987) Sorption of chemical agents and simulants: Measurement and estimation of octanol--water partition coefficients. Hanover, NH: Cold Regions Research and Engineering Laboratory, Special Report 87-18.

6. Sass, S., T.L. Fisher, R.J. Steger and G.A. Parker (1982) Gas chromatographic methods for the analysis of trace quantities of isopropyl methylphosphonofluoridate and associated compounds, in situ and in decontamination effluent. J. Chromatogr., 238:445–456.

7. Shih, M.L. and R.I. Ellin (1984) Stability of aqueous solutions of sarin and soman: Influence of concentration and an equation for determining concentration. Bull. Environ. Contamin. Toxicol., 33:1–5.

8. Shih, M.L. and R.I. Ellin (1986) Determination of toxic organophosphorus compounds by specific and nonspecific detectors. Anal. Lett., 19(23-24):2197–2205.

9. Leo, A., C. Hansch, and D. Elkins (1971) Partition coefficients and their uses. Chem. Revs., 71(6):525–616.

10. Hertz, C.D., J.G. Schnable and I.H. Suffet (1989) Isolation of polar organic compounds from water using salting out liquid-liquid extraction systems, Preprint, American Chemical Society Conf., Dallas, TX.

11. Leggett, D.C., T.F. Jenkins and P.H. Miyares (in press) Salting-out solvent extraction for preconcentration of nitroaromatics, nitramines, and nitrate esters from water. Anal. Chem.

12. Rosenthal, R.W., R. Proper and J. Epstein (1956) The distribution of some phosphonofluoridates between organic solvents and water. J. Phys. Chem., 60:1596–1598.

13. Chang, Y., J. Noriyan, D.R. Lloyd, and J.W. Barlow (1987). Polymer sorbents for phosphorus esters: 1. Selection of polymers by analog calorimetry. Polym. Engin. Sci., 27(10):693–702.

14. Barlow, J.W., P.E. Cassidy, D.R. Lloyd, C-J. You, Y. Chang, P.C. Wong, and J. Noriyan (1987). Polymer sorbents for phosphorus esters: II. Hydrogen bond driven sorption in fluoro-carbinol substituted polystyrene. Polym. Engin. Sci., 27(10):703–715.

15. Leggett, D.C. (in press) Complex formation between dimethylmethylphosphonate and hexafluoroisopropanol. CRREL Report.

16. Higuchi, T., J.H. Richards, S.S. Davis, A. Kamada, J.P. Hou, M. Nakano, N.I. Nakano and I.H. Pitman (1969) Solvency and hydrogen bonding interactions in non-aqueous systems. J. Pharm. Sci., 58(6):661–671.

17. Ruosteso, P., U. Salminen and R. Liias (1987) Thermodynamic and spectroscopic properties of phosphorus compounds and various OH and NH proton donors. Spectrochim. Acta, 43A(9):1135–139.

18. Taft, R.W., D. Gurka, L. Joris, P. von R. Schleyer and J.W. Rakshys (1969) Studies of hydrogen-bonded complex formation with p-fluorophenol. V. Linear free energy relationships with OH reference acids. J. Amer. Chem. Soc., 91(17):4801–4808.

BLANK

NICOTINIC ACETYLCHOLINE RECEPTOR/ION CHANNEL COMPLEX SHOWS IRREVERSIBLE ORGANOPHOSPHATE EFFECTS

D.E. Menking, R.G. Thompson, V.L. Wolff and J.J. Valdes
U.S. Army Chem. Res. Devel. & Engr. Ctr.
Aberdeen Proving Ground, MD

ABSTRACT

Organophosphate (OP) toxicity is primarily due to the inhibition of acetylcholinesterase. In sublethal doses, OP's induce symptoms which indicate a direct interaction with nicotinic acetylcholine receptors (nAChR). Torpedo electric organ membrane fragments were used to determine OP interactions with nAChR-coupled ion channel using ^{3}H-phencyclidine (^{3}H-PCP) as a probe. Highly toxic OP's [O-ethyl S-(diisopropylaminoethyl) methylphosphonothiolate, ethyl-N,N-dimethylphosphoramido-cyanidate, isopropyl methylphosphonofluoridate and pinacolyl methylphosphonofluoridate] were found to potentiate ^{3}H-PCP binding to nonactivated channels and to inhibit carbachol-activated binding. Membrane preparations were preincubated with OP's and washed several times with Tris-HCl buffer to assess reversibility of ^{3}H-PCP binding. Results show that OP's irreversibly potentiate ^{3}H-PCP binding. These results are consistent with the hypothesis that OP's bind to, and irreversibly phosphorylate, an allosteric site on the ion channel associated with the nAChR.

INTRODUCTION

The toxicity of organophosphorus (OP) compounds is primarily due to their irreversible inhibition of acetylcholinesterase (AChE), resulting in excess synaptic acetylcholine (ACh) accumulation. This excess results in receptor overstimulation, causing paralysis of the peripheral neuromuscular junction and inhibition of central respiratory neurons, and is thought to be responsible for the lethality of the OP's. In sublethal doses, OP's induce psychic disturbances, tremors and seizures which persist beyond the exposure period, symptoms which cannot be solely attributed to AChE inhibition.[1-3] Together these observations suggest some interaction with both cholinergic and non-cholinergic neurotransmitter systems. Recent data indicate a direct interaction of the OP compounds with postsynaptic nicotinic acetylcholine receptors (nAChR) that does not depend on the accumulation of ACh.[4]

The nAChR consists of five subunits- α_2, β, γ, and δ with an approximate molecular weight of 250,000. These subunits form a rosette-like structure with various binding sites for different drugs and toxins. These sites are the receptor active site, which binds ACh and toxins such as bungarotoxin and curare, and the allosteric, or ion channel site, which binds histrionicotoxin, batrachotoxin and phencyclidine, as well as other drugs and toxins. The binding of an agonist to the receptor site activates the ion channel, expcsing the ion channel sites allowing an increase in the binding of channel binding ligands. I^{n} the resting state, the receptor site is unoccupied; the ion channel remains closed and little binding to the channel site occurs.[5-6] The electric organ of the electric ray Torpedo nobiliana as used in these studies

contains a high density of nAChR that are similar to receptors in the neuromuscular junction. Receptor-rich membrane fragments were used to determine OP interactions with the nAChR-coupled ion channel. The ligand of choice to assess ion channel binding was ^{3}H-Phencyclidine (^{3}H-PCP). Its binding to Torpedo membranes is saturable and is inhibited by drugs that have been shown to interact with ion channels in muscle endplate, but not by drugs that bind to nAChR sites.[7-8]

The present studies were performed to screen a series of lethal chemical nerve agents for in vitro effects on the nAChR and the allosteric ion channel site. Activation of the receptor with subsequent ion channel opening is indicated by increased ^{3}H-PCP binding, and direct effects of OP's on the ion channel can therefore be measured as a function of ^{3}H-PCP binding. The in vivo turnover rate of nAChR is approximately 50 hours, and permanent disruption would be critical to survival during this period. These studies were therefore designed to determine the reversibility of OP effects on the ion channels.

MATERIALS AND METHODS

Materials.

Trizma base and poly-l-lysine were obtained from Sigma Chemical Company, St. Louis, MO. GF/B glass fiber filters were obtained from Whatman International, LTD., Clifton, NJ. ^{3}H-Phencyclidine and Formula 963 aqueous counting cocktail were obtained from New England Nuclear (NEN), Boston, MA.

The four OP nerve agents used in this study were: O-ethyl S-(2-diisopropylaminoethyl)-methylphosphonothiolate (VX); ethyl-N-N-dimethylphosphoramidocyanidate (tabun); isopropyl methylphosphonofluoridate (sarin); and pinacolyl methylphosphonofluoridate (soman). Dilutions were made in isopropanol and ranged from 500 nM to 37.5 μM. Torpedo electric organ was obtained from Biofish Associates, Gloucester, ME.

Preparation of Torpedo synaptosomes.

Frozen electric organ was minced in two volumes of 50 mM Tris buffer (pH 7.4) containing 154 mM NaCl, 5 mM Na_2HPO_4. and 1 mM EDTA (ethylenediaminetetraacetic acid). This mixture was homogenized with a Brinkman polytron (setting 5 for 1 min), set on ice for 2 min and rehomogenized. The mixture was centrifuged (1000 x g, 10 min, 4^0 C) and the supernatant stored on ice. Pellets were rehomogenized, centrifuged as before, and the supernatants combined and centrifuged (30,000 x g, 65 min). The resulting pellet was suspended in one volume of the Tris buffer with five up-down strokes (Wheaton homogenizer, setting 3) and stored at 4^0 C. Protein was determined by the Bradford method using gamma globulin standard.[9]

^{3}H-Phencylidine Assay.

Duplicate aliquots of tissue homogenate were preincubated with each agent for either 30 or 60 min. Fifty ul of the OP-treated membrane suspension was then added to glass test tubes containing 2 nM (final conc.) [^{3}H]-phencyclidine (^{3}H-PCP, 50 Ci/mmol), carbachol- 5 μM (CBC: for activation studies only) and 50mM Tris-HCl buffer (pH 7.4) to give a

final volume of 1 ml. The tubes were immediately vortexed and incubated for 30 sec before aspirating the contents onto GF/B filter disks. Test tubes and filter disks were soaked in 0.1% poly-l-lysine for 30 min prior to use to minimize PCP binding to glass. The filters were washed twice with 5 mls cold Tris buffer and placed in scintillation vials containing 5 mls Formula 963 (NEN). The vials were dark and cold adapted prior to counting in a Packard Model 300-C liquid scintillation spectrometer (62% efficiency).

RESULTS

Results of ^{3}H-PCP binding to the nonactivated, or resting, binding sites are shown in Figure 1. OP agents activated the channel at low concentrations as indicated by increased binding of ^{3}H-PCP. Maximal activation occurred at 1 μM for VX, 2 μM for sarin and 5 μM for soman and tabun.

Figure 2 shows the inhibition of ^{3}H-PCP binding by the OPs in the CBC-activated receptor/ion channel. At 37.5 μM, VX shows an inhibition from control of 52%; sarin, 19%; soman, 16%; and tabun, 8%. For the reversibility studies, duplicate aliquots of tissue homogenate were preincubated with each agent in a 1:9 agent-to-tissue ratio for ten minutes. The membranes were pelleted by centrifugation (23,000 x g, 20 min, 4^{0} C) and supernatant from one of each pair of tubes was discarded (wash set) and replaced with Tris-HCl. All pellets were resuspended and this wash procedure repeated, and the tissue suspension treated as above. The OP's tested irreversibly stimulated the binding of ^{3}H-PCP in the nonactivated receptor/ion channel as shown in Figure 3. Addition of 0.025 μg OP resulted in an increase in ^{3}H-PCP binding from the control: soman, 16%; sarin, 16%; VX, 8%; and tabun, 32%. There was an increase in binding observed even when the tissue had been washed after being exposed to the OP: soman, 44%; sarin, 40%; VX, 45%; and tabun, 43% over the washed control. This increase may be due to the removal of AChE during washing, allowing more OP to interact with the receptor.

CONCLUSIONS

The results of this study indicate that OP's interact with the ion channel associated with the nAChR in an irreversible manner. These anti-AChE's act primarily by binding irreversibly to AChE, resulting in the accumulation of ACh in the synapse, hence receptor activation. In our preparation, CBC was used to activate the receptor with subsequent channel opening. Under these conditions, OP's decreased ^{3}H-PCP binding in the channel. Since OP's stimulated ^{3}H-PCP binding in the nonactivated (ACh or CBC absent) receptor, there appears to be a direct interaction with the nAChR as well. The inhibition of CBC-activated binding suggests two possibilities: a direct interaction of OP's, possibly competing for the receptor binding sites, or the binding of OP's to allosteric sites which modulate the receptor and ion channel accordingly. These hypotheses are not mutually exclusive.

The differential effects of the OP's on ^{3}H-PCP binding may be a result of unique steric effects related to their molecular structures. In the wash experiments, OP's may form an irreversible complex with the receptor, changing its conformation and altering the dissociation rate of

^{3}H-PCP, resulting in binding of ^{3}H-PCP with a higher affinity. Tabun shows a significant decrease in ^{3}H-PCP binding when comparing the washed preparation with the unwashed preparation. This may result from the relative toxicities of the OP's. Soman, sarin, and VX, respectively, have median lethal dosages (MLD) in man of 70, 70, and 30 mg/min/m^3, whereas tabun has a MLD in man of 135 mg/min/m^3, only half as toxic as the others. Also, the rate of hydrolysis and breakdown in the pH range 7 +/- 1 is greater for tabun at 8.5 hr than the rates of soman, 45 hrs; sarin, 47 hrs; and VX, 40 hrs.[10]

In summary, the results of the present study show the activating of the ion channel by OP's, the inhibition of CBC-activated ^{3}H-PCP binding and the irreversible stimulation of ^{3}H-PCP binding. These results are consistent with the hypothesis that OP's activate, and irreversibly phosphorylate, an allosteric site associated with the nAChR.

REFERENCES

1. Valdes, J.J., Chester, N.A., Menking, D., Shih, T-M., and Whalley, C. Regional Sensitivity of Neuroleptic Receptors to Sub-Acute Soman Intoxication. Brain Research Bulletin 14, 117-121 (1985).

2. Biskind, M. and Mobbs, R.F. Psychiatric Manifestations from Insecticide Exposure. J. Amer. Med. Assoc. 220, 1248 (1972).

3. Korsak, R.J. and Safo, M.M. Effects of Chronic Organophosphate Pesticide Exposure on Central Nervous System. Clin. Toxicol. 11, 83-95 (1977).

4. Karczmar, A.G. Acute and Long Lasting Central Actions of Organophosphate Agents. Fund. and Applied Tox. 4, S1-S17 (1984).

5. Eldefrawi, A.T., Miller, E.R., Murphy, D.L. and Eldefrawi, M.E. [^{3}H-Phencyclidine Interactions with the Nicotinic Acetylcholine Receptor Channel and Its Inhibition by Psychotropic, Antipsychotic, Opiate, Antidepressant, Antibiotics, Antiviral and Antiarrhythmic Drugs. Mol. Pharmacol. 22, 72-81 (1982).

6. Oswald, R.E., Bamberger, M.J. and McLaughlin, J.T. Mechanisms of Phencyclidine Binding to the Acetylcholine Receptor from Torpedo Electroplaque. Mol. Pharmacol. 25, 360-368 (1984).

7. Albuquerque, E.X., Tsai, M-C., Aronstam, R.S., Witkop, B., Eldefrawi, A.T. and Eldefrawi, M.E. Phencyclidine Interactions with the Ionic Channel of the Acetylcholine Receptor and Electrogenic Membrane. Proc. Natl. Acad. Sci. USA. 77(2), 1224-1228 (1980).

8. Elefrawi, M.E., Eldefrawi, A.T., Aronstam, R.S., Maleque, M.A., Warnick, J.E. and Albuquerque, E.X. [^{3}H] Phencyclidine: A Probe for the Ion Channel of the Nicotinic Receptor. Proc. Natl. Acad. Sci. USA. 77(12), 7458-7462 (1980).

9. Bradford, M. A Rapid and Scientific Method for the Quantitation of Microgram Quantities of Protein Utilizing the Principle of Protein-Dye

Binding. Anal. Biochem. 72, 242 (1976).

10. Edgewood Arsenal Special Report. EO-SR-74001. Chemical Agent Data Sheets. Vol. 1, December (1974).

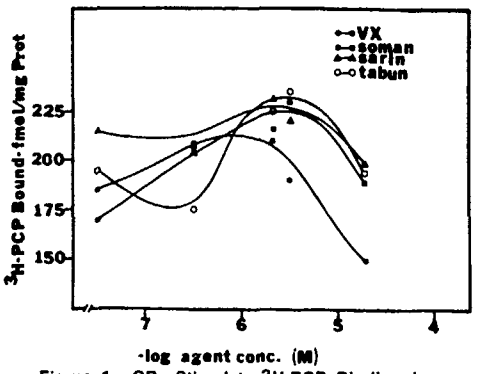

Figure 1. OPs Stimulate ^{3}H-PCP Binding in Resting nAChR System. Results are the average of 6 experiments.

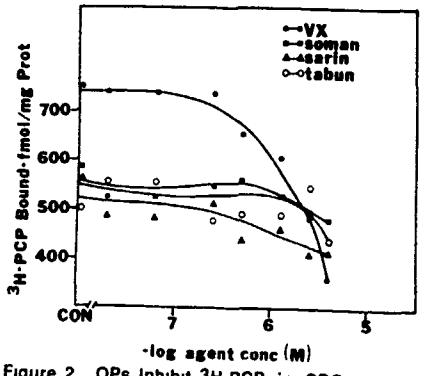

Figure 2 OPs Inhibit ^{3}H-PCP in CBC-activated nAChR System. Results are the average of 6 experiments

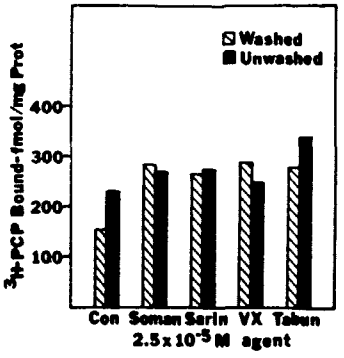

Figure 3. OPs Irreversibly Stimulate ^{3}H-PCP Binding. Results are the average of 6 experiments.

BLANK

PHARMACOLOGICAL EFFECTS OF OPIOID AGONIST AND ANTAGONIST COADMINISTRATION IN FERRETS

Robert Mioduszewski, Sharon Reutter and Dorothy Berg
U.S. Army Chemical Research, Development and Engineering Center
Aberdeen Proving Ground, MD 21010-5423

ABSTRACT

This study examined the feasibility of differentiating opiate-induced sedative and toxic effects by coadministration of an opiate agonist and antagonist in the ferret. Dose-response effects of carfentanil on sedative (akinesia, catalepsy and loss of righting reflex (LRR)) and toxic (convulsive movements, apnea, lethality) signs were compared with those following treatment with the coadministration of carfentanil + naltrexone. The coadministration of carfentanil + naltrexone in a molar ratio of 1.88:1 respectively, resulted in rapid onset, but limited duration of sedative effects, while toxic effects were minimized with a subsequent improvement in therapeutic index.

INTRODUCTION

The fentanyl family of synthetic opiates are recognized for their potent analgesic, anesthetic and immobilizing properties in both animals and humans[1,2]. However, they are equally potent in inducing toxic side-effects such as respiratory depression which limit their clinical use in higher species without mechanical respiratory support. This research was to characterize some of the pharmacological effects of carfentanil in the ferret and examine the feasibility of differentiating opioid-induced sedative/hypnotic from toxic/lethal effects in this species by adjuvant coadministration. It follows the work reported previously from this laboratory on the effects of carfentanil + adjuvant coadministration in the rat[3].

MATERIALS AND METHODS

Adult male castrated ferrets, weighing between 0.8 and 1.6 kg were used in this study. Carfentanil (Carf), methyl 4-N-(1-oxopropyl)phenylamino]-1-(2-phenylethyl)-4-piperidine carboxylate, was obtained from Organic Chemistry Branch, Chemical Div., Research Dir., CRDEC. Naltrexone (Nalt), (N-cyclopropyl-noroxymorphone), was obtained from Sigma Chemical Company, St. Louis, Mo. Test agents were diluted to working concentrations in double-distilled, sterile water and administered by intraperitoneal (IP) injection in a volume of 1 ml/kg body weight.

Three indices of sedative/hypnotic immobilization were measured as quantal(all or none) responses. The following signs were considered positive responses if they were observed to occur for a minimum of 30 sec following treatment: akinesia (the cessation of motor activity, including head movements), catalepsy (no movements with "lead pipe" muscular rigidity after placing the animal's front paws on a 10 cm high block of plastic), and loss of righting reflex (LRR), the failure of an animal to right itself after being placed on its back. Transient signs of abrupt muscular movements, from muscular twitches/jerks to those tonic/clonic movements associated with grand mal seizures, were considered treatment-induced convulsive movements in this study.

A Columbus Instruments "Oxymax" system used to monitor pressure and atmospheric gas (O_2, CO_2) concentration changes occurring as a result of a ferret breathing within an acrylic "whole body" plethysmograph chamber. This system allowed for simultaneous observation of motor activity and collection of respiratory data from awake, unrestrained and/or anesthetized (narcotized) animals. Apnea was considered to occur when measurable breathing stopped for at least 10 sec on at least two occasions within a one minute measurement period.

The effective doses (ED) and 95% confidence limits for treatment-induced effects were calculated by the Litchfield-Wilcoxen probit method[4]. Respiratory data were analyzed by a two-way ANOVA with repeated measures and Dunnett's test was used to test the differences between means, $p < 0.05$ was considered significant in these studies.

RESULTS AND DISCUSSION

The effective doses for several indices of Carf-induced immobilization/ toxicity and safety ratios in the ferret are summarized in Table 1. The onset and duration of immobilization, toxic and lethal effects, were directly correlated with the dose of Carf (Table 2).

TABLE 1.

Effective doses and safety ratios for carfentanil (top) and carfentanil + naltrexone (1.88:1) (bottom) coadministration in the ferret.

	Effective Doses (ug/kg)				
ED[1]	Akinesia	Catalepsy	LRR[2]	Lethality (24h)	Lethality (48h)
ED16	4.7	10.8	21.4	40.9	40.9
ED50	8.3	18.2	37.9	83.0	83.0
ED84	14.8	30.6	67.2	168.7	168.7
S.R.[3]	9.9	4.5	2.1		
ED16	8.4	10.6	18.2	227.7	100.2
ED50	25.0	30.0	59.7	1,054,952.0	9053.6
ED84	74.6	85.0	195.3	4.9 E+09	817951.0
S.R.[3]	361	301	151		

[1]Effective Dose, [2]Loss of Righting Reflex, [3]Safety Ratio (LD50,48h /ED50)

TABLE 2.

Effect of dose on onset times and duration of opioid responses in ferrets treated with Carf (top) and Carf + Nalt (bottom).

CARF[1] (ug/kg)	NALT[2] (ug/kg)	TIME	Mean Onset Times/Duration (minutes) AKIN[3]	CAT[4]	LRR[5]	CONV[6]	APNEA	LETHAL[7]
6.25	0	ONS.	10.0	-	-	-	-	-
		DUR.	3.8	-	-	-	-	-
12.5	0	ONS.	6.8	9.0	-	20.0	40.0	-
		DUR.	22.3	19.8	-	10.0	2.5	-
25.0	0	ONS.	4.0	5.5	4.0	15.0	17.0	-
		DUR.	34.8	33.3	14.0	7.8	9.0	-
50.0	0	ONS.	4.0	6.5	8.0	5.7	27.5	<18.0
		DUR.	144.8	142.3	140.8	22.3	21.3	-
100.0	0	ONS.	3.0	3.3	4.8	5.0	16.0	89.0[8]
		DUR.	72.0	71.8	70.3	6.0	44.0	-
200.0	0	ONS.	2.0	2.8	3.3	2.3	10.5	107.5[8]
		DUR.	101.8	101.0	100.5	6.3	93.3	-
10.62	4.00	ONS.	9.0	7.0	-	-	-	-
		DUR.	5.5	1.5	-	-	-	-
26.62	10.10	ONS.	6.4	4.0	-	-	-	-
		DUR.	6.3	3.5	-	-	-	-
66.93	25.36	ONS.	2.8	3.8	3.8	3.0	-	-
		DUR.	43.9	43.1	43.1	1.3	-	-
168.00	63.65	ONS.	2.4	3.5	2.5	1.7	-	-
		DUR.	11.5	10.6	8.9	0.5	-	-
1058.00	401.00	ONS.	0.7	1.1	1.1	0.8	-	<48.0
		DUR.	17.3	17.0	17.0	3.6	-	-
2656.00	1008.00	ONS.	0.5	0.6	0.7	0.4	-	<44.0
		DUR.	27.3	27.1	27.0	5.0	-	-
6666.00	2530.00	ONS.	0.4	0.6	0.6	0.5	-	<33.0
		DUR.	26.5	26.3	26.3	3.4	-	-
16733.00	6365.00	ONS.	0.5	0.5	0.5	0.5	-	<18.0
		DUR.	21.5	21.5	21.5	1.9	-	-

[1]Carfentanil, [2]Naltrexone, [3]Akinesia, [4]Catalepsy, [5]Loss of Righting Reflex, [6]Convulsive Movements, [7]Lethality (in hours), [8] In minutes.

One of the primary causes for mortality resulting from opioid overdosage is the inhibition of respiratory control centers within the brainstem, resulting in decreased respiratory frequency/tidal volume, dyspnea, periodic apnea, and finally the cessation of breathing. Respiratory frequency and VO2 were inversely correlated with the dose of Carf (Figures 1,2). Onset and duration of apnea were also dose-dependent, Table 2. Although signs of respiratory depression appeared to be transient during the test period, it is hypothesized that post-test period episodes of respiratory depression, including apnea, eventually resulted in lethality.

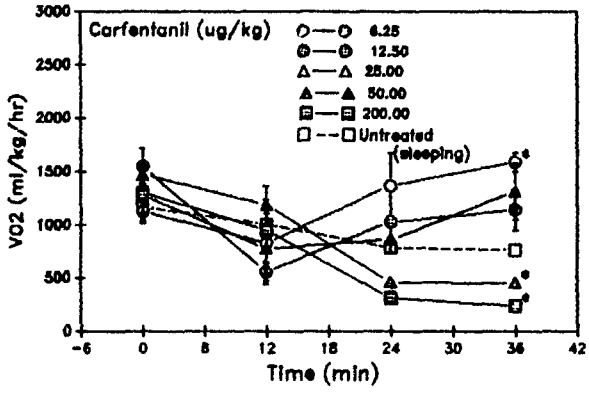

FIGURE 1.

Effects of Carf dose on respiratory rate, mean and S.E.M.. * p<0.05 vs. untreated.

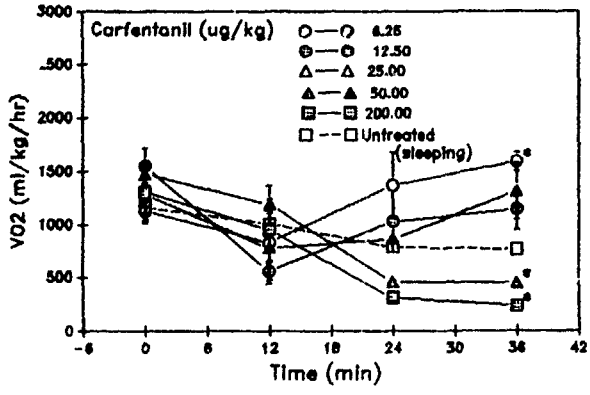

FIGURE 2.

Effects of Carf dose on VO2 in ferrets, mean and S.E.M.. * p <0.05 vs. Untreated.

Various convulsive movements (tonic/clonic jerks and spasmodic muscle twitches) usually occurred at doses less than 100 ug/kg, higher doses resulted in signs of grand mal seizures of less than one minute duration.

When a lethal dose of Carf (168 ug/kg) was coadministered with each of four doses of Nalt (21, 42, 84 and 168 ug/kg) or its vehicle (water), a separation of immobilizing and toxic signs was noted, depending upon the ratio of Carf to Nalt administered, Figure 3.

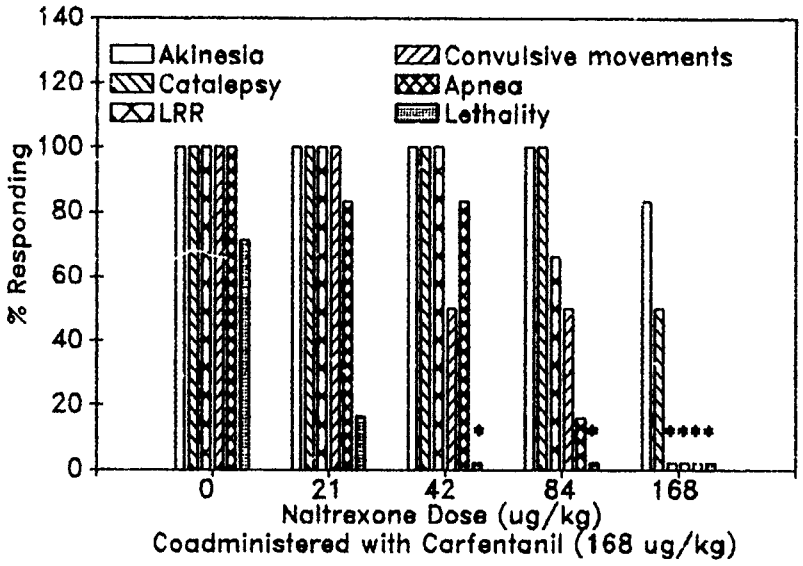

FIGURE 3.

Effects of Carf:Nalt dose-ratio on the incidence of opioid effects in ferrets. * p <0.05 vs. Carf + Nalt (0 ug/kg).

The cataleptic and lethal effects of various doses of Carf + Nalt administered in a fixed molar ratio (1.88:1, Carf:Nalt) are compared with those of Carf alone in Figure 4. Effective doses and safety ratios for Carf + Nalt-induced akinesia, catalepsy, LRR and lethality are summarized in Table 1.

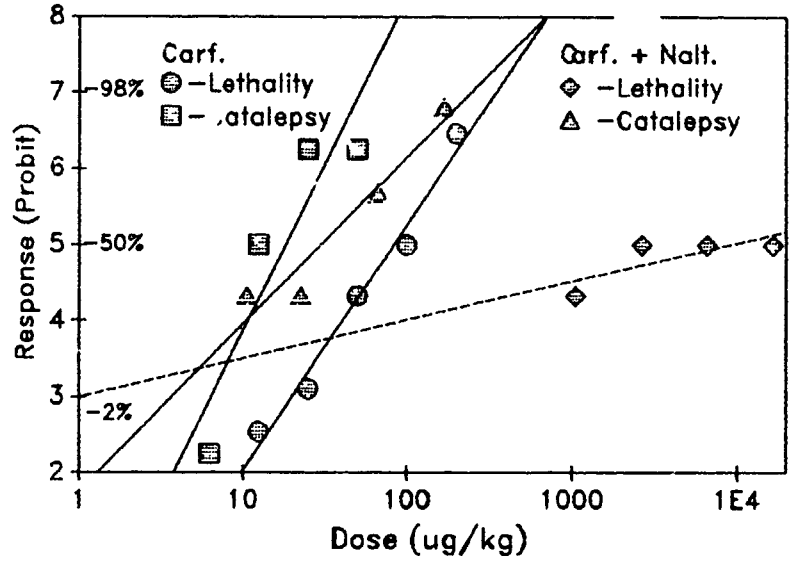

FIGURE 4.

Catalepsy and Lethal dose-response regression in ferrets treated with Carf (shaded) and Carf + Nalt (1.88:1) (open).

It is interesting to note that onset times for opioid effects were not delayed by increasing doses of Nalt, but were inversely correlated with Carf dose (Table 2, Figs. 1,2). In contrast, duration of opioid effects was limited to a maximum average of 27 min with combinations of Carf + Nalt Table 2, Figs. 5,6). Regardless of the combination dose received, ferrets showed rapid recovery from all narcotic effects within the 60 min observation period following injection. This recovery was characterized by a change from no spontaneous activity to vigorous digging motions and exploratory movements within a period of several seconds. However this "hyperactive" phase usually only lasted less than two hours and was followed by signs of sedation, especially after the highest doses of the combination.

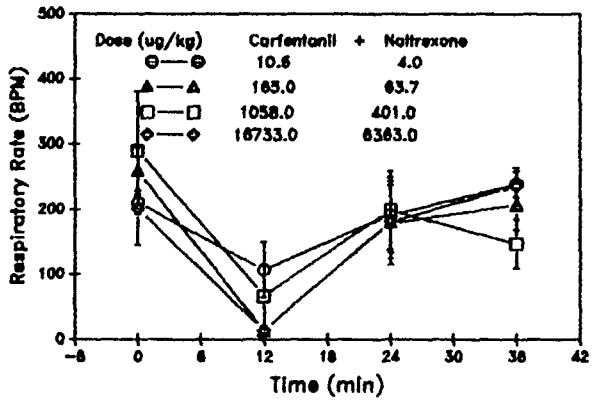

FIGURE 5.

Effects of Carf + Nalt dose on respiratory rate in ferrets, mean and S.E.M..

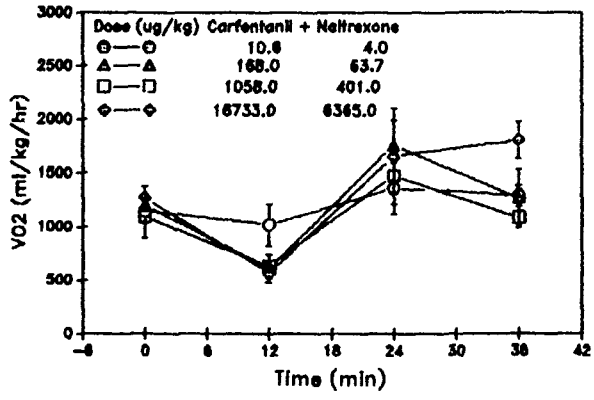

FIGURE 6.

Effects of Carf + Nalt dose on VO2 in ferrets, mean and S.E.M..

The data of this study suggest that coadministration of an opioid antagonist (Nalt) with an opioid agonist (Carf) can result in an expression of sedative/hypnotic effects with apparent limited toxicity and subsequent improvement in therapeutic index. These results are in agreement with earlier findings[3] reported from this laboratory in which the opioid antagonist, naloxone, attenuated the toxic/lethal effects of carfentanil when coadministered with it in rats, but had no apparent affect on sedative/hypnotic potency.

The renarcotization observed in the combination treated animals suggests that the balance between sedative and toxic effects achieved in this study was transient. It is postulated that differences in the relative amounts of Carf and Nalt, as well as their pharmacokinetics, were also involved in the rapid expression of sedative effects with minimal acute signs of toxicity.

CONCLUSIONS

These data suggest that clinically desirable effects (sedation) of opiates may be separated from toxic side-effects by opiate antagonist coadministration in the ferret. Coadministration of carfentanil + naltrexone in a molar ratio of 1.88:1 respectively, results in rapid onset but limited duration of sedative\hypnotic effects, while toxic effects are minimized with a subsequent improvement in therapeutic index.

REFERENCES

1. Hess, L., and Knakel. J., First Exposure with Immobilization with Carfentanil at Zoo Prague. Gazella (3/4), pp 87-90 (1985).

2. Stanley, Theodore H., M.D., Port, J. David, Pace, Nathan, M.D., Kimble, Melissa, and McJames, Scott, U. of Utah Sch of Med, and Ferguson, C. Parker, CRDEC, Chemical Immobilization Using New High Potency Opioids and Other Drugs and Drug Combinations with High Therapeutic Indices, CRDEC-CR-88077, June 1988.

3. Mioduszewski, R.J. and Farrand, R.L., Pharmacological Effects of Carfentanil and Adjuvant Coadministration in the Rat. CRDEC-TR-041, (1989).

4. Tallarida, R. and Murray, R., Eds., in Pharmacological Calculations with Computer Programs, Springer-Verlag, 2nd Edition (1987).

BLANK

EFFECTS OF CARFENTANIL ON AUDITORY BRAINSTEM RESPONSES (ABRs) IN FERRETS

[1]Sharon A. Reutter,
Nida Q. Legaspi, Robert D. Armstrong and Robert J. Mioduszewski

Carfentanil is a potent anesthetic with a low therapeutic index; apnea is the proximal cause of death. The purpose of the study was to use ABRs to monitor depressant effects of carfentanil upon brainstem neurons. The research was predicated by previous work in which ABRs demonstrated brainstem dysfunction in preterm infants with apnea.[1,2] Carfentanil produced abnormal responses to stimuli of $\leq$ 75 dB. The changes were not related to anesthetic-induced hypothermia and were compatible with a neuronal-type dysfunction. These data suggest that ABRs may be a good monitor of brainstem function, particularly when respiratory centers are compromised.

Carfentanil is a synthetic opiate belonging to the "Fentanyl" family. It is a potent anesthetic but has a low therapeutic index. Apnea is the apparent proximal cause of death. In order to better understand the mechanisms underlying the actions of carfentanil we employed ABRs to monitor the effects of carfentanil on brainstem neurons. The work was predicated by previous studies[1,2] in which ABRs proved useful in demonstrating brainstem dysfunction in preterm infants subject to apnea. It was hypothesized that ABRs would be a sensitive indicator of the effects of carfentanil upon the respiratory centers. The study was novel in that non-invasive clinical methods were used to record the ABRs so that the database which was developed would be as applicable as possible to humans.

METHODS

Castrated, de-scented male ferrets (approximately 3-4 months old) were obtained from Marshall Farms. The animals were housed in the Vivarium until testing at 9-12 months of age. Carfentanil data were obtained following intraperitoneal (IP) injection with carfentanil citrate (CRDEC) (25-100 ug/kg). ABR testing was begun an hour later, following respiratory measurements for another study. Control responses were obtained following IP injection with 40 mg/kg Na pentobarbital (Sigma). Temperature was monitored at 5 min intervals via a rectal probe. After suitable skin preparation standard 10 mm gold disk EEG electrodes were applied with electrode cream to the nose, "vertex" (defined as the mid-point between the eyes and the medial attachments of the auricular pinnae), and occipital protruberance. Standard earlobe clip electrodes were attached to the auricular pinnae. Impedances were symmetric and less than 5 kOhm. The stimulus was a rarefacting click delivered to the right ear, via a tubal insert earphone, at 19.1/sec. Filters were set at 100-3000 Hz. The gain was approximately 100,000. Artifact

rejection and 60 Hz notch filters were employed. The average n was 1024. The electrode montage was vertex-ipsilateral ear, with an occipital ground. Responses were recorded with a Bio-logic "Navigator" system, stored on floppy disks, and plotted off-line. Peak amplitudes and latencies were measured using cursors in the machine. ABRs were evaluated for latency, amplitude, and morphology of the four major peaks. Amplitudes were defined as follows: 1=1-1n; 2=2-1n; 3=3-3n; 4=4-4n.

Findings

Nine carfentanil studies were performed on seven animals. Control responses under pentobarbital anesthesia were obtained in 5/7 experimental animals, plus two others. Responses were classed as abnormal if they were of poor morphology, low amplitude, and/or absent. Peaks were considered to be absent if they were not obvious above background noise at the standard display gain; such peaks were given an amplitude of zero, but were not used in latency calculations. Following IP injection with carfentanil, abnormal responses to stimuli of $\leq$ 75 dB were observed in 7/9 experiments (Figs 1-3).

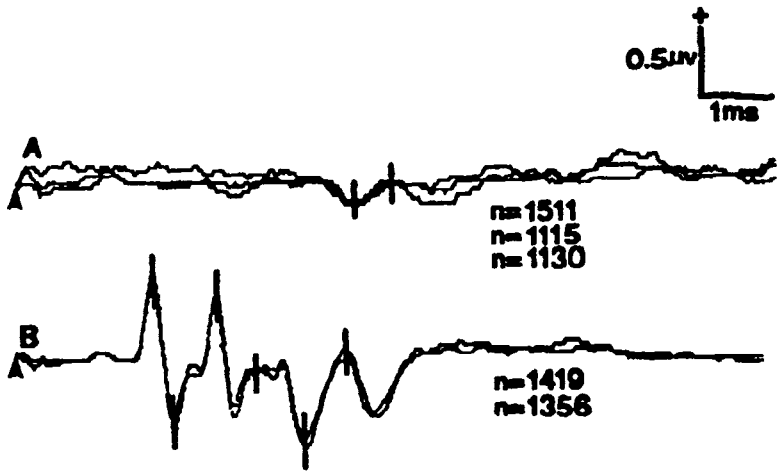

Figure 1. **Carfentanil Effects. ABRs. Ferret 7.** 75 dB responses. Stimulus delivered at arrow. Vertical bars indicate major peaks. **A.** Following IP injection with 50 ug/kg carfentanil. Three responses superimposed. **B.** Under pentobarbital anesthesia. Two responses superimposed.

In the other two studies normal responses were observed to 75 dB stimuli, but responses to stimuli of 50 or 60 dB were absent, an abnormal finding (Fig 3). Amplitudes of the four major peaks were significantly lower in the Carfentanil group (Table 1). Although several of the animals in both groups were relatively hypothermic during ABR testing (normal body temperature for ferrets is 101-104 ^{o}F) there was no significant difference in temperature between the two groups (Table 1), and there was no statistical correlation between body temperature and response amplitude. Latencies of the four major peaks were nearly identical for the two groups (Table 2). The responses of the carfentanil group to a 95 dB stimulus (Table 3) were quite similar to the 75 dB responses (Tables 1 and 2) of the Control group. There was no correlation

between dose of carfentanil and ABR findings. While more preliminary data indicated some correlation betweenresponse morphology and survivability following 100 ug/kg carfentanil, these studies neither enhanced nor refuted the observation.

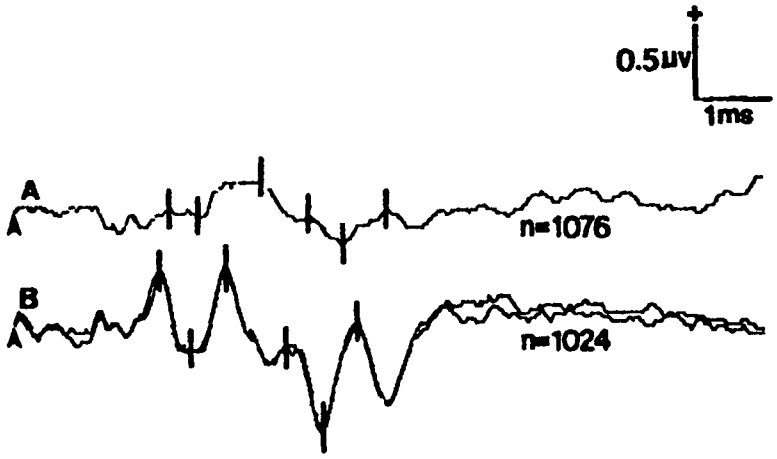

Figure 2. **Carfentanil Effects, ABRs, Ferret 10.** 75 dB Responses. Stimulus delivered at arrow. Vertical bars indicate major peaks. **A.** Following IP injection with 100 ug/kg carfentanil. **B.** Under pentobarbital anesthesia; two responses superimposed.

TABLE 1. COMPARISON OF AMPLITUDES TO A 75 dB STIMULUS

Group:	Pent	Carf	Pent	Carf	Pent	Carf	Pent	Carf	Pent	Carf	Carf
Wave:	1	1	2	2	3	3	4	4	temp*	temp	dose+
	0.58	0.12	0.46	0.31	0.53	0.22	0.48	0.23	98	96	100x
	0.46	0.11	0.34	0.00	0.52	0.00	0.49	0.24	98	100	100x
	0.60	0.77	0.58	0.71	0.29	0.67	0.39	0.63	100	101	100
* °F	0.85	1.08	0.70	0.72	0.41	0.62	0.60	0.68	101	101	100
	0.38	0.14	0.50	0.30	0.48	0.15	0.41	0.22	99	100	100
+ ug/kg	0.32	0.13	0.52	0.12	0.54	0.18	0.48	0.10	99	100	100
	0.98	0.68	0.92	0.53	0.58	0.46	0.67	0.41	100	97	50
	1.15	0.60	1.01	0.40	0.59	0.49	0.67	0.46	100	97	50
	0.62	0.00	0.59	0.00	0.65	0.00	0.81	0.15	97	100	50
	0.63	0.00	0.65	0.00	0.60	0.00	0.82	0.16	97	100	50
	1.12	0.41	0.81	0.61	0.53	0.45	0.55	0.41	102	100	50
	1.04	0.23	0.77	0.47	0.57	0.34	0.56	0.31	102	100	50
	1.09	0.19	1.12	0.11	0.69	0.24	0.66	0.18	98	95	50
	1.11	0.21	1.05	0.16	0.65	0.19	0.65	0.16	98	95	50
		1.01		0.54		0.80		0.25		99	25
		0.92		0.57		0.67		0.66		99	25
mean:	0.78	0.41	0.72	0.35	0.55	0.34	0.59	0.33	99	99	
s.e.m.:	0.08	0.09	0.06	0.06	0.03	0.07	0.04	0.05	1	1	
n:	14	16	14	16	14	16	14	16	14	16	
p:		0.0058		0.0004		0.0095		0.0002		0.50	

two responses from each animal are shown unless marked x

TABLE 2. COMPARISON OF LATENCIES TO A 75 dB STIMULUS

Group:	Pent	Carf	Pent	Carf	Pent	Carf	Pent	Carf	Pent	Carf	Carf
Wave:	1	1	2	2	3	3	4	4	temp*	temp*	dose+
	1.96	2.10	2.92	3.40	3.82	4.06	4.78	5.14	98	96	100x
	1.98	2.26	2.92		3.86		4.82	5.24	98	100	100x
	1.84	1.86	2.70	2.62	3.54	3.38	4.34	4.34	100	101	100
* °F	1.84	1.84	2.62	2.66	3.50	3.10	4.32	4.32	101	101	100
	1.86	2.18	2.94	3.16	3.60	3.92	4.74	5.06	99	100	100
+ ug/kg	1.80	2.34	3.00	3.02	3.62	3.74	4.70	4.64	99	100	100
	1.94	2.06	2.82	2.90	3.76	3.94	4.64	4.86	100	97	50
	1.94	2.06	2.82	2.92	3.76	3.98	4.66	4.88	100	97	50
	1.98		2.92		3.74		4.76	5.10	97	100	50
	1.98		2.92		3.74		4.76	5.18	97	100	50
	1.88	1.98	2.66	2.76	3.42	3.62	4.42	4.30	102	100	50
	1.88	2.02	2.66	2.82	3.42	3.58	4.38	4.26	102	100	50
	2.34	2.16	2.86	3.14	3.78	4.24	4.72	5.30	98	95	50
	2.36	2.20	2.86	3.18	3.70	4.28	4.80	5.30	98	95	50
		1.90		2.76		3.44		4.60		99	25
		1.90		2.72		3.46		4.70		99	25
mean:	1.97	2.06	2.83	2.93	3.66	3.75	4.63	4.83	99	99	
s.e.m.:		0.05	0.04	0.03	0.07	0.04	0.10	0.05	0.10	1	1
n:	14	14	14	13	14	13	14	16	14	16	

two responses from each animal are shown unless marked x

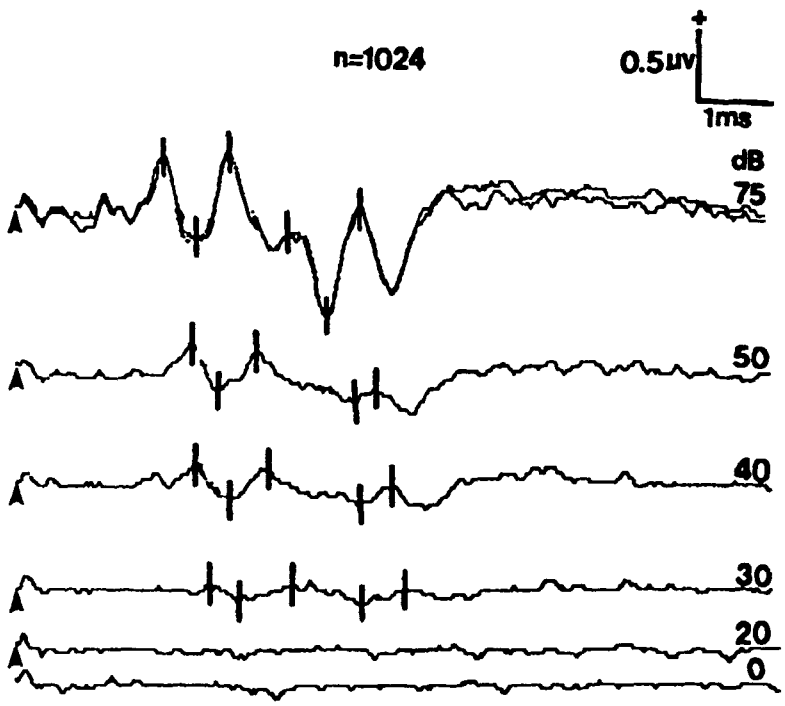

Figure 3. **Ferret ABR Intensity Series.** Pentobarbital anesthesia. Vertical bars indicate major peaks. Two responses superimposed at 75 dB.

TABLE 3. 95 dB RESPONSE WITH CARFENTANIL

Group:	Lat	Amp	Lat	Amp	Lat	Amp	Lat	Amp		
Wave:	1	1	2	2	3	3	4	4	temp*	dose+
	1.90	1.22	2.82	0.83	3.78	0.70	4.76	0.76	97	100x
	1.94	0.82	2.90	0.65	3.80	0.82	4.90	0.68	100	100x
	1.72	1.06	2.44	0.91	3.26	1.07	4.06	0.53	101	100x
* °F	1.96	0.34	2.90	0.38	3.82	0.44	4.88	0.20	96	100
	1.96	0.34	2.78	0.33	3.76	0.24	4.54	0.16	100	100
+ ug/kg	1.76	1.18	2.72	0.81	3.74	0.94	4.64	0.78	97	100
	1.98	0.76	2.72	0.50	3.54	0.32	4.52	0.42	101	100
	1.98	0.71	2.88	0.56	3.40	0.41	4.78	0.46	100	50
	1.98	0.71	2.88	0.52	3.46	0.44	4.82	0.53	100	50
	1.90	0.92	2.84	0.80	3.86	0.68	4.66	0.57	96	50
	1.88	0.95	2.86	0.88	3.76	0.80	4.70	0.62	96	50
	2.10	0.53	3.12	0.30	3.88	0.28	5.20	0.32	94	50
	2.12	0.65	3.10	0.44	3.94	0.52	5.20	0.41	94	50
mean:	1.94	0.78	2.84	0.61	3.69	0.59	4.74	0.50	98	
s.e.m.:		0.03	0.08	0.05	0.06	0.06	0.07	0.08	0.05	1
n:	13	13	13	13	13	13	13	13	13	

two responses from each animal are shown unless marked x

Discussion

ABRs are generally considered to be refractory to the drug effects, particularly those of pentobarbital. The changes observed herein following administration of carfentanil were quite striking. The characteristics of the abnormalities were similar to a sensorineural-type hearing loss in which responses above threshold level are fairly intact, while responses below threshold are absent. In humans this type of aberration is usually permanent. However, "temporary" sensorineural-type hearing losses as per ABR testing have been reported in premature infants subject to apnea, with normalization of the responses when the apnea had been outgrown.[2] These data are analogous in that the animals had normal ABRs on follow-up testing with pentobarbital.

It is well-documented (*vide infra*) that hypothermia can alter ABRs. Although several of the animals experienced hypothermia following injection with carfentanil, there was no statistical correlation between temperature and ABR amplitude--the criterion for detection. It should also be noted (Table 1) that although there was no significant difference in temperature between the Carfentanil and Control groups, the responses of the Carfentanil group were significantly lower in amplitude. Three of the animals were warmed to more normothermic temperatures (data not shown). The responses of one animal were unchanged and the responses of another had degraded. The third animal did have improved ABRs, but died precipitously within seconds of the last recording. This finding was attributed to some last agonal release of neurotransmitter. The data are interpreted as indicating that carfentanil-induced changes in the ABRs were not directly related to body temperature and that drug effects outweighed any temperature effects.

No clear dose-response effects on the ABRs were observed with carfentanil, but data were limited at the lower doses. There was some

correlation between ABR morphology at the highest dose, and survivability of the animals. Further studies are warranted.

Although respiration was not directly monitored during evoked potential testing, the animals were continuously observed. Apnea was noted with carfentanil, but not with pentobarbital. ABR changes were noted in both the presence and absence of clinical apnea. Further studies are underway to try to correlate changes in the respiratory pattern with changes in the ABR.

CONCLUSIONS

Taken together the data indicate that the findings reported herein represent effects of carfentanil upon brainstem neurons and that these effects were independent of body temperature and anesthesia. The data suggest that ABRs are a sensitive monitor of brainstem function, particularly when respiratory centers are compromised.

REFERENCES

1. Henderson-Smart, D.J. Pettigrew, A. G., and Campbell, D.J.: Clinical apnea and brain stem neural function in preterm infants. N. Engl. J. Med. 308:353-357, 1983.

2. Reutter, S.A.: Brainstem Evoked Responses and Apnea in Preterm Infants, PhD Dissertation, George Washington Univ., Washington, DC, 1985.

[1]Toxicology Division, U.S. Army Chemical Research, Development and Engineering Center, Aberdeen Proving Ground, MD 21010-5423

THE EVALUATION OF A SYNTHETIC OPIATE AEROSOL IN INDUCING NARCOTIC HYPNOSIS IN THE RAT

J. Carpin, C. Whalley, and R. Mioduszewski, U.S. Army Chemical Research, Development, and Engineering Center, Aberdeen Proving Ground, MD. 21020

ABSTRACT

The sedative/hypnotic properties of opiates have been widely studied in several mammalian species. Typically the route of administration is by bolus injection. It is likely that these drugs are at least as effective via the inhalation route, however, no quantitative data are available. To address this question, individual rats were exposed to different concentrations of an aerosolized synthetic opiate, carfentanil. Rats were judged to be in a state of narcotic hypnosis when loss of righting reflex (LRR) was exhibited during a post exposure exam. The EC_{50} for LRR was found to be 8.1 µg/liter. Based on this value, inhaled dose was estimated at 3.7 µg/kg, nearly an order of magnitude below the reported ED_{50} value for LRR by intraperitoneal injection. One can conclude that the drug is at least as potent when inhaled as an aerosol.

INTRODUCTION

Opiates are potent central nervous system depressants and they have been shown to exhibit a continuum of effects in several mammalian species ranging from sedation at low dose levels to general anesthesia at sufficiently high doses. Intermediate dose levels produce narcotic hypnosis, a sleeplike state in which the subject is incapable of voluntary movement and appears to be dissociated from the surrounding environment. A recent study examined the hypnotic/sedative properties of carfentanil, a synthetic opiate, in the rat when the compound was administered by intraperitoneal (IP) injection[1]. One of the neuromotor responses used to evaluate hypnotic effects in the study was loss of righting reflex (LRR). The ED_{50} value reported for LRR in the rat was 31.9 µg/kg.

The goal of this study has been to demonstrate the feasibility of achieving carfentanil-induced hypnosis in rat via the inhalation route. It was hypothesized that carfentanil, delivered in the form of an aerosol, would be at least as effective as an IP bolus injection in attaining the same neuromotor response. To test this hypothesis, a series of rat exposure experiments were conducted at various opiate concentration levels to evaluate the EC_{50} for loss of righting reflex. Using this EC_{50} value, together with reasonable values for minute ventilation and particle deposition fraction during the exposure, an estimate of lung dose was determined.

EXPERIMENTAL METHODS

Carfentanil, methyl 4-[(1-oxopropyl) phenylamino]-1-(2-phenylethyl)-4-piperidine carboxylate was obtained in crystalline form as the citrate salt. Varying amounts of compound (0.5 to 2.0 mg/ml) were dissolved in a citric acid/ethanol solution (66 mg/ml) which served as the vehicle for dissemination. The citric acid served to stabilize the particle size of the aerosol and also increase the total aerosol mass delivered during the exposures.

Experiments were conducted in a bench scale whole body exposure chamber consisting of a 4.5" I.D. by 12" long Plexiglass cylinder. Exposure aerosols were generated by compressed air nebulization of the opiate/vehicle solution. Aerosols emanating from the generator were diluted 2:1 with particle free air in a mixing chamber, prior to entering the exposure chamber, to promote solvent evaporation and subsequent drying of the particles. A Columbus Instruments respiration monitor, connected to the chamber, enabled continuous respiratory frequency monitoring throughout the exposure.

Six male albino (Sprague-Dawley) rats (0.35-0.42 kg) were individually exposed to equilog-spaced target concentrations of airborne carfentanil in an up-and-down sequence. The initial target concentration was based on a best estimate of the EC_{50} value using available data. Subsequent target exposure levels were set higher or lower depending on the animal response from the preceding exposure. Exposure concentration levels were altered by varying the amount of dissolved carfentanil in the nebulizer solution while maintaining the generator mass output constant. All exposures were 4 minutes in duration and were conducted under dynamic conditions at a total chamber flow of 19 lpm.

Following each exposure, the rat was temporarily removed from the chamber and it's ability to right itself was evaluated. An animal was considered to test positive for LRR if it made no attempt to right itself for 30 seconds.

Six additional rats were used in a series of vehicle control (citric acid/ethanol) exposures to rule out the possibility of neuromotor deficit as a consequence of ethanol exposure. The experimental conditions during these exposures were identical to those used in the opiate/vehicle exposures except for the fact that no opiate was added to the nebulizer solution.

Airborne carfentanil concentration was determined gravimetrically by collecting the entire aerosol flow exiting the chamber onto a 47mm open faced filter (i.e. sample flowrate = 19 lpm). After allowing sufficient time for any residual ethanol to evaporate, the filters were weighed on a Fisher Model XA200DS balance to determine the net weight gain. The amount of carfentanil present in the sample was computed from the total mass collected and the total chamber flow by assuming that the ratio of carfentanil to citric acid on the filter was the same as that in the nebulizer solution. Chamber aerosol particle size distribution was determined using a Sierra Instruments Model 220 cascade impactor.

RESULTS

All the exposure atmospheres in this study consisted of composite aerosols of citric acid laden with varying amounts of carfentanil citrate. Ethanol was assumed to be present only in the vapor state assuming that sufficient time was given for complete evaporation from the primary aerosol cloud to occur. The average aerodynamic mass median diameter (AMMD) of the aerosols was nearly constant at 1.0 μm with a range of 0.9 to 1.1 μm. The total mass concentration of citric acid, the major aerosol constituent, was 600 +/- 20 μg/liter for all experiments. Ethanol vapor concentration was estimated at 26,000 ug/liter based on the rate of solvent loss from the nebulizer.

Figure 1 illustrates the resulting carfentanil exposure levels to which individual rats were subjected and their ability to right themselves when tested at 6 minutes post exposure. Airborne carfentanil concentrations ranged from 4.5 to 18.3 μg/liter. The EC_{50} for LRR was estimated at 8.1 μg/liter using the up-and-down method for small samples[2]. The resulting 95% confidence limits ranged from 5.5 to 12.5 μg/liter.

Figure 2 depicts the changes in respiratory activity as a consequence of exposure to the opiate/vehicle aerosol. Monitoring was initiated at least 10 minutes prior to the

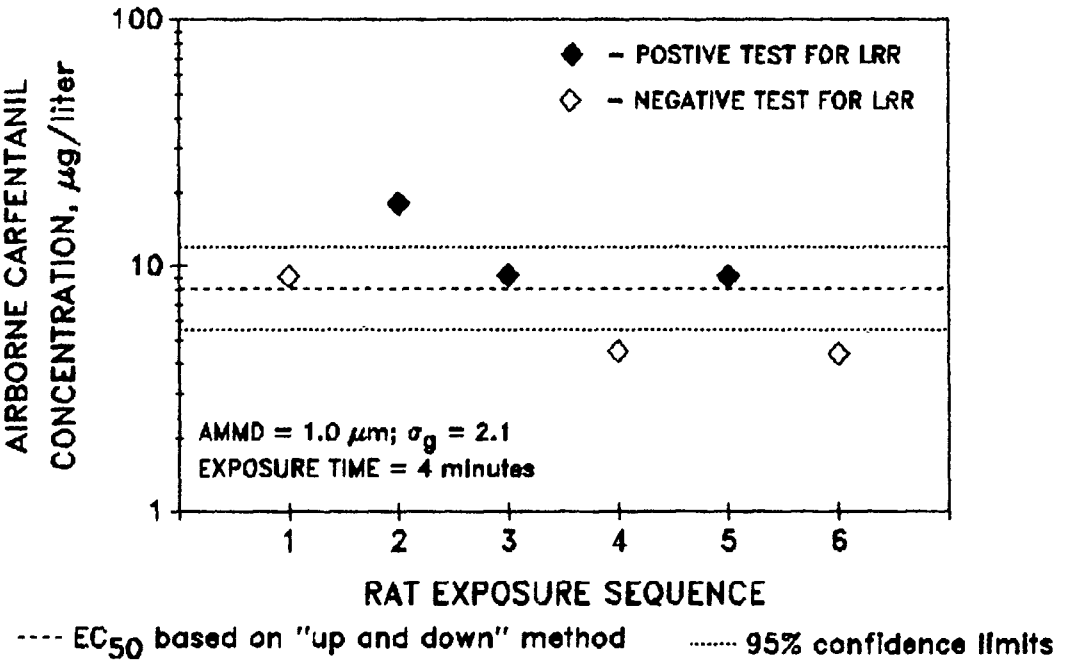

Figure 1
The effect of carfentanil exposure level on hypnosis as assessed by loss of righting reflex (LRR) in post exposure tests.

start of the exposure and continued throughout the exposure phase (bracketed by vertical lines). After a brief interruption at 6 minutes post exposure while the animal was removed for neuromotor evaluation, monitoring was continued for up to fifty six minutes post exposure. During the pre-exposure period, all rats exhibited normal respiratory activity with average rates as low as 120 bpm, indicative of quiescent tidal breathing, and, as high as 450 bpm during episodes of pronounced sniffing activity. In contrast, there was evidence of a fall in respiratory rates below pre-exposure values and cessation of sniffing activity after the first minute of the carfentanil exposure. Respiratory depression became more pronounced as the exposure proceeded and breathing rate continued to fall reaching a minimum value at two to four minutes post exposure. The degree and rate of respiratory depression was well correlated with the atmospheric concentration of carfentanil. Rates remained depressed during most of the post exposure phase showing some tendency towards recovery near the end of the monitoring period.

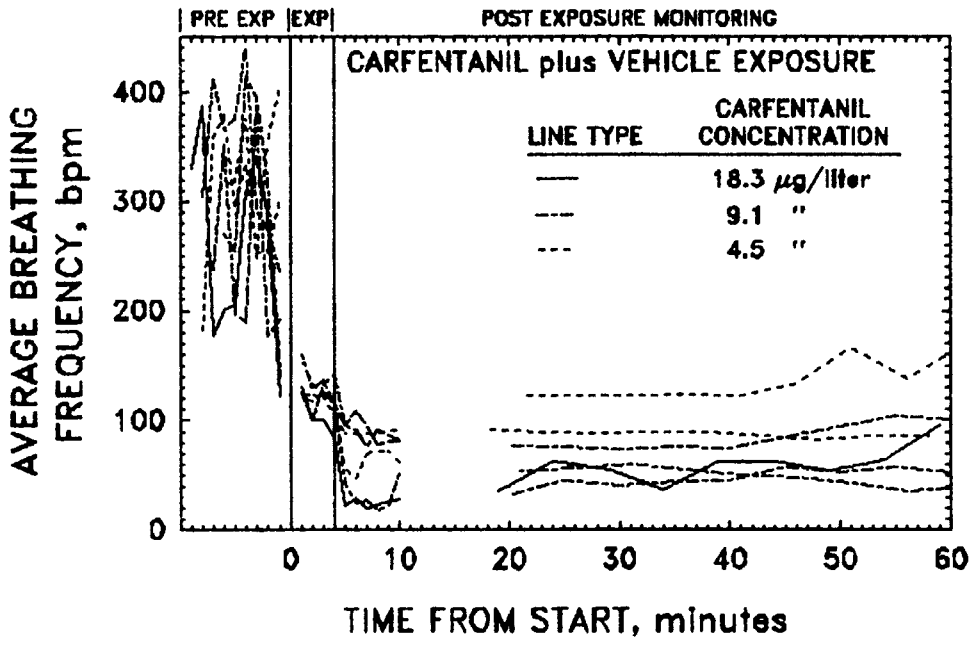

Figure 2
Respiratory response of individual rats before, during, and after exposure to carfentanil aerosol.

Control animals exposed to citric acid/ethanol (vehicle) atmospheres in the absence of opiate behaved normally before, during, and after the exposure showing no evidence of neuromotor deficit of any kind. In addition, no discernable differences were noted in the breathing patterns observed during the prexposure phase and those exhibited during the exposure and post exposure monitoring phases in any of the animals tested.

Other physiological responses observed during both the control and opiate exposures included eye blinking, salivation, and in a few animals rhinorrhea indicating that the vehicle aerosol was an irritant to the sensitive membranes of the eyes and respiratory tract. The irritant response ceased almost immediately after the exposure phase ended.

An estimate of the inhaled dose (ID) delivered to a rat exposed to a given concentration of airborne carfentanil was necessary in order to ascertain the effectiveness of administering the compound by the inhalation route. This was accomplished using Equation 1:

$$ID = \{\alpha (C * \Theta) V_T f\} / W \qquad (1)$$

α, aerosol deposition fraction; C, aerosol concentration; Θ, exposure duration; V_T, tidal volume; f, breathing frequency; W, average rat weight.

Four of the six parameter values needed to estimate ID, namely C, Θ, and W, were measured quantities. The remaining parameters (α and V_T) had to be obtained from literature sources. The total deposition fraction for the polydisperse aerosol used in this study was estimated from measurements of total deposition of monodisperse 0.2 to 3 µm AMMD aerosols in rats[3]. This was done by assuming a log normal distribution for the aerosol in this study (Mode = 1 µm; σ_g = 2.1) and weighting the rat deposition data accordingly. Linear interpolation was used to bridge the gaps between experimental deposition values. A summary of the values used in computing the inhaled dose necessary to produce LRR in 50% of the rats exposed is given in Table 1.

TABLE 1
Parameters values used in the estimate of inhaled dose.

α	= 0.25 (See explanation above)
C	= 8.1 µg/liter (EC_{50} for LRR)
Θ	= 4 minutes
V_T	= 0.0015 liters (Mean value for rat[4])
f	= 115 bpm (Average value measured during exposure phase)
W	= 0.38 kg

Given these values, the inhaled dose (ID_{50}) of carfentanil needed for induction of hypnosis calculates to be 3.7 µg/kg, nearly an order of magnitude lower than the previously reported ED_{50} value of 31.9 µg/kg via IP injection[1].

Although 95% confidence limits were reported for the effective IP injection dose data (12.1 to 86.6 µg/kg), there are unknown factors in the calculation of inhaled dose that make a precise comparison between the data sets difficult. For example, the value used above for the fraction of inhaled particles that deposit (α=0.25) is valid only for

non-hygroscopic aerosols. Since citric acid is soluble in water, the potential exists for hygroscopic growth in the saturated environment of the respiratory tract. This could result in a 2 to 3 fold increase in the value of α with a corresponding increase in the ID_{50}.

One could estimate the maximum likely ID50 by choosing a particle deposition fraction of 100% (α = 1) and substituting the upper confidence limit for the EC50 (12.5 µg/kg) into Equation 1. In doing so, one computes a maximum inhaled dose of 22.7 µg/kg, a value still less than the reported ED50 for LRR via IP injection.

CONCLUSIONS

Based on the above results, one can conclude that inhalation is a viable route of administration for potent synthetic opiates like carfentanil. We accept the hypothesis that an equivalent dose delivered to the lung by inhalation is at least as effective as a dose delivered by IP injection. It is likely that considerably less carfentanil is needed to induce narcotic hypnosis in the rat when administered in the form of an aerosol as compared to IP injection, however, the uncertainty in the deposition fraction of inhaled particles must be reduced by further experimentation before this contention can be supported.

REFERENCES

1. Mioduszewski, R. J., Farrand, R., Pharmacologic Effects of Carfentanil in Rats: Influence of Adjuvant Coadministration. CRDEC-TR-041, 1989.

2. Dixon, W. J., The Up-and-Down Method for Small Samples. J. Amer.Stat.Assoc., 60, 967-978. 1965.

3. Raabe, O. G., Yeh, H. C., Newton, G. J., Phalen, R. F., and Velasquez, D. J., Deposition of Inhaled Monodisperse Aerosols in Small Rodents, in Inhaled Particles IV, Walton, W. H., Ed., Permagon Press, Oxford, p1, 1977.

4. Phalen, R. F., Inhalation Studies: Foundations and Techniques. CRC Press, Boca Raton, Florida, p222, 1984.

BLANK

XVI. BIOTECHNOLOGY POSTERS

BLANK

DETERMINATION OF TOXINS USING ENZYME-AMPLIFIED RECEPTOR ASSAY

Susan F. Hallowell [a] and Garry A. Rechnitz [b]

Abstract: A new receptor based assay is described for the determination of toxins which have high affinities for the acetylcholine receptor. The method is based upon the hindrance of the normal binding of a synthetic enzyme-drug conjugate with a high affinity for the acetylcholine receptor protein by the presence of toxins which act as antagonists. The activity of the enzyme marker system, glucose-6-phosphate dehydrogenase covalently conjugated to desipramine, is monitored by colorimetric detection of the rate for NADH formation at 340 nm. The procedure proposed is designed to provide a simple toxin screen which can be done in a minimally equipped laboratory while achieving the required sensitivity. The technique is illustrated for snake venoms form *Bungarus multicintus*, *Naja naja*, and the alkaloid tubocurarine. Aspecific binding responses are shown to have minimal effect on the assay.

Introduction

Although the use of antibody/antigen and biocatalyst-based biosensor systems has emerged in the last 15 years, the use of isolated receptors as the molecular recognition element in a detector system is a fairly recent innovation. This concept appears to be very viable. Research done by CRDEC has demonstrated the ability to use receptor based technology for the determination of acetylcholine agonists and antagonist compounds using both capacitance sensors and fiber optic fluorosensor devices using fluorescent labeled bungarotoxin probes (1,2). These systems have the unique characteristic of pharmacological recognition of toxins at the level of toxicity, unlike immunogenic systems. The notion of coupling a receptor with other transducer-detection systems is limited only by the ability of the detector to sense the toxin binding reaction either directly or indirectly. This is done by the development of a physical or chemical environment which is both altered by the toxin binding reaction, and sensed by the detector. For instance, a new type of acetylcholine sensor was recently described using an Ion Sensitive Field Effect Transistor (ISFET) with an acetylcholine receptor which exploits the natural ion gating function of the receptor moiety as the signal producing event (3). Yet another receptor based sensor has been developed by incorporating receptors into the surface of a polymeric membrane cast onto the surface of an electrode, by which capacitance changes of the membrane were monitored as charged target compounds bound to the membrane's surface (4). The use of an enzyme marker system with a receptor recognition element has been shown to be an attractive, inherently sensitive system (5). The toxin binding reaction to the receptor is indirectly determined by its competition with an enzyme-labeled drug probe. The enzyme's activity is decreased by the binding of the drug attached to it as it binds to the receptor. Thus, the toxin binding reaction, which occurs at the nanomolar level, is catalytically enhanced by the presence of the enzyme, and the

a. Analytical Division, Chemical Research Development and Engineering Center, APG, MD.
b. Department of Chemistry, University of Hawaii, 2545 The Mall, Honolulu, Hawaii, 96822

signal detected is that of the amount of enzyme activity, determined by the measurement of the amount of conversion of substrate to product. Because the enzyme's activity has been linked to the amount of toxin present, and since it amplified this reaction by a factor of approximately 100,000 fold, this system does not rely on an ultrasensitive detection systems (such as the capacitance sensor) which can be subject to drift, reproducibility, and precision problems. A conventional detector can be used which is chosen to measure the signal created by the appearance of enzyme product. We have recently demonstrated the viability of this concept in our laboratory, and determined the theoretical limits of this assay (5,6). Last year, we developed and optimized a prototype Enzyme-Amplified Receptor Assay (ERA) system using the acetylcholine receptor and the drug desipramine, a channel binding compound, labeled with the enzyme glucose-6-phosphate dehydrogenase (7). The objectives of this present study were to determine the feasibility of applying the presently developed ERA system to the analysis of toxins which bind at the antagonist site on the receptor, which is allosteric to the actual site of binding of the enzyme labeled probe. Because of the demonstrated intramolecular communication phenomenon between these two sites, we believed that we could also use our channel binding drug labeled enzyme compound to detect the presence of drugs or toxins binding to the antagonist site.

METHODS

Reagents

Nicotinamide adenine dinucleotide (NAD, N7004), glucose-6-phosphate disodium salt (G6P, G7250), D-tubocurarine chloride (D-TC, T2379), carbamylcholine chloride (CARB, C4382), snake venoms from Bungarus multicinctus (a-BgT, V6625) and Naja-naja (Naja, V4378) were all purchased from Sigma Chemical company. The NAD, CARB, G6P, a-BgT, and Naja were reconstituted with a tris based buffer (54 mM NaCl, 50 mM Tris and 1mM EDTA) at pH 7.4. The D-TC was reconstituted in warmed, distilled, deionized water, and standards were prepared in the working buffer. The NAD, CARB and G6P were reconstituted with a tris based buffer (54 mM NaCl, 50 mM Tris and 1mM EDTA) at pH 7.4. The glucose-6-phosphate dehydrogenase conjugated with desipramine (G6PD-DES, which is not to be taken as a 1:1 stoichiometric conjugate) was purchased from Syva Co. (3J019) as a part of EMIT tricyclic antidepressant assay kit (7C319, reagent B), and was reconstituted according to the manufacturer's specifications in distilled, deionized water. No information was available on the enzyme activity or the DES concentration of this conjugate. (Under assay conditions comparable to unconjugated enzyme, the G6PD-DES was estimated to be 1.2 units/mL.). Buffer was made with Sigma Trizma Base (T-1503, tris(hydroxymethyl)aminomethane) and adjusted to pH 7.4 with HCl. Sodium chloride (NaCl, S271-500), disodium phosphate (Na_2HPO4, 3828-1), and disodium ethylenediaminetetraacetate (EDTA, S-311) were all purchased from Fisher Scientific. Distilled, deionized water was used throughout, and all reagents were stored at 4 ^{o}C when not in use.

Instruments

Centrifugations were carried out with an IET-HT centrifuge at 4^{o}C. Acetylcholine receptors were homogenized using a Polytron (Brinkman Instruments) setting at 5 (50% power). Reactions were carried out in 1.5 mL microcentrifuge tubes at room temperature (22^{o}C). Enzymatic activity of the G6PD and G6PD-DES was monitored in quartz cuvettes with the spectrophotometer at 340 nM at room temperature. Measurements were made with a Hitachi model 100-60 spectrophotometer. Responses were followed on a Heath strip chart recorder and initial rates calculated manually from recorder tracings.

Preparation of the Acetylcholine Receptor

Torpedo nobiliana was prepared as described elsewhere (7). This procedure yields receptors prepared as vesicles at an average protein concentration of about 5 mg/mL. The acetylcholine receptors were assayed with respect to total protein concentration by the method of Bradford (8).

Calibration Curves of d-Tubocurarine and Snake Venoms from Bungarus multicintus and Naja-naja

The primary standard solutions of the snake toxins were prepared in Torpedo buffer without Na_2HPO_4 at a concentration of 5 mg/mL. The working standard solutions D-TC were prepared in the working buffer system from the primary standard (prepared with deionized H_20.) The snake venom experiments were performed by adding a 9 µL quantity of 1 mM CARB to vials containing 150 µL of receptor protein or Torpedo buffer (as blank) and allowing them to stand for 2 minutes. Standard solutions of the toxins were then introduced (up to 30 µL of the standard solution, with buffer to make up the volume) and the mixtures were mixed thoroughly on a shaker for 10 minutes. A 15 µL volume of the G6PD-DES was then introduced, and this mixture was allowed to incubate for 40 minutes at room temperature. Two different blanks were run, one containing no toxin and the other set containing no receptor protein, some with or without the toxin.

The tubocurarine experiments were performed by adding a 10 µL quantity of 1 mM CARB to vials containing 200 µL of receptor protein or Torpedo buffer (as blank) and allowing them to stand for 2 minutes. A volume of 10 µL of the standard solutions of D-TC was then introduced and the mixtures were gently agitated on a shaker for 10 minutes. A 20 µL volume of the G6PD-DES was then introduced, and this mixture was allowed to incubate for 40 minutes at room temperature. Blanks were run as described previously.

After an incubation period, the vials were centrifuged at 3000 X g (8,000 rpm) for 10 minutes at 4°C. After centrifugation, 50 µL of supernatant from each vial were added to 750 µL of substrate containing 1mM G6P and NAD in a quartz cuvette and this was immediately followed by measurement of enzyme activity, by following the rate of production of NADH.

In most experiments, the data were normalized to indicate the percentage of initial enzyme activity remaining (or the percentage inhibition of enzyme activity) as a function of the toxin concentration.

RESULTS AND DISCUSSION

The acetylcholine receptor is an aggregate of five protein subunits with a molecular weight of 256,000. This protein approximates a rosette in appearance with a pore structure found in the center The chemical environment of this receptor dictates the conformation of the protein. These states (conformations) are nominally described as resting, activated, desensitized, or inactivated. Most of the time, the receptor assumes the resting conformation, with the pore structure shut, such that there is no ion flux transversing the membrane in which the receptor is incorporated. However, in the presence of an activator compound such as the physiological activator (acetylcholine) or synthetic analogs such as CARB, the pore structure is activated, and an ion channel is formed. The so called channel compounds are believed to bind within this pore region. Therefore, it is always necessary to first activate the receptor by the addition of an activator (agonist) compound to achieve the environment necessary to elicit binding of channel compounds, including the enyzme-labeled probe which we used in this study.

The reaction between agonist and receptor is shown in equation 1.

$$AchR_{(resting)} \underset{\text{(activator compound)}}{\rightleftharpoons} AchR_{(activated)} \qquad [1]$$

The assay employs commercially available G6PD, which has a ligand (desipramine) attached to it known to bind to the channel site. The binding of this marker system is dependent on the affinity equation in equation 2, with desipramine possessing an affinity of 10^6 /M to the receptor.

$$AchR_{(activated)} + \textit{G6PD-ligand}_{(channel\ compound)} \rightleftharpoons$$
$$\textit{G6PD-ligand}\text{:AchR (enzyme deactivated)} + \textit{G6PD-ligand (active)} \qquad [2]$$

When the enzyme-labeled drug is complexed with the acetylcholine receptor, the enzyme is rendered inactive. The exact mechanism for the enzyme inactivation is postulated to involve the steric exclusion of the enzyme substrate from the enzyme active site. The addition of the substrates for the enzyme G6PD result in the turnover of substrate to product only by the active enzyme remaining in solution which has not bound to the receptor, as shown in equation 3.

$$G6P + NAD^+ \underset{\textit{G6PD-ligand (active)}}{\rightleftharpoons} \text{6-phosphoglucono-d-lactone} + NADH + H^+ \qquad [3]$$

The rate of production of the NADH is monitored colorimetrically in this assay, and is used as an indication of enzyme activity.

The allosteric interactions between the acetylcholine and channel binding sites on the receptor provided some basis for the hypothesis that the presence of antagonist compounds could be assayed by using ERA with an enzyme labeled with a channel compound such as desipramine. Simply put, if antagonist compounds keep the receptor protein in a "locked" conformation (with no ionic channel formation), the ionic channel will not be accessible to bind with the enzyme-labeled channel compound. Therefore, in the presence of antagonists compounds, equation 5 also applies, which affects the material balance of the activated acetylcholine receptor, $AchR_{(activated)}$ shown in equation 1, available to participate in the bindng of the G6PD-DES shown in equation 2. Less enzyme is available to convert substrate to product, as shown in equation 3.

$$AchR_{(activated)} + \text{Antagonist} \rightleftharpoons \text{AchR-Antagonist}_{(inactivated)} \qquad [4]$$

Equation 5 proceeds in the forward direction in most cases because the affinity of many antagonist compounds for the receptor is greater (i.e. the Ka 10^{10} -10^{12}/M for snake neurotoxins) than that of the competing reaction shown in equation 1, of agonist compounds to the receptor (such as acetylcholine or carbamylcholine with Ka~10^5 - 10^6/M) Because the agonist compounds (which activate pore formation) and antagonist compound compete with the same binding site on the acetylcholine receptor, it seemed likely that dose response relationships (enzyme activity vs. antagonist concentration) could be developed. More antagonist compound should result in more desensitized receptors, resulting in greater enzyme activity relative to a blank experiment, with no antagonist compound. The neurotoxins found in *Bungarus multicintus* and *Naja-naja* venoms act as

extremely potent acetylcholine antagonists by virtue of their high affinity to the receptor; although the venom injected in a snake bite is typically very small, the results can be fatal. Similarly acting is another class of potent paralytic agents which are structurally quite different from the α-snake venoms namely, the alkaloid curares compounds. D-tubocurarine has a lower affinity for the receptor antagonists site (10^6-10^7) and has also been shown to bind to the channel site with an affinity of about 10^3/M. Thus, this compound is a dual acting drug.

The experimental procedure described previously produced calibration curves over the concentration range of 25 to 150 µg of Bungarus or Naja venoms. While there was a direct correlation between the increase of enzyme activity and the concentrations of toxins, it became apparent from the blank experiments that the crude BgT venom would also cross-react with the enzyme, causing some inhibition of its activity. Figure 1 shows the standard calibration curve for the BgT venom using ERA. The upper trace shows the binding of the toxin to the G6PD-DES enzyme only, with no receptors present while the bottom trace shows enzyme activity as a function of venom concentration in the presence of receptors. Although it may have decreased the overall sensitivity of this assay for BgT, the cross-reactivity of the venom to the enzyme did not prohibit the detection of this toxin. Figure 2 shows a plot of the normalized enzyme activity as a function of BgT venom. The data was collected in triplicate, and error bars indicate ± one standard deviation. Surprisingly, the Naja venom did not show cross reaction to the enzyme, as seen in Figure 3. (The relative average deviation between the enzyme activity with and without 150 µL of venom was 2.1%.) The increasing activity of the G6PD-DES as a function of increasing

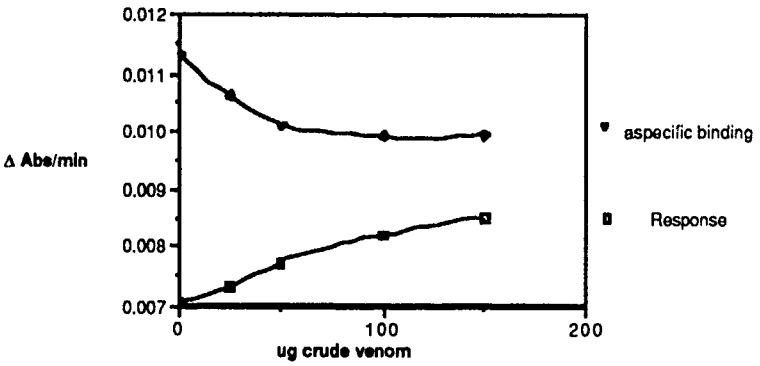

Figure 1

Standard calibration curve of *Bungarus multicintus* venom using ERA. Upper trace shows the binding of the toxin to the G6PD-DES enzyme only (no receptor present.) Bottom trace shows enzyme activity as a function of venom concentration, with receptor present. Receptor concentration is 4.5 µg/mL, CARB is 4.4 X 10^{-5} M, enzyme concentrations is 074 units/mL, 50 µL of sample solution was added to 750 uL of substrate containing 10^{-3} M G6P, NAD in Tris buffer.

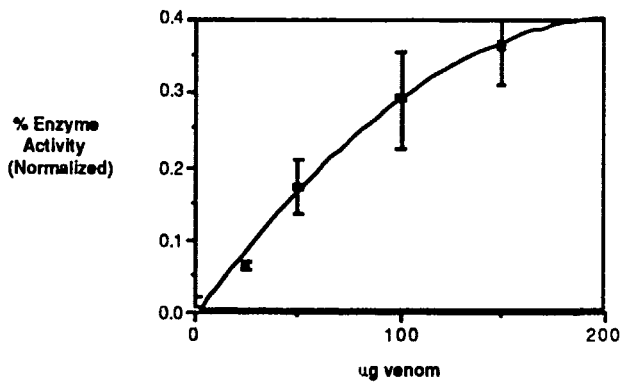

Figure 2:

Standard Calibration curve of *Bungarus multicintus* venom using ERA (Enzyme activity shown is normalized.) Receptor concentration is 4 5 µg/mL, CARB is 4.4 X 10^{-5}M, enzyme concentration is .074 units/mL, 50 µL of sample solution was added to 750 µL of substrate containing 10^{-3}M G6P, NAD in Tris buffer.

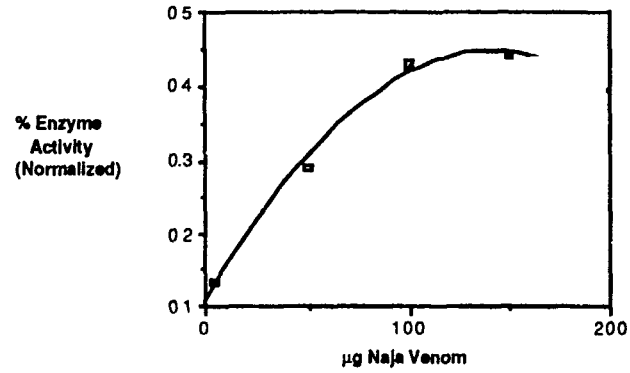

Figure 3:

Standard calibration curve of *Naja-naja* venom using ERA. Receptor concentration is 4.3 µg/mL, CARB is 4.4 X 10^{-5} M, enzyme concentration is .074 units/mL, 50 µL of sample solution was added to 750 uL of substrate containing 10^{-3} M G6P, NAD in Tris buffer.

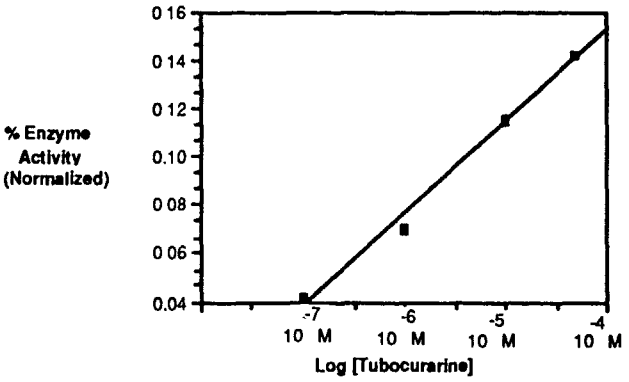

Figure 4:

Standard calibration curve of tubocurarine using ERA Receptor concentration is 4 8 µg/mL, CARB is 4 4 X 10^{-5} M, enzyme concentration is .100 units/mL, 50 µL of sample solution was added to 750 uL of substrate containing 10^{-3} M G6P, NAD in Tris buffer.

toxin concentration was fairly dramatic for the venom experiments, with the naja venom showing a slightly greater sensitivity than the BgT. In contrast, the ERA showed a much lower level of response to tubocurarine, as seen in Figure 4. Table 1 summarizes the response characteristics of these three analytes. These data confirmed the utility of the ERA experiment as a screen for antagonists with high affinities for the receptor site. However, it was apparent that the precision was not as good for antagonist compounds as it was for previously tested channel compounds. Also, the tubocurarine was only minimally responsive, probably due to the complicated and opposing interactions of this compound with both the receptor and ionic channel sites.

CONCLUSION

The development of a receptor based assay using a labeled enzyme probe has been demonstrated to be feasible. Here, we have

Table 1: Response Characteristics of Bungarus and Naja Venoms, and Tubocurarine using ERA.

	Regression Curve (Best Fit)	R	Lowest Standard
Bungarus Venom	$Y = -.0089 + 3.86 \times 10^{-3}X \quad 9.076 \times 10^{-6}X^2$	.998	25 µg
Naja Venom	$Y = 0.104 + 4.87 \times 10^{-3}X - 1.71 \times 10^{-5}X^2$	.997	25 µg
Tubocurarine	$Y = 6.83 \times 10^{-2} * X .2027$	.994	10^{-7}M

developed a homogeneous assay technique which can be used to screen for receptor antagonist compounds. This assay is notable since the analytes monitored in this case (the antagonistic toxins) bind to a distinctly different site that the enyzme-labeled probe used in the analysis. The assay works due to the allosteric communication between these two sites, since the presence of antagonist compounds do not allow the opening of the ion channel of the acetylcholine receptor . Thus, this binding site is not available for the enzyme probe used. It is notable that our demonstrated system produces analytical results: although the channel probe used (desipramine) has a much lower receptor affinity than the bungarotoxin, this probe can be successfully used in conjunction with the enzyme amplification feature. Because we were using the same enzyme probe as the EMIT kits, it can also be inferred that interferences with the EMIT assay due to interaction with the enzyme will also appear in the ERA assay.

The greatest significance of this study is the demonstration of the general feasibility of using receptor systems with enzyme amplification. This should prove to be a powerful general procedure, both for the clinician and for those interested in fabricating receptor based biosensors. Presumably, one can select a receptor system appropriate for a category of drugs or toxins, and then choose an enzyme system which will produce a signal compatible with the desired detection scheme, whether it be colorimetric, potentiometric, or electrochemical. The ERA technique should be suitable for transition to a number of different physical systems. For instance, the chemistry presented above should be directly transferable to the fiber optic system currently under development at CRDEC since NADH is fluorescent, assuming that the immobilization procedures for the receptor allows the functional recognition of channel binding compounds to the acetylcholine receptor, and the receptor density is sufficiently high to meet the previous established criteria for this procedure. If receptor technology can mature to the stage that receptors can be immobilized on to a paper tab, an ERA technique could be developed into a quick visual indicator kit, similar to commercially available home pregnancy kits, which employ antibody recognition in conjunction with enzyme amplification. Our ERA procedure could be developed into field kit configuration by the synthesis of a probe using an enzyme which results either directly or indirectly in a colored product, with the "detector" being the human eye. Our future plans include the synthesis of toxin labeled color producing enzymes, with this end objective.

Acknowledgement: This work was funded by CRDEC through the ILIR program in FY 89.

REFERENCES

1. Eldefrawi, M.E., Sherby, S.M., Andreou, A., Nansour, N.A., Annau, Z., Blum, N.A. and Valdes, J.J. (1988) Anlyt. Lett. **21**, 1665-1680.

2. Rogers, K.R., and Eldefrawi, M.E., Accepted to Analytical Biochemistry 7/18/89

3. Gotoh, M., Tarniya, E., Momoi, M., Kagawa, Y. and Karube, I. (1987) Analyt. Lett. **20**, 857.

4. Taylor, R.F., Marenchic, I.G. and Cook, E.J. (1988) Analyt. Chim. Acta. **213**, 131-138.

5. Hallowell, S.F. and Rechnitz, G.A.,(1988) Anal. Lett., **22** (1) .

6. Hallowell, S.F. and Rechnitz, G.A.,(1987) Anal. Lett., **20** (12) 1929.

7.Hallowell, S.F. and Rechnitz, G.A. (1989) CRDEC-SP-005, 23.

8. Bradford, M.M. (1976). Anal. Biochem., **72**, 255.

BLANK

A RADIOIMMUNOASSAY FOR PHYSOSTIGMINE

Howard G. Meyer, Brian J. Lukey, Robin T. Gepp,
Michael P. McCluskey and Claire N. Lieske

United States Army Medical Research Institute of Chemical Defense, Aberdeen Proving Ground, Maryland 21010-5425

ABSTRACT

Antiphysostigmine antibodies were produced in rabbits using a unique physostigmine analog conjugated to keyhole limpet hemocyanin. These antibodies were used to develop a radioimmunoassay ranging from 0.2 to 15.0 ng/ml of physostigmine in 100 ul plasma samples. This assay measures physostigmine in 100 ul plasma samples with better sensitivity and greater through-put than do current state-of-the-art HPLC techniques. Precision and accuracy were good, as indicated by within-day and among-day precision. Plasma levels of physostigmine were determined in rats after intramuscular administration of 27 ug/kg of physostigmine. Estimates of various pharmacokinetic parameters were calculated.

INTRODUCTION

Physostigmine, an alkaloid obtained from the Calabar bean, is a cholinergic drug that has been used for many years. Until now, a simple sensitive assay to measure low plasma levels associated with therapeutic dosages has been unavailable. Assay methods include a number of HPLC procedures.[1-3] All of these procedures have a number of shortcomings (poor sensitivity, large sample size, and time consuming sample preparation) that can be solved with a radioimmunoassay (RIA). We have been able to prepare antibodies to physostigmine that are specific and have a good binding affinity. These antibodies do not cross react with eseroline, the major hydrolysis product of physostigmine, with a variety of carbamates, or with selected compounds used in the management of organophosphate poisoning. We have used these antibodies to develop a sensitive RIA for physostigmine and have used this assay to estimate the pharmacokinetic parameters of physostigmine after i.m. injection in rats.

METHODS

Preparation of physostigmine analog hapten immunogen. A physostigmine analog, 1,3-dimethyl-3-{2-[N-methyl-N-(7-carboxyheptanoyl)]aminoethyl}-5-(N-methyl-carbamoyloxy)-2,3-dihydroindole hydrochloride, was covalently linked to keyhole limpet hemocyanin (KLH) with 1-(3-dimethylaminopropyl)-3-ethylcarbodiimide hydrochloride. The molar ratio of covalently bound physostigmine analog to KLH was approximately 341:1 as determined spectrophotometrically.

Immunization and antiserum collection procedures. One volume of hapten-KLH conjugate was incorporated into an equal volume of Freund's complete adjuvants, and two male New Zealand White rabbits, weighing approximately 3 kg each, were injected intradermally in 25 sites on their shaved backs, three times at two-week intervals. Antibodies that specifically bind physostigmine were detected in both animals. A pool of the serum from day 103 was used for development of the assay.

Radioimmunoassay procedure. The RIA for physostigmine was carried out at 4°C in 0.01 M phosphate buffer, pH 6.0. Neostigmine bromide in a final concentration of 10 ug/ml was added to all rat plasma used for standards, unknowns, and serially collected pharmacokinetic samples to prevent degradation of physostigmine by endogenous esterases in rat plasma. Standard curves were generated with reaction mixtures, each containing 0.1 ml of normal rat plasma (NRP) spiked with a known amount of physostigmine salicylate, 0.4 ml of phosphate buffer, 0.1 ml of tritiated physostigmine (10,000 dpm; specific activity, 16.1 Ci/mmol) and 0.1 ml of a 40x diluted antiserum. This dilution of the antiserum pool binds 50% of the tritiated physostigmine. Control reaction mixtures lacked the antibody solution. For physostigmine unknowns in NRP and plasma samples from the pharmacokinetic studies, the respective samples were substituted for spiked plasma in the reaction mixture. The total volume of the reaction mixture was 0.70 ml. Reaction mixtures were incubated overnight (18 hr) at 4°C. The antibody bound physostigmine was separated from free physostigmine by precipitation with an equal volume of cold, saturated ammonium sulfate solution adjusted to pH 6.0. After a single wash the pellet was dissolved in 2.0 ml of distilled water and transferred to a 20 ml glass scintillation vial and counted in a Beckman 5801 liquid scintillation counter. For data reduction we selected a weighted least squares regression coupled with logit transformation.[4] Standard curves of unlabeled physostigmine that ranged from 0.2 to 15.0 ng/ml were generated using a stock solution in NRP. The antibody was tested for cross reactivity with neostigmine bromide, pyridostigmine bromide, 5-(1,3,3-trimethyl)indolinyl-N,N-dimethyl carbamate hydrochloride (Cui Xing Ning hydrochloride), eseroline, artane hydrochloride, atropine sulfate, azaprophen hydrochloride, the chloride salt of N-methylpyridinium-2-aldoxime chloride (2-PAM), the chloride salt of 1-2-[(hydroxyimino)methyl]-pyridinium-2-(4-carboxyamido-pyridinium)dimethyl ether (HI-6), 1-(1,2-dimethyl-2-nitro-propyloxymethyl)-2-(hydroxyiminomethyl)-3-methylimidazolium chloride (ICD 467), and scopolamine hydrobromide.

Unknowns. Six coded batch concentrations of physostigmine in NRP were made containing 0.2, 1.0, 6.0, 10.0, 25.0, and 50.0 ng/ml. All samples were frozen at -80°C until the day of the analysis. The samples were subjected to a primary screen, and those containing more than 15 ng/ml were diluted so that they would fall within the 0.2 to 15 ng/ml standard curve range.

Precision and accuracy. For both precision and accuracy calculations, data were used from the above six unknown concentrations (0.2, 1.0, 6.0, 10.0, 25.0, and 50.0 ng/ml) of physostigmine in normal rat plasma.

Animal studies. A 27 ug/kg dose of physostigmine (free base equivalent) in the form of physostigmine salicylate was administered i.m. to each of 6 male rats weighing 250 to 350 g. Blood samples of 400 ul each were serially collected at multiple time points.

Pharmacokinetics. Concentration-time profiles of physostigmine for individual rats were fitted to standard pharmacokinetic models using PCNONLIN. Initial estimates of coefficients and exponentials required by PCNONLIN were obtained from the exponential curve-fitting program JANA.[5] For each animal, the product of systemic clearance and the fraction of drug absorbed was determined by dividing the dose by the area under the concentration-time curve. Parameters were averaged and reported with 95% confidence limits.

RESULTS

Standard curves. Standard titration curves for physostigmine in NRP were done for concentrations ranging from 0.2 ng/ml to 15.0 ng/ml. A typical standard curve using spiked NRP standards had an $r^2 = 0.992$.

Precision and accuracy. The precision and accuracy of the assay in the 0.2 to 50.0 ng/ml range were within acceptable limits.

TABLE 1.

Precision of physostigmine assay.

CONC. (ng/ml)	WITHIN-DAY CV (%)[a]	AMONG-DAY CV (%)[b]
0.2	9.1	21.3
1.0	4.6	7.4
6.0	6.7	6.4
10.0	14.2	15.2
25.0	8.3	11.3
50.0	12.5	16.8

[a] Coefficient of variation (CV) values were determined for each concentration each day (n=3). The average of six days' CV values represents the within-day CV.

[b] Among-day CV value was determined from 18 samples for a given concentration (3 each day for 6 days).

TABLE 2.

Accuracy of physostigmine assay.[a]

EXPECTED CONC. (ng/ml)	REPORTED ± 95% C.I. (ng/ml)	% BIAS
0.0	0.00 ± 0.00	0.0
0.2	0.16 ± 0.02	-22.1
1.0	0.99 ± 0.04	-0.5
6.0	6.17 ± 0.20	2.8
10.0	9.68 ± 0.73	-3.2
25.0	23.55 ± 1.33	-5.8
50.0	43.01 ± 3.60	-14.0

[a]The reported concentration and 95% confidence interval were determined from 18 samples of an expected concentration.

Specificity. We tested our antibody for cross reaction with eleven compounds. These included three carbamates, the major metabolite of physostigmine (eseroline), and seven compounds that have been used in the management of organophosphate poisoning. These compounds showed no cross-reaction at the concentrations tested.

TABLE 3.

Specificity of Physostigmine Antibody.

	IC_{50}*		IC_{50}*
Pyridostigmine Bromide	> 500 ng	Atropine Sulfate	> 500 ng
Neostigmine Bromide	> 500 ng	Scopolomine	> 500 ng
Physostigmine	0.6 ng	Artane	> 500 ng
Eseroline	> 500 ng	Cui Xing Ning	> 500 ng
ICD 467	> 500 ng	Azaprophen	> 500 ng
2-PAM Chloride	> 500 ng		

* Concentration needed to produce a 50% inhibition binding to inhibited physostigmine.

Pharmacokinetics. Plasma level-time curves were described adequately by an open, one-compartment model with first order absorption and elimination.

TABLE 4.

Pharmacokinetic parameters of physostigmine (27 ug/kg) injected i.m. into the rat.

PHARMACOKINETIC ESTIMATES	VALUE (n=6)	STANDARD DEVIATION
V_d/F (l/kg)[a]	5.87	1.43
k_{01} (min^{-1})[b]	0.435	0.271
k_{10} (min^{-1})[c]	0.041	0.006
AUC (ng x min/ml)[d]	118	13.0
$t_{1/2a}$ (min)[e]	2.7	2.0
$t_{1/2e}$ (min)[f]	17.4	2.9
T_{max} (min)[g]	7.7	3.6
C_{max} (ng/ml)[h]	3.5	0.8
Cl_s/F (ml/min/kg)[i]	232	27

[a] V_d = Apparent Volume of Distribution and F = Fraction of Drug Absorbed; [b] k_{01} = Absorption Rate Constant; [c] k_{10} = Elimination Rate Constant; [d] AUC = Area under the Curve; [e] $t_{1/2a}$ = Half Life of Absorption; [f] $t_{1/2e}$ = Half Life of Elimination; [g] T_{max} = Time to reach Maximal Concentration; [h] C_{max} = Maximal Concentration; [i] Cl_s = Systemic Clearance and F = Fraction of Drug Absorbed.

DISCUSSION

The RIA procedure has been used successfully since its introduction by Yalow and Berson in 1960 to measure physiological, toxicological, and therapeutic agents.[6] We were successful in designing a RIA for the cholinergic drug pyridostigmine,[7] and have now employed the same procedures to produce a RIA for physostigmine. We have demonstrated the utility of this assay by determining the pharmacokinetic parameters for i.m. administration of physostigmine in rats. The method is precise as indicated by CV values less than 20% for among-day and within-day, with but one exception. At 0.2 ng/ml, the among-day CV was 21%, which is acceptable considering the magnitude of the concentration. Within-day values approximated among-day values, signifying that day-to-day differences are very small. Concerning accuracy, the bias was acceptable within the 1 to 25 ng/ml concentration

range. The 50 ng/ml samples were found to be 14% low, probably due to a consistent error in the dilution of these samples to interpolate their concentration from the standard curve. Although the bias at 0.2 ng/ml appears large (22%), the standard error was only 0.04 ng/ml.

CONCLUSIONS

This RIA measures physostigmine concentrations with better sensitivity and greater through-put than do current state-of-the-art HPLC techniques. The small sample volume (100 ul) required permits pharmacokinetic studies of physostigmine by serial sampling in small laboratory animals as demonstrated in rats receiving an i.m. administration. Physostigmine absorption and elimination rates in our study were very rapid and comparable to those in prior rat studies.

REFERENCES

1. Somani S. M. and Khalique A.: Determination of physostigmine in plasma and brain by HPLC. J. Anal. Tox. **9**: 71-75, 1985.

2. Whelpton, R. and Moore, T.: Sensitive liquid chromatographic method for physostigmine in biological fluids using dual-electrode electrochemical detection. J. Chromatogr. **311**: 361-371, 1985.

3. Lukey, B. J., Clark, C. R., McCluskey, M. P. and Lieske, C. N.: A radiometric high performance liquid chromatographic assay for physostigmine. USAMRICD-TR-88-13, U.S. Army Medical Research Institute of Chemical Defense, Aberdeen Proving Ground, MD, November 1988. AD 203677.

4. Rodbard, D. and Lewald, J. E.: Computer analysis of radioligand assay and radioimmunoassay data. Acta Endocrinol. **64**: 79-103, 1970.

5. Statistical Consultants Inc.: PCNONLIN, NONLIN84, and JANA: Software for the statistical analysis of nonlinear models. Am. Stat. **40**: 52, 1986.

6. Yalow, R. S. and Berson, S. A.: Immunoassay of endogenous plasma insulin in man. J. Clin. Invest. **39**: 1157-1175, 1960.

7. Meyer, H. G., Lukey, B. J., Gepp, R. T., Corpuz, R. P. and Lieske, C. N.: A radioimmunoassay for pyridostigmine. J. Pharmacol. Exp. Ther. **247**: 432-438, 1988.

BIODEGRADATION OF THIODIGLYCOL

Steven P. Harvey*, Joseph J. DeFrank, Johnnie M. Albizo, James J. Valdes

Biotechnology Division, Research Directorate
U.S. Army Chemical, Research, Development and Engineering Center

Daphne Kamely

Scientific Advisor for Biotechnology
U.S. Army Chemical Research, Development & Engineering Center

A.M. Chakrabarty

Department of Microbiology and Immunology
University of Illinois at Chicago

ABSTRACT

Using a continuous-culture chemostat and bacteria collected from various sites in the Edgewood Area of Aberdeen Proving Ground, MD, a pure culture of gram-negative, aerobic bacteria was isolated which will utilize thiodiglycol (TDG) as its sole source of carbon and sulfur. The strain (SH18) was variously identified as Agrobacterium tumefaciens (by bacteriological methods) and Pseudomonas picketii (by fatty acid analysis). It was determined that SH18 would also utilize ethylene glycol as its sole source of carbon. Growth rates were determined with different concentrations of TDG and ethylene glycol and in enriched Luria broth. Gas chromatographic data combined with the growth curve data in TDG medium demonstrate that SH18 will degrade greater than 90% of the TDG in a 10 mM culture within 48 hours.

INTRODUCTION

Although enzymes have been isolated for the detoxification of organophosphate compounds[1,2,3], none have yet been found for the detoxification of 2,2'-dichlorodiethyl sulfide (mustard, HD). One way in which such enzymes might be found is via the isolation of bacteria which

utilize thiodiglycol (TDG, 2,2'-thiodiethanol) as a nutrient source. If enzymes from such an organism could hydrolytically cleave mustard at the sulfur-carbon (S-C) bond, detoxification would be effected.

TDG is used in various laboratory and industrial processes and is also a hydrolysis product and potential precursor of mustard. A literature search (1970 to present) found no previous reports of TDG biodegradation.

EXPERIMENTAL

Isolation of Bacteria from Soil Samples

Since thiodiglycol is a hydrolysis product of mustard and is typically found as an environmental contaminant in land sites previously contaminated with mustard, such sites from the Edgewood Area of Aberdeen Proving Grounds, MD were chosen from which to collect soil bacteria samples. Bacteria were extracted from soil samples by the procedure of Holben et al.[4] As opposed to procedures which grow organisms directly out of the soil, in this case they are physically removed from the soil matrix without any selection based on growth conditions. Presumably, this approach extracts a larger fraction of the total pool of microorganisms in the soil.

Continuous Culture Chemostat

A chemostat was constructed which allowed the continuous logarithmic growth of soil organisms in an environment which encouraged bacterial recombination. The essential features of the chemostat included a small culture flask for continuous growth and minimal usage of medium, a separate tube where new bacteria samples were added and slowly forced out into the culture flask, and a conjugation column filled with ceramic saddles and intended to provide a favorable environment for bacterial conjugation. Additionally, bacteria were continuously recirculated from the growth flask back over the conjugation column to encourage maximum recombination. Initially, a supplemental carbon source (glucose) and a potential intermediate in the TDG metabolic pathway (ethylene glycol) were added to the medium to allow all bacteria to grow. The glucose and ethylene glycol were gradually removed leaving only TDG as carbon and sulfur source. The chemostat was operated continuously for eight months in this way during which time other bacteria samples from various locations were periodically added. Samples were regularly checked for growth on TDG-Gelrite plates or in liquid medium in 5 ml tubes. After approximately eight months, strain SH18 was isolated based on its growth in liquid TDG medium and on TDG plates.

MATERIALS AND METHODS

Bacterial Medium

Minimal defined medium was a modification of M9 medium[5]. $MgCl_2$ was used in place of $MgSO_4$ to obtain sulfur-limiting growth conditions. M9 was supplemented with a salt solution consisting of 0.2 g $MgCl_2.7H_2O$, 0.012 g $FeCl_3.6H_2O$, 0.003 g $MnCl_2.4H_2O$, 0.003 g $ZnCl_2$, 0.003 g $CaCl_2.2H_2O$, 0.001 g $CoCl_2.6H_2O$, 0.003 g $CuCl_2.2H_2O$, 0.003 g $Na_2MoO_4.2H_2O$ and 0.001 g $NiCl_2.6H_2O$ per liter. Because an organic chelating agent such as nitrilotriacetic acid was not used, the inorganic salts did not dissolve completely. When the medium was used in the chemostat, it was stirred continuously in the medium jar to maintain homogeneity. When it was used for growth in tubes, it was filtered before use.

For growth in ethylene glycol or TDG as sole sources of carbon and/or sulfur, the organic compounds were added to a final concentration of 10 mM except when constructing growth curves which required higher concentrations. Luria broth contained 10 g tryptone, 5 g yeast extract and 5 g NaCl per liter and was supplemented with 0.3% glucose. Both Luria and minimal plates were made with 8 g per liter Gelrite (Kelco). Select Agar (BBL) was used initially but it appeared that the organisms were degrading the agar. With Gelrite, no growth was seen without other carbon sources added to the medium. In the case of the minimal plates, 2X M9 supplemented medium was mixed with a 16 g per liter solution of Gel-Rite immediately after autoclaving and plates were poured quickly to minimize salt precipitation.

Chemicals

Thiodiglycol was obtained from Sigma at a purity of 99+%. Ethylene glycol was obtained from Fisher at a purity of 99%.

Gas Chromotagraphy

All gas chromatographic determinations were done as described[6].

RESULTS

Isolation of SH18

After approximately eight months of continuous chemostat operation, a pure culture of gram-negative bacteria designated SH18 was isolated by growth on 10 mM TDG-Gelrite plates and in 10 mM TDG liquid minimal medium. Initially, a small aliquot from the chemostat was passed repeatedly (10 ul into 5 ml) in tubes with TDG as the sole source of carbon and sulfur. After five such passages, the organisms were streaked on a Luria plate yielding four distinct colony types. Each of these colonies was streaked repeatedly on Luria plates to ensure they were pure cultures. The colonies were inoculated into TDG medium singly and in all combinations to determine which were required for growth. One, SH18, was found to be necessary and sufficient for growth.

Identification of SH18

Using classical bacteriological techniques, SH18 was identified at the University of Illinois as Agrobacterium tumefaciens. Using fatty acid analysis and by comparison with their database of known organisms, Microbial I.D., Inc. identified the same organism as Pseudomonas pickettii (32.2% similarity to known strains). Both Agrobacterium and Pseudomonas are gram-negative, aerobic, rod-shaped organisms. Since the organism is gram-negative, it should be possible to use broad host-range plasmids for purposes of strain improvement.

Growth on TDG

In order to determine the optimal TDG concentration for growth of SH18, growth curves were measured in all TDG concentrations from 0 to 190 mM, in 10 mM increments. Representative data are shown in Fig. 1. A single colony from a Luria plate was suspended in sterile M9 supplemented medium with no carbon source and 50 ul aliquots were added to each tube containing different concentrations of TDG. Tubes were shaken at 29 C and cell growth was monitored by 595 nm absorbance readings taken every day on a Spectronic 20D spectrophotometer. Results show that SH18 will grow in all concentrations of TDG from 10 mM to 190 mM. Growth in 10 mM is the most definitive in that the lowest concentration contains the fewest impurities. Cells grown in 50 mM were the quickest to recover from lag phase and cells grown in the higher concentrations up to 190 mM took longer to recover but also eventually exhibited steady growth. The doubling time in all low to middle concentrations of TDG is approximately one day at 29 C. The doubling time in Luria broth + 0.3% glucose was approximately 150 min at 29 C.

FIGURE 1

Growth of SH18 in different concentrations of TDG at 29 C.

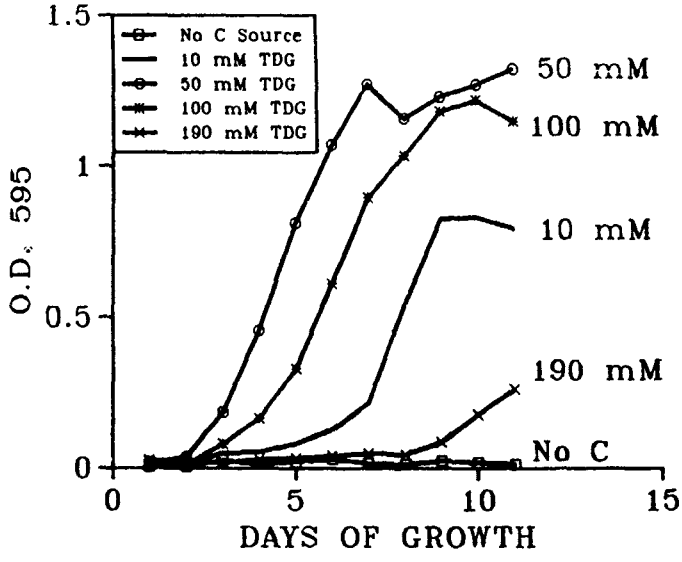

Growth in Ethylene Glycol

For the purpose of eventually isolating enzymes which catalyze the hydrolysis of the S-C bond of mustard, it would be most interesting if the TDG-degrading bacteria cleaved the S-C bond of TDG. Hydrolysis of this bond would yield ethylene glycol and beta-mercaptoethanol. Although the pathway of TDG degradation has not yet been elucidated, it was determined that SH18 would utilize 10 mM ethylene glycol as its sole carbon source. Growth rate of SH18 on ethylene glycol is similar to that seen on TDG.

Correlation of Growth of SH18 with Disappearance of TDG

Gas chromatography was used to monitor the disappearance of TDG with the increase in optical density of the culture. Bacteria were previously grown to late log phase in TDG in order to induce all necessary enzymes. Log phase bacteria were then inoculated into 10 mM TDG and the TDG concentration was monitored for 72 hours. Within 48 hours, greater than 90% of the TDG had disappeared. Within 72 hours, the TDG level was undetectable. A small peak was actually observed after 72 hours but it was insufficient for integration. Peaks from the 1 mM standard were always integrated so it was simply concluded that greater than 90% of the TDG had been degraded. Results are shown in Fig. 2.

FIGURE 2

Disappearance of TDG with increase in optical density of SH18.

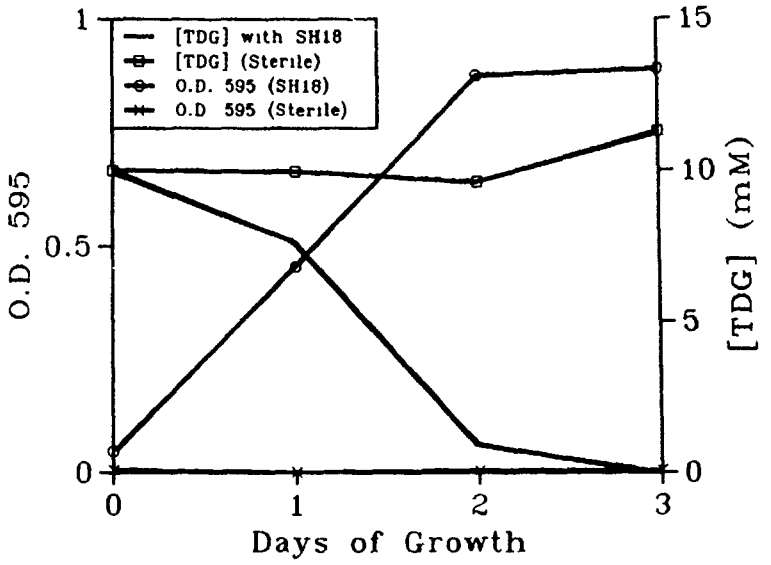

CONCLUSIONS

A pure culture of gram-negative, aerobic, TDG-degrading bacteria (SH18) has been isolated from a chemostat after eight months of intense selection. Gas chromatographic data demonstrate that SH18 will degrade greater than 90% of the TDG in a liquid culture within 48 hours. The pathway of TDG biodegradation has not yet been elucidated but it was demonstrated that SH18 will also utilize ethylene glycol as its sole source of carbon. Future experiments will be conducted to elucidate the pathway of TDG biodegradation and to determine if cell-free lysates of SH18 have enzymatic activity against mustard.

REFERENCES

1. Mazur, A. 1946. An Enzyme in Animal Tissue Capable of Hydrolyzing the Phosphorus-Fluorine Bond of Alkyl Fluorophosphates. *J. Biol. Chem.*, 164: 271-289.

2. Mounter, L.A. 1963. Metabolism of Organophosphorus Anticholinesterase Agents. In *Hanbuch de Experimentellen Pharmakologie: Cholinesterases and Anticholinesterase Agents*, Kolle, G.B. Eds., Springer-Verlag, Berlin, 486-504.

3. Hoskin, F.C.G., G. Chettur, S. Mainer, K.E. Steinmann, J.J. DeFrank, B.J. Gallo, F.M. Robbins, and J.E. Walker. 1989. Soman Hydrolysis and Detoxification by a Thermophilic Bacterial Enzyme. In *Enzymes Hydrolyzing Organophorus Compounds* (E. Reiner, W. N. Aldridge, and F.C.G. Hoskin, eds.), Ellis Horwood, Ltd. Chichester, England (John Wiley, American distributors), 53-64.

4. Holben, W.E., J.K. Jansson, B.K. Chelm and J.M. Tiedje. 1988. DNA Probe Method for the Detection of Specific Microorganisms in the Soil Bacteria Community. *Appl. Environ. Microbiol.* 54:703-711.

5. Maniatas, T., E.F. Fritsch, J. Sambrook. 1982. Molecular Cloning: A Laboratory Manual. Cold Spring Harbor Laboratory, Cold Spring Harbor, New York. pp.68-69.

6. Albizo, Johnnie, M. 1987. A Direct Aqueous Injection GC/FPD Method for Use in Monitoring the Hydrolysis of GD, VX, and HD by Chemical and Biological Catalysts in Aqueous Decontaminants Proceedings of the 1986 Scientific Conference on Chemical Defense Research. ERDEC-SP-87008.

BLANK

XVII. INDEXES

BLANK

AUTHORS FOR PAPERS IN THESE PROCEEDINGS

INDEX A

BLANK

ORGANIZATIONS OF AUTHORS IN THESE PROCEEDINGS

INDEX B

BLANK

XVIII. APPENDIXES

BLANK

LIST OF ATTENDEES
APPENDIX A

Dr. George F. Adams
US Army BRL
ATTN: SLCBR-IB-I
APG, MD 21005-5060
301/278-6197

Dr. Joseph A. Akkara
US Army Natick RD&E Center
ATTN: STRNC-YNT
Biotechnology Branch
Natick, MA 01760-5260
508/651-5260

Mr. Johnnie M. Albizo
US Army CRDEC
ATTN: SMCCR-RSB
APG-EA, MD 21010-5423
301/671-2761

Dr. Stephen C. Alter
Environmental Tech Group, Inc.
P.O. Box 9840
Baltimore, MD 21284-9840
301/321-5164

Ms. Kiyomi Amemiya
Ohio State University
College of Pharmacy
Lloyd M. Parks Hall
500 West 12th Avenue
Columbus, OH 43210-1291
614/292-9206

Dr. Yoshiya Amemiya
Ohio State University
College of Pharmacy
Lloyd M. Parks Hall
500 West 12th Avenue
Columbus, OH 43210-1291
614/292-9206

Dr. Zoltan Annau
Johns Hopkins University
School of Hygiene & Public Health
Dept of Env Health Sciences
Baltimore, MD 21205
301/955-3045

Mr. William P. Ashman
US Army CRDEC
Research Directorate
APG, MD 21010
301/671-3518

Dr. James A. Baker
US Army CRDEC
ATTN: SMCCR-PPD
APG, MD 21010-5423
301/671-5621

Dr. Barney L. Bales
California State University
Dept Phys & Ast
Northridge, CA 91330
818/885-2779

Dr. Harold D. Banks
US Army CRDEC
ATTN: SMCCR-RSC-O
APG, MD 21010-5423
301/671-2131

Ms. Hilda Bartley
US Army CRDEC
ATTN: SMCCR-RS
APG, MD 21010-5423
301/671-4144

Dr. J. J. Beaman
Univ of Texas at Austin
ATTN: ETC 5.160
Dept Mechanical Engineering
Austin, TX 78712
512/471-3058

Dr. William T. Beaudry
US Army CRDEC
ATTN: SMCCR-RSC-P
APG, MD 21010
301/671-3863

Mr. Scott H. Bergeson
Dugway Proving Ground
ATTN: STEDP-MT-C-T
Dugway, UT 84022
801/831-5225

Mr. Ammon Birenzvige
US Army CRDEC
ATTN: SMCCR-RSP-P
APG, MD 21010
301/671-3321

Mr. Wm. C. Blanchard
Blanchard & Co., Inc.
27 Glen Alpine Road
Phoenix, MD 21131
301/592-7507

Mr. Frank Block
US Army CRDEC
ATTN: SMCCR-RSC-C
APG, MD 21010
301/671-2357

Dr. M. J. Block
ORD
Box 148
North Salem, NH 03073
603/893-9419

Mr. K. Blomgren
Goucher College
Towson, MD 21204
301/337-6313

Mr. David Blyth
Geo-Centers, Inc.
Prospect Square Building
Suite 502
Ft. Washington, MD 20744
301/671-2416

Dr. Paul C. Bossle
US Army CRDEC
ATTN: SMCCR-RSL
APG, MD 21010
301/671-2794

Mr. Donald R. Bowie
US Army CRDEC
ATTN: SMCCR-RSC-P
Chemical Division
Research Directorate
APG, MD 21010-5423
301/671-3171

Dr. Ernest H. Braue, Jr.
USAMRICD
ATTN: SGRD-UV-DB
APG, MD 21010
301/671-4373

Dr. Burt Bronk
US Army CRDEC
ATTN: SMCCR-RSP-B
APG, MD 21010
301/671-2326

Mrs. Marguerite Brooks
CDR US Army CRDEC
ATTN: SMCCR-RSL
APG, MD 21010-5423
301/671-2560

Ms. Ann Brozena
US Army CRDEC
ATTN: SMCCR-RSC-P
APG, MD 21010-5423
301/671-3833

Dr. Joe L. Brumsfield
Naval Surface Warfare Center
Code HH305
Dahlgren, VA 22448
703/663-8621

Mr. James H. Buchanan
US Army CRDEC
ATTN: SMCCR-RSC-P
APG, MD 21010-5423
301/671-2366

Mr. Leonard Buettner
US Army CRDEC
ATTN: SMCCR-RST-E
APG, MD 21010
301/671-4822

Prof. Clifford A. Bunton
U of Calif at Santa Barbara
Chemistry
Santa Barbara, CA 93106
805/961-2605

Mr. Brent Busey
US Army CRDEC
ATTN: SMCCR-DDT
APG, MD 21010
301/671-5501

Dr. William Buttner
Argonne National Lab
9700 S. Cass Avenue
Argonne, IL 60439
708/972-8795

Dr. Edward J. Calabrese
University of Massachusetts
Division of Public Health
Amherst, MA 01003
413/545-3614

Dr. Robert J. Campbell
Army Research Office
P.O. Box 12211
Research Triangle Park, NC 27709
919/549-0641

Mr. Paul L. Cannon, Jr.
US Army CRDEC
ATTN: SMCCR-RSC-C
APG, MD 21010
301/671-3719

Mr. Hugh R. Carlon
US Army CRDEC
ATTN: SMCCR-RSP-P
APG, MD 21010
301/671-4106

Dr. John Carpin
US Army CRDEC
ATTN: SMCCR-RST-E
APG, MD 21010
301/671-4716

Mr. A. H. Carrieri
US Army CRDEC
ATTN: SMCCR-DDT
APG, MD 21010
301/671-2437

Dr. George D. Case
Resource Technologies Group, Inc.
400 Mississippi Street
Morgantown, WV 26505
304/291-6706

Mrs. E. L. Cerny
Utica College of Syracuse Univ.
Dept of Chemistry
Utica, NY 13502
315/792-3091

Prof. Lawrence C. Cerny
Utica College of Syracuse Univ.
Dept of Chemistry
Utica, NY 13502
315/792-3091

Dr. James P. Chambers
Univ. of Texas at San Antonio
Division of Life Sciences
Brain Res. Lab of Biochemistry
San Antonio, TX 78285
512/691-5477

Dr. Shib C. Chattoraj
ASD/AEEE
Wright Patterson AFB, OH 45433-6503
513/255-2568

Dr. Ronald T. Checkai
US Army CRDEC
ATTN: SMCCR-RST-E
APG, MD 21010
301/671-2036

Dr. Tu-Chen Cheng
US Army CRDEC
ATTN: SMCCR-RSB
E3220, Rm 209
Biotechnology
APG, MD 21010
301/671-3972

Dr. Steven Christesen
US Army CRDEC
ATTN: SMCCR-RSL
APG, MD 21010-5423
301/671-2437

Dr. Ben Chu
SUNY at Stony Brook
Dept of Chemistry
Stony Brook, NY 11794-3400
516/632-7928

Mr. Greg D. Clark
Howard University
Department of Chemistry
Washington, DC 20059
202/636-7678

Mr. James H. Clark
USAMRICD
Bldg E3100
APG, MD 21010
301/671-3836

Mr. Offie E. Clark
USAMRICD
Bldg E3100
APG, MD 21010
301/671-2626

Dr. Michael J. Coggiola
SRI International
333 Ravenswood Avenue
Menlo Park, CA 94025
415/859-3045

Dr. Daniel R. Coleman
CMS Research Corporation
1075 South 13th Street
Suite 205
Birmingham, AL 35205
205/934-9151

Ms. Carol A. Collier
Foreign Science & Technology Ctr
220 7th Street, NE
Charlottesville, VA 22901
804/980-7869

Dr. Kenneth R. Collins
US Army CRDEC
ATTN: SMCCR-RSC-P
APG, MD 21010
301/671-3171

Mr. William H. Collins
US Army CRDEC
ATTN: SMCCR-RS
APG, MD 21010
301/671-3210

Dr. Roger J. Combs
US Army CRDEC
ATTN: SMCCR-DDT
E5554
APG, MD 21010-5423
301/671-3021

Mr. Gale Connor
Blanchard & Co., Inc.
27 Glen Alpine Road
Phoenix, MD 21131
301/592-7507

CDR Thomas J. Contreras
Office of Naval Technology
Code 223
800 N. Quincy Street
Arlington, VA 22217-5000
301/696-4791

Mr. Phillip Coon
US Army CRDEC
ATTN: SMCCR-RSP-C
APG, MD 21010-5423
301/671-2775

LT Christopher Cramer
US Army CRDEC
ATTN: SMCCR-RSP-C
APG, MD 21010
301/671-3518

Ms. Ruth A. Cresson
ENS, USNR
33 University Square
Suite 130
Madison, WI 53715
608/262-2791

CPT L. B. Crowell
National Defence Headquarters
Health Services Res Coord
Surgeon General Branch
Maj Gen George R. Pearkes Bldg
Ottawa, K1A OK2
CANADA
613/995-4842

Dr. E. G. Cummings
US Army CRDEC
ATTN: SMCCR-RST-C
APG, MD 21010
301/671-2817

Mr. Fran D'Amico
US Army CRDEC
ATTN: SMCCR-DDT
APG, MD 21010
301/671-2437

Ms. Joyce A. Dabkowski
US Army CRDEC
ATTN: SMCCR-DDT
Bldg 3549
Edgewood, MD 21010
301/671-5579

Dr. Franklin A. Davis
Drexel University
Dept of Chemistry
Philadelphia, PA 19104
215/895-2647

Mr. Lynn H. Davis
US Army CRDEC
ATTN: SMCCR-ST
APG, MD 21010
301/671-3933

Mr. Paul M. Davis
Geo Centers, Inc.
10903 Indian Head Road
Ft. Washington, MD 20744
301/671-2357

Dr. Joseph J. DeFrank
US Army CRDEC
ATTN: SMCCR-RSB
Biotechnology Division
APG, MD 21001-5423
301/671-3972

Dr. Stephan DeLuca
Colorado School of Mines
Dept of Chemistry
Golden, CO 80401
303/273-3615

CPT Krisma D. DeWitt
USMA
Chemistry
West Point, NY 10996
914/938-3909

Mrs. Madelyn M. Decker
US Army CRDEC
ATTN: SMCCR-RSL-A
Bldg E3220, Room 130
APG, MD 21010-5423
301/671-2409

Dr. Victor R. Deitz
Naval Research Laboratory
Code 6170
Washington, DC 20375
202/767-2334

Dr. Jeff Deschamps
Naval Research Laboratory
Code 6030
Washington, DC 20375
202/767-0656

Mr. John T. Ditillo
US Army CRDEC
ATTN: SMCCR-DDT
APG, MD 21010-5423
301/671-3021

Dr. Eugene S. Domalski
Nat'l Inst for Standards & Tech
B348 Chemistry Bldg
Chemical Thermodynamics Division
Gaithersburg, MD 20899
301/975-2205

Dr. David T. Doughty
Calgon Carbon Corp.
P.O. Box 717
Pittsburgh, PA 15230-0717
412/787-6602

Mr. Bryce F. Doxzon
USAMRICD
Bldg E3100
APG, MD 21010
301/671-3691

Prof. Russell S. Drago
University of Florida
Chemistry Dept
Gainesville, FL 32605
904/392-6043

Mr. James B. Duncan
Eastman Kodak
Bldg 82A Rm 578
Rochester, NY 14650
716/477-3020

Dr. W. T. Elam
Naval Research Lab
Code 4683
Washington, DC 20375-5000
202/767-3014

Mr. Ilya Elashvili
US Army CRDEC
Attn: SMCCR-RSB
APG, MD 21010
301/671-3398

Dr. Mohyee Eldefrawi
University of Maryland
655 W. Baltimore Street
Baltimore, MD 21201
301/328-3564

Dr. Eugene L. Elmore
NSI Technology Services Corp
Environmental Science
P.O. Box 12313
Two Triangle Drive
Research Triangle Pk, NC 27709
919/549-0611

Dr. Silvio L. Emery
US Army CRDEC
ATTN: SMCCR-RSP-C
APG, MD 21010
301/671-3518

Mr. Erik E. Engwall
US Army Materials Tech Lab
ATTN: SLCMT-EMP
Watertown, MA 02172
617/923-5348

Mr. Sam Eure
Science and Technology Corp.
101 Research Drive
Hampton, VA 23666
804/865-0467

Dr. George R. Famini
US Army CRDEC
Attn: SMCCR-RSP-C
APG, MD 21010

Mr. Phillip K. Fasone
US Army CRDEC
ATTN: SMCCR-DDW
APG, MD 21010
301/671-2108

Dr. Paul D. Fedele
US Army CRDEC
ATTN: SMCCR-RSP-P
APG, MD 21010-5423
301/671-2262

Mr. C. Parker Ferguson
US Army CRDEC
ATTN: SMCCR-RSC-O
Research Directorate
APG, MD 21010-5423
301/671-3603

Mr. Foy E. Ferguson
US Army CRDEC
ATTN: SMCCR-RSL-A
APG, MD 21010
301/671-2712

Dr. Kim E. Ferris
Pacific Northwest Laboratory
Molecular Science Research Center
Richland, WA
509/375-3754

Mr. Donald Fielder
US Army CRDEC
ATTN: SMCCR-RSC-P
APG, MD 21010-5423
301/671-3833

Mr. George H. Fielding
Hughes Associates, Inc.
7610 Holiday Drive
Alexandria, VA 22308
703/765-8107

Mr. Edward S. Fisher
US Army FSTC
220 Seventh Street, NE
Charlottesville, VA 22901
804/980-7806

Mr. Alan Force
US Army CRDEC
ATTN: SMCCR-RSL
APG, MD 21010
301/671-2437

Mr. Karl W. Ford
USAMRICD
Bldg E-3100
APG, MD 21010
301/671-2626

Dr. R. H. Frickel
US Army CRDEC
ATTN: SMCCR-RSP-B
APG, MD 21010
301/671-3854

Dr. David K. Friday
US Army CRDEC
ATTN: SMCCR-RSC-A
APG, MD 21010
301/671-4822

Dr. Benedict J. Gallo
US Army Natick RD&E Center
ATTN: STRNC-YMT
Soldier Science Directorate
Natick, MA 01760-5020
508/651-5505

Dr. Donald E. Gardner
NSI Environmental Sciences
P.O. Box 12313
Research Triangle Pk, NC 27709
919/549-0611

Ms. Stephanie M. Garlick
Geo-Centers, Inc.
2231 Grubb Road
Wilmington, DE 19810
301/671-2131

Dr. David Garmer
Center for Adv Res in Biotech
9600 Gudelsky Drive
Rockville, MD 20850
301/251-2202

Mr. Nathan Gerber
BRL
514 Overbrook Road
Baltimore, MD 21212-2101
301/278-4591

Mr. Michael T. Goode
US Army CRDEC
ATTN: SMCCR-DDT
Edgewood Area
APG, MD 21010
301/671-5580

Mr. George A. Grant
G.A. Grant Scientific Consultants
46 Crystal Beach Drive
Nepean
Ontario, 1T2H 5M9
CANADA
613/998-2193

Mr. Paul Grasso
US Army CRDEC
ATTN: SMCCR-RSC-C
APG, MD 21010
301/671-3719

Prof. Michael Gratzel
Swiss Federal Inst of Technology
Institute of Physical Chemistry
Lausanne
SWITZERLAND
41216933112

Mr. Clark L. Gross
USAMRICD
ATTN: SGRD-UV-PB
Bldg E3100
APG, MD 21010
301/671-2847

COL Raymond A. Gross
US Army CRDEC
ATTN: SMCCR-CO
APG, MD 21010-5423
301/671-4363

Mr. Robert Gross
US Army CRDEC
ATTN: SMCCR-DDW
APG, MD 21010
301/671-3021

Mr. Robert J. Grula
US Army CRDEC
ATTN: SMCCR-RSC-P
APG, MD 21010
301/671-2366

Dr. Harold E. Guard
Office of Naval Research
800 North Quincy Street
Arlington, VA 22217-5000
202/696-4311

Dr. Keith G. Haddaway
Geo-Centers, Inc.
6102 Koala Ct
Waldorf, MD 20603
301/671-2131

Ms. Susan Hallowell
US Army CRDEC
ATTN: SMCCR-RSL
APG, MD 21010
301/671-2818

Dr. Hendrik F. Hameka
University of Pennsylvania
1503 Argyle Road
Berwyn, PA 19312
215/898-8303

Mr. James T. Hanley
Research Triangle Institute
P.O. Box 12194
Research Triangle Pk, NC 27709
919/541-5811

Mrs. Carol Hansen
US Army CRDEC
ATTN: SMCCR-RSP-A
APG, MD 21010
301/671-2158

Dr. Charles S. Harden
US Army CRDEC
ATTN: SMCCR-RSC
APG, MD 21010-5423
301/671-3129

Ms. Joan Hart
Allied-Signal Aerospace Co
AiResearch, Los Angeles Div
Dept 93190, T41
2525 W. 190th Street
Torrance, CA 90509
213/512-3715

Dr. Steve Harvey
US Army CRDEC
ATTN: SMCCR-RSB
Biotechnology Division
APG, MD 21010-5423
301/671-3972

Mr. Mark Haugland
Univ of Nebraska - Lincoln
Dept of Electrical Engr
209 NWSEC
Lincoln, NE 68588-0511
402/472-1966

Prof. Thorwald Herbert
Ohio State University
Dept Mechanical Engineering
206 West 18th Avenue
Columbus, OH 43210-1107
614/292-2902

Mr. Raymond E. Herd
US Army CRDEC
ATTN: SMCCR-RSL-A
APG, MD 21010
301/671-2409

Dr. Craig L. Hill
Emory University
Dept of Chemistry
Atlanta, GA 30322
404/727-6611

Mr. A. Jack Hitt, III
McDonnell Douglas
Dept 354 Bldg 32 Lev 3
Rm/PT 310 Mail Code 83
P.O. Box 516
St. Louis, MO 63166-0516
314/234-3511

Dr. Lynn D. Hoffland
US Army CRDEC
ATTN: SMCCR-RSL
APG, MD 21010
301/671-3129

Dr. Landa C. Hoke
Natick RD&E Center
Special Projects Branch
Natick, MA 01760-5020
508/651-4550

Dr. Donald E. Holness
Canadian Embassy
Res and Dev Liaison Staff
ATTN: CDLS(W)
501 Pennsylvania Ave NW
Washington, DC 20001
202/682-7648

Dr. Seok H. Hong
US Army CRDEC
ATTN: SMCCR-RSC-P
Bldg E3300
APG, MD 21010-5423
301/671-2721

Dr. Barton Houseman
Goucher College
Department of Chemistry
Towson, MD 21204
301/337-6313

Mr. Joseph W. Hovanec
US Army CRDEC
ATTN: SMCCR-RSC-C
APG, MD 21010
301/671-2761

Dr. Chen C. Hsu
US Army CRDEC
ATTN: SMCCR-RSC-A
APG, MD 21010-5423
301/671-3753

Dr. David S.Y. Hsu
Naval Research Lab
Code 6170H
Washington, DC 20375-5000
202/767-2742

Dr. Fu-Lian Hsu
US Army CRDEC
ATTN: SMCCR-RSC-O
APG, MD 21010-5423
301/671-2131

Dr. Paul F. Hudrlik
Howard University
Department of Chemistry
Washington, DC 20059
202/636-7678

Mr. Joseph Huerta
US Army CRDEC
Attn: SMCCR-RSP-A
APG, MD 21010
301/671-2158

Mr. Holcombe H. Hurt
USAMRICD
Bldg E3100
APG, MD 21010
301/671-2803

Dr. Stefan Hermann Huttenhain
Fraunhofer Inst
Umweltchemie und Okotoxikologie
Postfach 12 60
Schmallenberg
Grafschaft, D-5948
GERMANY
02972302313

Mr. William R. Hydro
US Army CRDEC
ATTN: SMCCR-RSC-O
APG, MD 21010
301/671-2422

Mr. Brian S. Ince
US Army CRDEC
ATTN: SMCCR-RSC-P
APG, MD 21010-5423
301/671-4125

Mr. Louis Isaacson
Geo-Centers, Inc.
10903 Indian Head Highway
Ft. Washington, MD 20744
301/767-2332

Mr. Jerry K. Jarboe
US Army Natick RD&E Center
ATTN: STRNC-YMA
Natick, MA 01761-5020
508/651-4573

Dr. Lynn Jarvis
Microsensor Systems, Inc.
5610 Sandy Lewis Drive
Fairfax, VA 22032
703/642-6919

Mr. Andrew T. Jeffers
WRDC/FIVE
Wright Patterson AFB, OH 45433-6553
513/255-3021

Dr. James Jensen
US Army CRDEC
ATTN: SMCCR-RSP-C
APG, MD 21010
301/671-3518

Ms. Janet Jensen
US Army CRDEC
ATTN: SMCCR-DDT
APG, MD 21010
301/671-3518

Mr. Robert A. Johnson
US Army Missile Command
ATTN: AMSMI-RD-RE-QP
Redstone Arsenal, AL 35898-5248
205/876-5937

Dr. Leonard A. Jonas
Hughes Associates Inc.
2730 University Blvd, West
Suite 902
Wheaton, MD 20902
301/949-0505

Dr. George C. Joy
Allied-Signal Res & Tech Ctr
P.O. Box 5016
Des Plaines, IL 60017-5016
708/391-3196

Mr. Louis Kanaras
US Army CRDEC
ATTN: SMCCR-PPD
APG, MD 21010
301/671-5647

Mr. Mark Kaplan
Eastman Kodak
5/82A RL-02156
Rochester, NY 14650-2156
716/722-1303

Mr. Chris Karwacki
US Army CRDEC
ATTN: SMCCR-PPC
APG, MD 21010
301/671-5782

Mr. Ronald J. Kassel
US Army CRDEC
ATTN: SMCCR-RSC-O
APG, MD 21010
301/671-4224

Mr. Lionel Katzoff
US Army CRDEC
ATTN: SMCCR-DDT
APG, MD 21010
301/671-5569

Dr. Joyce J. Kaufman
Johns Hopkins University
Chemistry Dept
Charles and 34th Streets
Baltimore, MD 21218
301/338-7417

Dr. Hae-Won Kim
Penn State Ogontz
Chemistry Dept
1600 Woodland Road
Abington, PA 19001
215/886-9400

Dr. James W. King
US Army CRDEC
ATTN: SMCCR-RSC-O
APG, MD 21010-5423
301/671-3482

Mr. Paul Kirk
Naval Surface Warfare Center
ATTN: H31(P.Kirk)
Dahlgren, VA 22448-5000
703/663-8621

Mr. Harold Klapper
US Army CRDEC
ATTN: SMCCR-RSC-P
Edgewood Area
APG, MD 21010
301/671-2265

Dr. Michael Koals
Rohm and Haas Co
Independence Mall West
Philadelphia, PA 19105
215/592-2953

Dr. Edward M. Kober
Los Alamos Nat'l Lab
T-14 MS B214
Los Alamos, NM 87545
505/667-5140

Dr. Philip Koga
ETC Inc.
1400 Taylor Avenue
P.O. Box 9840
Baltimore, MD 21284
301/321-5312

Mr. Jan E. Kolakowski
US Army CRDEC
ATTN: SMCCR-RSL
APG, MD 21010
301/671-2755

Ms. Karla Kopec-Smyth
Naval Research Laboratory
Code 6030
Washington, DC 20375
202/767-0656

Prof. Walter S. Koski
Johns Hopkins University
Chemistry Dept
Charles & 34th Streets
Baltimore, MD 21218
301/338-7418

Mr. John D. Koutsandreas
EPA
ATTN: OMMSQA/ORD/RD-680
401 M Street, SW
Washington, DC 20460
202/382-5789

Dr. Morris Krauss
NIST
Molecular Spectroscopy Div
Bldg 221, Rm B268
Gaithersburg, MD 20899
301/975-2598

Dr. Thaiya Krishnamurthy
US Army CRDEC
ATTN: SMCCR-RSL-M
APG, MD 21010-5423
301/671-3957

Dr. P. N. Krishnan
Coppin State College
Baltimore, MD 21216
301/671-4827

Dr. Robert Kroutil
US Army CRDEC
ATTN: SMCCR-RSL
APG, MD 21010-5423
301/671-3021

Mr. Thomas Kulle
US Army CRDEC
ATTN: SMCCR-PPI
APG, MD 21010
301/671-2519

Mr. Robert A. Kumpf
University of Delaware
Dept of Chemistry & Biochemistry
Newark, DE 19716
302/451-1544

Dr. Cynthia A. Ladouceur
US Army CRDEC
ATTN: SMCCR-RSB
APG, MD 21010-5423
301/671-4284

Mr. Robert A. Lamontagne
Naval Research Laboratory
Code 6180
Washington, DC 20375
202/767-2332

Mr. Vernon J. Laurie
US EPA
ATTN: RD-680
401 M Street
Washington, DC 20460
202/382-5795

Mr. Charles Lawson
US Army CRDEC
ATTN: SMCCR-PPC
APG, MD 21010-5423
301/671-5690

Mr. Daniel C. Leggett
US Army CRREL
72 Lyme Road
Hanover, NH 03775
603/646-4626

Dr. Bruce E. Lehnert
Los Alamos National Laboratory
LS-4 MS M888
Cell Biology Group
Los Alamos, NM 87545
505/667-2753

Mr. D. Ralph Leslie
US Army CRDEC
ATTN: SMCCR-RSC-P
APG, MD 21010-5423
301/671-3863

Dr. George R. Lester
Allied-Signal Inc.
Research and Technology
Des Plaines Research Center
50 E. Algonquin Road POB 5016
Des Plaines, IL 60017-5016
708/391-3314

Mr. Bruce Lewbart
US Army CRDEC
ATTN: SMCCR-PEV
APG, MD 21010-5423
301/671-3303

Dr. Shirley Liebman
Geo-Centers, Inc.
Prospect Square Building
Suite 502
Ft. Washington, MD 20744
301/671-2416

Ms. Claire Lieske
USAMRICD
Bldg E3100
APG, MD 21010
301/671-3836

Dr. William Limm
US Army CRDEC
ATTN: SMCCR-RSC-A
APG, MD 21010-5423
301/671-4297

Mr. J. Michael Lochner
US Army CRDEC
ATTN: SMCCR-RSL
APG, MD 21010-5423
301/671-2116

Dr. S. Randolph Long
US Army CRDEC
ATTN: SMCCR-RSL
APG, MD 21010
301/671-2437

Dr. Frederick R. Longo
US Army CRDEC
Applied Chemistry Branch
APG, MD 21010
301/671-2107

Dr. Alfred H. Lowrey
Naval Research Lab
Code 6030
Washington, DC 20375
202/767-6383

Dr. David M. Lubman
University of Michigan
Dept of Chemistry
930 North University Ave
Ann Arbor, MI 48109-1055
313/764-1669

Mr. Leonard Luskus
USAFSAM/VNC
Brooks AFB, TX 78235
512/536-3126

Mr. Brian MacIver
US Army CRDEC
ATTN: SMCCR-PPD
APG, MD 21010
301/671-5636

Dr. Raymond Mackay
US Army CRDEC
ATTN: SMCCR-DDT
APG, MD 21010
301/671-5581

Mr. John Mahle
US Army CRDEC
ATTN: SMCCR-RSC-A
APG, MD 21010
301/671-3753

Dr. Stephen Maroldo
Rohm and Haas Co.
727 Norristown Road
Springhouse, PA 19477
215/641-7318

Mr. John J. Martin
US Army CRDEC
ATTN: SMCCR-RSL-M
APG, MD 21010
301/671-2663

Mr. Richard A. Matuszko
Geo-Centers, Inc.
10903 Indian Head Highway
Ft. Washington, MD 20744
202/767-2332

LTC Edward W. Mayer
USMA
Dept of Chemistry
West Point, NY 10996
914/938-3902

Prof. Cynthia K. McClure
University of Delaware
Dept of Chem & Biochem
Newark, DE 19716
302/451-8848

Mr. Vincent M. McHugh
US Army CRDEC
ATTN: SMCCR-RSC-P
APG, MD 21010-5423
301/671-2721

Dr. Sam McManus
Univ of Alabama Huntsville
Chemistry Dept
Huntsville, AL 35899
205/895-6002

Mr. James J. McNeely
Battelle Edgewood Operations
2113 Emmorton Park Road
Edgewood, MD 21040
301/676-9030

Ms. Caryn F. Mee
USA MTL
ATTN: SLCMT-EMP
Watertown, MA 02172
617/923-5525

Mr. William Mego
Argonne National Labs
9700 S. Cass Avenue
Argonne, IL 60439
708/972-7564

Mr. Darrel E. Menking
US Army CRDEC
ATTN: SMCCR-RSB
APG, MD 21010-5423
301/671-3398

Dr. Millard M. Mershon
USAMRICD
Bldg E3100
APG, MD 21010
301/671-3591

Dr. Henk L.C. Meuzelaar
Univ of Utah
Ctr for MicroAnalysis/Reaction Chem
EMRL, Room 214
Salt Lake City, UT 84112
801/581-8431

Mr. Howard G. Meyer
USAMRICD
ATTN: SGRD-UV-PA
APG, MD 21010
301/671-4254

Mr. Alexander P. Mickiewicz
US Army CRDEC
ATTN: SMCCR-RSP-C
APG, MD 21010
301/671-3688

Mr. Merrill Milham
US Army CRDEC
ATTN: SMCCR-RSP-B
APG, MD 21010
301/671-3854

Dr. Duane D. Miller
Ohio State University
College of Pharmacy
Division of Medicinal Chem
and Phamacognosy
Columbus, OH 43210
614/292-9206

Mr. Miles C. Miller
US Army CRDEC
ATTN: SMCCR-RSP-A
APG, MD 21010
301/671-2186

Dr. Robert J. Mioduszewski
US Army CRDEC
ATTN: SMCCR-RST-C
APG, MD 21010
301/671-4101

Mr. Robert W. Morrison
US Army CRDEC
ATTN: SMCCR-PPC
APG, MD 21010
301/671-5689

Dr. Shekar Munavalli
Geo-Centers, Inc.
700 Paige Circle
Bel Air, MD 21014
301/671-2815

Mr. Kim D. Murphy
NAVEODTECHCEN
Code 50A23
Indian Head, MD 20640-5070
301/743-4538

Dr. W. C. Neely
Auburn University
Chemistry Department
Auburn University, AL 36849
205/844-5905

Mr. Doug Nelson
US Army Chemical School
ATTN: ATZN-CM-CS
Ft. McClellan, AL 36265
205/848-5569

Prof. Wilfred H. Nelson
University of Rhode Island
Dept of Chemistry
Kingston, RI 02881
401/792-2498

Mr. Thaddeus J. Novak
US Army CRDEC
ATTN: SMCCR-RSC-C
APG, MD 21010
301/671-2369

Mr. Michael J. Nusca
US Army BRL
ATTN: SLCBR-LF-A
APG, MD 21005
301/278-2057

BG David A. Nydam
PM for Chemical Demilitarization
APG, MD 21010
301/671-2658

Dr. Raymond T. O'Donnell
State Univ of New York
Chemistry Dept
Oswego, NY 13126
315/341-2697

Mr. Richard O'Donnell
US Army CRDEC
ATTN: SMCCR-PPD
APG, MD 21010
301/671-5645

Ms. Lousie Parker
USA CRREL
72 Lyme Road
Hanover, NH 03755
603/646-4393

Dr. Parmanand P. Patel
USAAMCCOM
ATTN: AMSMC-QAO-C(A)
Bldg E5100
APG, MD 21001-5423
301/671-3555

Ms. Dorothea Paterno
US Army CRDEC
ATTN: SMCCR-RSP-P
APG, MD 21010
301/671-4466

Dr. Richard J. Paur
US Army Research Office
P.O. Box 12211
Research Triangle Pk, NC 27701
919/549-0641

Mr. Elwin C. Penski
US Army CRDEC
ATTN: SMCCR-RSC-P
APG, MD 21010
301/671-3953

Mr. Joseph V. Pistritto
US Army CRDEC
ATTN: SMCCR-RSC-C
APG, MD 21010-5423
301/671-3614

Dr. Peter Politzer
University of New Orleans
Dept of Chemistry
Lakefront Campus
New Orleans, LA 70148
504/286-6850

Prof. Gary H. Posner
Johns Hopkins University
Dept of Chemistry
Baltimore, MD 21218
301/338-4677

Ms. Marie K. Potts
US Army Materials Tech Lab
ATTn: SLCMT-EMP
Watertown, MA 02172-0001
617/923-5009

Dr. Edward J. Poziomek
Univ of Nevada - Las Vegas
Environmental Research Ctr
4505 South Maryland Pkwy
Las Vegas, NV 89154
702/739-3382

Mr. Robert J. Puhala
US Army CRDEC
ATTN: SMCCR-PPC
APG, MD 21010
301/671-5688

Dr. K. S. Rajan
IIT Research Institute
10 West 35th Street
Chicago, IL 60616
312/567-4262

Dr. Vijay S. Rajput
Unitech Engineers, Inc.
654 Woodbourne Road
Langhorne, PA 19047
215/752-2240

COL James H. Ramsden
USMA
Dept of Chemistry
West Point, NY 10996
914/938-3900

Mr. R. Ray
USAMRICD
Bldg E3100
APG, MD 21010
301/671-3074

Dr. Michael Redmon
Chemical Dynamics Corp.
9560 Pennsylvania Avenue
Upper Marlboro, MD 20772
301/599-1050

Mr. Joseph Rehrmann
US Army CRDEC
ATTN: SMCCR-RSC-A
APG, MD 21010
301/671-3753

Dr. Sharon Reutter
US Army CRDEC
ATTN: SMCCR-RST-C
APG, MD 21010
301/671-2686

Mr. James Richmond
US Army CRDEC
ATTN: SMCCR-PPD
APG, MD 21010
301/671-5640

Dr. Chun-Hsun Rin
US Army CRDEC
ATTN: SMCCR-DDW
APG, MD 21010
301/671-2140

Dr. Steven M. Risser
Pacific Northwest Laboratory
Molecular Science Research Center
Richland, WA 99352
509/256-7482

Mr. David E. Roady
US Army CRDEC
ATTN: SMCCR-GS
APG, MD 21010
301/671-4339

Dr. Donald H. Robertson
US Army Natick RD&E Center
Soldier Science Directorate
Natick, MA 01760
508/651-5176

Dr. Kim Rogers
University of Maryland
School of Medicine
655 West Baltimore Street
Baltimore, MD 21201
301/328-3564

Mr. Dennis K. Rohrbaugh
US Army CRDEC
ATTN: SMCCR-RSC-P
APG, MD 21010-5423
301/671-2366

Dr. James A. Romano, Jr.
US Army MRDC
Medical Chemical Defense Res Prog
Frederick, MD 21701-2161
301/663-2161

Mr. Leonard C. Rowe
PM for Chem Demil
Bldg E4585
APG, MD 21010
301/671-3633

Dr. Asit Roy
Separation Industries
4 Leonard Street
Metuchen, NJ 08840
201/549-4011

Mr. Joseph M. Ruder
AiResearch-Los Angeles Div
2525 W. 190th Street
Torrance, CA 90509
213/512-4379

Ms. Maria Sadusky
US Army CRDEC
ATTN: SMCCR-RST-E
Bldg E3220
APG, MD 21010-5423
301/671-2036

Dr. Harry Salem
US Army CRDEC
ATTN: SMCCR-RS
APG, MD 21010-5423
301/671-3250

Mr. John B. Samuel
US Army CRDEC
1505 Northam Ct
Bel Air, MD 21014
301/671-2366

Dr. Emory W. Sarver
US Army CRDEC
ATTN: SMCCR-DDT
APG, MD 21010
301/671-5528

Dr. G. Paul Savage
University of Florida
Department of Chemistry
Gainesville, FL 32611
904/392-0554

Dr. James J. Savage
US Army CRDEC
ATTN: SMCCR-TDT
APG, MD 21010-5423
301/671-3498

Mr. Leon J. Schiff
US Army CRDEC
ATTN: SMCCR-RSC-C
APG, MD 21010
301/671-3111

Mr. John Schlager
USAMRICD
Bldg E3100
APG, MD 21010
301/671-3836

Mr. John C. Schmidt
Environmental Tech. Group, Inc.
1400 Taylor Avenue
P.O. Box 9840
Baltimore, MD 21284-9840
301/321-5163

Dr. Robert N. Schmidt
Life Systems Inc.
24755 Highpoint Road
Cleveland, OH 44122
216/464-3291

Dr. Nathaniel S. Schneider
US Army Materials Technology Lab
Watertown, MA 02172
617/923-5434

Dr. Donald P. Segers
Southern Research Institute
2000 Ninth Avenue South
Birmingham, AL 32355-5305
205/581-2664

Dr. Reginald P. Seiders
USARDSG (UK)
Box 65
FPO, NY 09510
4414094423

Dr. Robert W. Shaw
US Army Research Office
P.O. Box 12211
Research Triangle Pk, NC 27709
919/549-0641

Dr. M. Shih
USAMRICD
ATTN: SGRD-UV-VA
Bldg E3100
APG, MD 21010-5425
301/671-2591

Mr. Wendel J. Shuely
US Army CRDEC
ATTN: SMCCR-RSC-P
Bldg E3300
APG, MD 21010-5423
301/671-4125

Mr. William Shulman
US Army CRDEC
ATTN: SMCCR-PEV
APG, MD 21010-5423
301/671-3303

Dr. Gary D. Sides
CMS Research Corp
1075 South 13th Street
Suite 205
Birmingham, AL 35205
205/934-9151

Mr. Achille Silvestri
US Army CRDEC
ATTN: SMCCR-DDT
APG, MD 21010
301/671-5529

Mr. Gordon Sima
ETG, Inc.
1400 Taylor Avenue
Baltimore, MD 21204
301/321-5117

Mr. J. Richard Smith
USAMRICD
Analytical Chemistry Branch
Bldg E3100, Rm 33
APG, MD 21010-5425
301/671-2591

Mr. Alan Snelson
IIT Research Institute
10 West 35th Street
Chicago, IL 60616
312/567-4260

Dr. A. Peter Snyder
US Army CRDEC, AMCCOM
ATTN: SMCCR-RSL
APG, MD 21010-5423
301/671-2416

Mr. Jose Solivan
US Army CRDEC
ATTN: SMCCR-PPI
APG, MD 21010
301/671-4174

Dr. Ralph B. Spafford
Southern Research Institute
2000 Ninth Avenue South
Birmingham, AL 35255-5305
205/581-2219

Dr. Glenn E. Spangler
Environmental Tech Group, Inc.
1400 Taylor Avenue
Baltimore, MD 21204
301/321-5261

Dr. Lois M. Speaker
Eastman Kodak Company
Bldg 82A, RL
Rochester, NY 14650-2156
716/588-7057

Mr. Ralph J. Steger
US Army CRDEC
ATTN: SMCCR-DDT
APG, MD 21010-5423
301/671-5567

Dr. John R. Stephens
Los Alamos National Laboratory
MS C-348
P.O. Box 1663
Los Alamos, NM 87545
505/667-7363

Dr. J. Stetter
Transducer Research, Inc.
1228 Olympus Drive
Naperville, IL 60540
312/974-2107

Dr. John I. Stevens
US Army CRDEC
ATTN: SMCCR-OPI
APG, MD 21010-5423
301/671-4438

Dr. James J.P. Stewart
US Air Force Academy
FJSRL/NC
Colorado Springs, CO 80840
719/472-2655

CDR Rodney L. Stiling
USNR
NTIC 1313
AFRC
1430 Wright Street
Madison, WI 53704
608/233-8511

Mr. Peter J. Stopa
US Army CRDEC
ATTN: SMCCR-DDT
APG, MD 21010-5423
301/671-5578

Mr. John Strawbridge
US Army CRDEC
ATTN: SMCCR-PPP
APG, MD 21010
301/671-4827

Ms. Linda Strickler
US Army CRDEC
ATTN: SMCCR-PPI
APG, MD 21010
301/671-2519

Dr. Edward W. Stuebing
US Army CRDEC
ATTN: SMCCR-RSP-B
APG, MD 21010
301/671-3089

Mr. Arthur K. Stuempfle
US Army CRDEC
ATTN: SMCCR-RSP
APG, MD 21010-5423
301/671-2651

Mr. Larry M. Sturdivan
US Army CRDEC
ATTN: SMCCR-RSP-C
APG, MD 21010
301/671-3546

Mrs. Linda L. Szafraniec
US Army CRDEC
ATTN: SMCCR-RSC-P
APG, MD 21010-5423
301/671-3863

Mr. Pascal A. Tarantino
US Army CRDEC
ATTN: SMCCR-RSL
APG, MD 21010-5423
301/671-2409

Dr. David E. Tevault
US Army CRDEC
ATTN: SMCCR-RSC-A
APG, MD 21010
301/671-3753

Prof. Richard C. Thompson
University of Missouri
Dept of Chemistry
Columbia, MO 65211
314/882-7356

Dr. Sandra Thomson
US Army CRDEC
ATTN: SMCCR-RST-E
APG, MD 21010
301/671-4821

Mr. Nolan Tillman
Eastman Kodak
Federal Systems Division
Advanced Chemical Tech Group
Rochester, NY 14650-2156
716/477-5037

Mr. Robert Tom
AiResearch-Los Angeles Div
2525 West 190th Street
Torrance, CA 90509
213/512-4385

Dr. Donald A. Tomalia
Michigan Molecular Inst
463 W. Chippewa River Rd
Midland, MI 48640
517/636-5408

Prof. Paul J. Toscano
SUNY at Albany
Department of Chemistry
Albany, NY 12222
518/442-4465

Mr. Abe Turetsky
US Army CRDEC
ATTN: SMCCR-RSC-C
APG, MD 21010
301/671-2395

Ms. Mickey Tyler
US Army CRDEC
ATTN: SMCCR-RS
APG, MD 21010-5423
301/671-3777

Mr. Raymond P. Tytus
US Army CRDEC
ATTN: SMCCR-RSP-P
APG, MD 21010-5423
301/671-3594

Dr. James J. Valdes
US Army CRDEC
ATTN: SMCCR-RSB
APG, MD 21010-5423
301/671-3564

Dr. Raymond L. Venable
Univ of Missouri - Rolla
Chemistry Dept
Rolla, MO 65401
314/341-4394

Dr. David L. Venezky
Naval Research Laboratory
Code 6170
Washington, DC 20375
202/767-3550

Mr. Joseph J. Vervier
US Army CRDEC
ATTN: SMCCR-TD
APG, MD 21010-5423
301/671-4362

Mr. Eugene Vickers
US Army CRDEC
ATTN: SMCCR-RST-E
APG, MD 21010
301/671-3212

Ms. Jane C. Vizcarrondo
US Army CRDEC
ATTN: SMCCR-PPI
APG, MD 21010
301/671-4174

Mr. Gus Vlahacos
USAMRICD
ATTN: SGRD-UV-PB
APG, MD 21010
301/671-3074

Prof. Vitaly Vodyanoy
Auburn University
Dept of Physiology & Pharmacology
212 Green Hall
Auburn University, AL 36849-5520
205/844-5404

Mr. L. J. Vorgetts
AEHA
Bldg E2100
APG, MD 21010
301/671-3613

Dr. Norman J. Wagner
Calgon Carbon Corp
P.O. Box 717
Pittsburgh, PA 15230-0717
412/787-6617

Mr. Michael Waldman
Separation Industries
4 Leonard Street
Metuchen, NJ 08840
201/549-4011

Ms. Helen M. Walker
US Army CRDEC
ATTN: SMCCR-RSC-P
APG, MD 21010
301/671-2531

Mr. John E. Walker
US Army Natick RD&E Center
ATTN: STRNC-YSP
Soldier Science Directorate
Natick, MA 01760-5020
508/651-4374

Mr. J. H. Wallace
NRL/US Army CRDEC
ATTN: SMCCR-OPR
APG, MD 21010
301/671-2155

Dr. Edward D. Walton
CDR-USNR
P.O. Box 392
Mt. Baldy, CA 91759
714/869-3661

Dr. J. Richard Ward
US Army CRDEC
Research Directorate
Chemical Division
APG, MD 21010
301/671-2719

Mr. George H. Warner
ASD/AEEE
Wright Patterson AFB, OH 45433
513/785-9167

Mr. Daniel J. Weber
US Army CRDEC
ATTN: SMCCR-RSP-A
APG, MD 21010-5423
301/671-2158

Dr. John F. Weimaster
US Army CRDEC
ATTN: SMCCR-RSC-O
APG, MD 21010-5423
301/671-3603

Mr. Ronald A. Weiss
US Army CRDEC
ATTN: SMCCR-PP
APG, MD 21010
301/671-2313

Dr. Randy Wentsel
US Army CRDEC
ATTN: SMCCR-RST-E
APG, MD 21010
301/671-2036

Dr. Christopher E. Whalley
US Army CRDEC
ATTN: SMCCR-RST-E
APG, MD 21010-5423
301/671-4716

Dr. William E. White
US Army CRDEC
ATTN: SMCCR-RSP-C
APG, MD 21010
301/671-2670

Dr. Anthony F. Wilde
US Army Materials Tech Lab
ATTN: SLCMT-EMP
Polymer Research Branch
Watertown, MA 02172
617/923-5147

Mr. Joe Williams
US Army CRDEC
ATTN: SMCCR-RS
APG, MD 21010-5423
301/671-2849

Dr. Eugene Wilusz
Natick RD&E Center
Materials & Polymer Appl Branch
Room 304
Natick, MA 01760-5019
508/651-5486

Dr. Norman M. Witriol
Louisiana Tech University
Ruston, LA 71272
318/257-4670

Dr. Gerry Wood
Los Alamos Nat'l Lab
MS K484
Los Alamos, NM 87545
505/667-9824

Dr. Yu-Chu Yang
US Army CRDEC
ATTN: SMCCR-PPD
APG, MD 21010-5423
301/671-5917

Dr. Sidney Yaverbaum
USAMRICD
Bldg E3100
APG, MD 21010
301/671-3691

Mr. Homer R. Yeh
US Army CRDEC
ATTN: SMCCR-RSB
APG, MD 21010
301/671-3398

Dr. Kenneth C. Zahn
Andrulis Research Corp
31 Potter Street
RT Douglas
Salt Lake City, UT 84113
801/583-0336

Mr. J. H. Zarzycki
US Army CRDEC
ATTN: SMCCR-PP
APG, MD 21010
301/671-5601

Prof. Daniel Zeroka
Lehigh University
Dept of Chemistry 6
Bethlehem, PA 18015
215/758-3479

Mr. Anthony Zirnhelt
US Army CRDEC
ATTN: SMCCR-RSL
APG, MD 21010
301/671-3212

Mr. Alan Zulich
US Army CRDEC
ATTN: SMCCR-DDT
APG, MD 21010
301/671-5573

AGENDA
APPENDIX B

U.S. Army Chemical Research, Devleopment and Engineering Center

SCIENTIFIC CONFERENCE ON CHEMICAL DEFENSE RESEARCH

14-17 November 1989
Aberdeen Proving Ground (Edgewood Area), Maryland

Tuesday, 14 November 1989

0800 Registration
Post Conference Center (Seminar Bldg)

0900 OPENING SESSION
Welcome and Opening Remarks

0910 Keynote Address

0940 Presentation of Army Research and Development Achievement Awards
Congratulatory Remarks

1000 COFFEE BREAK

1020 Overview of the Chemical Defense Basic Research Program
Dr. Harry Salem, Acting Director of Research, U.S. Army Chemical Research, Development and Engineering Center

Overview of Other Chemical Defense Research Programs
Other Department of Defense Representatives

1200 Administrative Announcements

1215 LUNCH

Tuesday, 14 November 1989

SESSION 1 - DECONTAMINATION

Moderator: *Joseph W. Hovanec,* U.S. Army Chemical Research, Development and Engineering Center

Conference Center

1330 Improvement of the "German Emulsion"
S.H. Huttenhain, W. Balzer and R. Feldmann, Fraunhofer-Institut

1350 Effect of Reactive Ingredients in Decontamination by the M280 Kit
J.R. Ward, L.L. Szafraniec, W.T. Beaudry, S.E. Day and G.A. Dragunas, U.S. Army Chemical Research, Development and Engineering Center

1410 Decontamination of Soman in Freon Mixtures
W. Johnson, K. Collins and J.R. Ward, U.S. Army Chemical Research, Development and Engineering Center

1430 EPR Studies of Micelles as Compartments
B.L. Bales and J. Deaton, California State University

1450 Synthesis of Organo-Ruthenium Complexes for Luminescence Probes in Microemulsion Droplet Size Determination
H.D. Durst and L.L. Szafraniec, U.S. Army Chemical Research, Development and Engineering Center; *K.G. Haddaway and S.M. Garlick,* Geo-Centers, Inc.; *F.R. Longo,* Drexel University

1510 BREAK

1530 Chemical and Physical Studies in Microemulsions Containing 1-Alkyl-2-Pyrrolidinones as Cosurfactants
S.M. Garlick and K.G. Haddaway, Geo-Centers, Inc.; *R.A. Mackay, H.D. Durst and S.D. Christesen,* U.S. Army Chemical Research, Development and Engineering Center; *F.R. Longo,* Drexel University

1550 Electrochemical Impedance Spectroscopic Study of the Penetration of CARC by DS-2 and Experimental Microemulsions
P.L. Cannon, Jr., U.S. Army Chemical Research, Development and Engineering Center; *F.R. Longo,* Drexel University; *S.M. Garlick,* Geo-Centers, Inc.

1610 Soman Detoxifying Enzyme from Escherichia Coli
J.A. Akkara and D. Kaplan, U.S. Army Natick Research, Development and Engineering Center

1630 Biological Degradation of a Simulable Chemical Warfare Agent
A.V. Stiffey, Naval Ocean Research and Development Agency

1650 Studies in Microemulsions Similar to the MCBD Microemulsion
S.M. Garlick and K.G. Haddaway, Geo-Centers, Inc.; *R.A. MacKay and H.D. Durst,* U.S. Army Chemical Research, Development and Engineering Center; *F.R. Longo,* Drexel University

Tuesday, 14 November 1989

SESSION 1A - COMPUTATIONAL CHEMISTRY (CONCURRENT)
Moderator: *George R. Famini,* U.S. Army Chemical Research, Development and Engineering Center

Seminar Center

1330 Molecular Surface Properties as Guides to Chemical Reactivity
P. Sjoberg and P. Politzer, University of New Orleans

1350 Comparison of the Electronic Structure of the P-O and P-S Bonds
M. Krauss, National Institute for Standards and Technology

1410 Theoretical Studies of Reaction Rates: Application to H_2+CN
M.J. Redmon and B.C. Garrett, Chemical Dynamics Corporation; *C.F. Melius,* Sandia National Laboratories

1430 Computations of Vibrational Infrared Frequencies of Some Amines
H.F. Hameka, University of Pennsylvania; *G.R. Famini and J.O. Jensen,* U.S. Army Chemical Research, Development and Engineering Center; *E.I. Newhouse,* Auburn University

1450 Theoretical Prediction of VCD Spectra
D. Zeroka, Lehigh University; *G.R. Famini, J.O. Jensen and A.H. Carrieri,* U.S. Army Chemical Research, Development and Engineering Center; *C.F. Chabalowski,* Ballistic Research Laboratory

1510 BREAK

1530 Applications of "MNDO"-Type Semi-Empirical Methods
J.J.P. Stewart, U.S. Air Force Academy

1550 The Calculation of Hydrogen-Bonding Properties
E.M. Kober and J.P. Ritchie, Los Alamos National Laboratory

1610 Molecular Orbital Calculations on Copper (II)-N,N,N' N'-Tetramethylethylenediamine (TMEN) Type Complexes
L.C. Hoke, U.S. Army Natick Research, Development and Engineering Center

1630 Molecular Modeling of Selected Organophosphorus Compounds
W.E. White and G.R. Famini, U.S. Army Chemical Research, Development and Engineering Center

1650 Quantum Chemical Calculations Using a Grid of Evenly Space S-Functions
J.O. Jensen, U.S. Army Chemical Research, Development and Engineering Center

Wednesday, 15 November 1989

SESSION 2 - DECONTAMINATION
Moderator: *Joseph W. Hovanec,* U.S. Army Chemical Research, Development and Engineering Center

Conference Center

0800 Catalytic Decomposition of CW-Agents by Ternary Chelates of Copper (II)
K.S. Rajan and S. Mainer, IIT Research Institute; *J.E. Walker, D. Remy and J. Halliday,* U.S. Army Natick Research, Development and Engineering Center

0820 Reaction of 2-Chloroethyl Methyl Sulfide with Phenolates and Thiophenolates, Mechanistic Dependence on Solvent and Nucleophile
S.P. McManus, J.M. Harris, R. Sedaghat-Herati and M. Jalali-Heravi, University of Alabama in Huntsville

0840 Micellar Effects Upon the Reaction of Hydroxide Ion with Thiophenyl Phosphinates
C.A. Bunton and A. Blasko, University of California

0900 Sulfur-Assisted Oxidation of 2-Chloroethyl Sulfides to Sulfoxides by Dimethyl Sulfoxide
Y.-C. Yang, L.L. Szafraniec, W.T. Beaudry and F.-L. Hsu, U.S. Army Chemical Research, Development and Engineering Center

0920 Catalytic Agent Degradation on Oxide Films and in Microheterogeneous Solution Systems
M. Graetzel, Swiss Federal Institute of Technology

0940 BREAK

1000 The Metal Catalyzed Oxidation of Mustard Simulants with Peroxides
R.S. Drago, T.C. Cundari, A. Goldstein, D. Patton and J.P. Hage, University of Florida; *Y.-C. Yang,* U.S. Army Chemical Research, Development and Engineering Center

1020 Rapid, Selective, Catalytic Destruction of Sulfides (Thioethers) Including Half Mustard by Heteropoly and Isopoly Oxometalates
C.L. Hill, M. Faraj and R.C. Chambers, Emory University

1040 Mechanisms of VX Oxidation I. Oxidation by Peroxides and Oxone
Y.-C. Yang, L.L. Szafraniec, W.T. Beaudry and D.K. Rohrbaugh, U.S. Army Chemical Research, Development and Engineering Center

1100 Equilibria and Reactivity of Peroxo Complexes of Mo(VI) and W(VI) in Basic Solution
R.C. Thompson, University of Missouri

1120 Starburst Dendrimers: Molecular Level Control of Size, Shape, Surface Chemistry, Topology, and Flexibility from Atoms to Macroscopic Matter
D.A. Tomalia, Michigan Molecular Institute

Wednesday, 15 November 1989

SESSION 2A - FLUID DYNAMICS (CONCURRENT)

Moderator: *Miles C. Miller,* U.S. Army Chemical Research, Development and Engineering Center

Seminar Center

0800 Solvent Effects Which Influence the Rheological Behavior of Polymer Solutions
W.J. Shuely and B.S. Ince, U.S. Army Chemical Research, Development and Engineering Center

0825 Influence of Trace Amount of Organic Acids on the Viscoelastic Properties of Polymer Solutions
S.H. Hong, W. Limm and W. Shuely, U.S. Army Chemical Research, Development and Engineering Center

0850 Solution Behavior of A Random Copolymer of Poly (Isobutyl) Methacrylate-T-Butyl Aminoethyl Methacrylate
B. Chu and J. Wang, State University of New York at Stony Brook; *W.J. Shuely,* U.S. Army Chemical Research, Development and Engineering Center

0915 Liquid Stretching Using a Falling Cylinder
J.E. Matta and R.P. Tytus, U.S. Army Chemical Research, Development and Engineering Center

0940 Silicone Fluid Rheogoniometer Measurements and Their Application to Despin Moment Studies in a Spinning and Coning Cylinder
R.P. Tytus, U.S. Army Chemical Research, Development and Engineering Center

1005 BREAK

1020 Computational Fluid Dynamics Method for Low Reynolds Number Flow in a Precessing/Spinning Liquid-Filled Cylinder with Rounded Endcaps
M. Nusca, U.S. Army Ballistic Research Laboratory

1045 Effect of Partial-Fill Condition on the Destabilizing Moment Produced by a Viscous Liquid in a Spinning and Coning Cylinder
D.J. Weber and M.C. Miller, U.S. Army Chemical Research, Development and Engineering Center

1110 Reduction of Viscous Liquid-Fill Flight Instability by Addition of Immiscible, Low Viscosity Liquid
M.C. Miller, U.S. Army Chemical Research, Development and Engineering Center

1135 Two-Fluid Flows in Spinning and Nutating Cylinders
T. Herbert and M. Selmi, Ohio State University

Wednesday, 15 November 1989

SESSION 3 - SYNTHESIS AND PROPERTIES
Moderator: *Harold D. Banks,* U.S. Army Chemical Research, Development and Engineering Center

Conference Center

1330 An Overview of the Synthesis of ^{14}C Ring Labeled EA 4923
J.W. King and D.R. Bowie, U.S. Army Chemical Research, Development and Engineering Center

1355 Medetomidine Analogs as $Alpha_2$-Adrenergic Agonist
D.D. Miller and Y. Amemiya, Ohio State University; *F.-L. Hsu,* U.S. Army Chemical Research, Development and Engineering Center

1420 Recent Developments in the Physical Chemistry of Simulant Selection
E.C. Penski, D. Fielder, A.B. Livesey and H.M. Walker, U.S. Army Chemical Research, Development and Engineering Center

1445 BREAK

1500 Use of Pentacovalent Oxaphosphorane Chemistry in the Development of New Methodology for the Synthesis of Natural Products
C.K. McClure, K.-Y. Jung and C. Grote, University of Delaware

1525 Formation of C-C Bonds By Rearrangements from Silicon to Carbon
P.F. Hudrlik, A. Hudrlik and Y. Abdallah, Howard University

1550 New Approaches to the Synthesis of Fentanyl Derivatives
H.D. Banks, U.S. Army Chemical Research, Development and Engineering Center

1615 Thermochemistry of High Energy Reactions
E.S. Domalski, National Institute of Standards & Technology

Wednesday, 15 November 1989

1300-1700 SESSION 3A - POSTER SESSION (CONCURRENT)

Seminar Center/Chapel Annex

DECONTAMINATION POSTERS

Mechanisms of VX Oxidation II. Oxidation by Chlorine-Based Compounds
Y.-C. Yang, L.L. Szafraniec, W.T. Beaudry and D.K. Rohrbaugh, U.S. Army Chemical Research, Development and Engineering Center

The Effect of Biological Media on the Hydrolysis of Mustard Simulants
L.C. Cerny and E.L. Cerny, Utica College of Syracuse University

C-Agent Evaporation and Weathering on Surfaces: Effect of Surface Temperature
H.R. Carlon, U.S. Army Chemical Research, Development and Engineering Center

A Comparison of *o*-Iodosobenzoic Acid Derivatives in the Catalytic Hydrolysis of PNDP
C.A. Panetta, University of Mississippi; *H.D. Durst,* U.S. Army Chemical Research, Development and Engineering Center; *S.M. Garlick and K.G. Haddaway,* Geo-Centers, Inc.; *F.R. Longo and B.A. Burnside,* Drexel University

Photooxidation of Mustard and VX in Solutions and on Titania Surfaces
J.H. Buchanan, D.K. Rohrbaugh, L.L. Szafraniec, W.T. Beaudry and Y.-C. Yang, U.S. Army Chemical Research, Development and Engineering Center

Studies on the Reformulation of Agent Decontaminant DS-2
L.J. Schiff, J. Hovanec and A. Livesey, U.S. Army Chemical Research, Development and Engineering Center

Inhibition of Organophosphorous Acid Anhydrase from Squid Hepatopancreas by Specific Alkylating Reagents
K. Kopec-Smyth, L.D. Loomis, J.R. Deschamps and K.B. Ward, Naval Research Laboratory

Fractional Factorial Test Matrix Designed to Evaluate New Chemical Decontaminant Against Two Existing Decontaminants
B.K. MacIver, L.M. Sturdivan and J.H. Thompson, U.S. Army Chemical Research, Development and Engineering Center

Electrochemical Studies in Microemulsions
P.L. Cannon, Jr., U.S. Army Chemical Research, Development and Engineering Center; *S.M. Garlick,* Geo-Centers, Inc.; *F.R. Longo,* Drexel University

Polyester Carriers for Catalytic Reactants
N. Tillman, L.M. Speaker, G.M. Russo, Eastman Kodak Company

COMPUTATIONAL CHEMISTRY POSTERS

Molecular Modeling of Anatoxin and Selected Analogs
W.E. White, U.S. Army Chemical Research, Development and Engineering Center

A Computational Comparison of the Electronic Properties of G Agents with Selected Reaction Simulants
G.R. Famini, U.S. Army Chemical Research, Development and Engineering Center

Topological Molecular Transforms in Molecular Similarity Analysis
J.W. King, U.S. Army Chemical Research, Development and Engineering Center; *B.B. King,* Clemson University

Deuterium Electric Field Gradients of Diatomics by Variation-Perturbation Method: Comparison of Results Based on Slater and Gaussian Basis Sets
H.-W. Kim, Penn State Ogontz; *J.O. Jensen,* U.S. Army Chemical Research, Development and Engineering Center; *H.F. Hameka,* University of Pennsylvania

Theoretical Investigation of the Reactivity and Reaction Mechanisms of Perfluoroisobutene (PFIB)

N.M. Witriol, Louisiana Tech University; *G.R. Famini,* U.S. Army Chemical Research, Development and Engineering Center

Molecular Modeling of Some Alpha-2 Adrenergic Compounds

A. Mickiewicz and W. Ashman, U.S. Army Chemical Research, Development and Engineering Center

Accurate Calculations for Hydrogen Bonded Systems Using Molecular Mechanics Methods

R.A. Kumpf, W.C.F. Muhlbauer, J.J. Urban and J.R. Damewood, Jr., University of Delaware

DETECTION POSTERS

Detection and Identification of QL Degradation Products by Chemical Ionization Mass Spectrometry

D.K. Rohrbaugh, U.S. Army Chemical Research, Development and Engineering Center

2-Napthalenethiol as a Fluorogenic Reagent for Detection of the Blister Agent Simulant 2-Chloroethylethylsulfide

T.J. Novak, U.S. Army Chemical Research, Development and Engineering Center; *P.M. Davis,* Geo-Centers, Inc.

Distributed Air-Monitoring Network for Multipoint Determination of Chemical Agents

G.D. Sides, T.G. Thomas, D.R. Coleman and J.T. Brown, CMS Research Corporation

Novel GC-FTIR and GC-MS Techniques in the Analyses of Laser-Induced Reactions of Alcohols

R.A. Johnson, U.S. Army Missile Command

Determination of the Fragmentation Mechanisms of Organophosphorus Ions by H_2O and D_2O Atmospheric Pressure Ionization Tandem Mass Spectrometry

A.P. Snyder and C.S. Harden, U.S. Army Chemical Research, Development and Engineering Center

Surface Acoustic Wave and Chemiresistor Responses to Vapor Challenges Using Arylphosphonic Acids, Salts, and Esters as Microsensor Coatings

A.R. Katritzky, G.P. Savage, R.J. Offerman and B. Pilarski, University of Florida

Raman Spectroscopy for Contamination Monitoring
S.D. Christesen, U.S. Army Chemical Research, Development and Engineering Center

Thermal Catalysis of Toxic Vapors and its Application for Chemical Analysis
W.H. Buttner, Argonne National Laboratory; *C. Hsu,* U.S. Army Chemical Research, Development and Engineering Center

Chemical Agent Detection with Amplifying Bioresponse Simulator
G.D. Case, Resource Technologies Group; *M.M. Howton and D.S. Beattie,* West Virginia University; *S.N. Agathos,* Rutgers University; *L.J. Luskus,* USAF/SAM Brooks AFB

An Expert System for Interpreting IR Spectra of Organophosphorus Compounds
L. Hoffland and R. Piffath, U.S. Army Chemical Research, Development and Engineering Center; *B.J. Wythoff and S. Tomellini,* University of New Hampshire

Analysis of Fatty Acids in Bacteria by Pyrolysis/Tandem Mass Spectrometry
S.J. DeLuca, P.D. Harrington and K.J. Voorhees, Colorado School of Mines; *E.W. Sarver,* U.S. Army Chemical Research, Development and Engineering Center

MATERIALS POSTERS

A Novel Interaction of Acrylic Polymers with Protic Solvents: An FTIR Study
W. Limm and S.H. Hong, U.S. Army Chemical Research, Development and Engineering Center

Optical Properties of Inorganic Polymers
K.F. Ferris and S.M. Risser, Pacific Northwest Laboratory

PROTECTION POSTERS

AES and XPS Analyses of Plastic Welds
C.C. Hsu and J.A. Fritz, U.S. Army Chemical Research, Development and Engineering Center

Rapid Three Dimensional Anthropometric and Mold Measurement for Mask Design
R.A. Weiss and J. Solivan, U.S. Army Chemical Research, Development and Engineering Center

Improved Method for Investigating NBC Respirator Communication Capability
R.A. Weiss and J. Viscarrondo, U.S. Army Chemical Research, Development and Engineering Center

Respirator Lens Configuration for Optical Coupling to Sighting Systems
R.A. Weiss, U.S. Army Chemical Research, Development and Engineering Center

TOXICOLOGICAL AND ENVIRONMENTAL STUDIES POSTERS

Solvent-Water Partitioning and Extraction of Phosphonates
D.C. Leggett, U.S. Army Cold Regions Research and Engineering Laboratory

Nicotinic Acetylcholine Receptor/Ion Channel Complex Shows Irreversible Organophosphate Effects
D.E. Menking, R.G. Thompson and J.J. Valdes, U.S. Army Chemical Research, Development and Engineering Center

Pharmacological Effects of Opiate Agonist and Antagonist Coadministration in the Ferret
R.J. Mioduszewski, S. Reutter and D. Berg, U.S. Army Chemical Research, Development and Engineering Center

Effects of a Synthetic Opioid on Auditory Brainstem Responses in Ferrets
S. Reutter, N. Legaspi and R. Mioduszewski, U.S. Army Chemical Research, Development and Engineering Center

The Aquatic Toxicology of a Mixture of Isopropylamine, 2-Methylcyclohexanol and Pinalcolyl Alcohol
N.A. Chester, M.V. Haley, J. Buchanan, D.W. Johnson and W.G. Landis, U.S. Army Chemical Research, Development and Engineering Center

The Anesthetic Potency of a Synthetic Opiate Aerosol in the Rat
J. Carpin, C. Whalley and R. Mioduszewski, U.S. Army Chemical Research, Development and Engineering Center

BIOTECHNOLOGY POSTERS

Determination of Toxins Using Enzyme-Amplified Receptor Assay
S.F. Hallowell, U.S. Army Chemical Research, Development and Engineering Center; *G.A. Rechnitz,* University of Hawaii

A Radioimmunoassay for Physostigmine
H.G. Meyer, B.J. Lukey, R.T. Gepp, M.J. McCluskey and C.N. Lieske, U.S. Army Medical Research Institute of Chemical Defense

****

BEEF AND BURGUNDY DINNER
Aberdeen Area Officers' Club
Aberdeen Proving Ground (Aberdeen Area), Maryland
(301) 278-3062

Wednesday, November 15, 1989
1800-1900 Hours Cocktails
1900-2030 Hours Dinner

MENU

COMPLETE SALAD BAR
ROAST BEEF AU JUS * BAKED CHICKEN
MASHED POTATOES * RICE * CORN * GREEN BEANS
DESSERT TABLE
Burgundy wine, coffee, tea, water
$11.00 Tax and Gratuity Included

CASH BAR

2030-2130 Hours Guest Speaker

Dr. John R. Huizenga, University of Rochester
"Cold Fusion: An Evaluation of Reported Results"

****

Thursday, 16 November 1989

SESSION 4 - DETECTION
Moderator: *S. Randolph Long,* U.S. Army Chemical Research, Development and Engineering Center

Conference Center

0800 Laser Stand Off Detection of Atmospheric Species Using the CRDEC CO_2 LIDAR System
A.P. Force, S.L. Emery and F.M. D'Amico, U.S. Army Chemical Research, Development and Engineering Center

0820 Statistics for Identifying a Contaminated Rough Surface by Polarized IR Scattering: Full Wave Approach
S.M. Haugland, E. Bahar, University of Nebraska-Lincoln; *A.H. Carrieri,* U.S. Army Chemical Research, Development and Engineering Center

0840 Detection of Explosive Analogs Using Laser Induced Multiphoton Ionization and Discharge Methods in Atmospheric Pressure Ionization Mass Spectroscopy
D.M. Lubman and I. Sofer, University of Michigan

0900 The Effect of Cultural Conditions on Deep UV Resonance Raman Spectra of Bacteria
W.H. Nelson and J.F. Sperry, University of Rhode Island

0920 Progress in CB Detection by Transfer Line GC/MS^n Using a Miniaturized Ion Trap Mass Spectrometer
H.L.C. Meuzelaar, N.P. Arnold, W.H. McClennen, University of Utah; *A.P. Snyder,* U.S. Army Chemical Research, Development and Engineering Center

0940 BREAK

1000 Development of a Point Detector for Biological Agents
B. Busey, A. Zulich, M. Goode, P. Stopa, U.S. Army Chemical Research, Development and Engineering Center; *J.W. Parce and G. Kirk,* Molecular Devices Corporation; *S. Alter,* Environmental Technologies Group

1020 Micro-Electrochemical Detection Systems
J.R. Stetter, Transducer Research, Inc.

1040 Acada (XM22) and Cam CW Detector Hardware Emulation for Research with SCPS Shelters
B.L. Houseman and L.A. Walker, Goucher College; *L.J. Luskus,* USAFSAM/VNC Brooks AFB; *W.C. Blanchard,* Blanchard & Co.

1100 Digital Signal Processors for Real-Time Chemical Analysis
J.T. Ditillo and R. Kroutil, U.S. Army Chemical Research, Development and Engineering Center

1120 Emerging Technologies in Field Screening Methods for Hazardous Waste Site Investigations
E.J. Poziomek, Artech Associates

Thursday, 16 November 1989

SESSION 4A - MATERIALS (CONCURRENT)

Moderator: *Seok Hong,* U.S. Army Chemical Research, Development and Engineering Center

Seminar Center

0800 Non-Isothermal Sorption of Toluene Vapor in Natural Rubber
N.S. Schneider and L.S. Waksman, U.S. Army Materials Technology Laboratory

0820 Flooded Cell Permeation Testing of Butyl Rubber Barriers
E. Engwall, U.S. Army Materials Technology Laboratory

0840 Analysis of CW Liquid Droplet Permeation Tests Performed with a Series of Rubber Materials
A.F. Wilde, U.S. Army Materials Technology Laboratory

0900 Liquid Sorption and Desorption of Contaminants from Chemically Resistant and Protective Polymers
W.J. Shuely and B.S. Ince, U.S. Army Chemical Research, Development and Engineering Center

0920 The Interpretation of Sorption and Permeation Measurements in Polymers
N.S. Schneider and E. Engwall, U.S. Army Materials Technology Laboratory

0940 BREAK

1000 A New Method of Estimating Strain to Failure (Cracking/Crazing) of Polymeric Materials Under Chemical Stress
L. Sturdivan, E.W. Sarver and P. Grasso, U.S. Army Chemical Research, Development and Engineering Center

1020 An Experimental Test for Determining Resistance of Thin Polymeric Films to Penetration by Chemical Agents
E.W. Sarver, L. Sturdivan and P. Grasso, U.S. Army Chemical Research, Development and Engineering Center

1040 Stress Crazing in Transparent Materials Exposed to Chemical Agents
P. Grasso, U.S. Army Chemical Research, Development and Engineering Center

1100 Solubility Parameter of Poly (Methyl Methacrylate): An Inverse Gas Chromatography Study
W. Limm, U.S. Army Chemical Research, Development and Engineering Center

Thursday, 16 November 1989

SESSION 5 - PROTECTION

Moderator: *David Tevault,* U.S. Army Chemical Research, Development and Engineering Center

Conference Center

1330 Axial Dispersion Effects on the Breakthrough Behavior of Freon 113
D.K. Friday, Geo-Centers, Inc.; *J.J. Mahle and L.C. Buettner,* U.S. Army Chemical Research, Development and Engineering Center

1350 Batch Adsorption Equilibria and Rate Apparatus
J.J. Mahle and L.C. Buettner, U.S. Army Chemical Research, Development and Engineering Center; *D.K. Friday,* Geo-Centers, Inc.

1410 Characterization of a Weathered Carbon Displaying Agglomeration Tendencies
R. Lamontagne, R. Colton and H. Hoff, Naval Research Laboratory; *R. Matuszko and L. Isaacson,* Geo-Centers, Inc.; *J. Rossin,* U.S. Army Chemical Research, Development and Engineering Center

1430 Effects of Environmental Weathering on the Properties of an ASC-TEDA Radial Flow Carbon Filter: Metal Impregnants
L. Isaacson, Geo-Centers, Inc.; *R. Lamontagne,* Naval Research Laboratory; *E.R. Riley and J. Rossin,* U.S. Army Chemical Research, Development and Engineering Center

1450 Single and Binary Adsorption of n-Nonane and Xylene on BPL Carbon
R. Matuszko, D.K. Friday and L. Isaacson, Geo-Centers, Inc.; *R. Lamontagne,* Naval Research Laboratory

1510 BREAK

1530 Adsorption Bed Breakthrough Curve Data Fitting
G. Wood, Los Alamos National Lab

1550 CK Breakthrough and Surface Area of Whetlerite as a Function of Particle Density and Particle Size
V.R. Deitz, Naval Research Laboratory; *J.A. Rehrmann,* U.S. Army Chemical Research, Development and Engineering Center

1610 Effect of Impregnant Loading on the Adsorption Capacity of Activated Carbons
C. Karwacki and J.J. Mahle, U.S. Army Chemical Research, Development and Engineering Center; *D.K. Friday,* Geo-Centers, Inc.

1630 An Examination of How Exposure to Humid Air Can Result in Changes in the Adsorption Properties of Activated Carbons
L.B. Adams, C.R. Hall and R.J. Holmes, Chemical Defense Establishment, England; *R.A. Newton,* U.S. Army Chemical Research, Development and Engineering Center

1650 The Development of a New Chromium-Free Whetlerite Carbon for Adsorption of Toxic Gases
D.T. Doughty and N.J. Wagner, Calgon Carbon Corporation; *R.W. Morrison and R.J. Puhala,* U.S. Army Chemical Research, Development and Engineering Center

Thursday, 16 November 1989

SESSION 5A - TOXICOLOGICAL AND ENVIRONMENTAL STUDIES (CONCURRENT)
Moderator: *Edmund G. Cummings,* U.S. Army Chemical Research, Development and Engineering Center

Seminar Center

1330 Microbial Populations in Soil Maintained Under Anaerobic Conditions
W.A. Mego, Argonne National Laboratory

1355 Use of Open-Top Chambers to Assess the Toxicity of Chemicals to Plants
M.C. Sadusky, Geo-Centers, Inc.; *R.S. Wentsel and R.T. Checkai,* U.S. Army Chemical Research, Development and Engineering Center; *J.M. Skelly,* Pennsylvania State University

1420 Removal of Hazardous Substances from Contaminated Soil by Extraction and Washing Using Flow Through Column System
V.S. Rajput, Unitech Engineers; *M.E. Singley, A.J. Higgins and P.F. Strom,* Rutgers University

1445 A Charcoal Filter Test System Using a Combination of Chemical and Toxicological Detectors to Assess Performance
L.C. Buettner and J.J. Manle, U.S. Army Chemical Research, Development and Engineering Center; *D.K. Friday,* Geo-Centers, Inc.; *S. Hsu,* Fallston, MD

1510 BREAK

1525 Potentiation of Perfluoroisobutylene-Induced Lung Injury by Exercise
B.E. Lehnert and D.M. Stavert, Los Alamos National Laboratory

1550 The Pharmacokinetics of Volatile Anesthetics - A Brief Review
J.W. King, U.S. Army Chemical Research, Development and Engineering Center

1615 Growth Characteristics of Commercial Normal Human Abdominal Keratinocytes
S. Yaverbaum, J.P. Petrali, B.F. Doxzon, S.B. Oglesby and D.L. Kolb, U.S. Army Medical Research Institute of Chemical Defense

1640 Chemical Carcinogens from a Single Exposure: Documentation and Risk Assessment Implication
E.J. Calibrese, University of Massachusetts

Friday, 17 November 1989

SESSION 6 - PROTECTION
Moderator: *David E. Tevault,* U.S. Army Chemical Research, Development and Engineering Center

Conference Center

0800 Surface Characterization of Chromium-Free Impregnated Carbons
C.C. Hsu, U.S. Army Chemical Research, Development and Engineering Center

0820 Chemical Studies of ASC Whetlerites
A. Birenzvige and E. Petersen, U.S. Army Chemical Research, Development and Engineering Center; *P.N. Krisnan,* Coppin State College

0840 Synchrotron X-Ray Absorption Study of CR and Other Metals in Activated Charcoal Filters
W.T. Elam, Naval Research Laboratory

0900 Complete Catalytic Oxidation of Diethyl Sulfide Over a 1% Pt/Al_2O_3 Catalyst: Effects of Mass Transfer on Reactivity
J.A. Rossin, U.S. Army Chemical Research, Development and Engineering Center

0920 Catalytic Oxidation of Perfluoropropene Over a Monolithic Pt/TiO_2 Oxidation Catalyst
D.S.Y. Hsu and P. Nazario-Gonzalez, Naval Research Laboratory

0940 BREAK

1000 Removal of Toxic Catalytic Oxidation Products Via Adsorption
I.W. Kim, G.D. Munkvold and J.J. Beaman, University of Texas; *W.W. Choi and A.J. Hitt,* McDonnell Douglas Corporation

1020 Identification of a Species in a Silent Discharge Plasma
W.C. Neely, E.I. Newhouse, S. Parish, K. Walker, J.P. Wey, S. Pathirana and E.J. Clothiaux, Auburn University

1040 Model of Aerosol Protection Offered by Permeable Protective Garments
P. Fedele, U.S. Army Chemical Research, Development and Engineering Center; *J. Hanley, D. VanOsdell and D. Ensor,* Research Triangle Institute

1100 Recent Advances in Automated Permeation Testing of Chemical Defense Fabrics
D.R. Coleman, J.T. Brown, G.D. Sides and T.G. Thomas, CMS Research Corporation

1120 Updated Static Pulmonary Function Parameters for NBC Respirator Design
L. Strickler, J. Solivan, H. Froehlich, T. Kulle and R.A. Weiss, U.S. Army Chemical Research, Development and Engineering Center

Friday, 17 November 1989

SESSION 6A - BIOTECHNOLOGY (CONCURRENT)
Moderator: *James J. Valdes,* U.S. Army Chemical Research, Development and Engineering Center

Seminar Center

0800 Purification Procedures for OPA Anhydrase-2 from Halophile JD6.5
T.-C. Cheng, R.A. Deas, J.J. DeFrank and I. Elashvili, U.S. Army Chemical Research, Development and Engineering Center

0820 Properties of OPA Anhydrase-2 from Halophile JD6.5
T.-C. Cheng, R.A. Deas and J.J. DeFrank, U.S. Army Chemical Research, Development and Engineering Center

0840 Molecular Topography of Squid OPA Anhydrase (EC 3.1.8.1) as Revealed by Spectroscopic Studies
J.E. Walker, J. Connolly and D. Steeves, U.S. Army Natick Research, Development and Engineering Center; *F.C.G. Hoskin and K.S. Rajan,* IIT Research Institute

0900 Induction of Enhanced Strains of a Thermophile that Synthesizes an OPA Anhydrase Effective in Detoxifying Soman
B.J. Gallo, P. Scotland and D. Gowenlock, U.S. Army Natick Research, Development and Engineering Center

0920 Removal of Crude Oil from Valdez, Alaska Rock Samples with a Microbially-Produced Biosurfactant
S. Harvey, I. Elashvili and J. Height, U.S. Army Chemical Research, Development and Engineering Center; *A.M. Chakrabarty,* University of Illinois at Chicago

0940 BREAK

1000 Modification of the Ditam (Diffusion Through a Membrane) Assay and Apparatus for the Detection of Small Molecular Weight Substances
C. Ladouceur, U.S. Army Chemical Research, Development and Engineering Center

1020 Partial Purification and Characterization of a High Affinity Ca^{2+} Channel Receptor from Porcine Brain
J. Chambers, P. Kumar and M. Wayner, University of Texas at San Antonio; *J.J. Valdes,* U.S. Army Chemical Research, Development and Engineering Center

1040 Enzyme-Amplified Receptor Assay Screening Test for Chlorpromazine Trifluoperazine, and PCP
S.F. Hallowell, U.S. Army Chemical Research, Development and Engineering Center

1100 A Nicotinic Receptor Optical Biosensor
M. Eldefrawi and K. Rogers, University of Maryland

1120 Recent Hardware Advances in Evanescent Wave Fiber Optic Biosensors
S. Lackie, T. Glass and M.J. Block, ORD, Inc.

1989 U.S. ARMY CHEMICAL RESEARCH, DEVELOPMENT AND ENGINEERING CENTER SCIENTIFIC CONFERENCE ON CHEMICAL DEFENSE RESEARCH

ADDENDUM

SESSION 1 - DECONTAMINATION

Tuesday, 14 November 1989

1410 Decontamination of Soman in Freon Mixtures
W. Johnson, K. Collins and J.R. Ward, U.S. Army Chemical Research, Development and Engineering Center

WILL BE PRESENTED IN THE DECONTAMINATION POSTER SESSION

REPLACEMENT

1410 A Quantitative Description of the Effect of Micellized CTAB on the o-Iodosobenzoate Catalyzed Hydrolysis of G Agents
D.R. Leslie and S. Pantelidis Defence Science and Technology Organization

SESSION 6 - PROTECTION

Friday, 17 November 1989

WITHDRAWN

0820 Chemical Studies of ASC Whetlerites
A. Birenzvige and E. Petersen, U.S. Army Chemical Research, Development and Engineering Center

REPLACEMENT

0820 Catalytic Destruction of Hazardous Halogenated Organic Chemicals
G.R. Lester, Allied-Signal Engineered Materials Research Center

SESSION 6A - BIOTECHNOLOGY

Friday, 17 November 1989

1140 Functional Reconstitution of Olfactory Receptor for Analytical Application
V. Vodyanoy, Auburn University

SESSION 3A - POSTER SESSION

Wednesday, 15 November 1989
1300-1700

MATERIALS POSTERS

Dilute Solution Characterization of Poly(iBMA-CO-tBAEMA)
M.K. Potts, U.S. Army Materials Technology Laboratory

BIOTECHNOLOGY POSTERS

Biodegradation of Thiodiglycol
Steve Harvey and Joseph J. DeFrank, U.S. Army Chemical Research, Development and Engineering Center; *A.M. Chakrabarty*, University of Illinois

BLANK

APPENDIX C

DELAYED PAPERS*

*The papers contained in this appendix were received too late to be included in their proper sections.

BLANK

SOMAN-DETOXIFYING ENZYME FROM ESCHERICHIA COLI

Joseph A. Akkara, and David L. Kaplan
US Army Natick Research, Development, and Engineering Center,
Natick, MA 01760-5000.

ABSTRACT

Earlier studies with a partially purified enzyme from Escherichia coli (ATCC 25922) by cold ethanol precipitation showed that Soman was hydrolyzed but was not detoxified by the enzyme. Recent studies with this enzyme partially purified by column chromatography demonstrated that the enzyme not only hydrolyzed but also detoxified Soman. Substrate specificity and temperature and pH optima for the E. coli enzyme were determined. The partially purified enzyme from E. coli was covalently bound to cotton by tresyl chloride activation and this immobilized enzyme retained its hydrolytic activity against organophosphonates.

INTRODUCTION

Rapid and complete decontamination of chemical warfare agents is of extreme importance for the protection of personnel, equipment, operating systems, and the environment, once they are exposed to chemical agents and agent surrogates. A number of physical, chemical, and biological methods have been developed for the removal and/or degradation of chemical agents with varying degree of success. Biocatalytic degradation of chemical agents has the following advantages: rapid breakdown, mild reaction conditions are compatible with many of the functional finishes, and provide complete detoxification of the agent. A number of Organophosphorus Acid Anhydrase (OPA) enzymes that detoxify G-agents have been identified in organisms ranging from bacteria and protozoa to higher mammals.[1-5] Earlier studies have demonstrated that an enzyme from Escherichia coli (ATCC 25922) detoxifies Soman and a number of G-agent surrogates.[6] This report concentrates on the partial purification, characterization and covalent binding of this enzyme to cotton.

MATERIALS AND METHODS

Preparation of E. coli Cell-Free Extract: E. coli (ATCC 25922) was grown in 3% Trypticase Soy Broth (Difco Laboratories, Detroit, MI), the cells were harvested in mid log phase and a cell-free extract was prepared in bis Tris

APPENDIX C

buffer (pH 7.0, 0.05M). The cell free extract was kept frozen at -20°C until used.

OPA Anhydrase and Protein Assays: The enzyme activity was measured in bis Tris buffer (pH 7.0, 0.05M) in the presence of 1.0 mM $MnCl_2$ and 3 mM substrates at 37°C. The enzyme activity was measured by the rate of formation of p-nitrophenol at 405 nm with all agent surrogates without fluorine, and expressed as u moles of p-nitrophenol formed per minute per g of protein. The hydrolysis of diisopropypl fluorophophonate (DFP, Sigma Chem. Co., St.Louis, MO), Soman (1,2,2-trimethylpropyl methylphosphonofluoridate) and Dimebu (3,3-dimethylbutyl methylphosphonofluoridate) was determined using a fluoride specific electrode and the activity of the enzyme was expressed as u moles of fluoride released per minute per g of protein. The detoxification of Soman was quantified by measuring the decrease in the inhibition of eel acetylcholinesterase activty by Soman after its hydrolysis.[6] Hydrolysis and detoxification of Soman, and hydrolysis of Dimebu were carried out at Illinois Institute of Technology Research Institute (Chicago, IL) on contract with US Army Natick RDE Center (Natick, MA). The protein content of the enzyme preparations was determined by measuring the absorbance at 280 nm or by using a Bio-Rad Protein assay kit with Coomassie Brilliant Blue G-250 dye and using bovine serum albumin as standards (Bio-Rad Corp, Richmond, CA).

Purification of the Enzyme: The cell-free extract was partially purified by Sephadex G-100 (Pharmacia, Piscataway, NJ) equilibrated with bis Tris-HCl (pH 7.0, 0.05M) in a 1.25 cm X 50 cm column. The elution buffer was bis Tris-HCl (pH 7.0, 0.05M) and 5.0 mL fractions were collected. The protein concentration was monitored by the absorbance at 280 nm and the enzyme activity was determined as described above. The fractions containing the enzyme activity were pooled, lyophilized, reconstituted in Milli Q(R) water (Millipore Corp. Bedford, MA), and dialyzed twice against 10 volumes of bis Tris-HCl buffer (pH 7.0, 0.05M).

Immobilization of the Enzyme: The enzyme immobilization on cotton fabrics was carried out in three steps: a) preparation of the cotton fabric, b) activation of cellulose, and c) the covalent binding of the enzyme onto the activated cellulose. The cotton fabric (Army Cotton Duck, Oxford, 368 g/sq.cm) was cut into one square cm discs and treated with 1.0 N NaOH for one hour to swell the fabric. After complete swelling, the fabric was washed thoroughly in deionized water till the pH of the wash solution was neutral. The swelled fabric was treated with a series of acetone/water (V/V) solutions in sequence with increasing concentrations of acetone (30/70, 50/50, 70/30, and 90/10) and finally washed twice with 10 volumes of dry acetone. Swelled and acetone treated cotton fabric (30 g) was suspended in two volumes of dry acetone. One half mL of dry pyridine was added, followed by the drop wise addition of 1.0 mL of tresyl chloride (>97% pure, Fluka Chemical Corp., Ronkonkoma, NY) with vigorous stirring. After 15 minutes of mixing, the reaction was quenched by the addition of dry acetone followed by washing with 10 volumes of acetone. The acetone-washed fabric was further treated in sequence with a set of acetone/1.0 mM HCl (V/V) solutions with increasing concentrations of 1.0 mM HCl (70/30, 50/50, 30/70 and 15/85) and finally with 10 volumes of 1.0 mM HCl. The tresylated fabric was stored at 4°C before immobilization with an enzyme.

Before immobilization, the tresylated fabric was washed briefly with ten

volumes of PIPES buffer (pH 7.2, 0.05 M) at 4°C and resuspended in one volume of the same buffer, followed by the addition of the partially purified E. coli enzyme. The coupling reaction was carried out at 4°C for 24 hours. At the end of the reaction the cotton fabric with immobilized enzyme was washed twice with ten volumes of PIPES buffer at 4°C to remove uncoupled proteins. The immobilized enzyme was stored at 4°C in PIPES buffer (pH 7.2, 0.05 M). The activity of the immobilized enzyme preparation was determined in the same buffer with 1 mM $MnCl_2$ and 3 mM DFP.

RESULTS AND DISCUSSION

FIGURE 1 shows the enzyme activity of the E. coli enzyme with respect to temperature, when bis para nitrophenyl phosphate (bis pNPP) was used as the substrate. The activity of the enzyme increased with an increase in incubation temperature up to 45°C, above which the enzyme was deactivated rapidly. The second plot in the figure gives the rate of the reaction after three minutes into the reaction. The three minute plot indicates that the rate of the reaction dropped to about 75% of the initial reaction at 45°C. The pH optimum of the E. coli enzyme is given in FIGURE 2 with bis pNPP as the substrate. It appears from the figure that the pH optimum for the activity of the enzyme is fairly broad between 6.5 and 8.5.

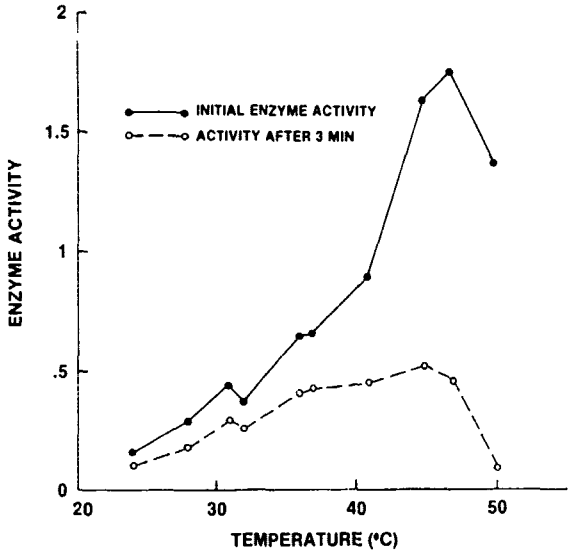

FIGURE 1. TEMP. PROFILE OF *E. COLI* ENZYME

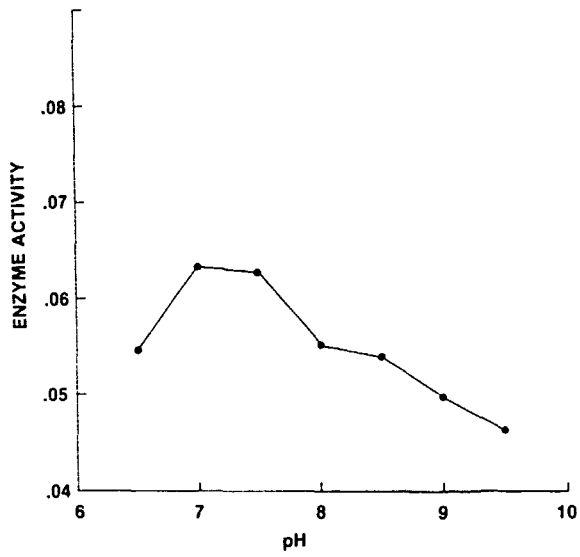

FIGURE 2. pH OPTIMUM OF *E. COLI* ENZYME ACTIVITY

FIGURE 3 shows the protein and enzyme activity profile of the E. coli cell-free preparation when passed through a Sephadex G-100 column. Two major protein peaks were observed by measuring the optical density of the fractions at 280 nm. The enzyme activity of the fractions was determined with two substrates - Soman and bis para nitrophenol - and these values are shown in the figure. Activity of the enzyme against both substrates was limited to the same fractions from the column and these two enzyme activity peaks were at the tail end of the first major protein peak. Earlier calibration of the column had indicated that this elution volume corresponds to a molecular weight greater than 68,000.

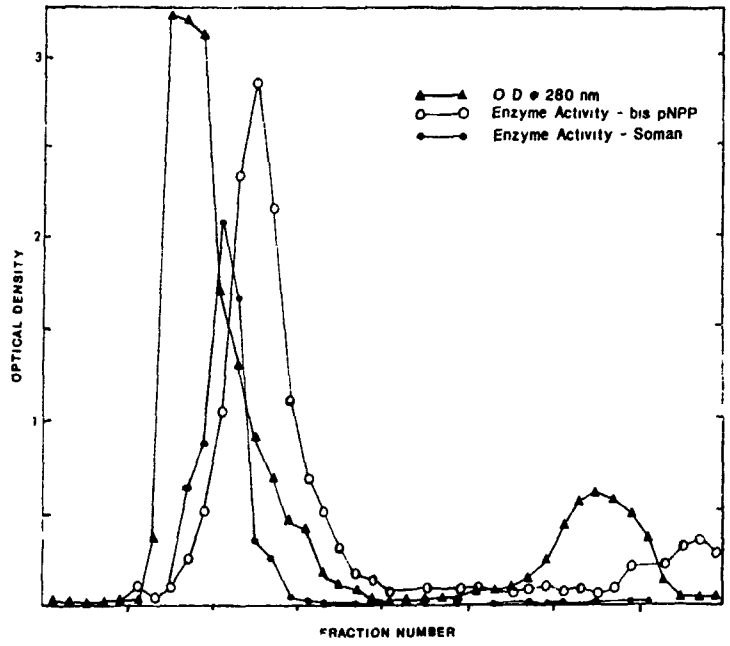

FIGURE 3. PURIFICATION OF E. coli ENZYME BY SEPHADEX G-100

A number of substrates were evaluated for enzyme activity with the partially purified E. coli enzyme and the results are given in TABLE 1. The table clearly indicates that the enzyme was active against Soman and a number of chemical agent surrogates, including a number of insecticides.

TABLE 1

Substrate Specificity of the E. coli Enzyme

SUBSTRATE	ACTIVITY (u moles/ min./g protein)
Soman	415.00
Dimebu	33.00
p-Nitrophenylmethyl(phenyl) phosphinate	152.10
p-Nitrophenylethyl(phenyl) phosphinate	100.40
p-Nitrophenylisopropyl(phenyl) phosphinate	0.17
bis p-Nitrophenyl phosphate	212.30
p-Nitrophenylmethyl phosphonate	51.96
Paraoxon	33.48
Parathion	45.63

TABLE 2 gives the distribution of enzyme activity (both hydrolysis and detoxification of Soman) in different Sephadex G-100 fractions of E. coli cell-free extract.[7] The table clearly indicates that the enzyme activity (both hydrolysis and detoxification) was retained in fractions 41 to 67 after Sephadex G-100 separation. However, the detoxification activity of the E. coli enzyme was destroyed by cold ethanol precipitation of the enzyme.[2,3]

TABLE 2

Hydrolysis and Detoxification of Soman by Sephadex G-100 Fractions from E. coli Cell-free Extract

SAMPLES	HYDROLYSIS (u moles/min./mL) No Mn^{++}	HYDROLYSIS (u moles/min./mL) Mn^{++}	HYDROLYSIS (%)	DETOXIFICATION (%)
Cell-free extract	3.06	3.8	42	30
Fractions 34-39	0.02	0.02	—	—
Fractions 41-53	0.96	1.13	39	29
Fractions 54-67	0.96	1.32	43	30
Cold ethanol precipitate			54	0

Data adopted from reference 7.

FIGURE 4 shows the rate of fluoride formation by the hydrolysis of DFP catalyzed by E. coli enzyme immobilized onto cotton. Cotton fabric with immobilized enzyme was added to the reaction mixture after 20 minutes incubation of the substrate in the buffer at room temperature, and the

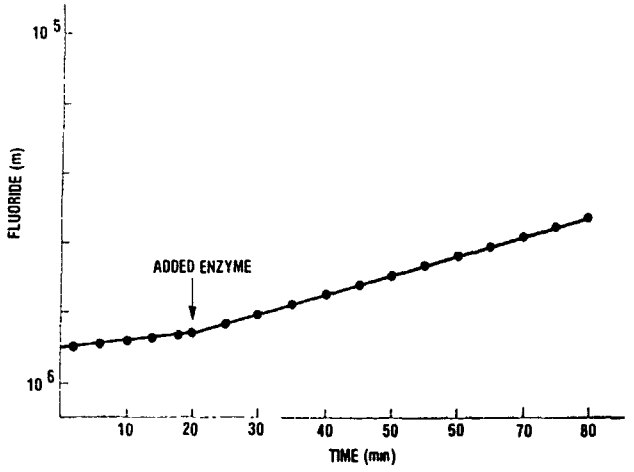

FIGURE 4. HYDROLYSIS OF DFP BY THE IMMOBILIZED ENZYME

reaction was continued another 50 minutes. The rate of hydrolysis of DFP in the presence of the immobilized enzyme was four fold faster than that observed in the buffer without the enzyme. Earlier studies with this enzyme have shown that Soman was hydrolyzed 7 to 15 fold faster than DFP, indicating that Soman could be detoxified rapidly by this immobilized enzyme preparation.[6]

ACKNOWLEDGMENT

We express our appreciation to Dr. Bendict J. Gallo, Biotechnology Br., US Army Natick RDE Center, for the supply of bacteria and to Dr. K. S. Rajan, Chemistry Div., IIT Research Institute, Chicago, IL for the agent testing that was conducted under Contracts DAAK-87-Q-0137 and DAAK60-89-A-0108.

REFERENCES

1. Attaway, H., Nelson, J. O., Baya, A. M., Voll, M. A., White, W. E., Grimes, D. J. and Colwell, R. R., "Bacterial Detoxification of Diisopropyl fluorophosphates," Appl. and Environ. Microbiol., 53: 1685-1689 (1987).

2. Hoskins, F. C. G., Chettur, G., Gallo, B. J., Robbins, F. M., and Walker, J. M., "Hydrolysis and Detoxification of Soman and Dimebu by Microbial and Squid DFP-ase," Proceedings of the 1986 U. S. Army Chemical Research Development and Engineering Center Scientific Conference on Chemical Defense, pp 283-288 (1987).

3. Chettur, G., Defrank, J. J., Gallo, B. J., Hoskin, F. C. G., Mainer, S., Robbins, F. M., Steinmann, K. E. and Walker, J. E., "Soman Hydrolyzing and Detoxifying Properties of an Enzyme from a Thermophilic Bacterium," Fund. Appl. Toxicol., 11: 373-380 (1988).

4. Landis, W. G., Anderson, R. S., Chester, N. A., Haley, M. V. and Johnson, D. W., "The Organophosphate Acid Anhydrase Systems of the Clam, Rangia cuneata," Proceeding of the 1987 CRDEC Conference on Chemical Defense, 1: 139-144 (1988), CRDEC-SP-88013.

5. Chemnitius, J.-M., Losch, H., Losch, K. and Zech, R., "Organophosphate Detoxicating Hydrolases in Different Vertebrate Species," Comp. Biochem. Physiol., 76C: 85-93 (1983).

6. Akkara, J. A., Kaplan, D. L. and Kaplan, A. M., "Enzyme Formulation for Laundering and Decontaminating Chemically Contaminated Clothing," Technical Report, Natick/TR-88/014 L, US Army Natick Research, Development, and Engineering Center, Natick, MA 1988 (AD B119 209L).

7. Walker, J. E. Unpublished Contract Report "Characterization of Enzymatic and Nonenzymatic Organophosphate Hydrolyzing Catalysts," IIT Research Institute, Chicago, IL July 10, 1987. Contract # DAAK-87-Q-0137, Purchase Request Number 14-13786-87H, Call #1, US Army Natick Research, Development, and Engineering Center, Natick, MA (1987).

GROWTH OF COMMERCIAL NORMAL HUMAN ABDOMINAL KERATINOCYTES

Sidney Yaverbaum, John P. Petrali, Bryce F. Doxzon,
Susan B. Oglesby and Dana L. Kolb
Pathophysiology Division, USAMRICD, APG, MARYLAND 21010-5425

ABSTRACT

The purpose of this study was to determine the suitability of commercially available human keratinocytes for the initiation of in vitro human epidermal organotypic models for vesicant research. Commercial keratinocytes can be used for short-term toxicologic-type assays in first and second passages with impunity, and with increasingly reduced reliability in the third and fourth passages. The data show that skin organotypic model research is better initiated and performed with primary cultures. Studies undertaken with commercial keratinocytes over an extended period of time should be conducted with the same keratinocyte cell preparation to insure reliable results.

INTRODUCTION

This study of in vitro grown second culture commercial human keratinocytes was conducted to assess their utility for developing organotypic skin models for vesicant research. It has been shown that such in vitro models (e.g., reconstructed human epidermis (RHE) and lining skin equivalents (LSE)) require normal basal keratinocytes that can proliferate long-term without loss of either viability for morphological integrity (1). Several commercial keratinocyte cultures were received for cytotoxic assays. Some cultures had many vacuolated cells regardless of site of epidermal origin, and did not appear normal by transmission electron microscope (TEM) analysis. Data from this study will be used to determine the utility of commercial keratinocytes to initiate and sustain in vitro human skin organotypic model systems.

MATERIALS AND METHODS

Keratinocyte culture. Duplicate EpiPack Kit keratinocytes (Clonetics Corporation, NHEK 46, Lot # 00762 Abdominal Keratinocytes, 1989) were handled and treated upon receipt as specified in the accompanying instruction insert with few modifications. Sterile conditions were used for all procedures. Following initial manipulation (supra), keratinocyte growth medium (KGM) was changed three times a week. Keratinocyte cultures were observed for morphological and ultrastructural changes at 24 to 72-hour intervals under standard conditions of serum free growth medium and incubation. The appearance of unusual changes in the cells were recorded and photographically

documented. Notice was taken of cultures which displayed unusual ultrastructural and pleomorphic characteristics. Subcultures were performed when cell surface growth became 50-80% confluent. Before initiating subculturing procedures, phase contrast inverted microscope (PCIM) photomicrographs were taken of each culture flask (25 cm^2/flask) of each representative pair/set of a passaged cell line was processed and analyzed by TEM.

Subculture. The commercial abdominal keratinocyte culture was subcultured (serially cultured) up to an additional six passages following receipt. Select early subconfluent serially cultured flasks were "recultured" immediately following routine subculture procedures (i.e., KGM was added to cells remaining in the subcultured flask, and the flask reincubated) to determine if any significant differences in growth parameters would occur in the recultured cell lines.

Total cell and viable cell counts were performed for the cell suspensions on a Neubauer Bright-line hemocytometer under a coverslip (2). New culture flasks were inoculated and observed microscopically every 24 hours for evidence of proliferation, and the medium changed every 2 or 3 days. When the growth in identically seeded flasks became 50-80% confluent, one was selected for subculturing, and the other for TEM processing and analysis.

Electron microscopy. Scrape-harvested cells from subconfluent culture flasks were treated by routine procedures used to prepare isolated cell samples for TEM observations (3).

Definitions. Serial cultures were consecutively passaged (subcultured) with a known viable cell count inoculum. A reculture cell line was initiated when a routinely subcultured flask, still containing an unknown number of viable cells, was incubated with fresh media and subsequently cultured and subcultured routinely.

Total and viable cell counts. Cells were stained with nigrosin dye, and total cell and viability counts were performed by procedures described previously (2). Total cell counts, viable cell count, percent viability, population doublings (PD), and population doublings/day (PD/D) were quantitated.

Estimation vs. quantitation of culture confluency. To gauge the accuracy of recorded subjective estimates, two types of quantitative analyses were performed on enlarged positive photographic prints of representative culture flask growth confluency fields. The first method was an image analysis system program (Quantimet 970, Cambridge Instruments, Cambridge, MA). The second was a photographic weight ratio analysis to determine percent confluency.

RESULTS

Morphological observations. Phase contrast microscopy. First passage cell population contained a mixture of columnar, spindle, and cubiodal shapes associated with normal epithelial keratinocytes. Ovate and columnar forms containing large nuclei (n) were predominant early in the first and second passages, as were pleomorphic forms. Cells initially attached and grew alone or in loosely associated clusters. Many of the keratinocytes had ruffled membranes consistent with migratory activity at this stage of culture growth (4). In 2-3 days, patches of nonconfluent cluster colonies grew having polygonal forms as the culture density increased, with many cells having paranuclear vacuoles (pnv) and cell inclusions (ci) (Fig.1). Second and third passage serially cultured cells had similar patterns. Fourth passage cell lines contained increased numbers of paranuclear vacuoles, and showed

morphological changes from, and loosening of, the tight polygonal growth pattern (Fig 2). Double nucleated (dn) and giant cells (gc) were present. Terminal differentiation occurred in the sixth passage.

FIGURE 1.

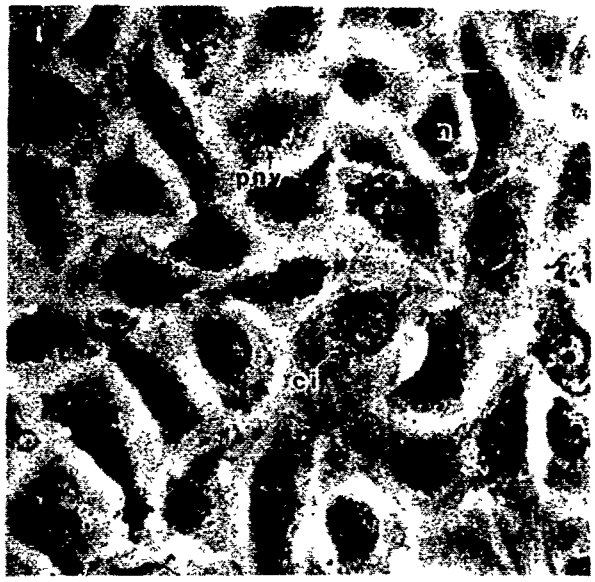

First passage. Magnified 1, 147x

FIGURE 2.

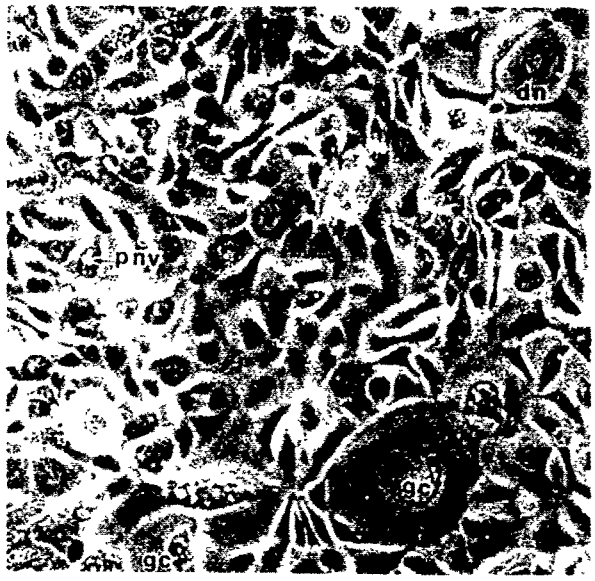

Fourth passage. Magnified 358x.

FIGURE 3.

Second passage. Magnified 8, 400x.

FIGURE 4.

Third passage. Magnified 5, 600x.

APPENDIX C

Paranuclear vacuoles were present during the lifespans of the cell lines. Nuclei with 1-3 paranuclear vacuoles were prominent in early and late passages. Cell size decreased slightly as the serial cultured cell lines approached senescence (fourth passage) but became large flat cells in passage 6, the terminal differentiation phase.

Ultrastructural observations. Transmission electron microscopy. TEM photomicrographs taken at each passage showed abdominal keratinocyte populations to be predominantly normal domed cells during the early passages. First and second passage keratinocytes had a rounded dense nucleus (n), distinct nucleoli (nc), intact, rounded nuclear membrane (nm) components, large prominent microvilli (mv), endocytotic vacuoles (ev), an abundance of mitochondria (m), rough endoplasmic reticula (rer), and a ring of perinuclear tonofilaments (t) (Fig. 3). No evidence was seen of junction attachment sites or desmosomal buildup at the cell membrane. Increased numbers of endocytotic vacuoles, an uneven nuclear membrane, and the appearance of lipid droplets (l) and lysosomes (ly) occurred in the third passage (Fig. 4). Stampfer et al. (5) and J. P. Petrali regard increased cytoplasmic vacuolization as the initiation of senescence. More concrete evidence of senescence was seen in the fourth passage which showed the onset of nuclear membrane indentation, rarified cytoplasm, smaller microvilli, and increasing numbers of lysosomes and lipid droplets. Terminal differentiation occurred in the sixth passage.

Cell viability and growth. Serial culture cell lines were highly viable in the first and second passages, but generally dropped below 90% viability thereafter (Fig. 5). Passage 6 was an outlier because a total of only 12 cells were countable. Reculture cell line viability never averaged over 87% (Fig. 6; passages 2-5). Population doublings of serial and reculture cell lines decreased from the third and fourth passages, respectively.

FIGURE 5.

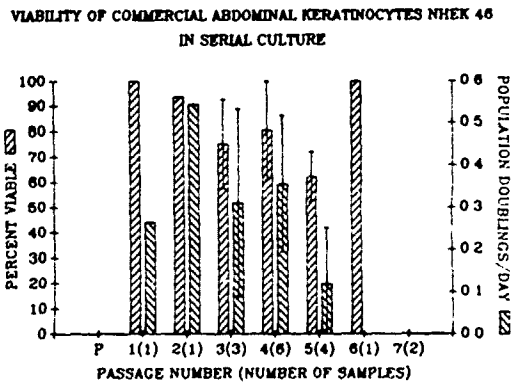

FIGURE 6.

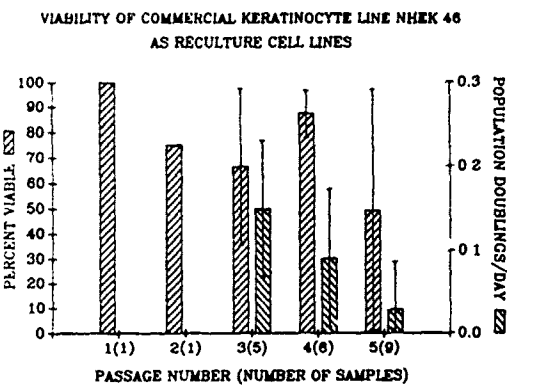

Culture confluency estimates. There were no significant differences for the seven samples at 95% C.I. between the quantitative and subjective methods estimates. The sample confluences ranged from 50-95%.

Relative sizes of abdominal keratinocytes in culture. Abdominal keratinocytes in serial cultured cell lines maintained an average relative size of 0.76 (passages 2-5) with respect to the culture initially received (passage 1). There was a tendency toward successively smaller sizes in these passages until the sixth and seventh passages when the sizes increased

perceptively. Recultured cell lines showed a markedly increased cell size with each succeeding passage. The average relative reculture keratinocyte size doubled over the previous cell size in passages four and five. These data agree with investigators who consider enlarging cells as the initial differentiation of senescence signal, or as the first stage of terminal differentiation (6). The recultured cells were two to seven times larger than the serial cells, especially in passages four and five.

DISCUSSION

As a result of this study, we found commercial abdominal keratinocyte cultures to be normal, proliferating cell lines through their second passage. Reduced viability and cellular ultrastructural changes signalling the onset of differentiation, senescence and ultimately terminal differentiation started in the third passage and ended in the sixth passage.

Human neonatal foreskin tissue cells produce 0.90 population doublings/day (PD/D) in the second passage and about 40 PDs/lifespan. The highest proliferation rate obtained with abdominal keratinocytes was 0.54 PD/D in the second passage (Fig. 5) with a total of 16-17 PDs from passages one to five, and 28-29 when including the estimated primary passage data. One possible reason for the difference is that the commercial abdominal cells were obtained by elective surgery from adult donors. It has been reported that skin site origin and ages of donors may have a bearing on cell response during cultivation (6).

Fusenig (6) reported that relative cell size of human neonatal foreskin increased with each succeeding passage as was seen in our reculture cell lines, but not in our serial cell line cultures. Cell enlargement is identified as one potential signal for differentiation. senescence, and terminal differentiation (6). It was reported that the proliferation potential of keratinocytes was inversely correlated with their size (6). Using this criterion with respect to our data (Figs. 5, 6), there was little or no change in the cell size or growth activity of serial cultures from passages 2-5, whereas all the reculture cell lines were increasingly larger on average and less active in this study.

The presence of abdominal epithelial keratinocytes were confirmed in this study by their morphology in light and electron microscopes. Their viability was confirmed by a dye exclusion procedure that can detect dying as well as dead cells. The only stress placed on the exponentially growing cells prior to the dye procedure was trypsinization. Trypsin adversely affects dead and dying cells, often digesting the former and damaging the latter.

The decline of cell growth and viability from the third passage on, and the initiation of differentiation and possible senescence at that time were of considerable importance and interest. Stampfer *et al.* (5) described a procedure in which a primary culture of human mammary keratinocytes was partially trypsinized and secondary cultures established periodically. They showed that the secondary cultures grew 3-7 times more actively than tertiary serial cultures. Since Stampfer *et al.* (5) were able to retrypsinize the primary culture persistently, it suggested the possibility that stem cells were present in the primary culture and perhaps in first passage cultures. Our reculture experiments did not emulate their results. Our results show that once stem cells are removed from the primary culture, diluted and subcultured, they become inactive, thus permitting senescence to occur (8).

CONCLUSION

Commercial abdominal cultures attain a useful zenith through their second passage, after which viability, growth, and cell integrity decrease rapidly, and senescence followed by terminal differentiation starts in the third or early fourth passage. Results of this study indicate that keratinocytes are useful for short-term experiments in the first and second passages, but have increasingly reduced reliability in the third and subsequent passages. Commercial keratinocytes were shown to have expended about 40% of their population doubling by the end of the first passage. Together with the second passage, these represent the prime of the cell culture lifespan. It is suggested that long-term skin organotypic model research be initiated and performed with primary cultures. Studies undertaken with commercial keratinocytes over an extended period of time should be conducted with the same keratinocyte preparation to insure reliable results.

ACKNOWLEDGEMENT

We would like to acknowledge the technical expertise of Tracey Justus and John Graham.

REFERENCES

1. Chamson, A., Germain, N., Claudy, A., Perier, C. and Frey, J.: Study of basement membrane formation in dermal-epidermal recombinants in vitro. Arch. Dermatol. Res. 281:267-272, 1989.

2. Kaltenbach, J. P., Kaltenbach, M. H. and Lyons, W. B.: Nigrosin as a dye for differentiating live and dead ascites cells. Exp. Cell Res. 15:112-117, 1958.

3. Petrali, J. P., Oglesby, S. B. and Meier, H. L.: Ultrastructural correlates of the protection afforded by niacinamide against sulfur mustard-induced cytotoxicity of human lymphocytes in vitro. TR-88-16, U.S. Army Medical Research Institute of Chemical Defense, Aberdeen Proving Ground MD., Dec. 1988. AD #A203118.

4. Magee, A. I., Lytton, N. A. and Watt, F. M.: Calcium-induced changes in cytoskeleton and motility of cultured human keratinocytes. Exp. Cell Res. 172:43-53, 1987.

5. Stampfer, M., Hallowes, R. C. and Hackett, A. J.: Growth of normal human mammary cells in culture. In Vitro 16:415-425, 1980.

6. Fusenig, N. E.: Mammalian epidermal cells in culture. In: Biology of the integument. Vol 2., Bereiter-Hahn, J., Matoltsy, A. G. and Richards, K. S., eds., Springer-Verlag, Berlin, Germany. 409-442, 1986.

7. Barrandon, Y. and Green, H.: Cell size as a determinant of the cloneforming ability of human keratinocytes. Proc, Nat. Acad. Sci. 82:5390-5394, 1985.

8. Watt, F. W.: Epidermal stem cells in culture. J. Cell Sci. Suppl. 10:85-94, 1988.

INDUCTION OF ENHANCED STRAINS OF A THERMOPHILE THAT SYNTHESIZE AN OPA ANHYDRASE EFFECTIVE IN DETOXIFYING SOMAN

Benedict J. Gallo, Paula M. Scotland and David A. Gowenlock

U.S. Army Research, Development and Engineering Center, Natick, MA 01760

A strain of Bacillus stearothermophilus JD100 previously reported to synthesize intracellular Soman-detoxifying enzyme was genetically altered in order to increase the synthesis of this enzyme. The approach involves traditional genetic methods of improving enzyme titers. The multistep process includes mutagenesis of parental strain I5D with UV light and subsequent screening of the surviving population for enhanced activity against p-nitrophenyl ethyl(phenyl)phosphinate. Several putative mutants have been isolated with enhanced synthesis of this OPA anhydrase.

Introduction

The bacterial thermophile JD100, a soil microbe, was identified as a strain of Bacillus stearothermophilus and has been reported to synthesize a unique endogenous organophosphorus acid anhydrase (OPA anhydrase), which cannot hydrolyze diisopropylfluorophosphate (DFP) but is very active in detoxifying soman.[1] The use of this and other similar OPA anhydrases in detoxifying organophosphorus nerve agents and pesticides has been suggested by a number of authors[2]. In order to make enzyme from this strain of B. stearothermophilus more available for research and development, we conducted a program to produce hyperproducing mutants. This paper describes the methodology and results from our studies.

Experimental methods

Organisms - Bacillus stearothermophilus JD100, JD200 and JD300 were obtained from Dr. J. DeFrank, CRDEC. They were maintained on LB (Lennox) agar slants at 55°C for 24-36 hours before storage at refrigerator temperatures. The streptomycin resistant (strE) strains of Bacillus stearothermophilus reported in this paper were maintained on the above medium but with the addition of 250 ug to 500 ug of streptomycin per mL medium.

Mutation and Mutant Screening - Log phase cells of Bacillus

stearothermophilus grown at 45°C were mutagenized with UV light at room temperatures at a kill rate in excess of 99.99%. Immediately after irradiation survivors were protected from light, cooled and stored at 4°C for 18 to 36 hours prior to use. The mutagenized cells were spread on agar plates to a average colony density of 100 per plate and incubated to maturity at 55°C. The screening protocol is described in the text.

Submerged Culture - The medium used for the growth of submerged cultures for enzyme synthesis was either that of Cook or Lennox basic broth with 0 - 0.5% dextrose and 125 ug streptomycin (minimum)/mL medium when required.[3,4] The growth vessels included 2 mL microfuge tubes, standard glass culture tubes, 300 mL culture flasks, 2800 mL Fernbach flasks and 14 liter stirred tank reactor (fermentor) with working volumes of 1.25 mL, 7 mL, 50 mL, 500 mL, and 10 liter, respectively.

Harvest and Pre-assay Processing - Ten liter cultures were harvested by cartridge flow filtration and centrifugation. For cultures of less volume, centrifugation at 12,000 rpm was used. The cell suspensions were washed free of medium by 1-3 centrifugations using normal saline without Mn++ or bis-tris propane - KCl - NaCl buffer, pH 7.15, with Mn++ (standard buffer).[6] Final pellets were resuspended in the standard buffer and immediately frozen to -30°C. Cells for dry weight measurements were most commonly made from nonwashed centrifugation pellets after drying at 80°C for 24 or more hours.

Enzyme Activity Estimations - OPA anhydrase activity estimations were made of washed whole cells ruptured by either 1 or 6 cycles of freezing and thawing in standard buffer.[6] The assay reaction mixture consisted of 5 uL of ruptured cell suspension and 47 uL of standard buffer made 0.2 mM with respect to 4-nitrophenyl methyl(phenyl)phosphinate (MPP).[6] OPA anhydrase hydrolysis of MPP was found to correlate directly with hydrolysis and detoxification of soman (unpublished data). The assay temperature was set at or about 28°C and optical density read at 400 or 405 nm. The extinction coefficient of p-nitrophenol used in computing activity was at pH 7.15, 11.85 X 10^3.[7] Activity is expressed as uM of substrate hydrolyzed/min·mg dry weight^{-1} or mL^{-1} culture at 28°C. Spectrophotometric readings were made either with LKB Ultrospec spectrophotometer or a Molecular Devices Thermomax microplate reader and the reaction mixture volumes used with each instrument were 2600 uL/tube and 260 uL/well, respectively.

Results

In 1984 three thermophilic strains (JD100, JD200 and JD300) were isolated at U. S. Army Chemical Research, Development and Engineering Center, whose whole cells had low hydrolytic activity against DFP (personal communication J. De Frank, CRDEC). Upon further investigation the isolates were found to be different strains of Bacillus stearothermophilus. Table 1 shows the major species-determining traits, and dissimilar strain-differentiating traits. The strains remain as originally designated JD100, JD200 and JD300. Fifty-two different traits were determined for these three different strains of B. stearothermophilus.

Strain JD100 was then mutagenized for the purpose of inducing two antibiotic markers on the chromosomal genome, resistance to streptomycin and resistance to ampicillin. Antibiotic markers are useful in growth and genetic studies as an aid in maintaining strain purity and for use as a parental stock for mutation studies. In addition it was determined earlier that the development of resistance to streptomycin in B. stearothermophilus

Table 1. Diagnostic Taxonomic Traits of Bacillus stearothermophilus strains JD100, JD200 and JD300

TAXONOMIC TRAIT	JD100	JD200	JD300
Respiration			
Obligate Aerobic	+	+	+
Endospore formation	+	+	+
Gram Strain	+	+	+
Rod Morphology	+	+	+
Growth Limits, ° C			
Maximum Temperature	<73	<75	<75
Minimum Temperature	40	40	35
Indole Production	+	-	-
D Xylose Oxidation	+	-	-
Nitrate Reductase	-	-	+
Growth with 5% NaCl	-	-	+
Gas Production			
Arabinose	-	+	+
L Xylose	-	-	+
Lactose	-	+	+
β-galactosidase	-	+	-

resulted in curing the bacterium of plasmids.* In this study several streptomycin-resistant strains of JD100 were induced by UV mutagenesis. However one strain, I5D, arose spontaneously and was chosen as the strain for further use because of the lack of any UV treatment. Mutants with resistance to ampicillin could not be obtained via UV irradiation. Figure 1 shows the geneology of strE I5D and subsequently derived hyperproducing OPA anhydrase strE mutants.

The mutagenized spores were spread on agar medium plates with streptomycin at a target concentration of 100 colonies per plate and incubated at 55°C for 24 to 36 hours or whenever the plate seemed ready for accurate replica plating. The protocol for primary plate screening for enhanced OPA anhydrase strains is shown and described in Figure 2. Approximately 14,000 colonies were screened in this manner. Initially replicate filter lifts were individually tested with the 4-nitrophenyl methyl(phenyl)phosphinate, 4-nitrophenyl ethyl(phenyl)phosphinate and

FIGURE 1. GENEOLOGY OF THE ENHANCED OPA ANHYDRASE MUTANTS OF BACILLUS STEAROTHERMOPHILUS

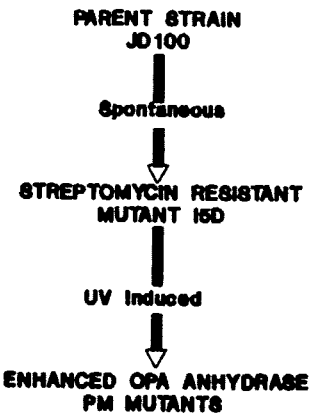

4-nitrophenyl isopropyl(phenyl)phosphinate. Use of 4-nitrophenyl methyl(phenyl)phosphinate was discontinued in the plate screening because of the very rapid hydrolysis (color development time) rate at room temperature, which would make hyperproducers and non hyperproducers indistinguishable. The bioassay overlays of 4-nitrophenyl isopropyl(phenyl)phosphinate had to be incubated at 37°C to 45°C in order to be developed but the development was poor in most cases. The

FIGURE 2

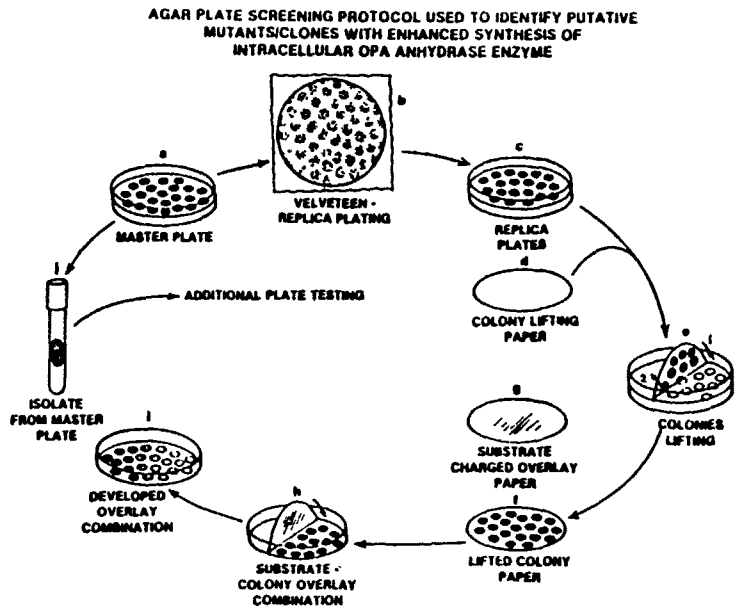

Explanation of Figure 2. a) About 100 viable, mutated bacteria are spread on a master plate and incubated until mature; b) 2 - 5 agar medium plates are inoculated with surface colonies from the master plate using short nap velveteen; and master plate is reincubated until colonies imaged and then stored at refrigerator temperatures; c) the replica plates are incubated for growth; d) heat-sterilized filter paper disks are cut to loosely fit into the lower plate; e) when mature, the colonies on the agar surface of the replicate are overlaid (1) with the prepared lift paper to which we apply gentle pressure to insure good contact between paper and colonies; after the disk is wetted from plate moisture it is carefully removed by lifting (2) and f) placed in a sterile petri plate and rapidly frozen to at least -20°C; g) sized paper disks are charged with substrate by solution impregnation and allowed to dry; h) the frozen test colony disk is placed in a petri plate, colonies face up, and moistened with a fine mist of buffer until saturated and then overlaid with a substrate-impregnated disk, moistened again and the disk-sandwiched colonies incubated for catalysis and color development at room temperature; i) during incubation the plates are observed periodically and noted for color development; j) bacterial isolates of promising reactions are transferred from the corresponding colonies on the master plate to agar slant and/or another master plate and incubated for growth and continued testing.

4-nitrophenyl ester of ethyl(phenyl)phosphinate was most suitable for the plate screening and its overlays generally developed within a few minutes. The substrate enzyme hydrolysis/color development controls were replicate bacteria-charged disk lifts of the experimental ones, which were denatured by heat sterilization temperatures. The selection process was strictly qualitative in nature and color development was compared within and among the combination development overlays. Three main phenotypes were selected for further testing: those that developed a strong yellow color rapidly, those that showed strong color development after a period of time, and those which showed no color development. Initially colonies that exhibited good agreement in color development on the different esters of the phosphinates were selected for further testing but this was not a prerequisite to selection for additional screening.

The primary plate screening was followed by the secondary plate screening, which involved the same plate bioassay except that eight putative mutants were grown on a plate with I5D control. Using the same qualitative process we selected 75 putative hyperproducing OPA anhydrase mutants for submerged culture testing for OPA anhydrase synthesis. The primary plate screening was discontinued after these putative mutants were obtained. A few strains found to lack activity were spurious and no negative strains were found.

The putative mutants were then tested for enhanced synthesis by growth in shaken culture in tubes containing 7 mL of medium at 55°C. After 18 to 24 hours and 44 to 48 hours the cultures were harvested for enzyme synthesis and for dry weights measurements. The amount of OPA anhydrase synthesized was computed against the dry weight of the sample. Twelve strains which showed a 25% or higher enzyme synthesis than I5D were again tested in culture tubes but samples were measured after 7 and 48 hours. In the final testing in submerged culture 8 enhanced mutants were tested for synthesis after 12, 18 and 36 hours. Figure 3 shows the putative mutants with enhanced synthesis 50% or higher than that of the control strains (JD100 and I5D). The other 4 mutants included in this testing showed enhanced activities greater than 25% but less than 50% over the controls (data not shown).

The production of OPA anhydrase synthesis by the parental strain I5D was scaled up to 10 liters by growing it in a stirred tank reactor and under constant temperature of 55°C and the pH was controlled at 6.8 with 1N KOH. Figure 4 shows the growth kinetics and OPA anhydrase synthesis during this fermentation. The fermentation was stopped upon the rise in pH to 7. The OPA anhydrase synthesis per gram dry weight follows the same pattern as that based on turbidity in Klett Units, an increase in OPA anhydrase synthesis with an increase in dry weight. The fermentation had an approximate OPA anhydrase productivity of 0.45 units per liter per hour. This fermentation and the post-harvest measurement of activity were not optimized and represent preliminary yields and productivities.

CONCLUSIONS AND DISCUSSION

This study describes an effective but qualitative protocol for screening for mutants/strains with enhanced synthesis of intracellular OPA anhydrase. Its use is not restricted to strains of the genus Bacillus and has been used with other bacteria including strains of Escherichia and Flavobacterium. The protocol should be applicable to other intracellular

FIGURE 3

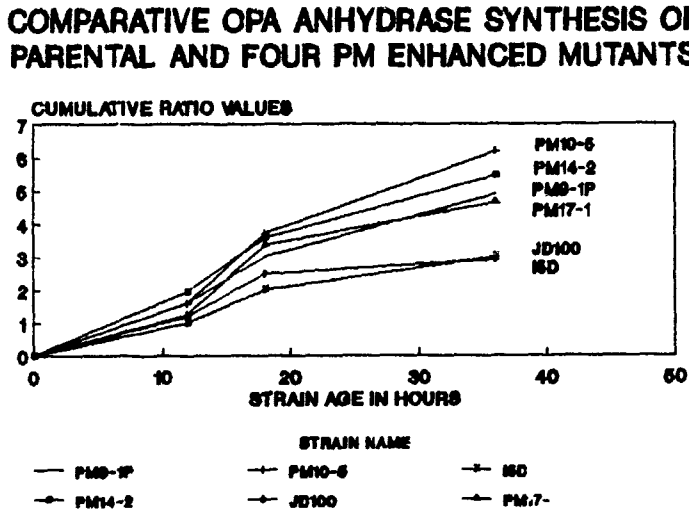

Explanation of Figure 3.
Graph showing the respective cumulative ratio values of 6 strains of B. stearothermophilus where each point represents the ratio of OPA anhydrase activity of tested strain :: opa anhydrase activity of I5D in OD of nitrophenol formed / min for cultures harvested after shaken incubation at 55°C. Each point represents the average duplicate assay value of cultures grown in triplicate. Parent strain B. stearothermophilus JD100 is also included for comparative purposes. The cumulative ratio values assigned to the control I5D are 1, 2 and 3, corresponding to 12, 18 and 36 hour cultures, respectively. The four other putative enhanced mutants are not shown but they all have a ratio at 36 hours that lies below that of PM17-1 and a value 25% greater than that of the standard strain I5D.

---

enzymes/proteins synthesized in cells whose activity or presence can be detected through some color-forming product, for example, intracellular protein. This simple protocol should also be usable with any colony-forming bacteria possessing moist, sticky surface that will adhere to filter paper. The process easily lends itself for use in robotization and computerization for large-scale screening for endogenous enzymes. The protocol also allows the testing of bacterial strains with different growth and substrate requirements on the same paper through the use of replica plating and multiple plate colony lifting.

Several forms of evidence indicate that the gene for this OPA anhydrase in B. stearothermophilus I5D has a chromosomal locus and not an extrachromosomal one. Preliminary but not exhaustive plasmid screening of its parental strain JD100 did not provide positive results for the presence of plasmids (unpublished results). Other evidence comes from the unsuccessful attempts to induce ampicillin resistance in this thermophile although spontaneous and UV-induced streptomycin resistance is obtained with relative ease. Streptomycin resistance in Bacillus can have a chromosomal origin.* It has been reported that induced streptomycin resistance in B. stearothermophilus clears the species of plasmids. The

FIGURE 4

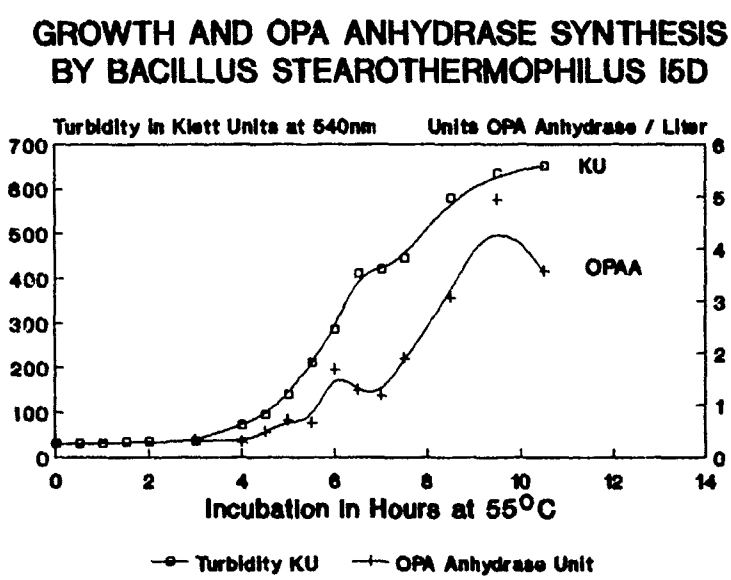

Explanation of Figure 4 - This figure describes the growth of B. stearothermophilus in a 10 Liter fermentation and accompanying OPA anhydrase synthesis. Each liter of LB broth was supplemented with 5 g glucose and 250 mg of streptomycin. A 10% inoculum with an age of 12 hours was used to seed the fermentation. The pH was not allowed to drop lower than pH 6.8 by 1N KOH titration. The culture was sparged with air at 5 L/min, agitated at 250 rpm and had a head pressure of 5 psi. Growth temperatures were controlled at 55°C. Washed, once frozen-thawed cells were used in estimating enzyme activity expressed as uM of methyl-O-nitrophenyl(phenyl)phosphinate hydrolyzed/min·L culture^{-1}

gene for a similar OPA anhydrase from unidentified bacterial halophilic strains was also reported to be chromosomal because of the failure to find any plasmids.[10]

Although this OPA anhydrase is unique in its properties, other similar OPA anhydrases are quite common among living things but their function and exact location in the cell remain unverified. No OPA anhydrase negative mutants were found, a fact that suggests that this OPA anhydrase plays an essential role in B. stearothermophilus. Its synthesis in B. stearothermophilus is associated with rapidly growing cultures (see Figure 4) and suggests a role in DNA replication or in protein synthesis. What further complicates the picture is that I5D is a spore former, and no attempt has yet been made to associate enzyme synthesis with sporulation.

Since the number of submerged culture samples that required testing was so large, the bacterial cells were ruptured by simple freezing to -30°C and thawing instead of using sound irradiation. The number of freeze and thaw cycles used in each study was either 6 or 1. Some studies show a decay of activity with repeated cycles of freezing and thawing. Even after mutant development, enzyme synthesis optimization and sound irradiation cell rupture pretreatment, the amount of OPA anhydrase synthesis is small as compared to other enzyme yields from other industrial microbes[11]. In

order to continue to reduce the cost of producing this unique and militarily important enzyme it must be available in larger amounts and be made more easily recoverable than at present. To accomplish this goal the gene from strain I5D is also being cloned and inserted into multicopy expression vectors for use in extracellular enzyme production.

REFERENCES

1. Chettur, G., J. J. DeFrank, B. J. Gallo, F. C. G. Hoskin, S. Mainer, F. M. Robbins, K. E. Steinmann, and J. E. Walker. "Soman Hydrolyzing and Detoxifying Properties of an Enzyme from a Thermophilic Bacterium". Fundam. Appl. Toxicol. Vol. 11, pp. 373-380, 1988.

2. Hoskin, F. C. G., G. Chettur, S. Mainer, K. E. Steinmann, J. J. DeFrank, B. J. Gallo, F. M. Robbins, and J. E. Walker. "Soman Hydrolysis and Detoxication Properties by a Thermophilic Bacterial Enzyme" in Enzymes Hydrolyzing Organophosphorus Compounds, Chapter 5, Ellis Horwood Publishing Ltd., Chichester, Eng., 1989.

3. Cook, A.M. and Brown, M. R. W. "The Relationship Between Heat Activation and Colony Formation for the Spores of Bacillus stearothermophilus". J. Pharm. Pharmacol. 16, 725-732, 1964.

4. Lennox, E. S., "Transduction of Linked Genetic Characters of the Host by Bacteriophage P1". Virology 1, 190, 1955.

5. Hoskin, F. C. G.,and Roush, A. H. "Hydrolysis of Nerve Gas by Squid Type Diisopropylphosphorofluoridate Hydrolyzing Enzyme on Agarose Resin. Science 215, 1255-1257, 1982.

6. Lieske, C. N., J. H. Clark, H. G. Meyer, M. A. Lawson, J. R. Lowe, P. Blumbergs, and M. A. Priest, "Inhibition of Two Acetylcholinesterases by the 4-Nitrophenyl Esters of Methyl-, Ethyl-, and Isopropyl(phenyl) phosphinic Acid. Pest. Biochem. Physiol. 17, 142-148, 1982.

7. Martin, C. C., J. Golubow, and A. E. Axelrod. "A Rapid and Sensitive Spectrophotometric Method for the Assay of Chymotrypsin". J. Biol. Chem. 234, 294-298, 1959.

8. Imanaka, T., M. Fujii, I. Amamori, I., and S. Aiba, "Transformation of Bacillus stearothermophilus with plasmid and characterization of shuttle vector plasmids Between Bacillus stearothermophilus and Bacillus subtilis". J. Bacteriol. 149, 824-830, 1982.

9. Staal, S. P. and J. A. Hoch, "Conditional Dihydrostreptomycin Resistance in Bacillus subtilis", J. Bacteriol., 110, 202-207, 1972.

10. Cheng, T. C., and J. J. DeFrank, "Screening for Plasmids in Halophiles". Technical Paper CRDEC-TR-094, 13 pp., US Army Chemical Research, Development and Engineering Center, Aberdeen Proving Ground, MD. 1989.

11. U.S. Patent No. 4,472,504, September 18, 1984. Benedict J. Gallo Inventor. "Cellulase-Producing Microorganism".

This paper reports research sponsored by US Army Natick Research, Development and Engineering Center and has been assigned TP-2834 in the series of papers approved for publication.

U.S. GOVERNMENT PRINTING OFFICE 1990 -281-507/A0001